AGARD CONFERENCE PROCEEDINGS No. 52

AGARD

ADVISORY GROUP FOR AEROSPACE RESEARCH & DEVELOPMENT

7 RUE ANCELLE 92 NEUILLY SUR SEINE FRANCE

Reactions between Gases and Solids

NORTH ATLANTIC TREATY ORGANIZATION

AGARD Conference Proceedings No.52

NORTH ATLANTIC TREATY ORGANIZATION

ADVISORY GROUP FOR AEROSPACE RESEARCH AND DEVELOPMENT

(ORGANISATION DU TRAITE DE L'ATLANTIQUE NORD)

REACTIONS BETWEEN GASES AND SOLIDS

Papers presented at the Propulsion and Energetics Panel 34th Meeting, 8th Colloquium held at the Aerospace Research Laboratories, Wright-Patterson Air Force Base, Dayton, Ohio USA, 13-17 October 1969.

The material in this publication has been produced directly from copy supplied by each author.

Published February 1970

541.124.012.4

Printed by Technical Editing and Reproduction Ltd
Harford House, 7-9 Charlotte St. London. W1P 1HD

AGARD PROPULSION AND ENERGETICS PANEL

PANEL CHAIRMAN Dr C.T.Hewson Rolls-Royce Ltd., UK

PANEL DEPUTY CHAIRMAN Professor J.Chauvin, Von Karman Institute, Rhode-St-Genese, Belgium.

PROGRAMME COMMITTEE FOR 34th MEETING (8th COLLOQUIUM)

Colonel P.G.Atkinson Jr USAF, Aerospace Research Laboratories, Wright-Patterson AFB, (CHAIRMAN) Dayton, Ohio, USA.

Dr D.I.Dawton, National Gas Turbine Establishment, Pyestock, Hants, UK.

Professor O.Lutz, Deutsche Forschungs und Versuchsanstalt für Luft und Raumfahrt, Brunswick, Germany.

Professor R.Monti, University of Naples, Italy.

Mr J.Surugue, Office National d'Etudes et de Recherches Aérospatiales, Châtillon-sous-Bagneux, France.

PANEL EXECUTIVE

Dr R.P.Hugerty, AGARD

FOREWORD

The kinetics and equilibria of gas-solid interactions are encountered in connection with a diversity of phenomena - combustion, ablation, corrosion, erosion, catalysis - each of which is usually studied and practised as a separate engineering speciality.

This colloquium brings together workers in all these disciplines. Research papers describe current advances in NATO laboratories and authoritative surveys afford a perspective to show the common thread of basic knowledge that connects these technologies as well as the differences in goals and emphasis that make each field unique.

Direct communication between specialists, crossing inter-disciplinary boundaries, is intended to stimulate new insights in dealing with the many practical problems which involve some aspect of gas-solid reactions.

CONTENTS

SESSION VII. EROSION AND ABLATION

Papers 1, 14, 17, 22, 31 and 32 were withdrawn.

THE REACTION OF METALS AND ALLOYS WITH GASES AT ELEVATED TEMPERATURES

by

Dr. Robert A. Rapp
Department of Metallurgical Engineering
The Ohio State University
116 West 19th Avenue
Columbus, Ohio 43210
U.S.A.

SUMMARY

The recent literature has been surveyed for theoretical and experimental contributions to the understanding of scale formation in the high-temperature reaction of metals and alloys with gases. The graphical representation of thermodynamic data is used to identify possible reactions between metals and alloys and gas mixtures. From a knowledge of the predominant vapor species in metal-oxygen systems and some limited vapor pressure data, graphical representations can be used to predict the vaporization rates of metals and their oxide scales as a function of oxygen activity.

Recent theoretical contributions in alloy oxidation are discussed. The role of grain boundaries of the scale in the dissociative mechanism for protective scale growth has been clarified. An alternating diffusional growth and scale fracture mechanism seems to account for the linear kinetics of scale formation in niobium oxidation. Impurities in the oxide scales of refractory metals probably account for the irrational dependences of these oxidation reactions on oxygen pressure.

The design of oxidation-resistant refractory metal alloys is discussed. Minor additions of rare earth and alkaline earth metals to oxidation-resistant alloys continue to be used to effect reduced scaling kinetics and improved scale adherence; the rationalization of this behavior is yet incomplete.

THE REACTION OF METALS AND ALLOYS WITH GASES AT ELEVATED TEMPERATURES

AN ATTEMPT WILL BE MADE in this paper to survey concisely some contributions made in the last few years to our fundamental knowledge of the theory and mechanisms of high-temperature reactions between gases and metals or alloys to form a scale of reaction products. In this regard, the author wishes to distinguish between the diffusional growth of scales on pure metals by the outward migration of cations and by the inward migration of anions, with their corresponding electronic transport processes. Likewise, the oxidation of alloys based on these two types of scales shall be considered separately.

GRAPHICAL REPRESENTATIONS OF THERMODYNAMIC DATA

Quets and Dresher (1) have recently demonstrated the application of graphical representations of thermodynamic data (the so-called Pourbaix-Ellingham plots which are well known in extractive metallurgy) to the rather complex problem of alloy oxidation in gas mixtures. By this method, reaction tendencies and impossibilities, and to some extent reaction morphologies, can be predicted or rationalized. Quets and Dresher (1) analyzed the "hot corrosion" or "sulfidation" reaction, i.e. the reaction of multi-component Ni-15Cr-base alloys with combustion product gases containing oxygen, sulfur, and sodium sulfate. Figure 1 is a log-log plot indicating the stabilities of phases in the Ni-S-O system at 1200°K; to construct such a plot, only values for the standard free energies of formation of the compounds, i.e., ΔG^{o}_{NiS}, $\Delta G^{o}_{Ni_3S_2}$, and ΔG^{o}_{NiO}, are required. In the analogous plot for the Cr-S-O system shown in Figure 2, it is seen that chromium forms both a more stable sulfide and oxide than nickel.

For a good approximation of the relative stabilities of products formed between gases containing oxygen plus sulfur and binary nickel-chromium alloys Figures 1 and 2 may be superimposed as shown in Figure 3. (Consideration of the reduction in activities of the nickel and chromium in Ni-Cr alloys would result in only small translations of the lines.) For the reaction of relatively dilute Ni-Cr alloys (such as Ni-1 to 15 Cr), for which a protective Cr_2O_3 external scale would not be formed by selective oxidation, both Cr_2O_3 and CrS could exist within a nickel matrix, as can be seen from Figure 3. Indeed, in the absence of sulfur, Cr_2O_3 precipitates are formed by internal oxidation beneath a NiO external scale. For the reaction of dilute Ni-Cr alloys with gases containing both oxygen and sufficient sulfur, CrS precipitates are found deep in the alloy, i.e, at oxygen activities which are too low for the formation of Cr_2O_3. Aluminum and titanium form even more stable sulfides than chromium and therefore their sulfides are formed even deeper in reacted multicomponent alloys. A film or layer of Ni_3S_2 may also be found beneath a NiO scale. These morphological arrangements of phases are consistent with the thermodynamic diagram (Figure 3.)

In the "hot-corrosion" of Ni-Cr-base turbine engine alloys, Na_2SO_4 vapor is present from injested sea water. Likewise, the reaction of injested NaCl vapor with the combustion product gases thermodynamically favors the formation of Na_2SO_4 (2). De Crescente and Bornstein (2) showed that Na_2SO_4 vapor does not effect accelerated attack, but that sulfide formation and "hot corrosion" occur beneath a condensed Na_2SO_4 surface layer. The shift of "hot corrosion" to a higher temperature range in engines with high compression ratios is in agreement with the effect of pressure on the dew point of Na_2SO_4. The following reactions have been proposed (2) for the reaction of Na_2SO_4 with base-metal nickel and the nickel oxide scale, respectively:

$$Na_2SO_4 + 9/2\ Ni \rightarrow Na_2O + 3NiO + \tfrac{1}{2}\ Ni_3S_2 \qquad \text{Eq (1)}$$

and

$$Na_2SO_4 + NiO \rightarrow NiS + Na_2O + 2O_2 \qquad \text{Eq (2)}$$

To examine the possibility of these reactions, Quets and Dresher (1) superimposed the Pourbaix-Ellingham plots of the Na-S-O and the Ni-S-O systems as shown in Figure 4. Also shown in Figure 4 are lines representing the stabilities of ternary compounds between Na_2O and the oxides of some common components in turbine engine alloys (Si, Al, Cr). As written, Eqs. (1) and (2) cannot occur because there is no set of oxygen and sulfur activities at which pure Na_2O can coexist with either Ni_3S_2 or NiS. (A criterion for a possible reaction is that all products

must coexist under some set of experimental conditions. Likewise, the reactant phases should not coexist under these local activities of sulfur and oxygen.) However, if a means is available to reduce the activity of Na_2O far below unity, such as the formation of a ternary compound, or the dissolution of Na_2O into another phase or the vaporization of Na_2O, Eqs. (1) and (2) could proceed, but not to form pure Na_2O. Thus, Quets and Dresher (1) have suggested that the formation of ternary oxides (such as those coexisting with the nickel sulfides in Figure 4 are necessary for the initiation of "hot corrosion". Considered mor generally, the thermodynamic Pourbaix-Ellingham diagrams are quite useful in the analysis of reactions between complex alloys and gas mixtures.

Kellogg (3) has treated in detail another type of graphical representation of thermodynamic data (also originating in extractive metallurgy) to describe the dependence of the vapor pressure of a compound on the non-metal activity. The formation of volatile oxide molecules represents a serious hindrance to the retention of protective diffusion-barrier scales for a number of oxides. Empirically, it is well appreciated that the oxides of W, Mo, and Cr are volatile in oxidizing atmospheres, while SiO_2 experiences vapor losses in reducing atmospheres.

Figure 5 is a Kellogg-type, log-log diagram describing the dependences on oxygen activity of the partial pressures of the volatile species Si(g) and SiO(g) over the condensed phases Si(s) and SiO_2(2) at 1500°K. The four lines of the diagram are derived from the four vapor-forming reactions:

$$Si(s) + \frac{1}{2}\ O_2 \rightarrow SiO(g) \qquad \text{Eq (3a)}$$

$$Si(s) \rightarrow Si(g) \qquad \text{Eq (3b)}$$

$$SiO_2(s) \rightarrow SiO(g) + \frac{1}{2}\ O_2 \qquad \text{Eq (3c)}$$

$$SiO_2(s) \rightarrow Si(g) + O_2 \qquad \text{Eq (3d)}$$

The slopes of the lines in Figure 5, d log P_{SiO}/d log P_{O_2} and d log P_{Si}/d log P_{O_2}, result from the differentiation of the logarithms of the equilibrium constants for Eqs. (3a-d). To construct a Kellogg vaporization diagram the following information is required: 1) knowledge of the stoichiometries of all existing condensed phases and vapor molecules, 2) ΔG^o of formation of each condensed phase (in order to place the vertical lines on the diagram), and 3) at least one value for the equilibrium vapor pressure of each vapor species over a condensed phase at a particular oxygen activity. The stoichiometries and vapor pressures of the volatile species are most readily obtained from mass spectrometric investigations, but reliable vapor pressures for many of the oxide molecules are not yet available, partly because the oxygen activity is not usually known or controlled in the mass spectrometer.

The value for P_{SiO} at Si-SiO_2 coexistence in Figure 5 is taken from Schäfer and and Hörnle (4). From Figure 5, it may be appreciated that the vapor pressure of a compound is not a single-valued function of the temperature (as is often assumed in tabulated data) whenever the stoichiometry of the predominant vapor species differs from that of the condensed phase. A SiO_2 scale at 1500°K would exhibit negligible vapor losses in a highly oxidizing environment (air), but SiO volatilization would be severe in highly reducing gases. (The annealing of research specimens in hydrogen gas in quartz combustion tubes at 1100°C should result in contamination of the speciments with silicon.)

Figure 6 is a Kellogg-type diagram to describe vaporization in the Cr-O system at 1473°K. The less important vapor species CrO_2 and CrO have been deleted from the diagram; the value of $P_{CrO_3} = 5 \times 10^{-5}$ atm at $P_{O_2} = 1$ atm is taken from Caplan and Cohen (5). As studied recently by Tedmon (6), the vaporization of CrO_3 molecules from Cr_2O_3 protective oxide scales is a serious engineering problem which results in paralinear kinetics for oxidation in highly oxidizing atmospheres. Actual vapor losses from protective scales cannot be predicted directly from Kellogg diagrams, only the maximum possible vapor loss through use of the Hertz-Langmuir equation:

$$J_i \left(\frac{\text{moles}}{\text{cm}^2\text{-sec}}\right) = \frac{P_i}{(2\pi M_i RT)^{1/2}} \qquad \text{Eq (4)}$$

A calculated mass transport coefficient is required to predict actual vapor losses from the known vapor pressure.

OXIDATION WITH SCALE GROWTH BY CATION DIFFUSION

PURE METALS. When the predominant ionic defects in an oxide scale are vacant cation sites, then the growth of a compact, protective layer occurs by the outward diffusion of cations with a counter flow of vacancies and positive holes. As the scale thickens, its resistance to plastic deformation increases, particularly at points of constraint such as the edges and corners of a specimen. With the continual arrival of vacancies through the oxide to the metal-scale interface, the reducted plasticity of the scale can lead to the condensation of vacancies to form voids and ultimately a porous zone at the metal-scale interface.

The scanning electron microscope seems to offer outstanding promise for the observation and rationalization of scale morphologies on metals. (In this regard, Wood (7) has completed a comprehensive review of experimental techniques for the study of oxidation rates, structures, morphologies, etc.) Howes (8) used the scanning electron microscope to examine the matching surfaces of a Cr_2O_3 scale which had spalled from an oxidized Fe-Cr alloy. This detailed observation of the inner, porous zone of the Cr_2O_3 scale showed large void areas with only oxide bridges retaining contact between the outer compact scale and the alloy. Deep grooves were seen in the grain boundaries of the alloy, and the scale above these grain boundaries had apparently buckeled outward because of the local loss of metal-scale contact and the existing compressive stresses. Only between 5 to 25 percent of the geometric area of the porous zone consisted of oxide bridges; many authors have recently suggested that a dissociative mechanism can result in the growth of the scale at the metal-scale interface by the inward transport of metalloid molecules across the voids within the porous inner scale.

The investigation of morphological details in the scale is difficult in the oxidation of metals because no suitable radioactive tracer of oxygen is available. However, in the sulfidation of silver, copper, iron, nickel, and several binary alloys, Brückman (9) and Mrowec (10) used sulfur radio-tracers to study the formation of the inner porous scale and the phenomena resulting from its formation. For slab specimens of the pure metals, the inner porous scale was initiated at corners and edges while metal-scale adherence was maintained along the flat faces of the specimen. Upon further oxidation, a perforation of the initially compact outer scale occurred in regions exterior to the inner porous scale. Thereafter, tracer molecules were not only consumed for scale growth at the scale-gas interface, but also reached the inner porous zone by diffusion through the perforations in the outer scale. Brückman and Mrowec suggested that the dissociative mechanism occurs in the porous inner scale, but that the dissociation is anisotropic, with preferential formation of molecules along grain boundaries which ultimately results in the perforation of the outer scale. In the sulfidation of alloys for which an insoluble internal precipitate is formed, the porous inner scale layer was initiated essentially at the start of the sulfidation at all areas on the specimen (not just corners and edges). For these alloys, the perforation of the outer scale also occurred early and generally over the specimens, and the sulfide which was formed at the metal-scale interface represented a large contribution to the scaling rate.

For the oxidation of metals, the possibility of scale perforation by the preferential dissocation along oxide grain boundaries of the inner porous scale has not been investigated. However, oxide scale morphologies resemble closely those for sulfide scales. Obviously, with the occurrence of a dissociative mechanism and scale perforation, i.e., morphological irregularities, kinetic data after long oxidation times cannot be simply related to self-diffusion in the scale according to Wagner's parabolic oxidation rate expressions.

ALLOYS. In the theory of alloy oxidation, C. Wagner has made two recent contributions. As a basis for calculating the scaling rates of binary alloys, Wagner (11) has derived expressions for the distribution of cations in solid solution oxide and sulfide scales. In the model chosen by Wagner, a two-component alloy was oxidized to form a plane, compact, single-phase, nearly stoichiometric, electronic conducting scale. Local equilibrium was assumed at the metal-scale and scale-gas interfaces so that the oxidation rate is controlled by the outward diffusion of the two cation species through the scale. Mathematical expressions

which required numerical evaluation showed that the different cations should not be uniformly distributed in a single phase scale because of their differing mobilities, so that the cation species with the greater mobility would be enriched at the scale-gas interface. The theory was evaluated for the sulfidation of Cu-Ag alloys and the oxidation of very dilute Ni-Cr alloys. Because most binary alloys exhibit either internal oxidation or selective scale formation by a single component (mechanisms for which Wagner has previously presented theoretical treatments), the new theory for the formation of solid solution, single-phase scales may not find numerous applications.

C. Wagner (12) has also examined theoretically the oxidation of binary Cu-Pd and Cu-Pt alloys in which the same oxide (Cu_2O) forms both as an external scale and as an internal oxide precipitate. A thermodynamic driving force to effect this somewhat unusual morphology only exists when a slowly diffusing, more-noble component is rejected and enriched at the metal-scale interface. Then the oxygen activity for coexistence of the scale and adjacent alloy is higher than that for the same oxide in coexistence with the original alloy composition. However, to form the oxide as an internal precipitate, a significant solubility and diffusivity of oxygen in the matrix is also required. As a criterion for the simultaneous formation of an external scale and an internal oxide precipitate from the same oxide AO, Wagner pointed out that the derivative $(\partial \ln N_A N_O / \partial x)_{x=X}$ at the metal-scale interface must be positive. From a solution of the diffusion equation, Wagner derived a quantitative expression for this derivative and showed that for Cu-Pd and Cu-Pt alloys positive values result from evaluation of the expression.

The Wagner-Hauffe "doping" effect in alloy oxidation has received some recent attention. To rationalize the enhanced oxidation rates of dilute Ni-Cr alloys, Meier and Rapp (13) studied the defect structure and chromium solubility in Cr-doped NiO. The previously proposed electrical neutrality condition, $[Cr_{Ni}^{\cdot}] = 2[V_{Ni}^{''}]$, was found to hold for all P_{O_2}. The solubility of chromium in NiO was found to be independent of P_{O_2}, but was rather low: 0.015 cation fraction at 1100°C, 0.012 at 1000°C, and 0.009 at 850°C. Several authors have previously reported a steady increase in oxidation rate compared to pure nickel with increased chromium content up to 8 or 10 atom percent. The question arises as to how chromium in excess of the solubility limit (about one percent) can effect increased scaling rates; the "doping" effect cannot be held responsible. Recently, Wood and Hodgkiess (14) and Giggins and Pettit (15) have reported a sharp increase in scaling rates for Ni-Cr alloys with very low chromium contents (1 to 2 percent), but then little or no further increase in kinetics with increasing chromium. This pattern is consistent with that expected from the "doping" effect.

To provide a basis for the use of the "doping" effect in reducing the oxidation rates of alloys which form Cr_2O_3 scales, Tedmon and Hagel (16) developed procedures for the electrodeposition of lithium onto chromium from molten lithium fluoride. Despite some irregularities in the coatings, the lithiated chromium oxidized slower both in oxygen and in air. The scales which formed were both more adherent and non-spalling. In air oxidation, less nitrification occurred beneath the "doped" oxide scale. Tedmon (17) also prepared ductile, lithiated Fe-25 Cr alloys by melting under pressure. In oxidation at 1300 and 1360°C, the reduced oxidation rates for lithiated alloys were ascribed to the diffusion of chromium ions over the Li-doped Cr_2O_3 scale which simultaneously suffered evaporation losses from CrO_3. At lower temperatures, 1000-1200°C, the formation of a ternary oxide barrier phase at the metal-scale interface apparently aided the "doping" effect in the reduction of the kinetics and the improvement of scale adherence.

In the space allowed, the author cannot discuss in detail all of the various recent contributions to our knowledge of morphologies, structures, mechanisms, kinetics, etc., for alloy oxidation. However, a few papers involving oxidation in practical alloy systems will be mentioned.

Pettit (18) investigated the oxidation of Ni-Al alloys. As a function of the temperature and composition three mechanisms were observed: for the most dilute alloys, an internal precipitation of Al_2O_3 occurred beneath the NiO scale; for the alloys with highest aluminum content, a protective Al_2O_3 scale was formed; for intermediate compositions, an initially formed Al_2O_3 scale could not be sufficiently maintained by the diffusion of aluminum in the alloy so that a reversion to the dilute-alloy mechanism occurred at longer times. Giggins and Pettit (15) reported three differing mechanisms for the oxidation of Ni-Cr alloys; the mechanisms

for the most dilute and the most concentrated alloys corresponded to those for Ni-Al alloys. For intermediate Ni-Cr compositions, an external Cr_2O_3 scale formed preferentially above the alloy grain boundaries while initially the centers for surface grains experienced internal oxidation of chromium and NiO scale formation. However, as the oxidation progressed, the compact grain boundary layer of Cr_2O_3 extended down along the grain boundaries until the surface grains were isolated by a protective Cr_2O_3 layer. Internal oxidation and NiO formation then stopped and the kinetics were correspondingly reduced. For Ni-Cr alloys in the intermediate composition range (10-30 wt. percent Cr), fine-grained specimens oxidized at slower rates than those with coarse grains because of this tendency to form protective Cr_2O_3 grain boundary films. Preliminary deformation of the surface prior to oxidation resulted in a recrystallized surface layer upon heating, so that specimens with surface deformation showed the preferred oxidation behavior of fine-grained specimens. (Incidentally, Pettit (15,18) has also used an informative graphical representation of thermodynamic data, i.e., a log-log plot of alloy content (activity) vs. oxygen activity which indicates the regions of phase stability.)

Kofstad and Hed (19) have reported an extensive investigation of the microstructures and kinetics for the oxidation of a Co-10 w/o Cr alloy. At relatively high P_{O_2} at temperatures between 800 to 1300°C, an internal precipitation of Cr_2O_3 occurs and a dual layer CoO scale is formed. In the inner scale with 33-35% porosity, the Cr_2O_3 precipitates reacted with CoO to form $CoCr_2O_4$ particles. In the outer "compact" scale, voids which were apparently closed and caused by mechanical stresses accounted for about 3-6% porosity. (The perforation of the outer scale by anisotropic dissociation (9,10) as is prevalent in sulfidation did not seem to occur.) Kofstad and Hed ascribed the rate control essentially to ionic diffusion of cobalt ions through CoO; however, the reaction was aided by a short-circuiting of the inner scale resulting from the dissociation mechanism, while $CoCr_2O_4$ particles served as barriers to ionic diffusion in the inner scale. The "doping" of CoO by trivalent Cr ions probably did not affect the rate significantly.

Wood and coworkers have reported recently several comprehensive oxidation studies of Cu-, Ni- and Fe-base alloys. Whittle and Wood (20) studied three differing oxidation mechanisms for Cu-Ni alloys containing 80,55, and 10% Ni. In this system, NiO is somewhat more stable than Cu_2O, and the oxides NiO, Cu_2O, and CuO are essentially mutually insoluble and nonreactive. For the Cu-80 Ni alloy, a compact NiO inner scale controlled the oxidation rate although a thin outer CuO was retained from the initial nucleation stage. The microstructure of the oxidized Cu-10Ni alloy was the usual type for a dilute alloy-internal oxide precipitates of NiO with a two-layered Cu_2O scale. The microstructure for the oxidized Cu-55 Ni alloy was complex, varying from two-layered to multilayered scale with large nodule formation.

Wood and Hodgkiess (14,21) have studied the oxidation of Ni-Cr alloys and Wood and Whittle (22,23) have investigated the oxidation of Fe-Cr alloys; Wood, et al. (24) have compared the oxidation behavior of Ni-Cr and Fe-Cr alloys. Of particular interest in both systems was the identification of Cr_2O_3 (and not a spinel) as the protective scale, as well as the description of scale failure and healing mechanisms. For dilute Fe-Cr alloys (14-18 Cr), a protective Cr_2O_3 scale is formed initially but then is lifted or cracked by mechanical stresses to allow the more rapid formation of a stratified scale rich in iron oxides. Healing of the stratified scale by the formation of an underlying Cr_2O_3 layer can occur only after some of the chromium-depleted alloy has been consumed. Scale adherence is generally poor for Fe-Cr alloys. Alloys of Ni-14 to 25 Cr retain a thin external NiO layer above the protective Cr_2O_3 layer. Thin layers of Cr_2O_3 loop around grain boundaries and stop any initial internal oxidation besides providing improved scale adherence compared to Fe-Cr alloys. Because interdiffusion is slower in f.c.c. Ni-Cr alloys than in b.c.c. Fe-Cr alloys, chromium depletion at the metal-scale interface beneath Cr_2O_3 scales is greater for Ni-Cr alloys, but the depletion does not extend as deeply into the alloy. Oxidation stresses also occasionally result in local failures of protective Cr_2O_3 scales on Ni-Cr alloys; scale failures on Ni-Cr alloys may occur at higher Cr contents than in the Fe-Cr system because of the more extensive chromium depletion. However, the healing of scale fractures on Ni-Cr alloys is facilitated by the shallowness of chromium depletion and the ability of Cr_2O_3 grain boundary loops to reestablish a protective scale.

For many years, additions of rare earth and alkaline earth metals or oxides have been used to improve the oxidation resistance of alloys which are protected by scales supporting cation diffusion. Because of the small amounts required and the reactivity and insolubility of the components, a clarification of the mechanisms involved in this effect has not been presented. Wood and Boustead (25) found that Y and Gd additions (as YFe_9 and Gd_2Fe_{17}) to Fe-Cr alloys resulted in reduced oxidation rates, the prevention of breakaway (scale failure) at long times, and better scale adherence on cooling. Mentioned as possible causes for the improvements were: a.) an accumulation of rare earth oxide precipitates in the metal-scale interface, b.) a convolution of this interface which keys the oxide to the metal, and c.) the condensation of vacancies at internal oxide precipitates which prevents the formation of voids at the metal-scale interface.

Seybolt (26), in the oxidation of Cr containing 5 vol.% Y_2O_3, found the kinetics to be much slower than parabolic at long times, and suggested that the Y_2O_3 particles collected in the metal-scale interface to form $YCrO_3$ which serves as a barrier to cation transport. In hot corrosion (sulfur plus oxygen) studies, Seybolt (27) found that a 0.5% Ce addition to the superalloy Udimet 500 effected reduced penetration of the sulfide precipitation in the matrix. Viswanathan (28) reported that small additions of Y and La reduced the hot corrosion attack of Udimet 700. Both before and after the reaction, the rare earths were located in the grain boundaries as $LaNi_x$ and LaS_x, resp. The rare earth sulfides (and oxides) seem to block effectively the grain boundaries to the inward diffusion of atomic sulfur and oxygen.

OXIDATION WITH SCALE GROWTH BY ANION DIFFUSION

PURE METALS. Considerable work has been accomplished recently toward the understanding of the complex high-temperature scaling behavior of niobium (columbium). The author will discuss briefly the oxidation of niobium with the exclusion of other metals of interest, such as V, Ta, Zr, Hf, Ti, etc. Roberson and Rapp(29) oxidized niobium at 900°C in a cuprous oxide vapor. Upon reduction of the cuprous oxide vapor species (the exact nature of which is unknown) by the niobium to form the high-temperature structure α-Nb_2O_5, two moles of copper are deposited at the site where each mole of oxygen is consumed. Microscopic observation of the scale with its copper markers showed a series of relatively compact layers, each of which had successively fractured to admit the oxidizing molecules to penetrate the scale. The oxidation of niobium was described as the diffusion-controlled growth of a compact Nb_2O_5 layer at the metal-scale interface to some critical thickness at which the scale fractures because of mechanical stresses, and then the process is repeated indefinitely. Linear kinetics would result if the growth of layers were "out-of-cycle" in various regions around the specimen.

Sheasby et al. (30) have examined the P_{O_2}-dependence of the ionic-diffusion-controlled, parabolic growth of the low-temperature γ-Nb_2O_5 modification at 720-850°C. A large dependence of the parabolic rate on oxygen pressure was found; this result is not expected for the diffusion of oxygen ions with a concentration-independent mobility. To rationalize this P_{O_2}- dependence, Sheasby et al. (31) determined the P_{O_2}-dependence of the oxygen diffusion coefficient for α-Nb_2O_5 and γ-Nb_2O_5. For both oxides, the oxygen diffusion coefficients were several orders of magnitude smaller for oxides with large deviation from stoichiometry, i.e., at lower P_{O_2}; apparently, a simple oxide structure and oxygen ion mobility behavior does not exist in Nb_2O_5. The authors suggested that a γ-Nb_2O_5 scale consists of a series of distinct phases or structures joined by regular discontinuities. In fact, Schafer et al. (32) have reported the compositions, diffraction patterns, and thermodynamic free energies of formation for seven equilibrium phases between NbO_2 and Nb_2O_5 at 1300°C.

Kofstad (33) has proposed an alternate interpretation for the large P_{O_2}-dependence for the parabolic oxidation of niobium reported by Sheasby et al. (30). Kofstad considered the effect of aliovalent impurities (doping) on the defect structure and associated properties of Nb_2O_5, as well as Ta_2O_5 and ZrO_2. The concentration on native oxygen vacancy defects in Nb_2O_5 at 900°C in one atm oxygen should be on the order of two parts per million, while the "pure" niobium metal and Nb_2O_5 used in laboratory experiments contains two or more orders of magnitude higher impurity contents. Near stoichiometry (at highest P_{O_2}), the defect concentrations in Nb_2O_5 must be established by the impurity content according to a neutrality condition

$[Mf''_{Nb}] = [V_O^{\cdot}]$ where Mf is a trivalent impurity ion. The consideration of doping leads to the prediction of a $P_{O_2}^{1/4}$-dependence of the electrical conductivity which is observed, as well as a logarithmic dependence of the parabolic rate constant on P_{O_2}, which is in agreement with the results of Sheasby et al. The consideration of impurities in the oxidation of refractory metals seems to clarify a major uncertainty in this area, i.e., the irrational P_{O_2}-dependence found for oxidation rate constants.

J. S. Sheasby (34) has oxidized niobium for extended times in the lower-temperature range 450-720°C. An initial parabolic growth of a compact γ-Nb_2O_5 scale was interrupted by scale fractures, and at long times, linear oxidation kinetics were observed. The final microstructure for specimens oxidized above 626°C revealed a scale consisting of a series of compact layers of γ-Nb_2O_5 of about equal thickness which were separated by fractures. With the assumption that the oxidation is controlled by ionic diffusion through a compact layer of γ-Nb_2O_5 at the metal-scale interface, Sheasby was able to show that the observed thicknesses of the scale layers could be calculated from the parabolic rate constant measured before scale fracture. Therefore, in the temperature range 625-720°C, the oxidation of niobium is controlled by the diffusion of oxygen ions in Nb_2O_5, but the scale periodically fractures to result in linear kinetics. At temperatures between 450 and 600°C, suboxide NbO_2 platelets form in the metal beneath the scale, and the scale fracture is facilitated, with a chevron pattern of pores appearing in the scale as previously reported for tantalum oxidation by Stringer (35).

ALLOYS. Although many screening studies of niobium-base (and other refractory-metal base) alloys have been carried out, little study of alloy oxidation mechanisms has been made in these alloy systems. With our recent significant improvement in the understanding of the oxidation of pure niobium, some meaningful alloy oxidation work should be forthcoming. For the development of strong, oxidation-resistant, uncoated refractory metal alloys, saturation of the matrix with dissolved oxygen must be prevented. The solubility of oxygen in niobium is 2 atom percent at 1000°C; the dissolution of oxygen into a niobium alloy under a Nb_2O_5 scale can only be prevented by the internal oxidation of a less noble alloying component, for which the selection is rather limited; Zr, Ti, Hf, and rare earth metals.

Rapp and Goldberg (36) investigated the combined internal oxidation and external scaling behavior of Nb-Zr alloys. (Because of their creep and stress-rupture properties Nb-Ti base alloys seem unattractive, but strong, oxidation resistant Nb-Hf base alloys are currently being developed by several groups.) At 1000°C in oxygen, binary Nb-Zr alloys with 10 and 20 atom percent Zr formed submicroscopic internal oxide precipitates and these alloys oxidized at linear rates higher than that for pure niobium. However, in the oxidation of Nb-30 Zr and Nb-40Zr alloys, lamellar ZrO_2 internal oxide platelets were formed, and these were oriented approximately normal to the metal-scale interface. The ZrO_2 platelets were apparently very strong because they withstood the expansive conversion of Nb to Nb_2O_5 at the metal-scale interface without immediate fracture. The linear oxidation rates for these concentrated Nb-Zr alloys were lower than that for pure niobium, presumably because with the mechanical support and keying of the ZrO_2 platelets a greater average thickness of compact Nb_2O_5 could be maintained at the metal-scale interface. The addition of a third alloying addition, such as Ti or Re, can effect yet lower scaling rates (and indeed parabolic kinetics) with better scale adherence and less scale porosity. Then qualitately, the design of an oxidation-resistant Nb-(or Ta-) base alloy seems to require a major (20 to 40%) alloying addition of a less noble component to support internal oxidation with a platelet morphology and at least one other minor alloying addition whose role is to either soften the Nb_2O_5 (to delay scale fracture) or to dope the Nb_2O_5 scale with plus 6 or plus 7 cations (to reduce the concentration of oxygen vacancies in the compact Nb_2O_5 layer). The third possible role of an alloying addition would be the formation of a ternary compound with Nb_2O_5 having low transport properties.

CONCLUDING REMARKS

The author has attempted to summarize some of the contributions made over the last two or three years to our understanding of the oxidation of metals and alloys. In this regard, only high-temperature scaling reactions were considered, and even with this limitation, some significant work in this area has surely been deleted. These deletions should be blamed on the limited available space and the author's limited interests and knowledge of the recent literature.

REFERENCES

(1) J. Quets and W. Dresher, J. Materials, March (1969).
(2) M. A. DeCrescente and N. Bornstein, Corrosion, 24, 127 (1968).
(3) H. H. Kellogg, Trans. Met. Soc. AIME, 236, 602 (1966).
(4) H. Schäfer and R. Hörnle, Z. anorg. allgem. Chem., 263, 261 (1950).
(5) D. Caplan and M. Cohen, J.E.C.S., 108, 438 (1961).
(6) C. S. Tedmon, J.E.C.S., 113, 766 (1966).
(7) G. C. Wood, "Experimental Techniques in the Oxidation of Metals", Chapter in Techniques in Metals Research, Vol. IV, Editor, R. A. Rapp, Wiley Publ., New York, 1970.
(8) V. R. Howes, Corr. Sci., 8, 221 (1968).
(9) A. Brückman, Corr. Sci., 7, 51 (1967).
(10) S. Mrowec, Corr. Sci., 7, 563 (1967).
(11) C. Wagner, Corr. Sci., 9, 91 (1969).
(12) C. Wagner, Corr. Sci., 8, 889 (1968).
(13) G. H. Meier and R. A. Rapp, "Electrical Conductivities and Defect Structures of Pure NiO and Chromium-Doped NiO", submitted for publication to Trans. Met. Soc. AIME.
(14) G. C. Wood and T. Hodgkiess, Nature, 211, 1358 (1966).
(15) C. S. Giggins and F. S. Pettit, "Oxidation of Nickel-Chromium Alloys at Temperatures between 800 and 1200°C, submitted for publication to Trans. Met. Soc. AIME.
(16) C. S. Tedmon and W. C. Hagel, J.E.C.S., 115, 147 and 151 (1968).
(17) C. S. Tedmon, Corr. Sci., 7, 525 (1967).
(18) F. S. Pettit, Trans. Met. Soc. AIME, 239, 1296 (1967).
(19) P. K. Kofstad and A. Z. Hed, J.E.C.S., 116, 224 and 229 (1969).
(20) D. P. Whittle and G. C. Wood, Corr. Sci., 8, 295 (1968).
(21) G. C. Wood and T. Hodgkiess, J.E.C.S., 113, 319 (1966).
(22) G. C. Wood and D. P. Whittle, Corr. Sci., 7, 763 (1967).
(23) G. C. Wood and D. P. Whittle, J.E.C.S., 115, 126 and 133 (1968).
(24) G. C. Wood, T. Hodgkiess and D. P. Whittle, Corr. Sci., 6, 129 (1966).
(25) G. C. Wood and J. Boustead, Corr. Sci., 8, 719 (1968).
(26) A. U. Seybolt, Corr. Sci., 6, 263 (1966).
(27) A. U. Seybolt, Trans. Met. Soc. AIME, 242, 1955 (1968).
(28) R. Viswanathan, Corrosion, 24, 359 (1968).
(29) J. A. Roberson and R. A. Rapp, Trans. Met. Soc. AIME, 239, 1327 (1967).
(30) J. S. Sheasby, G. R. Wallwork and W. W. Smeltzer, J.E.C.S., 113, 1255 (1966).
(31) J. S. Sheasby, W. W. Smeltzer and A. E. Jenkins, J.E.C.S., 115, 338 (1968).
(32) H. Schafer, D. Bergner and K. Gruehn, Z. anorg. allgem. Chem., 365, 31 (1969).
(33) P. K. Kofstad, Corrosion, 24, 379 (1968).
(34) J. S. Sheasby, J.E.C.S., 115, 695 (1968).
(35) J. Stringer, J. Less Common Metals, 11, 111 (1966).
(36) R. A. Rapp and G. Goldberg, Trans. Met. Soc. AIME, 236, 1619 (1966).

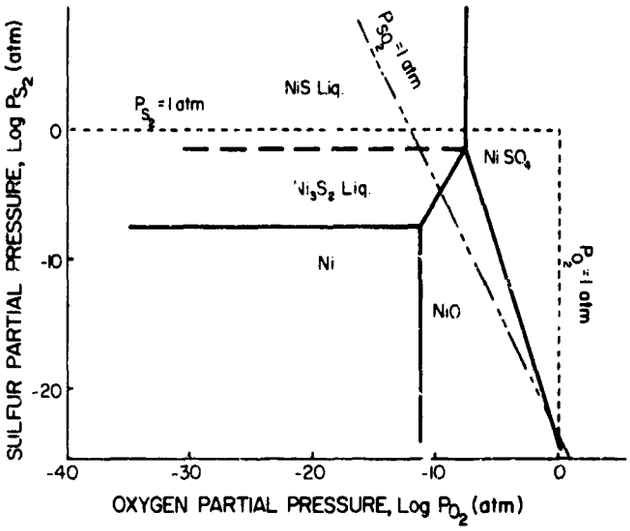

Fig. 1 - PHASE STABILITY in Ni-S-O SYSTEM at 1200°K (QUETS AND DRESHER)

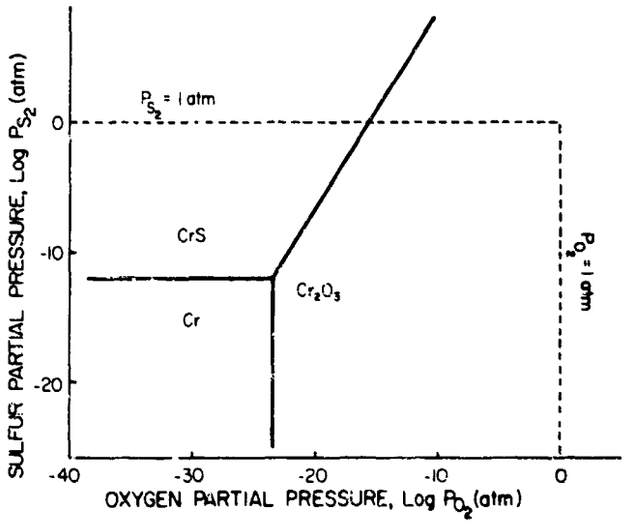

Fig. 2 - PHASE STABILITY in Cr-S-O SYSTEM at 1200°K (QUETS AND DRESHER)

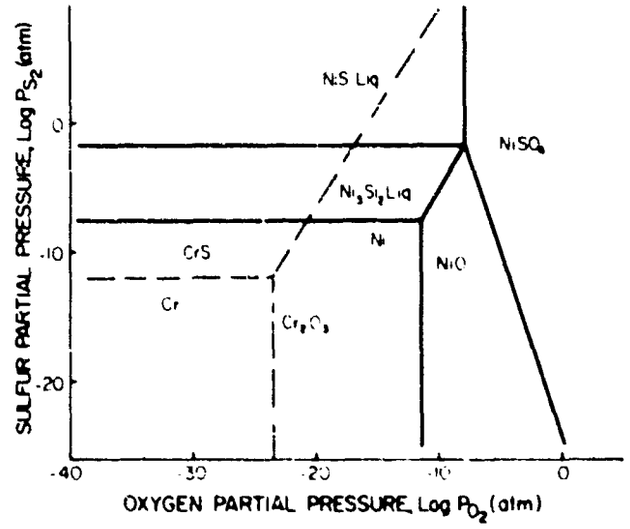

Fig 3 - SUPERPOSITION OF Ni-S-O AND Cr-S-O STABILITY DIAGRAMS AT 1200°C (QUETS AND DRESHER)

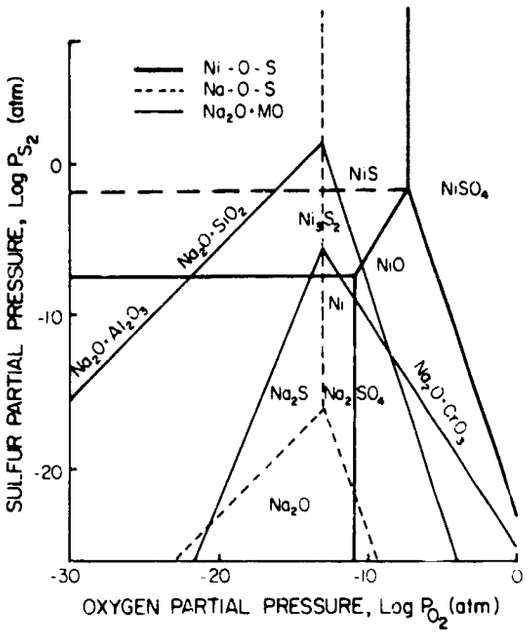

Fig 4 - VARITION OF Na_2O PHASE FIELD WITH A FEW METAL OXIDES AT 1200°K (QUETS AND DRESHER)

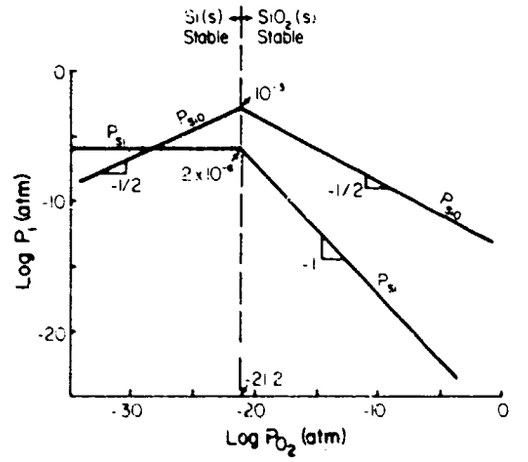

Fig 5 - VAPORIZATION in the Si - O SYSTEM at 1500°K

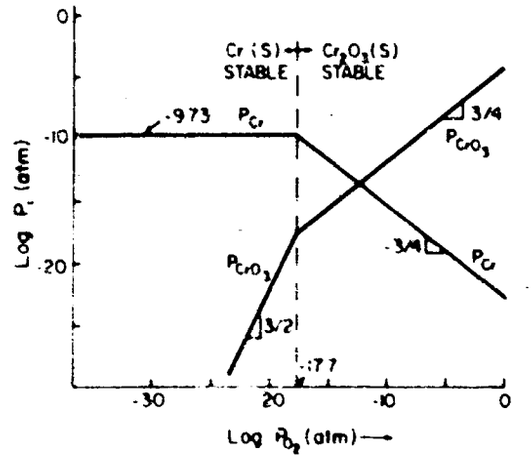

Fig 6 - VAPORIZATION IN THE Cr-O SYSTEM AT 1473°K

PARAMETRES THEORIQUES ET DETERMINATIONS EXPERIMENTALES DANS L'ETUDE DE MATERIAUX SOUMIS A L'ABLATION

by

E. GUERINI et R. JOATTON
INGENIEURS A SUD-AVIATION - FRANCE

S O M M A I R E

L'étude de l'ablation, phénomène de couplage entre le matériau et la couche limite, couvre schématiquement 3 domaines : matériau, couche limite, transferts de masse et d'énergie à la surface en recul.

Nous nous intéressons ici à l'étude du matériau, qui comprend l'étude des répartitions internes de température, de débits gazeux, de masse spécifique, de pression ; ces répartitions sont calculables par des modèles mathématiques établis en fonction de paramètres qui traduisent globalement les phénomènes physiques et chimiques prépondérants : parmi ces phénomènes citons la cinétique de la décomposition du matériau, repérée par la thermogravimétrie et la thermovolumétrie ; l'évolution des caractéristiques thermiques et aérotiques de la matrice poreuse cokéfiée, l'action du carbone résiduel sur les fibres de silice ... etc.

Des valeurs significatives de ces paramètres peuvent être obtenues, en dehors de l'exploitation de schémas inverses utilisant les répartitions de température mesurées, par des processus expérimentaux séparés dont la description est l'objet de ce rapport.

Le terme d'ablation qui, à l'origine, dépeignait l'enlèvement en surface d'un matériau de protection thermique, s'est peu à peu généralisé et il désigne aujourd'hui l'ensemble des phénomènes complexes qui régissent le comportement d'un bouclier thermique. Il comprend en effet toutes les réactions de pyrolyse qui provoquent une carbonisation progressive du matériau vierge pour aboutir au dégagement des gaz de cracking terminal et les phénomènes de combustion, de dissociation, de blocage de flux thermique aérodynamique, de convection résultant de l'injection des gaz de pyrolyse dans la couche limite. L'ablation est donc, dans son sens le plus général, un phénomène de couplage qui associe étroitement le matériau en transformation, la surface en recul et la couche limite.

Nous nous limiterons ici à l'étude du comportement des matériaux, étude orientée vers la détermination des caractéristiques nécessaires au fonctionnement de schémas de calculs représentatifs des phénomènes analysés.

Les premières tentatives de calculs des écrans thermiques étaient basées sur l'hypothèse simplificatrice suivante : on affectait au matériau des caractéristiques physiques apparentes, ces caractéristiques étant assimilées à une capacité calorifique et à une conductivité thermique. C'est-à-dire que l'on englobait sous ces deux paramètres tous les phénomènes complexes qui régissent la transformation du matériau. Dans ces conditions, l'équation de Fourrier permet la détermination des champs de température. Une troisième caractéristique, la chaleur d'ablation définit le recul de la surface.

Ces trois paramètres résultent , pour être valables dans un dimensionnement d'expériences réalisées dans des conditions d'échauffement voisines de celles rencontrées en vol. (Références 1 et 2). Toutefois, physiquement, ce schéma simplifié est très éloigné de la réalité et, les caractéristiques apparentes n'ayant aucun rapport direct avec des caractéristiques physiques, elles ne peuvent en aucun cas orienter le physicien et le chimiste lors de la conception de formules de matériaux nouvelles. La nécessité s'est donc faite sentir d'établir de nouveaux schémas serrant de plus près la réalité. Ce qui permet :

- des dimensionnements beaucoup plus précis.
- la connaissance plus approfondie du phénomène qui n'est plus masqué par des caractéristiques beaucoup trop simplifiées.
- l'élaboration plus scientifique de nouveaux matériaux.

THEME DE TRAVAIL

Le thème de travail que nous avons choisi pour cette étude est un matériau à 3 composants : une résine phénolique, des fibres de silice et des fibres de polyamides aromatiques.

Les fibres de polyamide et de silice se présentent sous forme de tissus mixtes, le polyamide étant destiné à amener d'importantes chaleurs de décomposition tout en laissant des résidus de cokes très durs et adhérents, le rôle de la silice consiste à armer ces cokes de manière à réduire les vitesses d'ablation.

Ce matériau a reçu la dénomination d'Orthostralon 60.

COMMENT ABORDER LE PROBLEME.

Résumons tout d'abord le processus général de dégradation (Figure 1). En partant de l'extérieur vers la surface pratiquement inaltérée, nous trouvons une zone vierge caractérisée par sa conductivité thermique, sa chaleur spécifique et sa masse spécifique. L'équation de Fourrier régit alors l'écoulement du flux calorifique. Nous abordons ensuite la zone ou s'amorce la pyrolyse, caractérisée d'abord par la température de pyrolyse commençante. Cette pyrolyse se traduit par la formation de toute une série d'hydrocarbures, notamment benzéniques.

La pyrolyse est accompagnée d'une augmentation de la porosité, [redacted], cette augmentation s'accentuant au fur et à mesure que nous approchons de la surface en ablation. Les gaz résultant de la première pyrolyse traversent donc, avec des vitesses de plus en plus importantes des zones de températures croissantes, d'où un cracking qui aboutit finalement en surface, pour des températures de l'ordre de 2400°K, à un dégagement d'hydrogène, d'azote et d'oxyde de carbone. Ce cracking entraîne par ailleurs des dépôts de carbone pyrolytique dans les zones les plus chaudes, l'oxygène étant en quantité insuffisante pour oxyder tout le carbone. Dans la zone en transformation interviennent également la conductivité thermique de la chaleur spécifique et la masse spécifique en fonction de la température. Toujours dans les zones les plus chaudes, la silice et le carbone réagissent et la silice disparait très vite sous forme de silicium, de monoxyde de silicium et de carbure de silicium.

Enfin au niveau de la surface, il faudra prendre en compte, les réactions d'oxydation des cokes ainsi que la fusion de la silice, si la stéochiométrie carbone-silice le permet.

./..

Des schémas de calculs représentatifs de cet ensemble de phénomènes sont concevables et relativement aisés. Ce qui l'est moins, c'est la mise en place de moyens expérimentaux capables de fournir avec suffisamment de représentativité les paramètres nécessaires. Nous reviendrons plus loin, lors de l'exposé des méthodes d'essais sur ces difficultés.

Un certain nombre d'étapes intermédiaires apparaissent donc nécessaires. Elles consisteront à considérer certains phénomènes sous une forme globale. Toutefois, afin de respecter l'image générale du schéma, et de lui conserver toute sa représentativité, ces intégrations partielles ne grouperont que des propriétés de même nature. Par exemple, les effets thermochimiques de la pyrolyse seront étudiées sous forme d'un "gaz moyen" mais ne seront pas englobés avec, par exemple, l'échauffement des gaz traversant les couches cokéfiées.

Malgré ces simplifications, des imprécisions résultant de la difficulté des expériences subsisteront et l'utilisation de schémas de calcul inverses seront encore nécessaires pour affiner les résultats de calculs. Enfin dans certains cas, les zones de transition ne seront pas accessibles à l'expérience. On procédera alors par interpolation entre les caractéristiques à l'état initial et l'état final. Les paramètres à prendre en charge expérimentalement sont donc les suivants :

- dans l'ensemble du matériau, la conductivité thermique, la chaleur spécifique et la masse spécifique en fonction de la température,
- les chaleurs de décomposition dans la zone en transformation,
- dans la zone en transformation également et dans la zone cokéfiée, l'étude des échanges gaz-structure ce qui entraine la connaissance,
  - . de la composition des gaz ainsi que la chaleur spécifique des constituants,
  - . de la porosité des structures ainsi que des pertes de charge.
- vers la surface, enfin l'étude,
  - . des réactions silice-carbone,
  - . de l'oxydation en surface.

RESULTATS EXPERIMENTAUX

L'acquisition directe des caractéristiques physiques se heurte à un obstacle majeur : la brièveté et surtout l'intensité des échauffements qui dans la plupart des cas ne permettent que des mesures globales insuffisantes pour meubler les schémas de calcul. Cette remarque est particulièrement vraie en ce qui concerne les paramètres liés à la pyrolyse. Nous avons donc pris les orientations suivantes : les phénomènes échappant à l'analyse fine en échauffement rapide sont étudiés avec précision au cours d'expériences de laboratoire réalisés avec des échauffements lents. Lorsque cela est possible, nous regardons si les résultats en sont directement applicables à des échauffements rapides. Cette vérification résultera en général de l'application de ces données expérimentales à des résultats d'essais globaux. Dans le cas où elle ne se révèle pas satisfaisante, les caractéristiques physiques sont adaptées à partir de ces résultats d'essais globaux.

Pour l'étude systématique des différents paramètres, nous avons défini, après de nombreuses expériences les domaines de température correspondant à des zones présentant un mode d'action déterminé. La zone de pyrolyse s'étend de

350°C ± 50°C (pyrolyse commençante)

à

800°C ± 100°C température à laquelle nous considérons que toutes les réactions de pyrolyse sont terminées.

Des essais en régime transitoire rapide au jet de plasma montrent que cette zone n'excède pas une épaisseur de 1 mm. Dans la zone cokéfiée, les réactions silice carbone s'amorcent vers 1200°C. Enfin, la température de la surface en ablation, pour des flux de l'ordre de 2000 KW/m^2 des frottements de 900 pascals et une température de paroi de 2200°C.

CONDUCTIVITE THERMIQUE - La conductivité thermique dans la zone en transformation est expérimentalement peu accessible. Nous procéderons ici par interpolation. La détermination de la conductivité aux températures inférieures à la pyrolyse commençante est très aisée, par des mesures en régime permanent sur des appareillages classiques. Pour obtenir la conductivité des résidus à haute température, nous procéderons de la manière suivante.

Une éprouvette d'Orthostralon 60 est chauffée sur un four à image d'arc sous un flux de 2000 KW/m^2 pendant un temps assez long (6 minutes). On élimine ensuite en surface, une zone superficielle de 2 mm, dans laquelle les réactions silice carbone ont, par suite de la longueur du temps d'échauffement, perturbé la structure du matériau. Des couples thermo électriques tungstène-tungstène Rhenium sont alors disposés dans l'éprouvette qui subit ensuite un nouveau chauffage intensif mais plus modéré que le précédent. Le flux est de 1500 KW. La température de paroi atteinte est supérieure à 1800°C. Le temps d'exposition est de 30 secondes. Ces conditions expérimentales ont été définies afin de laisser une certaine pureté à l'essai et de ne pas le perturber par

- des réactions silice carbone,
- un échauffement trop intensif de la zone froide de l'éprouvette, phénomène qui aurait entraîné une pyrolyse avec circulation de gaz.

./...

Ces échauffements sont toutefois du même ordre de grandeur que ceux rencontrés sur un corps de rentrée IRB4. Les essais ont été réalisés, et nous sommes en attente des résultats de dépouillement.

CHALEUR SPECIFIQUE EN FONCTION DE LA TEMPERATURE - Nous procéderons ici encore par interpolation entre les valeurs à températures modérées et à hautes températures. A basse température, nous définissons la chaleur spécifique par micro calorimétrie différentielle. Les mesures sont réalisées jusqu'à 300°C, température jusqu'à laquelle le matériau peut être considéré comme suffisamment stable. A haute température, des analyses de résidus après essais au jet de plasma, nous permettent de déterminer les proportions silice carbone, seuls matériaux restant en place .Les chaleurs spécifiques globales de ces résidus sont celles calculées à partir des tables de constantes physiques. L'interpolation (figure n° 2) n'offre ici, aucune difficulté.

VARIATION DE LA MASSE SPECIFIQUE EN FONCTION DE LA TEMPERATURE - Etant donné la difficulté d'une telle détermination en régime transitoire rapide, les expériences sont réalisées en régime transitoire lent. Nous examinerons par la suite si ces résultats sont adaptables à des échauffements rapides par leur application sur des essais globaux. Ils seront éventuellement retouchés et adaptés.

Les courbes obtenues montrent une faible dispersion (Figure n° 3). La bosse systématique observée aux environs de 900° correspond à la deuxième décomposition du polyamide. L'allure générale des courbes nous a incité à considérer une réaction globale qui peut analytiquement se mettre sous une forme de loi d'Arrhénius (Figure n°4).

Il existe une infinité de trios de constantes A,B,n qui satisfait correctement l'expérience. Nous choisissons celui qui vérifie au mieux les résultats dans la zone de forte pyrolyse et nous et nous adoptons

Ordre de grandeur de la réaction $n = 8$

$A = 9.10^{18}\ mn^{-1}$

$B = 2{,}575.10^{4}\ °K$

ce qui correspond à une énergie d'activation de 51,5 Kcal.
La valeur de n adoptée parait évidemment trop importante pour attacher à ces coefficients une signification thermo-chimique. Elle résulte probablement de l'hypothèse simplificatrice d'une réaction globale. Toutefois notre but était l'acquisition d'une forme analytique succeptible d'être introduite dans les calculs et cette loi satisfait à notre objectif.

L'adaptation de cette loi à des échauffements rapides a porté sur deux séries d'essais :

- la vérification des densités finales définies par dissection sur des éprouvettes chauffées par rayonnement infra-rouge (flux 200 KW/m^2, température maximale 1100°C) et au jet de plasma (flux 2000 KW/m^2, température de surface maximale 2200°C). On constate une concordance très satisfaisante (figures 5 et 6).
- la vérification sur des courbes de thermo-gravimétrie en régime rapide (8°C/s) réalisée par rayonnement infra-rouge (figure n° 7). Nous constatons ici aussi une bonne concordance.

Sans réserve de vérifications ultérieures, nous adoptons donc la loi analytique de la forme Arrhénius avec les coefficients que nous avons définis plus haut.

CHALEUR DE DECOMPOSITION - La chaleur de décomposition est définie comme étant la différence entre, l'enthalpie totale et la quantité de chaleur nécessaire à l'échauffement du matériau. Cette dernière est parfaitement définie par les deux caractéristiques que nous avons étudiées précédemment : la masse spécifique et la chaleur spécifique. Pour acquérir la chaleur de décomposition, il nous suffit donc de déterminer l'enthalpie totale, valeur accessible par analyse thermique différentielle.

La figure 8 montre l'allure générale des thermogrammes qui mettent en évidence :

- à 290°C, une inflexion d'allure exothermique qui correspond à une fin de polymérisation de la résine.
- à 440°C, un premier pic de décomposition du polyamide (pic endothermique) .
- à 500°C, le pic de décomposition de la résine.
- à 700°C, enfin le deuxième pic de décomposition du polyamide.

La figure 9 définit les valeurs relatives en fonction de la température de l'enthalpie totale et des chaleurs de décomposition. Nous admettons qu'à 800°C les décompositions sont pratiquement totales.

./...

Nous adoptons donc comme chaleur de décomposition totale 560 KJ/Kg à 800°C. Les vérifications en régime transitoire rapide sont peu accessibles. Nous nous trouvons ici en présence d'un cas où les valeurs définitives devront être précisées au cours de l'application des schémas de calculs, soit par balayage soit par l'utilisation de schémas inverses appliqués à des expériences globales d'ablation.

DETERMINATION DU GAZ MOYEN - En attendant l'aboutissement d'études thermochimiques permettant de prendre en compte toutes les réactions de dépolymérisation, nous nous attachons à la détermination d'un "gaz moyen". Cette hypothèse parait acceptable car, la zone de pyrolyse, nous l'avons vu, présente une très faible épaisseur et l'enthalpie de décomposition est suffisante pour prendre en compte l'ensemble des phénomènes. Les gaz sortant de la zone de pyrolyse pénètrent dans la zone cokéfiée à une température de l'ordre de 800°C et vont s'échauffer progressivement, c'est-à-dire que seuls pourront subsister, en quantité notable, l'hydrogène, l'oxyde de carbone et le méthane. Nous nous attachons donc, pour l'instant à l'étude de la composition d'un gaz de pyrolyse à 800°C. Malheureusement, l'échauffement de l'éprouvette ne peut pas être instantané, et aux faibles températures, des carbures benzéniques non crackés se condensent et échappent à l'analyse.

Actuellement nous récupérons dans ces essais réalisés en analyse thermique différentielle avec injection des gaz dans un chromatographe, environ 40 % de l'ensemble des volatils sous la forme (figure n° 10).

- Hydrogène ..... 68,9 %
- Azote ..... 4,4 %
- Oxyde de carbone .. 10,7 %
- Gaz carbonique .... 9,0 %
- Méthane ..... 7,0 %
- Poids moléculaire moyen 10,8

Les essais se poursuivent actuellement avec les objectifs suivants :

- augmentation de la vitesse de chauffe
- post chauffage des condensables afin de parfaire leur cracking jusqu'à 800°C.

STRUCTURE DU MATERIAU DE PYROLYSE - Cette structure est caractérisée par :

- le diamètre des porosités,
- les pertes de charge dans les matériaux.

Le diamètre des porosités ouvertes et leur répartition sont déterminées sur un porosimètre à mercure. Des mesures sont réalisées sur des matériaux ayant subi des échauffements rapides à différents niveaux de température. Les premiers essais nous ont montré des différences fondamentales entre les diamètres de porosités en fonction de la vitesse de chauffe. Pour des échauffements de l'ordre d'un corps de rentrée IRBm (flux 2000 KW/m^2, température de paroi 2200°C) le diamètre moyen des porosités ouvertes est de 10 microns. Les essais de mesure de perte de charge sont en cours d'exécution.

REACTIONS SILICE CARBONE - Nous les avons mises qualitativement en évidence :

- la figure 11 montre une éprouvette exposée au four à image d'arc. On constate la disparition de fibres de silice en profondeur.
- la figure 12 montre la même éprouvette vue de face après essais. On voit les trous précédemment occupés par les fibres de silice perpendiculaires à la surface ainsi que la trace de fils parallèles à la surface et qui ont disparu.
- la figure 13 montre une éprouvette essayée au jet de plasma. Cette éprouvette était constituée de couches alternées de tissus de polyamide et de résine. On constate (parties en creux) que la silice a été réduite, alors que les résidus cokéfiés du polyamide restent en place.
- enfin, nous constatons, au cours d'essais thermiques au jet de plasma, une inflexion systématique et importante des relevés thermocouples vers 1700°C. Cette inflexion disparait aussitôt que nous opérons sur un matériau constitué uniquement de polyamide et de résine phénolique.

Ces phénomènes sont très complexes et donnent lieu à des réactions chimiques qui aboutissent essentiellement à la formation de mono-oxyde de silicium, de Silicium, de carbure de Silicium et de dioxyde de carbone. Des essais sont envisagés afin de déterminer globalement la cinétique de ces réactions.

Pour l'instant, nous considérons uniquement la réaction jugée essentielle :

$$Si\,O_2 + C \rightleftharpoons Si\,O + CO + 144\ K\ Cal/mole$$

./...

CONCLUSIONS

Les travaux que nous venons d'exposer brièvement marquent un progrès considérable dans la représentation de l'ablation, par rapport aux schémas simplifiés qui ne serraient que de très loin les phénomènes réels. Outre les progrès dans les dimensionnements d'écrans thermiques, ils permettent la mise en place de procédures expérimentales représentatives qui seront précieuses lors de la conception de compositions nouvelles.

Bien sûr, les caractérisations actuelles laissent encore bien des incertitudes et certaines adaptations des données expérimentales sont encore nécessaires. Ces adaptations toutefois seront admissibles dans la mesure où les résultats des calculs seront interprétés avec prudence en gardant parfaitement conscience des approximations admises.

R E F E R E N C E S

1 - G. MOUNIS — 4th European Space Symposium Rome 1964.
"Méthodes et données nécessaires pour le calcul d'un écran thermique"
Traduction . NASATTS 294 Février 1965.
On Methods and Data required for heat shield calculation.

2 - H. LACAZE — La protection thermique par ablation.
Doc. Air-Espace n° 105 - 106 - 107 Juillet 1967.

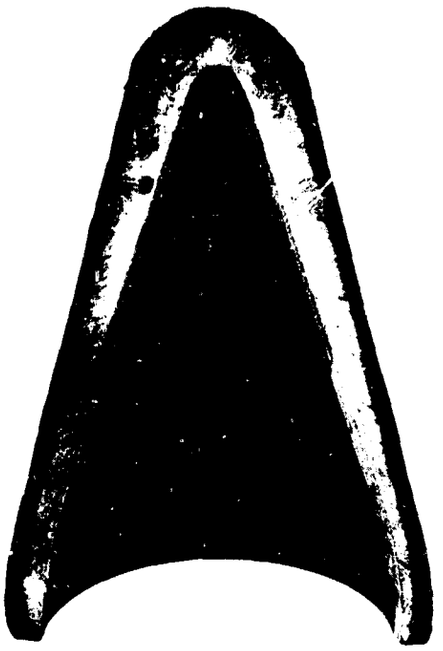

FIG 1. OGIVE VUE EN COUPE APRES ESSAI D'ABLATION

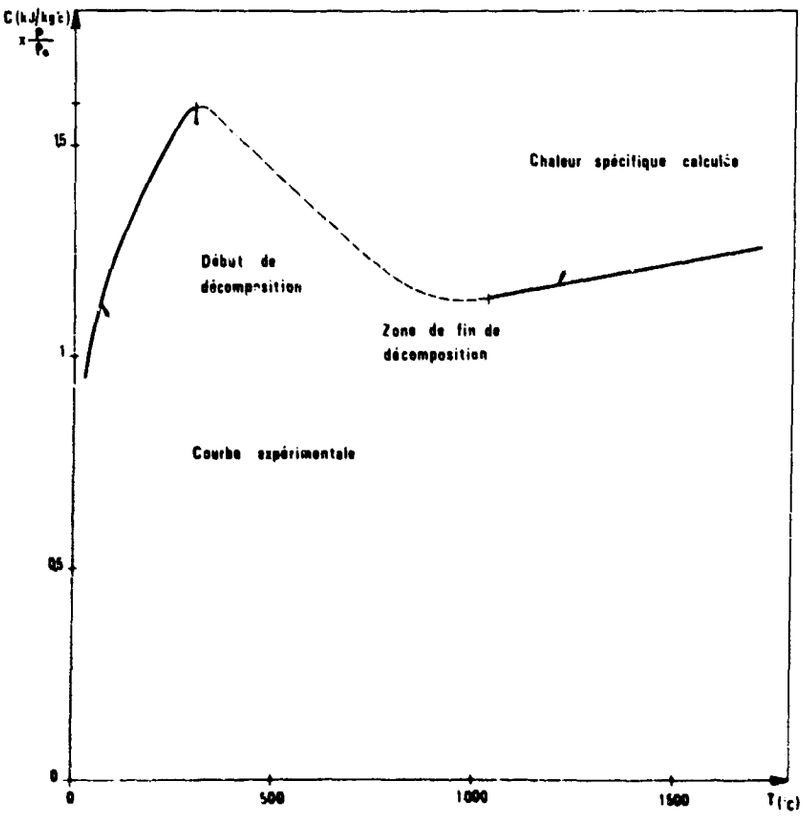

Fig 2. CHALEUR SPECIFIQUE APPARENTE

ORTHOSTRALON 60

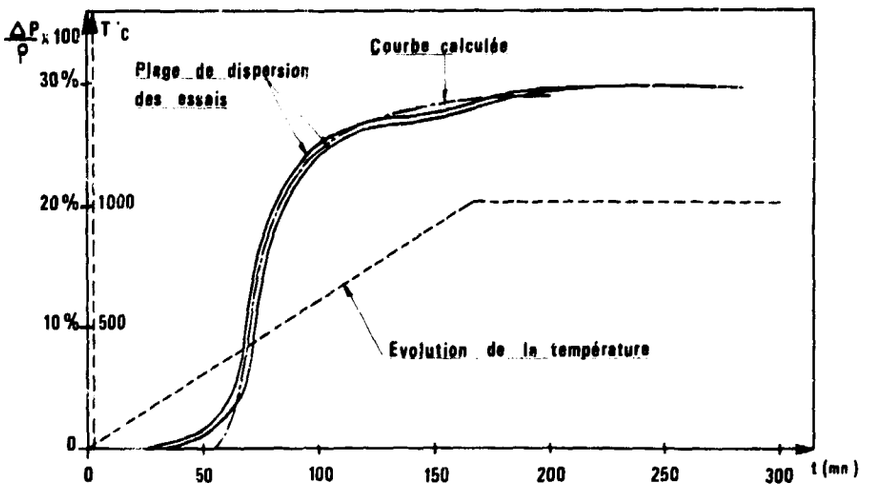

Fig 3. THERMOGRAVIMETRIE

CRTHOSTRALON 60

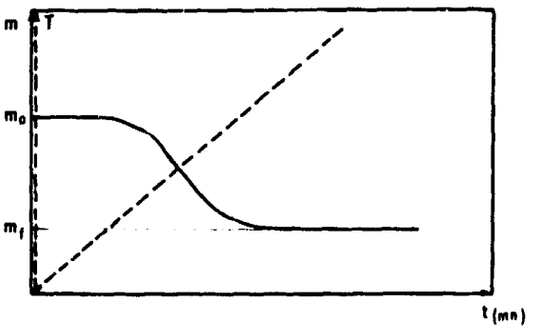

$$-\frac{1}{m_o}\left(-\frac{dm}{dt}\right) = \left(\frac{m-m_f}{m_o}\right)^n A\, e^{-B/T}$$

m = masse de l'échantillon à l'instant t

m_o = masse initiale de l'échantillon

m_f = masse final de l'échantillon

T = température (°K)

A = facteur de fréquence (mn^{-1})

$B = \frac{\text{énergie d'activation}}{\text{constante des gaz}}$ (°K)

n = ordre de la réaction

Fig 4. Loi du type ARHENIUS adoptée

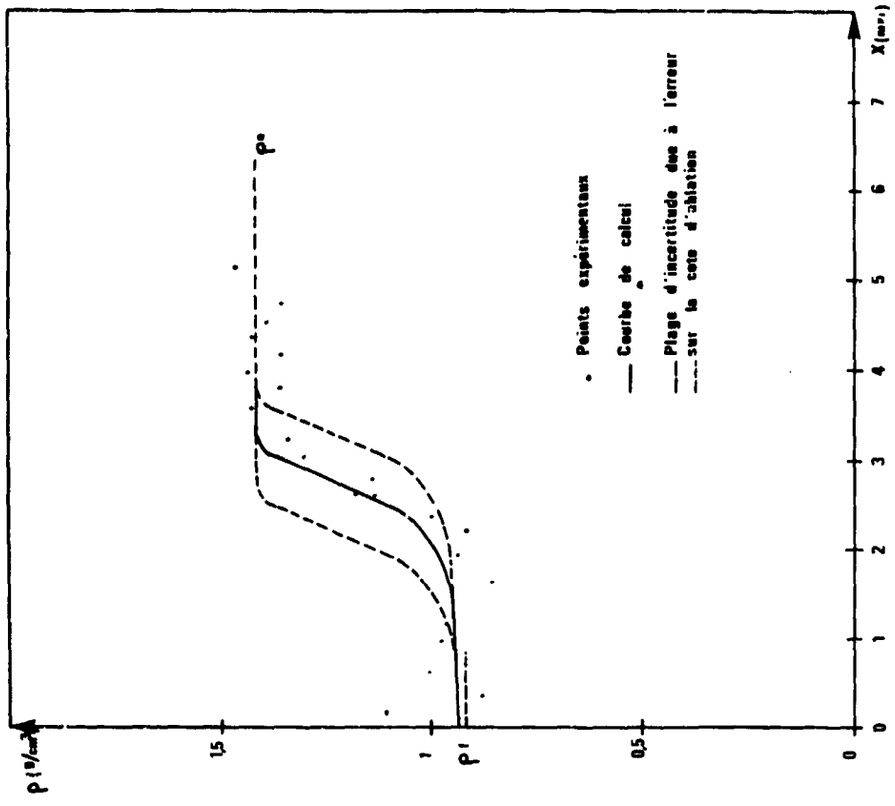

Fig.6 ESSAIS AU JET DE PLASMA

DENSITES APRES ESSAIS EN FONCTION DE LA PROFONDEUR

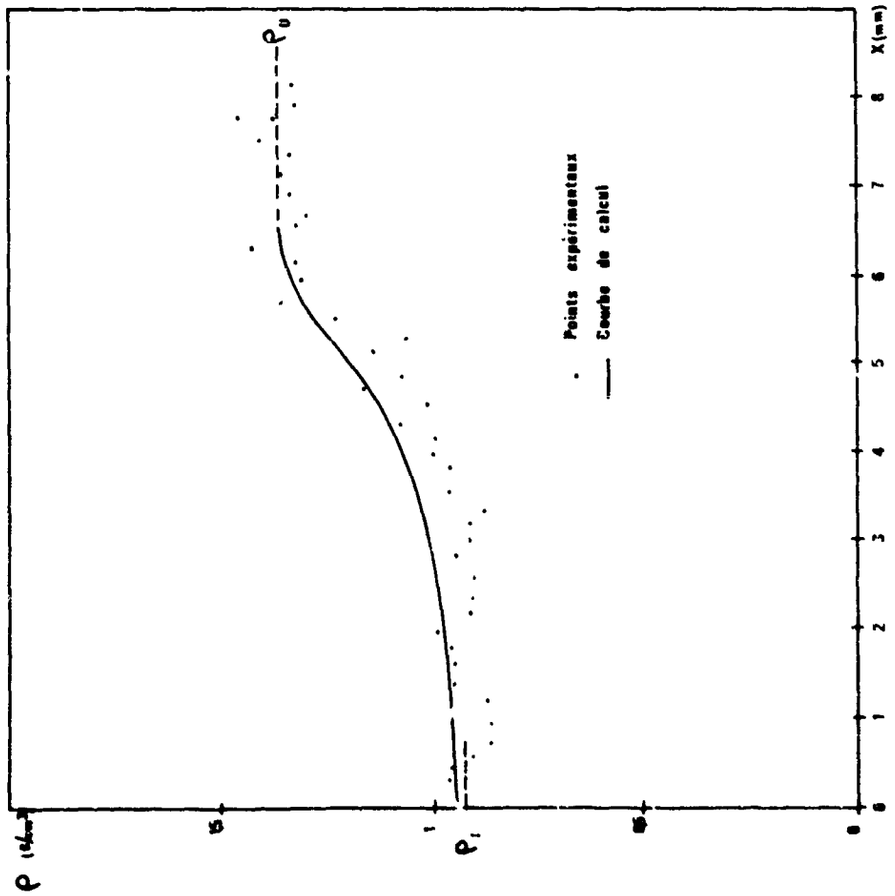

Fig 5. ESSAIS PAR RAYONNEMENT INFRA-ROUGE

DENSITES APRES ESSAIS EN FONCTION DE LA PROFONDEUR

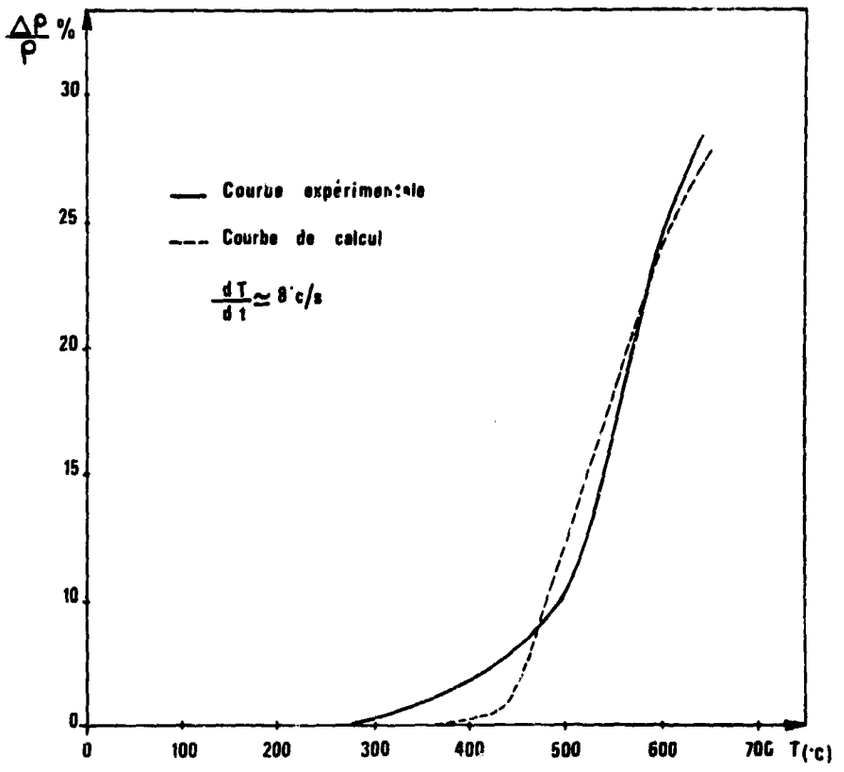

Fig 7. TERMOGRAVIMETRIE RAPIDE

(8°C/SECONDE)

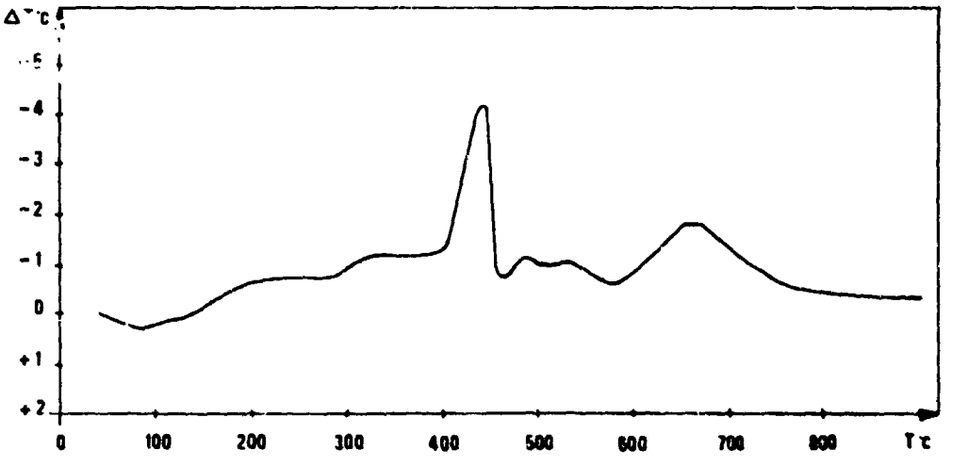

Fig.8 THERMOGRAMME D'ANALYSE THERMIQUE DIFFERENTIELLE DE L'ORTHOSTRALON 60

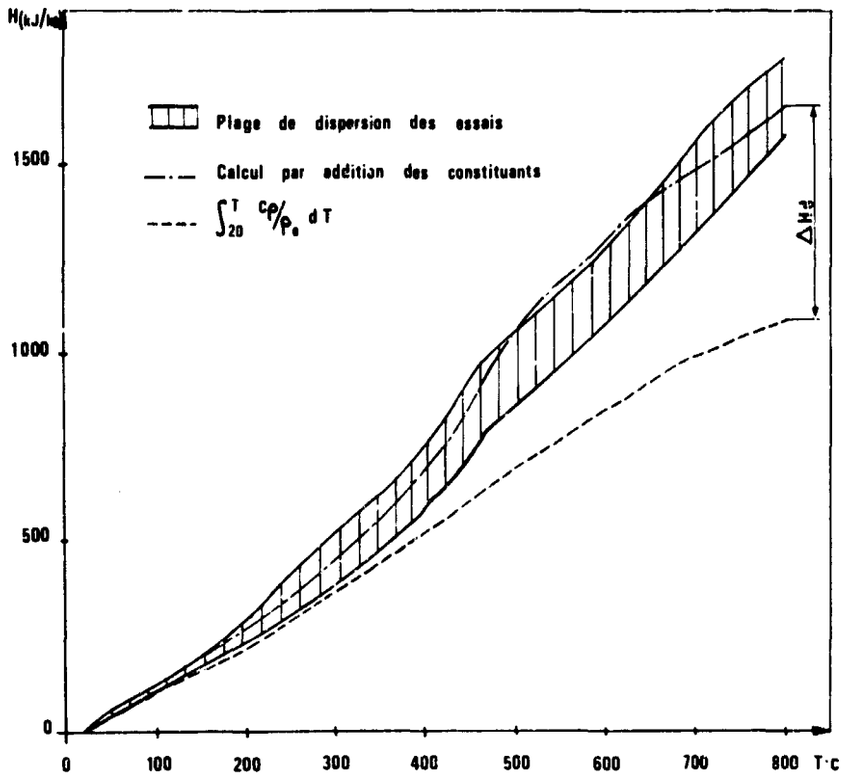

Fig 9. ENTHALPIE DE L'ORTHOSTRALON 60

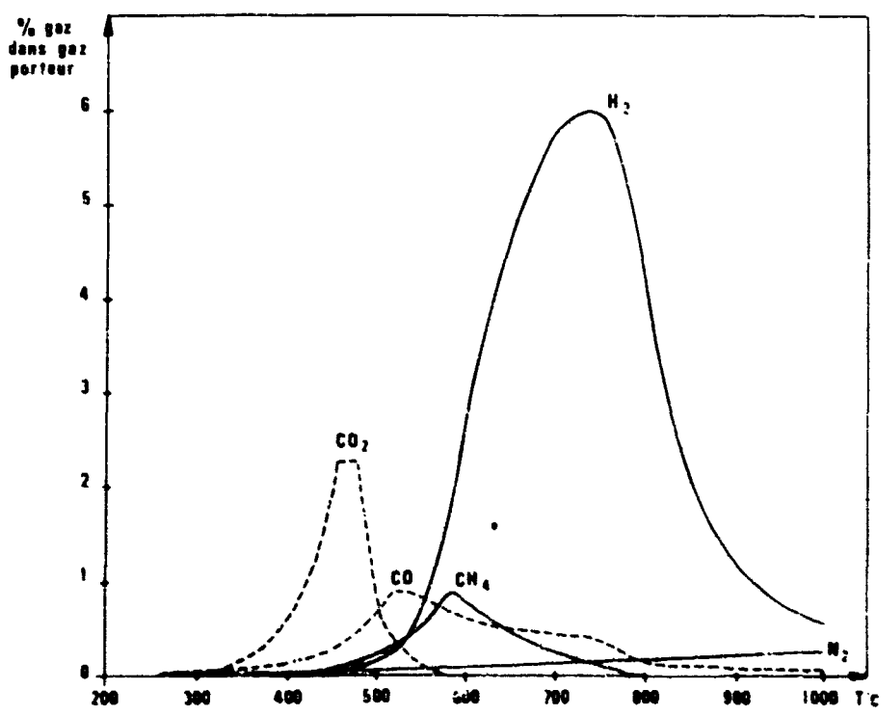

Fig 10. EMISSION DES GAZ

ORTHOSTRALON 60

FIG 11. ESSAI AU FOUR A IMAGE D'ARC
EPROUVETTE VUE EN COUPE

FIG 12. ESSAIS AU FOUR A IMAGE D'ARC
VUE DE LA FACE EXPOSEE

FIG 13. ESSAIS AU JET DE PLASMA
EPROUVETTE EN COUCHES ALTERNEES POLYAMIDE-
SILICE VUE EN COUPE APRES ESSAI

CHEMISORPTION ON REFRACTORY METALS

by

T. W. Haas
Aerospace Research Laboratories
Wright-Patterson Air Force Base, Ohio

SUMMARY

The chemisorption of reactive gases (H_2, N_2, CO and O_2) onto the low index planes of the refractory metals Cr, Mo, W, V, Nb, Ta and Re has been studied, using low energy electron diffraction. Trends observed are discussed and contrasted. It is suggested that strong covalent, directional bonds are responsible in many cases for the structures observed, rather than adsorbate-adsorbate lateral interactions.

MANY STUDIES OF THE chemisorption of gases onto refractory metals have been carried out over the past 50 years or so. Despite the large amount of effort put into such studies a really satisfying knowledge of the chemisorption process is lacking. If one looks at the development of other areas of chemistry and physics one finds that great progress was made following elucidation of the elementary structure and the energetics of the systems being studied. In the case of surface studies a fair amount of reliable information exists on the energetics of gas-solid interactions, although many such measurements were carried out on poorly defined systems. A real lack of structural information exists and this in turn inhibits attempts to understand the kinetics and energetics of chemisorption in terms of fundamental parameters. In recent years widespread use of low energy electron diffraction (LEED) (1) as well as field electron and field ion microscopy has improved our position on the structural aspects of surface studies but a lack of a detailed theory for LEED intensity variations prevents unequivocal structure determination. The studies to be reported here were carried out principally using LEED and represent an attempt to gain some detailed knowledge of chemisorbed structures by studying a variety of crystal faces of a number of refractory metals. The metals studied were V, Cr, Mo, W, Nb, Ta which are all body centered cubic and Re which is hexagonal close packed. Thus we are able to gain a certain amount of information on the importance of crystal structure, chemistry of adsorbate, and lattice constant effects, by studying the interaction of simple reactive gases (CO, O_2, CO_2, H_2 and N_2) with several low index crystal planes of these materials. Table 1 gives some pertinent data on the arrangement of these elements in the periodic chart as well as their lattice constants (2). From a chemical standpoint one expects elements in the same group to give similar results, while for any given crystal plane one might expect some trend in behavior with the lattice constant if packing or orientation effects are important. The trends we are looking for include reactivity, similarities in chemisorbed structures and faceting.

Table 1. Arrangement of elements studied in periodic chart. Lattice constants for each material are shown in parentheses.

V B	VI B	VII B
V (3.03)	Cr (2.89)	
Nb (3.30)	Mo (3.14)	
Ta (3.30)	W (3.16)	Re
BCC		HCP

TECHNIQUE

EXPERIMENTAL. The LEED systems used in these studies were of the post-diffraction acceleration display type which are available commercially from Varian Associates. External electronic modifications to the system allowed measurements of the energy distribution of inelastically scattered electrons (3, 4). The samples used were all electron-beam three-pass zone-refined single crystals and were oriented, cut, and polished using standard metallographic techniques. In most cases the specimens were resistance heated and temperatures were measured by optical and infrared pyrometers. The gases used were reagent grade gases and purities during the chemisorption process were monitored with a quadrupole residual gas analyzer. With the exception of oxygen, background levels of residual gases were less than one part in 1000. For oxygen, carbon monoxide was always a problem and could only be kept at a level of one part in 300.

SURFACE PREPARATION. To insure that one is studying a surface free from large quantities of impurities one needs a surface chemical analysis, preferably carried out in-situ. In this work the technique of Auger electron spectroscopy (4, 5, 6, 7) was employed by using the LEED optics to measure energy distributions of inelastically scattered electrons. Common impurities found on these refractory metals after mild heating (500°C) in vacuo are S, N, Cl, O and C. S appears when virtually any metal is heated in vacuum and can be removed in most cases by simple heating to temperatures around 1000°C. A typical Auger spectrum from a contaminated V(110)surface is shown in fig. 1. The techniques for producing clean surfaces for the materials discussed here included high temperature heating, chemical reaction to produce volatile products with the impurities (e.g. oxidation) and argon ion bombardment followed by thermal annealing. Each material and crystal face must be treated individually; a technique which is effective for Nb is frequently not effective for Mo.

INTERPRETATION. The number of LEED studies has increased very rapidly in recent years (1). The technique is by now relatively familiar so only a few words will be said about

interpretation of data. The chemisorption of a gas onto a surface can be characterized by LEED in three ways. The simplest case obtains when the gas adsorbs in a crystalline layer on the surface having a different unit cell than the underlying substrate. In this case one gets a change in the diffraction pattern like that shown in fig. 2. This set of LEED patterns shows changes in the oxidation of a Mo(112) surface. The clean pattern is shown in fig. 2(a). Short exposure of this surface to oxygen produced the changes leading to fig. 2(b). The new spots are half way between the original spots in the vertical direction. Since the patterns reflect periodicity in reciprocal space, this new pattern represents a new unit cell in real space having twice the dimension in the vertical direction as the substrate, and no change in the horizontal direction. This new unit cell would be indexed in terms of the old unit cell as a (2x1) pattern (8). Further oxidation produces patterns which can be indexed as (2x2), (1x2), etc.

In some cases gases will adsorb onto a surface in such a way as to give no change in the size or shape of the diffraction pattern. Two cases can be distinguished here on the basis of how intensities of diffracted beams change. The measurement consists in following the brightness of one of the diffracted beams as the incident beam energy is scanned, using photometric techniques. The resulting plot is fairly complex and shows intensity maxima at many places not predicted on the basis of the simple kinematic diffraction theory that is used in X-ray work. No detailed discussion of these curves can be given here other than to point out that the ultimate aim of LEED, as with any diffraction experiment, is to use the experimental intensity variations to compare with predicted intensities for various proposed atomic arrangements. In fig. 3 a typical intensity curve is given for one of the diffracted beams from Nb(110) surface before and after the chemisorption of hydrogen (9). The point to notice is that the curve shows a distinctive change of shape after hydrogen is adsorbed. This indicates that the hydrogen is adsorbed in a crystalline layer on the surface but since no new diffracted beams appear it must be in a lattice which has the same size, shape and orientation as the underlying Nb(110). If CO is adsorbed onto the clean Nb(110) surface at room temperature, then again no new diffracted beams appear (10). In this case, however, there is no change in the shape of the intensity curve. What is observed is a general and steady decrease in intensity of all the features in this curve while the background intensity readily increases. This behavior is interpreted as due to an amorphous immobile layer of CO on the surface.

RESULTS AND DISCUSSION

The first point to make in discussing these results is that no correlation was found between structures of adsorbed layers and structures of underlying substrate; this includes both symmetry and lattice constant effects. Thus, Ta and W although both BCC crystals, with lattice constants 3.30A and 3.16A, give entirely different structures and reactivities. Conversely, V and Ta, also BCC crystals with lattice constants differing by 10%, give very similar results for the crystal faces studied so far. This suggests that correlations in structure and reactivity will follow rather closely the arrangement of materials by groups in the periodic chart. Reference to Table I then shows that V, Nb, and Ta should behave similarly while Cr, Mo and W should give similar results, with Re being altogether different. In most cases this is the behavior observed. A summary of many of the available results is given in Table 2. The W(110) work was reported in references (11, 12); the W(100) work can be found in (13, 14, 15, 16); the W(112) work is given in (17, 18). The remainder of the work was carried out in our laboratories and some of it was reported in (9, 10, 19, 20, 21, 22). Studies of Cr are not included in Table 2, but have been carried out in this laboratory for the Cr(110) and (100) surfaces (23). In this case a rather reversed behavior was obtained in that the (110) surface faceted into (100) planes so that the surface had a sawtooth-like appearance. The lattice constant for Cr is 2.89A which is considerably smaller than for Mo and W. In the BCC structure the (110) plane is the most densely packed and hence is expected to be quite stable, but apparently size effects in Cr cause the (100) surface to be more stable. The (100) surface of Cr parallels some of the results from the W and Mo(100) surfaces.

Re(0001) was found to be an unusual surface in that it showed very low reactivity. Oxygen adsorbs at room temperature to give a (2x2) structure but CO, N_2 and H_2 do not adsorb at any temperature from 25°C to 2000°C. In fact Re(0001) is one of the very few materials studied in this laboratory that will give good LEED patterns after cycling the LEED system to atmospheric pressure, with no heating or other treatment of the Re. Even many noble metals will not give LEED patterns under similar conditions.

A very noticeable trend is the tendency for CO to be adsorbed onto metal surfaces at room temperature in an amorphous immobile layer. In all cases reported here this is the result which obtains and indicates that there is a random filling of sites by the CO. There is in general more than one type of site involved as flash desorption experiments show. Heating a pre-adsorbed layer of CO on Mo or W in general causes some desorption and gives complex patterns from the CO still adsorbed on the surface. On V, Ta and Nb surfaces very good evidence from both LEED and Auger electron spectroscopy shows that heating preadsorbed CO causes a dissociation of the CO giving the various oxide patterns. The carbon appears to diffuse into the bulk or to cooler parts of the crystal.

Very little desorption of CO takes place. Thus heating V, Nb, Ta and also probably Cr, in CO, and probably in CO_2, environments causes these metals to begin to oxidize. Whether very thick layers of oxide could be built up and what their structures might then be was not investigated.

Nitrogen was not found to interact with the densest (i.e. the (110)) faces of any of these materials. It does not react with the (100) of (112) face of Mo, but does adsorb on W(100) and on the (112) face of Nb, Ta and W. With the Nb and Ta(112) surface a cubic nitride is formed on the surface in a faceted epitaxial layer with the facets paralliel to the {113} planes of the substrate.

Hydrogen does not adsorb on (110) Mo or W but does adsorb on all the other materials and crystal faces studied. It is interesting to note that hydrogen is a sufficiently strong scatterer of low energy electrons to produce new diffracted beams when adsorbed on surfaces as it does on the W and Mo(100) and Mo (112) surfaces. In most cases the interaction of hydrogen with these refractory metals is weak and it is easily removed by heating to about 400°C. In some cases the electron beam itself will destroy it.

Oxidation of these surfaces gives a variety of patterns. With coverages of less than one monolayer a great similarity in structures formed is noted between Mo and W and among V, Nb and Ta. For greater coverages a difference shows up between Mo and W for faces other than the (110). The result is that W facets into (110) planes while Mo does not. Apparently in the presence of oxygen the W(110) plane is very much favored thermodynamically but not so with Mo. The V, Nb and Ta surfaces studied thus far have shown no tendency to facet when oxidized.

What we have tried to point out, then, is the great similarity in reactivity and structure for materials in the same group in the periodic chart. The correlation is best with V, Nb and Ta, and is still good for Mo and W. If the correct model for adsorbed atoms on surfaces were one of ions or atoms sitting on the surface in region of minimum potential energy one would not expect to see this correlation. Instead, a very strong effect of directed covalent bonds is indicated. This suggests that, at least in submonolayer regions, calculations using the methods of crystal field theory might be very useful in determining atom locations and models which fit the experimental LEED data.

Table 2. Reactivities of Mo, W, V, Nb and Ta Surfaces. Fractions refer to coverage in monolayers; other nomenclature explained in text.

Plane Exposed \ Gas		O_2	N_2	H_2	CO
(100)	Mo	1/4, 1/2, 3/4, 1, complex; no facets	NA	NA	amorphous at room temp. complex with heat
	W	1/4, 1/2, 3/4, 1, complex; no facets	NA	NA	amorphous at room temp. complex with heat
(100)	Mo	no facets; c(4X4), c(2X2), complex	NA	1/4(m/4, n/2), 1	amorphous at room temp. c(2X2), complex
	W	c(2X2), 3/4 facets to (110)	1/2(c2X2)	1/2(c2X2), complex, 1	amorphous at room temp. (c2X2), 1
(112)	Mo	(2X1), (2X2), (1X2), (1X3), (4X4); facets	NA	(1X2)	amorphous at room temp. complex with heat
	W	(2X1), (1X1), (1X2), (1X3), (1X4); facets to (110)	complex	?	amorphous at room temp. c(6X4), (2X1), c(2X4) complex
(111)	Mo	facets	?	?	amorphous at room temp. facets to (433) with heat
	W	facets to (112) then to (110)	?	?	?
(110)	V	1/6, 1/3, complex	NA	(1X1)	amorphous at room temp heat dissociates CO giving various oxide patterns
	Nb	1/6, 1/3, complex	NA	(1X1)	" " "
	Ta	1/6, 1/3, complex	NA	(1X1)	" " "
(112)	Nb	(1X3) complex	amorphous at room facets with heat, cubic nitride grows	(1X1)	amorphous at room temp heat dissociates CO giving various oxide patterns
	Ta	(1X3) complex		(1X1)	" " "
(0001)	Re	(2X2)	NA	NA	NA

NA - No adsorption
? - No information

REFERENCES

1. J. J. Lander, "Recent Progress in Solid State Chemistry", (Pergamon Press, N. Y.) Vol 2, p. 26 (1965).
2. C. A. Hanpel, Ed., Rare Metals Handbook, (Reinhold Publishing Corp., N. Y.) 1961.
3. E. J. Scheibner and L. N. Tharp, Surface Sci. 8, 247 (1967).
4. P. W. Palmberg and T. N. Rhodin, J. Appl. Phys. 39, 2425 (1968).
5. J. J. Lander, Phys. Rev. 91, 1382 (1953).
6. R. E. Weber and W. T. Peria, J. Appl. Phys. 38, 4355 (1967).
7. L. A. Harris, J. Appl. Phys. 39, 1419 (1968).
8. E. A. Wood, J. Appl. Phys. 35, 1306 (1964).
9. T. W. Haas, J. Appl. Phys. 39, 5854 (1968).
10. T. W. Haas, A. G. Jackson, M. P. Hooker, J. Chem. Phys. 56, 3025 (1967).
11. L. H. Germer and J. W. May, Surface Sci. 4, 452 (1966).
12. J. W. May and L. H. Germer, J. Chem. Phys. 44, 2895 (1966).
13. J. Anderson and W. E. Danforth, J. Franklin Inst. 279, 160 (1965).
14. P. J. Estrup and J. Anderson, J. Chem. Phys. 45, 2254 (1966).
15. J. Anderson and P. J. Estrup, J. Chem. Phys. 46, 563 (1967).
16. P. J. Estrup and J. Anderson, J. Chem. Phys. 46, 567 (1967).
17. C. C. Chang and L. H. Germer, Surface Sci. 8, 115 (1967).
18. C. C. Chang, J. Electrochem. Soc. 115, 354 (1968).
19. T. W. Haas and A. G. Jackson, J. Chem. Phys. 44, 2921 (1966).
20. T. W. Haas, Surface Sci., 5, 345 (1966).
21. A. G. Jackson and M. P. Hooker, Surface Sci. 6, 297 (1967).
22. T. W. Haas, Proceedings 4th International Materials Symposium, (John Wiley & Sons, N. Y.) 1969.
23. J. T. Grant and T. W. Haas, Surface Sci., to be published.

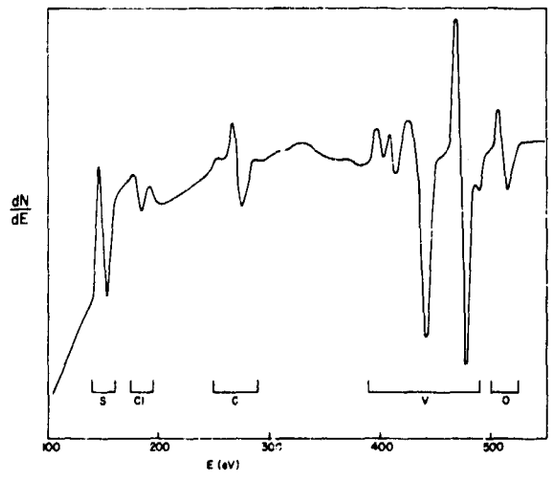

1. Derivative of the energy distribution, N(E), vs energy, E, of inelastically scattered electrons from V(110) sample. Some of the Auger peaks observed are labeled.

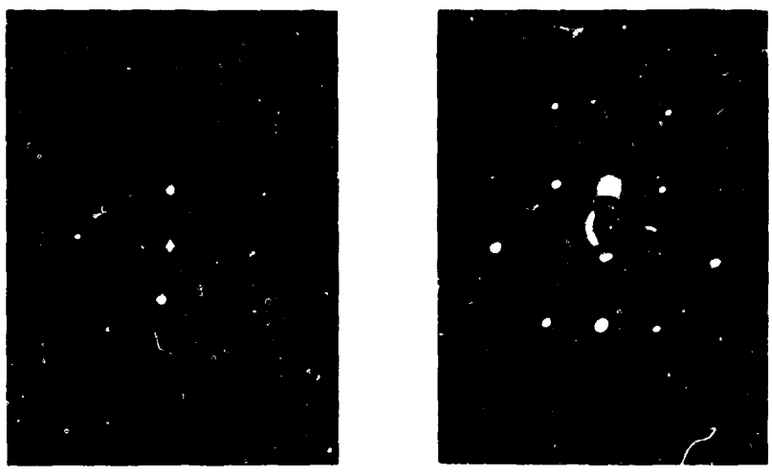

2. Changes in LEED patterns from Mo(112) due to oxidation a) Clean Mo(112) b) (2xl) oxide.

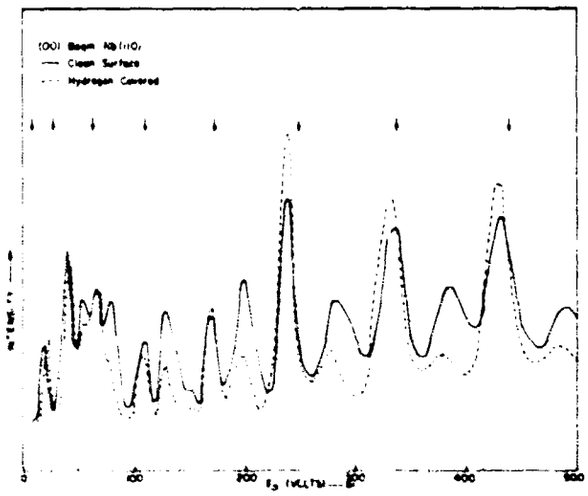

3. Changes in intensity of (00) beam from Nb(110) due to adsorption of one monolayer of hydrogen.

TRANSFERT DE CHALEUR ET DE MATIERE AU DESSUS D'UNE SURFACE CATALYTIQUE DANS UN ECOULEMENT TURBULENT

par

M. TRINITE et P. VALENTIN

Faculté des Sciences
Université de Rouen - FRANCE

SOMMAIRE

Des renseignements intéressants sur l'hypothèse d'égalité des viscosités, conductivités et diffusivités turbulentes, nous sont donnés par l'étude d'un transfert simultané de chaleur et de matière. Ce transfert a lieu lors d'une combustion catalytique de surface d'hydrogène dans l'air dans une couche limite turbulente préétablie au-dessus d'une plaque plane. Par des explorations fines des couches limites, nous calculons les différents flux au voisinage d'une discontinuité de type "échelon" à la paroi et nous examinons l'influence de la température de paroi. Les valeurs expérimentales de la conductivité et de la diffusivité turbulente mettent en défaut les hypothèses du nombre de Prandtl turbulent égal à l'unité juste après la discontinuité, le nombre de Lewis turbulent, par contre, n'est pas affecté par cette condition à la limite.

LES TRAVAUX EXPERIMENTAUX concernant les explorations de couches limites turbulentes avec transfert de chaleur et de matière sont rares, notamment dans le cas où les variations des propriétés physiques de l'écoulement avec la température ne peuvent être négligées. Dans le cas de discontinuité à la paroi de type "Step", les théories semi-empiriques classiques doivent être adaptées. D.B. Spalding (1) (2), dans le cas de propriétés physiques constantes donne une solution corrigeant avec une bonne approximation la théorie de Seban (3) et Rubesin (4) pour les abscisses proches de la discontinuité.

Nous nous proposons dans le cas d'un transfert simultané de chaleur et de matière par catalyse de surface d'hydrogène contenu dans de l'air à faible concentration, d'aborder expérimentalement la validité des hypothèses concernant les diffusivités turbulentes et les nombres de Prandtl et Lewis turbulents. Les premiers résultats concernant un transfert de chaleur seul, dans les mêmes conditions expérimentales, ont été donnés dans (5). A partir des équations de transfert, nous évaluons expérimentalement l'influence des différents termes dans l'intégrale première.

LES EQUATIONS

Nous considérons les équations de conservation a deux dimensions utilisées en écoulement laminaire compressible pour un mélange binaire de gaz (6). La pression statique est constante et la variation de la chaleur massique C_p en fonction de la température est négligée. Pour adapter ces équations au cas de l'écoulement turbulent, nous considérerons les valeurs moyennes des variables et nous remplaçons les paramètres moléculaires de transport par leur équivalent en turbulent. La faible vitesse de l'écoulement libre (30 m/s) permet de négliger la contribution de l'énergie cinétique dans l'équation de l'enthalpie, d'autre part l'apport d'enthalpie dû au flux de diffusion d'hydrogène peut être négligé compte tenu de sa faible concentration.

Dans ces conditions, x et y étant respectivement les coordonnées longitudinale et normale, les équations s'écrivent :

Equation de conservation

$$\frac{\partial}{\partial x}(\rho u) + \frac{\partial}{\partial y}(\rho v) = 0 \quad (1)$$

Equation de la quantité de mouvement

$$\rho u \frac{\partial u}{\partial x} + \rho v \frac{\partial u}{\partial y} = \frac{\partial}{\partial y}\left|(\mu+\mu_t)\frac{\partial u}{\partial y}\right| \quad (2)$$

Equation de l'enthalpie

$$C_p \rho u \frac{\partial T}{\partial x} + C_p \rho v \frac{\partial T}{\partial y} = \frac{\partial}{\partial y}\left|(k+k_t)\frac{\partial T}{\partial y}\right| \quad (3)$$

Equation de diffusion

$$\rho u \frac{\partial c}{\partial x} + \rho v \frac{\partial c}{\partial y} = \frac{\partial}{\partial y}\left\{\left|(\rho D)_l + (\rho D)_t\right| \frac{\partial c}{\partial y} + (D\rho)_l \frac{K_T}{T}\frac{\partial T}{\partial y}\right\} \quad (4)$$

avec comme conditions aux limites

$$\begin{array}{lll} y = 0 & x < L & T = T_0 \quad c = c_0 \\ & x > L & T = T_p \quad c = 0 \\ y = \infty & & T = T_0 \quad c = c_0 \end{array}$$

Introduisons les coefficients sans dimensions tels qu'ils sont définis dans (7) :

nombre de Prandtl effectif Pr_e

$$\frac{1}{Pr_e} = \frac{1}{Pr_e\left(1+\frac{\mu_t}{\mu}\right)} + \frac{1}{Pr_t\left(1+\frac{\mu}{\mu_t}\right)}$$

nombre de Schmidt effectif Sc_e

$$\frac{1}{Sc_e} = \frac{1}{Sc_l\ (1 + \frac{\mu_t}{\mu})} + \frac{1}{Sc_t\ (1 + \frac{\mu}{\mu_t})}$$

Les indices l et t se rapportant respectivement aux propriétés laminaires et turbulentes. Les équations (3) et (4) deviennent :

$$\rho u \frac{\partial T}{\partial x} + \rho v \frac{\partial T}{\partial y} = \frac{\partial}{\partial y} \left(\frac{\mu_t + \mu}{Pr_e} \frac{\partial T}{\partial y}\right) \quad (5)$$

$$\rho u \frac{\partial c}{\partial x} + \rho v \frac{\partial c}{\partial y} = \frac{\partial}{\partial y} \left\{\left(\frac{\mu_t + \mu}{Sc_e} \frac{\partial c}{\partial y}\right) + \frac{\mu}{Sc_l} \frac{K_T}{T} \frac{\partial T}{\partial y}\right\} \quad (6)$$

Remarque : la concentration c dans l'équation (6) est le rapport molaire n/N, en toute rigueur il faudrait prendre la concentration massique nm/NM, mais on suppose la masse molaire du mélange constante étant donné la faible teneur en hydrogène.

CONDITIONS EXPERIMENTALES

La soufflerie (schématisée sur la figure 1) est à circuit fermé afin de maintenir constant un taux d'hydrogène de 0 à 5 % dans de l'air ; le contrôle se fait au moyen d'un cathoromètre commandant une vanne électromagnétique, le taux peut ainsi être maintenu à 1 % près de la valeur nominale. La vitesse dans l'écoulement libre de la veine est d'environ 29 m/s. Le circuit comprend un condenseur afin d'éliminer la vapeur d'eau formée par combustion, un thermostat maintient constante la température d'entrée du fluide dans la veine. Les gradients de pression statique au-dessus de la plaque sont éliminés grâce à une paroi supérieure mobile.

Les conditions aux limite sont résumées sur la figure 2. La couche limite de concentrations et de température se développe dans la couche dynamique qui elle-même se développe depuis 36 cm. Une légère saillie à la jonction plaque-collecteur permet d'accélérer l'établissement du régime turbulent. La zone de réaction a une longueur de 15 cm, la plaque chauffante est en palladium, la combustion catalytique de l'hydrogène commence à partir de 250°C. Afin de maintenir constante la température de paroi, nous avons construit un dispositif de chauffage réglable par tranches dont le contrôle se fait par des thermocouples logés sous la plaque. L'origine fictive de la couche limite dynamique est déterminée expérimentalement par une méthode classique (8), le nombre de Reynolds en X = 0 est $6{,}2.10^5$.

Les mesures des valeurs moyennes sont effectuées au tube de pitot pour les vitesses, au thermocouple pour les températures (la soudure étant aplatie de façon à ce que la hauteur de mesure soit de l'ordre de $3/100e^{mm}$). Les mesures des fluctuations de températures de vitesse et de concentration sont effectuées au "thermoanémomètre", un fil chaud est commandé par un train d'impulsions, les détails de ce prototype seront donnés dans (9). Des corrections de mesure des concentrations moyennes près de la paroi sont nécessaires par suite de la présence de vapeur d'eau d'une part et d'autre part à cause de la hauteur d'aspiration de la sonde dans les régions à forts gradients.

RESULTATS

EXPLORATIONS DES COUCHES LIMITES. Les mesures de vitesse effectuées à température ambiante en l'absence de catalyse et de transfert de chaleur, exprimées en termes $u^+ = \frac{u}{u_\tau \sqrt{Cf/2}}$ et $y^+ = y \sqrt{Cf/2}\ \frac{\rho_e u_\tau}{\mu_e}$, se regroupent sur la loi de paroi avec des approximations du même ordre que celles faites dans les travaux de différents auteurs collectés par Kestin et Richardson (10). La figure 3 donne les valeurs du coefficient de frottement Cf/2 dans la zone d'étude ; en abscisse sur cette courbe nous avons inscrit la correspondance entre X distance à l'origine de la plaque catalysante et x distance à l'origine fictive de la couche limite dynamique ; entre parenthèses, nous donnons les valeurs de X^+ définies à froid, X^+ étant la distance sans dimension donnée par Spalding dans (1)

$$X^+ = \int_0^X \frac{\rho_e u_\tau}{\mu_e} \sqrt{Cf/2}\ dx \quad (7)$$

La transformation donnant X^+ dans le cas du fluide compressible reste à définir.

Sur la figure 4, nous donnons quelques profils de température exprimés en Θ/Θ_0, Θ étant l'écart entre la température locale et la température à la paroi : $\Theta = T_p - T$. La valeur moyenne de T_p est de 430°C. Nous avons également effectué des mesures sans transfert de matière pour T_p = 63°C, 210°C et 480°C. Les répartitions ont été faites à partir de X = 0,5 mm tous les 1,5 cm. La figure 6 représente un profil de fluctuations de vitesse et de température au près de la paroi mesuré simultanément pour T_p = 63°C.

Nous montrons sur la figure 5, les profils correspondants en concentrations, le taux d'hydrogène dans l'écoulement libre, c_0, était de 3 %. Pour que les mesures tout près de la paroi soient valables, il faut tenir compte des corrections. On peut montrer facilement que la concentration en vapeur d'eau à la paroi atteint une valeur double de c_0, donc 6 % à la paroi, elle décroit très vite avec y par suite de l'infériorité du coefficient de diffusion de la vapeur d'eau à celui de l'hydrogène, ainsi pour $c/c_0 = 0,5$, l'erreur tombe à 2 %. L'erreur provenant de la sonde d'aspiration qui n'est pas infiniment mince, est plus importante, nous pouvons la chiffrer par la formule suivante :

$$c(y)\ \text{mes.} \int_{y-\frac{e}{2}}^{y+\frac{e}{2}} \rho u\, dy = \int_{y-\frac{e}{2}}^{y+\frac{e}{2}} \rho u c\, dy$$

e étant l'épaisseur d'aspiration. Pour la valeur minimum mesurable de y, soit 0,09 mm, l'erreur atteint 30 %, elle devient négligeable pour y = 0,5 mm. En effectuant ces corrections, le profil c/c_0 passe par zéro pour y = 0, ce qui correspond à une combustion catalytique complète à la paroi.

INTEGRALES PREMIERES. Effectuons le bilan local correspondant aux intégrales premières des équations (5) et (6)

$$\frac{\mu+\mu_t}{Pr_e\ \rho_0 u_0} \frac{\partial \frac{\Theta}{\Theta_0}}{\partial y} = + \frac{\partial}{\partial x} \int_y^\infty \frac{\rho}{\rho_0} \frac{u}{u_0} \left(1 - \frac{\Theta}{\Theta_0}\right) + \left(1 - \frac{\Theta}{\Theta_0}\right) \frac{\partial}{\partial x} \int_0^y \frac{\rho}{\rho_0} \frac{u}{u_0} dy \quad (8)$$

$$\frac{\mu+\mu_t}{Sc_e\ \rho_0 u_0} \frac{\partial \frac{c}{c_0}}{\partial y} + \frac{\mu}{Sc_1} \frac{1}{\rho_0 u_0} \frac{K_T}{T} \frac{\partial T}{\partial y} =$$

$$= \frac{\partial}{\partial x} \int_y^\infty \left(1 - \frac{c}{c_0}\right) \frac{\rho}{\rho_0} \frac{u}{u_0} dy + \left(1 - \frac{c}{c_0}\right) \frac{\partial}{\partial x} \int_0^y \frac{\rho}{\rho_0} \frac{u}{u_0} dy \quad (9)$$

De ces équations, on tire les valeurs des conductivités totales $\varepsilon_h = k + k_t$ et diffusivité totale $\varepsilon_d = (\rho D) + (\rho D)_t$.

$$\frac{\mu+\mu_t}{Pr_e\ \rho_0 u_0} = \frac{\varepsilon_h}{\rho_0 c_p u_0} \quad (10)$$

$$\frac{\mu+\mu_t}{Sc_e\ \rho_0 u_0} = \frac{\varepsilon_d}{\rho_0 u_0} \quad (11)$$

L'intégration sur toute l'épaisseur de la couche limite nous donne le flux total sous forme du nombre de Stanton, St_h pour le flux de chaleur et St_d pour la diffusion.

$$St_h = - \frac{\partial}{\partial x} \int_0^{\delta_h} \frac{\rho}{\rho_0} \frac{u}{u_0} \left(1 - \frac{\Theta}{\Theta_0}\right) dy \quad (12)$$

$$St_d = - \frac{\partial}{\partial x} \int_0^{\delta_d} \frac{\rho}{\rho_0} \frac{u}{u_0} \left(1 - \frac{c}{c_0}\right) dy \quad (13)$$

δ_h et δ_d étant respectivement les épaisseurs de couche limite en température et en concentration. L'élimination de la thermodiffusion dans l'équation (13) provient de la forme de $K_T = -0,167\ c$, donc nul à la paroi et $\partial T/\partial y = 0$ pour $y > \delta_h$.

La thermodiffusion, en général négligée dans les écoulements turbulents, occupe une place notable dans le transfert auprès de la paroi pour des valeurs de X proches de la discontinuité. Nous avons tracé sur la figure 7 l'importance de la

thermodiffusion par rapport au flux total pour $X = 0{,}5$ cm, $X = 2$ cm, $X = 5$ cm et $X = 14$ cm. Le maximum est atteint à la fin de la sous-couche ; il a une valeur de 10 % au proche voisinage de l'origine du transfert, cette valeur tombe à 4 % en fin de plaque.

FLUX TOTAL A LA PAROI. Nous donnons sur la figure 8 les valeurs expérimentales de $\int_0^X St\, dx$ déduites des équations (12) et (13). En l'absence de catalyse le fluide étant de l'air pur, les points, pour les trois températures de paroi 63°C, 210°C et 480°C, se regroupent sur une courbe unique à 4 % près. Nous pouvons donc en déduire que l'influence des propriétés physiques variables ne change pas notablement le transfert total de chaleur à la paroi. La courbe théorique est déduite de la théorie de D.B. Spalding (2) en incompressible.

L'hypothèse fondamentale dans cette théorie est $\varepsilon_u^+ \left(\frac{du^+}{dy^+}\right) = 1$ où ε_u^+ est la viscosité totale sans dimension. Cette hypothèse permet de ramener l'équation de l'enthalpie à :

$$\frac{\partial \frac{\Theta}{\Theta_0}}{\partial X^+} = \frac{1}{\varepsilon_u^+ u^+} \frac{\partial}{\partial u^+} \frac{\varepsilon_h^+}{\varepsilon_u^+} \left(\frac{\partial \frac{\Theta}{\Theta_0}}{\partial u^+}\right) \qquad (14)$$

Pour obtenir la solution par calcul machine ou approchée sous la forme d'une série, il est nécessaire de supposer $\varepsilon_h^+/\varepsilon_u^+$ constant. Les valeurs de la fonction de Spalding $St_h\, Pr/|(1/2)\, Cf|^{1/2}$ ont été calculées pour différentes valeurs du nombre de Prandtl laminaire, par Gardner et Kestin (11) en supposant le nombre de Prandtl constant et égal à l'unité. A partir de ce calcul pour $Pr_L = 0{,}72$ et des valeurs de X^+ correspondant à X à froid comme cela est indiqué sur la figure 3, nous avons tracé la courbe théorique, elle s'écarte des points expérimentaux pour les faibles valeurs de X.

L'écart de la courbe expérimentale dans le cas où il y a catalyse peut s'expliquer par la variation du nombre de Prandtl, due à la présence de 3 % d'hydrogène dans l'air. En effet, si la viscosité du mélange varie d'une façon négligeable, il n'en est pas de même pour la conductivité K qui varie de 10 % pour 3 % d'H_2 d'après l'équation de Wassiljewa (12). Si l'on admet une affinité en $Pr_l^{-2/3}$ les deux courbes se regroupent avec une bonne approximation. La courbe supérieure regroupe les points expérimentaux correspondant au transfert de matière ($T_p = 440$°C). L'affinité avec la courbe théorique doit se faire suivant une puissance du nombre de Lewis $\frac{(D\rho)_l c_p}{k}$, D.B. Spalding dans (13) conseille une puissance voisine de 0,5 pour les faibles valeurs du nombre de Prandtl (ou Schmidt égal ici à 0,22).

CONDUCTIVITES ET DIFFUSIVITES TURBULENTES. La figure 9 rapporte les valeurs sans dimension de la conductivité turbulente $\varepsilon_h^+ - 1/Pr_l$ dans le cas où il n'y a pas de transfert de matière et pour $T_p = 63$°C. ε_h^+ est tiré expérimentalement des équations (8) et (10):

$$\varepsilon_h^+ = \frac{\varepsilon_h}{c_p \mu} = \frac{1 + \frac{\mu_t}{\mu}}{Pr_e} \qquad (15)$$

en abscisse, nous avons porté y^+ défini en incompressible (l'écart de température à l'écoulement libre étant faible, nous pouvons considérer les propriétés physiques constantes). La formule de Spalding (2) donnant $(\varepsilon^+ u - 1)$ dans les mêmes conditions apparaît comme une limite pour des X^+ suffisamment éloignés de la discontinuité. Par suite le nombre de Prandtl turbulent $Pr_t = (\varepsilon_u^+ - 1)/(\varepsilon_h^+ - 1/Pr_l)$ tend vers une valeur voisine de 1 pour ces mêmes X.

Sur la figure 10, nous avons porté les valeurs correspondantes de $\varepsilon_d^+ - 1/Sc_l$ et $\varepsilon_h^+ - 1/Pr_l$ pour X voisin de la discontinuité lors du transfert simultané de chaleur et de matière. ε_d^+ est déduit de la même manière que l'équation (15)

$$\varepsilon_d^+ = \frac{\varepsilon_d}{\mu} = \frac{1 + \frac{\mu_t}{\mu}}{Sc_e} \qquad (16)$$

Nous n'avons pas porté en abscisse la variable y^+ car on ne peut plus considérer le fluide comme incompressible, toutefois si nous supposons que le coefficient de

frottement à la paroi n'est pas affecté par la discontinuité en température, nous pouvons appliquer le changement de variables proposé par Baronti et Libby (14) en remplaçant y par $\int_0^y (\rho/\rho_0)\, dy$. Nous avons ainsi tracé la courbe théorique correspondant à celle de la figure 9, nous voyons que là encore les valeurs de ε_h^+ tendent vers cette limite avec une bonne approximation. Etant donné le voisinage de $(\varepsilon_d^+ - 1/Sc_1)$ et $(\varepsilon_h^+ - 1/Pr_1)$ le nombre de Lewis turbulent peut être considéré comme égal à l'unité, même tout près de la discontinuité.

CONCLUSION

Etant donné le très fort gradient qui règne après une discontinuité, l'hypothèse du nombre de Prandtl turbulent constant et égal à l'unité n'est pas valable. Les termes provenant des dérivées longitudinales généralement négligés dont les équations de la couche limite sont peut-être à prendre en considération pour les λ faibles, seule une étude détaillée des fluctuations de température et de concentration peut nous fournir les renseignements nécessaires. De la figure 10, nous pouvons déduire que le nombre de Lewis par contre peut être considéré égal à l'unité.

BIBLIOGRAPHIE

(1) - SPALDING D.B. : Intern. Develop. Heat Transfert, Amer. Soc. Mech. Engrs., Inst. Mech. Eng. 11, 1961, p. 439.
(2) - SPALDING D.B. : J. Heat and Mass Transfert, G.B. 7, 1964, p. 743-761.
(3) - SEBAN R. : "Experimental investigation of convective Heat transfert to air from a Flat Plate with a Stepwire discontinuous Surface Temperature". M.S. Thesis, Univ. of California, Berkeley (1951).
(4) - RUBESIN M.W. : The effect of on Arbitrary Surface Temperature Variation along a Flat Plate in on incompressible turbulent Boundary layer" (1951). N.A.C.A. TN 2345.
(5) - TRINITE M., BELORGEY M. et VALENTIN P. : C.R. Acad. Sc. Paris, t.266, 1968, p.664
(6) - SCALA S.M., BAULKNIGHT C.W. : Transport and thermodynamic properties in a Laminar Boundary layer. A.R.S. Journal, Vol. 29, 1960, p. 329.
(7) - ROSENBAUM H. : Turbulent compressible Boundary layer on a Flat Plate with heat Transfert and moss diffusion. A.I.A.A. Journal, Vol. 4, n° 9, 1966, p. 1548.
(8) - SOGIN H.A. and GOLSTEIN R.S. : Turbulent Transfert from isothermal Spanwire Strips on a Flat Plate. Amer. Soc. Mech. Engrs, New York 1961, p. 468-474.
(9) - CALVET P., LIOUSSE L. et TRINITE M. : Congrès de l'AFITAE, Toulouse 1969. (A paraître).
(10)- KESTIN J., RICHARDSON P.D. : Heat Transfert across turbulent, incompressible boundary layers. Int. J. Heat Mass Transfert, 1963, 6, 147-189.
(11)- GARDNER G.O., KESTIN J. : Calculation of the Spalding Functions over a range of Prandtl nombers. Int. J. Heat Mass Transfert, 6, 289-99 (1963).
(12)- REID and SHERWOOD : Properties of Gases and Liquids : Mac Graw Hill Book Company 1963.
(13)- SPALDING D.B. : Convective Mass Transfert. Edward Arnold LTD London 1963.
(14)- BARONTI P.O. and LIBBY P.A. : Velocity Profiles in Turbulent compressible Boundary Layers. A.I.A.A., 4, 1966, p. 193.

SYMBOLES

u Composante longitudinale de la vitesse (cm/s).
v Composante normale de la vitesse (cm/s).
x Distance le long de la plaque (origine fictive de la couche limite dynamique (cm).
X Distance le long de la plaque (origine à discontinuité) (cm).
L Valeur de x à la discontinuité.
y Distance normale à la plaque (cm).
ρ Masse volumique du mélange (g/cm^3).
C_p Chaleur massique du mélange (cal/g °C).
n Nombre de molécules de gaz combustible par unité de volume.
N Nombre de molécules de mélange par unité de volume.
C Concentration en gaz combustible = n/N
m Masse molaire du gaz combustible (g)
M Masse molaire du mélange (g)
T Température (absolue en °K sans autre précision).
θ Ecart à la température de paroi (T_p-T) (°C).
μ Viscosité moléculaire (poises)
μ_t viscosité turbulente (poises)
k Conductivité thermique moléculaire (cal/s °C.cm).
k_t Conductivité thermique turbulente (cal/s °C.cm).
D Coefficient de diffusion binaire (cm^2/s).
$(\rho D)_l$ Diffusivité laminaire (g/cm.s).
$(\rho D)_t$ Diffusivité turbulente (g/cm.s).
K_T Coefficient de diffusion thermique (sans dimension) (= 0,167c pour l'hydrogène).
δ_d Epaisseur de la couche limite de diffusion (cm).
δ_h Epaisseur de la couche limite thermique (cm).
ε_u Viscosité totale (poises).
ε_h Conductivité totale (cal/s °C.cm).
ε_d Diffusivité totale (g/cm.s).
u' Fluctuation de vitesse (cm/s).
θ' Fluctuation de température (°K).

- Grandeurs sans dimension

Pr Nombre de Prandtl
Sc Nombre de Schmidt
Le Nombre de Lewis
St Nombre de Stanton
Cf Coefficient de frottement à la paroi.

X^+ Distance $= \int_L^X \frac{\rho_0 u_0}{\mu_0} \sqrt{Cf/2}\, dX$

y^+ Distance $= y \frac{\rho_0 u_0}{\mu_0} \frac{1}{\sqrt{Cf/2}}$

u^+ Vitesse $= \frac{u}{u_0} \frac{1}{\sqrt{Cf/2}}$

$\varepsilon_u^+ = \frac{\varepsilon_u}{\mu}$

$\varepsilon_h^+ = \frac{\varepsilon_h}{C_p \mu}$

$\varepsilon_d^+ = \frac{\varepsilon_d}{\mu}$

- Indices

e dans l'écoulement libre.
p à la paroi
l se rapportant au laminaire
t se rapportant au turbulent
u se rapportant au transfert de quantité de mouvement
h se rapportant au transfert de chaleur
d se rapportant au transfert de matière.

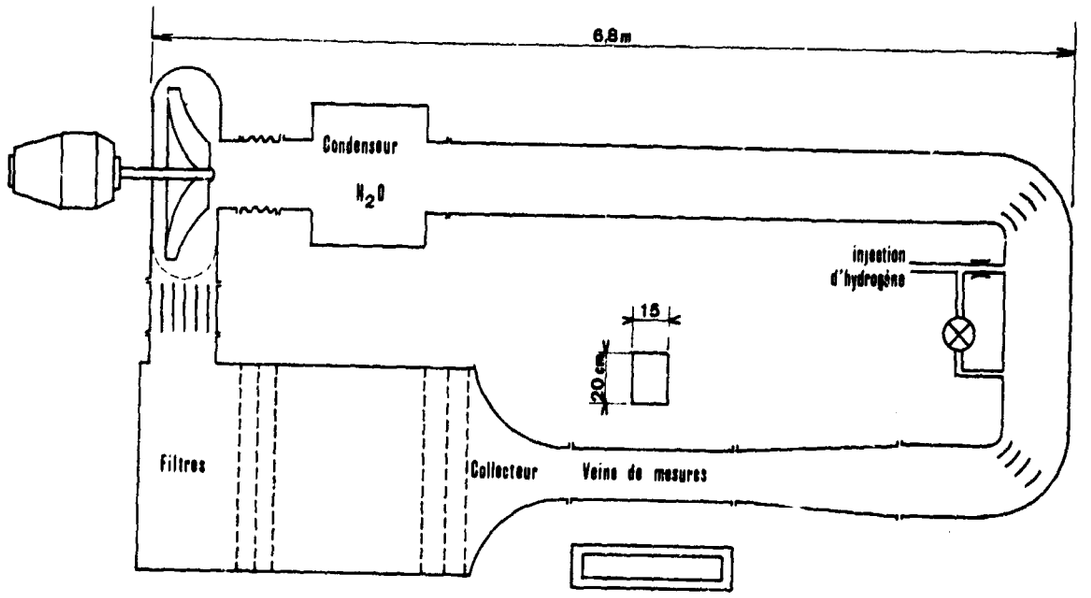

FIGURE 1 : Schéma du montage

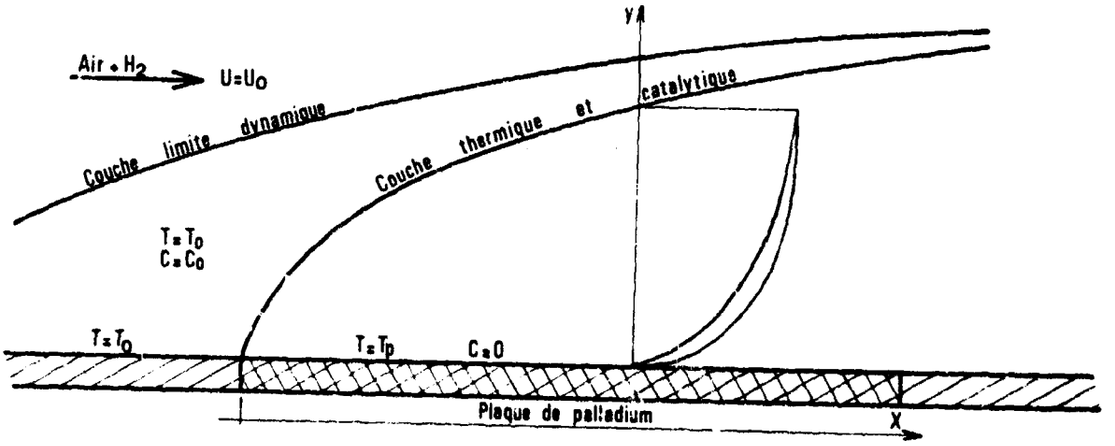

FIGURE 2 : Conditions aux limites

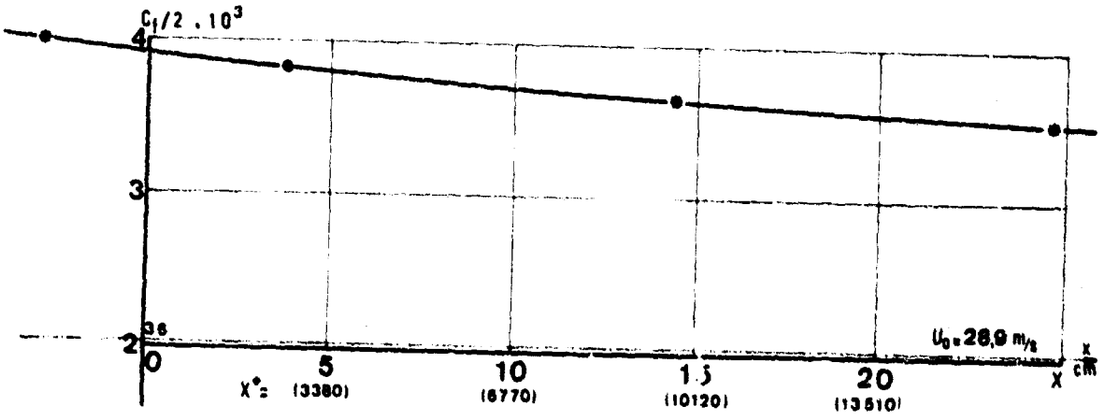

FIGURE 3 : Valeur du coefficient de frottement

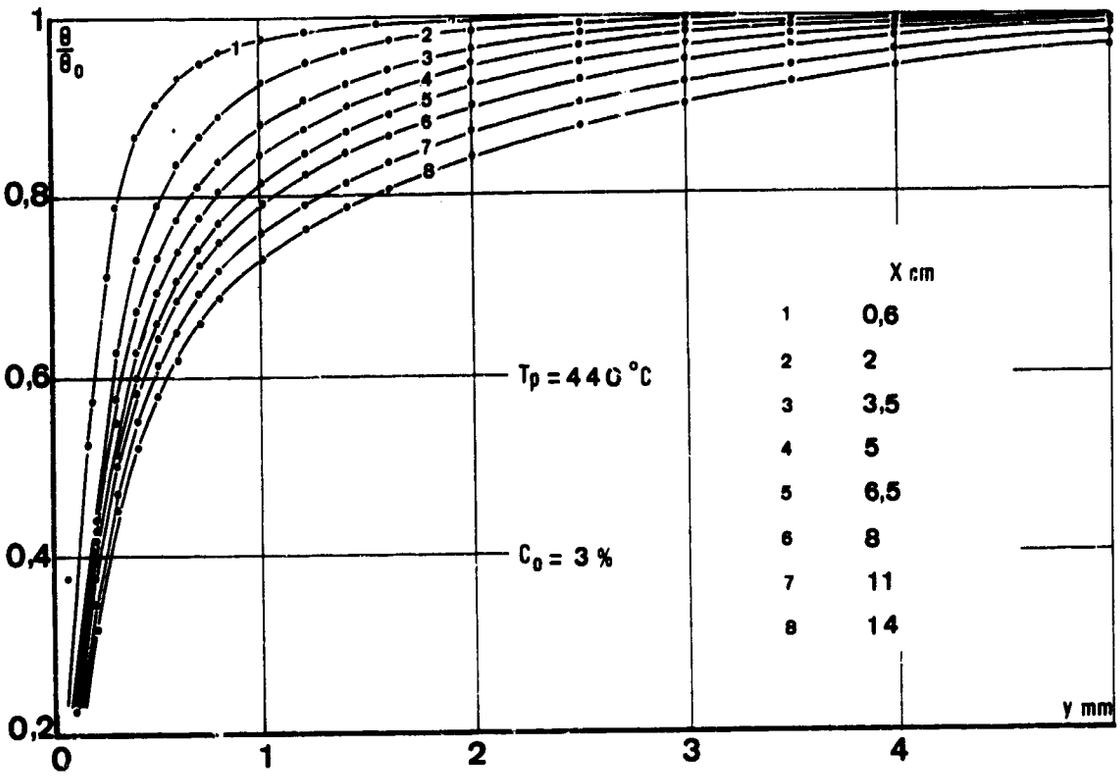

FIGURE 4 : Quelques points des explorations en température

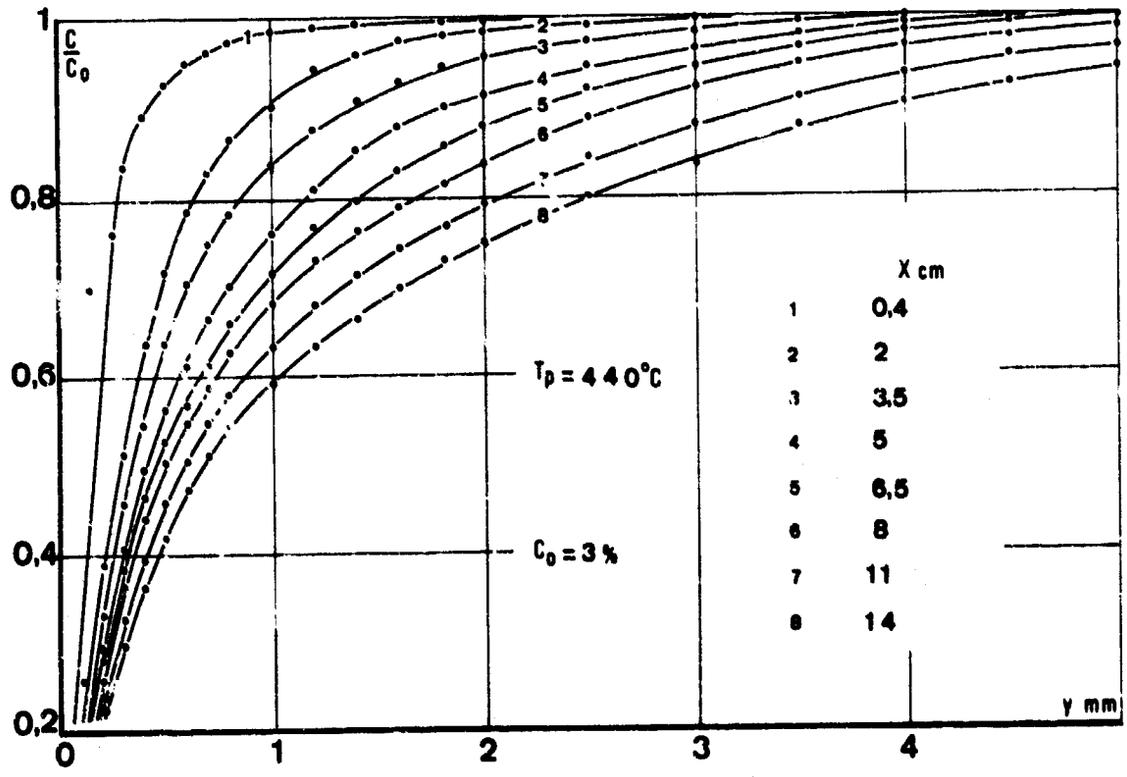

FIGURE 5 : Quelques points des explorations en concentration

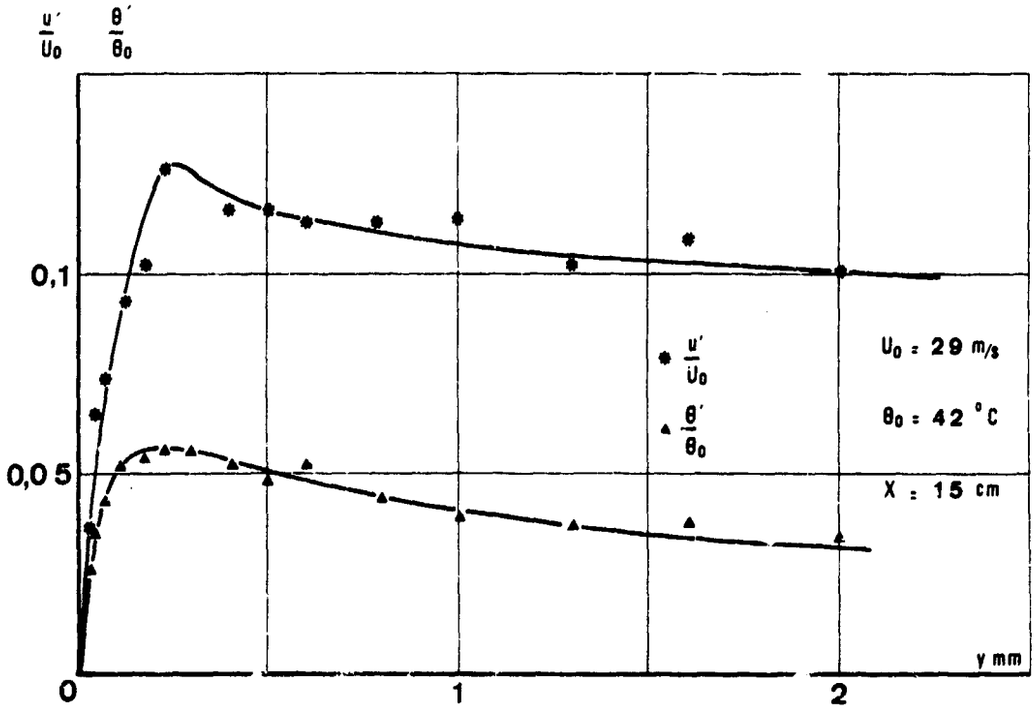

FIGURE 6 : Quelques mesures de fluctuations

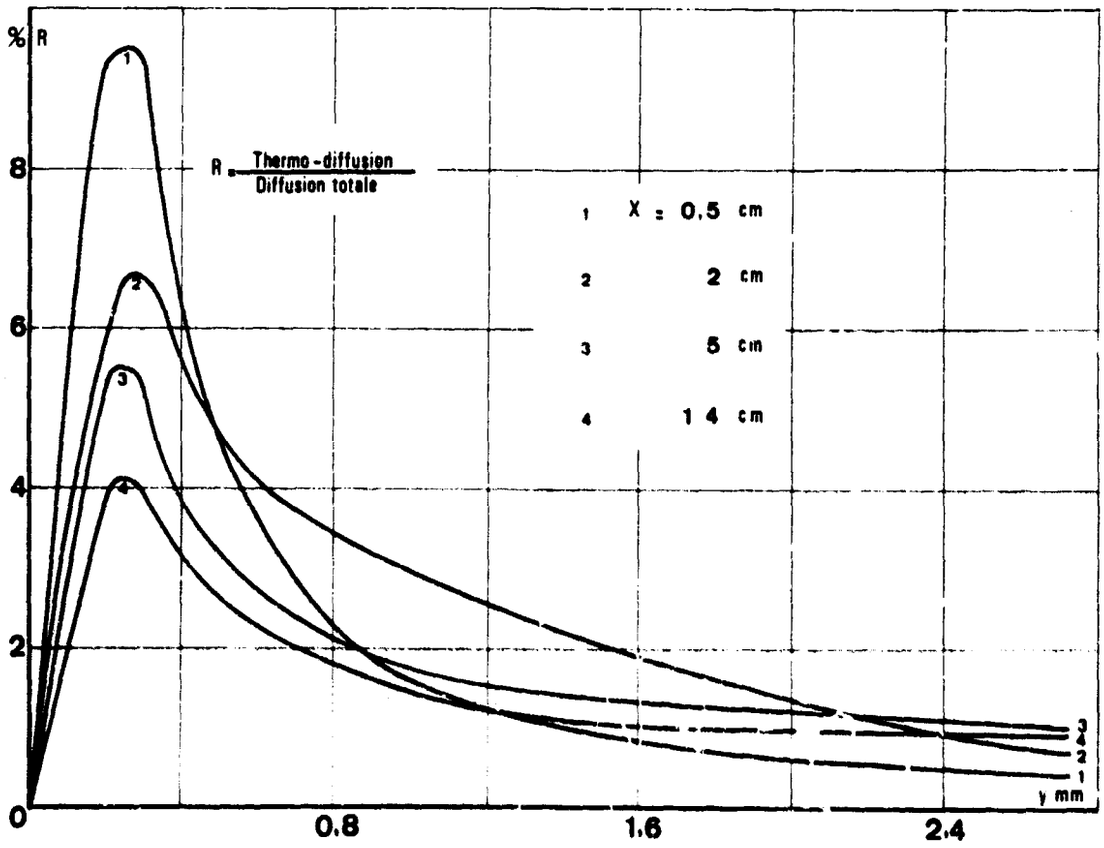

FIGURE 7 : Importance de la thermodiffusion

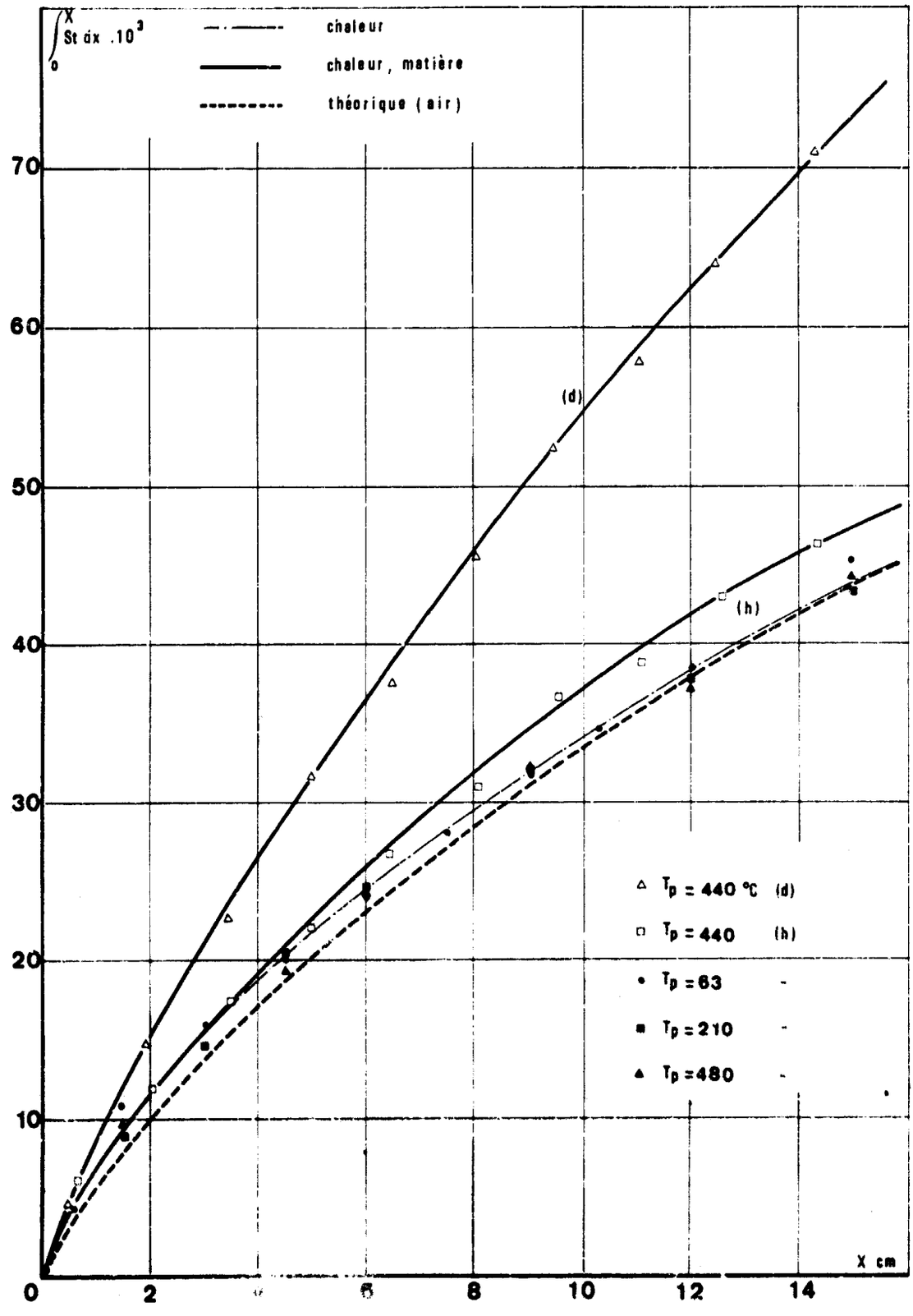

FIGURE 8 : Flux de [illegible]tal (indice h) avec et sans hydrogène et flux de diffus[illegible] (indice d).

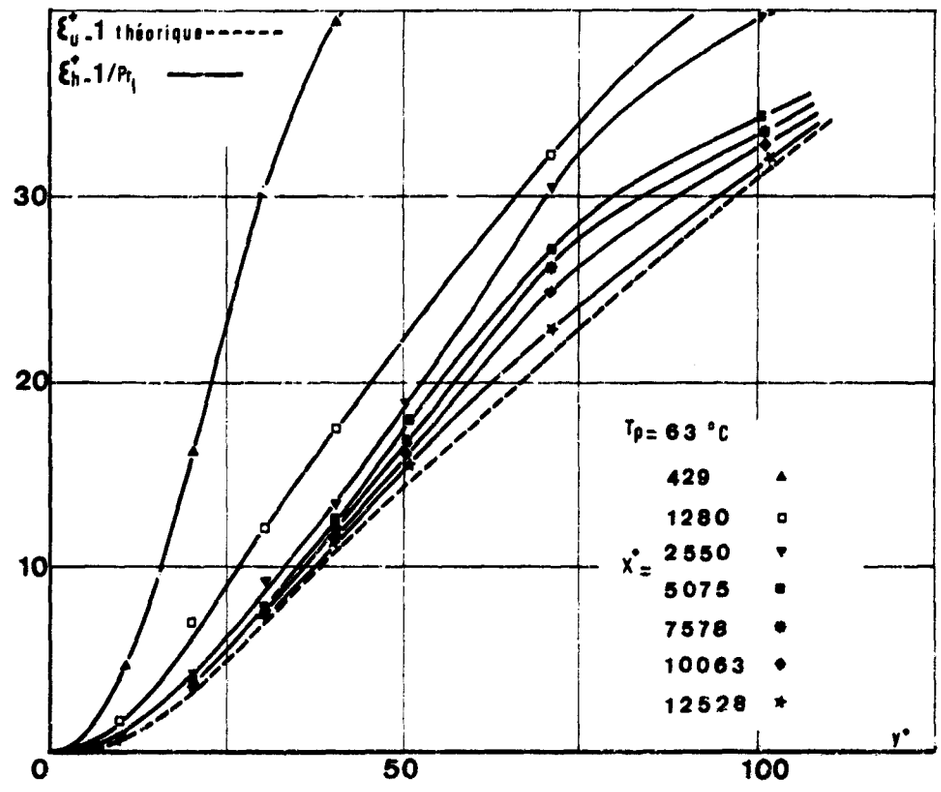

FIGURE 9 : Conductivité totale sans transfert de matière

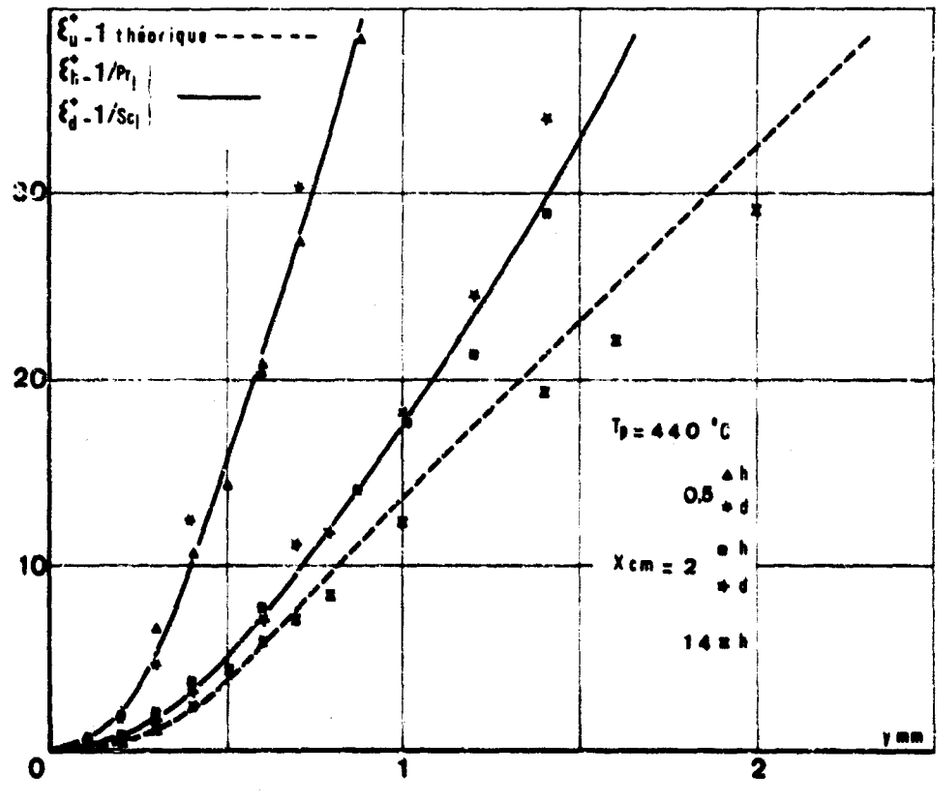

FIGURE 10 : Conductivité et diffusivité totale

A MODEL FOR THE INDEPENDENT REVERSIBLE POISONING OF POROUS CATALYSTS BY FEED STREAM IMPURITIES

F.Gioia, L.G.Gibilaro* and G.Greco Jr.,
Istituto di Principi di Ingegneria Chimica
Facoltà Ingegneria - Università di Napoli
Italy.

* Present Address
Department of Chemical Engineering
University of Technology
Loughborough
LEICS
ENGLAND

SUMMARY

A mathematical model is developed for the penetration of a reversible poison that is adsorbed on the catalyst surface; its application to isothermal reaction systems is discussed.

The model predictions are found to be in reasonable agreement with experimental results obtained for the hydrogenation of ethylene on a copper-magnesia catalyst in the presence of water vapour which acts as a reversible poison.

THE PROBLEM OF CATALYST DEACTIVATION is of current interest. In particular the optimisation of reactor performance in cases where the catalyst activity decreases with operating time has received much attention in the literature. The deactivation may be due to the presence of impurities in the feed stream or to reaction products both of which may either occupy the active sites or in some way impede access to them. In mechanistic studies of the process the usual assumption is that the poison species bonds irreversibly to the catalyst surface. The poison is generally considered either to advance as a step from the outer surfaces completely deactivating the regions it has reached (pore-mouth penetration), or to act uniformly throughout the catalyst particle (homogeneous poisoning).

But there exist many processes where the removal of a poison from the feed stream results in the complete restoration of catalyst activity. A theoretical basis for the study of such systems has great potentiality because, as demonstrated by ROSENMUND and ZETSCHE and quoted in reference [1], a poison can be used to improve catalyst selectivity; and, for the case of a suitable reversible poison, metered quantities can be added to the reactor feed stream to continuously control the product composition.

Such techniques are used industrially. An interesting example is the hydrocarbon reforming process carried out on a bifunctional catalyst of platinum supported on an alumina base. Dehydrogenation, dealkylation and dehydrocyclization reactions take place on the platinum sites; dealkylations, hydrocracking and isomerisations occur on the acidic sites; and two poisons, H_2S and H_2O, that block the platinum and acidic sites respectively are used, in trace quantities, to adjust the overall performance.

However to make the most of these techniques some basic model of the process is required: an industrial reactor subjected to a trace introduction of poison is likely to reveal transients lasting perhaps several days so that a purely feedback control system is out of the question. It is the purpose of this paper to present a model for the reversible independent poisoning of a porous catalyst by feed stream impurities to serve as a basis for such studies.

THE MATHEMATICAL MODEL

We consider the poison penetration to be quite independent of other components in the reaction system there being no competition for available active sites between the poison and reactant and product species. Rather the poison, when adsorbed on the catalyst surface, prevents reactants from reaching these centers.

A poison mass balance on an incremental element of a flat slab of porous catalyst yields:

$$D \frac{\partial^2 C}{\partial x^2} = \frac{\partial C}{\partial t} + \frac{\partial \bar{C}}{\partial t} \qquad (1)$$

With the assumption that the gas and adsorbed phase concentrations are always in equilibrium, they may be related by means of the Langmuir adsorption isotherm as follows:

$$\alpha = \frac{\bar{C}}{\bar{C}_{max}} = \frac{KC}{1+KC} \qquad (2)$$

In practice the gas phase accumulation term, $\frac{\partial C}{\partial t}$, is negligibly small compared with that in the adsorbed phase and can be ignored.

The adsorbed phase accumulation term, $\frac{\partial \bar{C}}{\partial t}$, is obtained by differentiating Eq (2). Substituting for this in Eq (1) yields the dimensionless equation

$$\frac{\partial^2 C_r}{\partial \xi^2} = \frac{1}{(1+KC_iC_r)^2} \cdot \frac{\partial C_r}{\partial \tau} \qquad (3)$$

where

$$C_r = C/C_i$$
$$\xi = x/R$$
$$\tau = Dt/R^2K\bar{C}_{max}$$

Boundary conditions for the introduction of poison at the pellet surface ($\xi = 0$) at time zero are

$$\tau = 0 \ , \quad C_r = 0$$
$$\xi = 0 \ , \quad C_r = 1$$
$$\xi = \infty \ , \quad C_r = 0$$

This last boundary condition requires some explanation. A more sensible way of writing it, from the physical point of view, would be

$$\xi = 1 \ , \quad C_r = 0$$

which is valid only for small τ , before any appreciable concentration of poison has reached the center; as solutions of the flat slab case are of practical utility at small times, where they can be applied to all pellet geometries, this is not unduly restrictive. Mathematically the two alternatives are virtually identical at small τ . The form chosen. however, has the advantage that it allows Eq (3) to be tackled by means of the similarity transformation

$$q = \xi \tau^{-\frac{1}{2}} \qquad (4)$$

which reduces it to the ordinary differential equation

$$\frac{d^2 C_r}{dq^2} + \frac{q}{2(1+KC_i C_r)^2} \frac{dC_r}{dq} = 0 \qquad (5)$$

subject to

$$q = 0 \ , \quad C_r = 1$$
$$q = \infty \ , \quad C_r = 0$$

The nature of the poison penetration is thus influenced solely by the parameter KC_i; the real time scale depends on the system constants D, R, K and C_{max} incorporated in the dimensionless time τ .

Figure (1) shows computer solutions of Eq (5) for the range of KC_i values of practical interest. The advantage of the similarity transformation is that, although a numerical solution is eventually resorted to, results for the full range of KC_i values can be expressed as a single family of curves; computation time is also greatly reduced.

The actual poison profiles within the pellet at discrete values of τ are readily obtained from Figure (1) by making use of the relationships of Eqs (2) and (4). Figures (2) and (3) show the poison concentration profiles in the gas phase and adsorbed phase respec tively for KC_i equal to 1.

The ordinate of Figure (3) provides a direct measure of the fraction of catalyst surface, α , blocked by poison. In the steady state this is given by $KC_i/(1+KC_i)$; so that the catalyst can retain considerable activity in the presences of a reversible poison for small values of KC_i.

LIMITING VALUES OF KC_i

KC_i LARGE. Figure (4) illustrates how the penetration is affected by the parameter KC_i. For KC_i larger than about 10 the poison advance approaches that of a step and pore-mouth penetration can be assumed without significant error. This follows from a consideration of Eq (2): at the outer regions of the pellet, where $C \triangleq C_i$, α approaches unity; it is these almost totally poisoned regions that will most affect the catalyst performance. This means that solutions of irreversible pore-mouth poisoning problems (for example those of SADA and WEN [2] on selectivity in double reaction systems) can be applied in this case.

KC_i SMALL. The linearised version of Eq (3) which applies for

$$KC_i \ll 1$$

has been considered by GIOIA [3] . It is

$$\frac{\partial^2 C_r}{\partial \xi^2} = \frac{\partial C_r}{\partial \tau} \qquad (6)$$

which represents purely diffusional transport of poison governed by a pseudo diffusivity given by

$$D_p = \frac{D}{KC_{max}} \qquad (7)$$

which in practice is very much smaller that D. The solution of Eq (6), subject to the same boundary conditions as for Eq (3), is

$$C_r = \text{erfc}\left(\frac{\xi}{\sqrt{4\tau}}\right) \qquad (8)$$

which agrees with the numerical solution shown in Figure (1) for $KC_i < .1$

Figure (1) also indicates that this analytical solution can be used as a reasonable approximation for KC_i values up to about 1.

SPHERICAL PELLETS

We have obtained solutions to the general model (Eq (1)) valid for all geometries at small τ . For all but small values of KC_i, solutions at larger values are of little practical importance because of the large drop in catalyst activity that would then obtain. However, for systems where small quantities of a reversible poison are introduced to adjust selectivity, the long time poison concentration response is of some interest; and of particular interest is the time required to reach a new steady state.

We consider therefore finite spherical pellets and small values of KC_i. The model equation for this situation is given by:

$$\frac{\partial^2 C_r}{\partial \xi^2} + \frac{2}{\xi}\frac{\partial C_r}{\partial \xi} = \frac{\partial C_r}{\partial \tau} \qquad (9)$$

subject to

$$\tau = 0 \ , \quad C_r = 0$$

$$\xi = 0 \ , \quad C_r = 1$$

$$\xi = 1 \ , \quad \frac{\partial C_r}{\partial \xi} = 0$$

Eq (9) can be readily solved by means of the Laplace transform. The transfer function solution is given by

$$C_r(s) = \frac{\text{Sinh}\sqrt{s(1-\xi)^2}}{(1-\xi)\ \text{Sinh}\sqrt{s}} \qquad (10)$$

and the time domain solution for the step input by

$$C_r = -2\sum_{n=1}^{\infty}(-1)^n \frac{\text{Sin}(n\pi(1-\xi))}{n\pi(1-\xi)} \cdot (1 - \exp(-n^2\pi^2\tau)) \qquad (11)$$

To get an idea of the time required to reach the steady state it is not necessary to compute Eq (11). The average response time can be obtained from the transfer function (Eq(10)) by the well known technique of differentiating with respect to s and setting s equal to zero. This gives the mean response time to be

$$\tau\ (\text{mean}) = \frac{\xi}{6}(2-\xi) \qquad (12)$$

Eq (12) tells us that the pellet surface ($\xi = 0$) instantaneously reaches the concentration of the surroundings, and that at the centre the mean response occurs at $\tau = 1/6$.

For practical purposes the steady state can be said to have been reached at about three times the mean response time at the pellet centre. So that

$$\tau\ (\text{steady state}) \simeq 0.5 \qquad (13)$$

APPLICATION TO ISOTHERMAL SYSTEMS

One of the basic postulates of the proposed model is that the poison penetration is unaffected by the presences of other reaction components. This has enabled the equations for poison penetration to be derived independently of the chemical reactions taking place within the catalyst pellet. We now consider briefly the application of the model to isothermal reaction systems.

For an incremental length of catalyst pellet the following material balance can be written for each component in the reaction system.

Net Rate of entry by diffusion	−	Net Rate of disappearance by reaction	−	Net rate of accumulation	+	Net rate of entry by convection	=	0

The convection term can usually be ignored except where large volume changes accompany the reactions. The accumulation term is included because the poisoning process is essentially an unsteady state phenomenon. However, as the rate of change of catalyst activity may be generally regarded as low, it is reasonable to ignor reaction transients in the component mass balances. We are left, therefore, with the first two terms of the preceeding mass balance for each reaction component; it remains to solve these equations at discrete τ values to determine how the catalyst performance varies with poisoning time. A specific example will make this clear.

Consider the first order isothermal scheme

$$A \xrightarrow{k_A} B \xrightarrow{k_B} C$$

taking place in spherical catalyst pellets and in which only the reaction $B \rightarrow C$ is affected by a reversible poison suddenly included in the feed stream. In view of the proceeding discussion a dimensionless material balance on component B may be written

$$\frac{d^2C_B}{d\xi^2} + \frac{2}{\xi}\frac{dC_B}{d\xi} + \frac{D_A}{D_B}\phi_A^2 C_A - \phi_B^2 (1-\alpha)C_B = 0 \qquad (14)$$

where the Thiele modulus is given by

$$\phi_i = R\sqrt{\frac{k_i a_o}{D_i}} \quad , \quad i = A, B$$

Similar equations may be written for components A and C.

α is the fraction of surface area poisoned and is a function of both ξ and the poisoning time τ. Functional and numerical forms for α at discrete values of τ have been derived in the preceding section so that the equations can be readly solved by computer methods to yield the catalyst activity and selectivity as functions of τ.

For this example these may be defined as:

$$\text{Activity} = D_A \left.\frac{d C_A}{d \xi}\right|_{\xi=0} \qquad (15)$$

which provides a direct measure of the rate of consumption of reactant A and

$$\text{Selectivity} = \frac{D_B \left.\frac{dC_B}{d\xi}\right|_{\xi=0}}{D_C \left.\frac{dC_C}{d\xi}\right|_{\xi=0}} \qquad (16)$$

which measures the relative rate of production of B to C.

Clearly the activity is unaffected by the poisoning of the second reaction; the selectivity however increases with poisoning time reaching a maximum when the steady state is attained. For a more complicated reaction scheme (for instance one consisting of a number of reactions of the type considered above) the performance criteria may not be capable of such compact expression as in Eqs (15) or (16) but once they are defined the basic computation required remains essentially the same.

EXPERIMENTAL

The system studied experimentally was that of ethylene hydrogenation on a copper-magnesia catalyst.

$$C_2H_4 + H_2 \longrightarrow C_2H_6$$

Under the experimental conditions maintained this reaction may be safely assumed to be first order in hydrogen [4]. Water vapour was used as the reversible poison.

The reader is refered to the paper by GIOIA [5] for details of the experimental

method and of the evaluation of the results. Briefly, two series of kinetic experiments were carried out in a differential reactor; both consisted of the sudden introduction of poison into the feed stream and the measurement of the subsequent decrease in conversion as a function of time.

For the first series of runs the catalyst was in the form of a powder of sufficiently small particle size to effectively eliminate diffusional resistances: the gas phase concentrations of all components (including the poison) within the catalyst grains were substantially the same as those in the surrounding gas.

These runs showed the poison adsorption to be very rapid (an important finding as the proposed model implicitly postulates instantaneous adsorption), and enabled the Langmuir parameter, K, to be calculated.

The second series of runs was carried out with larger catalyst particles. However experimental conditions were arranged to ensure that the Thiele modulus, ϕ (defined after Eq (14)) was much smaller than 1. This excludes the possibility of diffusional effects for the reactants so that, in the absence of poison, all elements of the catalyst surface contribute equally to the reaction process; and in the presence of poison the reactor conversion is directly proportional to the fraction of catalyst surface unpoisoned.

Under these conditions the suitability of the model can be easily checked. The total fraction of area poisoned, α_T, at any time, τ , is obtained from the integration of the relevant adsorbed poison concentration profiles (for example those shown in Figure 4 for $\tau = 0.1$).

Figure 5 shows these integrated forms of the poison penetration for values of τ up to 0.1; for high values of KC_i these curves are not valid for τ values large enough to result in appreciable poison concentration in the centre of the pellet and are consequently terminated at the point corresponding to a value of C_r equal to 0.1 at ξ equal to unity.

The values of α_T obtained experimentally from the conversion data are shown plotted against those predicted by the model in Figure 6 for τ equal to 0.025; this corresponded to real times covering a range from 28 to 130 minutes. KC_i values ranged from 1 to 19.

The results shown in Figure 6 are really quite good when one considers the many uncertainties in the interpretation of the experimental findings. These are discussed in reference [5] and include the correction for non-isothermal effects, the evaluation of the effective diffusivity, D, and the assumption of monolayer adsorption used for the estimation of $\bar{C}_{max}$.

DISCUSSION

The most questionable assumption in the derivation of the poison penetration equations is that of independence. Deactivation by poison adsorption is discussed by Innes [6] who describes two mechanisms both of which have been advocated by a number of workers. Although the distinction is somewhat vague the first mechanism stresses reaction between the poison and active centers whereas the second considers a less direct interference, the number of free electrons, unpaired electrons or reaction sites being in some way affected by the presences of adsorbed poison molecules. The first mechanism suggests a direct competition between the poison and reaction components while the second lends itself more plausibly to the interpretation of independent poisoning considered in this paper.

Typical poisoning curves quoted in the literature [1] are in qualitative agreement with the proposed model and suggest the assumption of independence to be valid for many systems. They show the relationship between the steady state catalyst activity (proportional to the fraction of catalyst surface unpoised) and poison concentration to be linear at low concentrations (ie. at low KC_i values); for higher concentrations the activity decreases more slowly as indicated by the Langmuir isotherm. The initial linear portion of these curves is strongly indicative of independence: if there were competition between the poison and reaction components for available active sites the KC_i term would appear in the denominator of the reaction rate expression regardless of the controlling mechanism [7] ; the catalyst activity would therefore decrease with increasing KC_i but not linearly as generally found in practice.

When there are temperature differences between the catalyst particles and the surrounding gas stream the effect of poisoning is likely to be far greater than for the isothermal schemes considered above. For exothermic reactions the immediate effect of the poison will be to reduce the overtemperature with the consequence of

an exponentially amplified drop in the reaction rate; a point will be reached, however, when the overtemperature becomes negligibly small making applicable the assumption of isothermal operation to the final stages of the deactivation curves. This was the case for the experiments reported in this paper and considered in more detail in reference [5] .

Temperature effects could also be expected to invalidate the assumption of independent poisoning, the Langmuir constant bearing an Arrhenius relationship with temperature. However available evidence suggests the effect of temperature on the fraction of catalyst surface poisoned to be generally small. Maxted [1] , for example, found that a temperature rise sufficient to produce a fivefold increase in the rate of hydrogenation on a platinum catalyst, made no significant difference to the poisoning effect of thiophene.

For large values of KC_i this low temperature dependence is to be expected from the form of Eq (2). And for small KC_i values, where Eq (2) indicates a linear dependence of area poisoned with the Langmuir constant K, adsorption will be less than mono-layer with consequentally low energies of activation.

ACKNOWLEDGEMENTS

This work was financed by a research grant from the "Ente Nazionale Idrocarburi" of Italy. Dr. Gibilaro also received partial personal support from the Science Research Council of Great Britain.

REFERENCES

1 MAXTED E.B., Advances in Catalysis, Volume 3, Academic Press, New York, 1951

2 SADA E., and WEN C.Y., Chem.Engng.Sci., 1967 22 559

3 GIOIA F., Rend. Acc. Lincei, 1967, VIII-42, 515

4 CUNNINGHAM R.A., CARBERRY J.J., and SMITH J.M., A.I.Ch.E. Journal, 1965, 11 636

5 GIOIA F., Paper submitted to Ind.Eng.Chem.Fundamentals and available from the publishers

6 INNES W.B., Catalysis, Volume I, Chapter 6. Reinhold Publishing Company, New York 1954 (Edited by P.H.Emmett)

7 HOUGEN O.A., and WATSON K.M., Chemical Process Principles, Part 3, John Wiley and sons, New York, 1947.

NOTATION

a_o	Catalyst surface area available for reaction	cm^2/cm^3
C	gas phase poison concentration	$gmols/cm^3$
$\bar{C}$	adsorbed phase poison concentration	$gmols/cm^3$
$\bar{C}_{max}$	maximum adsorbed phase poison concentration	$gmols/cm^3$
C_i	gas phase poison concentration at pellet surface	$gmols/cm^3$
C_r	C/C_i	[0]
$C_{r(s)}$	transfer function solution of poison penetration	[0]
C_A, C_B	concentrations of components A, B	$gmols/cm^3$
D	effective diffusivity of poison	cm^2/sec
D_p	pseudo diffusivity of poison defined by Eq (7)	cm^2/sec
D_A, D_B	effective diffusivities of components A and B	cm^2/sec
K	Langmuir constant	$cm^3/gmol$
k_A, k_B	reaction velocity constants	cm/sec
q	defined by Eq (4)	[0]
R	catalyst pellet half dimension	cm
s	Laplace variable	sec^{-1}
t	time	sec
x	distance into pellet	cm
α	fraction of catalyst surface poisoned (point value)	[0]
α_T	total fraction of catalyst surface poisoned	[0]
ϕ	Thiele modulus. Defined after Eq (14)	[0]
τ	dimensionless time. Defined after Eq (3)	[0]
ξ	dimensionless distance. Defined after Eq (3)	[0]

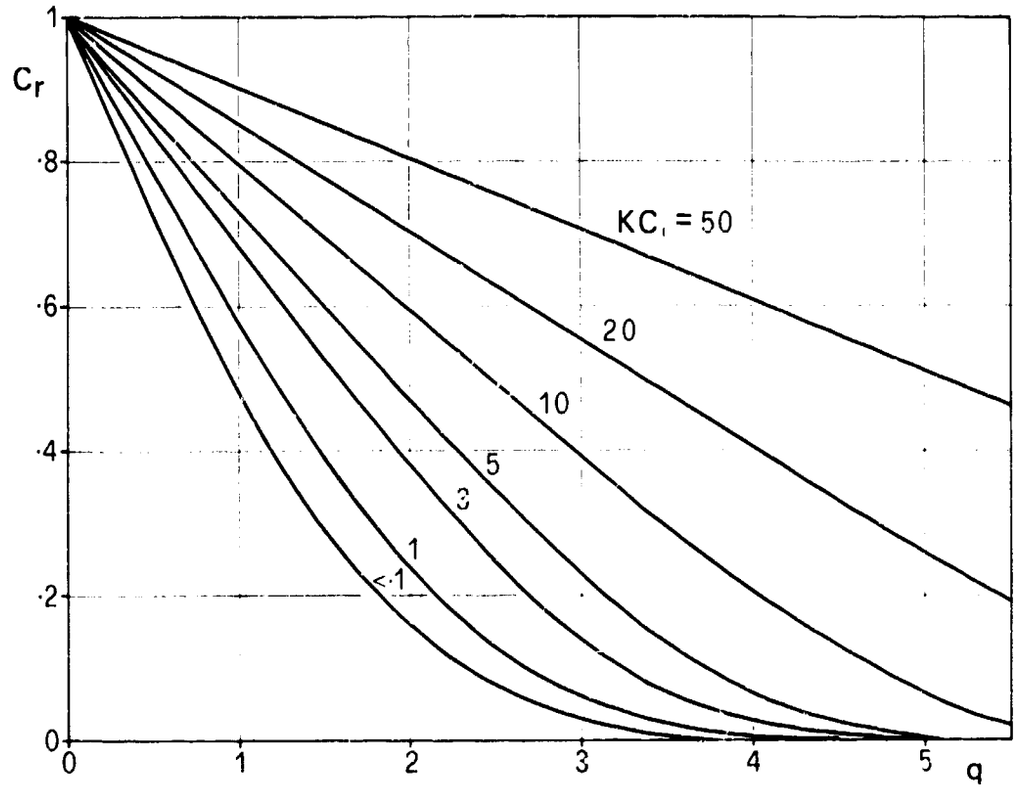

Figure 1 Numerical solutions of Eq (5)

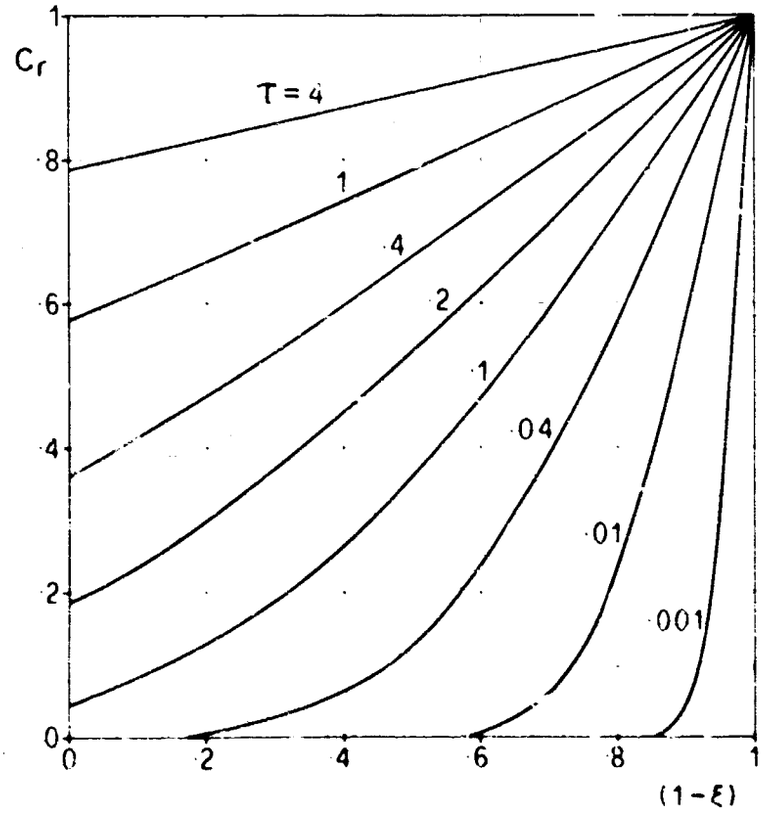

Figure 2 Gas phase poison concentration profiles for KC_1 equal to 1

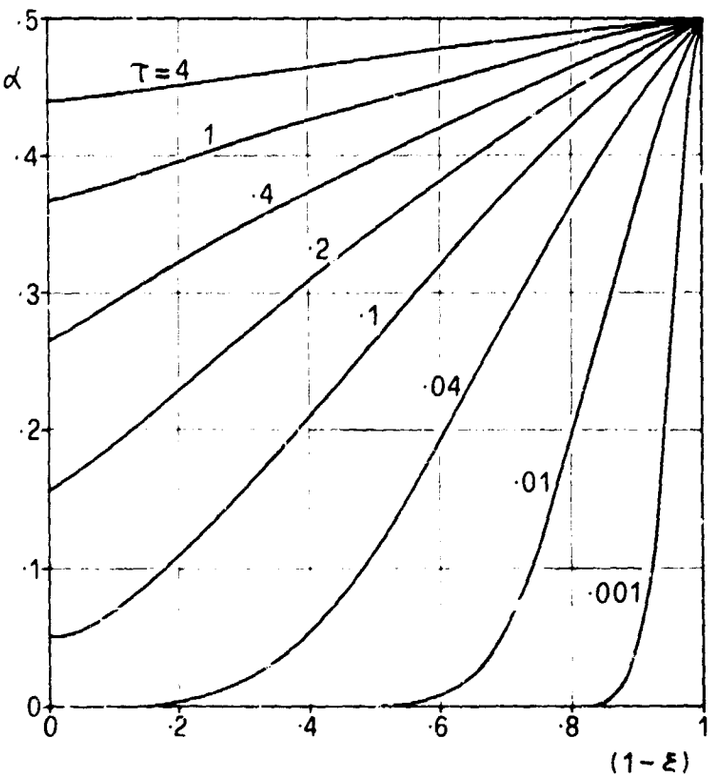

Figure 3 Adsorbed phase poison concentration profiles for KC_1 equal to 1

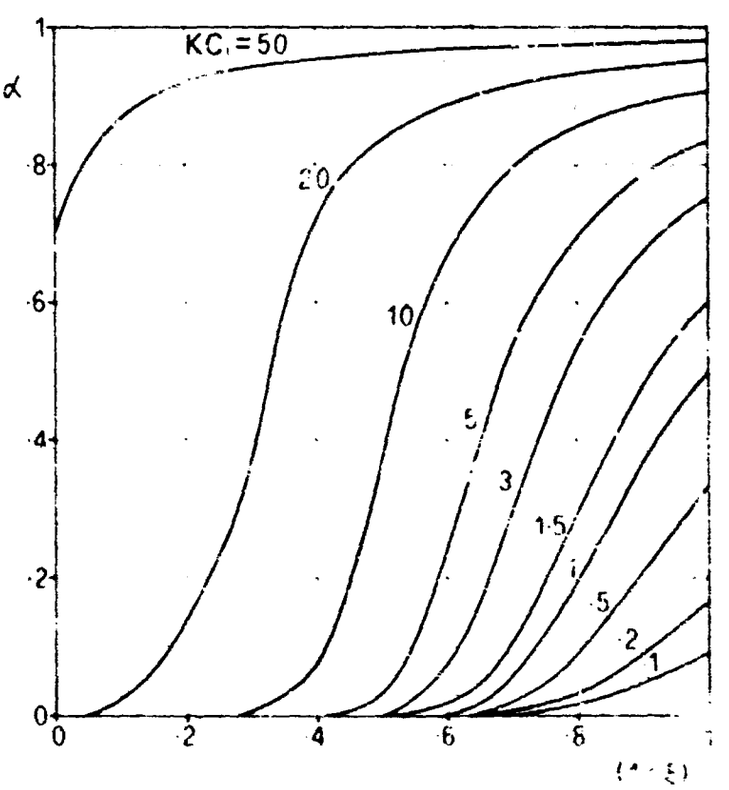

Figure 4 Adsorbed phase poison concentration profiles for τ equal to 0.01

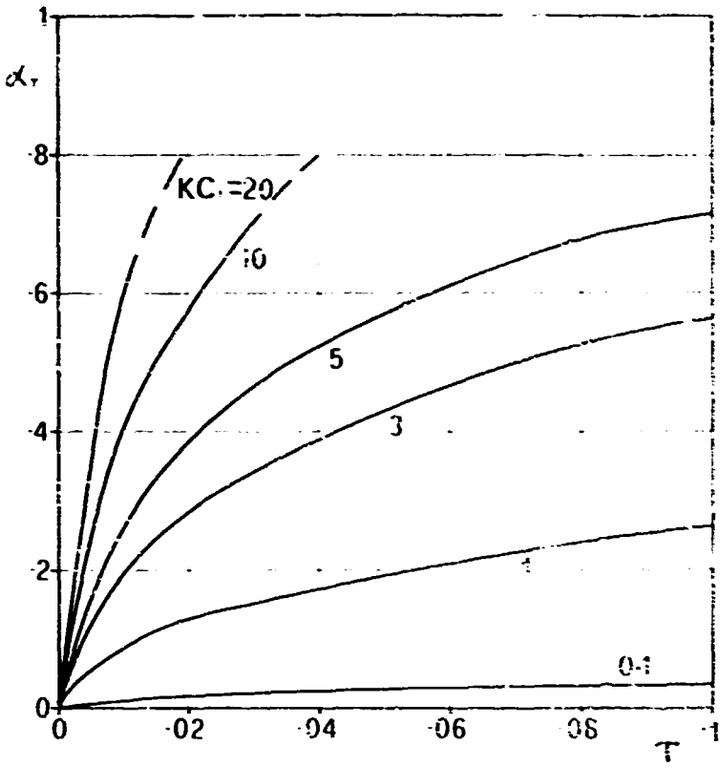

Figure 5 Overall fraction of surface area poisoned α_τ as a function of τ.

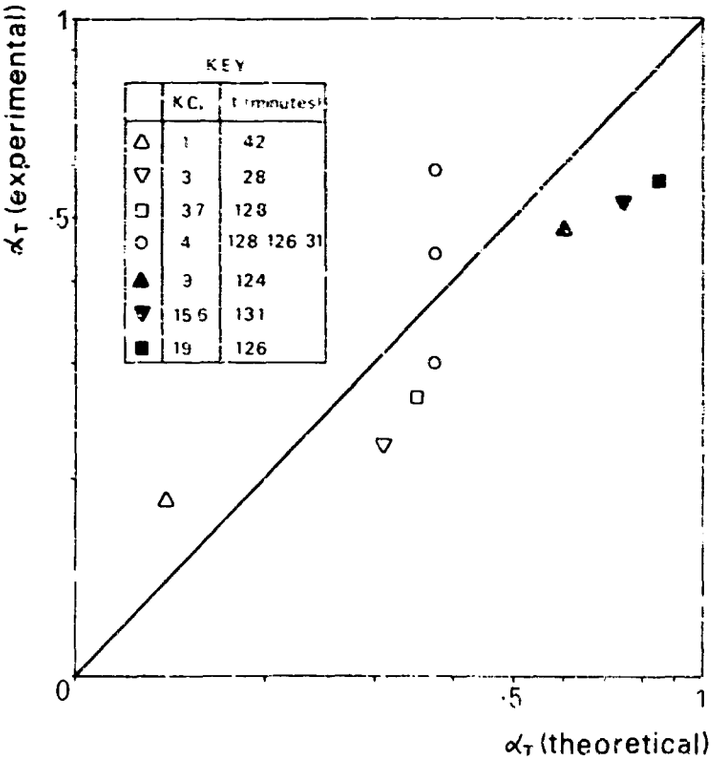

Figure 6 Comparison of model predictions with experimental results for τ equal to 0,025

THERMIONIC EMISSION OF ELECTRONS IN THE PRESENCE OF ADSORBED GASES

by

F. M. Page and J. I. Wright

The University of Aston in Birmingham

Gosta Green,
Birmingham 4,
England.

SUMMARY

Many of the gaseous products of combustion are adsorbed on surfaces, even at temperatures above 1500°K and these adsorbed layers strongly affect thermionic emission of electrons. The ionisation of solid particles in flames is therefore not to be compared directly with ionisation in vacuo. Experimental work on the systems CO/W, O_2/Pt and SO_2/Pt is presented and analysed in terms of the heat of adsorption of the gas; and of the kinetics of adsorption. In all these systems there is a large rise in the thermionic work function. Certain systems particularly those involving highly unsaturated organic materials, analogous to soot, have the opposite effect and lower the work function with a consequent large increase in the emission of electrons. Some observations on these systems are discussed and their consequences at low temperatures considered.

The general understanding of ionisation in flames has been developed from a simple equilibrium description[1] based on the Saha[2] equation, through the modification of such a description by including interaction with the flame gases[3], to a kinetic description of both natural ionisation and the ionisation of additives through the work of Calcote, Sugden and Williams and their collaborators. The technology of fuels has, however, advanced more rapidly than the laboratory studies, and consideration must now be given to the effects of solid particles on the levels of ionisation in flames, both to explore the possibility of increasing this level for purposes of MHD generation, or as an unwanted source of radio attenuation in other fields. The earliest description of the effect of solid particles was due to Sugden & Thrush[4] who put forward the relation

$$n_e = \frac{2(2\pi m_e kT)^{3/2}}{h^3} \exp\left(-(\chi + n_e e^2/Na)/kT\right)$$

This has been modified by Einbinder[5], F.T. Smith[6], and Soo & Dimich[7] but the modifications are of importance only for small particles and heavy ionisations[8]. The crucial point in equation (1) is the exponential dependence on the work function.

Work functions have usually been determined under high vacuum conditions and the importance of using very clean surfaces was realised at a very early stage. Kingdon[9] demonstrated that the work function of tungsten (4.54 eV, 437 kJ) was raised to approximately twice this value when the measurements were carried out in the presence of 0.1 Nm^{-2} of oxygen. This result has been quantitatively reproduced in these laboratories[10], and it has also been shown that other strongly adsorbed materials such as tetracyanoethylene[11] or acetylene[12] may lower the work function by 100 kJ. The origin of these changes will be discussed later, for the present it is enough to note that they do occur, and that therefore any attempts to describe phenomena at atmospheric pressure must take such changes into account. A change in work function of 1 ev (100 kJ) at a temperature of 1500°K corresponds to a change of 1000 in the current density, so that the use of clean surface work functions could be misleading in the extreme.

E. R. Miller[13] has studied a variety of solid particles in flames, using a Langmuir/Williams[14] rotating probe. As such a probe is swept through a flame where there is gaseous ionisation, a smoothly profiled response is found, but if the flame contains solid particles as well, the smooth profile is lost, and a spiky response is found. The heights of the spikes are a function of the solid material and of the temperature of the flame, and Miller described his results in terms of the following model:

A single particle in the flame will be at or near the temperature of the flame and will therefore lose (or gain) electrons until it is in equilibrium with the local concentration of electrons. In so doing, it will of necessity become charged and the loss of electrons will rapidly cease. The cold probe in passing through the flame can act only as a current collector, and the response will be limited by the plasma density. If however the cold probe passes sufficiently near to the hot particle to interact with it, the combination is equivalent to an emitting probe, and the response is governed by the temperature and work function of the system. A steady state response is not obtained, because the particle is rapidly cooled by the massive probe, but a ballistic response yields the typical spike. Miller was able to evaluate the work function of various materials by a statistical survey of the spike heights with the following results (Table 1).

Table 1

Material	Observed Work Function (eV)	Literature value (15) (eV)
Carbon	1.5	3.93
Tungsten carbide	2.5	3.60
Lanthanum Hexaboride	2.2	2.66
Barium oxide	(0.60 Low temp. (1.95 High temp.	1.66

It is apparent that even allowing for the crudeness of the experiment, it would be most injudicious to attempt to use the literature values to account quantitatively for the observation.

RAISED WORK FUNCTIONS

In considering the origin of these changes in work function consequent upon adsorption, two distinct factors must be separated - the actual change under an absorbed layer and the change in the amount of the adsorbed layer. It is commonly found that the surface potential of a clean surface is about 1 volt for that of a surface covered with an adsorbed layer. As already pointed out, this potential difference will correspond to a factor of 1000 in the current density and therefore the electron emission will be dominated by the surface of lower work function unless it represents less than 10^{-3} of the whole surface. If the fraction of surface covered is temperature dependant through adsorption, such dependence will be added to the work function when determined thermionically thus accounting for the observation of Kingdon.

It is generally accepted that the presence of an adsorbed film on a metal surface will produce an electrical double layer, and that the effect of this double layer will be to produce a surface potential which will modify the work function. The various theories and experimental data are

discussed by Kaminskey[16] Burshtein[17] and Mignolet[18] while Gomer[19] and Ehrlich[20] have demonstrated the effect of adsorption on field emission. For the purpose of the present discussion the finer details of this surface potential and the variation with degree of surface coverage, may be neglected and the simplifying assumption made that the work function χ_o of the clean surface is increased by an amount $\Delta\chi$ by covering with an adsorbed layer.

The current density for either surface will be given by Richardson's equation.

$$j_e = BT^2 \exp(-\chi/RT) \qquad (2)$$

If a fraction θ of surface is covered by an adsorbed film, not necessarily continuous, but composed of particles whose dimensions are comparable to the distance of the Schottky barrier, then the current density will be given by

$$j_e = B_o T^2(1 - \theta) \exp\left(-\chi_o/RT\right) + B_1 T^2\theta \exp\left(-(\chi_o + \Delta\chi)/RT\right) \qquad (3)$$

The mean thermionic work functions is defined by

$$\bar{\chi} = -RT^2 \frac{d \ln j}{dT} \qquad (4)$$

If, furthermore, the fraction of the total current derived from the ith patch is defined as ϕ_i, differentiation of equation 3 and substitution in equation (4) yields for the general case

$$\bar{\chi} = \sum_i \phi_i \chi_i + \sum_i \phi_i \, d \ln \theta_i/dT \qquad (5)$$

Under conditions where the degree of surface coverage varies slowly with the temperature, the last term in equation (4) may be neglected and the mean thermionic work function then becomes

$$\bar{\chi}_m = \sum_i \phi_i \chi_i \qquad (6)$$

This is not identical with the mean work function derived from contact potential measurements, where the weighting factor is the fraction of surface covered, not the current derived for the surface

$$\chi_p = \sum \theta_i \chi_i \qquad (7)$$

Farragher has developed this approach to the thermionic emission for covered surfaces and has incorporated a simple Langmuir expression for the fraction of surface covered. The resultant expression for the total current density is

$$j_T = \frac{BkT^{(2+n)}}{p^x} \quad \frac{\theta}{1 - \theta} \quad \exp\left(-(\chi_o + q_o)/RT\right) \qquad (8)$$

where the pressure exponent x and temperature exponent n depend on the type of adsorption, and χ_o and q_o are the work function of the clean surface and heat of adsorption at zero coverage respectively. He has studied a number of systems with the following results

TABLE 2

System	NO_2/W	NO/W		CO/W		O_2/W	O_2/Ir	O_2/Pt
T°K	1792	1788	1640	1750	1610	1800	1590	1500
$(q_o + nRT)$ (kJ)	464	246	552	222	492	410	306	294
x	0.5	0.5	1.0	0.5	1.0	0.5	0.5	0.5

These values for the heat of adsorption are upper limits, and must be reduced by approximately 80 kJ to obtain the values at normal surface coverage. The most reliable measurement in these systems is that of Redhead[21] on the system CO/W. His value for the heat of adsorption of 375 kJ is so close to the corrected value for this work as to suggest that the model is correct. For many simple systems where the effect of adsorption of a gas is to raise the work function of the surface, the thermionic current density may be predicted from a consideration of the properties of the clean surface and of the degree of surface coverage.

LOWERED WORK FUNCTIONS

Certain vapours, notably acetylene[12] and tetracyanoethylene[11] have the opposite effect to that just described in that the thermionic work functions are lowered by about 1 volt. Surface potential studies have not been made on these systems so that it is not possible to say how great a portion of the observed change is due to electrostatic effects and how much to adsorption, but it is apparent from the geometry of the current-temperature graphs that there must be an effect other than on the work function if the clean and covered surface current densities are to be comparable in magnitude. Such an alternative effect is to be found in the transmission coefficient for electrons

across the barrier field.

The phenomenon of electron emission from one of the most widely studied systems, a tantalum surface in the presence of tetracyanoethylene, is illustrated in Figure 1. Generally, two lines are obtained, one (A) being the current density obtained from a clean surface and the other (B), slightly higher and with a lower slope, being the current density in the presence of tetracyanoethylene. At a given pressure of tetracyanoethylene, the measurements starting from a low temperature would follow line B until a well defined transition to line A occurred. This transition was completely reproducible and reversible, measurements extending well above and below the transition point. It was frequently possible to make several measurements in the region between the lines, thus defining the transition clearly.

The point at which the transition occurred was a function of the pressure of vapour, being at higher temperatures for higher pressures, and was clearly a function of the adsorption process. The difference in slopes of the lines was about 90 kJ, which was disproportionately greater than their actual separation, so that the pre-exponential factor for the covered surface must be much less than that of the clean surface. Fowler[22] has given an expression for the alteration in the transmission coefficient which is applicable to this phenomenon.

$$a = 4\left\{\frac{\chi_o - \Delta\chi}{\chi_o}\right\}^{\frac{1}{2}} \exp\left(-4zl(\Delta\chi)^{\frac{1}{2}}/3\right) \qquad (9)$$

when a is the ratio of the transmission coefficient, $\Delta\chi$ the lowering of the work function, l the thickness of the barrier and $z^2 = 8\pi^2 m_e/h^2$.

In applying this result, equation (3) is used in the form

$$j_c = d_c BA\theta T^2 \exp\left(-(\chi_o - \Delta\chi)/RT\right)$$

$$j_o = d_o BAT^2 \exp\left(-\chi_o/RT\right)$$

whereas $\log(j_c/j_o) = \log(d_c\theta/d_o) + \Delta\chi/RT$

$$\text{or } RT \log(j_c/j_o) = RT \log a\theta + \Delta\chi \qquad (10)$$

As Figure 2 shows, $\Delta\chi$ and $a\theta$ may readily be evaluated, with the result, under most conditions, that $a\theta$ is of the order of 0.03 but that for certain carefully prepared surfaces it could be as high as 0.1. A reasonable estimate of the barrier thickness would encompass the first layer of atoms in the metal, together with the adsorbed molecule, and a summation of the appropriate radii gives values 4.4 - 5.5 Å for l depending on the model used. The value of 5.3 Å has been chosen to evaluate a from Fowler's result, since this makes $\theta = 1$ for the special surfaces and is within the range estimated. As will be seen for table 3, the other surfaces all suggest a value of about 0.3 for θ, the fraction of surface covered

TABLE 3

Filament	Pressure	$\Delta\chi$	$a\theta$	θ
Ta	1.3×10^{-3} Nm^{-2}	49 kJ	9.3×10^{-2}	0.32
Ta	6.5×10^{-2} Nm^{-2}	92 kJ	3.3×10^{-2}	0.32
WC	1.3×10^{-2} Nm^{-2}	94 kJ	1.1×10^{-1}	1.0
MoC	1.5×10^{-2} Nm^{-2}	28 kJ	3.3×10^{-2}	0.56
TaC	1.5×10^{-2} Nm^{-2}	58 kJ	6.6×10^{-2}	0.29

This value is entirely reasonable, since for an immobile film any space between adjacent molecules will be inaccessible if it is of smaller dimensions than the molecule. For diatomic species this is only of marginal importance, but for tetracyanoethylene which can occupy 30 (5 x 6) sites it is significant. Such an extended molecule will on average be surrounded by a clear space of half its diameter, and the upper limit for coverage will therefore be 0.25 in reasonable agreement with observation. The specially conditioned surface of tungsten carbide is then attributable to the formation of a highly mobile film in which close packing can occur.

KINETIC EFFECTS

The results, and theoretical approach outlined so far are applicable to what are essentially static conditions. The final state was reached rapidly, usually too fast to see any intermediate stage, and the results appeared to be reversible. In the analysis of the results, it is assumed that everything is at a steady state. By contrast, electron emission from many surfaces in the presence of sulphur compounds shows a strongly time-dependent effect (Figure 3).

At temperatures below 1450°K electron emission from a platinum surface is not particularly dependent on the pressure of sulphur compound (sulphur dioxide has been used for most of the work though the same results have been obtained with SO_3, CS_2 and sulphur vapour). Above this temperature, there is a slow fall in the electron emission over a considerable period of time followed by a catastrophic drop over a very short time. The actual time scale involved depended on the sample of metal and on

its history but typically the slow fall corresponded to a drop to one half of the electron current and occupied 90% of the time, while the catastropy reduced the electron current by a factor of 10^3 in the remaining 10%.

It was found possible to fit these curves empirically by an expression of the form

$$\frac{j - j_\infty}{j_o - j_\infty} = 1 - \exp(kt^n) \qquad (11)$$

where t is the time and n is an exponent between 2 and 3.

In searching for a theoretical basis for this empirical expression, certain facts were noted. Firstly, although a very slow evaporation of the platinum occurred, it was too slow to be attributed to the intermediate formation of massive platinum sulphide. On the other hand, very significant thermal etching had occurred during a run. Secondly, although the fall in electron emission could be completely reversed by pumping off the sulphur dioxide, and the emission restored to its original value, subsequent runs using the same filament showed the same general behaviour, but with a progressively increasing time scale. Thirdly, the adsorption of sulphur dioxide on platinum has been studied extensively and there appears to be no anomalies. As a result of considering these facts, a hypothesis of conditional adsorption is advanced. Under this hypothesis, the adsorption of sulphur dioxide as such does not contribute directly to the loss of electron emission, and is at a steady state at all temperatures. Sulphur atoms can however be adsorbed, either as atoms or in combination and reduce the electron emission, but such adsorption can only occur at suitable sites, which are associated with a particular condition of the platinum surface, and are not present on a normal clean surface. The particular surface configuration is localised as a patch, and these patches can grow in size in the presence of sulphur. In order that they can start to grow, nuclei, or patches of minimal area must be present. Such nuclei may be present at the start of a run, or may be created during a run. When the sulphur dioxide is pumped out of the system, the surface reverts to the clean condition.

The necessary mathematics to develop this model have been worked out by Avrami[23] for the case of nuclei already present, and by Poisson[24], who considered the chance that part of a pool would remain undisturbed by the ripples spreading during a shower of rain, for the case of continuous generation of nuclei. The approach of Poisson may readily be extended to include a finite number of nuclei present initially.

The final result is naturally complex, but it is of the correct form, and reduces to the equation of Avrami and Poisson under appropriate conditions. The theory of Avrami predicts an exponent in equation (11) of 2 while that of Poisson, one of 3. The intermediate values found empirically reflect the varying importance of the two processes. Generally, successive runs not only show an increased time scale, but also are fitted to higher values of the exponent n. This is support for the model advanced, in that the nuclei present initially tend to be consumed in patch growth, so that the initial rate is therefore lower in successive runs, and depends more on generation of new nuclei.

CONCLUSION

The three different aspects of the interaction of gases with surfaces and the consequent effect on electron emission indicate quite clearly the many difficulties which beset any attempt to predict such emission which is based solely on the properties of clean surfaces. The variations which are found can be understood in terms of the simple kinetic feature of adsorption and surface change, but the prediction of the variations is a more formidable task. One comment which may rightly be made is that the majority of the work described herein is concerned with rather exotic systems. While this is true, the complex nature of the problem forces attention first to those systems which show simple and markedly dominant features which are amenable to experimental investigation. When the general nature of the phenomena have been made clear, they may be then studied in greater detail with more sophisticated techniques, and in systems where several of the phenomena play a contributory role.

REFERENCES

1. Wilson, H.A., Rev. Mod. Phys. 3, 156 (1931).
2. Saha, M.N., Phil. Mag. 40, 472 (1920).
3. Padley, P.J., Page, F.M., and Sugden, T.M., Trans. Farad. Soc. 57, 1552 (1961).
4. Sugden, T.M. and Thrush, B.A., Nature, 168, 703 (1951).
5. Einbinder, H., J. Chem. Phys. 26, 948 (1957).
6. Smith, F.T., Proceedings of Third Conference on Carbon, 419, Pergamon (1959).
7. Dimich, R.C. and Soo, S.L., Multi-phase Flow Symposium, Am. Soc. Mech. Eng. (1963).
8. Woolley, D.E., Ph.D. Dissertation, University of Aston (1969).
9. Kingdon, K.H., Phys. Rev. 24, 510 (1924).
10. Page, F.M., Trans. Farad. Soc. 57, 359 (1961).
11. Farragher, A.L., Ph.D. Dissertation, University of Aston (1966).
12. Goode, G.C., Unpublished Work.
13. Miller, E.R., Ph.D. Dissertation, University of Aston (1969).
14. Travers, B.E.L. and Williams, H., 10th Symposium (International) on Combustion p.657, Combustion Institute (1965).
15. Fromanko, V.S. and Samsonov, G.V., "Handbook of Thermionic Properties", Plenum Press (1966).

16. Kaminsky, M., "Atomic and Ionic Impact Phenomena on Metal Surfaces", Springer-Verlag, Berlin (1965).
17. Burshtein, R.Ch. and Surova, M.D., Dokl. Akad. Nauk. 61, 75, (1968).
18. Mignolet, J.C.P., Bull. soc. chim. Belg. 64, 126 (1955).
19. Gomer, R., J. Chem. Phys. 21, 1869 (1953).
20. Ehrlich, G., J. Chem. Phys. 34, 39 (1961).
21. Redhead, P.A., Trans. Farad. Soc. 57, 641 (1961).
22. Fowler, R.H., "Statistical Mechanics", C.U.P. (1936).
23. Avrami, I.M., J. Chem. Phys. 7, 1103 (1939); J.Chem. Phys. 8, 212 (1940); J. Chem. Phys. 9, 177 (1941).
24. Poisson, S.D., "Recherches sur la Probabilité des Jugements en materiere criminelle et en matiere civile", Bachelier Paris p. 206 (1837).

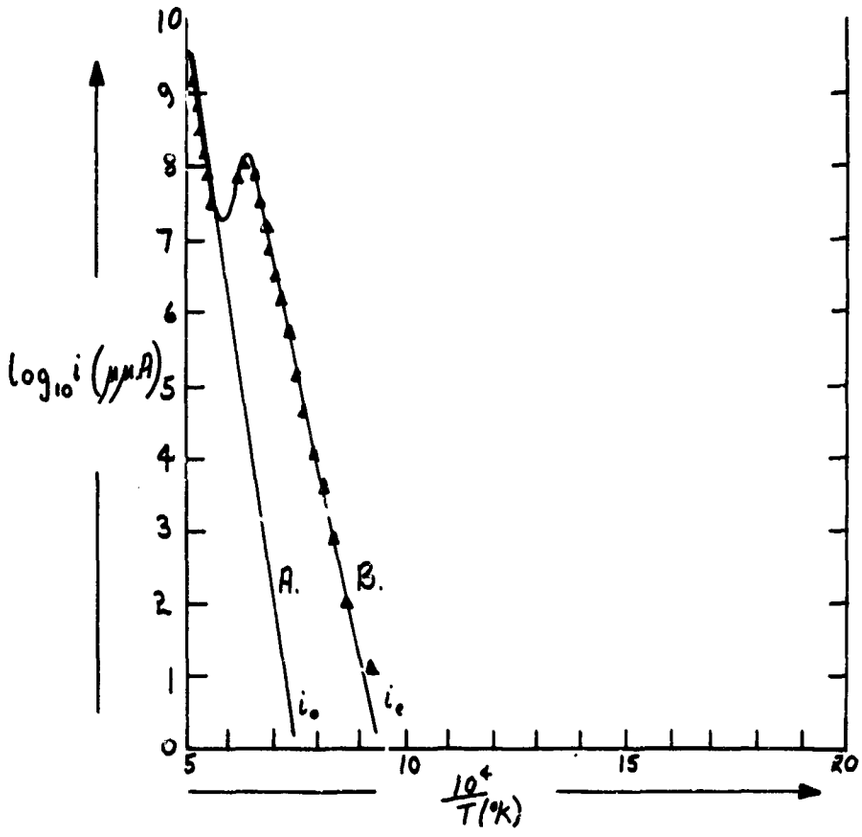

Fig.1 Electron emission from tantalum in presence of tetracyanoethylene

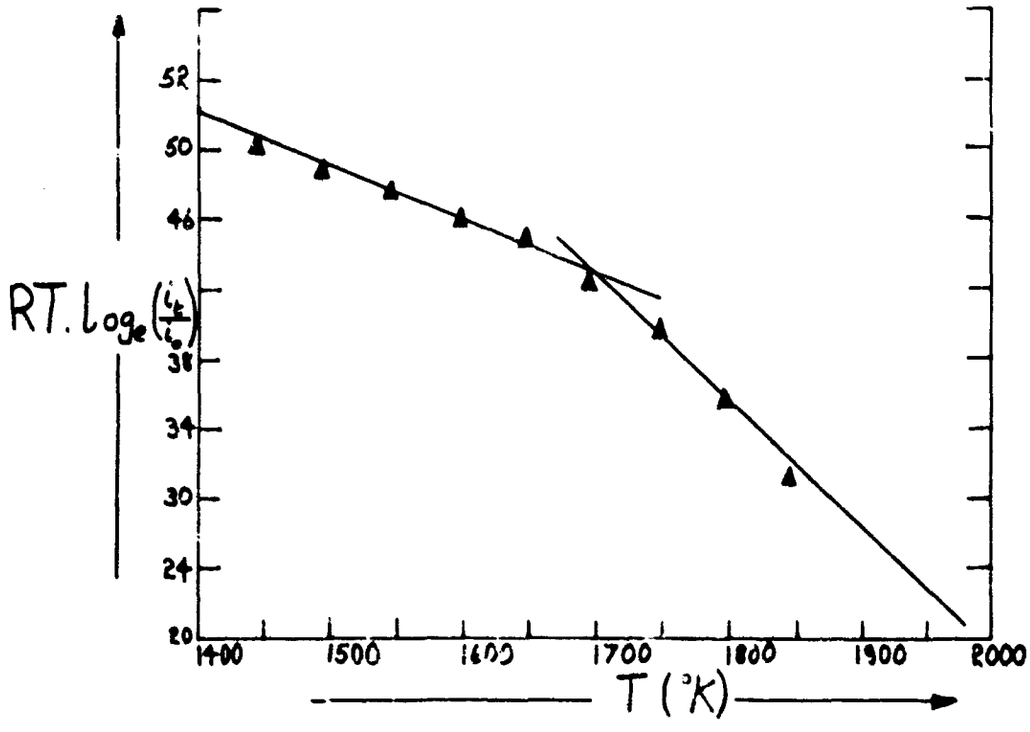

Fig.2 Relative thermionic currents, tetracyanoethylene/tantalum

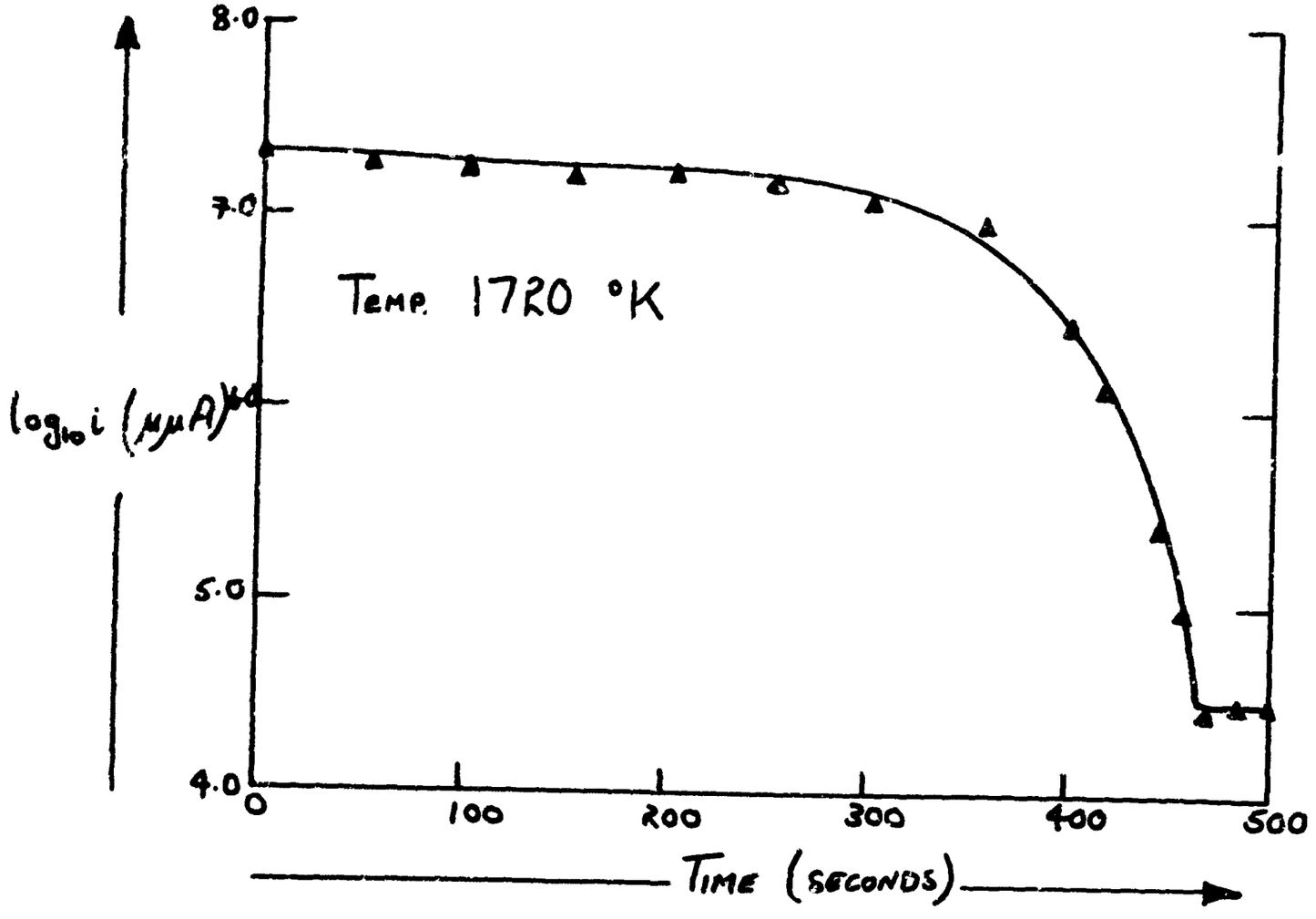

Fig.3 Electron emission from platinum in presence of sulphur dioxide

"KINETICS OF PHASE BOUNDARY REACTIONS BETWEEN GASES AND METALS"

by

H.J.Grabke

Max-Planck-Institut für Metallforschung, Institut für Metallkunde

Stuttgart, Seestr. 75

Germany

SUMMARY

Phase boundary reactions often determine the rate of interactions of metals with gases. Adsorption and stepwise dissoziation of the gas molecules must occur before the nonmetal atoms from the gas phase can be dissolved in the metal or can react with the metal.
The kinetics of the surface reactions of iron and other metals with NH_3-H_2, CH_4-H_2, H_2S-H_2, H_2O-H_2, CO_2-CO and N_2-H_2 mixtures have been studied at high temperatures.
From the experimentally determined kinetics, the dependence of the forward and backward reaction rate on the partial pressures or activities of the reactants and reaction products, the rate determining step of the investigated reactions could be detected. The rate determining step can also be found out by the comparison of the overall reaction rate with the rate of an appropriate isotope exchange reaction. Depending on the temperature or other reaction conditions different reaction steps can act as the rate determining step of a reaction.

From the knowledge of one or two elementary steps the mechanism of the overall reaction could be deduced for the investigated reactions of metals with gases. The occurence of individual elementary steps involving intermediate products such as adsorbed atoms or radicals was proved.

AT SUFFICIENT HIGH TEMPERATURES equilibria between the solid phase and the gas atmosphere are established, if a gas or a gas mixture is passed over a metal. In equilibrium the activity of each of the atomic species, of which the gas phase is composed, is the same in the gas atmosphere, in the solid and at the surface of the solid. Depending on the activity of A and chemical affinity to the metal either a solution of A in the metal and an adsorbed layer of A atoms at the metal surface is established, or a compound is formed.

At the phase boundary adsorption and dissociation of the gas molecules must occur before the nonmetal atoms can be dissolved or can react with the metal. In most cases the dissociation is the rate determining step in the sequence :

a) transport of the molecules to the surface of the solid,
b) adsorption at the surface,
c) dissoziation of the adsorbed molecule and
d) entry of the atoms into the solid.

In the following, only studies will be discussed, in which chemical dissoziation reactions at metal surfaces were rate determining. The diffusion process, which establishes the equilibrium in the bulk phase, will not be considered.

Typical reactions which transfer nonmetal atoms A from the gas phase to a metal are the dissoziation reactions of diatomic molecules, O_2, H_2, N_2, etc.

$$A_2 \rightleftharpoons 2A \quad \text{(adsorbed and dissolved)}$$

From CO_2-CO mixtures both O and C can be transferred to a metal. Nonmetal atoms A also can be transferred to a metal by equilibration with gas mixtures $AH_x - H_2$, for example $NH_3 - H_2$, $CH_4 - H_2$, $H_2S - H_2$ and $H_2O - H_2$. In these reactions a stepwise dehydrogenation or hydrogenation (in the back reaction) of the nonmetal atom A must occur and it was considered very interesting to detect the separate elementary reaction steps.

To eliminate rate control by diffusion, thin film techniques can be used. Dissolution reactions of gases in metals can be studied with thin metal foils. This way the distances are small enough that no considerable concentration gradients occur. The mean concentration change of A in the solid and thus the rate of the transfer of A to the solid can be measured.

Relaxation measurements of weight or resistance are very convenient. The activity of A in the gas phase is changed abruptly and the resulting change of the concentration of A in the metal from its initial value to the new equilibrium value can be observed by recording the change in the weight or the resistance of the thin foil used. The electrical resistance and the concentration of dissolved A are correlated by a linear relation. The principle of the relaxation method is shown in fig. 1. The retardation of the absorption and desorption of A is caused by the reaction at the surface of the thin metal foil.

Another means for the measurement of surface reaction kinetics is the study of isotope exchange reactions. These reactions can be studied while equilibrium between the gas and the solid prevails.

REACTIONS OF THE TYPE $AH_x \rightleftharpoons \underset{\text{RESULTS}}{x/2\ H_2 + A\ (\text{dissolved})}$

A relaxation method was used to study the reaction

$$NH_3 \rightleftharpoons N\ (\text{dissolved in } \alpha\text{-iron}) + 3/2\ H_2 \qquad (1)$$

The resistance changes produced by the nitriding of thin iron foils in NH_3-H_2 mixtures and the denitriding in H_2 have been studied in a flow apparatus at temperatures between 300 °C and 800 °C (1). The following mechanism is assumed for reaction Eq (1)

$$\begin{aligned}
NH_3 &\rightleftharpoons NH_3\ (\text{ads}) \\
NH_3\ (\text{ads}) &\rightleftharpoons NH_2\ (\text{ads}) + H\ (\text{ads}) \qquad \text{III} \\
NH_2\ (\text{ads}) &\rightleftharpoons NH\ (\text{ads}) + H\ (\text{ads}) \qquad \text{II} \\
NH\ (\text{ads}) &\rightleftharpoons N\ (\text{ads}) + H\ (\text{ads}) \qquad \text{I} \\
N\ (\text{ads}) &\rightleftharpoons N\ (\text{dissolved}) \\
H_2 &\rightleftharpoons 2H\ (\text{ads})
\end{aligned}$$

With some reasonable assumptions, rate laws can be derived for the case that one of the dehydrogenation and hydrogenation steps I, II or III is rate determining. The NH_3-formation on an iron foil containing nitrogen, over which H_2 is passed, will be discussed.

The rate of the first hydrogenation step, backward reaction I, is proportional to the product of the surface concentrations Γ_i of N and H. It is assumed that

the surface concentrations of all adsorbed species are low, so that the surface concentration of N is proportional to its concentration in solution $\Gamma_N \propto [N]$ and the surface concentration of H is proportional to the activity of H $\Gamma_H \propto p_{H_2}^{1/2}$. The rate of step I equals

$$v_I = -k_I^{\times} \Gamma_N \Gamma_H = -k_I [N] p_{H_2}^{1/2} \qquad (2)$$

These dependences of the overall reaction would be expected if step I were rate determining.
But if forward and backward reaction of step I are fast compared with rate of the backward reaction II, there will be approximate equilibrium for the reaction I and the surface concentration of NH is given by

$$\Gamma_{NH} = K_I [N] p_{H_2}^{1/2} \qquad (3)$$

The rate of the backward reaction II is proportional to the product of the surface concentrations of NH and H.

$$v_I = -k_I^{\times} \Gamma_{NH} \Gamma_H = -k_{II} [N] p_{H_2}^{2/2} \qquad (4)$$

These dependencies of the overall reaction would be expected if step II were rate determining.
Suppose that the forward and backward reaction of step I and of step II are fast compared with the rate of the backward reaction III. Then virtually equilibrium for reaction I and II prevails and the surface concentration of NH_2 is given by

$$\Gamma_{NH_2} = K_{II} [N] p_{H_2} \qquad (5)$$

The rate of the backward reaction III is proportional to the product of the surface concentrations of NH_2 and H

$$v_{III} = -k_{III}^{\times} \Gamma_{NH_2} \Gamma_H = -k_{III} [N] p_{H_2}^{3/2} \qquad (6)$$

Thus one expects for the dependences of the reaction rate on the nitrogen concentration and the hydrogen partial pressure the following general equation :

$$v_\nu = -k_\nu [N] p_{H_2}^{\nu/2} \qquad (7)$$

with ν = 1,2 or 3 according to which of the hydrogenation and dehydrogenation steps is rate determining.
The Eq (7) was verified by denitriding experiments. The decrease of nitrogen content in the iron foil may be written

$$v_\nu = -\frac{1}{S}\frac{dn_N}{dt} = -\frac{\delta}{2}\frac{d[N]}{dt} = -k_\nu p_{H_2}^{\nu/2} [N] \qquad (8)$$

with S = surface area and δ = thickness of the iron foil. The denitriding experiments can be plotted according to the integrated equation (fig.2).

$$\log \frac{[N]_0}{[N]_t} = \frac{2}{2{,}3\,\delta} k_\nu p_{H_2}^{\nu/2} t \qquad (9)$$

The linearity of plots of log ($[N]_0 / [N]_t$) vs. t proves that the reaction is of first order concerning the concentration of dissolved nitrogen. From the slope of this plot $k_\nu p_{H_2}^{\nu/2}$ can be determined. Experiments with different H_2-pressures gave the double-logarithmic plot of $k_\nu p_{H_2}^{\nu/2}$ vs. p_{H_2} (fig.3), which must deliver straight lines with the slopes 1/2, 2/2 or 3/2. The measurements yield lines with the slope changing from 2/2 to 3/2. At higher H_2-pressures the exponent ν = 2 shows that reaction II, the formation of NH_2 (ads), is rate-determining. At lower pressures the exponent ν = 3 shows that reaction III, the formation of NH_3 (ads), is rate determining. At H_2-pressures higher than 1 atm the reaction I may become rate determining, but this could not be investigated.
The results confirm the mechanism and the other assumptions which were made to derive Eq (7).
The rate control by the reaction steps II and III is also demonstrated by measurements of the temperature dependence of the rate of denitriding (fig.4). These measurements also show, that at high temperatures or at low H_2-pressures desorption of N_2 occurs. The N_2-desorption 2N (dissolved) $\rightarrow N_2$ is characterized by a high activation energy and is independent of the H_2-pressure.
A similar mechanism as for the reaction Eq (1) can be assumed for the decarburization of metals in H_2 and the carburization in CH_4-H_2 mixtures. Here four hydrogenation-dehydrogenation steps occur:

$$CH_4\ (ads) \rightleftharpoons CH_3\ (ads) + H\ (ads) \qquad IV$$
$$CH_3\ (ads) \rightleftharpoons CH_2\ (ads) + H\ (ads) \qquad III$$
$$CH_2\ (ads) \rightleftharpoons CH\ (ads) + H\ (ads) \qquad II$$
$$CH\ (ads) \rightleftharpoons C\ (ads) + H\ (ads) \qquad I$$

The exponent ν can assume the values 1,2,3 or 4 in the rate equation for the decarburization

$$-\frac{\delta}{2}\frac{d[C]}{dt} = k_\nu\, p_{H_2}^{\nu/2}\,[C] \qquad (10)$$

The decarburization of γ-iron was studied in the temperature range 910° to 1050 °C (2). The usual first order plot $\log([C]_0/[C]_t)$ vs. t is linear (fig.5), thus the proportionality of the decarburization rate to the carbon concentration could be proved. It was found for the range of H_2-pressures which have been applied that $\nu = 3$ (fig.6), obviously the formation of the CH_3-radical, backward reaction step III, is the rate determining reaction.
Likewise the desulfurization can be described by a mechanism with two hydrogenation-dehydrogenation steps.

$$H_2S\ (ads) \rightleftharpoons SH\ (ads) + H\ (ads) \qquad II$$
$$SH\ (ads) \rightleftharpoons S\ (ads) + H\ (ads) \qquad I$$

Studies of this reaction have been made with iron at 950 °C (3). The desulfurization is of first order concerning the sulfur concentration in the iron (fig.7) and the result $\nu = 2$ from (fig.8) shows that reaction step II is rate determining. With other metals also $\nu = 1$ has been found.
According to these results for the reactions of the mentioned nonmetal atoms A from their solution in iron (and other metals) with hydrogen a general rate equation can be given

$$v_\nu = -k_\nu\, p_{H_2}^{\nu/2}\,[A] \qquad (11)$$

This law describes the rate, if the reaction

$$AH_x \rightleftharpoons A\ (\text{dissolved}) + x/2\ H_2 \qquad (12)$$

only occurs in the backward direction, in absence of AH_x. The rate law for the total reaction is obtained from the equilibrium condition . In equilibrium ($d[A]/dt = 0$) the rate of the forward and backward reaction must be equal for all hydrogenation and dehydrogenation steps and must yield the equilibrium condition

$$\frac{p_{AH_x}}{[A]_{eq}\, p_{H_2}^{x/2}} = K \qquad (13)$$

This is fulfilled by the rate equation

$$\frac{\delta}{2}\frac{d[A]}{dt} = k_\nu' \frac{p_{AH_x}}{\left(p_{H_2}\right)^{\frac{x-\nu}{2}}} - k_\nu\, p_{H_2}^{\nu/2}\,[A] \qquad (14)$$

This general rate equation could be confirmed for all studied reactions, nitriding, carburization and sulfurization . In this equation the expression for the forward reaction contains the activity of the radical AH_ν, which is determined by equilibria of the reactions preceding the rate determining step. The expression for the backward reaction contains the product of the activity of H and the activity of $AH_{\nu-1}$. The latter is determined by equilibria of the reactions which follow after the rate determining step. The forward reaction is determined by the decomposition of the radical AH_ν, the backward reaction is determined by its formation. This is in agreement with the principle of microscopic reversibility which must be fulfilled for reactions not too far from equilibrium.

REACTIONS OF THE TYPE $A_2 \rightleftharpoons 2A$ (DISSOLVED)

The dissolution of nitrogen from N_2 in iron

$$N_2 \rightleftharpoons 2N \quad \text{(dissolved)} \qquad (15)$$

could be investigated at 7oo °C to 1ooo °C by measuring the relaxation of the electrical resistance (4). Thin iron foils were nitrided in N_2 with 1% H_2, in Ar with 1 % H_2 the iron foil desorbed its nitrogen as N_2. The nitrogen desorption curve (fig.9) is characterized by a fast decreasing slope, indicating a reaction of second order. The initial rates of experiments with various partial pressures of N_2 are proportional to the partial pressure of p_{N_2} (fig.1o). Thus one has the rate equation

$$\frac{1}{S}\frac{dn_N}{dt} = k' p_{N_2} - k [N]^2 \qquad (16)$$

This equation can be rewritten as follows

$$\frac{\delta}{2}\frac{d[N]}{dt} = k' p_{N_2}\left[1 - \left(\frac{[N]}{[N]_{eq}}\right)^2\right] \qquad (17)$$

The integrated form describes the nitrogenization of α-iron at temperatures between 7oo °C and 9oo °C (fig.11)

$$\log \frac{[N]_{eq} + [N]_t}{[N]_{eq} - [N]_t} = \frac{4}{2{,}3\,\delta}\,\frac{k' p_{N_2}}{[N]_{eq}}\,t \qquad (18)$$

The desorption rate in absence of N_2 is given by the equation

$$\frac{\delta}{2}\frac{d[N]}{dt} = -k [N]^2 \qquad (19)$$

According to the integrated form of this equation

$$\frac{[N]_0 - [N]_t}{[N]_t} = \frac{2}{\delta}\,k\,[N]_0\,t \qquad (2o)$$

the desorption curves can be plotted (fig.12).
The following reaction sequence is proposed for the atomistic mechanism of the reaction

$$N_2 \rightleftharpoons N_2 \text{ (ads)}$$
$$N_2 \text{ (ads)} \rightleftharpoons 2N \text{ (ads)}$$
$$N \text{ (ads)} \rightleftharpoons N \text{ (dissolved)}$$

The observed rate equation can be attached to the second step. The forward reaction is the dissociation of adsorbed nitrogen, the backward reaction is the recombination of two adsorbed nitrogen atoms. Again the linear relations $\Gamma_{N_2} \propto p_{N_2}$ and $\Gamma_N \propto [N]$ must be valid, and written with the surface concentrations of the reacting species the equation reads as follows

$$\frac{1}{S}\frac{dn_N}{dt} = k^* \Gamma_{N_2} - k^* (\Gamma_N)^2 \qquad (21)$$

The reaction

$$A_2 \text{ (ads)} \rightleftharpoons 2\,A \text{ (ads)} \qquad (22)$$

with its rate equation

$$\frac{1}{S}\frac{dn_A}{dt} = k' p_{A_2} - k [A]^2 \qquad (23)$$

presumably will be rate determining in several systems gas-metal.
Complications arise at lower temperatures or high nonmetal activities and for other conditions if the coverage with the atoms A is not very small.
The equation (16) for the nitriding in N_2 and the nitrogen desorption is only valid for low nitrogen concentrations. For as high nitrogen concentrations as one can establish in γ-iron by nitriding with N_2 or in α-iron by nitriding with NH_3-H_2 mixtures, the equation (16) must be completed according to

$$\frac{1}{s}\frac{dn_N}{dt} = k' \frac{\Gamma_L p_{N_2}}{1 + K[N]} - k \frac{[N]^2}{1 + K[N]} \qquad (24)$$

The expression for the backward reaction shows that the nitrogen desorption is of second order only at low nitrogen concentrations, for high nitrogen concentrations the desorption apparently becomes of first order. This is illustrated by a plot which shows the dependence of desorption rates on high nitrogen contents. The iron foils had been nitrided with NH_3-H_2 mixtures and after that were denitrided in Ar (fig.13). In Ar the nitrogen can only be desorbed as N_2 not as NH_3.
In order to derive equation (24) the following mechanism is proposed. The dissociation of the N_2 molecule occurs at special sites with a high enthalpy of adsorption for N-atoms, may be at a kink L. The recombination takes place at a kink, one nitrogen atom, which is adsorbed with high-enthalpy at the kink reacts with another mobile N-atom, which is adsorbed with less adsorption enthalpy.

$L + N_2$	$\rightleftharpoons$	$L\,N_2$ (ads)	I
$L\,N_2$ (ads)	$\rightleftharpoons$	$L\,N$ (ads) + N (ads)	II
$L\,N$ (ads)	$\rightleftharpoons$	N (diss.) + L	III
N (ads)	$\rightleftharpoons$	N (diss.)	IV

The rate determining step would be reaction II. The rate equation can be written with the surface concentrations of the reacting species

$$v_{II} = k_{II}' \Gamma_{LN_2} - k_{II} \Gamma_{LN} \Gamma_N \qquad (25)$$

For the equilibrium III a Langmuir-Isotherm is introduced

$$\Gamma_{LN} = \frac{\Gamma_L K_{III} [N]}{1 + K_{III} [N]} \qquad (26)$$

The N_2-molecules presumably are less strong adsorbed at the sites of the reaction than the N-atoms, therefore one has for the surface concentration

$$\Gamma_{LN_2} = \frac{\Gamma_L K_I p_{N_2}}{1 + K_{III} [N]} \qquad (27)$$

The adsorption equilibrium IV is described by a linear relation

$$\Gamma_N = K_{IV} [N] \qquad (28)$$

as it was assumed for the discussion of reaction (1). These expressions for the surface concentrations of the reacting species are introduced in Eq (25) and one receives a rate equation

$$v_{II} = k_{II} \frac{\Gamma_L K_I}{1 + K_{III} [N]} p_{N_2} - k_{II} \frac{\Gamma_L K_{III} [N]}{1 + K_{III} [N]} K_{IV} [N] \qquad (29)$$

which can be converted to the experimentally obtained Eq (24), if the constants are combined.
There is another possible mechanism which explains the rate Eq (24) and that is a dissociation of N_2 (ads) under formation of one adsorbed and one dissolved N-atom. The backward reaction would be a recombination of one adsorbed and one dissolved N-atom. The derivation of the rate equation for this second mechanism is similar to the considerations given above, excepted that the adsorption equilibrium IV would play no part. Thus the assumption of special sites is not needed.

N_2	$\rightleftharpoons$	N_2 (ads)	I
N_2 (ads)	$\rightleftharpoons$	N (ads) + N (dissolved)	II
N (ads)	$\rightleftharpoons$	N (dissolved)	III

The rate equation (24) in a generalized form

$$\frac{1}{s}\frac{dn_A}{dt} = k p_{A_2} \frac{1}{1 + K[A]} - k \frac{[A]^2}{1 + K[A]} \qquad (30)$$

and the inherent mechanism probably is of general importance for several reactions $A_2 \rightleftharpoons 2A$ (dissolved in a metal), since measurements of the dissolution reactions of H_2 with Pd (5) and O_2 with Ag (6) have given rate equations, which are in accord with equation (30).

ELEMENTARY REACTIONS IN CO_2-CO-MIXTURES

By measuring the rates of isotope exchange reactions at metals the rates of elementary steps of other more complicated reactions can be measured. This is shown for the decarburization and carburization of iron in CO_2-CO mixtures. The isotope exchange in a mixture of tagged CO_2, labelled with radioactive ^{14}C, and of inactive CO occurs by oxygen transfer from the CO_2 to the surface of the metal

$$^{14}CO_2 \rightleftharpoons {}^{14}CO + O\ (ads) \qquad (31)$$

and by the reaction of carbon monoxide with the adsorbed oxygen

$$O\ (ads) + CO \rightleftharpoons CO_2 \qquad (32)$$

Therefore by measuring the rate of the overall reaction

$$^{14}CO_2 + CO = {}^{14}CO + CO_2 \qquad (33)$$

the rate of the decomposition of CO_2 can be determined at any surface (7,8). It is virtually equal to the rate of the first step of the exchange reaction, since the isotope effect may be neglected. For the rate of the first step can be written

$$\frac{1}{S}\ \frac{dn_{^{14}CO}}{dt} = k(a_0)\, p_{^{14}CO_2} - k'(a_0)\, p_{^{14}CO} \qquad (34)$$

It is assumed that the surface coverages with CO_2 and CO are low, but the surface coverage with O (ads) may be high. Therefore the rate constants may depend on the activity of oxygen, which is determined by the equilibrium Eq (32) and can be defined by $a_0 = p_{CO_2}/p_{CO}$. In equilibrium of reaction Eq (33) the concentration of radiocarbon must be same in both gases

$$\left(\frac{p_{^{14}CO_2}}{p_{^{14}CO}}\right)_{eq} = \frac{p_{CO_2}}{p_{CO}} = a_0 \qquad (35)$$

With the help of the equilibrium condition $k'(a_0)$ can be eliminated

$$\frac{1}{S}\ \frac{dn_{^{14}CO}}{dt} = k(a_0)\,(1+a_0)\left[(p_{^{14}CO})_{eq} - p_{^{14}CO}\right] \qquad (36)$$

The exchange reaction was measured in a flow reactor. The amount of ^{14}CO, formed by the decomposition of $^{14}CO_2$ at the metal surface, is proportional to the counting rate found for the carbon monoxide behind the reaction vessel. At 800 °C the rate constant $k\ (a_0)$ was measured at iron in the interval of CO_2/CO-ratios between 0,116 and 0,532. At higher CO_2/CO-ratios oxidation of the iron occurs, at lower CO_2/CO-ratios carbon can be deposited. In this range the phases α- and γ-iron with dissolved carbon, ferrite and austenite occur, the boundary is at $CO_2/CO = 0{,}372$. It was found that the rate constant depends on a_0 (fig.14) according to

$$k\ (a_0) = k \cdot a_0^{\ -m} \qquad (37)$$

Measurements on metals more noble than iron showed no variation of $k\ (a_0)$ with a_0, obviously on these metals the surface coverage with O (ads) is low (fig.15).

At 800 °C also the decarburization and carburization of austenite was studied (7). This reaction proceeds according to

$$CO_2 + C\ (\text{in } \gamma\text{-Fe}) \rightleftharpoons 2\ CO \qquad (38)$$

A change in the CO_2/CO-ratio causes a change in the carbon content of the iron sample. For the decarburization the following mechanism may be assumed

	CO_2	$\rightleftharpoons$	CO_2 (ads)		I
CO_2 (ads)		$\rightleftharpoons$	CO (ads)	+ O (ads)	II
O (ads) + C (ads)		$\rightleftharpoons$	CO (ads)		III
CO (ads)		$\rightleftharpoons$	CO		IV
C (ads)		$\rightleftharpoons$	C (dissolved)		V

If the decomposition of the adsorbed CO_2 is rate determining the rate equation for the change in carbon content is analogous to the rate equation for the exchange reaction, which was discussed above.

$$-\frac{1}{S}\frac{dn_C}{dt} = k(a_0)\,p_{CO_2} - k'(a_0)\,p_{CO} \qquad (39)$$

By elimination of $k'(a_0)$ the following rate equation is derived

$$-\frac{\delta}{2}\frac{d[C]}{dt} = k(a_0)\,p_{CO_2}\left(1 - \frac{[C]_{eq}}{[C]}\right) \qquad (40)$$

which shows that the rate of decarburization should be proportional to the partial pressure of CO_2.
The decarburization and carburization could be investigated at 800 °C by measuring the relaxation of the electrical resistance after changes in the CO_2/CO-ratio of the flowing gas. The experiments could be performed in the interval of CO_2/CO-ratios where austenite is stable. The measurements showed that the rate of the decarburization is proportional to the partial pressure of CO_2 and is independent of the initial concentration of carbon. The rate contant $k(a_0)$, calculated from the decarburization measurements is virtually the same as the value found for the rate constant, calculated from the ^{14}C-exchange results.
These results prove that in both reactions the CO_2-decomposition occurs as an elementary step and that the reactions can be described by the assumed mechanisms.

CONCLUSION

For surface reactions at metals simple rate equations have been measured, from which the rate determining step could be recognized. In one case the comparison with isotope exchange studies helped to identify the elementary rate determining step.
Measurements have been performed of some reactions which lead to the formation of a solid solution of a nonmetal A in the metal. In reactions of the type

$$AH_x \rightleftharpoons A \text{ (dissolved)} + x/2\ H_2 \qquad (A = C,N,S,O)$$

a stepwise dehydrogenation or hydrogenation (in the backward reaction) of the nonmetal atom occurs. One of the reaction steps

$$AH_\nu \text{ (ads)} \rightleftharpoons AH_{\nu-1} \text{ (ads)} + H \text{ (ads)}$$

determines the rate of the reaction sequence and the dependences on partial pressures and concentrations, see Eq.(14). Obviously the rates of these consecutive steps are not very different and a variation of the reaction conditions or the metal substrate often displays other dependences and thus another rate determining step.
For dissolution reactions of diatomic gases $A_2 = N_2$, H_2, O_2 usually the dissoziation of the adsorbed molecule is rate determining. In several investigations the simple rate law Eq.(23) for the dissoziation and its back reaction, the recombination of two adsorbed A-atoms was found.
Complications arise at lower temperatures or high nonmetal activities and if nonmetal atoms are involved in the reactions, which are very strongly adsorbed such as oxygen. Then appropriate isotherms must be introduced for the equilibria of these atoms in the gaseous state and in the adsorbed state or in the dissolved state and in the adsorbed state, in order to adapt the rate equations to the results (see Eq.30 and Eq.37).
In principle the same considerations are valid and similar rate laws are to be expected, if no solid solutions but compounds of the metal and the nonmetal atom are formed, nitrides, carbides, sulfides or oxides.

REFERENCES

1) H.J.Grabke, Ber.Bunsenges. physik.Chem. 72, 533 (1968)
2) H.J.Grabke, Ber.Bunsenges. physik.Chem. 72, 541 (1968)
3) S.J.Wang and H.J.Grabke, to be published
4) H.J.Grabke, Ber.Bunsenges. physik.Chem. 69, 409 (1965)
5) W.Auer and H.J.Grabke, to be published
6) L.Imre, Ber.Bunsenges. physik.Chem. 72, 863 (1968)
7) H.J.Grabke, Proc. IIIrd Int.Congr.Catalysis, p.928 Amsterdam 1965
8) H.J.Grabke Ber.Bunsenges. physik.Chem. 69,48 (1965),7o,664 (1966),71,1o67 (1967)

FIGURE CAPTIONS

1) Principle of the relaxation method
2) Denitriding measurements with iron foil
3) Double-logarithmic plot of k_γ $p_{H_2}^{\gamma/2}$ vs. p_{H_2} from denitriding measurements with iron foil
4) Temperature dependence of the denitriding rate measured at 1 atm •, o,5 atm ◘, o,1 atm ⊙ and o,ool atm ▫ .
5) Decarburization measurements with iron foil
6) Double-logarithmic plot of k_γ $p_{H_2}^{\gamma/2}$ vs. p_{H_2} from decarburization measurements with iron foil
7) Desulfurization measurements with iron foil
8) Plot of k_γ $p_{H_2}^{\gamma/2}$ vs. pH_2 from desulfurization measurements
9) Relaxation measurement of the nitriding with N_2 and of the N_2-desorption
10) Rate of the nitriding with N_2 at various N_2-partial pressures
11) Plot of the nitriding measurements with α-iron
12) Plot of the denitriding measurements with α-iron
13) Dependence of the N_2-desorption on high nitrogen concentrations in the iron sample
14) Double-logarithmic plot of k (a_0) vs. a_0 for measurements on iron
15) Double-logarithmic plot of k (a_0) vs. a_0 for measurements on copper and nickel.

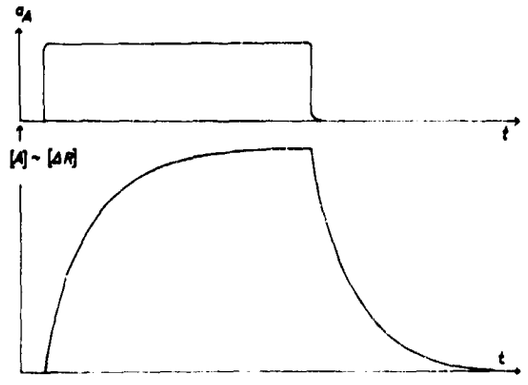

(1) Principle of the relaxation method

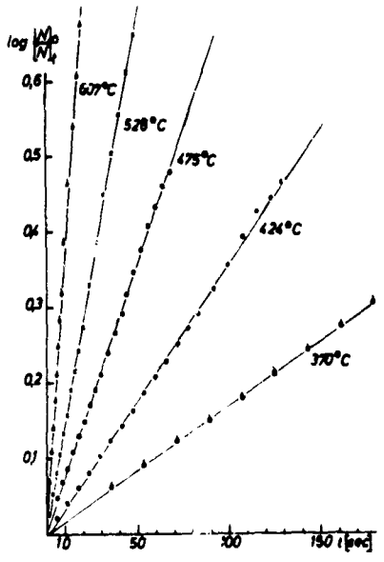

(2) Denitriding measurements with iron foil

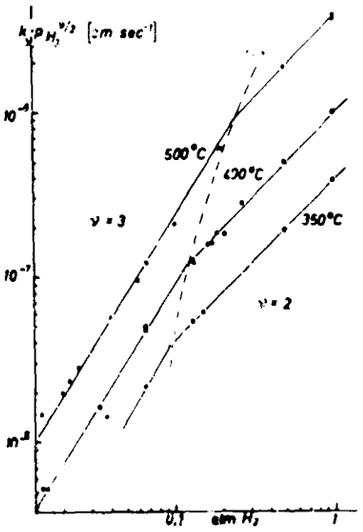

(3) Double-logarithmic plot of $k_\gamma p_{H_2}^{\nu/2}$ vs. p_{H_2} from denitriding measurements

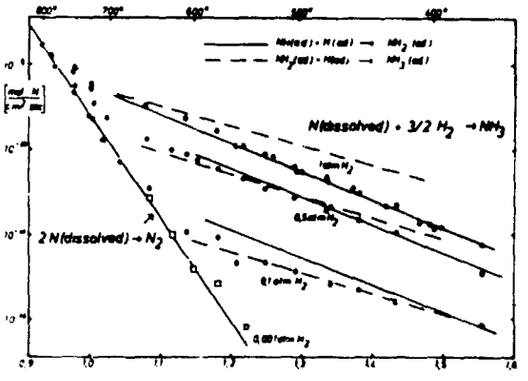

(4) Temperature dependence of the denitriding rate, measured at 1atm H_2 • , 0,5 atm • 0,1 atm • and 0,001 atm ▫

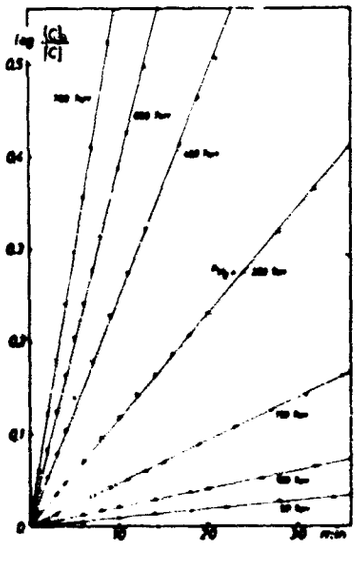

(5) Decarburization measurements with iron foil

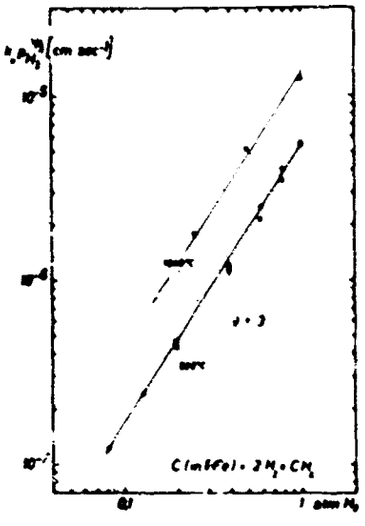

(6) Double-logarithmic plot of $k_\gamma p_{H_2}^{\nu/2}$ vs. p_{H_2} from decarburization measurements

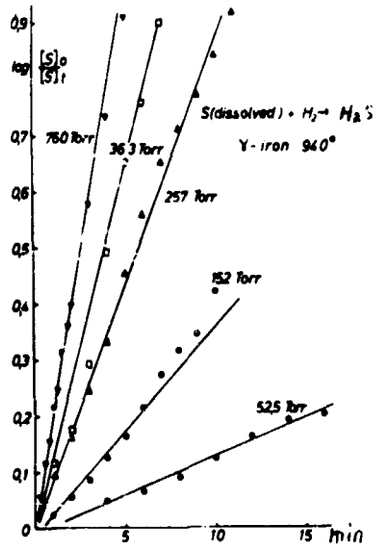

(7) Desulfurization measurements with iron foil

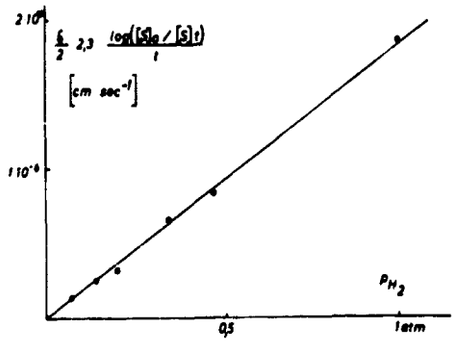

(8) Plot of $k_\gamma p_{H_2}^{1/2}$ vs. p_{H_2} from desulfurization measurements

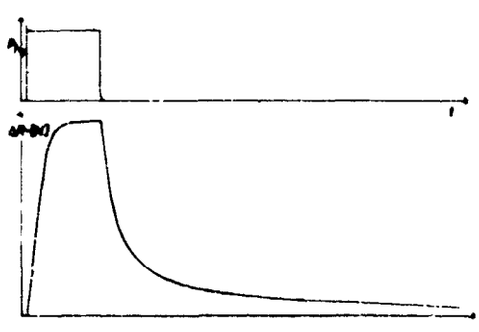

(9) Relaxation measurement of the nitriding with N_2 and of the N_2-desorption

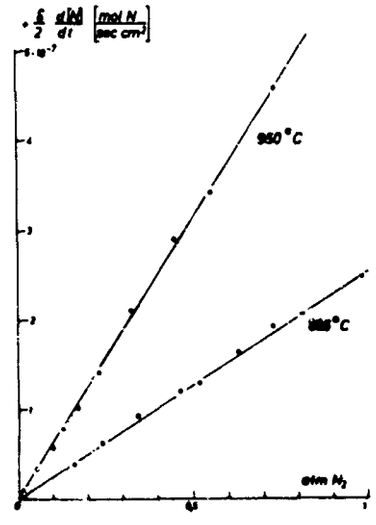

(10) Rate of the nitriding with N_2 at various nitrogen pressures

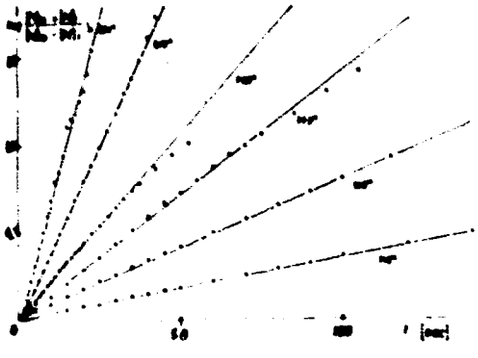

(11) Plot of the nitriding measurements with α-iron in N_2

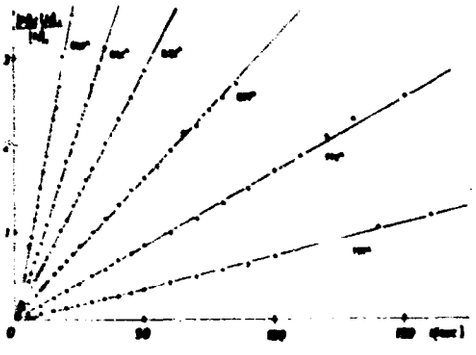

(12) Plot of the N_2-desorption measurements after nitriding α-iron in N_2

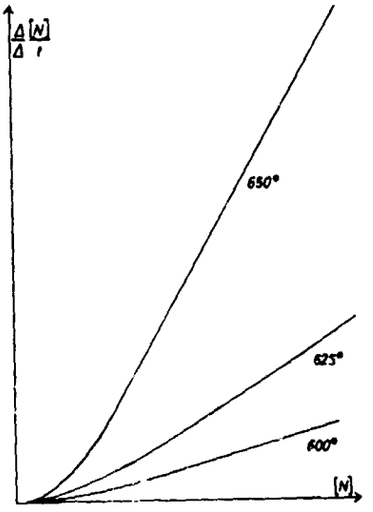

(13) Dependence of the N_2-desorption rate on high nitrogen concentrations in the iron sample

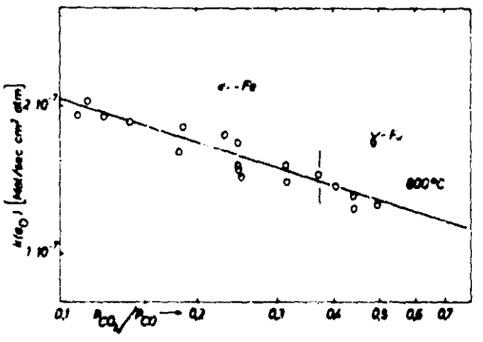

(14) Double-logarithmic plot of $k(a_O)$ vs. a_O from ^{14}C -exchange measurements on iron

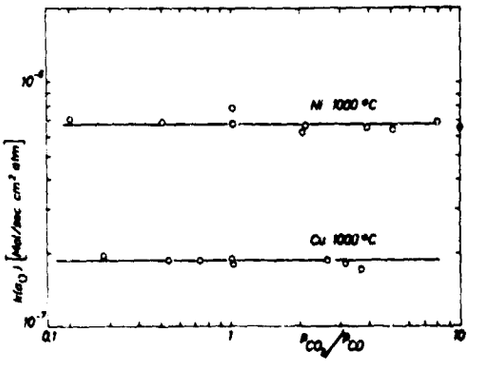

(15) Double-logarithmic plot of $k(a_O)$ vs. from ^{14}C-exchange measurements on copper and nickel

OXIDATION STUDY OF ZIRCONIUM DIBORIDE WITH VARIOUS ADDITIVES

July 1969

H.C. Graham

AEROSPACE RESEARCH LABORATORIES
WRIGHT-PATTERSON AIR FORCE BASE
DAYTON, OHIO 45433 USA

W.C. Tripp

SYSTEMS RESEARCH LABORATORIES INC.
DAYTON, OHIO 45440 USA

SUMMARY

The relative oxidation resistances of (1) ZrB_2, (2) ZrB_2 + 20 v/o SiC, and (3) ZrB_2 + 14 v/o SiC + 30 v/o C were studied thermogravimetrically over the range 800 to 1600°C and over a range of three orders of magnitude in oxygen partial pressure. In undoped ZrB_2 the relative amounts of B_2O_3 and ZrO_2 formed could be determined by measuring total oxygen consumption and the amount of B_2O_3 formed. Below 1100°C very little of the B_2O_3 formed evaporated at the total pressure used (250 mm). The kinetics of the oxidation process were difficult to define and appear to depend on sample composition, temperature, and oxygen partial pressure. Logarithmic and cubic as well as parabolic dependencies were observed in some cases. In those cases where the process was consistent over a wide enough range of conditions, values for the rate constants and activation energies are calculated and compared with values found by other investigators.

A GROUP OF MATERIALS of current interest for high temperature applications is the refractory metal borides. A thorough survey of the borides of niobium, titanium, zirconium, and hafnium has been made for the Air Force Materials Laboratory at Wright-Patterson AFB under the direction of Manlabs, Inc. Through their efforts several of the borides and borides with additives have been developed with sufficient thermal properties to be considered for practical uses in such applications as rocket nozzles, turbine parts, and leading edges of space vehicles.

The study of the oxidation of zirconium diboride with certain additives was undertaken to compliment and extend the extensive survey work of Manlabs. The measurements made at Manlabs consisted principally of recession rates for times of 30 to 60 minutes in air at temperatures of 1800° to 2100°C, whereas the measurements conducted in this study are weight change measurements in oxygen for larger periods of time over the temperature range of 800° to 1500°C. The goal is to derive the mechanism of corrosion of these materials. The studies accomplished to date show clearly the complexity of the problem and have shown the necessity of combining more than one type of measurement to determine insight into the processes involved.

The specific materials that have been investigated are:

Material I, ZrB_2 without any intentional additives, Manlabs billet number IO3AD0563.

Material V, ZrB_2 with 20 v/o SiC, billet number VO7DO717K.

Material VIII, ZrB_2 with 14 v/o SiC and 30 v/o Regal C, billet number VIII07D0725K.

Out of the many materials developed in the Manlabs program these three studied here appear to be the most promising for immediate applications based on their thermal properties, ease of fabrication, and the cost of manufacture. A similar group of materials with hafnium replacing zirconium was studied by Manlabs and generally exhibited better thermal properties but was both heavier and more costly.

This manuscript is the initial report of a continuing study of the oxidation of boride compounds and as such is not intended to be complete. More measurements, complimentary to the weight change data, are in progress. These include weight change measurements where the volatile products are collected and weighed simultaneously with the sample, weight change measurements where only the volatile products are weighed, oxygen consumption measurements, and microstructure studies. The results of these measurements will be reported upon completion.

EXPERIMENTAL The material was received in three inch diameter billets approximately one inch long. The billets were sliced with a diamond saw to make coupons approximately 1 mm thick having an average surface area of 4 cm^2. After sawing, the samples were smoothed on a diamond grinding wheel to remove the saw marks and no further polishing was done.

Each sample had a small hole drilled in the center at one end from which it was suspended for the weight change measurements. The area used for a sample was the geometric area obtained by measuring with a micrometer.

Before a run was made the sample was washed with acetone and alcohol in an ultrasonic cleaner, then hung from the balance in the furnace which was evacuated to about 10^{-5} torr and heated to 600°C. Each sample was held at 600°C for 15 to 18 hours before heating to the temperature of the measurements.

Two methods were used to establish a value for zero weight at zero time. Below 1000°C, where no significant reaction occurs in vacuum for short periods of time, the vacuum weight could be compared before and after a run to get the total weight gained. This weight could be subtracted from the last weight measured before evacuating to obtain a weight for zero time. Above 1000°C where some reaction could be observed in vacuum it was necessary to extrapolate back to zero time to get zero weight values. The values obtained by the first method are much more accurate.

The balance system used in this study has been previously described.[1], [2] Two Ainsworth balances were used; one a model 14F, the other a model AU1. Both balances worked extremely well in this application. The one limitation necessary was imposed by the small weight change that could be measured. The 14F measures a total change of only 80 mg and the AU1, 100 mg. This required samples small enough that the total change in weight observed would be within these limits.

Most all the measurements were made at a total pressure of 250 mm of oxygen. This pressure was chosen so that evaporation could be kept as low as possible. At 250 mm total pressure, the balance trace starts to show noise because of thermal convection currents and gets much worse as the pressure is increased.

Commercial breathing type oxygen was used with no further purification. The flow dependence of the weight change was checked and although flows of only 150 ml/min were used it was found to provide enough oxygen at all temperatures with the small samples that were used.

RESULTS The results presented here contain only weight change measurements to 1500°C with the exception of one 20 min run on material V at 1600°C.

Figure 9-1 is the weight change per unit area vs time for material I covering the temperature range of 800° to 1400°C. The first two hours of these data can be fit reasonably well to a parabolic rate. However, it was also found that most of these data could be plotted equally well to a cubic equation. The next two hours appear to be linear but here also the data could be fit to another dependence, i.e. logarithmic. This graph indicates a change in the oxidation process between 1100° and 1200°C. This can be seen by the relative closeness of the two curves. Above 1100° the boron oxide formed appears to be completely vaporized and although the oxidation rate is expected to increase with temperature it does not since these gravimetric measurements only measure the weight of the material remaining.

Material I was oxidized at 1500°C but because of a reaction occurring between the sample and the material used to hang the sample the sample droped off after 20 minutes. No satisfactory material has been found for suspending the boride materials at temperatures above 1500°. Calcia stabilized zirconia, thoria, alumina, rodium, and iridium have been tried for the higher temperature work, but in each case the reaction occurring proved to be distructive.

The effects of oxygen pressure on the oxidation rate over long periods of time was examined at 1100°C as shown in Figure 9-2. The oxygen pressures are also the total pressure. . . quite difficult to explain from these measurements what change in mechanism(s) is occurring as the pressure is lowered. However, the weight change measurements shown on Figures 9-1 and 9-2 do indicate that the mechanism of oxidation in material I does depend on both the temperature and the pressure.

Material V with 20 v/o silicon carbide added shows different behavior at the higher temperatures than material I. Figure 9-3 presents the weight change data for material V over the same temperature range. Below 1000°C the oxidation behavior for both materials is quite similar. At 1100°C there is a marked decrease in the weight gain. After several hours the sample appears to be losing weight which is an indication that the boron oxide is vaporizing about as fast as it is formed. The 1200° data appear anomalous showing a larger weight gain than fits in with the data at other temperatures. This sample had a very thick glass-like coating on it that apparently forms in this temperature range and does not evaporate very rapidly. The glass-like coating is observed at other temperatures, but never as thick as at 1200°C. At 1300° the glass formed appears to be evaporating. After several hours a decrease in weight is observed probably due to the rate of formation being slower than the rate of evaporation. At 1400°C and above the weight shows a steady increase for long periods of time. This is an indication that the formation and retention of solid ZrO_2 predominates. The 1500° run on this material was successful, but at 1600° the reaction between the suspension and the sample occurred as it did at 1500° in material I.

The pressure dependence is shown in Figure 9-4. Again combining the data of Figures 9-3 and 9-4 indicates an oxidation process which is both pressure and temperature dependent. However, it was possible to take the first 60 minutes of these data and calculate a parabolic rate constant. Figure 9-5 shows that the pressure dependence is nearly linear for the first hour of oxidation at 1100°C.

Figure 9-6 shows the weight change data for material VIII which contains 14 v/o silicon carbide and 30 v/o regal carbon. These data indicate behavior quite similar to material V. The reproducibility of these measurements was quite poor probably due to inhomogenity caused by the large carbon content. The data on materials I and V were reproducible to better than 10% so the comparison of the oxidation behavior will be confined to these two materials.

An indication of the rates involved in the weight change can be seen from Figures 9-7 and 9-8. Figure 9-7 is a log - log plot of the weight change per unit area for material I and 250 torr oxygen pressure and Figure 9-8 shows the same data for material V. A line is drawn in the figures representing parabolic kinetics.

The agreement is not good because as shown previously the oxidation rates are a combination of more than one process. However, to compare the rates of the two materials and also to compare our data with other investigators the shorter times can be plotted reasonably well to a parabolic equation.

The addition of silicon carbide was made to improve the oxidation resistance of these materials at the higher temperatures. It is expected that the usable temperature range will be above 2000°C. No weight change measurements have been successful at temperatures this high because of the problem of supporting the sample. The measurements made to 1500°C do show the improved oxidation behavior of material V when compared to material I.

Figures 9-9 and 9-10 compare the high temperature and low temperature behavior of materials I and V. These data are plotted to a parabolic fit for the first two hours of oxidation.

Below 1300° material V shows larger weight gains than material I. Above 1300° this behavior is reversed as shown in Figure 9-10.

Keeping in mind that these data are weight measurements of remaining sample it would be difficult to fairly evaluate the material from these data only. However, the recession rate measurements to 2100°C by Manlabs do show that it is at the high temperatures that material V is superior to material I in resisting oxidation.

Other investigators have made oxidation studies on materials equivalent to material I used in these experiments. Figure 9-11 is a plot of the parabolic rate constant derived from these weight measurements. In this figure are shown the data of two other investigators, one of weight change[3], the other oxygen consumption measurements[4]. Below 1100°C there is reasonable agreement between all investigators. Since all the oxidation products should be retained at these temperatures the measurements should be directly comparable. Above 1100° where a rate change was shown to occur, Figure 9-1, our data and that of Kuriakose and Margrave are still in good agreement, however, Berkowitz's data shows a much greater oxygen consumption which could not be shown on this plot.

CONCLUSIONS A complete picture of the oxidation of zirconium diboride or any oxidation process resulting in part in the formation of one or more volatile products cannot be deduced from weight change measurements alone. However, continuous weight change measurements are extremely sensitive indicators, perhaps more so than any other type of measurement, of any change taking place with time, temperature, pressure etc. which results in a loss or gain in weight. The results presented here show quite clearly the oxidation of the diborides, particularly with additives, is complicated.

Material I, without additives, does not show a clear parabolic dependence to the oxidation process even at temperatures below 1100° where the vaporization of boron oxide should be negligible, although most of the oxidation data found in the literature does interpret the oxidations process as parabolic. The weight change rate at temperatures below 1100° could be controlled by more than one process. The boron oxide formed is liquid at these temperatures. A diffusion controlled process theoretically requires a constant film thickness which is difficult to maintain with the measurements being made here.

The data above 1200° shown in Figure 9-7 appears to be approaching closer to a 1/2 slope as the temperature is increased. At these higher temperatures the vaporization of boron oxide is probably complete and the process being measured is the formation of zirconium oxide. What the rate controlling process is cannot be derived without additional information but it is not unreasonable to assume that the process is controlled by the diffusion of oxygen through ZrO_2. The energies obtained from the weight change measurements are reasonable for this type of process.

The behavior of material V is shown by these weight change measurements to be much more complicated than material I. The long time data presented in Figure 9-3 show the behavior expected when the compounds formed have different temperature dependence for vaporization. Below 1100°C the behavior, especially at times less than 4 hours, is quite similar to material I. This would indicate that the SiC addition does not enhance the oxidation resistance of ZrB_2 at these temperatures and does not significantly affect the weight change. However, at 1200°C the formation of a glassy layer on the surface of material V appears to be the largest contributor to the weight change. The composition of this layer is not known but could possibly contain boron and/or zirconium compounds as well as SiO_2. At 1300°C and above the evaporation of the silica layer begins and as the temperature is increased the formation of ZrO_2 should be the predominant process increasing the sample weight. For the first four hours of oxidation shown in Figure 9-8 the data appears to fit a 1/2 slope better at the higher temperatures as did material I.

The non-reproducibility of the measurements on material VIII precludes this material from a qualitative discussion. However, as can be seen by comparing Figure 9-3 with Figure 9-5 there is a great deal of similarity in the weight change data for both of these materials. A variation of material VIII has been developed by Manlabs which contains only 18 v/o carbon and 10 v/o silicon carbide. This material which is much more homogeneous and retains all the desirable properties of material VIII (i.e., oxidation resistance with better thermal stress properties and increased machinability).

REFERENCES

(1) W.C. Tripp, R.W. Vest, and N.M. Tallan, "Vacuum Microbalance Techniques", Vol. 4 pp. 141-157 Plenum Press (1965).

(2) H.C. Graham and W.C. Tripp, "Vacuum Microbalance Techniques", Vol. 6, pp. 63-73, Plenum Press (1967).

(3) A.K. Kuriakose and J.L. Margrave, J. Electrochem Soc. III 827 (1964).

(4) J.B. Berkowitz - Nattuck, J. Electrochem Soc. 113 908 (1966).

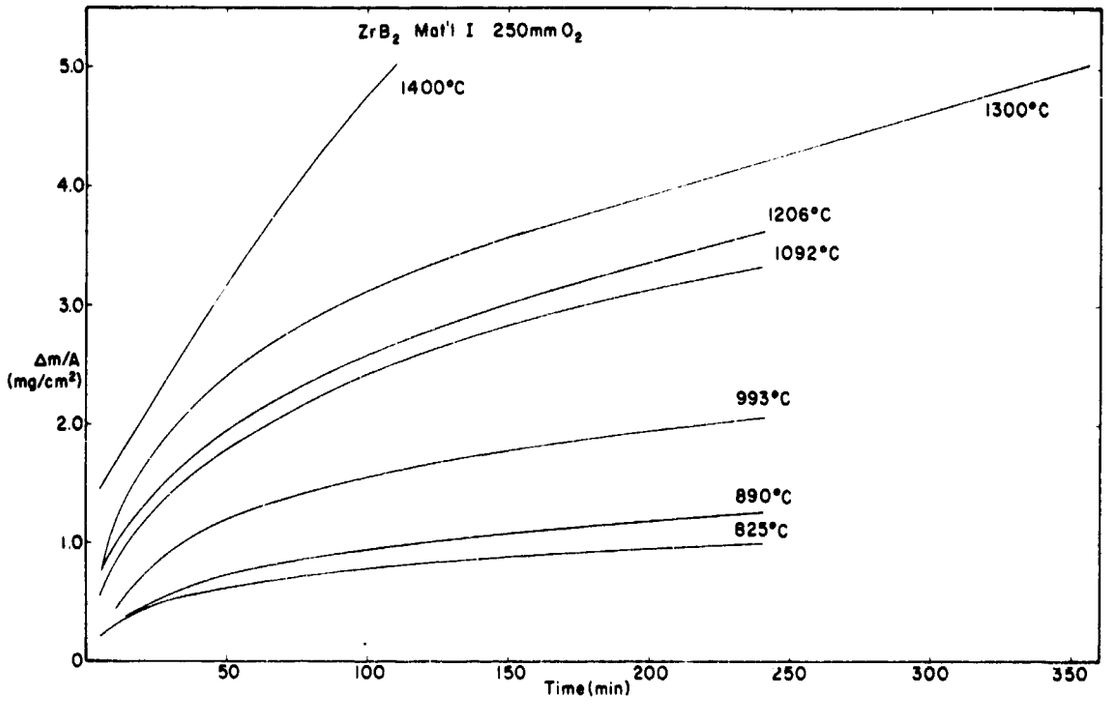

Fig. 9-1 Oxidation of Material I, ZrB_2; 800° to 1400°C, 250 torr Oxygen.

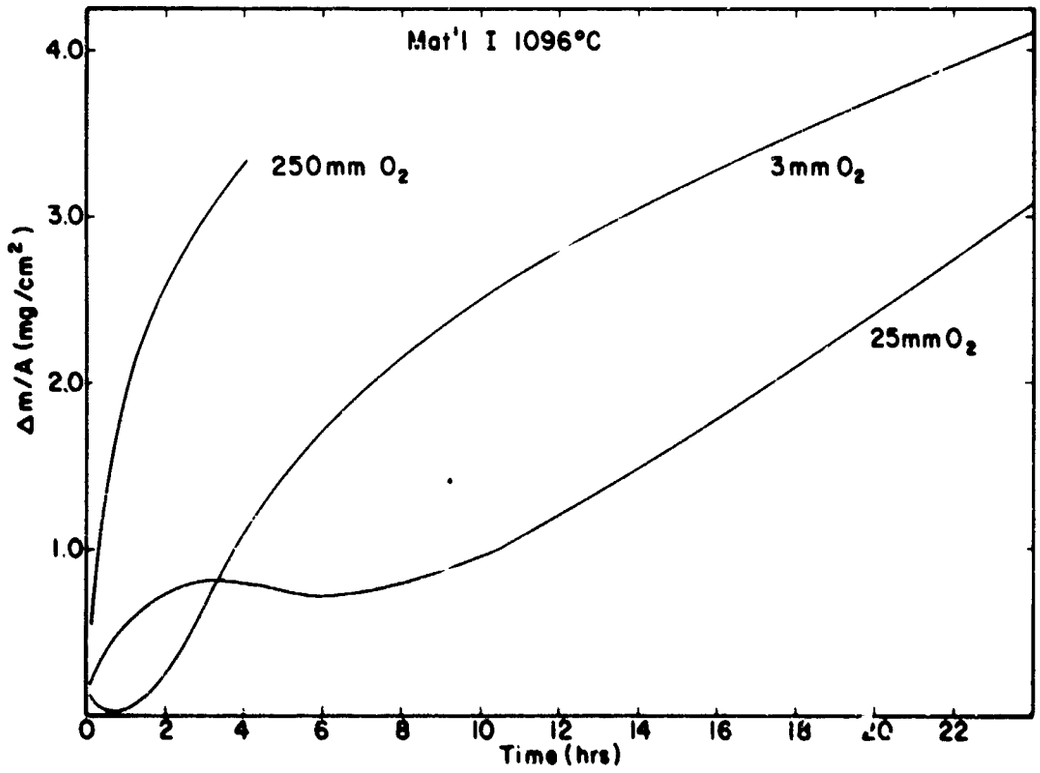

Fig. 9-2 Pressure Effect on the Oxidation of Material I, ZrB_2; 1096°C, 250, 25, & 3 torr Oxygen.

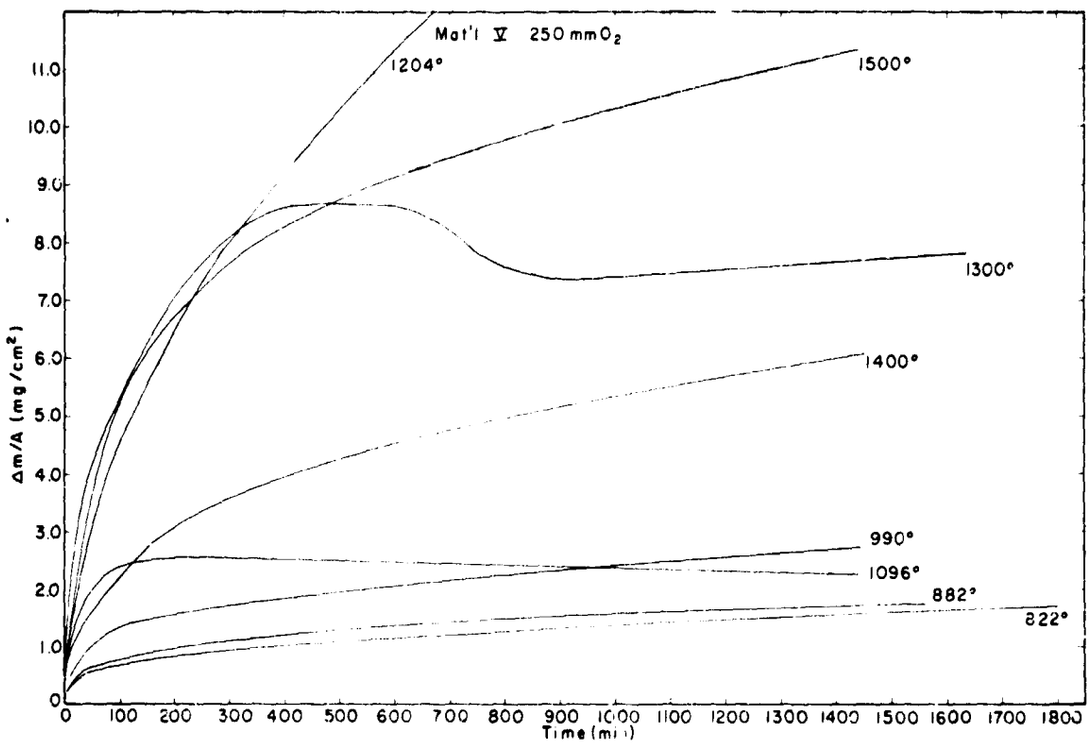

Fig. 9-3 Oxidation of Material V, ZrB_2 + 20 v/o SiC 800° to 1500°C, 250 torr Oxygen.

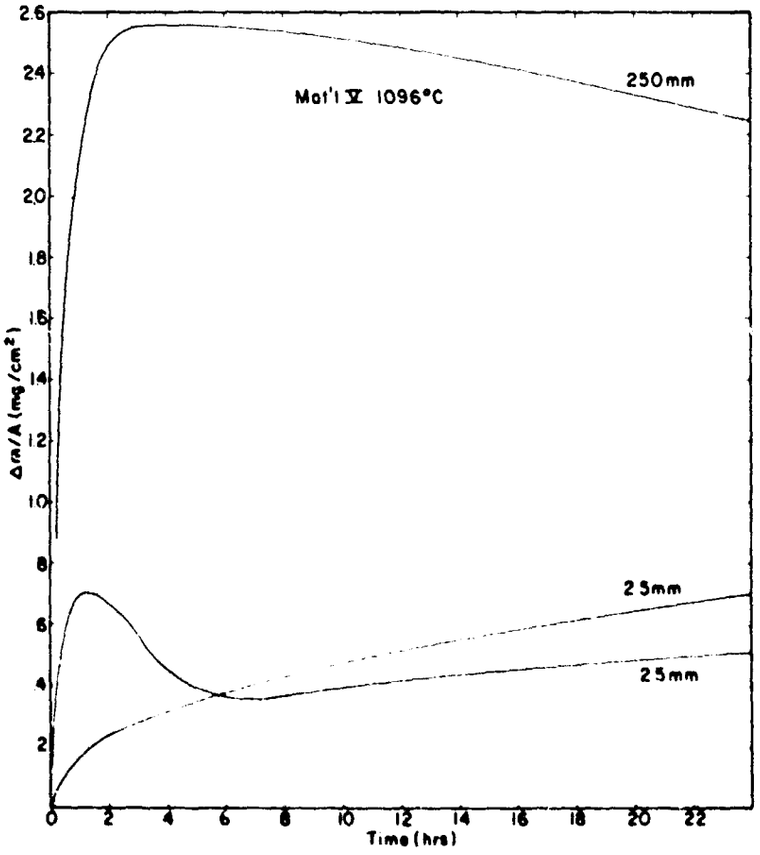

Fig. 9-4 Pressure Effect on the Oxidation of Material V, ZrB_2 + 20 v/o SiC, 1096°C, 250, 25, & 2.5 torr Oxygen

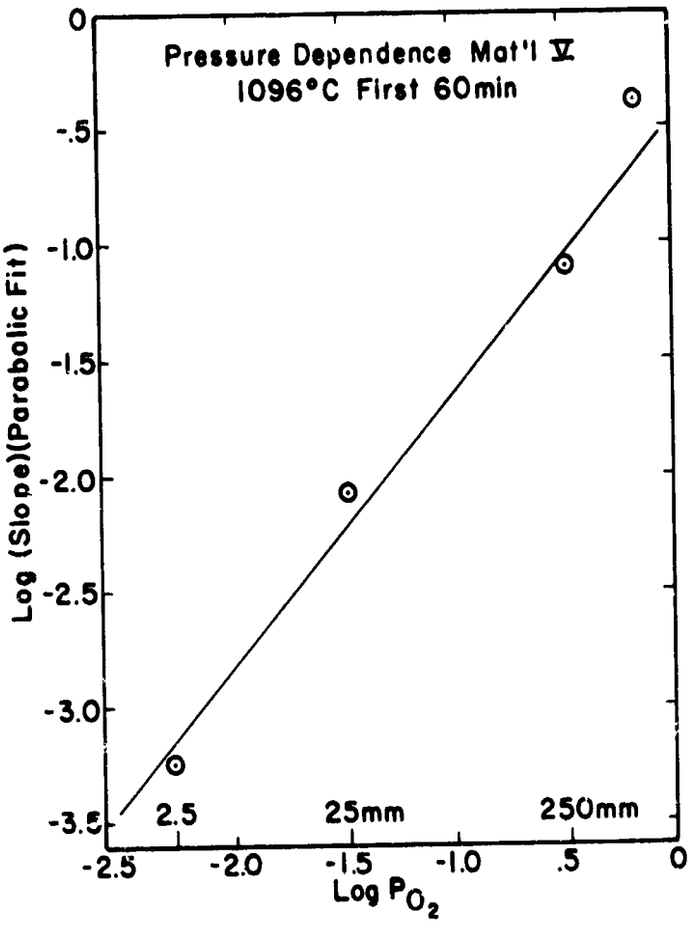

Fig.9-5 Linear Pressure Dependence of the Oxidation of Material V, ZrB_2+20 v/o SiC, 1096°C.

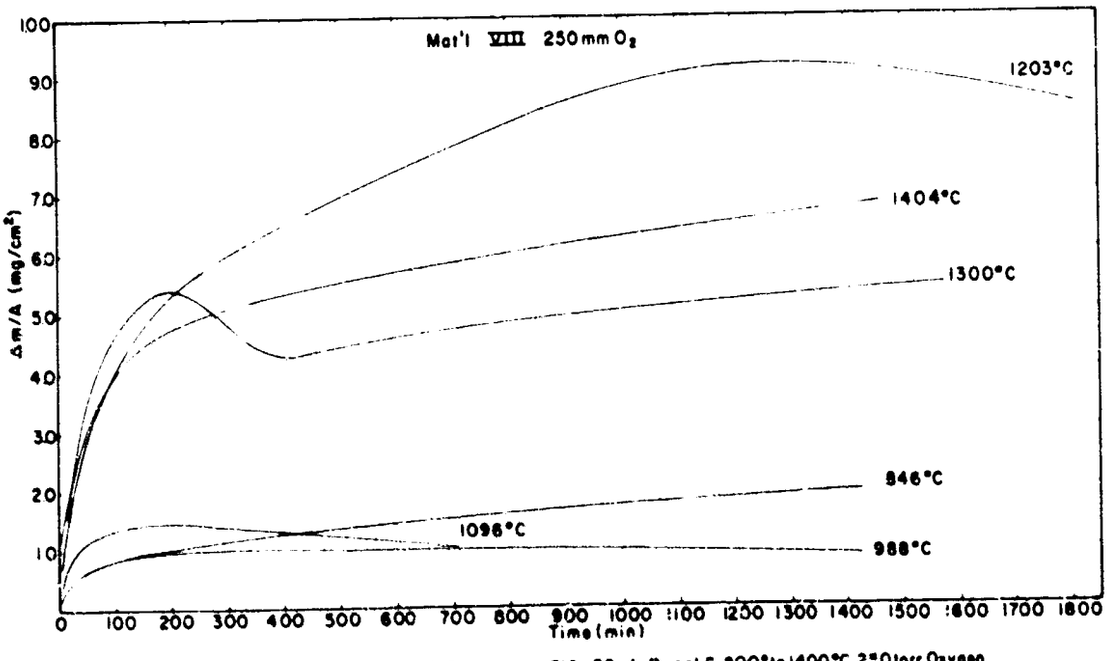

Fig 9-6 Oxidation of Material VIII, ZrB_2+14 v/o SiC + 30 v/o Regal C, 800° to 1400°C, 250 torr Oxygen

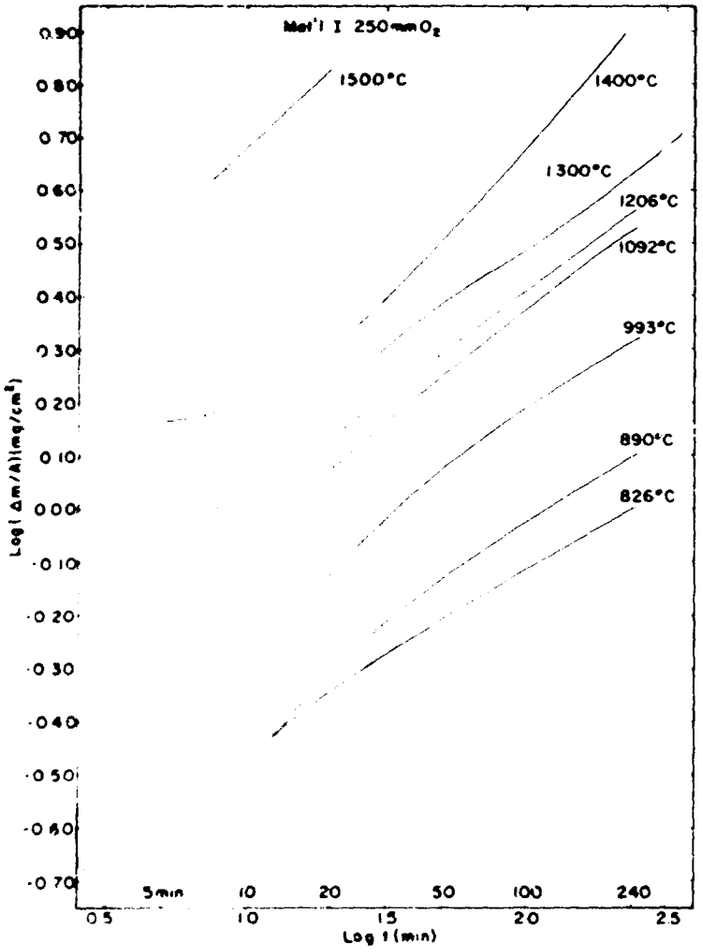

Fig 9-7 Log-Log Plot of the Oxidation of Material I, ZrB_2, 800° to 1500°C, 250 torr Oxygen

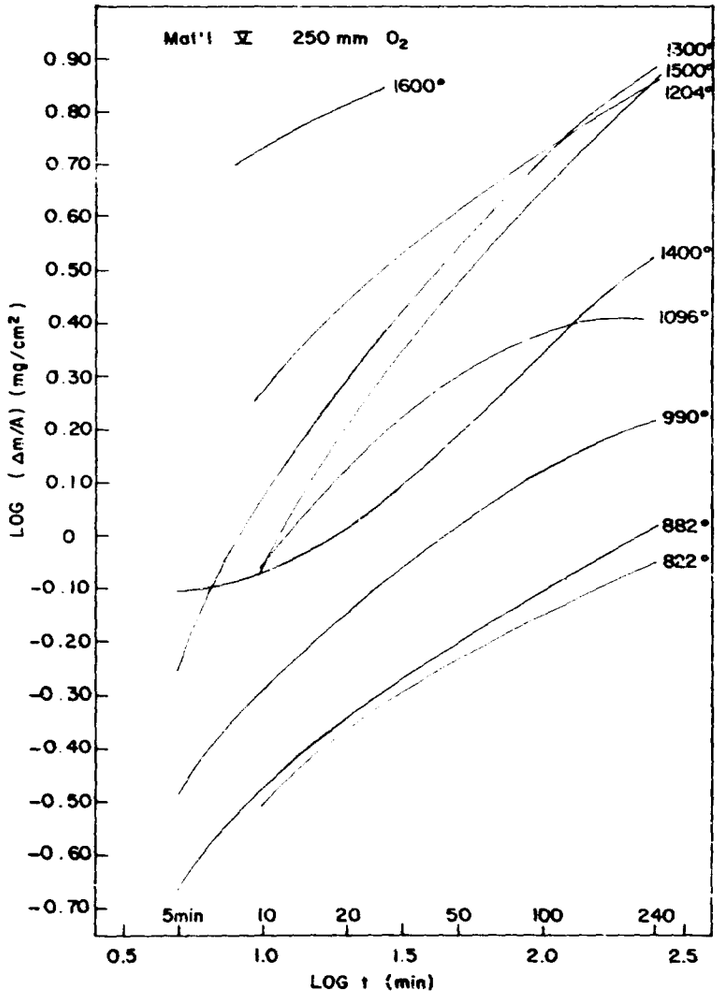

Fig. 9-8 Log-Log Plot of the Oxidation of Material V, ZrB_2 + 20v/o SiC, 800° to 1600°C, 250 torr Oxygen

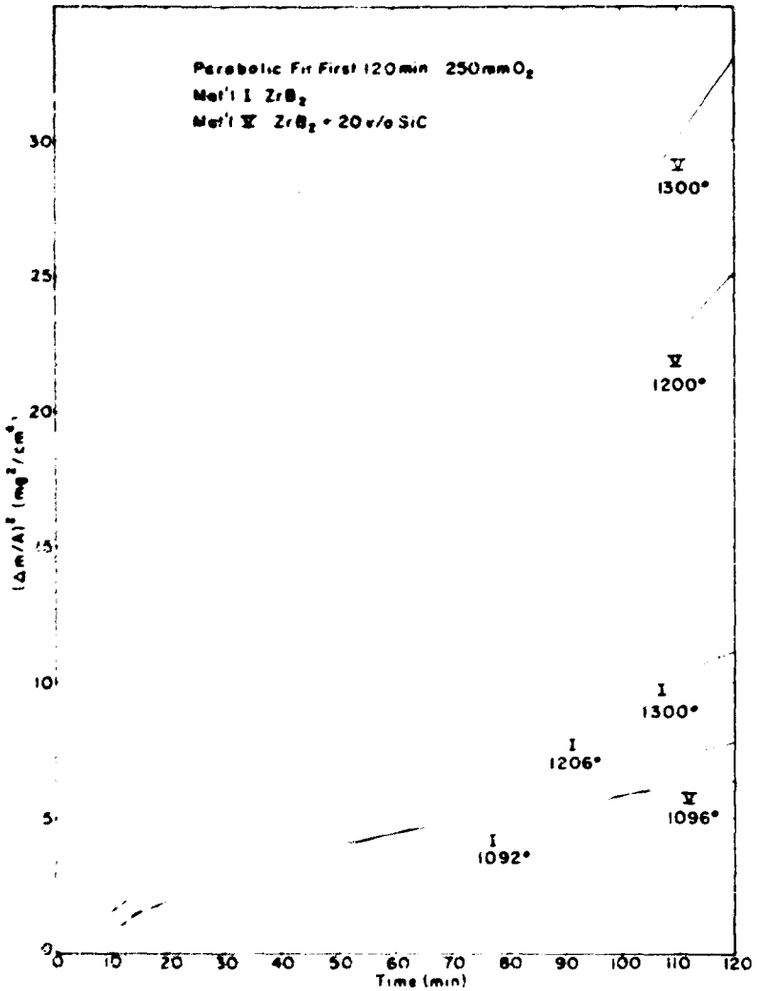

Fig 9-9 Parabolic Fit to the Data for the First 2 Hours of Oxidation at 250 torr Oxygen Comparing Materials I & V at 1100°, 1200, & 1300°C

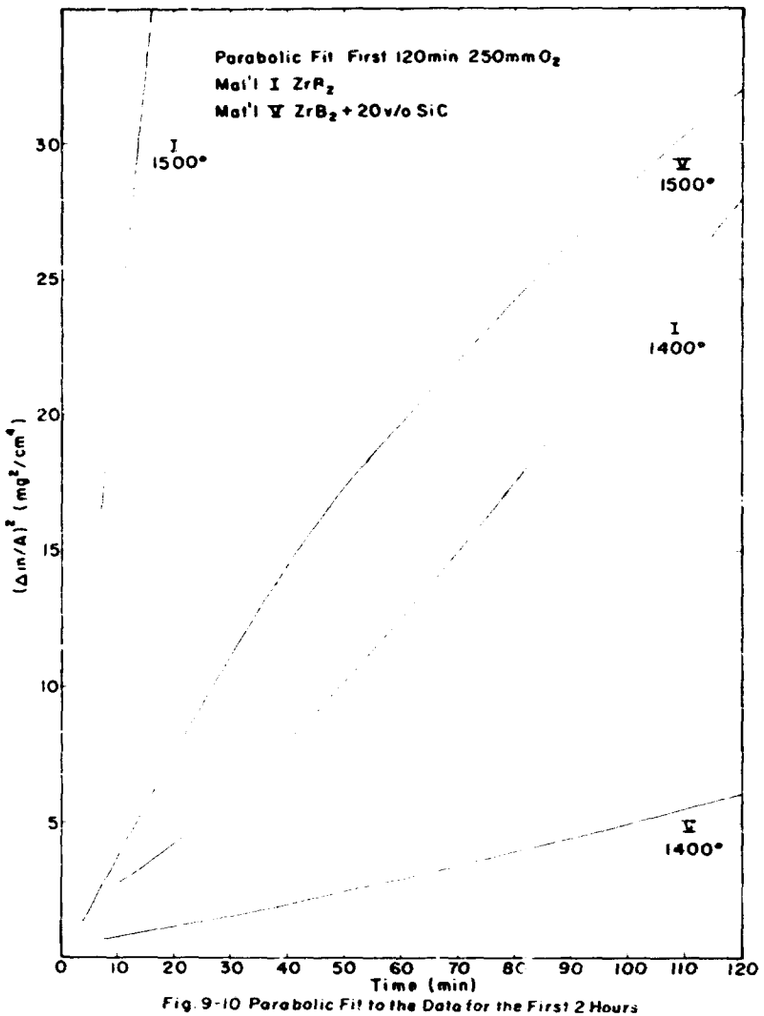

Fig. 9-10 Parabolic Fit to the Data for the First 2 Hours of Oxidation at 250 torr Oxygen Comparing Materials I & V at 1400° & 1500°C

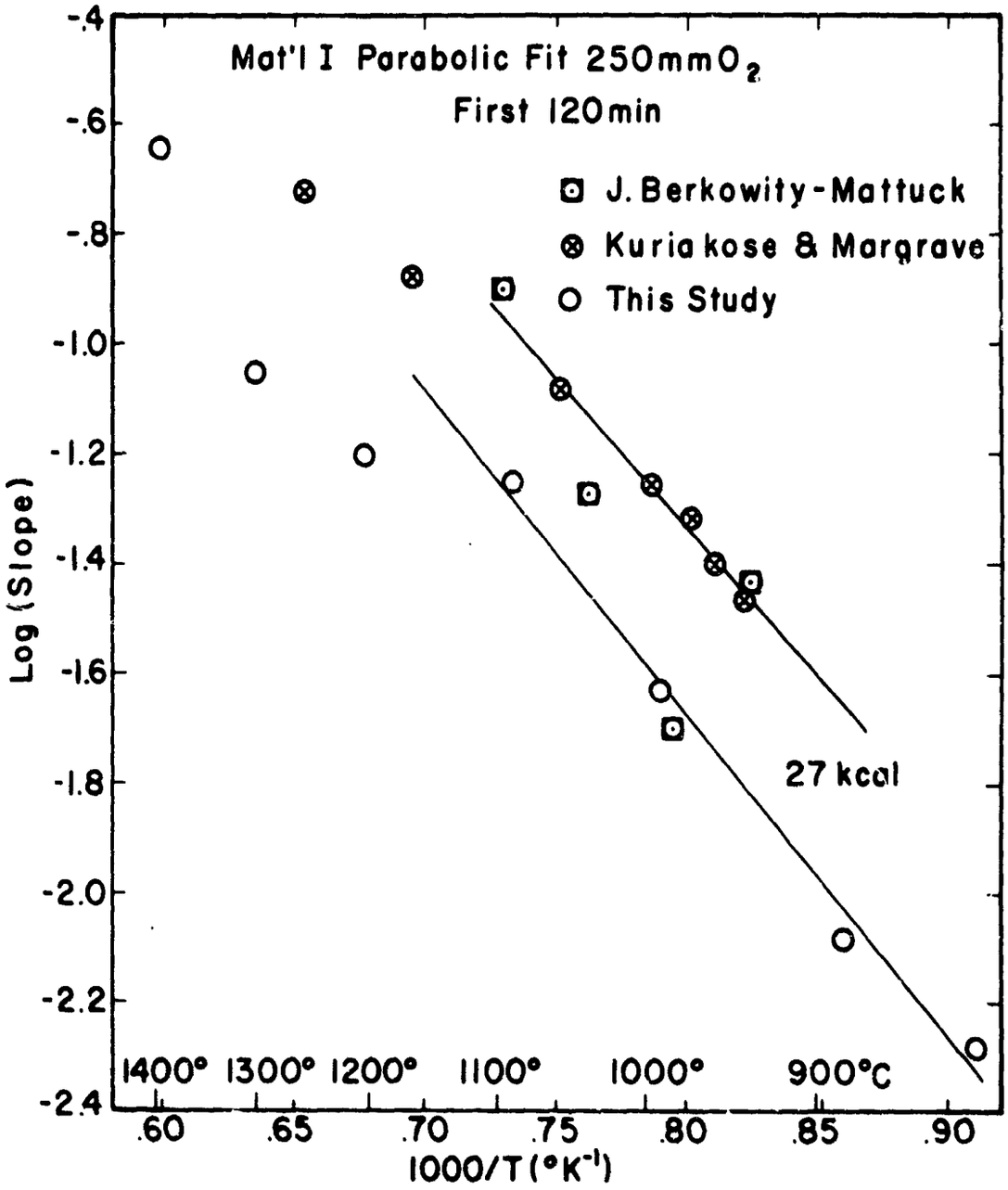

Fig.9-11 Comparison of the Weight Change Measurements of this Study with the Work of Other Investigators. Material I, Parabolic Fit, 250 torr Oxygen.

OXIDATION OF SILICON AND SILICON CARBIDE IN GASEOUS ATMOSPHERES AT 1000 - 1300°C

J. E. Antill and J. B. Warburton
Solid State Division, A.E.R.E., Nr. Didcot, Berkshire U.K.

SUMMARY

The behaviour of silicon, a self bonded silicon carbide containing silicon and pure silicon carbide has been assessed in carbon dioxide, water vapour, oxygen, carbon monoxide, vacua and helium at 1000 - 1300°C. Particular attention has been paid to the conditions governing the formation of protective silica films and to the passage of material into the gas phase as SiO and silicon vapour. A detailed review of published data is given together with an account of additional experimental work.

When silica films are formed a parabolic rate law is in general obeyed and there are no marked differences in behaviour of the three materials, with the exception that silicon is oxidised more readily than silicon carbide in water vapour at 1000°C. The reactivities of the oxidants decrease in the order water vapour, oxygen and carbon dioxide with carbon monoxide being completely inert. The data have been interpreted on the basis that the silica films grow by the diffusion of hydroxyl ions in water vapour.

The formation of SiO with silicon carbide in low partial pressures of oxidant leads to high corrosion rates. It has been deduced that under these conditions silica is an intermediary and the rate determining step is the desorption of the gaseous products. Silicon carbide is not dissociated into silicon vapour and carbon at temperatures $< 1200°C$ although decomposition may be significant at 1300°C

SILICON CARBIDE has established itself for many applications, its essential properties being excellent oxidation resistance and mechanical strength at high temperatures. The work covered by the present paper was carried out on its corrosion behaviour in the nuclear context for the possible use of silicon carbide based materials in nuclear reactors, and hence the environments considered are of particular relevance to the nuclear field. However the work is of general applicability in that the fundamentals covered apply to many non-nuclear applications including the aerospace field.

The work has been concerned with self bonded silicon carbide, a well established impervious product containing free silicon, pure silicon carbide and for reference purposes and because silicon is present in the bonded material, pure silicon. The behaviour of these materials has been assessed in carbon dioxide, water vapour, oxygen, carbon monoxide, vacua and flowing helium over the temperature range 1000 - 1300°C. For presentation purposes the paper is divided into a review of previous work, application of previous work, a description of an experimental programme with finally a discussion of the available data.

PREVIOUS WORK

The oxidation behaviour of both silicon and silicon carbide can be classified as either "passive" with the formation of protective silica films, or "active" with the formation of gaseous SiO, leading to high corrosion rates. A limited supply of oxidant with low partial pressures of the oxidising gas is a necessary condition for active corrosion, the SiO being produced possibly by direct reaction with the gas or by reduction of temporarily formed silica, by the underlying silicon or silicon carbide e.g.

$$2\,Si + O_2 \longrightarrow 2\,SiO$$

$$Si + SiO_2 \longrightarrow 2\,SiO$$

A high pressure of oxidant lowers the partial pressure of SiO according to the reaction

$$SiO + \tfrac{1}{2}O_2 \longrightarrow SiO_2 \qquad \ldots\ldots(1)$$

and thereby results in the formation of a protective film of silica.

PASSIVE REGION With regard to the passive region, numerous studies have been carried out for both silicon[1-3] and silicon carbide[4-9] in oxygen and water vapour, with only a very limited amount of work on the behaviour in carbon dioxide and carbon monoxide. The data in general only refer to short exposures with a maximum time of 100h and in the case of silicon carbide only to powder samples. Also much of the data are inconsistent with regard to the influence of important variables such as gas pressure.

The kinetics may in general be approximated to a parabolic law, although there may be an appreciable period in the early stages when a linear law is obeyed, particularly at low temperatures. With silicon carbide limited studies indicate that the carbon is released to the gas phase as carbon dioxide or carbon monoxide on oxidation of the silicon atoms, and most data are interpreted on this basis. Motzfeldt[10] has summarised most of the information for both materials in oxygen published up to 1964 in a parabolic rate constant versus $\frac{1}{T}$ plot, which indicates that the kinetics of the thickening of the silica film are similar for both materials and hence are not influenced by the passage of carbon through the films formed on silicon carbide. The oxidation rates for both materials in water vapour are considerably faster than those for oxygen. Cappelen et al.[9] have shown for silicon carbide at 1500°C that silica films preformed in oxygen do not inhibit attack by water vapour and that a subsequent return to oxygen results in rates slightly higher than those obtained in oxygen initially. Also the behaviour in a gas mixture containing equal parts of oxygen and water vapour was equivalent to that for the water vapour alone. Deal and Grove[3] in a study of the behaviour of silicon have shown that the parabolic rate constant for water vapour is greater than that in oxygen by a factor of approximately 100 at 1000 - 1100°C and that in agreement with the data of Cappelen et al. for silicon carbide a small amount (17%) of oxygen does not significantly influence the attack by water vapour.

Considerable differences exist between the various sets of data on the influence of pressure. Jorgensen et al. have reported that the parabolic rate constant (k) for silicon carbide in oxygen[7] and water vapour[8] from 1300 - 1556°C and 1218 to 1514°C respectively varies logarithmically with gas pressure (p)

$$k = A \log p + C \qquad A \text{ and } C = \text{constants}$$

whilst Deal and Grove[3] have deduced that the parabolic rate constant for silicon in these gases at 1100 - 1200°C is directly proportional to gas pressure. However, Law[1] has reported a logarithmic relationship for silicon in oxygen at 792 - 927°C. Much of the apparent inconsistency could be due to the fact that different materials, gases, temperatures and pressures have been covered by the different workers and therefore that the relationship varies with the environmental conditions, although it is more likely that basic disagreements exist between the various sets of work.

The films are generally believed to consist primarily of amorphous silica although at the higher temperatures after long times and particularly in the presence of water vapour crystalline

tridymite or cristobalite may form[6,8]. There is evidence that the transformation to crystobalite decreases the protective properties of the films[6]. Several marker studies[2, 11-13] have shown that the films grow at the metal/oxide interface by the passage of oxygen through the films. There has been considerable speculation[14] as to the nature of the diffusing species although it is accepted that the diffusion is rate controlling when a parabolic law operates. In support of the theoretical analyses correlations have been obtained between the diffusion of gases through silica and oxidation rates for silicon and silicon carbide in oxygen[3,10] and silicon in water vapour[3]. The agreement includes activation energies as well as particular rates and involves a linear as distinct from a logarithmic dependence of rate constant on gas pressure. For water vapour the lower diffusion constant is more than counterbalanced by its high solubility in silica by comparison with oxygen, thereby explaining the high oxidation rates with water vapour.

Information on the behaviour in carbon dioxide and carbon monoxide is restricted to brief statements that the kinetics of oxidation of silicon carbide in carbon dioxide are similar to those for oxygen[5], that silicon reacts with carbon dioxide according to a parabolic law but with an extremely low rate constant and with the formation of extremely rough films[13], and that silicon carbide is unattacked by carbon monoxide at temperatures up to 1250°C[5].

ACTIVE REGION The exact mechanisms by which SiO forms under various conditions does not appear to have been studied, in particular it is not known whether silica is always an intermediary. However, several studies have demonstrated that silicon and silicon carbide reduce silica at 1300 - 1500°C and it may be deduced that the reactions still occur readily at lower temperatures. Hertl and Pults[15,16] have shown that the presence of various gases inhibits the reduction by silicon carbide, the efficacy of the gases decreasing in the order NO, HCl, Cl_2, CO, N_2. These workers deduced that the gases inhibited the desorption of the gaseous products and that in vacua the rate determining step was the desorption of carbon monoxide. It should also be noted that silica films may be lost with the formation of SiO by the reverse of reaction (1).

Wagner[17] has analysed theoretically the active/passive transition for helium-oxygen mixtures and calculated the oxygen partial pressures necessary to form and maintain a protective film of silica. The pressure necessary to maintain a film is naturally less than that to form it, but unfortunately from theoretical considerations alone, only a lower limit can be determined for the former pressure. For example at 1410°C, the melting point of silicon, oxygen pressures of 6.1×10^{-3} atm and $> 3 \times 10^{-8}$ atm are necessary to form and maintain respectively, films of silica. Gulbransen et al. have studied experimentally the oxidation of silicon[18] and silicon carbide[19] in low partial pressures of oxygen at 1100 - 1300°C and obtained good agreement with Wagner's theory on the partial pressures required to form silica films. They have also shown qualitatively that lower pressures are required to maintain the films on silicon carbide and have suggested that traces of carbon containing gases (e.g. CO_2) markedly influence the oxidation and volatilisation of silicon by the formation of thin surface films of silicon carbide.

APPLICATION OF PREVIOUS WORK

PASSIVE REGION At high oxygen potentials in particular with oxygen and carbon dioxide at pressures above 10^{-2} atm the published data indicate that thin protective films of silica should form on both silicon and silicon carbide at temperatures up to 1400°C with there being no significant corrosion of these materials. However, quantitative data on the extent of the attack by carbon dioxide are not available and corrosion could become severe in the presence of water vapour. An aspect not clear from the previous work but which is of considerable importance in the application of the data, is the influence of the pressure of the oxidant, in particular in the case of water vapour.

With carbon monoxide it may be predicted that passive silica films will be formed according to the reactions

$$Si + 2CO \longrightarrow SiO_2 + 2C$$

$$SiC + 2CO \longrightarrow SiO_2 + 3C$$

when the pressure of carbon monoxide exceeds the equilibrium value. For example with silicon carbide the equilibrium pressures are 2×10^{-4}, 9×10^{-3} and 4×10^{-2} atm at 1000°, 1200° and 1300°C respectively. However, at lower pressures or with low rates for the gas/solid interface reaction, there is the possibility of SiO formation.

ACTIVE REGION In the absence, or with only a low partial pressure of an oxidising gas, corrosion may be severe with corrosion rates several orders of magnitude greater than those obtained in the passive region, due to the formation of volatile species. Without an oxidising gas, pure silicon may volatilise and silicon carbide may decompose to give silicon vapour and carbon

$$Si(s) \longrightarrow Si(g)$$

$$SiC(s) \longrightarrow Si(g) + C \qquad \ldots\ldots(2)$$

As stated in the previous sections a low partial pressure of an oxidising gas leads to the formation of SiO. The rate at which the materials corrode under these conditions is governed by the partial pressures of the gaseous species at the surface of the specimens and the diffusion of the gases to and from the surface. The equilibrium gas pressures associated with the important reactions

are given in Fig. 1 (20). The diffusion processes would be influenced by the presence of an inert gas. High vacua would facilitate fast gas transport away from a specimen and could be considered to represent the worst case. The maximum free volatilisation rates in a vacuum can be calculated from the Langmuir equation

$$r = \frac{44.4\ p}{\sqrt{MT}} \quad \text{moles/cm}^2 \text{ sec.}$$

where p = partial pressure of volatilising species (atm)
M = molecular weight " " "

The penetration rates resulting from the volatilisation of silicon from silicon and silicon carbide and SiO formed by the relevant reactions, are given in Fig. 2. They represent maximum values and could be reduced in practice, possibly considerably, by reaction kinetics, by long narrow diffusion paths, by the presence of an inert cover gas and in the case of SiO by the supply of oxidant. With an inert cover gas the interdiffusion coefficient (D_{1-2}) for the various volatile species may be calculated from the equation

$$D_{1-2} = \frac{9.292 \times 10^{-4} T^{3/2} \left(\frac{1}{M_1} + \frac{1}{M_2}\right)^{\frac{1}{2}}}{p\ \alpha_{1-2}^2\ f\left(kT/\epsilon_{1-2}\right)}$$

where α_{1-2} = molecular separation at collision (Å)
p = total pressure (atm)
ϵ_{1-2} = energy of molecular interaction (erg)
$f\left(kT/\epsilon_{1-2}\right)$ = collision function evaluated by Treybal (21)

α and ϵ may be calculated from the properties of gases such as viscosity, but if necessary they may be estimated for each gas from the relationships

$$\frac{\epsilon}{k} = 0.75\ T_{crit} = 1.39\ T_{bp}$$

$$\alpha = 0.835\ V_{crit}^{\frac{1}{3}}$$

where T_{crit} and T_{bp} = critical temperature and normal boiling point respectively (°K)

V_{crit} = critical volume cm³/mole

It follows that when transport through an inert gas layer is rate controlling, the rate is inversely proportional to the inert gas pressure and the thickness of the gas layer.

As an example the maximum penetration rates for the reactions covered in Fig. 2 for vacuum, have been calculated for a helium atmosphere at 20 atm pressure with a stagnant gas layer 0.32 mm thick; the results are given in Fig. 3. Points of particular note arising from these figures are that the presence of oxygen atoms available for the formation of SiO can increase volatilisation rates by up to 4-7 orders of magnitude and the inert helium atmosphere decreases the rates by factors up to 10^4.

PASSIVE-ACTIVE TRANSITION REGION The minimum partial pressure of oxidant which will lead to the formation of a passive silica film in flowing helium may be calculated from a modified theory of Wagner. Firstly assume equilibrium between silicon or silicon carbide, silica and SiO.

$$Si + SiO_2 \rightleftharpoons 2SiO$$

With oxygen as the oxidant the rate of transport of oxygen atoms to the surface

$$= D_{O_2} \frac{2P_{O_2}}{d_{O_2} RT} \quad (d_{O_2} = \text{diffusion path for } O_2)$$

(P_{O_2} = partial pressure of O_2 in main gas stream)

Rate of transport of oxygen atoms away as SiO

$$= D_{SiO} \frac{P_{SiO}}{d_{SiO} RT} \quad (d_{SiO} = \text{diffusion path for SiO}$$

(P_{SiO} = equilibrium partial pressure of SiO)

Under steady state conditions

$$P_{SiO} = \frac{D_{O_2}}{D_{SiO}} \frac{d_{SiO}}{d_{O_2}} 2P_{O_2}$$

With a turbulent helium gas stream $d_{SiO}/d_{O_2} = 1$

The minimum oxygen pressure therefore which will lead to the formation of a silica film is

$$P_{O_2} = \frac{D_{SiO}}{2 D_{O_2}} P_{SiO}$$

Similarly for carbon dioxide and water vapour

$$P_{CO_2} = \frac{D_{SiO}}{D_{CO_2}} P_{SiO}$$

$$P_{H_2O} = \frac{D_{SiO}}{D_{H_2O}} P_{SiO}$$

The ratios of the diffusion coefficients in the equations may be taken as 0.9, 1.2 and 1.0 for oxygen, carbon dioxide and water vapour respectively in helium from which it follows that the critical partial pressure of oxidant leading to the formation of a passive film is, within an order of magnitude similar for all three oxidants and approximately equal to the equilibrium partial pressures of SiO given in Fig. 1. The minimum values for the partial pressure of oxidant necessary to maintain a preformed oxide film may also be calculated from Wagner's paper. However these calculations do not appear appropriate here as the values applying in practice depend in a complex manner on the diffusion rates of oxygen and silicon in the silica films and hence lie between the calculated minimum pressures and the minimum pressures for a bare surface.

In theory limited volatilisation may still occur with passive silica films when the partial pressures of oxidant are low but above the minimum values to stabilise the films; this volatilisation results from the dissociation of the silica according to the reaction

$$SiO_2 \longrightarrow SiO + \tfrac{1}{2}O_2$$

With this reasoning a given partial pressure of oxygen should result in a steady state film thickness being achieved such that the rate of film formation matches the rate of volatilisation. With carbon dioxide or water vapour as the major oxidant the associated low partial pressures of oxygen, given by reactions

$$CO_2 \longrightarrow \tfrac{1}{2}O_2 + CO \qquad \text{.....(3)}$$

$$H_2C \longrightarrow \tfrac{1}{2}O_2 + H_2$$

should enhance the volatilisation. However in practice the volatilisation is small and can usually be neglected. For example, with the minimum partial pressure of carbon dioxide necessary to form a silica film at 1400°C the penetration rate resulting from volatilisation would be $< 5 \times 10^{-9}$ cm/h for both silicon carbide and silicon in a flowing helium coolant at 20 atm.

EXPERIMENTAL PROGRAMME

In the present experimental programme the behaviour of three materials, a self bonded silicon carbide, pure silicon carbide coatings on uranium dioxide particles, and pure silicon, has been studied in various environments within the temperature range 1000 - 1300°C. The kinetics of silica film formation have been determined for pure carbon dioxide at 0.1 and 1 atm, for water vapour at 0.013 and 1 atm, for carbon monoxide at 0.1 atm and to a limited extent for oxygen at 1 atm. Also volatilisation rates in various vacua have been obtained for silicon carbide with and without a preoxidised surface.

TECHNIQUES Behaviour at subatmospheric pressures was studied by determining changes in weight of specimens in vacuum microbalances. In cases of passive oxidation the oxidants were static with the carbon monoxide and hydrogen formed being continuously converted to carbon dioxide and water vapour in a bed of cupric oxide at 350°C in a separate portion of the apparatus. Other experiments at 1 atm pressure utilised thermal balances with a continuous flow of oxidant. The silicon and self bonded carbide material were suspended from alumina rods whilst the silicon carbide coated particles were contained in alumina crucibles under passivating conditions and in graphite crucibles in carbon monoxide and vacuum. Mullite reaction tubes were used although with water vapour these had to be sleeved with silica to stop the transfer of iron oxide from the refractory to the specimens by the water vapour.

MATERIALS The self bonded material was fully dense and consisted of equal portions of α and β silicon carbide with a small amount of free silicon. The material was tested in the form of sections cut longitudinally from tubes 1.3 cm diameter 0.13 cm wall thickness. The inner surface was in the as-received condition whilst the outer surface was ground smooth. There was a rim 80μm thick on the inner surface which was rich in the silicon phase, the volume concentrations of silicon in this rim and the remainder of the material being 23 and 7% respectively.

The coated particles consisted of 800μm diameter, 95% dense spheres of uranium dioxide coated first with a 30μm thick layer of porous pyrolytic carbon, then a 60μm thick layer of dense pyrolytic carbon and finally a 40μm thick layer of β silicon carbide. The silicon carbide was obtained by the decomposition of methyltrichlorosilane in hydrogen at 1500°C and chemical analysis indicated that it might have contained some (8%) excess carbon.

The silicon was semiconductor grade >99.999% Si obtained from Kooh-Light Laboratories in the form of small bars. Specimens in the form of discs were cut from the bars on a slitting wheel and degreased before testing.

RESULTS

PASSIVE REGION The formation of silica films in carbon dioxide or water vapour usually obeyed a parabolic law up to at least 500h and in many instances up to 1000h exposure, although in some cases during the latter stages of oxidation the reaction rate decreased at a greater rate than is predicted by a parabolic law. For convenience therefore the data are reported in the form of parabolic rate constants, the use of which could in some instances lead to over-estimates of the extent of the oxidation.

An interpretation of the weight gain data together with a comparison of the behaviour of silicon carbide with silicon, necessitates knowledge of the behaviour of the carbon in the silicon carbide on oxidation of the silicon atoms. Accurate data on this point could only be obtained for oxidation by water vapour where any carbon released to the gas phase formed carbon dioxide which could be subsequently collected and measured. The results given in Table I demonstrate that within experimental error the carbon freed from the silicon atoms by the formation of silica, transferred to the gas phase rather than remaining as carbon within the specimen or reacting with free silicon to form fresh silicon carbide. Here it should be noted that the carbon release exceeded slightly the predicted values, especially when the presence of the free silicon in the tube material is taken into account; however the limits of error are such that further discussion of this point is not warranted other than to suggest that the discrepancy could be associated with a slight excess of carbon in the carbide materials. On the basis therefore of Table I, together with the published literature, it has been assumed that the carbon is transferred stoichiometrically to the gas phase during silica film formation in all the environments, and the parabolic rate constants have been presented for convenience in terms of the calculated silica film thickness.

TABLE I

Release of carbon from silicon carbide oxidised in water vapour at 0.013 atm

Material	Oxidation conditions	Wt gain μg/cm²	Carbon released μg/cm²	Predicted carbon* release μg/cm²
SiC tube	1300°C 496h	128 ± 10	85 ± 1	76 ± 6
" "	1200°C 381h	81 ± 10	47 ± 1	48 ± 6
" "	1000°C 500h	47 ± 5	28 ± 1	28 ± 3
SiC particles	1300°C 592h	137 ± 20	95 ± 2	82 ± 12
" "	1200°C 475h	121 ± 10	74 ± 1	73 ± 6
" "	1000°C 743h	46 ± 5	29 ± 1	27 ± 3

* The predicted carbon release is based upon the assumptions that the surface is composed entirely of stoichiometric SiC and that oxidation of the silicon atoms results in the release to the gas phase of the associated carbon atoms.

The results obtained for carbon dioxide at temperatures of 1000 - 1300°C are summarised in Fig. 4 together with the data published for oxygen by Motzfeldt[10]. Appreciable scatter was obtained which it is believed results primarily from the small amount of reaction. Essential features of the results were that there was no significant influence of carbon dioxide pressure over the range 0.1 - 1 atm and the reactivities of silicon and silicon carbide were similar at 1200 - 1300°C, indicating that the release of carbon to the gas phase, and therefore its passage through the silica films, did not affect the protective properties of the films, although there was an indication that silicon might be more reactive than its carbide at 1000°C. The rate constants published for oxygen at 1 atm were greater than those obtained for carbon dioxide by a factor of approximately 20, whilst the activation energies for the two gases were similar. To ensure that the behaviour of the materials under investigation was typical of the materials covered in the

previous studies, their behaviour in oxygen at 1 atm at 1200°C was determined and as shown in Fig.4 was found to agree well with the data summarized by Motzfeldt. In view of the belief of Gulbransen et al. that carbon is transferred to silicon from carbon containing gases, two experiments were carried out with silicon in carbon dioxide labelled with ^{14}C. The conditions were 355h at 1000°C, and 43h at 1200°C followed by 190h at 1300°C. The final weight gains were 110 and 60 $\mu g/cm^2$ respectively. Surface counting gave the carbon pick-ups as 0.06 $\mu g/cm^2$ for both specimens demonstrating that the carbon transfer represented <0.1% of the weight gain.

The behaviour in water vapour has been studied over the temperature range 1000 - 1300°C at 0.013 and 1.0 atm pressure. The parabolic rate constants obtained are summarized in Fig. 5 together with the data of Deal and Grove for silicon in 1 atm of water vapour. Unlike the results for carbon dioxide there was a pronounced dependence of the rate constant on pressure of water vapour with the values for the lower pressure being of the same order as those for carbon dioxide. The slight difference in behaviour between silicon and silicon carbide obtained in carbon dioxide at the lowest temperature, 1000°C, was accentuated such that silicon was substantially more reactive than its carbide at both pressures at this temperature, but not at higher temperatures. The protective character of the silica reaction product increased with temperature as the log (k) against $\frac{1}{T}$ plots for silicon carbide (Fig 5) appeared to flatten at the higher temperatures or in the case of silicon, had a positive slope such that reaction rates decreased as the temperature increased. To obtain more information on the influence of pressure experiments were carried out with silicon at 1000°C in which the pressure was increased from 2.6×10^{-3} to 2.6×10^{-2} atm during the oxidation. The parabolic plots (Fig. 6) demonstrate the marked pressure dependence and confirm the greater reactivity at the lower temperature. All the results on the influence of pressure for silicon have been plotted in Fig. 7; the graph demonstrates that the data may conveniently be expressed by an equation

$$k \propto p^n$$

where n equals 0.67 at both 1000° and 1200°C. The limited results available for silicon carbide indicate that a similar dependence on pressure applies for this material.

A selection of the specimens oxidised in carbon dioxide and water vapour was examined by the Weissenberg X-ray camera technique to identify the silica corrosion product. In no instance was evidence obtained for the presence of appreciable amounts of amorphous oxide. With both silicon and silicon carbide in water vapour α cristobalite was the predominant phase. For silicon in water vapour the presence of one line indicated the presence also of α quartz or tridymite at 1200 - 1300°C whilst two broad diffractions at 4.95 and 3.64 Å indicated an unidentified phase for temperatures of 1000 - 1200°C. With silicon in carbon dioxide diffraction lines were obtained on various specimens corresponding to both α cristobalite and the unidentified phase.

The primary experiments with carbon monoxide were carried out with the gas at 0.1 atm for 100h in a microbalance. The self bonded carbide was exposed at 1000° and 1200°C and the coated particles at 1000°, 1200° and 1300°C. In all instances the weight changes were small and could be represented by a gain or loss within the limits of error of ± 10 $\mu g/cm^2$. With a pressure of 0.013 atm appreciable weight losses were obtained due to the formation of SiO; experiments with ^{14}C labelled gas established that the SiO was formed by reaction with gaseous impurities in the containment rather than with the carbon monoxide as carbon was not deposited from the gas phase.

ACTIVE REGION The initial experiments on active oxidation were carried out with a specimen of the self bonded silicon carbide tube from which the majority of the free silicon had been removed by prior heat treatment in vacuum at 1300 - 1400°C. This specimen was heated in vacua of 10^{-6} - 10^{-7} atm obtained with rotary and mercury diffusion pumps and a liquid nitrogen trap and the rate of weight loss determined over the temperature range 1000 - 1300°C. The rates were linear and not noticeably dependent on the partial pressure of gas in the system within the above range. They were attributed solely to reaction at the geometric surface, the contribution from the pores created by the removal of the silicon being considered small, as the mean free path of the gas molecules was large by comparison with the dimensions of the pores, and metallographic evidence indicated no enlargement of the pores during the experiments. The rates are summarized as a function of temperature in Fig. 8, together with the maximum theoretical rate which could be obtained by dissociation of silicon carbide according to reaction 2. The high values obtained indicated that appreciable amounts of SiO were formed under these conditions. Further experiments in which a tantalum getter was placed in the neighbourhood of the specimen confirmed this view, in that the rates were lowered by a factor > 10 whilst the gas pressure was reduced to 10^{-7} - 10^{-9} atm by the getter. These lower rates could still be due to SiO formation or to dissociation of silicon carbide according to reaction 2 together with the volatilisation of small isolated particles of silicon freed by either of the other two reactions. To distinguish the latter possibility experiments were carried out at 1200° and 1300°C with silicon carbide coated particles in a graphite crucible in the gettered system. The weight loss was not measurable (i.e. rate < 0.1 $\mu g/cm^2h$) at 1200°C but was significant at 1300°C (Fig. 6). From these results it was concluded that the dissociation of silicon carbide may take place to a limited extent at 1300°C but does not occur at 1200°C.

To obtain data on the reduction of silica by silicon carbide, the specimen of the tube material used in the previous experiments was oxidised in air at 1200°C and its volatilisation behaviour then studied in the gettered system. The rates of weight loss obtained were 0.37, 4-10 and 30-50 $\mu g/cm^2h$ at 1000°, 1200° and 1300°C respectively, and hence were slightly less than those for the unoxidised silicon carbide in the ungettered system. On completion of the reduction the rates returned to the original values for the unoxidised material in the gettered system (e.g. 0.6 $\mu g/cm^2h$ at 1200°C). Limited experiments with the particles preoxidised in carbon dioxide at 1300°C confirmed the previous

data at 1200°C, with a rate of 26 $\mu g/cm^2 h$, but gave no significant reaction at 1000°C (i.e. rate < 0.1 $\mu g/cm^2 h$).

DISCUSSION

The results obtained have fully substantiated the excellent protective character of the silica films formed on silicon and silicon carbide. The high reactivity of water vapour by comparison with other environments and the inert behaviour of carbon monoxide are in agreement with previous work whilst the data obtained on the influence of partial pressure of water vapour represent a compromise between the various sets of published work. However a clear inconsistency arises with the reaction rates for silicon in water vapour decreasing as the temperature increases, such that the parabolic rate constant for 1200°C and 1 atm pressure is less than the value given by Deal and Grove by a factor of 10. No explanation can be offered for this discrepancy although it should be pointed out that high rates comparable with those of Deal and Grove were obtained for both silicon and silicon carbide at 1200°C when the water vapour was contaminated with air. The unusual temperature dependence must be due to differences in the structure of the films at different temperatures, leading to more protective films at the higher temperatures. The indication of some tridymite or quartz at the higher temperatures together with the observation of Jorgensen[6] that cristobalite has poor protective properties is consistent with this reasoning.

A point of considerable interest is the mechanism of growth of the films. Marker experiments previously have demonstrated that growth occurs at the inner film surface with the passage of oxygen through the films. However, the mechanism by which this diffusion occurs is not known although it must be tied to the form in which the oxygen enters the silica. On the Wagner lattice defect model oxygen ions would diffuse by lattice vacancies and the parabolic rate constant would be almost independent of p_{O_2}. Alternatively the gases could dissolve in or react with the silica and then diffuse as O_2 molecules, ions or atoms. For example water vapour could react to form hydroxyl ions according to the reaction

$$Si - O + H_2O \longrightarrow 2OH^-$$

For these latter possibilities the parabolic rate constants would be directly proportional to gas pressure for the diffusion of gas molecules or proportional to the square root of pressure for oxygen and water vapour dissolved as atoms or hydroxyl ions respectively. In this context the data for carbon dioxide and oxygen may be conveniently compared on the basis of oxygen partial pressure. With carbon dioxide at 0.1 atm the partial pressure of oxygen in the gas according to reaction 3 is 3×10^{-7} atm at 1200°C. The difference in rate constant between oxygen at 1 atm and carbon dioxide at 0.1 atm is approximately a factor of 20 and hence if the corrosion in both cases is governed by the oxygen potential of the gas, the dependence on the oxygen partial pressure does not agree with any of the proposals. The high reactivity of water vapour although it has a low oxygen potential establishes that a special mechanism applies for this corrodant. The formation and diffusion of hydroxyl ions appears the most likely mechanism with the $p_{O_2}^{0.67}$ dependence for the rate constant rather than $p_{O_2}^{0.5}$ indicating that not all the hydroxyl ions are identical and able to partake in the growth of the films.

Other points of interest which are probably related are the mechanisms of transfer of carbon through the films to the gas phase during the oxidation of silicon carbide and the reasons for the different reactivities of silicon and silicon carbide in water vapour at 1000°C. None of the data however provides positive information on these points.

For the active region reaction rates of silicon carbide in poor vacua were high as expected, but were considerably less than the maximum theoretical rates in Fig. 2 (i.e. by a factor of 10^5) showing that reaction was not controlled by the gaseous diffusion of SiO away from the specimen. Also the rates were unlikely to have been controlled by the supply of oxidant as they were not significantly affected by gas pressure. However their similarity with the rates of reduction of preformed silica films in high vacua indicate that during active oxidation silica is an intermediary and the solid/solid reaction is the rate determining step. Further it may be deduced from the work of Hertl and Pultz that the slowest step in this reaction is the desorption of the gaseous products, and that the basic considerations in the previous section on the active-passive transition are not applicable in their present form.

ACKNOWLEDGMENTS

The authors gratefully acknowledge the assistance given by K. A. Peakall and E. N. Hodkin of A.E.R.E. with experimental work, W. A. Gutteridge of the Palmer Research Institute with the X-ray studies and the U.K.A.E.A. Springfields Laboratories with the provision of the silicon carbide materials.

REFERENCES

1. J. T. Law, J. Phys. Chem. 61 1200 (1957).
2. J. R. Ligenza and W. G. Spitzer, J. Phys. Chem. Solids 14 131 (1960).
3. B. E. Deal and A. S. Grove, J. Appl. Phys. 36 3770 (1965).
4. R. F. Adamsky, J. Phys. Chem. 63 305 (1959).
5. C. Ervin, J. Amer. Cer. Soc. 41 347 (1958).
6. P. J. Jorgensen et al. J. Amer. Cer. Soc. 48 613 (1965).
7. P. J. Jorgensen et al. J. Amer. Cer. Soc. 43 207 (1960).

REFERENCES CONTINUED

8. P. J. Jorgensen et al. J. Amer. Cer. Soc. 44 258 (1961).
9. H. Cappelen, K. H. Johansen and K. Motzfeldt. Paper presented at the Joint Symposium on the Inorganic and Applied Chemistry of the Solid State 19th International Congress of Pure and Applied Chemistry, London 10-17 July 1963.
10. K. Motzfeldt, Acta Chem. Scandinavica 18 1596 (1964).
11. P. J. Jorgensen, J. Chem. Phy. 37 874 (1962).
12. W. A. Pliskin and R. P. Grall, J. Electrochem Soc. 111 872 (1964).
13. P. Balk, C. F. Aliotta and L. V. Gregor, Trans. AIME 233 563 (1965).
14. D. O. Raleigh, J. Electrochem. Soc. 133 782 (1966).
15. W. W. Pultz and W. Hertl, Trans. Faraday Soc. 62 2499 (1966).
16. W. Hertl, W. W. Pultz, Trans. Faraday Soc. 62 3440 (1966).
17. C. Wagner, J. App. Phys. 29 1295 (1958).
18. E. A. Gulbransen et al. J. Electrochem. Soc. 113 834 (1966).
19. E. A. Gulbransen et al. J. Electrochem. Soc. 113 1311 (1966).
20. O. Kubaschewski, E. W. Evans and C. B. Alcock, Metallurgical Thermochemistry 4th Edition Pergamon Press, Oxford, (1967).
21. R. E. Treybal, Mass Transfer Operations, McGraw-Hill NY (1955).

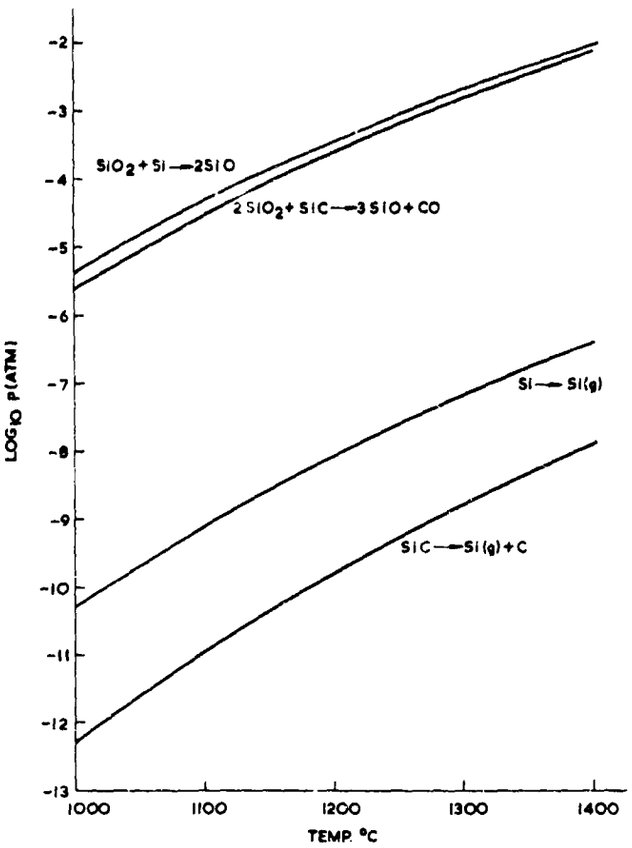

FIG. 1. EQUILIBRIUM PARTIAL PRESSURES OF Si AND SiO.

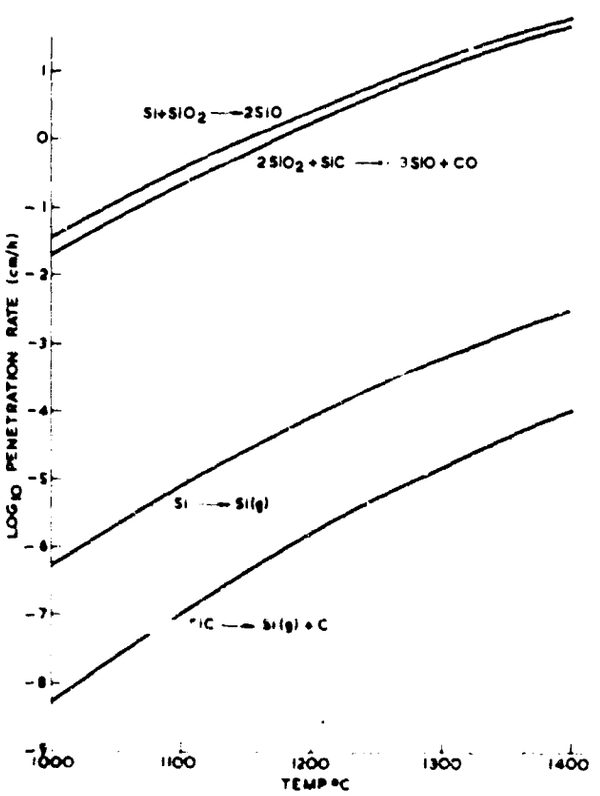

FIG 2 MAXIMUM PENETRATION RATES IN VACUUM

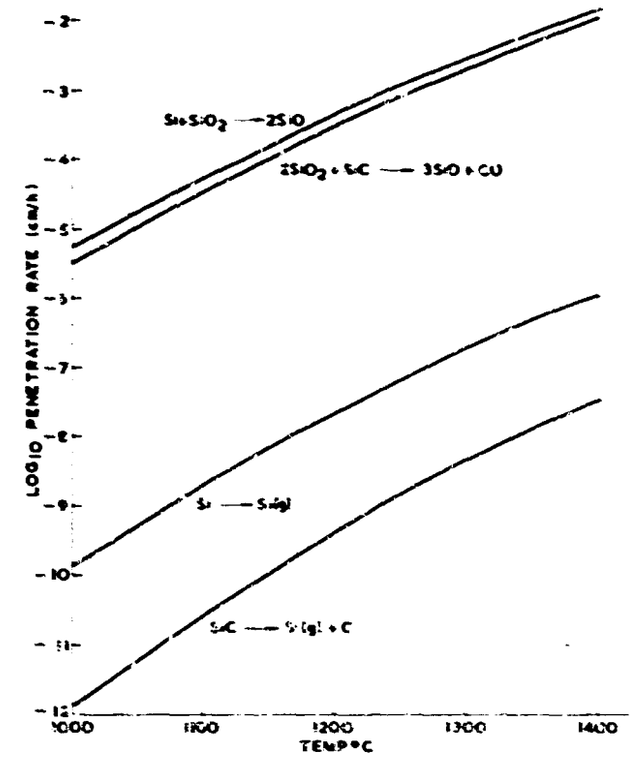

FIG.3. MAXIMUM PENETRATION RATES IN A FLOWING HELIUM ATMOSPHERE

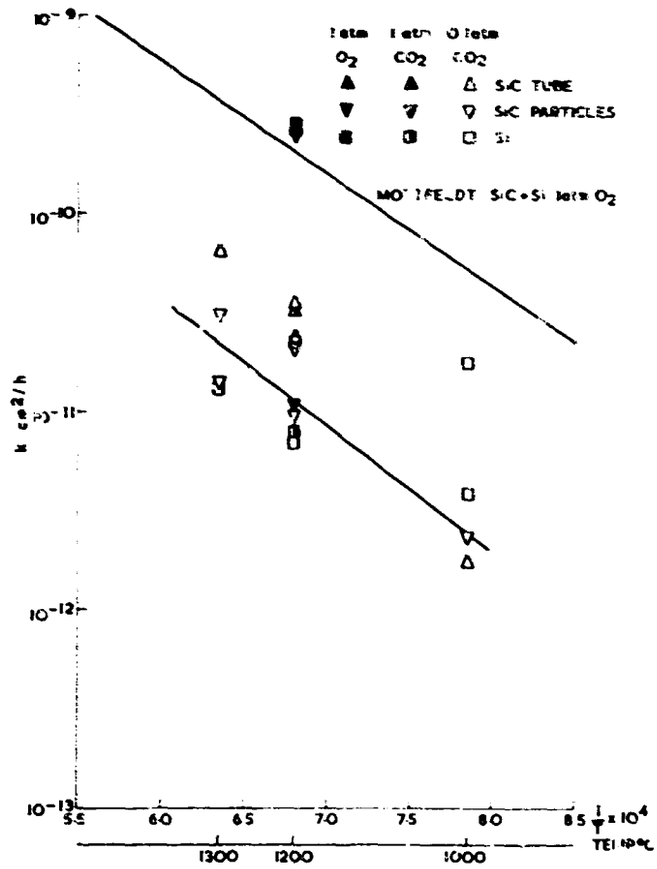

FIG.4. PARABOLIC RATE CONSTANTS FOR CARBON DIOXIDE AND OXYGEN

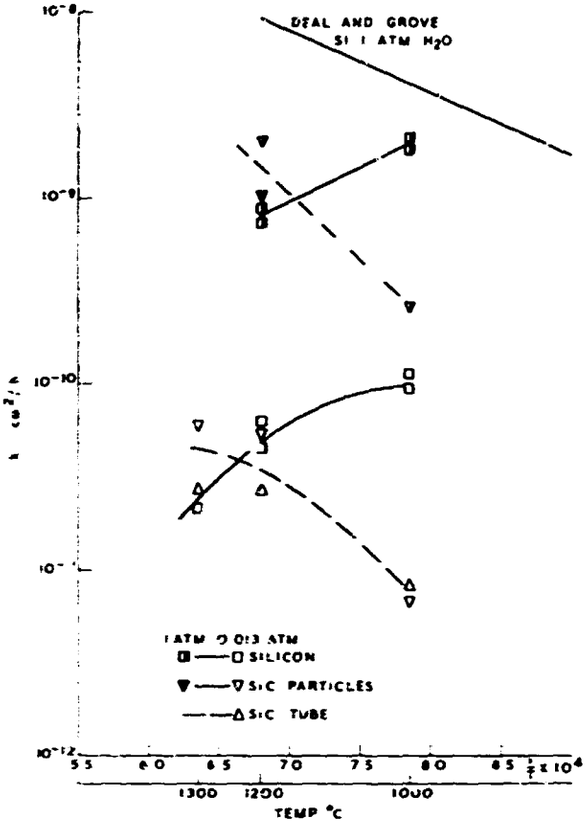

FIG 5 PARABOLIC RATE CONSTANTS FOR WATER VAPOUR

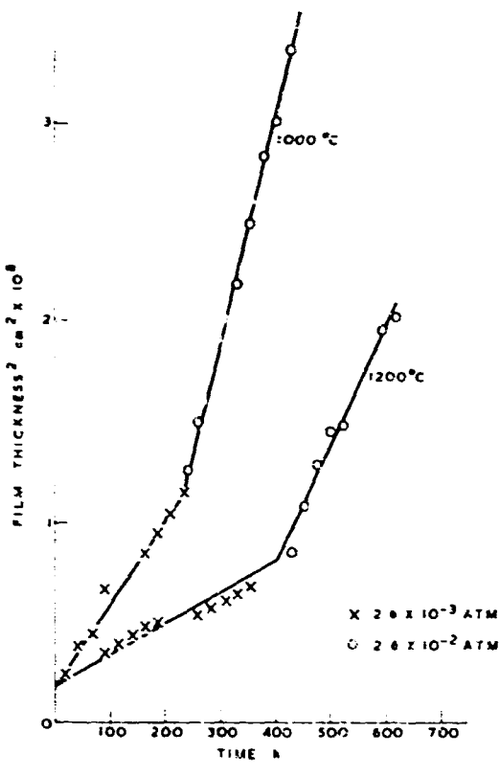

FIG 6 PARABOLIC PLOTS FOR THE OXIDATION OF SILICON IN WATER VAPOUR WITH A CHANGE IN OXIDANT PRESSURE

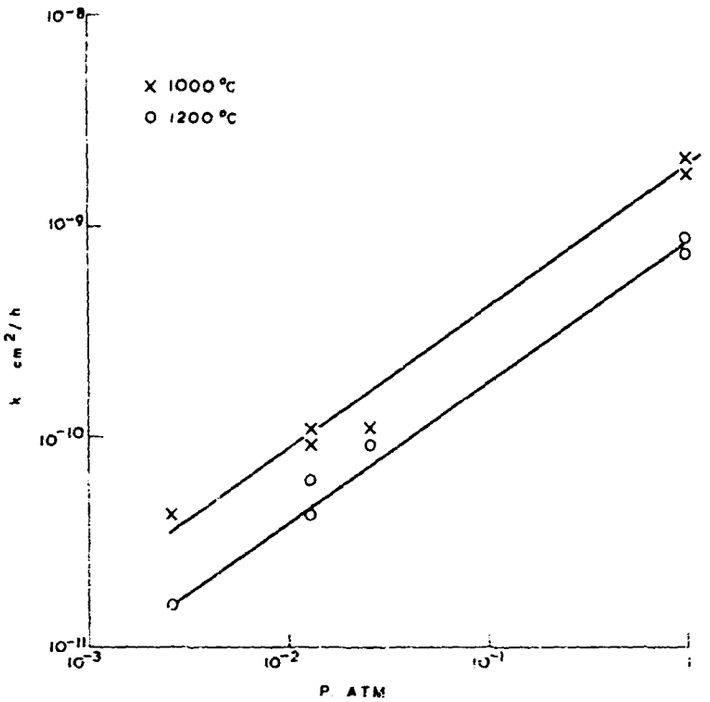

FIG 7 DEPENDENCE OF THE PARABOLIC RATE CONSTANT FOR SILICON ON THE PARTIAL PRESSURE OF WATER VAPOUR

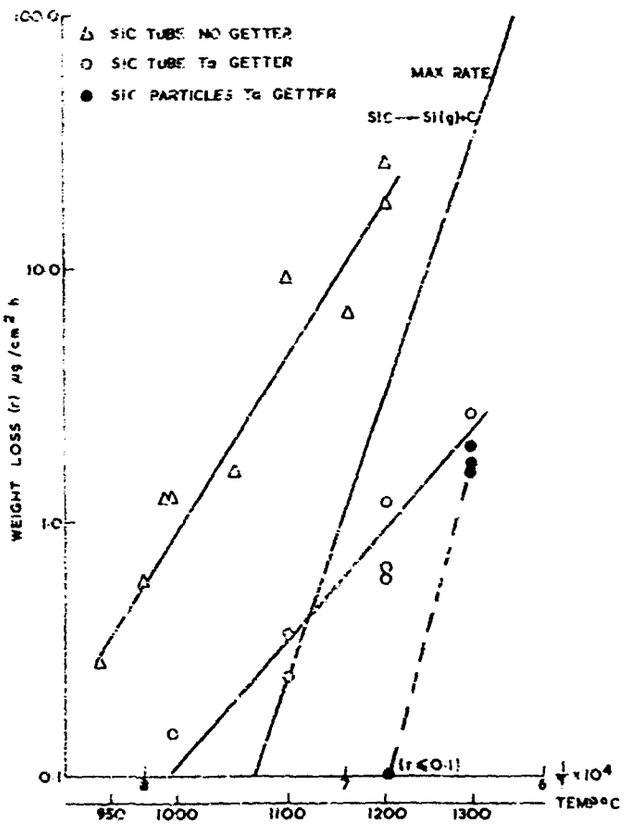

FIG.8. SUMMARY OF VOLATILISATION RATES

THE OXIDATION OF NIOBIUM IN THE TEMPERATURE RANGE 350°-600°C

J.S. SHEASBY
FACULTY OF ENGINEERING SCIENCE
THE UNIVERSITY OF WESTERN ONTARIO
LONDON CANADA

SUMMARY

THE OXIDATION PROPERTIES OF NIOBIUM were studied in the temperature range 350° - 600°C at an oxygen pressure of 380 Torr. Particular emphasis was placed on correlating the reaction products with the oxidation kinetics. The oxidation rate in this temperature range is predominantly time independent, and a sharp change in the temperature dependence of this linear rate has been detected at 440°C. On the basis of kinetic and metallographic evidence it is considered that above this temperature the linear rate is of the type known as "paralinear" in which the reaction rate is controlled by the diffusional properties of the oxide layer in contact with the metal phase. Below 440°C the morphology of the reaction products is quite different and it appears that the reaction rate is controlled by a surface reaction at an oxide-gas interface. After long periods of oxidation at temperatures above 440°C a localized breakaway reaction occurs. This breakaway reaction is an extreme form of grain boundary attack and causes severe specimen self-heating. However, no evidence was found of a fundamental change in the rate controlling mechanism throughout this transition.

THE OXIDATION BEHAVIOUR of niobium has been studied by many workers, and the literature was reviewed most recently by Kofstad (1). Niobium exhibits unusual oxidation features, for at each temperature and oxidation pressure the oxidation rate is found to follow a complex series of time laws. This paper describes an investigation into the oxidation behaviour of niobium in the temperature range 350°-600°C, at oxygen pressures near atmospheric, for times from 10 seconds to 1 month. The field under study is characterized by a time independent rate (linear reaction rate law), which is preceded by a period (a few minutes at 600°C and days at 350 C) of non-linear behaviour. After extensive oxidation at temperatures above 440°C a second breakaway reaction occurs. The major part of the weight gain is associated with the formation of niobium pentoxide although oxygen is also consumed by the formation of sub-oxides and by solution in the metal phase. Although there is good agreement between previous studies on the rates of oxidation and types of time laws observed at various oxidation conditions, there is no agreement as to the physical events nor the nature of the rate controlling steps associated with each stage. Particular areas of disagreement are: (i) the reaction products formed during the pre-transition period, (ii) the mechanism of the transition to linear oxidation kinetics, (iii) the rate controlling step during linear oxidation.

Earlier work by the author on the morphology of the products of reaction elucidated the mechanism of oxidation in the temperature range 625°C-825°C. In the temperature range 720°-825°C (2) it was found that the niobium pentoxide scale grows protectively when not too close to sharp changes of radii on the specimen, and that the parabolic rate constant of its formation was pressure sensitive. Extension of this work to lower temperatures (3) where the parabolic oxidation breaks away to linear kinetics revealed that during the initial parabolic oxidation period the scale appears compact, and at the transition to linear kinetics the scale blisters and cracks. Scale formed during linear oxidation grows in a series of crude layers. Because of the correlation between the morphology of the oxide scale with the variations in the weight gain curve it was proposed that the oxidation reaction was an example of the class of oxidation reactions known as "paralinear" in which a layered oxide scale emanates from the growth of the oxide to a critical thickness, cracking and regrowth of the adherent oxide to the critical thickness when the cycle repeats.

The columnar grain structure across the layered niobium pentoxide scale indicated that there would be no pause in the reaction rate associated with the nucleation of new oxide layers, and further, the layer of oxide in contact with the metal phase was not observed to be significantly thicker than the other layers. It follows that the "paralinear" oxidation rate Kl should be related by the mean oxide layer width, w_c, to an underlying parabolic rate constant, Kp, for the reaction by the equation

$$Kl = Kp/w_c$$

Kp and Kl are defined by the equations $w^2 = Kpt + a$

$w = Klt + b$

respectively; w is the weight of oxygen absorbed at time t, and a and b are reaction constants.

The good agreement found between the derived parabolic rate constant, Kp, and that measured from weight gain determinations, Kp_v, confirmed the paralinear mechanism, indicating that the rate of reaction is controlled by diffusion across the layer of oxide that is in the process of growing. This agreement has been improved (Fig. 15) by the use of a more recent determination of the density of $T\text{-}Nb_2O_5$ (notation of Schafer et al. (5)), by Terao (6).

Below 625°C the disappearance of layers of NbO and NbO_2 from the reaction zone causes an abrupt increase in the linear reaction rate and the derived parabolic rate constant Kp. Although the scale formed during linear oxidation had essentially the same morphology as that formed at higher temperatures, the difficulty in obtaining an initial parabolic rate constant, Kp_v, prevented confirmation of the continued operation of the paralinear oxidation mechanism. This paper describes a further study of the pre-linear and linear behaviour in the temperature range 450°- 600°C, and extends the morphological study of the reaction products down to 350°C.

EXPERIMENTAL: THE NIOBIUM SHEET used was produced by Fansteel and had a strong {100}<011> annealing texture. An analysis of the major impurities as supplied by the manufacturer is shown in Table 1. Specimens were cut in the form of squares measuring approximately 2 x 2 x 0.1 cm. Unless otherwise stated, specimens were prepared for oxidation by abrasion up to 600 grade silicon carbide paper, followed by electropolishing for 30 sec in a nitric acid - 30% hydrofluoric acid electrolyte at 24v using a carbon cathode.

The kinetics of oxidation were examined in a volumetric type of apparatus. Experimental runs were initiated by admitting oxygen to a specimen brought to temperature under vacuum. Estimates of self-heating during reaction were made by embedding the head of a Pt/Pt-Rh thermocouple in a small hole in each test specimen. After reaction all the specimens were examined metallographically.

EXPERIMENTAL RESULTS: A SERIES OF SPECIMENS was oxidized at 380 Torr oxygen at approximately 25 deg C intervals over the temperature range 450°- 650°C to measure specimen self-heating. These specimens were not prepared beyond abrasion on 600 grade silicon carbide paper. The difference in temperature between the specimen and furnace was found to be a complicated function of oxidation time and temperature, and examples are shown in Fig. 1. The curves show a variety of inflexions depending upon the furnace temperature, but duplicate specimens at the same temperature agree very well both to the time of occurrence and size of the inflexions. The significance of these results will be considered from two points of view, (a) the effect of self-heating on the kinetics of oxidation, and (b) the insight given to the events occurring during oxidation.

Below 525°C self-heating is small and kinetically insignificant. At 550°C the initial temperature rise of 25 deg C falls to within 5 deg C of the furnace temperature after 110 seconds, but after 30 minutes of oxidation the temperature slowly rises to 10 deg C above the furnace temperature over the next 100 minutes. This slow rise is attributed to thermal insulation of the specimens by the growing oxide scale. Above 575°C the slow temperature rise due to "blanketing" is important immediately after a second temperature maximum occurring at 3 min oxidation. Specimen temperatures are always at least 6 deg C above the furnace temperature and later in the reaction this rises to 20 deg C. Above 625°C as described previously (3), only one temperature maximum occurs and the specimen then cools to within a few degrees of the furnace temperature. The breakaway reaction occurring at long oxidation times (7,8) causes large self-heating effects and a consequence of this will be discussed later.

Measurements of self-heating at various oxygen pressures were made at 586°C on specimens in the fully blanketed condition, and these values are given in Table 2. Also given in Table 2 is the enhancement in rate to be expected from the known temperature coefficient of the reaction due to this self-heating. Although the enhancement is not large it should be incorporated in detailed studies of the mechanism of the effect of pressure on the rate of reaction.

At temperatures below 525°C a notable feature is the occurrence of a second temperature maximum higher than the first. For instance at 500°C the first peak at 12 sec with a temperature of 1.2 deg C in excess of the furnace temperature is followed by a second maximum of 6.9 deg C at 14 sec. Examination of specimens suggest that the first peak is caused by the initial oxygen adsorption (9) and the second peak by the major oxide nucleation event. Traces of this behaviour can be seen on the initial temperature rise at temperatures up to 600°C, see Fig.7. 585°C curve.

One of the main purposes of this work was to look for protective oxide formation early in the reaction so that measured values, Kp_v, could be compared with parabolic rate constants, Kp, derived from the subsequent linear rates of reaction. For this discussion it is useful to know that the oxide layers formed during linear oxidation were about 1μ thick at 400°C increasing to about 2μ at 600°C, i.e., weight gains of 1.75 to 3.5 x 10^{-4}g(0)cm^{-2} respectively. Series of specimens with different surface preparations were reacted in 380 Torr oxygen for short times in the temperature range 400°- 600°C. At temperatures below 500°C for weight gains of less than 3 x 10^{-5}g(0)cm^{-2} the metal grains showed bright interference colours. These films have been observed previously (9,10), but have eluded identification. At weight gains of about 5 x 10^{-5}g(0)cm^{-2} isolated growths of niobium pentoxide were observed, and lateral spreading and thickening of these growths, to the extent of layering several times took place at longer reaction times, Fig. 2. Several grains were remarkably slow to change to the rapid oxidation mode, remaining with a gold coloured interference film in one instance for 30 days at 350°C. X-ray examination indicated that the oxidation resistant grains had a (100) orientation agreeing with the results of Pawel et al. (11). Changing the surface preparation to abraded or mechanically polished speeded the transition to rapid oxidation but did not prevent uneven attack in the early stages. The influence of specimen preparation on the kinetics of oxidation is seen in Fig. 3.

At 550°C after 10 seconds of oxidation, polished specimens still showed anisotropic oxidation to the extent of gold grains. Ground specimens oxidized more uniformly, but because of the irregularity of the interface the first layers that formed had no long range continuity and were very thin. At 600°C polished specimens formed a uniform layer of niobium pentoxide within the first seconds of reaction. As far as can be determined within the confines of the non-isothermal

reaction conditions the oxide grew at a parabolic rate with a rate constant of $4.0 \times 10^{-9} g(O)^2.cm^{-4}.sec^{-1}$. Later in the reaction this oxide blistered and cracked away from the metal in a manner quite analogous to the paralinear behaviour observed at higher temperatures (3).

To examine the morphology of scales formed on specimens reacted for longer times a series of specimens was oxidized at 380 Torr at approximately 25 deg C intervals over the temperature range 350 - 600 C to a weight gain of about $0.02 g/cm^{-2}$. Further specimens were oxidized as required for specific times and temperatures. The initial stages of typical weight gain curves are shown in Fig. 4. and as far as can be estimated there is good agreement between these values and previous investigations (7-15). After the formation of about 10μ of niobium pentoxide the reaction rates are time independent and the values of Kl obtained are plotted in Fig. 5. An abrupt change can be seen in the temperature coefficient of the reaction at about 450°C, and much of the remainder of this study is concerned with observations relating to this transition. After reaction for several hours at temperatures above 450 C the second breakaway reaction reported previously by Kolski (7) and by McLintock and Stringer (8) was observed.

A striking change in the morphology of the niobium pentoxide scale was observed between specimens reacted above and below 440°C, whereas changes within the temperature ranges 440°- 600°C and 350°- 440°C are comparatively minor. The scale formed on specimens reacted in the high temperature range is thicker at specimen corners and edges than on the main faces, Fig. 7a. The scale contains blister type fractures running parallel to the surface over distances of at least one metal grain diameter giving the scale a laminar appearance. Fig. 6. The width of these laminations, w_c , is used to derive the parabolic rate constant Kp and it was therefore important to determine that the scale is sound between blisters. This was verified from the appearance of the scale in the scanning electron microscope, Fig. 9. The metal-oxide interface is comparatively flat on a microscopic scale, Fig. 8a and only part of the adjacent layer of oxide appears dark in polarized light, Fig. 8b.

In contrast the scale formed on specimens reacted in the low temperature range does not show enhanced oxidation at specimen corners, Fig. 7b. The structure of the scale varies in appearance with the reaction temperature. At 430°C blisters are present but do not appear to be joined by cracks, Fig. 10a. At 375°- 400°C the scale is crudely layered but does not contain blisters, Fig. 10b, whilst at 350°C the scale appears similar to that formed at 430°C. The metal-oxide interface is flat on a macroscopic scale but is irregular on a microscopic scale to the extent that there are detached pieces of metal in the oxide. Fig. 8c. In polarized light the dark, non-stoichiometric oxide is more extensive than at higher temperatures, Fig.8d.

Platelets of a sub-oxide were observed in the metal phase of specimens reacted at temperatures above 440°C. At temperatures between 525°- 600°C platelets are numerous and predominantly alligned at 45° to the metal-oxide interface, whereas platelets formed between 440°- 525°C are less numerous and tend to be alligned either parallel or perpendicular to the interface. These changes may be associated with the transition of the platelet structure from NbO_2 to NbO_x reported to occur by Norman (16) as the temperature is lowered. Platelets perpendicular to the metal-oxide interface cause lines of pores to form in the oxide scale by a mechanism described and discussed by Stringer (17). These pores do not cause the laminated structure, but are incorporated in it, Fig. 11, so that oxidation at low temperatures is isotropic at all times. (Fig. 6). At higher temperatures oxidation is initially isotropic but after the formation of many oxide layers grains with platelets at approximately 45° to the interface oxidize more rapidly. Fig. 12. It is considered that platelets initiate early failure of the protective scale on these grains thus causing a faster oxidation, rather than the more rapid oxidation of certain metal planes as suggested by Kofstad and Kjollesdal (15).

In agreement with McLintock and Stringer (8) the breakaway reaction observed after long periods of oxidation is associated with the formation of a powder oxide at a relatively small number of sites on the metal surface. These sites are usually at edges or ends of specimens but are occasionally found in the centre of main faces. Macroscopically the sites are hemispherical cavities, Fig. 13, but in detail the surface of the cavity shows extreme grain boundary penetration, Fig. 14. In some cases grains of metal are parted from the surface and oxidize from all sides within the cavity. There is no doubt that the damaging cracks follow grain boundaries in the metal, and they progress at a fairly slow rate for oxygen-penetrated metal shows clearly in partially polished specimens round all parts of the crack tip. The large volume of oxide that forms on the side of a crack apparently opens it further, allowing oxidation on the new surface and the wedge to be driven deeper. The comparative rarity of pits and their more frequent occurence near the ends of specimens suggests that unusual

stress conditions are required for their initiation and growth. Once started, the strain at one grain boundary triggers those adjacent and the cavity spreads spherically from the point of initiation.

The mechanism by which the first pit forms is not known; grain boundaries do not normally show enhanced oxidation and defects in the original specimen preparation should have been passed by the receding metal interface. Platelets oxidize more rapidly than the metal, see Fig. 11, and Stringer (18) has suggested that cracks start at such points and run to grain boundaries. However, Kolski (7) reports that the breakaway reaction occurs at temperatures as low as 400°C, at which temperature platelets are not observed.

DISCUSSION: from the morphological and kinetic evidence presented there appears to be an abrupt change in the mechanism of the linear oxidation rate of niobium at temperatures above and below 440°C. Only at temperatures close to 600°C is the linear reaction rate preceded by a period of parabolic behaviour that can be associated with the growth of a protective niobium pentoxide layer. At lower temperatures oxide growth in the initial stages is too irregular for weight gain data to be so interpreted. The excellent agreement of this one data point, Kp_y, with that derived from the linear rate at this temperature, Kp, Fig. 15, and the supporting morphological features of the reaction, leave little doubt that linear oxidation in the temperature range 440°- 600°C is the result of a "repeated parabolic" or "paralinear" scaling process. Hence the mechanism of oxidation is a natural extension of that observed at higher temperatures as shown in Fig. 15, and described previously (3). The inversion in the temperature coefficient of the parabolic rate constant as the temperature is decreased from 625°- 600°C was shown to be associated with the disappearance of layers of NbO and NbO_2 from the reaction zone and the appearance of the metastable platelet phase NbO_2. This causes an enhancement of the oxygen concentration gradient across the growing oxide layer and hence a larger value for the parabolic rate constant.

A consequence of the paralinear mechanism is that the linear oxidation rate in this temperature range is sensitive to any variations that can affect the protective layer width; such as the presence of suitably oriented platelets or the stress conditions at specimen corners. In particular the conditions prevailing during the growth of the oxide from 2μ - 10μ at temperatures below 550 C allow the protective layers to form and increase in range and width; hence the rate of oxidation falls throughout this phase of the reaction.

At temperatures below 440°C in contrast to this behaviour, it is observed that the rate of oxidation continually increases from the time of the appearance of the first growths of niobium pentoxide in the interference colour film to the establishment of the steady state oxidation rate. The oxidation rate is apparently proportional to the area covered by growths. Further, as the rate is completely insensitive to stresses in the oxide caused by corners on the specimens, it is deduced that the oxidation rate is truly linear in that the rate controlling step is an interface reaction. The phase change $T\text{-}TTNb_2O_5$ was considered as an alternative explanation for the abrupt change in oxidation characteristics. However, an x-ray diffraction study of the oxides showed that this transition was quite gradual, in agreement with the results of Terao(19). The scale is $T\text{-}Nb_2O_5$ when formed at 600°C and a mixture of T and $TT\text{-}Nb_2O_5$ at 350°C with no marked change in the vicinity of 450 C.

Supporting evidence for the proposed change in mechanism is obtained by consideration of the anomalous temperature coefficient of the steady state oxidation rate shown in Fig. 5, as the temperature is lowered from 445°- 430°C. A paralinear rate is an average rate of oxidation, being composed of much faster rates when a layer is new, and slower rates as it approaches the layering width w_c . However, at 430°C the phase boundary reaction does not permit the faster oxidation rates thus inhibiting the paralinear mechanism. At higher temperatures where the paralinear mechanism can first operate it therefore results in a slower linear or average rate than the sustained maximum obtainable at lower temperatures.

Further information about the phase boundary control of the linear oxidation reaction in the temperature range 350 - 440 C can be obtained from observations made on cross-sections of reacted specimens. The thick band of non-stoichiometric oxide adjacent to the metal interface and the extreme irregularity of this interface, Fig. 8c,d, indicates that in this region the oxygen activity gradient is small and the oxygen potential very low. Hence the phase boundary controlling the reaction rate is at an oxide interface in contact with molecular oxygen. In which case the metal-oxide interface should more closely approach equilibrium conditions than at higher temperatures, and as platelets are apparently absent the possibility arises of the reappearance of the oxides NbO and NbO_2.

It is difficult to be certain about the absence of very thin layers but for the following reasons the oxides NbO and NbO_2 are thought not to be present.

1. Microhardness curves of the oxygen gradient in the metal core extrapolate to surface hardnesses similar to those in specimens containing platelets which is a value much higher than that from specimens known to contain layers of NbO and NbO_2.

2. A diligent search on taper sections of oxidized specimens using scanning electron microscopy failed to detect these oxides.*

3. Calculations of the kinetically expected thickness of NbO (Appendix 1) showed that this thickness was no greater (and therefore the oxide no more likely to form) than that calculated for specimens oxidized in the temperature range 450°- 600°C when this oxide is absent.

If the oxides NbO and NbO_2 are absent, the question then becomes, "Why are there no platelets?" NbO_x is known to be stable in this temperature range (9). Calculations of the oxygen concentration gradient at the metal-oxide interface (Appendix 1) indicate that the volume of oxygen super-saturated metal at this interface is similar to that in which platelets are observed when oxidizing at higher temperatures. Superficially it appears that conditions should be favourable for their formation.

The breakaway reaction at long oxidation times, which was shown to be due to an extreme grain boundary attack, was also associated with severe specimen self-heating, i.e., at 555°C an extra 45 deg C at 380 Torr oxygen, and 65 deg C at 760 Torr oxygen. The enhancement in rate due to this temperature rise is more than sufficient to reduce the apparent pressure sensitivity of the post-breakaway reaction rate to the pre-breakaway value reported by McLintock and Stringer (8). For this reason, and because the oxide forming on the exposed grain surfaces has many of the growth characteristics of the oxide forming on a free surface, it is considered that the observed oxidation rate is still under diffusion control in the oxide and not, as postulated by these workers, to a change in the rate controlling mechanism.

ACKNOWLEDGEMENTS. THE AUTHOR is grateful to Mr. H. Allin for his assistance with the experimental work, and to Dr. J. Stringer of the Department of Metallurgy, University of Liverpool, for his helpful discussions. The research was supported by the National Research Council of Canada.

*This examination was done by Dr. B. Cox of the Atomic Energy Commission, Chalk River, Ontario, Canada and the author is grateful for the sophistication of his approach to the problem.

APPENDIX 1.

CALCULATION OF THE OXYGEN GRADIENT in the metal at the metal oxide interface and the kinetically expected thickness of NbO.

Thanks are due to Dr. G.W. Cox of the Australian Atomic Energy Commission, Lucas Heights, Australia, who provided this analysis (20).

The solutions presented are integrations of Fick's Law in a phase with a linear boundary movement. The assumption is made that the linear oxidation rate starts from time zero and so provides reasonably accurate solutions only at some time after the transition to linear kinetics.

The concentration penetration C at some time t at a distance x from the metal surface is

$$C = \tfrac{1}{2} C_o \left[exp\ (-mx) erfc(x/2\sqrt{Dt} - \tfrac{1}{2}m\sqrt{Dt}) + erfc(x/2\sqrt{Dt} + \quad \sqrt{Dt}) \right]$$

where C_o = surface concentration
m = Kl/D
Kl = rate of movement of the interface
D = diffusion coefficient of mobile species

Differentiation of this equation and substitution of $x=0$ gives the gradient at the surface of the metal as

$$\frac{\partial C}{\partial x}_{x=0} = \tfrac{1}{2} C_o \quad -m.erfc(-\tfrac{1}{2}m\sqrt{Dt} - \frac{2}{\sqrt{\pi Dt}} .exp(-\tfrac{1}{4}Dm^2 t)$$

The equation describing the thickness of the NbO layer Δx_{NbO} is

$$\Delta x_{NbO} = \frac{D_{NbO} \Delta C_{NbO}}{\Delta C_{NbO-Nb} \cdot Kl + D_o \quad \frac{-\partial C}{\partial x} \quad x=0}$$

where D_{NbO}, D_o are the diffusivities in the NbO and Nb phases,
ΔC_{NbO-Nb} the change in oxygen concentration from NbO to the metal surface
$\frac{\partial C}{\partial x}_{x=0}$ the oxygen concentration gradient at this surface.

This equation makes the assumption that the rate of growth of NbO is small compared with the movement of the metal oxide interface.

As neither D_{NbO} nor ΔC_{NbO} is known accurately, their product was estimated as a function of temperature from observations of NbO thicknesses in specimens which had been reacted at higher temperatures, where the layers were comparatively thick and uniform (21). These thicknesses were used with the appropriate interface movements to calculate the product $(D\Delta C)_{NbO}$. The line of best fit on an Arrhenius plot was found to be:

$$(D\Delta C)_{NbO} = 3.2 \times 10^{-4}\ exp\ (-25,400/RT)$$

This relationship with values of D_o (22) and C_o (23) was used to calculate the kinetically expected thickness of NbO in specimens in which NbO could not be observed.

REFERENCES

1. P.Kofstad, High Temperature Oxidation of Metals, John Wiley and Sons,Inc., New York, 1966.
2. J.S.Sheasby,G.R.Wallwork and W.W.Smeltzer, J.Electrochem.Soc., 113,1255(1966).
3. J.S.Sheasby, ibid., 115, 695(1968).
4. J.Stringer, Met.Rev.,11, 113(1966).
5. H.Schäfer, R.Gruchn and F.Schulte,Angew Chem.Internat.Edit.,5,40(1966).
6. N.Terao, Japanese J.Appl.Physics, 4, 8(1965).
7. T.L.Kolski, Trans.ASM, 55, 119(1962).
8. C.H.McLintock and J.Stringer,J.Less Common Metals, 5, 278(1963).
9. T.Hurlen, J.Inst.Metals, 89,273(1960-61).
10. B.Cox and T.Johnston, Trans.Met.Soc. AIME, 227,36(1963).
11. R.E.Pawel,J.V.Cathcart and J.J.Campbell, Columbium Metallurgy, p.667, AIME., Conf. (1960).
12. E.A.Gulbransen and K.F.Andrew, J.Electrochem. Soc., 105, 4(1955).
13. D.W.Bridges and W.M.Fassell, Jr., ibid, 103, 326(1956).
14. D.W.Aylmore, S.J.Greggand W.B.Jepson, ibid, 107, 495(1960).
15. P.Kofstad and H.Kjollesdal, Trans.Met.Soc. AIME, 221,285 (1961).
16. N.Norman, J.Less Common Metals, 4, 52 (1962).
17. J.Stringer, J.Less Common Metals
18. J.Stringer, private discussion
19. N.Terao, Japanese J.Appl. Physics, 2, 156(1963).
20. G.W.Cox, Ph.D. Thesis, University of N.S.W. (1965).
21. J.S.Sheasby, Ph.D. Thesis, University of N.S.W. (1963).
22. R.E.Pawel and J.J.Campbell, J.Electrochem.Soc., 116, 828 (1969).
23. R.P.Elliot, Trans. A.S.M., 52, 990(1960).

Table 1. Manufacturer's analysis of the niobium sheet.

Element	P_{pm}	Element	P_{pm}
C	30	Cr	20-
O	75	V	20-
N	19	Co	20-
H	5-	B	2-
Ti	20-	Cd	5-
Fe	50-	Hf	100-
Ni	20-	Mo	100-
Si	50-	Mg	20-
Mn	20-	Zr	50-
Ca	20-	Cb	Bal
Al	20-	W	100-
Cu	20-	Ta	360
Sn	20-		

Table 2. Dependence of the excess specimen temperature and the calculated rate enhancement factor upon oxygen pressure when oxidizing niobium at a furnace temperature of 586°C.

Oxygen Pressure Torr	Specimen temperature above furnace temperature °C	Oxidation rate enhancement
50	2	1.08
100	6	1.16
200	12	1.33
380	22	1.62
600	27	1.83
760	31	2.0

REFERENCES

1. P.Kofstad, High Temperature Oxidation of Metals, John Wiley and Sons,Inc., New York, 1966.
2. J.S.Sheasby,G.R.Wallwork and W.W.Smeltzer, J.Electrochem.Soc., 113,1255(1966).
3. J.S.Sheasby, ibid., 115, 695(1968).
4. J.Stringer, Met.Rev.,11, 113(1966).
5. H.Schäfer, R.Gruchn and F.Schulte,Angew Chem.Internat.Edit.,5,40(1966).
6. N.Terao, Japanese J.Appl.Physics, 4, 8(1965).
7. T.L.Kolski, Trans.ASM, 55, 119(1962).
8. C.H.McLintock and J.Stringer,J.Less Common Metals, 5, 278(1963).
9. T.Hurlen, J.Inst.Metals, 89,273(1960-61).
10. B.Cox and T.Johnston, Trans.Met.Soc. AIME, 227,36(1963).
11. R.E.Pawel,J.V.Cathcart and J.J.Campbell, Columbium Metallurgy, p.667, AIME., Conf. (1960).
12. E.A.Gulbransen and K.F.Andrew, J.Electrochem. Soc., 105, 4(1955).
13. D.W.Bridges and W.M.Fassell, Jr., ibid, 103, 326(1956).
14. D.W.Aylmore, S.J.Greggand W.B.Jepson, ibid, 107, 495(1960).
15. P.Kofstad and H.Kjollesdal, Trans.Met.Soc. AIME, 221,285 (1961).
16. N.Norman, J.Less Common Metals, 4, 52 (1962).
17. J.Stringer, J.Less Common Metals
18. J.Stringer, private discussion
19. N.Terao, Japanese J.Appl. Physics, 2, 156(1963).
20. G.W.Cox, Ph.D. Thesis, University of N.S.W. (1965).
21. J.S.Sheasby, Ph.D. Thesis, University of N.S.W. (1963).
22. R.E.Pawel and J.J.Campbell, J.Electrochem.Soc., 116, 828 (1969).
23. R.P.Elliot, Trans. A.S.M., 52, 990(1960).

Table 1. Manufacturer's analysis of the niobium sheet.

Element	P_{pm}	Element	P_{pm}
C	30	Cr	20-
O	75	V	20-
N	19	Co	20-
H	5-	B	2-
Ti	20-	Cd	5-
Fe	50-	Hf	100-
Ni	20-	Mo	100-
Si	50-	Mg	20-
Mn	20-	Zr	50-
Ca	20-	Cb	Bal
Al	20-	W	100-
Cu	20-	Ta	360
Sn	20-		

Table 2. Dependence of the excess specimen temperature and the calculated rate enhancement factor upon oxygen pressure when oxidizing niobium at a furnace temperature of 586°C.

Oxygen Pressure Torr	Specimen temperature above furnace temperature °C	Oxidation rate enhancement
50	2	1.08
100	6	1.16
200	12	1.33
380	22	1.62
600	27	1.83
760	31	2.0

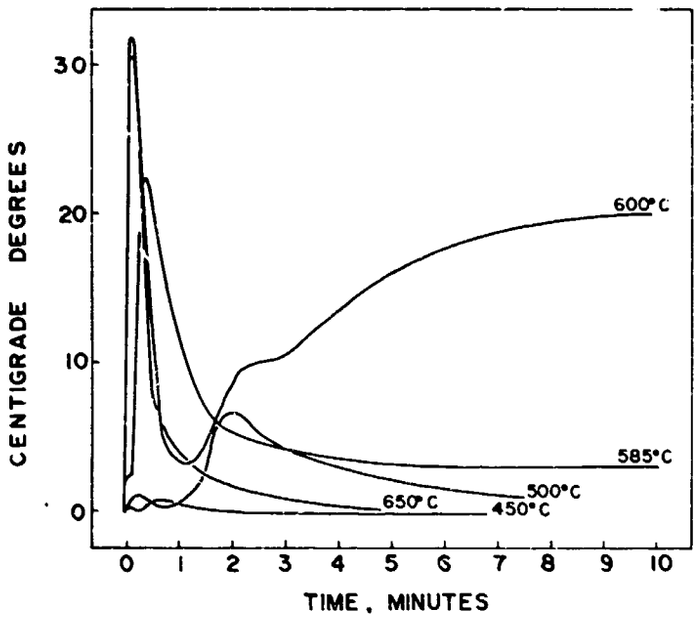

Fig. 1. Temperature of niobium specimens above the furnace temperature as a function of time at several furnace temperatures.

(a)

(b)

Fig. 2. Cross sections of specimen oxidized at 431°C, 380 Torr oxygen for 60 min. showing uneven oxidation, (a) Magnification 200X, (b) Etched, Magnification 1000X.

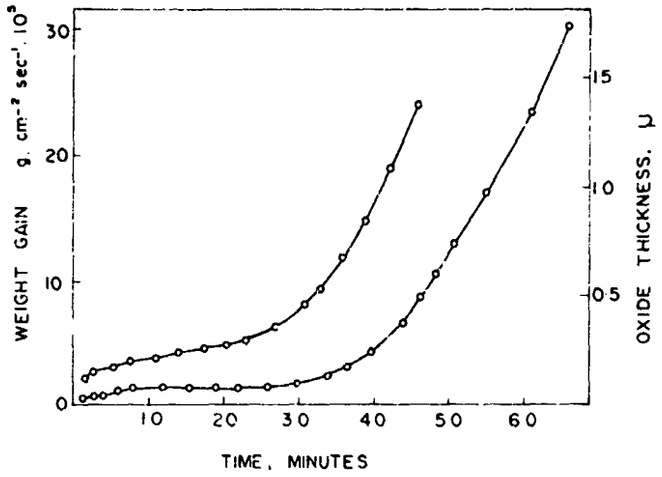

Fig. 3. Oxidation of niobium at 431°C, 380 Torr oxygen, effect of surface preparation.

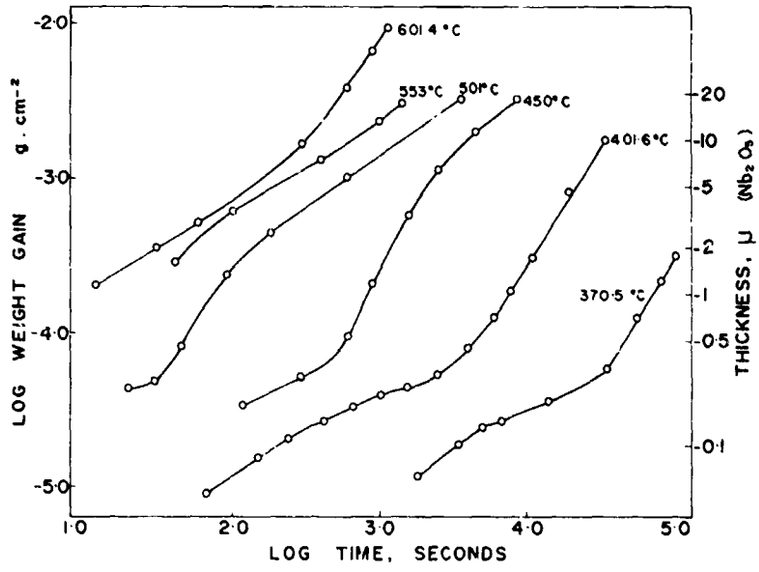

Fig. 4. Typical weight gain curves for the oxidation of niobium in the temperature range 350-600°C, 380 Torr oxygen.

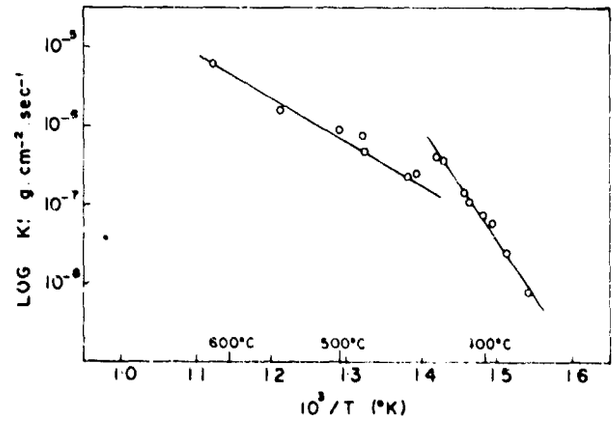

Fig. 5. Dependence of the linear rate of oxidation of niobium at 380 Torr oxygen on temperature.

Fig. 6. Cross section of specimen oxidized at 450°C, 380 Torr oxygen for 1443 min. showing a typical laminated scale. Magnification 150X.

(a)

(b)

Fig. 7. Cross sections of specimens comparing edge effects above and below 440°C. (a) 575°C,380 Torr oxygen, 29 min. Magnification 200X. (b) 430°C, 380 Torr oxygen, 385 min. Magnification 250X.

a.1

a.2

b.1

b.2

Fig. 8. Cross sections of specimens comparing the metal-oxide interface above and below 440°C. a) 625°C, 380 Torr oxygen, 65 min. b) 430°C, 380 Torr oxygen, 385 min. a.1, b.1, plain light, a.2, b.2, polarized light. Magnification 1000X.

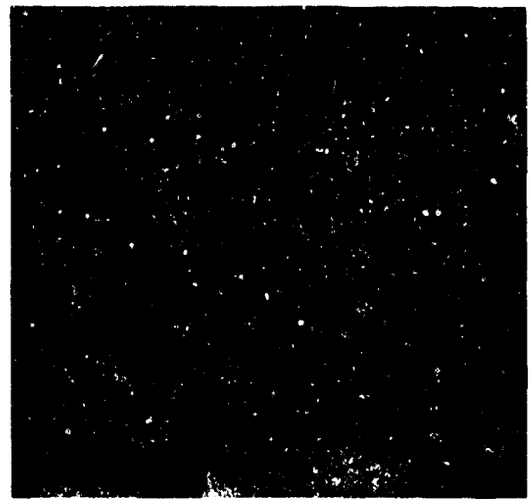

Fig. 9. Cross section of specimen oxidized at 500°C, 380 Torr oxygen for 140 min. showing the scale structure at high magnification. Magnification 10,500X.

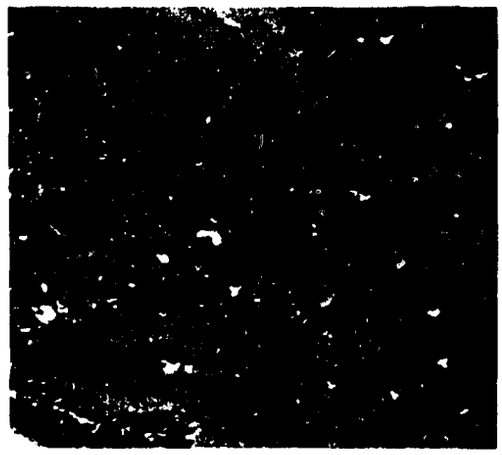

(a)

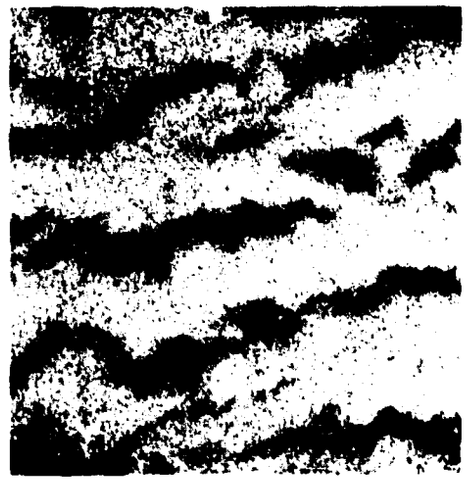

(b)

Fig. 10. Cross sections of the scale formed on specimens oxidized below 440°C showing the scale structure at high magnification. (a) 425°C, 380 Torr oxygen, 1275 min. Magnification 5,750X. (b) 401°C, 380 Torr oxygen, 4090 min. Magnification 10,700X.

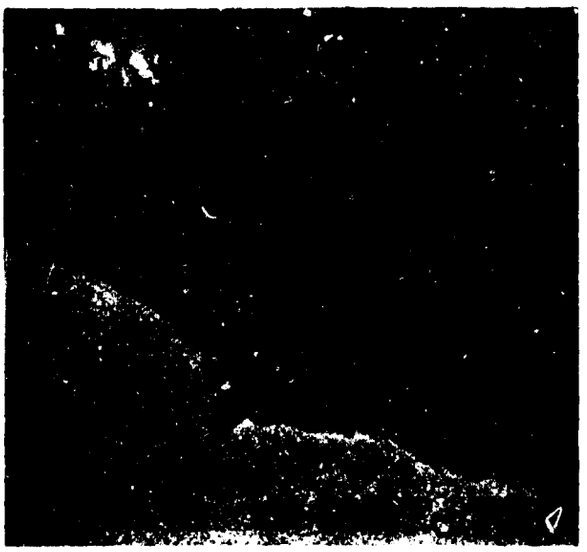

Fig. 11. Cross section of specimen oxidized at 550°C, 380 Torr oxygen, for 240 min. showing the incorporation of sub-oxide plates into the scale. Magnification 5,500X.

Fig. 12. Cross section of specimen oxidized at 550°C, 380 Torr oxygen for 240 min. showing the development of anisotropic oxidation. Magnification 25X.

Fig. 13. Cross section of specimen oxidized at 444°C, 380 Torr oxygen, for 2840 min. showing a site of breakaway oxidation. Magnification 35X.

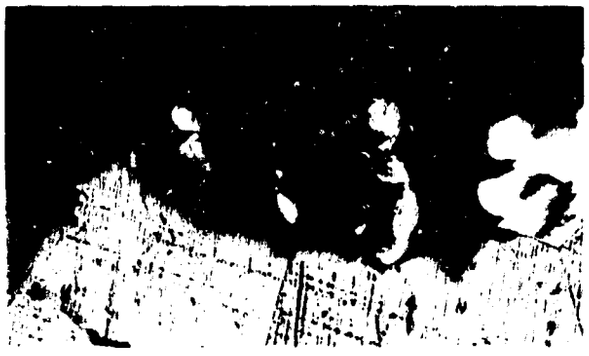

(a)

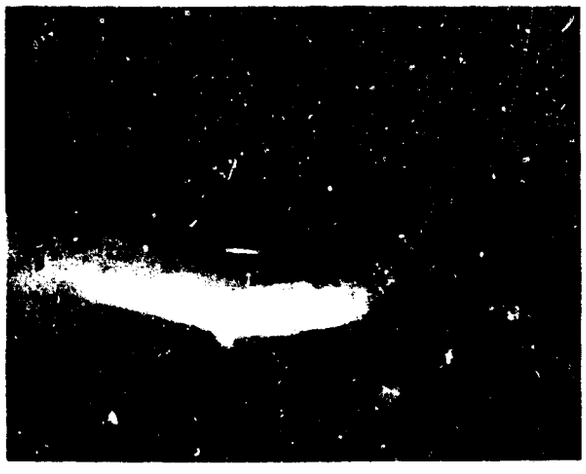

(b)

Fig. 14. Cross section of specimen oxidized at 450°C, 380 Torr oxygen for 1443 min. showing details of sites of breakaway oxidation. (a) Etched, Magnification 200X. (b) Polarized light, Magnification 1000X.

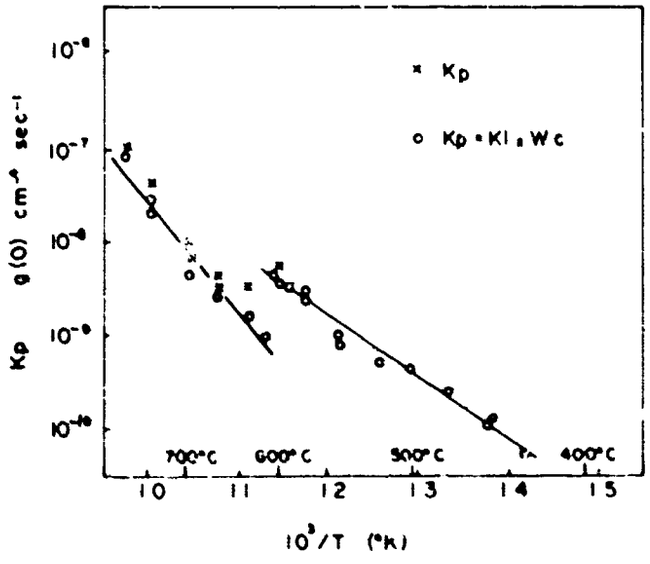

Fig. 15. Dependence of the derived and measured parabolic rate constants of oxidation of niobium at 380 Torr on temperature.

SUMMARY

Nickel-base superalloys, utilized extensively in the hot components of jet engines, are subjected to environmental conditions which vary widely dependent on a number of factors. Principal among the critical variables are temperature, pressure, gas velocity, and gas contamination due to ingestion of gaseous, liquid and solid compounds.

The basic oxidation behavior of Ni-base superalloys is briefly reviewed. Typical alloys are evaluated as to type of oxides (both surface and subsurface) formed, matrix chemistry changes during oxidation, effects of surface preparation and gas velocity.

The phenomenon of accelerated oxidation (hot corrosion) is reviewed. The effects of NaCl in the atmosphere and sulfur in the fuel on the surface stability of typical alloys are examined. Examples of accelerated oxidation encountered in service are presented. The various theories which have been developed to explain the "hot corrosion" reactions are examined and correlations with experimental observation are attempted.

THE OXIDATION OF NI-BASE SUPERALLOYS UNDER AIRCRAFT ENGINE CONDITIONS

C. S. Wukusick

Materials and Processes Technology Laboratory

General Electric Company

Evendale, Ohio

NICKEL-BASE SUPERALLOYS are used extensively in the hot components of aircraft turbine engines because of their unexcelled combination of high-temperature strength and corrosion resistance. The alloys derive their strength primarily from the precipitation of a coherent Ni_3 (Al, Ti) compound and, because of the high stability of the precipitate, useful strengths are retained to at least $0.75T_M$. Further strengthening is obtained through additions of refractory metal elements which solution-harden the matrix and stabilize carbide precipitates. The structures of the alloys are thus relatively simple, consisting of gamma prime and carbide precipitates in a Ni-base matrix. The chemical compositions of the alloys, however, are quite complex, generally consisting of over 10 elements intentionally added. The compositions of typical alloys are listed in Table I.

As a result of the complexity in chemistry the oxidation behavior of the alloys is also complex. The alloying elements form oxides and nitrides of varying stability and complexity. Surface and subscale reactions vary not only with chemical composition of the alloy but also with time and temperature of exposure, environment and surface condition. In spite of all the problems involved, an improved understanding of the factors which control the oxidation behavior of the alloys is critical to the development of improved alloys. The development of alloys with higher strength has generally proceeded without too much concern for oxidation behavior. In the past few years, however, the development of alloys with improved oxidation resistance has received increasing emphasis because oxidation resistance has been approaching the status of a life-limiting property. This is partially a result of the projected increased in life of aircraft engines. Critical parts such as turbine blades must exhibit lives of thousands of hours rather than hundreds.

In service, many superalloy components are exposed to a variety of environmental conditions. Generally the atmosphere created by the products of combustion is of high velocity and contains O_2, N_2, CO_2, H_2O and perhaps SO_2 or Na_2SO_4. The components are also subject to foreign particle erosion and rapid temperature cycles.[2]

It is the purpose of this paper to critically examine the oxidation-corrosion behavior of nickel-base superalloys in aircraft gas turbines, to establish the general level of present understanding and to point out areas where further study is needed.

BASIC OXIDATION BEHAVIOR

The Ni-base superalloys are based on Ni-Cr and Ni-Cr-Al alloys and their oxidation behavior can be closely related to these systems. The effects of Cr + Al on the oxidation of Ni are indicated in Figure 1. Below about 10%, Cr increases the rate of oxidation of Ni[1]. Up to about 3% Cr the reaction data fit Wagner's mechanism of oxidation as would be expected by the addition of a high valence Cr ion to a p-type metal deficit divalent lattice. At higher Cr levels the presence of spinel oxide in the inner NiO zone as well as the complexing effect of internally oxidized Cr_2O_3 particles does not allow a good fit with the Wagner mechanism. At higher Cr levels (> 10%) either Cr_2O_3 or a $NiCr_2O_4$ spinel oxide is responsible for the reduced oxidation rate. Some dispute over which of these two[4] oxides is the controlling one has not been resolved. It is quite possible that both oxides are present and in some cases one oxide is stabilized over the other depending on the presence of trace elements.

The addition of Al to Ni and Ni-Cr alloys increases the oxidation resistance. Based on the Wagner mechanism, it might be expected that in Al-Ni alloys, due to the trivalent nature of the Al ion, the rate of oxidation would be increased in the region where Al is soluble in NiO. This effect has not been experimentally observed in alloys containing as little as 1% Al. This is apparently due to the very low dissociation pressure of Al_2O_3 which precludes Al solution in NiO. The oxides formed on Ni-Al alloys are Al_2O_3 (α or γ), $NiAl_2O_4$ spinel and NiO. Comparing the results of various studies, it is likely that at low temperatures thin films of Al_2O_3 form and subsequently become overgrown with spinel and NiO. At high temperatures α Al_2O_3 appears to form at the exclusion of other phases. The beneficial effect of Al on the oxidation behavior of Ni-Cr alloys has been ascribed to the formation of more protective $Ni-Al_2O_4$ spinels as well as adherent Al_2O_3 films next to the metal/oxide interface which in the presence of Cr can be stabilized to lower temperatures.[3]

The oxidation behavior of turbine blade alloys is somewhat more complex than the simple alloys outlined above. In order to obtain a sufficient understanding of the alloys, careful studies utilizing a number of analytical tools are necessary. A number of superalloys have been well documented.[4,5] As an example of a typical alloy the behavior of U-700 alloy is here briefly reviewed. The rates of oxidation of U-700 from utilization of thermo-gravimetric techniques are shown in Figure 2. It is apparent that the oxidation rate is controlled not by a single process, but perhaps several. Initially at all temperatures a linear rate law is obeyed. It is followed by nearly parabolic kinetics at most temperatures. However, an inversion in kinetics is noted at 1900°F where, after a time, the rate of oxidation decreases and becomes less than at 1800°F. The reason for this will become apparent upon establishing the identity of the oxides which are formed. From the results of the studies a time-temperature diagram can be constructed to show the oxides formed. The resulting diagram for U-700 alloy is shown in Figure 3.

During initial oxidation at 1600 to 1800°F, a continuous film of α-Al_2O_3 forms with smaller areas of Cr_2O_3 nucleating over grain boundary and twin boundary areas. The aluminum is depleted from the metal adjacent to the oxide-metal interface and little further growth of the Al_2O_3 occurs. Cr_2O_3 continues to form as Cr diffuses along short-circuits such as grain boundaries.[3] The initial period of linear oxidation is believed to reflect the formation and lateral growth of Cr_2O_3

colonies while the Al_2O_3 film retains virtually a constant thickness. At longer times, the continual solution of Cr^{+3} converts the α/Al_2O_3 film into an $(Al, Cr)_2O_3$ solid solution. Subsequent parabolic oxidation then causes growth of the film and its continual enrichment in Cr. At the same time, subscale Al_2O_3 and TiN are formed because of a high degree of stability of the compounds and a low rate of diffusion of the metal ions to the surface.

Prolonged exposure at 1600-1800 (region 3) results in Cr_2O_3, spinel and overgrowths of TiO_2 as well as subscale Al_2O_3, TiN and a complex Mo-Ni nitride. At higher temperatures 1800-1900°F (region 4), the availability of Al is greater due to solution of the Ni_3Al (gamma-prime phase). The resulting scale which contains only traces of Cr_2O_3 consists predominately of spinel ($NiAl_2O_4$) which contains a high aluminum content. Note also that no subscale products are formed in the 1800-1900°F temperature range. This is due to the high stability of the Al-rich surface oxide. At higher temperatures, the Al concentration is not sufficient to establish and maintain an Al-rich oxide and as a result Cr_2O_3, $NiCr_2O_4$ spinel and NiO are formed at the surface, with subscale Al_2O_3 and TiN. The decrease in oxidation kinetics at 1800-1900°F is explained by the formation of a Al_2O_3 surface oxide rich in Al which grows slowly and whose extremely low dissociation pressure precludes the back diffusion of oxygen into the alloy in amounts sufficient to produce internal oxidation.

Other Ni-base superalloys exhibit oxidation behavior similar to U-700 except in most cases the 1800-1900°F inversion is absent. In U-700 the Al content (4%) and the Al/Ti ratio (4/3) are in the proper range to exhibit the inversion. Rene' 41 alloy does not exhibit the effect as indicated in Figure 4 because of unfavorable chemical composition. Rene' 41 contains only 1.5% Al and a low Al/Ti ratio (1.5/3). Among the many factors which are important in the oxidation of most metals and alloys is the method of surface preparation used. We might expect that in the case of U-700 alloy, cold working of the surface would increase diffusion rates and reduce the temperature at which internal oxidation is eliminated. This effect has been noted.[5] In other alloys such as Rene' 41 we expect and obtain increased internal oxidation when the surface is abraded prior to test.

The kinetic studies outlined above, while establishing the type of scale and subscale products formed do not accurately predict the performance of an alloy. Other major factors which contribute to increased oxidation are:

1. Oxide spalling
2. Excessive localized intergranular oxidation
3. Oxide volatilization

Due to cyclic temperatures encounter in service, oxide spalling can result in greatly increased oxidation rates. In general, during cyclic tests the oxidation rate of most superalloys is increased by a factor of up to about 4 to 1. The effect of cyclic exposures on the oxidation rate of U-700 is indicated in Figure 5.

Preferential oxidation of grain boundaries can result in deep penetration and in some cases act as nuclei for fatigue cracks.

In aircraft engines the gas velocities are much higher than in most laboratory tests. Higher velocities can increase the rate of formation of volatile oxides, presumably by removal of protective boundary layers. Many of the superalloys form Cr_2O_3-rich surface oxides because of the high Cr contents. In a high velocity gas stream a volatile species CrO_3 is formed by the reaction:

$$2\ Cr_2O_3 + 3\ O_2 \rightarrow 4\ CrO_3$$

More stable oxides such as Al_2O_3 or the spinels such as $MnCr_2O_4$ are preferred for high temperature, high velocity applications. For this reason the Al/Cr ratio in an alloy is extremely important, since it will determine which oxide predominates at high temperatures.

ENGINE OXIDATION

In gas turbines, in addition to the normal oxidation processes encountered, an additional mode of attack can occur. As a result of contamination of the gas stream, accelerated oxidation, also termed "hot corrosion" occurs. A number of comprehensive reviews of the "hot corrosion" problem have been published, the most notable being one by Hancock.[6] In spite of the volumious literature on the subject, the basic mechanisms by which "hot corrosion" occurs have not been completely defined. This is in part due to the wide range of contaminants, variations in materials, and differing time - temperature regimes encountered in various equipments. In the aircraft engine we can limit our discussions principally to atmospheric contamination by sodium chlorides and sulfur contamination in the fuel, although carbonaceous deposits also can contribute to accelerated attack. The actual engine environment is difficult to describe but it is known that Na_2SO_4 is formed by reaction between Na in the air and S in the fuel.[6]

A series of typical microstructures showing oxidation which occurred during service is shown in Figure 6. The structures range from those expected during normal oxidation to those exhibiting moderate and severe accelerated oxidation. The microstructures vary widely because of widely differing service conditions. Pronounced internal sulfidation occurs in some cases where overall attack is slight. In other cases very little internal sulfidation is evident even when corrosion is moderate. Depletion of Cr due to reaction with carbonaceous deposits to form carbides tends to increase the oxidation rate, particularly in grain boundaries. This form of attack is sometimes

called "green rot" due to the characteristic color of the resultant oxide. A turbine blade which exhibited severely accelerated oxidation is shown in Figure 7. The phenomenon is characterized by voluminous NiO formation and internal sulfidation.

The corrosion reaction is markedly temperature dependent as indicated in Figure 8 compared to normal oxidation behavior. It is generally believed that the critical temperature regime is dependent on the presence of Na_2SO_4 condensate. At higher temperatures the dew point is exceeded and condensation does not occur. As a result, the reactivity decreases and eventually is controlled by more normal oxidation processes. Recent work by Bornstein and DeCrescente[7] indicates that a shift in the critical temperature range should occur as pressure is increased due to a shift in the vapor-condensate transition temperature as indicated in Figure 9.

The mechanisms involved in the corrosion reaction have not been completely defined. It is clear that reaction consists of two steps. First, breakdown of the normally protective oxide scale must occur. This event can result from mechanical abrasion, spalling of the scale due to thermally induced stresses or fluxing of the oxide by the liquid corrodent. Secondly, oxidation proceeds at an extremely rapid rate in the absence of a protective oxide. Considering first the breakdown of the surface oxide, it is likely that all three mechanisms can operate. Loss of the scale will expose material which is somewhat depleted in the less noble elements required for scale re-formation. However, loss of surface scale during normal oxidation does not usually result in catastrophic oxidation. Therefore, fluxing of the surface oxide would appear to be a necessary condition for catastrophic attack. In this way the re-formed oxide films are dissolved as fast as they are formed.

Next, it is critical to explain the catastrophic nature of the attack. In early work, Seybolt[8] postulated that internal sulfidation caused depletion of Cr from the matrix thereby reducing the oxidation resistance. However, this can only be a contributing factor since complete depletion of Cr or other less noble elements would not be expected to result in catastrophic attack. Recent work by Seybolt[9] indicates that sulfur may not be a necessary part of the reaction, having produced accelerated oxidation by reaction with NaCl. In a Ni-20 Cr alloy, reaction with molten salt resulted in migration of Cr to the surface to form non-adherent, granular and thus non-protective oxides. The loss of alloy constituent caused a counter current flow of vacancies which condensed into an interconnecting pore network filled with the Na compound. It is suggested that since the salt penetrates into the structure, the loss of Cr does not require intermetallic diffusion over long distances, but instead corrosion products are largely removed by solution of alloying metals as ions in the pore-salt network. Seybolt presented evidence that suggests that an integral part of the catastrophic process is recrystallization, occurring in the porous zone, and that in the Ni-20 Cr alloy Cr diffuses down grain boundaries of the grain network to be deposited at grain boundary-pore intersections as Cr ions. The concentration gradient of Cr ions in the salt phase forces Cr diffusion out to the surface where the higher effective oxygen pressure forms Cr_2O_3. Seybolt's proposed mechanism seems capable of explaining the catastrophic oxidation which occurs; however, it probably should be modified for the case of Na_2SO_4 - alloy reactions.

Turning to the effects of alloying elements, there is general agreement[10] that the higher the Cr content, the greater the resistance to hot corrosion. Bergman et al[10] found that alloys readily susceptible to corrosion contain less than 15% Cr while the better alloys contain 18 to 21% Cr. The effect of Al additions on the corrosion behavior of Ni-base alloys is not clear. Both high and low resistances to corrosive environments have been obtained with high Al alloys. It is suggested that if a continuous, adherent aluminum rich oxide is formed, resistance to Na_2SO_4 attack may be high. It is however difficult to obtain good Al_2O_3 adherence on Ni-base alloys[3,4]. Also, the rate of Al_2O_3 formation is extremely slow and the resultant thin film may be easily disrupted mechanically or by reaction with the Na compounds. In Ni-Cr-Al alloys, the presence of Al may accelerate the corrosion reaction once the surface oxide is rendered non-protective. Through the mechanism suggested by Seybolt, Al would tend to reduce the effective oxygen pressure in the pores due to Al-O reaction, thereby speeding up the rate of Cr-ion diffusion outward.

Titanium additions were found by Bergman et al to be beneficial in improving corrosion resistance even though Ti generally reduces the resistance to normal oxidation. It is possible that at high Ti levels the formation of Ti-rich oxides may occur at a faster rate than can be removed by reaction with Na_2SO_4. In this regard the Ti/Al ratio appears to be important. A number of new alloys have recently been developed with increased Ti/Al ratios. Alloys such as U-710, and IN-738 exhibit improved corrosion resistance compared to U-700 and Inconel 713C.

RECOMMENDATIONS

In order to develop Ni-base superalloys with improved combinations of strength and surface stability, a much better understanding of the interactions between alloy chemistry and actual or simulated engine environments must be obtained. In order to obtain higher strength alloys, reductions in Cr seem unavoidable. The levels of other critical elements such as Al, Ti and refractory elements must be adjusted to make up for the reduced Cr and maintain adequate surface stability. Further studies of rare-earth type elements additions appear warranted since they have been found to improve both oxidation and corrosion resistance[10]. In the evaluation of materials, conditions closely approximating those encountered in service must be utilized to obtain the proper relationships between contaminants and oxide formation and reduction.

REFERENCES

1. C. Lund et al, "Oxidation of Nickel and Cobalt Base Superalloys", DMIC Report No. 214, March 1, 1965.

2. C. Wagner and K. Gruenwald, Phys. Chem., B40, 455 (1938).

3. W. C. Hagel, "Proceedings Second, Int'l Conference on Corrosion", 1963.

4. G. E. Wasielewski, "Oxidation of Ni and Co Superalloys", G.E. Co., R68AEG141, January 1968.

5. S. T. Wlodek, "The Oxidation of Rene' 41 and U-700", Trans. AIME 1964, p. 107.

6. P. Hancock, "Corrosion of Alloys at High Temperatures in Atmospheres Consisting of Fuel Combustion Products and Associated Impurities", London, 1968.

7. M. A. DeCrescente & N. S. Bornstein, "Formation and Reactivity Thermo-dynamics of Sodium Sulfate with Gas Turbine Alloys", Corrosion, Vol. 24, May 1968.

8. A. U. Seybolt and A. Beltran, "High Temperature Sulfur-Oxygen Corrosion of Ni and Co", Amer. Soc. for Testing & Matl's, STP-421, September 1967.

9. A. U. Seybolt, "Mechanisms of Salt-Induced Accelerated Oxidation of Ni-20Cr Alloy and Stainless Steels", GERL Report 69-C-223, May 1969.

10. P. A. Bergman, C. T. Sims, A. Beltran, "Development of Hot Corrosion Resistant Alloys for Marine Gas Turbine Service", Amer. Soc. for Testing and Matl's, STP-421, September 1967

TABLE I

COMPOSITIONS OF TYPICAL Ni-BASE SUPERALLOYS

Name	Composition (Wt. %)										
	Cr	Co	Al	Ti	W	Mo	Ta	B	Zr	C	Other
U-700	14.5	15.0	4.3	3.5	-	4.2	-	.015	-	.10	
Rene' 100	9.5	15.0	5.5	4.2	-	3.0	-	.015	.06	.17	1.0 V
Rene' 41	19.0	11.0	1.5	3.1	-	10.0	-	.005	-	.09	
I-713C	13.0	-	6.0	0.7	-	4.5	-	.012	.10	.12	2.0 Cb
U-500	19.0	18.0	3.0	3.0	-	4.0	-	.006	-	.08	
W-710	18.0	15.0	2.5	5.0	1.5	3.0	-	.02	-	.07	
IN-738	16.0	8.5	3.4	3.4	2.6	1.75	1.75	.01	.10	.17	0.9 Cb

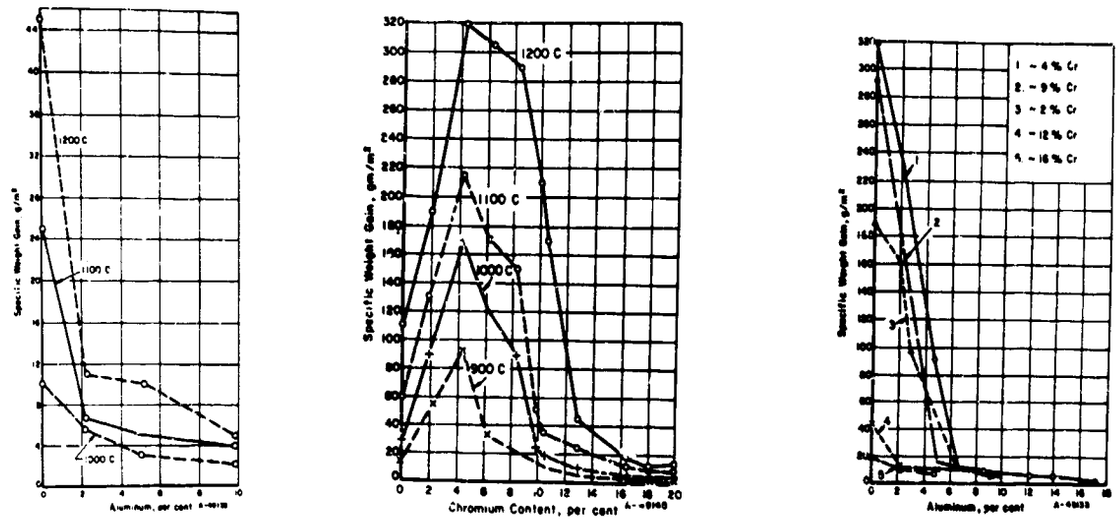

Effect Of Aluminum | Effect Of Chromium | Combined Effect Of Al & Cr

Fig.1 Effects of aluminum and chromium alloy additions on the oxidation resistance of nickel base alloys[1]

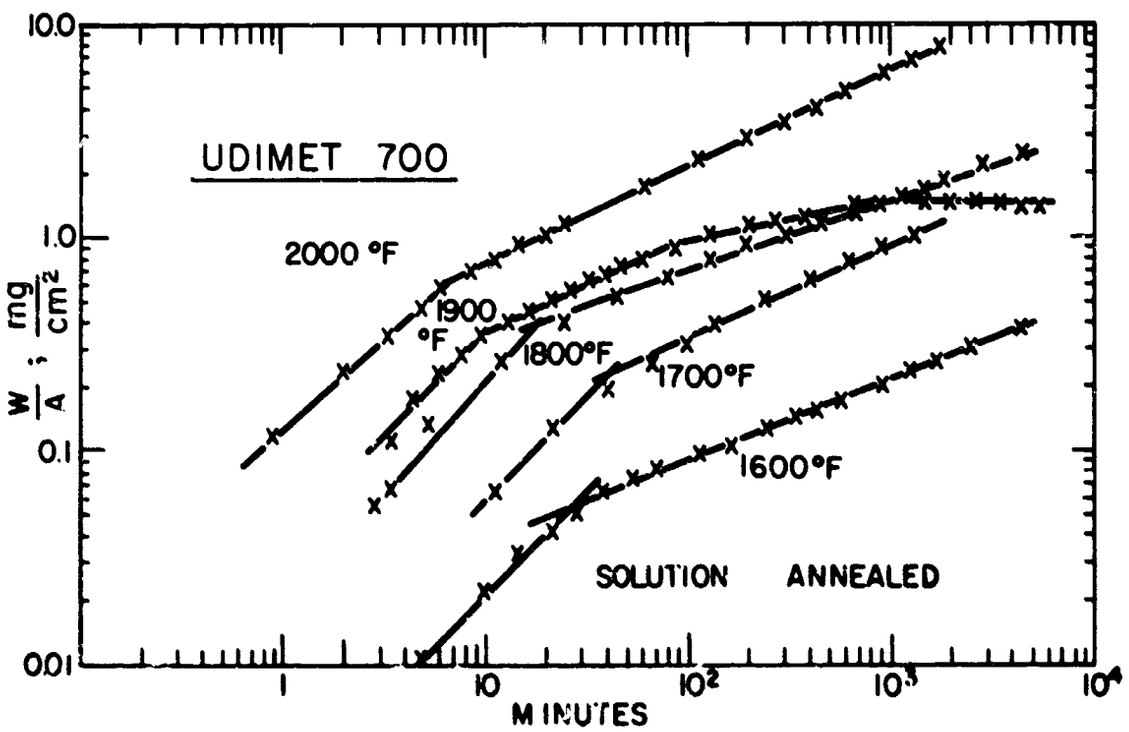

Fig.2 Logarithmic weight gain plot for Udimet 700 indicating initial linear and subsequent parabolic behavior and a complete cessation of weight gain at 1900°F after 1,000 minutes

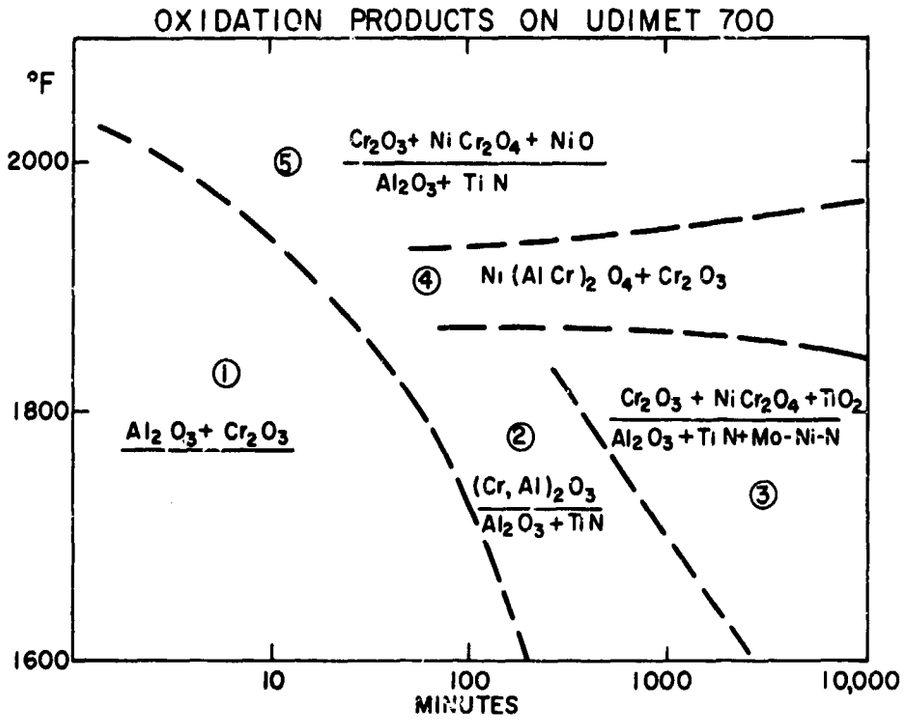

Fig.3 Simplified summary of the four main phenomelogical stages of oxidation encountered by Udimet 700. Subscale and scale reaction products expressed as numerator and denominator of a quotient which identifies the reaction species in each region. Note absence of internal oxidation in Regions 1 and 4. Scaling kinetics linear in Region 1, parabolic in others, except 4 where weight gain reaches a constant value in some 1,000 minutes

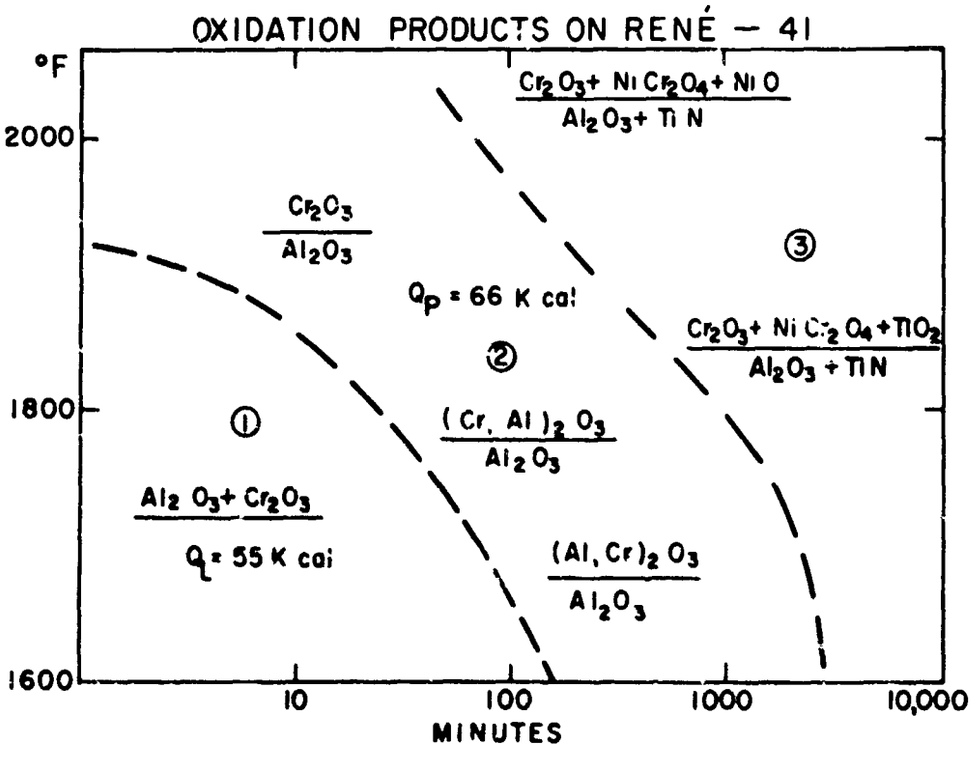

Fig.4 Schematic presentation of the major reaction products that can form during the oxidation of Rene' 41 and the associated kinetic regions 1 - linear, 2 and 3 parabolic. The phases present in the numerator are the scale constituents, those in the denominator are the products of internal oxidation

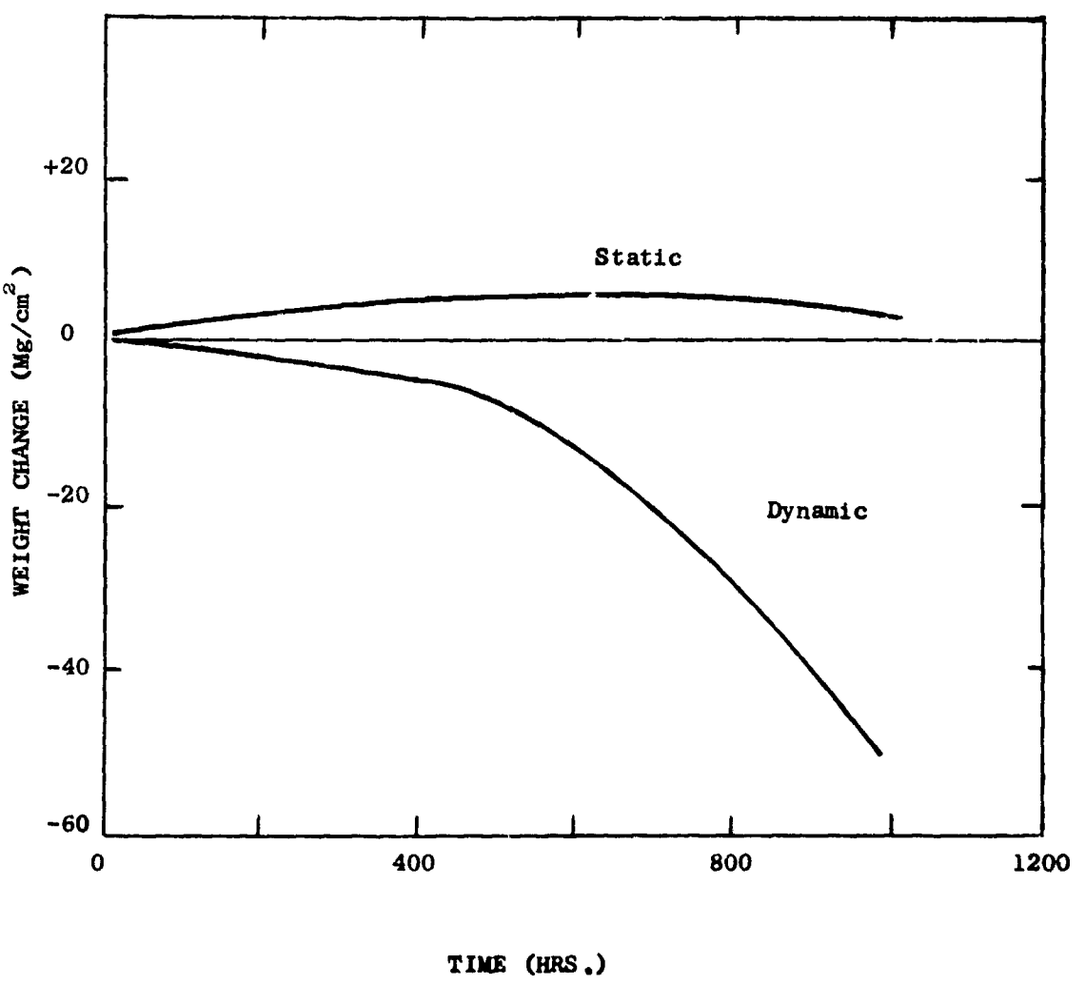

Fig.5 Effects of cyclic exposure on the oxidation rate of U-700 alloy at 1800°F

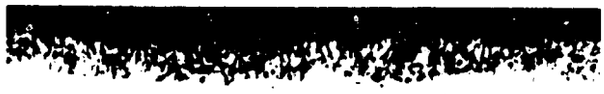

(a) Typical Oxidation

(b) Increased Attack

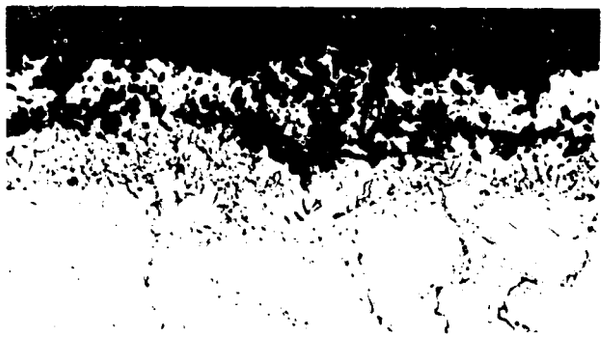

(c) Sulfidation

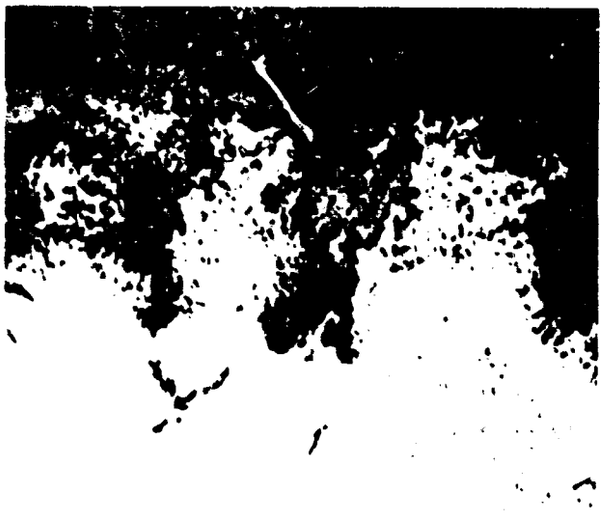

(d) Advanced Corrosion

Fig. 6 Oxidation of U-500 alloy turbine blades during service. 50 X

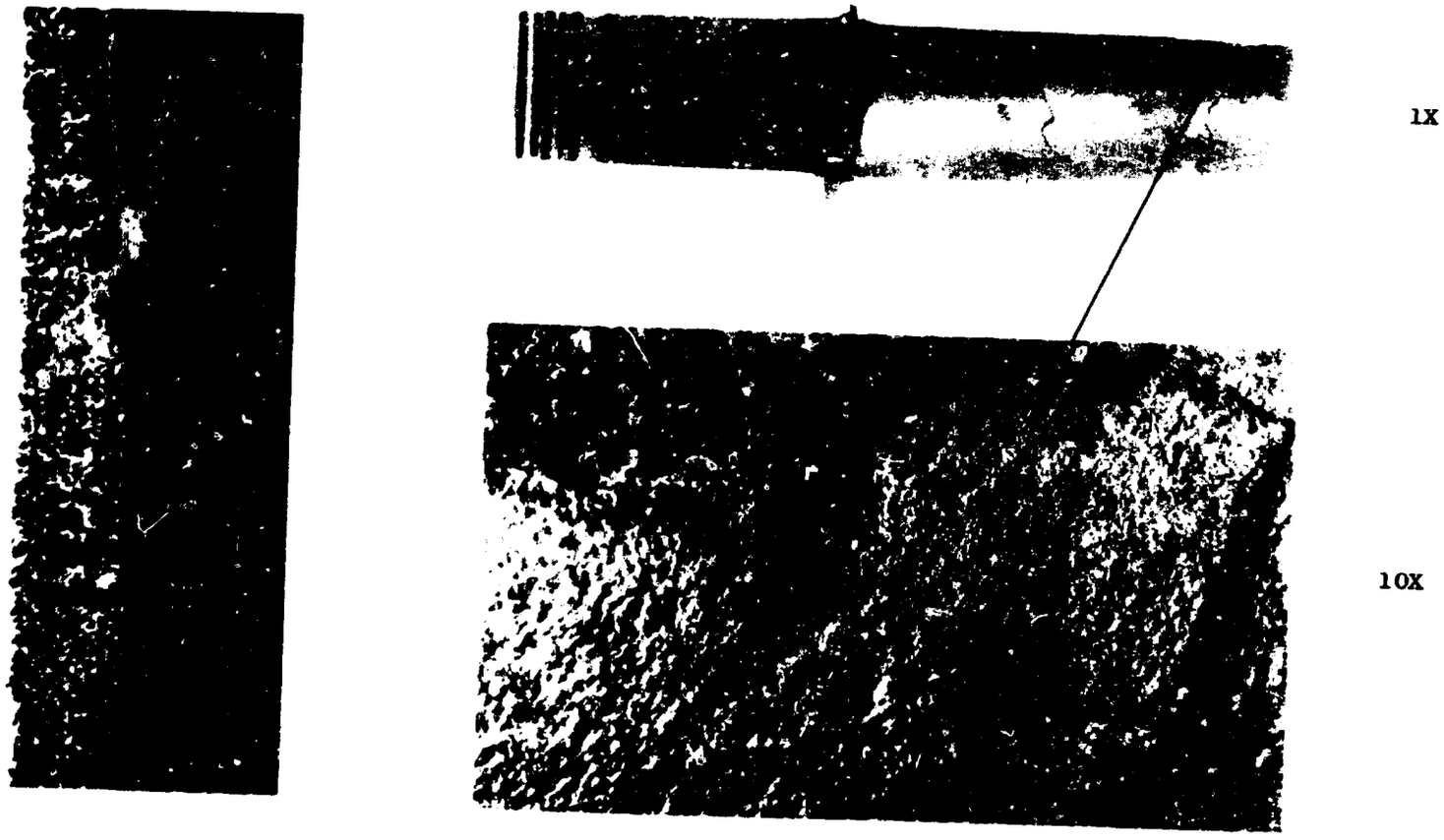

Fig. 7 Turbine blade showing accelerated oxidation

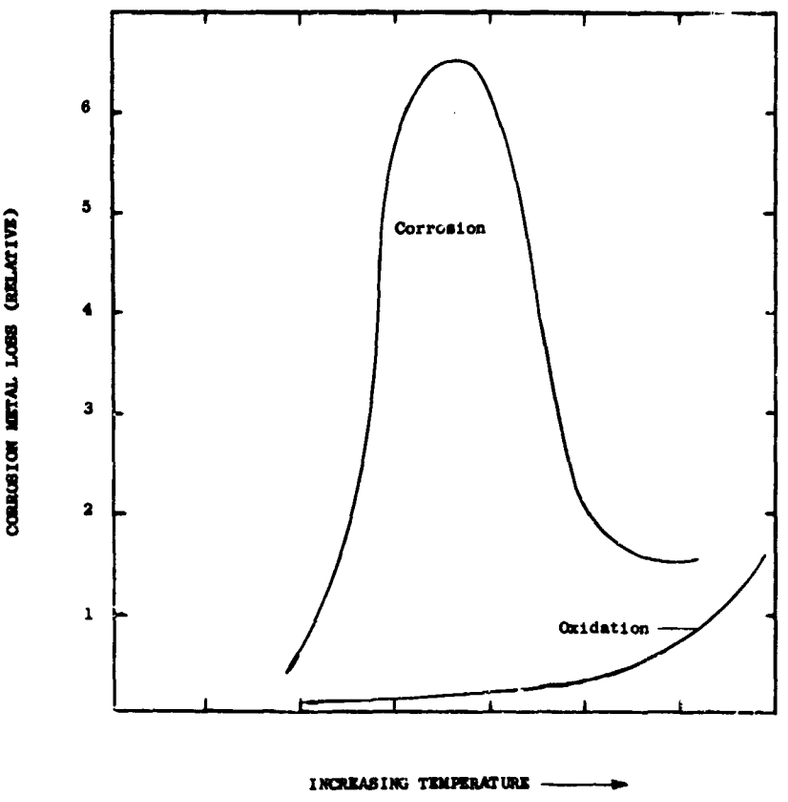

Fig.8 Schematic representation of the temperature dependence of accelerated and normal oxidation

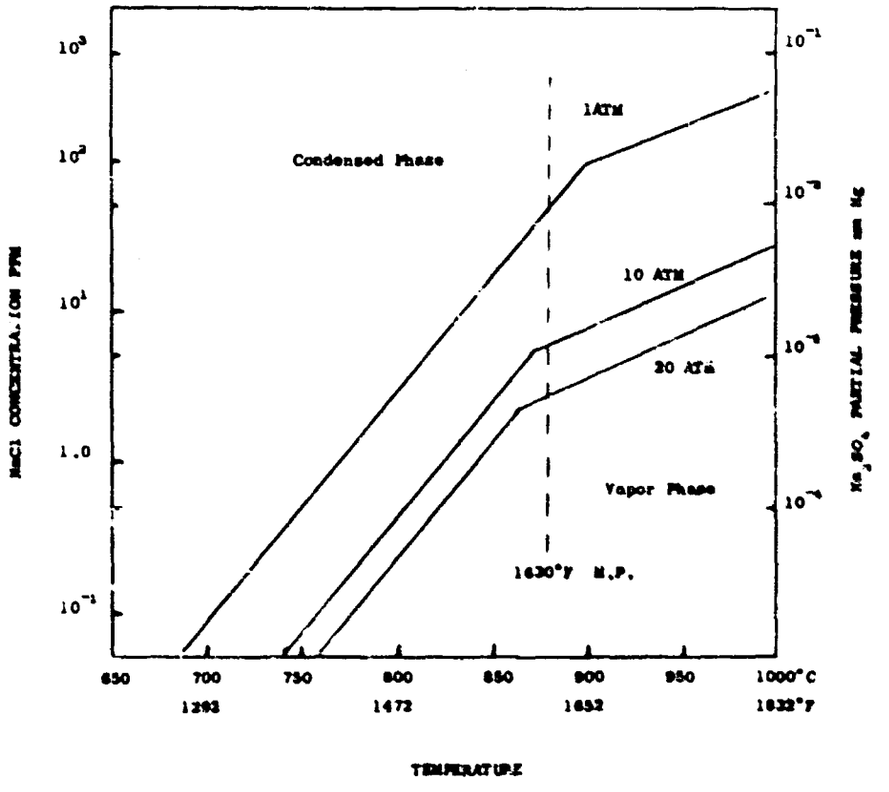

Fig.9 Dew point of Na_2SO_4 as a function of NaCl concentration and pressure

REACTIONS BETWEEN HIGH-TEMPERATURE-RESISTANT ALLOYS AND GASES

H. Pfeiffer

Vacuumschmelze GmbH,
Hanau, Western Germany

SUMMARY

Normally the Gibbs-potential of the reaction between metals and oxygen is much higher than that of any other reactions between solids and gases and, therefore, this process takes place in gases with oxygen contents of 20 % or less, especially in air.

The phenomenon of selective or preferential oxidation of the one or the other alloying element is one of the most interesting facts regarding the rate of oxidation processes. It has been discussed in detail on the system of iron-chromium alloys which may be thought to be a model of temperature-resistant alloys.

Another important influence has to be attributed to the adhesion between the metallic surface and the oxide scale. It proved to be true for all heat-resistant alloys that diffusion processes are determining the rate of oxidation. Consequently, the growing scale acts as a protective layer, the efficiency depending on the concentration of lattice defects in the oxide scale. But the protective effect will be small unless the demand for a sufficient adhesion is satisfied.

A third point of view is the plastic flow of oxide layers which influences the kinetics of oxidation reactions. It reduces the cooling stresses and may cause the oxide scale to remain in tight contact with the metal in spite of the formation of holes due to the preferred migration of metal ions to the outer surface.

A considerably different situation is observed if the content of oxygen in the surrounding atmosphere is not as high as to form pure oxide scales. Other reactions can take place, for example, the attack by gases containing nitrogen, carbon, or sulphur. In many cases reactions are observed running at very high rates: catastrophic oxidation processes due to the formation of molten phases. Finally it has been discussed the so-called green rot oxidation arising from internal oxidation of chromium, especially obtained in furnace atmospheres either alternating between carburizing and oxidizing.

OXIDATION PROCESSES OF METALS often are marked by the formation of coherent oxide layers acting as a barrier between the metal surface and the oxygen containing gas. The high values of the free energies of oxides are responsible for the phenomenon that most of the scales arising at high temperatures are oxides and not other possible reaction products as, for instance, nitrides. Already a very low content of oxygen in the surrounding atmosphere is sufficient for this scaling process and in most cases of annealing in air the existence of oxides as sole reaction products should be observed.

SELECTIVE OXIDATION

Another question is the composition of oxide scales or, in other words, the extent of selective oxidation. This problem has been receiving considerable interest during the past ten years. In view of its importance specifically with regard to reaction kinetics the following deals first of all with questions connected with selective oxidation. The specially interested reader may be referred to two summarized representations (1, 2). It is quite clear that the growing oxide scale acting as a barrier will have important influence on composition and consequently on nature and concentration of lattice defects in these layers. Furthermore, some other factors are interesting, as scale density and adherence, oxide volatilization, blistering and cracking phenomena, and so on. In other words, selective oxidation and the extent of preferred oxidation of one or the other component of alloy respectively is an essential point of view with regard to oxidative attack at high temperatures. Selective oxidation not at last determines the rate of the heterogenous chemical reaction.

Oxide layers formed by oxidation of alloys may be composed as follows:

1. The oxide of only one component of the alloy has been obtained; hence, only selective oxidation had taken place.
2. The reaction product consists of a mixture of insoluble oxides.
3. Several oxides reacting together are obtained and spinels are formed which either alone or more frequently together with an excess oxide produce the protective layer.
4. The oxide consists of several layers of different composition.

The case of nearly exclusive selective oxidation certainly is the most important one with regard to considerable reduction of the oxidation rate at increasing thickness of the layer. This is realized best in the case of an alloy containing an oxidizable base metal and a noble metal. Thermodynamic facts allow only the base metal component to be oxidized at higher temperatures. But also in other cases very exclusive selective oxidation is frequently observed and that the more probable the more the free energies of the oxides differ. Beside thermodynamic facts there are kinetic problems which may influence the preferred oxidation of a component of alloy as far as a sufficient diffusion rate of this specially oxygen affine element in the metallic phase is a necessary precondition. Add to that other factors of influence as composition of alloy, temperature and oxygen pressure of the environment, test time, structure of the oxide layer, and the diffusion rates of the components contained in the layer. It was above all Wagner (3) who has dealt in detail with the qualitative and quantitative relations of selective oxidation.

This kind of oxidation is observed at high temperatures at some resistance alloys as CrAl 25 5 (iron rest) which shows, moreover, clearly the influence of the temperature on the extent of selectivity. Annealing of such alloys in air or oxygen produces practically pure Al_2O_3 as may be proved by X-ray examination and chemical analysis. Kornilov and Sidorishin (4) observed with an analogous alloy of 30 weight % of chromium a different oxidation process at medium and higher temperatures. In the first case a mixture consisting of the spinels $FeAl_2O_4$ and $FeCr_2O_4$ is obtained. With increasing temperature finally selective oxidation of aluminum becomes predominant. Up to temperatures of about 1000°C γ-Al_2O_3 is formed, beyond that α-Al_2O_3. Concentration of aluminum decreases near the surface of the alloy and diffusion from the bulk material becomes important. Determination of the lattice constants (table 1) of the oxides obtained at different temperatures shows clearly the facts described before.

Table 1: Lattice constants of oxide layers on FeCrAl (4)

Temperature, °C	400	600	700	800	1000
Lattice constant, Å	8,328	8,195	8,077	8,050	7,882

According to ASTM-card-index (5) the lattice constant of γ-Al_2O_3 is 7,90 Å whereas the spinels $FeAl_2O_4$ and $FeCr_2O_4$ show lattice constants of 8,113 and 8,348 Å respectively.

While testing the alloy for oxidation at 1200°C in long runs with alternate heating and cooling at intervals of 12 and 42 hours, Kornilov (4) carried out chemical and X-ray analyses of the cracked off portion of the oxide film. He has shown that it consists of 98,7 % of alumina, the rest being chromic and ferric oxide.

These small additions of blackening oxides are extraordinarily important and

useful. They influence the spectral emissivity $\varepsilon(\lambda,T)$ of the oxide film in such a way that the difference between true temperature and temperatures measured e.g. by means of a selective-radiation pyrometer is only small. Quantitative estimation supplies the following result which has been proved experimentally in some analogous cases (6):
According to Wien's approximation to the law of radiation by Planck the following compendency exists between true temperature T_1, brightness temperature T_2, and spectral emissivity $\varepsilon(\lambda,T)$

$$\frac{\lambda}{c_2} \ln \varepsilon(\lambda,T) = \frac{1}{T_1} - \frac{1}{T_2}$$

$\lambda = 0{,}65.10^{-4}$ cm is the effective wavelength of the monochromatic screen of the selective-radiation pyrometer, $c_2 = 1{,}44$ cm.deg is a constant.

The spectral emissivity of pure Al_2O_3 is 0,14 ±0,05 at 1100 - 1600°K (7) and a true temperature of, e.g., 1200°C corresponds to $\Delta T = T_1 - T_2 \approx 170$°C, whilst an alloy of CrAl 25 5 with normally developed oxide layer shows an emissivity of 0,86 (8) and therefore only a difference of 15°C is found for the same temperature $T_1 = 1200$°C.

In this case the mentioned additions of oxides have no disadvantageous influence. Their valency is congruent with that of the bulk oxide and there is no influence on the lattice defect concentration and the rate of oxidation.

The advantage of the formation of an extensively pure layer of Al_2O_3 at high temperatures is the excellent protective effect of just this oxide due to its low lattice defect concentration. As the concentrations of defect ions and electrons are equivalent in pure oxides, it may be advantageous to know their conductivities. Then in some cases it may be possible to make predictions about the protective effect of the concerning oxides if neglecting different electron mobilities in different oxides. Table 2 shows the electric conductivities of metal oxides at 1000°C (9). Simultaneously has been indicated whether the oxides belong to the n-type or p-type conducting systems (10).

Table 2: Electric conductivities of some oxides at 1000°C

Oxide	BeO	Al_2O_3	CaO	SiO_2	MgO	NiO	Cr_2O_3	CoO	Cu_2O	FeO
$\kappa, \Omega^{-1}\cdot cm^{-1}$	10^{-9}	10^{-7}	10^{-7}	10^{-6}	10^{-5}	10^{-2}	10^{-1}	10^{+1}	10^{+1}	10^{+2}
Conducting system	n	n	n	n	n	p	p	p	p	p

Supposing the formation of pure oxides in compact form and of an oxidation rate depending on diffusion processes the oxides left in the table about up to MgO included are expected to have particularly good protective properties owing to their low conductivities. Yet, this does not apply on principle as a number of other factors are of more or less essential influence. Anyhow, the distinct protective effect of BeO, Al_2O_3, and SiO_2 is generally known and used for many materials.

Presumably the low lattice defect concentrations and by that also electric conductivities of the oxides of comparatively unnoble elements are based on the high oxygen-affinity of those elements. It is believed that the equilibrium concentration of ions in interstitial lattice positions and excess electrons in n-type conducting systems (the oxides indicated left in table 2) decreases with increasing oxygen-affinity of the concerning metal. The conditions are more complicated with p-type conducting systems where the stability of the various possible valencies of the concerning metals are very important and cannot be directly overlooked with regard to the tarnishing properties of the oxide scales.

In the right part of the table Cr_2O_3 represents an exception as it shows remarkable protective effect in spite of quite good conductivity. This may be based on the peculiarity of the defect phenomena of this oxide (11). With regard to the diffusion rates within the layer it may be noted that Cr_2O_3 shows a special irregularity. It is to be assumed that not all cation defects in the lattice are produced at one of the two phase boundaries and, consequently, are not subject either to a concentration gradient and directed diffusion.

Often also chromium oxide is formed as nearly exclusive oxide phase, for instance with FeCr-alloys with chromium contents >13 % in the temperature range between 1000 and 1300°C (12). Below 13 % of chromium the spinel $FeCr_2O_4$ is observed preponderantly proving the important influence of only small differencies in concentration. Other authors, however, indicate also other oxide compositions. Undoubtedly this disagreement is connected with the different conditions chosen as test time, atmosphere, and impurities of alloys. Also the formed oxide film influences internal oxidation which occured notably during formation of the spinel, but had not been observed, on the contrary, if a pure Cr_2O_3 layer is formed.

OXIDATION OF FeCr-ALLOYS

Oxidation of FeCr-alloys is probably the reaction system examined best and it seems

useful out of the present results and interpretations to list the most essential ones and check them with regard to their general application. First of all must be stated that all authors agree in saying that parabolic kinetics are generally observed for all compositions and temperatures. By that the preliminary conditions for the Wagner theory of oxidation are accomplished and, in particular, diffusion processes in the oxide film on the condition of chemical equilibrium at the phase boundaries are the rate controlling steps of the entire reaction. This secures in principle the possibility of an influence on the oxidation rate by impurity ions in the sense of Wagner and Hauffe (13). Whittle and Wood (14, 15), for instance, believe that the slow increase of the oxidation rate with growing chromium contents could be due to the decreasing concentration of Fe^{++}-ions. Solution of lower valent cations in Cr_2O_3 would, corresponding to the equation

$$2\ FeO + 1/2\ O_2^{(g)} = 2\ Fe_{\bullet}'(Cr) + 2\ \oplus + Cr_2O_3$$

(wherein $Fe_{\bullet}'(Cr)$ means a bivalent Fe-ion at a regular lattice site and $\oplus$ an electron hole), results in a concentration growth of electron holes and by that in a concentration decrease of cation vacancies. On the other hand they imagine Fe^{3+}-ions to be in solution exerting no influence according to the Wagner-Hauffe valency rules. Yet, in this case the dependence of the oxidation rate on the Cr-content would, indeed, have to be caused by the composition of the oxide layer consisting of metal-deficient p-type Cr_2O_3 and oxygen-deficient n-type Fe_2O_3. They consider it possible that, taking a certain concentration of iron, an optimum content of lattice defects in Cr_2O_3 is obtained.

And finally the concentrations of vacancies at the alloy/oxide interface depends on the chromium content of the alloy. This concentration of vacancies decreases, while the concentration gradient in the oxide increases with growing chromium content at the phase boundary. Consequently, with increasing chromium content the rate of oxidation must also grow.

It maybe noted (16) that at constant oxygen pressure the chromium activity decreases at the metal/oxide interface with decreasing concentration. The consequence is a decreasing chromium activity gradient within the oxide scale causing the diminution of the oxidation rates at smaller chromium contents.

According to Caplan and Cohen (17), on the contrary, the chromium content would not notably influence the oxidation behaviour. They show, for instance, that the oxidation rate of Fe-26 % Cr is comparable to that of pure chromium. Their examinations to clear up the discrepancies were only partially successful. They particularly referred to the considerable influence of surface treatment.

Whenever selective oxidation is observed, depletion of the preferentially oxidized element in the metallic surface must occur at the same time unless a concentration equalization happens quickly enough. Corresponding examinations have been carried out recently by means of the electron probe microanalyser. Fig. 1 shows the results by Wood and Whittle (14) with a FeCr-alloy of high chromium content. Inside the alloy the chromium content drops starting from the initial concentration towards the phase boundary alloy/oxide in order to rise to about the value of stoichiometric Cr_2O_3 of 68,5 weight % in the oxide layer. The iron content shows just reciprocal relations. The variations of the chromium content in the practically pure oxide phase Cr_2O_3 can be attributed to the inadequate resolving power due to the size of the X-ray source and to microporosity and relief polishing. In contrast to the important depletion of chromium with that alloy of very high chromium content it is remarkable that an FeCr-alloy containing only 28 % of chromium does not show any mentionable changes of the alloy concentrations under the same conditions, although pure Cr_2O_3 is formed in this case as well.

This phenomenon is explainable too by the different oxidation rates: the higher the reaction rate the greater is the demand for the preferably oxidized element at the phase boundary alloy/oxide and by that also the probability of depletion. In this connection it must, however, be mentioned that it is almost impossible to determine exactly the concentration gradients in an alloy in a distance from the phase boundary alloy/oxide of only a few microns (18).

A similar result of electron probe microanalyses may be demonstrated on the basis of the sulphurization of a Co-20 % Cr-alloy. The same test conditions would have caused severe attack on the Ni-20 % Cr-heater alloy due to formation of the $Ni-Ni_3S_2$-eutectic, the melting point of which is 645°C. Fig. 2 shows the contents of Co, Cr, and S after annealing in dried H_2-H_2S containing 65 % H_2S. The sum of the concentrations of these three elements (upper curve) has been determined at the positions indicated and the measurements are seen to have been carried out at very compact material. Remarkable deviations of some concentration, as, for instance, at 700 µm, find their equivalent in an inverse deviation of the concentration of some other element. Above about 750 µm a sudden diminution of the chromium content is found which finally decreases to zero. This was likewise observed after annealing for 15 and 60 min. respectively under the same conditions and applies also to corresponding NiCr and FeCr-alloys. They all consist of two layers, the inner one adhering fast to the alloy and consisting mainly of CrS, the outer one without any content of chromium.

The formation of two layers of different composition is being observed in other cases as well. Reported by Saunders and Pryor (20), for instance, the oxide film on Cu-3 % Al-alloys formed at 450 - 750°C consists of an inner layer of γ-Al_2O_3 and an outer one of Cu_xO. Both oxides are insoluble together and diffusion of copper-ions through Al_2O_3 is possible. If the formation of two layers is observed, an inner layer identical with the oxide of the unnoble alloy component and an outer layer identical with the oxide of the basic metal are the constituents of the scale.

Particularly complicating with regard to the discussion of the test results is the fact of blistering and spalling of the growing oxide, as observed, for instance, with FeCr-alloys. This may occur during isothermal oxidation, certainly during cooling, above a certain thickness of layer. No agreement exists regarding the question which of these two possibilities will be right. Whereas Caplan and Cohen (17) assume that the stresses in the oxide arise during isothermal oxidation and could be accounted on anion diffusion, other authors (14, 15, 16) emphasize that the cooling stresses would be responsible for the spalling behaviour. Westbrook (21) tends to the latter assumption revealing only a small effect of stresses arising during oxidation at constant temperature. He observed that hardness of most common oxides drops strongly at temperatures higher than about half the absolute melting temperature. This would be 860°C for Cr_2O_3 and above this temperature plastic deformation should be possible. Since the same behaviour of the oxide layers is being observed, however, also after oxidation at far higher temperatures, the cooling effect proves more probable.

INFLUENCE OF MINOR ELEMENTS

The cooling effect is also evident by the results obtained by Betteridge (22) who examined some NiCr 80 20-alloys in an intermittent oxidation test similar to the ASTM-Specification B 76-39. In these tests wires of about 0,9 mm diameter were suspended vertically and heated electrically reducing the heating current every 2 minutes from the value required to maintain the wire at the normal test temperature to a value maintaining the wire at a lower temperature. The lower one has been varied from almost room temperature up to close to the upper temperature. The results (Fig. 3) are remarkable in two different respects. Firstly, exceeding of certain temperature differencies $T_{upper}-T_{lower}$ shows decreasing lifetime indicating the damage of the oxide layer happening during cooling down. A small difference between upper and lower annealing temperature has no disadvantageous effect. On the contrary, the lifetime increases first as the advantage of the lower mean value of the temperature compensates more than enough the resulting thermal stresses and their consequences.

Secondly, the figure demonstrates essential differences in the behaviour of the two alloys which differ with regard to the calcium and cerium contents, thus showing different resistance to oxidation at high temperatures. The influence of these additions is shown also in the useful life under the normal intermittent test conditions of 37 and 606 hours respectively at 1175°C. With decreasing lower limit temperature a maximum lifetime is reached the earlier and the following reduction the more considerable, the smaller contents of these minor elements are used. It may be noted,for instance, that the alloy containing such additions at a lower temperature of 1000°C showed still nearly the highest lifetime attained in these experiments of approximately 1000 hours. But the alloy without additions showed only a lifetime of less than 100 hours under the same conditions.

Those additional elements prove efficient to such extent that nowadays no heater alloys are produced any more in which this possible quality improvement would not have been widely realized. They cause considerable improvement in adherence of the oxide layer, either by improved adaption of the oxide lattice to the metallic substrate or by better keying of both phases (23). In any case, owing to their very high oxygen affinity they concentrate in the form of their oxides at the inside of the scales, and, consequently, only those elements can be effective, which are solved in metallic form and therefore diffusible.

This may be one of the reasons why some authors have different views on the composition of oxide layers on NiCr-alloys since, on the one hand, pure alloys and, on the other hand, commercial ones have been examined. Other reasons are of course the testing conditions, particularly the test time, and by that the oxide thickness (24). Thus it seems not surprising that if taking alloys with Cr-contents >10 %, the oxide layer either consists mainly of the spinel $NiCr_2O_4$ (25, 26), or, under certain conditions, the formation of Cr_2O_3 is observed (27, 28), or, as a further possibility, both constituents were found (24). Own tests with commercial NiCr-alloys containing 20 and 30 % Cr were carried out at 1200°C, a temperature which can only be realized using alloys improved by minor elements. These tests prove that thicker oxide layers show heterogenous composition and consist predominantly of Cr_2O_3 and $NiCr_2O_4$.

Comparing the oxidation behaviour of NiCr-alloys of chromium contents ≥20 % with FeCr-alloys of the same chromium contents, it is interesting to see that in the latter case no spinel phase has been observed. The different compositions of oxide layers of the one and the other alloy system may be assumed to cause the different oxidation resistance. Perhaps it would be possible to improve the

FeCr-alloys by addition of some minor elements. Tedmon (29), for instance, succeeded in improving the oxidation resistance of Fe-25 % Cr alloys by adding 0,1 to 0,5 % of lithium. Obviously the influence of lithium consists in reduction of cation vacancies in Cr_2O_3 and by that the reduction of the diffusion rate of chromium-ions through the scale. The parabolic rate constant obtained for an Fe-25Cr-0,5Li-alloy at 1300°C was 7,o x 10^{-11} $g^2cm^{-4}sec^{-1}$, whereas with the corresponding lithium-free alloy there had been found a rate constant of 5,o x 10^{-10} $g^2cm^{-4}sec^{-1}$. It should be of interest to compare the latter value with the value of 6,9 x 10^{-10} $g^2cm^{-4}sec^{-1}$ (30) indicated for pure chromium at the same temperature. The good conformity shows only the oxide layer being responsible for the oxidation rate, whether it is formed on pure chromium or, for instance, on Fe-25Cr. Apparently the influence of iron-ions at such high temperatures may be neglected. This corresponds to results on the oxidation of the alloys Fe-27Cr and Fe-59Cr reported by Whittle and Wood (15) who found the greater the differences of the parabolic rate constants are, the lower the temperature is. This is shown in table 3 for runs of 5 hours.

Table 3: Comparison of short-term parabolic rate constants for Fe-59%Cr and Fe-27%Cr at 800 - 1200°C (5 h values)

Temperature, °C	Parabolic rate constant, $g^2cm^{-4}sec^{-1}$	
	Fe-59%Cr	Fe-27%Cr
800	1,9 x 10^{-12}	1,4 x 10^{-11}
900	1,1 x 10^{-11}	3,7 x 10^{-11}
1000	5,3 x 10^{-11}	1,4 x 10^{-10}
1100	7,o x 10^{-10}	4,1 x 10^{-10}
1200	1,4 x 10^{-9}	1,2 x 10^{-9}

According to examinations carried out by Evans (31) the analogous comparison applies also to pure chromium and Ni-20%Cr-heater alloys, of course only on the condition of pure chromium oxide formation. This statement refers, moreover, only to the reaction at constant temperature, whereas cyclic tests are not expected to show conformity of results due to differential spalling of the oxide scale. This corresponds to the observation of conforming oxidation rate of three Ni-20%Cr-alloys continuously oxidized (32). The same alloys, owing to different contents of small amounts of Si, Zr, Ca, Al, and Mg, differ essentially in intermittent oxidation tests showing ASTM-lifetimes of 25, 86, and 157 hours respectively. The results are given in Fig. 4. The broken-line curve applies to all three alloys at continuous annealing, the other curves to intermittent annealing.

Analogous observations are also concerning other alloys as, for instance, Fe-27%Cr-5%Al-alloys both with and without a cerium addition. Fig. 5 shows the good conformity of the rate constants at constant temperature, whereas the ASTM-lifetimes differ about by the factor 5 (33).

PLASTIC FLOW OF OXIDE SCALES

According to the explanations given before two things are prominent with regard to the oxidation rate of metallic materials at high temperatures: the composition of the oxide layer produced, on the one hand, and its adherence to the metallic surface, on the other hand. A third point, finally, is to be mentioned which refers to the plastic flow of the oxide layers. Oxides generally are very brittle substances which, nevertheless, may show slight plastic behaviour, especially at high temperatures. This property is important for two reasons. First, stresses in the oxide layer as produced at changing temperatures because of the differential expansion coefficients of alloy and oxide, can be equalized more or less by a plastic flow of the oxide layer. The second reason refers to the mechanism of metal oxidation which in most cases is characterized by diffusion of cations and electrons through the oxide layer towards the phase boundary oxide/gas. The consequence of this directed transport of metal should be the formation of cracks and holes at the phase boundary alloy/oxide. Plastic flow may be effective against this porosity by maintaining, at least partially, the contact between metallic substrate and oxide layer. These phenomena have been tested metodically at pure iron (34, 35), the behaviour of which under oxidising conditions at high temperatures has been interpreted by different plastic behaviour of the various iron-oxide modifications (35).

The possibility of plastic flow depends, besides the properties of the oxide itself, strongly on the shape of the metallic specimen as different geometric shapes cause differential flow resistance. A very usual form to apply the heater-alloys is that of round wires. Unfortunately, in this case inward flow of oxide to fill up the cavities arisen inside is nearly impossible for geometric reasons. At the edges of strip-shaped material only little plastic deformations may occur

because two oxide layers meeting perpendicularly upon another become very stiff. In these positions, the contact between the two phases gets preferably interrupted and further oxidation is suspended or at least retarded.

REACTIONS IN CONTROLLED ATMOSPHERES

So far considerations related mainly to the behaviour of temperature-resistant alloys in oxygen-containing gases. Yet, there is a steady increase of annealing in certain controlled atmospheres which are suited, for instance, for carburization or decarburization of materials, for nitriding, and for brazing, or which shall only just inhibit oxidation of materials. Furthermore, often reactions with other substances are possible originating, for instance, from unsuited ceramic materials or combustion residues of fuels thus preventing the normal formation of a protective oxide layer. In such cases, the requirements to the resistance-alloy in an electric furnace are quite different. Possibly the protective effect of the oxide layer is not sufficient to prevent elements as carbon, nitrogen, and sulphur - and these are only the most important ones - to get contact with the metallic surface and to diffuse into the alloy. There, they react mostly just with those elements required for the formation of outer protective layers which, therefore, are not available any more for this purpose. Another consequence is frequently a considerable lowering of the melting point of the alloy which, eventually, may cause instantaneous destruction. By that the most essential disadvantages of such possible attacks have already been quoted. Perhaps they have to be reduced by reasonable modifications of the conditions, specifically of the composition of the annealing atmosphere, by constructive methods, choice of suitable alloys, or even by the development of alloys with higher resistance, under special conditions.

Especially the formation of molten phases results in any case in a catastrophic increase of the oxidation rate. The term of "catastrophic oxidation" (36) introduced first for reactions with low-melting oxides as MoO_3 and V_2O_5 ought to be used generally for all reactions which are forming, outside or inside, locally or widespread, molten phases. Beginning of the melting process is observed along the grain boundaries into the bulk material. The diffusion rate of all elements taking part in the chemical reaction is essentially higher in molten phases than in solid state, and the reaction rate increases correspondingly. Furthermore, partial melting at grain boundaries may diminish the bond between the grains of the polycristalline metal structure and so may cause vigorous deformations as a result.

Those appearances of catastrophic oxidation referring to the following four possibilities of attack have been best examined because of their frequent occurence in practice:

1. contact of low-melting oxides with the scale of the temperature-resistant material,
2. sediments of alkali-sulphates in the presence of SO_3 on iron-containing alloys,
3. sulphur attack,
4. carbon attack.

Amongst the low-melting oxides it is specifically the vanadium oxide V_2O_5 which shows itself already a melting point of only 715°C and eutectic mixtures of this oxide are known with a number of other oxides (37). For this reason it is one of the most aggressive constituents of heavy fuel oils, used, for instance, for gas turbines or heating of boilers. Up to the present no possibilities have yet been found to prevent effectively this type of chemical attack. Searching for suitable alloys, for improving inhibitors, and for protecting coatings has not been very successful.

Subject to similar heavy chemical attacks are heat-resistant steels which may be also in contact with combustion gases and are used, for instance, as basic material for superheater pipes in steam production plants. They are often subject to attack caused by alkali-sulphates which in presence of SO_3 may react with iron oxide according to the equation

$$Fe_2O_3 + 3\ K_2SO_4 + 3\ SO_3 = 2\ K_3Fe\ (SO_4)_3$$

forming complex sulphate-compounds (38). Substances of this type give accelerated corrosion at temperatures of about 600 up to 800°C (39). This critical temperature range reaches from the melting point of this compound, which can be lowered by K_2SO_4 depending on the SO_3-content of the furnace atmosphere to about 600°C, up to its decomposition temperature (40). Hence, also in this case it is the liquid phase which causes catastrophic effects increasing the diffusion rate and - as in other cases too - may possibly dissolve oxide scales. SO_3-formation is catalytically accelerated by iron oxide and flue ash (41). From Fig. 6 it can be seen that such attacks may be very severe. It shows the weight-losses of a Cb-stabilized CrNi-steel embedded in K_2SO_4 with and without an addition of Fe_2O_3, depending on the temperature (42). The annealing atmosphere has been an SO_3-containing mixture of air and water vapour of a dew point of 165°C. The corresponding results for not embedded specimens have also been recorded. Above 600°C the weight-loss increases vigorously in case of embedment whereas it decreases again at about 800°C. The reduced attack in case of embedment in K_2SO_4 and Fe_2O_3 is due to partial reaction of the SO_3 with the iron oxide of the embedding material, and therefore less SO_3 is available for reaction with the oxide layer.

Sulphur-attack on nickel-containing temperature-resistant alloys is mostly very severe. Mainly, if H_2S is present in the annealing atmospheres even in a small concentration, there will be heavy damages. Billington (43) reports of severe sulphur-attack on Nimonic 75 that arises from the contact with an insulating material containing only 0,04% S. The depth of local corrosion in a few hours at 800°C was more than 1 mm.

The reason for the low resistance of nickel-containing alloys to sulphur-containing environment is the formation of the eutectic phase Ni-Ni_3S_2 with a sulphide concentration of about 80 weight %. The melting point of this eutectic mixture is 645°C. Actually preferred formation of chromium sulphide ought to be expected as the standard free energy of the formation of CrS corresponding to

$$2\ Cr + 2\ H_2S = 2\ CrS + 2\ H_2$$

is given by $\Delta G^o = -76.660$ cal at 800°K (44) whereas Ni_3S_2 shows an analogous value of only -23.750 cal (45). There exists no unanimous view about the modification of the chromium sulphide produced, especially as CrS, the lowest sulphide, dissociates upon cooling at some as yet undefined temperature, but presumably below 1000°C, to Cr_7S_8 and chromium (46). Some other sulphides, especially Cr_2S_3 may also be stable. Their ΔG^o-values are unknown, but Seybolt supposes they would be less negative (less stable) than that of CrS. According to the different ΔG^o-values of the sulphides of nickel and chromium one must imagine the corrosion process as follows (43): The first sulphur diffusing into the metal would combine with the chromium at the surface and grain boundaries. As soon as chromium-depletion has reached locally a certain extent, nickel sulphide is produced and by that the catastrophic reaction will be started. Fig. 7 shows severe sulphur attack on a NiCr 80 20 heater-alloy. The widespread branching of the low-melting phase causes simultaneously intense brittleness of the material. The outer zones show the additional influence of the oxygen which is present in all annealing atmospheres converting the sulphides into oxides.

Finally, it is still to be mentioned that carbon lowers the melting point of alloys on the basis of nickel-chromium. If these temperature-resistant materials are used in controlled atmospheres carbon in contact with the metallic surface can diffuse into the alloy. Köster and Kabermann (47) have examined melting equilibria in the ternary system nickel-chromium-carbon and found several eutectic phases in the temperature range between 1045 and 1305°C. Hence, in this temperature range catastrophic reaction is possible. This does not apply to nickel-free, ferritic heat-resistant alloys, as, for instance, Fe-25%Cr-5%Al, which do not show any mentionable decrease of the melting point in the case of carbon-absorption. These alloys, on the contrary, are sensitive to nitrogen which mostly is a main component of controlled atmospheres. As there is only little oxygen present and correspondingly less protection by oxide layers is given, nitrogen can easily diffuse into the alloy. Due to the high nitrogen affinity of aluminum they react to form AlN within the bulk material and further formation of the Al_2O_3-layer at the surface is questionable at all.

The following possibility seems to be suitable to overcome the difficulties and ought to be examined as to its technical realization. Carbon attack is inevitable but that of nitrogen is not. Generally, controlled atmospheres are obteined by partial combustion of natural gas, propan, or similar gases, with air. By using a gas-oxygen combustion mixture instead of an air-containing one, a nitrogen-free gas would be obtained. Then the use of iron-chromium-aluminum alloys would be possible, especially as these alloys are also less sensitive to sulphur than the alloys containing nickel.

Finally, it is still to be mentioned another reaction which runs at an abnormal rate although it does not concern the formation of molten phases: the green rot oxidation. This one has been observed with alloys on the basis of nickel-chromium in gases of low oxygen content and is characterized by the inner oxidation of chromium exclusively. Especially furnace atmospheres alternating between carburizing and oxidizing may lead to this type of attack. The subsurface oxidation prevents the formation of an external oxide scale. The surface swells and cracks and the alloy becomes brittle and can be broken easily, showing a typical green fracture. Fig. 8 shows an Ni-20%Cr-alloy destroyed by green rot oxidation. The heterogenously composed and completely loosened outer layer being strongly ferromagnetic because of its high nickel content cannot give any essential protection against the proceeding attack.

The last years efforts have been made to develop alloys showing higher resistance to all attacks possible in controlled atmospheres, especially to nitrogen, carbon, sulphur, and green rot oxidation. For this purpose, there has been made use of experiences gathered by the US-Navy with nickel-chromium-cast alloys of high chromium contents used as tube support materials in oil fired marine boilers. The corrosion caused by fuel ashes has been diminished strongly with these alloys compared with all other alloys used so far. These experiences suggested the development of heater alloys with higher chromium-contents. Because of the miscibility gap in the Ni-Cr-alloy system the chromium-content has to be limited to about 30 weight % of chromium, thus assuring this alloy to be situated within the γ-region above 600°C up to its melting point. A final estimation of the quality of this alloy under

various conditions seems still premature. Anyhow, the advantage of the high chromium content has already become clear in some cases where this alloy has been used in controlled atmospheres. The alloy Ni-30%Cr shows, moreover, under normal working conditions, especially at high temperatures in air, a heat resistance being at least equivalent to that of the best classical nickel-chromium-heater alloys.

REFERENCES

1. P. Kofstad, High Temperature Oxidation of Metals, John Wiley & Sons, New York, 1966, p. 269
2. H. Pfeiffer and H. Thomas, Zunderfeste Legierungen, Springer-Verlag, Berlin, 1963, p. 55
3. C. Wagner and K. Grünewald, Z. phys. Chem. (B) 40 (1938) 455. - C. Wagner, J. electrochem. Soc. 99 (1952) 369; 103 (1956) 571; 103 (1956) 627; Z. Elektrochem. 63 (1959) 772. - F. Maak and C. Wagner, Werkstoffe und Korrosion 5 (1961) 273
4. I. I. Kornilov and I. I. Sidorishin, Comptes Rendus (Doklody) de l'Académie des Sciences de l'URSS 42 (1944). Volume XLII, Nr. 1, p. 20
5. ASTM Powder Diffraction File 1966, Philadelphia
6. H. Pfeiffer and G. Sommer, Z. Elektrochem. 66 (1962) 671
7. M. Pirani and K. Conrad, Z. techn. Physik 5 (1924) 266
8. E. Walther, Elektrowärme 17 (1959) 527
9. L. E. Price and G.J. Thomas, J. Inst. Met. 63 (1938) 21
10. O. Kubaschewski and B.E. Hopkins, Oxidation of Metals and Alloys, Butterworth, London, 1962, p. 24
11. K. Hauffe u. J. Block, Z. Physik. Chem. 198 (1951) 232
12. A.N. Seybolt, J. electrochem. Soc. 107 (1960) 147
13. K. Hauffe, Progress in Metal Physics 4 (1953) p. 89
14. G.C. Wood and D.P. Whittle, J. Iron Steel Inst. 202 (1964) 979
15. D.P. Whittle and G.C. Wood, J. electrochem. Soc. 115 (1968) 133
16. C.S. Tedmon, Jr., J. electrochem. Soc. 114 (1967) 788
17. D. Caplan and M. Cohen, J. electrochem. Soc. 112 (1965) 471
18. I.A. Menzies, Werkstoffe und Korrosion, 19 (1968) 1050
19. A. Davin, D. Coutsouradis, M. Urbain and L. Habraken, Industrie Chimique Belge 30 (1965) 340
20. S.R.J. Saunders and M.J. Pryor, J. electrochem. Soc. 115 (1968) 1037
21. J.H. Westbrook, Rev. Hautes Temper. et Refract., 3 (1966) 45
22. W. Betteridge, IV. Congrès International du Chauffage Industriel, Rep. 18, group 1, sect. 16, Paris 1952; Brit. J. appl. Physics 6 (1955) 301
23. H. Pfeiffer and H. Thomas, Zunderfeste Legierungen, Springer-Verlag, Berlin, 1963, p. 254
24. I. Pfeiffer, Z. Metallkde. 51 (1960) 322
25. I. Iitaka and S. Miyake, Nature 137 (1936) 457
26. K. Hauffe and K. Pschera, Z. anorg. allg. Chem. 262 (1950) 147; K. Hauffe, Oxidation of Metals, Plenum Press, New York, 1965, p. 184
27. E.A. Gulbransen and K.F. Andrew, J. electrochem. Soc. 106 (1959) 941
28. N. Birks and H. Rickert, J. Inst. Metals 91 (1962-63) 308
29. C.S. Tedmon, Jr., Corr. Sci. 7 (1967) 525
30. W.C. Hagel, Trans. ASM, 56 (1963) 583
31. E.B. Evans, Corrosion 21 (1965) 274
32. B. Lustman, Trans. AIME 188 (1950) 995
33. H. Pfeiffer, Werkstoffe und Korrosion, 8 (1957) 573
34. H.J. Engell and F. Wever, Acta Met. 5 (1957) 695
35. J.D. Mackenzie and C.E. Birchenall, Corrosion 13 (1957) 783; D.W. Juenker, R.A. Meussner and C.E. Birchenall, Corrosion 14 (1958) 57
36. W.C. Leslie and M.G. Fontana, Trans. Amer. Soc. Metals 41 (1949) 1213
37. G. Lucas, M. Weddle and A. Preece, J. Iron Steel Inst. 179 (1955) 342
38. R.C. Corey, B.J. Cross and W.T. Reid, Trans. Amer. Soc. mech. Eng. 67 (1945)289; R.C. Corey, H.A. Grabowski and B.J. Cross, Trans. Amer. Soc. mech. Eng. 71 (1949) 951
39. A. Rahmel, The Mechanism of Corrosion by Fuel Impurities, Butterworth, London, 1963, p. 556
40. A. Rahmel and W. Jäger, Z. anorg. allg. Chem. 303 (1960) 9
41. S.A. Goldberg, J.J. Gallagher u. A.A. Orning, J. Eng. Power 90 (1968) 193
42. A. Rahmel, Arch. Eisenhüttenw. 31 (1960) 59
43. S.R. Billington, Metallurgia, Jan. 1962, 3
44. J.P. Hager and J.F. Elliott, Trans. Met. Soc. AIME 239 (1967) 513
45. O. Kubaschewski, E.Ll. Evans and C.B. Alcock, Metallurgical Thermochemistry, Pergamon Press, London, New York, 1967
46. A.N. Seybolt, Trans. Met. Soc. AIME 242 (1968) 1955
47. W. Koster and S. Kabermann, Arch. Eisenhüttenw. 26 (1955) 627

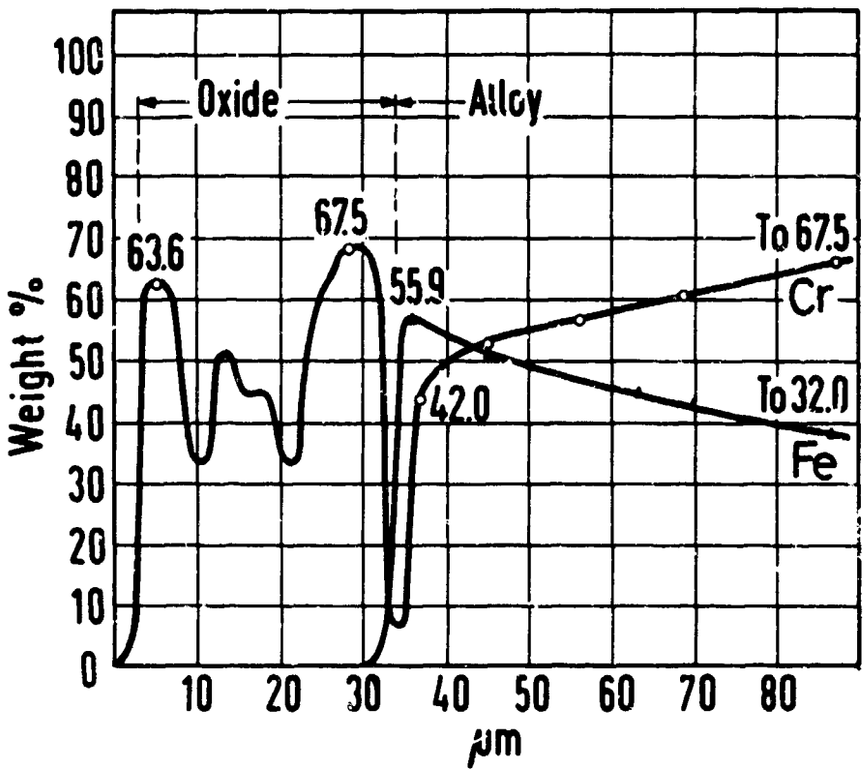
Oxide
Alloy
63.6
67.5
55.9
42.0
To 67.5
Cr
To 32.0
Fe
Weight %
µm

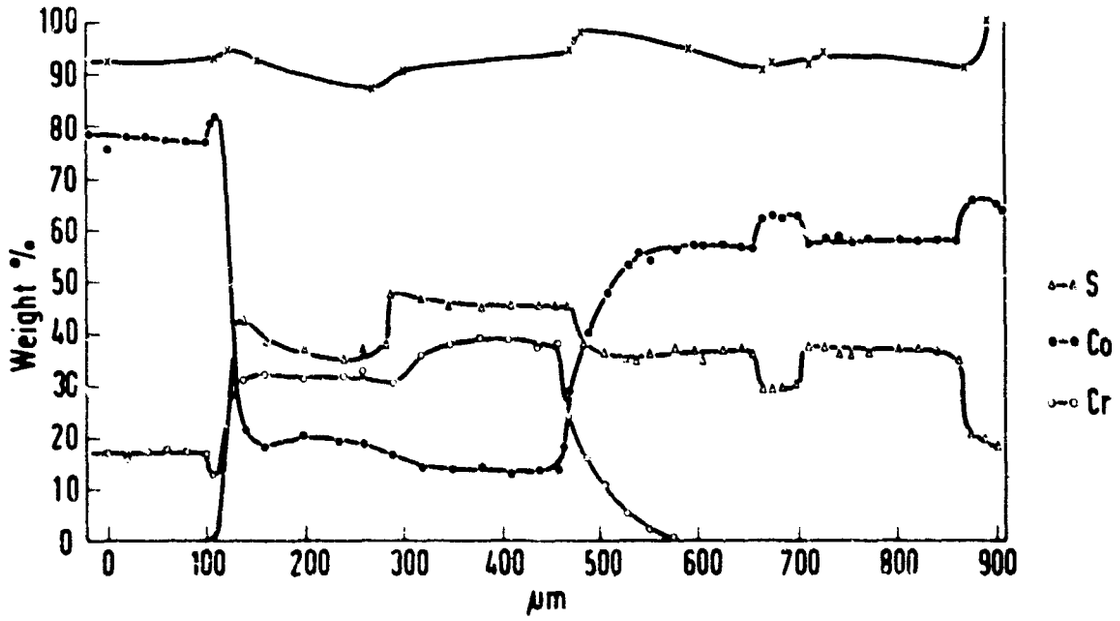
S
Co
Cr
Weight %
µm

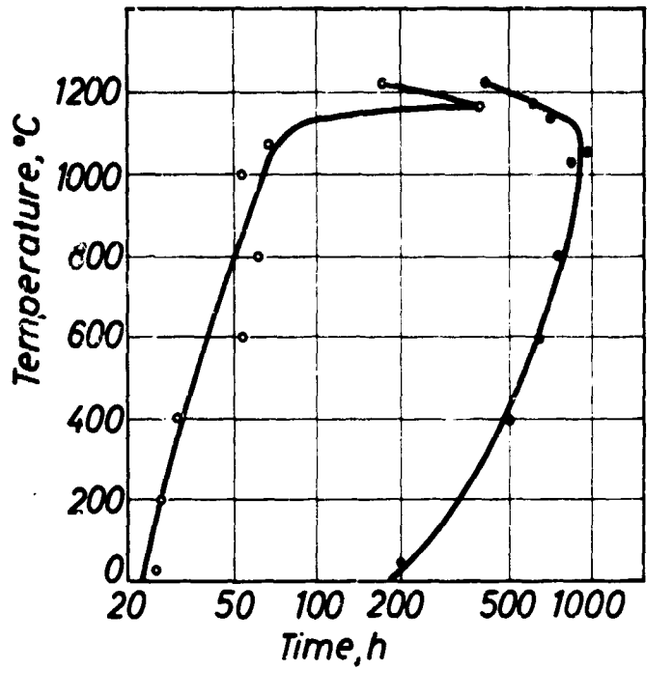

Curve	Additive element	Hours life in ASTM-test
•——•	Ce-Ca	606
○——○	none	37

Fig. 3 Dependence of lifetime upon the difference $T_{upper} - T_{lower}$

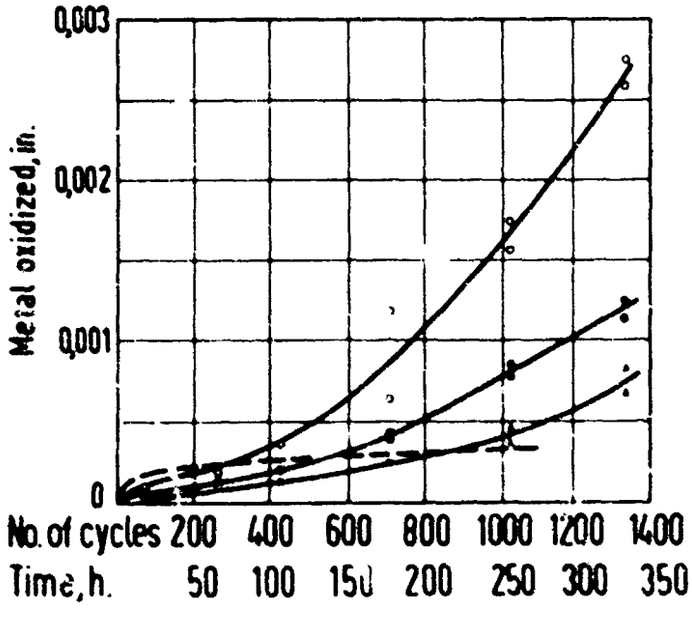

Sign	Additive element	Hours life in ASTM test
○	none	25
•	Zr-Co-Al	86
·	Zr-Co-Al-Si	175
----	Continuous oxidation, mean of all alloys.	

Fig. 4 Results of intermittent and cyclic oxidation tests at 1150°C (Eastman)

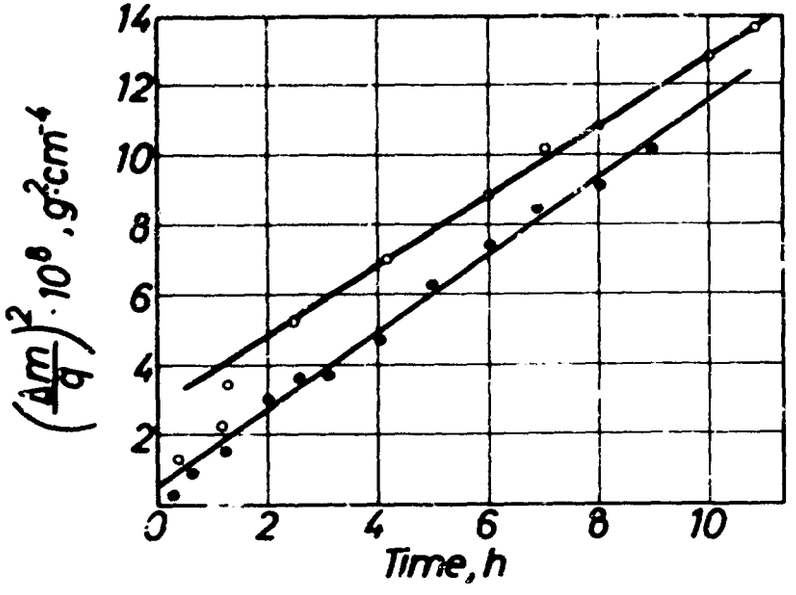

Fig. 5 Oxidation of FeCrAl in pure oxygen at 1100°C

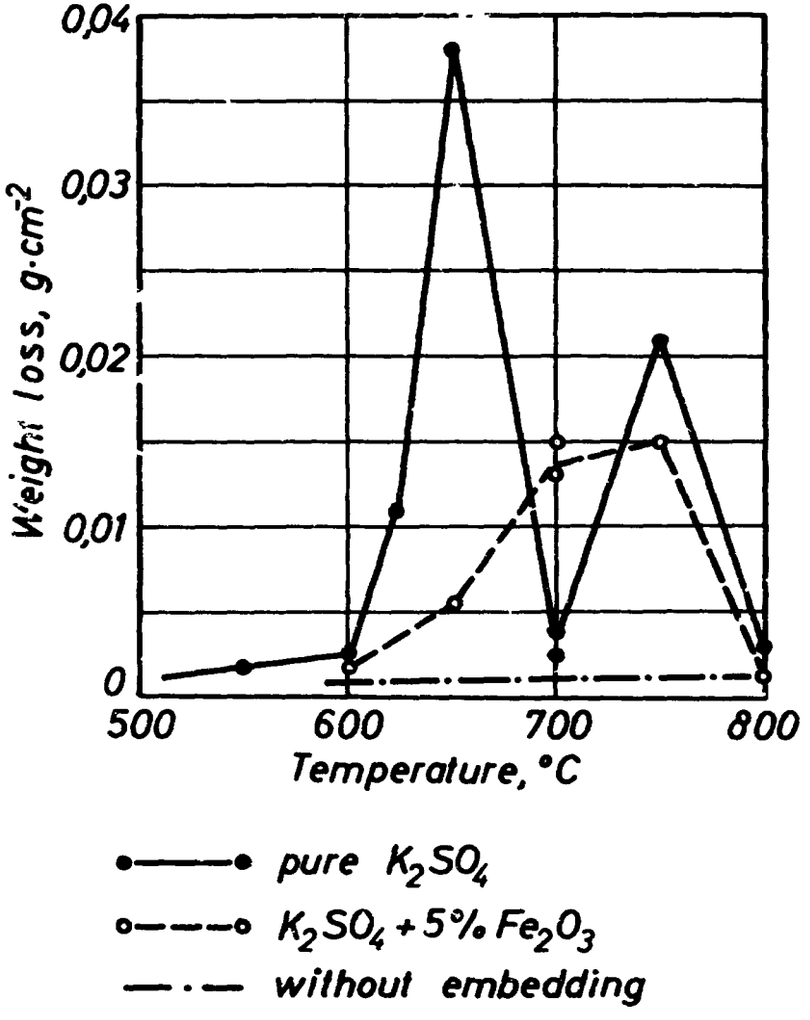

Fig. 6 Attack by K_2SO_4 with and without 5% Fe_2O_3 (Rahmel)

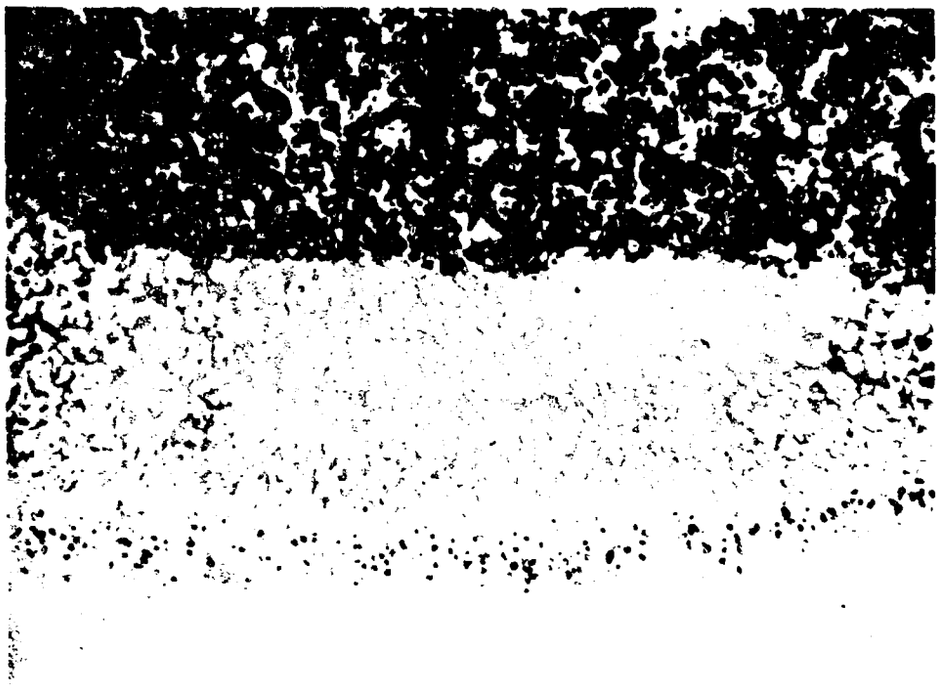

Fig.7 Ni-20% Cr-alloy, heavy attack by sulphur

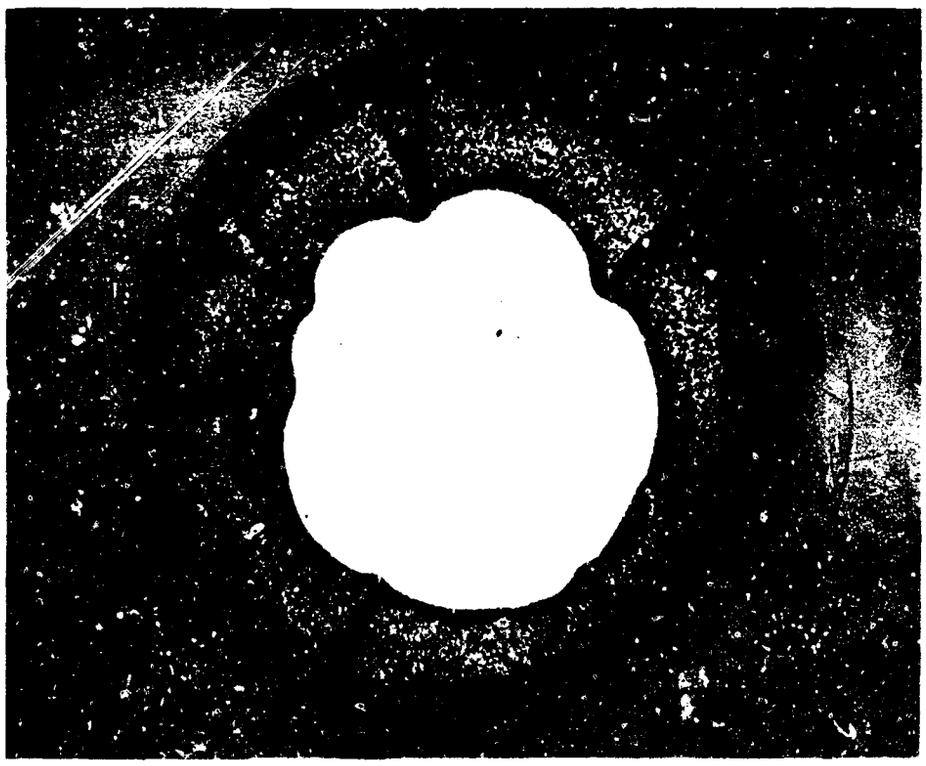

Fig.8 Ni-20% Cr-alloy, destroyed by green rot oxidation

MECHANICAL PROPERTIES
OF
SURFACE OXIDE FILMS
AND
THEIR EFFECT ON THE KINETICS
OF
OXIDE GROWTH

BY

Dr P. Hancock
Glasgow University

SUMMARY

A new technique for measuring the mechanical properties of growing oxide films, by observing the natural frequency of a freely suspended metal specimen, is described.

Values are given of the Young's modulus, adhesion and plasticity of oxides on Armco iron and 0.2% carbon steel, at temperatures from 570° to 800°C and on pure nickel, at temperatures from 800° to 1000°C.

Young's modulus values on iron decrease with increasing temperature from 27×10^6 lb in^{-2} at 570°C to 22×10^6 lb in^{-2} at 800°C. Adhesion values increase with increasing temperature and the value of plastic strain before failure increases from 2×10^{-4} at 500°C to 10×10^{-4} at 800°C.

The Young's modulus of growing nickel oxide scales varies from $46 - 60 \times 10^6$ to 30×10^6 lb in^{-2} over the temperature range 800 - 1000°C and its excellent adhesion is explained in terms of the mechanical properties.

The influence of mechanical properties on oxidation behaviour is demonstrated and the effects of specimen geometry and thermal shock on oxidation behaviour are discussed.

MOST WORK ON THE KINETICS OF OXIDATION of metals and alloys completely ignores the effect of the mechanical properties of the surface scale that is formed. However it has been demonstrated by several workers (1)(2)(3)(4) that internal stresses develop in the surface oxide film during growth and therefore subsequent growth kinetics will be largely dictated by the ability of the oxide to withstand these stresses without cracking or spalling.

Previously there was no way of measuring the mechanical properties of a surface oxide scale during growth at high temperatures but recently a method has been developed at Glasgow (5)(6) which enables this to be done. The method of measuring the mechanical properties of growing oxides is described and their effect on oxidation kinetics is demonstrated.

METHOD OF MEASURING MECHANICAL PROPERTIES OF SURFACE OXIDES AT HIGH TEMPERATURES.

The method used is based on measuring the change in frequency of the natural flexural vibration of a freely supported cylindrical specimen at the operating temperature, as the surface of the specimen becomes progressively oxidised.

Rayleigh (7) showed that the characteristic frequency of the first mode of vibration (fo) is related to the dimensions and Young's modulus (E_1) of the bar by the following equation.

$$fo^2 = \frac{(4.73)^4 E_1 a^4}{16\pi \ell^3 \, mo} \qquad \text{- - - - - - (1)}$$

where a, ℓ and mo are the radius length and mass of the rod before oxidation.

As the rod oxidises the frequency will change and at any time will be given by

$$f^2 = (4.73)^4 \left[E_1 c^4 + E_2 (b^4 - c^4)\right] \qquad \text{- - - - - - (2)}$$

where f is the characteristic frequency of the oxidised rod,
b is the outer radius of the oxidised bar,
c is the inner radius of the metal core and
E_2 is the Young's modulus of the oxide.

The change in dimensions of the specimen can be related to the mass gain due to oxidation by an equation of the form (5)

$$\frac{f^2 - fo^2}{fo^2} = \Delta\left[\frac{2\beta M_1}{M_2 - M_1} - \frac{M_2 + M_1}{M_2 - M_1}\right] \qquad \text{- - - - - - (3)}$$

where Δ is defined by $m = mo(1 + \Delta)$

$$\text{and } \beta = \frac{E_2 \rho_1 M_2}{E_1 \rho_2 M_1} \qquad \text{- - - - - - (4)}$$

where ρ_1 and M_1 are the density and atomic weight of the metal
ρ_2 and M_2 are the density and molecular weight of the oxide considered as MO_x

Equation (3) neglects higher order terms of Δ but the error involved by using this simplification is <2%. (5) This equation shows that the progress of oxidation can be followed by frequency measurements and, as flexural vibration is used, it is extremely sensitive to surface effects. The method has the advantage over gravimetric techniques that if cracking of the oxide does occur during growth then this will be shown as a sudden discontinuity in the frequency response.

The apparatus is shown diagrammatically in Figure 1, construction details and operation procedure have been recently described in detail elsewhere.(5) The specimens used are 0.2 inch diameter cylinders 6 inches long and must be accurately ground so that the variation in diameter is less than $\pm$ 0.0003 in. Measurements can be made at temperatures up to 1000°C and in any chosen atmosphere so that the influence of gaseous contamination could be readily investigated if required.

Detailed studies have been made of the oxidation of Armco iron (0.038%C, 0.009%S, 0.01%P, 0.075% Mn, Trace Ni.) and 0.2% carbon steel (0.196%C, 0.126%S, 0.052%P, 0.058% Mn, Trace Ni, 0.017%Cr). and the behaviour of these materials has been compared with that of pure nickel (Al<1, Ca<1, Cu3, Fe 20-30, Mg<1, Si2, Ag<1 ppm). Nickel was chosen as a comparative material because it is known to have a highly adherent oxide film.(8)

Measurements have been made on the vibration apparatus and compared with gravimetric measurements made on a conventional Stanton HT-D recording thermobalance.

OXIDES FORMED ON IRON AND NICKEL. The results of oxidation tests using the thermobalance are shown in Figure 2 for both Armco iron and 0.2% carbon steel. The usual

smooth oxidation curves are obtained with no evidence of discontinuities. However, results using the vibrational technique are shown in Figure 3 for Armco iron and Figure 4 for the 0.2% carbon steel, these demonstrate that the oxide film is cracking sporadically during growth as shown by the sudden discontinuities in the curves obtained. Measurements have been taken up to 200 hours exposure and this initial pattern of behaviour is found to continue throughout the period of oxidation.

Comparison tests, using nickel in the vibration apparatus at a temperature that would give similar values of Δ to those on iron, showed that the vibration curves were smooth and continuous, Figure 5, as obtained with the thermobalance technique and showed no evidence of the discontinuities observed with the iron specimens. This is in agreement with the observed behaviour of oxides on iron and nickel under these conditions. The oxide film on iron is friable and spalls easily whereas that of nickel is extremely adherent.

To explain the difference in behaviour of the oxides on iron and nickel it is necessary to examine the mechanical properties of the oxides formed.

YOUNG'S MODULUS OF THE OXIDES FORMED ON IRON AND NICKEL. Examination of equation (3) shows that if values of $(f^2 - fo^2)/fo^2$ are plotted against values of Δ, a linear relationship should be obtained and the gradient of the line will give a value of β and hence a value for the modulus of the surface oxide at any temperature. At each temperature, values of $(f^2 - fo^2)/fo^2$ can be obtained from frequency results and values of Δ, corresponding to the same exposure times, can be obtained from thermobalance results. The values will be inaccurate due to the oxide cracking when only a thin layer of oxide is present at short time exposure, but the inaccuracy decreases as the exposure time is increased, when the total frequency change due to the oxide layer is large compared to the instantaneous change due to individual cracking. The values obtained for Young's modulus are accurate to within $\pm$ 10% and are shown in Figure 6; (5) the modulus values decrease with increasing temperature from 27 x 10^6 lb in^{-2} at 570°C to 22 x 10^6 lb in^{-2} at 800°C and similar results are found for both Armco iron and 0.2% carbon steel.

Modulus values for nickel oxide have also been measured in this way (6) and are shown in Table 1 together with earlier values measured on bulk oxides by Menzies and Strafford.(9) The nickel results are not as accurate as the iron results because the number of experiments performed was much less and there is always some scatter when measuring oxide properties. The values obtained are higher than those of Menzies and Strafford but this is to be expected for in their samples, which were made by completely oxidising nickel specimens, appreciable voidage is present which would give lower values. However considering the different oxide forms tested the results are comparable.

TABLE 1 (6)

Values of Young's Modulus for Nickel Oxide

Temp °C	Modulus, lb in^{-2}	
	Present work	Menzies and Strafford (9)
700		25.4 - 35.4 x 10^6
800	40 - 60 x 10^6	
850		19.4 - 25.4 x 10^6
900	30 x 10^6	
1000	37 x 10^6	

ADHESION OF OXIDES. Measurements of the adhesive force between oxides and iron have been made by Gulyaev,(10) who recorded the force required to separate a plate and a cone attached by oxide and by Peters and Engell,(11) who determined the adhesion of surface oxides on steel by fluing the oxide to a solid base and measuring the force required to pull it off. Both these measurements require attachment of a pulling device to transmit the force to the oxide and hence the measurements are rather artificial.

But using the vibration technique it is possible to measure adhesion by subjecting the scale to thermal stresses by rapid cooling and noting the temperature drop which is just sufficient to cause cracking and loss of adhesion. This is possible because the technique is so sensitive to surface cracking.

The coefficient of thermal expansion of the metal is greater than that of the oxide and therefore during cooling the oxide is subjected to compressive stresses in both the hoop and longitudinal direction, but the circumferential stress can be shown to be the dominant stress (6) and the appearance of oxide ridges which run along the specimen after cooling confirms this observation.

Considering a cylinder of diameter 'c' with an oxide film of thickness δ, if the oxide is to remain in contact with the metal when the temperature drops by T°C then a radial inward force will be exerted on the oxide film. If the inward force is P per unit area of surface contact then, if contact is to be maintained (6)

$$P = \frac{E_s (\alpha_m - \alpha_o) T \delta}{c} \qquad \text{- - - - - - (5)}$$

where α_m and α_o are the coefficients of thermal expansion of the metal and oxide respectively.

The adherence A is the value of P at the temperature drop Ta that just produces cracking, therefore

$$A = \frac{E_s (\alpha_m - \alpha_o) Ta\ \delta}{c} \qquad \text{- - - - - - (6)}$$

Adhesion values were obtained with the vibration apparatus by measuring the frequency of an oxidising specimen after the initial large frequency change was completed and the frequency was only varying slightly due to the local oxide cracking, the temperature was then dropped a given amount by switching off the furnace. When it had dropped the required amount the furnace was switched on again and the specimen returned to the original test temperature whilst the frequency change was noted. If there was little or no change the procedure was repeated with a larger temperature drop until the subsequent frequency response showed that appreciable failure of the oxide had occurred, as shown in Figure 7 (6) when drops of 50°, 100°, 175° and 250°C had little effect but a drop of 325° caused appreciable damage. In this way the adhesion values at any temperature could be bracketed using the values of Young's modulus of the oxides obtained in the previous section and values of coefficients of expansion of iron and iron oxides given by Tylecote(12) (Fe - 12.2 x 10^{-6} and FeO - 15.3 x 10^{-6} deg C^{-1}). The value for FeO has been taken because the film formed during oxidation consists mainly of FeO in the temperature range considered.

The results of the adhesion tests for both Armco iron and 0.2% carbon steel are given in Figure 8 which shows that the oxide adhesion increased as the testing temperature increased. The reasons for the increased adhesion at high temperatures is closely linked with the plasticity of the oxide scale, which is discussed in the following section.

The adhesion values of nickel oxide proved to be impossible to bracket, because appreciable scale damage could not be produced even on cooling from the test temperature down to 20°C and the reasons for the excellent adhesion of nickel oxide is discussed in the following section.

PLASTICITY OF SURFACE OXIDE SCALES. During cooling of an oxidised specimen the total oxide strain 'ϵ_{ox}' after a drop of T°C is given by

$$\epsilon_{ox} = (\alpha_m - \alpha_o) T \qquad \text{- - - - - - (7)}$$

The value of oxide strain for each temperature drop made during the adhesion tests has been measured and in Figure 9 (6) it is plotted against the original test temperature. The temperature drop to produce this strain is given by the scale at the right hand side of Figure 9.

Tylecote (12) has measured the ultimate tensile strength of wüstite at various temperatures and he found no measurable elongation. Therefore using his results and the values of oxide modulus measured by the vibration technique, given in Figure 6, values of the elastic strains to the ultimate at each temperature can be measured and these are also shown in Figure 9. But as the two curves in Figure 9 do not overlap, this means that in the thermal shock tests some plastic strain was present in the oxide even when oxide fracture did not occur. However the amount of available plastic strain before fracture and loss of adhesion occurs at any temperature, given by the separation of the two curves in Figure 9, is very small and lies between 1→2 x 10^{-4} at 500°C and 7→10 x 10^{-4} at 800°C. Therefore at temperatures of 500°C a temperature drop of 100°C will exceed the plastic availability in the oxide and failure will result whereas at 800°C a temperature drop of 300°C is required before plastic flow can no longer accommodate the imposed strains and failure ensues. Similar results for nickel are shown in Figure 10, taken from reference 6. However the coefficients of expansion (12) of nickel (17.6 x 10^{-6} deg C^{-1}) and nickel oxide (17.1 x 10^{-6} deg C^{-1}) are very similar and therefore the oxide strains produced on cooling are smaller than with iron. In fact Figure 10 shows that at temperatures below 900°C, the oxide strain on cooling to room temperature can be accommodated by <u>elastic</u> deformation of the oxide and at higher temperatures there is only a very small amount of plastic deformation required for compatibility and this can be easily accommodated by the oxide, for nickel oxide has been shown to deform plastically at temperatures above 700°C(13).

THE EFFECT OF MECHANICAL PROPERTIES ON OXIDATION KINETICS

The effect of the mechanical properties of the oxide scales on oxidation kinetics are usually ignored, mainly because the mechanical data does not exist, however the work

described in Section 2 shows that the difference in the type of oxidation behaviour between nickel and iron can be largely accounted for in terms of the mechanical properties of the oxides formed.

When nickel oxidises it has been shown that the surface scale grows without appreciable cracking and therefore kinetic studies using conventional diffusion data should not be appreciably in error due to oxide cracking.

Results on iron show that the oxide film cracks continually during growth and, under these circumstances, kinetic studies will be governed by mechanical considerations. However the specimens used were cylindrical in shape and it is known that the effect of specimen geometry has a marked influence on the oxidation kinetics of iron. Juenker, Meussner and Birchenall (13) showed that cylindrical specimens produced voided oxides with loss of adhesion at the metal:oxide interface; whereas flat specimens produced a much more coherent scale. These effects were attributed to stresses in the oxide but the stresses could not be measured. However with the values of oxide strain to fracture given in Section 2 it is now possible to explain and predict the effects of specimen geometry.

When flat specimens of iron are used (14)(15) the oxide scales are adherent and consist of an inner layer of FeO, an intermediate layer of Fe_3O_4 and a thin outer layer of Fe_2O_3. The oxides present are in the ratio 95% FeO, 5% Fe_3O_4 and 1% Fe_2O_3. However with cylindrical specimens, over the same temperature range, non adherent oxides are formed, the local scale composition depends upon whether or not it is in contact with the underlying metal, but the average scale composition (16) is 34% FeO, 65% Fe_3O_4, 1% Fe_2O_3 which is very different from that observed with flat specimens. In the FeO and Fe_2O_3 layers, which constitute the major part of the oxide scale on both type of specimen, Hauffe (17) has shown that these scales grow by outward diffusion of iron ions. On flat specimens this means that there will be little internal stress generated during growth. On cylindrical specimens however the metal core will be reduced as the specimen oxidises and, if the oxide is to remain adherent, it must deform. Section 2 showed that if the oxide was subjected to strains greater than 2×10^{-4} at 500°C and 10×10^{-4} at 800°C then failure and loss of adhesion occurs. This means that at 500°C, on a specimen of 0.2 in. diameter, failure will occur when the metal diameter is reduced by $0.2 \times 2 \times 10^{-4} = 4 \times 10^{-5}$ in. and at 800°C when the diameter reduces by $0.2 \times 10 \times 10^{-4} = 2 \times 10^{-4}$ in. It can easily be calculated from gravimetric measurements or shown from microscopical observation (16) that such reductions in diameter occur after short term exposure at either temperature and therefore in 0.2 in. diameter specimens cracking and loss of adhesion occur throughout the exposure time as can be clearly seen in Figure 11. Thus the mechanical properties of the oxide and the geometry of the specimen will largely control both the rate of oxidation and chemical composition of the scale produced.(16) The marked lack of adhesion in the cylindrical specimens shown in Figure 11 appreciably reduces the effective rate of transport of metal ions through the oxide scale and accounts for the fact that, in spite of local oxide cracking, the rate of scale growth is slower than the familiar parabolic behaviour.

These results demonstrate that for a thorough understanding of the oxidation behaviour the mechanical properties are of equal importance to kinetic transport studies and, under cyclic oxidation conditions or contaminated atmosphere, where spalling and lack of adhesion invariably occur (18) the mechanical properties should probably be the primary consideration.

REFERENCES

1. P.D. Dankov and I.R. Churaev, Doklady Akad. Nauk. S.S.S.R., 1950, v73, 1221.
2. R.F. Tylecote, Mem. Sci., Rev. Met., 1965, v62, 241.
3. W. Jaenicke, S. Leistikow, and A. Stadler, J. Electrochem. Soc., 1964, v111, 1031.
4. B. Boric, C.J. Sparks, and J.V. Cathcart, Acta Met., 1962, v10, 691.
5. D. Bruce and P. Hancock, J. Inst. Metals, 1969 v97, 140.
6. D. Bruce and P. Hancock, Paper 2, J. Inst Metals. 1969 v97, 148.
7. Lord Rayleigh, "Theory of Sound", 2nd Ed., Vol.1. 1894-96; London (Macmillan) reprinted 1945; New York (Dover Publications).
8. P. Hancock and R. Fletcher, Metallurgia, 1966, v6, 1.
9. I.A. Menzies and K.R. Strafford, J. Materials Sci., 1967, v2, 559.
10. V.I. Kulyaev, Zavod. Lab., 1958, v24, (10), 1275.
11. F.K. Peters and J.H. Engell, Arch. Eisenhuttenwesen, 1959, v30, 275.
12. R.F. Tylecote, J. Iron Steel Inst., 1960, 196, p 135.
13. D.W. Juenker, R.A. Meussner, and J.E. Birchenall, Corrosion, 1958, v14, 57.
14. M.H. Davies, M.T. Simnad, and C.E. Birchenall, J. Metals, 1951; v3, 889 and 1953, v5, 1250.
15. J. Paidassi, Acta Met., 1958, v6, 184.
16. P. Hancock and D. Bruce. To be published.
17. K. Hauffe. 'Oxidation of Metals', p.280, 1965, New York, Plenium Press.
18. P. Hancock, 'Corrosion of Alloys at High Temperatures in Atmospheres Consisting of Fuel Combustion Products and Associated Impurities'. H.M.S.O., London 1968.

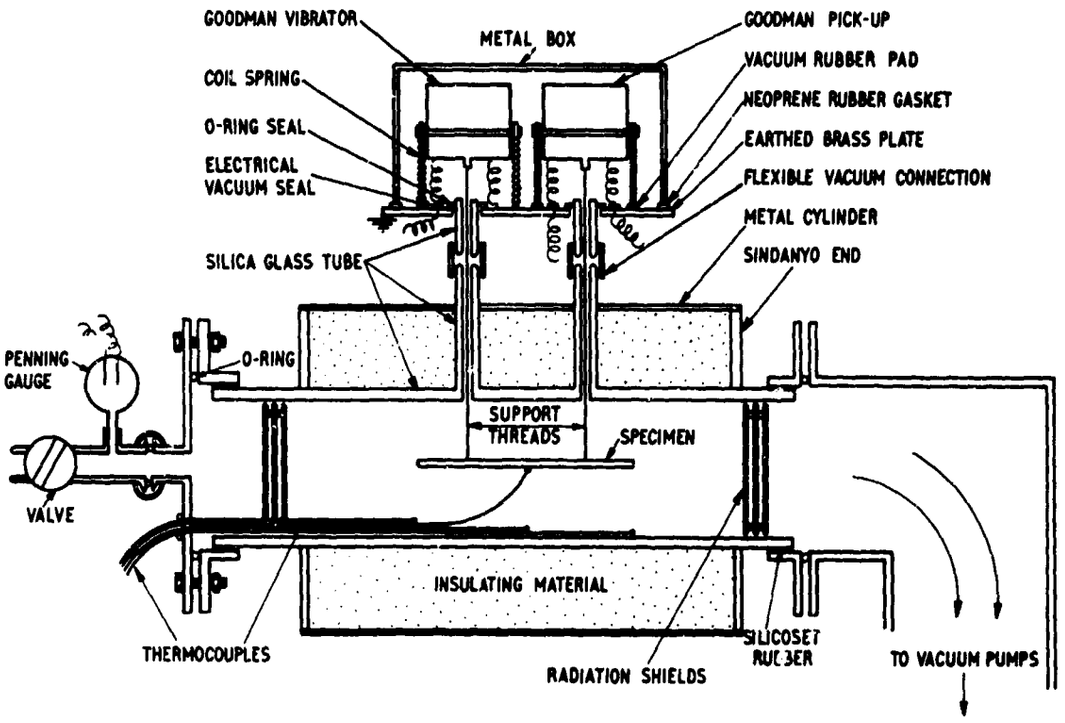

Fig. 1. Diagram of vibration apparatus. (from Ref.5)

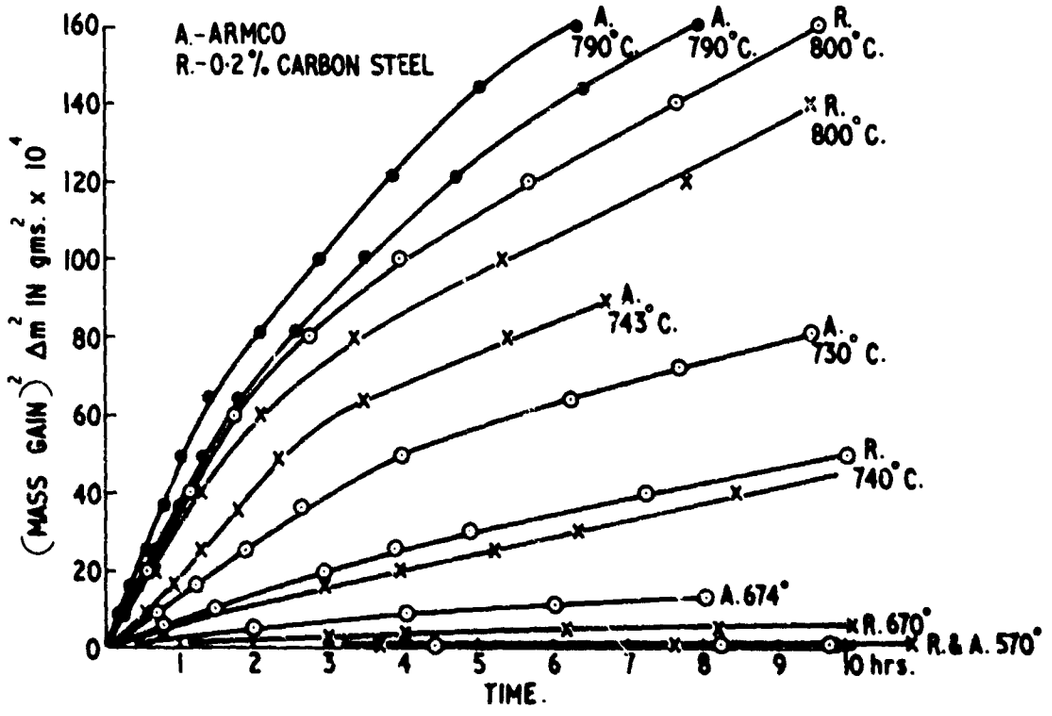

Fig. 2. Mass gain squared vs. time curves for oxidising Armco iron (A) and 0.2% carbon steel (R), measured on a thermobalance at temperatures from 570°C to 800°C (from Ref.6)

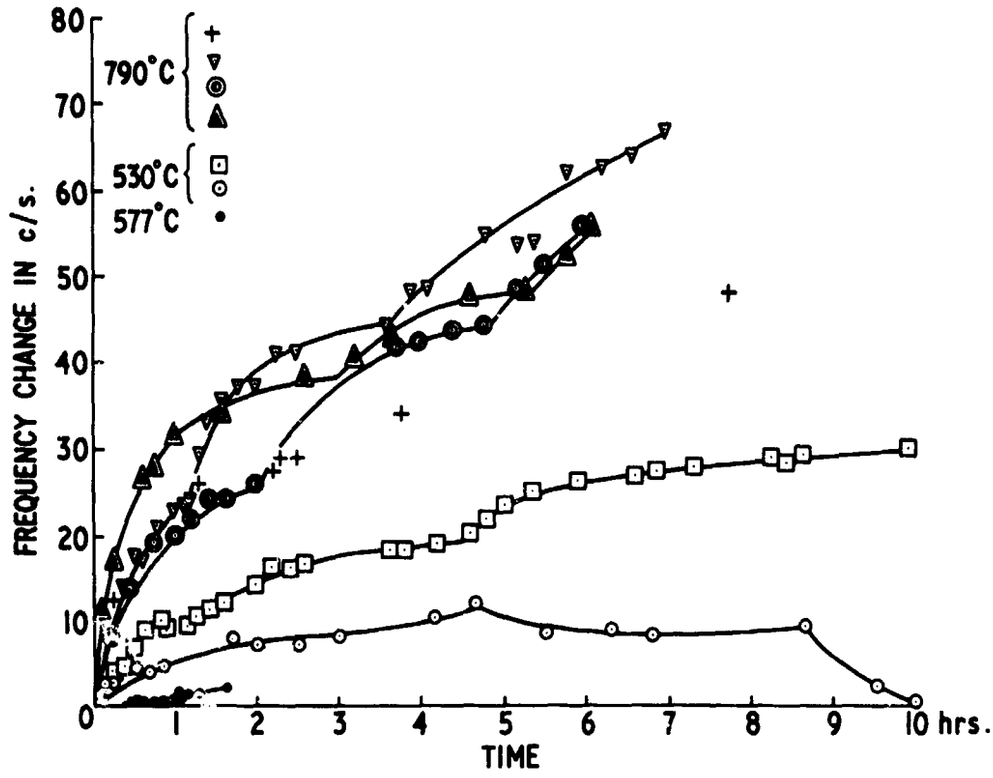

Fig. 3. Frequency change on oxidising Armco iron specimens. (after Ref.5)

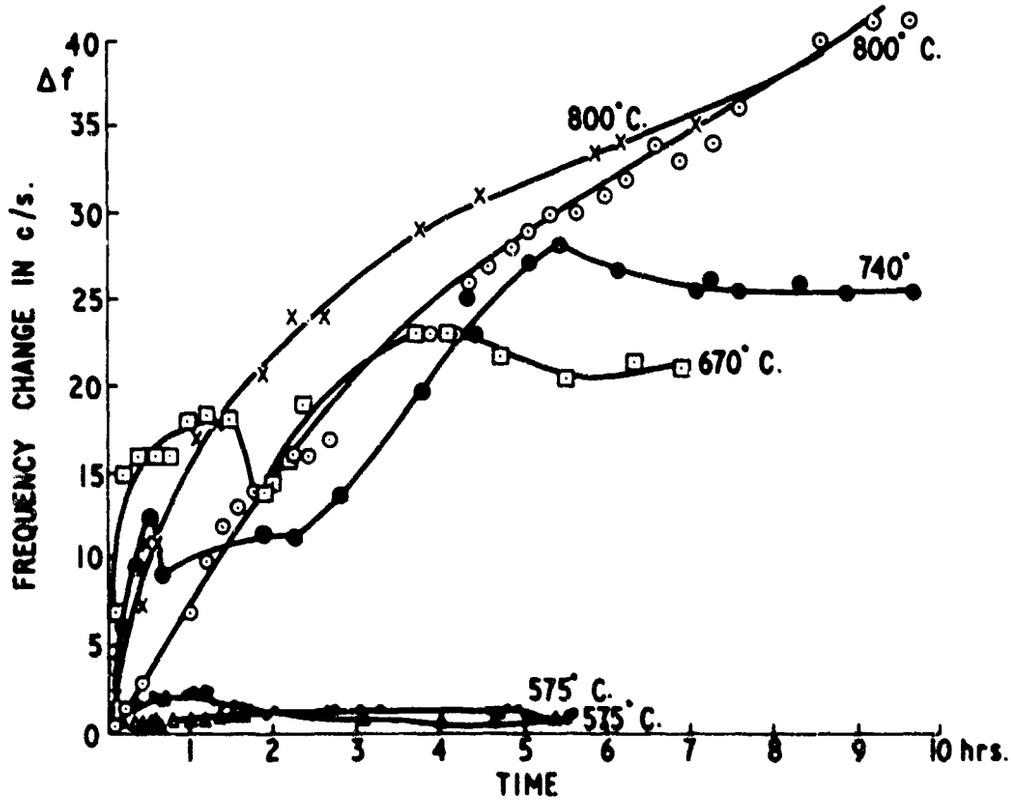

Fig. 4. Frequency change of 0.2% carbon steel specimens during oxidation at temperatures from 750° to 800° C. (from Ref.6)

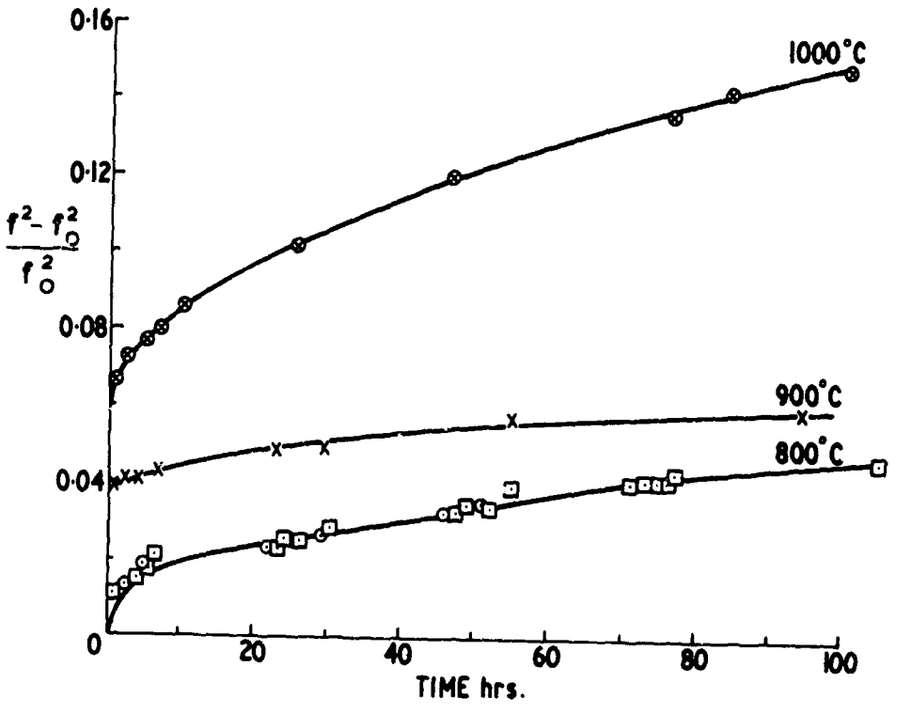

Fig. 5. Frequency change of nickel specimens during oxidation at temperatures from 800 to 1000°C (from Ref.6)

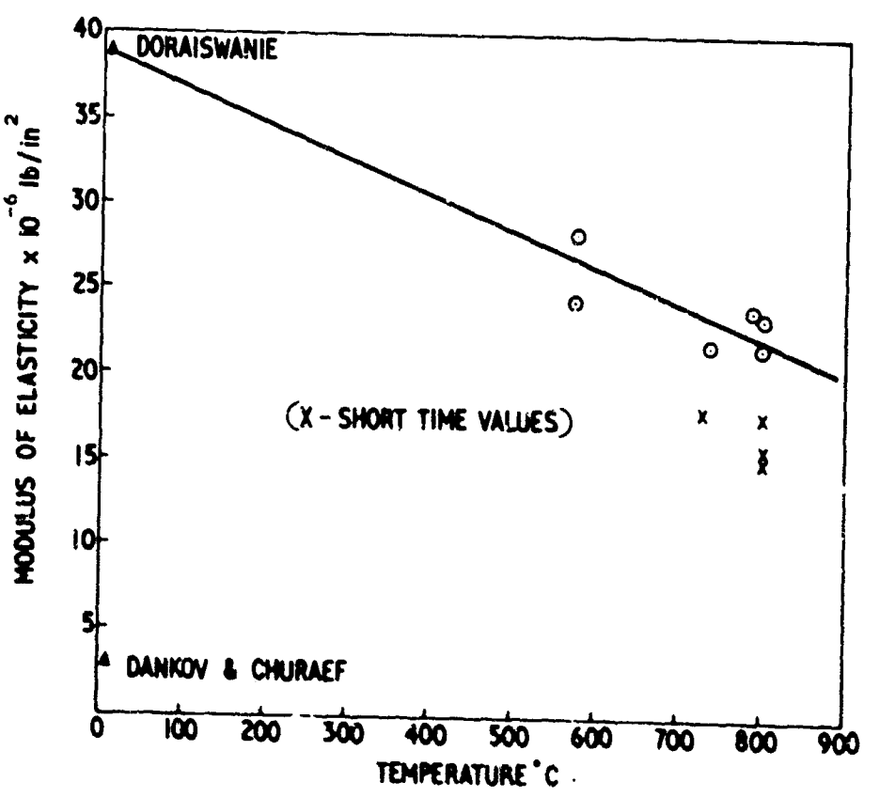

Fig. 6. Young's modulus of surface oxide scales on [illegible] vs. temperature. (from Ref.

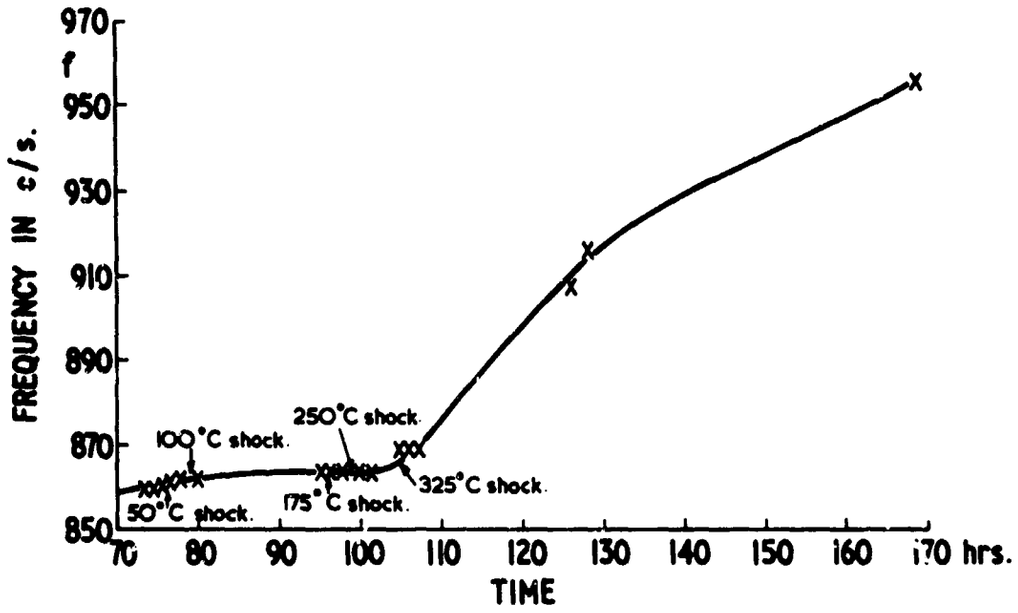

Fig. 7. Effect of various thermal shocks on the vibration response of 0.2% carbon steel at 800°C. (from Ref.6)

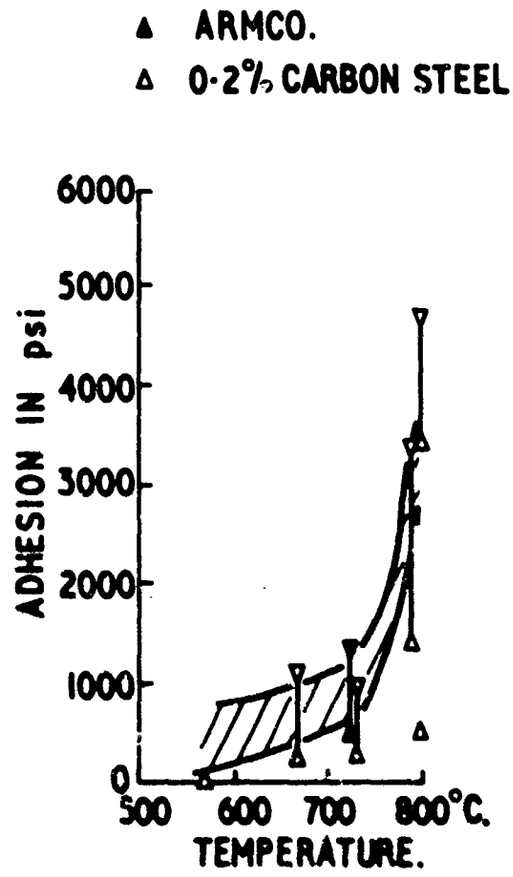

Fig. 8. Adhesion of oxides on Armco iron and 0.2% carbon steel, measured by the vibration apparatus. (after Ref.6)

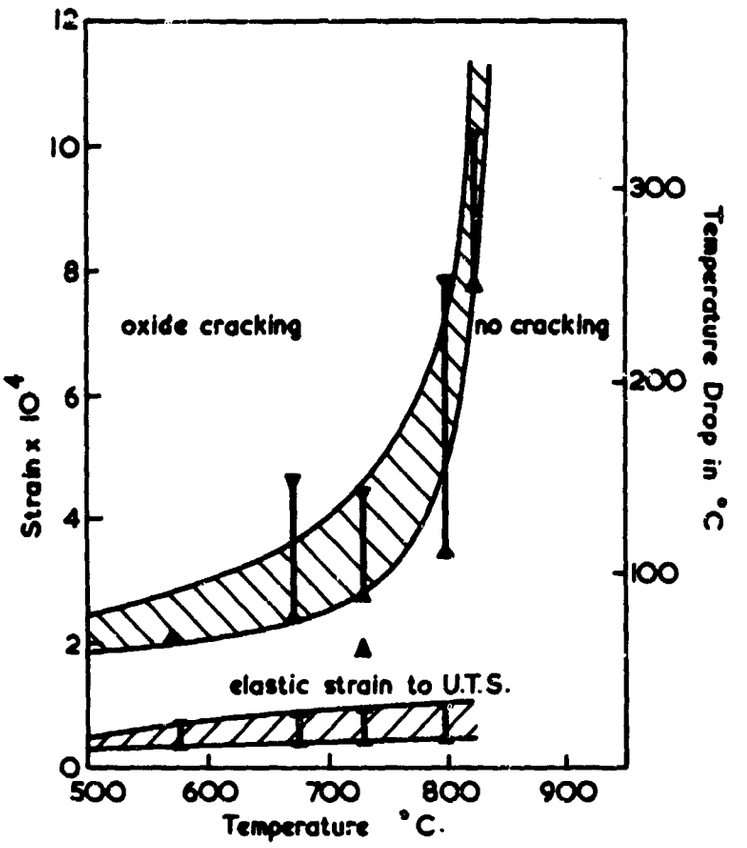

Fig. 9. Oxide strains involved during thermal shock of growing oxide scales. The right hand scale gives the temperature drop to produce cracking at each test temperature. Values of the elastic strains of the oxide at its ultimate tensile strength are also included. (from Ref.6)

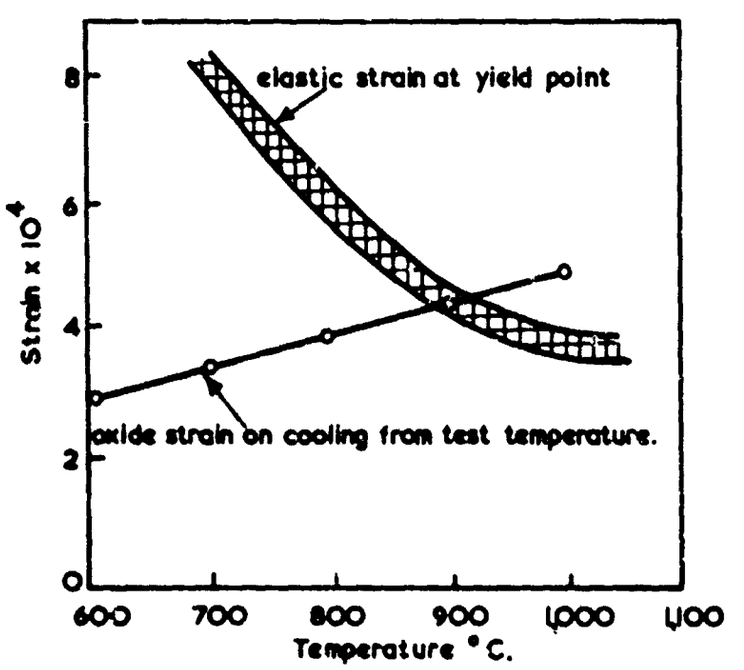

Fig. 10. Strains produced by cooling oxide scales on nickel to room temperature from various test temperatures, compared with the elastic strain of nickel oxide at its yeild point (from Ref.6)

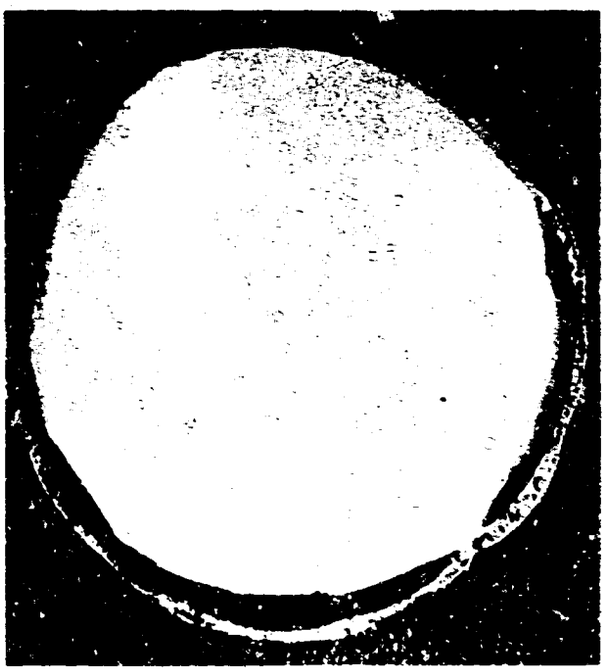

Fig. 11. Section of Armco iron specimen oxidised at 790°C.

REACTION BETWEEN SOLIDS AND GASES IN RADIATION FIELDS

by

J. M HUTCHEON

United Kingdom Atomic Energy Authority
Reactor Materials Laboratory
Culcheth, Lancs., England

SUMMARY

The paper reviews the effects of reactor radiation on corrosion.

In particular it discusses in some detail the reaction between CO_2 and graphite under irradiation where the main effects arise from gamma irradiation of the gas. The effects on corrosion rate of dose rate, pressure, temperature, gaseous additives and modifications to the graphite pore structure are described and contrasted, where relevant, with the corresponding effects in the absence of irradiation. Differences are also noted between the thermal and radiolytic processes in regard to the changes in pore structure and mechanical properties derived from corrosion to the same weight loss.

A short section is devoted to the changes in the (out-of-pile) reactivity of graphite towards air resulting from pre-irradiation of the graphite by fast neutrons and the effects are compared with other effects of fast neutron damage to graphite.

Finally, the paper examines briefly the current state of knowledge concerning the effects of irradiation in the corrosion rate of zirconium alloys in steam or water and related phenomena. It concludes that the effects arise from the production of interstitial oxygen atoms in the zirconium oxide scale but that the explanation of their enhanced mobility is not yet available.

SYMBOLS

D	Diffusion Coefficient
h	Planck's Constant
K	Equilibrium Constant
K', K''	Constants
l	Distance Through Scale
$\dot{n}$	Flux of Atoms
P_{O_2}	Partial Pressure of Oxygen
ϵ	Electron
Δ (O^{2-})	Interstitial Oxygen Ion
$\square$	Vacancy

IT IS TO BE EXPECTED that gas-solid corrosion reactions will be considerably modified in irradiation fields. This paper discusses results obtained from technological studies relating to three examples which have occurred in the development of important nuclear reactor systems. The first concerns the reaction between carbon dioxide and graphite in an irradiation field where the main effect is the modification of the carbon dioxide by γ-radiation; this has been an important problem in the development of the Advanced Gas-cooled Reactor. The second concerns the enhanced chemical reactivity of graphite towards air resulting from neutron damage to the graphite; this is not a normal operational problem for current reactor types, but was very relevant to the early air-cooled graphite moderated reactor, and has to be taken account of in safety studies for any graphite moderated reactor if an air leak into the system can be postulated. The third concerns the corrosion of the zirconium in an aqueous environment, and is relevant to most types of water moderated and cooled reactor, since these use zirconium alloys either as fuel cladding materials or as pressure tubes, or both. The paper suggests that the role of irradiation here is to change the defect structure of the oxide scale on the zirconium, and thus to modify transport processes through this scale.

THE CO_2 GRAPHITE REACTION

In a reactor moderated by graphite and cooled by carbon dioxide the radiation is of mixed type. As far as the gas is concerned the extent of absorption of energy from neutrons and gamma rays is relatively small and the great bulk of the radiation damage to the coolant arises from secondary electrons. It is a point of experimental demonstration that the gas which is significant to the radiolytic reaction between CO_2 and graphite is, almost entirely, gas contained within the pore of the graphite and not the gas contained in the free space in fuel element channels, for example. In this regard the reaction is analogous to the low temperature chemically-limited regime of the thermal reaction between CO_2 and graphite rather than to the high temperature diffusion controlled regime, as indeed would be expected from comparison of the numerical values of the rates of reactions under practical conditions. In normal commercial graphites the open pores make up about 10-20% of the total volume. The diameters of these pores have a fairly wide distribution but commonly show a peak in the neighbourhood of 5-10 microns. Under these conditions the pores can be regarded as Bragg-Gray cavities (1). Since the electron densities of CO_2 and graphite are identical the secondary electron flux to the CO_2 can be calculated directly from the dose to the graphite, which can be measured calorimetrically.

RADIATION STABILITY OF CO_2 - High yields of CO are obtained by the irradiation of CO_2 in the presence of small amounts of oxygen acceptors. Even in the absence of these vacuum ultraviolet radiation leads to the production of CO with a yield dependent on rate of gas flow (2). It therefore seems likely that the apparent stability shown in some experiments arises from a rapid recombination of the primary radiolytic products. Analysis of likely reactions in terms of their energy requirements (3) indicates that a number of processes leading to the formation of CO and oxygen atoms are possible with minimum energy requirements of 5.5 eV. Excited CO_2 molecules, which may be an intermediate step in the dissociation of CO_2, require smaller energies. The available experimental evidence does not distinguish between the two possibilities of excited molecules and oxygen atoms as the active oxidising species produced. But it is clear that in the presence of a gamma field the CO_2 is transformed to produce some species very much more reactive towards graphite than the normal CO_2 molecule, and that this species dominates the reaction between CO_2 and graphite under irradiation. This is demonstrated in the following sections where the effects of temperature, pressure, dose rate, type of graphite, and gaseous inhibitor upon the reaction are presented and contrasted with those where appropriate for the thermal CO_2 graphite reaction.

EFFECT OF TEMPERATURE - It is well established from many earlier experiments that the thermal reaction between CO_2 and graphite occurs in two parts. Initially a surface oxide is formed on the graphite with no removal of carbon atoms from the matrix, Eq (1). Subsequently the surface oxide is disengaged from the matrix bringing with it carbon atoms as CO, Eq (2).

$$RC- + CO_2 \rightleftarrows RC(O) + CO \qquad \ldots\ldots (1)$$

$$RC(O) \longrightarrow R- + CO \qquad \ldots\ldots (2)$$

RC- and R- represent graphite surfaces with three valency sites.

The second stage of carbon removal only comes into play at temperatures above about 600°C, where the equilibrium constant of reaction (1) permits a sufficient number of occupied sites to exist. The activation energy of the gasification reaction is 59 K cal/mol. (4). By contrast the radiolytic reaction proceeds, for realistic dose rates, at a measurable rate at room temperature, and this rate is almost independent of temperature between 200°C and 550°C as indicated in Fig. 1.

EFFECT OF DOSE RATE AND PRESSURE - We can regard the primary step as a bi-molecular reaction

$$h\nu + CO_2 \longrightarrow CO_2^* \qquad \ldots\ldots (3)$$

where CO_2^* represents the active species first produced. We would therefore expect the rate of production of the active species to be proportional to dose rate and, for a given graphite, to gas pressure. Figures 2(a) and 2(b) taken from Reference (5) shows the rate of loss of carbon plotted against dose rate, and pressure respectively, the results being obtained from experiments carried out in a materials test reactor. If it is assumed that the rate of carbon removal is proportional to the rate of production of active species then these data follow the expected form. In regard to dose rate, there is obviously no comparison with the thermal reaction; in regard to pressure, the

direct proportionality in the radiation dose is to be compared (4) with the lack of dependence of rate of the thermal reaction on total pressure.

DEPENDENCE ON GRAPHITE PORE STRUCTURE - Technical carbons and graphites vary very widely in their physical and chemical properties, and it is customary to analyse such variation, impurity effects being excluded, into two classes related to crystallographic and pore structure parameters respectively. Thermal reaction rates towards CO_2 for different types of carbon are therefore correlated through a specific reaction rate constant which allows for surface area differences between the materials, always provided that the reaction is taking place in the chemically-controlled regime (temperature up to about 1,000°C). At higher temperatures the thermal reaction becomes diffusion limited, and the rate is therefore dependent only on the external surface and not on the internal pore surface.

By contrast, a set of measurements carried out in pile, at 350°C and 200 p.s.i. pressure, with a wide range of graphites, showed no correlation whatever with surface area, despite the fact that the weight loss rate per unit dose varied almost over an order of magnitude. Of several pore structure parameters which were investigated, the only one which gave a useful correlation of the data was the simplest, namely the open porosity of the graphite derived from density measurements in mercury and helium. Results are shown in Fig. 3, taken from Ref. (6), which indicates a good linear correlation.

With the same assumption as before, namely that the number of carbon atoms removed is proportional to, if not equal to, the number of active species produced, this again is the result expected from Eq (3) above. The effective concentration of CO_2 will be the mass of CO_2 in the pores of the graphite per unit mass of graphite, i.e. for a given temperature it is the product of pressure and pore volume per unit mass of graphite.

The insensitiveness of radiolytic corrosion rate to graphite surface area follows from the absence of thermodynamic equilibrium in the gas phase. The excited molecules can lose their excess energy by collision with a graphite surface but cannot recover it by further collisions. Hence, an excited CO_2 molecule having once collided with the graphite surface has then lost its energy; on a further collision it is no longer excited and therefore no longer capable of reaction. Reaction rate is therefore not dependent on the number of collisions per unit time and therefore not dependent on graphite surface area. It is dictated instead by the rate of supply of active species, i.e. by the product of flux and mass of gas in the pores, as experimentally found.

DEACTIVATION OF EXCITED SPECIES - It has been already noted that the theoretical picture enunciated makes predictions about the rate of production of active species from CO_2, whereas the experimental data recorded refers to the rate of removal of carbon from the solid, so that the agreement between experiment and prediction implies a direct relationship between these two quantities. This in turn implies that any other processes for de-activation of the CO_2 molecules must either be absent or must remove a constant proportion of the active species under the experimental conditions examined. It would be expected that some de-activation should occur by gas phase collisions. If the active species is an excited CO_2 molecule then the appropriate equation can be written as

$$CO_2^* + CO_2 \longrightarrow 2CO_2 \qquad \ldots\ldots (4)$$

If, on the other hand, the active species is an oxygen atom, then the de-activation process can be written as

$$O + CO + M \longrightarrow CO_2 + M \qquad \ldots\ldots (5)$$

In this equation M is a CO_2 molecule; the binary reaction between an oxygen atom and a CO molecule to produce CO_2 is energetically unlikely and a third body is required to dissipate the energy released.

In fact the agreement illustrated by Fig. 3 must be regarded as somewhat fortuitous. It arises because in the graphites examined the range of the active species, i.e. the average distance which this species will travel, before it has lost its energy by gas phase collisions, is greater than the effective radius of the pores in the graphite studied. Hence, in these materials the contribution of de-activation reactions such as those indicated in Eq (4) and (5) is negligible, and it may be assumed that all the active species produced by the radiation are removed by reaction with the graphite.

We should therefore expect to find this simple relationship to break down in experiments in which pore diameters are significantly larger than this range. Labaton et al. (7) have described such experiments in which the large pores were obtained by two different methods. In the first procedure the manufacturing route for the graphite was selected in order to produce pores with diameters up to 25 microns, and in the second procedure a standard graphite (mean pore diameter about 5 microns) was oxidised radiolytically up to a maximum weight loss of about 28%. Fig. 4(a) shows the experimental results for mean oxidation rate plotted as a function of open pore volume, assuming that the total accessible pore volume was operative, while Fig. 4(b) shows a similar plot where the measured open pore volume has been corrected on the assumption that only pores in the size range 0.1 to 5.0 microns are effective from the point of view of radiolytic oxidation. Calculation of the coefficient of correlation by linear regression analysis confirms the view obtained by inspection of the curves. The correlation coefficient is 0.898 for Fig. 4(a) and 0.975 for Fig. 4(b). Fig. 5 shows data obtained from the radiolytic oxidation of a single specimen, progressively oxidised up to 28% weight

loss. At each stage the open porosity of the specimen was measured and it is therefore possible to obtain an experimental relation between rate of weight loss and open porosity from the single specimen. It is seen that the results are very far from showing a linear relationship. In fact the oxidation rate goes through a maximum and then decreases as the open porosity passes through a value of around 26%. Clearly the pore volume produced at the highest weight losses is for some reason not contributing to the radiolytic oxidation rate as expected.

Labaton et al. have analysed their experimental data on the basis both of Eq (4) and (5) above. They conclude that neither explanation can be accepted unequivocally and adduce evidence for both types of de-activation mechanism. Comparison of their experimental data with those of Dominey and Morley (8) and with the data given by Mahan and Solo (9) and by Avramenko and Kolesnikova (10) for the recombination cross-section of O(3P) and CO strongly suggest that an oxygen species, not necessarily an oxygen atom in its ground state, is present in the radiolysed gas.

EFFECTS OF OXIDATION ON PORE STRUCTURE - The ideas discussed above can be used for a calculation not only of the change in total porosity of the graphite with radiolytic corrosion, but also to calculate how the pore size distribution in the material changes. Since the rate of the thermal reaction (in the chemically-controlled régime) depends on the internal pore surface, and that of the radiolytic reaction depends, to a first approximation at least, upon the internal pore volume, then the porosity distribution function will change with burn-up in a different way according to whether the oxidation is carried out thermally or radiolytically. In practice the distinction is blurred because the manner of change also depends to some extent on assumptions about the shape of the pores. For the graphites which have been examined experimentally, the most probable shape is slab or cylindrical, and on this basis Labaton et al. have calculated pore size distribution curves for different radiolytically-produced weight losses. The resulting curves are shown in Fig. 6, compared with experimental data. It is seen that the agreement is very good for a 13% weight loss graphite, and at least fair for the 27.6% weight loss material.

EFFECTS OF RADIOLYTIC OXIDATION ON MECHANICAL PROPERTIES - For reasons already discussed, the change in mechanical properties of graphite for a given amount of burn-off produced by thermal reaction with CO_2 depends upon the seat of the reaction interface and therefore is greater for the chemically- than for the diffusion-controlled régime. The radiolytic reaction discussed above takes place within the body of the graphite, and thus corresponds more to the chemically-controlled situation. However, there is in addition the factor that reaction rate at the walls of a given pore depends on the pore diameter. Thus, unit area of carbon present as walls of fine pores will, at least to a first approximation, suffer loss during radiolytic oxidation than will unit area in the form of walls of large pores. Hence, if the graphite concerned is (as is common with the industrial product) a multi-phase material, and these phases differ in the distribution of pore sizes contained within them, then selective removal of one phase with respect to another may occur differently in the two processes. This seems the likeliest explanation of Fig. 7 (from Ref. 11) which compares the effect on Young's modulus and strength of graphite for a given amount of oxidation by CO_2 when produced either thermally, in the diffusion régime, or radiolytically. The implication of this curve on this reasoning is that the large pores in the materials examined occur in those parts of the structure which are of less significance to its mechanical integrity.

EFFECT OF INHIBITORS - Inhibition of the thermal CO_2 graphite reaction by carbon monoxide arises (4) from the effect of the latter on the oxygen-exchange equilibrium of Eq (1). The supposition that radiolysed CO_2 contains excited species implies that molecules which can scavenge these species should reduce the rate of radiolytic reaction. In the technological studies carbon monoxide was an obvious scavenger to try. Many experiments were done on these lines, and typically gave results indicated by Fig. 8 taken from Ref. (8). Since the inhibition obtained in this way was inadequate for practical purposes, more powerful inhibitors were sought. Fig. 9 from a paper (12) by Hutcheon and Prince shows the results of one set of experiments in which different concentrations of methane were added to CO_2 in radiolytic oxidation experiments. It is clear that this inhibitor can exert a profound effect in slowing down the rate of attack, here measured by the rate of evolution of $C^{14}O$ from C^{14} labelled graphite. This behaviour is shown by other hydrocarbons as well as methane. Fig. 10 from unpublished work at Culcheth shows that the inhibitive effect is roughly proportional to the size of the hydrocarbon molecule.

It is naturally of interest to speculate on the mechanism by which methane operates. Two possible reactions are indicated by the following equations:-

$$O + CH_4 = CH_2{:} + H_2O \qquad \ldots\ldots (6)$$

$$CO_2^* + CH_4 = CO{:}CH_2 + H_2O \qquad \ldots\ldots (7)$$

A useful experimental pointer towards the mechanism is provided by Fig. 11 based on work in Culcheth. In this graph the results of two experiments are plotted together. In one experiment a graphite specimen was exposed to CO_2 in pile before the reactor was shut down, while in the other experiment the specimen was exposed to a gas containing methane before the reactor was shut down. After the shut-down the reactor was then re-started with the specimens exposed to pure CO_2. The specimen which had not previously been exposed to methane very rapidly indicated a C^{14} evolution rate characteristic of the uninhibited reaction. In the second experiment there was a relatively long transition period before the uninhibited CO_2 rate was attained. The result implies that the methane bearing atmosphere in which the specimen had previously been running had in some way conditioned the surface, so that a chemisorbed surface layer of a protective nature had first to be removed before the specimen reacted at a rate corresponding to a methane free gas. The inhibitive property of methane therefore

arises, to a large degree, from a surface process.

SUMMARY OF GRAPHITE-CO_2 REACTION - Examples have been quoted to show that the corrosion of graphite by CO_2 is substantially modified when the process takes place in an irradiation field. These modifications appear as differences in the effect of temperature, pressure and inhibitors on the rate of reaction, and differences in the effects on the graphite itself in relation to pore structure and mechanical properties.

CHEMICAL REACTIVITY OF NEUTRON - DAMAGED GRAPHITE

THE REACTIVITY TO AIR of solid carbons in general is of course a highly variable parameter. However, for a closely controlled product such as reactor graphite, with tight specifications in particular on impurity content, and with a standardised test procedure, reproducible measurements can be made. A typical value for the U.K. reactor graphite PGA, measured at 450°C, is recorded (13) as 24×10^{-6} h^{-1} with an activation energy of ca. 40 K cal/mol^{-1}. The unit used for reactivity is a convenient practical one which assumes constant surface area between different specimens. For this material the surface area is about 0.25 $m^2 g^{-1}$ so that the figure quoted above corresponds to a specific reactivity of ca. 1.5×10^{11} atoms $cm^{-2} sec^{-1}$.

When graphite is irradiated by fast (> 1 MeV) neutrons, atoms are displaced from their lattice positions. In the core temperature range of practical interest to the Magnox and AGR reactor systems (200-500°C) the great majority of these displaced atoms will return to vacant lattice positions. A small fraction however will migrate to layer plane boundaries or remain as interstitials (single or compound) leaving some lattice vacancies. These interstitials and vacancies will correspond to sites of higher energy than atoms in their stable lattice positions. Energy deriving from the fast neutrons is thus stored in the lattice - the "Wigner energy". Increase of graphite temperature will cause some of the interstitials to migrate through the lattice, eventually to combine with vacancies and to release stored energy in the process.

We should expect to find this increased stored energy therefore to be associated with an enhanced chemical reactivity in so far as we expect the displaced atoms and the vacancy sites to be more reactive than atoms in their stable lattice positions. This enhancement should increase with dose and reduce as irradiation temperature is increased.

The safety of operating graphite-moderated reactors is guaranteed by monitoring the core for this increase in reactivity as well as (for CO_2- or helium-cooled reactors) by precautions to avoid the ingress of oxygen to the hot core. Any observed reactivity increases may clearly have several origins in the practical case - changes in pore structure have already been discussed above. In order to obtain a better understanding of such monitoring data, experiments have been done (13) to evaluate specific effects due to neutron irradiation.

The specimens of graphite used which had been irradiated in nominally pure helium to doses up to 20×10^{20} nvt (> 1 MeV) in a Materials Testing Reactor at known temperatures between 225°C and 450°C with the primary purpose of determining changes in dimensions and physical properties. Some of the specimens were subjected, after removal of possibly contaminated outer layers by skimming, to a standard oxygen reactivity test. This test involved oxidising the specimens to about 1 per cent weight loss by exposure to air in a furnace at 450°C $\pm$ 5°C. Results are shown in Fig. 12. Because of the history of the experiment there is some doubt about the original (unirradiated) value for these particular specimens but "standard" values for unirradiated material of similar origin are indicated in the graph.

The results show, as expected, a linear dependence of reactivity on neutron dose under these conditions and a reduction in magnitude of the effect as the irradiation temperature of material is increased. These effects, which closely parallel the effects of irradiation on stored energy and thermal conductivity, and are almost certainly to be ascribed to neutron-induced displacements.

CORROSION OF ZIRCONIUM ALLOYS IN AQUEOUS ENVIRONMENTS

OUT-OF-PILE CORROSION OF ZIRCALOY-2 - Results for the out-of-pile oxidation of Zircaloy-2 by water or steam at ca. 300°C are shown in Fig. 13 taken from Ref. (14). Zircaloy-2 is the zirconium-based alloy containing 1.5 per cent of tin which has been developed for use as a cladding and pressure tube material in water reactors and has been studied by workers in several countries.

Initially the weight gain/time curve found at these temperatures is approximately cubic rather than of the parabolic form expected on classical models. Nevertheless, it indicates that oxidation of the alloy is essentially controlled by a diffusion process through the oxide scale. Marker experiments have shown that the oxide grows apparently entirely at the metal/oxide interface so that diffusion must be by movement of oxygen rather than of zirconium. As, under reducing conditions, the oxide is slightly oxygen deficient, the corrosion process is currently explained as the diffusion of oxygen vacancies down a concentration gradient either in the oxide lattice, or, in view of the discrepancies between diffusion coefficients calculated from corrosion rates and some recent (15) measurements by "easy paths", for example at crystallite boundaries. If the mobility of the vacancies can be taken as substantially constant over the range of vacancy concentrations, the transport through any given scale should be directly dependent on the difference in vacancy concentrations across the scale. These will be related, assuming the vacancies to be doubly charged to the local partial pressure of oxygen, by the reaction:-

$$\square + 2\epsilon + \tfrac{1}{2}O_2 \rightleftharpoons O_{lattice} \qquad \ldots\ldots (8)$$

It follows that

$$[\square] \propto \frac{1}{(Po_2)}^{1/6} \qquad \ldots\ldots (9)$$

Hence, the difference in vacancy concentration across the scale is given by

$$\left(\frac{1}{(Po_2)_i}\right)^{1/6} - \left(\frac{1}{(Po_2)_o}\right)^{1/6}$$

where $(Po_2)_i$ is the partial pressure of oxygen at the metal/scale interface. Since, as noted above, $(Po_2)_i \ll (Po_2)_o$ the second term in this expression is negligible in comparison to the first, and the measured corrosion rate should be independent of the partial pressure of oxygen in the water. This is in fact the experimental result.

IN-PILE CORROSION BEHAVIOUR OF ZIRCALOY-2 - The subject has recently been reviewed (16) in considerable detail by Cox. The ensuing discussion picks out only the main features of the argument. When Zircaloy-2 is corroded by steam or water while simultaneously being irradiated, the observed behaviour is quite different from that out-of-pile. In the first place the reported corrosion rate for temperatures up to 400°C is in general considerably faster than the out-of-pile rate as indicated, for example, by Fig. 14.

However, as Cox's review brings out, when comparisons are made between results from different laboratories there are wide discrepancies in the data. Variations in sources of material, in surface condition and state of preoxidation of the metal, and uncertainties about dose rate and temperature no doubt contribute to these discrepancies. However, when due allowance is made for these, there remains an apparent sensitivity of corrosion rate in pile to oxidising conditions, whether due to molecular oxygen as such or the presence of oxidising species produced by the radiation, such that, depending on the flux level, temperature and environment, rates may be increased by a factor approaching two orders of magnitude.

A quantitative explanation of these observations is not yet available and is perhaps not to be expected. Aside from the fact that the experimental techniques are difficult and expensive, so that the results themselves have not been repeated as often and as closely as might be wished, the models even of the out-of-pile process which have been suggested over the last twenty years or so still only apply to relatively simple systems (see, for example, Stringer (17)). The review by Cox, quoted above, considers, and rejects, explanations based solely on phase transformations of the oxide, enhanced dissolution of ZrO_2, radiation damage in the metal, enhanced electrical conductivity, oxide film embrittlement and radiation chemical effects, as well as other explanations of more limited applicability which have been proposed. Most of these require little further discussion here since Cox's arguments will receive fairly general acceptance. In view of the earlier sections of this paper it is worth noting, however, that explanations based entirely on radiation chemical effects are rejected. Such effects should be produced by γ-radiation alone whereas the experimental evidence is that γ-radiation produces (18) only very small effects and then only in the thin film region. Moreover, it is difficult to visualise changes in transport rate through a thick scale resulting from an increased agressiveness of the corroding medium.

Cox notes the difficulties involved in an explanation based on enhanced diffusion through the oxide film. First, the rate of production of defects by practical irradiation doses does not serve by itself to account for the increased oxidation rate, and it is therefore necessary to invoke some permanent damage to the film, derived from irradiation, which will provide an easy path for oxygen diffusion. As noted above, such "easy paths" have been invoked, also for the unirradiated case. Secondly, irradiation damage to the oxide film does not provide an obvious explanation for the sensitivity to oxygen level in the environment which appears when Zircaloy-2 is irradiated. Cox's method of dealing with this second difficulty is to suggest that the transport rate may be controlled, depending on circumstances, either by ionic transport or by the electronic transport in the other direction. Thus, even if irradiation facilitates ionic transport, this will not increase the transport rate if a limit is set by electronic transport in the opposite direction. Hence, no effect will be observed unless the environment is also changed. If, however, this is made more oxidising then, in his view, the properties of a thin barrier at the oxide/environment interface, which he takes to be the main resistance to electron flow, may be so modified as to facilitate electron transport and thus to remove the limit on overall transport.

ANALOGY BETWEEN IRRADIATED ZIRCALOY-2 AND UNIRRADIATED ZIRCONIUM NIOBIUM - Campbell and Tyzack note (20) that the alloy of zirconium with 2.5% niobium (Zr/Nb) corrodes out-of-pile at a rate generally faster than does Zircaloy-2 but is distinctly sensitive to the oxygen partial pressure of the environment and that this rate is little, if any, enhanced (21) by irradiation. Since, therefore, the effect of irradiation on zirconium is in a sense similar to that of alloying with niobium in regard to corrosion behaviour, they suggest that a satisfactory theory of the latter effect may provide a useful starting point for understanding the effect of irradiation on Zircaloy-2.

The niobium ion on size grounds should fit into the ZrO_2 lattice. Niobium, however, can exert a valency of 5, although it can also have valency 4. With valency 5 charge balance can be maintained

by oxygen interstitials, and thus can therefore be an equilibrium between Nb^{IV}, Nb^{V}, oxygen interstitials and external oxygen atoms.

$$2\ Nb^{IV} + \tfrac{1}{2}O_2 \rightleftharpoons 2\ Nb^{V} + \Delta\ O^{2-} \qquad \ldots\ldots (10)$$

$$[\Delta\ (O^{2-})] = K.P_{O_2}^{\frac{1}{2}} \cdot \frac{[Nb^{IV}]^2}{[Nb^{V}]^2} \qquad \ldots\ldots (11)$$

$$\text{and}\quad [Nb^{V}] = 2\ [\Delta\ (O^{2-})] \qquad \ldots\ldots (12)$$

$$\text{so that}\quad [\Delta\ O^{2-}]^3 = \frac{K}{4} \cdot P_{O_2}^{\frac{1}{2}} \cdot [Nb^{IV}]^2 \qquad \ldots\ldots (13)$$

The next step is to relate oxygen transport rate to interstitial concentration. In this connection Campbell and Tyzack note that for hyperstoichiometric uranium oxide ($UO_{2.006}$ to $UO_{2.015}$) the diffusion coefficient for oxygen experimentally (21) observed is some orders of magnitude higher, depending on the degree of non-stoichiometry, than in the stoichiometric oxide.

The data are scattered, but Compbell has observed (22) that, very approximately the oxygen mobility increases as $[\Delta\ O^{2-}]^3$ so that the diffusion coefficient increases approximately as $[\Delta\ O^{2-}]^2$. Assuming, for want of better information, similar behaviour in Zr-Nb, then in this case the oxygen flux

$$\dot{n} = D\ \frac{d}{dl}\ [\Delta\ O^{2-}] \qquad \ldots\ldots (14)$$

$$= K'\ [\Delta\ O^{2-}]^2\ \frac{d}{dl}\ [\Delta\ O^{2-}] \qquad \ldots\ldots (15)$$

and, since $\dot{n}$ is constant through the film

$$\dot{n}l = \frac{K}{3}\ [\Delta\ O^{2}]_o^3 - [\Delta\ O^{2}]_i^3 \qquad \ldots\ldots (16)$$

Now $(P_{O_2})_i \ll (P_{O_2})_o$ hence, by Eq (11), $[\Delta\ O^{2-}]_i \ll [\Delta\ O^{2-}]_o$

$$\text{so that}\quad \dot{n}l \simeq \frac{K}{3}\ [\Delta\ O^{2-}]_o^3 \qquad \ldots\ldots (17)$$

$$\text{which, from Eq (13),}\quad \simeq K'' \cdot P_{O_2}^{\frac{1}{2}} \cdot [Nb^{IV}]_o^2 \qquad \ldots\ldots (18)$$

If, as has been suggested, $[Nb^{V}]_o \ll [Nb^{IV}]_o$ then, approximately $\dot{n}l = K'' \cdot P_{O_2}^{\frac{1}{2}} \cdot [Nb]^2$.

The results of recent unpublished work (23) at Culcheth, in Fig. 15, give some confirmation to the predicted dependence on $P_{O_2}^{\frac{1}{2}}$. Other recent work at Culcheth using specimens of as-quenched Zr-Nb in order to obtain uniform dispersion of Nb through the oxide film also show an approximate dependence of oxidation rate on the square of the niobium content.

The equilibrium of Eq (10) provides a mechanism for the scale to accept oxygen atoms, as interstitials, from an oxidising medium at an interface. Given an oxygen gradient across the scale it also provides a mechanism for transferring them from the oxygen source to an oxygen sink, namely the metal interface. The dependence on external oxygen level seems to have the right form, although a quantitative theoretical prediction of the mobility has not been presented.

For the case of irradiated Zircaloy-2 there is no difficulty in postulating the presence of interstitials. Even without irradiation zirconia shows (24) p-type semi-conducting properties, consistent with the presence of interstitials, at 1200°C and the analogy between irradiation and high temperature effects is very obvious. It therefore seems reasonable to ascribe to interstitials the enhanced oxygen mobility resulting from irradiation.

The difficulty remains that the direct effects of interstitial production are quantitatively inadequate to account for the enhanced transport rate. On the other hand, evidence has been quoted from out-of-pile work which indicates that a small excess of oxygen over stoichiometric requirements, and presumably therefore present in interstitial form, produces surprisingly large increase in oxygen mobility. A better account of this effect in unirradiated materials seems required before the effects of irradiation can be completely understood. However, if it can be granted that irradiation damage in zirconium oxide can interact with the external oxygen pressure so as to give a relatively small continuing population of interstitials, the observed effects on corrosion rate of Zircaloy-2 should follow.

REFERENCES

1. L. H. Gray (1964), Proc. Cambridge Phil. Soc., 42, 72.

2. W. A. Noyes and P. A. Leighton (1941), A.C.S. Monograph Series No. 86 (Reinhold).

3. J. Wright (1963), Private communication from AERE Harwell.

4. S. Ergun (1956), J. Phys. Chem. 60, 480.

5. R. Lind and J. Wright (1963), J. Brit. Nuc. Eng. Soc., 2, 287.

6. J. M. Hutcheon, H. C. Cowen and N. F. Godwin (1963), Proc. 5th Carbon Conf., 2, 379 (Pergamon Press, Oxford).

7. V. Y. Labaton, B. W. Ashton, R. Lind and J. N. Tait (1969) Carbon, 7. 59.

8. D. A. Dominey and H. Morley (1966), Atom. Ener. Res. Estab. (Harwell) Report R/4989.

9. B. H. Mahan and R. B. Solo (1962), J. Chem. Phys., 37, 2669.

10. I. Avramenko and R. V. Kolesnikova (1959), Bull. Acad. Sci. USSR, 9, 1506.

11. N. Hawkins (1965), Proc. 2nd Conf. on Industrial Carbon and Graphite, Soc. Chem. Ind. (London)

12. J. M. Hutcheon and K. Prince (1965), Nuclear Engineering, October, 1965.

13. H. C. Cowen and D. M. Clare (1963), Unpublished work - RML Culcheth.

14. J. E. Draley, J. A. Ayres, W. E. Berry, E. Hillner and S. P. Rideout (1964), 3rd U.N. Int. Conf. on the Peaceful Uses of Atomic Energy, A/Conf.28/P/243.

15. B. Cox and J. P. Pemsler (1968), J. Nucl. Mats. 28, 73.

16. B. Cox (1968), J. Nucl. Mats. 28, 1.

17. J. Stringer (1966), J. Inst. Metals, Metall. Revs., Vol.11, p.113.

18. R. C. Asher and B. Cox (1962), Proc. IAEA Symp. Corrosion of Reactor Materials, Salzburg, p.209.

19. C. S. Campbell and C. Tyzack (1969a), Paper to Conference "[illegible]ium 68", Mariánske Lázně, Czechoslovakia.

20. J. E. LeSurf and P. E. C. Bryant (1967), At.En. of Canada Report AECL 2797.

21. A. B. Auskern and J. Belle (1961), J. Nucl. Mats., 3, 367.

22. C. S. Campbell (1969), Private communication.

23. C. S. Campbell and C. Tyzack (1969b), UKAEA Internal Report.

24. P. Kofstad and D. J. Ruzicka (1963), J. Electrochem. Soc., 110, 181.

25. J. E. Irvin (1966), J. Electrochem. Tech. 4, 240.

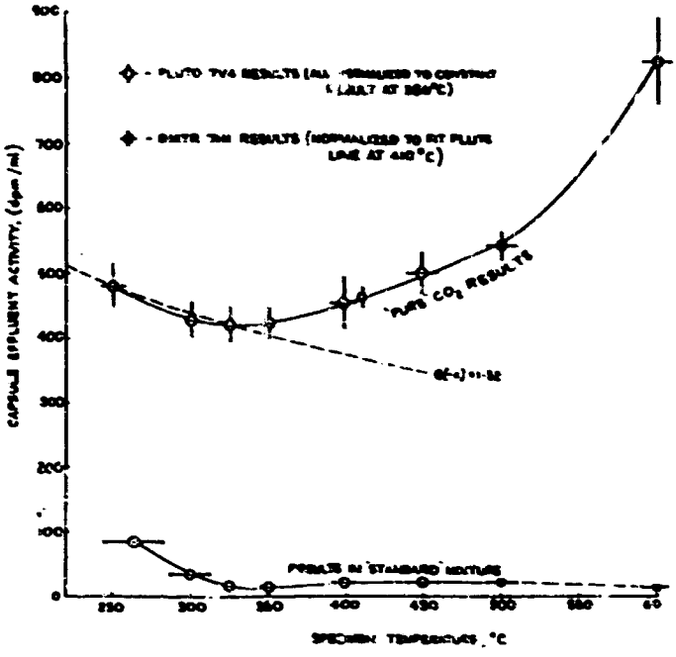

Fig.1 Effect of temperature on attack rate

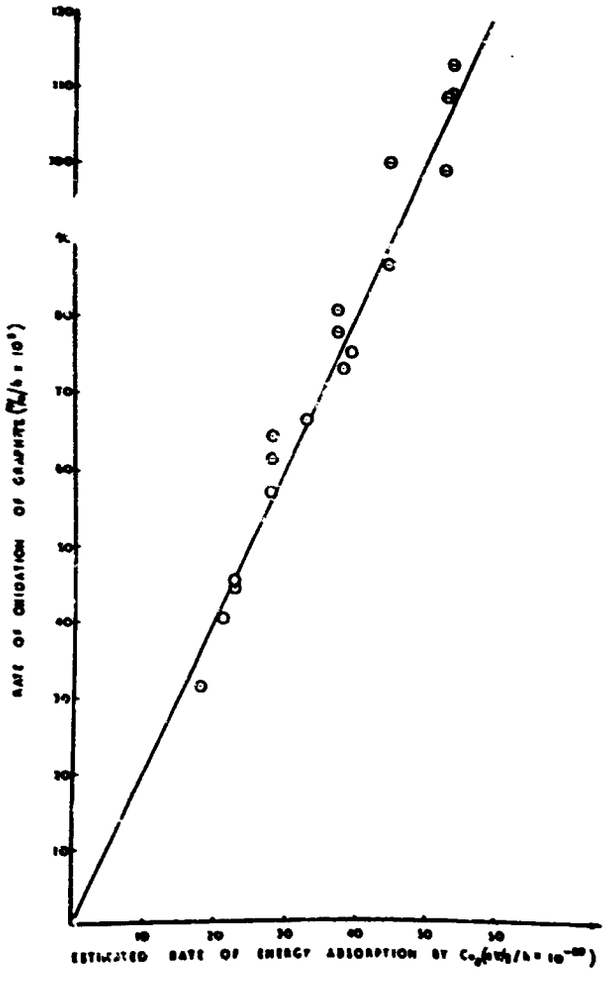

Fig.2(a) M.T.R.Experiment illustrating effect of dose rate on rate of oxidation (CO_2 at 40 atm. and 200°C)

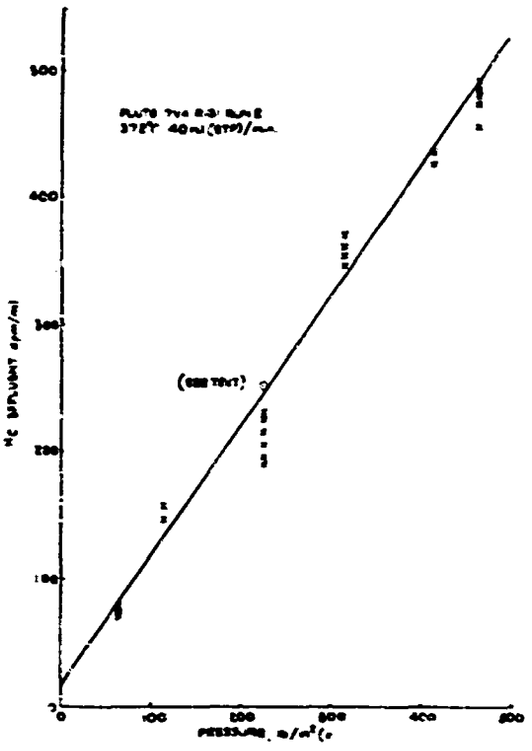

Fig.2(b) Effect of pressure on the radiation-induced reaction of CO_2 with ^{14}C-Graphite

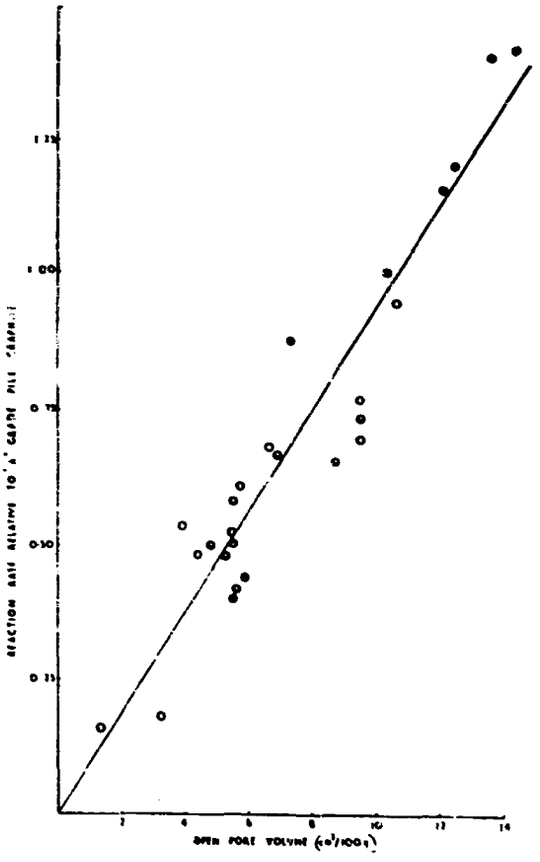

Fig.3 Effect of Open pore volume on reaction rate

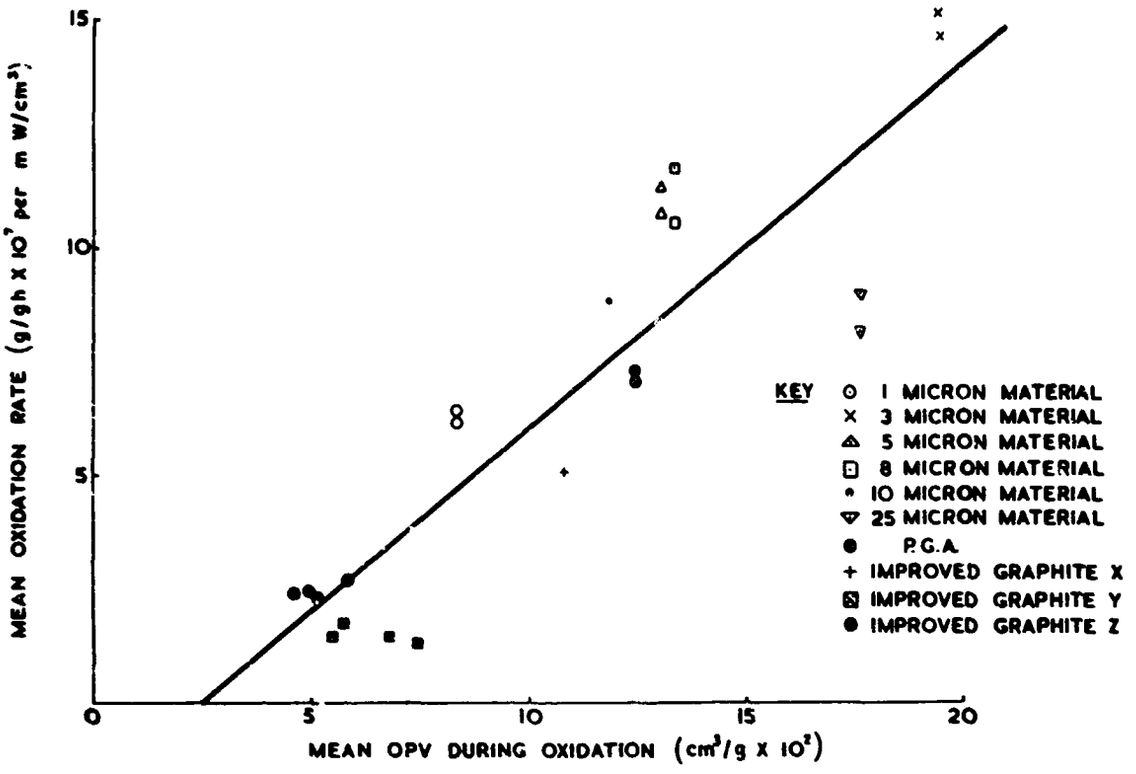

Fig.4(a) Oxidation rate as a function of total accessible pore volume

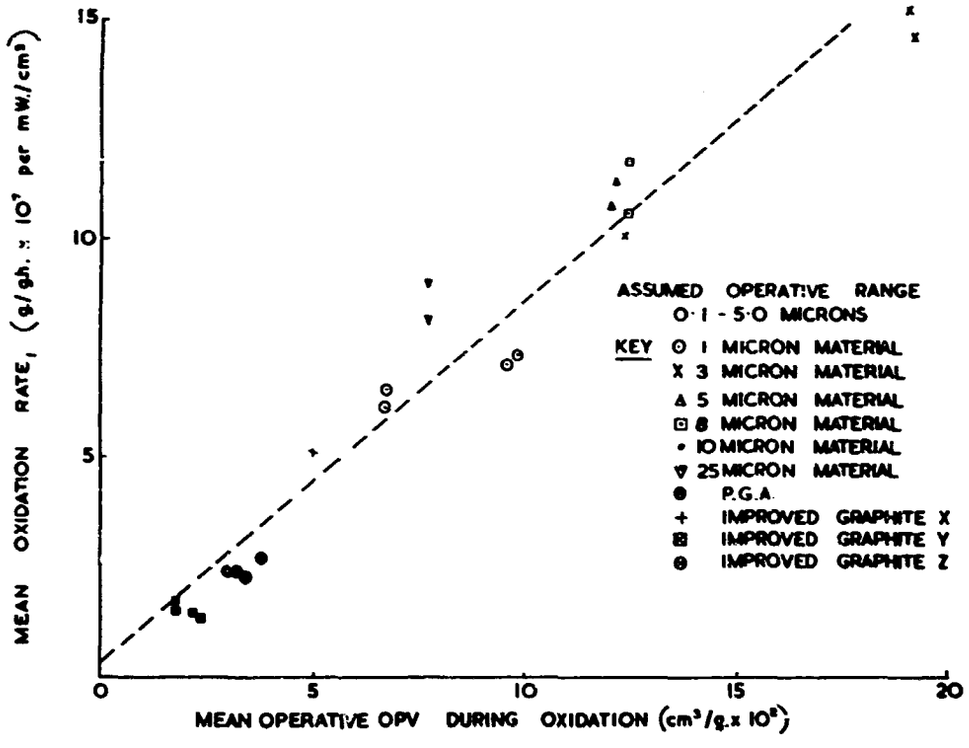

Fig.4(b) Oxidation rate as a function of the operative OPV

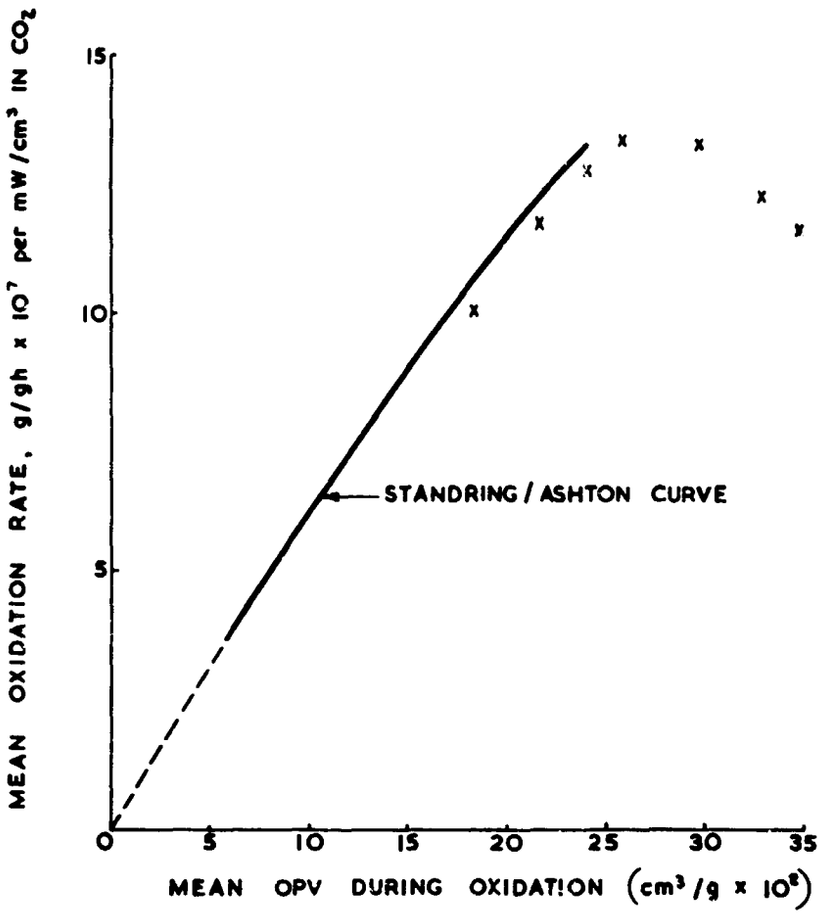

Fig.5 Oxidation rate of a P.G.A.Specimen taken to high weight loss as a function of total accessible pore volume

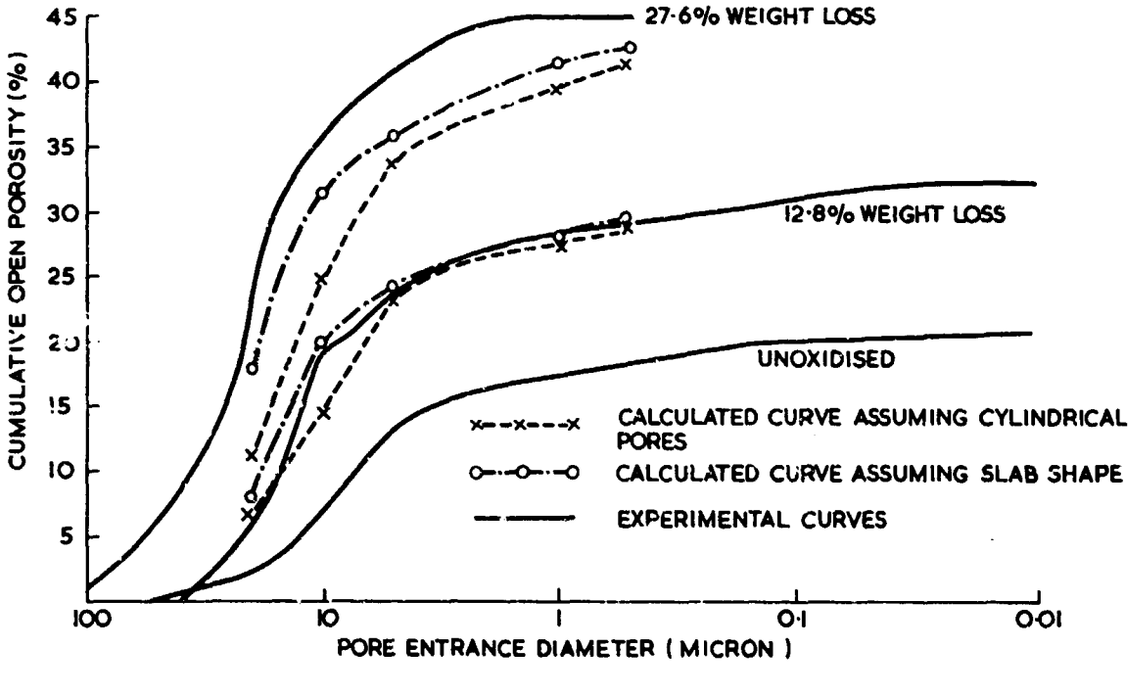

Fig.6 Comparison of experimental and calculated pore size distribution

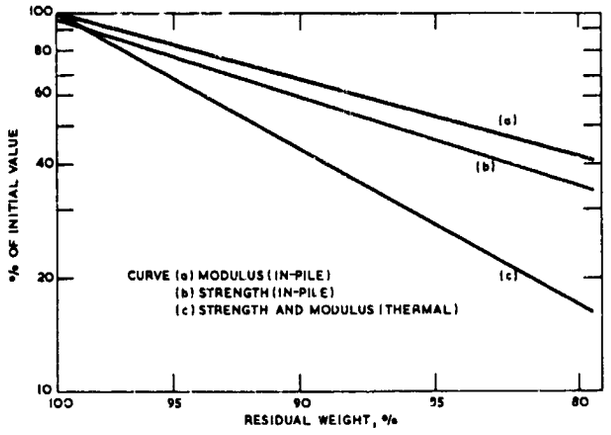

Fig.7 Relationship between residual strength modulus and residual weight for thermal and in-pile oxidised graphite

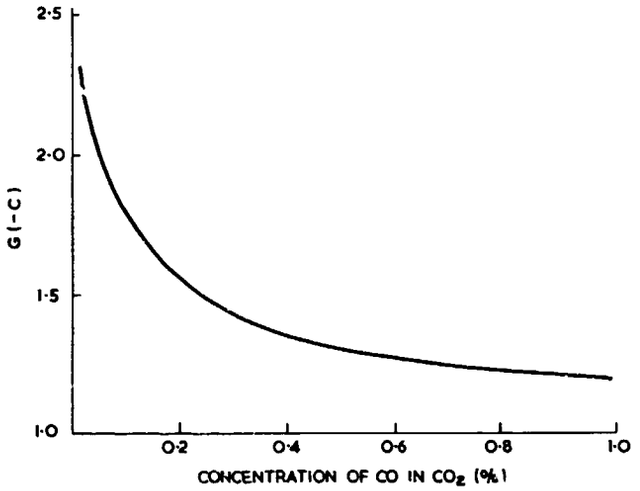

Fig.8 Variation of G(-C) with concentration of CO

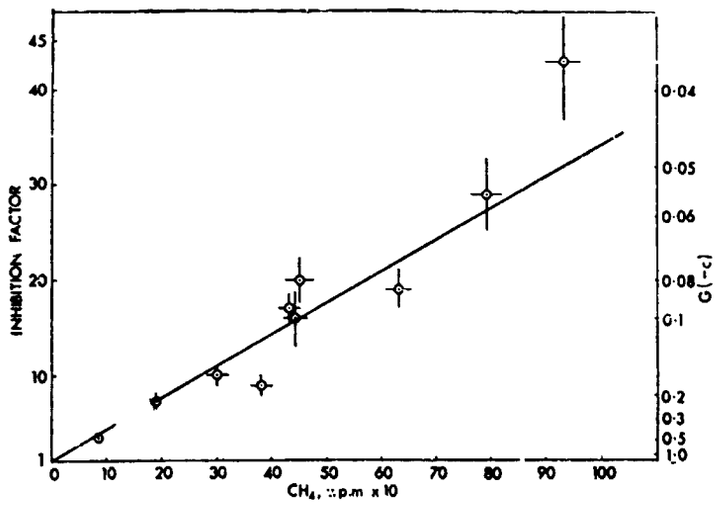

Fig.9 Reduction in coolant aggressiveness by methane. CO concentrations between 0.4 and 1.8% ; water concentrations less than 150 vpm

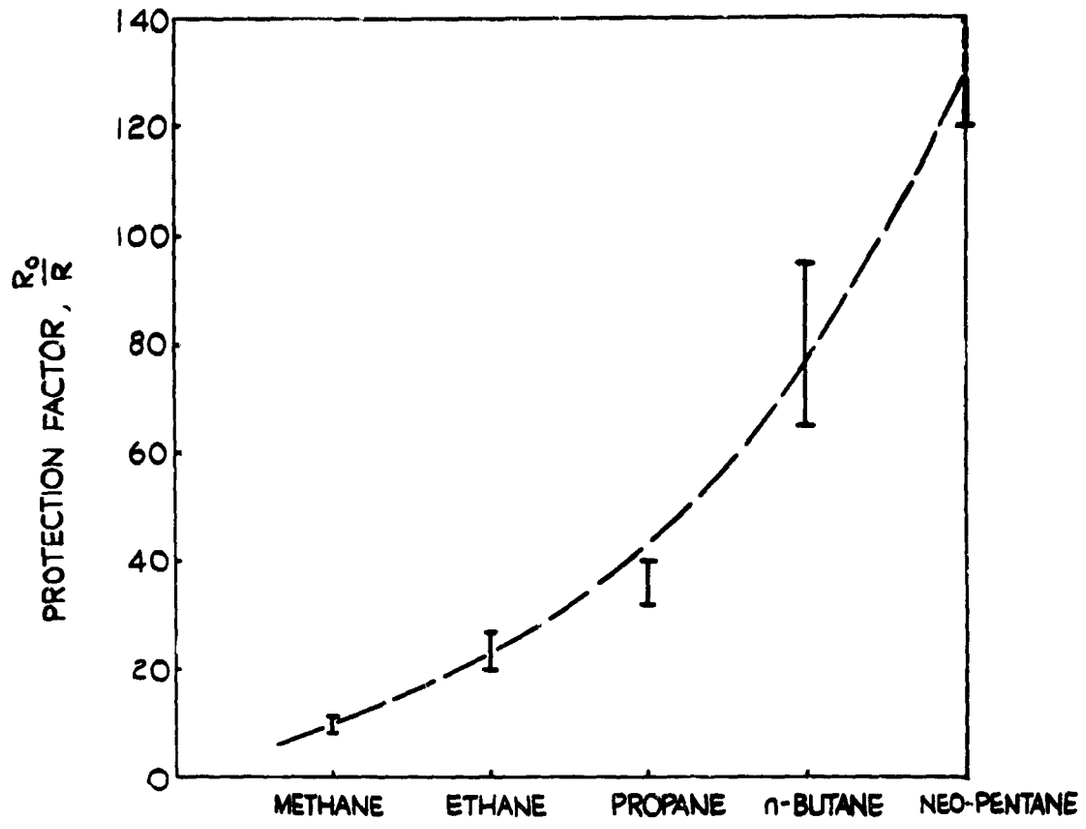

Fig. 10 Effect of 200 vol. ppm. Additions of different hydrocarbons on the CO_2/graphite reaction

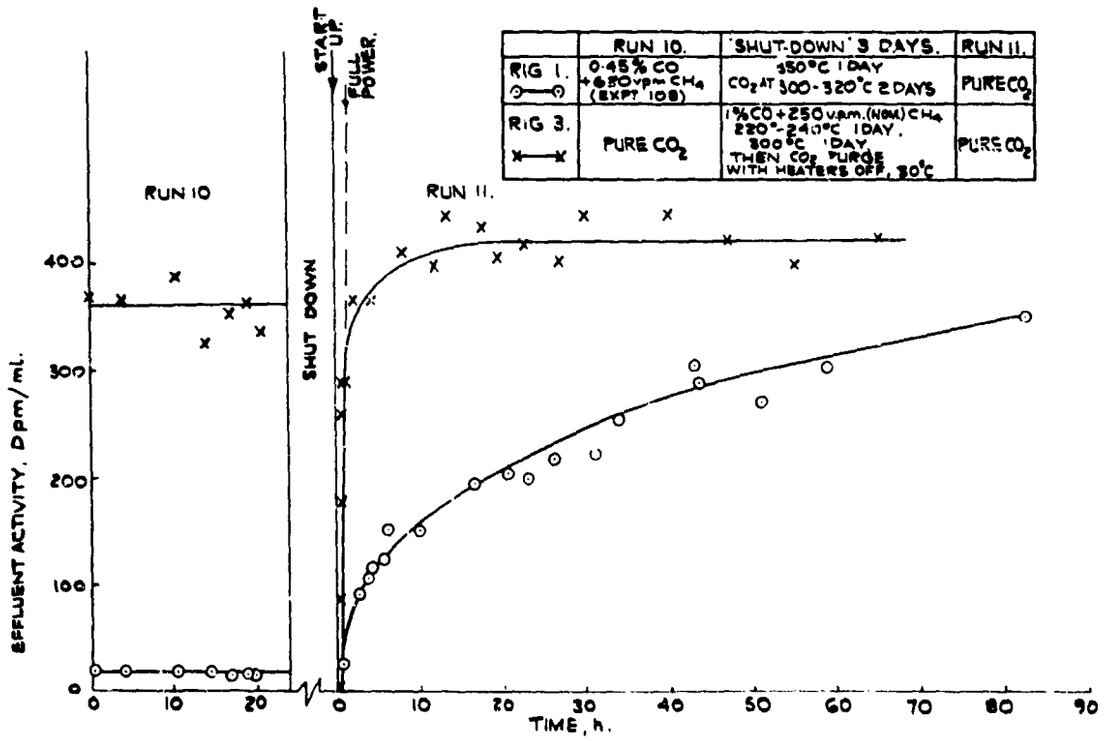

Fig. 11 Special "shut-down" experiment to investigate methane inhibition

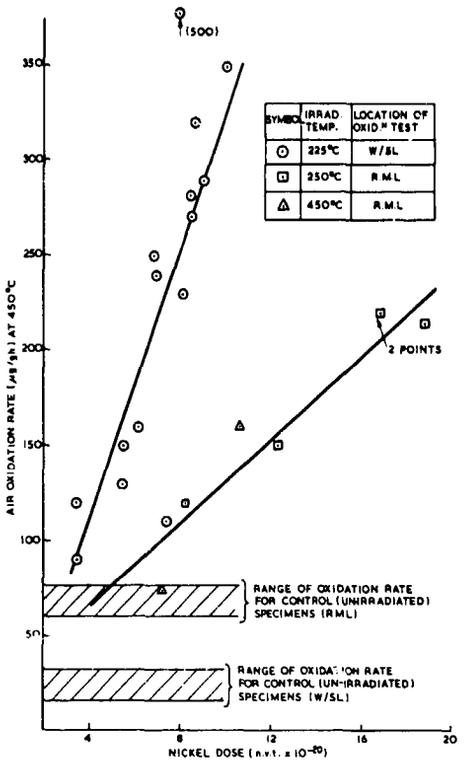

Fig. 12 Oxidation rate after skimming as a function of dose

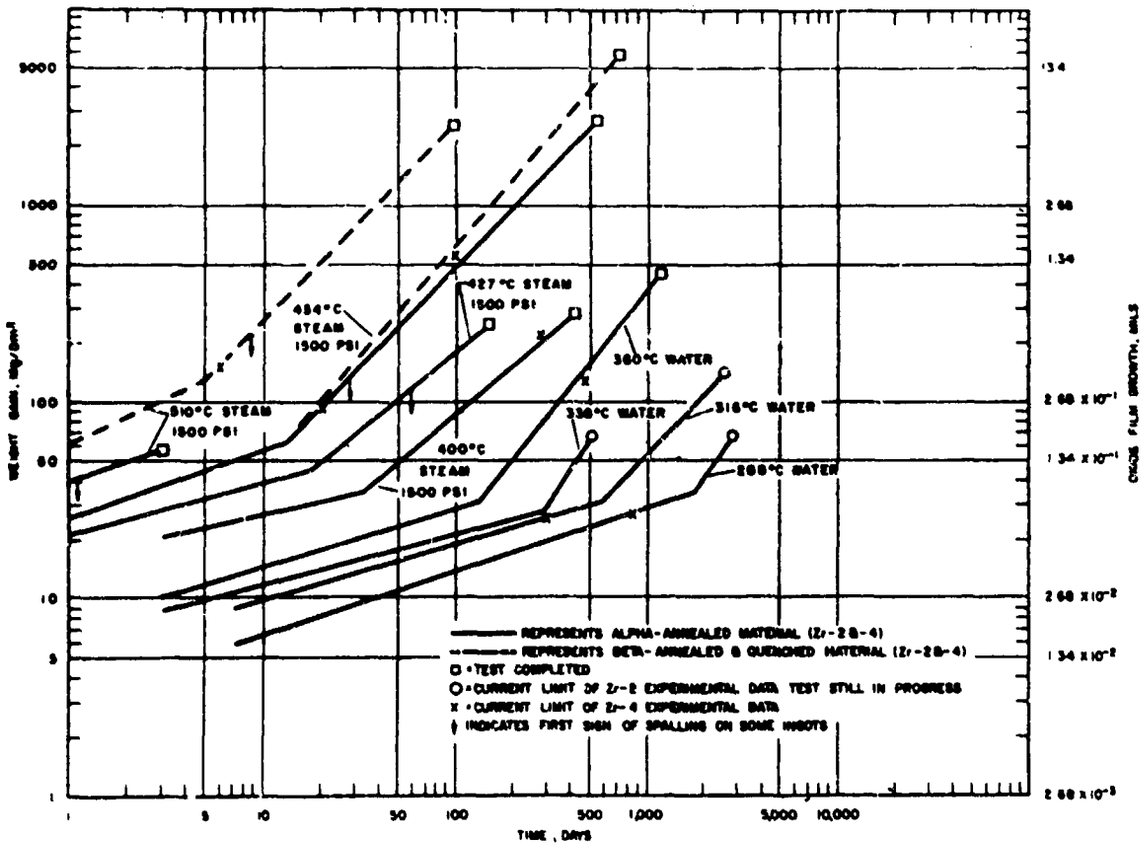

Fig. 13 Weight gain as a function of time for Zircaloy-2 and Zircaloy-4 exposed to high temperature water and steam

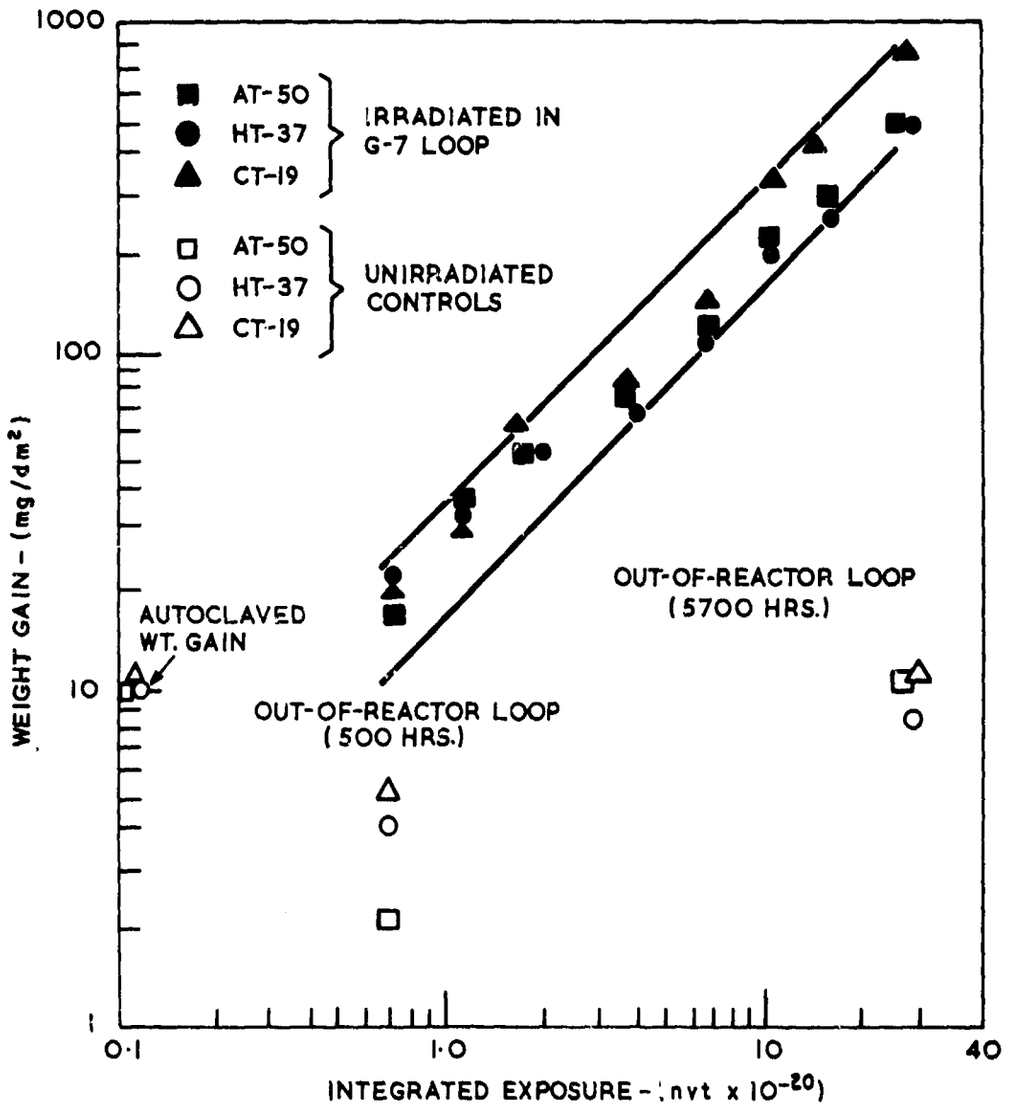

Fig. 14 The results from Fig. 11b, obtained in pH10 LiOH in the G-7 loop in ETR, plotted as a function of fast neutron dose (after Irvin [1966])

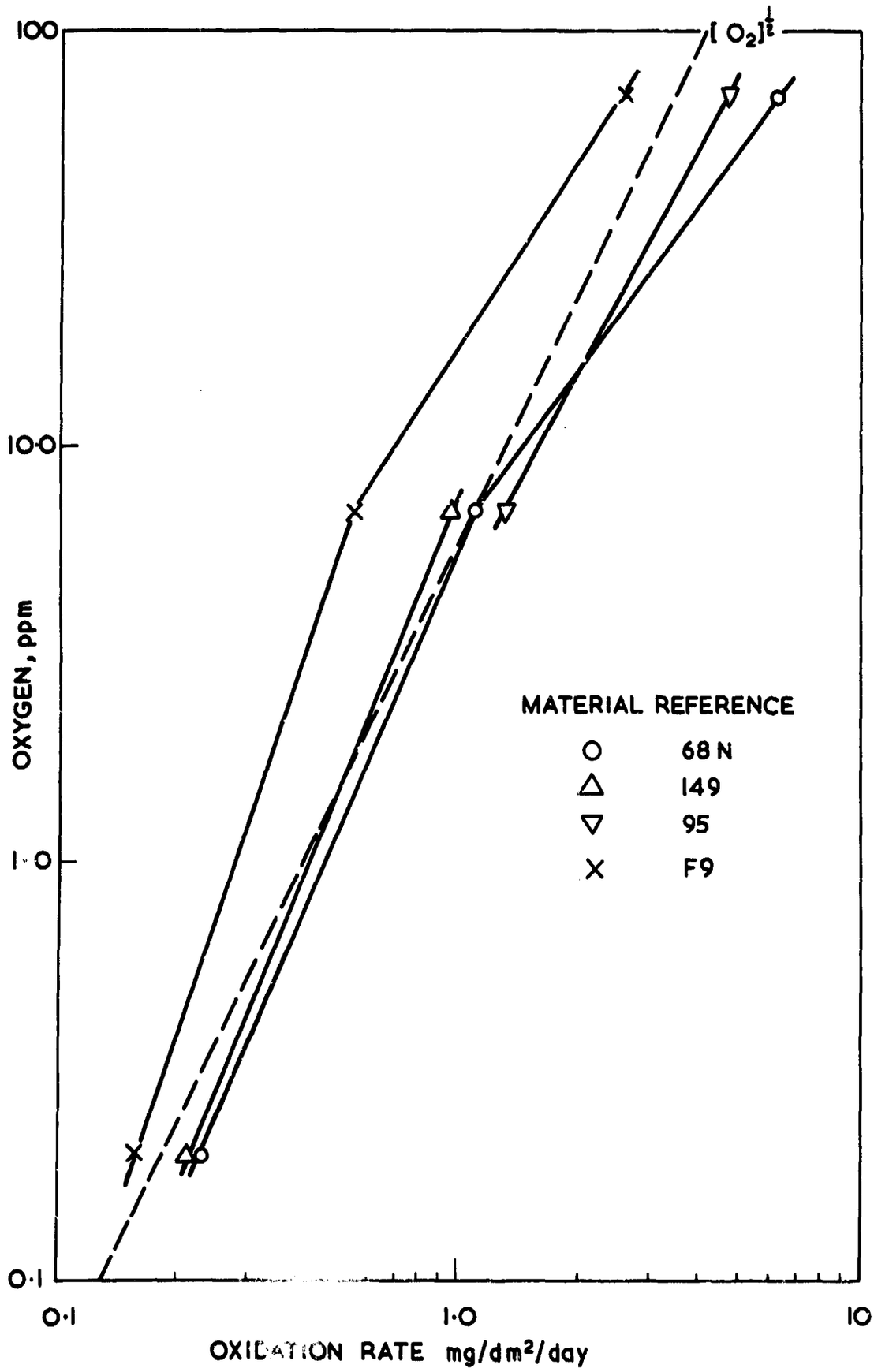

Fig. 15 Oxidation of Zr-2½% Nb alloy in 290°C water containing various levels of oxygen

LOW-TEMPERATURE REACTIONS BETWEEN SOLIDS AND GASES

by

Professor Dr.-Ing. Karl HAUFFE

Institut für physikalische Chemie
der Universität
34 Göttingen, Bürgerstr.50

SUMMARY

Because of the fact that all reactions between a solid and a gas are initiated by a chemisorption, in the first chapter of this paper the mechanism of the chemisorption is contributed under the viewpoint of the first step of metal oxidation and the ore reduction. The chemisorption, however, is mainly influenced by the presence of lattice defects and traps in and near the surface. Since often the mass transport through the solid due to a diffusion gradient and/or an electric field is the rate-determining step, the various transport phenomena are discussed. The utility of the understanding of these theoretical relations is demonstrated, especially, by means of the oxidation of nickel and of desorption and evaporation processes in the dark and under illumination. As examples zinc oxide and cadmium sulfide have been chosen.

LOW-TEMPERATURE REACTIONS BETWEEN SOLIDS AND GASES

Karl Hauffe

Institut für physikalische Chemie der Universität Göttingen, Germany

1. INTRODUCTION

Every chemical reaction between a solid and a gas (for example between a metal or an oxide or a sulfide and for instance oxygen, gaseous sulfur or hydrogen) is initiated by chemisorption of the corresponding gas. Chemisorption is often accompanied by a dissociation if molecules are the reacting species. Generally, at high temperatures the chemisorption of the gas is fast enough so that other steps can become rate-determining. At low temperature, however, chemisorption can also become the slowest step. The fact that a slow chemisorption does indeed take place can be expected if an electric field transport or a steep concentration gradient of lattice defects cause a fast movement of the corresponding ions towards the reaction front.

Since chemisorption is the initial step both in the oxidation of a metal and the reduction of an ore, the mechanism of chemisorption will be dealt with in the first chapter under consideration of the presence of lattice defects, electrons and holes as well as traps in and near the surface of a solid. In view of the fact that both in the oxidation of a metal and the reduction of an ore, one of the reacting solids is a semiconductor, it seems reasonable to discuss the chemisorption of various gases on a semiconductor surface. Subsequently, the various transport phenomena are described because the mass transport through the solid due to a concentration gradient and/or an electric field is often the rate-determining step. With regard to the topic under consideration, the oxidation of nickel is one of the most instructive examples for the demonstration of the different rate laws obtained under various experimental conditions.

Another very interesting problem is the elucidation of the mechanism of desorption as the initiating step in ore reduction and in the evaporation of photoconducting solids under strong irradiation in high vacuo. The experi-

mental conditions for evaporation processes should be realized, for instance, on the surface of the moon where a strong irradiation and a sufficiently high vacuum are available. Since ultraviolet light enhances evaporation, especially, of non-metals (for example oxygen and sulfur) of photoconducting solids much more than the evaporation of the corresponding species of non-photoconducting solid compounds, it should be expected that the surface of the moon should be free from photoconducting solids, such as ZnO, CdS, PbS, PbSe, TiO_2 and Cu_2O. To what extent metals with very low vapor pressure in the temperature range between 100 and 200°C, for instance titanium and copper, are present on the moon's surface is an open question.

2. CHEMISORPTION ON SEMICONDUCTING SOLIDS

As mentioned above, chemisorption is not only the decisive initiating step in metal oxidation and ore reduction but also in heterogeneous catalysis. Therefore, it seems appropriate to discuss first of all some of the actual problems in chemisorption. Under the topic of the oxidation of nickel in the next chapter, we shall discuss the chemisorption and the reaction of oxygen with nickel oxide. As is well known, nickel oxide is a p-type semiconductor with a more or less equivalent concentration of nickel-ion vacancies $|Ni|''$ or $|Ni|'$ and electron holes $|e|^{\cdot}$. The amount of these concentrations is a function of the temperature and the oxygen pressure. At high temperatures, if the ion mobility is large enough, the following equilibrium

$$O_2(gas) \rightleftharpoons 2\ NiO + 2\ |Ni|'' + 4\ |e|^{\cdot} \qquad (1)$$

is established throughout the entire crystal as can be demonstrated by conductivity measurements [1]. According to Eq. (1), oxygen is incorporated into the NiO lattice under generation of nickel-ion vacancies and holes. Eq. (1), however, represents the overall-reaction which can be separated into the following steps:

$$O_2(gas) \rightleftharpoons O_2^-(ads) + |e|^{\cdot} \qquad (2a)$$

whereby the first step represents the chemisorption characterized by chemisorbed oxygen molecules with a trapped electron. The following surface reaction steps can occur the faster the higher the temperature:

$$O_2^-(ads) = NiO + |Ni|'' + O^-(ads) + 2\ |e|^{\cdot} \qquad (2b)$$

and

$$O^-(ads) = NiO + |Ni|'' + |e|^{\cdot}\ . \qquad (2c)$$

With decreasing temperatures, however, the steps (2b) and (2c) become smaller and smaller so that the pure chemisorption step (2a) becomes more and more important. According to Eq. (2a), the chemisorption of oxygen causes a negative surface charge which is compensated by a positive space-charge layer with an enrichment of holes and an exhaustion of nickel-ion vacancies [2]. This mechanism is responsible for the appearance of a strong electric field through this space-charge layer with a width between 10^{-4} and 10^{-3} cm depending on the temperature and the oxygen pressure. As will be discussed later, under special experimental conditions this strong electric field should be responsible for the rather fast occuring surface reaction steps (2b) and (2c) which are accompanied by an ion movement.

According to equilibrium (2a), the chemisorption of oxygen should become smaller with increasing concentration of holes $|e|^{\cdot}$, a state which can be realized by incorporation of lithium ions into the nickel-oxide lattice, according to

$$\frac{1}{2}\,O_2(gas) + Li_2O = 2\,Li|Ni|' + 2\,|e|^{\cdot} + 2\,NiO \qquad (3a)$$

and the corresponding equation

$$Li_2O + |Ni|'' = 2\,Li|Ni|' + NiO\,. \qquad (3b)$$

As can be seen from the Eq.s (3a) and (3b), the concentration of holes will be increased and the concentration of nickel-ion vacancies decreased. If one considers that the nickel-ion transport is a direct function of the concentration of the nickel-ion vacancies and that the chemisorption of oxygen will be strongly decreased with increasing hole concentration, it can be expected that no noticeable occurence of oxygen up-take, according to Eqs. (1) and (2), should be detected.

Rather embarrassing results have been reported on the chemisorption and desorption of oxygen on illuminated zinc-oxide surfaces. Several authors [3] [4] [5] [7] have stated that a vacuum treated and, therefore, reduced zinc-oxide powder exhibits oxygen desorption under illumination with light of 370 mμ necessary for the production of electron-hole pairs. On the other hand, that zinc-oxide powder annealed at high temperatures in high oxygen pressure exhibits an oxygen chemisorption during illumination between 20 and 200°C. The experimental procedure, however, is not free of error concerning the chemical composition of the surface region of the ZnO sample. Therefore, the interpretation of the experimental results is not very convincing. Since this

phenomenon might be of general interest, it is discussed in what follows.

As is well known, zinc oxide is an n-type semiconductor with a more or less amount either of zinc metal in excess or of oxygen deficiency. This lattice-defect mechanism can be schematically represented by the following equations under equilibrium conditions established at high temperatures:

$$ZnO \rightleftharpoons Zn^{\cdot\cdot} + 2\,e' + \tfrac{1}{2}\,O_2(gas) \qquad (4)$$

or

$$Null \rightleftharpoons |O|^{\cdot\cdot} + 2\,e' + \tfrac{1}{2}\,O_2(gas) \qquad (5)$$

with the additional equilibrium

$$Zn^{\cdot\cdot} + e' \rightleftharpoons Zn^{\cdot} \qquad (6)$$

or

$$|O|^{\cdot\cdot} + e' \rightleftharpoons |O|^{\cdot} \qquad (7)$$

shifted at low temperatures largely to the right hand side. Here, e' denotes a free electron and $Zn^{\cdot}$ and $|O|^{\cdot}$ indicate zinc ions in interstitial positions and oxygen-ion vacancies, respectively. The one and two dots denote the single and double positive excess charge.

For further discussion, we prefer the lattice-defect mechanism represented by the Eqs. (4) and (6). It should be mentioned that the equilibrium (4) is shifted to the left hand side with increasing oxygen pressure and to the right hand side with increasing temperature at constant oxygen pressure and also under vacuum. At lower temperatures, the chemisorption can be described according to

$$O_2(gas) + e' \rightleftharpoons O_2^-(ads) \qquad (8)$$

followed by the two surface-reaction steps:

$$O_2^-(ads) + Zn^{\cdot} + e' = ZnO + O^-(ads) \qquad (9)$$

and

$$O^-(ads) + Zn^{\cdot} = ZnO\,. \qquad (10)$$

Now, let us discuss the possible presuppositions for chemisorption and desorption of oxygen on dark and illuminated zinc-oxide surfaces. According to Eq. (8), the extent of chemisorption of oxygen on ZnO in the dark will be larger the higher the concentration of free electrons. Therefore, we may assume that the chemisorption of oxygen is large on ZnO samples annealed at high temperatures in vacuum because of the significant generation of free electrons. In contrast, chemisorption should be expected to be very low on

ZnO samples annealed at high temperatures under high oxygen pressure since the equilibrium (4) is shifted far to the left hand side. Therefore, only a small concentration of free electrons is available for chemisorption.

In view of these facts, we may conclude that a ZnO specimen annealed in vacuo develops a large chemisorption capacity for oxygen in the dark even at room temperature. Since this chemisorbed oxygen, however, is only loosely bonded, it is not astonishing that during illumination a significant desorption could be detected. In the other case, however, an oxidized ZnO sample with a small amount of chemisorbed oxygen can exhibit photoadsorption. Only the steady-state concentration of chemisorbed oxygen particles present on the surface before the illumination determines whether a photodesorption or a photoadsorption does occur in order to approach a new steady state. At coverages exceeding a special concentration of adsorbed charged oxygen species, neutral oxygen molecules can also be adsorbed. This could be demonstrated by ESR measurements [7].

As discussed elsewhere, during illumination electron-hole pairs $e' \sim |e|^{\cdot}$ are produced which are very reactive to the particles on the surface, for instance oxygen, and to lattice defects in the bulk according to the equations:

$$e' \sim |e|^{\cdot} + O_2^-(ads) \longrightarrow O_2^{\times}(gas) + e' \qquad (11)$$

causing a photodesorption and

$$e' \sim |e|^{\cdot} + O_2^{\times}(ads) \longrightarrow O_2^-(ads) + |e|^{\cdot} \qquad (12)$$

with the hole trapping

$$|e|^{\cdot} + Zn^{\cdot} \longrightarrow Zn^{\cdot\cdot} \qquad (12a)$$

causing a photoadsorption. These two possibilities can be demonstrated by photoconductivity measurements at various oxygen pressures under illumination, represented in Fig. 1. As can be seen, the steady-state conductivity of zinc oxide under illumination with light of 365 mμ is independent of the chronological sequence of the admission of oxygen. In any case, the same conductivity will be reached independent whether oxygen of 20 torr is already present at the very beginning of the illumination or is added later during exposure to light [6]. This experiment confirmed by KWAN [7] demonstrates the possibility of a photoadsorption if the oxygen pressure is increased during illumination.

In view of this point, it is evident that a strong photodesorption occurred when the reduced zinc oxide was in contact with oxygen before illumination because of the large amount of loosely chemisorbed oxygen due to the large

concentration of free electrons near the surface of the zinc oxide. In contrast to these results, a photoadsorption is possible on ZnO samples annealed between 500 and 600°C at high oxygen pressures because of a lack of a sufficient number of free electrons which are now only available during illumination. Since a weak doping with lithium oxide strongly decreases the concentration of free electrons, according to

$$Li_2O + e' = 2\,Li|Zn|' + Zn^{\cdot} + ZnO\,, \qquad (13)$$

such a doping should, therefore, cause an extensive photoadsorption of oxygen, theoretically predicted by us [8]. This could be confirmed by measurements of the surface potential difference in the dark and under illumination [9]. While on pure ZnO single crystals, the surface photovoltage always exhibits a positive value, the lithium doped crystals exhibited at the very beginning of illumination a strong negative voltage which, however, changes over to a positive value after few minutes. The course of the surface photovoltage for pure and lithium-doped zinc oxide is represented in Fig. 2. The mechanism is at present not yet understood.

The chemisorption of carbon monoxide and hydrogen was extensively investigated on nickel oxide and zinc oxide in the dark and under illumination [10] [11] [12] using the concept of the space-charge theory [13].

3. TRANSPORT PHENOMENA THROUGH SOLID REACTION PRODUCTS DEMONSTRATED BY MEANS OF NICKEL OXIDATION

The oxidation of a metal is an important example of a reaction between a solid and a gas with surface interactions and transport phenomena through the oxide layer. This shall be discussed in greater detail in what follows. The first period of oxidation is usually determined by nucleation processes and crystal growth as well as by formation of pores. Therefore, a uniform and compact oxide layer cannot often be expected at the very beginning of oxidation.

As was discussed elsewhere [14] [15] [16], at sufficiently high temperatures oxidation generally occurs in accordance with a parabolic rate law because a diffusion process through the oxide layer is the rate-determining step. If a phase-boundary reaction becomes rate-determining then another - mainly a linear - rate law is observed. At low temperatures, other time laws have been found besides the parabolic and linear rate laws. Here, preferentially cubic, fourth power, logarithmic and reciprocal-logarithmic rate laws have been established. The last mentioned rate laws are observed for thin oxide layers in which a strong electric field causes the transport of ions.

Fundamental considerations have been published by MOTT and CABRERA [17]. On the basis of this paper, several authors have modified and improved the theoretical models [18] [19] [20]. An understanding of the logarithmic rate law is at present unsatisfactory. The most reasonable discussion is that by EVANS [21].

According to the oxidation experiments with nickel available in the literature [18] [22], the oxide-layer growth follows a logarithmic rate law at the very beginning of oxidation. The period of this rate law becomes smaller with increasing temperature. At 400°C, this period lasted about 6 hours up to an oxide thickness of 400 Å while at 500°C, the period was only 1 hour with a corresponding thickness of the oxide layer of about 1000 Å. After the logarithmic period of oxidation, the experimental data obtained at longer exposure time both at 400 and 500°C fit very well the fourth power rate law as can be seen in Fig. 3. This rate law could be derived under the reasonable assumption of established equilibria at both interfaces and under the presupposition of a rate-determining field transport of nickel ions through the NiO layer via nickel-ion vacancies. Therefore, with

$$\left| D \frac{dc}{dx} \right| \ll \left| c\, u \frac{dV}{dx} \right| \tag{14}$$

where D and u denote the diffusion coefficient and the mobility of the nickel ions via vacancies, respectively, and c the concentration of the vacancies, we obtain the transport equation

$$j(x) = - c\, u \frac{dV}{dx} \tag{15}$$

Here, j(x) is the mass flux in g-atoms·cm^{-2}·sec^{-1} and dV/dx the gradient of the electrical potential with x as local coordinate. Applying the POISSON equation

$$d^2V/dx^2 = - z\, c\, e/\varepsilon \tag{16}$$

with ε as dielectric constant and e as elementary charge, the fourth power rate law was obtained

$$\frac{dx}{dt} = \frac{k}{4} \frac{1}{x^3} \tag{17}$$

with

$$k = \frac{9\, \varepsilon\, u\, V^2}{2\, z\, e\, c_{Ni}} \tag{18}$$

Here, c_{Ni} denotes the volume concentration of the nickel ions in the oxide and z the valency of the migrating ion.

The measurements of the rate of nickel oxidation between 400 and 500°C at

higher oxygen pressures performed by ENGELL et al [18] were evaluated with the cubic rate law. Since the plot of the logarithmic values of the thickness of the oxide x versus the time t results in $x \sim t^{1/3,7} \rightarrow t^{1/3,9}$, the cubic rate law can no longer be maintained. Independent of this result, however, a cubic rate law was recently derived by WAGNER [23] under reasonable assumptions stimulated by oxygen isotope exchange experiments carried out by BORESKOV [24] on oxidized nickel foils. A plausible mechanism for the cubic rate law will be obtained if it is assumed that the rate of dissociation of oxygen molecules both for the exchange and for the nickel oxidation becomes rate-determining. Furthermore, the rate of both processes is inversely proportional to the thickness of the NiO film. According to Fig. 4, the slope of a plot of log $\vec{n}_O$ (= the rate of the oxygen exchange in mole/cm^{2}sec) and of log dx/dt (= the rate of nickel oxidation in mole/cm^{2}sec) versus log N (= the number of monolayers of consumed oxygen) is about -2. Thus, the following relation which was theoretically derived by WAGNER [23] results:

$$\log(dx/dt) = -2 \log N + \text{constant} \qquad (19)$$

or

$$dx/dt = k/x^2 \qquad (20)$$

if one considers that N is proportional to the oxide-layer thickness x. Upon integration of Eq. (20) with x = 0 at t = 0, it results in

$$x \sim t^{1/3} \; . \qquad (21)$$

This result, however, becomes understandable only if it is assumed that the rate of dissociation of the adsorbing oxygen molecules is proportional to the local concentration of free electrons present in thin NiO films in contact with metallic nickel, an assumption which is not yet verified for the p-type nickel oxide. Since the concentration of free electrons decreases with increasing distance from the Ni/NiO interface, the rate of oxidation decreases simultaneously. A rate-determining dissociation of oxygen molecules on NiO and Cu_2O films was also discussed by STOTZ [25]. This mechanism, however, is no longer applicable when a critical thickness of the NiO layer has been attained where the hole concentration and the nickel ion-vacancy concentration are now the predominant lattice-defect concentrations.

4. DESORPTION AND EVAPORATION OF SOLIDS BY ILLUMINATION IN HIGH VACUO

Desorption and evaporation often occur by the same mechanism. Generally, these processes are enhanced by increasing temperatures, high vacuum and strong illumination with light of sufficient energy if the solid is a photo-

conductor. Under the concept of this paper, photodesorption and photoevaporation shall be discussed for ZnO and CdS as typical examples of photoconductors. It could be demonstrated by several authors [26] [27] [28] that the decrease and increase of photocurrent is closely related with photoadsorption and photodesorption of oxygen on zinc oxide. Besides the photocurrent, the time function of the pressure also decreases or increases and the investigation of the ESR spectra represent useful methods for the study of these phenomena.

A photodesorption of oxygen could be studied under evacuation of ZnO at 10^{-5} torr at room temperature and under illumination with light of 370 mμ. It has been found that due to irradiation the desorption was indicated by the decrease of the g = 2,0 triplet signal indicating O_2^- species adsorbed on ZnO and by the increase of the g = 1,96 signal of the ESR measurements indicating free electrons and/or electrons in a donor level and, furthermore, by the simultaneous increase of the current [7] [31]. These results were confirmed by measurements of the surface photovoltage [9], of the field effect [29] and of the conductivity of ZnO single crystals [30]. Both an illumination with light of 370 mμ and a γ-irradiation of zinc oxide cause a desorption, especially, of oxygen weakly adsorbed at higher coverages [32].

The rate of evaporation of ZnO powder in a high vacuum of 10^{-5} torr between 450 and 525°C was independent of the absolute amount of ZnO and its specific surface but only dependent on the geometrical area like a vaporizing liquid. From the temperature dependence of the rate of evaporation, represented in Fig. 5, the activation energy was determined and found to be 30,2 kcal/mole [33] in agreement with the activation energy both of the reduction of ZnO with hydrogen [34] and of the evaporation of zinc metal [35]. The volatility was enhanced by the presence of water vapor.

The evaporation of cadmium sulfide with various deviations from the stochiometric composition between 680 and 740°C in the dark and under illumination is also worth mentioning. According to SOMORJAI [36] [37], it was found that a sulfur-doped CdS crystal with a resistivity at room temperature of about 10^{10} ohm.cm showed in high vacuo of about 10^{-6} torr at 696°C an evaporation rate in light which was five times larger than that in the dark. Fig. 6 represents some evaporation measurements. Studies of the wave-length dependence of the evaporation under illumination required that a light of = 640 mμ was necessary, in agreement with the band gap of CdS at 700°C. Furthermore, it was observed that the rate of evaporation increased linearly with the light intensity. The quantum efficiency of the light effect was approximately = 0,7

atom/photon in all experiments.

The results can be explained by a charge-transfer controlled evaporation and by the light-induced change in the composition of the CdS crystals. Noticeable is the fact that the rate of evaporation of a cadmium-doped CdS crystal started with a low value of $0{,}9 \cdot 10^{-5}$ g $cm^{-2}sec^{-1}$ and reached after 6 hours the speed of $1 \cdot 10^{-4}$ g $cm^{-2}sec^{-1}$, approximately equal to the rate of evaporation of a sulfur-doped CdS crystal under illumination with a light intensity of $2 \cdot 10^5$ μwatts/cm^2. The vacuum evaporation rate of pure cadmium sulfide is decreased by 50% if copper ions have been incorporated in the vaporizing surface. If copper ions are present in the bulk of the CdS crystal, the rate of vacuum evaporation is increased. With the incorporation of copper ions into the CdS lattice, according to

$$Cu_2S + e' = 2\,Cu|Cd|' + |S|^{\cdot} + 2\,CdS\,, \qquad (22)$$

the concentration of free electrons e' is decreased and the concentration of sulfur-ion vacancies $|S|^{\cdot}$ is increased. The yellow cadmium sulfide with the band gap of 2,4 ev at room temperature becomes black as a result of the copper acceptor centers with the electron exchange level between 0,6 and 1,0 ev above the valence-band edge [38] [39]. Furthermore, we have to consider that the rate of diffusion of sulfur vacancies is much larger than that of copper ions in CdS ($D_{700}(S) = 6{,}5 \cdot 10^{-6}$ and $D_{700}(Cu) = 1{,}6 \cdot 10^{-7}$ cm^2/sec) and that the rate of copper diffusion in CdS and the rate of evaporation of CdS are of the same order of magnitude.

Similarly to the light-induced desorption of oxygen from ZnO, we propose tentatively the following mechanism for the evaporation of cadmium sulfide under illumination. If it is assumed that the surface equilibrium is established

$$CdS \rightleftharpoons S^{-}(ads) + Cd^{+}(ads) \qquad (23)$$

the electron-hole pairs generated by light

$$h\nu \xrightarrow[700^{\circ}C]{640\ m\mu} e' \sim |e|^{\cdot} \qquad (24)$$

can cause the following sequence of reaction steps resulting in a simultaneous evaporation of cadmium and sulfur:

$$e' \sim |e|^{\cdot} + S^{-}(ads) \longrightarrow S^{x}(ads) + e' \qquad (25)$$

$$2\,S^{x}(ads) \longrightarrow S_2(gas) \qquad (26)$$

$$e' + Cd^{+}(ads) \longrightarrow Cd(gas) \qquad (27)$$

Further experiments are necessary in order to get more detailed information.

REFERENCES

[1] See for instance K. HAUFFE: Reaktionen in und an festen Stoffen, Springer-Verlag Berlin 1965, p. 187 ff.

[2] H.J. ENGELL and K. HAUFFE: Z. Elektrochem. Ber.Bunsenges.phys.Chem. 57 762 (1953).

[3] Y.P. SOLONITZIN: J.phys.Chem. USSR 32 2142 (1958).- A. TERENIN and Y.P. SOLONITZIN: Disc.Faraday Soc. 28 28 (1959).

[4] Y. FUJITA and T. KWAN: Bull.Chem.Soc. Japan 31 370 (1958).

[5] T.I. BARRY and F.S. STONE: Proc.Roy.Soc.(A) 255 124 (1960).- F. ROMERO-ROSSI and F.S. STONE: II. Congrès International de Catalyse, Paris 1960.

[6] W. DOERFFLER and K. HAUFFE: J. Catalysis 3 156, 171 (1964).

[7] T. KWAN, K.M. SANCIER, Y. FUJITA, M. SETAKA, S. FUKUZAWA and Y. KIRINO: J.Res.Inst. Catalysis, Hokkaido Univ. 16 53 (1968).

[8] K. HAUFFE and R. STECHEMESSER: Zur Randschicht-Theorie der Adsorption und Katalyse an Halbleiter-Katalysatoren, De Gruyter-Verlag Berlin 1970.

[9] K. HAUFFE and R. SCHMIDT: unpublished results.

[10] W. HERZOG and E.G. SCHLOSSER: Ber.Bunsenges.phys.Chem. 71 344, 358 (1967). - E.G. SCHLOSSER: Ber.Bunsenges.phys.Chem. 71 352 (1967).- K. HAUFFE: Ber. Bunsenges.phys.Chem. 65 321 (1961).

[11] A. CIMINO, E. MOLINARI and E. CIPOLLINI: Gazz.Chim.Ital. 90 79, 90, 120 (1960).- A. CIMINO, E. MOLINARI, P. CRAMAROSSA and G. GHERSINI: J.Catalysis 1 275 (1962).

[12] L. KÜCHLER and E.G. SCHLOSSER: Z.Naturforsch. 19a 54 (1964).

[13] P. AIGRAIN and C. DUGAS : Z. Elektrochem. 56 363 (1952).- K. HAUFFE and H.J. ENGELL: Z.Elektrochem. 56 366 (1952).- P.B. WEISZ: J.Chem.Phys. 20 1483 (1952); 21 1531 (1953).

[14] O. KUBASCHEWSKI and B.E. HOPKINS: Oxidation of Metals and Alloys, London 1962.

[15] K. HAUFFE: Oxidation of Metals, Plenum Press New York 1965.

[16] P. KOFSTAD: High-Temperature Oxidation of Metals, John Wiley New York 1966.

[17] N. CABRERA and N.F. MOTT: Rep.Progr.Phys. 12 163 (1949).

[18] H.J. ENGELL and K. HAUFFE: Metall 6 285 (1952).- K. HAUFFE and B. ILLSCHNER: Z.Elektrochem. 58 382, 467 (1954).- H.J. ENGELL, K. HAUFFE and B. ILLSCHNER: Z.Elektrochem. 58 478 (1954).

[19] T.B. GRIMLEY and R.M.W. TRAPNELL: Proc.Roy.Soc.(A) 234 [illegible]5 (1956).

[20] A.T. FROMHOLD, jr.: Nature 200 1309 (1963); J.Chem.Phys. 38 282, 2041 (1963); 40 3335 (1964); J.Phys.Chem.Solids 24 1081, 1309 (1963).

[21] U.R. EVANS: The Corrosion and Oxidation of Metals, London 1960.

[22] E.A. GULBRANSEN and K.F. ANDREW: J.Electrochem.Soc. 101 128 (1954).

[23] C. WAGNER: Written Paper, not yet published.

[24] G.K. BORESKOV: Disc.Faraday Soc. 41 263 (1966).

[25] S. STOTZ: Ber.Bunsenges.phys.Chem. 70 769 (1966).

[26] I.A. MYASNIKOV and S.Y. PSHEZHETSKII: Doklad.Akad.Nauk SSSR 99 125 (1954).

[27] D. MELNICK: J.Chem.Phys. 26 1136 (1957).

[28] D. MEDVED: J.Chem.Phys. 28 870 (1958).

[29] G. HEILAND: Disc.Faraday Soc. 28 168 (1959); J.Phys.Chem.Solids 22 227(1961)

[30] E. MOLINARI, F. CRAMAROSSA and F. PANICCIA: J.Catalysis 4 415 (1965).

[31] K.M. SANCIER: J.Catalysis 6 313 (1966).

[32] T.I. BARRY and K. KLIER: Disc.Faraday Soc. 31 219 (1961).

[33] K. HAUFFE and A.J. HEGEDÜS: unpublished results.

[34] A.J. HEGEDÜS and A.B. KISS: Microchim.Acta 8 813 (1966).

[35] L. GMELIN: Handbuch der anorg. Chem., 8. Auflage, System Nr. 32, Zink und Erg-Bd. Leipzig-Berlin 1924 u. 1956.

[36] G.A. SOMORJAI and J. LESTER: J.Chem.Phys. 43 1450, 1456 (1965).

[37] G.A. SOMORJAI: Surafce Sci. 2 298 (1964).

[38] R.H. BUBE: Photoconductivity of Solids, John Wiley & Sons, New York 1960.

[39] A. DREEBEN: J.Electrochem.Soc. 111 174 (1964).

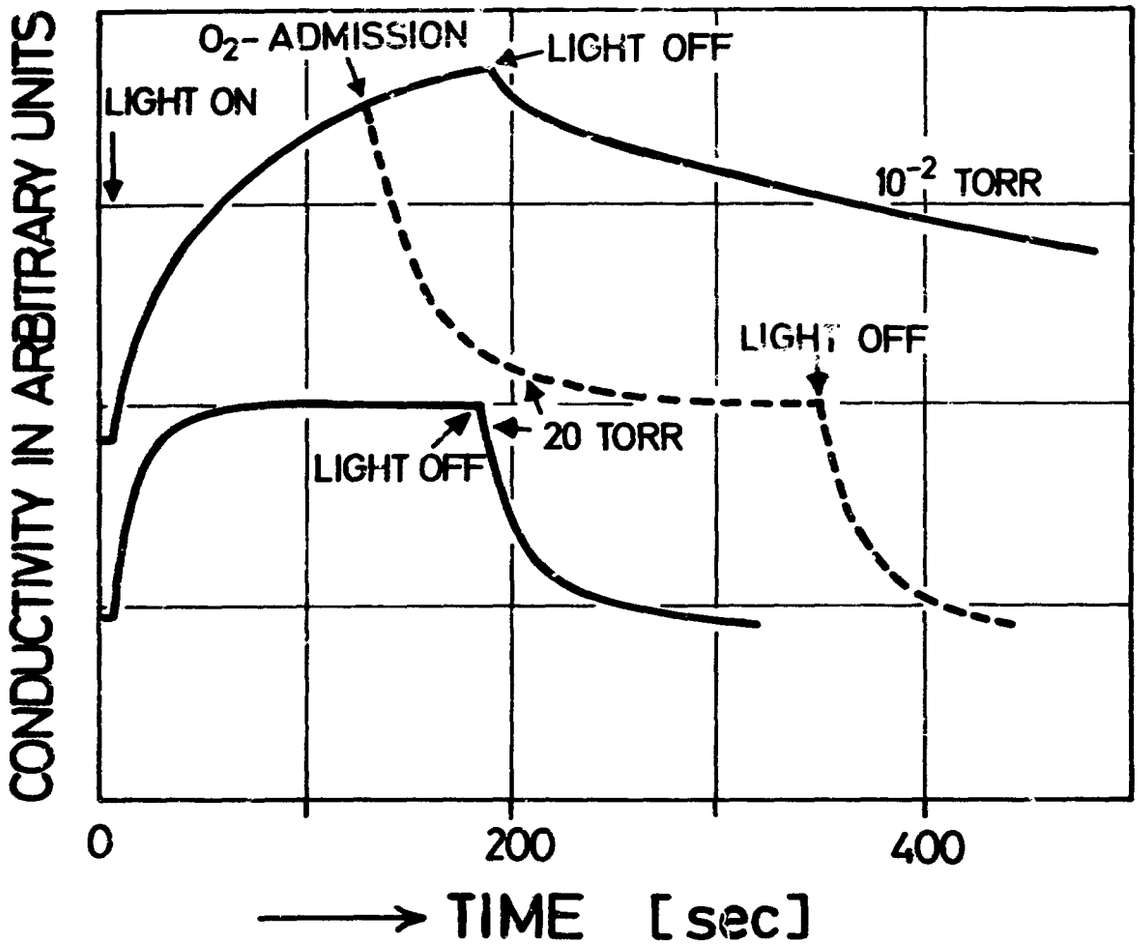

Fig. 1 The decrease of the photoconductivity of zinc oxide (sintered powder) due to admission of oxygen of 20 torr at 160°C, according to DOERFFLER and HAUFFE.

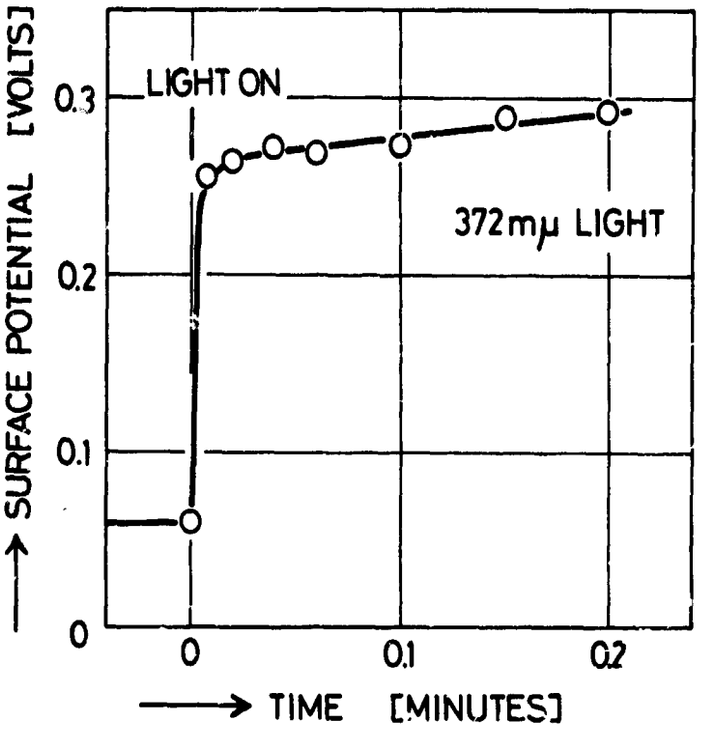

a) for an undoped crystal

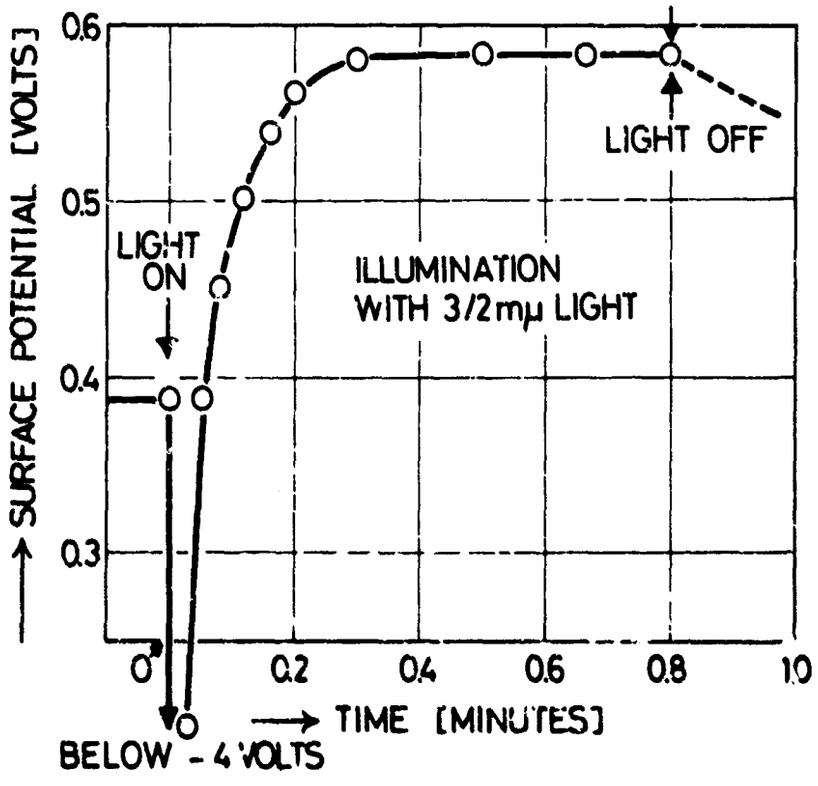

b) for a Li_2O doped crystal

Fig. 2 The surface photovoltage of pure and doped zinc oxide single crystals at 23°C versus the time under illumination at 370 mμ, according to HAUFFE and SCHMIDT.

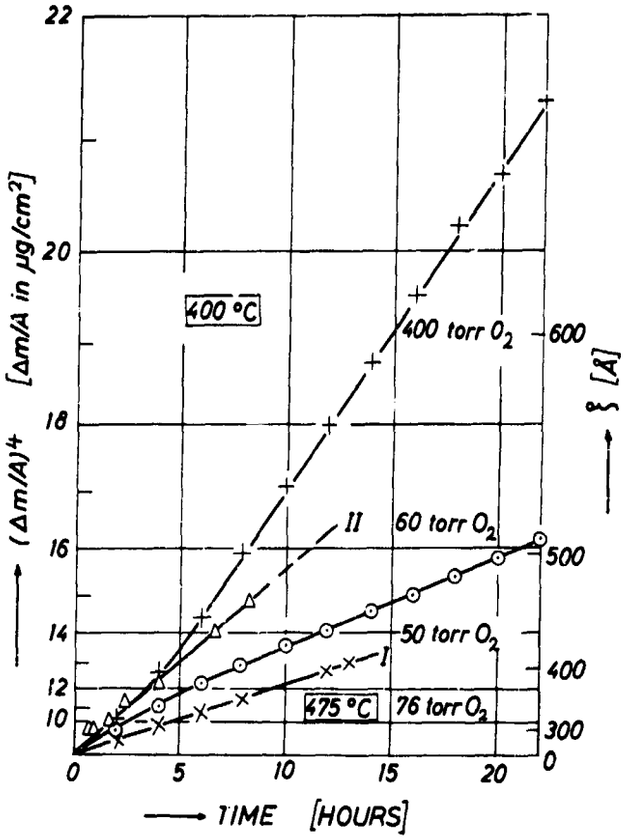

Fig. 3 Time dependence of nickel oxidation in the thin oxide layer region at 400°C and various oxygen pressures obeys the fourth power rate law, according to HAUFFE et al.

\+ 400, Δ 60, ⊙ 50 torr oxygen;

× at 475°C and 76 torr oxygen (experimental data from GULBRANSEN)

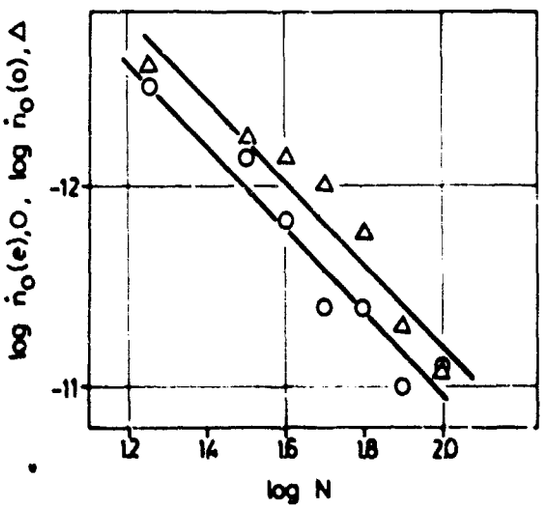

Fig. 4 The dependence of the rate $\dot{n}_0(e)$ of the oxygen exchange on NiO and the rate $\dot{n}_0(o)$ of nickel oxidation at 250°C on the numbers N of monolayers of consumed oxygen, according to BORESKOV.

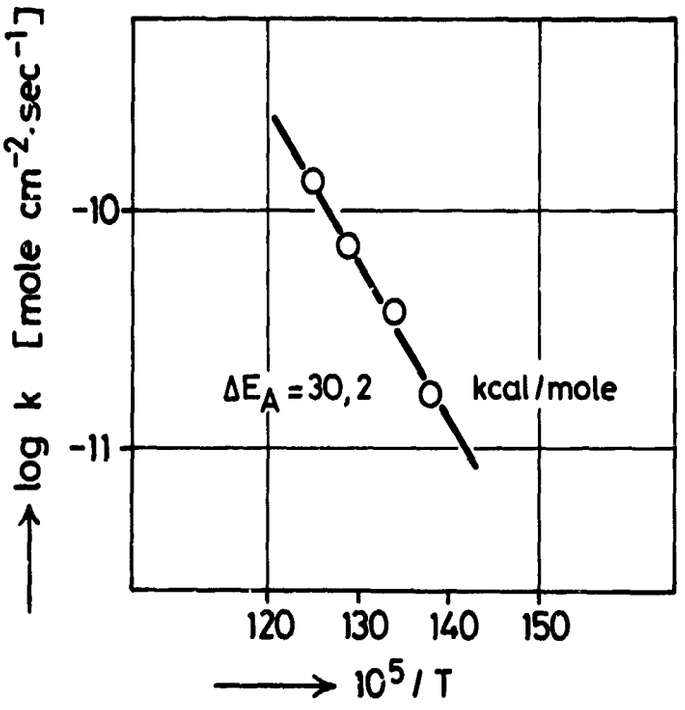

Fig. 5 Temperature dependence of the rate of ZnO evaporation in vacuo of 10^{-5} torr between 450 and 525°C, according to HAUFFE and HEGEDÜS.

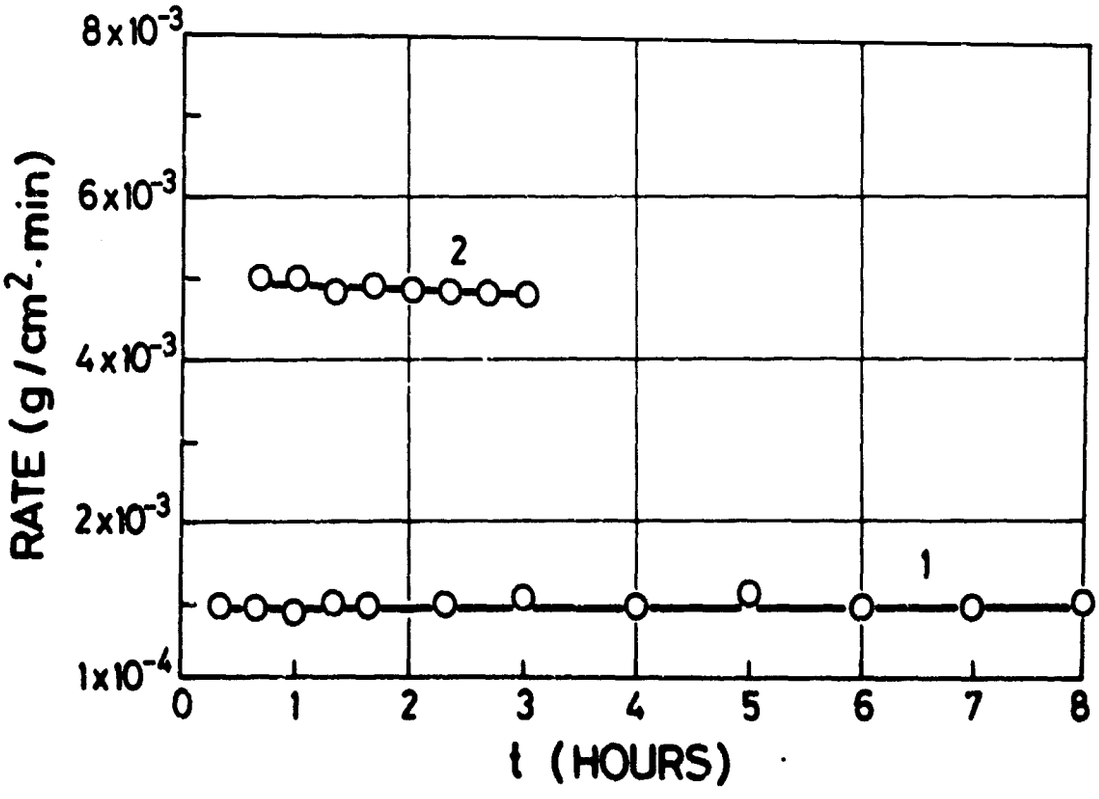

Fig. 6 The evaporation rate of sulfur-doped (at 1200°C and 20 atm sulfur) CdS single crystal from the (0001) surface at 696°C both in the dark (1) and under illumination (2), according to SOMORJAI and LESTER.

A REVIEW OF METAL IGNITION AND FLAME MODELS

by

I. Glassman, A. M. Mellor, H. F. Sullivan and N. M. Laurendeau

Princeton University, Princeton, USA

SUMMARY

Based upon the classic work of Frank Kamenetskii, a physical model of the heterogeneous ignition process of metals was developed. This model is compared with other theories of metal ignition concerned with bulk samples, quiescent piles, single particles and dust dispersions. The new model is based upon the concept of a transition temperature - the temperature at which the oxide layer on the metal becomes non-protective in the sense that a reaction rate independent of time describes the behaviour of the system at constant temperature. The model postulates that the ignition temperature must be greater than both the transition and the critical temperatures. It further relates pyrophoricity to the concept of a transition temperature.

The transition temperature thought to be a unique value characteristic to the metal, such as the oxide melting point, has been shown by Kuehl to be pressure dependent in the case of aluminum. Kuehl's work and the recent supporting evidence of Laurendeau on zinc are reviewed.

With respect to the burning mechanisms of metals, reviewed are the finite reaction zone model of Coffin, liquid oxide bubble model of Fassell, collapsed reaction zone model of Brzustowski and Glassman, extension of the Brzustowski-Glassman model by Knipe, the heterogeneous reaction model of Markstein and the very recent, broad homogeneous reaction zone model of Sullivan.

IN THIS REVIEW OF IGNITION AND FLAME MODELS OF METALS, the authors will use their own work as the central basis of discussion. The work of others will be well-referenced and discussed and various ignition theories will be reviewed extensively in an appendix. The early work in metal combustion at Princeton (1), (2), (3), (4) will be mentioned only briefly. Various compendia and general reviews (5), (6), (7), (8) of metal combustion are readily available.

IGNITION MODELS*

The impetus at Princeton for a study of ignition phenomena came about through certain results obtained in earlier work on combustion which made use of the technique of ohmic heating of wire samples (4), (9), (10), (11), (12).

While investigating the flames produced by aluminum wires, Brzustowski (4), (9), found that the ignition temperature of aluminum in oxygen-argon atmospheres was very close to the melting point of aluminum oxide at pressures greater than 300 torr. In addition, Friedman and Macek (13) had shown that the Al_2O_3 coating must melt in order that aluminum undergo vapor-phase combustion. Later Kuehl (14) showed that in general the ignition temperature of aluminum is very close to 2042°C., the melting point of the metal oxide.

Mellor (10), (11) carried out similar experiments with anodized aluminum wires in carbon dioxide-oxygen atmospheres. He observed two things that were very different from the results of Brzustowski. First, in the carbon dioxide-argon mixtures at pressures below 300 torr, a cylindrical vapor-phase diffusion flame appeared before the wire broke. On the other hand, in the oxygen-argon mixtures, the wire broke thereby exposing molten aluminum to the oxidizing atmosphere before a vapor-phase flame appeared (4), (9). Secondly, on the basis of total power required at ignition, it was easier to ignite anodized aluminum wires at similar pressures in CO_2-Ar atmospheres than it was to ignite them in O_2-Ar atmospheres (10), (11).

To explain these results it was necessary to consider the pre-ignition oxidation of the metal. In CO_2-Ar mixtures, little oxidation occurs during the pre-ignition period while in O_2-Ar mixtures, a very thick oxide coating builds up on the surface of the metal. In general, the anodized film is porous but in oxygen containing atmospheres, these pores are filled by the natural oxidation process during this preignition period (15). Thus, in this case, melting of the oxide occurs before ignition can take place.

For an anodized film of Al_2O_3 considered here, a thin barrier layer of oxide exists between the outer porous layer and the metal substrate. Even in the case of a CO_2-Ar atmosphere, however, it is suggested that the ignition temperature is still equal to the melting point of Al_2O_3 since only the barrier layer need be melted to expose the molten aluminum to this oxidizing atmosphere (15). Thus, in summary, since little oxidation occurs before ignition in a CO_2-Ar atmosphere and since the anodized coating is porous, ignition occurs in a cylindrical vapor-phase flame upon melting of the barrier layer before the wire breaks at that point when the anodized coating completely melts**. Obviously, because of the little oxide built up before ignition, the total power at ignition for the anodized wire is less in the CO_2-Ar mixtures than in the O_2-Ar mixtures.

This work with aluminum and other work with magnesium ribbons (4), (9), (10), (11) showed primarily that the ignition of metals is strongly dependent on the pre-ignition surface oxidation reaction in the environment of interest. Surface oxidation reactions determine whether or not a particular metal coating is protective in a certain environment in a particular temperature range. If the metal coating is protective, then the metal sample cannot ignite. However, usually the oxide coating becomes nonprotective at higher temperatures and the sample may then ignite.

This surface coating is the unique property of the metal ignition problem that makes it very difficult to analyze mathematically. The ignition problem has been well treated for the homogeneous case, but is not at all well understood in the case of a simple heterogeneous reaction. Here the situation becomes even more difficult since one must consider the complicating factor brought about by the low temperature oxidation process common to all metals of interest.

---

* This section has been extracted from the M.S.E. thesis of Laurendeau (17). The content is based extensively on the earlier Ph.D. thesis of Mellor (12).

** A more appropriate explanation for the appearance of this cylindrical vapor-phase flame will be offered in a later section.

These findings coupled with the well-known concepts of the homogeneous problem led to Mellor's work on the development of both a model for the heterogeneous ignition of metals and subsequent experimental verification of certain trends predicted by that model (15), (12). Later work by Laurendeau (17) further substantiated and clarified some aspects of the model primarily through an experimental determination of the ignition temperatures of many common non-toxic metals in an oxygen atmosphere.

THE STEADY STATE MODEL OF METAL IGNITION - As mentioned previously, any model which attempts to describe the metal ignition process must take into consideration the formation of solid phase products on the surface during the pre-ignition reaction. Thus, metal ignition is usually much more complicated than the heterogeneous ignition of other simple fuel-oxidizer systems. Because of this difficulty, Mellor developed a qualitative model of metal ignition based to a large extent on the classical thermal theories of homogeneous ignition as demonstrated most lucidly by Frank-Kamenetskii in his comprehensive work describing the effects of heat and mass transfer in chemical kinetics (16).

As is well known, both a stationary and a non-stationary approach exists for the description of the homogeneous ignition phenomena. Because of the complications involved in any heterogeneous process, it is best to emphasize the stationary approach in this case. It may be shown that the non-stationary approach can equally well describe the metal ignition process, but the argument is somewhat laborious (See Ref. 12). Therefore, since it is of interest here to only describe those aspects of the model directly essential to this particular work, the steady-state approach will be followed in order to make the principal ideas as clear as possible to the reader. Those interested in a detailed description of both the stationary and non-stationary aspects of the model along with an excellent discussion of the relationship between the classical thermal theories of homogeneous ignition and the present model may wish to consult Chapter II of Ref. 12.

It seems important at this time to indicate the intent of the early work at Princeton by Mellor. He attempted to construct a qualitative model which would take into consideration metals of all types and sizes in all possible atmospheres. An investigation of other models of metal ignition (12) (see Appendix I) indicate that they are much more quantitative than the present description in that they attempt to calculate ignition temperatures; however, each of these models is restricted to only a very limited range of practical experimental situations.

HETEROGENEOUS IGNITION WITH GAS-PHASE REACTION PRODUCTS - Before metal ignition, i.e., heterogeneous ignition with solid-phase reaction products is considered, it is of paramount importance that a slightly simpler case be investigated, that is, the ignition of a solid fuel via reaction with a gaseous oxidizer involving only gaseous reaction products. An example of this might perhaps be a carbon particle reacting in air or oxygen (12).

As pointed out by Mellor (12), in the case of a heterogeneous system, where the exothermic reaction occurs on the surface as opposed to throughout a reaction volume as in a homogeneous system, the interaction is characterized by a uniform surface temperature T_s instead of a gas temperature, and all heating terms are expressed per unit area instead of per unit volume. Thus, in order to investigate the case of a spherical metal particle in a static gaseous atmosphere for which all the products are assumed to be in the gaseous state, a heat balance is conveniently made in a thin control volume at uniform surface temperature T_s enclosing only the reacting surface of the metal*.

This heat balance is constructed by examining the rate of heat input and the rate of heat loss from the aforementioned thin control volume, both quantities being functions of the surface temperature T_s. Consider** first then the chemical energy release rate in cal/cm^2 -sec. It may be written as:

$$\dot{q}_{chem} = \dot{m} Q \qquad \text{Eq (1)}$$

where $\dot{m}$ is the molar reaction rate in moles of fuel per cm^2 per second and Q is the chemical energy release in calories per mole of fuel.

---

* Since a steady state is being considered here, it is necessary that the control surface be stationary. Therefore, in this development, reactant depletion is neglected.

** In the present discussion, only chemical heat input will be considered.

The chemical energy release is given by the expression:

$$Q = \sum_{\substack{\text{react.} \\ i}} n_i \, \Delta H_{i,T_s} - \sum_{\substack{\text{Prod.} \\ j}} n_j \, \Delta H_{j,T_s} \qquad \text{Eq (2)}$$

where the subscript i indicates reactants and the subscript j products, where

$$\Delta H_{k,T_s} = \Delta H_{f,k}^{298} + (H_{T_s} - H_{298})_k \qquad \text{Eq (3)}$$

and where
T_s = surface temperature, $^\circ$K;
n_k = no. of moles of species k per mole of fuel;
$H_{f,k}$ = standard heat of formation of species k at 298°K, cal/mole of k;
$H_{T,k}$ = enthalpy of species k at T$^\circ$K, cal/mole of k.

The molar reaction rate is given by two expressions, depending on whether the surface temperature T_s is such that the reaction rate is controlled by kinetics or by diffusion of the oxidizer. At lower temperature, $\dot{m}$ may be given by:

$$\dot{m} = A e^{-E/RT_s} C_s^n \qquad \text{Eq (4)}$$

where
A = pre-exponential factor, $cm^{3n-2}/moles^{n-1}$. sec;
E = activation energy, cal/mole;
R = universal gas constant, cal/mole.$^\circ$K;
C_s = oxidizer concentration at the surface, mole of fuel/cm^3;
n = order of the reaction, dimensionless, and, therefore, here the dependence of $\dot{q}_{chem}$ on T_s is exponential due to the controlling kinetic Arrhenius factor.

At higher temperatures, $\dot{m}$ may be given by:

$$\dot{m} = \frac{Nu \, D}{r} (C - C_s) \qquad \text{Eq (5)}$$

where
Nu = diffusion Nusselt number, dimensionless;
D = diffusivity of the oxidizer, cm^2/sec;
r = a characteristic dimension of the system, cm;
C = oxidizer concentration in the gas, moles of fuel/cm^3;
and, therefore, here the dependence of $\dot{q}_{chem}$ on T_s is given predominantly by the diffusivity D which varies as the 1.67 power of temperature (18).

Thus, as T_s is increased, the value of $\dot{q}_{chem}$ also increases due to the variation of Q with T_s, but the form of $\dot{q}_{chem}$ vs T_s is given by an S-shaped curve (See Fig. 1a) which emphasizes the control of the chemical heat release by the molar reaction rate, $\dot{m}$. At lower temperatures $\dot{m}$ is controlled by kinetics, but as T_s is increased, diffusion of the oxidizer through the inert gas to the particle surface becomes important and, therefore, $\dot{m}$ then is controlled by the diffusion process. In addition to diffusion, the drop in the slope of the $\dot{q}_{chem}$ vs T_s curve at higher temperatures is partially due to a small amount of dissociation of the reaction products.

Consider next the heat loss rate in cal/cm^2. sec from the same control volume described previously. Recalling that this control volume includes only the reaction surface, then the rate of heat loss $\dot{q}_{loss}$ may be written as follows:

$$\dot{q}_{loss} = \dot{q}_{cond,f} + \dot{q}_{cond,g} + \dot{q}_r \qquad \text{Eq (6)}$$

where
$\dot{q}_{cond,f}$ = conductive heat loss into the fuel particle, cal/cm^2.sec;
$\dot{q}_{cond,g}$ = conductive heat loss into the ambient static gas, cal/cm^2.sec;
$\dot{q}_r$ = radiative heat loss to the environment, cal/cm^2.sec;
all where each of these terms is of course a function of the surface temperature T_s.

Notice that in this equation, there is no term indicating heat loss by means of mass transfer of gaseous products to the environment. In this analysis, the gas phase products are considered to be instantaneously removed as they are produced at temperature T_s and they are not allowed to participate in any heat trans-

fer to the environment. This approach is taken not solely for simplicity, but in looking forward to the adaptation of this model to the case of heterogeneous metal ignition as characterized by the deposition of a solid-phase product on the surface, it is recognized that such a product cannot participate in the transport of heat from the reacting surface to the environment.

By expressing each of the above terms explicitly, Eq (6) can then be written in the following manner:

$$\dot{q}_{loss} = k_f \left.\frac{\partial T}{\partial r}\right|_{r=r_o^-} + k_g \left.\frac{\partial T}{\partial r}\right|_{r=r_o^+} + \epsilon\sigma\left(T_s^4 - T_r^4\right) \qquad \text{Eq (7)}$$

where

k = thermal conductivity of the fuel or oxidizer gas mixture (denoted respectively by subscript f or g), cal/cm.sec.°K;

= temperature gradient evaluated at the surface of the particle ($r=r_o$) either into the fuel ($r=r_{o-}$) or into the oxidizer ($r=r_{o+}$), °K/cm;

= total surface emissivity, dimensionless;

= Stephen-Boltzmann constant, cal/cm^2·sec. (°K)^4;

T_r = effective radiation temperature of the environment, °K.

The general form of the $\dot{q}_{loss}$ vs T_s curve as obtained from the addition of these three heat loss terms is depicted in Fig. 1b. Notice that at the origin, where T_s is equal to the ambient gas temperature T_{amb}, $\dot{q}_{loss}$ is equal to zero. In order that this be true, it is necessary that the overall temperature (both internal and surface) of the sample be equal to T_{amb} before heating begins. If T_{amb} is taken to be room temperature (298°K), then this becomes a perfectly reasonable approximation of an actual physical heating process. In other words, for convenience, the heating of the sample is considered to take place in a room temperature environment in which the original temperature of the sample is also 298°K. Thus, if $T_s = T_{amb} = 298$°K, then $\dot{q}_{loss}$ is equal to zero since only then is $\dot{q}_{cond,f}$ equal to zero.

Other values of T_{amb} can also be considered, but it is felt that this example is the easiest to visualize; indeed the curves can quite simply be extended to other values of T_{amb}, as will be made clearer in a discussion of Fig. 2 at the end of this section.

If the most general case is considered, the $\dot{q}_{chem}$ and $\dot{q}_{loss}$ curves may be combined in the fashion depicted in Fig. 1c in which three points of intersection defining equilibrium conditions at the sample surface are obtained. The end points of intersection at the low and high temperature regions of Fig. 1c are both stable equilibrium temperatures with respect to small perturbations of the surface temperature T_s since:

$$\left(\frac{\partial \dot{q}_{chem}}{\partial T_s}\right)\Bigg|_{T_s = T_{oxid}} < \left(\frac{\partial \dot{q}_{loss}}{\partial T_s}\right)\Bigg|_{T_s = T_{oxid}} \qquad \text{Eq (8)}$$

and

$$\left(\frac{\partial \dot{q}_{chem}}{\partial T_s}\right)\Bigg|_{T_s = T_f} < \left(\frac{\partial \dot{q}_{loss}}{\partial T_s}\right)\Bigg|_{T_s = T_f} \qquad \text{Eq (9)}$$

Physically this means that at temperatures somewhat greater than T_{oxid} or T_f, $\dot{q}_{loss}$ is greater than $\dot{q}_{chem}$ and thus T_s tends to decrease; at temperatures somewhat less than T_{oxid} or T_f, $\dot{q}_{loss}$ is less than $\dot{q}_{chem}$ and T_s tends to increase. Therefore, T_{oxid} and T_f are stable temperatures to which the system tends to converge.

The high temperature intersection T_f physically represents the flame temperature and is then the steady-state self-sustained combustion mode of the system. For metals, the flame temperature is limited by enthalpy considerations to the boiling point of the metal oxide.

The low temperature intersection T_{oxid} is referred to as the oxidation temperature. It physically represents the ordinary slow, kinetically controlled, surface oxidation reaction common at this low temperature. However, as can be seen by the fact that the $\dot{q}_{chem}$ and $\dot{q}_{loss}$ curves are nearly tangent at T_{oxid}, the true oxidation process realistically occurs over a short temperature range [12].

The center point of intersection, denoted by T_{crit}, is called the critical temperature and is an unstable equilibrium surface temperature since:

$$\left(\dot{q}_{chem}\right)\Big|_{T_s = T_{crit}} = \left(\dot{q}_{loss}\right)_{T_s = T_{crit}}$$

$$\left(\frac{\partial \dot{q}_{chem}}{\partial T_s}\right)\Big|_{T_s = T_{crit}} > \left(\frac{\partial \dot{q}_{loss}}{\partial T_s}\right)_{T_s = T_{crit}} \qquad \text{Eq (10)}$$

Thus, surface temperatures less than T_{crit} tend to decrease to T_{oxid} since here $\dot{q}_{loss}$ is greater than $\dot{q}_{chem}$ and surface temperatures greater than T_{crit} tend to increase to T_f since here $\dot{q}_{loss}$ is less than $\dot{q}_{chem}$. It is the latter of the above situations that is so important in this development, i.e., once the critical temperature is reached, the system tends to higher temperatures. Because this phenomenon is so vital to a complete understanding of the ignition problem, the critical temperature T_{crit} is defined as follows: T_{crit} is the lowest initial surface temperature from which the surface may self-heat to reach the steady-state combustion configuration.

The critical temperature is commonly called the spontaneous ignition temperature in the literature. It is here labeled the critical temperature in order to avoid confusion with the experimental ignition temperature shortly to be discussed. The existence of this critical temperature is the basic cause of the metal dust explosions that on occasion occur in various industrial plants.

It is now important to define an ignition temperature T_{ign} which can be easily related to the experimental ignition temperature. For most systems, the experimental ignition temperature is usually taken to be that temperature at which the flame appears. When the flame appears, whether it be vapor-phase or surface combustion, there occurs simultaneously the most rapid rate of change with time of both light intensity and sample temperature*. Since temperature runaway is the most obvious phenomenon of the ignition process and since it is the easiest to measure, especially for metals which burn of the surface, it is convenient to define a theoretical ignition temperature in terms of this particular property of the ignition process.

Now, since the aforementioned control volume is assumed to be at a uniform temperature T_s, the time rate of change of the surface temperature can be expressed as a linear function of the quantity $(\dot{q}_{chem}-\dot{q}_{loss})$ as follows:

$$\rho\,\delta\,c_p\,\frac{\partial T_s}{\partial t} = \dot{q}_{chem} - \dot{q}_{loss} \qquad \text{Eq (11)}$$

where

ρ = density of the fuel, g/cm^3;
δ = thickness of the control volume ($\delta \neq 0$), cm;
c_p = fuel specific heat, cal/g.°K.

According to Eq. (11) then, the ignition temperature can be defined by that point at which the maximum difference between $\dot{q}_{chem}$ and $\dot{q}_{loss}$ exists. Now since the ignition temperature must be above the critical temperature, and below the flame temperature, then the ignition temperature T_{ign} can be represented graphically as in Fig. 2**.

Mathematically, the ignition temperature is defined by looking for the maximum value of $(\dot{q}_{chem}-\dot{q}_{loss})$ above T_{crit} but below T_f. Therefore:

$$\frac{\partial}{\partial T_s}\left(\dot{q}_{chem} - \dot{q}_{loss}\right)\Big|_{T_s = T_{ign}} = 0 \qquad \text{Eq (12)}$$

where

$$T_{crit} \leq T_{ign} \leq T_f \qquad \text{Eq (13)}$$

---

* In the course of many experiments with various metals, the maximum change of light intensity and temperature appear to always coincide.

** In this graph, the internal coordinate system is identical to Fig. 1c.

Thus, the full definition of the experimental ignition temperature becomes the following:

$$\left\{ \left(\frac{\partial \dot{q}_{chem}}{\partial T_s}\right)\Big|_{T_s=T_{ign}} = \left(\frac{\partial \dot{q}_{loss}}{\partial T_s}\right)\Big|_{T_s=T_{ign}} \right\} \quad \text{Eq (14)}$$

$$T_{crit} \leq T_{ign} \leq T_f$$

The above then points out the theoretical difference between T_{crit} and T_{ign} as interpreted on a $\dot{q}$ vs T_s diagram. At T_{crit}, the magnitudes of $\dot{q}_{chem}$ and $\dot{q}_{loss}$ are equal; at T_{ign}, the slopes of the $\dot{q}_{chem}$ and $\dot{q}_{loss}$ curves are equal. Physically, this distinction that has been introduced between the ignition temperature and the critical or spontaneous ignition temperature is a very important one, since it allows for the distinct possibility of the existence of an ignition delay time. This possibly long self-heating time, possibly due to an oxide accumulation on the surface, is what must be prevented when metal particles are used to increase the performance of rocket combustion chambers, for example. Thus, in these applications, the ignition temperature, not the critical temperature, is of prime importance in dealing with ignition inefficiencies.

As intimated above, the ignition delay time in metal ignition may be of the order of minutes rather than a few seconds or milliseconds as in a homogeneous gaseous ignition process. This large difference in ignition delay time between heterogeneous and homogeneous systems is essentially due to the need for oxidizer diffusion to, and absorption on, the fuel surface in the case of a heterogeneous chemical reaction. If the rate of chemical heat input, $\dot{q}_{chem}$, for a heterogeneous system is represented in Arrhenius form, as for a homogeneous system, then the computed values of $\dot{q}_{chem}$ will indicate the influence upon heterogeneous reaction of the physical processes of diffusion and absorption. The much lower value of $\dot{q}_{chem}$ for a heterogeneous system, as compared to that in a homogeneous syste, accounts for the large ignition delay time for such reactions, since $\partial T/\partial \tau$ is a linear function of $(\dot{q}_{chem}-\dot{q}_{loss})$ for homogeneous as well as heterogeneous systems.

Now, for both homogeneous and heterogeneous systems in the kinetic range, $\dot{q}_{chem}$ and thus the ignition delay time is a strong function of the kinetic frequency or pre-exponential factor if the appropriate reaction rate is expressed in Arrhenius form (19). On the basis of collision theory, it has been found that in general the more complicated the chemical reaction process, the smaller in magnitude is the kinetic frequency factor and thus the slower is the reaction rate (20). For homogeneous bimolecular reactions, the frequency factor is on the order of 10^{10} to 10^{14} cm^3/mole-sec and for unimolecular reactions, around 10^{13} to 10^{17} sec^{-1} (19,20). For heterogeneous reactions, the pre-exponential factor has a value for metal systems of 10^{-3} to 10^{-8} gm^2/cm^4-sec for protective oxide systems and 10^{-1} to 10^{-6} gm/cm^2-sec for non-protective oxide systems (21,22). Thus, for a complicated heterogeneous metal reaction, $\dot{q}_{chem}$ is much smaller in magnitude; in addition, there is a further reduction of $\dot{q}_{chem}$ and thus a longer ignition delay time for a heterogeneous reaction due to the onset of the diffusional control of the reaction rate at higher surface temperatures.

Fig. 2 displays all of the above defined surface temperatures on a diagram covering the entire temperature range starting at 0°K. The internal coordinate system has its origin at $\dot{q}=0$, $T_s=T_{amb}$ and is the coordinate system used in Fig. 1. However, the extension to 0°K is made here in order to discuss some of the properties of the heterogeneous ignition system in more detail.

At 0°K, $\dot{q}_{chem}$ goes to zero; this is appropriate since at lower temperature the molar reaction rate $\dot{m}$ which is a factor in determining $\dot{q}_{chem}$ is in the kinetic regime and as T_s goes to zero, indeed the exponential term in Eq. (4) approaches zero thereby forcing $\dot{m}$ and thus $\dot{q}_{chem}$ to also approach zero. As discussed previously $\dot{q}_{loss}$ approaches zero as T_s approaches T_{amb} if the temperature of the sample before heating (at $t=0^-$) is also T_{amb}. The ambient temperature is usually taken to be 298°K since the process is much easier to visualize at room temperature. However, any other value of T_{amb} may be used, but the initial temperature of the sample must also be raised to T_{amb} in order that $\dot{q}_{loss}$ be equal to zero at T_{amb}. This may seem very artificial, but again, it is done in this manner simply for the sake of clarity in the development of the model.

More importantly, however, the ambient temperature is taken to be 298°k because this will give the most general results in terms of the three points of intersection shown in Fig. 1c. In other words, by varying T_{amb} for a fixed value of T_s, $\dot{q}_{chem}$ stays essentially constant while $\dot{q}_{loss}$ varies a great deal and thus it is possible that only one point of intersection, either at the low temperature or high temperature end of the scale, will appear. In this case, the sample will either never ignite or always ignite. This situation is not of general interest here and thus

T_{amb} is taken to be near room temperature. However, even in this case, if the initial temperature of the sample is kept at the appropriate T_{amb} for the system, then $\dot{q}_{loss}$ is equal to zero at that particular $T_s = T_{amb}$.

In the unsteady problem, $\dot{q}_{loss}$ need not always be equal to zero at $T_s = T_{amb}$. At any constant value of T_s, once the heating process has begun, $\dot{q}_{loss}$ decreases equally over the entire temperature range, due to the conduction losses to the interior of the metal sample (12). In fact, $\dot{q}_{loss}$ takes on negative values at $T_s = T_{amb}$ since now the internal energy of the sample tends to heat the surface because the interior temperature is greater than the surface temperature, and therefore $\dot{q}_{loss}$ actually becomes a heat source. Now, a diagram similar to Fig. 2 can be graphed for any time t* in the heating process. But for any time greater than t=0, $\dot{q}_{loss}$ will not be equal to zero at $T_s = T_{amb}$ since the entire sample has now gained energy from the heating process at a higher surface temperature.

This last paragraph deserves a little more clarification since it implies other details of the model as interpreted here that are not so obvious. Recall that Fig. 2 represents a strictly time-independent system and, therefore, one must use extreme caution in analyzing for example the variation of surface temperature with time in an actual physical heating process. This graph then strictly represents the instantaneous attainment of a surface temperature T_s artificially put on the surface of a fuel sample of original overall temperature T_{amb} in a gaseous atmosphere of temperature T_{amb}. This is somewhat analogous to the dumping of a sample in a heat bath in which the sample surface instantaneously attains the bath temperature, except that here there is another variable in that the atmosphere has an independent temperature T_{amb} equal to the overall temperature of the sample at time $t = 0^-$.

Now, imagine the sample in equilibrium with the oxidizing atmosphere at T_{amb}. Instantaneously a higher temperature T_s is made to appear on the fuel surface; it remains there until at a later time when instantaneously the original ambient temperature T_{amb} is put on the surface. At this juncture, $\dot{q}_{loss}$ cannot be equal to zero at $T_s = T_{amb}$ since the interior of the sample is not at temperature T_{amb}, but at a higher temperature, which tends to heat the surface thus making $\dot{q}_{loss}$ a negative quantity since indeed this process represents a heat gain. Therefore, all the diagrams in this report represent steady-state situations at time $t=0^+$ when $\dot{q}_{loss}$ is equal to zero at $T_s = T_{amb}$.

Not only is this done for better visualization of the actual theoretical ignition process, but also for a much more practical reason. The essential use for these diagrams is to be able to predict if a fuel sample will or will not ignite. If it does not ignite, it must stabilize at T_{oxid}; if it does ignite, it must reach T_f. Although the actual values of T_{oxid} and T_f will vary with time somewhat (12), whatever values they represent will eventually be reached in the final steady-state configuration of the fuel sample. In application, the main query is to whether or not the sample will ignite with a given set of initial conditions on the problem. Therefore, the determination of whether or not ignition will take place must be answered practically at time $t = 0^+$, which is really the main reason for graphing these curves at this particular value of time.

Looking again at the $\dot{q}_{loss}$ curve in Fig. 3, it can be seen that at $T_s > T_{amb}$, $\dot{q}_{loss}$ becomes an actual heat gain even at time $t=0^+$. This is again true because at $T_s > T_{amb}$, the interior temperature of the sample is greater than the surface temperature.

Also, because $\dot{q}_{loss}$ is equal to zero at T_{amb}, then for this case in which there is no solid phase product deposited on the sample surface, the stable low-temperature oxidation temperature T_{oxid} is somewhat higher than T_{amb}. Although this may seem peculiar in light of practical experiences with metals, there is a fairly simple explanation that will be discussed in detail in the following section.

HETEROGENEOUS IGNITION WITH SOLID-PHASE REACTION PRODUCTS - All of the preceding has been for the case where the products of combustion appear in the gas phase. For metals, the greatest difficulty comes about through the fact that a solid state metal oxide coating appears on the surface of the sample. This represents one more level of difficulty in the treatment of the heterogeneous ignition problem.

Again, a spherical fuel sample in a static oxidizing atmosphere is considered. The control volume includes those products formed on the reaction surface. In addition, the product temperature is uniform and equal to the surface temperature so that the solid-phase products do not contribute to the heat transfer characteristics of the configuration. Indeed, all the assumptions of the previous section are maintained such that the equations and concepts developed there remain valid for the case of solid-phase product formation.

It has been well-established in isothermal oxidation experiments that, in general, at low temperatures, the presence of the metal oxide film leads to the so-

called protective oxidation rate laws while at higher temperatures, the product film offers no protection to further oxidation and the linear rate law is observed (21,23,24)*. These rate laws in general are of the form:

$$\frac{dx}{dt} = k_n / x^{n-1} \qquad \text{Eq (15)}$$

where

x = mass of oxygen consumed per unit surface area at time t, gm/cm^2;
k_n = rate constant, $(gm/cm^2)^n/sec$;
n = oxidation law index, dimensionless.

The variable x may alternatively represent the mass of metal transformed to the oxide or the thickness of the oxide layer in the case of a uniform, plane parallel oxide film. However, the amount of oxygen consumed in the oxidation process per unit surface area is most widely applicable to metals of interest and most measurements of the rate constant have been made in this form (21,22).

Integration of equation (Eq. 15) with n=2 or n=3 gives respectively the parabolic or cubic protective rate law:

$$x^2 = 2k_2 t + C_2 \qquad \text{Eq (16)}$$

$$x^3 = 3k_3 t + C_3 \qquad \text{Eq (17)}$$

The logarithmic law is another common example of a protective rate law:

$$x = k \ln t + C \qquad \text{Eq (18)}$$

Integration of equation (15) with n=1 gives the linear rate law:

$$x = k_1 t + C_1 \qquad \text{Eq (19)}$$

In contrast to the protective rate laws (parabolic, cubic, logarithmic), for which the rate of reaction dx/dt decreases with time, the rate of reaction for linear oxidation is independent of time and is thus independent of the amount of gas or metal previously consumed in the reaction. In other words, here the rate of reaction is independent of the amount or thickness of the oxide film on the sample. One explanation of this phenomenon that is most usually experimentally observed (21,23) is that the oxide film has either become porous or has cracked so that the metal surface is not protected from the oxidizing atmosphere.

In most circumstances the parabolic protective oxidation rate law appears at average temperatures; as the temperature increases, the non-protective linear rate law usually appears before ignition occurs. Thus, at lower temperatures, the heterogeneous reaction rate is inhibited by this product film, while at higher temperatures the reaction rate is essentially independent of the product film. Now the temperature at which this changeover occurs is called the transition temperature, T_{trans}. It is the lowest temperature above which the metal-oxidizer system is controlled by a linear oxidation rate law that persists until metal ignition occurs.

Now, since below this transition temperature the metal is protected, the transition temperature must be less than or equal to the ignition temperature. In fact, the transition temperature is the lowest possible ignition temperature for any metal-oxidizer system. This fact will become clearer in the next section.

Mellor (12) attributed the appearance of the transition temperature to a phase change or other changes leading to stress or thermal cracking of the oxide film or perhaps melting of the oxide as in the case of aluminum. Now the linear rate law may not only be due to the non-protectiveness of the oxide layer as intimated by the above mechanisms, but may also arise from other physical mechanisms such as a non-porous barrier layer between the metal substrate and a porous outer oxide layer (12, 23). Therefore, the transition temperature only defines the appearance of a <u>non-protective</u> linear rate law which persists at all higher temperatures between T_{trans} and T_{ign}.

---

* See these same references for a discussion of the microscopic mechanisms behind these laws.

In view of the significance of the transition temperature in defining the effect of the solid oxide layer in metals, this problem may be graphically analyzed via an uncomplicated extension of the simpler problem of heterogeneous ignition with gas-phase reaction products as displayed in Fig. 1c. At lower temperatures the molar reaction rate $\dot{m}$ will be reduced due to the presence of the protective product film. Since $\dot{m}$ here is in the kinetic regime, $\dot{q}_{chem}$ will decrease following Eqs. (1) and (4) due to a decrease in the pre-exponential factor and an increase in the activation energy. At temperatures above T_{trans}, $\dot{q}_{chem}$ is assumed to approach the value for a clean surface although this is not strictly true in the real case since some oxide always adheres to the exterior of the metal. The $\dot{q}_{loss}$ curve remains the same since the solid oxide coating has been included in the control volume.

Consider now the region near the critical temperature which represents the area of changeover from high temperature oxidation to ignition and subsequent steady-state combustion. Fig. 3a depicts this region for the case of no solid-phase product formation. Figs. 3b and 3c depict the case of solid-phase product formation for the two possible subcases: $T_{trans} < T_{crit_o}$; $T_{trans} > T_{crit_o}$ where T_{crit_o} is the original critical temperature for the clean surface*. From these graphs, a criterion for metal ignition may be proposed:

$$\text{If } T_{trans} < T_{crit_o}; \text{ then } T_{ign} \geq T_{crit_o}; \qquad \text{Eq (20)}$$

$$\text{If } T_{trans} > T_{crit_o}; \text{ then } T_{ign} \geq T_{trans}. \qquad \text{Eq (21)}$$

If $T_{trans} < T_{crit_o}$, then the ignition temperature is called critical temperature controlled, whereas if $T_{trans} > T_{crit_o}$, the ignition temperature is called transition temperature controlled. Most metals are critical temperature controlled, while a few metals such as aluminum and beryllium are thought to be transition temperature controlled.

It is important to note here that a transition temperature controlled metal sample of reasonable size cannot in general self-heat to ignition. This statement is supported by the fact that an impervious oxide layer covering the bare metal should protect the surface from producing a large heat of reaction until $T_s \geq T_{trans}$. Thus, the sample would be expected to stabilize at T_{oxid_o} for all original $T_s \leq T_{trans}$. In order that this occur, it is necessary that the actual critical temperature, as determined by the protective surface (the solid rather than the dashed curve in Fig. 3c) be greater than T_{crit_o}, but not less than T_{trans}, so that self-heating may not occur below T_{trans}. In other words, $\dot{q}_{loss}$ must be greater than $\dot{q}_{chem}$ for all $T_s \leq T_{trans}$ and necessarily $T_{trans}=T_{crit}$ for the oxide-protected surface of the bulk metal as depicted in Fig. 3c.

In order to summarize the effects of T_{trans} on all previously defined temperatures of interest, it is necessary to study in detail Fig. 4. Fig. 4 is an extension of Fig. 2 to the case of a heterogeneous reaction with a solid-phase oxide product. The typical decrease in $\dot{q}_{chem}$ below T_{trans} for both a critical and a transition temperature controlled metal is shown here but with emphasis on the critical temperature controlled subcase (the T_{trans} controlled subcase is represented by the dashed $\dot{q}_{chem}$ curve). For this subcase, there is theoretically no change in T_{crit}, as well as no change in T_{ign} and T_f, from the case of a heterogeneous reaction with gas-phase reaction products.

For both subcases, the protective quality of the low temperature oxide film results in a significant lowering of the oxidation temperature from T_{oxid_o} to T_{oxid}. The original value of the oxidation temperature T_{oxid_o} is, as mentioned in the previous section, somewhat higher than the ambient temperature T_{amb}. However, due to the protective qualities of the oxide layer the new value of the oxidation temperature T_{oxid} is postulated to be very near T_{amb}, as would physically be expected for most metals. For example, calcium is known to get fairly warm if exposed to a room temperature environment, and would be expected to stabilize to some temperature higher than T_{amb} if the oxide coating were continually removed during the oxidation reaction. However, it is also a matter of experience that calcium quickly develops a protective oxide coating and that after some time, the temperature stabilizes close to T_{amb}. Also, since some metal oxides, such as Al_2O_3, are more protective than others, then metals like aluminum stabilize extremely close to room temperature and thus do have $T_{oxid} \approx T_{amb}$ as shown in Fig. 4.

---

* The $\dot{q}_{chem}$ curve for the clean surface is represented in these figures by the dashed line.

In summary then, a transition temperature has been defined which separates regions of time-dependent and time-independent reaction rates for heterogeneous metal-oxidizer systems. Ignition is postulated to occur only after this temperature is exceeded and, furthermore, the ignition process occurs exactly as in other heterogeneous systems.

APPLICATION OF THE STEADY-STATE MODEL TO METAL PYROPHORICITY - One of the more interesting properties of metals is the ability of a well-dispersed group of small metal particles to spontaneously ignite when exposed to an oxidizer at room temperature. Although this is a difficult problem to analyze because of the cooperative effort between the particles to minimize the rate of heat loss, it is still possible to study instead the effect of metal sample size on the ignition temperature of a single particle. Such studies have indeed been made on this pyrophoric behavior of metal particles, and it has been concluded that a decrease in sample size generally results in a decrease in ignition temperature. It is of interest here to attempt to explain this phenomenon in terms of the present model of metal ignition. First, however, an overall discussion of this problem seems appropriate.

In order for a metal particle to be able to first, self-heat, and second, self-heat to a fairly low ignition temperature, it is necessary that the total heat release increase with respect to the total heat loss as metal particle size is reduced. Now, as particle size decreases, sample surface area increases with respect to sample volume; that is, the ratio of surface area to volume of the sample (S/V, a suitable size index) increases. This increase in S/V is indicative of a relative increase in the total chemical heat release with respect to the total heat capacity of the fuel particle. Therefore, pyrophoric action can be attributed to an increase in the amount of free surface of the metal, since this is responsible for the inability of the metal particle to dissipate its heat of oxidation rapidly enough, because with more surface area and less volume, more heat is liberated that cannot be dissipated by the metal particle itself.

Of course, the heat of oxidation of the metal will be greatly reduced by a protective oxide coating and thus, a metal with a low transition temperature which in all probability is then a critical temperature controlled metal will tend to be more pyrophoric. Of these critical temperature controlled metals, those which have the highest heat of reaction with the oxidizer in the atmosphere of interest will retain the ability to burn spontaneously for a larger-sized particle. In other words, it is generally true that for an oxygen atmosphere, the higher the heat of formation of the metal oxide, the more pyrophoric is the parent metal (27).

TABLE 1

HEATS OF FORMATION OF PREDOMINATING METAL OXIDES*

Oxide	$-\Delta H_f^{298}$	Oxide	$-\Delta H_f^{298}$
Ta_2O_5	488.80	SnO_2	142.01
Al_2O_3	400.40	SrO	141.10
V_2O_5	381.96	WO_2	140.94
B_2O_3	303.64	Bi_2O_3	139.00
ThO_2	293.20	BaO	133.50
Cr_2O_3	272.65	ZnO	83.25
HfO_2	266.05	FeO	63.50
ZrO_2	261.50	CdO	62.20
UO_2	259.20	NiO	57.30
TiO_2	225.50	CoO	57.10
SiO_2	217.50	PbO	50.39
MoO_3	182.65	Cu_2O	41.80
MgO	143.70	Ag_2O	7.20
BeO	143.10	Au_2O_3	0.80

*Data in kcal/gmole taken from Refs. (21,25).

Table 1 lists the heats of formation of the predominant metal oxide of some metals of interest in order of decreasing magnitude of their heat of formation. In general, those metals which are known to be pyrophoric such as uranium, zirconium, thorium, and vanadium occur at the head of the list while metals which barely oxidize such as silver and gold indeed are at the end of this table.

Now, in dealing with the phenomenon of metal pyrophoricity in terms of the model developed here, it is necessary to ascertain the degree of influence of metal sample size (S/V) on the critical and transition temperatures. Mellor (12) analyzed by means of the available literature the influence of several variables on the latter and found that although the transition temperature may be dependent to some extent on sample purity and non-isothermal conditions, it is generally independent of such things as surface pretreatment, experimental environment, sample size and is so postulated. On the other hand, the critical temperature may be a strong function of some of these environmental factors since the relative values of $\dot{q}_{chem}$ and $\dot{q}_{loss}$ could change with these parameters. In particular, as the sample size decreases, S/V increases and therefore the effect of heat loss will decrease since the main heat loss term, the conduction heat loss into the sample, will decrease*. Since $\dot{q}_{chem}$ is not a function of S/V in the kinetic regime (See Eqs. 1,2,4), then as S/V increases, the critical temperature will decrease, thus theoretically making it possible for a metal sample to self-heat to ignition from a lower value of the initial surface temperature.

Recall that it has been previously postulated that a metal has its ignition temperature controlled by either its critical or transition temperature depending on whether T_{crit} is greater than or less than T_{trans}. Since the transition temperature is here assumed to be independent of sample size, a transition temperature controlled metal is postulated to have its ignition temperature independent of sample size even though its critical temperature is not, while a critical temperature controlled metal has both its critical and ignition temperatures decrease with a decrease in metal sample size**. In short then, metals whose ignition is controlled by T_{crit} will experience a size effect while metals whose ignition is controlled by T_{trans} will experience no size effect.

It is interesting to note that as a sample size is reduced, and thus $\dot{q}_{loss}$ is decreased, the metal-oxidizer system will shift from a critical temperature controlled system (Figure 3b) to the appropriate transition temperature controlled system (Fig. 3c). As the particle size is further decreased, it is possible as mentioned in the previous section to have $\dot{q}_{loss}$ become so small that T_{crit} becomes less than T_{trans} and, therefore, the sample may self-heat from temperatures below T_{trans} to eventual ignition. Indeed, it might perhaps be possible that such a process occur for a transition temperature controlled metal of bulk size, but here the sudden increase in $\dot{q}_{chem}$ at T_{trans} is usually much larger and the ignition temperature is thus maintained at its bulk value.

When the size of a metal particle has decreased to the point where the system, which was critical temperature controlled in the bulk regime, is now transition temperature controlled, any further decrease in sample size will have little effect on the ignition temperature, as in any transition temperature controlled situation. In other words, as the particle size decreases, the critical temperature will continue to decrease; however, the ignition temperature will never become less than the appropriate transition temperature for that system.

Turning for a moment to the bulk regime, it is postulated that once the sample reaches a certain bulk size, in reference to the surface, the sample volume is infinite. Thus, the $\dot{q}_{loss}$ curve will tend to stabilize and consequently the critical and ignition temperatures will tend to remain relatively constant with further increases in size.

In summary then, for metals whose bulk ignition is controlled by the critical temperature, the ignition temperature will decrease with decreasing sample size due to a decrease in the critical temperature. For large samples, the ignition temperature is equal to the bulk ignition temperature; in this regime, the critical and ignition temperatures are relatively independent of size. For intermediate-sized samples, the critical and ignition temperatures will decrease with decreasing sample size until the latter nears the transition temperature. Upon further reduction in sample size, the critical temperature continues to decrease, but the ignition temperature remains relatively constant and approaches the transition temperature. This then is the problem of pyrophoricity, where a small particle may self-heat to the transition temperature and thus ignition, but where a larger sample is not allowed to undergo this physical process.

---

* Inspection of Eq. (7) for $\dot{q}_{loss}$ shows that only $\dot{q}_{cond,g}$ and $\dot{q}_{cond,f}$ are dependent on samples size with the latter much larger since k_f is much larger than k_g in most all cases.

** See Mellor (12) for a mathematically orientated argument that outlines the influence of T_{crit} and T_{trans} on the ignition temperature.

One of the more notable achievements of this theory is the prediction of the size effect as demonstrated by Mellor with the aid of an induction furnace facility and two critical temperature controlled metals, magnesium and calcium (12). The induction furnace accentuates the size effect since it heats on the surface of the sample as is done in the model, and, thus, makes the conduction losses into the sample very important. In other experimental environments where the metal sample is heated uniformly, it is expected that the size effect will be diminished if the source of the size effect has been correctly assured to be the conduction heat loss into the metal.

Figs. 5 and 6 demonstrate clearly the size effect in various oxidizing atmospheres at 300 torr for the two metals, magnesium and calcium. Unfortunately, it was not possible in both cases to obtain metal samples with a larger S/V ratio because of the difficulties with industrial production of thin sheets of such metals (12). However, the general trend can be seen on these graphs and furthermore, it appears that the ignition temperature may indeed be minimized at the appropriate transition temperature for the metal under consideration.

THE VARIATION OF THE TRANSITION TEMPERATURE

PREVIOUS RESULTS WITH ALUMINUM - In the early work with aluminum at Princeton, Brzustowski (4,9) found, as had other investigators, that the ignition temperature of this metal in oxygen-argon atmospheres was very close to the melting point of its oxide. Brzustowski also noted, however, that the brightness temperature at ignition for anodized aluminum wires, though constant from 20 atm. to 1 atm., slowly decreased from total pressures of 300 torr to 50 torr. Although Brzustowski (4) attributed this behavior to a change in emissivity, it is very possible that the ignition temperature of aluminum decreases with decreasing oxidizer pressure at these lower ambient pressures. Indeed, Kuehl (14) later found that, whereas the ignition temperature of aluminum is constant at the oxide melting point at higher pressures, for pressures lower than approximately 250 torr, the ignition temperature slowly decreases with decreasing ambient pressure.

Since aluminum is transition temperature controlled, the above behavior of its ignition temperature may logically be explained via some mechanism that would allow the transition temperature to decrease with decreasing pressure below 300 torr. Such a mechanism has been proposed by Kuehl (14) and is depicted on the pressure vs. temperature plot in Fig. 7.

The normal transition temperature for aluminum is known to be its metal oxide melting point, 2042°C. This is represented by the straight vertical line in Fig. 7. Consider now the vapor pressure curve for aluminum metal; from Fig. 7, it can be seen that the oxide melting point is equal to the metal boiling point at a pressure of about 700 torr. Thus, at pressures above 700 torr, the pressure of the aluminum vapor enclosed by the oxide coating can never exceed the total ambient pressure without having the temperature of the sample become greater than the melting point of Al_2O_3. Therefore, at pressures greater than 700 torr, the transition (and ignition) temperature of aluminum is postulated to be the melting point of the metal oxide.

For ambient pressures below 700 torr, the vapor pressure of aluminum inside the solid oxide shell will become larger than the outside ambient pressure for temperatures greater than the appropriate boiling point of aluminum at the pressure of interest. Thus, it is not possible in this pressure range to reach the oxide melting point without causing a pressure differential across the oxide shell. Depending on the strength of the oxide layer then, it is possible that a certain pressure differential may break the oxide coating at temperatures below the melting point of Al_2O_3. If the oxide coating is thin and weak, but impervious to the ambient oxidizer, then the transition (and ignition) temperature below 700 torr will closely follow the vapor pressure curve. On the other hand, if the oxide coating is thick, strong, and protective, as is usually the case with aluminum, a higher than ambient metal vapor pressure will be needed to break the oxide coating. Therefore, the transition temperature for pressures below 700 torr will folow a path similar to that found by Kuehl (14) as depicted by the lower curve in Fig. 7*. (Note that a pressure drop from 700 to 250 torr is needed in the case of aluminum to have a large enough pressure differential to break the oxide coat.)

In summary then, the ignition temperature for aluminum is postulated to be controlled by the oxide melting point at higher pressures and the metal boiling point at lower pressures. However, aluminum still remains completely transition temperature controlled since the metal boiling point, like the oxide melting point, is a physical

---

* Notice that the lower curve approaches the vapor pressure curve at very low pressures. This is to be expected since at very low pressures, the oxide shell naturally becomes thin and weak. The heavy lines in Fig. 11 denote the transition temperature variation for both a strong and weak oxide shell.

property of the metal-oxidizer system and not a chemical property, dependent on the heating characteristics of the system. Thus, it is concluded that the transition temperature may vary considerably with the pressure when the metal boiling point interferes with the natural melting process of the oxide.

Adding even more credance to this argument is the fact that it can be used to explain the cylindrical vapor-phase flame that appears upon ignition of aluminum wires in carbon dioxide-argon atmospheres at pressures below 300 torr (14). Earlier this type of flame was explained by arguing that a barrier layer of Al_2O_3 exists which melts before the porous outer layer of oxide, thus, enabling metal vapor to escape before the wire breaks. Although this process may have a part in establishing the vapor-phase flame, the following argument seems to explain the observed phenomenon much more appropriately.

In heating the wire, the pores in the outer layer are only slightly filled by the pre-ignition oxidation process when the atmosphere contains CO_2-Ar mixtures. At ambient pressures above 300 torr, the oxide coat must melt before ignition can occur and, hence, a cylindrical vapor-phase flame does not appear. However, at pressures less than 300 torr (in agreement with Fig. 7), there exists a large enough pressure differential across the oxide shell to break the coating at its weakest points, specifically, near large pores, and thus allow metal vapor to escape without completely destroying the integrity of the oxide coat and, hence, the anodized aluminum wire. Consequently, it is indeed possible to observe the cylindrical vapor-phase diffusion flame at these lower pressures.

THE INVESTIGATION OF ZINC (17) - Although the boiling point effect as described above seems to bring together and explain various results with aluminum, only Kuehl (14), using pyrometric means, has offered any evidence at all that indeed the ignition temperature of aluminum at low pressures is controlled by a variable transition temperature which is in turn controlled by the metal boiling point. The fact that the ignition temperature of aluminum may be significantly reduced by using low pressures could be very useful in rocket applications (low pressure solid rockets for space applications). Therefore, it appears to be very important to determine if this phenomenon really does occur for metals such as aluminum.

TABLE 2

FUNDAMENTAL TEMPERATURES OF INTEREST FOR METALS*

Metal	Metal Oxide	Metal Melting Point	Metal Oxide Melting Point	Metal Boiling Point	Metal Oxide Boiling Point	Transition Temperature
Ba	BaO	710	1923	1527	2000	17
Bi	Bi_2O_3	271	860	1470	1890	-
Ca	CaO	848	2580	1240	2850	400
Fe	FeO	1536	1420	2872	-	1200
Pb	PbO	328	897	1753	1516	550
Mg	MgO	650	2800	1105	3600	450
Mo	MoO_3	2620	795	4507	1155	700
Sr	SrO	774	2430	1366	3000	-
Sn	SnO_2	232	1127	2260	1850	475
Zn	ZnO	419	1975	907	-	700
Co	CoO	1495	1935	3550	-	1350
Cu	Cu_2O	1083	1235	2595	-	1000
Ti	TiO_2	1677	1855	3277	2750	850
W	WO_2	3410	1580	5900	-	1000
Zr	ZrO_2	1855	2677	4474	4300	1300

* Taken and extrapolated from Refs. (12,21,23,24,25,26,27); given in °C. Boiling points are for atmospheric pressure (760 torr).

Unfortunately, direct temperature measurements of bulk aluminum in the induction furnace at Princeton was not possible. Consequently, it was though that perhaps some other metal might be found which would also demonstrate this behavior at lower pressures. By using existing data on ignition temperatures and boiling points, and the data in Table 2, zinc was chosen as perhaps having a transition temperature controlled by a protective oxide layer, and that at lower pressures, its ignition temperature would be controlled by its boiling point. Laurendeau (17) obtained data

using the Princeton induction furnace facility and the data appeared to bear out these original suppositions. Table 3 lists the measured ignition temperatures of zinc to the nearest five degrees.

TABLE 3

IGNITION TEMPERATURES FOR ZINC METAL

Pressure	Ignition Temperature (°C)	Average Ignition Temperature (°C)
200 torr	785	790±5
	795	
300 torr	815	840±30
	835	(830±15
	840	
	880	
1 atm	895	905±15
	905	
	920	
3 atm	1035	1040±5
	1040	
	1045	
5 atm	1090	1135±35
	1095	(1095±5
	1140	
	1150	
	1160	
	1165	
7.5 atm	1160	1165±5
	1170	
10 atm	1140	1160±20
	1175	
12.5 atm	1185	-
15 atm	1290	-

In order to ascertain the validity of the boiling point effect, it is necessary to compare the average ignition temperature at each pressure to the boiling point of zinc at these pressures. The vapor pressure curve for zinc metal, as taken and extrapolated from Refs. (28,35 and 36) is shown in Fig. 8. The data are not plotted as a lnp vs. 1/T to accentuate the constantcy of the ignition temperature above 5 atm. Note the near perfect correlation of the average ignition temperature at each pressure up to 7.5 atm with the boiling point of zinc. This indicates that zinc oxide is in all probability a protective oxide, but that it is thin and weak, and therefore only a slight pressure differential is needed to break the oxide shell. In order to see this point better, it is of interest to look closer at the data listed in Table 3.

At the lower pressures, especially at 200 torr, 1 atm, and 3 atm, there is almost perfect correlation with the zinc boiling point (At 760 torr, Table 2 gives 907°C as the boiling point of zinc, for example.). However, at 300 torr, there is a first indication that the oxide coat may at times require a sizeable pressure differential before it will crack. Nevertheless, in most cases at this pressure, the ignition temperature closely follows the vapor pressure curve as can be seen by comparing the average of the three lower experimental points (the average ignition temperature in parentheses) to the boiling point of zinc at 300 torr. A similar behavior is noted at 5 atm, but here the majority of the data points indicates that a higher pressure gives rise to a stronger oxide coat that, in general, remains protective until 1150°C. When, for some reason, a certain oxide shell is unprotective at this pressure, an ignition temperature comparable to the zinc boiling point at 5 atm (~1100°C) is obtained.

For those runs at 300 torr and 5 atm where the oxide shell is protective to a higher temperature than the corresponding metal boiling point, zinc metal scraps are usually found attached to the sides of the pressure vessel after the run has been completed. This indicates that the ignition process here was "explosive" in the sense that the large pressure differential across the oxide shell caused a spewing out of zinc metal upon breaking of the oxide coating just before ignition occurred. In addition, the temperature traces for these particular runs show that immediately upon ignition, the molten zinc metal almost instantaneously drops in temperature to the appropriate metal boiling point. These particular experimental findings again seem to indicate that the zinc oxide shell is indeed protective to fairly high temperatures.

At higher pressures, the reaction is of course very rapid and, at times, the metal is almost completely consumed before the metal fire can be extinguished. At both 7.5 and 10 atm, the ignition temperature is near 1160°C. This corresponds to the zinc boiling point at 7.5 atm, but to a temperature lower than the metal boiling

at 10 atm. It appears then that the protective qualities of the oxide coat are experimentally beginning to level off near 1150°C. Thermal oxidation data indicates that the zinc transition temperature is greater than 700°C; the present results increase the maximum value of the transition temperature to 1150°C or perhaps higher. This, however, is still significantly less than the melting point of ZnO at 1975°C (See Table 4).

The experimental data at 12.5 and 15 atm are not plotted in Fig. 8 because there is some doubt as to the significance of these results. At both of these pressures, the reaction is almost instantaneous and very explosive in the sense described above. At 15 atm, there was a sudden flash of light and no more; however, reaction had occurred since there was a thick layer of zinc oxide particles covering the entire inner surface of the pressure vessel. At 12.5 atm, there was no flash, but the furnace automatically shut down when the metal explosion occurred due to a short circuit across the work coil caused by the flying zinc metal. (This also happened at 15 atm.). After a few seconds, light appeared from the remaining portion of the sample and reaction then proceeded.

Because of the extremely vigorous reaction and the imminent danger that it posed to the work coil, only one run was made at each of these pressures. However, even these very scanty data perhaps indicate that at higher pressures, the oxide coat becomes much thicker, leading to either the possibility of early cracking of the oxide layer or the presence of an extremely strong oxide shell which causes the transition temperature to increase with increasing pressure. The above statement, however, is to be considered very hypothetical in light of the lack of data supporting it*.

The experimental investigation of the ignition temperatures of bulk zinc shows that, in general, the ignition temperature of zinc increases with increasing pressure in almost perfect correlation with its boiling point at the respective pressures involved. Because the ignition temperature may be greater than the metal boiling point, and the range of ignition temperatures is very large, it would appear that the oxide is protective to some high temperature, although not to the oxide melting point as for aluminum**. Indeed the maximum transition temperature, over the observable pressure range investigated here, appears to be near 1150°C, much less than the maximum possible transition temperature for zinc at the melting point of ZnO (1975°C). This maximum transition temperature (1150°C) denotes the end of the control of T_{trans} by the boiling point and the beginning of the control of T_{trans} by the physical characteristics of the zinc oxide coat as determined by the low temperature oxidation process prevalent in all metals.

Assuming that 1150°C is indeed the maximum transition temperature for zinc***, then below the vapor pressure at 1150°C (7.5 atm), the boiling point of zinc will control the transition and thus the ignition temperatures. However, the oxide coat for zinc, although impervious, is thin and weak; therefore, the ignition temperature will follow the vapor pressure curve instead of a curve similar to the lower curve for aluminum below 700 torr as depicted in Fig. 7. At very low pressures, both aluminum and zinc will follow their vapor pressure curves since very little oxidation takes place at these pressures and thus the aluminum oxide coat also becomes thin and weak. At pressures above 7.5 atm, the ignition and transition temperatures are here assumed to be constant at near 1150°C.

The overall results of the zinc investigation show then that a transition temperature controlled metal can have its ignition temperature controlled by its boiling point for a certain range of low pressures. Thus, for metals like zinc and aluminum, the transition temperature is not necessarily a constant but may be a strong function of pressure if the boiling point becomes the controlling influence in the ignition process. Consequently, although not common to most metals, the boiling point effect is indeed a proven influencing factor that very clearly explains the previously observed lowering of the ignition temperature and the cylindrical vapor-phase diffusion flame below 300 torr in early experimental work with aluminum metal.

---

* In fact, due to the explosive nature of these reactions, it may be possible that the Al_2O_3 crucible perhaps acted as a catalytic agent or even entered into the reaction. There is, however, no evidence for or against this hypothesis.

** If this were true, the ignition temperature would continue to rise until the ambient pressure increased over 260 atm at which pressure, the boiling point is equal to the melting point of the oxide (1975°C). This is highly unlikely based on the high pressure results obtained in the present investigation.

*** Any other assumption for the maximum transition temperature will not change the reasoning in the argument outlined here. Thus, 1150°C corresponds to the melting point of Al_2O_3 at 2042°C shown in Fig. 7. However, 1150°C is not the melting point of ZnO, but instead represents the simple physical failure of the oxide layer to protect the metal substrate. This phenomenon, as for all other metals, is characterized and defined by the transition temperature.

FLAME MODELS*

In this section the various models that have been presented in the literature to represent the flame structure of metal-oxygen diffusion flames will be reviewed. Attention is focused strictly on those metals which burn in the vapor phase.

The evidence to support the proposed models varies significantly. In some cases visual observation alone is the sole criterion suggesting a flame model. Burning rate calculations performed under the guidelines of this postulated model are then compared with experimentally determined burning rates to judge the validity of the model. Other models result from more complete experimental determinations including such diagnostic measurements as optical spectroscopy, electron microscopy and x-ray diffraction studies of the combustion products, quench studies of metal particles in all stages of combustion, and determination of kinetic rate constants. No effort is made to describe the methods of making burning rate calculations. Such methods are described adequately in Ref. (4). The important aspect of the problem is to establish the proper flame model.

It should be pointed out that unknown or uncertain high temperature values for many of the parameters required in order to be able to perform an analytical calculation of a burning rate, preclude the possibility of definitely establishing one flame model as correct on the basis of comparing calculated and measured burning rates. In the same manner it has not been possible to assess critically the various assumptions that have been made in all of these admittedly idealized and simplified models.

FINITE REACTION ZONE MODEL DUE TO COFFIN - The earliest of these models is due to Coffin (9). In his experiments Coffin studied the burning of magnesium ribbons in various mixtures of oxygen with argon, nitrogen, helium and argon-water vapor. His evidence indicated a vapor phase reaction for magnesium combustion bearing some analogy to the combustion of liquid fuel drops. However, the model generally used for liquel droplets, was not used by Coffin. Instead of this "collapsed flame front" model, a finite thickness for the reaction zone was adopted. Coffin's model is illustrated in Figure 9.

In this cylindrical model, there are three concentric zones. The inner zone AB contains only the metal vapor and the inert diluent. Metal, which is vaporized at the fuel surface by the heat conducted back from the reaction zone, diffuses from the ribbon surface at A, where it is at a temperature close to the boiling point of the metal, to the reaction zone which starts at B. The reaction zone was considered to be at the boiling point of the magnesium oxide, as had been suggested by experimental flame temperature measurements (28,29). It was also believed that the oxide dissociated almost completely upon vaporization (30).

The reaction zone BB' thus consisted of a mixture of magnesium vapor, oxygen and condensed oxide at the boiling point of the metal oxide in a stagnant film of inert gas. It was assumed that chemical equilibrium existed among the species in this zone.

The third zone B'C is the zone through which oxidizer diffuses from the surroundings to the constant temperature reaction zone. The oxygen is heated from the ambient temperature of the surroundings to the flame temperature as it diffuses inward. The condensed oxide from the reaction zone cools as it moves outward from the reaction zone through the zone B'C.

Idealized assumptions which were made for this model were as follows: free convection was ignored; the pressure was considered to be 1 atmosphere throughout the system; the inert gas was considered as a stagnant film throughout the system.

LIQUID OXIDE BUBBLE MODEL DUE TO FASSELL AND CO-WORKERS - A second model for the combustion of metal particles has been proposed by Fassell and co-workers (31,32). Although these authors indicated that the gas phase spherical diffusion flame theory adequately accounted for the combustion of magnesium, they suggested that higher boiling metals did not burn in conformity with this model. A particular case of this latter category of metals was aluminum. In the experiments of Fassell et al, aluminum and various aluminum-magnesium alloy particles were burned in two different types of torches in either methane-oxygen mixtures, or a combination of methane, oxygen and air.

Visual observations, high speed photographic measurements and detailed observations including x-ray diffraction of the combustion products suggested to these workers that the diffusion flame model which had apparently been successfully applied to the combustion of magnesium, did not in fact represent the case of aluminum combustion. Based largely on the appearance of the combustion products, Fassell et al proposed the model which is depicted schematically in Figure 10.

* This section is extracted almost in its entirety from Ph.D. thesis of Sullivan.

A continuous layer of molten oxide covers the metal droplet. The evaporating metal from the droplet, which is considered to be at its boiling point, causes the molten oxide layer to form a bubble. The limiting step to further reaction is considered to be diffusion, through this molten oxide layer, of either metal vapor diffusing outward, or oxygen diffusing inward. Reaction is considered to take place at the liquid oxide interface. The authors considered the possibility of the molten oxide bubble exceeding a critical size and bursting, thus scattering fragments of both oxide and freshly exposed metal.

It was thought that this model provided the explanation of the numerous hollow oxide spheres present in the combustion products. It also satisfied one of the difficulties which arose from the x-ray diffraction studies, namely the appearance of species such as $MgAl_2O_4$ which would not be thought likely to occur in a vapor phase diffusion flame.

COLLAPSED REACTION ZONE MODEL DUE TO BRZUSTOWSKI AND GLASSMAN -The first model due to Coffin subsequently came under criticism by Brzustowski and Glassman (9). In addition to certain facets which they felt had to be included in the analytical model (thermal radiation from the flame front to the surroundings and to the droplet surface; diffusion of oxygen toward the flame front being affected by the condensed product), they stated that the thick reaction zone used by Coffin predicted a flame structure "notably different" from observed flames. Coffin's contribution was felt to be the comparison of the diffusion flames of metals and of hydrocarbons. This comparison of the diffusion flames of metals and of hydrocarbons. This comparison was the basis on which Brzustowski and Glassman proceeded to develop a flame model which is outlined below.

The analysis was based on the theory developed to describe the combustion of hydrocarbon droplets, namely the collapsed flame front model depicted in Figure 11, but was modified to account for specific characteristics pertaining to metal combustion. These particular features are presented below:

(1) The flame temperature will be fixed at the boiling point of the oxide. Some oxide will always form in the condensed state. (Coffin's model was a particular case of this general statement. His model was specifically for magnesium.)

(2) The presence of the condensed oxide products will affect the diffusion of oxygen to the reaction zone. Movement of these solid or liquid products must occur due to bulk motion of gaseous species since they cannot diffuse.

(3) Thermal radiation will probably be an important consideration because of the existence of these condensed species in the high temperature regions of the flame. It can possibly result in higher evaporation rates for the fuel due to an increased heat feedback, but it can also lead to significant losses to the surroundings.

(4) In the case of metal combustion, evaporation rates of the fuel may not be fast compared to diffusional processes.

With the above considerations in mind, the collapsed flame zone model of Figure 11 becomes the metal combustion model proposed by Brzustowski and Glassman. Heat feedback (due to both conduction and radiation) from the thin flame front B, evaporates metal from the fuel surface at A. This metal vapor, at a temperature which may be several hundred degrees lower than the metal boiling point, diffuses through the stagnant film AB toward the high temperature flame front at B.

Oxidizer from the surroundings diffuses toward the flame front through the film BC. This diffusion of the oxidizer is opposed by the outward movement of combustion products which were formed in the thin flame front at B. Heat is conducted and radiated to the surroundings through this film BC.

As in the case of the earlier model of Coffin, idealizations considered in this model include uniform pressures throughout the system, and a system steady in time. It was assumed that combustion products did not diffuse back to the fuel surface through the film AB, but that all products diffused through the film BC to the surroundings. This last assumption was justified in part by the observation of Brzustowski that although oxide was observed on the wire surface (probably from back diffusion of the products) it did not appear to have an appreciable effect on the observed burning mechanism. As will be pointed out later in this chapter, more recent experimental work of other investigators does not support this assumption of no back diffusion of the combustion products.

An important feature of the Brzustowski-Glassman model is the attention paid to the condensed oxide products. Condensed oxide particles can be transported out of the flame zone only if a bulk outward gas velocity exists in the zone BC. The diffusion equation for this zone gives the conditions under which such a bulk velocity can be achieved.

A parameter α is defined as the fraction of the condensed oxide product that is vaporized. This parameter is a function of the flame radius when there is dissociation in the flame zone and subsequent recombination in the zone BC. The result, derived analytically by Brzustowski, illustrates that an outward bulk velocity in the zone BC occurs when more than one mole of gaseous products is formed for every mole of oxidizer participating in the reaction.

In the reaction zone itself, the degree of dissociation of the oxide varies according to the balance between heat liberated in the reaction and heat radiated or conducted to the surroundings. If heat losses are large enough, it would be expected that condensed oxide deposits would appear in the flame front itself.

It has sometimes been incorrectly stated in the literature that a collapsed reaction zone assumption would define zero concentrations for the reacting species at the flame front. Brzustowski (4) points out the correct definition of a collapsed flame front as follows: "..... to a desired degree of accuracy, the dimensions of the reaction zone and the changes in reactant concentrations through it are small with respect to the dimensions and concentration differences involved in the diffusion processes."

Brzustowski found Coffin's thick flame zone model unacceptable because, firstly, it assumed that no gaseous oxide was present because of complete dissociation, whereas spectroscopic observations showed significant oxide vapor radiation and, secondly, Brzustowski's interpretation of his flame photographs showed an entirely different structure. Over a large pressure range from 50 torr to 12 atmospheres the bright flame zone thickness was small in comparison with the dimension between the metal surface and the flame front.

EXTENSIONS OF THE BRZUSTOWSKI-GLASSMAN MODEL DUE TO KNIPE - In a survey paper on aluminum particle combustion by Christensen, Knipe and Gordon (6), a critical discussion of aluminum particle combustion models was presented. The two models discussed were the models due to Fassell et al and the Brzustowski-Glassman model discussed in the previous two sections of this chapter.

One of the criticisms of the model of Fassell and co-workers is that the postulated rate-controlling step of diffusion through the oxide shell must be accepted with some caution because of considerable uncertainty about the magnitude of this diffusion rate. This model does take into account the normal metal oxide coating which exists on the metal particle prior to ignition, but the bubble of oxide which is proposed may be unstable.

A criticism of the Brzustowski-Glassman model is that it does not explain the fate of the normal oxide coating which exists on the metal surface. A suggestion is that the oxide may accumulate in one area giving rise to a metal sphere with an agglomerated oxide cap. The basis for this suggestion comes from observations of such metal-oxide configurations in quench studies. However, this is then a considerable departure from the idealized one-dimensional, spherically symmetric model of Brzustowski and Glassman.

Another criticism of this model is the treatment of dissociation fragments in the reaction zone. Allowing for the fact that their precise nature is not known, aluminum and oxygen atoms are the major fragments of dissociation of the oxide. Since the reaction zone is at a high temperature, it is expected that a heterogeneous reaction will be more likely than vapor-phase reaction to gaseous oxides, and as a consequence the conditions favorable to the nucleation of the condensed oxide may play some role in determining the location of the reaction zone.

Christensen et al conclude from this survey of combustion models that the Brzustowski-Glassman model does describe the gross features of aluminum particle combustion but that there are significant features not contained in the idealized model. As a consequence, Knipe (6) sought to extend the Brzustowski-Glassman model as is indicated below.

The Brzustowski-Glassman model does indicate the conditions under which condensed oxide may build up in the reaction zone. Knipe suggests that this fact should raise strong questions about the applicability of a steady state approximation especially in view of the many statements in the literature suggesting that, because of the condensed nature of the products, radiation will be an important heat trnasfer mechanism in metal flames. As pointed out previously, Knipe also proposes that the principle reaction path will be via heterogeneous processes on the condensed oxide within the reaction zone. It is also stated that the zone of condensed oxide particles has been observed experimentally to possess considerable thickness. This is a plausible observation for such a proposed heterogeneous reaction zone since dissipation of heat, which occurs most efficiently at the edges of this thick zone, significantly affects the progress of the reaction.

In the Brzustowski-Glassman model, back-diffusion of the gaseous combustion products to the metal surface was assumed not to take place. However, experimental observations of Prentice (33) showed that significant amounts of oxide did build up on the metal surface during combustion, indicating that oxygen-containing species were present in the region between the metal particle and the flame front.

Figure 12 is an attempt to represent schematically the model which Knipe proposes.

This model is characterized by a heterogeneous reaction zone of appreciable thickness which probably extends in both directions with time as mentioned previously. A narrow nucleation zone is expected to exist between the reaction zone and a position where the inward-diffusing oxygen-containing species (both evaporation products and partially reacted species) make up a saturated vapor relative to condensation. A second nucleation zone is proposed on the oxidizer side of the reaction zone.

Note that the importance of recognizing the back diffusion of gaseous combustion products is of more significance than merely explaining some of the features attributed to a non-symmetrical burning configuration (e.g., particle spinning). Condensation of oxide on the metal surface would be an appreciable heat transfer mechanism operating between the reaction zone and the particle surface since much of the heat of reaction is in the heat of condensation.

HETEROGENEOUS REACTION MODEL DUE TO MARKSTEIN - Markstein (34), although he has not set out a specific flame model, has discussed vapor-phase burning of metals and has contributed significantly to the problem of whether or not heterogeneous reaction or homogeneous reaction dominates metal combustion, in particular in the case of magnesium.

Figure 13 is reproduced from Markstein's paper (34) and represents a schematic representation of most of the processes that might possibly play a role in vapor-phase combustion.

Markstein states that heterogeneous reaction on the metal surface is not likely a significant process once the vapor phase flame is fully developed. This statement is reflected in the schematic by the dashed lines used to depict this process.

Back diffusion of oxide vapor is also expected to be significant as evidenced by a consideration of the experimental evidence of Macek (35).

Markstein agrees that the question of heterogeneous versus homogeneous reaction is far from settled and, thus far has been an area of speculation and controversy. In an earlier work (36) Markstein seems to have demonstrated the strong role played by heterogeneous reactions in low pressure dilute magnesium-oxygen flames. In these experiments magnesium vapor was carried in an inert carrier gas (Argon). The mixture of magnesium and argon carrier gas entered the stagnant oxygen-argon atmosphere of the combustion chamber through an orifice. Total pressures ranged from about 2 to 10 torr. The spectra of the resulting flame showed no line and band radiation at all, but instead consisted of continuum radiation with several maxima. In addition, it was observed that oxide growths were present near the orifice. The luminescence of these oxide growths was also characterized by a broad maximum in the blue closely resembling that of the dilute flame spectrum. Markstein suggested that the reaction path was following a heterogeneous route. Recent work of Markstein (34,37,38) has been an attempt to determine rate constants for this proposed heterogeneous reaction and to obtain further experimental evidence to elucidate details of the mechanism.

Markstein is cautious about the interpretation of emission spectra by other authors as being an indication of homogeneous reaction, suggesting that the high electronic energies of the states observed in spectra may be difficult to explain on the basis of kinetic steps that are probably not highly exothermic.

If one were to postulate the structure of a combustion model which would fit the particular conditions of Markstein's experiments, namely low pressure highly-diluted flames, it would appear schematically as indicated in Figure 14.

Note that nucleation zones are not specifically defined. Markstein stated (36) that some homogeneous reaction may be required initially to furnish sites for the ensuing heterogeneous reaction but that in the fully developed reaction it would be expected that homogeneous reaction would not be significant. Since oxide vapor is not present due to the lack of homogeneous reaction, it would also be likely that not much oxide would appear on the metal surfaces. This statement is based on two facts. Firstly, most evaporation products dissociate, and thus, very little oxide vapor for back diffusion could be expected from this process. Secondly, it was pointed out earlier that Markstein felt that heterogeneous reaction on the metal

surface was unimportant when fully developed reaction had been established. Thus, the schematic in Figure 14 indicates no back diffusion of oxide vapor to the metal surface.

THE NEW PRINCETON INNER REACTION ZONE MODEL - Sullivan (39) undertook an experimental investigation to determine the flame structure of metal vapor-phase diffusion flames, in particular the low-pressure flames of the alkaline-earth metals Mg, Ca and Sr. In these studies the flames were generated in two types of experiments. In the first type, metal samples in the form of wires or strands were mounted between electrodes and heated to ignition by passing an electric current through the sample. The resulting "wire flame" was studied by color photography and space-resolved spectroscopy which defined the location of emitters in the cylindrically-symmetric flames. In the second type of experiment, a two-dimensional diffusion flame burner was adapted to low-pressure metal combustion studies. The burner provided a flame with a geometry particularly suited for space-resolved spectroscopic observations. The longer exposure times available for obtaining spectra in the burner experiments permitted the observation of oxide band systems which had not been observed in the wire experiments. The observation of these additional band systems aided in the interpretation of the spectral results obtained from the wire experiments.

This investigation has shown that a reaction exists in the inner zone of the luminous envelope surrounding the metal sample. The production of oxide vapor by homogeneous reaction causes a supersaturation of oxide vapor leading to rapid nucleation. Thus, the inner reaction zone is expected to be a high temperature region of the flame due to the liberation of the heat of condensation. Sullivan demonstrated that the major contribution to the observed radiation is due to a thermal excitation mechanism, although some contribution from chemiluminescent radiation may occur in the inner reaction zone. Based on the thermal nature of the radiation, the self-reversal over a portion of their length of the resonance lines of the metals Ca and Sr respectively, indicates that the inner zone of colored radiation in the flame is hotter than the outer zone.

If the trend shown by Markstein's results (38) illustrating the decrease of collision efficiency (for surface reaction) with increasing temperature continues at higher temperatures, it is anticipated that the inner reaction zone of the flames of Ca and Sr is thus a zone of predominantly homogeneous reaction. Heterogeneous reaction would tend to become more important at larger flame radii where it is expected that the temperature is decreasing.

The model described above is pictured schematically in Figure 15. A comparison of this figure with the figures presented at the beginning of this section demonstrates the differences in the flame model as a result of Sullivan's investigation.

The flame zone does not appear to be a "collapsed reaction zone" as in the model of Brzustowski and Glassman. The peak flame temperature is not expected to be located at the outer edge of the luminous envelope. The reaction zone appears to extend to regions very close to the wire surface, and makes it difficult to determine the size of an inner zone such as in the Brzustowski-Glassman model, zone AB, which is assumed to contain only metal vapor and the inert diluent.

The model due to Coffin (40) assumes an extended reaction zone such as the present investigation indicates, but in Coffin's model this zone is assumed to contain no MgO vapor. It would be impossible to explain the spectroscopic observations of Brzustowski (4,9), Courtney (41), and the present investigation, on the basis of Coffin's model. In addition, the two zones observed in the Ca and Sr flames, namely a reaction zone extending almost to the wire surface, and a second zone containing oxide particles surrounding the zone of colored radiation, are not distinguished by Coffin.

In the proposed extensions of the Brzustowski-Glassman model by Knipe (6), it is assumed that reaction probably proceeds predominantly by heterogeneous reaction in the case of aluminum combustion, and that this reaction proceeds at the cloud boundaries. The role played by heterogeneous reaction in the case of aluminum combustion could be significantly different than for the combustion of the alkaline-earth oxides. Unlike the aluminum oxides, the alkaline-earth oxides are observed to have the same composition in the condensed and gaseous phases. However, Knipe's suggestion that reaction proceeds at the cloud boundaries is appropriate to the flames of the alkaline-earth metals as well, in view of the trend illustrated by Markstein's results showing a strong dependence of the heterogeneous reaction mechanism on temperature. It should be stressed, however, that Markstein's results are for a limited temperature range (410°K to 840°K) and that he states that the results should not be taken as "unqualified evidence" that heterogeneous reaction may be unimportant at higher temperatures.

In summary, Sullivan defines a flame structure model in which a predominantly

homogeneous reaction zone is located well inside the luminous envelope. Heat release, which occurs throughout this reaction zone due to oxide vapor condensation, accounts for the excitation of the species observed to radiate. Oxide particles, formed throughout the reaction zone, are swept out of the inner zone of the flame by the bulk velocity of the gaseous product species and thermophoresis effects. Since both effect decrease with increasing distance from the reaction zone, there is a region in which the particles pile up to form the outer luminous edge of the flame which is characteristic of most metal flame photographs.

REFERENCES

1. GLASSMAN, I., "Metal Combustion Processes", Amer. Rocket Soc. Preprint 938-59, 1959.
2. GLASSMAN, I., "Combustion of Metals. Physical Considerations", in Solid Propellant Rocket Research, Ed. by M. Summerfield, Academic Press, New York, 1960, pp 253-258.
3. BRZUSTOWSKI, T. A. and GLASSMAN, I., "Spectroscopic Investigation of Metal Combustion", in Heterogeneous Combustion, Ed. by Wolfhard, H. G., Glassman, I., and Green, L., Jr., Academic Press, New York, 1964, pp 41-74.
4. BRZUSTOWSKI, T. A., "Vapor-Phase Diffusion Flames in the Combustion of Magnesium and Aluminum", Ph.D. Thesis, Princeton University, Dept. of Aeronautical Engineering, 1963.
5. MARKSTEIN, G. H., "Combustion of Metals", AIAA Journal, 1, (1963), pp 550-562.
6. CHRISTENSEN, H. C., KNIPE, R. H., and GORDON, A. S., "Survey of Aluminum Particle Combustion", Pyrodynamics, 3 (1965), pp 91-119.
7. WOLFHARD, H. G., GLASSMAN, I., and GREEN, L., JR., Eds. Heterogeneous Combustion Academic Press, New York, 1964.
8. BAHN, G. S., Ed., Pyrodynamics, 3 (1965), pp 29-168.
9. BRZUSTOWSKI, T. A. and GLASSMAN, I., "Vapor-Phase Diffusion Flames in the Combustion of Magnesium and Aluminum: II. Experimental Observations in Oxygen Atmospheres", in Heterogeneous Combustion, Ed. by Wolfhard, H. G., Glassman, I., and Green, L., Jr., Academic Press, New York, 1964, pp 117-158.
10. MELLOR, A. M., "The Combustion of Aluminum and Magnesium in Carbon Dioxide - Oxygen and Carbon Dioxide-Argon Mixtures", B.S.E. Thesis, Princeton University, Dept. of Aeronautical Engineering, 1963.
11. MELLOR, A. M. and GLASSMAN, I., "Vapor-Phase Diffusion Flames in the Combustion of Magnesium and Aluminum: III. Experimental Observations in Carbon Dioxide Atmospheres", in Heterogeneous Combustion, Ed. by Wolfhard, H. G., Glassman, I., and Green, L., Jr., Academic Press, New York, 1964, pp. 159-176.
12. MELLOR, A. M., "Heterogeneous Ignition of Metals: Model and Experiment", Ph.D. Thesis, Princeton University, Department of Aerospace and Mechanical Sciences, 1967.
13. FRIEDMAN, R. and MACEK, A., "Ignition and Combustion of Aluminum Particles in in Hot Ambient Gases", Combustion and Flame, 6 (1965), pp 9-19.
14. KUEHL, D. K., "Ignition and Combustion of Aluminum and Beryllium", AIAA Journal 3, (1965), pp 2239-2247.
15. MELLOR, A. M. and GLASSMAN, I., "A Physical Criterion for Metal Ignition", Pyrodynamics, 3 (1965), pp. 43-64.
16. FRANK-KAMENETSKII, D. A., Diffusion and Heat Exchange in Chemical Kinetics, Thon, N., Translator, Princeton University Press, Princeton, N. J., 1955.
17. LAURENDEAU, N. M., "The Ignition Characteristics of Metals in Oxygen Atmospheres, M.S.E. Thesis, Princeton University, Department of Aerospace and Mechanical Sciences (1968); also AMS Report No. 851 (1968).
18. FRISTOM, R. M. and WESTENBERG, A. A., Flame Structure, McGraw-Hill, New York, 1965.
19. GRAY, P. and HARPER, M. J., "The Thermal Theory of Induction Periods and Ignition Delays", in Seventh Symposium (International) on Combustion, Butterworths, London, 1959, pp. 425-430.
20. LAIDLER, K. J., Chemical Kinetics, Second Edition, McGraw-Hill, New York, 1965.
21. KUBASCHEWSKI, O. and HOPKINS, B. E., Oxidation of Metals and Alloys, Second Revised Edition, Butterworths, London, 1967.
22. REYNOLDS, W. C., "Investigation of Ignition Temperatures of Solid Metals", NASA TN D-182, 1959.
23. KOFSTAD, P., High-Temperature Oxidation of Metals, Wiley, New York, 1966.
24. HAUFFE, K., Oxidation of Metals, English Edition, Plenum Press, New York, 1965.
25. HODGMAN, C. D., Editor, Handbook of Chemistry and Physics, 46th Edition, Chemical Rubber Publishing Co., Cleveland, 1964.
26. JANAF Thermochemical Tables, The Dow Chemical Co., Midland, Mich., March 31, 1965.
27. KAYE, G. W. C. and LABY, T. H., Table of Physical and Chemical Constants, Wiley, New York, 1966.
28. WOLFHARD, H. G. and PARKER, W. G., "Temperature Measurements of Flames Containing Incandescent Particles", Proc. Phy. Soc., (London) 62B, 523-9 (1949).
29. SCARTAZZINI, H., "Combustion du magnesium en poudre dans l'oxygene", Compt. Rend. 230, 97-8 (1950).
30. BREWER, L., "The Thermodynamic Properties of the Oxides and Their Vaporization Processes", Chem. Rev. 52, 1-75 (1953).

31. FASSELL, W. M., PAPP, C. A., HILDENBRAND, D. L. and SERNKA, R. P., "The Experimental Nature of the Combustion of Metallic Powders" in Solid Propellant Rocket Research, ed. by M. Summerfield, Progress in Astronautics and Rocketry, Vol. 1, Academic Press, 1960, p. 259-60.
32. BARTLETT, R. W., ONG, J. N., FASSELL, W. M. and PAPP, C. A., "Estimating Aluminum Particle Combustion Kinetics", Combustion and Flame, 7, 227-34 (1963).
33. THE METAL COMBUSTION STUDY GROUP "Aluminum Particle Combustion Progress Report, 1 April 1964-30 June 1965", Technical Progress Report 415, NOTS TD 3916, U. S. Naval Ordinance Test Station (1966).
34. MARKSTEIN, G. H., "Heterogeneous Reaction Processes in Metal Combustion 11th Symposium (International) on Combustion, The Combustion Institute, Pittsburgh, Pa., (1967).
35. MACEK, A., "Fundamentals of Combustion of Single Aluminum and Beryllium Particles", 11th Symposium (International) on Combustion, The Combustion Institute, Pittsburgh, Pa. (1967).
36. MARKSTEIN, G. H., "Magnesium-Oxygen Dilute Diffusion Flame", 9th Symposium (International) on Combustion, Academic Press, New York, (1963).
37. MARKSTEIN, G. H., "Rate of Growth of Magnesium Oxide Deposits Formed by Surface Reaction of Magnesium Vapor and Oxygen", presented at the Spring Meeting of the Western States Section of the Combustion Institute, Denver, Colorado, 25-26 April 1966.
38. MARKSTEIN, G. H., "Study of the Reaction of Magnesium Vapor and Oxygen at the Surface of MgO Deposits by Atomic-Absorption Spectrophotometry" presented at the 12th International Symposium on Combustion, Poitiers, France, July 1968.
39. SULLIVAN, H. F., "The Structure of the Alkaline-Earth Metal Diffusion Flame", Princeton University Ph.D. Thesis (1969), Department of Aerospace and Mechanical Sciences; also AMS Report No. 865 (1969).
40. COFFIN, K. P., "Some Physical Aspects of the Combustion of Magnesium Ribbons", Fifth Symposium (International) on Combustion, Rheinhold, New York, (1955) pp 267-76.
41. COURTNEY, W. G., "Homogeneous Nucleation from Simple and Complex Systems", pp 677-699 Heterogeneous Combustion, Wolfhard, H. G., Glassman, I., and Green, L., Jr., Editors Academic Press, New York (1964).
42. EYRING, H. and ZWOLINSKI, B. J., "The Foundations of Reaction Rate Theory and Some Recent Applications", Record Chem. Prog. 8, (1947), pp 87-102.
43. FASSELL, W. M., JR., GULBRANSEN, L. B., LEWIS, J. R., and HAMILTON, J. H., "Ignition Temperatures of Magnesium and Magnesium Alloys", J. Metals 3, (1951), pp 522-528.
44. HILL, P. R., ADAMSON, D., FOLAND, D. H., and BRESSETTE, W. E., "High-Temperature Oxidation and Ignition of Metals", NACA RM L55L23b, (1956).
45. TALLEY, C. P., "The Combustion of Elemental Boron", Solid Propellant Rocket Research, Summerfield, M., Editor, Academic Press, New York, (pp 279-285) (1960).
46. MACEK, A., FRIEDMAN, R., and SEMPLE, J. M., "Techniques for the Study of Combustion of Beryllium and Aluminum Particles", Heterogeneous Combustion, Wolfhard, H. G., Glassman, I., and Green, L., Jr., Editors, Academic Press, New York, (1964) pp 3-16.
47. NAGY, J. and SURINCIK, D. J., "Thermal Phenomena During Ignition of a Heated Dust Dispersion", Bureau of Mines RI 6811, (1966).
48. ANDERSON, H. C. and BELZ, L. H., "Factors Controlling the Combustion of Zirconium Powders", J. Electrochem. Soc. 100, (1953), pp. 240-249.
49. TETENBAUM, M., MISHLER, L., and SCHNIZLEIN, G., "Uranium Powder Ignition Studies", Nucl. Sci. Eng. 14, (1962), pp. 230-238.

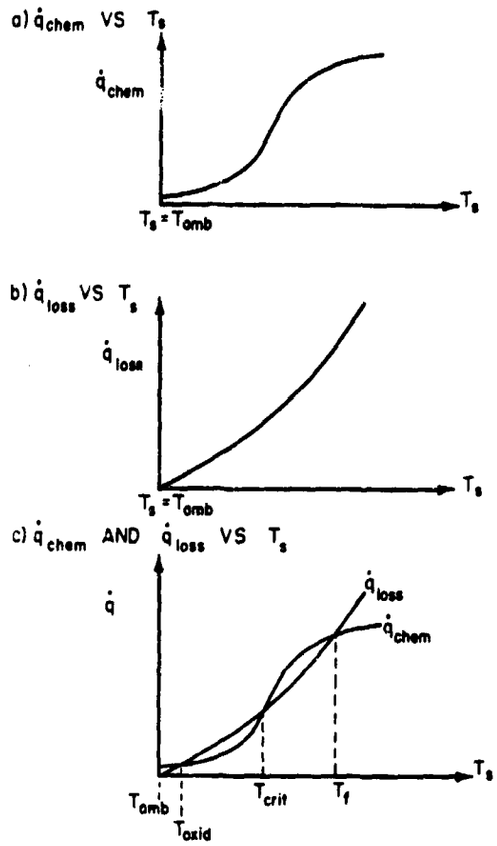

Fig. 1 Heterogeneous ignition: rate of chemical energy release and rate of heat loss vs. surface temperature

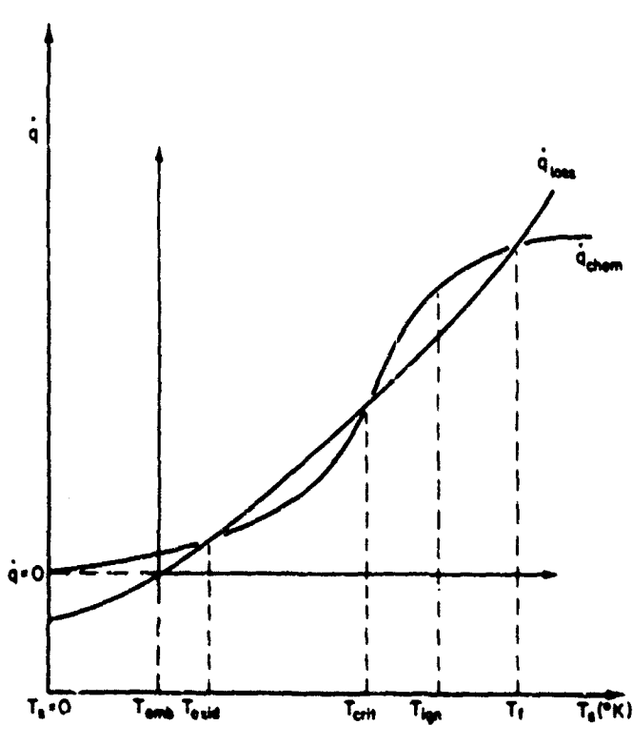

Fig. 2 Heterogeneous ignition: complete variation with temperature

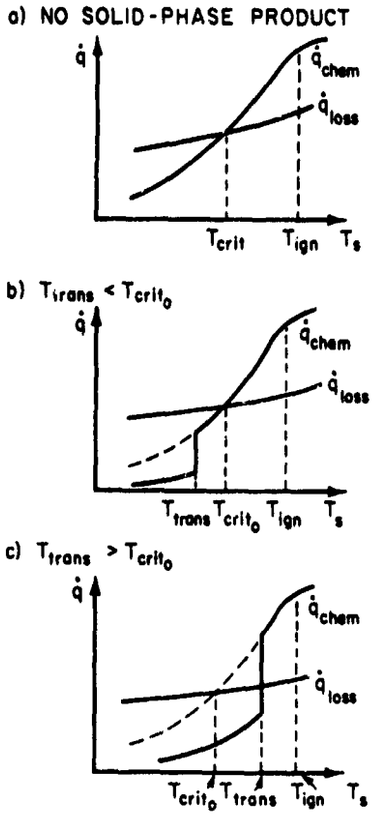

Fig. 3 The ignition criterion

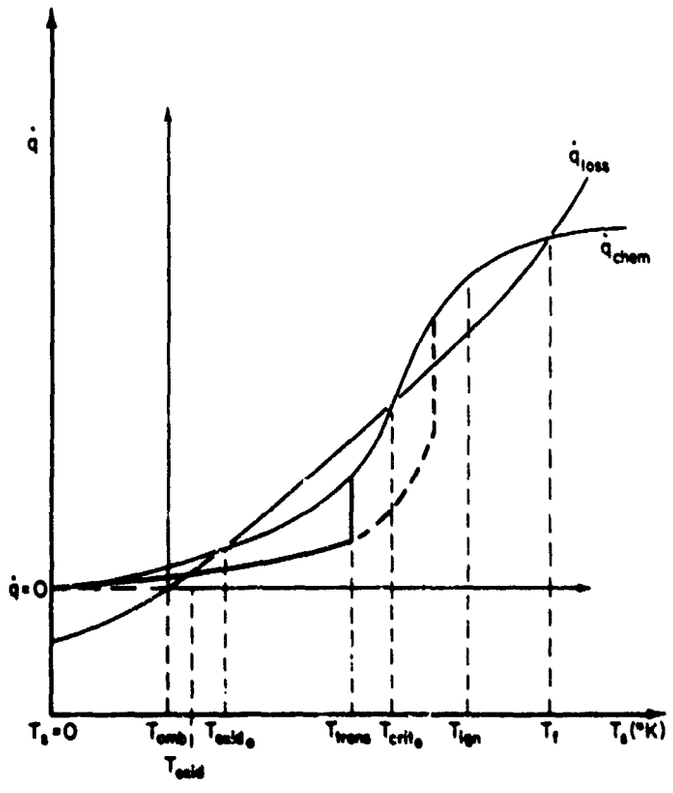

Fig. 4 The low temperature effects of the transition temperature

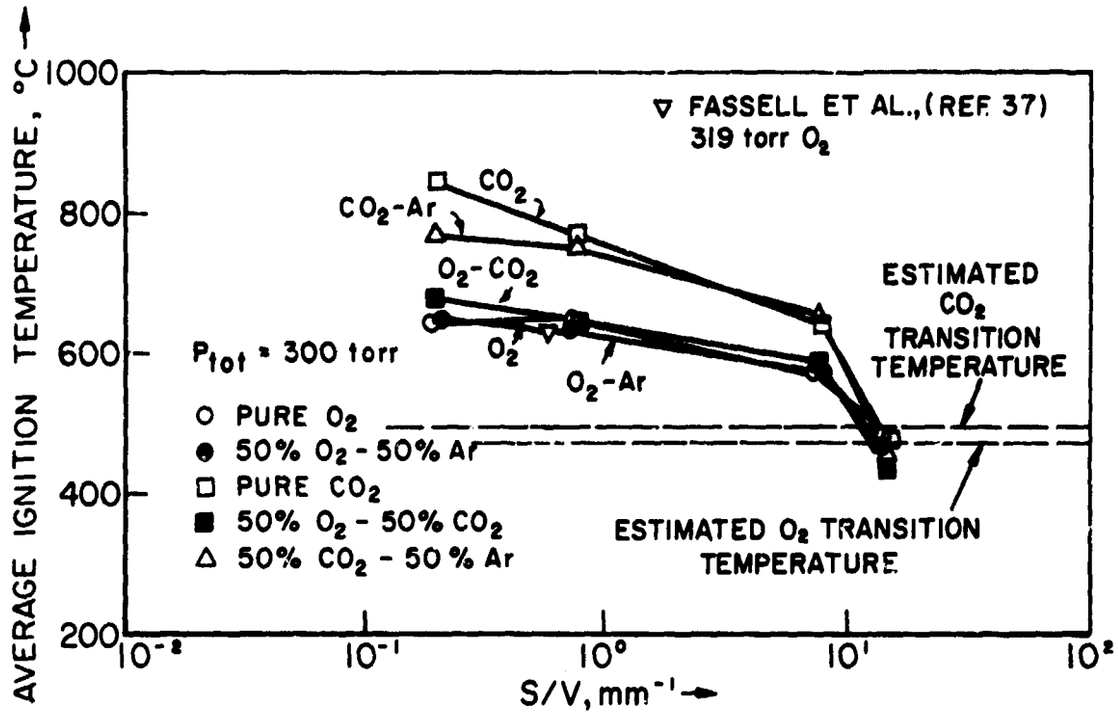

Fig.5 Magnesium average ignition temperature in various oxidizing gases vs. surface to volume ratio (total pressure = 300 torr)

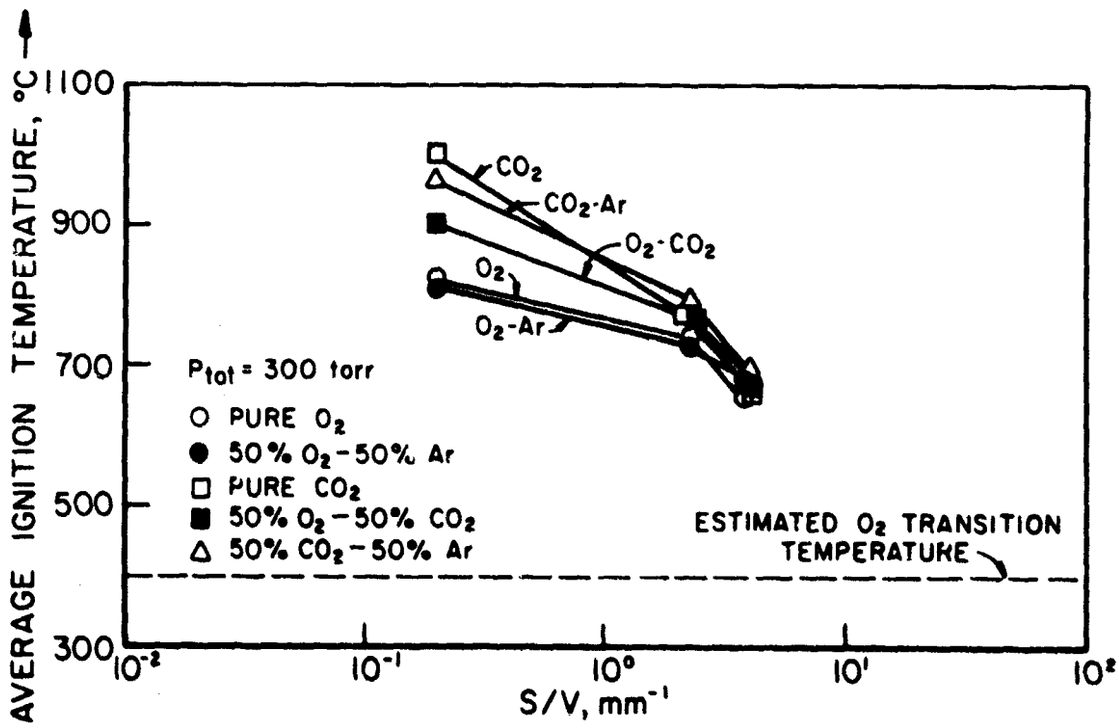

Fig.6 Calcium average ignition temperature in various oxidizing gases vs. surface to volume ratio (total pressure = 300 torr)

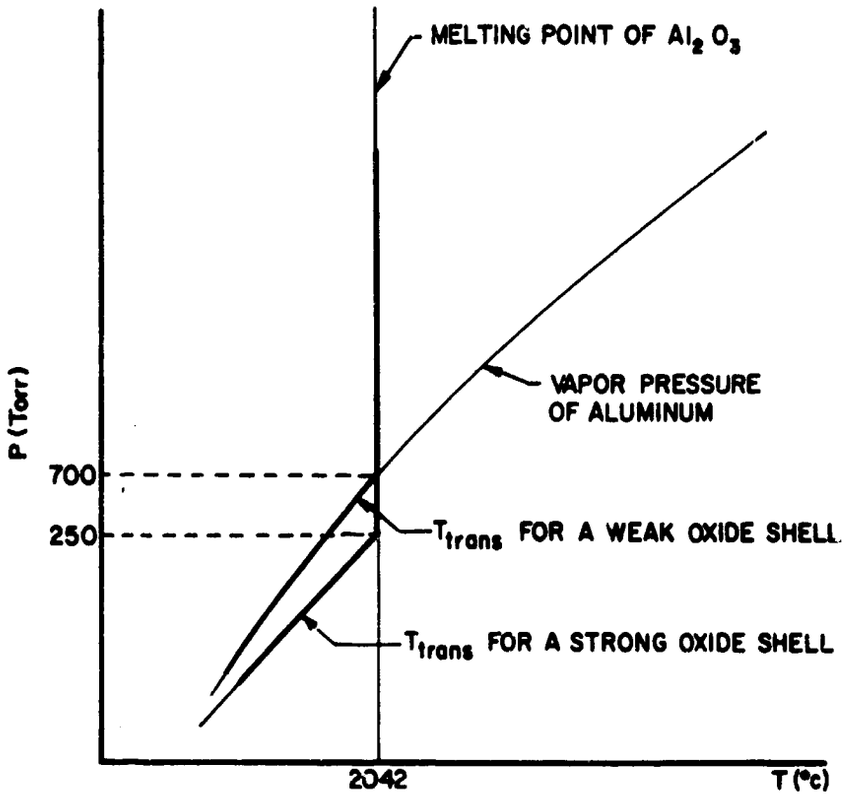

Fig. 7 Transition temperature vs. pressure for aluminum

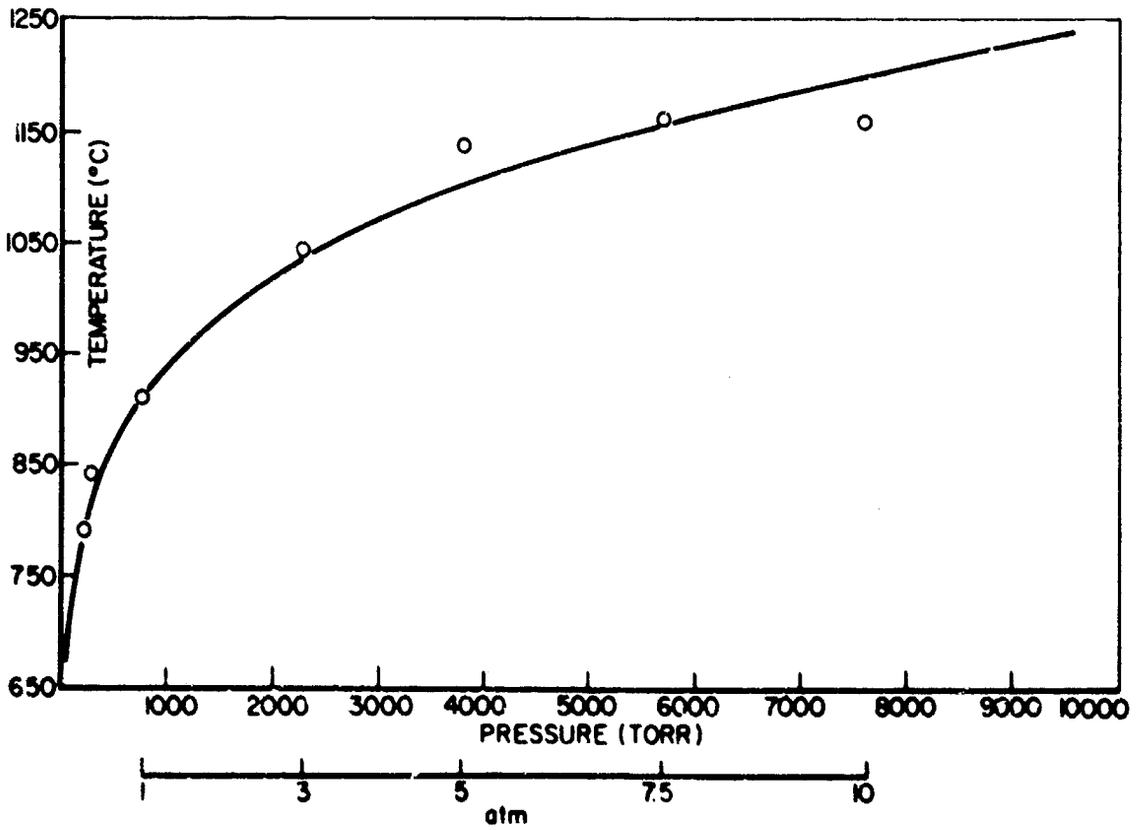

Fig. 8 Ignition temperatures vs. boiling points for zinc

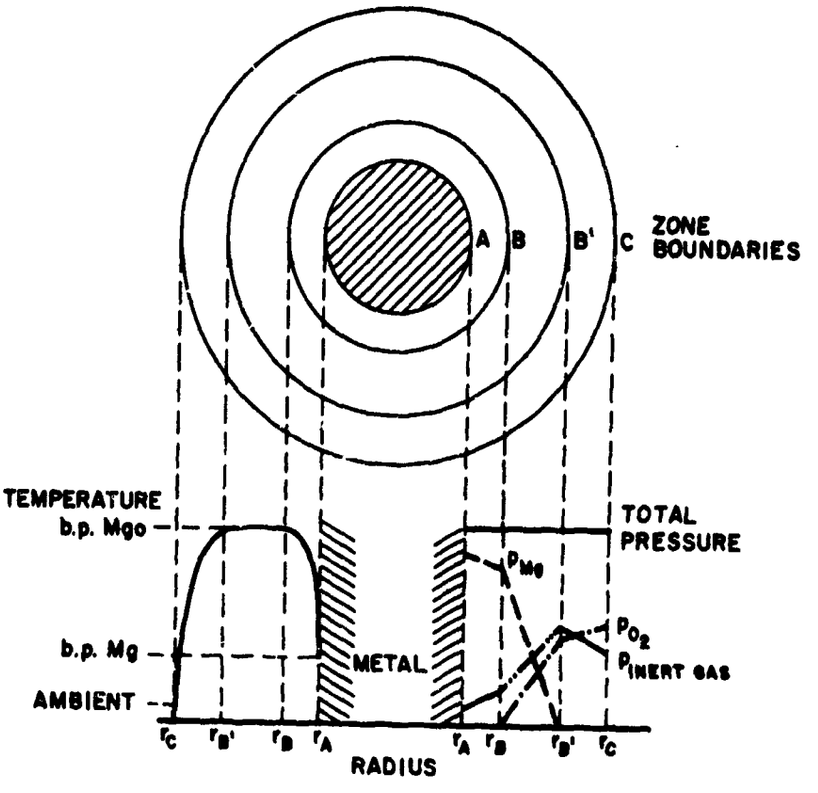

Fig. 9 Cross section of cylindrical stagnant-film model with finite reaction zone; p , partial pressure. Reproduced from Ref. 10

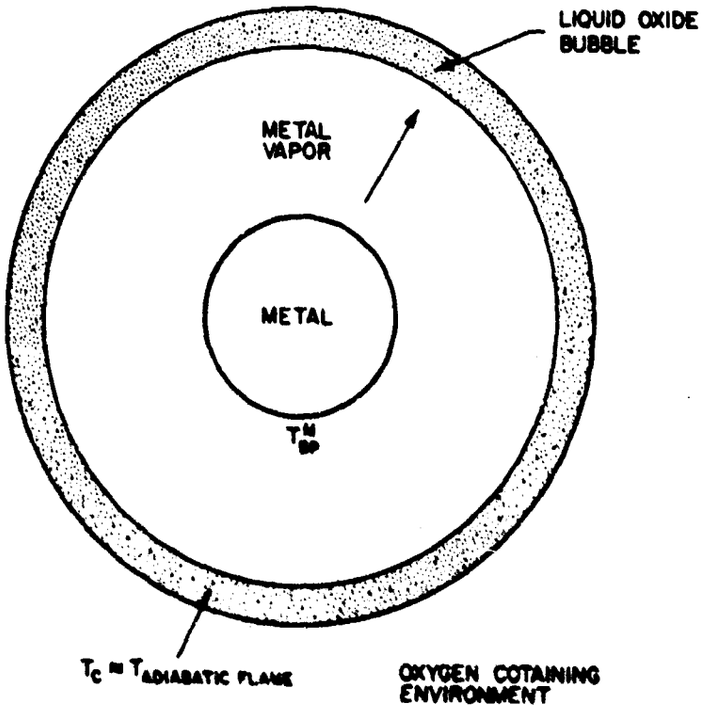

Fig. 10 Model for combustion with metal evaporation and expansion of the liquid oxide shell.
Ref: Fassell et al. Combustion and Flame 7, 237 34 (1963)

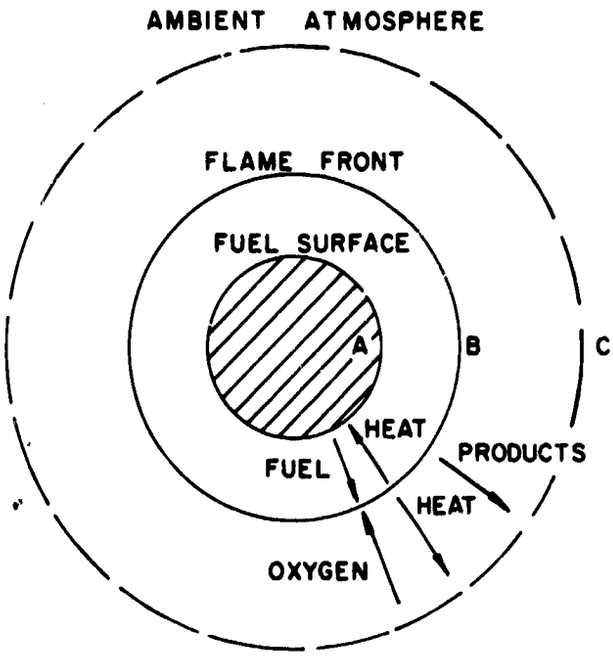

Fig.11 Droplet burning theory model

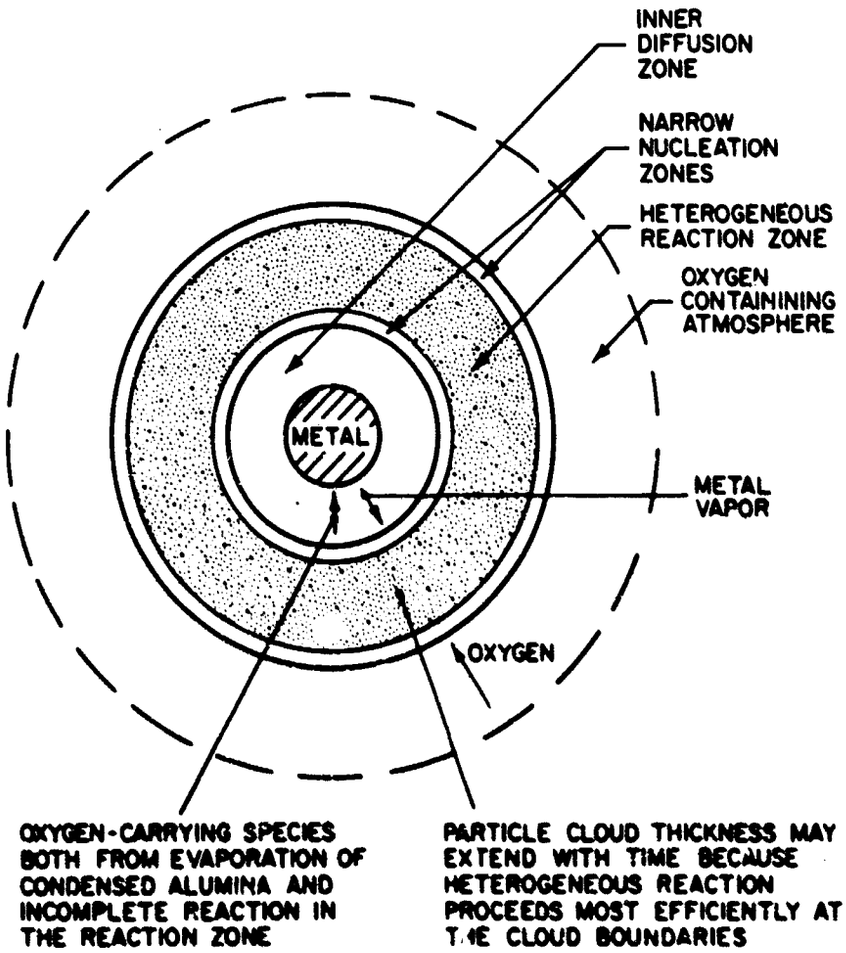

Fig.12 A mouel of aluminium particle combustion. Ref: R.H.Knipe. [illegible] TP 3916 April 1966. Technical progress report 415

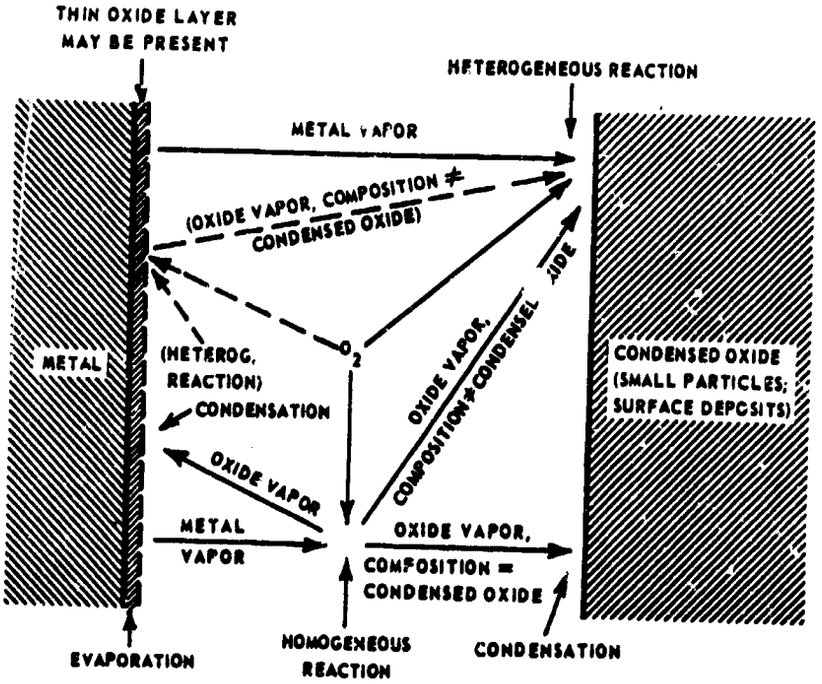

Fig. 13 Schematic representation of vapor-phase burning. Ref: Markstein, G.H. 11th Symposium (International) on combustion pg 219-234, The Combustion Institute, Pittsburgh, Penna.

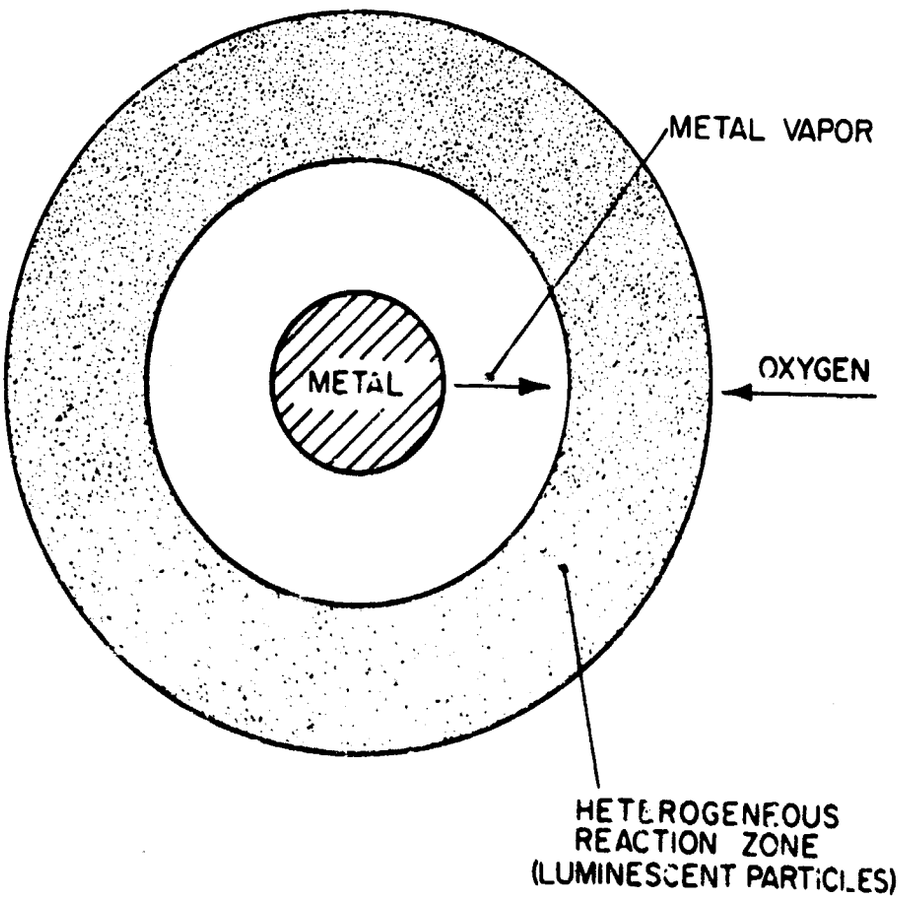

Fig. 14 [illegible]

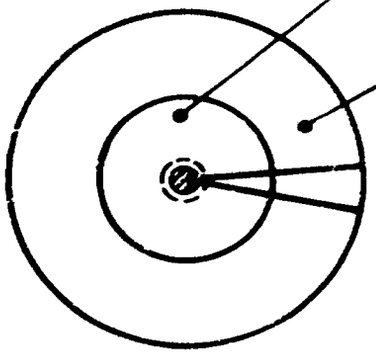

INNER FLAME ZONE
(COLORED RADIATION DUE TO METAL AND METAL OXIDE VAPOR)

OUTER FLAME ZONE
(RADIATING CONDENSED OXIDE PARTICLES)

CROSS-SECTION OF TWO ZONE CYLINDRICAL FLAME MODEL

INDICATES CONDENSED OXIDE PARTICLES WHICH GROW IN SIZE AS THEY ARE CONVECTED OUTWARD BY BULK VELOCITY AND POSSIBLE THERMOPHORESIS.

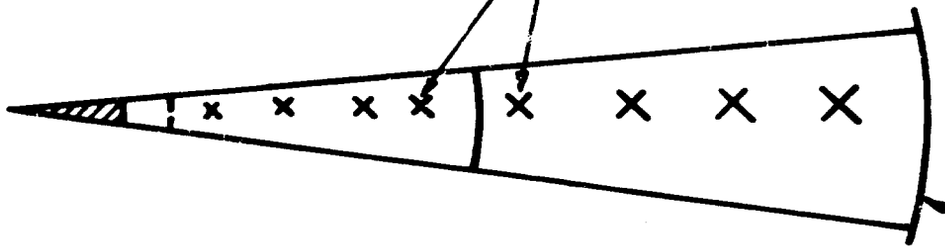

EDGE OF LUMINOUS ENVELOPE

INNER ZONE

(1) PREDOMINANTLY HOMOGENEOUS REACTION
(2) HIGHEST TEMPERATURE ZONE
(3) PARTICLE NUCLEATION AND SOME CONDENSATION

OUTER ZONE

(1) POSSIBLY HETEROGENEOUS REACTION
(2) REGION WHERE CONDENSED OXIDE PARTICLES PILE UP.

Fig. 12 Schematic representation of flame structure

APPENDIX A - THEORIES OF METAL IGNITION*

Several theories of metal ignition have been given by various investigators in the literature; these will now be reviewed. In order to facilitate comparison, the defining equations for the critical and ignition temperatures in Mellor's model are repeated:

$$\left(\dot{q}_{chem}\right)\Big|_{T_s = T_{crit}} = \left(\dot{q}_{loss}\right)\Big|_{T_s = T_{crit}} \qquad \text{Eq (10)}$$

$$\left(\frac{\partial \dot{q}_{chem}}{\partial T_s}\right)\Big|_{T_s = T_{ign}} = \left(\frac{\partial \dot{q}_{Loss}}{\partial T_s}\right)\Big|_{T_s = T_{ign}} \qquad \text{Eq (14)}$$

Some of the theories to be discussed are appropriate to systems of any size, that is, are size independent, and others are for particular types of experiments such as those involving dust dispersions.

A - BULK IGNITION ACCORDING TO THE THEORY OF EYRING AND ZWOLINSKI - The earliest theory of metal ignition is due to Eyring and Zwolinski (42). This theory, in terms of the present model, is a calculation for the critical temperatures of a bulk system based on the Theory of Absolute Reaction Rates.

The temperature under consideration was defined by the following heat balance equation:

$$\dot{q}_{chem} = \dot{q}_{loss} \qquad \text{Eq (A-19)}$$

The $\dot{q}_{chem}$ term was expressed as:

$$\dot{q}_{chem} = \dot{m}\, \Delta H_f / N \qquad \text{Eq (A-20)}$$

where $\dot{m}$ is the reaction rate (number of metal atoms/cm^{2}sec). ΔH_f is the heat of formation of the product (kcal/mole), and N is Avogadro's number.

It was stated that "the ignition of metal samples will occur when the conduction of heat through the oxide film is inadequate for the removal of the heat produced at the metal-film interface as a result of corrosion". Radiation, conduction into the metal, and conduction into the ambient oxidizing gas are neglected, and thus, $\dot{q}_{loss}$ was written:

$$\dot{q}_{loss} = k_{ox}\left(T_s - T_o\right)/d_{ox} \qquad \text{Eq (A-21)}$$

where k_{ox} is the thermal conductivity of the oxide (cal/°C cm sec), T_s is the temperature at the metal-oxide interface, T_o is the temperature at the oxide-gas interface (both in °K), and d_{ox} is the oxide film thickness (cm). Eq. (A-19) then becomes:

$$\dot{m}\, \Delta H_f / N = k_{ox}\left(T_s - T_o\right)/d_{ox} \qquad \text{Eq (A-22)}$$

The expression for the reaction rate was developed from the Theory of Absolute Reaction Rates and was written:

$$\dot{m} = \left(C_s\, k\, T_s\, F/h\right) e^{-E/kT_s} \qquad \text{Eq (A-23)}$$

where C_s is the number of absorption sites or metal atoms per unit surface area, k is the Boltzmann constant (ergs/°K), h is Planck's constant (erg sec), E is the activation energy (erg), and F is the ratio of the reaction surface area to the outer area of the oxide film. This rate expression is valid only for regimes of linear oxidation.

Eq. (A-22) and A-23) may be rewritten:

$$T_o = T_s\left[1 - \left(C_s\, k\, F\, d_{ox}\, \Delta H_f / k_{ox}\, h\, N\right) e^{-E/kT_s}\right] \qquad \text{Eq (A-24)}$$

Since ignition will occur when the heat balance represented by Eq. (A-22) is destroyed, T_s as calculated from Eq. (A-24) is the ignition temperature, which is seen to depend strongly on the oxide film thickness d_{ox}. Note, however, that in terms of the present model, T_s as calculated from Eq. (A-24) is actually the critical temperature by virtue of Eq. (10).

Upon comparison of temperatures calculated from Eq. (A-24) with ignition temperatures measured experimentally for Mg in O_2, Fassell et al. (43) noted the following difficulties withe the theory: firstly, the experimental ignition temperature is independent of oxide thickness; secondly, self-heating below the temperature predicted by Eq. (A-24) is impossible (that is, these authors recognized that self-heating below the ignition temperature is possible); and thirdly, the

* Extracted in its entirety from the Ph.D. thesis of Mellor (12).

observed pressure dependence of the ignition temperature is not explained or predicted by the theory.

Recalling that the temperatures calculated by Eyring and Zwolinski are actually critical temperatures, two of the failures of the theory noted by Fassell and co-workers can be explained. It is possible that the critical temperature is a function of oxide film thickness and self-heating is not only possible, but also expected above the critical temperature. A pressure dependence of ignition or critical temperature is predicted by a more complete theory.

Other difficulties with the theory of Eyring and Zwolinski are the independence of critical temperature with respect to sample size and the failure of the theory for zero oxide thicknesses. Also, the theory as developed applies only to temperature regimes of linear oxidation.

In view of the difficulties noted with the theory of Eyring and Zwolinski, Higgins and Schultz proposed the following modifications in which T_s and T_o were defined in terms of microscopic granules of metal: T_s is the mean temperature in the interior of a metallic granule at the metal-oxide interface; T_o is a mean temperature at the external surface of the oxide film associated with the granule; and, allowing for non-uniformities in the oxide film on the granule, d_{ox} is taken as a mean oxide thickness. It was then argued that for an aggregate of small granules, because of the near equality of T_s and T_o from granule to granule, the temperature gradient $(T_s - T_o)/d_{ox}$ becomes vanishingly small and ignition occurs. However, no calculations were attempted.

B-BULK IGNITION ACCORDING TO THE THEORY OF HILL, ADAMSON, FOLAND AND BRESSETTE- A second theory, also based on Eq. (10), was proposed by Hill and co-workers (44). These authors, however, noted that the calculation provided an estimate of the spontaneous ignition temperature, rather than ignition temperature, and is thus consistent with the definitions of the present model.

These authors balanced a rate of chemical energy release with a convection and radiation heat loss:

$$\dot{q}_{chem} = \dot{q}_{conv} + \dot{q}_{rad} \qquad \text{Eq (A-25)}$$

A conduction term into the metal was neglected because in their experiments the samples were heated uniformly. Using engineering approximations to the three terms in Eq. (A-25), good agreement between calculated and measured spontaneous ignition temperatures was obtained for 1020 steel in air. The appropriate oxidation rate involved in $\dot{q}_{chem}$ was measured in their own experiments. The calculated values were dependent on the oxide thickness (as in the theory of Eyring and Zwolinski).

A major difficulty with the theory of Hill et al. is that the wrong size dependence of critical temperature is predicted. In their approximation of $\dot{q}_{conv}$ the sample size dependence enters as follows:

$$\dot{q}_{conv} \sim Re^{1/2}/d \qquad \text{Eq (A-26)}$$

where de is now the characteristic size of the sample, and Re is the Reynolds number based on this size. Therefore, by virtue of the definition of Reynolds number:

$$\dot{q}_{conv} \sim d^{-1/2} \qquad \text{Eq (A-27)}$$

That is, as the sample size is decreased, $\dot{q}_{conv}$ increases, and so does the critical temperature.

As in the theory of Eyring and Zwolinski, the theory of Hill et al fails for clean metal surfaces, that is, for zero oxide thicknesses, because in this case the reaction rate is inversely proportional to oxide film thickness.

C-BULK IGNITION ACCORDING TO THE THEORY OF REYNOLDS - A theory of metal ignition was advanced by Reynolds (22), in which the temperature history of the metallic sample was described by the following energy equation, where conduction into the fuel is neglected:

$$\frac{C}{S}\frac{dT_s}{dt} = \dot{q}_{chem} - h(T_s - T_g) - \epsilon\sigma(T_s^4 - T_a^4) + \dot{q}_{input} \qquad \text{Eq (A-28)}$$

where C = total heat capacity of the sample, cal/°K;
s = surface area of the sample, cm^2;
T_s = surface temperature of the sample, °K;
t = time, sec;
$\dot{q}_{chem}$ = chemical energy release rate per unit area, $cal/cm^2 sec$;
h = heat transfer coefficient, $cal/cm^2 sec\,°K$;
T_g = sample recovery temperature, °K;
σ = Stefan-Boltzmann constant, $cal/cm^2 sec\,(°K)^4$;

ϵ = surface emissivity, dimensionless;
T_r = effective radiation temperature of the environment, °K;
$\dot{q}_{input}$ = any heat input independent of the body temperature, cal/cm^{2}sec.

According to Reynolds, "the ignition temperature is seen to be equivalent to the temperature at which the body temperature begins to increase at an increasing rate. This may be expressed mathematically as the temperature at which dT_s/dt is a minimum. Thus, at ignition:

$$\frac{d}{dT_s}\left(\frac{c}{s}\frac{dT_s}{d\tau}\right) = 0 \qquad \text{Eq (A-29)}$$

or, from Eq. (A-28)=

$$\frac{d\dot{q}_{chem}}{dT_s} - h - 4\epsilon\sigma T_s^3 = 0 \qquad \text{Eq (A-30)}$$

Reynolds defined ignition to occur at an inflection point in the surface temperature-time curve; as no equilibrium positions (with respect to time) are indicated in his model and as the surface temperature is rising in time, by definition, the critical temperature has been exceeded. He then incorrectly indicated that dT_s/dt goes through a minimum at ignition, above the critical temperature.

In the present model ignition occurs at a maximum value of dT_s/dt above the critical temperature, which is indeed an experimental criterion for ignition. Mathematically, of course, there is no difference in the defining equation for ignition temperature, but the intuitive difference in approach to this equation is stressed.

Reynolds wrote $\dot{q}_{chem}$ as follows:

$$\dot{q}_{chem} = \dot{m}\, Q_{chem} \qquad \text{Eq (A-31)}$$

where $\dot{m}$ is the reaction rate (g O_2/cm^{2}sec) and Q_{chem} is the heat of reaction (cal/g O_2). He considered both linear

$$w = K_l t = A_l t\, e^{-E_l/RT_s} \qquad \text{Eq (A-32)}$$

and parabolic regimes of oxidation

$$w^2 = K_p t = A_p t\, e^{-E_p/RT_s} \qquad \text{Eq (A-33)}$$

where the K_i are the appropriate rate constants, A_i are the appropriate pre-exponential factors, E_i are the appropriate activation energies, and R is the universal gas constant. w is the weight of O_2 per unit area that has reacted with the metal at time t.

Since

$$\dot{m} = \partial w/\partial t \qquad \text{Eq (A-34}$$

then

$$\dot{m}_l = K_l = A_l\, e^{-E_l/RT_s} \qquad \text{Eq (A-35)}$$

and

$$\dot{m}_p = K_p/2w = K_p\gamma/2\rho_{ox}\, d_{ox} \qquad \text{Eq (A-36)}$$

Therefore*:

$$\dot{m} = \left(A_p\gamma/2\rho_{ox}\, d_{ox}\right) e^{-E_p/RT_s} \qquad \text{Eq (A-37)}$$

where ρ_{ox} is the oxide density, d_{ox} is the oxide thickness, and γ is the ratio of the mass or oxide to the mass of O_2 forming it. Multiplying by the heat release per gram O_2, Q_{chem}, the heat release rates are obtained:

$$\dot{q}_{chem,l} = A_l\, Q_{chem}\, e^{-E_l/RT_s} \qquad \text{Eq (A-38)}$$

$$\dot{q}_{chem,p} = \left(A_p\gamma Q_{chem}/2\rho_{ox}\, d_{ox}\right) e^{-E_p/RT_s} \qquad \text{Eq (A-39)}$$

Substitution of Eq. (A-38) or (A-39) into Eq. (A-30) yields:

$$e^{-1/T_{s,i}^*} = (T_{s,i}^*)^5/\eta_i + h_i^*(T_{s,i}^*)^2 \qquad \text{Eq (A-40)}$$

---

* Markstein (5) has shown that the placement of in the denominators of Eq. (A-36) and A-37), as in the original paper of Reynolds, is in error.

where subscript i equals 1 or p, and where

$$T^*_{s,i} = T_s R/E_i \qquad \text{Eq (A-41)}$$

$$\eta_1 = A_1 Q_{chem} R^4/4\epsilon\sigma E_1^4 \qquad \text{Eq (A-42)}$$

$$\eta_p = A_p \gamma Q_{chem} R^4/8\epsilon\sigma \rho_{ox} d_{ox} E_p^4 \qquad \text{Eq (A-43)}$$

$$h_1^* = h E_1/A_1 Q_{chem} R \qquad \text{Eq (A-44)}$$

$$h_p^* = 2h E_p \rho_{ox} d_{ox}/A_p \gamma Q_{chem} R \qquad \text{Eq (A-45)}$$

The $T^*_{s,i}$ are dimensionless ignition temperatures, h^*_i are dimensionless heat transfer coefficients, and the η_i are called pyrophoricities by Reynolds.

Reynolds noted that either an increase or decrease in the rate of convective heat transfer (and, furthermore, when this term represents either heating or cooling) will increase the calculated ignition temperature.

Since the ignition temperature is expressed by the universal curve Eq (A-40), all metal-oxidizer systems were expected to agree with this prediction. Reynolds calculated a family of curves of T^*_s versus η for various values of h*. He then measured ignition temperatures for various massive systems. For the specific systems, the oxidation rate data were taken from the oxidation literature. Extremely good agreement between the curve of T^*_s versus η with h* equal to zero was obtained in all the cases investigated. Reynolds argued that this agreement with the case of zero convective heat transfer was a result of his measuring the ignition temperatures in quiescent atmospheres. Experimentally, ignition was defined by "a sharp break in the temperature curve."

As noted previously, Reynolds' resulting theoretical definition of the ignition temperature, Eq. (A-30), is equivalent to that of the present investigation, Eq. (14). The experimental definition is also equivalent. Thus agreement between theory and experiment, within the experimental error and the theoretical error in estimating the various parameters which appear in Eq. (A-41) - (A-43), is not unexpected. However, in the theory of Reynolds, the ignition temperature is predicted to be independent of sample size, and, furthermore, no pressure dependence is predicted, because of the experimental indication that convective heat losses to the ambient gases are negligible.

D-BULK IGNITION ACCORDING TO THE THEORY OF TALLEY - Talley (45) made a calculation of "the minimum temperature above which the combustion of boron is self-sustaining. . . . by equating the rate of heat generation by chemical reaction with the rate of heat loss by radiation as functions of temperature." He referred to this temperature as an ignition temperature, but, of course, in the present model this temperature is defined as the critical temperature. Estimates of the reaction rate were acquired from data about 700°C below the ignition temperature in a temperature regime in which the evaporation of B_2O_3 from the metal surface is rate-determining.

As Talley recognized, because only a radiation heat loss mechanism is assumed, the theory is valid only for large samples. Under these assumptions, an ignition temperature of about 1925°C was predicted for large B samples in O_2. Because of the experiment employed to investigate the ignition process, critical and ignition temperatures could not be distinguished.

By introducing a 1 mm diameter B rod into an O_2-rich natural gas flame and using a corrected optical pyrometer to measure surface temperature, Talley made the following observations: "at temperatures about 1800°K the boron was observed to burn relatively slowly. Between 1800 and 2100°K the rate increased evenly. A temperature of 2230°K (1957°C) was the highest temperature before there was a sudden increase in burning rate." The correspondence of the temperature of this sudden rate change and the calculated ignition temperature is excellent.

As is the case with most of the other theories discussed to this point, Talley's theory predicts that the calculated critical temperature is independent of sample size and oxidizer pressure.

E-SINGLE PARTICLE IGNITION ACCORDING TO THE THEORY OF FRIEDMAN AND MACEK - Friedman and Macek (13) developed an ignition theory in order to explain their experimental results on the ignition of Al particles. They later applied similar ideas to the ignition of Be (46).

The attempt to explain their results on the basis of a simple heat balance led to several discrepancies with their experimental results. The theory predicted a strong dependence of the ignition temperature on particle size and on ambient oxidizer concentration, whereas experimentally these parameters had little influence on ignition temperatures. Also, predicted ignition temperatures were considerably higher than the measured temperatures.

In order to circumvent these difficulties, on the basis of the experimental association of the Al ignition temperature with the melting point of Al_2O_3 they assume that a discontinuous increase in reaction rate occurs at the melting point of the oxide, T_{MP}^{MO} (T_s is the particle temperature):

$$\dot{q}_{chem} = Q_{chem}\, C_g\, K \qquad T_s < T_{MP}^{MO} \qquad \text{Eq (A-46)}$$

$$\dot{q}_{chem} = Q_{chem}\, C_g\, K' \qquad T_s \geq T_{MP}^{MO} \qquad \text{Eq (A-47)}$$

where Q_{chem} is the heat of reaction (cal/mole), c_g is the concentration of oxidizer at the particle surface (mole/cm^3), and k and k' are rate constants (cm/sec), with $k' >> k$.

Two heat fluxes in the ambient gas were considered:

$$\dot{q}_{cond,g} = 2K_g\,(T_s - T_g)/d \qquad \text{Eq (A-48)}$$

$$\dot{q}_{diff} = 2Q_{chem}\, D\,(C_{g,\infty} - C_g)/d \qquad \text{Eq (A-49)}$$

where $\dot{q}_{cond,g}$ is the heat lost by conduction, k_g is the thermal conductivity of the gas (cal/cm sec $^\circ$K), T_g is the gas temperature ($^\circ$K), d is the particle diameter (cm), $\dot{q}_{diff}$ is the heat flux due to oxidizer diffusion to the reaction zone, D is the oxidizer diffusivity (cm^2/sec), and $c_{g,\infty}$ is the oxidizer concentration at infinity (mole/cm^3).

Because the particle is assumed to be at uniform temperature T_s, conduction into the particle is neglected. Radiation losses are also neglected in the ignition process.

A temperature defined by an equilibrium:

$$\dot{q}_{cond,g} = \dot{q}_{diff} \qquad \text{Eq (A-50)}$$

$$\dot{q}_{chem} = \dot{q}_{cond,g} \qquad \text{Eq (A-51)}$$

exists below the oxide melting point; above this temperature the particle may self-heat (that is, this temperature is, in terms of the physical model, the critical temperature). The authors referred to this temperature as the minimum ambient temperature required for ignition.

Friedman and Macek proceeded in this manner in order to evaluate the oxidizer concentration at the particle surface from Eq. (A-50), (A-48), and (A-49):

$$C_g = C_{g,\infty} - K_g\,(T_s - T_g)/D\,Q_{chem} \qquad \text{Eq (A-52)}$$

Eq. (A-51) may be rewritten:

$$Q_{chem}\, C_g\, K = 2K_g\,(T_s - T_g)/d \qquad \text{Eq (A-53)}$$

Eq. (A-52) is then substituted into Eq. (A-53) and the expression for the minimum ambient temperature required for ignition is obtained:

$$T_g = T_s - C_{g,\infty}\, Q_{chem} \Big/ \left[K_g\left(\frac{1}{D} + \frac{2}{dK}\right)\right] \qquad \text{Eq (A-54)}$$

Since at ignition, $T_s = T_{MP}^{MO}$, Eq. (A-54) becomes:

$$T_g = T_{MP}^{MO} - C_{g,\infty}\, Q_{chem} \Big/ \left[K_g\left(\frac{1}{D} + \frac{2}{dK}\right)\right] \qquad \text{Eq (A-55)}$$

Friedman and Macek noted that the correction term, the second term on the right hand side of Eq. (A-55), is extremely small compared to T_{MP}^{MO}, which explains the observed small dependence of ignition temperature on d and D.

The theory is applicable only to small particles because conduction into the interior of the particle and radiation to the surroundings are neglected.

A major difficulty with the theory is that as the particle diameter is increased, the minimum ambient temperature required for ignition (or critical temperature) decreases. Also, k, the reaction rate, which appears in Eq. (A-55) is a function of temperature, and pressure.

F-DUST DISPERSION IGNITION ACCORDING TO THE THEORY OF NAGY AND SURINCIK - Nagy and Surincik (47) have recently developed a theory for ignition of dust dispersions. Their theory was tested against experimental results on the ignition of dust dispersions. Their theory was tested against experimental results on the ignition of cornstarch; nevertheless, inasmuch as dust dispersion experiments give ignition temperatures which have little correlation with transition temperatures (12), the ignition temperatures of dust dispersions of cornstarch or metal powders are expected to be predicted equally well by a theory which does not include a transition temperature concept.

Again a simple heat balance is used to define ignition, so that in actuality, a critical rather than ignition temperature is estimated:

$$\dot{q}_{chem} = \dot{q}_{loss} \qquad \text{Eq (A-56)}$$

Because of the nature of the sample configuration, somewhat more complicated expressions for the heat fluxes result. Also, heat fluxes per unit volume rather than per unit area are considered.

The following assumptions were made:

1. The entire system (gas plus particles) is described by the equation of state pV = RT, where p is pressure, V is volume, R is the universal gas constant, and T is the temperature.

2. The dispersion is uniform with respect to volume, and the volume of the particles is negligible with respect to that of the gas.

3. Mass transfer is negligible during ignition.

4. Heat capacities are temperature independent.

5. Heat transfer occurs primarily by conduction and convection and is linearly proportional to the temperature difference.

6. Any action of the addition of an inert dust to the dispersion is strictly thermal.

7. A bimolecular oxidation process is assumed, and the rate variation of this process with respect to temperature is expressed by an Arrhenius-type function.

The heat release due to reaction per unit volume may then be expressed:

$$\dot{q}_{chem} = A\, Q_{chem}\, (F)^{\alpha} (OX)^{\beta} (\rho/RT)^{2} e^{E/RT} \qquad \text{Eq (A-57)}$$

where all symbols have their previous meanings, and where α is the order of the reaction with respect to fuel (F) and β with respect to oxidizer (OX). (F) and (OX) are the relative molar concentrations per unit volume. Several simplifications of Eq. (A-59) are made as indicated below.

Since O_2 is the only reacting component of the gas phase, "the system may be considered unimolecular with respect to the gaseous phase. Thus the term p/RT is taken at the first power rather than at the second power, and the units of A become 1/sec. The system contains the inert gases nitrogen and admixed carbon dioxide, and the rate of reaction is lowered by the fraction , which represents the proportion of oxygen in the atmosphere." Since at ignition, by definition the concentration of products is negligible:

$$(F) + (OX) = 1 \qquad \text{Eq (A-58)}$$

Because the number of moles of O_2 per unit volume is p /RT, the weight of O_2 per unit volume, Z, is:

$$Z = \rho\, \mathcal{O}\, \mathcal{M}_{O_2} / RT \qquad \text{Eq (A-59)}$$

where $\mathcal{M}_{O_2}$ is the molecular weight of O_2.

The effective surface area of the dust is included in the chemical heat release rate by modification of the activation energy, that is, exp (-E/RT) is replaced by exp (-σ E/RT), where σ is the effective surface area of the dust, and E is a property only of the fuel. Finally,

$$(F) = (x/m_d)/(x/m_d + z/m_{O_2}) \qquad \text{Eq (A-60)}$$

where X is the initial dust concentration in g/cm^3 and m_d is the molecular weight of the dust. Then:

$$(F)^{\alpha}[1-(F)]^{\beta} = [x/(x+bz)]^{\alpha}[1-x/(x+bz)]^{\beta} \qquad \text{Eq (A-61)}$$

$$\equiv f(x) \qquad \text{Eq (A-62)}$$

where

$$b \equiv m_d/m_{O_2} \qquad \text{Eq (A-63)}$$

Thus combining Eq. (A-57) through (A-62):

$$q_{chem} = \{A Q_{chem} z f(x)/m_{O_2}\} e^{-\sigma E/RT} \qquad \text{Eq (A-64)}$$

The rate of heat loss per unit volume is expressed in the following manner:

$$q_{loss} = [\sum k_i N_i c_{p_i} + V'](T - T_f) \qquad \text{Eq (A-65)}$$

where subscript i includes all constituents of the dust and gas system, k_i is the coefficient of heat transfer of species i (including conduction, convection, and radiation), (1/sec), N_i is the concentration of species i at the furnace temperature T_f (g/cm^3), $c_{p,i}$ is the specific heat of species i at T_f (cal/g ^{o}K), and V' is the rate of heat loss per degree per unit volume to the vessel walls (cal/sec ^{o}Kcm^3).

The experimental results indicated that the heat transfer coefficients, k_i, are all of the same order of magnitude. Thus,

$$K_i = K \qquad \text{Eq (A-66)}$$

and

$$V = V'/K \qquad \text{Eq (A-67)}$$

Following Semenov, the approximation is made:

$$T - T_f \cong RT_f^2/\sigma E \qquad \text{Eq (A-68)}$$

(A-65) becomes in its final form:

$$q_{loss} = (KRT_f^2/\sigma E)[\sum_i N_i c_{p_i} + V] \qquad \text{Eq (A-69)}$$

The condition for ignition, Eq. (A-56), is then:

$$\{A Q_{chem} z f(x)/m_{O_2}\} e^{-\sigma E/RT} = \{KRT_f^2/\sigma E\}[\sum_i N_i c_{p_i} + V] \qquad \text{Eq (A-70)}$$

Nagy and Surincik obtained the values of σ, k', V, α, β, and b, where

$$K' \equiv KR m_{O_2}/\sigma A Q_{chem} E \qquad \text{Eq (A-71)}$$

from their experimental results on the ignition of cornstarch. They then varied the furnace temperature and concentrations of fuel dust, inert dust, and oxygen over wide ranges, and found an excellent correlation between theory and experiment. Predictions of ignition limits were also verified experimentally.

G-QUIESCENT PILE IGNITION ACCORDING TO THE THEORY OF ANDERSON AND BELZ - Anderson and Belz (48) proposed a qualitative theory of the ignition of quiescent piles of metal powders. In particular, they considered the ignition of Zr in O_2. It was assumed that a spherical mass of powder of radius r is in perfect contact with a heat reservoir at temperature T_o. This spherical mass of powder consists of spherical particles of diameter d. "If the rate of heat development at the center of the mass is greater than the rate at which the heat can be transported to the container, ignition eventually occurs. Then, the following condition is necessary to ignition: rate of exothermic heat development > rate of heat loss." Therefore, this theory is a discussion of the critical temperature for a quiescent pile experiment.

The appropriate reaction rate law for Zr in O_2 was taken as

$$w^2 = k_p t + const \qquad \text{Eq (A-72)}$$

where w is the increase in weight of the metal sample per unit area. The reaction rate per unit area is then:

$$\frac{dw}{dt} = \frac{1}{2}\sqrt{\frac{K_2}{t}} = \frac{\sqrt{A'}\,e^{-E/2RT}}{2\sqrt{t}} \qquad \text{Eq (A-73)}$$

where all symbols have their previous meanings.

The total surface area per gram of a system of uniformly sized particles is $6/\rho d$, where ρ is the metal density*. Anderson and Belz then wrote the rate of heat generation by the center element as

$$q_{chem} = (A' Q_{chem}/\sqrt{t}\,\delta)\,e^{-E/2RT} \qquad \text{Eq (A-74)}$$

where A' includes all previous constants.

The heat loss term is assumed to be of the form:

$$q_{loss} = K(T - T_a)/r \qquad \text{Eq (A-75)}$$

where k is the appropriate thermal conductivity of the particle plus void configuration. The criterion for ignition then becomes:

$$(A' Q_{chem}/\sqrt{t}\,\delta)\,e^{-E/2RT} > K(T - T_0)/r \qquad \text{Eq (A-76)}$$

Anderson and Belz noted that this expression could not be solved for the ignition temperature T in terms of the ambient temperature T_0. However, simplifications are possible if the assumption that $(T - T_0)$ is equal to a small constant value is made. Then Eq. (A-76) may be written:

$$e^{-E/2RT_0} > A''\sqrt{t}\,\delta/r \qquad \text{Eq (A-77)}$$

or

$$T_0 > E/\{2R\ln(r/A''\sqrt{t}\,\delta)\} \qquad \text{Eq (A-78)}$$

Anderson and Belz stated that "various interpretations of the time factor in this expression are possible. If it is interpreted as an inverse function of the external heating rate, then the expression predicts a decrease in ignition temperature with heating rate. This is the experimental case for small samples. In the case of larger samples, the increase of ignition temperature with heating rate is attributed to increased lag of internal temperature with respect to external temperature. . . . The expression is in qualitative agreement with the data, as regards particle size." The trend predicted is that the ignition temperature will decrease with decreasing particle diameter, d.

H-QUIESCENT PILE IGNITION ACCORDING TO THE THEORY OF TETENBAUM, MISHLER, AND SCHNIZLEIN - Tetenbaum et al (49) correlated their experimental results on the ignition of quiescent piles of U powder in O_2 on the basis of the ignition theory of Frank-Kamenetskii. They also applied an ignition theory of Murray, Buddery, and Taylor, which was originally developed in light of the data of Anderson and Belz (48).

Using the stationary homogeneous ignition theory of Frank-Kamenetskii, Tetenbaum and co-workers found excellent agreement between their experimental results and ignition temperatures calculated on the basis of the critical size result of Frank-Kamenetskii (16) with , the shape constant, equal to 0.88, that is, for a one-dimensional container.

The agreement between a theory developed for homogeneous gas-phase systems with results obtained in a quiescent pile powder experiment no doubt results from the homogeneous nature of this latter experimental configuration, that is, the small metal particles separated by spaces filled with O_2. Again, Eq (10) is the defining equation in this theory, a critical temperature has been calculated.

Tetenbaum et al then applied a theory due to Murray, Buddery, and Taylor; the physical basis of this theory is questionable. Here no heat losses are included, and all the heat generated by the chemical reaction is used to increase the temperature of the pile of powder. Effectively, then, the critical temperature for this theoretical model is zero, for as long as any exothermic reaction occurs, the temperature of the sample will increase until ignition occurs.

According to Murray et al as quoted by Tetenbaum and co-workers, the rate of heating due to chemical reaction of a metal powder in the linear oxidation rate regime is:

---

* Anderson and Belz erroneously gave this expression as $6/\rho d^5$, but apparently used $6/\rho d$ in their subsequent calculations.

$$\frac{dH}{dt} = \frac{6MQ_{chem}Ae^{-E/RT}}{\rho D} \qquad \text{Eq (A-79)}$$

where H is enthalpy, M is the mass of the powder, d is the diameter of a particle within the powder, and ρ is the density. If the container is heated at the rate $dT/dt = \phi$, then the total enthalpy generated upon heating from 298°K to T°K is:

$$H = \int_{298}^{T} \frac{6MQ_{chem}Ae^{-E/RT}}{\phi\rho\alpha}\,dT \qquad \text{Eq (A-80)}$$

Also,

$$H = MC_p\Delta T \qquad \text{Eq (A-81)}$$

where c_p is the specific heat of the powder and ΔT is the temperature rise resulting from reaction upon raising the container temperature from 298°K to T°K at a rate of ϕ°K/min*. Thus,

$$\Delta T = \int_{298}^{T} \frac{6Q_{chem}Ae^{-E/RT}}{\phi\rho C_p\alpha}\,dT \qquad \text{Eq (A-82)}$$

After integration, Eq. (A-82) may be written:

$$\log\{R\rho d\phi C_p\Delta T/6Q_{chem}AE\} = -E/4.56T_0 + \log\left\{\left(\frac{RT_0}{E}\right)^2 - 2\left(\frac{RT_0}{E}\right)^3\right\} \qquad \text{Eq (A-83)}$$

where T_0 is the container temperature at which ignition occurs. ΔT is "the difference in temperature between the sample and container at ignition."

On the basis of the data of Anderson and Belz obtained with Zr powder (48), Murray and co-workers took T=50°K. Tetenbaum et al. used this value of T and calculated ignition temperatures, T_0, for their experiments from Eq. (A-83). Again, excellent agreement between theory and experiment was obtained.

At first sight, there is an apparent contradiction between these two theories. Critical temperatures are calculated from the theory of Frank-Kamenetskii because of the starting equation, Eq. (10). Because no heat losses are involved in the theory of Murray et al., the critical temperature is zero and the calculated temperature may be an ignition temperature. Yet temperatures calculated from both theories agree extremely well with each other and with experiment. This could mean that the critical and ignition temperatures are equivalent in this particular experiment.

First, however, it is not clear that the temperature calculated from the Murray theory is an ignition temperature, and particularly the ignition temperature as defined in the physical model of metal ignition. Secondly, in this theory, ignition is regarded to occur when the amount of sample self-heating over the container temperature, ΔT, is equal to 50°K. This value, however, was estimated on the basis of results of Anderson and Belz.

It was shown in the previous sections of this chapter that these latter investigators most likely measured critical temperatures rather than ignition temperatures. Thus, the agreement of the Murray and Frank-Kamenetskii theories is not fortuitous, because the choice of ΔT=50°K was based on critical temperature data.

---

* There is a typographical error in the definition of H in Ref. (49), in which $H = Nc_p\Delta T$. Eq. (A-81) above is correct.

RESULTATS EXPERIMENTAUX RECENTS SUR LA COMBUSTION DE L'ALUMINIUM ET D'AUTRES METAUX

RECENT EXPERIMENTAL RESULTS ON THE COMBUSTION OF ALUMINIUM AND OTHER METALS

par Marcel BARRERE

OFFICE NATIONAL D'ETUDES ET DE RECHERCHES AEROSPATIALES

92 CHATILLON - France

- SOMMAIRE -

L'étude de la combustion des métaux a pris ces derniers temps de l'importance depuis que ceux-ci sont utilisés comme combustibles dans les systèmes de propulsion moderne. Le délai d'allumage et le temps de combustion des particules métalliques, le rendement de combustion et la nature des produits brûlés sont les points importants qui intéressent le spécialiste de la propulsion et qui sont pris en considération dans cet exposé.

La première partie est consacrée aux techniques expérimentales utilisées pour l'étude de la combustion d'un métal. Deux groupes principaux ont été définis, l'un se rapportant à la combustion des particules, l'autre à celle des fils. Dans le premier groupe, quelques méthodes statiques ont été développées, la particule étant fixée à un support, mais les plus courants consistent à placer les particules dans un écoulement. Dans le deuxième groupe, l'allumage est simple et la combustion plus facile à étudier. L'analyse des phénomènes de combustion est effectuée par cinémicrographie, par figeage de la combustion sur des parois froides, par spectographie... Une étude critique de ces diverses techniques est présentée.

La deuxième partie est une synthèse des résultats expérimentaux mettant en évidence pour chaque métal et en particulier pour l'aluminium, le béryllium, le magnésium et le bore, l'influence de divers paramètres comme la nature des gaz environnants, leur pression et la température, l'influence de l'état de surface du métal au [illegible] de l'allumage. La nature des dépôts est également discutée.

A partir de ces résultats, les schémas de combustion sont proposés faisant l'objet de la troisième partie. Une première classification de ces schémas a été donnée par GLASSMAN en faisant intervenir les températures de fusion et d'ébullition du métal et de l'oxyde; MARKSTEIN a montré que ces schémas dépendaient non seulement des températures d'ébullition du métal et de l'oxyde, mais aussi de la température à laquelle les réactions de surface et dans la phase gazeuse démarrent. Le choix entre combustion homogène et hétérogène est encore assez mal défini, les deux mécanismes pouvant coexister.

La quatrième partie est relative à l'étude de la combustion dans un milieu hétérogène qui existe en particulier lorsque le métal est utilisé dans un propergol ou dans un combustible solide. Les résultats exposés dans ce paragraphe se rapportent donc à l'étude de la combustion d'un métal dans les systèmes à propergol solide ou hybride.

- SUMMARY -

The study of the combustion of metals has recently become important since they are used as a fuel in modern rocket propulsion systems. The ignition delay and burning time of metal particles, the combustion efficiency as well as the nature of the combustion products are the most important points which are of interest to the propulsion expert and they are taken in consideration in this paper.

The first part is devoted to the experimental techniques used for the study of metal combustion. Two main groups of techniques are defined. One concerning metal particle combustion, the other concerning the combustion of metal wires. In the first group some static methods were developed, the metal particle being attached to a holder but the most widely used techniques consist in studying the metal particles in a flow. In the second group, ignition is simple and combustion is easy to study. The analysis of combustion phenomena is done by cinemicrography, by freezing the combustion on cold plates, by spectrography, ... A critical study of these various techniques is presented.

The second part is a synthesis of the experimental results showing for each metal and in particular for aluminium, beryllium, magnesium and boron, the influence of various parameters such as the nature of the gas atmosphere, its pressure and temperature, the influence of the surface conditions on the metal at ignition. The nature of the deposits is also discussed.

From these results some combustion models are proposed and are dealt with in the third part. A first classification of these models was given by GLASSMAN considering the melting and boiling points of the metal and those of its oxide. MARKSTEIN has shown that these models depend not only on the melting and boiling points of the metal and of its oxide but also on the temperature at which surface and gas phase reactions can start. The choice between homogeneous and heterogeneous combustion is still ill defined since both mechanisms can take place simultaneously.

The fourth part is relative to the study of combustion in a heterogeneous environment which exists in particular when the metal is included in a propellant or in a solid fuel. The results given in this paragraph are based on the study of the combustion of a metal in solid or hybrid propellant systems.

DEPUIS QUELQUES ANNEES un effort important est fait pour définir les conditions de combustion des métaux et pour comprendre le mécanisme permettant de libérer par voie chimique une importante quantité d'énergie avec un bon rendement . Le problème au départ interessait l'industrie, il s'agissait de prévenir la combustion et l'explosion de poussières métalliques dans les mines et dans certaines industries où ces poussières métalliques étaient utilisées . La combustion des métaux conduisant à des températures de fin de combustion élevées et le rayonnement produit étant intense, les métaux sont utilisés pour produire des éclairs . Dans un passé plus récent l'emploi de métaux dans des conditions de températures élevées , en particulier pour les vols supersoniques et dans les foyers de réacteurs a stimulé les recherches dans ce domaine , mais c'est surtout l'utilisation de métaux comme combustible qui a fait progresser ce domaine de recherches . L'aluminium est maintenant un combustible courant entrant dans la composition de la plupart des propergols solides , l'introduction de l'aluminium a pour effet d'augmenter l'impulsion spécifique , d'accroître la densité du propergol et dans certains cas d'améliorer la stabilité de la combustion du propergol. Le béryllium malgré sa toxicité entre dans la composition de certains propergols . D'autres métaux comme le bore , le magnésium sont également envisagés comme propergol en particulier dans les statoréacteurs. Dans les systèmes hybrides le lithium est un métal qui conduit à de très bonnes performances avec les comburants fluorés. L'ensemble de ces applications a donné naissance à de nouveaux sujets de recherche et nous analyserons ici ce ... s qui interessent la propulsion c'est pourquoi nous limiterons nos propos à des métaux susceptibles d'utiliser comme combustible l'aluminium , le béryllium , le magnésium , le bore ....;. en analysant plus particulièrement les paramètres interessant le spécialiste de la propulsion tels le délai d'allumage, le temps de combustion de particules métalliques, le rendement de combustion , la nature des produits formés , le mécanisme de combustion .

La première partie est consacrée aux techniques expérimentales utilisées. Deux groupes ont été définis : l'un se rapportant à la combustion des particules, l'autre à la combustion des fils , nous avons également décrit une technique permettant d'étudier la combustion d'un métal à l'état de vapeur.

La deuxième partie est une synthèse des résultats expérimentaux obtenus dans plusieurs laboratoires mettant en évidence pour chaque métal l'influence des principaux paramètres qui agissent sur les phénomènes de combustion : pression , composition des gaz environnants .

La troisième partie analyse les différents modèles proposés permettant de décrire le mécanisme de combustion des métaux et de dégager les paramètres importants qui régissent ce mécanisme. Ce problème est complexe , pour chaque métal et dans chaque domaine de combustion le modèle peut évoluer et il n'est pas possible de décrire un modèle unique valable pour tous les métaux .

Il nous a paru utile, le métal étant utilisé comme combustible dans un propergol solide ou dans un combustible solide de donner quelques résultats sur la combustion des métaux dans les fovers de systèmes à propergols solides ou hybrides . La combustion a lieu dans un milieu hétérogène , ce qui complique encore les phénomènes, les expériences fondamentales décrites plus haut peuvent cependant servir de guide pour obtenir dans la chambre de combustion un allumage rapide et une combustion aussi complète que possible des métaux .

TECHNIQUES EXPERIMENTALES

Elles peuvent être classées de diverses manières , pour faciliter l'exposé nous distinguerons ici trois techniques principales suivant que le métal est pris : a - sous forme de particules ,b - sous forme de fils ou de rubans , c - à l'état de vapeur . Pour chacune d'elles nous indiquerons les moyens employés pour définir les conditions d'allumage, pour suivre les processus d'allumage , enfin pour analyser les phases gazeuses et condensées présentes dans les produits de combustion .

TECHNIQUES UTILISANT DES PARTICULES - Pour faciliter l'interprétation des résultats , la plupart des chercheurs ont tout d'abord travaillé sur une particule mais des techniques interessantes ont été développées en utilisant plusieurs particules de manière à se rapprocher des conditions réelles de combustion que l'on observe avec les propergols solides ou hybrides .

COMBUSTION D'UNE PARTICULE ISOLEE - Le diamètre des particules varie suivant la technique expérimentale de quelques microns à quelques millimètres . Lorsque la particule est de faible diamètre on utilise une injection pneumatique , la particule est placée dans un écoulement et entraînée par celui-ci. Si v_0 est la vitesse de l'écoulement et v_{p_0} la vitesse de la particule à l'injection, la vitesse de la particule v_p , en admettant la loi de traînée de STOCKE , est donnée par la relation :

$$v_p - v_0 = (v_{p_0} - v_0)\, e^{-t/\tau_v}$$

la constante de temps τ_v dépend du diamètre de la particule d , de sa masse volumique ρ et de la viscosité du gaz μ_g , $\tau_v = d^2 \rho / 18 \mu_g$.

Cette technique a été particulièrement étudiée par FRIEDMAN et MACEK (1) . Une autre méthode développée par la NOTE consiste à utiliser les forces de pesanteur et à étudier l'évolution de la combustion pendant la chute de la particule, le gaz comburant entourant le métal étant en général au repos (2). Rien n'empêche de combiner les deux effets (écoulement et pesanteur) pour augmenter le temps de séjour de la particule dans la chambre d'expérience. Il est possible également par des forces extérieures à distance de maintenir la particule dans une position donnée (3) .

Lorsque la particule a un diamètre de quelques millimètres le problème de support est complexe à résoudre, des solutions ont été apportées par MURIAUMEX et WILLIAMS , le support peut dans certains cas venir perturber les phénomènes de combustion. Il est possible également de former des gouttes par fusion de fils métalliques, cette technique est avantageuse lorsque la température de fusion est faible (sodium) Un dispositif de production de gouttes d'un diamètre de l'ordre du millimètre a été mis au point par RICHARD (4) . Le problème de support étant réglé , il faut fournir à cette particule une quantité d'énergie suffisante pour obtenir l'allumage du métal. La solution la plus courante consiste à utiliser un brûleur à flamme plate du type FOWLING produisant des gaz brûlés comburants à haute température. Le brûleur de FRIEDMAN et MACEK (1) par exemple est alimenté par un mélange de propane-oxygène -azote , en faisant varier la proportion de ces trois composants on modifie la température des gaz brûlés et la composition (teneur en oxygène et vapeur d'eau) ; pour éviter la présence d'eau ils utilisent le

mélange monoxyde de carbone-oxygène (5). Cette technique ne permet pas cependant de choisir à volonté la composition et la température. Les particules sont introduites dans l'axe du brûleur par un tube de faible diamètre (250 μ) , elles sont portées par un gaz vecteur neutre généralement de l'hélium ou de l'azote. La nature du gaz porteur dont le débit est extrêmement faible par rapport au débit du brûleur n'a pratiquement aucun effet sur la combustion . La température de la particule T_p placée dans un gaz à température T_g varie en fonction du temps suivant la loi :

$$T_p - T_g = (T_{p_0} - T_g)\, e^{-t/\tau_T}$$

la constante de temps $\tau_T = d^2 \rho C / 12\, \lambda_g$ où C est la chaleur spécifique de la particule et λ_g la conductibilité thermique du gaz ; en introduisant le nombre de Prandtl $P_r = \mu_g C_p / \lambda_g$ où C_p est la chaleur spécifique du gaz , on obtient entre τ_v et τ_T la relation :

$$\tau_T = \frac{3}{2} P_r \frac{C}{C_p} \tau_v \ .$$

On peut donc dire que les retards de vitesse et de température entre le gaz et la particule sont voisins.

Quelques tentatives ont été faites pour remplacer le brûleur par un générateur de plasma fonctionnant avec un gaz neutre , les particules sont injectées dans le plasma et pénètrent après chauffage dans une atmosphère oxydante mais cette technique est d'une mise en oeuvre délicate .

Une solution élégante consiste à utiliser une source intense de lumière. NELSON par exemple pour étudier la combustion de particules de zirconium a obtenu de bons résultats en utilisant une lampe à éclairs au Xénon (6) . Un tube de quartz de 8 mm de diamètre rempli de Xénon est enroulé en hélice sur le tube d'expérience placé verticalement et dans lequel une particule de métal tombe suivant l'axe. Le tube de Xénon est enroulé sur 5 spires, le volume chauffé est d'environ 35 cm^3 , la durée de l'éclair est d'environ 1 ms .

Une autre technique ayant donné de bons résultats avec l'aluminium est basée sur l'emploi d'un laser continu à gaz (CO_2) d'environ 120 w ; des particules de 5 μ d'aluminium ont pu ainsi être allumées. Avec un laser continu on évite la synchronisation toujours délicate entre l'éclair et le passage de la particule. Avec cette méthode il est cependant difficile de connaître les conditions d'allumage et en particulier de connaître l'énergie transmise à la particule. Elle offre cependant l'avantage d'initier la combustion dans des temps brefs et d'éviter la formation d'oxyde à la surface .

L'emploi d'un four est limité à des métaux dont la température d'inflammation est faible (sodium par exemple) .

Après l'allumage de la particule quelques méthodes ont été développées pour suivre la combustion . La plus simple consiste à prendre une photographie de la particule pendant toute la combustion, on observe alors sur le cliché une traînée lumineuse laissée par la particule en combustion pendant son déplacement . De la structure de cette traînée on en déduit l'allure des phénomènes de combustion (évolution du diamètre de la particule, évolution du diamètre de la flamme, combustion dissymétrique et rotation de la particule, explosion de la particule. Les gouttes de métal ainsi étudiées sont en général de faible diamètre (quelques dizaines de microns) il est donc difficile de concilier un fort grossissement pour détailler la zone de combustion et obtenir également un long trajet. Par des procédés optiques il est possible de prendre sur la même photographie plusieurs parties du trajet . On peut également filmer le mouvement de la particule en synchronisant la prise de vue avec une lampe à éclairs placée à contre jour . Là encore un fort grossissement limite le champ d'observation.

Une technique très utile consiste à figer la combustion à un instant donné , en faisant varier cet instant de l'allumage à la fin de combustion on peut reconstituer l'évolution de la combustion mais une expérience est nécessaire à chaque fois . Pour figer la combustion on recueille la particule sur une plaque froide placée à une certaine distance du point d'allumage , cette distance est variable d'une expérience à l'autre . Cette plaque est parfois une lame de microscope en verre ou une plaque refroidie polie. Dans certains cas un figeage rapide est nécessaire et on recueille la particule dans de l'argon liquide (7). Avec la plupart des métaux (aluminium, magnésium, béryllium) il est préférable de ne pas refroidir trop brusquement pour ne pas changer la structure de la combustion et la nature des dépôts . Le figeage sur une plaque de verre donne de très bons résultats comme en témoigne la photographie de la figure 1 prise par PRENTICE , il s'agit d'une particule d'aluminium de 400 μ brûlant dans l'air et figée à 23 cm de son point de chute, l'allumage est obtenu par un éclair de Xénon ; on note une combustion symétrique de la goutte avec un nuage de fines particules d'alumine condensée. Il s'agit d'une combustion en phase gazeuse du métal vaporisé avec le comburant gazeux environnant la goutte . Les différentes structures autour de la particule mettent en évidence la complexité du phénomène de combustion (8) . Avec cette technique il est possible d'étudier la combustion d'une particule en fonction des deux paramètres fondamentaux , nature des gaz comburants et pression , notons que les expériences de combustion des particules à haute pression sont peu nombreuses. L'analyse des produits issus de la combustion peut se faire par spectrographie directe pour la partie gazeuse et par analyse chimique classique pour la phase condensée (9) . La structure de cette phase condensée peut être mieux décrite si l'on utilise un microscope électronique à balayage comme en témoignent les trois photographies de la figure 2 montrant des échantillons d'alumine recueillis après combustion .

COMBUSTION DE PLUSIEURS PARTICULES - La combustion d'un nuage de particules métalliques pourraient être étudiée à l'aide d'un brûleur du type MACEK ou de ceux qui sont décrits à la référence (2) , mais on préfère dans ce cas se rapprocher des conditions réelles de combustion et en particulier analyser l'évolution des particules en partant d'échantillons de propergols mis au point pour cette recherche ou utilisés sur propulseur.

Dans le premier cas on forme des échantillons par compression en partant d'un comburant solide, d'un métal pris sous forme de fines particules , d'un combustible plastique et de catalyseurs également solides . On peut avec cette technique changer rapidement la composition du mélange et la nature des composants. L'évolution de la combustion des particules métalliques est suivie par cinémicrographie , on peut également figer la combustion à un certain stade et recueillir des dépôts .

Dans le deuxième cas on utilise des échantillons de pronergol obtenus par coulée d'un mélange de comburant, de particules métalliques enrobées dans une matière plastique . Cette façon d'opérer a donné des résultats intéressants . On trouve en particulier de nombreux travaux en URSS (10) .

TECHNIQUES UTILISANT DES FILS - La mise en oeuvre de cette technique est simple , le fil métallique est pris entre deux électrodes et l'allumage est obtenu par effet joule . La température du fil est enregistrée pendant la phase d'allumage . En plaçant le fil dans une bombe , il est donc possible de faire varier simplement la composition du comburant et la pression . La cinématographie de la zone de combustion , la spectrographie de la zone de flamme, l'analyse des dépôts permettent une étude complète de la combustion des métaux . Cette technique a permis à GLASSMAN et BRZUSTOWSKI d'étudier en détail la combustion de l'aluminium et du magnésium (11) (12) dans une atmosphère contenant O_2 et CO_2.

Des difficultés peuvent apparaître à l'allumage si la température d'inflammation est supérieure à la température de fusion du métal, car la rupture du fil intervient avant l'apparition de la flamme . Avec l'aluminium par exemple il suffit de chauffer suffisamment lentement pour qu'une mince couche d'oxyde se forme à la surface maintenant le fil en place jusqu'à la phase d'allumage . L'aspect de la flamme est celui de la figure 3 montrant le chauffage du fil et sa combustion dans une atmosphère d'oxygène . Après la rupture du fil la combustion se poursuit autour du métal fondu .

Une autre façon de procéder consiste à suspendre un fil et à apporter à l'extrémité libre une quantité d'énergie suffisante pour obtenir l'inflammation . On obtient dans ce cas une donnée supplémentaire qui est la vitesse de combustion du fil (13) , l'influence de la convection est assez minime , la vitesse de régression du fil est principalement réglée par des phénomènes de diffusion et la formation d'oxyde .

TECHNIQUES UTILISANT LE METAL EN PHASE VAPEUR - Dans la combustion de nombreux métaux les produits de combustion comportent une phase condensée, il est donc très utile de comprendre ce mécanisme de formation de la phase condensée qui est celui d'une réaction chimique hétérogène . Suivant cette idée MARKSTEIN a obtenu des résultats importants en étudiant à basse pression la réaction d'un métal en phase vapeur avec l'oxygène . La vapeur de métal est injectée en un point de la bombe diluée d'argon ; le métal réagit avec l'oxygène et un dépôt d'oxyde se forme sur un miroir placé à environ 2 cm de l'orifice d'injection du métal . L'épaisseur du dépôt est mesurée par le déplacement de franges d'interférence . Ce déplacement est symétrique par rapport à l'orifice . Cette technique permet de mettre en évidence l'importance relative de la diffusion et de la cinétique chimique Le dosage des atomes métalliques peut être fait par spectrophotométrie d'absorption (14) . Des expériences de ce type en plus grand nombre pourraient apporter de nombreux renseignements sur la combustion hétérogène du métal .

Il n'existe pas pour l'étude de la combustion des métaux de technique idéale, chacune de celles que nous venons d'examiner possède des avantages et des inconvénients. Le but visé par le chercheur est double : comprendre le mécanisme de combustion du métal , améliorer le rendement de combustion , chacune d'elles apportant une contribution à ces deux préoccupations .

La technique utilisant des particules est intéressante car elle se rapproche des conditions réelles d'utilisation mais certaines difficultés apparaissent dans l'inflammation et dans la description des phénomènes de combustion; exception faite pour la particule brûlant dans un milieu au repos , la combustion a lieu dans un comburant vicié et il est difficile de jouer à la fois sur la composition et la température du gaz . On note peu de recherches effectuées à haute pression c'est à dire dans des conditions voisines de celles de l'emploi sur propulseur, les difficultés apparaissent dans ce domaine, flammes près de la surface , luminosité importante qui gêne les forts grossissements .

L'emploi de fils ou de rubans est d'une mise en oeuvre beaucoup plus simple mais la quantité de métal brûlé est plus importante (pertes le long du fil également plus grandes), des difficultés apparaissent au moment de l'allumage .

La technique de combustion des métaux en phase vapeur nous paraît fort utile pour décrire le mécanisme de combustion hétérogène et de formation des dépôts, la vaporisation de certains métaux à haut point d'ébullition rend cette technique d'une mise en oeuvre difficile , elle nous paraît cependant très utile pour acquérir des données fondamentales sur le mécanisme de diffusion des oxydes et sur la nature et la vitesse des réactions chimiques de combustion .

RESULTATS EXPERIMENTAUX

Il nous paraît plus simple dans la présentation des résultats de prendre chaque métal et de discuter les conditions d'allumage et les modes de combustion propres à chacun en insistant plus particulièrement sur les métaux les plus utilisés en propulsion .

ALUMINIUM - Le point de fusion de l' aluminium est de 923 °K , son point d'ébullition 2740°K donc très au dessus du point de fusion de l'oxyde 2318°K , la température de décomposition de Al_2O_3 étant de l'ordre de la température de fin de combustion (3800°K) . Cette disposition de la température d'ébullition du métal T_{EM} et de fusion de l'oxyde T_{FO} fait apparaître un certain nombre de phénomènes spécifiques de l'aluminium .

A - ALLUMAGE - Les expériences les plus probantes sont celles de MAČEK , la particule étant injectée dans un écoulement comburant chaud , il est facile d'évaluer le délai d'allumage τ . Une théorie élémentaire assez bien vérifiée par l'expérience indique que ce délai τ est donné par la relation :

$$\tau = \frac{\rho d^2}{12 \lambda_g N_u} \left[c \ln \frac{T_g - T_0}{T_g - T_i} + \frac{L}{T_g - T_{FM}} \right]$$

ce délai est donc proportionnel au carré du diamètre de la particule et dépend du nombre de NUSSELT Nu de la chaleur latente de fusion du métal L, de la température initiale de la particule T_0 , de la température du gaz entourant la particule T_g et de la température d'inflammation T_i (1) . Outre le délai d'allumage il est important de connaître la température du gaz T_{gi} à laquelle l'inflammation se produit. Les expériences de MAČEK montrent que cette température est voisine de la température de fusion de l'oxyde

T_{Fo} et dépend de la concentration en oxygène :

$$T_{gi} = T_{Fo} - \frac{\Delta h\, d}{2\lambda_g} k \left(\frac{p_g}{R T_{Fo}}\right)^n .$$

La température T_{gi} diminue lorsque la pression partielle en oxygène p_{O_2} augmente , l'exposant n est de l'ordre de 0,5 . Cette loi a été vérifiée pour des pressions allant de 1 à 10 atm . Ce niveau de température indique que pendant la phase précédant l'allumage une faible couche protectrice d'alumine s'est formée à la surface du métal enrobant complètement celui-ci , cette couche pouvant se constituer par une oxydation lente si la particule est stockée dans une atmosphère oxydante ou encore pendant le délai τ . Des expériences ont montré que cette oxydation est très rapide et peut intervenir dans le délai τ . Cette couche protectrice a été mise en évidence en plaçant des échantillons d'aluminium dans une atmosphère portée à 1300 °K , l'aluminium fondu n'est libéré que lorsque cette couche d'oxyde se ramolit, le liquide s'échappe alors par des fissures qui se sont formées à la surface sous forme de filaments (figure 4) . Lorsque cette couche protectrice est présente il est donc nécessaire d'atteindre T_{Fo} pour obtenir une libération du métal et l'allumage de la particule . Toutes les techniques qui empêchent la formation de cette couche diminue la température d'inflammation du métal .

Les méthodes d'étude de la combustion des fils conduisent à la même conclusion . La température de fusion du fil étant inférieure à la température d'inflammation , il est donc nécessaire pour obtenir une bonne tenue durant le chauffage de réaliser un chauffage lent pour permettre la formation d'une couche d'oxyde qui assure une bonne tenue pendant cette période . Dans une atmosphère contenant uniquement de l'oxygène la température du fil à laquelle l'inflammation apparaît croît lorsque la pression dans laquelle s'effectue la combustion augmente : elle passe de 1700°K à 0,2 atm à la température de fusion de l'oxyde 2318°K à 2 atm pour rester sensiblement constante jusqu'à 70 atm . La puissance nécessaire à l'obtention de l'allumage augmente avec la pression (voir figure 5) (15) . Cette série d'expériences tend à montrer que de 0,2 à 2 atm la couche d'oxyde est plus perméable qu'aux pressions élevées . La concentration en oxygène agit légèrement sur la température du fil au moment de l'allumage , on note que la température augmente légèrement lorsque la fraction molaire en oxygène croît . Cette tendance est en désaccord avec celle trouvée à partir des expériences de MACEK, il serait logique de conclure à une augmentation de la température d'inflammation avec la fraction molaire en oxygène puisque dans ce cas la couche d'oxyde devrait devenir plus épaisse et donc plus protectrice, signalons toutefois que cet effet est faible . La pression limite d'allumage dépend de la concentration en oxygène et celle-ci diminue lorsque le pourcentage en oxygène augmente . Une pression limite supérieure peut apparaître sous certaines conditions par exemple pour une fraction molaire en O_2 de 0,5 ,la pression limite inférieure est de 0,34 atm et la pression limite supérieure de 17 atm (15) . La nature du diluant a peu d'importance , notons cependant que l'allumage avec l'hélium est obtenu avec une puissance plus importante que pour l'argon et l'azote . Par contre la nature du comburant joue un grand rôle : avec le ClF_3 par exemple , l'allumage a été obtenu à des températures inférieures au point de fusion de l'halide (953°K) . Cette propriété des composés fluorés permettant d'abaisser la température d'allumage des particules métalliques peut être utilisée pour faciliter la combustion des propergols solides ou hybrides métallisés . Des combustions ont été obtenues dans l'azote pur, l'allumage a lieu à des pressions supérieures à 27 atm, la température d'inflammation (1380°K) étant nettement inférieure à la température de fusion de AlN (2473°K) , la couche d'AlN formée étant vraisemblablement non protectrice . Les conditions d'allumage dépendent donc dans une large mesure de la possibilité de formation d'une couche protectrice et de sa destruction . On note en général qu'une couche protectrice se forme lorsque le volume de l'oxyde est plus élevé que le volume de métal qui intervient dans sa formation (cas de Al et de Al_2O_3) , l'épaisseur de la couche formée dépend de la concentration en comburant près de la surface et de la température du gaz environnant suivant une loi d'Arrhénius, il est donc difficile d'agir sur toute la surface , on peut néanmoins, par des apports locaux de certaines substances empêcher en certains points de la particule la formation locale d'oxyde. Cette façon de faire peut diminuer la température d'allumage de la particule .

B- COMBUSTION - Examinons tout d'abord la combustion des particules dans une ambiance comburante oxygénée . A la pression atmosphérique on observe deux mécanismes de combustion possibles, l'un éloigné de la surface , régi par un processus de diffusion avec combustion des vapeurs métalliques avec le comburant gazeux et formation d'une phase condensée qui se présente sous forme d'un nuage de fines particules dont les dimensions sont de l'ordre de quelques centaines d'Angströms, l'autre près ou sur la surface avec formation de la phase condensée à la surface du métal, ce mécanisme étant d'ailleurs assez mal défini. Ces deux mécanismes peuvent d'ailleurs coexister sur la même particule comme l'indiquent les photographies de la figure 6 . La photographie 6A a été obtenue par cinémicrographie de la zone de combustion , on distingue nettement sur la particule une calotte d'alumine, il n'y a pas au-dessus de cette calotte d'émission de vapeur métallique et de combustion d'alumine, le métal peut se vaporiser librement et on observe en phase vapeur,à une certaine distance de la particule, une flamme de diffusion provenant de la combustion du métal vaporisé avec le gaz comburant entourant la particule . Lorsqu'on recueille sur une plaque de verre des particules en cours de combustion (figures 6B et 6C) , on observe sur la même particule la calotte d'oxyde et le métal , autour de la particule , on note également une fine poussière d'alumine dont les dimensions sont voisines de 10^2 Å et qui provient de la combustion en phase vapeur avec formation d'un nuage d'alumine. Ces deux modes de combustion apparaissent simultanément ou séparément suivant les conditions expérimentales (pression et composition des gaz environnants) .

Examinons les résultats obtenus lorsqu'une particule d'aluminium brûle dans une atmosphère comburante contenant de l'hydrogène et de la vapeur d'eau. L'allumage est progressif, le diamètre de la zone de combustion varie de une fois à une fois et demie le diamètre de la particule; on observe dans ce cas simultanément les deux types de combustion mentionnés plus haut ; les produits de combustion renferment des sphères creuses d'alumine, pour des particules de 70 μ , on obtient des sphères de 150 μ. La photographie de la figure 7 montre l'aspect extérieur de ces ballons (photographie 7A) , lorsque la sphère est brisée (photographie 7B) on remarque à l'intérieur la goutte métallique attachée ou noyée dans la sphère creuse d'alumine . On recueille également des sphères ayant une surface moins lisse mettant en évidence le processus de formation par apports successifs ou par coalescence de particules (photographie 7C) . Le mécanisme de formation de ces sphères creuses est encore obscur , il ne semble pas cependant influen-

cer le processus de combustion .

Toujours en présence d'hydrogène, on note une rotation très rapide de la particule (la vitesse angulaire pouvant aller jusqu'à 10^4 t s^{-1}) . Cette rotation est vraisemblablement due à une dissymétrie dans la combustion des particules et donc à une dissymétrie dans le débit de métal vaporisé compliqué par un effet de jet pouvant provenir du [redacted] métal vaporisé sous la couche d'alumine située près de la surface et qui s'échappe d'une manière dissymétrique en bordure de la calotte d'alumine . Cet effet de jet peut être décelé en remarquant en certains points à la lisière de la calotte une combustion intense due au jet de vapeur issu de la calotte brûlant avec le gaz comburant environnant . Le mouvement de la particule est assez complexe:dans de nombreux cas l'axe de rotation de la particule est perpendiculaire à l'axe de symétrie de la calotte d'alumine, une queue formée par un nuage d'alumine s'étalant le long de l'axe de rotation ; l'effet de jet de vapeur issu du pourtour de la calotte pourrait être responsable de cette rotation . A cette rotation s'ajoute parfois un mouvement en spirale de la particule dû également à l'effet de jet ainsi qu'au débit de métal vaporisé issu de la surface de la particule non protégée par l'alumine .

Toujours dans un milieu contenant de l'hydrogène et de la vapeur d'eau on observe une fragmentation de la particule, le pourcentage de fragmentation augmente lorsque le taux d'oxygène croît . Certains expérimentateurs pensent que cette fragmentation provient de la rupture des sphères creuses d'alumine, rupture due à la pression règnant à l'intérieur de la sphère par suite de la vaporisation du métal. Il semble plutôt que cette fragmentation intervienne lorsqu'une combustion dissymétrique a lieu, la couche d'alumine formée près de la surface conduit dans cette zone à un transfert de chaleur important et cette dissymétrie dans le chauffage peut provoquer une rupture de la particule . En l'absence de fragmentation en atmosphère contenant H_2 et H_2O le temps de combustion des particules est sensiblement proportionnel au diamètre de la particule à la puissance 1,5 .

Pour éviter la présence d'hydrogène et de vapeur d'eau MAČEK a étudié la combustion de particules dans les gaz de combustion de CO avec O_2 . On observe tout de suite après l'allumage une augmentation rapide du diamètre de la flamme . La zone de combustion est éloignée de la surface de la particule et le processus de combustion est celui d'une goutte combustible brûlant dans l'air, les phénomènes de diffusion étant prépondérants; la combustion est sensiblement symétrique et le temps de combustion comme dans le cas de gouttes combustibles est proportionnel au carré du diamètre de la particule et inversement proportionnel à la fraction molaire d'oxygène . Avec ce comburant on retrouve dans les produits de combustion des sphères creuses d'alumine , on note dans certains cas une rotation de la particule et une fragmentation . La présence d'azote peut également favoriser la rotation de la particule et la fragmentation . Les expériences de PRENTICE (5) ont en effet montré que la combustion des particules dans un mélange à 80% d'argon et 20% d'oxygène s'effectue sans rotation et sans fragmentation et l'introduction d'une faible quantité d'azote 10% conduit à une rotation qui se termine par une fragmentation de la particule .

Les résultats que nous venons de donner correspondent à des expériences effectuées à la pression atmosphérique , on dispose de peu de résultats à des pressions élevées . La combustion des fils est assez semblable à celle des particules . BRZUSTOWSKI et GLASSMAN ainsi que KUEHL et ZWILLENBERG ont étudié en détail la combustion de fils d'aluminium . Les photographies de la figure 8 indiquent quelques modes de combustion possible des fils avec formation de gouttes ou explosion du fil .

Les modes de combustion sont indiqués sur la figure 9 et dépendent de la fraction molaire d'oxygène X_{O_2} , le diluant étant de l'argon , et de la pression . Comme on peut le constater c'est principalement la fraction molaire X_{O_2} qui définit le processus , la pression intervenant surtout aux basses pressions : au dessous de 20% d'oxygène il est impossible d'allumer le fil (domaine 1) , entre 20 et 30% une couche d'alumine se forme à la surface du fil dans une flamme diffuse (domaine 2 et 3) ; entre 30 et 80% d'oxygène on peut distinguer deux zones avec extinction aux fortes pressions, la flamme est très près de la surface et le métal brûle sous forme de gouttes suspendues au tube d'oxyde formé à la surface du fil (domaine 5) ; à des fractions molaires supérieures à 0,8 on note une combustion très rapide et très intense qui progresse vers les electrodes (domaine 6) ; aux basses pressions (50 mm de Hg) la combustion s'effectue suivant une flamme de diffusion caractéristique (domaine 7) . D'une manière générale , on observe que le rapport du rayon de la flamme au rayon du fil ou de la goutte formée par fusion décroît lorsque la pression ou la fraction molaire d'oxygène augmente, à une pression de 1 atm , ce rapport est de l'ordre de 1,5 . C'est pourquoi GLASSMAN pense que dans la plupart des cas une flamme de diffusion apparaît (combustion en phase gaseuse) plus ou moins près de la surface du métal; les particules d'oxydes formées au cours de cette combustion ne peuvent s'éloigner de cette zone que si le débit issu de la goutte est suffisamment important, sans cela on note une accumulation des produits condensés près de la surface ou dans la zone de combustion . Dans la phase de combustion à basse pression , on remarque , à la surface du fil, des gouttelettes très lumineuses constituées par de l'alumine liquide portée à une température bien supérieure à celle du métal et également supérieure à la température de fusion de l'oxyde . Cette alumine peut provenir comme dans le cas des particules d'une réaction hétérogène de surface, à cette pression (50mm de Hg) la température d'ébullition du métal est égale à 2260°K donc inférieure à la température de fusion de l'oxyde. On note également des traînées lumineuses venant du métal mais il est difficile de préciser la nature de ces particules incandescentes . Dans les produits de combustion on trouve des sphères creuses attachées à la couche d'alumine entourant le fil .

L'influence de la pression peut être discutée par les expériences de LONG et SERALD (13) relatives à la détermination de la vitesse de combustion d'un fil placé dans de l'oxygène et allumé à une extrémité . Cette vitesse est donnée sur la figure 10 en fonction de la pression d'oxygène . On remarque tout d'abord entre 1 et 3 atm une augmentation rapide de la vitesse , la combustion est contrôlée par la diffusion du comburant et des vapeurs métalliques ; les dépôts sont constitués par de fines particules dont le diamètre est inférieur au micron , dépôts caractéristiques d'une combustion en phase vapeur . Entre 3 et 8 atm on observe une légère diminution de la vitesse puis entre 8 et 14 atm une légère augmentation . Cette variation peut être due à une diminution relative du flux d'oxygène allant vers la surface du métal, diminution due aux produits de combustion venant de la zone de réaction vive et s'accumulant dans cette zone et freinant la diffusion de l'oxygène . Le mouvement des particules d'oxyde est dû principalement à l'écoulement général allant de la surface du métal vers l'extérieur, la vitesse des gaz étant égale pour un débit $\dot{m}$ vaporisé à : $v = \frac{RT\dot{m}}{4\pi r^2 p}$, diminue donc lorsque la pression augmente et lors-

que l'on s'éloigne de la surface , de ce fait les particules d'alumine éprouvent de la difficulté à sortir de cette zone de réaction . Une agglomération des particules peut se produire, se traduisant par la formation de sphères creuses ou pleines d'alumine . Le débit de métal vaporisé varie peu en fonction de la pression , ce qui limite la vitesse de combustion . Dans ce domaine des pressions les résidus sont formés de fines particules et de sphères creuses d'alumine . Au delà de 14 atm , on observe une chute de la vitesse de combustion et le niveau le plus bas correspond à la valeur de la vitesse trouvée à la pression atmosphérique , le minimum se situant à environ 22 atm, après cela , la vitesse de combustion croît progressivement avec la pression , d'après KIRSCHFELD (13) on ne note aucune particularité jusqu'à 100 atm , la vitesse continuant à croître . Entre 16 et 38 atm les dépôts sont formés de fines particules , de sphères creuses et également de gouttes d'alumine translucide dont le diamètre moyen se situe entre 100 et 200 μ et pouvant aller jusqu'à $10^3 \mu$, ces gouttes d'alumine se détachent du fil en cours de combustion .

La diminution de la vitesse de combustion observée entre 16 et 22 atm peut être due à l'accumulation d'alumine près de la surface du fil qui limite le taux d'évapcration du métal , la combustion ayant lieu non en phase vapeur mais tout près de la surface, phénomène déjà observé avec les particules , cette combustion de surface limitant également le flux d'oxygène arrivant près du métal . Cette formation d'oxyde protecteur à la surface atteint son maximum à 22 atm , au delà les phénomènes de diffusion reprennent l'avantage , la vitesse de combustion augmente progressivement avec la pression . C'est donc l'action combinée d'une réaction homogène en phase vapeur , d'une réaction hétérogène en fin de combustion (condensation d'alumine) , d'une réaction hétérogène à la surface du métal qui peuvent avoir lieu simultanément qui conditionne la vitesse de combustion du fil . Tels sont très schématisés les principaux résultats obtenus sur la combustion de l'aluminium .

BERYLLIUM - On souligne souvent que le mécanisme de combustion du béryllium est très voisin de celui de l'aluminium, nous allons voir qu'il existe une certaine analogie mais des différences très nettes apparaissent également . La température de fusion du béryllium est plus élevée que celle de l'aluminium 1556°K pour 932°K ; les températures de vaporisation sont sensiblement les mêmes 2757°K pour Be et 2740°K pour Al ; la température de fusion des oxydes passe de 2820°K pour Be à 2318°K pour Al et la température d'ébullition des oxydes est de 4123°K pour Be et 3800°K pour Al . Le rapport du volume d'oxyde au volume de métal est de 2,5 pour l'aluminium et de 1,66 pour le béryllium .

A- ALLUMAGE - Examinons tout d'abord les conditions d'allumage de particules de quelques dizaines de microns de diamètre. Les résultats expérimentaux de MACEK montrent que la température d'inflammation du béryllium est plus élevée que celle de l'aluminium entre 2400 et 2600 °K sans pour cela atteindre la température de fusion de l'oxyde 2820°K . La nature des gaz environnants a d'ailleurs une très grande influence sur la température d'allumage . Les valeurs expérimentales obtenues lors de la combustion du beryllium sont très dispersées et s'il est possible de fournir des tendances , il est difficile d'établir des lois reliant par exemple le délai d'allumage ou la température d'inflammation avec le diamètre des particules et la composition des gaz environnants . Cela tient surtout à la formation aléatoire au départ d'oxyde à la surface. La température de vaporisation du métal et la température de fusion de l'oxyde sont voisines et il est difficile de savoir celle qui est déterminante . Le délai d'allumage n'est pas en général proportionnel au carré du diamètre de la particule, l'exposant dépendant des pertes par rayonnement et de l'énergie apportée à la surface par réaction chimique, étudions tout d'abord les phénomènes qui rendent le processus d'allumage aléatoire .

- Pendant la période de préchauffage on note tout d'abord des réactions chimiques importantes avec formation de dépôt d'oxyde principalement lorsque le gaz environnant contient de la vapeur d'eau . Ces réactions démarrent à 1800°K c'est à dire nettement au dessous de la température d'allumage, les réactions possibles seraient les suivantes :

$$Be + H_2O \longrightarrow BeO + H_2$$

l'hydrogène formé pouvant réagir avec l'oxygène présent . Ces réactions exothermiques de surface, très sensibles à la nature des gaz environnants modifient par l'apport local d'énergie les conditions d'allumage . D'après diverses observations il ressort que l'oxyde de béryllium ainsi formé est moins protecteur que l'alumine et la température de 2820°K n'est pas une température limite .

- L'épaisseur de la couche d'oxyde formée dépend beaucoup des conditions expérimentales et en particulier du temps de séjour de la particule dans les gaz environnants, ce temps de séjour étant fonction du diamètre de la particule, l'épaisseur d'oxyde dépend donc également de ce diamètre . Une particule de grand diamètre ($\sim$1mm) peut être recouverte d'une couche d'oxyde importante qui va diminuer le flux de métal vaporisé et limiter le taux de réaction, pour cette raison le démarrage de l'allumage est lent . Au contraire pour les particules de petit diamètre, la couche d'oxyde peut être faible ou même inexistante et le mécanisme de l'allumage peut être celui d'un métal volatil, c'est pourquoi on peut noter suivant le diamètre des particules des températures d'inflammation différentes .

- Les pertes par rayonnement sont plus grandes dans le cas du béryllium que dans le cas de l'aluminium , ceci pour deux raisons : l'émissivité du béryllium est de 0,6 alors qu'elle est de l'ordre de 0,1 avec l'aluminium , la température d'allumage du béryllium est plus élevée que celle de l'aluminium. Le temps nécessaire pour porter la particule de T_0 à T en tenant compte du rayonnement est égal à :

$$t = \frac{\rho c d^2}{6} \int_{T_0}^{T} \frac{dT}{\lambda N_u (T_g - T) - \varepsilon \sigma T^4 d}$$

MAČEK indique que pour amener une particule de 29 μ de la température ambiante au point de fusion du métal (1556°K) , 4,3 ms sont nécessaires et 7 ms pour passer de 1556°K à T_g = 2900°K ($\lambda_g = 3\ 10^{-4}$ cal.cm^{-1}. deg^{-1}. s^{-1}, Nu =2 , ε=0,6) , soit au total 11,3 ms, avec une particule de 35μ on obtient un temps global de 17,6 ms ce qui correspond à un exposant du diamètre de l'ordre de 2,4 . Si nous admettons une réaction chimique de surface l'énergie libérée étant fonction de T et de la composition X_j , on obtient :

$$t = \frac{\rho c d^2}{6} \int_{T_0}^{T} \frac{dT}{\lambda N_u (T_g - T) + [q(T, X_j) - \varepsilon \sigma T^4] d}$$

l'apport d'énergie à la surface tendant à diminuer l'exposant de d .

L'allumage des fils fait apparaître les mêmes difficultés , on constate que le béryllium est d'un allumage difficile , dans l'oxygène pur la pression doit être supérieure à 1,1 atm. Les essais sont très peu reproductibles. Dans l'oxygène la température d'allumage est de l'ordre de 2600°K . On voit très nettement se former pendant la phase d'initiation de la combustion une couche d'oxyde mais qui ne protège pas le métal puisque la température d'allumage est inférieure à la température de fusion de l'oxyde . Le traitement subi par le fil de béryllium a une grosse importance , il détermine la tenue mécanique du fil pendant la période de chauffage ohmique .La température d'allumage est abaissée au voisinage de 1500°K si les gaz environnants contiennent de la vapeur d'eau; dans l'azote la combustion démarre à une pression supérieure à 35 atm et la combustion du béryllium peut être initiée à 1100°K en présence de trifluorure de chlore, la présence de ClF_3 améliore l'allumage en réduisant de façon appréciable le délai d'allumage .

Les principales conclusions sont reprises en ce qui concerne les fils dans le tableau suivant du KUEHL :

Comburant	pression (atm)	Température d'allumage	Comburant	Pression(atm)	Température d'allumage
O_2	0,17- 68	2400 T_i 2600°K	H_2O	6,8	1000 -1500°K
O_2 + inerte	6,8 - 68	allum. aléatoire	H_2O + inerte	6,8 - 34	1000 - 1500
N_2	34	2350°K	$CO_2/HCl/N_2$	34	2100 - 2500
ClF_3	0,5 - 1,2	1073 °K	$CO_2/H_2O/N_2$	34	1200 - 1500
ClF_3 + inerte	10 - 11	1100 °K	$ClF_3/CO_2/HCl/N_2$	1,7	1550°K

- B - COMBUSTION - La combustion est relativement aisée avec des particules et très difficile et aléatoire lorsqu'en part de fils . Considérons comme pour l'aluminium deux cas suivant que la combustion a lieu dans un gaz dépourvu d'hydrogène et de vapeur d'eau ou dans un gaz contenant de l'hydrogène .

Dans le premier cas le temps de combustion est plus court que celui de l'aluminium et le processus de combustion est celui d'une flamme de diffusion résultant de la rencontre d'un flux de vapeur de béryllium avec un flux gazeux comburant. Le rapport du diamètre de la flamme au diamètre de la particule métallique décroit lorsque la fraction molaire d'oxygène augmente (1,3 à 1,4 pour X_{O_2} =0,36 et de 1,1 à 1,2 pour X_{O_2} = 0,16 , le diamètre de la particule étant de 32 μ) . Cette décroissance peut être attribuée à la décroissance de la température avec X_{O_2} mais également à la diminution du flux d'oxyde à la surface du métal venant de la zone de combustion . Le temps de combustion est sensiblement proportionnel au carré du diamètre de la particule, ce qui justifie le modèle classique avec une flamme de diffusion en phase gazeuse et inversement proportionnel à la fraction molaire d'oxygène avec un exposant inférieur à l'unité. Une étude théorique conduit pour une particule de 32 μ à un temps de combustion de 1,2 ms et l'expérience donne 1,8 ms pour X_{O_2} = 0,43 . Lorsque la température du gaz environnant est supérieur à la température de fusion de l'oxyde , on recueille après combustion , des sphères d'oxyde de béryllium dont le diamètre est inférieur au micron , par contre lorsque la température est inférieure , les dépôts sont beaucoup plus grossiers et l'on observe par exemple des bâtonnets de BeO de 10 μ de hauteur environ . L'oxyde de béryllium peut diffuser à la fois vers la particule et vers l'extérieur,c'est pourquoi on trouve en fin de combustion et pour les faibles concentrations en oxygène des particules dont le diamètre est un peu inférieur à celui de la particule avant combustion . Une forte partie de BeO (environ 60%) se retrouve sous cette forme. Le mécanisme de régression de la particule devant comprendre une vaporisation du métal et une agglomération continue d'oxyde à la surface. Une légère rotation des particules est observée durant la combustion , due à une dissymétrie dans le dépôt d'oxyde à la surface .

Dans le cas d'une combustion dans un gaz comburant contenant de la vapeur d'eau , le mode de combustion est assez voisin de celui observé dans un gaz sec .

On observe que le rapport du diamètre de la flamme à celui de la particule est plus faible (de l'ordre de 1,1) , on observe dans ce cas peu de fines particules d'oxydes mais plutôt des fragments de géométrie irrégulière ; l'introduction de H_2O allonge légèrement le temps de combustion .

La combustion du fil de béryllium a donné des résultats décevants et il est difficile d'en déduire une philosophie cohérente .

MAGNESIUM - Le point de fusion du magnésium est voisin de celui de l'aluminium 923°K et le point de vaporisation beaucoup plus faible 1376°K , par contre le point de fusion de l'oxyde est beaucoup plus élevé 3073 °K et peu éloigné de sa température de vaporisation 3373°K . L'allumage du magnésium est relativement facile et nécessite des températures nettement inférieures à celles précédemment trouvées pour l'aluminium et le béryllium.Les expériences de CASSEL et LIEBMAN ont donné les résultats suivants (17)

Composition du comburant	Température d'allumage en fonction du diamètre de la particule (°K)			
	20	50	80	120
AIR	1015	950	925	910
O_2 + 4 A	1005	940	915	900
O_2 + 4 He	1085	1025	995	975

On note une diminution de la température lorsque le diamètre de la particule croît , la nature du diluant modifie la température, l'augmentation de la température avec l'hélium peut être due à un accroissement de la conductibilité thermique du gaz $\lambda_{(O_2+4\ A)} < \lambda_{AIR} < \lambda_{O_2 + 4\ He}$.

Les températures d'allumage obtenues avec l'oxygène sont assez voisines de celles déterminées dans l'air . Les particules de magnésium brûlent dans l'air, dans l'oxygène et dans des mélanges O_2 ,A, He avec une flamme de diffusion et la réaction est gouvernée par la diffusion de l'oxygène ; les résidus sont constitués par de fines particules et des sphères creuses d'oxyde de magnésium .

La combustion des fils et des rubans de magnésium a fait apparaître les mêmes phénomènes et a lieu dans une large gamme de pressions et de températures en phase vapeur . La variation de la vitesse

de combustion d'un fil est donnée en fonction de la pression sur la figure 11 (13) . La vitesse varie rapidement jusqu'à 5 atm , la combustion étant contrôlée par la diffusion du comburant vers la zone de réaction , les dépôts sont constitués par des fines particules de MgO . Au delà de cette pression la diffusion de l'oxygène est freinée par les particules solides de MgO présentes dans la zone de combustion . A des pressions plus élevées , on note des irrégularités qui peuvent provenir du changement de propriétés physiques de la couche solide ou liquide d'oxyde poreux entourant la particule et formant une coquille , KIRSCHFELD pense en effet qu'à haute pression autour de la partie la plus basse du fil se forme une coquille liquide ou solide, l'intérieur de la coquille est rempli de vapeur métallique à haute pression qui diffuse à travers la paroi de la coquille , la combustion prenant place à l'extérieur de celle-ci , le mécanisme déterminant étant dans ce cas la diffusion du métal . On peut également concevoir une diffusion de l'oxygène vers l'intérieur et une combustion dans cette zone . Si la combustion a lieu dans une atmosphère contenant de la vapeur d'eau on note une diminution de la vitesse de combustion lorsque la concentration en eau augmente . MELLOR et GLASSMAN ont trouvé que les rubans de magnésium ne brûlent pas dans une atmosphère de CO_2 .

Dans de nombreuses conditions la combustion du magnésium se fait suivant un processus de diffusion avec production d'une fumée contenant de fines particules de MgO , MARKSTEIN a étudié cette réaction hétérogène et a pu comparer le processus chimique et le processus de diffusion qui intervient durant la condensation du MgO (14) . La comparaison de ces deux mécanismes (de diffusion et chimique) se fait en général à l'aide du module de THIELE $\gamma_0^2 R(C_0)/\vartheta C_0$ comparant par exemple dans le problème plan un temps de diffusion γ_0^2/ϑ (où γ_0 est une longueur d'échange et ϑ un coefficient de diffusion) et un temps chimique $C_0/R(C_0)$ (où C_0 est la concentration d'une espèce réagissante à l'abscisse $\gamma = \gamma_0$ et $R(C_0)$ le taux de production chimique). Pour une réaction du premier ordre MARKSTEIN utilise le paramètre $\gamma_0 k/\vartheta$ où k est la vitesse spécifique de réaction . En admettant pour k la valeur $\beta \omega/4$ où β est l'efficacité de collision et ω la vitesse moléculaire moyenne , on obtient $\frac{\gamma_0 k}{\vartheta} = \frac{\beta \gamma_0}{4\ell}$.

ℓ étant le libre parcours moyen ; le passage d'un processus contrôlé par diffusion à un processus contrôlé par réaction chimique se fait à une longueur caractéristique de 40ℓ ($\beta \approx 0{,}1$) . La détermination de $k\gamma_0/\vartheta$ a montré , dans le cas du magnésium , la prédominance des réactions hétérogènes sur des réactions en phase gazeuse suivies d'une condensation .

BORE - Une étude fondamentale sur la combustion du bore a été entreprise à A R C par MACEK (16) . Notons tout d'abord que les points de fusion et de vaporisation du métal sont respectivement de 2450°K et 3931°K et pour B_2O_3 723°K et 2316°K . L'allumage par laser des particules de bore de 60 à 80μ dans l'air à la pression atmosphérique conduit à une combustion en deux étapes, après 10 à 20 ms , la combustion démarre puis s'arrête brusquement , l'extinction est souvent complète mais parfois la particule se réallume et brûle complètement avec une flamme brillante , le temps total de combustion étant de l'ordre de 100 ms . Des particules de 40 et 45μ introduites dans des gaz brûlés comburants (pression partielle de O_2 = 0,2 atm) dont la température est comprise entre 2300 et 2900 °K brûlent également en deux étapes, ce phénomène étant observé dans une flamme exempte ou contenant H_2O . L'allumage de la particule a lieu lorsque sa température atteint environ 2000°K , le départ de la combustion est franc, on note un noyau central très lumineux entouré par une enveloppe gazeuse de couleur verte caractéristique des systèmes gazeux à haute température contenant du bore ; ensuite la combustion s'arrête . D'après MACEK , le temps de combustion pour des particules de 40 μ est de 2 à 3 ms , le temps d'extinction de 3 ms . On assiste ensuite à un réallumage et à une combustion complète de la particule durant environ 15 ms . Dans les mêmes conditions le temps de combustion d'une particule d'aluminium ou de béryllium est d'environ 5 ms . Cette combustion en deux étapes pourrait s'expliquer par un dépôt d'oxyde protecteur se formant à la surface de la particule pendant la phase d'allumage et de combustion primaire ; cette couche fait écran entre le gaz comburant et le métal stoppant tout échange entre comburant et combustible et provoquant l'extinction . Par la suite les gaz chauds entourant la particule vaporisent la couche d'oxyde dont la température d'ébullition est de 2316°K , cette vaporisation d'oxyde réduit encore momentanément la diffusion du comburant vers la particule , lorsque la couche d'oxyde a disparu un deuxième allumage intervient avec combustion complète de la particule . Il semble que durant cette deuxième combustion la couche d'oxyde, si elle se forme , n'est plus protectrice , cela peut tenir à une augmentation de la température de surface de la particule supérieure à la température de vaporisation de l'oxyde alors que , lors du premier allumage, la température de surface est de l'ordre de 2000°K .

MODE DE COMBUSTION DES METAUX

L'exposé des résultats expérimentaux montre la complexité des problèmes et la difficulté qu'il y a à construire un schéma représentatif de la combustion des métaux. BRZUSTOWSKI et GLASSMAN (18) ont divisé les métaux en deux groupes : a - les métaux volatils comme Li, Na, K , Mg, Ca qui ont les propriétés suivantes:

- le métal a une tension de vapeur de plus de 1 mm de Hg à 1000°K
- la phase liquide du métal se situe dans un domaine de température inférieur à la phase liquide de l'oxyde ,
- la température d'ébullition du métal est nettement inférieure à celle de l'oxyde ,
- la température de fusion du métal est basse comparée à la température de fin de combustion ,
- les oxydes formés sont poreux car le volume de l'oxyde est inférieur au volume du métal consumé pour former l'oxyde .

b - les métaux non volatils divisés en trois groupes comme Al, Be , Si qui ont des oxydes insolubles , Ti, Zr dont les oxydes sont solubles et B ayant son oxyde volatil et pour lesquels nous pouvons faire les remarques suivantes :

- les métaux classés à partir de la propriété des oxydes car celle-ci définit le mécanisme de combustion , Al, Be, Si ont des oxydes qui adhèrent à la surface métallique freinant la pénétration du comburant,
- lorsque la solubilité entre l'oxyde et le métal l'interface disparait et l'oxygène peut diffuser à travers l'oxyde,
- les oxydes des métaux Al, Be, Ti, Zr ont une température d'ébullition qui excède la température d'ébul-

lition du métal,; les oxydes du Si et du Bore ont un point d'ébullition inférieur au point d'ébullition du métal, de ce fait Al, Be, Ti et Zr peuvent brûler en phase vapeur suivant une flamme de diffusion alors que Si et B ne le peuvent pas .

A l'aide de cette classification BRZUSTOWSKI et GLASSMAN ont essayé de prédire les modes de combustion possibles du métal en décrivant chaque fois le mécanisme de transfert prépondérant. MARKSTEIN (14) classe les modes possibles de combustion en trois cas :

a- oxydation lente lorsque la température de réaction est inférieure à la température d'ébullition du métal et de l'oxyde (figure 12 a) (cas du zirconium). Une couche d'oxyde se forme à la surface du métal , l'oxygène allant jusqu'à la surface du métal si la couche est poreuse et s'arrêtant à la surface de l'oxyde lorsque la couche est protectrice ,

b - combustion à la surface si la température de réaction est de l'ordre de grandeur de la température d'ébullition de l'oxyde elle-même étant inférieure à la température d'ébullition du métal (cas du molybdène) , on note dans ce cas une réaction hétérogène de combustion à la surface ,

c- enfin combustion en phase vapeur, lorsque la température de réaction est comprise entre la température d'ébullition du métal et de l'oxyde (cas de l'aluminium). Dans ce schéma (figure 12 c) une réaction chimique homogène en phase gazeuse a lieu loin de la surface et deux réactions chimiques hétérogènes peuvent prendre naissance l'une près de la surface, l'autre en fin de combustion avec formation d'oxyde condensé.

La classification des modes de combustion à partir des propriétés physiques et chimiques du métal et des oxydes nous paraît intéressante et permet d'obtenir pour chaque métal un schéma valable, il nous semble cependant que le problème est beaucoup plus complexe et que, suivant le domaine expérimenté, on peut définir pour un même métal plusieurs modes de combustion possibles. Si nous prenons par exemple le Bore, la combustion se fait en deux étapes, le processus change donc en fonction du temps, ce processus est modifié également suivant le niveau de pression utilisé et selon la nature des gaz comburants , il n'y aura donc pas, pour un métal , un schéma unique . Pour expliquer ce point de vue nous allons analyser quelques modes possibles intervenant dans la combustion de l'aluminium . Lorsqu'on examine la figure 1 représentant la combustion interrompue d'une particule d'aluminium, on note une combustion symétrique en phase vapeur etle processus principal semble être celui qui régit la combustion d'une goutte d'hydrocarbure brûlant dans l'air. Sous l'effet de la température de fin de combustion élevée le flux de chaleur transmis à la goutte vaporise le métal, un écoulement de vapeur s'établit ayant pour source la surface du métal , une zone de combustion apparaît à une certaine distance de la particule. Le comburant pénètre par diffusion dans la zone de combustion et les produits gazeux formés diffusent vers la particule et vers l'extérieur. Ce schéma simple a été le support de nombreuses théories. La dernière en date de R.P. WILSON (19) indique que cette théorie simplifiée permet de prévoir la constante de combustion à ± 50 %, cette différence provient surtout d'une méconnaissance des paramètres de transfert entrant dans le calcul. Cette théorie simplifiée prévoir une loi en d^2 en fonction du temps, loi vérifiée par les résultats expérimentaux (voir figure 13).Cette loi en d^2 indique une prédominance des phénomènes de diffusion, les réactions chimiques ayant moins d'importance . Signalons cependant pour des particules dont le diamètre est compris entre 350 et 450 μ PRENTICE indique (comburant O_2,Ar) une variation linéaire du temps de combustion avec le diamètre des particules (20) . Ce schéma se complique un peu par suite de la formation en fin de combustion d'une poussière d'alumine, cette présence de particules étant le résultat d'une réaction hétérogène ou d'une réaction homogène suivie d'une condensation de l'oxyde formé ; il semble que dans le cas de l'alumine on soit plutôt en présence d'une réaction hétérogène. Ce nuage de fines particules prend naissance dans la zone de combustion puis est entraîné par les gaz brûlés. Une étude balistique de la trajectoire de ces particules d'alumine serait interessante; en première approximation, le diamètre de celles-ci étant inférieur au micron , on peut dire qu'elles suivent sans retard les gaz brûlés, on fait alors l'hypothèse du quasi-gaz . La goute d'aluminium en combustion étant placée dans un écoulement il en résulte que la zone de combustion est en partie sphérique, les produits brûlés s'échappent dans le sens de l'écoulement en formant une queue . Les particules d'alumine sont pour la plupart situées à la frontière de l'écoulement comburant extérieur et de l'écoulement formé par les gaz brûlés, du côté des gaz brûlés. Il serait donc utile dans le schéma de tenir compte de cet effet convectif. On note sur la figure 1 plusieurs zones d'accumulation des particules et PRENTICE conclut (8) : " les zones de distribution observées sur la figure 1 indique une structure de flamme complexe". Il faut cependant être présent dans l'interprétation , une zone de combustion simple peut donner naissance à des zones de départ complexes. Si nous examinons la figure 14 par exemple, la plaque de verre étant placée perpendiculairement à la trajectoire de la goutte d'aluminium, on aura une première zone d'accumulation correspondant à la sphère entourant la goutte, ensuite une deuxième zone provenant des poussières situées à la surface de la queue.

La présence d'hydrogène ou d'azote dans le gaz comburant fait naître à la surface de l'aluminium une calotte d'oxyde qui s'étale sur la goutte au cours de la combustion . Ce phénomène apparaissant avec certaines espèces doit donc avoir une origine chimique . On admet en général que sa formation est due à des réactions de surface, mais on peut envisager une combustion dissymétrique comme indiqué sur la figure 15. Durant la période d'allumage une couche d'oxyde s'est formée à la surface et après cette phase la pellicule est brisée et l'alumine se rassemble en un point de la surface; par suite de la présence de cet écran il n'y a plus au dessus de l'oxyde de vapeur d'aluminium puisque nous avons vu que l'alumine formait une couche non poreuse, cet écran a deux effets : tout d'abord l'aluminium vaporisé n'est plus injecté à la surface de la calotte, le gaz comburant présent tout près de la calotte est entraîné par l'écoulement venant soit de la surface du métal soit du dessous de la calotte dans le cas où il n'y a pas un contact parfait entre le métal et l'oxyde. On réalise donc deux jets parallèles de comburant et de combustible avec possibilité de combustion tout près de la surface , l'alumine formée dans cette zone de combustion et de condensation a la possibilité de se déposer à la périphérie de la calotte augmentant progressivement ses dimensions . Nous voyons donc apparaître deux schémas possibles : a - un schéma symétrique avec combustion en phase vapeur et possibilité de diffusion de l'oxygène jusqu'à la surface et d'oxydation secondaire à la surface avec formation d'une couche d'alumine diminuant le flux de métal vaporisé , des parcelles d'alumine liquide pouvant être entraînées par l'écoulement de la surface vers la flamme ; dans cette représentation il est difficile d'admettre la diffusion de l'alumine condensée vers la surface , la présence d'alumine ne peut provenir, dans un schéma symétrique , que de la diffusion de l'oxygène ou de certaines espèces comme l'azote (formation de nitrure d'aluminium condensé ou de compo-

sés faisant intervenir (N , Al , et O) ou de la condensation d'un oxyde gazeux, le produit gazeux Al_2O_3 s'il existe diffusant de la zone de combustion vers la goutte et venant se condenser à la surface du métal . b - Un schéma dissymétrique car la présence à la surface d'oxyde change complètement l'écoulement de combustible venant de la goutte et de comburant arrivant de la périphérie , les échanges sont donc modifiés ainsi que les processus de combustion et de condensation . De plus par suite de la présence d'un écoulement général les produits de combustion ne s'échappent pas de la zone de combustion avec une symétrie sphérique mais cette dissymétrie agit peu sur le temps de combustion . Soulignons que les deux modèles symétriques et dissymétriques sont une vue simplifiée des choses car au fur et à mesure que l'on analyse en détail les phénomènes , on découvre une très grande complexité caractérisée par une surface hétérogène , une combustion hétérogène et donc des procédés de transfert de masse et d'énergie hétérogènes et il est difficile pour l'instant de tenir compte dans une analyse mathématique de cette hétérogénéité. Celle-ci varie non seulement avec la nature du métal , la nature du comburant , la pression mais encore avec le temps et le diamètre des particules par exemple, par exemple les dépôts d'alumine à la surface de la goutte métallique n'ont pas la même épaisseur et la même structure avec les petites ou les grosses particules .

On observe en gros durant la combustion trois sortes de dépôts :

a- une poussière de particules d'alumine provenant d'une combustion en phase vapeur ,

b - des sphères creuses d'alumine dont la structure est lisse et ridée, la formation de ces sphères n'est pas encore élucidée; à notre avis plusieurs mécanismes de formation peuvent intervenir, tout d'abord lorsqu'on augmente la pression , la vitesse de l'écoulement vers l'extérieur de la goutte diminue et les particules d'alumine éprouvent de la difficulté pour suivre l'écoulement gazeux, ces particules s'accumulent et s'agglomèrent pour former au refroidissement une sphère creuse. Ces sphères peuvent être formées également à partir du mécanisme décrit sur la figure 15 , l'alumine se déposant au point de rencontre des deux écoulements comburant et combustible , on note bien dans certains cas sur les capsules un dépôt d'alumine par strates parallèles (figure n°5 de la référence 20) , les dépôts présentent dans ce cas une ouverture .

c - des gouttes d'alumine due à une combustion en surface que l'on rencontre dans des combustions à haute pression .

COMBUSTION DU METAL DANS UN PROPERGOL SOLIDE ET DANS UN COMBUSTIBLE SOLIDE

Dans les foyers utilisés pour la propulsion, la combustion des particules métalliques s'effectue dans une ambiance très hétérogène en composition , dans ce domaine de pression différent de celui utilisé dans l'expérimentation décrite précédemment et dans un écoulement dont la vitesse varie de quelques mètres à plusieurs centaines de mètres par seconde. On peut donc se demander si le mécanisme de combustion est modifié ou non par de telles conditions .

COMBUSTION DE L'ALUMINIUM DANS LES PROPERGOLS SOLIDES - Les particules d'aluminium introduites dans le propergol sont enrobées en général dans la matière plastique . Sous l'effet de l'énergie libérée par la combustion , la matière plastique disparait laissant à la surface une dentelle constituée par les particules d'aluminium . Ces particules sont recouvertes en partie d'une mince couche d'oxyde qui empêche toute agglomération , sous l'effet de la température élevée des gaz brûlés, cette couche est détruite , une flamme apparait à une extrémité de cet édifice de particules puis la combustion gagne tout l'édifice et une agglomération de l'aluminium se produit avec formation d'une goutte . La dimension des gouttes dépend dans une large mesure de l'aluminium contenu dans les interstices laissés entre les cristaux de perchlorate et la granulométrie des gouttes dépend de la distribution de ces interstices . On obtient donc à la surface du propergol des gouttes dont le diamètre peut atteindre quelques centaines de microns. Le temps de fusion de la particule d'aluminium est de 0,2 ms à 70 atm pour une particule de 10 μ et de 2,4 ms à 1 atm , il est de 6 ms à 70 atm pour une particule de 100 μ . Le temps d'agglomération est également court de l'ordre de la milliseconde. Les gouttes d'aluminium sont ensuite entraînées dans l'écoulement , la combustion démarrant près de la surface du propergol . Le mouvement des gouttes en combustion dépend des forces appliquées : pesanteur, accélération, forces aérodynamiques. Si la vitesse des gaz perpendiculaires à la surface est relativement faible (de l'ordre du mètre par seconde) dans un propulseur à canal central la vitesse le long de la surface croit très vite puisqu'elle peut atteindre le quart de la vitesse des gaz dans le canal central à une distance de la surface de l'ordre de 100 μ . La cinémicrographie à grande vitesse montre que la combustion des gouttes d'aluminium sur échantillon de propergol est assez voisines de celle décrite à partir des expériences précédentes lorsque le gaz comburant contient de l'hydrogène , de la vapeur d'eau et de l'azote . On observe près de la surface une première zone de combustion avec formation d'une calotte et une flamme de diffusion autour de la partie non protégée . On observe également une rotation de la particule au cours de la combustion et une fragmentation de celle-ci . Les produits condensés issus de la combustion se composent de fines particules de sphères creuses et de sphères pleines d'alumine (21) . Dans un propulseur la vitesse de l'écoulement dans le canal central a pour effet d'intensifier les échanges de masse et d'énergie entre la particule et la flamme et de diminuer le temps de combustion , l'alumine recueillie dans l'écoulement se présente sous forme de gouttes dont le diamètre moyen est de l'ordre du micron , on ne retrouve plus de sphères creuses ou de grosses gouttes . Une goutte d'aluminium de 50 μ de diamètre initial partant de la surface du propergol et pénétrant dans l'écoulement du canal central atteint au bout de 2 ms une vitesse de l'ordre de 180 ms^{-1} (figure 16) et parcourt 30 cm . Il est alors très difficile à de telles vitesses d'avoir expérimentalement une visualisation des phénomènes de combustion . Nous avons vu que la goutte d'aluminium quittait la surface sous l'effet combiné des forces appliquées (pesanteur, accélération , traînée) . Dans un propulseur en rotation , et sous l'effet de la force centrifuge , un plus grand nombre de gouttes reste à la surface produisant des irrégularités (formation de puits) .

Les techniciens de la propulsion sont intéressés par une combustion complète du métal et par la formation dans les produits brûlés de gouttes d'alumine dont le diamètre ne dépasse pas le micron . Ces deux conditions peuvent être réalisées : a - en formant à la surface des gouttes d'aluminium de petit diamètre , b - en empêchant pendant la phase d'allumage la formation à la surface du métal d'une couche d'oxyde protectrice , c - en augmentant la turbulence dans le canal central , la pulvérisation

de l'alumine formée pouvant être obtenue par un effet mécanique .

COMBUSTION DE L'ALUMINIUM DANS LES COMBUSTIBLES SOLIDES - (Application aux systèmes hybrides). Les particules métalliques sont introduites dans une matière plastique dans des proportions pouvant aller de 20 à 50% afin d'obtenir le maximum de performances (avec les propergols solides le maximum de performances se situe aux environs de 20%) . Le comburant est injecté dans le canal central d'un bloc cylindrique combustible . Sous l'effet de l'énergie libérée par la combustion la matière plastique est vaporisée libérant le métal . Contrairement à ce qui a lieu avec les propergols solides , le comburant est près de la surface en très faible concentration de sorte que les particules métalliques sont libérées dans une atmosphère combustible . La formation d'oxydes ou de nitrures à la surface est peu probable et la fusion de ces particules est très rapide , il se forme à la surface du combustible des gouttes de gros diamètre des filets liquides ou un film liquide continu entraîné par l'écoulement gazeux . La combustion de ce métal est donc très difficile et le rendement du foyer faible . Pour améliorer ce rendement on dispose de nombreux moyens physiques et chimiques . Une première technique consiste à augmenter la turbulence de l'écoulement de manière à ce que le comburant soit amené près de la surface; on peut également placer en bout de bloc des écrans qui créent des tourbillons dans lequels les échanges entre gaz comburant chaud et métal sont accrus . Il est également possible d'agir en plaçant dans le combustible et près du métal des substances qui empêchent la formation d'oxydes ou de nitrures,qui favorisent le démarrage de la combustion (abaissement de la température d'allumage) et qui augmentent le rendement de combustion . Ces substances doivent agir tout près de la surface, et doivent donc être de faibles dimensions (environ le centième du diamètre de la particule).

CONCLUSION

L'étude de la combustion des métaux est , comme nous venons de le voir, complexe, mais des résultats interessants ont été obtenus au cours de ces dernières années. Dans les progrès obtenus , nous noterons tout d'abord la définition des paramètres qui agissent sur le temps d'allumage et le temps de combustion; ces données intéressent directement les spécialistes de propulsion . La nature des gaz environnants joue un très grand rôle et par suite il est possible d'orienter le choix des ergols de manière à réduire le temps de combustion global et à accroître l'efficacité de la combustion .

Les progrès sont moins probants sur le plan fondamental et en particulier sur la définition des mécanismes de combustion des métaux. C'est un problème compliqué car il n'est pas possible de définir un processus unique mais une intéraction de plusieurs qui peuvent même évoluer pendant le temps de combustion .

Dans quelques cas cependant des hypothèses simplificatrices peuvent être faites et les résultats théoriques obtenus sont assez voisins de l'expérience . L'abord du problème complet est cependant difficile puisqu'il s'agit d'aérothermochimie instationnaire , tridimensionnelle avec transfert de masse et d'énergie par diffusion et réactions chimiques , ces réactions chimiques pouvant être homogènes ou hétérogènes .

BIBLIOGRAPHIE

1 – FRIEDMAN,R – MACEK ,A – Ignition and Combustion of Aluminum Particles in Hot Ambient Gases – Combustion and Flame vol 6 n°1 March 1962 pp9-19

2 – CHRISTENSEN , H.C, KNIPE R.H ,GORDON A.S – Survey of Aluminum Particle Combustion – Meeting of the Western States Section of the Combustion Institute – SALT LAKE CITY 26-27 October 1964 – Preprint n°64-19

3 – NELSON L.S, RICHARDSON,R,L. PRENTICE,J.L – Apparatus for the Production and Ignition of Metal Droplets with a Pulsed Laser – Rev Sc. Instr. vol 39 N°5 May 1968 .

4 – MICHAEL,J.R, BELBOURDO,R . LAFFITTE,P – Spontaneous Ignition and Combustion of Sodium Droplets in Various Oxidising Atmosphere at Atmosphere Pressure – Presented of the XII th Symposium (International) on Combustion – 14-20 July 1968 POITIERS –FRANCE

5 – MACEK, A. – Fundamentals of Combustion of Single Aluminum and Beryllium Particles – XIth Symposium(International) on Combustion – The Combustion Institute Pittsburg Pennsylvania 1967 pp 203 – 217

6 – NELSON ,L.S – Combustion of Metal Droplets Ignited by Flash Heating – XIth Symposium (International) on Combustion – The Combustion Institute –Pittsburg Pennsylvania 1967 pp.409 – 416 .

7 – NELSON , L.S , BOOKER , D.R, KURZIUS , S.C, LEVINE ,H.S. – Combustion of Zirconium Droplets in Oxygen/Inert Gas Mixtures Kinetics and Mechanism . Presented at the XII th Symposium (International) on Combustion –POITIERS –France 14 – 20 July 1968

8 – PRENTICE ,J.L – On the Combustion of Single Aluminum Particles Combustion and Flame vol 9 n°2 pp.205 – 210 .

9 – MACEK ,A, SEMPLE ,J.M. Experimental Burning Rates and Combustion Mechanisms of Single Beryllium Particles – Presented at the XII th Symposium (International) on Combustion – 14 –20 July 1968 – POITIERS –FRANCE

10 – ZENIN ,A.A, GLASKOVA,A.P. LAPUSHKIN,G.I, BOBOLEV,V.K. – Effects of Metallic Additives on the Deflagration of Condensed Systems – Institute of Chemical Physics USSR Academy of Sciences – C.R. Acd .Sci.USSR – 151 – 604 (1963)

11 – SHUSTOVSKI,T.A. GLASSMAN,I – Vapor-Phase Diffusion Flames in the Combustion of Magnesium and Aluminum II –Experimental Observations in Oxygen Atmospheres – Heterogeneous Combustion – Progress in Astronautics and Aeronautics vol 15 pp 117 – 158 .

12 – MELOR , A.M, GLASSMAN ,I – Vapor –Phase Diffusion Flames in the Combustion of Magnesium and Aluminum III Experimental Observations in Carbon Dioxydes Atmospheres Heterogeneous Combustion – Progress in Astronautics and Aeronautics vol 15 pp.159 – 176

13 – LORD , C.E , SEBAID , E . – The Burning Rate of Aluminum and Magnesium Wire in Pure Oxygen and Oxygen Water Vapor Atmospheres at High Pressures . Western States Combustion Institute April 1968 – Preprint 68-8 .

14 – FAINSTEIN , G.E. – Heterogeneous Reaction Process in Metal Combustion – XIth Symposium (International) on Combustion – The Combustion Institute , Pittsburg Pennsylvania 1967 pp 219 – 234 .

15 – KUEHL , D.K , ZWILLENBERG , H.L– Investigation of the Ignition and Combustion of Metal Wires May 1967 Contract NAS 7-353

16 – MACEK, A, SEMPLE , J.M – Solid-Propellant Flame Mechanisms – Projet Squid 1 oct.1968

17 – CASSEL H.M, LIEBMAN – Combustion of Magnesium Particles – Combustion and Flame vol 7 n°1 March 1963 pp79-82

18 – SHUSTOVSKI , T.A , GLASSMAN I – Spectroscopic Investigation of Metal Combustion – Heterogeneous Combustion – Progress in Astronautics and Aeronautics pp 41 – 73 vol 15

19 – WILSON , R.P– Studies on Combustion of Aluminum Particles – Spring Meeting Western States Section / The Combustion Institute China-Lake California 28-29 April 1969 Paper n°69-3

20 – PRENTICE , J.L– Combustion of Pulse Heated Singles Particles of Aluminum and Beryllium Spring Meeting Western States Section / The Combustion Institute China-Lake California 28-29 April 1969 – Paper n°69-2 .

21 – BAULARD J – Contribution à l'Etude de la Combustion des Particules d'Aluminium La Recherche Aérospatiale n°118 (1967) pp 25 – 49 .

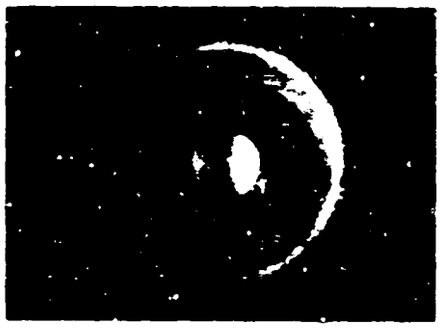

Fig. 1 - Particule d'aluminium de 400 brûlant dans l'air, combustion figée sur une plaque de verre (PRENTICE)

16 μ

Fig. 2 b - Structure d'une particule d'alumine après combustion

Fig. 2 c - Structure d'une particule d'alumine après combustion

Fig. 2 a - Structure d'une particule d'alumine après combustion

Fig. 3 - Combustion d'un fil d'aluminium

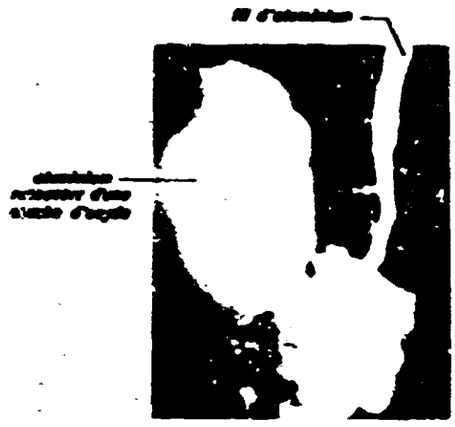

Fig. 4 - Formation de fils d'aluminium

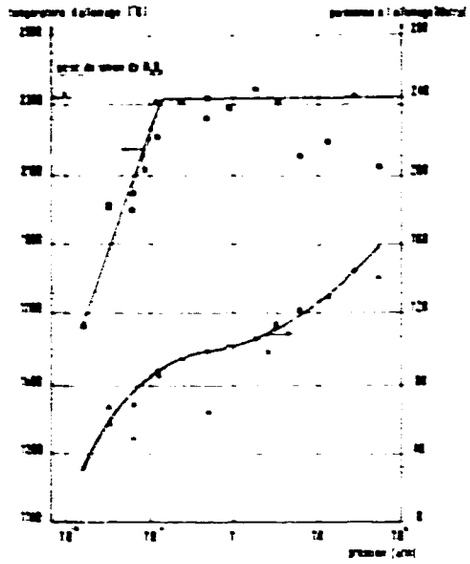

Fig. 5 - Effet de la pression sur la température d'allumage (15)

Structure de la particule après figeage de la combustion

Fig. 6 - Combustion près de la surface et flamme de diffusion

Fig. 7 a - Aspect extérieur des ballons d'alumine

Fig. 7 b - Structure interne des ballons d'alumine

Fig. 7 c - Structure de la surface des dépôts d'alumine

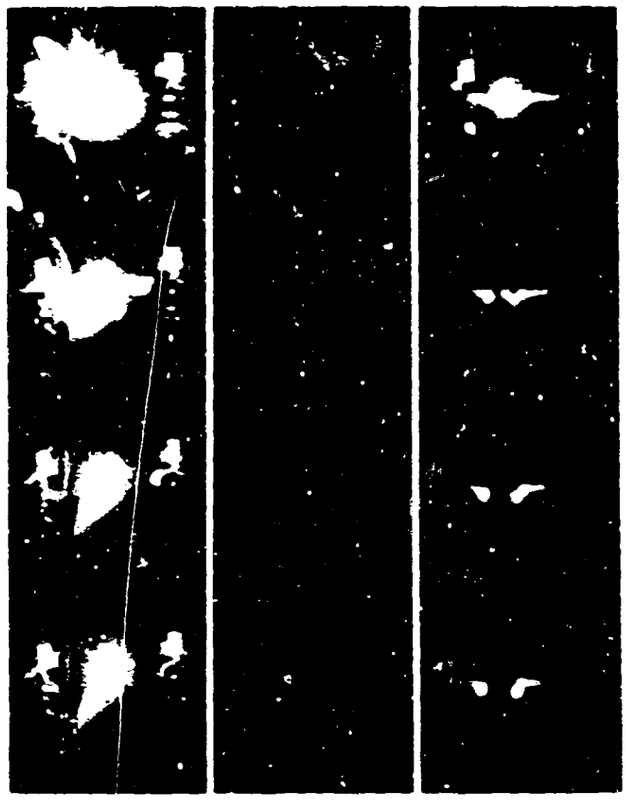

Formation d'une goutte | Explosion du fil | Arrêt de la combustion

Fig. 8 - Différents modes de combustion d'un fil d'aluminium

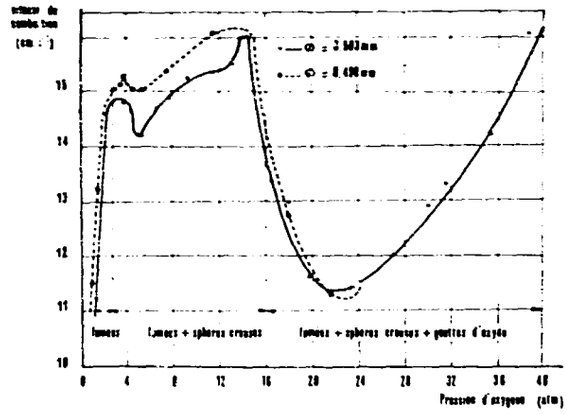

Fig. 10 - Vitesse de combustion d'un fil d'aluminium (13)

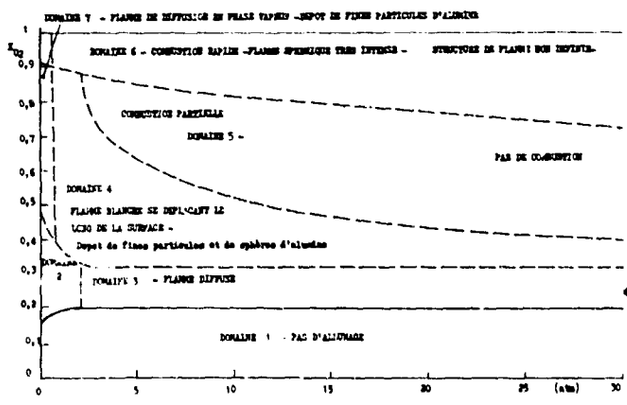

Fig. 9 - Modes de combustion d'un fil d'aluminium dans une atmosphère OXYGENE - ARGON (11)

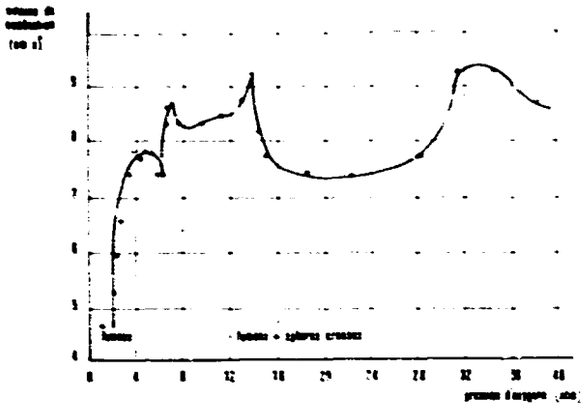

Fig. 11 - Vitesse de combustion d'un fil de magnésium (13)

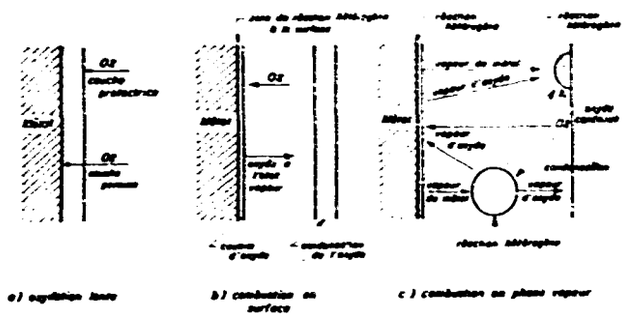

Fig. 12 - Schéma de combustion des métaux

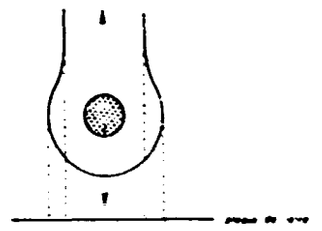

Fig. 14 - Structure des projections d'alumine sur une plaque de verre

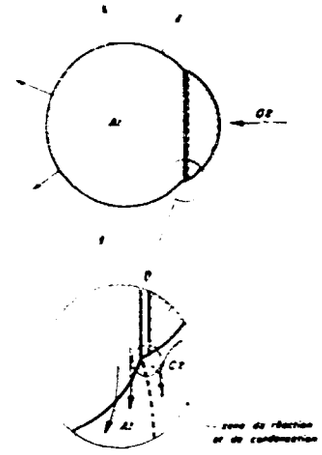

Fig. 15 - Formation de la calotte d'oxyde

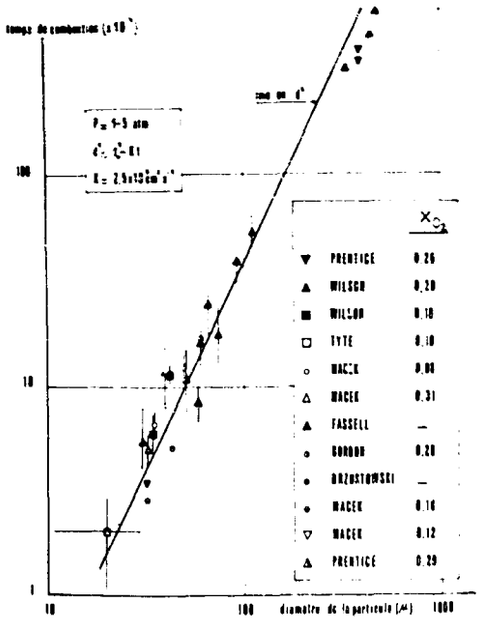

Fig. 13 - Combustion de particules d'aluminium dans de l'oxygène dilué (WILSON)

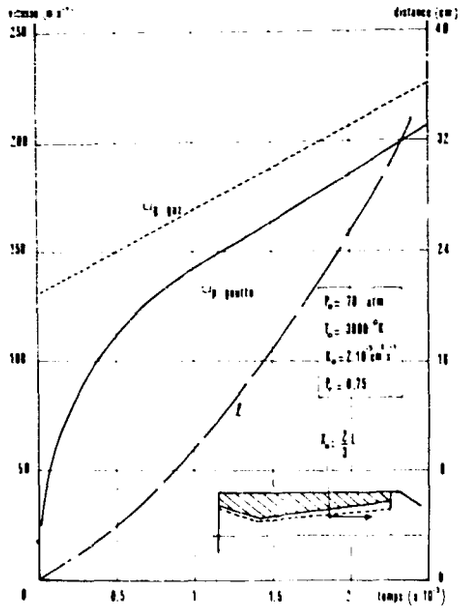

Fig. 16 - Vitesse de la goutte et distance parcourue en fonction du temps

COMBUSTION OF SOLID PARTICLES IN A TURBULENT STREAM WITH RECIRCULATION

M. M. GIBSON *
Northern Research and Engineering Corporation
London, U.K.

and

B. B. MORGAN
BCURA Industrial Laboratories
Leatherhead, U.K.

* Present address: Department of Mechanical Engineering, Imperial College, London, U.K.

SUMMARY

The paper describes a calculation procedure used to predict mass, momentum and energy transfer in a turbulent pulverised-coal flame in a cylindrical chamber, the geometry of which produces a zone of recirculatory flow. The flame, which may be swirling, is axisymmetric. The elliptic partial-differential equations describing the flame are solved numerically at a finite number of points in the flow field. The procedure includes a simple model of thermal radiation which assumes that net transfer along the length of the flame is zero.

Results of calculation are compared with data from six flames that differ in respect of burner size, fuel fineness and input swirl. Prediction is fairly good for the non-swirling flames but is less satisfactory for swirling ones.

Possible improvements to the calculation procedure are outlined.

SYMBOLS

C	numerical coefficient, as defined locally	
D	diameter of chamber	m
H	calorific value	J/kg
I	radiant intensity in outward radial direction	W/m^2 sterad
J	radiant intensity in inward radial direction	W/m^2 sterad
K, K_C, K_D	proportionality factors in char reaction equation	s/m
L	length of chamber	m
M	mass concentration of char per unit diameter interval	kg/m^4
$\dot{M}$	mass flowrate	kg/s
Q	radiant flux, not explicitly defined	W/m^2
T	temperature (absolute)	K
VM_o	initial volatile matter in unit mass of dry ash-free coal	-
W	fractional loss of weight by coal	-
a	numerical coefficient in convection term of Eq (5)	
b	numerical coefficient in diffusion term of Eq (5)	
c	numerical coefficient in diffusion term of Eq (5)	
c(T)	specific heat at temperature T	J/kg K
d	source term in Eq (5)	
e	enthalpy	J/kg
f	mixture fraction	-
k	absorption coefficient for thermal radiation	m^{-1}
l	burner dimension, defined in Figure 1	m
m	mass fraction	-
$\dot{m}''$	rate of burning of char per unit external surface	kg/m^2s
p	partial pressure	kg/ms^2
q	net radiant flux in outward radial direction	W/m^2
r	distance from symmetry axis	m
s	scattering coefficient for thermal radiation	m^{-1}
t	time	s
u	velocity	m/s
x	diameter of particle	m
z	axial distance from burner	m
ε	radiant emissivity	-
θ	angle of rotation about symmetry axis	rad
λ	mass of oxygen combining with unit mass of reactant	-
μ	viscosity	kg/ms
μ_*	numerical coefficient in viscosity expression	-
ρ	density	kg/m^3
σ	Schmidt or Prandtl number	-
σ_R	Stefan-Boltzmann constant	W/m^2K^4
ϕ	dependent variable	
ψ	stream function	kg/s
ω	vorticity	s^{-1}

Subscripts

c	char
eff	effective value in turbulent flow
g	gas
O2	oxygen
p	primary
r, z, θ	cylindrical polar co-ordinates
s	secondary
v	volatiles
w	wall

IN THE FIVE YEARS 1963-68, The British Coal Utilisation Research Association (BCURA) devoted a considerable effort to the study of the combustion of pulverised coal. This is coal that has been crushed and ground to a fine powder so that it can be carried as a suspension in a stream of air, injected into a combustion chamber, and burnt in a matter of seconds or less.

A comprehensive review of the information needed in the construction of mathematical models of pulverised-coal combustors was made by Field, Gill, Morgan and Hawksley (1). The review collected such numerical data as were available and described simple one-dimensional models that had been developed in BCURA and elsewhere. At the same time the meagre supply of basic data was being augmented by measurements of devolatilisation and burning rates of closely-graded coal particles under conditions of rapid heating similar to those experienced in a combustion chamber. These measurements are equivalent to ones for a single particle in a uniform environment. A third activity was to design and run a highly-instrumented rig, burning pulverised coal at rates up to 660 kg/h (2,3). Using this, the aerodynamic, combustion and heat-transfer phenomena in a real flame were studied systematically. It is the behaviour of this rig that we are attempting to calculate, using results from the reaction rate studies.

Earlier attempts at calculation (1,4) have assumed either plug flow and lateral uniformity along the whole length of the chamber, or, at best, a simple known pattern of jet spread and recirculation. Here we attempt to calculate the flow pattern, as well as burning rates and heat transfer, and we also permit lateral variation of properties.

The method of calculation is one for steady turbulent flow that was developed by Spalding and co-workers (5). The procedure is to integrate the differential equations for mass, momentum and energy transfer over small volumes of the flow field and to solve the finite-difference formulae so obtained by iteration, starting with a series of guessed values. A critical feature in the success of the method is the use of 'upwind' values in evaluation of convective transfer. One of the early applications of the Spalding method was the treatment by Pun & Spalding (5,6) of a cylindrical chamber into which flow two gases through concentric inlets at one end. The flow, although axisymmetric, may be swirling. The walls are impermeable, non-reacting and adiabatic. The gases react at infinite chemical rate to give a single gaseous product. They, and the product, are non-radiating. Fluid density and other properties vary greatly from point to point and the method successfully overcomes the computational difficulties that this presents.

The calculations of this paper derive directly from those of Pun & Spalding but treat a system more complex in three respects. Firstly, the flow contains solid particles that react at a finite rate with the gas. Secondly, the system is thermally radiating. Thirdly, the chamber is not adiabatic but has cooled isothermal walls.

COMBUSTION OF PULVERISED COAL IN TEST RIG

The combustion chamber, shown in outline in Figure 1, consists of a horizontal cylinder 1.1 metres diameter, 6.1 metres long (2). The outlet is unrestricted, so combustion effectively takes place at atmospheric pressure. A double-concentric-jet burner is mounted on the centreline at the inlet end. The inner, or primary, jet carries the pulverised coal suspended in about 15 per cent of the total air admitted. This is preheated to 375K. The annulus admitting the remaining (secondary) air, which is at 620K, is separated from the primary inlet by a water-cooled metal ring. Burner geometry is known to have a marked effect on mixing patterns in the chamber. This has been studied using a number of different (detachable) burners, some of which contain swirl vanes in either or both inlets.

The furnace wall is of steel and is water-cooled along its length. Entry ports for sampling probes are provided along one side. There is some asymmetry of the flame, both horizontal and vertical, but it is small enough to be neglected. Apparent asymmetry of non-simultaneous measurements is more likely to arise from fluctuations in the coal feedrate, which is the most difficult variable to control. The maximum coal feedrate was 660 kg/h but in most tests it was 300 kg/h. The overall air-fuel ratio was normally some 20% above the stoichiometric value. Fuel type was not investigated, low-rank bituminous coals being used throughout. The fuel normally had a weight median particle diameter of 45μm, although 25μm and 80μm powders were used as well. The overall diameter range of the standard fuel was 2 to 200μm.

Combustion of pulverised coal is difficult to represent quantitatively owing to the variety of coal types, the heterogeneity of even a single type, and to the complexity of the changes that take place on heating. A typical fuel fired in the rig contains 5% by weight of water, and 10% incombustible mineral matter. Much of the mineral matter exists as separate particles but there are composite particles also, some having a layered structure; about 2% of minerals is intimately distributed throughout the coal. The dry ash-free coal is 80% carbon, 11% oxygen, 5% hydrogen, the balance being mostly nitrogen and sulphur. It has a calorific value of 33 MJ/kg and requires 10.6 times its mass of air for complete combustion to carbon dioxide and water.

In a pulverised-coal flame the particles heat to 1200K in 0.1 s or less. During heating they soften and swell, and above 800K they lose mass by emission of combustible volatile matter. At this stage the particles may be quite rounded and have large internal voids. But there is no uniformity of behaviour and up to five different types have been distinguished visually. The char residue is mostly carbon and burns by heterogeneous reaction with oxygen diffusing to the surface. Burning may occur internally as well as at the outer surface; it results partly in a reduction of particle density, partly in a reduction of particle size. This char-burning stage may overlap decomposition.

Studies of isothermal decomposition of coal particles in an inert atmosphere under conditions of rapid heating have been made by Badzioch, Sainsbury and Hawksley (1,7). They showed that the fractional loss of mass W could be related to the time t spent at the decomposition temperature T and to the initial volatile-matter content VM_o, as estimated by a standard slow-decomposition test. The relation is

$$W = VM_oC(1 - C_1)\{1 - \exp\left[-C_2 \exp(-C_3/T)t\right]\} \quad (1)$$

C, C_1, C_2 and C_3 are experimentally-determined constants. Typical values for 20μm particles of a low-rank coal (VM_o = 0.37) decomposed at temperatures in the range 800 - 1300K are C = 1.3, C_1 = 0.14, C_2 = 1.5 x 10^5s and C_3 = 8900K.

Isothermal combustion of a devolatilized char has been studied by Field (8,9). The rate of removal of carbon per unit of geometric surface was found to be proportional to the mainstream concentration of oxygen. The proportionality factor K could be formed from two coefficients, one (K_D) expressing the rate of transport of oxygen to the particle surface, and the other (K_C) expressing the rate of chemical reaction at the surface. Thus

$$\dot{m}''_c = Kp_{O2} = p_{O2}/(1/K_D + 1/K_C) \quad (2)$$

$$K_D = C_4 T_g^{0.75}/x \quad (3)$$

$$K_C = -C_5 + C_6 T_c \quad : T_c > C_5/C_6 \quad (4)$$

where $\dot{m}''_c$ = rate of carbon removal (kg/m^{2}s)

p_{O2} = partial pressure of oxygen (kg/s^{2}m)

T_g = temperature of gas (K)

x = particle diameter (m)

T_c = temperature of particle surface (K)

Constant C_4 is calculated from diffusion theory as 4.99 x 10^{-12}s/K$^{0.75}$. It is implicit in this that the first product of reaction at the surface is carbon monoxide. C_5 and C_6 are experimentally-determined constants, specific to the coal. For low-rank coals, such as were burnt in the rig tests, typical values found are C_5 = 7.90 x 10^{-5} s/m and C_6 = 6.4 x 10^{-8} s/mK. For simplicity, the reaction rate is supposed zero at temperatures below 1230K.

Partly because of the difficulty of identifying precisely the processes occurring, and partly because of the need to avoid excessive complications in the computational procedure, a number of simplifying assumptions have been made concerning the behaviour of the coal during heating and combustion. These are described in subsequent sections of the paper.

METHOD OF CALCULATION

The work of Pun & Spalding, mentioned above, forms the point of departure for the present calculations. These authors reduced the partial-differential equations for the transfer of mass, momentum and energy to the general form, in cylindrical polar coordinates:

$$\frac{a}{r}\left(\frac{\partial}{\partial z}\left(\phi\frac{\partial\psi}{\partial r}\right) - \frac{\partial}{\partial r}\left(\phi\frac{\partial\psi}{\partial z}\right)\right) - \frac{1}{r}\left[\frac{\partial}{\partial z}\left\{br\frac{\partial(c\phi)}{\partial z}\right\} + \frac{\partial}{\partial r}\left\{br\frac{\partial(c\phi)}{\partial r}\right\}\right] + d = 0 \quad (5)$$

Here ϕ represents a dependent variable; a, b, c and d are known functions of the variables; and the remaining symbols are explained in the nomenclature. A hypothesis for the transport properties of turbulent gas flows finds its mathematical expression in the function b, as an effective diffusion coefficient; d is a "source" term, which in the case of the mass transfer equations contains the appropriate chemical kinetic terms.

The dependent variables in the case analysed by Pun & Spalding were vorticity, stream function, swirl velocity, chemical species (mixture fraction), and enthalpy. Only three chemical species (fuel, oxidant, product) were considered and by postulating an infinitely-fast reaction rate the corresponding species equations were reduced to a single (mixture-fraction) equation. Because there was no thermal radiation and the chamber was adiabatic the enthalpy equation was identical to this.

We do not intend to dwell on the basic treatment, which is fully described in the referenced papers, but will focus attention on the new features introduced for pulverised-coal combustion.

BURNING OF FUEL. The combustible volatile content of the fuel is supposed to be admitted separately in gaseous form and to combine instantaneously when mixed with oxidant. The oxygen, nitrogen and water content is added to the primary gas stream. Minerals are treated as separate inert particles.

The residual char particles are assumed to be spherical, to consist wholly of carbon and to burn at constant density. A series of particle diameter classes is specified, five in the present calculations, and the mass fraction of solids in each class is treated as a separate dependent variable requiring an equation of the general form (Eq (5)).

The effect of particle burning on the mass fraction in each diameter class is embodied in the source term d. This is made up of three components: a) loss of mass to the gas phase; b) loss of mass by transfer of particles across the lower diameter limit to the class below; c) gain of mass by transfer of particles across the upper diameter limit from the class above. Thus the particle-fraction equation for the i th diameter interval contains a source term

$$d_i = - M_i\left(\frac{dx}{dt}\right)_i + M_{i+1}\left(\frac{dx}{dt}\right)_{i+1} - 3\int_{x_i}^{x_{i+1}} \frac{M}{x}\left(\frac{dx}{dt}\right) dx \qquad (6)$$

where M denotes mass concentration per unit diameter interval, and x is the diameter.

It is assumed that, within each size class, concentration M is constant at value $M_{av,i}$ given by

$$M_{av,i} = \rho m_i/(x_{i+1} - x_i)$$

and that the value at class limit x_i is related to the two values of M_{av} in classes (i - 1) and i by

$$M_i = \frac{M_{av,i-1}(x_{i+1} - x_i) + M_{av,i}(x_i - x_{i-1})}{x_{i+1} - x_{i-1}} \qquad (7)$$

The integral in Eq (6) is approximated to by the finite-difference form

$$3\int_{x_i}^{x_{i+1}} \frac{M}{x}\left(\frac{dx}{dt}\right) dx = \frac{3M_{av,i}}{x_{av,i}}\left(\frac{dx}{dt}\right)_{av,i} (x_{i+1} - x_i) \qquad (8)$$

where $x_{av,i}$ is the arithmetic mean diameter for the i th class. The final expression for the source term becomes

$$d_i = - M_i\left(\frac{dx}{dt}\right)_i + M_{av,i+1}\frac{(x_{i+1} - x_i)}{(x_{i+2} - x_i)}\left(\frac{dx}{dt}\right)_{i+1} \qquad (9)$$

$$+ m_i\left[\rho\frac{(x_{i+2} - x_{i+1})}{(x_{i+2} - x_i)(x_{i+1} - x_i)}\left(\frac{dx}{dt}\right)_{i+1} - \frac{3\rho}{x_{av,i}}\left(\frac{dx}{dt}\right)_{av,i}\right]$$

This formulation of d, was found to overcome difficulties in regard to stability that were at first experienced. The rate of change of particle diameter is obtained from Eq (2), using numerical values given by Field (9).

Before the particles start to burn, their temperature is held at the inlet value. Thereafter they are given a temperature higher than that of the gas by a constant specified amount.

SPECIES COMPOSITION OF GAS. In addition to the inert component nitrogen the gas is supposed to contain only oxygen, volatiles, carbon dioxide and water vapour. Their mass fractions are related to each other, and to that of the solid char, and it is found that the species composition of the gas may be treated by a single dependent variable, the equation for which contains no source term. By analogy with the Pun & Spalding case this is called mixture fraction (f) but is differently defined. Here it represents conservation of the quantity $(m_{02} - \lambda_c m_c - \lambda_v m_v)$ where m is a mass fraction and λ is the corresponding stoichiometric ratio. The subscripts denote oxygen, char and volatiles.

THERMAL RADIATION. The treatment of thermal radiation, which is described fully in another report (10), is an extension of the Milne-Eddington method (11) to axisymmetric systems. There are two main simplifying assumptions: firstly, that net transfer of radiant energy in the z (axial) direction is zero; secondly, that net transfer q in the r (radial) direction is

$$q = \pi(I-J) \qquad (10)$$

where I and J is each a (supposed) uniform intensity of radiation over a solid angle of 2π, in outward and inward radial directions respectively. With the aid of these, and other, assumptions, the general integro-differential equation of transfer reduces to the two ordinary differential equations

$$\frac{1}{r}\frac{d}{dr}(qr) = k(4\sigma_R T^4 - 3Q) \qquad (11)$$

$$\frac{dQ}{dr} = - \frac{k + s}{r}(qr) \qquad (12)$$

in which k and s are the absorption and scattering coefficients of the radiating medium, and σ_R is the Stefan-Boltzmann constant; Q is a radiant flux that need not be evaluated explicitly for present purposes.

Equations (11) and (12) are readily cast in finite-difference form, for evaluation of q in the calculation scheme, and solved numerically at each step of the iteration process. Boundary conditions are that on the centreline q = 0, and at the wall:

$$\pi J_w = \epsilon_w \sigma_R T_w^4 - (1 - \epsilon_w)\pi I_w \tag{13}$$

$$Q_w = \frac{4}{3} J_R T_w^4 + \frac{4}{3} q_w \left(\frac{1}{\epsilon_w} \cdot \frac{1}{2}\right) \tag{14}$$

In the present calculations the scattering coefficient is set to zero. The absorption coefficient is computed from the concentration and sizes of the char particles, assuming them to have a particle emissivity of 1; to this is added a constant contribution of 0.1 m^{-1}, to represent radiation by all other species. The wall is assigned an emissivity of 0.7. Greyness is assumed throughout.

ENERGY CONSERVATION. The enthalpy of the flow, a dependent variable in a partial-differential equation of the general form (Eq (5)), is defined by:

$$e = \int_T c(T)dT + m_c H_c + m_v H_v \tag{15}$$

where H_c and H_v are heats of combustion of char and volatiles. A linear temperature dependence is assumed for specific heat c(T) such that

$$\int_T c(T)dT = (-419 + 0.151T)T \qquad \text{joules per kg} \tag{16}$$

The energy contributed by thermal radiation forms the source term of the enthalpy equation. Since there is only a radial component in our simplified model the source term becomes

$$d_e = \frac{1}{r}\frac{d}{dr}(qr) \tag{17}$$

The enthalpy is used to evaluate temperature at all points of the field, using prevailing values of m_c and m_v.

TURBULENT DIFFUSION. The term b appearing in the general conservation equation contains the effective diffusion coefficient for the dependent variable in question. This is obtained by dividing the effective viscosity μ_{eff} by the effective Prandtl or Schmidt number σ_{eff}, as appropriate. Assumptions made earlier require that the Prandtl and Schmidt numbers be equal at each point in the field; they are assigned the value 1 throughout. Various hypotheses for eddy viscosity in turbulent gas streams are available; the one used here is that given by Pun & Spalding:

$$\mu_{eff} = \frac{\mu_* D^{2/3}(\dot{m}_p u_p^2 + \dot{m}_s u_s^2)^{1/3}}{L^{1/3}} \rho^{2/3} \tag{18}$$

where μ_* = a specified constant (the value 0.018 has been used)

D = chamber diameter (m)

L = chamber length (m)

$\dot{m}_p, \dot{m}_s$ = mass flow through primary and secondary nozzles (kg/s)

u_p, u_s = velocities in primary and secondary nozzles (m/s)

ρ = stream density (kg/m^3)

Thus the local value of viscosity is taken to vary only with stream density, the other parameters being constant for each flame. Viscosity increases with kinetic energy of the stream and with chamber diameter, but decreases with chamber length.

SOLUTION PROCEDURE. The coefficients a, b, c, d used for each variable in the general partial-differential equation are listed in Table 1. The set of equations so formed, together with suitably-chosen boundary conditions and the perfect gas laws, suffice for solution of the problem. The procedures employed for the numerical solution of the equations follow those used by Spalding and his co-workers (5,6), whose papers should be consulted for a full description.

In brief, the flow field is supposed covered by a rectangular mesh, a section of which, surrounding a nodal point P, is shown in Figure 2. Each partial-differential equation is cast in finite-difference form, with respect to the mesh, and is then integrated over a control volume surrounding the node. Thus for each dependent variable, each node on the calculation mesh provides an algebraic, finite-difference equation giving the value at node P in terms of those at surrounding nodes. The solution starts from a set of guessed values for all variables, and the sets of equations are solved successively at all points taken in turn to yield a new set of values. The cycle is repeated until the difference between values obtained from successive cycles is acceptably small. The radiation equations are not integrated across a control volume but solved, in finite-difference form, by a straightforward step-by-step procedure using prevailing values of the other variables.

Special procedures have been adopted in calculating heat transfer to the cooled walls. The steep gradients occurring in the near-wall region cannot be adequately described on a calculation mesh of practical dimensions. To overcome the difficulty it is assumed that the flow adjacent to the wall is one-dimensional; that it can be joined to the main flow; and that fluxes to the wall may be obtained from pre-determined "wall functions", calculated from analysis of the one-dimensional flow. A detailed account of the procedure has been given by Spalding & Patankar (12) and Runchal (13).

Table 1. Coefficients in Differential Equation for Dependent Variable

Dependent variable ϕ	Coefficients in Equation (5)			
	a	b	c	$\dot{s}$
ω/r (vorticity)	1	1	μ_{eff}	$-\frac{1}{r}\left[-\text{grad}\left(\frac{u_z^2+u_\theta^2}{2}\right).\text{iso}\ \rho+\frac{\partial}{\partial z}\left(\frac{\rho u_\theta^2}{r}\right)+2\mu_{eff}\frac{\partial}{\partial r}\left(\frac{\omega}{r}\right)\right]$
ψ (stream function)	0	$\frac{1}{r^2}$	1	$-\frac{\rho\omega}{r}+\frac{1}{r^2}\left[\text{grad}\ \psi.\ \text{grad}(\ln\rho)\right]$
u_θ (swirl velocity)	1	μ_{eff}	-1	$\frac{u_\theta}{r}\left(\rho u_r+\frac{\mu_{eff}}{r}+\frac{\partial\mu_{eff}}{\partial r}\right)$
f (mixture fraction)	1	$\frac{\mu_{eff}}{\sigma_{f,eff}}$	1	0
e (enthalpy)	1	$\frac{\mu_{eff}}{\sigma_{e,eff}}$	1	$\frac{1}{r}\frac{d}{dr}(qr)$
m_i (solid particles)	1	$\frac{\mu_{eff}}{\sigma_{i,eff}}$	1	$-M_i\left(\frac{dx}{dt}\right)_i+M_{i+1}\left(\frac{dx}{dt}\right)_{i+1}-3\int_{x_i}^{x_{i+1}}\frac{M}{x}\left(\frac{dx}{dt}\right)dx$

CALCULATIONS FOR TEST RIG

Calculations have been made for six flames of pulverised coal in the test rig described earlier, chosen to cover the range of the main variables investigated (3). They test the ability of the method to predict the effect on the flame of burner size, fuel fineness and input swirl.

Input conditions for the flames are summarised in Table 2. Fuel composition and mass flowrates of air and fuel are much the same throughout, as are inlet temperatures. But Flame 85 is a slight exception in that fuel flowrate is higher and secondary-inlet temperature is lower. The first four flames are without swirl. Flames 30 and 34 differ only in fuel fineness; they utilise a burner (Burner E) that has proportions in the middle of the range investigated. Extreme designs of burner (M and I) are used in Flames 43 and 49. Burner M has a very narrow interface between primary and secondary inlets, and a wide secondary inlet. In contrast Burner I has a very wide interface and a narrower secondary inlet; the primary inlet is narrower too. Other conditions are the same and the fuel is one of medium fineness. The last two flames (79 and 85) are swirling ones utilising Burner M. In Flame 79 there is swirl in the primary stream only; in Flame 85 it is present in both primary and secondary. The intensity of swirl is not very precisely established, but approximately the tangential component of velocity is 1.2 times the forward component.

CALCULATION MESH. For the calculations reported here eleven internal grid nodes were used in the radial direction, and thirteen in the axial. This is barely adequate but the limit was set by the size of store of the computer in use and by the cost of computation. The axial positioning of nodes was constant throughout; the radial positioning varied with the proportions of the burner. Values are given in Table 3. The first two nodes in the axial direction lie within the burner inlets.

It will be seen that grid-line spacing is small, as it must be, close to the primary inlet where conditions change very rapidly with distance, but expands gradually as one moves downstream or towards the chamber wall. Thus the control volume used in the solution process may have a cross-sectional area in the rz plane as small as 0.02 x 0.10 m, or as large as 0.10 x 1.00 m. Its third dimension is proportional to the radial distance from the axis.

CONVERGENCE. Each solution was started independently from a very simple set of guessed values at internal nodes except for Flame 34, when the final estimates resulting from Flame 30 were used. These two flames have almost identical flow patterns. Typically, 110 - 120 iterations were made,

Table 2. Input Conditions for Flames

Flame number		30	34	43	49	79	85
Fuel flowrate	(kg/s)	0.086	0.084	0.086	0.086	0.083	0.105
Primary air flowrate	(kg/s)	0.123	0.122	0.110	0.104	0.120	0.121
Secondary air flowrate	(kg/s)	0.825	0.819	0.810	0.822	0.737	0.953
Swirl in primary jet (fraction of u_z)		0.0	0.0	0.0	0.0	1.2	1.2
Swirl in secondary jet (fraction of u_z)		0.0	0.0	0.0	0.0	0.0	1.2
Temperature of primary air	(K)	373	373	372	373	375	376
Temperature of secondary air	(K)	622	623	625	626	613	577
Temperature of wall	(K)	400	400	400	400	400	400
Burner : code letter		E	E	M	I	M	M
diameter l_1	(m)	0.10	0.10	0.10	0.08	0.10	0.10
diameter l_2	(m)	0.26	0.26	0.15	0.30	0.15	0.15
diameter l_3	(m)	0.40	0.40	0.40	0.38	0.40	0.40
Fuel : weight median size	(μm)	25	80	47	43	47	41
5% larger than size	(μm)	77	360	150	140	150	140
5% smaller than size	(μm)	6	26	10	9	10	9
carbon (as-fired basis)		0.646	0.651	0.683	0.690	0.677	0.687
hydrogen -do-		0.042	0.042	0.044	0.044	0.044	0.044
oxygen -do-		0.088	0.095	0.098	0.099	0.098	0.099
nitrogen -do-		0.014	0.014	0.016	0.016	0.016	0.016
sulphur -do-		0.014	0.016	0.007	0.007	0.007	0.007
ash -do-		0.114	0.117	0.109	0.103	0.074	0.072
moisture -do-		0.082	0.065	0.043	0.041	0.084	0.075
volatile matter, VM_o (dry, ash-free basis)		0.408	0.408	0.374	0.374	0.374	0.374
calorific value (MJ/kg) (as-fired basis)		26.3	26.3	27.6	27.9	27.4	27.8

although with Flame 34 in consequence of the more realistic starting values, only 81 were necessary to achieve the pre-selected criterion for termination.

Convergence of the solution, which is heavily damped, is achieved first near the burner and the axis, and moves very slowly downstream and outwards. No solution when terminated was properly converged in the sense that the change in successive iterations was reducing at a rapidly increasing rate. It is possible, then, that estimates near the outlet could still move very slowly to significantly different values. But it is judged that this would not in fact happen to an extent that would invalidate the conclusions drawn from the results about the effect of major flame variables. As examples of the level of convergence accepted, one may say that on termination the enthalpy change in successive iterations was never greater than 10^{-3} of the value that would have prevailed at the outlet of an adiabatic chamber, and the change in char mass fraction was never greater than 10^{-3} of the outlet value that would have prevailed if no burning had occurred.

RESULTS FOR FLAMES WITHOUT SWIRL. Direct comparison of some calculated results for non-swirling flames with measured data from the rig is made in Table 4 and Figures 3 to 5. A calculated streamline pattern is shown in Figure 6.

The performance of our mathematical model in predicting overall behaviour of the rig as a device for release and transfer of heat is revealed by the first four energy balances of Table 4. One must first note that up to 150 kW, 7% of the available energy, is unaccounted for in these balances. In the case of the measurements this discrepancy may be attributed to experimental error; in the case of the calculations it is the result of failure to achieve conservation of the dependent variables throughout the whole field. The chief contributory factor is the procedure adopted for the regions near a boundary. There, the outer limits of a control volume (Figure 2) lie midway been the boundary and the nearest node. This leaves a significant region (with the present mesh, not at all small) in which no attempt is made explicitly to ensure conservation; instead, the dependent variables are given power-law profiles designed to satisfy the boundary conditions. The error may be reduced

Table 3. Positioning of Calculation Mesh

Grid-line number, axial or radial	Axial position relative to burner (m)	Radial position (m)		
		Burner E	Burner I	Burner M
1	- 0.16	0.000	0.000	0.000
2	- 0.08	0.025	0.020	0.025
3	0.00	0.050	0.042	0.050
4	0.11	0.076	0.074	0.075
5	0.21	0.104	0.122	0.102
6	0.37	0.132	0.151	0.132
7	0.59	0.166	0.169	0.166
8	0.84	0.202	0.188	0.202
9	1.34	0.255	0.220	0.255
10	1.84	0.322	0.279	0.322
11	2.59	0.407	0.335	0.407
12	3.34	0.490	0.488	0.490
13	4.34	0.550	0.550	0.550
14	5.34	-	-	-
15	6.10	-	-	-
Primary-inlet number	-	3	3	3
Secondary-inlet numbers	-	6, 8	6, 8	4, 8

Table 4. Energy Balances (kW) for Six Flames

Flame number		30	34	43	49	79	85
Chemical energy of fuel input		2270	2210	2380	2380	2280	2920
Sensible heat of input above 0 K		550	550	540	540	490	570
Total energy input		2820	2760	2920	2920	2770	3490
Heat transfer to wall,	calculated	1210	1050	1130	1270	1110	1410
	measured	1300*	1160	1210	1350	1370	1700
Sensible heat of outflow,	calculated	1610	1600	1600	1480	1510	1910
	measured	1430	1350	1420	1340	1240	1610
Chemical energy of char,	calculated	10	120	60	20	50	50
	measured	20	170	140	120	100	30
Input unaccounted for,	calculated	-10	-10	130	150	100	120
	measured	70	80	150	110	60	150

* value from Flame 97, which is similar to Flame 30

substantially, at the expense of computer storage and time, by specifying a finer mesh close to the boundaries. This would reduce also errors due to the finite-difference approximation, such as truncation and linear interpolation between mesh points.

As regards the enthalpy due to incomplete burning of the fuel, the model matches measurement in showing the loss to be small and in fact overestimates the amount of burn-out somewhat. Estimation of heat transfer to the wall is good although consistently low by about 100 kW. This is within the precision set by the size of the error terms. At the present stage of development the pattern of prediction is of more importance than precise numerical values, and it is correct as to the effect of fuel fineness and burner size.

Passing now to prediction of the distribution of heat transfer to the cooled wall, this is shown in the top four sections of Figure 3. Accuracy is quite good except for the region near the burner. A typical pair of temperature patterns, calculated and measured, is shown in Figure 4. It will be seen that the model predicts peak temperatures, near the axis and the burner, far higher than were measured. These explain the discrepancy in the calculated rate of heat transfer to the wall in the first metre or so from the inlet. When mixing is well advanced, the calculated temperatures become more accurate and in the last metre or so before the outlet are about right.

It is thought that the discrepancies in temperature and heat transfer arise from the assumptions made about release and burning of coal volatiles. It will be remembered that we have supposed the volatiles to be immediately available on entry to the chamber, and to burn at infinite rate provided oxygen is available. The temperature that would be achieved by adiabatic burning of the volatiles in a stoichiometric quantity of air is about 2560K and temperatures approaching this are computed for the inlet region, little mixing and little radiant transfer having occurred. In contrast, measured values show a peak of 1700K at about 2.5 metre from the burner. Gas samples taken on the axis show appreciable concentrations of carbon monoxide, hydrogen, methane and other combustible gases at distances up to 3 metre, with a peak at 1.5 metre. In contrast the calculations predict no volatiles beyond 1.5 metre and the peak to be at the burner itself.

Features consistent with the observations made above are revealed in the plots of fuel burn-out on the axis presented in Figure 5. Thus the pattern of change with fuel fineness or burner size is correct, but too short a distance of travel is predicted as being necessary for any given degree of burn-out.

RESULTS FOR FLAMES WITH SWIRL. The same comparisons as are made for the four non-swirling flames in Table 4 and Figures 3 and 5 are presented for the two swirling flames also. These are Flame 79 (primary swirl only) and Flame 35; their non-swirling equivalent is Flame 43.

Comparison of results computed for the swirling flames with those for Flame 43 show that the model is relatively insensitive to input swirl. Presence of primary swirl changes predicted values scarcely at all; swirl of both primary and secondary inputs produces changes much smaller than were observed on the rig. Thus for Flame 85 total heat transfer to the wall is 300 kW too low (Table 4). This is due to gross underestimation of the rate in the first two metres from the burner (Figure 3). And far too great an axial distance is predicted for a given degree of burn-out (Figure 5).

Film of a flame with swirl in both inputs shows it to be visually uniform across the whole width of the chamber, even adjacent to the burner. Measured profiles of temperature are very uniform too, whereas predicted profiles are not markedly different from those for the non-swirling case. A possible reason is that, in effect, one has assumed the solid particles to be at rest relative to the gas. Swirl will encourage relative motion. On a local scale, this will increase burning rates unless they should happen to be chemically controlled; on a coarser scale, the larger particles may be centrifuged outwards to regions richer in oxygen.

CALCULATED STREAMLINE PATTERNS. Measured flow patterns are not available for presentation here and would be imprecise because of turbulent fluctuations and other instabilities of the flow. Therefore we restrict ourselves to calculated values.

Predicted patterns of flow are illustrated in Figure 6, which shows plots of streamlines, i.e. lines of constant stream function. Burner M without swirl gives relatively weak recirculation and a slowly spreading jet, which does not strike the wall until 3 m from the burner. Addition of swirl to both primary and secondary inputs shortens the recirculation zone greatly, to about 1 m. But the mass of recirculating fluid is not changed. Streamlines are almost parallel to the axis from about 3 m onwards.

Characteristics of the recirculation zone for all six flames are summarised in Table 5. As one expects from studies of isothermal scaled models by Wingfield (14), Burner I gives much more recirculation than Burner M, with Burner E intermediate. The distance of the outer edge of the secondary inlet from the wall is almost the same for all these burners and it is presumably this that causes the radial position of the core of the recirculation eddy to be constant. The axial position of the core, too, is constant for the non-swirling flames, in spite of considerable variation in the distance to impingement, and is very close to the burner face. How realistic this is, one does not know.

Table 5. Calculated Characteristics of Recirculation Zone for Six Flames

Flame number	30	34	43	49	79	85
Mass of recirculating flow: fraction of total mass inflow	0.35	0.37	0.26	0.67	0.25	0.26
Axial distance from burner to point of impingement of jet on wall : m	2.5	2.4	3.0	1.8	3.3	0.9
Axial distance from burner to point of maximum recirculation : m	0.37	0.37	0.37	0.37	0.40	0.25
Radial distance from axis to point of maximum recirculation : m	0.34	0.35	0.35	0.33	0.34	0.35

PRESENT ACHIEVEMENT AND FURTHER DEVELOPMENT

When the relative simplicity of the flow model is taken into account the predictions made must be considered remarkably good. Nevertheless, there is considerable scope for improvement both in respect of the physical assumptions and the details of the numerical methods. Many of the simplifying and restrictive assumptions made for our calculations were introduced for reasons of computational convenience and economy. The calculation procedure itself is sufficiently flexible to permit considerable relaxation in this respect.

As already stated, many of the present inaccuracies can be traced to the treatment of the volatile fraction of the solid fuel. (Whether the model would predict a stable flame for a fuel without volatiles is not known, nor was such a fuel fired in the rig.) As a first step in correcting the inadequacy here one could impose a finite rate on the combustion of the volatiles, similar to what has been done in the most recent form of a one-dimensional model of the rig (4). This would add one more dependent variable and require one more partial-differential equation of the general form to be solved. To treat decomposition of the particles in any precise way would introduce too many variables to be feasible, as would allowing the char to burn with change of size and change of density. (One can see readily that one would need a separate variable for each combination of size, density and volatile content.)

Neglect of the effects of longitudinal radiation undoubtedly contributes to the over-high temperatures predicted for the inlet region of the chamber. However, a thorough treatment of radiant transfer is outside the scope of the present project and for the time being the analysis seems reasonably satisfactory. One possibility for simple improvement would be to introduce an axial flux analogous to the radial. One would then have a second radiation variable as a partner to q.

The calculation of a turbulent flow by the methods described here requires a mathematical description of the mechanics of turbulent diffusion. At present the transport properties of a turbulent fluid cannot be reliably expressed as analytic functions of local flow variables, so a quasi-empirical expression has had to be used for the effective viscosity. This appears to be satisfactory for our problem. When information from current researches in this field becomes available a better treatment will be possible. It may be noted that the restrictions we laid on the Schmidt and Prandtl numbers are not obligatory; they may be lifted at the cost of introducing additional equations to solve.

Considerations of computational economy have contributed to some of the errors occurring in the predictions. The enforced use of a coarse calculation mesh has exaggerated defects in the flow specification near the walls, as described above, as well as producing truncation and similar errors always associated with finite-difference methods.

To conclude, a first attempt has been made to apply finite-difference solution procedures to a turbulent gas flow containing burning solid particles. The results are highly encouraging for non-swirling flows in view of the complexity of the system, although less satisfactory for swirling ones. It is considered that major progress has been made in the task of predicting the behaviour of solid-particle combustors of the type treated.

ACKNOWLEDGMENTS

The extensions to the calculation method were made under contract to the British Coal Utilisation Research Association by Northern Research and Engineering Corporation. This was done by M.M.G., with contributions by Mr. J. A. Monahan. The authors are indebted to Professor D. B. Spalding (Imperial College) for his constant encouragement and help, and wish to thank also his colleagues, Dr. W. M. Pun and Mr. A. K. Runchal. Helpful discussions were held throughout the work with Mr. D. W. Gill and Mr. P. G. W. Hawksley (BCURA).

REFERENCES

1. M. A. Field, D. W. Gill, B. B. Morgan & P. G. W. Hawksley 1967 'Combustion of Pulverised Coal', BCURA, Leatherhead, U.K.
2. P. C. Baker, M. H. Barker, D. J. Loveridge, G. G. Thurlow & C. J. Wingfield 1969 J. Inst. Fuel (In the press).

3. D. J. Loveridge & co-authors 1969 BCURA Private Communication.
4. D. W. Gill 1969 BCURA Research Report No. 356.
5. A. D. Gosman, W. M. Pun, A. K. Runchal, D. B. Spalding & M. W. Wolfshtein 1969 'Heat & Mass Transfer in Recirculating Flows'. (To be published by Academic Press).
6. W. M. Pun & D. B. Spalding 1967 International Astronautical Federation Conference, Belgrade.
7. S. Badzioch, R. B. Sainsbury & P. G. W. Hawksley 1968 BCURA Members' Information Circular No. 340.
8. M. A. Field 1969 Combustion & Flame (In the press).
9. M. A. Field 1969 BCURA Private Communication.
10. M. M. Gibson & B. B. Morgan 1969 BCURA Research Report (In the press).
11. R. Viskanta 1966 'Advances in Heat Transfer', Vol. 3 (Eds: T. F. Irvine & J. P. Hartnett). Academic Press.
12. D. B. Spalding & S. V. Patankar 1967 'Heat & Mass Transfer in Boundary Layers'. Morgan-Grampian, London.
13. A. K. Runchal 1969 University of London, Ph.D. Thesis.
14. G. J. Wingfield 1967 J. Inst. Fuel 40 (October) 456-464.

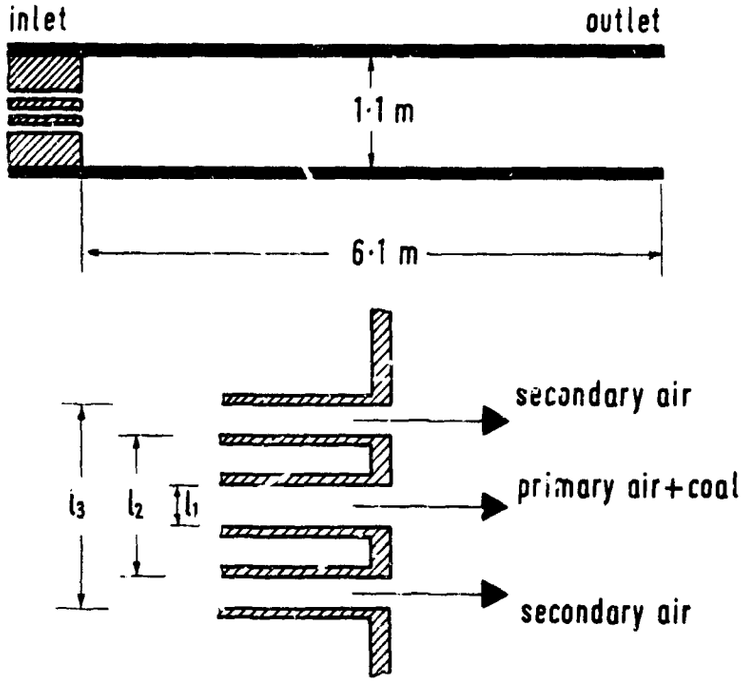

Enlarged view of burner

Figure 1. Geometry of combustion chamber and burner

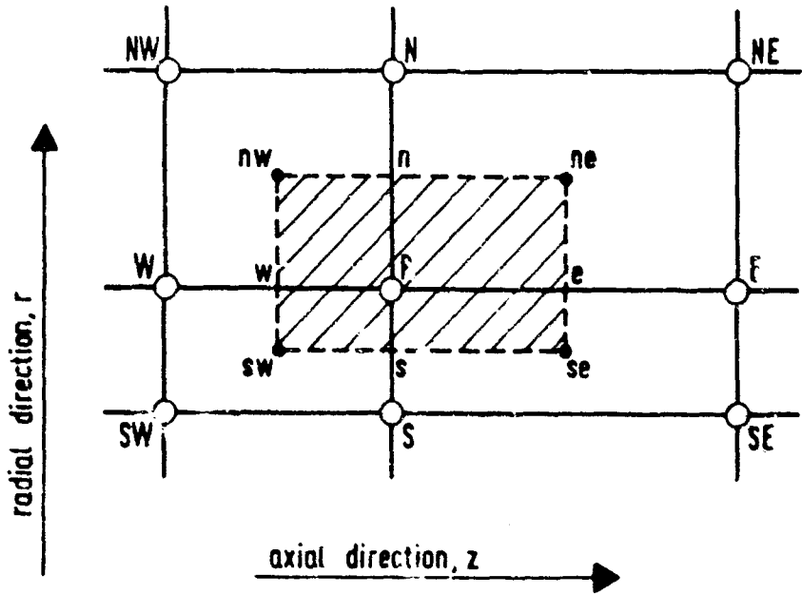

Figure 2. Portion of grid, showing control volume around node P

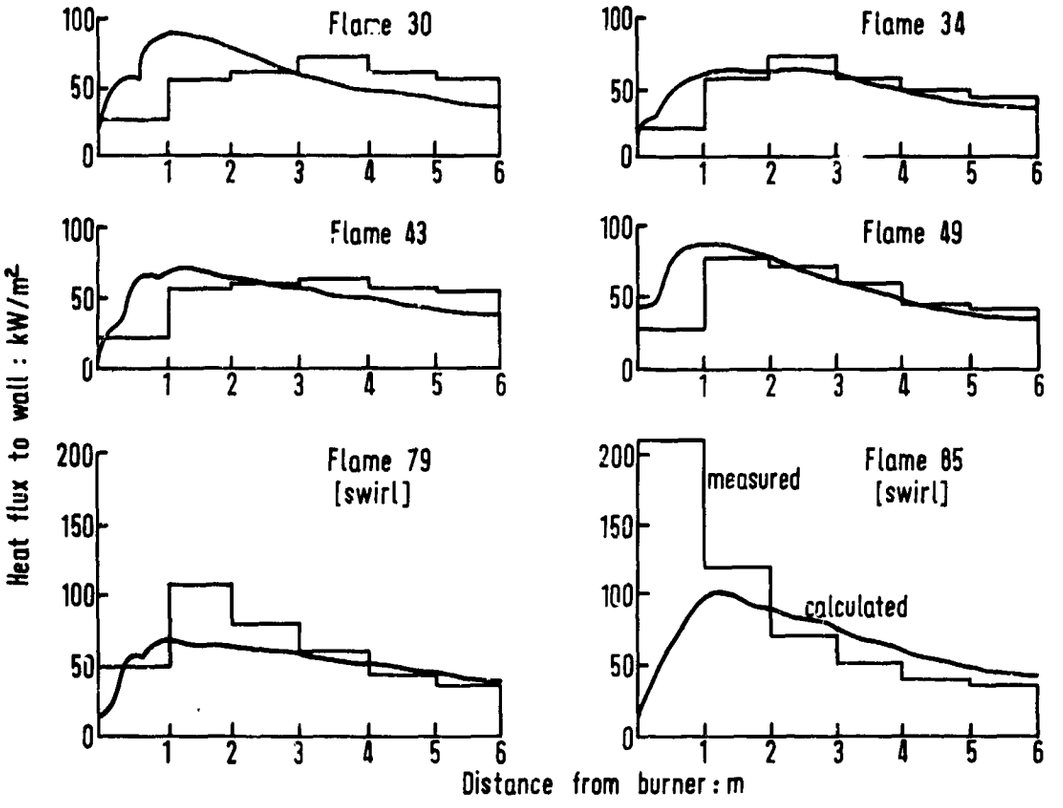

Figure 3. Comparison of calculated distribution of heat flux to chamber wall with measurement

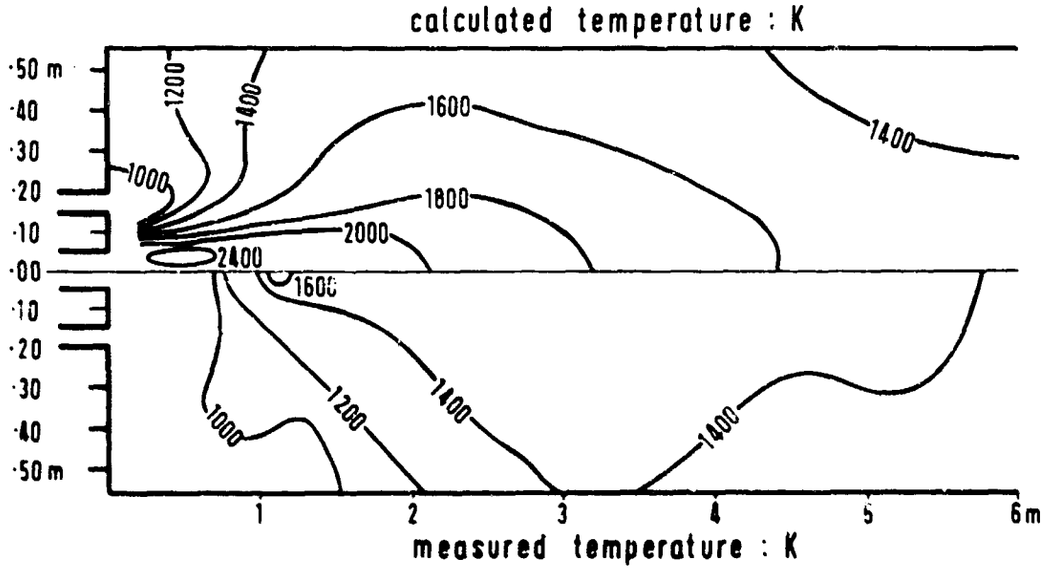

Figure 4. Comparison of calculated temperature contours with measurement for Flame 49

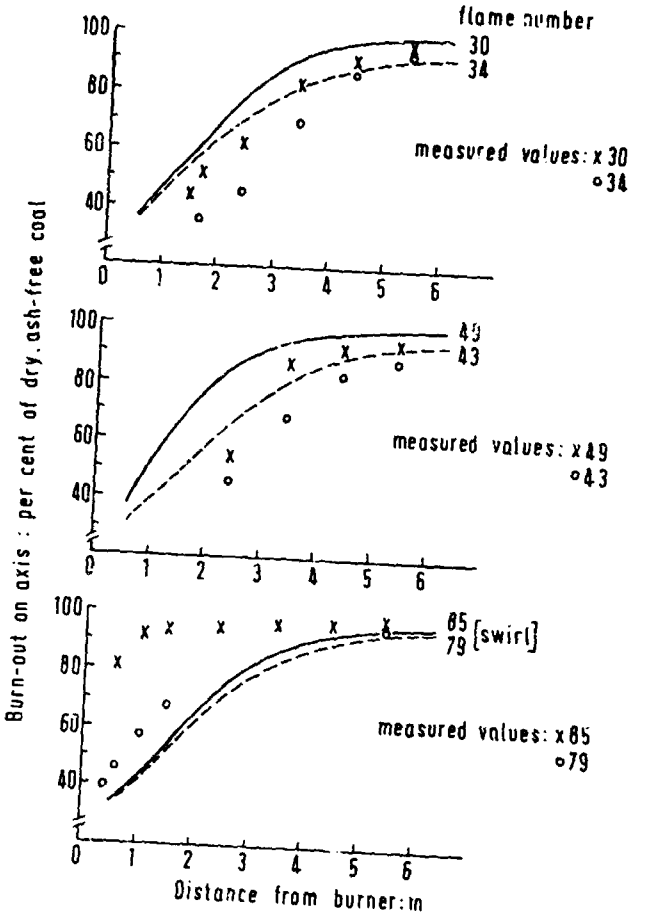

Figure 5. Comparison of calculated values of burn-out with measurement

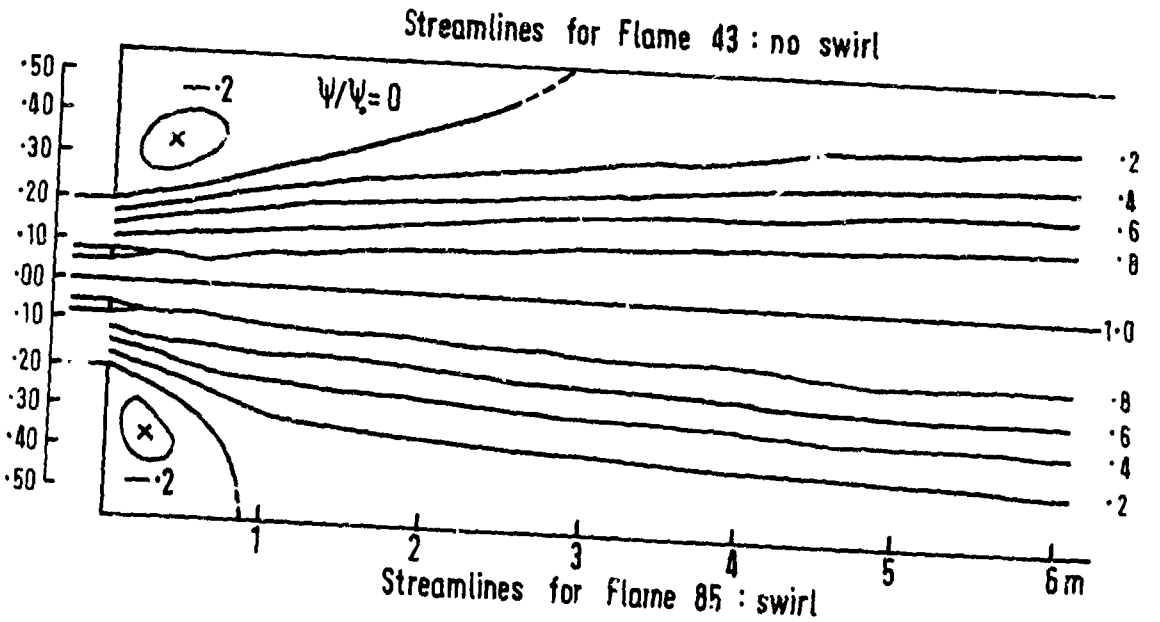

Figure 6. Calculated streamlines for Burner M, showing effect of swirl

PHENOMENES DE FUSION ET REACTIONS DE SURFACE DANS LA COMBUSTION DES LITHERGOLS

par Jean-François LIEBERHERR

OFFICE NATIONAL D'ETUDES ET DE RECHERCHES AEROSPATIALES (ONERA)
92 - CHATILLON-SOUS-BAGNEUX

SOMMAIRE

Au début des travaux sur les lithergols les modèles employés étaient basés sur le transfert de chaleur des gaz vers le solide, ce transfert provoquant l'évaporation ou la sublimation du solide. Les nombreux points de désaccord entre l'expérience et ces théories simplifiées ont conduit à penser que d'autres éléments entraient en jeu. On a assez rapidement envisagé la possibilité d'une réaction chimique de surface ou très près de la surface. Divers modèles ont été ainsi établis et rendent raisonnablement compte des phénomènes, à l'exception de ceux observés à l'ONERA sur les lithergols organiques à forte vitesse de régression et sur les hydrures métalliques. Quoiqu'il faille garder les réactions de surface comme mécanisme important, l'étude théorique qui fait l'objet de ce travail montre qu'elle ne doivent pas être liées à un mécanisme de vaporisation seul mais à un mécanisme de fusion et d'écoulement du liquide. On montre ainsi que la vitesse de régression est de la forme :

$$\dot{m} \propto (\rho u)^{0,5 \div 0,6}$$

et dépend fortement du rapport B/Pr du paramètre de transfert d'enthalpie à travers la couche liquide au nombre de Prandtl du liquide.

Le taux de fusion dépend également du taux de gasification du liquide mais ce taux doit être très important (de l'ordre de 0,5 $g/cm^2.s$) pour faire sentir son effet. La pression agit par une sensibilité inverse sur le taux de fusion ($\dot{m} p^{-0,33}$) et une sensibilité directe sur le taux de gasification.

Les conclusions pratiques de ce travail font qu'il semble difficile d'imaginer un moyen qui permette de bons rendements de combustion, c'est-à-dire l'absence de phase liquide, en dehors de systèmes de diaphragmes mélangeurs. Une voie dans cette direction peut consister à tirer le maximum de bénéfice des réactions de surface et à éviter les propergols ayant un nombre de Prandtl trop faible en phase liquide. Une autre voie peut consister à faire usage des conditions très particulières dans lesquelles la combustion a lieu dans la zone d'injection.

SUMMARY

The first models used in hybrid combustion studies were based upon heat transfer from a gaz to an evaporating or subliming solid. Many disagreements between experiment and these simplified models have led to think that other mechanisms are involved. The possibility of a chemical surface reaction was rapidly considered, this reaction taking place at the surface or very close to it. Various models have thus been established and account reasonably for the experimental observations, except for those observed at ONERA on high regression rate hybrid fuels and on metallic hydrides. Although the surface reactions remain as an important mechanism the theoretical study presented here shows that they must not be connected to a simple vaporization model but to a melting mechanism, and to the subsequent liquid flow. It can then be shown that the regression rate is of the form :

$$\dot{m} \propto (\rho u)^{0,5 \div 0,6}$$

and is a strong function of B/Pr, ratio of the enthalpy transfer parameter through the liquid layer to the Prandtl number of the liquid.

The melting rate depends also on the gasification rate of the liquid but this rate must be large to have a notigeable influence (of the order of 0.5 $g/cm^2.s$). The melting rate has an inverse pressure sensitivity (law in $p^{-0,33}$) and the gasification rate a direct pressure sensitivity.

The practical conclusions of this study are that it is difficult to imagine means which will destroy the liquid layer and promote the combustion efficiency, other them the already existing turbulators. A possible way in this direction is to make use as much as possible of the surface reactions and to avoid propellants which have too low a Prandtl number in liquid phase. Another way could be to take advantage of the particular conditions under which combustion takes place in the injection zone.

NOTATIONS

a diffusivité thermique du liquide

$$a = \lambda_\ell / \rho_\ell c_{p_\ell}$$

b coefficient de la loi de frottement

$$c_f/2 = b Re_o^{-\gamma}$$

C_{p_ℓ} chaleur massique du liquide

C_f coefficient de frottement

C_{f_o} coefficient de frottement sans injection pariétale

h_{ℓ_s} enthalpie du liquide à l'interface liquide gaz

$h_{\ell f}$ enthalpie du liquide à la surface de fusion

h_{fe} enthalpie effective de fusion

$\dot{m}$ taux de fusion

$\dot{m}_s$ taux de gazéification

x abscisse axiale

$\bar{x}$ abscisse axiale non dimensionnalisée

$$\bar{x} = x/D$$

y épaisseur de couche liquide

y distance à partir de l'interface solide-liquide, perpendiculairement à l'écoulement

$\bar{y}$ épaisseur non dimensionnalisée

$$\bar{y} = y/D$$

B paramètre de transfert d'enthalpie

$$B = h_{\ell_s} - h_{\ell f}/h_{fe}$$

D diamètre du canal central

M débit de liquide par unité de longueur de la circonférence du canal (g/cm.s)

Pr nombre de Prandtl de la phase liquide

$$Pr = \mu_\ell C_{p_\ell} / \lambda_\ell$$

Re_x nombre de Reynolds

$$Re_x = \rho_\ell U_e x / \mu_\ell$$

$Re_o = T$

T nombre de Reynolds

$$T = \rho_\ell U_e D / \mu_\ell$$

T_ℓ température de fusion solide

T_s température à l'interface liquide-gaz

U vitesse du liquide au point courant

U_s vitesse du liquide à l'interface liquide-gaz

U_e vitesse qu'aurait le liquide à l'extérieur de la couche limite si celle-ci était entièrement développée

V_s vitesse des gaz à l'interface liquide-gaz

V_e vitesse des gaz au sein de l'écoulement gazeux

W différence de vitesse $V_e - V_s$

X nombre de Reynolds

$$X = \rho_g WD/\mu_g$$

Y nombre de Reynolds

$$Y = \rho_g V_e D/\mu_g$$

β groupe adimensionnel $= \bar{y}\sqrt{T}/\sqrt{\bar{x}}$

γ exposant de la loi de frottement

$$C_f/2 = b Re_o^{-\gamma}$$

η rapport des viscosité $= \mu_\ell / \mu_g$

θ rapport des masses volumiques $= \rho_g / \rho_\ell$

μ_g viscosité du gaz

μ_ℓ viscosité du liquide

ρ_g masse volumique du gaz

ρ_ℓ masse volumique du liquide

ρu débit massique unitaire de gaz dans un repère lié à l'interface liquide-gaz.

Δh différence d'enthalpie :

$$= C_{p_\ell}(T_\ell - T_s)$$

π coefficient du profil

$$\beta \cdot \eta \bar{x}^{q/8}$$

ψ coefficient du profil $\bar{y} = \psi \bar{x}$

indice O : en l'absence d'injection pariétale

lettres soulignées : point courant

1 - INTRODUCTION

De nombreuses études ont été consacrées à la combustion dans les moteurs à lithergol par suite des avantages que ces moteurs présentent dans leur conception. Partant de schéma très simplifiés pour expliquer le mécanisme de combustion il a fallu les rendre de plus en plus complexes, car on s'est rapidement aperçu qu'il n'était pas facile de restituer sur le plan pratique les avantages offerts par les lithergols sur le plan théorique et qu'une connaissance plus approfondie des mécanismes était indispensable.

En particulier, lorsqu'il a fallu admettre que les modèles fondés sur l'analogie de Reynolds et faisant appel à une simple vaporisation par transfert de chaleur sont incapables d'expliquer l'écart de l'indice de sensibilité de la vitesse de régression au débit massique unitaire $(d\log \dot{m}/d \log \rho u)$ par rapport à la valeur théorique de 0,8 , ni les diverses valeurs de l'indice de sensibilité à la pression, ni même rendre compte de la valeur mesurée de la vitesse de régression, il a fallu faire intervenir la cinétique chimique.

2 - RAPPEL DES MODELES AVEC CINETIQUE CHIMIQUE.

Parmi les premiers à introduire, la cinétique chimique dans un modèle de combustion comparable à la combustion hybride, il faut citer Marxman, Wooldridge et Muzzy (1) à (6) . Cependant leur utilisation d'un modèle fondée presque exclusivement sur l'existence d'une combustion en phase gazeuse dans une couche limite établie et stabilisée rend son application aux moteurs hybrides discutable, sans rien retirer à sa valeur fondamentale.

Smoot, Price et Mihlfeith (7) à (9) ont considéré que l'ablation se fait essentiellement par une attaque chimique de la surface de combustible, le flux de comburant vers la surface dépendant de la différence des fractions massiques de comburant dans les gaz du canal central et ceux à la surface. Il s'agit donc d'une théorie avec réaction hétérogène à la surface. Les conditions dynamiques de l'écoulement définissent alors le taux de transfert de comburant. Cette théorie ne tient pas compte de l'interaction de l'ablation thermique et de l'ablation chimique.

La théorie de Miller (10), (11) offre des similitudes avec la précédente mais propose une interprétation par réaction en phase gazeuse. Il introduit une longueur de réaction chimique (épaisseur de flamme) et admet que la vitesse de régression est proportionnelle au taux auquel le comburant est consommé dans dans cette zone.

Sans présenter de théorie complète Kosdon et Williams (12) ont proposé un certain nombre de remarques relatives aux travaux de Smoot et Price et ceux de Miller. Ils concluent que les phénomènes observés peuvent être aussi bien interprétés par une réaction hétérogène que par une réaction homogène. Leur manière d'aborder le problème consiste à étudier par une méthode de perturbation le modèle classique d'ablation en y introduisant une réaction en phase gazeuse. Leur interprétation conduit cependant à admettre que cette réaction en phase gazeuse puisse devenir quasi-unimoléculaire et nécessité des hypothèses relatives au niveau de température de surface.

Une tentative récente (13) a cherché à tenir compte de la coexistence de l'ablation thermique et de l'ablation chimique. Une erreur dans l'application numérique en a cependant limité la portée. Il est certain que l'interaction entre ablation chimique et ablation thermique est un domaine d'étude intéressant qui doit permettre d'arriver à une évaluation de la température de surface. En effet cette température intervient dans le paramètre de transfert d'enthalpie B . Il est classique de dire que ce terme intervient par un coefficient de la forme $\log(1+B)$ qui est donc relativement insensible à la température de surface. Cependant une étude actuellement en cours (14) montre que dans le cas d'une vaporisation pure le paramètre B est très sensible à la température de surface lorsqu'on tient compte à la fois du transfert de chaleur et du transfert de masse. Par exemple, on trouve que la valeur de B peut être doublée lorsque la fraction massique du combustible vaporisé à la surface passe de 0,9 à 0,95.

C'est pourtant un autre aspect du problème de l'ablation que la présente étude se propose de traiter, l'ablation avec fusion du combustible solide. Pratiquement dépourvue d'intérêt en ce qui concerne les combustibles répandus aux Etats-Unis (caoutchouc butyle, plexiglas) puisque les théories antérieures permettent une corrélation satisfaisante des résultats, elle s'est avérée indispensable avec les propergols utilisés à l'O.N.E.R.A. (propergols organiques comprenant des ingrédients à bas point de fusion ou hydrures métalliques). Notre but n'est donc pas de discuter les théories antérieures ni de les mettre en question mais d'élargir l'éventail des cas traités et d'expliquer les phénomènes observés au cours des travaux menés à l'O.N.E.R.A. La cinétique chimique interviendra par un terme de réaction de surface dont nous montrerons l'importance.

3 - MODELE THEORIQUE AVEC TEMPERATURE DE SURFACE FIXEE

3.1 - Etablissement du modèle

Considérons un canal percé dans le combustible solide d'un moteur à lithergol. L'écoulement des gaz de combustion dans ce canal de diamètre interne D peut être laminaire ou turbulent. Les gaz chauds provoquent la fusion du solide qui se recouvre d'une couche liquide. Cette couche s'écoule vers l'aval en écoulement laminaire. Une couche limite s'établit donc dans le liquide. Nous supposerons qu'à l'interface entre le liquide et le gaz il y a continuité de la contrainte de frottement et de la vitesse. Nous admettrons cependant que la couche limite dans le liquide n'est pas entièrement développée

(épaisseur de liquide inférieure à l'épaisseur de couche limite) et que cette anomalie ne modifie pas le profil des vitesses, pas plus que l'injection pariétale.

Soient :

V_e la vitesse du gaz dans le canal central

V_s la vitesse du gaz à l'interface liquide-gaz

U_s la vitesse du liquide à l'interface liquide-gaz

U la vitesse du liquide au sein de l'écoulement

U_e la vitesse qu'aurait le liquide à l'extérieur de la couche limite si celle-ci était entièrement développée.

x la distance de l'entrée du canal au point considéré

y la hauteur dans la couche de liquide à partir de l'interface solide-liquide et δ l'épaisseur de la couche liquide. Nous supposerons $y \leq \delta \ll D$

Re_x et $Re_D = T$ sont les nombres de Reynolds de l'écoulement de liquide relatifs à l'abscisse x et au diamètre D .

W est la différence de vitesse $V_e - V_s$ caractérisant l'écoulement de gaz.

La vitesse dans la couche de liquide est donnée par une forme approchée de la solution de Blasius de l'équation de la couche limite laminaire :

$$\frac{U}{U_e} = 1 - \left(1 - \frac{y}{5x}\sqrt{Re_x}\right)^2 = 1 - \left(1 - \frac{y\sqrt{T}}{5\sqrt{xD}}\right)^2 .$$

Le gradient de vitesse, perpendiculairement au sens de l'écoulement, est :

$$\frac{dU}{dy} = 2U_e \frac{\sqrt{T}}{5\sqrt{xD}}\left(1 - \frac{y\sqrt{T}}{5\sqrt{xD}}\right) .$$

La continuité de la contrainte de frottement donne :

$$\tau = \frac{C_f}{2}\rho_g (V_e - V_s)^2 = \mu_e \left(\frac{dU}{dy}\right)_s ,$$

soit, en notant que $U_e = \frac{T\mu_g}{\rho_e D}$:

$$\frac{C_f}{2}\rho_g W^2 = \frac{2\mu_e^2}{5\rho_e D}\,\frac{T^{3/2}}{\sqrt{xD}}\left(1 - \frac{y\sqrt{T}}{5\sqrt{xD}}\right) .$$

Or $\frac{C_f}{2}$ n'est fonction que d'un nombre de Reynolds X qui s'écrit :

$$X = \frac{\rho_g W D}{\mu_g} .$$

Nous admettrons ici que le coefficient de frottement n'est pas modifié par l'injection pariétale de gaz due à une éventuelle vaporisation ou réaction de surface :

$$\frac{C_f}{2} = \frac{C_{f_e}}{2} .$$

L'élimination de W permet d'obtenir, après avoir introduit

$\eta = \frac{\mu_e}{\mu_g}$, $\theta = \frac{\rho_g}{\rho_\ell}$, $\bar{x} = \frac{x}{D}$ et $\bar{y} = \frac{y}{D}$:

$$\frac{C_f}{2}(X) X^2 = \frac{2}{5}\eta^2\theta \frac{T^{3/2}}{\sqrt{\bar{x}}}\left(1 - \frac{\bar{y}\sqrt{T}}{5\sqrt{\bar{x}}}\right) . \quad (1)$$

On voit alors facilement que la vitesse à la surface est :

$$V_s = \frac{\mu_\ell}{\rho_\ell D} T^{3/2} \frac{\bar{y}}{5\sqrt{\bar{x}}}\left(2 - \frac{\bar{y}\sqrt{T}}{5\sqrt{\bar{x}}}\right) . \quad (2)$$

La vitesse V_e est une donnée du problème. Si l'on écrit $W = V_e - V_s$ on peut aussi écrire

$$X = \frac{\rho_g V_e D}{\mu_g} - \frac{\rho_g V_s D}{\mu_g} .$$

En posant $Y = \rho_g V_e D / \mu_g$ l'expression de X devient, en utilisant (2) :

$$X = Y - \eta\theta T^{3/2} \frac{\bar{y}}{5\sqrt{\bar{x}}}\left(2 - \frac{\bar{y}\sqrt{T}}{5\sqrt{\bar{x}}}\right) . \quad (3)$$

Désignons par $\dot{m}$ le taux massique de fusion du solide (g/cm²-s) et par $\dot{m}_s$ le taux auquel le liquide passe en phase gazeuse (par réaction de surface ou par évaporation). La conservation de la masse permet d'écrire :

$$\rho_\ell \int_0^y U\,dy = \int_0^x (\dot{m} - \dot{m}_s)\,d\bar{x} .$$

Nous supposerons que $\dot{m}_s$ est constant.

La fusion se fait grâce à la conduction de la chaleur à travers la pellicule de liquide. T_e étant la température de l'interface liquide-gaz et T_s la température de l'interface liquide-solide nous désignerons par $\Delta h = C_{p_\ell}(T_e - T_s)$ la différence d'enthalpie du liquide à travers le film. Si l'on désigne par h_{f_e} l'enthalpie effective de liquéfaction du solide et par B le rapport $\Delta h / h_{f_e}$ on peut linéariser l'équation de conduction de la chaleur :

$$\lambda_\ell \frac{T_e - T_s}{y} = \dot{m} h_{f_e} ,$$

qui s'écrit, en introduisant la diffusivité thermique $a = \lambda_\ell / \rho_\ell C_{p_\ell}$:

$$\dot{m} = a\rho_e \frac{B}{y} .$$

L'équation de conservation de la masse s'écrit :

$$\int_0^y U\,dy = \int_0^x \left(a\frac{B}{y} - \dot{m}_s\right)dx \quad \text{soit :}$$

$$\frac{aB}{y} - \dot{m}_s = \frac{d}{dx}\left(\int_0^y U\,dy\right) . \quad (4)$$

L'expression (2) peut être considérée comme l'expression de U en un point d'ordonnée y et on a :

$$\int_0^y U\,dy = \frac{\mu_\ell}{\rho_\ell D}\frac{y^2 T^{3/2}}{5\sqrt{x D}}\left(1 - \frac{y\sqrt{T}}{15\sqrt{xD}}\right) .$$

L'équation (4) devient alors, en introduisant les variables réduites $\bar{x}$ et $\bar{y}$:

$$a\frac{B}{y} - \dot{m}_s = \frac{d}{d\bar{x}}\left(\frac{\mu_\ell}{\rho_\ell}\frac{\bar{y}^2 T^{3/2}}{5\sqrt{\bar{x}}}\left[1 - \frac{\bar{y}\sqrt{T}}{15\sqrt{\bar{x}}}\right]\right) \quad (4^{bis})$$

En remplaçant $\rho_a\, aB/\mu_\ell$ par B/Pr où Pr est le nombre de Prandtl de la phase liquide et en remplaçant la variable T par la variable $\beta = \bar{y}\sqrt{T}/\sqrt{\bar{x}}$ on obtient :

$$\left(\frac{3}{10} - \frac{2}{75}\beta\right)2\beta^2\bar{x}\frac{d\beta}{d\bar{x}} + \frac{\beta^2\bar{x}}{\bar{y}}\left(-\frac{2\beta}{10} + \frac{\beta^2}{75}\right)\frac{d\bar{y}}{d\bar{x}}$$

$$+ \frac{2\beta^3}{10} - \frac{\beta^4}{75} - \frac{B}{Pr} + \frac{\dot{m}_s\,\bar{y}\,D}{\mu_\ell} = 0 . \quad (5)$$

On sait que la forme habituelle de représentation des coefficients de frottement en fonction du nombre de Reynolds X est :

$$\frac{C_{f_0}}{2} = b X^{-\gamma} .$$

En écoulement laminaire $\gamma = 0{,}5$ et en écoulement turbulent $\gamma = 0{,}2$. L'équation résultant de (1) et de (3) est donc :

$$b\left(Y - \eta\theta T^{3/2}\frac{\bar{y}}{5\sqrt{\bar{x}}}\left[2 - \frac{\bar{y}\sqrt{T}}{5\sqrt{\bar{x}}}\right]\right)^{2-\gamma} =$$

$$\frac{2}{5}\eta^2\theta\frac{T^{3/2}}{\sqrt{\bar{x}}}\left(1 - \frac{\bar{y}\sqrt{T}}{5\sqrt{\bar{x}}}\right) .$$

Soit, en introduisant β :

$$b\left(Y - \eta\theta\frac{\beta^3\bar{x}}{5\bar{y}^2}\left[2 - \frac{\beta}{5}\right]\right)^{2-\gamma} =$$

$$\frac{2}{5}\eta^2\theta\frac{\beta^3\bar{x}}{\bar{y}^3}\left(1 - \frac{\beta}{5}\right) . \quad (6)$$

Cette équation doit être dérivée afin de pouvoir former avec (5) un système différentiel. On a alors, en notant :

$$Y - \eta\theta\frac{\beta^3\bar{x}}{5\bar{y}^2}\left(2 - \frac{\beta}{5}\right) = X$$

$$(2-\gamma)\,b\,X^{1-\gamma} = \alpha ,$$

$$\left[2\bar{x}\left(-3 + \frac{2\beta}{5}\right)\alpha - 2\eta\frac{\bar{x}}{\bar{y}}\left(3 - \frac{4\beta}{5}\right)\right]\frac{d\beta}{d\bar{x}}$$

$$+\left[\frac{2\alpha\beta\bar{x}}{\bar{y}}\left(2 - \frac{\beta}{5}\right) + 6\eta\frac{\beta\bar{x}}{\bar{y}^2}\left(1 - \frac{\beta}{5}\right)\right]\frac{d\bar{y}}{d\bar{x}}$$

$$-\alpha\beta\left(2 - \frac{\beta}{5}\right) - 2\eta\frac{\beta}{\bar{y}}\left(1 - \frac{\beta}{5}\right) = 0 . \quad (7)$$

Ces équations permettent de calculer $\bar{y}(\bar{x})$ et $\beta(\bar{x})$ puis la vitesse de fusion $\dot{m} = \mu_\ell B/Pr\,\bar{y}\,D$ ainsi que le débit de liquide par unité de longueur de la circonférence du canal central :

$$M = \mu_\ell\frac{\bar{x}\beta^3}{5\bar{y}}\left(1 - \frac{\beta}{15}\right) .$$

A titre de vérification on peut montrer que les résultats sont tels que :

$$M = \mu_\ell\frac{\bar{x}\beta^3}{5\bar{y}}\left(1 - \frac{\beta}{15}\right)$$

$$= \int_0^{\bar{x}}\left(\frac{\mu_\ell}{Pr}\frac{B}{\bar{y}} - \dot{m}_s D\right)d\bar{x} .$$

Les conditions initiales de l'intégration sont $\bar{x} = 0$, $\bar{y} = 0$. La valeur initiale de β ne peut cependant pas être donnée par l'équation (6) qui conduit à une

indétermination, on l'obtient par une approximation. Supposons que β soit fini au voisinage de l'origine, l'équation (4 bis) s'écrit, en introduisant Pr et β :

$$\frac{B}{Pr} - \frac{\dot{m}_s \bar{y} D}{\mu_\ell} = \bar{y} \frac{d}{d\bar{x}} \left(\bar{y} \frac{\beta^3 \bar{x}}{5 \bar{y}^2} \left[1 - \frac{\beta}{15} \right] \right) .$$

Si au voisinage de l'origine $\bar{x}$ et $\bar{y}^3$ sont des infiniment petits du même ordre $\bar{x}/\bar{y}^2$ tend vers zéro. On a alors, dans l'équation (6) :

$$b^{\gamma^2 - \gamma} = \frac{2}{3} \eta^2 \theta \frac{\beta^3 \bar{x}}{\bar{y}^3} \left(1 - \frac{\beta}{5} \right) . \quad (8)$$

L'équation différentielle ci-dessus se réduit à :

$$\frac{B}{Pr} = \bar{y} \frac{d}{d\bar{x}} \left(\frac{\beta^3 \bar{x}}{5 \bar{y}} \left[1 - \frac{\beta}{15} \right] \right) ;$$

et en éliminant $\beta^3 x$ à :

$$\frac{B}{Pr} = \bar{y} \frac{d}{d\bar{x}} \left(\frac{b \gamma^{2-\gamma} \bar{y}^2 \left(1 - \frac{\beta}{15} \right)}{2 \eta^2 \theta \left(1 - \frac{\beta}{5} \right)} \right) .$$

Soit :

$$\frac{\bar{y}^3}{3} = \frac{B}{Pr} \frac{\eta^2 \theta}{b \gamma^{2-\gamma}} \frac{1 - \beta/5}{1 - \beta/15} \bar{x} . \quad (9)$$

$\bar{x}$ et $\bar{y}^3$ sont bien des infiniment petits de même ordre et les équations (8) et (9) permettent d'exprimer β par :

$$\frac{2\beta^4}{75} - 0{,}4\beta^3 + 3\frac{B}{Pr} = 0 .$$

Cette équation n'admet de solution que si $\frac{B}{Pr} < 47{,}46093$. Cette solution n'est inférieure à 5 , condition pour que la couche limite soit moins épaisse que la couche entièrement développée dans le liquide, que si B/Pr est inférieur à 11,11.

On montre facilement qu'il est nécessaire que β soit fini et $\bar{y}$ proportionnel à $\bar{x}^{1/3}$ pour que β puisse être ainsi exprimé. On en tire au voisinage de l'origine :

$$\bar{y} = \left[\frac{3B}{Pr} \frac{\eta^2 \theta}{b \gamma^{2-\gamma}} \frac{1 - \beta/5}{1 - \beta/15} \bar{x} \right]^{1/3}$$

$$= \beta \left[\frac{2\eta^2 \theta}{5 \beta \gamma^{2-\gamma}} \left(1 - \frac{\beta}{5} \right) \right]^{1/3} \bar{x}^{1/3} , \quad (10)$$

et la vitesse de fusion est :

$$\dot{m} = \frac{B}{Pr} \frac{\mu_\ell}{\bar{y} D} =$$

$$= \frac{B}{Pr} \frac{\mu_\ell}{D \beta} \left[\frac{5b}{2\eta^2 \theta (1 - \beta/5)} \right]^{1/3} \gamma^{\frac{2-\gamma}{3}} \bar{x}^{-1/3} \quad (11)$$

On a vu que le débit de liquide s'écrit :

$$M = \mu_\ell \frac{\bar{x}}{\bar{y}} \frac{\beta^3}{5} \left(1 - \frac{\beta}{15} \right) ,$$

qui vaut au voisinage de l'origine :

$$M = \mu_\ell \frac{\bar{x}}{\bar{y}} \frac{3}{2} \frac{B}{Pr} .$$

L'équation de vérification est :

$$M = \int_0^{\bar{x}} \frac{B}{Pr} \frac{\mu_\ell}{\bar{y} D} D \, d\bar{x} ,$$

soit :

$$\mu_\ell \frac{\bar{x}}{\bar{y}} \frac{3}{2} \frac{B}{Pr} = \int_0^{\bar{x}} \frac{B}{Pr} \frac{\mu_\ell}{\bar{y}} d\bar{x} .$$

Cette équation est vérifiée si $\bar{y}$ est de la forme $\bar{y} = A \bar{x}^{1/3}$.

L'expression (11) de la vitesse de fusion appelle plusieurs remarques :

- L'exposant du débit massique unitaire (de γ) est peu sensible à la nature (laminaire ou turbulente) de l'écoulement et ne varie que de 0,5 à 0,6.
- L'influence du diamètre D est négligeable puisque, à débit global de gaz constant, l'exposant de D n'est que de $-\frac{1}{3}$
- Comme θ est proportionnel à la pression la vitesse de fusion est inversement proportionnelle à la racine cubique de la pression. Cette sensibilité inverse, qui n'a pas été observée dans la réalité, est vraisemblablement compensée par la vitesse de passage en phase vapeur $\dot{m}_s$, qui est sensible à la pression.

- La nature de la phase liquide intervient pour le nombre de Prandtl du liquide et pour sa viscosité. Si l'on admet que $\frac{1-\beta/5}{1-\beta/15}$ reste voisin de l'unité $\bar{v} \propto \left(\frac{B}{Pr}\right)^{1/3}$ et $\dot{m} \propto \left(\frac{B}{Pr}\right)^{2/3} \mu_\ell$. La valeur du nombre de Prandtl peut varier de 100 pour les corps organiques à 0,01 pour un métal. Si, comme on le verra plus loin, la vitesse de fusion ainsi calculée correspond approximativement aux vitesses de régression mesurées sur les combustibles organiques, il faut s'attendre à la voir croître très vite avec les métaux.

- La température des gaz intervient par θ puisque ρ_g est inversement proportionnel à la température. De plus B dépend linéairement de la température de l'interface liquide-gaz. Il en résulte que la vitesse de fusion et l'épaisseur de la phase liquide seront d'autant plus importantes que la température des gaz sera plus élevée, c'est-à-dire que le couple de propergols sera plus énergétique.

- Rappelons que tout le calcul suppose $\beta < 5$, c'est-à-dire que l'épaisseur de liquide ne dépasse pas l'épaisseur de couche limite dans le liquide.

3.2.1 - Influence d'une réaction de surface.

Dans l'équation (4 bis) on tient compte de la réaction de surface (réaction chimique ou mécanisme de vaporisation) en remplaçant $\alpha \frac{B}{\bar{v}}$ par $\alpha \frac{B}{\bar{v}} - \dot{m}_s$, donc $\frac{B}{Pr}$ par $B/Pr - \dot{m}_s \bar{v} D/\mu_\ell$. On montre facilement que l'effet de $\dot{m}_s$ est de faire décroître $\bar{v}$ pour une valeur donnée de $\bar{x}$, donc d'augmenter la vitesse de fusion.

Dans l'exploitation numérique de cette partie théorique nous supposons $\dot{m}_s$ constant le long du canal central ainsi que la valeur de la température de surface donc celle de B. En effectuant plusieurs calculs successifs avec différentes valeurs de B et de $\dot{m}_s$ on pourra déterminer l'influence sur la vitesse de fusion de ces deux paramètres.

Cette manière de procéder n'est qu'une approximation et suppose la température de l'interface liquide-gaz connue et égale par exemple à la température d'ébullition. Cette température peut également être fixée par un bilan énergétique qui fait intervenir une réaction hétérogène de surface. Nous utiliserons cependant la première méthode de façon à bien mettre en évidence l'influence du terme $\dot{m}_s$.

3.3 - Etude numérique.

- Cas asymptotique pour $x \sim 0$.

Nous choisirons arbitrairement des données afin de montrer l'ordre de grandeur des résultats obtenus. Prenons :

μ_ℓ = 5 centipoises, $\rho_g = 10^{-3}$ g/cm3,
μ_g = 500 micropoises, ρ_ℓ = 1 g/cm3,
(η = 100) ($\theta = 10^{-3}$)

b = 0,023, γ = 0,2 (lois du frottement turbulent)

D = 5 cm
ρu = 50 g/cm^2-s $\Big\}$ $Y = Re_D = 5.10^5$

On pourra prendre $B = \frac{0,3(1000-300)}{100} = 21$ et Pr = 100 (combustible organique) et $\bar{x}$ = 1.

On calcule ainsi β = 0,54 et $\dot{m}$ = 0,19 g/cm^2-s. Cette valeur est comparable aux valeurs obtenues dans les moteurs à lithergol. L'épaisseur de couche liquide qui résulte de ce calcul est très faible ($1,1\ 10^{-3}$ cm).

- Calcul complet

Le calcul est effectué avec les mêmes données que le calcul d'ordre de grandeur ci-dessus (η = 100, $\theta = 10^{-3}$, b = 0,023, γ = 0,2). La valeur de $\bar{x}$ variera de 0 à 20 et la valeur de Y de 4 10^5 à 10^6. On prendra pour valeur de B/Pr diverses valeurs, pour μ_ℓ et D : 5 centipoises et 5 cm respectivement.

Le calcul proprement dit a été effectué sur un ordinateur IBM 360/50 en utilisant pour l'intégration du système d'équations le sous-programme IBM HPCG.

Nous prendrons pour cas de calcul typique le cas où B/Pr = 0,1 et $\dot{m}_s$ = 0,1 g/cm2-s. $x/D = 5$ et $Re_D = 4.10^5$

La figure 1 montre l'évolution de la vitesse de régression, du débit du liquide et de l'épaisseur de la couche liquide pour un nombre de Reynolds de l'écoulement de gaz de 400 000. On voit que la vitesse de régression est de l'ordre de 1 mm/s alors que le débit de liquide est de l'ordre de 10 g/cm.s et l'épaisseur de liquide de l'ordre de 0,05 cm pour une valeur de x/D de 10.

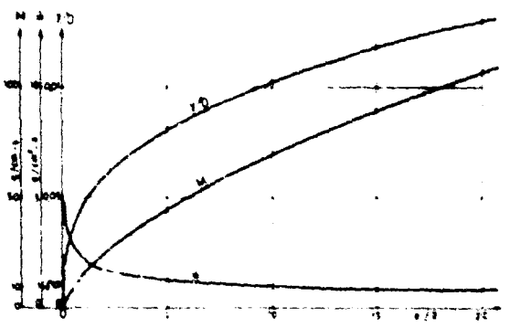

Fig. 1 - Profils d'épaisseur de liquide, de débit de liquide et de vitesse de fusion en fonction de l'abscisse axiale

La figure 2 représente les mêmes profils dans un diagramme logarithmique. Les profils sont rectilignes et montrent que les résultats peuvent s'exprimer sous la forme :

$$\dot{m} \propto \left(\frac{x}{D}\right)^{-1/3} ; \quad \frac{y}{D} \propto \left(\frac{x}{D}\right)^{1/3} ; \quad M \propto \left(\frac{x}{D}\right)^{2/3}.$$

Ces formes correspondent à celles trouvées analytiquement dans la solution asymptotique valable au voisinage de $x = 0$.

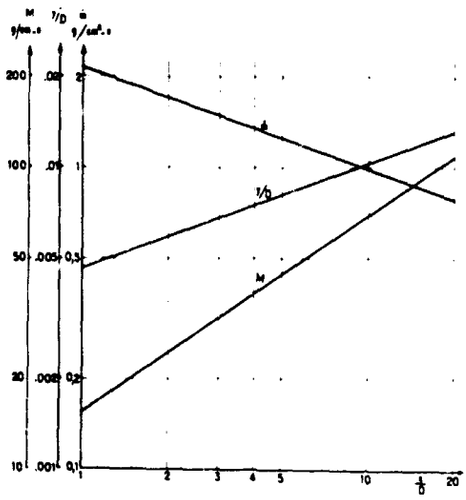

Fig. 2 - Profils de vitesse de fusion, d'épaisseur de liquide et de débit de liquide en fonction de l'abscisse axiale

- Influence du nombre de Reynolds.

La figure 3 représente la variation du taux de fusion pour diverses valeurs du rapport B/Pr en fonction du nombre de Reynolds, à valeur constante du taux de réaction de surface. Les valeurs numériques obtenues correspondent en ordre de grandeur à celles obtenues dans les expériences menées à l'ONERA. La pente des parties rectilignes est de l'ordre de 0,5 , conforme aux valeurs obtenues expérimentalement lors de tirs sur moteurs. La valeur du rapport B/Pr a une grande influence, celle de $\dot{m}_s$ aussi si $\dot{m}$ et $\dot{m}_s$ sont du même ordre.

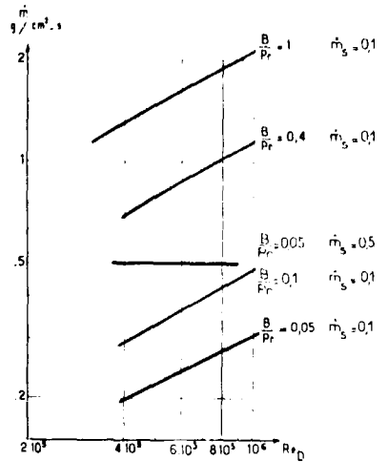

Fig. 3 - Influence du nombre de Reynolds sur la vitesse de fusion ($x/D = 5$, $\dot{m}_s$ en $g/cm^2.s$)

Le débit de liquide par unité de longueur de la circonférence du canal central est également sensible au nombre de Reynolds (fig. 4 , indice de sensibilité 0,6) et à la valeur de B/Pr mais également à la valeur du taux de réaction de surface.

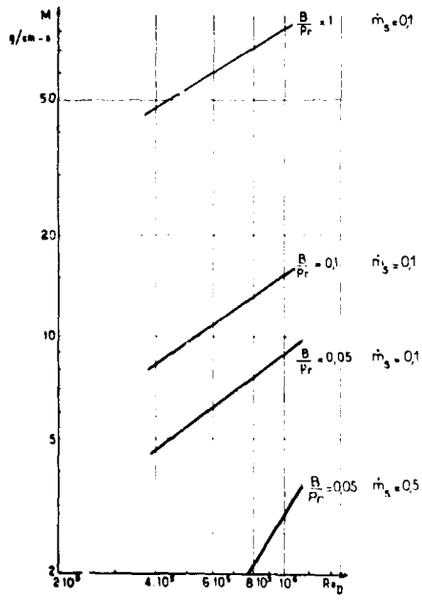

Fig. 4 - Influence du nombre de Reynolds sur le débit de liquide ($x/D = 5$, $\dot{m}_s$ en $g/cm^2.s$)

L'épaisseur de liquide est une fonction décroissante du nombre de Reynolds (figure 5) et du rapport B/Pr . Cette épaisseur est faible puisque pour $D = 5$ cm elle est de 0,1 à 1 mm. L'épaisseur du liquide est sensible au taux de réaction de surface, quand celui-ci est de l'ordre de $\dot{m}$.

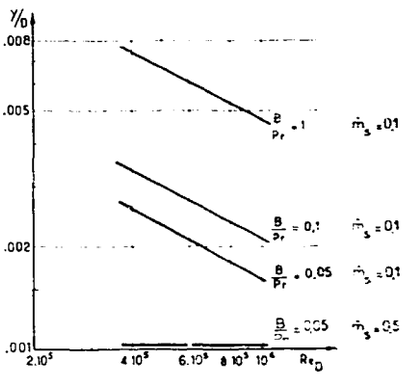

Fig. 5 - Influence de Re_D sur l'épaisseur de liquide ($x/D=5$, $\dot{m}_s$ en $g/cm^2.s$)

De la valeur du débit de liquide et du taux de réaction de surface on peut calculer la vitesse moyenne à laquelle le solide passe en phase liquide ou gazeuse par :

$$\dot{m}_f = \frac{M}{x} + \dot{m}_s .$$

Cette vitesse est comparée au taux de fusion instantané sur la figure 6. On constate un écart appréciable entre valeur instantanée et valeur moyenne quoique la sensibilité des deux au nombre de Reynolds soit la même. Cet écart montre qu'il faut bien distinguer entre les résultats obtenus par des mesures globales et les résultats obtenus par des mesures instantanées et locales.

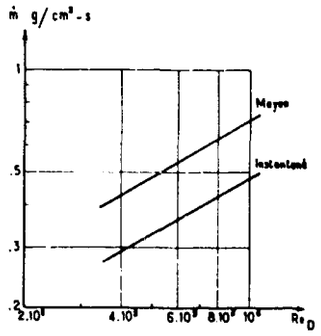

Fig. 6 - Comparaison entre taux de fusion instantané et taux de fusion moyen

- Influence du rapport B/Pr.

On a vu que les courbes représentant $\dot{m}$, M et y/D en fonction de Re_D sont sensibles à la valeur de B/Pr . La figure 7 montre la forme de cette sensibilité en ce qui concerne $\dot{m}$.

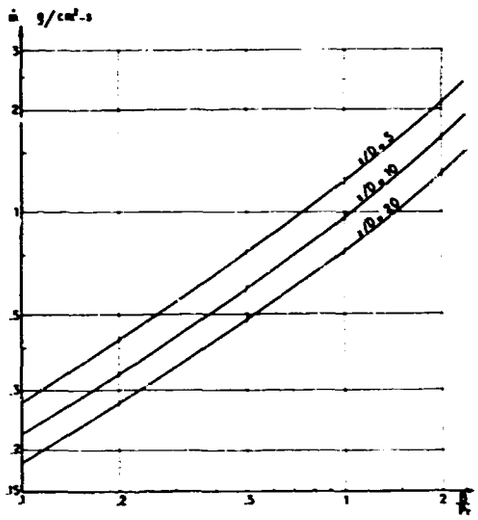

Fig. 7 - Influence de B/Pr sur la vitesse de fusion

Bien que la courbe ne soit pas rectiligne elle correspond approximativement à un indice de sensibilité de l'ordre de 2/3 comme le laisse prévoir la théorie. Le débit de liquide est également sensible à la valeur de B/Pr avec un indice de sensibilité de 0,78 ainsi que l'épaisseur du liquide avec un indice de sensibilité de -0,33.

- Influence du taux de réaction de surface.

Le taux de réaction de surface n'a pas une grande influence si la valeur est faible comparée à la vitesse de fusion. Celle-ci est alors une fonction légèrement croissante de $\dot{m}_s$ (figure 8) tandis que M et y/D sont des fonctions décroissantes.

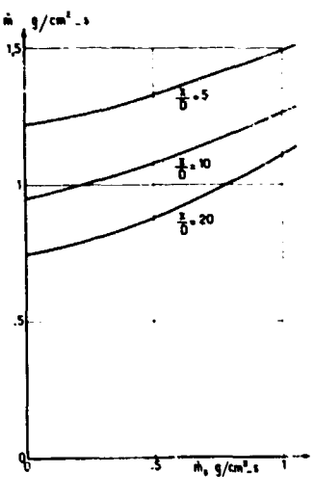

Fig. 8-Influence du taux de réaction de surface sur la vitesse de fusion. ($B/Pr = 1$, $Re_D = 4.10^5$)

Aux valeurs élevées de $\dot{m}_s$ ou aux faibles valeurs de B/Pr le comportement tend à être différent. Pour $B/Pr = 0,05$ et $\dot{m}_s = 0,5$ g/cm^2-s $\dot{m}$ est indépendant de Re_D et égal à $\dot{m}_s$ (figure 3). Dans ce cas y/D vaut 0,05 et est également indépendant de Re_D (figure 5). La valeur de M est nettement plus faible que dans le cas de calcul typique mais par contre est beaucoup plus sensible à Re_D (figure 4).

- Influence de la pression.

La pression s'introduit par le terme $\theta = \rho_g / \rho_l$. Le calcul montre que tandis que la vitesse de fusion est bien proportionnelle à $\theta^{-1/3}$ si $\dot{m}_s \ll \dot{m}$ elle tend à devenir indépendante aux fortes valeurs de θ, donc de la pression. Comme on tend alors vers l'égalité entre $\dot{m}$ et $\dot{m}_s$ la sensibilité de $\dot{m}$ à Re_D tend à devenir nulle, le débit de liquide M décroît fortement tandis que sa sensibilité à Re_D croît.

On constate enfin que si x/D croît, la vitesse de fusion décroît et tend vers $\dot{m}_s$. Il est à noter que bien que $\dot{m}$ puisse tendre vers $\dot{m}_s$ et devenir insensible à Re_D, la vitesse moyenne $\dot{m}_1 = M/x + \dot{m}_s$ reste sensible à Re_D puisque la sensibilité de M à Re_D croît.

Notons aussi que nous désignons ici par réaction de surface la réaction de gazéification sans préjuger du type de réaction chimique qui la provoque (réaction homogène près de la surface ou réaction hétérogène).

L'influence de la pression sur la vitesse de fusion se fera donc d'abord sentir par son action sur θ conduisant à une sensibilité en $p^{-1/3}$. Si p croît $\dot{m}$ décroît et devient plus sensible à $\dot{m}_s$, lequel peut être fonction de la pression. La réaction de gazéification peut également jouer par son effet énergétique par l'intermédiaire de B/Pr alors que nous n'en avons tenu compte que dans le bilan massique.

La figure 9 montre comment se déforme la courbe $\dot{m}(\dot{m}_s)$ lorsqu'on fait varier B/Pr, Re_D, x/D. Les déformations sous l'influence de θ ne sont pas indiquées mais sont comparables à celles sous l'influence de x/D.

3.3 - Conclusions relatives à l'étude théorique.

L'étude de l'ablation avec fusion, dans le cadre d'une hypothèse de température de surface fixée, montre que la vitesse de fusion peut être exprimée en fonction du débit massique unitaire par une relation de la forme :

$$\dot{m} \propto (\rho u)^{0,5}.$$

L'étude numérique montre que les ordres de grandeur des vitesses de fusion sont de l'ordre de plusieurs dixièmes de g/cm^2-s, ce qui correspond aux valeurs trouvées expérimentalement sur les propergols ONERA.

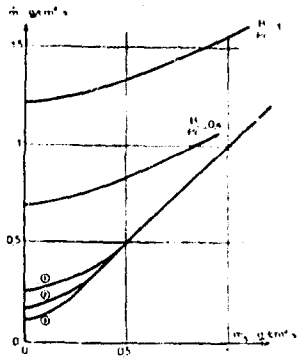

Fig. 9 - Influence du taux de réaction de surface sur la vitesse de fusion

B/Pr= 0,4 et 1 : $Re_D = 4.10^5$; x/D=5
B/Pr= 0,05 : (1) $Re_D = 8,3.10^5$; x/D=5
(2) $Re_D = 4.10^5$; x/D=5
(3) $Re_D = 4.10^5$; x/D=20

$\dot{m}_s$ en g/cm^2-s

Le débit de liquide qui s'écoule le long du canal central peut être important et dans certains cas représenter une fraction appréciable de la contribution du combustible à la combustion. En effet si $\rho u = 50$ g/cm^2-s et $D = 5$ cm, le débit de gaz est de 3930 g/s. Avec un rapport de mélange de 0,125 le taux d'ablation du combustible doit être de 492 g/s. Dans un moteur de configuration classique ($L/D \sim 20$) avec $Re_D = 5.10^6$, $B/Pr = 2,1$ et $\dot{m}_s = 0,1$ g/cm^2-s la présente théorie donne un débit de liquide de 235 g/s et un débit de gaz de 157 g/s soit un total de 492 g/s et pourtant l'épaisseur du liquide ne dépasse pas 0,7 mm. C'est ce qui explique pourquoi ces couches liquides n'ont pas été observées expérimentalement.

La vitesse de fusion est peu sensible au taux de réaction de surface. Par contre elle est très sensible au rapport B/Pr dans lequel la réaction de surface peut intervenir par son aspect énergétique alors que dans la présente théorie elle n'intervient que dans le bilan massique.

Dans l'utilisation pratique de cette théorie on se heurte à une difficulté, l'évaluation numérique des différents paramètres. Passons sur l'évaluation de Pr, θ, η etc.. Il importe de pouvoir se fixer la température de surface afin de pouvoir déterminer B. Dans les présents calculs on s'est imposé arbitrairement la valeur de B mais T_s peut être effectivement déterminé. En effet lorsqu'on étudie le phénomène de vaporisation pure par transfert de chaleur il est possible de montrer (14) que la température de surface est voisine de la température d'ébullition du liquide, sans jamais toutefois l'atteindre. L'écart avec la température d'ébullition est cependant suffisamment faible pour que l'on puisse confondre ces températures dans le calcul de B. Si une réaction de surface intervient, elle pourra élever la température de surface sans toutefois dépasser la température d'ébullition, du moins dans le cadre des hypothèses d'équilibre du travail déjà cité (14). On peut alors considérer T_s comme défini.

Il faut également noter que cette théorie ne laisse pas prévoir d'une manière simple l'effet de la pression puisque celle-ci intervient aussi bien sur $\theta = \rho_g/\rho_\ell$ que sur $\dot{m}_s$ et B par l'intermédiaire de T_s.

Les indices de sensibilité du taux de régression à $R\alpha_D$, θ et $\dot{m}_s$ varient donc suivant la valeur de B/Pr et de $\dot{m}_s$. Aux valeurs faibles de $\dot{m}_s$ ces indices sont respectivement de 0,6, - 0,33 et 0 ; aux fortes valeurs de $\dot{m}_s$ et aux faibles valeurs de B/Pr ils sont de 0, 0 et 1 ; enfin aux fortes valeurs de $\dot{m}_s$ et de B/Pr ils prennent des valeurs intermédiaires entre ces valeurs extrêmes. Nous dirons que dans le premier cas les phénomènes de fusion prédominent, tandis que dans le deuxième, les phénomènes de surface sont plus importants, sans préjuger de ce que peuvent être ces mécanismes de surface (réaction chimique hétérogène ou homogène etc..).

4 - ASPECT EXPERIMENTAL

4.1 - Généralités

La comparaison entre les résultats expérimentaux et les prévisions de la théorie est délicate car le domaine de validité de cette dernière se limite au cas de moteurs où la couche liquide peut se développer. Ceci exclut les expériences sur brûleurs de laboratoire où la longueur de l'échantillon est faible ainsi que les résultats obtenus sur des moteurs munis de dispositifs turbulateurs dans le canal central. Parmi les résultats obtenus sur moteurs on est également limité car il est rare que l'on connaisse l'évolution du débit massique unitaire de gaz et celle du taux de régression au cours du tir. Il faudra donc se limiter à l'étude de résultats globaux, en particulier à la relation entre pression et richesse.

Considérons un moteur dans lequel le taux de réaction de surface est constant et égal à $\dot{m}_s$; soit L la longueur du pain de combustible et D le diamètre du canal central.

Compte tenu du phénomène de fusion le débit de combustible est :

$$\dot{m}_H = \pi D L \dot{m}_s + \pi D M .$$

Or on sait que M est de la forme :

$$M \propto Y^{0,6} p^{-1/5} .$$

On sait également que le débit issu de la tuyère est : $\dot{m}_t = C_D P_c A_c$ et nous supposerons C_D constant dans le domaine de richesse considéré.

Y est proportionnel au débit massique unitaire des gaz donc pratiquement du débit de gaz issu de la tuyère. Si l'on écrit la fonction de la richesse:

$$\Psi = \frac{\varphi}{1+m_{st}\varphi} = \frac{1}{m_{st}} \frac{\dot{m}_H}{\dot{m}_o+\dot{m}_H} = \frac{1}{m_{st}} \frac{\dot{m}_H}{\dot{m}_t},$$

on a :

$$\Psi = K_1 \frac{\dot{m}_s}{p} + K_2 p^{-0,73} .$$

Cette expression permet de voir que dans un diagramme $\Psi(p)$ les couples propergoliques pour lesquels les phénomènes de fusion prédominent donneront, en coordonnées logarithmiques, des droites dont la pente sera voisine de -0,73 alors que si la vaporisation (ou la chimie de surface) prédomine l'exposant pourra être supérieur.

Nous tenterons de vérifier dans quelle mesure cette relation est vérifiée mais avant d'aborder cette discussion quantitative nous donnerons quelques observations d'ordre qualitatif destinées à mettre en évidence cette phase liquide dont on avait jusqu'ici assez peu parlé.

4.2 - Résultats qualitatifs

Si l'existence de phénomènes de fusion n'a pu être mise en évidence dans la combustion de lithergols organiques ces phénomènes ont pu être observés dans la combustion d'hydrures métalliques, conformément à la présente théorie.

En effet, on a observé :

- Des dépôts de HLi fondu et resolidifié à la partie la plus basse des moteurs à HLi + ClF_3 après fonctionnement.
- Dans les expériences de visualisation de la combustion de HLi + ClF_3 liquide l'écoulement gazeux est tacheté de points rouges, très probablement dus à la présence de gouttes de HLi dans l'écoulement. Ces gouttes proviennent de la couche liquide et sont projetées par le dégagement d'hydrogène gazeux lors de la décomposition de HLi fondu. Cette décomposition est la cause pour laquelle le HLi initial est blanc alors qu'une fois fondu et resolidifié il devient gris du fait de la présence de lithium métal.
- Dans les expériences de visualisation de la combustion de HLi + ClF_3 gazeux on a pu non seulement observer des résidus de HLi fondu et resolidifié mais également des gouttes de diamètre important (atteignant 4 mm) qui se déposent sur les hublots d'observation.

Dans certaines de ces expériences, où le rapport L/D de la longueur de l'échantillon étudié au diamètre de passage des gaz était important (L/D = 10 pour D = 5 mm) il est arrivé que la phase liquide obstrue le canal central, causant l'explosion de la chambre.

- Dans ces mêmes expériences de visualisation on a, dans certains cas, utilisé des chambres bidimensionnelles dont les parois étaient des plaques transparentes. Ces plaques ont été attaquées par HLi fondu à la partie la plus basse tandis que les autres parties, soumises aux gaz chauds seuls, étaient peu attaquées.

- Une tentative faite pour utiliser un combustible métallique a donné des résultats très décevants mais en accord avec les prévisions de cette théorie. Un tir de moteur effectué avec un pain de lithium métal a donné une fusion quasi-instantanée du combustible, confirmant l'influence défavorable des très faibles valeurs de Pr.

4.3 - Résultats quantitatifs

Pour de nombreux lithergols organiques classiques la vitesse de régression est de la forme :

$$\dot{m} \propto (\rho u)^{0,6}\, p^{0,2}.$$

En coordonnées logarithmiques la pente de la courbe $\Psi(p)$ est alors - 0,2. Les essais avec le lithergol PTC 85/15 confirment ces résultats. Les essais cités en (15) donnent une valeur de la pente de - 0,24 à - 0,35 et les essais de la figure 10 à une pente de - 0,32. Nous sommes donc loin de la valeur prévue par la théorie de fusion ce qui peut être attribué à la facilité avec laquelle les composants de ce combustible se vaporisent, c'est-à-dire à l'importance que prend $\dot{m}_3$. Par contre le couple polybutadiène - H_2O_2 (16) donne une pente de - 0,68 (figure 11) ce qui indique que la fusion prédomine.

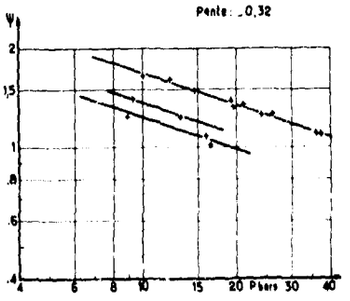

Fig. 10 - Variation de Ψ en fonction de la pression pour le lithergol PTC 85/15 + NO_3H.

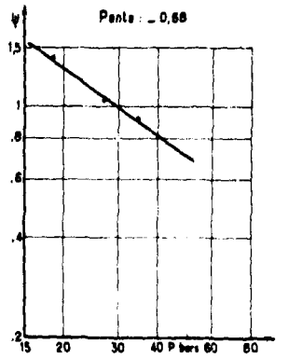

Fig. 11 - Variation de Ψ en fonction de la pression pour le lithergol Polybutadiène + H_2O_2

On a vu que les hydrures métalliques doivent présenter à un degré accentué ce phénomène de fusion. C'est ce que confirme l'expérience puisque la pente de la courbe $\Psi(p)$ est de - 0,64 (Figure 12).

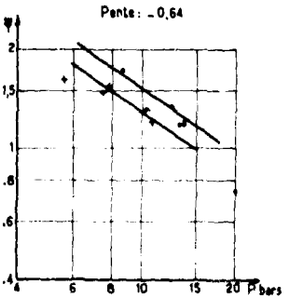

Fig. 12 - Variation de Ψ en fonction de la pression pour le lithergol HLi + ClF_3.

Les résultats expérimentaux confirment donc bien que si les exposants du débit massique unitaire sont de l'ordre de 0,5 (ou supérieurs) les pentes des courbes ne peuvent prendre des valeurs inférieures à - 0,5 que s'il existe un mécanisme présentant une sensibilité inverse à la pression, du type du mécanisme de fusion que propose la présente théorie.

CONCLUSION

Il apparait que l'existence d'une phase liquide dans les moteurs à lithergol est néfaste au rendement de combustion et que l'effet se fait surtout sentir avec les combustibles ayant un faible nombre de Prandtl en phase liquide (métaux et hydrures métalliques). Cette conclusion est conforme à celle trouvée par un traitement plus complet d'un cas de fusion appliqué à la protection par ablation (16) mais qui ne conduit pas à une expression explicite approchée de la vitesse de fusion. D'autres manières de mener le présent calcul montrent que la vitesse de fusion est peu sensible au profil de vitesse choisi dans le liquide.

Dans un moteur la couche liquide qui se développe brûle mal avec le comburant et conduit à une diminution de la sensibilité du taux de régression à la pression, diminution qui n'est que partiellement compensée par la sensibilité directe des phénomènes thermochimiques.

Cet effet de fusion est favorisé par les températures élevées rencontrées avec les propergols à haute énergie. Il se fait surtout sentir dans les moteurs où la longueur est suffisante pour permettre à la couche liquide de se développer.

Pour être assuré d'un bon rendement de combustion il est donc indispensable d'empêcher la couche liquide de se développer ou bien, lorsqu'elle existe, de permettre la combustion du liquide. Le premier effet est obtenu par la technique des diaphragmes mis au point à l'ONERA. Ces diaphragmes divisent le moteur en deux chambres, une chambre amont et une chambre aval. Le diaphragme interrompt la couche de liquide et provoque une turbulence suffisante pour rompre le film liquide qui se forme dans la chambre aval. Le deuxième effet est obtenu par les diaphragmes mélangeurs dont sont munis tous les moteurs actuellement en service. La combustion principale se fait alors en aval de ce diaphragme, dans le convergent. Il est significatif que la combustion puisse se faire de façon complète dans le convergent même en l'absence de ce diaphragme si le volume compris entre la section de sortie du canal central et le col est suffisamment grand.

En ce qui concerne le choix des propergols pour la réalisation d'un propulseur hybride, on constate qu'il n'est pas possible de choisir des combustibles qui rendent m maximum et M minimum. Par contre on peut éviter un excès de liquide en évitant les moteurs qui ont un rapport $\frac{L}{D}$ trop élevé. Il semble également favorable d'obtenir des valeurs de m_s élevées mais pour que l'effet de cette réaction de surface se fasse sentir il faut que m_s soit au moins de l'ordre de $0,5\ g/cm^2.s$. Il est également possible d'étudier d'autres dispositions de moteurs qui permettent de rompre la couche liquide.

On peut se demander si la mise au point de moteurs modulables à richesse constante et faisant appel à des propergols à haute énergie est possible en conservant la simplicité de l'injection unique du comburant en amont et en évitant la présence de systèmes mélangeurs en aval du combustible. Les résultats obtenus jusqu'ici tendent à faire répondre par la négative mais il reste à explorer les conditions très particulières de la régression dans la zone d'injection, conditions qui semblaient donner une sensibilité suffisante à la pression tout en limitant le débit de liquide. En effet, les essais effectués à l'ONERA (17) montrent qu'au voisinage de la zone d'injection la vitesse de régression est plus sensible à la pression qu'en aval, ce qui peut s'expliquer par le niveau élevé de l'intensité de combustion. Cette haute intensité de combustion peut conduire à des valeurs élevées du taux de réaction de surface, donc à de fortes sensibilité à la pression. Il est donc vraisemblable que la réalisation de moteurs modulables à richesse constante doive faire largement appel à ce mécanisme encore inconnu.

REFERENCES

(1) G.A. MARXMAN & M. GILBERT -
Turbulent Boundary Layer Combustion in the hybrid Rocket.
IXè Sympesium sur la Combustion.
Academic Press - N.Y. 1963, p. 371.

(2) G.A. MARXMAN & C.E. WOOLDRIDGE -
Fundamentals of Hybrid Boundary Layer Combustion.
Heterogeneous Combustion. Progress in Astronautics and Aeronautics. Vol. 15.
Academic Press N.Y. 1964 -

(3) G.A. MARXMAN -
Combustion in the Turbulent Boundary Layer on a Vaporizing Surface.
Xème Symposium sur la Combustion 1964 - The Combustion Institute.

(4) G.A. MARXMAN & C.E. WOOLDRIDGE -
Research on the Combustion Mechanism of Hybrid Rockets.
25ème Réunion AGARD Combustion and Propulsion Panel (1965)
AGARD Conference Proceedings n° 1
Advances in Tactical Rocket Propulsion
AGARD 1968.

(5) G.A. MARXMAN -
Boundary Layer Combustion in Propulsion.
XIème Sympesium sur la Combustion - 1966.
The Combustion Institute.

(6) C.E. WOOLDRIDGE & R.J. MUZZY.-
Internal Ballistics Considerations in Hybrid Rocket Design.
AIAA Paper n° 66-628.

(7) L.D. SMOOT & C.F. PRICE -
Regression Rate of Nonmétalized Hybrid Fuel Systems
AIAA J. 3, 8, 1408-1413 - Août 1965.

(8) L.D. SMOOT, C.F. PRICE & C.M. MIHLFEITH

Pressure Dependance of Hybrid Fuel Regression Rates.
AIAA J. 5, 1, 102-106, Janv. 1967.

(9) L.D. SMOOT & C.F. PRICE -

Regression Rate of Metalized Hybrid Fuel Systems.
AIAA J. 4, 5, 919-915, Mai 1965.

(10) E. MILLER -

Boundary layer combustion in Hybrid Rockets.
AIAA Preprint n° 67 - 471.

(11) E. MILLER -

Hybrid Rocket Combustion Regression Rate Model.
AIAA J. 4, 4, 752-753 - Avril 1966.

(12) F.J. KOSDON & F.A. WILLIAMS -

Pressure Dependance of Nonmetalized Hybrid Fuel Regression Rates.
AIAA J. 5, 4, 774-778 - Avril 1967.

(13) J.F. LIEBERHERR -

Ablation thermique et ablation chimique dans la combustion des lithergols.
XVIIIème Congrès I.A.F. - BELGRADE 1967.

(14) J.F. LIEBERHERR -

Evaluation de la température de surface dans l'ablation par évaporation.
La RECHERCHE AEROSPATIALE (à paraître).

(15) A. MOUTET & M. BARRERE -

Les fusées à lithergol ou fusées hybrides.
La RECHERCHE AERONAUTIQUE - Mars-Avril 1960

(16) G.W. SUTTON -

The hydrodynamics and heat conduction of a multing surface.
J. Aero. Sci. Janvier 1958.

(17) M. PUGIBET & A MOUTET -

Utilisation dans les systèmes hybrides de l'eau oxygénée comme comburant.
La RECHERCHE AEROSPATIALE n° 131 - Sept.-Oct. 1969.

SURFACE REACTIONS IN SOLID PROPELLANTS

H. Selzer

DEUTSCHE FORSCHUNGS- U. VERSUCHSANSTALT FÜR LUFT- U. RAUMFAHRT E.V.
Institut fur Strahlantriebe
Inst-Teil Chem. Raketenantriebe
Trauen, W.Germany

SUMMARY

The state-of-the art of the combustion mechanism of AP-propellants is reviewed and some new experimental facts are given concerning the influence of lattice defects and condensed phase behaviour on the burning process.
The findings demand a revision of the theoretical models to account for the lattice defect, for a change from fast to slow decomposition, and for reactivity spots.

THE THEME OF THIS PAPER incorporates a great variety of propellants and still rather hypothetical mechanisms. Therefore, attention will be centered on ammonium perchlorate based composite solid propellants, the most commonly used in modern-day rocketry. The combustion of pure ammonium perchlorate and AP based propellants has been extensively investigated and to review such work would require the discussion of some 500 separate papers, a task already admirably done by Hall and Pearson(1), Jacobs and Whitehead(2), and also Pearson(3). Because the details of the mechanism of AP combustion and the pros and cons of many individual viewpoints can be found in these review papers, the main purpose of the present paper is to review some new findings and also to point to those steps in the mechanism where more new information is needed.

THE CONDENSED PHASE REACTION OF AP

AP has an orthorhombic crystal structure between -190°C and 240°C(4). Above 240°C, the lattice changes to the cubic structure and at 592 ± 20°C it melts according to Hightower(5) and Cordes(6). But this transition to the melt needs more discussion in respect to its influence on the decomposition. Though AP is a rather stable compound in propellants, nearly all measurements of the behaviour of AP are complicated by the fact that all physical properties are influenced by inevitable chemical reactions.
Three different regions must be considered depending on the consumption rate:

(a) the slow decomposition (up to 0.1 mm/sec)

(b) the fast decomposition (the region of the normal burning)

(c) and the explosive decomposition.

Most detailed measurements have been performed in region (a) and partly into region (b).
Region (c) is of less interest because AP is mainly used for propellants. Therefore (c) falls out of the scope of this paper.

At room temperature, the unit cell of AP has the dimension a = 9.231 Å, b = 5.813 Å, and c = 7.453 Å(4) with the ions NH_4^+ and ClO_4^- in the lattice sites. Even in single crystals, there is a certain amount of disorder. Consequently, we expect to find vacant NH_4^+ or ClO_4^- sites, positively and negatively charged interstitials, and also neutral defects.

Furthermore, we must expect some free electrons (even if they are short-lived), photons, and mechanical excitation. Briefly expressed, the material possesses all kinds of interactions we know from the solid state physics. The question is what influence these distrubances have on the combustion of AP.

THE SLOW DECOMPOSITION OF AP. As mentioned above, there are several possibilities of defects in the AP-crystals. Besides the macroscopic dislocations, only two defects have been shown to influence the low temperature decomposition, up to now.
Herly and Levy(7) showed that the decomposition of AP-crystals was closely bound up with defects which could likewise be produced by gamma-ray irradiation (50 KV). Different radiation doses decreased induction time and increased the reaction rate for the acceleratory period. As shown in Fig. 1, this irradiation is only effective up to a certain degree of decomposition giving evidence that the number of effective defects is limited.

Cole(8) and Manelis et al(9) identified two types of x-ray created defects by EPR analysis. They noticed a longlived NH_3^+ ion and a shortlived ClO_3 ion. The number of defects was limited to 10^{20} defects/gm in the case of NH_3^+, corresponding to a maximum irradiation dose of 2×10^7 rad at a temperature of 150°K. In the temperature region from 20°C to 100°C, the maximum defect concentration was determined to be 5×10^{17} defects/gm. At low temperature the concentration remained stable whereas at the high temperature a slow decay was noticed due to the recombination rate:

$$k_{NH_3^+} = 10^{8.5} \exp(-6.3/RT) \qquad (1)$$

The recombination rate for the ClO_3 defects was measured to be

$$k_{ClO_3} = 10^{18} \exp(-20/RT) \qquad (2)$$

though due to the fast decay the measurements were difficult. The number of the ClO_3-defects was at least 2 orders of magnitude less than the NH_3^+ ions.

Herly and Levy(10) showed that the nucleation rate increases very rapidly at a radiation dose of 10^7 rad indicating the onset of chemical reaction induced by the defects. The magnitude of the dose corresponds to the value reported by Manelis(9) for the maximum concentration of NH_3^+ ions. Hence we have to assume a limiting defect number of 5×10^{17} defects/gm at room temperature for the slow decomposition. At room temperature, there are 1.3×10^{21} lattice cells per gram giving a rough estimate of the distribution ratio of the defects:

1 within 2600 lattice cells.

This concentration seems to enable a self sustained chemical reaction. However, this idea needs further confirmation.
Because the existence of large quantities of NH_3^+ and ClO_3 ions has been proven, we have to consider what happens to the H atom and O^- ion or to the proton and oxygen. Jacobs(2) proposed the following reaction equations:

$$NH_4^+ \longrightarrow NH_4^{++} + e^- \qquad (3)$$

$$NH_4^{++} \longrightarrow NH_3^+ + H^+ \qquad (4)$$

$$ClO_4^- \longrightarrow ClO_4 + e^- \qquad (5)$$

$$ClO_4 \longrightarrow ClO_3 + O \qquad (6)$$

$$ClO_4^- + H^+ \longrightarrow HClO_4 \qquad (7)$$

But we also have to consider the other possibilities:

$$NH_4^+ \longrightarrow NH_3^+ + H \qquad (8)$$

$$H + O \longrightarrow OH \qquad (9)$$

$$H^+ + e^- \longrightarrow H \qquad (10)$$

$$ClO_4^- \longrightarrow ClO_3 + O^- \quad ClO_3 + O + e^- \qquad (11)$$

$$ClO_3 + OH \longrightarrow HOClO_3 \qquad (12)$$

Which of the ways is correct or privileged, or whether other possible processes play a role, must still be determined. Attention must be confined to the high reaction rate of AP to see whether by chance the lattice vibration tends towards the highest possible frequencies and whether no thermodynamic equilibrium can be achieved.

Another series of experiments takes advantage of the electrical behaviour of AP. The present author tried to use a special electron-microscope (by the Balzers Comp., Lichtenstein) for the visualization of the electronic processes at the surface. The principle was as follows: a strong UV-radiation supplied the energy for the electrons in the crystal to surmount the surface work function. These electrons were extracted by a potential of 100 kV and then conventionally focussed on a screen by three lenses. Though the pictures of the AP-crystal were not of the highest quality, due to the partial sublimation of the material, one striking effect was noticed. At ambient temperature, nearly no electrons could be determined, but at 240°C the intensity increased sharply by several orders of magnitude.
The same effect was noticed by the author in an investigation which was intended to study the energy levels of defects. Prior to the change from the orthorhombic to the cubic lattice, a great number of electrons were released corresponding to an activation energy of E = 33 kcal/mole. This finding is being further analysed.

Some investigators measured the electrical conductivity to analyse the charge carriers and the defect mechanism. The most striking results were reported by Maycock et al(11). They found 5 different regions in the temperature range 25°C - 350°C (see Fig. 2). The increasing activation energies (0.18 eV, 0.54 eV, 0.82 eV, 2.0 eV, 5.6 eV) were ascribed to surface, extrinsic, intrinsic (orthorhombic and cubic), and electronic conduction. Unfortunately, the conduction did not remain constant versus time and therefore a correct interpretation of the measurements seems questionable as the conductivity is superimposed by some complicated chemical-electronic mechanism. Furthermore, the used DC-voltage caused a polarization zone due to the fact that the positive side of the sample became opaque during the treatment, an indication of negative defects.

A similar measurement using AC-voltages however was carried out by Wise(12) resulting in a simple exponential function of the conductance versus the reciprocal of the temperature. In contrast to Maycock, there is no change of the mechanism, not even at the temperature of the lattice transition.

These short notes on the electrical behaviour of AP should be sufficient to demonstrate the complex relations. As far as the authors knows, more investigations are underway. We may therefore look forward to more meaningful experimental data and a better background in the near future.

Other experiments were conducted to elucidate the influence of catalysts or artificial defects on the burning or deflagration rate. In most cases the differential thermoanalysis and thermogravimetric techniques were used. In most cases, the results depend on a mixture of condensed phase and gas phase reactions. Therefore some details will be discussed later. The DTA-measurements gave quantitative values for the temperature of deflagration, of phase changes, and the amounts of heat involved.

One difficulty in interpreting the reported results stems from the use of different catalysts and different procedures in preparing the samples. The results are hard to compare. Because they are in fact inconsistent, the reader should look up the details in the literature.
Two facts must be mentioned, however. Firstly, there is a great difference between impurities which can be substituted isomorphously into the lattice and those which are mixed mechanically(13).
Secondly, most of the DTA or TGA-measurements have not been considered with respect to dislocations and their possible influence. There are however a few exceptions such as those investigations of Herley(10) and Schmidt(4).

Schmidt and Stammler(4) found a dependency between the deflagration temperature and the burning rate. The onset of the free rotation of the ClO_4^- ion was given as an explanation for any chemical reaction. This is one of the few cases that data from low temperature measurements was connected to practical burning rate data.
As a final point in this section on the low temperature decomposition, the "magic" 30% decomposition first reported by Bircumshaw and Newman(14) must be repeated. We all know the defects which make the transparent crystal opaque and sometimes brownish indicating colour-centers, but we do not have the knowledge of the exact mechanism how they form and why they stop at 30% decomposed.

THE FAST DECOMPOSITION OF AP. The linear regression rate of AP is in the order of 0.1 cm/sec to 2 cm/sec. In self sustained burning, the lattice is being heated at a rate of approximately 10^6 °C/sec(15). Compared to the temperature rise in most of the laboratory experiments (appr. 10°C/min or even less) it is obvious that the extrapolation of the slow decomposition measurements must be looked at very critically.
One way to learn whether the extrapolation is correct takes advantage of a Scanning Electron Microscope (SEM) to study the surface of quenched propellants. Due to the stored energy in the surface, one has to keep in mind some post-reactions. An analysis(16) of propellants quenched by compressed air at 1 atm showed a particle distribution (see Fig. 3 and 4) deviating from the normal one. Beyond 30 μ, the number of AP-particles decreased rapidly while there was an increase in the number of particles greater than 100 μ.

The reason was given by the post-decomposition of small particles in the order of 30 μ and in the consumption of a thin fuel-cover over the big particles.

More details of the quenched surfaces are given in the following pictures. One great difficulty to be borne in mind is that AP has many different modes of behaviour.
Figure 5 shows the start of a reaction produced by some small dislocations which are not spread all over the crystal. The next series of pictures (Fig. 6) points out a powdering mechanism at some preferred spots. The pictures e and f show a particle quenched by cold N_2, which reduces post-reaction on the surface. Despite this drastic quenching procedure the same surface structure to that of the earlier pictures was apparent. However, some recondensed material was present.
Some important consequences can be derived from Figs. 7 and 8. The AP-crystal surfaces have isolated activity regions with many holes that dig deep into the solid interior. Finally, the tenuous structure collapses and a large deep hole of circular shape remains (see lower left corner of Fig. 7 b). That these holes are to be ascribed to the burning process, follows from Fig. 8 a and b with cold N_2-quenched samples. Here, the surface consisted of small residues adhering together and thus forming a porous layer. The pictures e and f (Fig. 8) give evidence of interpreting all hexagonal shapes to be recrystallized material. Yet, at the bottom of the holes, the material looked similar to that which was left behind by slow decomposition (Fig. 9 a). A rather rare crystal produced tetragonal holes (b and c, Fig. 9) and even cold N_2-quenched samples give evidence of rectangular pores (Fig. 9, d, e).
In summary, the SEM-analysis gives clear evidence of a nonsteady burning process of AP starting in activity sites of the dimension of 1 to 10 μ. At 1 atm, no liquid phase could be detected.

As shown by Boggs(17) pores exist at pressure levels up to 130 atm, even during burning of pure single crystals of AP. His very interesting findings need more investigation to eliminate the influence of the stored energy during quenching, though they will be correct in general. Depending on pressure, he defined four different regions in accord to the burning rate (Fig. 10).
The explanation for the negative pressure exponent was found in an intermittent flame. The same mechanism was reported by the present author for the combustion of composite propellants(18). Hence, the accumulated experimental evidence should now be strong enough to influence and correct existing theoretical models.

Is there any correlation between the slow and fast decomposition in the condensed phase? The appearance of dislocations point at a similar mechanism though the rates differ by several orders of magnitudes. In the first case we have a migration of defects whilst in the second case the defects must be assumed to be fixed and to influence the growth of big dislocation sites and holes. Despite the steep temperature rise, no other ion bond breakages seem to occur that do not occur during slow decomposition. The existence of pores implicates the differentiation whether the gas phase reactions start "above" the surface. The easy recondensation or sublimation of AP indicates the existence of $HClO_4$ as a decomposition product, thus contradicting the formation of OH or H_2O within the lattice.

An interesting fact arises from the negative pressure exponent in the pressure range 150 atm to 300 atm. As the gas phase reactions are accelerated by pressure, the reason must be looked for in the condensed phase. It is unlikely, though not yet measured, that the physical properties of AP change drastically. Therefore, the reason must be assumed to originate from a change in the different processes (equations 3 - 12) or in a still unknown recombination process. In this connection the question arises as to what influence is exercised by the surface melt reported by Price et coworkers(5). Those observations came from very big AP-crystals never used in this dimension in propellants. Cordes(6) supported the existence of a melting point of AP at $592^{\circ}C \pm 20^{\circ}C$ by a semitheoretical extrapolation (Fig. 11). Despite these evidences it is doubtful that a melt will occur in the commonly used reactive systems such as composite propellants.

Arguments against the melt come from the rather small particle diameter and the dependence of the burning rate of propellants on pre-irradiation as reported by Flanagan and Gray(19). At 70 atm, the burning rate of one type increased by 30% thus proving the influence of the lattice defects. Those defects should have been equalized in a melt. On the other hand, the surface temperatures measured by several investigators and different methods resulted in nearly the same value as the proposed melting point. Therefore, one has to admit that in most cases the vibration is fully excited and a question of less importance remains: whether the reactivity of AP predominates, i.e. sublimation occurs, or some influences will delay the decomposition, i.e. enabling a melt.

THE GAS PHASE REACTION OF AP

Compared to the reactions in the condensed phase of AP we know much more, though not enough, of those in the gas phase, because in the latter case the different steps could be analysed separately. Representative of the great number of investigations, only the latest publication can be cited. Pearson and Jacobs(20) proposed the following mechanism:
A proton transfer(21) in the solid produces

$$NH_3\ (gas) + HClO_4\ (gas) \qquad (13)$$

The next important step is given by the oxidation of NH_3 by ClO after the decomposition of $HClO_4$ (ClO + OH + O_2):

$$NH_3 + ClO \longrightarrow NH_2 + ClOH \qquad (14)$$

The third step reaction should involve:

$$ClOH + OH \longrightarrow ClO + H_2O \qquad (15)$$

$$NH_2 + O_2 \longrightarrow HNO + OH \qquad (16)$$

Then the scheme becomes more obscured by the different possible combinations resulting in the formation of H_2O, O_2, Cl_2, HCl, NO, N_2O, NO_2, and N_2, at last.

This paper cannot follow all the various details of the analysis of Jacobs and Pearson yet some remarks are necessary here. The overall heat balance shows that the decomposition flame will not be endothermic prior to reaction following equations 15 and 16. This fact stresses the importance of catalytic acceleration of the previous reactions in order to increase the energy feedback to the surface. In accordance with this idea, Pittman proved the effectiveness of iron containing catalysts in relation to the $HClO_4$-decomposition(22).

Though such a conclusive investigation is not available for other catalysts, the general impression tends to the exclusion of remarkable catalytic effects in the condensed phase. In the case of metal compounds, the strong influence on the deflagration of AP is ascribed to the formation of metal perchlorates prior to the decomposition.

Two ways must be considered as possible realistic models for the theoretical analysis: isothermal horizontal layers or vertical streams. As there is no thermal equilibrium, the way seems more promising to study the influence of the heat generated by the exothermic decomposition of the initial decomposition products of $HClO_4$, on the condensed phase though the oxidization of NH_3 needs 5.1 kcal/mole and this energy will partially be taken from the previous reactions. Unfortunately, the question is still open whether the sublimation energy will mainly be supplied by the reactions following equation 15 and 16 or by the local exotherm of the $HClO_4$ decomposition. In this respect, the existence of pores and holes in the AP needs attention again for they provide an excellent physical basis for an increased heat transfer from the initial exothermic reaction steps.

THE DECOMPOSITION OF THE BINDER

The combustion of polymers was studied extensively though not yet completely. The most informative data is to be derived from pyrolysis experiments. There are too many polymers to deal with the details here. But generally, they do not differ very much with respect to the burning behaviour in propellants. The mechanism includes two steps: depolymerization followed by desorption of the monomer from the surface of the propellant. As these processes are endothermic, the energy feedback plays an important role. The gaseous products react with the oxidizers' products in a diffusion flame. Therefore, the burning rate can be influenced by the degree of polymerization and on the other side by catalysts, though the margin is rather limited. This is not true for NO-containing binders or similar ones which can increase the burning rate of composites considerably. As far as the author knows, the once supposed subsurface reaction between fuel and AP could not be answered positively. But for some special purpose, a dependence on the fuel surface was reported by Steinz(23) with respect to the existence of a liquid phase.

THE COMBUSTION MECHANISM OF COMPOSITE PROPELLANTS

The main heat release of heterogeneous propellants occurs in a diffusion flame consisting of decomposition products of both the binder and the oxidizer. The latter forms a premixed type decomposition flame with a significant exotherm. Whether there is an exothermic decomposition in the condensed phase remains dubious. Generally spoken, the combustion mechanism seems to be rate controlled by energy feedback from the gas reactions though the mechanism is rather complex and the controlling steps may vary in different regions of temperature, pressure, and mixture ratio. Several combustion models and theories exist, the most developed one by Summerfield and coworkers(24). As this theory is based on an essentially one-dimensional steady model, Fenn(25) developed a "Phalanx" flame model that takes account of the heterogeneity of the propellants. So did Hermance(26) in a rather close approach to the complex mechanism. Despite this complexity, the model should be considered again for all the models treat the combustion as a steady process.

The present author(18) reported that most propellants burn by small flame nuclei. Thus, the surface is attacked by an unsteady process on a microscopic scale. Of course, the influence of these nuclei averages statistically all over the surface and establishes a steady regression rate. Yet, the nucleus burning may cause great instabilities and seems to be important in the quenching mechanism.

Now, the microscopic pictures of Boggs(17) and this author prove that even the AP crystals do not burn steadily but show priviledged reactivity sites. On the other hand, shadowgraph pictures of the author(18) showed that the AP particles in a propellant need a rather long time before they burn very fast (Fig. 12). It is apparent that ammonium perchlorate has many different modes of burning behaviour. The causes of these differing modes must be included in a theoretical propellant combustion model. Three such facts to be included, though the domains in which they are important have not yet been exactly defined, are:

(a) the existence and influence of lattice defects,

(b) the existence of a mechanism causing periods of slow and fast decomposition, and

(c) the existence of priviledged reactivity spots of the order of 1 - 10 μ.

ACKNOWLEDGEMENT:

Thanks are due to Dr. J.A. Steinz for discussions of this paper.

REFERENCES

1 Hall, A.R., Pearson, G.S.
Ammonium Perchlorate: A Review of its Role in Composite Propellant Combustion
R.P.E. Technical Report No. 67/1

2 Jacobs, P.W.M., Whitehead, H.M.
Decomposition and Combustion of Ammonium Perchlorate
Final Report Contract N 60530-12591, Febr. 1968

3 Pearson, G.S.
Perchlorates: A Review of Their Thermal Decomposition and Combustion, with an Appendix on Perchloric Acid
R.P.E. Technical Report No. 68/II

4 Stammler, M., Schmidt, W.G.
Oxidizer properties that affect combustion rates of solid propellants
The Combustion Institute Western States Section Meeting, 1966, Paper WSCI 66-26

5 Hightower, J.D., Price, E.W.
Combustion of Ammonium Perchlorate
Eleventh Symposium (International) on Combustion
(The Combustion Institute, Pittsburgh, 1967)
pp. 463 - 472

6 Cordes, H.F.
An estimate of the melting point of ammonium perchlorate
AIAA Journal, vol. 7, No. 6, 1969, pp. 1193 - 1195

7 Herley, P.J., Levy, P.W.
Effects of X- and γ-Ray radiation on the thermal decomposition of solid orthorhombic ammonium perchlorate. I. Experimental and results
J. of Chem. Phys., vol. 49, No. 4, Aug. 1968, pp. 1493-1500

8 Cole, T.
Paramagnetic defects in irradiated NH_4ClO_4
J. Chem. Phys. 65, pp. 1636-1637, 1961

9 Boyarchuk, Yu.M., Buben, N.Ya., Dubovitskii, A.V., Manelis, G.B.
EPR investigation of irradiated ammonium perchlorate
Kinetika i Kataliz 5, 823-830, 1964; Translation in Kinetics and Catalysis (USSR), 5, 723-728, 1964

10 Herley, P.J., Levy, P.W.
Effects of X- and γ-Ray Radiation on the Thermal Decomposition of Solid Orthorhombic Ammonium Perchlorate. II. Kinetics and Discussion
J. of Chem. Phys., vol. 49, No.4, 1500-1509, Aug. 1968

11 Maycock, J.N., Pai Verneker, V.R.
Role of point defects in the thermal decomposition of ammonium perchlorate
Proc. Roy. Soc. A 307, pp. 303-315, 1968

12 Wise, H.
Electrical conductivity of solid ammonium perchlorate
J. Phys. Chem. 71, pp. 2843-2846, 1967

13 Schmidt, W.G., Stammler, K.
Thermal decomposition of catalyzed ammonium perchlorate
21st Interagency Solid Propulsion Meeting, June 1965, Vol. I, pp. 71-88

14 Bircumshaw, L.L., Newman, B.H.
The thermal decomposition of ammonium perchlorate.
I. Introduction, experimental, analysis of gaseous products and thermal decomposition experiments
Proc. Roy. Soc. (London), A 227, pp. 115-132, 1954

15 Selzer, H.
The temperature profile beneath the burning surface of a composite ammonium perchlorate propellant
Eleventh Symposium (International) on Combustion

16 Furchert, E., Selzer, H.
Kathodenlumineszenzuntersuchungen von Festtreibstoffen mit Hilfe des Raster-Elektronenmikroskopes
Ein Vortrag gehalten auf der Tagung für Ultrastruktur-forschung und Elektronenmikroskopie, 22.-25. Sept, 1969, Wien

17 Boggs, T.L.
The deflagration of pure single crystals of ammonium perchlorate
AIAA 7th Aerospace Sciences Meeting, New York, Jan. 20-22, 1963, AIAA Paper No. 69-142

18 Selzer, H.
The unstable nature of the burning mechanism of AP-propellants
AIAA 7th Aerospace Sciences Meeting, New York, Jan. 20-22, 1969, AIAA Paper No. 69-177

19 Flanagan, J.E., Gray, J.C.
A study of composite solid propellants containing irradiated ammonium perchlorate
J. Spacecraft, vol. 3, No. 1, Jan. 1966

20 Jacobs, P.W.M., Pearson, G.S.
Mechanism of the decomposition of ammonium perchlorate
Comb. and Flame, vol. 13, No. 4, Aug. 1969

21 Jacobs, P.W.M., Russel-Jones, A.
The thermal decomposition and ignition of mixtures of ammonium perchlorate and copper chromite
Eleventh Symp. on Combustion, pp. 457-462

22 Pittmann, C.U., Jr.
Location of action of burning-rate catalysts in composite propellant combustion
AIAA Journal, vol. 7, No. 2, 1969

23 Steinz, J.A., Stang, P.L., Summerfield, M.
The burning mechanism of ammonium perchlorate-based composite solid propellants
AIAA 4th Propulsion Joint Specialist Conference, Cleveland, AIAA Preprint 68-658, June 1968

24 Steinz, J.A., Stang, P.L., Summerfield, M.
The burning mechanism of AP-based composite solid propellants
Aerospace and Mechanical Sciences Report No. 830, Princeton University, Febr. 1969

25 Fenn, J.B.
A phalanx flame model for the combustion of composite solid propellants
Comb. Flame, 12, pp. 201-216, 1968

26 Hermance, C.E.
A model of composite propellant combustion including surface heterogeneity and heat generation
AIAA Journal 4, pp. 1629-1637, 1966

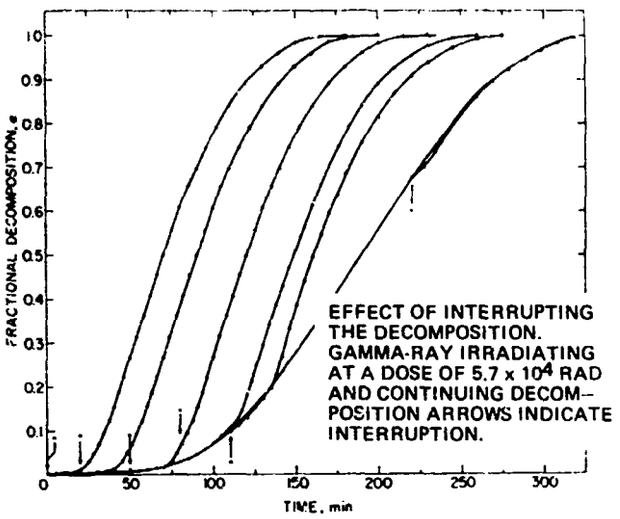

FIG. 6. Curves showing the effect observed when the decomposition of unirradiated whole crystals is interrupted, the sample irradiated, and the decomposition resumed. The decomposition temperature was 227°C and the dose 5.7×10^4 rad. The decomposition of the unirradiated material was interrupted, corresponding to the curves from left to right, at 0, 20, 50, 80, 110, and 220 min after the decomposition was started. The right most curve is for unirradiated material. (Solid line).

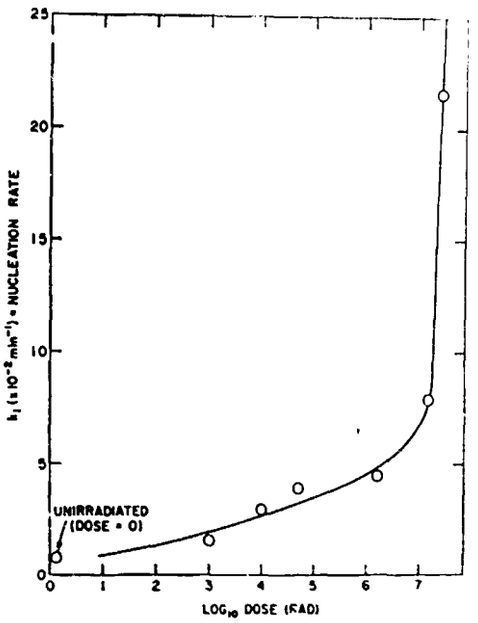

FIG. 5. The effect of gamma-ray irradiation prior to decomposition on the nucleation rate k_1 in the Avrami-Erofeyev theory. This was derived from a fit of Eq. (12) to the acceleratory region data given in Fig. 3 of Paper I (preceding paper).

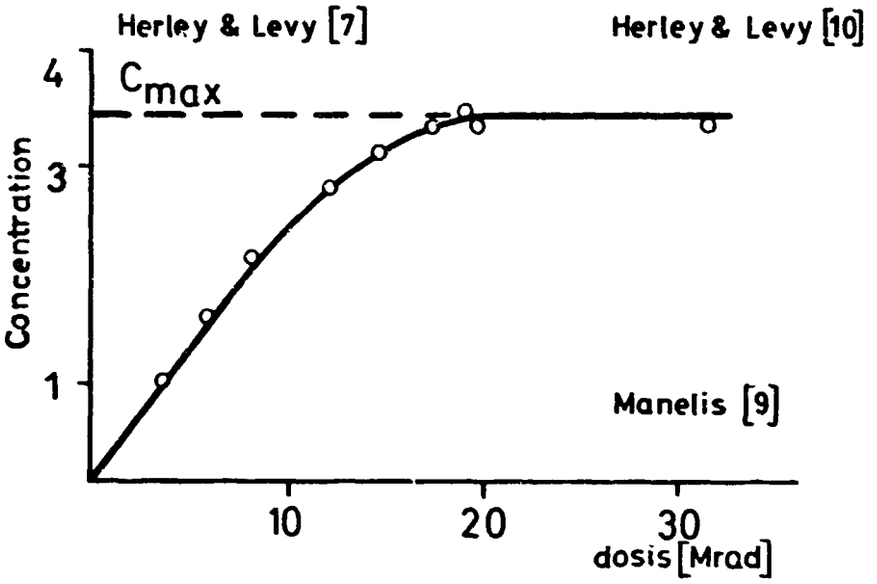

Concentration of the paramagn. centers versus the dosis of irradiation, Temp. 150°K

$C_{max} = 10^{20}$ paramagn.particles/g

Fig. 1 The influence of the number of defects on decomposition of AP

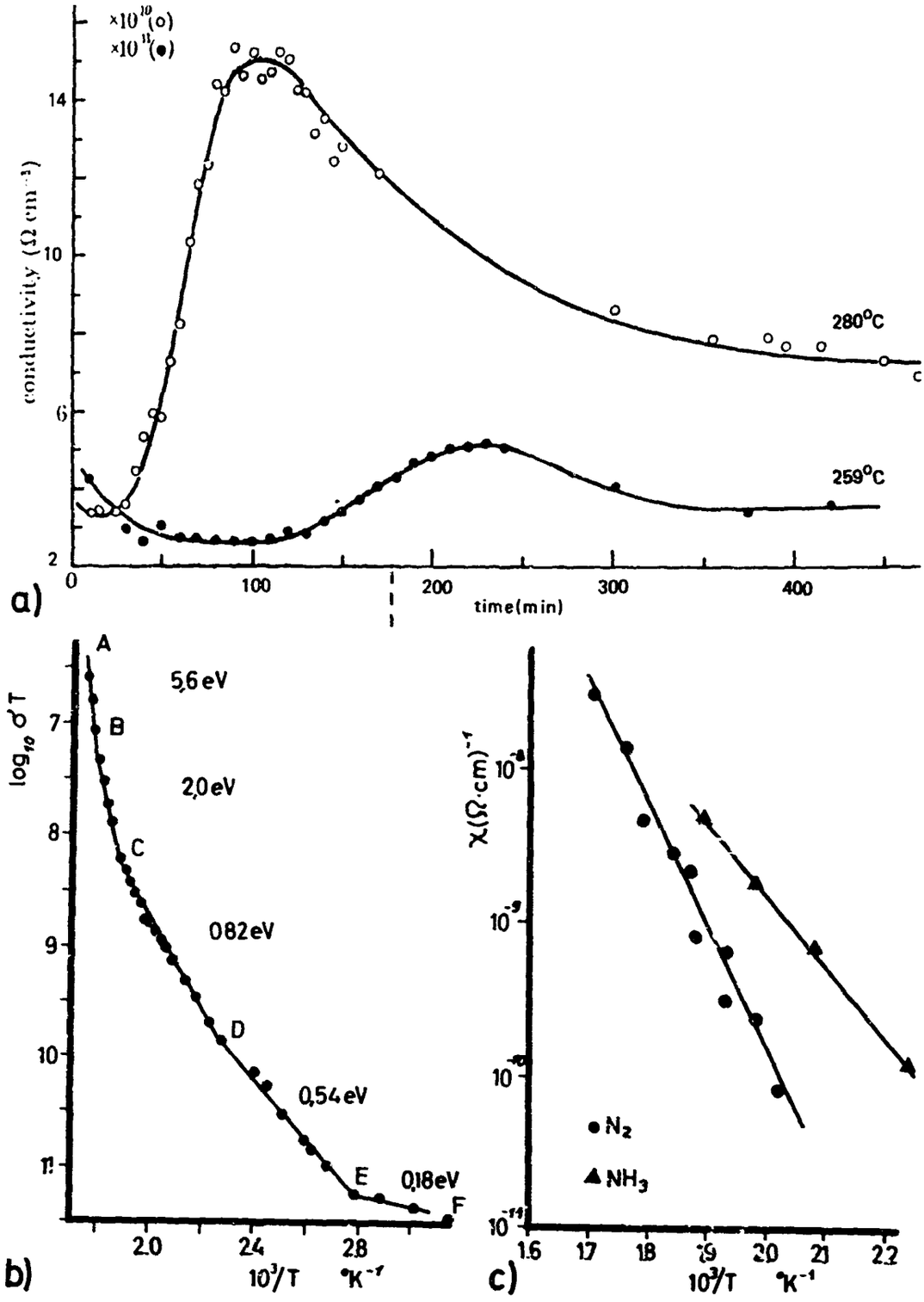

Fig. 2 Electricalconductivity of AP: a, b after Maycock et al(11); c after Wise(12)

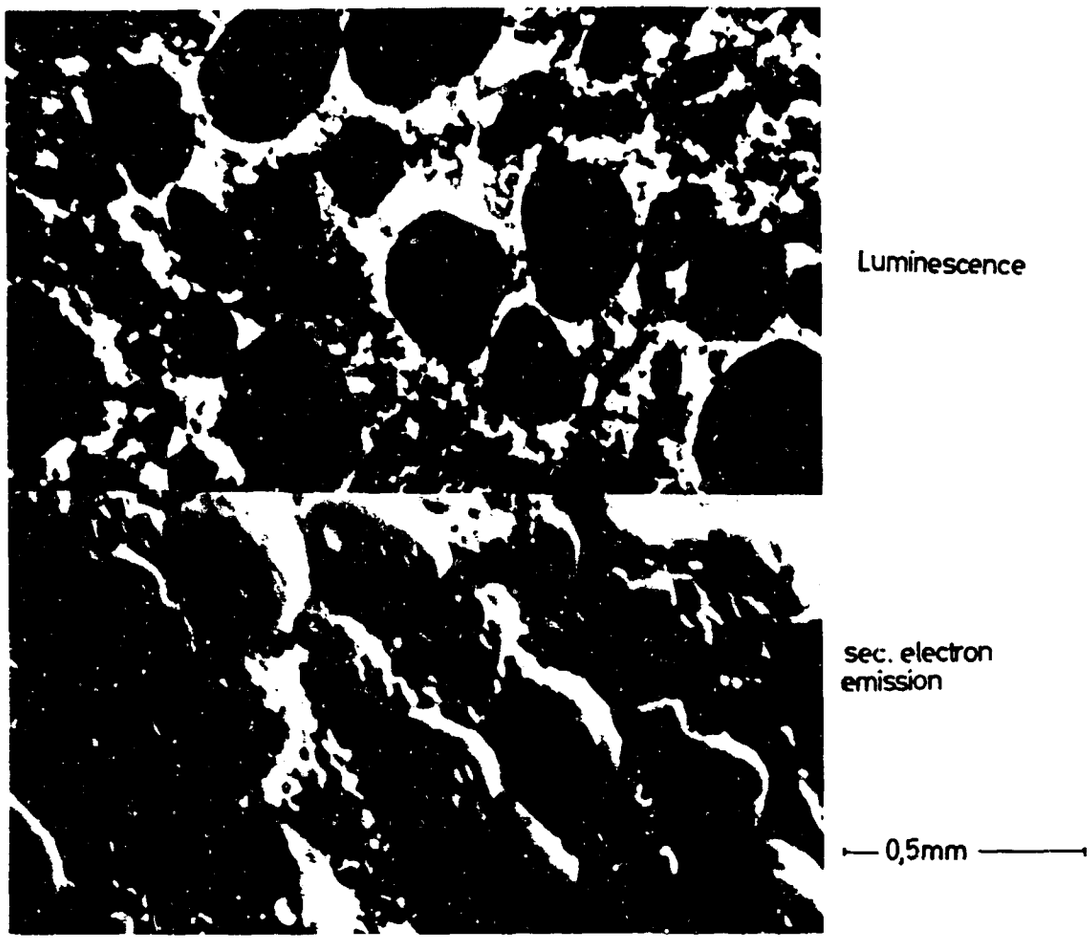

Fig. 3 A quenched surface in two SEM-modes

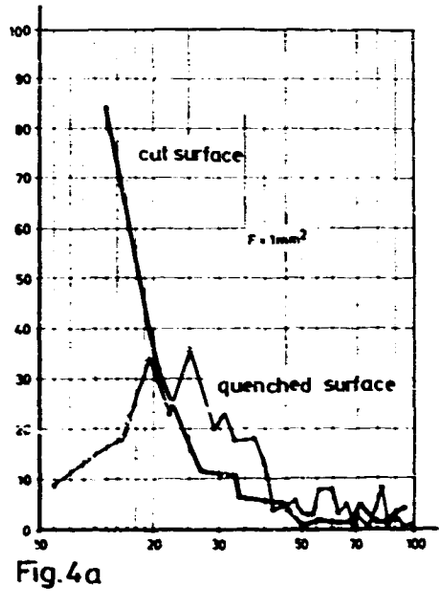

Fig.4a

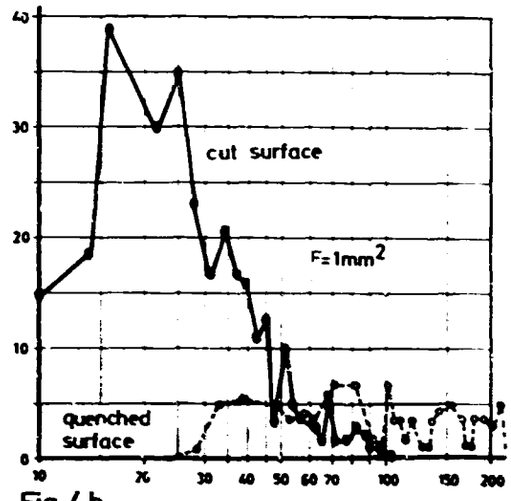

Fig.4b

Fig. 4 Comparison of quenched and cut surfaces

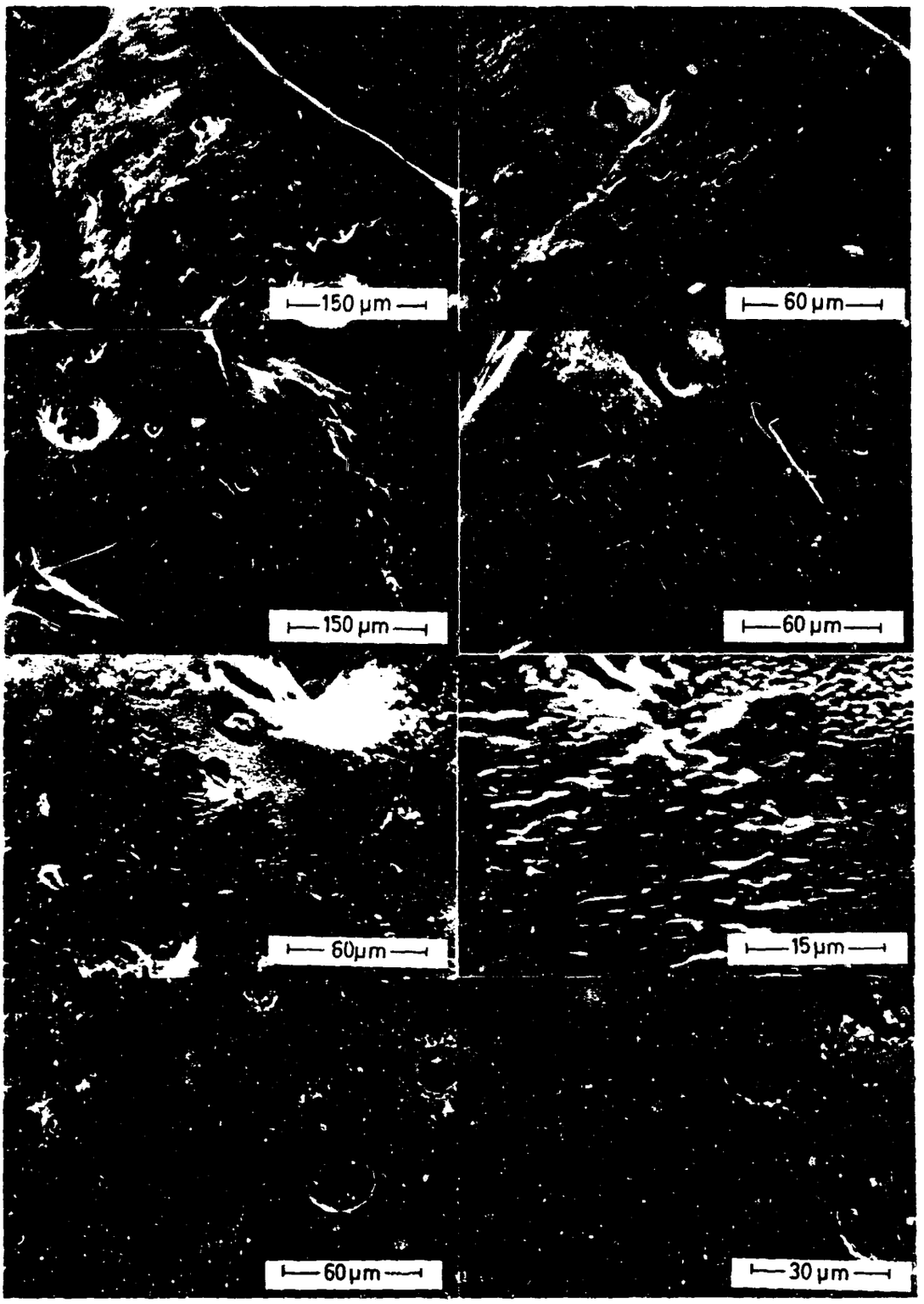

Fig. 5 SEM-pictures of the onset of the AP-reaction in a burning propellant at 1 atm

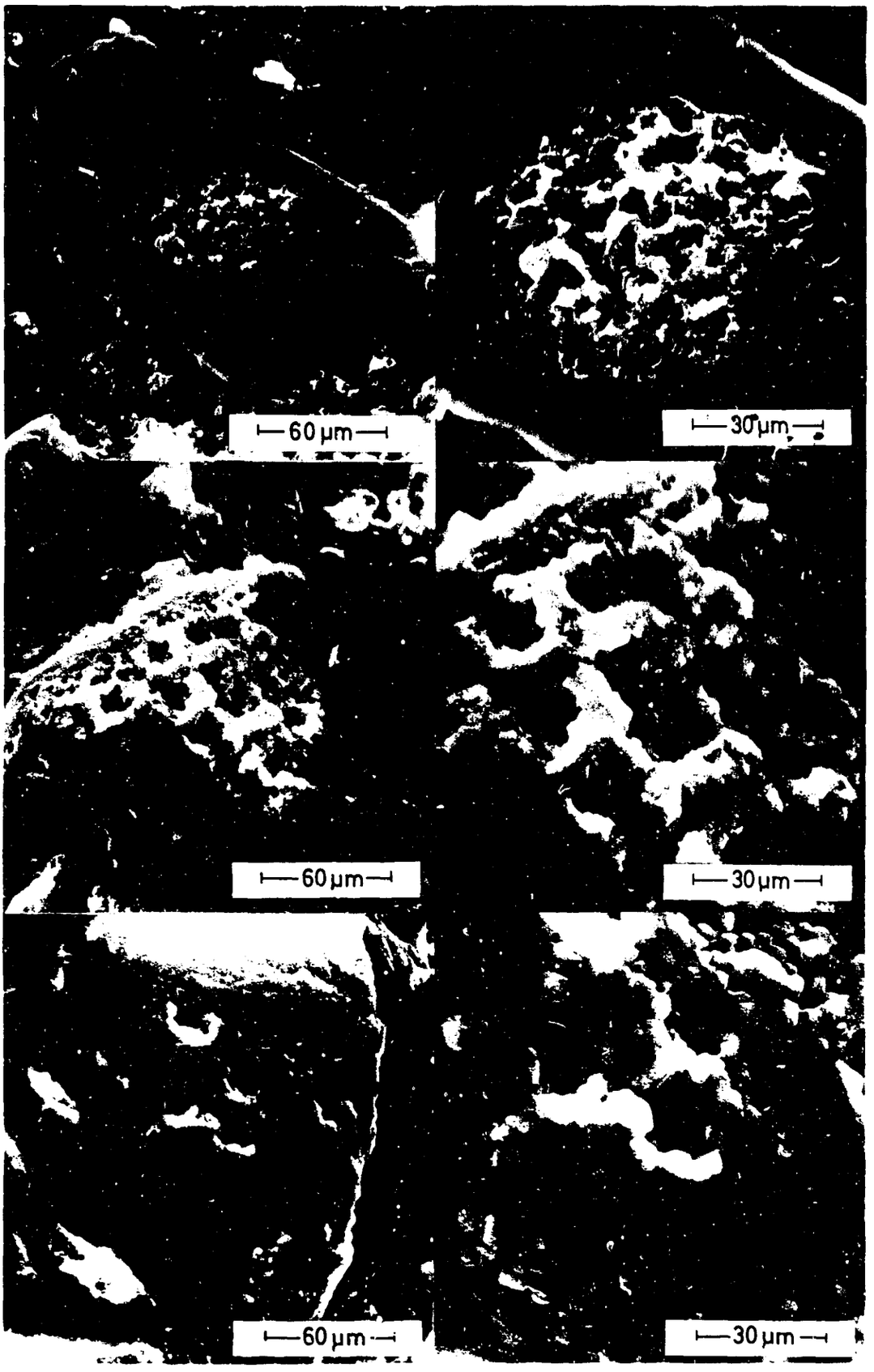

Fig. 6 SEM-pictures of the onset of the AP-reaction in a burning propellant at 1 atm

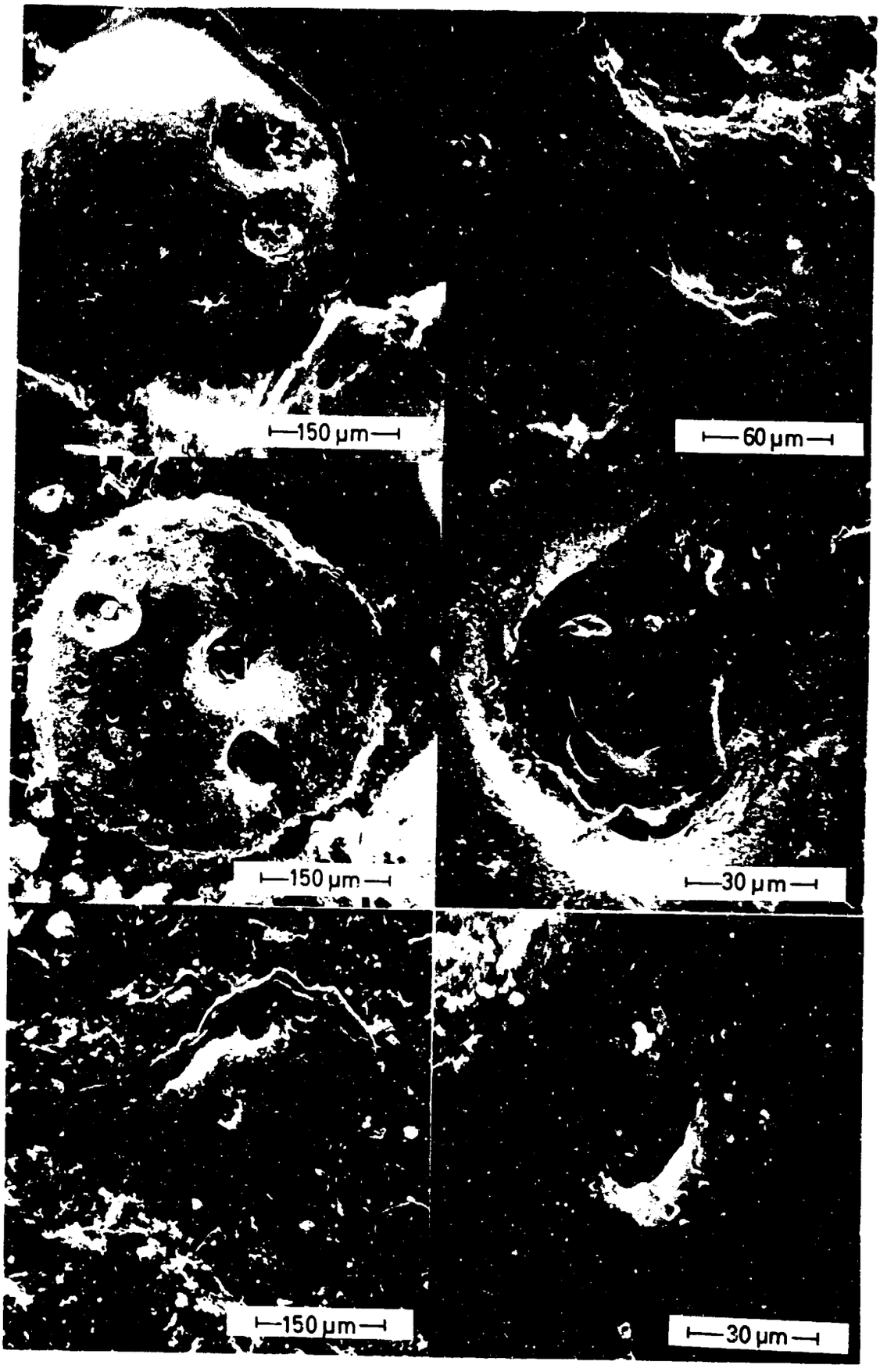

Fig. 7 SEM-pictures of the holes of a propellant at 1 atm

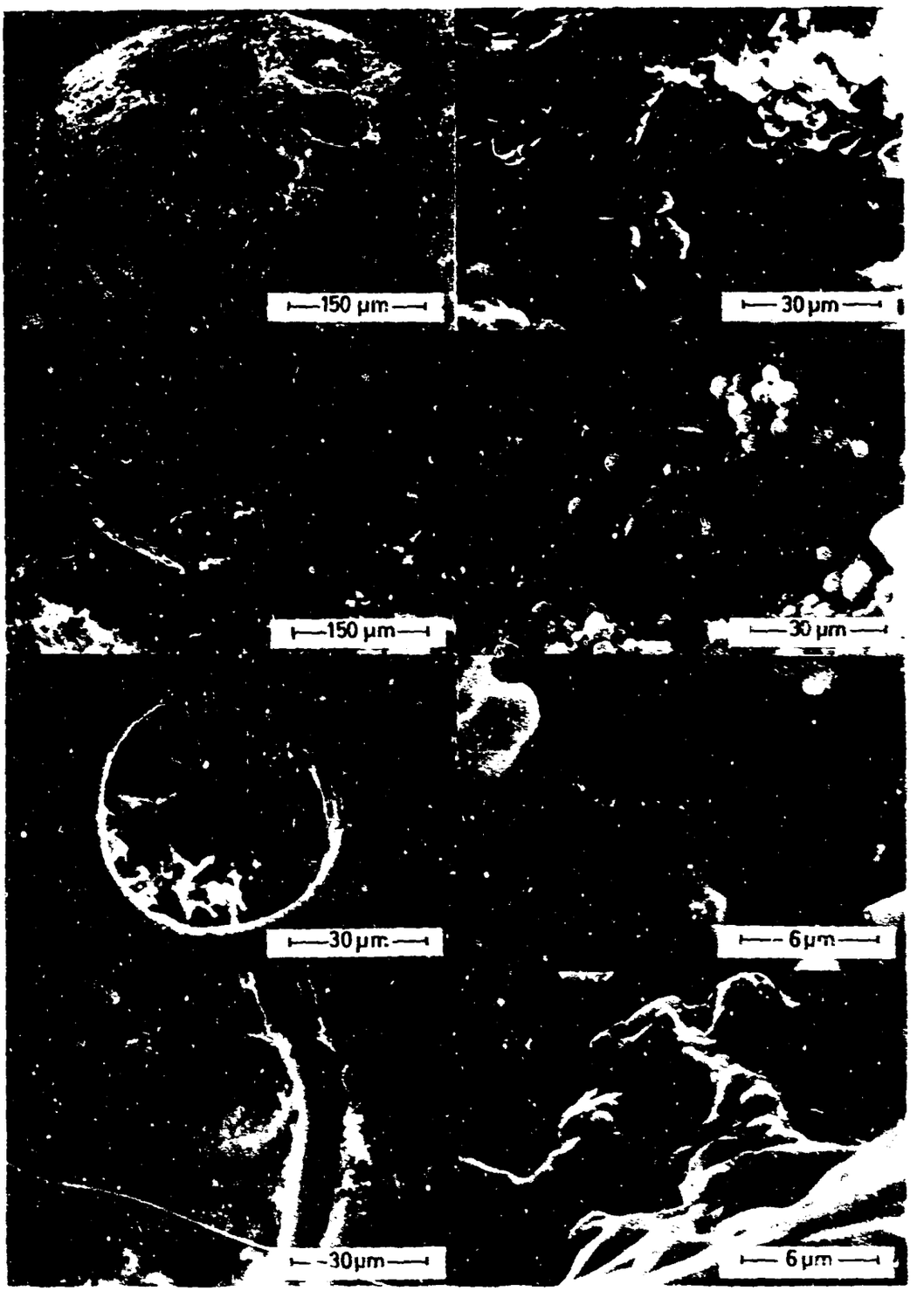

Fig. 8 The interior of holes in quenched AP-particles; pressure 1 atm

Low temperature decomposition at 230°C for 500 h

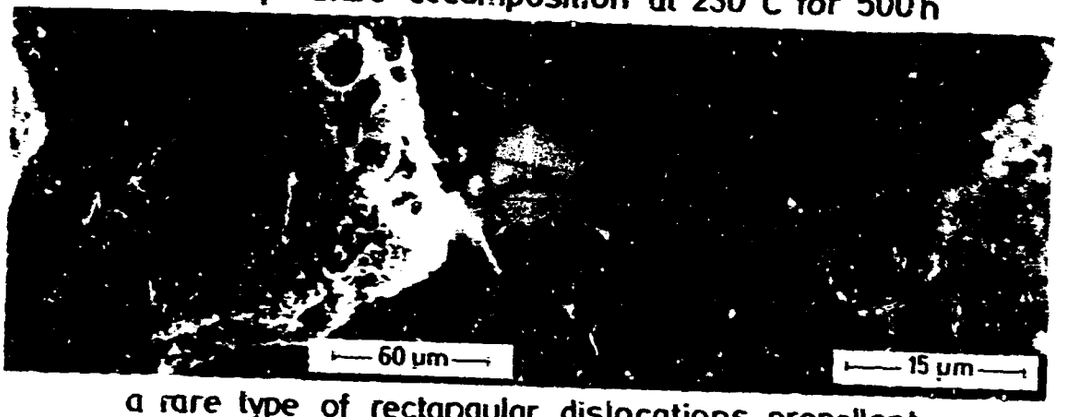

a rare type of rectangular dislocations propellant, quenchend by air

surface of an AP-particle on a propellant quenched by cold N_2

Fig. 9 Different Kinds of dislocations in AP-particles; pressure 1 atm

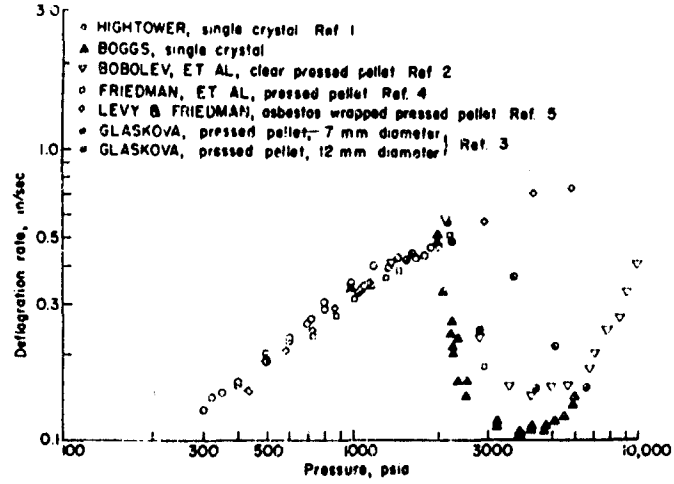

Fig. 10 Burning rate of AP (Boggs(17))

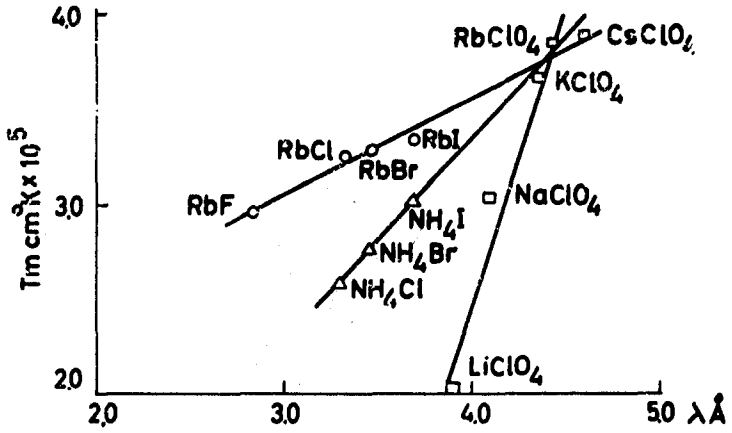

Fig. 11 Reduced melting point vs. interionic distance (after Cordes(6))

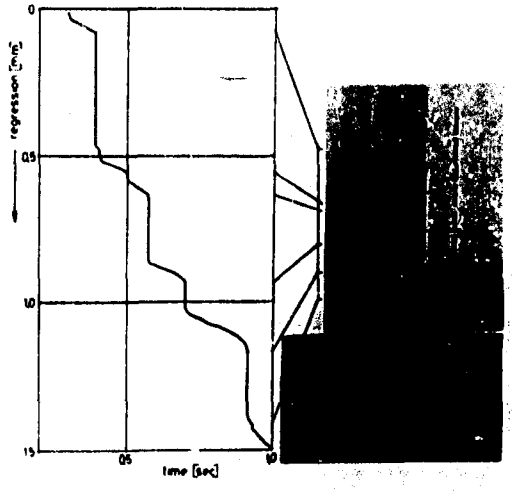

Fig. 12 Shadowgraph of burning AP propellant(18)

MIXING AND COMBUSTION OF SOLID PARTICLES IN TURBULENT STREAMS

By

Paolo O. Baronti
Advanced Technology Laboratories, Inc.
Jericho, N. Y.

and

Antonio Ferri
New York University, N. Y.

SUMMARY

The problem of mixing and combustion in adjacent turbulent streams, one of which contains solid particles, is analyzed. The analysis considers the response of solid particles to the spectrum of turbulent fluctuations in the surrounding medium, and determines the turbulent transport properties of particle clouds in terms of particle size, characteristic flow time and properties of the surrounding flow field. The conservation equations for turbulent mixing are then derived. Various particle sizes are considered, resulting in a multi-component particle diffusion process. Also, a new mechanism for particle combustion, based on the relative turbulent velocity between the particles and their surrounding oxidizing medium, is analyzed. The conservation equations are amenable to numerical integration; numerical examples are given, which show the characteristics of the particle diffusion and combustion process.

LIST OF SYMBOLS

a	defined by Eq. (1,a)
c_p	coefficient of specific heat
D	turbulent diffusion coefficient
E	energy spectrum function
h	static enthalpy
K	combustion efficiency coefficient, also coefficient of turbulent conductivity
L_e	Lewis number
m	mass
M	molecular weight
N_p	particle number density
p	static pressure
P_r	Prandtl number
$r_{\frac{1}{2}}$	half radius of mixing region
r_p	particle radius
R	jet radius
R_o	universal gas constant
S	particle surface area
t	time
T	static temperature
u,v	velocity components, also lagrangian components of velocity turbulent fluctuations
v_r	particle-fluid relative velocity
v_w	"washing velocity"
x,y	physical coordinates, also lagrangian coordinates
Z	random function, defined by Eq. (2)
α	mass fraction
γ_p	ratio between diffusion coefficients of solid particles and fluid particles
δ	height of mixing boundary
ε	diffusion coefficient
μ	viscosity coefficient
ρ	mass density
σ_p	specific gravity of solid particle
τ	shear stress
ω	angular frequency
$\dot{\omega}$	mass rate of production

SUBSCRIPTS AND SUPERSCRIPTS

f,g	refers to fluid or gas
i	refers to gaseous species i, also initial condition
L	lagrangian
p	refers to particle of radius r_p
T	refers to gas plus particles, also turbulent quantity
c	centerline value
(g)	gaseous phase
(s)	solid phase
$(\bar{\ })$	mean value
$(\ )'$	fluctuating value
$(\ )_t$	time derivative
$(\ )^*$	complex conjugate

THE STUDY OF TWO-PHASE FLOWS has received much attention in the past. Two main areas have been the object of investigation: a) inviscid and viscous laminar gas-particle flows, of which a comprehensive treatment is contained in the work of Marble (1), b) the flow of discrete solid particles in a homogeneous field of turbulence, as described and properly referenced in Hinze's textbook (2). An extension of Marble's treatment to include mixing of parallel streams containing solid particles has been carried out, later on, by Channapagadra et.al. (3), for laminar mixing and by Tirumalesa (4), for turbulent mixing. However, in the latter case, no detailed information on particle turbulent transport coefficients is provided.

A novel approach to the treatment of mixing and combustion of solid particles in a turbulent stream is presented here. Rational models for the contribution of turbulence in the mixing and combustion of solid particle clouds in turbulent streams are developed. These are then incorporated in the analysis of an inner stream, containing solid particles of different sizes, which mix and burn with an adjacent gaseous stream.

In synthesis, our approach is the following. We study first the motion of single solid particles in a homogeneous field of turbulence and determine, in terms of particle size, spectrum of turbulence and time, particle diffusion lengths and particle turbulent velocities. In doing so, concepts from statistical theory of turbulence, as well as results from previous investigations, are utilized; c.f., (5), (6) and (7). We then apply these results to define turbulent transport properties of clouds of solid particles in non-homogeneous turbulent flow fields and to determine the dependence of particle combustion upon the turbulence of the surrounding medium. With this information, we then formulate the conservation equations of the system composed of solid particles and gaseous species.

In general, when writing the conservation equations one must add to the contributions of turbulence, those contributions due to molecular effects, such as mean velocity and mean thermal lags as defined, e.g., by Marble, as well as all the other contributions associated with possible changes of state of solid or condensed phases. For simplicity these contributions will be disregarded here, but they can be easily included if desired. Indeed, the primary object of the present research is to emphasize the effects of turbulence on particle diffusion and combustion.

MOTION OF SOLID PARTICLES IN HOMOGENEOUS FIELDS OF TURBULENCE

The relevant feature in the motion of a solid particle in a turbulent medium, is its dynamical response to the spectrum of the turbulent fluctuations of the surrounding fluid. Because of inertia, the particle tends to lag with respect to the motion of the fluid; the greater the mass of the particle the greater is the lag. The velocity lag of the particle with respect to the fluid has important consequences: a) the particles will diffuse, in general, less than the fluid. b) if the relative motion between particle and surrounding fluid is strong enough, the classical concepts of particle combustion by diffusion controlled processes must be revised and a new interpretation of particle combustion in turbulent media is required.

A quantitative evaluation of particle diffusion and of particle-fluid relative velocity will be first obtained for the case of single particles in homogeneous turbulent fields. When the particle is spherical and follows Stokes drag law, the equation of motion of the particle is

$$\dot{v}_p(t) + a\, v_p(t) = a\, v_f(t) \tag{1}$$

where

$$a = 4.5\, \mu_f / \sigma_p r_p^2 \tag{1,a}$$

and where v_p and v_f are turbulent velocity components. The several restrictions under which such equation may be written are stated, e.g., in Hinze (2). Nevertheless, fairly conclusive results on the effects of inertia on particle motion can be obtained by solutions of Eq (1).

Solution of Eq (1) may now be obtained as follows. Represent the turbulent velocity of the fluid by the stochastic Fourier-Stieltjes integral

$$v_f(t) = \int_{-\infty}^{\infty} e^{i\omega t}\, dZ(\omega)$$

where ω is an angular frequency and where $dZ(\omega)$ is related to the Lagrangian energy spectrum by the relationship

$$\overline{dZ(\omega)\, dZ^*(\omega)} = E_L(\omega)\, d\omega \tag{2}$$

such that

$$\overline{v_f^2} = \int_{-\infty}^{\infty} E_L(\omega)\, d\omega \tag{3}$$

Then solution of Eq (1) yields

$$v_p(t) - e^{-at}\left[v_p(o) - \int_{-\infty}^{\infty} \frac{a}{a+i\omega}\, dZ(\omega)\right] + \int_{-\infty}^{\infty} \frac{a}{a+i\omega}\, e^{i\omega t}\, dZ(\omega) \tag{4}$$

where $v_p(o)$ is the initial turbulent velocity of the particle, at time t=0. A statistical description of $v_p(o)$ must now be specified in order to complete solution (4). For the mixing problem under study, where particles may be assumed to be injected into the mixing region with no initial turbulent velocity, it is realistic to take $v_p(o)=0$. Then:

$$v_p(t) = \int_{-\infty}^{\infty} \frac{a}{a+i\omega}\left[e^{i\omega t} - e^{-at}\right]\, dZ(\omega)$$

and

$$v_r(t) = v_f(t) - v_p(t) = \int_{-\infty}^{\infty} \frac{1}{a+i\omega}\, \left[i\omega e^{i\omega t} + ae^{-at}\right] dZ(\omega)$$

We then take averages with respect to a large number of particles and obtain, by invoking Eq (3)

$$\overline{v_r^2} = \int_{-\infty}^{\infty} \frac{\omega^2 + a^2 e^{-2at} - 2a\omega \sin \omega t e^{-at}}{a^2+\omega^2} E_L(\omega) d\omega \tag{5}$$

Consider now the displacement

$$y_p(t) = \int_o^t v_p(t)\, dt$$

of those particles which intersect, at t=0, the plane x=0. Then

$$y_p(t) = \int_{-\infty}^{\infty} \frac{a}{a+i\omega}\left[\frac{1}{i\omega}\, (e^{i\omega t}-1) + \frac{1}{a}(e^{-at}-1)\right] dZ(\omega),$$

and by taking averages

$$\overline{y_p^2}(t) = \int_{-\infty}^{\infty} \frac{a^2}{a^2+\omega^2}\left[2\, \frac{(1-\cos \omega t)}{\omega^2} + \frac{1}{a}\, (1-e^{-at})^2 \right. \tag{6}$$

$$\left. - \frac{1}{a}\, (1-e^{-at})\, \frac{2 \sin \omega t}{\omega}\right] E_L(\omega)\, d\omega$$

Finally, by representing the diffusion coefficient in the usual manner

$$\varepsilon = \frac{1}{2}\, \frac{d}{dt}\, \overline{y^2}(t)$$

one obtains

$$\varepsilon_p = (1-e^{-at}) \int_{-\infty}^{\infty} \frac{a^2}{a^2+\omega^2}\left[\frac{\sin \omega t}{\omega} + \frac{1}{a} e^{-at} - \frac{1}{a} \cos \omega t\right] E_L(\omega)\, d\omega \tag{7}$$

as compared with the diffusion coefficient

$$\varepsilon_f = \int_{-\infty}^{\infty} \frac{\sin \omega t}{\omega}\, E_L(\omega)\, d\omega \tag{8}$$

pertaining to fluid particles.

A description of the energy spectrum of the turbulent flow field is now required in order to evaluate the integrals of Eqs (3), (5), (7) and (8). The difficulties associated with the description of Lagrangian energy spectra are well known, c.f. (2) and (8); the point of view will be taken here of representing Lagrangian spectra by available Eulerian time spectra and of determining particle diffusion coefficient and particle relative velocity in a turbulent flow field of known spectral distribution $E(\omega)$.

For this purpose we select the energy spectrum of Figure (1) which is due to Favre (9) and determine in terms of a and in terms of time t, the ratios ϵ_p/ϵ_f and v_r^2/v_f^2. For typical particles having specific gravity of 1 gram/cm^3 and radii of 1, 10, 50 and 100 μ, respectively, the results are shown in Figures (2) and (3).

Clearly indicated by these figures is the dependence of particle diffusion coefficient and particle-fluid relative velocity, upon particle size. Also indicated is the strong dependence upon particle residence time, t. It follows, therefore, that the selection of the ratios ϵ_p/ϵ_f and v_r^2/v_f^2 is contingent upon the characteristic flow time of the problem one is interested in.

With these results, the study of turbulent mixing and combustion of solid particle clouds may now be undertaken.

TRANSPORT PROPERTIES OF PARTICLE CLOUDS IN MIXING REGIONS

The motion of solid particle clouds in a turbulent flow field must recognize the interaction among the particles themselves as well as the interactions with the surrounding gas. To a first approximation, the interactions among particles having random distribution of turbulent velocities are formally analogous to interactions among molecules in a gas; thus a representation along the lines of classical kinetic theory of gases would be in order. We present here an analysis of the simplest case, namely that of negligible interaction among the particles themselves.

With regard to interaction between turbulent gas flows and solid particles a suitable novel model must be developed. But the basic component of this model is provided by the analysis of the response of a solid particle to the turbulent velocity fluctuations described earlier.

The flow field produced by the mixing of two gaseous streams is non-homogeneous and has its own characteristic diffusion time. However, it appears reasonable to assume that local conditions of fluid density and velocity conform to conditions of homogeneity, with respect to the overall scale of the mixing process. With regard to diffusion times, for representative particles as those considered in Figures (2) and (3), the dynamical relaxation time of the particle may be of comparable magnitude to the gaseous diffusion time. Then, a piece-wise (with time) integration of the particle response at the prevailing local conditions is required.

Our approach to the solution of the problem at hand may be clarified now. We intend, in fact, to utilize the ratios ϵ_p/ϵ_f and v_r^2/v_f^2 pertaining to homogeneous turbulent flows and postulate that the same ratios hold for mixing problems at corresponding characteristic flow times. Then we regard the solid particle flow as a continuum turbulent flow and treat it by the usual type of conservation equations pertaining to turbulent gas flows. The only difference between these equations and those for the gaseous species present in the mixture, is that in the case of particles, different turbulent transport properties must be introduced.

Traditionally, in the case of turbulent gaseous mixing, the turbulent transport coefficients are described in terms of empirical expressions based on experimental data. Several models have been proposed in the past. Usually, the coefficients are taken to be constant at each cross section, that is, functions of the x-coordinate only. Most important, no matter what kind of model one selects, the momentum transport coefficient or eddy viscosity, is essentially expressed in the form

$$\mu_g \sim \ell\, \rho\, u$$

where ℓ ρ and u are characteristic lengths, densities and velocities, respectively. Eddy diffusivity and eddy conductivity are then provided by the relationships

$$(\rho D)_g = \frac{L_e}{P_r}\, \mu_g$$

and

$$K_g = \frac{\mu_g\, C_p}{P_r}$$

where L_e and P_r are the turbulent Lewis and Prandlt numbers, usually assumed to be of order one.

The formulation of the transport coefficients for the particle clouds is now immediately available by invoking previous conclusions. Indeed we may write

$$D_p = \gamma_p\, D_g$$

$$\mu_p = \gamma_p \mu_g$$

$$K_p = \gamma_p K_g$$

where $\gamma_p \equiv \epsilon_p/\epsilon_f$ is, in general, a function of particle size and flow time, and is given by the expressions previously derived.

EFFECTS OF TURBULENCE ON PARTICLE COMBUSTION

The previous results indicate not only different diffusion coefficients for the solid particles, but also the existence of a relative velocity between particles of larger size and the surrounding fluid. The implication of this relative velocity is of importance in defining particle combustion in a turbulent medium.

Assume for a moment that turbulence is not present, and that particle combustion is initiated. Then, during the steady process of combustion, according to classical combustion models, a combustion zone several times larger than the size of the particle is formed around the particle. Both the arrival rate of oxidizer to either the flame front or the surface, and the heating of the particle surface, are controlled by a diffusion process within this zone.

Consider then the effects of turbulence. The turbulence produces, for large size particles, a relative motion between the particle and the surrounding fluid. This motion is time dependent, has high frequencies, and its direction, relative to the particle, changes continuously and rapidly. Therefore, the configuration and the steadiness of the combustion zone as corresponding to the classical concept, is continuously disrupted and the classical models become inapplicable.

The very reasons which exclude the diffusion flame model suggest a new combustion mechanism. In fact, if there exists a turbulent relative velocity between the particle and the turbulent fluctuations around the particle, there also exists a relative mass flow. This brings oxidizer to the particle surface, initiates combustion if the particle surface is sufficiently hot, removes the combustion products from the surface and, therefore, creates a condition of continuous burning.

The relative velocity between particles and fluid defines, on the mean, the amount of oxidizer brought to the particle surface and represents the controlling mechanism of large particle combustion in a turbulent environment. We identify this relative velocity as the "washing velocity" and define it by the quantity.

$$v_w = (\overline{v_r^2})^{\frac{1}{2}} = (\overline{v_r^2}/\overline{v_f^2})^{\frac{1}{2}} \quad (\overline{v_f^2})^{\frac{1}{2}}$$

where $\overline{v_f^2}$ is the local mean square value of the turbulent velocity, and where $(\overline{v_r^2}/\overline{v_f^2})$ is, as discussed before, a function of particle size and particle residence time.

With these premises we are now in the position of defining the mass rate of arrival of oxidizer to the particle surface due to washing. This is given by

$$\dot{m}_{O_2} = S\, v_w\, \bar{\rho}_{O_2}$$

where S is the particle surface area, v_w the washing velocity, and $\bar{\rho}_{O_2}$ the average local concentration of oxygen around the particle. Then, for a general reaction of the type

$$a\, F(s) + b\, O_2(g) \rightarrow c\, P(g) \quad ,$$

the burning rate of the solid particle of chemical species F and molecular weight M_f is given by

$$\dot{m}_F = -K(aM_F/bM_{O_2})\dot{m}_{O_2}$$

and the rate of production of combustion products P(g) by

$$\dot{m}_p(g) = K\left[(aM_F + bM_{O_2})/bM_{O_2}\right]\dot{m}_{O_2}$$

where K is an efficiency coefficient.

Admittedly, more detailed analyses, and, more likely, experimental results are warranted for a detailed quantitative evaluation of the coefficient K, to account for effects such as molecular scale effects, surface reaction efficiency and particle-particle interaction. However, the overall feature of the washing mechanism on particle combustion is indicated by the previous discussion.

These concepts have been applied by the authors, (10), for the determination of combustion times of hot spherical boron particles of different sizes. Typical results pertaining to flow conditions encountered in the secondary combustor of an air-augmented solid rocket engine are presented in Figure (4). Shown in the figure is the percent variation of the boron particle mass during a combustion process controlled by washing for a chemical reaction of the type

$$2\ B(s) + 3/2\ O_2 \rightarrow B_2\ O_3 \quad (g)$$

(The validity of this reaction for hot boron particles has been discussed in (10)). Particles having an initial radius of 50 and 100 μ and entering the turbulent flow field with zero initial turbulent velocity, are considered. The fluid surrounding the particle has been taken to be air at a temperature of 500°K and with a turbulent velocity of about 50 ft/sec. A value of the coefficient K equal to unity was assumed.

The combustion mechanism based on washing applies only to larger size particles, say particles having a radius of more than 50 μ. For smaller particles, no washing occurs and in the limit of very small particles, say of the order of 1 μ, free molecular transfer will prevail. For intermediate size particles a proper superposition of the two effects must be considered. This is also discussed in (10).

THE CONSERVATION EQUATIONS

With the assumptions, previously stipulated, of no mean velocity and thermal lag between particles and surrounding fluid, we formulate here the conservation equations for the mixing of two coaxial streams containing several gaseous species and clouds of reacting solid particles of different sizes. The usual boundary layer approximations are made. It is also assumed that the mixing occurs at constant pressure and that the laminar viscous terms are negligible with respect to the turbulent ones.

In deriving the conservation equations we first relate instantaneous values to mean and fluctuating values by the relationships

$$u_g = \bar{u} + u' \qquad u_p = \bar{u} + u'_p$$

$$v_g = \bar{v} + v' \qquad v_p = \bar{v} + v'_p$$

$$\rho_i = \bar{\rho}_i + \rho'_i \qquad \rho_p = \bar{\rho}_p + \rho'_p$$

$$h_i = \bar{h}_i + h'_i \qquad h_p = \bar{h}_p + h'_p$$

where i refers to the ith gaseous species and where p refers to the particle cloud composed of spherical particles of radius r_p.

We then perform the averaging procedures by the standard rules. The resulting equations are written below. For convenience mean quantities will be now indicated without a bar.

CONSERVATION OF MASS. For the ith gaseous species; the diffusion equation is

$$\frac{\partial}{\partial x}\, y\, \rho_i\, u + \frac{\partial}{\partial y}\, y\, \rho_i\, v = -\frac{\partial}{\partial y}\, y\, \overline{\rho'_i\, v'} + \dot{\omega}_i$$

where $\dot{\omega}_i$ is the mass rate of formation of species i.

For the pth particle cloud,

$$\frac{\partial}{\partial x}\, y\, \rho_p\, u + \frac{\partial}{\partial y}\, y\, \rho_p\, v = -\frac{\partial}{\partial y}\, y\, \overline{\rho'_p\, v'_p} + \dot{\omega}_p$$

where $\dot{\omega}_p$ is the mass rate of burning of the pth particle cloud.

We now impose the condition

$$\sum_i \overline{\rho'_i\, v'} + \sum_p \overline{\rho'_p\, v'_p} = 0 \qquad (9)$$

and obtain the overall continuity equation

$$\frac{\partial}{\partial x}\, y\, \rho_T\, u + \frac{\partial}{\partial y}\, y\, \rho_T\, v = 0 \qquad (10)$$

where

$$\rho_T = \sum_i \rho_i + \sum_p \rho_p$$

We then express the correlations $\overline{\rho_i' v_i'}$ and $\overline{\rho_p' v_p'}$ in the form

$$\overline{\rho_i' v'} = -D_g \frac{\partial \rho_i}{\partial y}$$

$$\overline{\rho_p' v_p'} = -D_p \frac{\partial \rho_p}{\partial y} = -\gamma_p D_g \frac{\partial \rho_p}{\partial y}$$

by invoking the general relationship $\overline{v' \Gamma'} = \varepsilon \frac{\partial \bar{\Gamma}}{\partial y}$ for the turbulent diffusion of the scalar $\Gamma = \bar{\Gamma} + \Gamma'$.

Finally, by defining

$$\alpha_i = \rho_i / \rho_T \; ; \; \alpha_p = \rho_p / \rho_T$$

and imposing conditions (9), we obtain

$$\rho_T u \frac{\partial \alpha_i}{\partial x} + \rho_T v \frac{\partial \alpha_i}{\partial y} = \frac{1}{y} \frac{\partial}{\partial y} \left[y \rho_T D_g \left(\frac{\partial \alpha_i}{\partial y} + \alpha_i \frac{\sum_p (1-\gamma_p) \partial \alpha_p / \partial y}{1 - \sum_p \alpha_p (1-\gamma_p)} \right) \right] + \dot{\omega}_i \qquad (11)$$

$$\rho_T u \frac{\partial \alpha_p}{\partial x} + \rho_T v \frac{\partial \alpha_p}{\partial y} = \frac{1}{y} \frac{\partial}{\partial y} \left[y \rho_T \gamma_p D_g \left(\frac{\partial \alpha_p}{\partial y} + \alpha_p \frac{\sum_p (1-\gamma_p) \partial \alpha_p / \partial y}{1 - \sum_p \alpha_p (1-\gamma_p)} \right) \right] + \dot{\omega}_p \qquad (12)$$

OVERALL MOMENTUM. The overall momentum equation of the gas-particle system is obtained by summation of the individual equations of conservation of momentum of all gaseous species and of all particle clouds. The result is

$$\rho_T u \frac{\partial u}{\partial y} + \rho_T v \frac{\partial u}{\partial y} = \frac{1}{y} \frac{\partial}{\partial y} \left[y \left(\rho_g \overline{u' v'} + \sum_p \rho_p \overline{v_p' u_p'} \right) \right] \qquad (13)$$

$$= \frac{1}{y} \frac{\partial}{\partial y} \left[y \left(\tau_g + \sum_p \tau_p \right) \right]$$

$$= \frac{1}{y} \frac{\partial}{\partial y} \left[y \left(\mu_g + \sum_p \mu_p \right) \frac{\partial u}{\partial y} \right]$$

ENERGY. Again, the overall energy equation is obtained by adding together the contributions of the individual gaseous species and solid particle clouds, to yield

$$\rho_T u \frac{\partial h_T}{\partial x} + \rho_T v \frac{\partial h_T}{\partial y} = \left(\tau_g + \sum_p \tau_p \right) \frac{\partial u}{\partial y} - \frac{1}{y} \frac{\partial}{\partial y} \left[y \left(\sum_i \rho_i \overline{v' h_i'} \right. \right.$$

$$\left. \left. + \sum_i h_i \overline{\rho_i' v'} + \sum_p \rho_p \overline{v_p' h_p'} + \sum_p h_p \overline{\rho_p' v_p'} \right) \right]$$

where

$$h_T = \sum_i \alpha_i h_i + \sum_p \alpha_p h_p$$

We now define

$$\overline{v' h_i'} = - D_g \frac{\partial h_i}{\partial y}$$

$$\overline{v_p' h_p'} = - D_p \frac{\partial h_p}{\partial y} = - \gamma_p D_g \frac{\partial h_p}{\partial y}$$

and then, by invoking the two diffusion Equations, (11) and (12), we obtain

$$\rho_T u c_p \frac{\partial T}{\partial x} + \rho_T v c_p \frac{\partial T}{\partial y} = \left(\tau_g + \sum_p \tau_p \right) \frac{\partial u}{\partial y} \qquad (14)$$

$$+ \frac{\partial}{\partial y} \left[y \rho_T D_g \frac{\partial T}{\partial y} \left(\sum_i \alpha_i c_{pi} + \sum_p \gamma_p \alpha_p c_{pp} \right) \right]$$

$$+ \frac{\partial T}{\partial y} \left[\sum_i c_{pi} \rho_T D_g \left(\frac{\partial \alpha_i}{\partial y} + \alpha_i \frac{\sum_p (1-\gamma_p) \partial \alpha_p / \partial y}{1 - \sum_p \alpha_p (1-\gamma_p)} \right) \right.$$

$$+ \sum_p c_{pp} \gamma_p \rho_T D_g \left(\frac{\partial \alpha_p}{\partial y} + \alpha_p \frac{\Sigma (1-\gamma_p) \partial \alpha_p / \partial y}{1 - \Sigma \alpha_p (1-\gamma_p)} \right) \Big] - \sum_p h_p \dot{\omega}_p - \sum_i h_i \dot{\omega}_i$$

The conservation equations, Eqs. (10), (11), (12), (13) and (14), are then complemented by the equation of state, by a description of the turbulent transport coefficients and of the production terms ω_i, ω_p, and by a specification of the initial and boundary conditions.

For a system of solid particles and gaseous species, by disregarding the volume occupied by the particles, the equation of state may be written in the form

$$\rho_T = p \left(R_o T \sum_i \frac{\alpha_i}{M_i} \right)^{-1}$$

where the summation over i includes the gaseous species only.

Turbulent transport properties, production terms, and initial conditions for particle clouds will be detailed below for a set of typical numerical examples.

INTEGRATION OF THE CONSERVATION EQUATIONS AND NUMERICAL EXAMPLES

Eqs. (10) to (14) have been transformed from the x-y variables to the x-ψ variables, where ψ is the stream function or von Mises coordinate. The equations have then been cast in a finite difference form and solved by an explicit finite difference scheme. The formulation of Zeiberg and Bleich, (11), has been followed.

A few applications of these equations to problems of mixing and burning of solid particles have then been performed. In this connection an eddy viscosity for gaseous species of the form

$$\mu_g = \kappa \, r_{\frac{1}{2}} \, (\rho u)_{\ell}$$

has been assumed, by following Zakkay, (12). It then results, for particle clouds, that

$$\mu_p = \gamma_p \, \mu_g \, (\rho_p / \rho_g)_{\ell}$$

and

$$D_p = \gamma_p \, D_g$$

Combustion of solid boron particles by the washing mechanism has also been considered. Then, for the chemical reaction

$$2B\,(s) + O_2(g) \rightarrow B_2O_3(g) \quad ,$$

one has

$$\dot{\omega}_B = - \Sigma N_p \dot{m}_B$$

$$\dot{\omega}_{B_2O_3} = \Sigma N_p \dot{m}_{B_2O_3}$$

$$\dot{\omega}_{O_2} = - \Sigma N_p \dot{m}_{O_2}$$

where $\dot{m}_{O_2} = K S v_w \rho_{O_2}$, $\dot{m}_B = 0.455 \, \dot{m}_{O_2}$, $\dot{m}_{B_2O_3} = 1.45 \, \dot{m}_{O_2}$ and where $N_p \equiv \alpha_p \rho_T / m_p$ is the number density of solid particles of radius r_p.

Step profiles for the initial distribution $N_p(y)$ of particle number density have been taken here. However, the program is capable of handling arbitrary distributions of particle number density and any large (although discrete) number of particle initial radii.

Typical numerical results are given in Figures (5) to (8). Figures (5) and (6) refer to a jet of nitrogen containing particles characterized by values of γ_p equal to unity, one-half and zero. The jet exhausts into an air stream. The two streams are parallel. The velocity of the jet is 500 ft/sec., the velocity of the external stream is 700 ft/sec. The temperature of both streams is 300°K, the pressure is 1 atm. The initial mass density of each particle cloud is 16% that of nitrogen. Clearly indicated by these Figures is the different mixing of the three particle clouds. No combustion has been assumed in this case.

Shown in Figures (7) and (8) are some characteristic features of the mixing and combustion of a solid particle cloud. The solid particles have an initial radius of 100 μ and are contained in a nitrogen jet which exhausts into an air stream. The jet has a radius of 0.1 ft., an initial velocity of 500 ft/sec., and a temperature of 2000°K. The initial mass density of the particles is one-half that of nitrogen. The external stream has a velocity of 700 ft/sec. and a temperature of 1000°K. The pressure is 10 atm. A particle combustion process based on "washing" is considered. The assumption is made that the combustion efficiency coefficient, K, is equal to unity and that the washing velocity is 6% the local mean velocity in the mixing region. Indicated by the figures are the mixing boundaries of the particle cloud and of the combustion products and typical radial distributions.

CONCLUSIONS

The aim of this effort has been that of defining some new physical concepts and of providing analytical expressions for the mixing and combustion of solid particles in turbulent streams. It was found that existing analytical models for gaseous mixtures cannot be readily applied to mixtures containing solid particles. Depending upon their inertia, and upon the properties of the surrounding medium and the residence time, the solid particles exhibit a characteristic dynamical response to the fluctuations of the surrounding turbulent flow field. This response controls particle diffusion and, for particles having a radius of 50 μ or more, the particle combustion process. Outlined in the paper, is the derivation of analytical models which take such effects into account. Specific expressions for diffusion coefficients and combustion rates have been derived and typical examples of mixing and combustion of particle clouds have been investigated numerically.

REFERENCES

1. Marble, R.E., "Dynamics of a Gas Containing Small Solid Particles," Fifth AGARD Combustion and Propulsion Colloquium, Pergamon Press, Oxford, England 1963.

2. Hinze, J.O., "Turbulence," McGraw Hill Book Company, Inc., New York, 1959.

3. Channapragada, R.S., Anderson, R., Duvvuri, T., and Gopelakrishnan, A., "Mixing, Ignition and Combustion Analysis of Air Augmented Solid Rockets with Boron Particles," AIAA 3rd Propulsion Joint Specialist Conference, Washington, D.C., 1967.

4. Tirumalesa, D., "Two-Phase Flow Equations for Turbulent Boundary-Layer-Type Flows," AIAA J. 5, 2077-2079, 1967.

5. Friedlander, S.K., "Behavior of Suspended Particles in a Turbulent Fluid," AI.Ch.E. J. 3, 381-385, 1967.

6. Soo, S.L., "Statistical Properties of Momentum Transfer in Two-Phase Flow," Chem. Eng. Sci., 5, 57-67, 1956.

7. Csandy, G.T., "Turbulent Diffusion of Heavy Particles in the Atmosphere," J. Atmos. Sci., 20, 201-208, 1963.

8. Lumley, J.L. and Panofsky, H.A., "The Structure of Atmospheric Turbulence," Interscience Publishers, New York 1964.

9. Favre, A., Gaviglio, J. and Dumas, R., "Recherche Aeronaut," No. 32, p 21, 1953.

10. Baronti, P. and Ferri, A., "Mixing and Combustion of Solid Particles in Turbulent Streams, Part I," ATL TR-112, 1968.

11. Zeiberg, S. and Bleich, G., "Finite Difference Calculation of Supersonic Wakes," AIAA J. 2, 1396-1404, 1964.

12. Zakkay, V., Krause, E. and Woo, S.D.L., "Turbulent Transport Properties for Axisymmetric Heterogeneous Mixing," AIAA J. 2, 1939-1947, 1964.

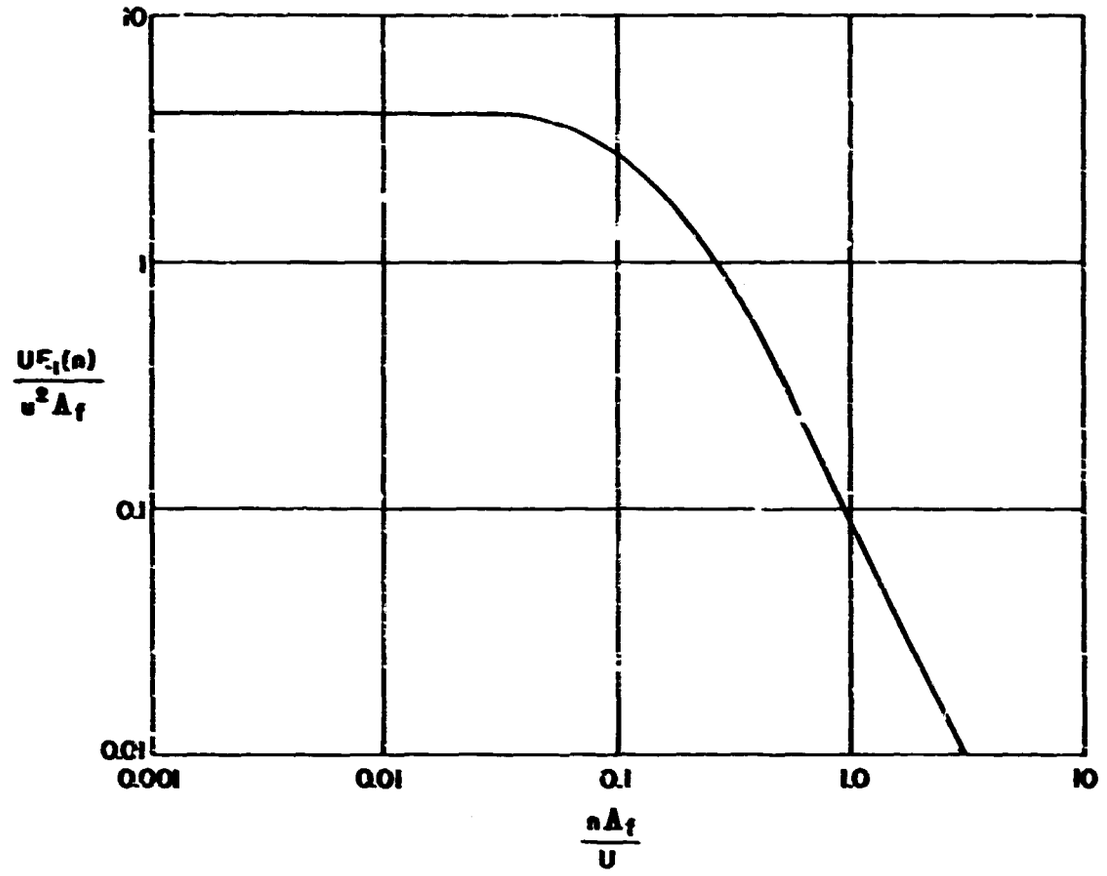

FIGURE 1. ENERGY SPECTRUM TAKEN FROM FAVRE, (9)

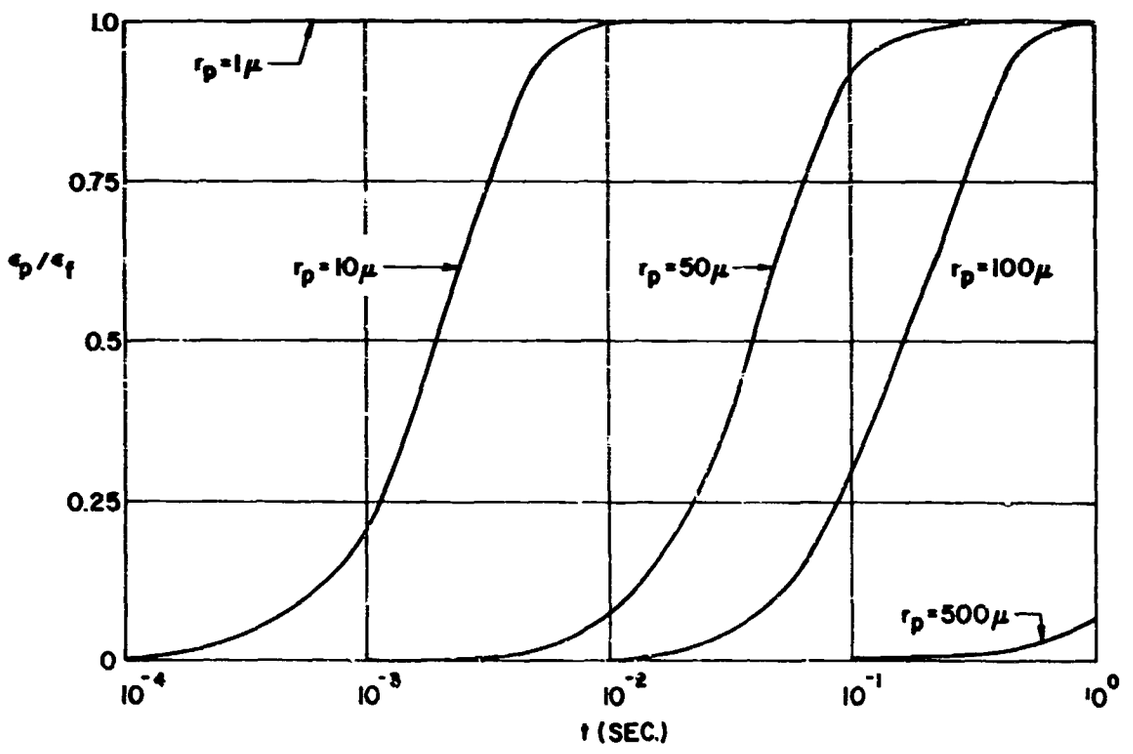

FIGURE 2. PARTICLE-FLUID DIFFUSIVITY RATIOS

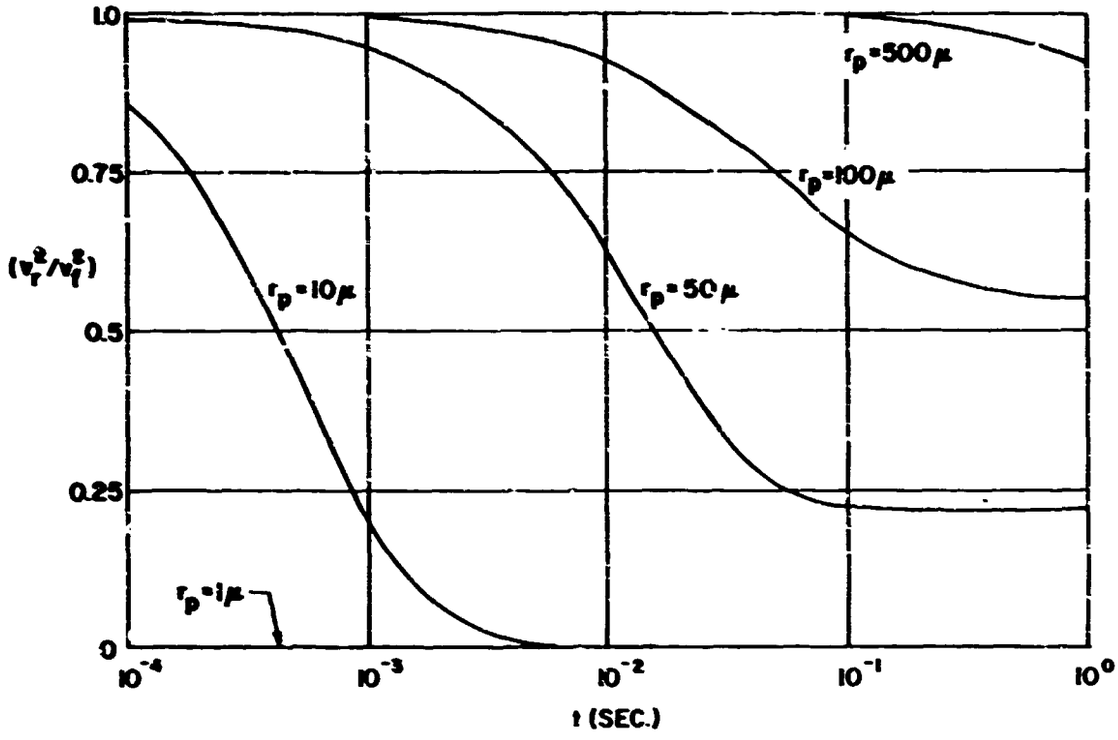

FIGURE 3. PARTICLE-FLUID MEAN SQUARE RELATIVE VELOCITIES

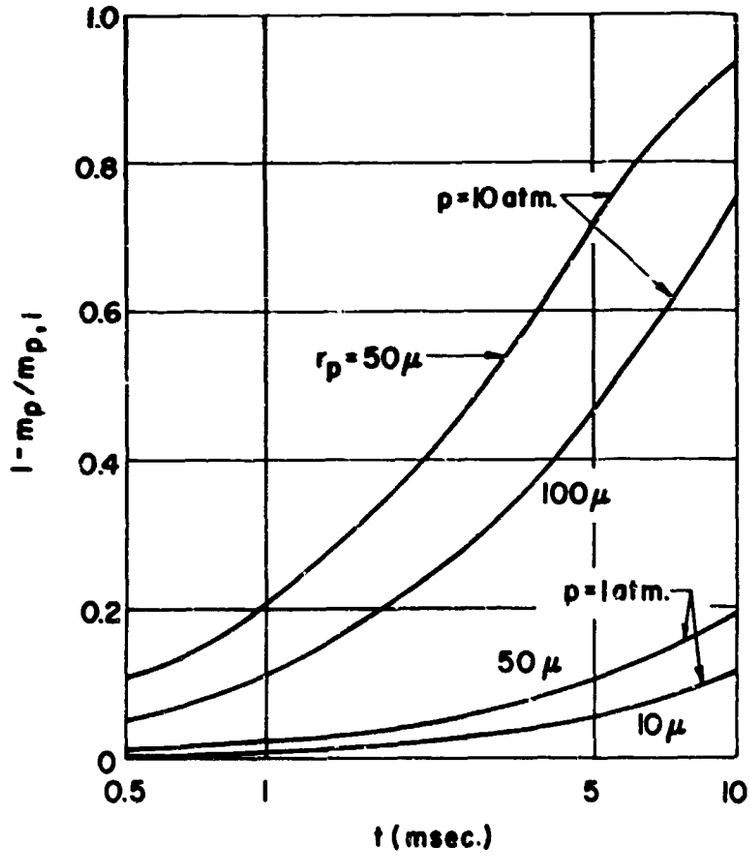

FIGURE 4. COMBUSTION OF BORON PARTICLES BY "WASHING." TYPICAL EXAMPLES

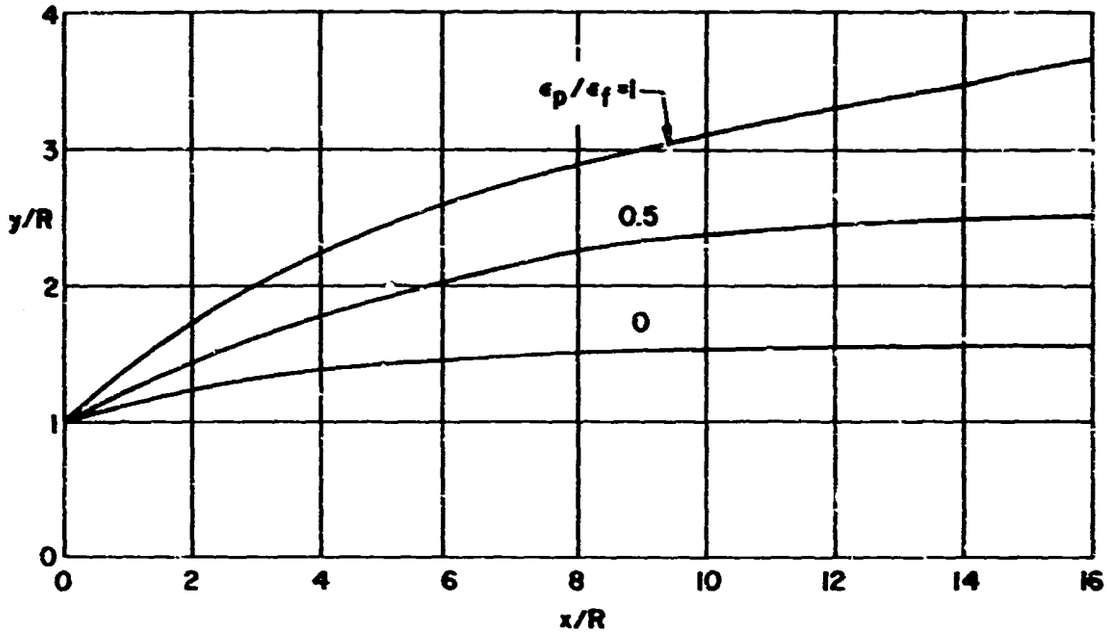

FIGURE 5. MIXING BOUNDARIES OF PARTICLE CLOUDS

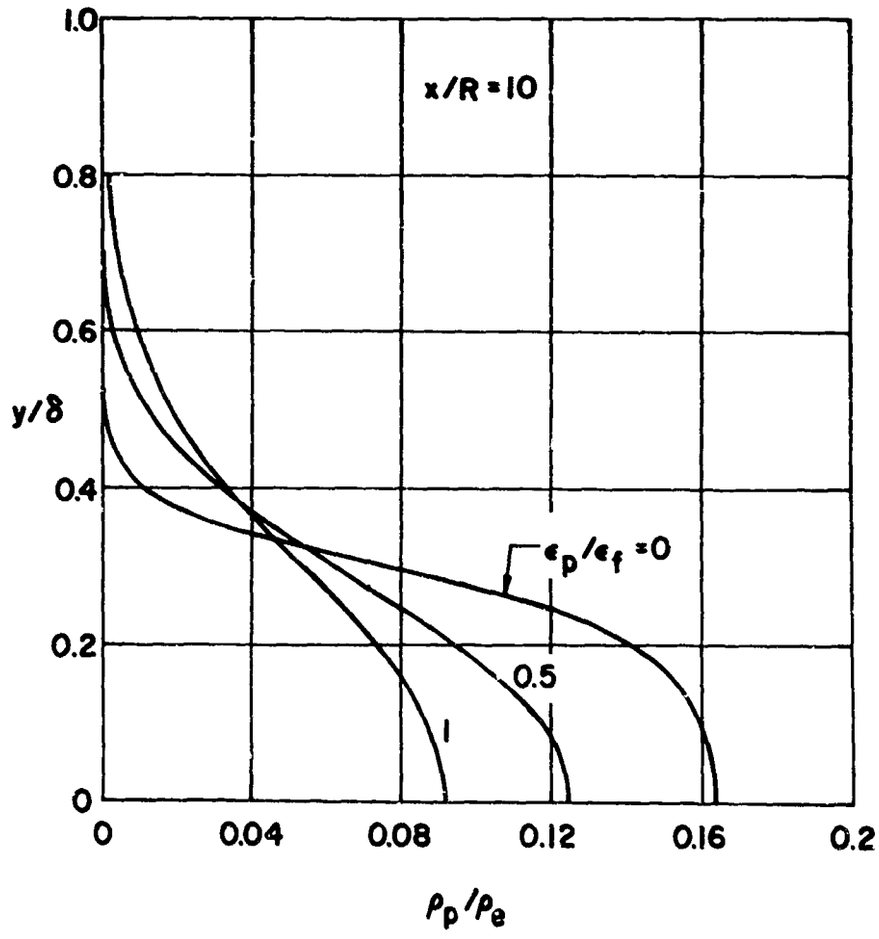

FIGURE 6. RADIAL DISTRIBUTION OF PARTICLE NUMBER DENSITIES

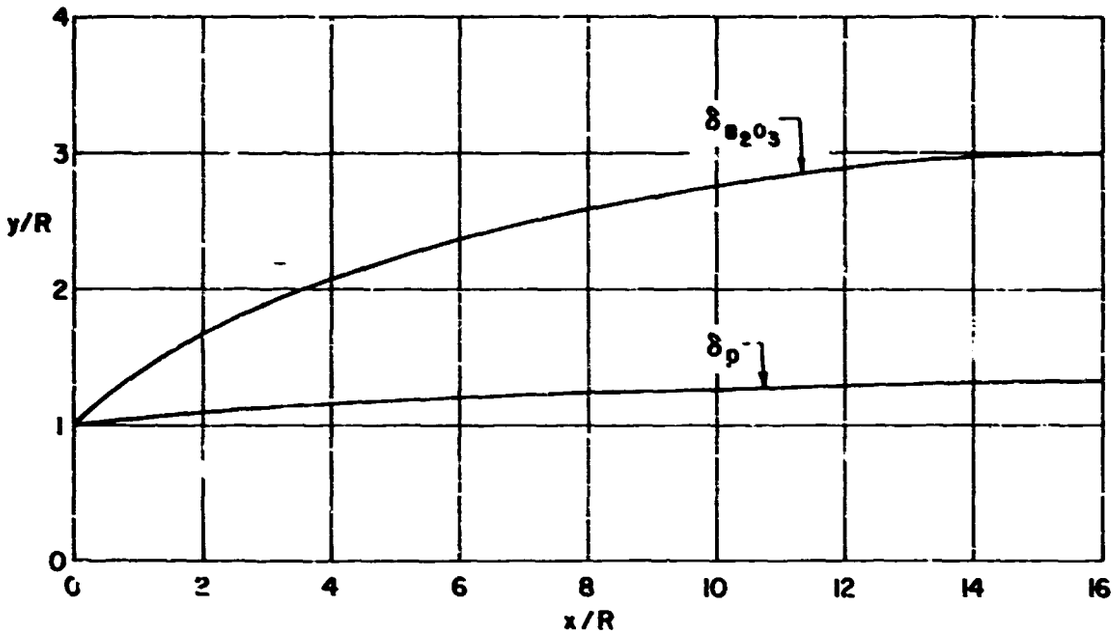

FIGURE 7. MIXING BOUNDARIES OF BORON PARTICLE CLOUD AND OF COMBUSTION PRODUCTS

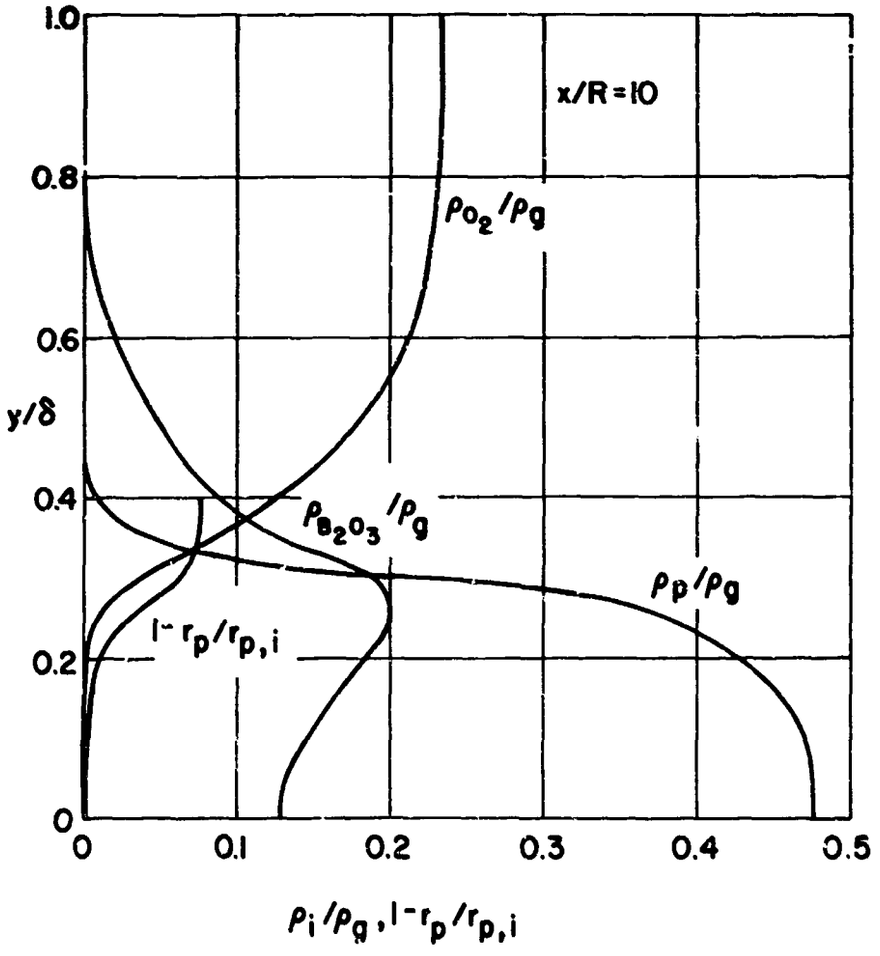

FIGURE 8. RADIAL DISTRIBUTIONS OF BORON PARTICLES AND GASEOUS MASS FRACTIONS AND OF PARTICLE RADII

DIFFUSION FLAMES OF MAGNESIUM VAPOUR AND OXYGEN AT LOW PRESSURES

by

B.E.L. Deckker and B.K.G. Rao

Department of Mechanical Engineering
University of Saskatchewan
Saskatoon, Canada

SUMMARY

The combustion of magnesium vapour in a quiscent atmosphere of oxygen and argon has been studied at low pressures (0.5 to 0.9 torr). The gross structure of these flames has been found to depend on the composition of the environment, the pressure in the combustion chamber, and on the temperature of vaporization. Steady flame conditions are difficult to maintain because of the deposition of oxide in the nozzle passage, but by the proper selection of the experimental variables reasonably steady conditions can be achieved for 2 to 4 minutes. The temperature distribution in the flame has been determined using sub-miniature sheathed, and grounded junction, thermocouples. Higher temperatures and lower intensities of emitted radiations have been recorded with decreasing oxygen concentrations. A critical value of oxygen concentration exists below which total combustion of the vapour does not occur.

The applicability of Polanyi's dilute diffusion flame method to these flames has been discussed. Reaction rate parameters have been obtained from the temperature pattern method and from the method of photographic photometry. These methods are based on the dilute diffusion flame model, and the results favour the predominance of homogeneous rather than heterogeneous reaction, as has been suggested in the literature.

SYMBOLS

A	A constant
C	Concentration
D	Diffusion coefficient of magnesium vapour and Argon
k	Reaction Rate Constant
n	Index used to designate order of reaction with respect to atmospheric reactant concentration
r	Radius in flame: r' denotes a particular radius
T	Absolute Temperature: T' denotes temperature at radius r'
V	Jet Velocity
α	A constant
ω	Reaction Rade Parameter ($\omega^2 = \frac{k}{D} C_A^n$)

Subscripts

A	Denotes atmospheric reactant (Oxygen)
N	Denotes nozzle reactant (Magnesium vapour)

THE COMBUSTION of metals such as magnesium is characterised by the burning taking place at some distance from the surface in the vapour phase, as distinct from surface burning. Following Glassman (1), the mode of burning can be predicted from a knowledge of the melting and boiling points of metals and their oxides. Glassman postulated that if the boiling point of the oxide is greater than that of the metal, then, burning occurs in the vapour phase; if the boiling point of the metal is greater, then, surface burning takes place. According to this hypothesis magnesium, among other metals such as, aluminium, beryllium, and lithium, burn in the vapour phase; whereas, metals such as boron, titanium and zirconium burn at the surface.

The investigation which forms the basis of this paper is concerned with the determination of the gross structure, and certain other features of the reaction, of magnesium-oxygen diffusion flames at low pressures. When the vapour is generated in sufficient quantity, the gross structure of these flames may be studied in a similar manner to that used for gaseous hydrocarbon flames. However, an important difference between gaseous flames and metal diffusion flames is the presence of condensed products in the reaction zone. The presence of these products gives metal flames a distinctive character, and also creates additional problems in their study. A difficulty that has been encountered in this investigation, and in that of Markstein (2) as well, is the accumulation of the oxide not only on a surface introduced into the flame but also in the flow passage at the tip of the burner. However, the presence of oxide particles in the flame might well be exploited to reveal certain aspects of the structure of these flames. Some problems that have arisen in the course of this investigation due to oxide deposition are briefly discussed.

A property of a flame that is essential to the description of its structure is the local temperature and its distribution in the flame. These have systematically been measured by the authors in low pressure magnesium vapour-oxygen flames, using sub-miniature sheathed and grounded-junction thermocouples. Although thermocouples have been used in low pressure gaseous flames, the authors have not been able to find a published reference to their use in metal flames. There are, of course, experimental difficulties involved in this technique of temperature measurement due to the deposition of oxide on the probe surface, and, also, in the interpretation of data obtained by this means. Attempts appear to have been made to determine the temperature of magnesium vapour flames by optical methods (3), the success of which is not generally known.

Apart from a systematic determination of the gross structure such as, shape, size and colour of magnesium vapour-oxygen flames under different environmental conditions, the nature of the reaction, and an estimate of the reaction rate constant are also relevant matters of interest. The nature of the reaction of these flames at low pressures is not clearly known at present. From the results of his early investigation of $Mg-O_2-Ar$ flames, Markstein has suggested that, after nucleation, the oxide particles may grow predominantly by reaction on their surfaces (2), (heterogeneous reaction). Later, however, he suggested that his earlier interpretation may have to be qualified, but he does not appear to have reached a final conclusion on this point (4). The results of the authors' investigation have led them to the view that the reaction process could be predominantly homogeneous. It is clear, therefore, that the uncertainty regarding the nature of the reaction in these flames has not yet been resolved.

It is difficult to produce steady magnesium vapour flames for any length of time, due, mainly, to continually changing flow conditions as a result of the accumulation of the oxide in the flow passage near the flame. Thus, the time during which the flame is reasonably steady is limited. The accumulation of oxide on a thermocouple surface immersed in the flame is a more serious problem and severely restricts the time during which the probe can be so exposed. The effects of the composition and pressure of the environment on the rate of oxide accumulation in the flow passage, and on some features of magnesium flames are also briefly discussed.

EXPERIMENTAL DESIGN

Details of the apparatus and experimental procedures used during this investigation may be found in references (5), (6) and (7). Flames have been obtained in a slowly moving environment of oxygen diluted with argon, in a stainless steel combustion chamber of large volume (about 30 litres). Magnesium vapour is generated from turnings contained in a cylindrical boron nitride crucible in a stainless steel vaporizer tube. A sectional view of the combustion chamber is given in Figure 1. The temperature required for vaporizing the magnesium at the pressure prevailing in the combustion chamber is obtained by joule-heating the vaporizer tube. The vapour is entrained by the flow of carrier gas (argon) through the annular space between the crucible and the vaporizer tube, and discharged into the combustion chamber through a nozzle located at the tip of the tube. The vapour burns in the form of a spherical flame while diffusing outwards, Figure 2.

The current for heating the vaporizer tube is supplied by a power controller in conjunction with a temperature controller. The temperature of the tube can be maintained to within $\pm \frac{1}{2}\%$ of the desired value. The crucible temperature is measured by means of a stainless steel, sheathed Chromel-Alumel thermocouple which not only supports the crucible but also actuates the temperature controller. The combustion chamber is continuously evacuated at a rate compatible with the desired pressure. The oxygen and argon which provide the environment are commercially pure, and are dried before being admitted into the combustion chamber. The partial pressure of oxygen in the combustion chamber is determined by means of an oxygen transducer (Chemtronics Inc. Model GP 10S), and the consumption of oxygen is given by the difference between the output of the transducer before, and during, combustion. The transducer is calibrated by exposing it to the ambient air.

Temperatures in magnesium vapour flames have been measured by means of a sub-miniature, sheathed Chromel-Alumel thermocouple with a grounded junction (Omega Engineering Inc.). The overall diameter of the thermocouple probe is 0.010 inch, which is considered satisfactory both from kinetic considerations and from the point of view of removal of the oxide by mechanical means. The thermocouple probe is mounted in a traversing mechanism which allows the probe to be located at any desired position in that sector of the flame nearest to the vertical pillar of the traverse mechanism, Figure 3, the spatial resolution of measurement being about 0.010 inch. The length of the thermocouple probe ex-

posed in the flame is kept as short as possible because of the difficulty of removing, by mechanical means, the oxide deposited on it.

Flames have been photographed using a 35 mm camera. A microphotometer (Jarrel Ash, J.A. 203) has been used to obtain the relative percent transmission values of black and white negatives of these photographs along a line through the apparent centre of the flame, and perpendicular to the nozzle axis. X-ray diffraction methods have been used to analyse the deposits found on exposed surfaces in the combustion chamber and on glass slides which were inserted horizontally in the flame, at the position of the apparent centre, for a very short time.

PRODUCTION OF STEADY FLAMES

The variation of the vaporizer tube temperature which is limited only by the temperature controller, and, also, the accumulation of oxide in the nozzle passage make if difficult to obtain absolutely steady flames for any length of time. The rate at which the oxide accumulates in the nozzle passage has been found to depend on the pressure and relative concentrations of oxygen and argon in the environment, on the vaporizer tube temperature, and on the concentration of carrier gas. The external profile of the nozzle also influences to some extent the rate of accumulation, probably as a result of changes in the local flow pattern (5). For example, in a nozzle with a plane circular apron at exit, accumulation of the oxide was rapid, forming spherically on the outside and penetrating into the nozzle passage, which was quickly closed.

The reduction in area of the flow passage due to oxide accumulation has been determined for durations of 2 and 4 minutes under the following experimental conditions: total pressure, 0.5 to 0.8 torr; vaporizer tube temperature 580° to 612°C carrier gas concentration 10 to 20 percent mole fraction, and oxygen concentration 5 to 35 percent mole fraction. These experiments have indicated that the rate of accumulation increases with pressure, but decreases as the carrier gas concentration and vaporizer tube temperature are increased. Also, in the lower range of oxygen concentrations, the rate of accumulation increases with oxygen concentration. For oxygen concentrations of less than 10 percent mole fraction, the area of the nozzle flow passage may be reduced by about 5 percent in 2 to 4 minutes, and is regarded as a tolerable level of departure from ideal conditions.

EXTERNAL APPEARANCE OF FLAMES

A flame which is suitable for observation and measurement is obtained only if the vaporizer tube temperature is at least equal to the saturation temperature of magnesium at the pressure prevailing in the combustion chamber. The flame is spherical, although slight departures from that shape may occur at high nozzle velocities (> 2000 cm/sec). Depending on the pressure and composition of the environment, and on the vaporizer tube temperature, the flame colour may vary from a bluish-white to pale blue. Normally, bluish-white flames are obtained either when the pressure is relatively high, or when the vaporizer tube temperature is high; while, at lower pressures and at lower vaporizer tube temperatures, pale blue flames are obtained. At the extremes of the latter pressure and temperature conditions, reaction may not be visible, although the presence of glowing oxide at the nozzle tip is evidence that reaction is occuring. The outer boundaries of these low pressure flames are not well defined.

The effects of the experimental variables on the appearance of magnesium-oxygen flames have been systematically determined from flame photographs, and the results are summarized here. Details may be found in reference (7). As the pressure in the combustion chamber is increased, both the flame size and intensity of emitted radiations increase. Similar changes have been observed when the oxygen concentration in the environment is increased and the pressure is held constant. There appears to be a limiting value of the oxygen concentration, about 20 percent mole fraction, beyond which the intensity of emission increases but the size of the flame decreases. An increase in carrier gas concentration, while the pressure in the combustion chamber is held constant, results in a reduction in flame size, and also in the intensity of emitted radiations.

TEMPERATURE DISTRIBUTION AND FLAME EMISSION

TEMPERATURE DISTRIBUTION The measurement of temperatures in a metal vapour flame in which the oxide is present in one or more condensed phases is difficult when a probe is used. These difficulties are primarily due to the accumulation of oxide on the thermocouple, as well as in the nozzle passage, the latter resulting in changing conditions in the flame during the time measurements are being made. These effects of oxide deposition on the recorded temperatures have been assessed by control experiments conducted under identical conditions (total pressure: 0.9 torr, Oxygen concentration: 10 percent mole fraction, carrier gas concentration 8 percent mole fraction, and vaporizer tube temperature: 610 $\pm$ 5°C). The results have led the authors to conclude that the time during which temperatures can be recorded is limited to the first 90 seconds of each experiment. During this period the temperature at any position does not vary by more than $\pm$ 5 percent of the mean.

A typical temperature-time record is reproduced in Figure 4. It is evident that thermal equilibrium between the thermocouple and the surroundings in which it is immersed is attained in about 15 seconds, the temperature remaining constant, thereafter, for a period of time. During the experimental time of 90 seconds it is possible to locate the probe at 4 or 5 positions in a flame and to record the corresponding temperatures. The temperatures reported are uncorrected values. Although it has been established experimentally that the conduction error is negligible, it is difficult to estimate the radiation correction, since the efficiency of the oxide particles surrounding the thermocouple as a radiation shield cannot be determined. Nevertheless, an upper bound can be obtained for the correction by considering only the prove and using a suitable value of the emissivity of magnesium oxide.

The distribution of temperature in a vertical plane through the nozzle axis is shown in Figure 5. The actual temperature contours shown in this Figure are compatible with the observed shape of

the flame. It is seen that the apparent circular contours of temperature agree with the actual temperature contours, for the greater part. Differences between the circular and actual contours near the tip of the flame may be attributed to convective effects. The temperature distribution has also been obtained in a horizontal plane through the apparent centre, and, in this plane, the apparent circular contours of temperature coincide with the actual contours. The measured temperature distributions in the vertical and horizontal planes confirm the sphericity of the flame when the carrier gas velocity is not too high.

The radial distribution of temperature in a horizontal plane through the apparent centre, for different oxygen concentrations, is shown in Figure 6. It is clear that there is a substantial variation of temperature. It is worth noting that flame temperatures are maximum when the oxygen concentration in the environment is 5 percent. At higher oxygen concentrations the recorded radial temperatures are lower, and it is also evident that the curves show a tendency to merge. This behaviour is thought to indicate that flame temperatures would reach a limiting distribution as the oxygen concentration was further increased.

The radial distribution of temperature of a mixture of magnesium vapour and carrier gas (in the absence of oxygen) is also shown in Figure 6. The temperature of the mixture is always lower than that of the vaporizer tube, and can only be due to the heat loss to the relatively cold carrier gas, and to the surroundings. The curves in that Figure have points of inflection, and there is reason to believe that about 90 percent of the reaction is completed at a radial position corresponding to the inflection point of each curve.

When the oxygen concentration is less than 5 percent, black deposits of magnesium have been found on the inner surfaces of the combustion chamber. The presence of these deposits is evidence that the vapour generated has not been totally consumed. Although the consumption of oxygen, in terms of partial pressure, is less than 1 percent of the total pressure, the minimum value of the concentration of oxygen in the environment for which magnesium deposition does not occur is about 5 percent. It is for this reason that the value of 5 percent mole fraction of oxygen in the environment is regarded as being 'critical' in the present investigation.

FLAME EMISSION The relative percent transmission values of flames produced with different concentrations of oxygen in the environment are shown in Figure 7. It is seen that the flame brightness increases (relative transmission decreases) as the concentration of oxygen is increased. On the other hand, as stated in an earlier paragraph, the flame temperature decreases as the concentration of oxygen is increased beyond the critical value of 5 percent mole fraction. Inspite of their lower temperatures, high oxygen flames are brighter, and their greater brightness may be attributed to the increased population density of the radiating species, if the excitation is thermal.

Flame emissions may be due also to chemical excitation. Although the present experiments do not establish the nature of the excitation, nevertheless, the temperature distributions (Figure 6), and the patterns of deposits obtained on glass slides (Figure 8), suggest that the principal mode of excitation is thermal. Attention was drawn in Figure 6 to the existence of temperature inflections, and it may be seen that these inflection points move towards the axis as the oxygen concentration is increased. As the greatest part of the reaction is believed to occur in the region between the point of inflection and the flame centre, and since this region shrinks as the oxygen concentration is increased, the population density of the radiating species in the central region increases. This suggests that the excitation may be thermal.

DEPOSIT PATTERNS Figure 8 shows the patterns formed by deposits on glass slides placed horizontally at the apparent centre of flames produced with different oxygen concentrations. In these, the central black region is surrounded by a dense white ring of magnesium oxide. The material of the central region is predominantly magnesium. The formation of the oxide ring may be explained in the following manner. Oxide particles that are formed as a result of reaction in the central region are carried radially outwards under the influence of the expanding jet of vapour and carrier gas and tend to accumulate in that region where the effects of jet momentum exchange are small. Markstein (2) obtained a shell-like crust of oxide on a glass slide placed vertically in a $Mg-O_2-Ar$ flame; the dense white ring in Figure 8 is a horizontal cross section of such a shell.

The shrinkage of the white ring that has been observed as the oxygen concentration is increased may be due to the greater availability of oxygen in the central region, in other words, the rate at which oxygen is depleted in that region may be decreased. The extent of the annular region in which the oxide particles tend to accumulate, or pile-up, depends on the number density of particles, in the central region, since the particles are very likely to be of approximately the same size.

AN INTERPRETATION OF THE REACTION DATA

The appearance of magnesium vapour-oxygen flames, and the important factor of the low absolute pressures, led the authors to the view that the requirements of Polanyi's dilute diffusion flame model (8) were being substantially fulfilled, although at the time no attempt had been made to examine the temperature distribution. It is, perhaps, pertinent at this stage to briefly recapitulate the assumptions underlying the mathematical model of the dilute diffusion flame, since these are central to the discussion that follows later regarding the validity of the temperature pattern method.

In the mathematical model, it is assumed that the nozzle reactant diffuses radially from a point source into the environment containing an excess of the atmospheric reactant. The concentration of atmospheric reactant, C_A, is assumed to remain constant everywhere in the reaction zone, while the nozzle reactant is assumed to react at a rate which is determined by the local reactant concentrations. One of the most important assumptions which simplifies the mass conservation equation and leads to a simple analytical expression for the distribution of the nozzle reactant concentration, C_N, is that the temperature in the system must be constant. The other assumption of importance is that the velocity of the gas leaving the nozzle must be small.

Experiments in which this model was used (9), (10) were designed to meet the requirement of a near-isothermal condition but the requirement of a negligibly small jet velocity, apparently, could not be met. However, the importance of the ratio of the linear velocity, V, in the nozzle to the

diffusion coefficient, D, of the mixture of nozzle reactant and diluent, rather than the velocity V itself, was quickly recognised, and limiting values of this ratio were determined experimentally (11) and from a simple mathematical analysis (9) within which the model conditions would not be invalidated.

In the present experiments the ratio V/D was within the prescribed limits, and on the tacit assumption that the temperature was nearly constant, systematic experimental data were obtained and analysed by the method of photographic photometry. The results of this analysis are presented in a later section. Details of the photometric method, which has been developed from the dilute diffusion flame model, may be found in reference (9) but a very brief description is given here for continuity.

In this method, the emission density at a point in the flame is assumed to be proportional to the nozzle reactant concentration at that point. The integrated value of the emission along a sighting path containing this point, and normal to the sensitive film, gives the emission intensity. When the photographic reciprocity law (12) is satisfied the film exposure, or the product of the emission intensity and time, is proportional to the film blackening. It is the film blackening and the time of exposure that are the measurable quantities in an experiment. The theoretical relationship between the relative film blackening measured by means of a microphotometer, and the reaction rate parameter, ω, permits the latter value to be obtained from the experimental data. Values of the reaction rate parameter for flames with different oxygen concentrations have been obtained in this manner.

Once the temperature distributions in these low pressure magnesium vapour flames had been ascertained, it was obvious that the isothermal condition of the dilute diffusion flame model had not been fulfilled. Notwithstanding the existence of large temperature variations in these flames, it was decided to proceed with an analysis of the temperature distribution data using the temperature pattern method developed by Garvin et al (13) and by Garvin and Kistiakowsky (10). In the temperature pattern method, the isothermal requirement of the model is relaxed to the extent that the variation of temperature must be sufficiently small so that temperature-dependent properties such as, activation energy, diffusion coefficient and thermal conductivity, could be regarded as being sensibly constant.

As in the photometric method, the temperature pattern method hinges on the expression for the nozzle reactant concentration, namely, $C_N = \text{const} \frac{1}{r} \exp(-\omega r)$ obtained from the dilute diffusion flame model. From energy considerations an integral relationship may then be found between the temperature T(r) at any radius, the reaction rate parameter, ω. By referring to a known temperature, $\bar{T}$, at a fixed radius r' in the flame an equation is obtained in the form:

$$\Delta T = T(r) - \bar{T}(r') = A\left[\frac{1}{r}(1-e^{-\omega r}) - \frac{1}{r'}(1-e^{-\omega r'})\right] \qquad \text{Eq. 1}$$

where A is a constant.
Multiplying both sides of this equation by r, there follows,

$$r \cdot \Delta T = A(1-\alpha r) - A\exp(-\omega r) \qquad \text{Eq. 2}$$

where $\alpha = \frac{1-\exp(-\omega r')}{r'} = \text{constant}$.

It is evident from the form of this equation that $r \cdot \Delta T$ may be presented graphically as the superimposition of a straight line and an exponential curve. It is on this basis that a graphical method of determining ω from experimental data for $r \cdot \Delta T$ has been derived. The reaction rate parameter, ω, is a shape parameter which is very sensitive to the temperature distribution.

The temperature data obtained in the present investigation have been used to construct curves showing the variation of $r \cdot \Delta T$ with radius, r, and are strikingly similar to the curve published by Garvin et al (13). Because of this similarity it was decided to determine values of the reaction rate parameter for flames with different oxygen concentrations in the manner outlined in reference (13). These values of the reaction rate parameter were then substituted in the theoretical expression for the variation of $r \cdot \Delta T$ with r, Eq. (2), and from these calculations the corresponding theoretical radial temperature distributions were obtained.

The theoretical variation of $r \cdot \Delta T$ with flame radius for three different oxygen concentrations are shown in Figure 9, on which the experimental data are superimposed. In Figure 10 the theoretical radial distributions of temperature are shown for the three flame conditions, and the experimental data have also been plotted. It is clear from these Figures that, for the most part, the experimental points lie on the corresponding theoretical curves, except in the region (at a radius approximately equal to one nozzle diameter) close to the nozzle axis. This deviation is a consequence of the assumption of a point source of diffusion.

It is remarkable, in spite of the marked sensitivity of the reaction parameter to the temperature distribution, that the experimental data agree so well with the theoretical curves. This is all the more surprising in view of the assumed constancy of the parameter ω, which, even from a cursory examination, is so strongly dependent on temperature. The agreement may be fortuitous, of course, but, then, it is improbable that the observed consistency would have been achieved. The one other possible explanation for the anomalous congruency of theory and experiment is that the group k/D which is contained in the reaction parameter, ω, is constant in which case the activation energy must be small so that the effect of the large variation in temperature would also be small, and of the same order as the variation of the diffusion coefficient with temperature.

The situation revealed by the foregoing treatment is certainly an intriguing one, and a first approach to an answer is, perhaps, to be found in a more rigorous analysis of the fundamental equations for a point source of diffusion with reaction, by numerical methods. From such a solution it would be possible to gain an insight into the role of the temperature in the radial variation of nozzle reactant concentration, and in the conservation of energy.

What is clear, however, is that low pressure $Mg-O_2-Ar$ flames appear to fit into Polanyi's model of the dilute diffusion flame. If this fact has any physical significance, then, one may propose that these magnesium vapour flames are also homogeneous. This proposition stems from the belief that the temperatures recorded in the relevant part of the investigation are those of the mixture of vapour

condensed phases which exist in a state of thermodynamic equilibrium.

This conclusion is an important, but contentious, one because the question of what is the preferred reaction path in the vapour phase burning of magnesium is obviously still open to investigation. While it is recognized that no precise meaning can be given to the rate constant k in the reaction rate parameter ($\omega^2 = k C_A^2$), nevertheless the order of magnitude of k may be obtained if an average temperature can be assigned. For example, it can be shown that bulk of the reaction occurs in the region between the axis of the flame and the position where $r \cdot \Delta T$ has a maximum value, Figure 9. This position where $r \cdot \Delta T$ has a maximum value almost coincides the position of the inflection point, Figure 6. Thus, a suitable temperature may be the arithmetic mean of the temperature at the axis and that at the position of the point of inflection.

RESULTS OF THE REACTION RATE STUDIES The reaction rate parameters obtained from the method of photographic photometry and from the temperature pattern method for different concentrations of oxygen in the environment are shown in Table 1 below.

Table 1. Experimental Results

Total pressure: 0.9 mm Hg, Total flow: 3.964×10^{-3} litres/sec. at standard conditions

Vaporizer tube temperature: $610^{\circ} \pm 5^{\circ}C$

Oxygen Conc, percent mole fraction	Reaction Rate parameter, ω, cm^{-1}	
	Photographic photometry method	Temperature pattern method
5.4	7.38	2.72
9.6	3.77	3.13
14.5	4.08	3.15
19.0	3.12	3.27

It is evident that agreement between the values of ω obtained by the two methods are in reasonable agreement. In any case, the latter concentration is near the critical value and, from the general observations made under these conditions, the value of the parameter ω is likely to be unreliable. Flames produced with sub-critical oxygen concentrations may be regarded in a similar light to the under-ventilated gaseous flames of Burke and Schumann (14). However, the dilute diffusion flame model can only be applied to over-ventilated flames corresponding to higher oxygen concentrations for which values of the reaction rate parameter are substantially constant.

CONCLUDING REMARKS

An attempt has been made to systematically study the gross structural features of $Mg-O_2-Ar$ flames at low pressures (0.5 - 1.0 torr). The effects of pressure and of the relative concentrations of oxygen and argon on the appearance of these flames, and on the intensity of the emitted radiations, were examined by photographs taken under controlled conditions. Because of their spherical shape, and the low pressured employed, the method of photographic photometry was used to determine the reaction rate parameter, ω, for nominal oxygen concentrations of 5, 10, 15 and 20 percent mole fraction and at a constant pressure.

A grounded junction thermocouple probe was used to explore the temperatures in the flame. The consistent pattern of the recorded response of the thermocouple was interpreted, in the light of the known complexity of the $Mg-O_2-Ar$ system, as being compatible with a state of thermodynamic equilibrium. In conjunction with other evidence, it was concluded that the temperature recorded was approximately that of the gas phase. Accurate corrections for the radiative loss could not be made, but the maximum correction was predicted to be about $40^{\circ}C$. The precision error of the measurements was estimated to be ± 5 percent.

Notwithstanding the large variation of temperature in these flames, the temperature pattern method was used to determine the reaction rate parameter, and was found to be in good agreement with that obtained by photometry. The most striking feature of the analysis was that nearly exact coincidence between the calculated and experimental temperature distributions were obtained in the three cases examined. Since it had been ascertained that the reaction rate parameter used in the calculations was extremely sensitive to the temperature distribution, the congruency was believed to be physically significant. In view of the interpretation of the temperature as that of the gas phase, it was tentatively concluded that the reaction could be predominantly homogeneous.

ACKNOWLEDGEMENTS

The work was supported by the National Research Council (Grant-in-aid No. A-1618). The authors are grateful to the University of Saskatchewan for the provision of laboratory facilities.

REFERENCES

1. Glassman, I., "Combustion of Metals: Physical Considerations", Solid Propellant Rocket Research (Summerfield, M. ed): pp 253-258, Academic Press, New York (1960).
2. Markstein, G.H., "Magnesium-Oxygen Dilute Diffusion Flame", Ninth Symposium (International) on Combustion, pp 137-147, Academic Press: New York (1963).
3. Sullivan, H.F., Gouldin, F.C. and Glassman, I., "Metal Flame Structure studies Employing Optical Techniques", Paper No. WSS/CI 67-40, Fall Meeting, Western States Section/The Combustion Institute, Seattle, Washington, U.S.A. (October 1967).
4. Markstein, G.H., "Correlation Between Vaporizer Temperature and Collision Efficiency of Heterogeneous Reaction in Magnesium-Oxygen-Argon Dilute Diffusion Flames", Combustion and Flame, Vol. 13, pp. 212-214, (1969).
5. Rao, B.K.G. and Deckker, B.E.L., "Low Pressure Magnesium Vapour Diffusion Flames", Paper No. WSCI-67-32, Fall Meeting, Western States Section/The Combustion Institute, Seattle, Washington, U.S.A. (October 1967).
6. Rao, B.K.G. and Deckker, B.E.L., "Temperature Distribution in Low Pressure Magnesium Vapour-Oxygen Diffusion Flames", Paper No. WSCI 68-20, Fall Meeting, Western States Section/The Combustion Institute, Menlo Park, California, U.S.A. (October 1968).
7. Rao, B.K.G., "Some aspects of the structure of Diffusion Flames of Magnesium Vapour and Oxygen at Low Pressures", A Thesis submitted for the Ph.D. Degree, Mechanical Engineering, University of Saskatchewan, Canada (1969).
8. Polanyi, M., Atomic Reactions, Williams & Norgate Ltd.: London (1932).
9. Repp, D. and Johnston, H.S., "Nitric Oxide-Fluorine Dilute Diffusion Flame", J. Chem. Phys., Vol. 33, pp. 695-699 (1960).
10. Garvin D. and Kistiakowsky, G.B., "The Kinetics of Co-ordinate Bond Formation", J. Chem. Phy., Vol. 20, pp. 105-113 (1952).
11. Heller, W., "A critical Investigation and Development of the 'Diffusion Method' for Determining Speeds of Atomic Reactions", Trans. Faraday Soc., Vol. 33, pp. 1556-1570 (1937).
12. Sawyer, R.A., Experimental Spectroscopy, Third Ed., pp. 203-205; Dover Publications, Inc., New York, (1963).
13. Garvin, D., Guinn, V.P., and Kistiakowsky, G.B., "The Temperature Pattern Method in the Study of Fast Chemcial Reactions", Discussion, The Faraday Society, No. 17, pp. 32-39 (1954).
14. Burke, S.P. and Schumann, T.E.W., "Diffusion Flames", Proceedings of the First and Second Symposia on Combustion, pp. 2-11, The Combustion Institute: Pittsburgh (1965).

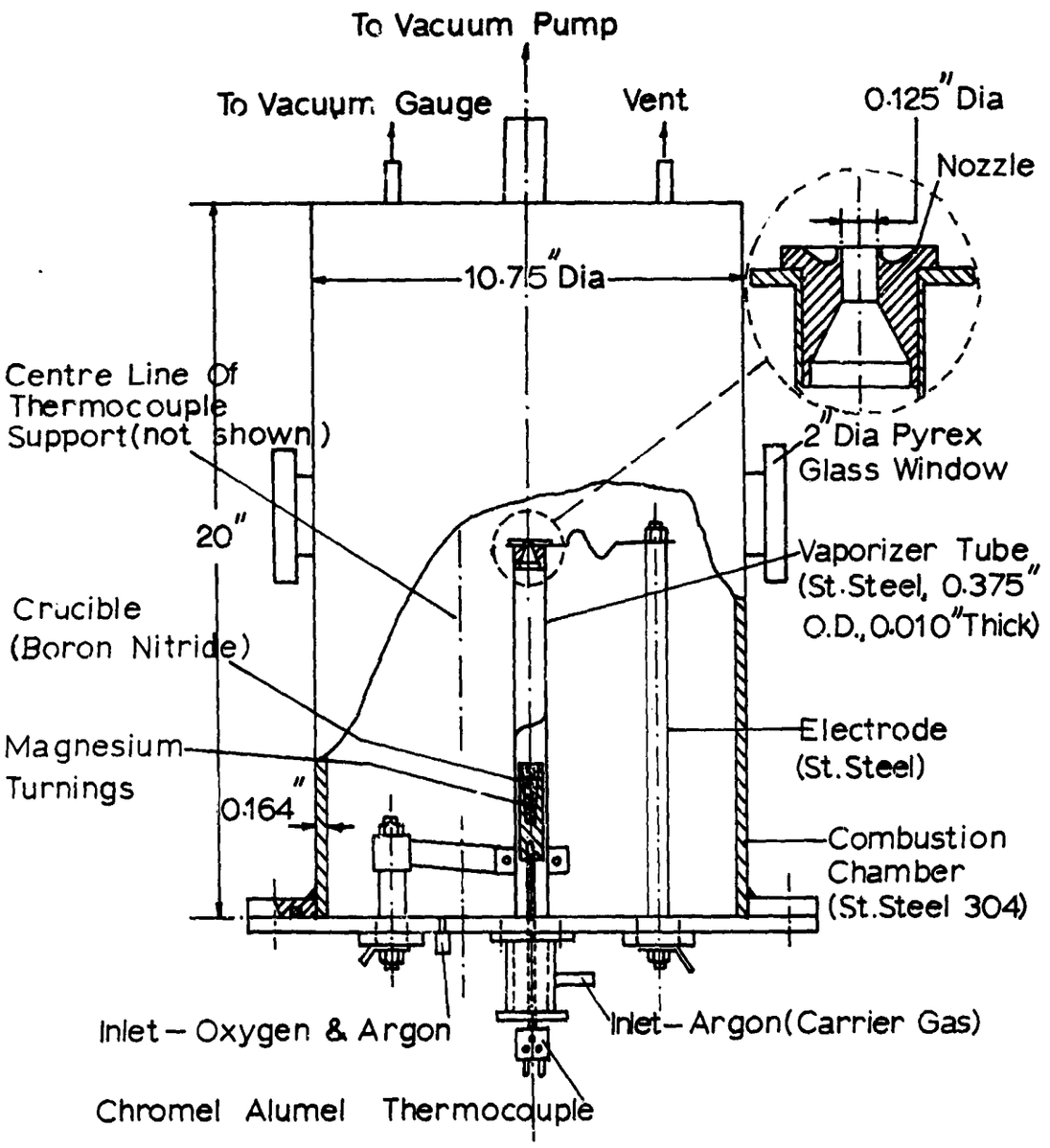

Figure 1. Sectional View of Combustion Chamber

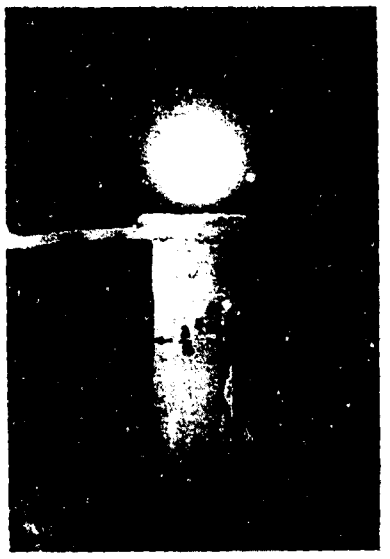

Figure 2. Typical Magnesium Vapour–Oxygen Diffusion Flame

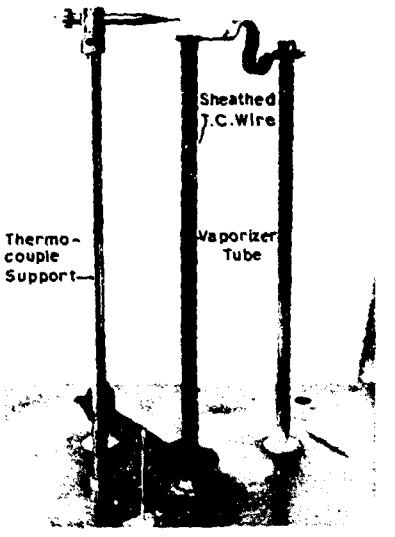

Figure 3. Thermocouple Probe and Vaporizer Tube

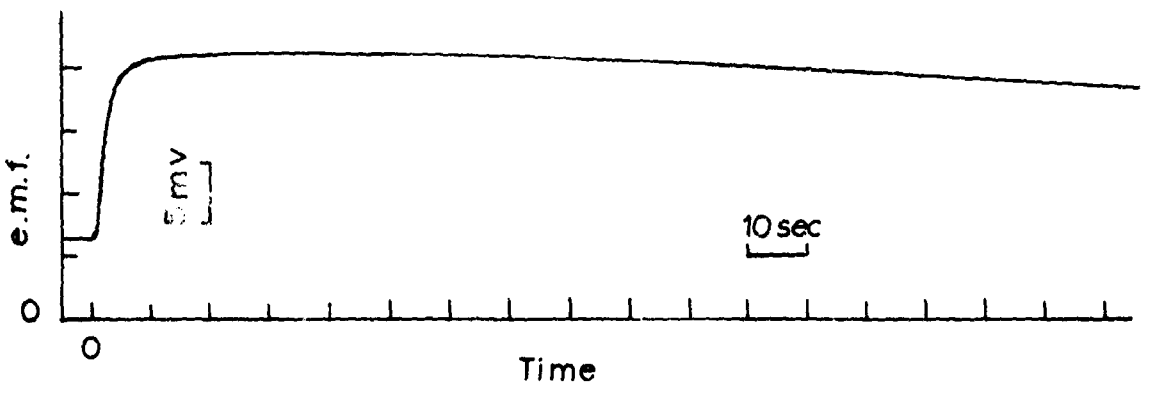

Figure 4. Typical Temperature – Time Record

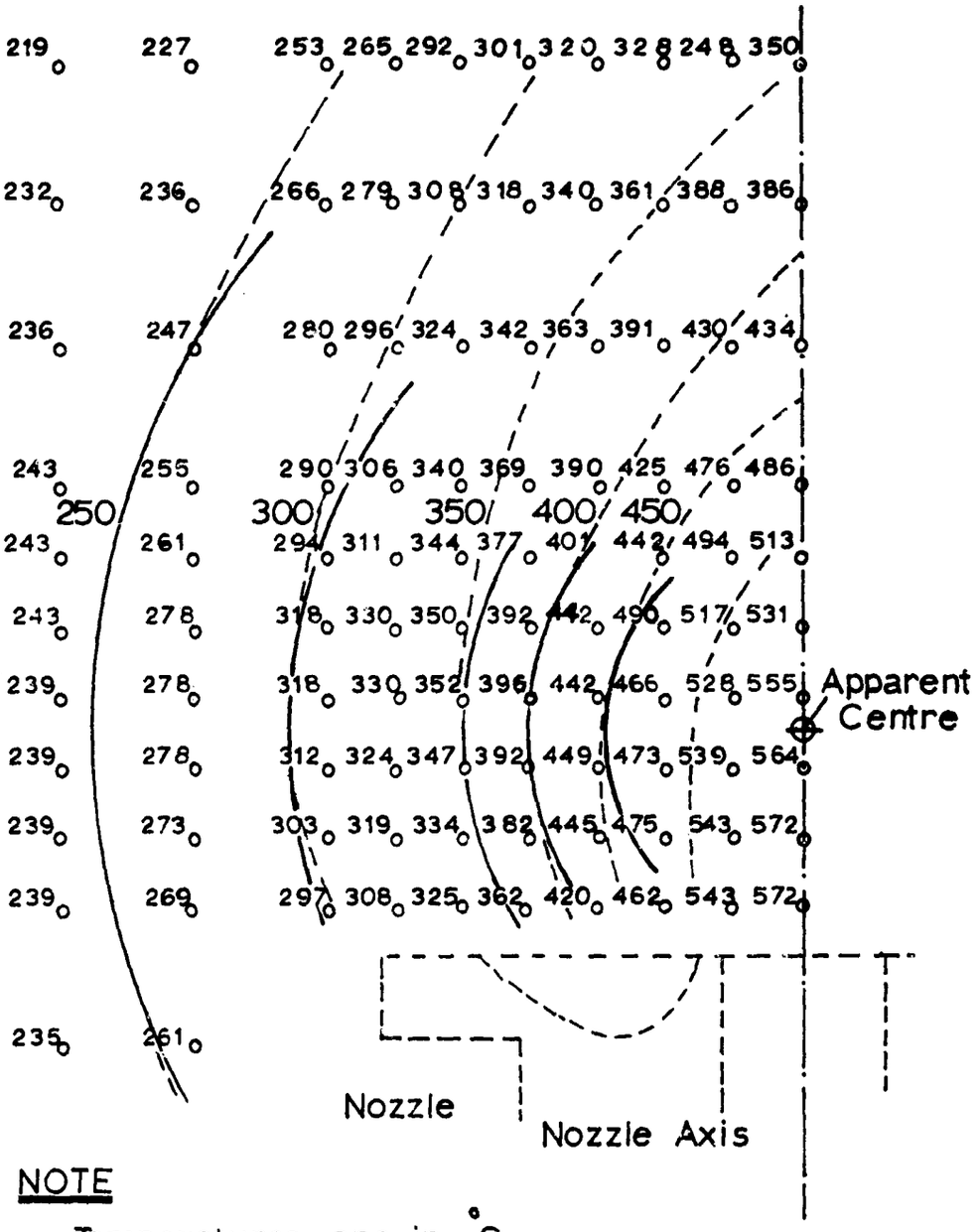

NOTE

Temperatures are in °C

---- Actual Temperature Contour

——— Apparent Circular Contour of Temperature

0.1 In

Vaporizer Tube Temperature: 610 °C

Total Pressure: 0.9 mm Hg abs.

Oxygen Conc.: 10 %,

Carrier Gas Conc.: 8 %

Figure 5. Vertical Temperature Distribution, Through Nozzle Axis

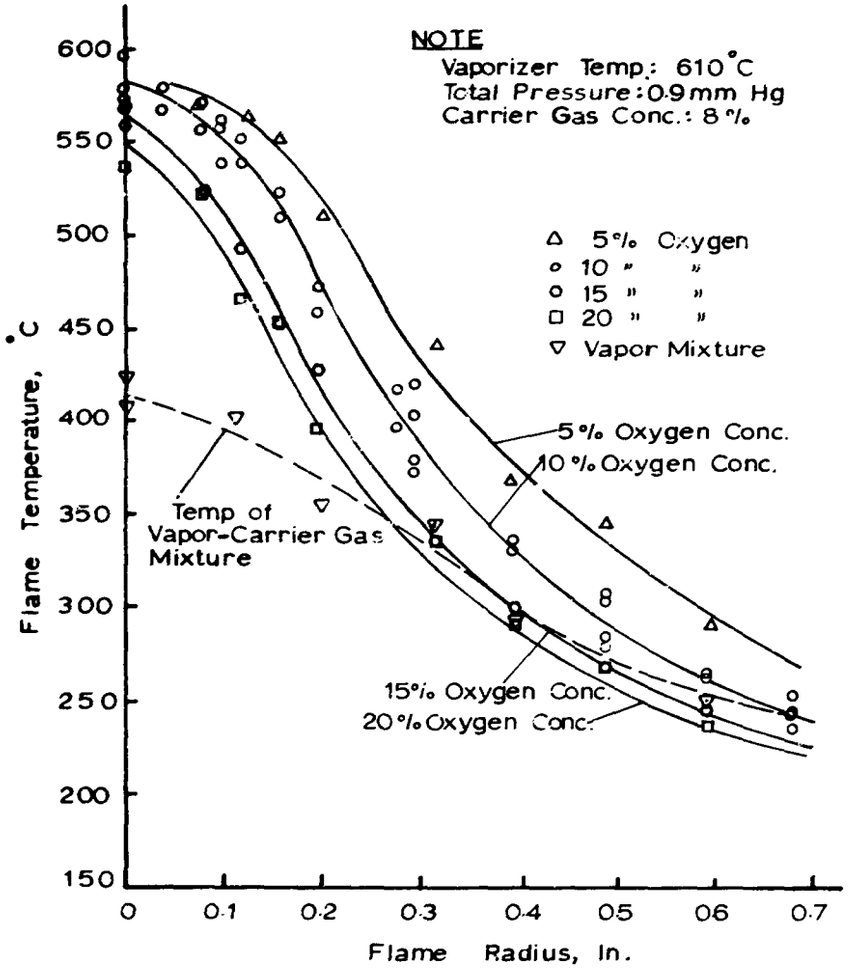

Figure 6. Radial Temperature Distribution, Through Apparent Centre

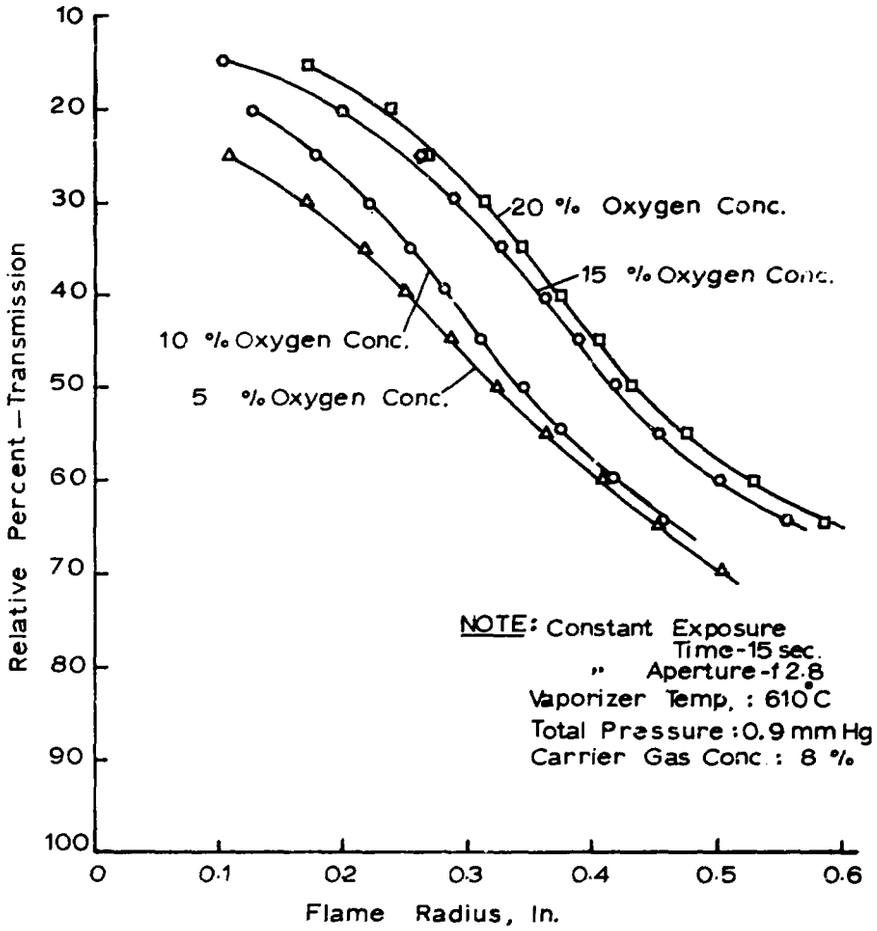

Figure 7. Radial Distribution of Relative Intensity, through Apparent Centre

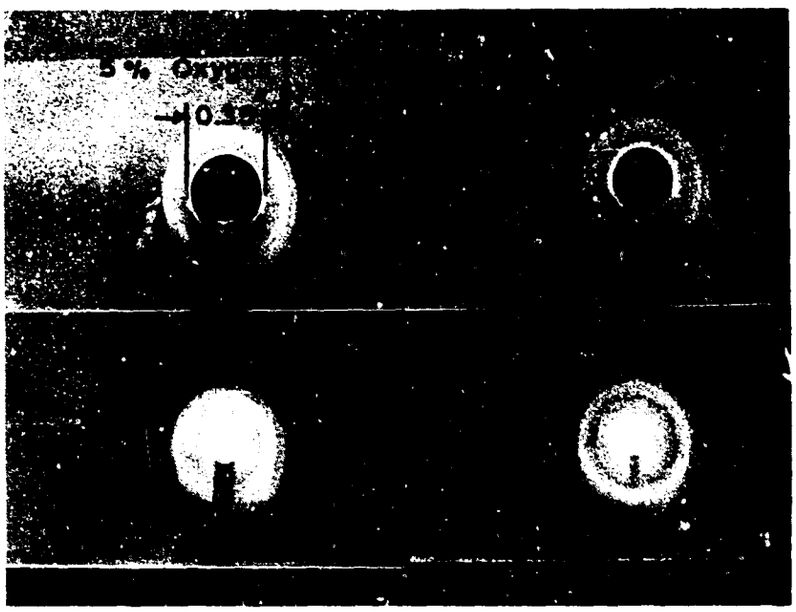

Figure 8 Deposit Patterns

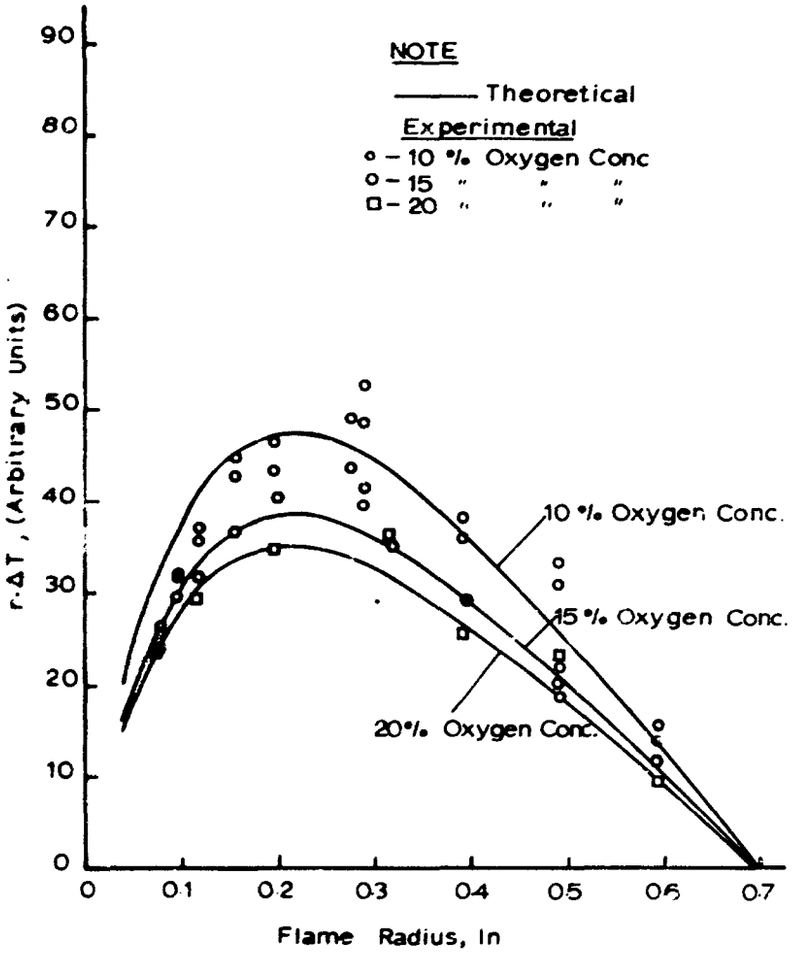

Figure 9. Comparison of Theoretical and Experimental Radial Distribution of r·ΔT

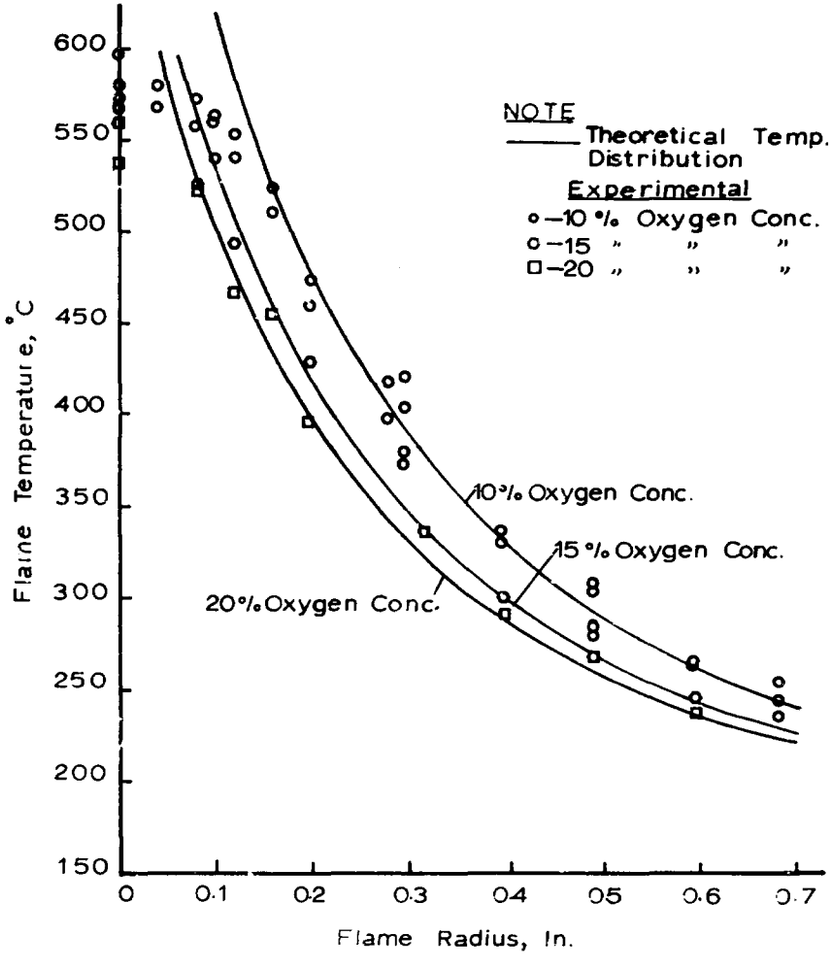

Figure 10. Comparison of Theoretical and Experimental Radial Temperature Distribution

SURVEY PAPER ON EROSION PRODUCED BY HIGH-SPEED TWO-PHASE FLOW IN SOLID PROPELLANT ROCKET MOTORS

by

Richard J. Zeamer

Hercules Incorporated
Magna, Utah, USA

SUMMARY

EROSION PRODUCED BY TWO-PHASE FLOW can be a serious problem in solid propellant rockets. The nongaseous phase originates from the powdered metals that are commonly added to solid propellants to increase their energy and density. As much as 40 percent of the exhaust flow can be in the form of liquid or solid particles.

The combustion of metal in a solid propellant and the associated particle changes involve formation of metal agglomerates on the burning surface, ejection, ignition and then combustion in the gas stream producing tiny oxide smoke particles. These oxide droplets grow rapidly from diameters as small as 0.01 micron to around 0.2 micron because of collisions caused by Brownian motion. Continued growth is due to turbulence and acoustic agitation. Large gas velocity gradients in the nozzle region cause more frequent collisions and very rapid growth in particle size with average oxide particle diameters increasing five to ten times from nozzle entry to exit.

The boundary layer effectively protects the wall from impingement by average sized particles in flow passages having good aerodynamic design. However, poor combustion may produce particles so large that they will impinge even under the best flow conditions.

In a solid propellant rocket motor the particles arriving at wall surfaces generally have releasable heat and chemical energy in addition to kinetic energy. Usually a large portion of this energy is transferred to the wall. Erosion by mechanical impact is negligible except in the nozzle exit cone and jet. Heating, together with high-temperature chemical reactions, is the principal cause of erosion in the nozzle entry and throat for all the commonly used materials including reinforced plastics, graphites and tungsten.

Impingement heating is highly localized and erratic. In tungsten and other refractories it may cause cracking due to abnormal thermal stresses or it may cause melting. In graphites and plastics it causes uneven erosion and gouging. In elastomeric insulation on chamber walls it causes deep charring in small areas.

Solid propellant motors that are free of two-phase flow erosion problems generally have efficient metal combustion and good interior aerodynamic design.

SURVEY PAPER ON EROSION PRODUCED BY HIGH-SPEED TWO-PHASE FLOW IN SOLID PROPELLANT ROCKET MOTORS

Richard J. Zeamer

OUR PURPOSE IS TO REVIEW two-phase flow in solid propellant rocket motors, erosion and deposition produced by it, methods available for its analysis, and techniques for avoiding erosion problems.

TWO-PHASE FLOW as it occurs in solid propellant rocket motors is described in sufficient detail to provide the necessary background for our review of erosion. Understanding of the unique and transiently changing character of this gas-particle mixture that travels through the motor is essential to any meaningful analysis of the erosion problem.

INTERACTION of a two-phase flow with a wall is reviewed using available data and theory. The boundary layer is considered as a barrier that prevents incoming particles from reaching the wall or reduces their arrival velocity and releasible energy.

PARTICLE TRANSPORT to the surface is treated as high velocity impingement and low velocity diffusion through the boundary layer.

THE RESULTING IMPACT, heating, chemical and melting effects are considered in regard to their contributions to erosion and deposition. Deposition of matter on the surface is included because it may either protect the surface or it may change flow and heat transfer so as to increase erosion.

THE EROSION PROCESS

Two-phase flow in solid propellant motors is not generally destructive. The boundary layer covers all exposed surfaces providing protection that is usually adequate. Potentially harmful particles are either diverted or stripped of their excess energy.

SPECIAL CONDITIONS are necessary to allow two-phase flow to cause erosion. The basic requirement is that particles with sufficient energy to cause damage must be delivered to the surface. To study this problem we must first investigate the region from which the particles came, the two-phase flow of the motor.

TWO-PHASE FLOW IN SOLID PROPELLANT ROCKETS

IN A SOLID PROPELLANT ROCKET two-phase flow is a condition that is continually changing. From point to point along the path of the flow the mean size and size distribution of the particles are varying. Also as the flow moves away from the propellant surface the proportion of aluminum (or other metal) decreases and the proportion of oxide increases. Typical two-phase flow inside a rocket motor is summarized in Figure 1. The various stages of the flow are reviewed in the following.

THE PARTICULATE MATERIAL ORIGINATES at the propellant burning surface. For normal propellants of average efficiency the small (30 microns typical diameter) particles of aluminum fuel are exposed on the burning surface and are quickly melted by the heat. As more aluminum particles emerge on the surface and melt, neighboring particles touch and merge (1,2). Typically these grow to sizes of around 150 microns in about eight milliseconds.

However, solid propellants differ widely in their manner of burning. At one extreme, for inefficiently burning propellants, the burning surface can be almost covered with a "filigree" of partially molten aluminum and oxide. Gas flow from the propellant lifts and breaks off irregular solid portions which are further heated, ignite at localized points and eventually melt into large spheres (3). Metal fuel agglomerates as large as 1,000 microns have been observed entering the gas stream.

At the other extreme, for propellants having high burning rates and high combustion efficiencies, the aluminum particles, for the most part, seem to move into the gas stream almost without agglomeration, retaining their original small size.

These burning phenomena are observed in micro-window bomb tests. In these tests small strands of propellant are burned in a high pressure atmosphere and observed through a heavy optical-glass window and lenses by a movie camera (1,2,3,4).

IGNITION AND COMBUSTION behavior of aluminum and the other metals most commonly used in solid propellants are similar. Ignition generally occurs when the metal is locally heated to its melting point; therefore, metals with higher melting points require more heating before they ignite (5).

Combustion generally occurs in the vapor phase (6) as shown in Figure 2. Metal vapor is assumed to diffuse away from an evaporating metal droplet. It appears certain that inside typical rocket motors with propellant containing aluminum, the droplets are thoroughly molten because the gas temperatures (which range from about 2400K to 4000K) are above the melting points of aluminum (933K) and aluminum oxide (2320K). Oxidizing species diffuse in toward the droplet. The reaction takes place in a very hot luminous combustion zone surrounding the droplet. Combustion is in the vapor phase controlled by diffusion of the oxidant (5). The combustion rate has an inverse relation to the melting points of the metal and its oxide. Thus in similar environments beryllium ignites and burns only about half as fast as aluminum (7). The resulting combustion lag for slower burning metals can have serious erosion consequences if agglomeration has formed large particles of metal fuel.

The time required to burn up a metal particle increases about with the square of its diameter as shown in Figure 3. Lower oxygen concentration and lower pressure also increase the burning time but not as drastically (8). Calculated combustion times for the largest agglomerates are found to exceed residence time for small rocket motors (4). As one would expect, in such cases there are erosion and deposition problems as well as substantial losses of specific impulse efficiency.

OXIDE PARTICLES IN THE CHAMBER first appear as tiny droplets in the smoke cloud produced by a burning particle of metal. These droplets are formed by condensation of oxide vapor in or just beyond the reaction zone, see Figure 2. They are very small, having diameters from 0.01 micron to 0.5 micron (9). However, under poor combustion conditions these can range in size up to 5 microns. Where appreciable amounts of oxide form on the surface of the burning metal oxide droplets as large as 50 microns can be formed (3).

The tiny particles first grow very rapidly by collision due to Brownian motion (10). However, the efficiency of coagulation by Brownian motion decreases with increase in size and becomes negligible for particles above 0.2 microns. Another mechanism, that of acoustic coagulation, further increases the size and reduces the number of oxide droplets (11,12). Brown has calculated that 0.5 percent or more of the thrust energy from a rocket motor is converted into sound; the power densities are in the range found necessary to coagulate aerosols. The rate of acoustic coagulation depends upon droplet concentration (hence, on the gas pressure and percent metal), the acoustic power and the residence time in the motor (10).

Turbulent agglomeration resulting from collisions due to eddy diffusion and particle lag in turbulent fluctuations also contributes to particle growth in the chamber (12).

The result is that the oxide particles grow with time during their residence in the chamber to a mean diameter ranging from 1 micron based on direct sampling of chamber gas (13) to 2 microns based on calculation from theory (12).

OXIDE PARTICLES IN THE NOZZLE grow rapidly, increasing diameter five time or more, mainly because the acceleration of the gas greatly increases particle collisions (14). The acoustic effect also increases but is of second order, (about five percent), importance (12). The velocity gradients in the flow result in different velocity lags for larger and smaller particles and, therefore, the smaller particles tend to catch up with the larger particles and coalesce with them (14). Particle growth continues into the exit cone to expansion ratios of 3 to 5 beyond which the particles become solid and little further growth takes place, except possibly close to the wall. But by this time they have grown to sizes approaching the limit imposed by maximum stable drop size theory (15) which is about 18 microns for the largest rocket motor and grades downward with motor size, see Figure 4.

Jenkins and Hoglund (12) have recently presented a unified theory of particle growth which combines the above effects in a kinetic coagulation model. Their calculated results for the Titan III-C Motor are shown in Figure 5. The particle diameters in the chamber appear large in comparison with the particle size summary in Figure 1; however, this would seem reasonable for such a large motor in which the residence times are long.

AMOUNT OF METAL in the propellant appears to have only a small effect on oxide particle size. Cheung and Cohen, in a typical test, found that an increase in aluminum from 3 to 17 percent resulted in an increase of exhaust particle size from 3.1 to 4.5 microns (16). Sehgal found no effect with a change in aluminum from 12 to 16 percent.

LARGE PARTICLES are of most concern in erosion analysis because of their potential for impinging and causing damage. Motor size is an important factor.

Small motors loaded with good ordinary propellants can have erosion problems due to relatively large (up to about 150 micron) burning metal fuel particles present throughout their flow because of the short residence times. In the throat any oversized burning fuel droplets still remaining in the flow are shattered by shear due to the high velocity gradients and thereby reduced to or below their maximum stable drop size. This size is about 5 microns for a nozzle with a 2-inch throat diameter (17). The same effect limits growth of oxide particles in the throat and exit cone.

In medium-sized motors with good combustion efficiency small (1 to 2 micron) particles are the rule except near the propellant surface where the flow is dominated by large particles (150 micron typical size) of burning metal fuel and in the exit cone where oxide particles can grow to sizes up to 10 micron.

In medium-sized motors having poor metal combustion efficiency large burning metal particles (up to 1000 microns in size) can be present in varying amounts through most or all of the interior. In the exit cone any oversized burning fuel droplets still remaining in the flow are shattered and reduced to or below their maximum stable drop size.

In very large motors the long residence time usually allows combustion and coagulation processes to approach completion. Even poorly burning metal fuel can be almost completely consumed before flow reaches the nozzle. Growth of oxide goes farther to produce particles of 2 microns or possibly larger in the chamber. Low velocity gradients in the large nozzle allow particles to grow to sizes approaching 18 microns (17).

THE FLOW FIELD

Concentration of particles in rockets is low enough that the velocity distribution in the gas stream may be calculated by methods used for clean gas but employing the simple corrections for gas properties of two-phase mixtures as presented by Marble (18).

Computer programs are used to solve the equations of potential incompressible flow (19,20) or potential compressible flow to determine the irrotational portion of the rocket interior flow. This usually involves almost all of the flow including the very important nozzle entrance region. Velocities in rotational flow regions are calculated, assuming a wheel-flow pattern and integrating the momentum equation over the eddy and its boundaries.

The supersonic exit flow is calculated by a method-of-characteristics computer program, such as that developed by Lockheed for NASA (21).

PARTICLE PATHS

Particle trajectories in the flow field are calculated by use of the equation of motion of a particle in which the particle inertia is equated with its aerodynamic drag. Stokes drag is a widely used approximation because it is simple and reasonably valid for low slip velocities. In regions of high slip, Stokes drag is too low and more sophisticated recent correlations should be used (22,23,24).

Burning droplets have been found to have two or more times the drag of inert particles (25).

The result of a typical rocket motor flow field and particle trajectory calculation is shown in Figure 6. As the particles shown are particles of burning fuel, the ends of their paths indicates the points at which they are completely consumed.

BOUNDARY LAYER

All internal surfaces of a rocket motor are covered by a boundary layer within which gas velocities and temperatures grade from free stream to wall values. As this boundary layer is the main protection of the wall from particle damage, determination of its thickness and character is an important part of an erosion study.

The rigorous analysis of the two-phase boundary layer is a complex and formidable problem. Marble has laid the groundwork for such an analysis (18) and Isaacson has investigated the feasibility of applying it to rocket heat transfer problems (26). Soo has applied the momentum integral method with some success (27).

Fortunately for our purposes, the two-phase flow boundary layer can be analyzed as a gas boundary layer. Farber and Morely (28) have shown that there is little heat transfer caused by the solid particles until the volume percent of solids reaches about 0.05%. Current solid rockets have volume percent particles in the throat region of 0.01 to 0.04%; thus little effect would be expected. This has been amply confirmed in rocket heat transfer studies (29,30,33) and throat erosion correlations (31,32).

That the velocity profile of the boundary layer is not changed by particles at loading ratios in our range of interest was noted as early as 1933 by Nikuradse and subsequently shown by Baw and Peskin (35) and Soo (27).

For rough estimates of boundary layer thickness the classical flat-plate formulas available in the text books can be used, but more rigorous methods may be preferred depending on the importance of the problem. Figure 7 shows the results of a calculation of the thickness of the boundary layer on an aft dome and nozzle. The thickness as shown illustrates the typical variation in the protection that the boundary layer provides to impingement.

PARTICLE IMPINGEMENT occurs when particles in the free stream are moving toward a wall with sufficient momentum to pierce the boundary layer along their line of travel and strike the wall. Using calculated flow velocity and boundary layer results, dimensionless parameters can be employed to predict the tendency for particles to impinge from a two-phase flow.

In 1946 Langmuir (36) proposed an "inertia parameter" in connection with his studies of water droplet impingement on airfoils. Larger parameter values indicated greater tendency to impinge. It is useful mainly in correlating data for specific experiments and geometries. In 1964 Adelberg (37) demonstrated the use of this parameter for flow in ducts using the data of Hacker and Brun (38) for 90° elbows. This parameter is defined as

$$K = \frac{S}{L} = \frac{d^2 V \rho_p}{18 \mu L}$$

where

$S = \frac{Vd^2\rho_p}{18\mu}$ = particle stopping distance; this is the distance that the moving particle would be carried by its momentum if it suddenly entered still gas. Stokes drag is assumed.

L = a characteristic length, such as the wing chord length or the duct diameter.

V = the flow velocity.

ρ_p = density of the particle material

μ = gas viscosity.

d = particle diameter

In 1965 Soo (27) proposed an almost identical parameter which he called a "gas-solid momentum number".

$$N_m = \frac{\text{particle inertia force}}{\text{gas viscous force}} = \frac{V/X}{18\mu/d^2\rho_p} = \frac{d^2 V \rho_p}{18 \mu X}$$

The only difference between the two parameters, N_m and K is in the length parameter which Soo defined as the same length that would be used in the Reynolds number for the same flow.

The author has found useful an "impingement number," defined as the ratio of the particle stopping distance to the boundary layer thickness as measured along the expected particle path length. This ratio is stated as follows:

$$N_I = \frac{\text{Particle stopping distance}}{\text{Boundary layer Thickness}/\sin\theta} = \frac{S \sin\theta}{\delta}$$

where

S = the particle stopping distance as defined above for Langmuir's inertia parameter.

θ = the impingement angle measured between the path line and the surface

δ = the boundary layer thickness.

Values of N_I that are greater than 1.0 generally indicate impingement while values less than 1.0 indicate safety from impingement. N_I has been calculated for a number of typical impingement situations in a solid propellant rocket motor. These are illustrated in Figure 8 and the impingement numbers and their interpretation are presented in Table I.

PARTICLE DIFFUSION is the migration of particles from the two-phase flow through the boundary layer to the wall. It is a slow and gentle process compared with impingement.

In laminar flow there is essentially no particle diffusion to the wall. However, Marble showed that in a laminar boundary layer there is a tendency for particles to collect near a wall. Soo also found this result by analysis and suggested that there would be a tendency for particles to impinge at a distance downstream of the leading edge. Friedlander and Johnstone found experimentally with air-particle flow in tubes that no wall impingement took place in the laminar boundary layer.

In turbulent boundary layers tests Friedlander and Johnstone found that uniform and well defined impingement takes place and they used von Karman's approach for the rate of transport of momentum and mass in a turbulent diffusion and impingement. Alternately they used tubes of glass and brass but were unable to detect any difference that would indicate the influence of electrostatic forces (40). Allen, Bloemer and Chapman subsequently used the method to interpret boron oxide deposition test data (41). Grinberg and Ungar in 1953 applied the method to solid propellant rocket nozzle problems with apparent success (42).

Although turbulent forces appear to be dominant in particle diffusion in rocket motors, there is evidence that electrostatic forces can be significantly large second-order effects.

Soo found that charged particles would impinge through a laminar or turbulent boundary layer on to a conductive wall that was either neutral and grounded or oppositely charged. Conductive walls with the same sign of charge received less-than-normal or no impingement (27). Hobbs demonstrated these effects in rocket motors. He further showed that the sign and amount of charge on the particles varied with changes in the propellant formulation(43).

The possible amount of electrostatic diffusion in solid propellant rocket motors appears limited because wall surfaces are not highly conductive and are neither neutral and grounded nor oppositely charged.

The other modes of particle diffusion through the boundary layer are, in order of their probable importance in rocket motors, transport by inertial forces, gravity forces, thermal diffusion, and Brownian motion.

Inertial and gravity forces are important only where particle mass is large relative to gas drag such as occurs in low velocity regions of the chamber.

Thermal diffusion would tend to drive particles from a hot free stream toward a cold wall. Breitweiser reported that analysis of data on deposition of boron oxide particles to a cold wall showed that thermal diffusion of the particles was very small compared with turbulent diffusion (44). Brownian forces would be negligible except for particles less than 0.2 micron diameter.

Erosion due to particle diffusion is generally less and more evenly distributed than that due to impingement and it may be confused with erosion due to gas flow.

SURFACE EROSION MECHANISMS

The particles which reach the surface bring with them more or less energy. In simple cases this includes only kinetic energy. However, in solid propellant rockets the particles also bring thermal and chemical energy.

The surface is subjected to localized impacts, accompanied by heat flux and when the surface temperature gets high enough, chemical attack. Usually only one of these modes is dominant at a particular time. The response of the surface depends greatly on the nature of the material. The results may be failure by mechanical abrasion, thermal shock, chemical corrosion or melting, or, on the other hand, deposition may protectively coat the material.

IMPACT

Impact due to impingement of droplets or particles is not an important mechanism except in the supersonic exhaust jet.

An impinging droplet produces a compressive force immediately beneath its center of impact. The impacting material flows outward from the center at velocities much higher than before impact. The resulting surface shear force produces tensile forces in a circular belt around the impact zone in which cracks may develop. Erosion due to impact usually does not begin immediately, but only after impact has been in progress for a period of time. This cumulative damage behavior is explained by the theory that localized cracks or fractures are produced one at a time, and for a piece of the surface to be released, there must have accumulated a minimum of three intersecting cracks around a single cell of surface material (45,46,47). It is possible that the time duration of a typical solid propellant rocket firing is just too short in comparison with the cumulative damage delay period.

The small importance of impact in the motor and nozzle entry and throat is attributed by Vidya to the relatively low kinetic energy of the droplet in comparison with its thermal energy (48). Cothran and Barnes discussed the possibility of mechanical impact damage in their subsonic-elbow blast-tube tests but then dropped the mechanical impact term in their analysis (49).

In the exhaust jet mechanical impact is generally the important cause of erosion. In travel through the exit cone the particles typically are accelerated to about three times their throat velocity. Their kinetic energy increases with the square of their velocity, and, accordingly their potential for eroding surfaces by mechanical impact goes up by about an order of magnitude.

Ungar studied the effect of solid aluminum and liquid glass particles from rocket exhausts impacting on ablating materials. He found that the surfaces of the reinforced plastics initially were mechanically eroded but then a melt layer accumulated which decelerated the impinging particles and reduced their ability to damage the underlying structure. Eventually all of the energy of the impinging particles was converted to heat without significant mechanical damage being done and heating became the dominant destructive mechanism. Other conditions being equal there did not seem to be any difference whether the impinging particles were solid aluminum or liquid glass. Ungar developed correlations from which erosion rates could be computed (50).

Kuby and Lewis tested erosion due to gas-particle exhaust impingement from a normal rocket and from a hot helium exhaust jet. By analysis of heat transfer into the target they were able to isolate the mechanical impact contribution of the exhaust. Also they compared their results with hypersonic impact data for large single projectiles, in particular with the correlation of Sorensen (51). They found that their surface erosion was always much less than would be predicted by single particle impact theory, usually several orders of magnitude less. This was caused by the accumulation of a thin layer of spent particles and particle fragments over the surface which effectively dissipated most of the kinetic energy of the impacting particles. As a result, increases in the particle impingement rate were accompanied by only relative slight increases in surface erosion. Surface damage was independent of angle of incidence probably due to roughening of the surface. They suggest that surface damage is reduced with reduction in particle size for a constant weight-rate of impingement (52,53).

HEAT TRANSFER

PARTICLES IN GAS FLOW usually increase heat transfer but may decrease it. In either case, as erosion is strongly dependent on surface heating, it is important for us to assess the ways in which particles change heat transfer to the wall.

RADIATION of heat from particles in a two-phase flow typically contributes the major part of the heat flux in the chamber and diminishing fractions as the flow moves out of the motor. Typical fractions for a solid propellant motor with an exit flow about 35% Al_2O_3 are as follows:

Region	*Radiant Flux/Total Flux*
Chamber	.90
Entry (ϵ = -3)	.36
Throat	.13
Exit (ϵ = 14)	.015

The gas produces a small proportion, probably less than 5%, of these radiant fluxes.

Photons of radiant energy originate from the particles. These particles are at all times hotter than the gas or the walls because of their very high temperature of combustion. The photons moving at the speed of light diffuse from the hottest regions of the flow. Because of collisions with particles their paths are changed almost randomly by scattering, absorption and re-emission. They are heavily absorbed by the relatively cool walls and by the cooler expanding gas mixture in the nozzle entry.

Price has developed a widely used practical method for calculating the radiant heat flux from an Al_2O_3 particle cloud inside a rocket motor. Their result depends on the particle-to-gas weight ratio, pressure, temperature, gas molecular weight and cloud thickness (30).

McIntosh developed a special method for calculating particle cloud heating to walls in semi-stagnant regions of rocket motors (54).

Radiant heat moves through the entry and exit cone at a speed far exceeding that of the gas flow and illuminates the plume with the "searchlight" effect. Stockham and Love have recently calculated that the "searchlight" effect may contribute as much heat to the motor base as does direct radiation (55). The radiant heat from the particles in the plume necessitates exterior insulation on the parts of the motor closest to the plume.

The radiant heat flux from two-phase solid propellant rocket plumes is most frequently calculated by the method of Morizumi and Carpenter (56). Carlson suggests some improvements to improve its accuracy (57).

CONVECTIVE HEATING by two-phase flow was analyzed by Marble, who found that for low particle-to-gas weight ratios the effect of the particles on convective heating was primarily to add heat capacity to the flow. In other words, the effect of the particles could be provided for simply by correcting the gas density and the gas specific heat to allow for their effective change due to the presence of the particles (18). Farber and Morely had previously found this result experimentally for particle-to-gas weight ratios from 0 to above 1.0 (28). For solid propellant rockets this ratio ranges from 0 to about 0.6 and is therefore well within the above limit, so this rule can be considered generally applicable for all solid propellant heat transfer.

Particles also perturb convective heat transfer by changing the character of the boundary layer. Farber and Morely and, later, Price found that the presence of particles made the flow and boundary layer more turbulent, thereby increasing heat transfer (28,30). On the other hand Soo found that there was a range of solids loading in which the particles apparently acted through their added inertia to stabilize a turbulent flow and reduce heat transfer (27).

Experimentally, it has been shown in solid propellant rockets that deposits on the wall which make it more irregular will disturb the boundary layer. Also, impingement which does not stick to the wall will increase the turbulence of the boundary layer close to the wall. In either case heat transfer will be increased (30).

IMPINGEMENT HEATING occurs when particles deliver heat energy to the surface during contact.

Experiments by Vidya indicate that when aluminum oxide droplets from a solid propellant gas flow impinge on a wall they lose heat to the wall only until they have changed phase and then are swept away (48). Cothan and Barnes assumed that the particles cooled completely to wall temperature before being swept away, but they reduced their calculated heat flux by an arbitrary "impaction efficiency" in reconciling their test data (49).

Tests at Battelle show that impinging droplets that were at or close to the wall temperature had no observable effect on heat transfer (41).

Impingement of particles of burning metal fuel on solid propellant rocket insulation and nozzle surfaces has been reported (58). Unless the wall is cold enough to extinguish the particle, impingement of this type is usually accompanied by severe erosion and heating. The deposited metal as it continues to burn on the surface produces abnormally high heat fluxes. This is because the heating potential of the droplet of metal due to its unspent heat of combustion is two to five times greater than that of the oxide.

The heating effectiveness of the burning metal is further aided by its high temperature of combustion for aluminum (about 6200°F) which provides a high local temperature gradient greatly increasing conduction into the surface.

Impingement has also been observed to cause reduction of heat flux. In such cases the deposits are nonburning and form protective layers which effectively shield the surface from erosion and add to its thermal insulation (30,34).

Rockets which accumulate heavy particle depositions on nozzle entry surfaces have been observed to lose these deposits in successive runoffs through the throat and exit. These waves of surface flow have been traceable in the heat transfer data. Heat flux is abnormally high during deposition, but then drops and becomes abnormally low as the layer of deposits becomes thicker and insulates the surface. Flux becomes high again when the deposits slough off (30,34).

In exit-plume impingement heat transfer Kuby and Lewis show that the thermal energy delivered by the particles has been found to be small compared with the kinetic energy delivered by the particles. However, if the impingement rate is sufficiently large a protective layer of spent particles builds up on the surface which cushions the impacts and converts the kinetic energy to heat. The layer of spent particles becomes hotter than the surface and carries away a large portion of the heat. It is assumed that the surface is in thermal equilibrium with the layer of particle debris, the resulting calculation overestimates the heating by factors ranging from 4 to 100. The heating reduces the strength of the surface and thereby increases the mechanical erosion (52,53).

CHEMICAL EFFECTS

Chemical attack by the oxidizing species of the exhaust gas is the dominant erosive mechanism in the high velocity regions of the chamber and the nozzle for refractory metals, graphites and ablative materials (48,59).

A high rate of heat transfer is an essential condition for chemical erosion because the chemical reactions of the gas with the surface are dependent on temperature for initiation and rate (48). Whether the heat is transferred by radiation, convection, or impingement does not seem important.

McDonald and Hedman present both theory and correlated data which show nozzle throat erosion to be controlled by temperature and the oxidizing potential of the gas. For a series of propellants with increasing aluminum content they show decreasing erosion rates. This is explained by the fact that the more fuel rich propellants are oxygen lean (59). This is confirmed by Olcott and Batchelor (60).

Reactions of deposited metal oxides with the surface material are possible but are usually considered a negligible factor (58).

EROSION PROBLEMS

The two-phase flow effects described in the above sections cause practically all of the erosion problems experienced in solid propellant rocket motors. Ten typical locations where these usually occur are shown in Figure 9. These common erosion occurrences are briefly described in the following:

(1) Particles of oxide impinge on the entry nose causing either very high heat transfer, rapid erosion and gouging, or, where deposition is heavy, accumulated deposits may coat and protect the nozzle nose until the deposits melt and slough off.

(2) Impingement on the nozzle entry causes high heat transfer and erosion. If deposited fuel from the nozzle nose migrates to the entry it will cause very high local heat transfer. In either case nonsymmetric abnormal thermal stresses and heavy erosion result. On the other hand a coating of deposition may protect the surface, at least until it melts away.

(3) The nozzle throat generally escapes impingement but oxide or burning fuel deposits from upstream may move to and through the throat. The heat transfer due to such deposits are irregular and may unevenly heat the throat causing local magnified thermal stresses which spall or shatter brittle materials (61). High local heating causes high local erosion. Surface geometry degradation distorts flow causing impingement, erosion and gouging.

(4) Split-line ridges in the nozzle area which project beyond the boundary layer receiving heavy impingement even from small particles. Unless such surfaces are made of refractory metals they will rapidly be eroded away.

(5) The downstream portion of the exit cone contour may, if the contour is excessively curved, receive solid particle impingement and be mechanically eroded.

(6) A jet vane inserted into the exhaust receives direct impingement by solid particles travelling at supersonic speed. Erosion is heavy due to impingement heat transfer which heats and weakens the material with heavy mechanical erosion by particles.

(7) An object in the path of the exhaust plume receives heavy solid particle impingement. Particles are travelling at close to hypersonic velocities, but the gases are relatively cool and of very low density. The damage to the surface is mainly due to mechanical impact.

(8) Particles of burning fuel deposit on the backside of the submerged nozzle or on the aft dome near the nozzle. The burning fuel may run down over the aft dome or into semi-stagnant crevices delivering very large heat fluxes to relatively thinly insulated surfaces causing burn-through.

(9) Burning fuel may be deposited on the forward dome or igniter surfaces and run down into semi-stagnant crevices carrying large heat fluxes to thinly insulated areas causing burn-through.

(10) The outside of the aft dome receives a high heat flux from the solid particles in the exit plume. These not only emit due to their own radiant heat but scatter radiation from the chamber due to the "searchlight effect". The aft dome exterior, if unprotected by insulation, could be seriously charred.

CONCLUSIONS

We have traced the formation of two-phase flow, its movement through the chamber and its effects on motor surfaces. An analysis to predict erosion due to two-phase flow should follow this same sequence and use, as appropriate, the analytic methods illustrated or referred to.

It should be evident that the designer in understanding two-phase flow and its consequences can design to avoid these problems.

In particular, it is recommended that the designer: (1) select a fuel that will completely burn before its gases reach the nozzle surfaces, (2) give the motor internal spaces good aerodynamic design that will make large flow turns only at low velocities and, at high speeds, make only gradual turns that will not cause particles to penetrate the boundary layers and to impinge and (3) avoid ridges and obstacles of any kind in the high-speed flow regions (including the entry, throat and exit cone).

REFERENCES

1 Crump, J.E. — ICRPG 2nd Combustion Conference, Los Angeles, November 1965, CPIA Publication No. 105, May 1966.

2 — *Combustion of Solid Propellants and Low Frequency Combustion Instability*, by Aerothermochemistry Division. China Lake, California, NOTS, June 1967. p.244 (NOTS TP 4244).

3 — *Combustion of Solid Propellants and Low Frequency Combustion Instability* Progress Report 1 April - 30 September 1967, by Aerothermochemistry Division. China Lake, California, NWC, April 1968. p.108 (NWC TP 4478).

4 Miller, R.R. — ICRPG 2nd Combustion Conference, Los Angeles, November 1965, CPIA Publication No. 105, May 1966.

5 Macek, A. — *Fundamentals of Combustion of Single Aluminum and Beryllium Particles*, Project Squid Tech. Report ARC-9-P, 9 June 1969.

6 Brzustowski, T.A. Glassman, I. — *Vapor-Phase Diffusion Flames in the Combustion of Magnesium and Aluminum, I., Analytical Development*, Progress in Astronautics and Aeronautics, Vol.15, Heterogeneous Combustion, Academic Press (1964).

7 Kuehl, D.K. — *Ignition and Combustion of Aluminum and Beryllium*, United Aircraft Corp., Research Lab., AIAA J., Vol.3, No.12, (December 1965).

8 Davis, A. — *Solid Propellants: The Combustion of Particles of Metal Ingredients*, E.R.D.E., 17/R/62, Explosives Research and Development Establishment, 4 December 1962.

9 Drew, C.M. et al. — *Study of Quenched Aluminum Particle Combustion*, Progress in Astronautics and Aeronautics, Vol.15, Heterogeneous Combustion, Academic Press (1964).

10 Brown, R. — *Oxide Particles in Solid Rocket Exhausts*, Remarks by the Session Chairman, Two-Phase Flow Conference, 15-16 March 1967, AFRPL-TR-67-223.

11 Mednikov, E.P. — *Acoustic Coagulation and Precipitation of Aerosols*, Translation from Russian, 1965.

12 Jenkins, R.M. Hoglund, R.F. — *A Unified Theory of Particle Growth in Rocket Chambers and Nozzles.* AIAA Paper No.69-541, 5th Propulsion Joint Specialist Conference, June 1969.

13 Crowe, C.T. et al. — *Analytical and Experimental Studies of Nozzle Performance and Al_2O_3 Particle Size.* Two-Phase Flow Conference, 15-16 March 1967, AFRPL-TR-67-223.

14 Nack, T.H. — *Theory of Particle Agglomeration, Mean Size Determination and Chamber Coagulation in Rocket Motors.* Two-Phase Flow Conference, 15-16 March 1967, AFRPL-TR-67-223.

15 Bartlett, R.W. Delaney, L.J. — *Effect of Liquid Surface Tension on Maximum Particle Size in Two-Phase Nozzle Flow.* Pyrodynamics 4, No.4, October 1966.

16 Cheung, H Cohen, N.S. — *Performance of Solid Propellants Containing Metal Additives.* AIAA J., 3, February 1965.

17 Delaney, L.J. — *Particle Characteristics in Two-Phase Plumes.* Martin Marietta Corp., Rocket Plume Phenomena Specialists Meeting, 11-12 July 1968, Report No.TOR-0200(S4960-10)-1.

18 Marble, F.E. — *Dynamics of a Gas Containing Small Solid Particles.* Combustion and Propulsion (5th Agardograph Colloquim), pp.175-213, 1963.

19 Travis, L.P. — *Heat Transfer and Particle Trajectories in Solid-Rocket Nozzles.* Aerojet Report No.0162-01TN-17, AFBSD Tech. Note BSD-TDR-62-165, October 1962.

20 Zeamer, R.J. — *Methods for Predicting Particle Behavior in Two-Phase Flow.* Two-Phase Flow Conference, 15-16 March 1967, AFRPL-TR-67-223.

21 Prozan, R.J. — *Development of a Method of Characteristics Solution for Supersonic Flow of an Ideal, Frozen or Equilibrium Reacting Gas Mixture.* Lockheed Missile and Space Company, LMSC/HREC A782535-A, Contract NAS 8-20082, April 1966.

22 Carlson, D.J. — *Particle Drag and Heat Transfer in Rocket Nozzles.* AIAA Journal, Vol.2, November 1964.

23 Crowe, C.T. — *Drag Coefficient of Particles in a Rocket Nozzle.* AIAA Journal, Vol.5 No.5, May 1967.

24 Selberg, B.P. Nicholls, J.A. — *Drag Coefficient of Small Spherical Particles.* AIAA Journal, Vol.6, March 1968.

25 Marshall, R.L. Pellett, G.L. — *An Experimental Study of the Drag Coefficient of Burning Aluminum Droplets.* NASA Langley Research Center, Hampton, Va., Third ICRPG Combustion Conference, October 1966.

26 — Informal memorandum from L.K.Isaacson of the University of Utah, Salt Lake City, Utah, August 1967.

27 Soo, S.L. — *Gas-Solid Flow.* Single and Multi-Component Flow Processes Symposium Engineering Res. Publ. No.45, Rutgers, College of Engineering, New Brunswick, N.J., 1965.

28 Farber, L. Morley, M.J. — *Heat Transfer to Flowing Gas-Solids Mixtures in a Circular Tube.* Industrial and Engineering Chemistry, July 1957.

29 Ungar, E.W. — *Heat Transfer to a Solid Propellant Rocket Motor Nozzle.* ARS Preprint 2333-62 (January 1962).

30 Price, F.C. et al. — *Internal Environment of Solid Rocket Nozzles.* Philco Publication No.U-2709, RPL-TDR-64-140, July 1964.

31 Gowariker, V.R. — *Mechanical and Chemical Contributions to the Erosion Rates of Graphite Throats in Rocket Motor Nozzles.* J. of Spacecraft, October 1966.

32 Mayberry, J.L. et al. — *Correlation of Graphite Nozzle Throat Erosion in Solid Rocket Motors.* AIAA Journal, November 1968.

33 Moody, H.L. Price, F.C. — *Prediction of Nozzle Material Performance for NASA's 260 SL-3 Motor.* J. of Spacecraft, March 1969.

34 — Informal communication from W.L.Smallwood of Philco Laboratories, Newport Beach, California, April 1968.

35 Baw, P.S.
Peskin, R.L.
Density Profiles in Gas-Solid Suspension Flow. AIAA Journal, April 1967.

36 Langmuir, I.
Blodgett, K.B.
A Mathematical Investigation of Water Droplet Trajectories. AAF TN 5418, ATI No.25,333, Air Material Command, February 1946 (Contract No.W-33-038-ac-9151 with General Electric Co.).

37 Adelberg, M.
The Inertia Parameter in Gas Particle Flow. Douglas Aircraft Co., MSCA-444-62; TN-110-D-1-4-64, March 1964.

38 Hacker, P.T.
Brun, R.J.
Impingement of Droplets in 90-degree Elbows with Potential Flow. NACA TN 2999, September 1953.

39 von Karman, T.
Transactions of American Society Mechanical Engineering. Vol.61, p.705 (1939).

40 Friedlander, S.K.
Johnstone, H.F.
Deposition of Suspended Particles from Turbulent Gas Streams. Industrial and Engineering Chemistry, July 1957.

41 Allen, J.M.
et al.
An Experimental Investigation of the Deposition of Small Particles from a Moving Gas Stream. Battelle Memorial Institute Report (sponsored by AEDC, Contract No. AF 40(600)-710) AEDC-TN 58-73, ASTIA Doc. N1. AD-201518, September 1958.

42 Grinberg, I.M.
Unger, E.W.
Determination of Temperature History of a Solid-Propellant Rocket Motor Nozzle. Battelle Memorial Institute Report, May 1963.

43 Hobbs, J.M.
Evaluation of the Electrically Charged Nozzle Concept. AFRPL, Edwards, California, AD 487 729, FLD/GP 21/8.1, May 1966.

44 Breitwieser, R.
On Deposits in Jet Engines. Lewis Research Center, The Chemistry of Propellants Meeting, AGARD Combustion and Propulsion Panel, 8-12 June 1959.

45 Engel, Olive,
Summary of Turbine Erosion Meeting. Jet Propulsion Laboratory, NASA-CR-88487, N67-37102, p.129, June 1967.

46 Mok, Chi-Hung,
A Cumulative Damage Concept in Rain Erosion Study. Technical Notes, pp.751-753, April 1969.

47 Engel, O.G.
Mechanism of Rain Erosion, Part 1, Impact Pressure in Solid-Liquid Sphere Collisions. Wright Air Development Center, AEDC Technical Report 5-132, July 1953.

48 McCuen, P.A.
et al.
A Study of Solid Propellant Rocket Motor Exposed Materials Behavior. Vidya, Palo Alto, California. Vidya Report No.149, AFRPL-TR-65-33, February 1965.

49 Cothran, L.E.
Barnes, S.V.
Behavior of Plastic and Refractory Materials in the Particle-Impingement Areas of Solid Propellant Ducting Systems. 1st AIAA Annual Meeting, Washington, DC AIAA Paper No.64-224, June 29-July 2, 1964.

50 Ungar, E.W.
Particle Impacts on the Melt Layer of an Ablating Body. ARS Journal. Battelle Memorial Institute Report, September 1960.

51 Sorensen, N.R.
Systematic Investigation of Crater Formation in Metals. Proceedings of the Seventh Symposium on Hyper-Velocity Impact, Vol.VI, 1965, pp.281-325.

52 Kuby, W.C.
Lewis, C.H.
An Experimental Study of the Effects of Particle Cloud Impingement, Technical Notes. Philco-Ford Corporation, Newport Beach, California, July 1966.

53 Lederman, A.J.
et al.
Two-Phase Impingement Forces. Aeronautics Proceedings of the Rocket Plume Phenomena Specialists Meeting, Vol.I, Aerospace Corporation, Report No.TOR-0200 (S4960-10)-1, October 1968.

54 McIntosh, M.J.
Heat-Transfer Solution for a Gas/Particle Mixture Losing Heat to Parallel Boundaries. Engineering Notes. Hercules Incorporated, Magna, Utah, January 1968.

55 Stockham, L.W.
Love, T.J.
Radiative Heat Transfer from a Cylindrical Cloud of Particles, AIAA Journal, Vol.6, No.10, October 1968.

56 Morizumi, S.J.
Carpenter, H.J.
Thermal Radiation from the Exhaust Plume of an Aluminized Composite Propellant Rocket. Aerospace Sciences Meeting, New York, January 20-22, 1964. Preprint No.64-61.

57 Huffaker, R.M.
Carlson, D.J.
Radiation from Rocket Exhaust Plumes. AIAA Second Propulsion Joint Specialist Conference, Colorado Springs, Colorado, 13-17 June 1966. AIAA Paper No.66-652.

58 Schaefer, J.W. et al.
Studies of Ablative Material Performance for Solid Rocket Nozzle Applications. Prepared for NASA (Contract NAS7-534). Aerotherm Corp. Report No.68-30, NASA CR-72429, 1 March 1968.

59 McDonald, A.J.
Hedman, P.O.
Erosion of Graphite In Solid-Propellant Combustion Gases and Effects on Heat Transfer. AIAA Journal, Vol.3, No.7. Thiokol Chemical Corporation, Brigham City, Utah, July 1965.

60 Olcott, E.L.
Batchelor, J.D.
Failure Mechanisms in Dense Tungsten Alloy Rocket Nozzles. AIAA Solid Propellant Rocket Conference, Palo Alto, California, 29-31 January 1964. Preprint No.64-103.

61 Tang, S.
Thermal Stresses in Hollow Graphite Cylinders with Asymmetric Heating. AIAA Journal, Engineering Notes, May 1968.

TABLE I

Impingement Numbers (N_I) for Typical Solid Propellant Rocket Two-Phase Flow

	Location	Particle	Re	δ(ft)	S(ft)	S/δ	Sin θ	N_I = S/δ Sin θ	Interpretation
A.	Chamber	150 Micron burning Al.	7×10^4	0.01	2.1	229	0.1	23.	Large particles of burning fuel would impinge.
B.	Chamber	0.5 Micron Al_2O_3 Smoke	7×10^0	0.01	2.4×10^{-5}	0.0025	0.9	0.0025	Tiny smoke particles would not impinge.
C.	Nozzle Nose	100 Micron burning Al.	2.2×10^5	0.001	1.7×10	16.000	0.9	14.000	Large particles of burning fuel would impinge.
D.	Nozzle Nose	1 Micron Al_2O_3	2.2×10^5	0.001	1.7×10^{-3}	1.6	0.2	0.32	Particles of oxide would not impinge but could if the flow approach angle were increased
E.	Nozzle Entry	2 Micron Al_2O_3	1.4×10^6	0.01	1.2×10^{-2}	1.1	0.05	0.055	In low angle flow over well designed entry, oxide particles would not impinge.
F.	Nozzle Throat	5 Micron Al_2O_3	5.6×10^6	0.017	2.1×10^{-1}	12.5	0.05	0.62	Impingement condition is marginal.
G.	Joint at Nozzle Throat	5 Micron Al_2O_3	5.6×10^6	0.004	2.1×10^{-1}	52	1.0	52.	Flow approaching a step joint at the throat would result in heavy impingement of oxide particles.
H.	Nozzle Exit Cone	9 Micron Al_2O_3	9×10^3	0.27	3.2	12.3	0.05	0.61	In grazing flow along the inward curving contour particles would be close to impinging.
I.	Jet Vane at Exit	9 Micron Al_2O_3	1.8×10^2	0.04	3.2	87	1.0	87	A jet vane inserted into the exhaust stream would receive very heavy impingement.
J.	Object in Plume	9 Micron Al_2O_3	3×10	0.02	4.7	240	1.0	240	An object in the expanded plume would receive very heavy impingement.

NOTE: Values of N_p above 1.0 indicate probable impingement

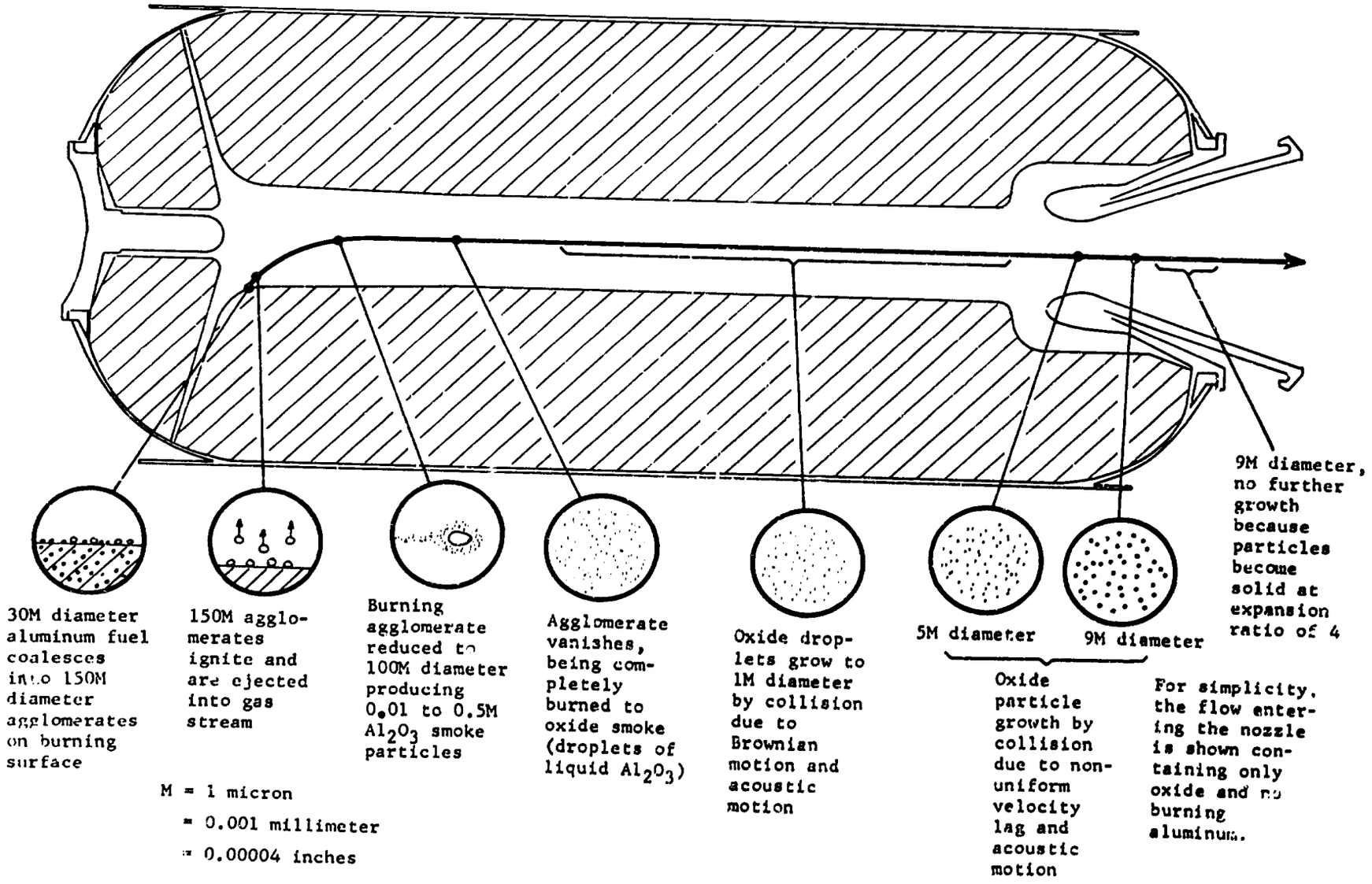

Fig.1 The changing state of two-phase flow in a typical medium-sized solid propellant rocket motor (nozzle throat about 12-inches diameter)

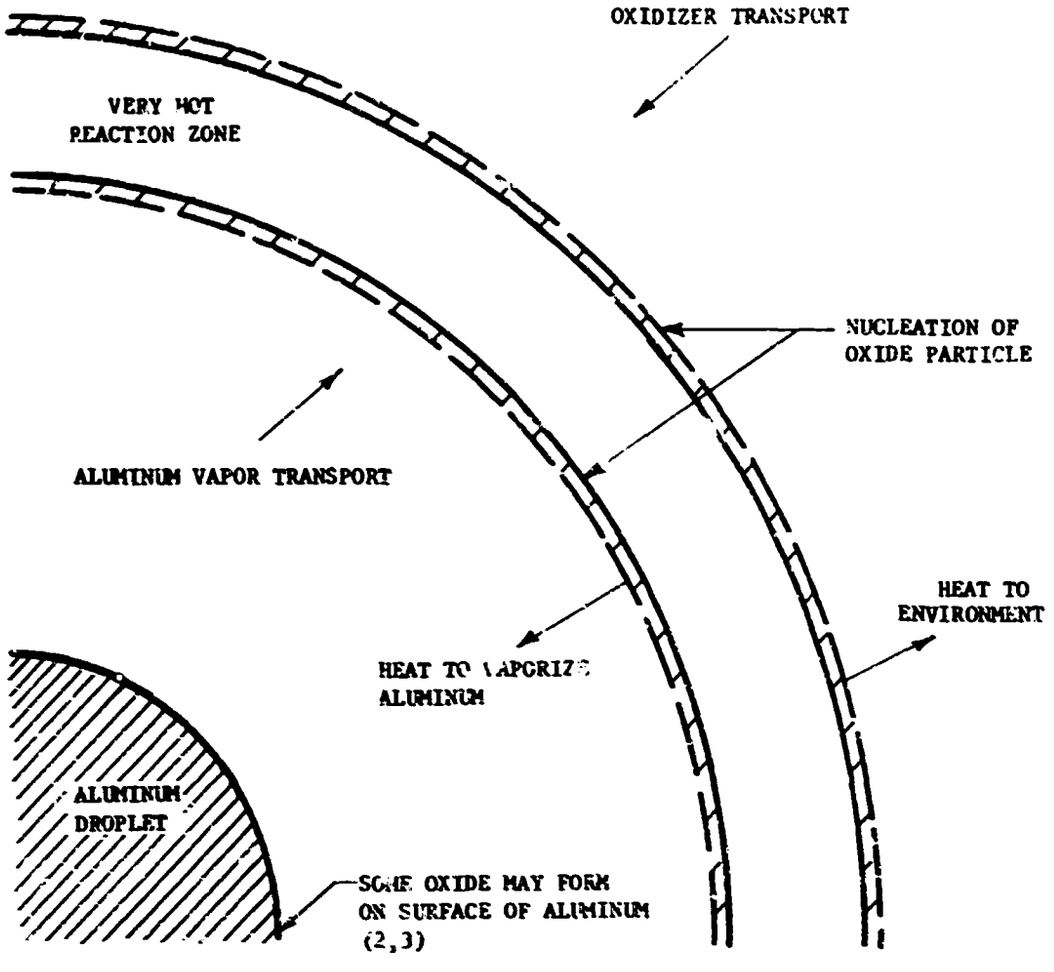

Fig. 2 Aluminum combustion in the vapor phase (reference 6)

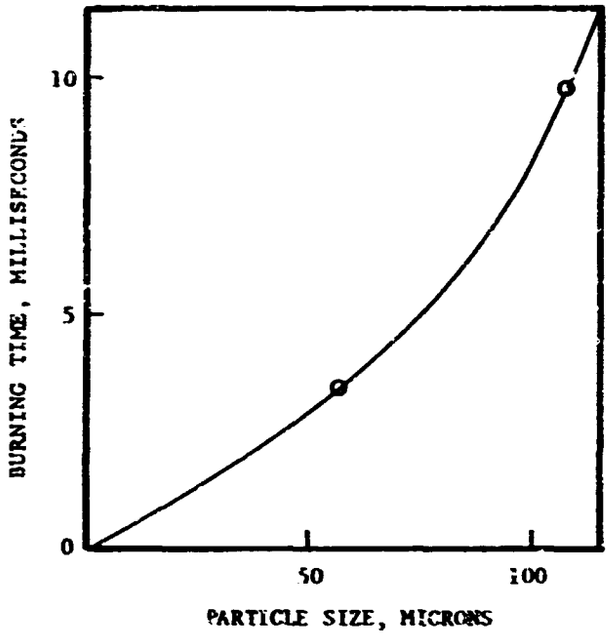

PELLET COMPOSITION
15% PARAFORMALDEHYDE
85% AMMONIUM PERCHLORATE
0.01% ALUMINUM

Fig. 3 Effect of particle size on burning time at 1000 psi (reference 8)

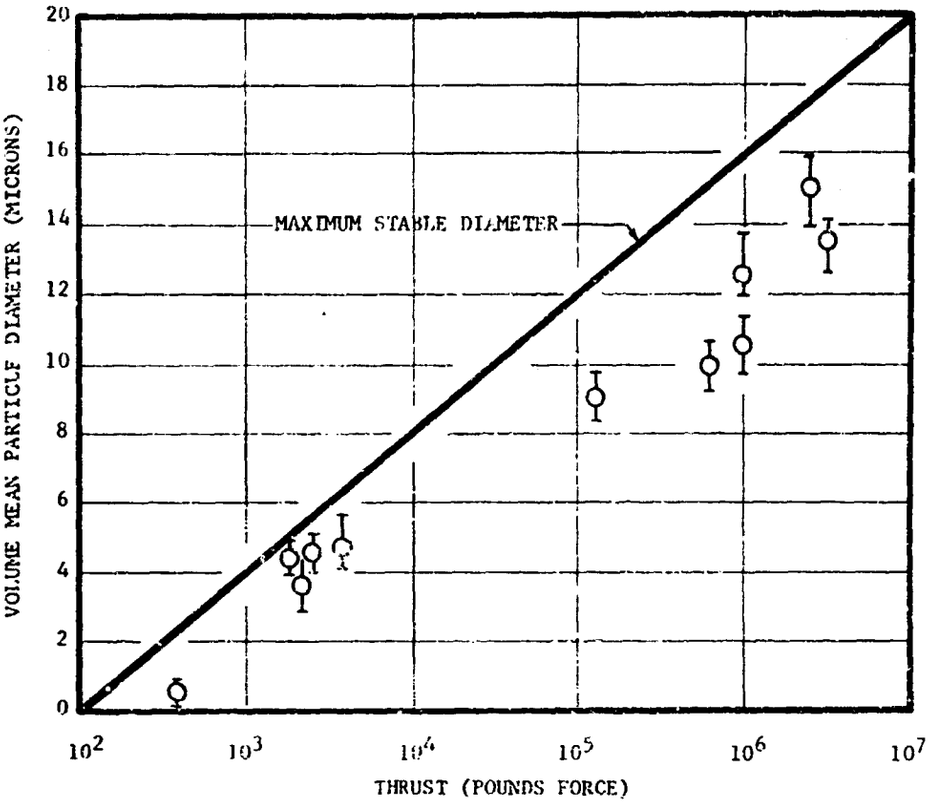

Fig. 4 Variation of Al_2O_3 particle diameter with motor thrust (reference 10)

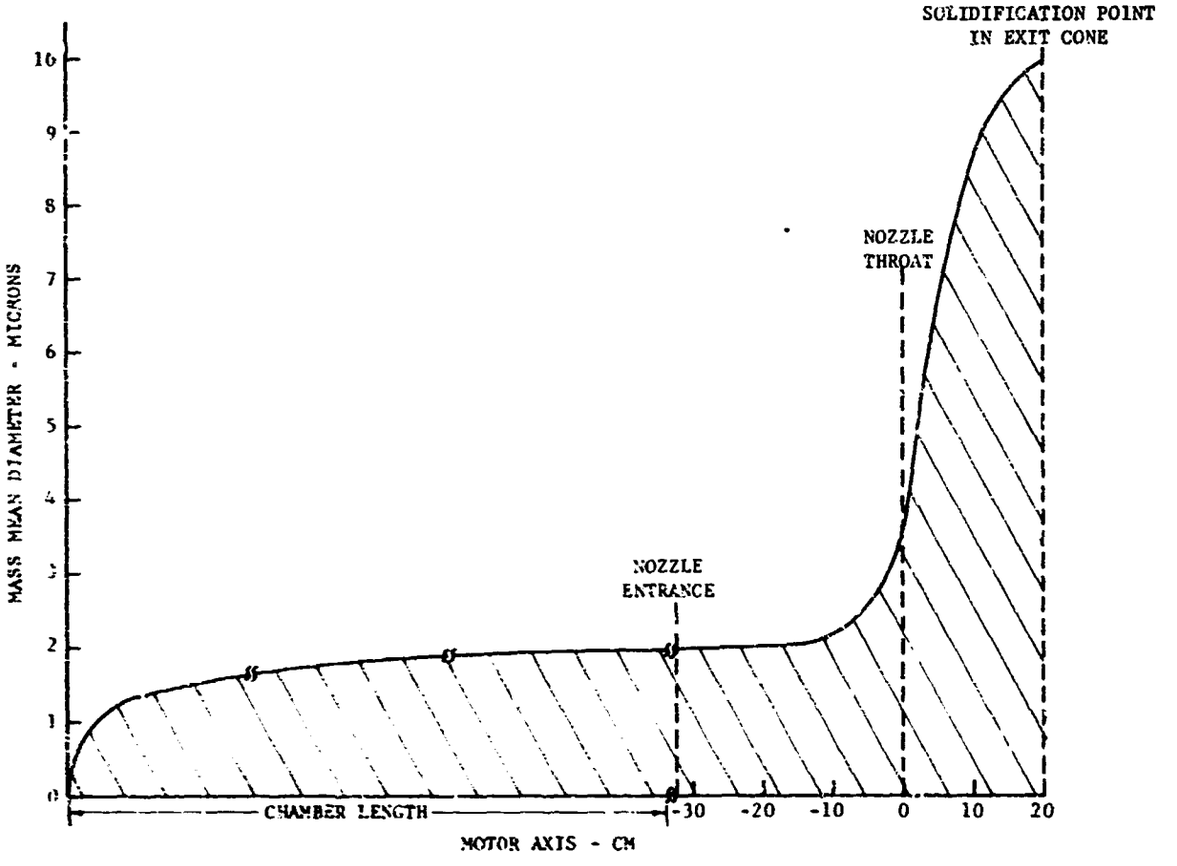

Fig. 5 Calculated particle growth history for Titan III-C motor. (reference 12)

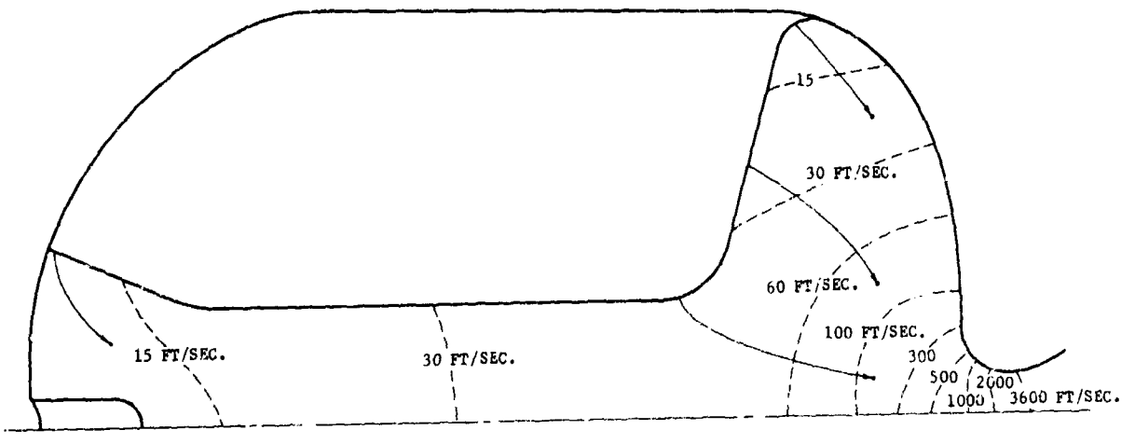

Fig.6 Calculated flow velocities (feet/second) and paths of burning 160 micron aluminum particles. End of path line indicates point at which particle is completely consumed

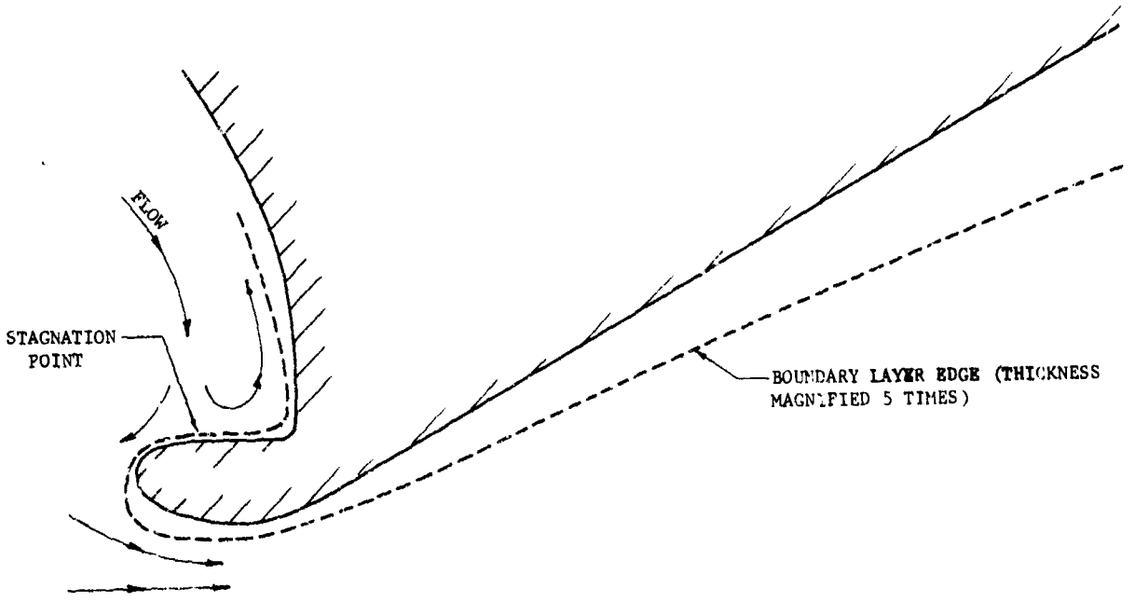

Fig.7 Boundary layer thickness on a typical solid propellant rocket nozzle

NOTE: HEAVY ARROWS ⟶ INDICATE IMPINGEMENT, LIGHT ARROWS ⟶ INDICATE NO IMPINGEMENT, TURBULENT DIFFUSION OF PARTICLES INDICATED BY - - - - - -.

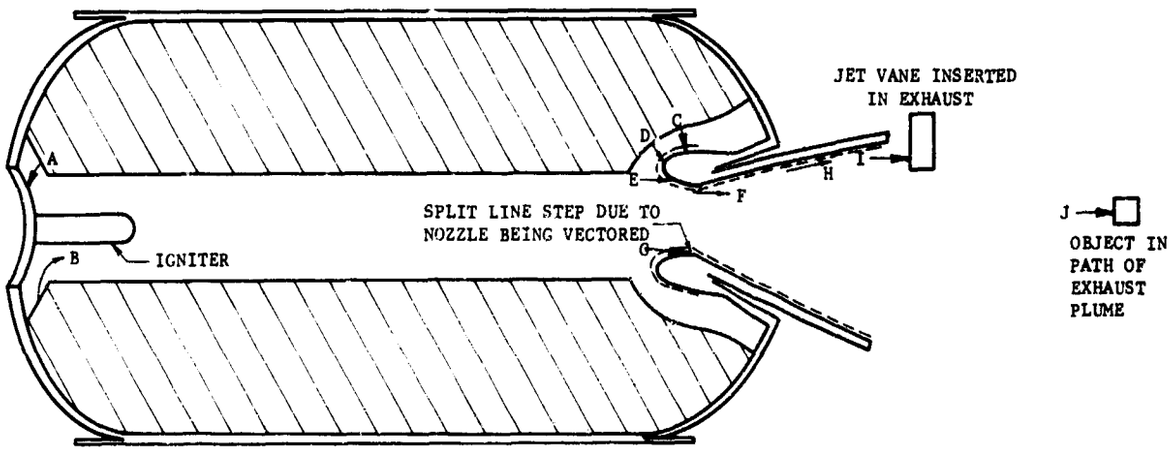

Fig.8 Typical particle impingement locations in a solid propellant rocket motor, (see table I for impingement data and interpretation)

NOTE: ARROWS INDICATE FLOW OF DEPOSITED MATERIAL

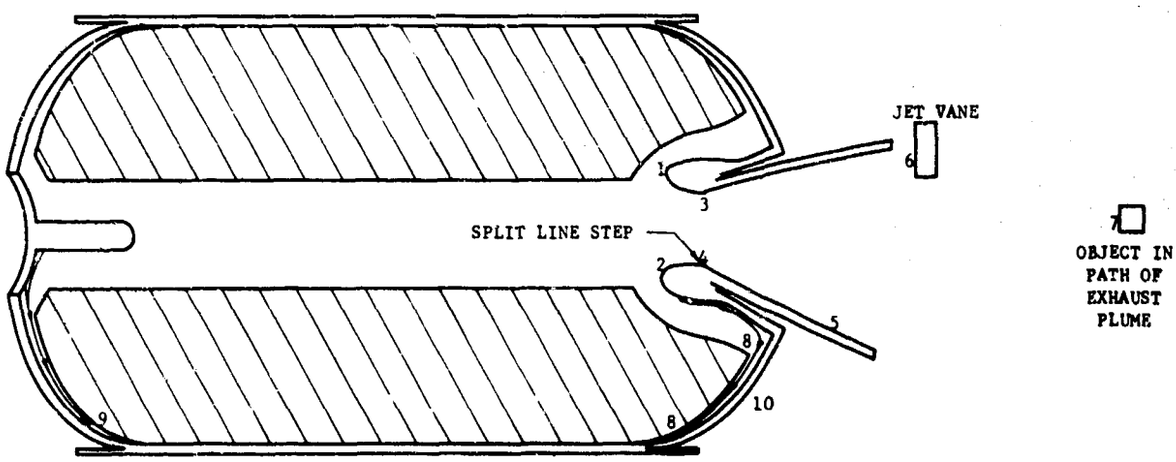

Fig.9 Typical locations of erosion due to two-phase flow, (see pages 27-7 and 27-8 for interpretation)

THE ROLE OF CARBON-GAS REACTIONS IN THE EROSION OF ROCKET NOZZLES

by

G. A. HEATH and R. W. THACKRAY

Ministry of Technology, Rocket Propulsion Establishment,
Westcott, Aylesbury, Buckinghamshire, U.K.

SUMMARY

Graphites have excellent physical and mechanical properties for use at high temperatures in uncooled rocket nozzles but undergo erosion, apparently arising from chemical reactions with gaseous combustion products. Recent chemical kinetic data on carbon-gas reactions relevant to rocket conditions have enabled chemical rate controlled erosion to be calculated and compared with experimental observations on specific graphite nozzles. The reactivity of the nozzle surface depends on its temperature which rises progressively during the rocket operation. Preliminary work has shown that at surface temperatures up to about 1600°K the erosion agrees with that predicted by a chemical rate control mechanism whereas at higher temperatures the predicted values are too high, probably because of boundary layer effects which hinder transfer of reactants from the free stream to the surface. Among graphites currently available pyrolytic graphite has the lowest reactivity to oxidising gases and the highest resistance to erosion in nozzles. This highly anisotropic material may be used with advantage in practical designs.

LIST OF SYMBOLS

k_i	first order reaction rate constant for gas species, i
$c_{w,i}$	concentration of gas species, i , at wall
$c_{e,i}$	concentration of gas species, i , at edge of boundary layer, i.e. free stream value
D_i	effective diffusion coefficient for gas species, i
r	radial distance from axis of nozzle
K	thermal diffusivity of nozzle throat material
t	time
δ	thickness of boundary layer
θ	temperature

THE NOZZLE IS AN ESSENTIAL PART OF A ROCKET MOTOR and has the function of converting the thermal energy produced in a combustion process into propulsive kinetic energy in an exhaust jet. The nozzle is usually of the convergent-divergent type, in which the combustion products are accelerated to sonic velocity in the convergent section and to supersonic velocity in the divergent section. The maximum heat transfer occurs at the smallest cross-section or "throat" where the mass velocity per unit cross-sectional area reaches a maximum value and this is where nozzle materials problems are most severe.

The nozzle is required to maintain its contour and structural integrity throughout the period of combustion which may range from a fraction of a second to several minutes. The use of uncooled nozzles, particularly for solid propellent rocket motors, is preferable to the use of cooling techniques which usually involve penalties in terms of complication, cost and weight. Only a limited number of materials are sufficiently refractory for use in uncooled nozzles and these are invariably brittle and susceptible to thermal shock. Of these materials, graphite is the most widely used because of its low density, good specific strength, high sublimation temperature and high resistance of thermal shock. Many different types of graphite have been produced but they all, to some extent, undergo erosion when used in rocket nozzles. It is important for the rocket designer to be able to make reasonable predictions of the dimensional changes in the nozzle throat which occur throughout the firing since they affect the variation of thrust with time. There will also be some limit to the tolerable amount of erosion. Furthermore, any non-uniformity of erosion may lead to undesirable misalignment of thrust. Since, as will be shown later, the erosion of graphite nozzles is believed to arise mainly from chemical reactions with the rocket exhaust gases, it is clear that carbon-gas reactions play an important role in determining the extent of this erosion. This paper draws some preliminary conclusions about the relationship between the extent of erosion and the chemical kinetics of the relevant carbon-gas reactions.

MECHANISMS CONTROLLING EROSION RATE

The erosion of graphite nozzles may be considered to arise from both chemical and mechanical processes. Graphite is known to react chemically with oxidising species such as water vapour, carbon dioxide, oxygen, hydroxyl radicals and oxygen atoms, which may be present in the rocket exhaust, to form carbon monoxide, a gaseous product. These and other possible reactions, e.g. with hydrogen, will lead to surface regression. Mechanical erosion may result from the action of shearing forces exerted by the high velocity rocket exhaust, often containing liquid and solid particles.

Although some attempts have been made to predict the erosion as a combination of both chemical and mechanical processes, e.g. by Gowariker (1), there is considerable experimental evidence, summarised below, to suggest that chemical erosion predominates.

(i) For any particular grade of graphite, erosion rate is very dependent on the concentration of oxidising gases in the rocket exhaust. This observation has been widely reported, e.g. (2,3) and a common finding is that an aluminised propellent often produces less erosion than the corresponding non-aluminised propellent, even though the former has a significantly higher combustion temperature and produces alumina which would be expected to accentuate mechanical erosion. However, the non-aluminised propellent produces larger concentrations of oxidising gases.

(ii) In laboratory experiments different types of graphite have been shown to exhibit different reactivities towards oxidising gases, e.g. (4). The rates of erosion of these graphites in rocket nozzles fall into the same general pattern, e.g. pyrolytic graphite can exhibit up to twenty times less erosion than high density conventional graphites (5).

(iii) Laboratory experiments on carbon-gas reactions carried out with flow reactors, e.g. (4), have shown that, at constant temperature, reaction rate increases with flow velocity in the region where there are boundary layer effects, eventually reaching a value independent of flow velocity, which is considered to be the true chemical rate. Mechanical erosion would be expected to increase indefinitely with flow velocity. Also, in this type of experiment, inert gases such as argon produce negligible erosion at all velocities, except at very high temperatures where vaporisation of carbon can occur.

Even with the assumption that erosion is caused only by chemical reaction, i.e. mechanical erosion is negligible, the rate controlling mechanism is not necessarily the "true" chemical rate of the surface reaction since the presence of a boundary layer may hinder the supply of reactive species to the surface. This situation has been treated extensively elsewhere, particularly by Rosner, e.g. (6). In the simplest case for a first order reaction of a gaseous species, the reaction rate at the surface is given by $k_i c_w$. This is balanced by the rate of flow of reactive species by diffusion through the boundary layer to the surface, given by $D_i (c_{e,i} - c_{w,i})/\delta$. The relative magnitudes of the velocity constants k_i and D_i/δ may be used to define three different rate controlling mechanisms.

(a) Chemical rate control
When the reaction rate constant is very small, such that $k_i << D_i/\delta$, then $c_{w,i} \rightarrow c_{e,i}$, i.e. the concentration of reactive species at the wall is very similar to that in the free stream. Under this condition the erosion rate is controlled by the "true" chemical rate at the surface. The calculation of erosion rate requires a knowledge of the surface temperature (which influences the value of k_i), the concentrations of reactive species in the gas stream and the relevant chemical kinetic data.

(b) Transition region
When the reaction rate constant, k_i , is significant compared to D_i/δ then there will be a concentration gradient of reactive species across the boundary layer such that the concentration at the wall will be less than in the free stream. For instance if $k_i = D_i/\delta$, then $c_{w,i} = c_{e,i}/2$. The erosion rate will depend on the values of both k_i and D_i/δ . The calculation of erosion rate requires all the same data as for (a) above and, in addition, the relevant data for mass transfer through the boundary layer.

(c) Diffusion control
When the reaction rate constant is large, such that $k_i >> D_i/\delta$, then $c_{w,i} \rightarrow 0$, i.e. any reactive species reaching the wall is immediately removed and the concentration is effectively zero. The erosion rate is thus dependent only on the rate of diffusion of reactive species through the boundary layer to the surface. The calculation of erosion rate requires only a knowledge of mass transfer data.

During the operation of a rocket motor the temperature of the exposed surface of the nozzle rises progressively and the reaction rate constants would be expected to increase with temperature. Thus all the above mechanisms may be operative at some time during the firing. It can be seen that the surface temperature is of paramount significance. It should also be noted that the erosion rate cannot exceed that predicted by chemical rate control.

CHEMICAL REACTIVITY OF GRAPHITES

Reactions between graphites and gases have been studied extensively and there is a considerable literature dealing with the topic. An excellent review has been made by Lewis (7).

The conditions under which the nozzle operates depend on the propellant system, combustion pressure and burning time. At the nozzle throat the gas temperature (approximately 0.9 of the combustion temperature) may be over 3000°C, the pressure (approximately 0.5 of combustion pressure) may be up to a hundred atmospheres and the burning time may be up to several minutes. The gas stream may contain significant amounts of reactive species (e.g. see Table 1) and is at sonic velocity, typically about 1000 metres/sec. It is desirable to be able to make use of chemical kinetic data appropriate to these conditions but, unfortunately, most experimental data have been obtained at either low temperature or low pressure. Extrapolation to rocket nozzle conditions is not reliable because of the complex nature of the reactions. The shortage of useful data is no doubt due to the difficulty of devising experimental methods which lead to the acquisition of true chemical rates not influenced by boundary layer effects. Another complication is that the reactivity of different graphites has been shown to vary widely according to their structure.

In the combustion products from many propellents the principal reactive species are water vapour, carbon dioxide, oxygen, hydrogen, hydroxyl radicals and oxygen atoms. Recent work (8) has yielded chemical rates for the first four of these reactants at temperatures up to 3000°K and pressures up to 100 psia, i.e. more relevant to nozzle conditions than previous data, and for two graphites in particular, viz. Le Carbone 5890 and pyrolytic graphite, which we have investigated in our rocket nozzle tests. Some extrapolation of these data was still required in order to apply them to our nozzle tests and therefore consideration had to be given to the influence of temperature, pressure and mixtures of gases on the basic data.

APPLICATION OF CHEMICAL KINETICS TO PREDICTION OF NOZZLE EROSION

PREVIOUS WORK. No satisfactory comprehensive method of predicting the erosion of graphite nozzles had yet been devised. However, considerable progress has been made in this direction and some notable contributions may be considered very briefly.

(i) Delaney, Eagleton and Jones (2)
Calculations were made of the surface temperature history of the nozzle and the erosion was predicted, taking into account both chemical rates and boundary layer diffusion. The kinetic data for the C/CO_2 reaction were extrapolated from the results of Khitrin (9) which had been obtained for electrode carbon at a gas pressure of one atmosphere and over the temperature range 1000-2000°K. It was assumed that the C/H_2O reaction had the same rate as the C/CO_2 reaction under all conditions (although it was recognised that the C/H_2O rate may be considerably faster) and that both reactions are first order. The C/H_2 reaction was assumed to be negligible below 2500°K and the C/O_2, C/OH and C/O reactions were assumed to be negligible because of the low concentrations involved. They concluded that chemical rate control operates at surface temperatures below about 1500°K and that at about 2000°K chemical and diffusion processes are equally important.

(ii) McCuen, Schaefer, Lundberg and Kendall (10)
A similar approach to that of the previous example was made but with a comprehensive analysis of heat and mass transfer for a multi-component gas stream. The chemical reactions considered to be important were C/CO_2, C/H_2O and C/H_2. The C/CO_2 rate constants were from extrapolation of the results of Gulbransen and Andrew (11) for a synthetic graphite in the temperature range 800-1200°K at one atmosphere in a static system and the C/H_2O rate constants were from extrapolation of the results of Blyholder and Eyring (12) for a spectroscopic grade graphite at 1200-1600°K and in the pressure range of approximately 10^{-5} to 10^{-4} atmospheres. The C/H_2 reaction kinetics were taken from Lowrie (13). All reactions were assumed to be first order. This work has produced very useful computer

programs for the prediction of erosion rates of graphites and ablative materials such as reinforced plastics.

(iii) McDonald and Hedman (3)
These authors pointed out the wide variation in reported chemical kinetic data for carbon-gas reactions and therefore they adopted an approach whereby the relevant carbon-gas reactions were assumed to have an infinite rate such that chemical equilibrium is reached in the gas adjacent to the surface. In this way the maximum possible erosion rate could be estimated. It was considered that erosion is diffusion controlled at temperatures above 2000°K.

(iv) Gowariker (1)
Both chemical and mechanical processes were considered. It was concluded that the chemical reactivity of a graphite is related to its bulk density whereas the susceptibility to mechanical erosion is related to its open porosity. Chemical kinetic data for C/CO_2 and C/H_2O reactions were the same as used in (i) above. The surface temperature of the nozzle was assumed to be identical to that of the exhaust gas.

(v) Mayberry, Kordig, Zeamer and Browning (14)
The average erosion rate was assumed to be a function of variables associated with rocket motor operation and a dimensional analysis of the variables enabled some correlations to be obtained with results from actual rocket firings. It was considered that the rates of carbon-gas reactions are very high under nozzle conditions and that erosion was therefore diffusion limited. It was recognised that for short burning times chemical rate control was probable.

Summarising the papers listed above, it is clear that they all suffer from lack of reliable chemical kinetic data for the particular graphites under investigation. There is little doubt that chemical rates are important in the erosion of all graphite nozzles since different graphites are known to exhibit different amounts of erosion under similar test conditions. For example, pyrolytic graphite may undergo an erosion of twenty times less than high quality conventional graphites (5). Furthermore, the boundary layer, which is assumed to modify the concentration of reactive species at the surface is ill-defined and its role in controlling erosion rate may have been over-emphasized. In a rocket motor firing the total erosion should be regarded as the integrated effect of erosion over a range of temperatures and pressures and not as an average erosion rate multiplied by the firing time, if reasonable predictions are to be made.

PRESENT WORK. In order to investigate the role of carbon-gas reactions in the erosion of graphite rocket nozzles we have made use of a liquid bi-propellent rocket engine (hydrogen peroxide/kerosene) because of the following advantages over a solid propellent rocket motor for this work.

(i) The combustion products contain a very high proportion of reactive species (see Table 1) and are free from condensed phases. Hence the role of chemical reactions should be highlighted.

(ii) The combustion pressure can be kept constant throughout a firing, thus removing one of the variables in solid propellent rocket tests.

(iii) The combustion temperature (2500°K) is lower than for most solid propellents such that after a reasonable firing time of 10 seconds the surface temperature of a graphite nozzle does not exceed 1700°K. Previous investigators have concluded that erosion is probably chemical rate controlled under this condition.

(iv) The mixture ratio of the two propellents may be varied to achieve variations in combustion temperature and relative amounts of combustion products.

(v) The exhaust gas is transparent in the visible region, permitting the application of optical techniques to the measurement of surface temperature.

The nozzle assembly used in all tests is shown in Fig. 1 and is identical to that used in our assessment tests with solid propellent rockets. Two different graphites, viz. Le Carbone 5890 and pyrolytic graphite (edge surface exposed) were investigated since the relevant chemical kinetic data were available for these (8).

Because of the obvious importance of the surface temperature, several methods of measurement were investigated.

(a) Embedded thermocouples
Spring-loaded thermocouples (Pt/Pt - 13% Rh, diameter 0.005 inch) were positioned radially at known depths of from 0.1 to 0.25 inch from the original exposed surface. They incorporated, at the junction, a small platinum disc, blackened with carbon, to act as a radiation collector. This obviated the need for perfect mechanical contact with the nozzle material. The surface temperature was obtained by the extrapolation of these thermocouple readings, making an allowance for surface recession.

(b) Ciné photography
This method was based on that devised by Hall (15). An 8 mm ciné film was taken of the

nozzle throat during the rocket firings, using an interference filter at 6643 Å. A calibrated tungsten strip lamp at a number of known brightness temperatures was also recorded under identical conditions on the same length of film. The strip lamp images were used to construct a calibration curve of optical density versus reciprocal of brightness temperature. Thus the brightness temperature of the nozzle could be determined from the optical density of its image, and the true temperature obtained from a knowledge of the emissivity of the graphite.

(c) Optical pyrometry
Use was made of an automatic optical pyrometer (Ircon Inc.) with a fast response recorder.

The first method, using thermocouples, enabled a complete temperature record to be obtained throughout the firing. The other two methods could be applied only above about 1000°K. The ciné method, in conjunction with a microdensitometer, provided a map of temperature distribution on the surface of the nozzle. Although optical pyrometry is basically the simplest method it has the disadvantage of having limited temperature ranges, i.e. no single range would cover a complete firing in all cases.

The total erosion was measured from the projected image of the nozzle throat before and after firing.

The theoretical estimation of graphite nozzle erosion by chemical rate control was carried out in the following way. First of all the surface temperature and internal temperature distribution were calculated by a method based on the radial flow of heat through a hollow cylinder, using a numerical solution of the standard equation

$$\frac{d^2\theta}{dr^2} + \frac{1}{r}\frac{d\theta}{dr} + \frac{1}{K}\frac{d\theta}{dt} = 0 \quad .$$

The convective heat transfer coefficient at the hot face was calculated using the method developed by Parkinson (16). This approach yields the surface temperature (and internal temperature distribution) as a function of time. Secondly, the conditions in the gas stream i.e. composition, pressure and temperature were calculated by standard methods assuming equilibrium flow. Finally the rate of erosion of the graphite throat as a function of surface temperature (and therefore time) throughout the firing was calculated on the basis of chemical rate control. The reactions considered were C/CO_2, C/H_2O, C/O_2, C/H_2 for which the recent data had been obtained (8). For the purposes of the present work the concentration of hydroxyl radicals was included in that of water vapour and the concentration of oxygen atoms was included in that of molecular oxygen. The C/H_2 reaction makes a negligible contribution to erosion since the reaction rate is a factor of 10^4 less than for C/CO_2. Evaporation of carbon is also negligible at temperatures below 2500°K (17). For the three remaining reactions, viz. C/CO_2, C/H_2O and C/O_2 some extrapolation of the data (8) to lower temperatures and higher pressures was required. At temperatures well below the rate maximum there is a linear relationship between log (reaction rate) and reciprocal of absolute temperature and extrapolation was made on this basis. Extrapolation to higher pressures for all the reactions was based on the general findings of Lewis (8) in the range 1 to 3 atmospheres that these reactions are first order, i.e. reaction rate is proportional to concentration (partial pressure) of reacting gas. An apparent exception is the reaction between pyrolytic graphite (edge surface) and carbon dioxide at temperatures below that for the rate maximum (approximately 1800°K). However, carbon dioxide significantly diluted with inert gases more nearly follows the first order relationship and this seems more appropriate to our conditions. It was also assumed that each reacting species acts independently. Although Lewis (8) found that additions of carbon monoxide retarded the C/CO_2 reaction, this effect was only significant for relative amounts of carbon monoxide greater than present in our conditions.

The theoretical and experimental results for the two types of graphite, Le Carbone 5890 and pyrolytic (edge surface) in the liquid propellent rocket engine are given in Fig. 2. It can be seen that agreement is obtained between measured and calculated surface temperatures and erosions for both graphites.

It is worth noting that the choice of chemical kinetic data has a profound effect on the predicted erosion rates, assuming chemical rate control. In Tables 2 and 3 a comparison is made between the use of the data from Lewis (8) and the data used by McCuen (10) and by Gowariker (1) to which previous reference has been made.

We have extended our chemical rate control predictions to the same two graphites in typical solid propellent rocket motor tests. The conditions in the free gas stream are included in Table 1 and the predicted erosions are compared with experimental values in Figs. 3 and 4. It can be seen that the measured erosion is considerably less than that predicted showing that diffusion processes become significant during the firing.

CONCLUSIONS

Carbon-gas reactions have been shown to play a significant role in the erosion of graphite rocket nozzles and, in fact, at moderate temperatures the amount of erosion can be accounted for on the basis of chemical rate control. Even at higher temperatures where the boundary layer is

believed to have an effect, the erosion rate is influenced by carbon-gas reaction rates. It follows that in the selection of a graphite for use in an uncooled rocket nozzle, the chemical reactivity should be an important consideration.

Although some progress has been made there is still no adequate theory which will give a quantitative prediction of the erosion of graphite nozzles under all conditions. However, previously proposed mechanisms which take some account of chemical kinetics could be re-assessed in the light of the latest data (8). The presence of a rate maximum in the C/CO_2 and C/O_2 reactions is of particular significance since it follows that the erosion due to these gases will decrease with increasing temperature in the range 1900-2500°K. Thus it is possible that, in this region, the erosion due to carbon dioxide and oxygen is chemical rate controlled whereas that due to water vapour, which does not exhibit a rate maximum, is diffusion controlled.

In order to investigate further the mechanisms controlling nozzle erosion and their interchange during a rocket firing it would be desirable to know the instantaneous surface temperature and erosion rate. The latter, although not normally available, could be obtained from continuous precise measurement of thrust, pressure and mass flow rate of propellent.

Improved graphites for nozzle applications will be characterised by improved oxidation resistance under rocket conditions. Pyrolytic graphite is superior in this respect and, typically, undergoes a total erosion of one-twentieth of that of conventional graphites (5). Furthermore this material is highly anisotropic. Thus in a rocket nozzle two configurations are possible, viz. "stacked disc" and "shell". The stacked disc (edge surface exposed) arrangement has the higher chemical reactivity (although still much lower than for other graphites) but reaches a lower surface temperature because of the high thermal conductivity normal to the surface. It is interesting to note that under certain conditions in the C/CO_2 reaction Lewis (8) shows zero order behaviour for this configuration. This implies chemical rate controlled erosion independent of pressure - a desirable feature if obtainable in a practical nozzle. The shell (basal plane surface exposed) arrangement has the lower chemical reactivity but reaches higher surface temperature because of the low thermal conductivity normal to the surface. This configuration is particularly attractive because its high thermal insulation allows the use of non-refractory materials of high specific strength, e.g. fibre-reinforced plastics, in the construction of a lightweight nozzle assembly. By a judicious combination, the two configurations of pyrolytic graphite may be used advantageously in the same nozzle design.

ACKNOWLEDGEMENTS

We wish to acknowledge the assistance given by Mr. S. W. P. Woodhouse in carrying out all rocket motor firings and that given by Mr. W. H. Williams and Mrs. D. A. Bailey in supplying data on the rocket exhaust conditions.

REFERENCES

1 Gowariker, V. R.
Mechanical and chemical contributions to the erosion rates of graphite throats in rocket motor nozzles. J. Spacecraft, 3, 1490-1494, (1966)

2 Delaney, L. J., Eagleton, L. C., and Jones, W. H.
A semi-quantitative prediction of the erosion of graphite nozzle inserts. AIAA Journal, 2, 1428-1433, (1964)

3 McDonald, A. J., and Hedman, P. O.
Erosion of graphite in solid propellant combustion gases and effects on heat transfer. AIAA Journal, 3, 1250-1257, (1965)

4 Lewis, J. C., Floyd, I. J., and Cowlard, F. C.
A comparative study of the gaseous oxidation of vitreous carbon and various graphites at 1500-3000°K. 8th Carbon Conference, Buffalo, (1967)

5 Parmee, A. C.
Material requirements for rocket nozzles, with particular reference to pyrolytic graphite. Special Ceramics 4, Ed. Popper, P., British Ceramic Research Association, 297-305, (1968)

6 Rosner, D. E.
Convective diffusion limitations on the rates of chemical reactions at solid surfaces - kinetic implications. 11th Symposium on Combustion, 181-196, (1966)

7 Lewis, J. B.
Thermal gas reactions of graphites. U.K./A.E.A. Atomic Energy Research Establishment, Report No. R 5321, March, 1967

8 Lewis, J. C., Floyd, I. J., and Cowlard, F. C.
A laboratory investigation of carbon-gas reactions of relevance to rocket nozzle erosion. AGARD Propulsion and Energetics Panel 34th Meeting on Reactions between Gases and Solids, Wright-Patterson AFB, 13-17 October, 1969, Paper No. 29

9 Khitrin, L. N.
Fundamental principles of carbon combustion and factors intensifying the burning of solid fuels. 6th Symposium on Combustion, 565-573, (1956)

10 McCuen, P. A., Schaefer, J. W., Lundberg, R. E., and Kendall, R. M.
A study of solid propellant rocket motor exposed materials behavior. Report 149, AFRPL-TR-65-33, Feb. 26, 1965, Vidya Corpn.

11 Gulbransen, E. A., and Andrew, K. F.
Reaction of carbon dioxide with pure artificial graphite at temperatures of 500 to 900°C. Ind. and Eng. Chemistry, 44, 1048-1051, (1952)

12 Blyholder, G., and Eyring, H.
Kinetics of the steam-carbon reaction. J. Phys. Chem., 63, 693-696, (1959)

13 Lowrie, R.
Research on physical and chemical principles affecting high temperature materials for rocket nozzles. Contract No. DA-30-069-ORD-2787, Union Carbide Research Institute, (1961)

14 Mayberry, J. L., Kordig, J. W., Zeamer, R. J., and Browning, S. C.
Correlation of graphite nozzle throat erosion in solid-rocket motors. AIAA Journal, 6, 2222-2224, (1968)

15 Hall, J. A.
A photographic investigation of the brightness temperatures of liquid steel streams. J. Iron and Steel Inst., 155, 55-85, (1947)

16 Parkinson, R. C.
Unpublished Ministry of Technology Report

17 Ladd, I. R., and Walsh, P. N.
Complex temperature dependence of the oxidation of pyrolytic graphite by CO_2. Carbon, 4, 539-541, (1966)

TABLE 1

Conditions in free gas stream at nozzle throat

	Hydrogen peroxide/kerosene stoichiometric mixture combustion pressure 500 psia (34.02 atm)	Non-aluminized solid propellent combustion pressure 500 psia (34.02 atm)	17% aluminized solid propellent combustion pressure 500 psia (34.02 atm)
Gas composition (mole fraction)			
CO	$2.448_{10} - 2$	$1.444_{10} - 1$	$2.380_{10} - 1$
CO_2	$1.519_{10} - 1$	$8.796_{10} - 2$	$1.140_{10} - 2$
H	$8.935_{10} - 4$	$1.846_{10} - 3$	$2.855_{10} - 2$
OH	$7.498_{10} - 3$	$1.467_{10} - 3$	$3.778_{10} - 3$
H_2	$2.078_{10} - 2$	$1.059_{10} - 1$	$3.531_{10} - 1$
H_2O	$7.910_{10} - 1$	$3.917_{10} - 1$	$1.250_{10} - 1$
O	$2.048_{10} - 4$	$1.631_{10} - 5$	$1.801_{10} - 4$
O_2	$3.235_{10} - 3$	$2.508_{10} - 5$	$2.563_{10} - 5$
N_2	-	$8.885_{10} - 2$	$7.988_{10} - 2$
HCl	-	$1.756_{10} - 1$	$1.479_{10} - 1$
Cl	-	$2.185_{10} - 3$	$8.156_{10} - 3$
AlCl	-	-	$2.711_{10} - 3$
Condensed phase liquid Al_2O_3 per 100 - of mixture	-	-	$3.173_{10} + 1$
Temperature (^oK)	2520	2498	3101
Pressure (atm)	19.57	19.19	19.55
Enthalpy (cal/g)	-1649	-724.6	-607.6
Molecular weight (g/mol)	21.90	24.19	24.88
Discharge coefficient (lbm/sec lbf)	$6.170_{10} - 3$	$6.541_{10} - 3$	$6.18_{10} - 3$
Area (cm^2 sec/g)	$4.611_{10} - 3$	$4.349_{10} - 3$	$4.606_{10} - 3$
Density (g/cm^3)	$2.072_{10} - 3$	$2.264_{10} - 3$	$2.072_{10} - 3$

TABLE 2

Le Carbone graphite grade 5890

Chemical rate controlled erosion rates, at 1 atm absolute pressure, calculated from various sources of kinetic data

Temp (°K)	Linear erosion rate (10^{-3} inch/sec)					
	Data from Lewis (8)			Data used in Ref. (10)		Data used in Ref. (1)
	CO_2	H_2O	O_2	CO_2	H_2O	All
600	$8.49_{10}-18$	$1.10_{10}-03$	$9.73_{10}-03$	$5.73_{10}-21$	$4.26_{10}-11$	$8.58_{10}-07$
800	$2.82_{10}-11$	$1.28_{10}-02$	$8.86_{10}-02$	$2.28_{10}-13$	$5.53_{10}-08$	$5.88_{10}-03$
1000	$2.31_{10}-07$	$5.54_{10}-02$	$3.33_{10}-01$	$8.28_{10}-09$	$3.85_{10}-06$	$1.18_{10}+00$
1200	$9.38_{10}-05$	$1.47_{10}-01$	$8.06_{10}-01$	$9.08_{10}-06$	$6.08_{10}-05$	$4.03_{10}+01$
1400	$6.85_{10}-03$	$2.97_{10}-01$	$1.51_{10}+00$	$1.35_{10}-03$	$3.94_{10}-04$	$5.03_{10}+02$
1600	$1.71_{10}-01$	$5.01_{10}-01$	$2.43_{10}+00$	$5.73_{10}-02$	$1.40_{10}-03$	$3.34_{10}+03$
1800	$6.86_{10}-01$	$7.64_{10}-01$	$3.22_{10}+00$	$1.06_{10}+00$	$3.21_{10}-03$	$1.46_{10}+04$
2000	$6.56_{10}-01$	$1.06_{10}+00$	$3.19_{10}+00$	$1.09_{10}+01$	$5.45_{10}-03$	$4.73_{10}+04$
2200	$3.26_{10}-01$	$1.38_{10}+00$	$2.77_{10}+00$	$7.37_{10}+01$	$7.51_{10}-03$	$1.24_{10}+05$
2400	$2.00_{10}-01$	$1.72_{10}+00$	$2.11_{10}+00$	$3.62_{10}+02$	$9.04_{10}-03$	$2.77_{10}+05$
2600	$1.91_{10}-01$	$2.08_{10}+00$	$1.89_{10}+00$	$1.39_{10}+03$	$1.00_{10}-02$	$5.46_{10}+05$
2800	$2.39_{10}-01$	$2.44_{10}+00$	$2.16_{10}+00$	$4.41_{10}+03$	$1.05_{10}-02$	$9.77_{10}+05$
3000	$6.41_{10}-01$	$2.80_{10}+00$	$3.03_{10}+00$	$1.20_{10}+04$	$1.06_{10}-02$	$1.62_{10}+06$

TABLE 3

Pyrolytic graphite

Chemical rate controlled erosion rates, at 1 atm absolute pressure, calculated from various sources of kinetic data

Temp (°K)	Linear erosion rate (10^{-3} inch/sec)					
	Data from Lewis (8)			Data used in Ref. (10)		Data used in Ref. (1)
	CO_2	H_2O	O_2	CO_2	H_2O	All
600	$2.40_{10}-17$	$3.33_{10}-14$	$7.84_{10}-06$	$4.82_{10}-21$	$3.58_{10}-11$	$7.21_{10}-07$
800	$2.61_{10}-11$	$2.27_{10}-09$	$5.73_{10}-04$	$1.92_{10}-13$	$4.65_{10}-08$	illegible
1000	$1.09_{10}-07$	$1.81_{10}-06$	$7.53_{10}-03$	$6.97_{10}-09$	$3.24_{10}-06$	$9.91_{10}-01$
1200	$2.85_{10}-05$	$1.55_{10}-04$	$4.19_{10}-02$	$7.64_{10}-06$	$5.11_{10}-05$	$3.39_{10}-01$
1400	$1.51_{10}-03$	$3.73_{10}-03$	$1.43_{10}-01$	$1.13_{10}-03$	$3.32_{10}-04$	$4.23_{10}+02$
1600	$2.97_{10}-02$	$4.05_{10}-02$	$3.58_{10}-01$	$4.82_{10}-02$	illegible	$2.81_{10}+03$
1800	$2.15_{10}-01$	$4.28_{10}-02$	$2.11_{10}+00$	$8.91_{10}-01$	$2.70_{10}-03$	$1.22_{10}+04$
2000	$1.44_{10}-01$	$1.89_{10}-01$	$1.97_{10}+00$	$9.19_{10}+00$	$4.58_{10}-03$	$3.98_{10}+04$
2200	$8.54_{10}-02$	illegible	$1.40_{10}+00$	$6.20_{10}+01$	$6.31_{10}-03$	$1.04_{10}+05$
2400	$5.38_{10}-02$	$1.22_{10}+00$	$1.05_{10}+00$	$3.04_{10}+02$	$7.60_{10}-03$	$2.33_{10}+05$
2600	$4.60_{10}-02$	$1.60_{10}+00$	$8.63_{10}-01$	$1.17_{10}+03$	$8.41_{10}-03$	$4.59_{10}+05$
2800	$7.44_{10}-02$	$1.79_{10}+00$	$1.01_{10}+00$	$3.71_{10}+03$	$8.81_{10}-03$	$8.22_{10}+05$
3000	$1.75_{10}-01$	$1.89_{10}+00$	$1.82_{10}+00$	$1.01_{10}+04$	$8.92_{10}-03$	$1.36_{10}+06$

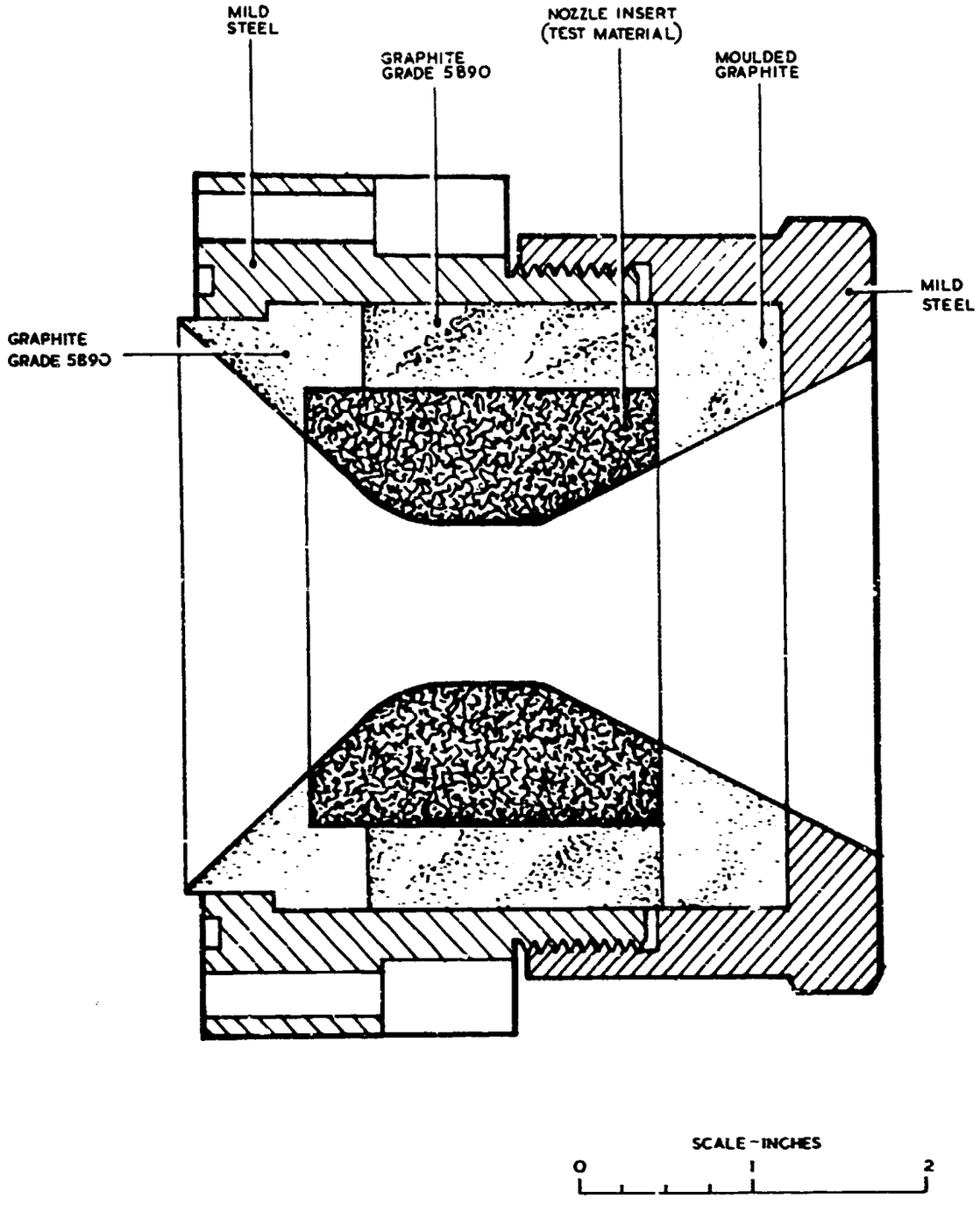

Fig. 1 Nozzle assembly

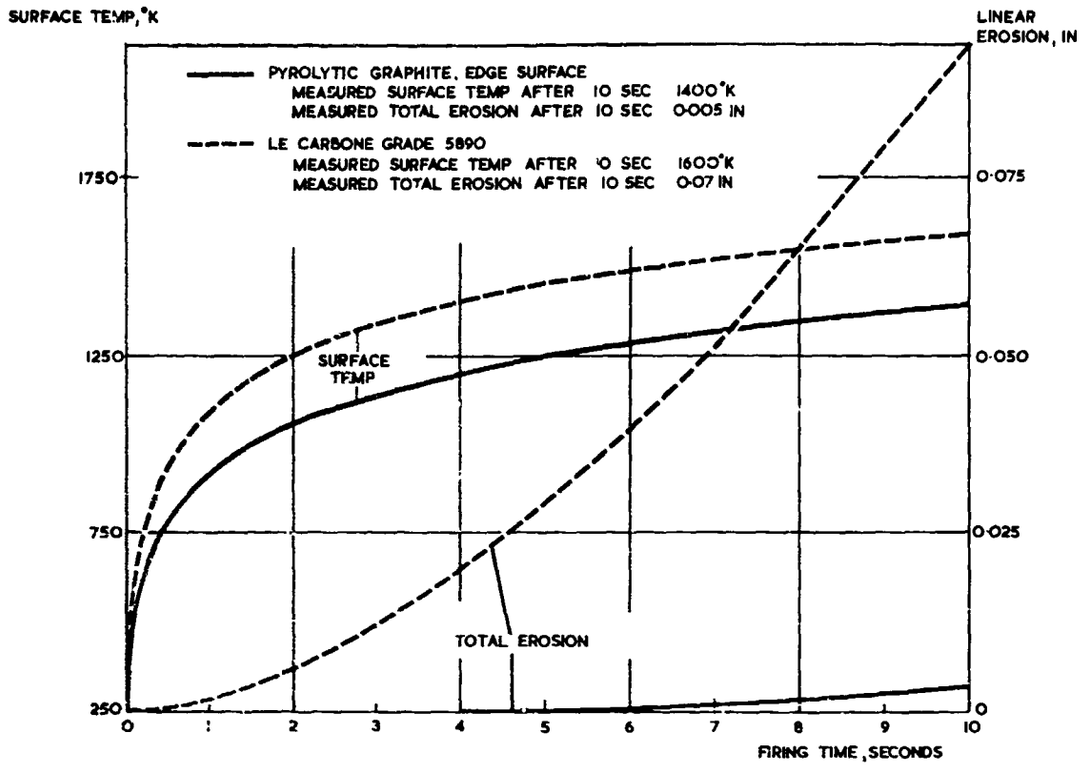

Fig. 2 Predicted surface temperature and total erosion, hydrogen peroxide/kerosene propellent engine

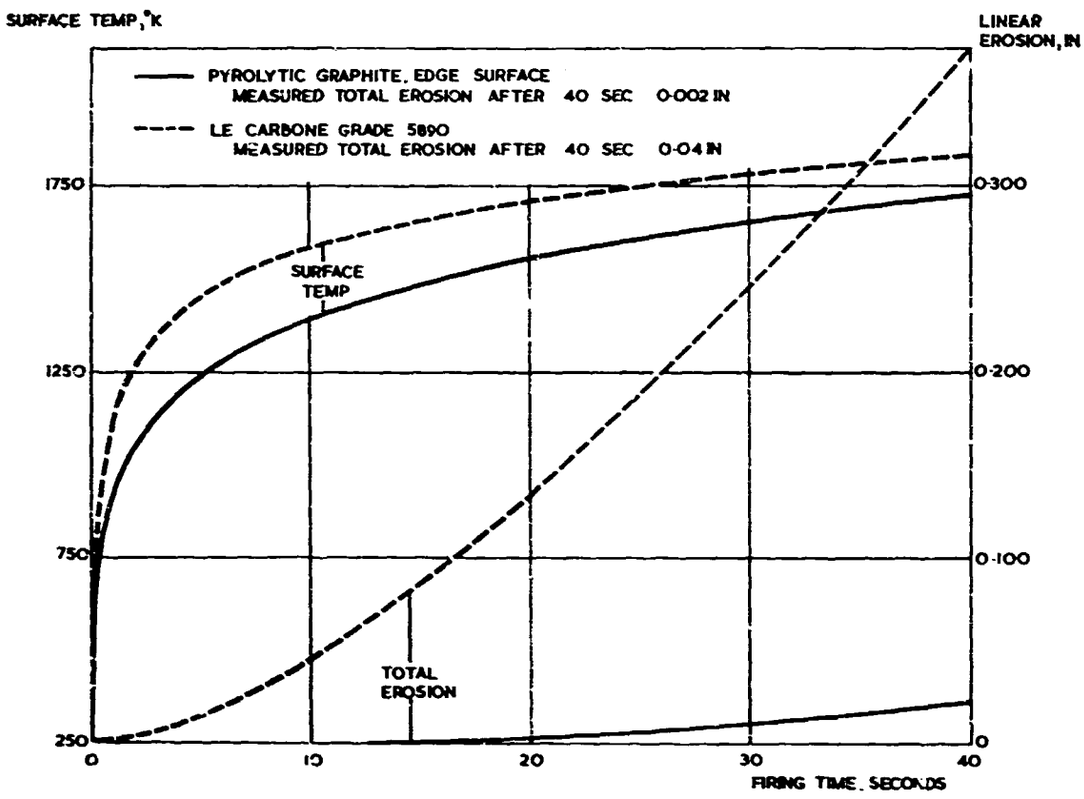

Fig. 3 Predicted surface temperature and total erosion, non-aluminised solid propellent motor

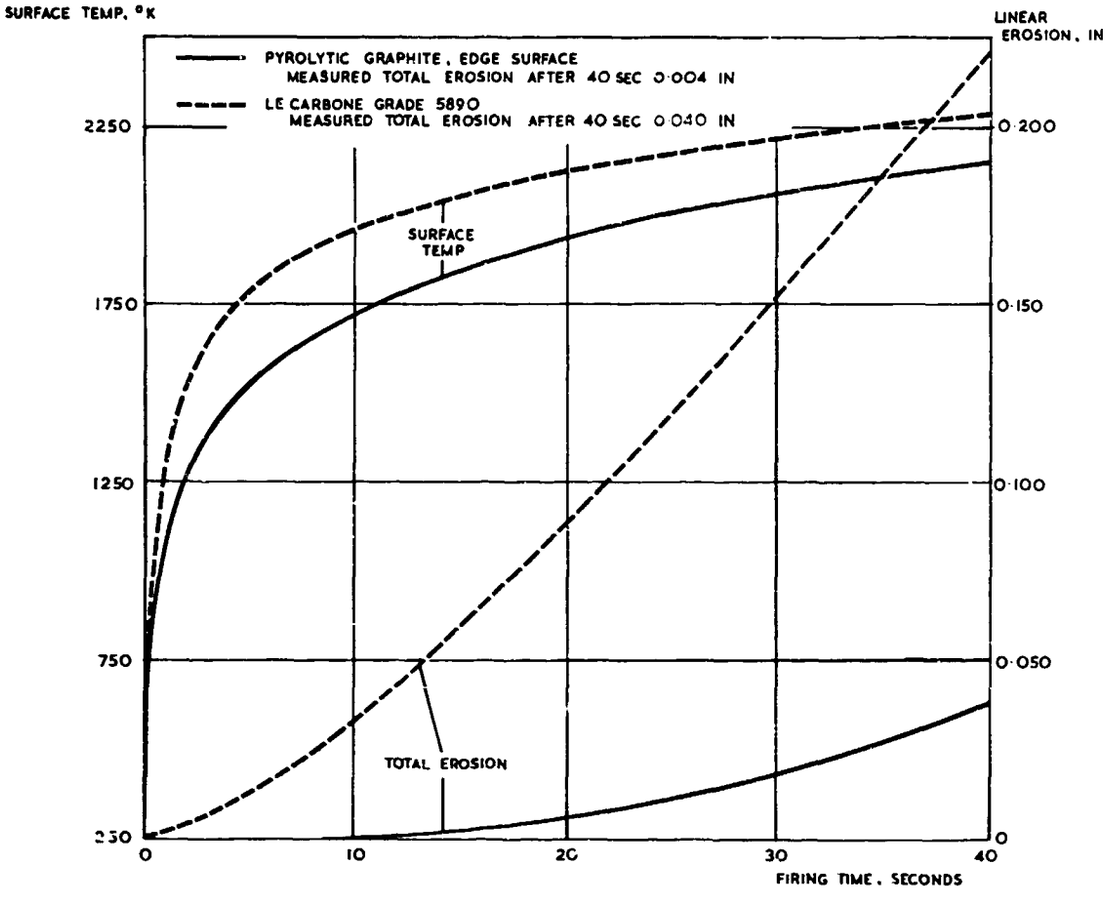

Fig. 4 Predicted surface temperature and total erosion, aluminized solid propellent motor

A LABORATORY INVESTIGATION OF CARBON-GAS REACTIONS OF RELEVANCE TO ROCKET NOZZLE EROSION

by

J.C. Lewis, I.J. Floyd and F.C. Cowlard

The Plessey Company Limited,
Allen Clark Research Centre,
Caswell, Towcester, Northants., U.K.

SUMMARY

The interaction of various carbons (pyrolytic graphite, vitreous carbon and an erosion-resistant synthetic graphite) with oxidising gases present in solid-propellant exhausts (CO_2, H_2O and O_2) was investigated at pressures of 1 - 3 atmospheres and surface temperatures of 1500 - 3000°K. The use of high gas flow velocities (up to 4 x 10^4 cm/sec) ensured freedom from boundary layer diffusion control in all but the most reactive conditions studied.

Graphs of weight loss rate versus temperature exhibited a maximum and a minimum for reactions in CO_2 and O_2, but not in H_2O. Significant departures from first order behaviour were observed in some cases.

Variations of the reaction rate with the type of carbon and the reactant gas were in general less pronounced than at lower temperatures. However, the synthetic graphite was still found to be markedly more reactive to CO_2 than pyrolytic graphite or vitreous carbon, the best pyrolytic graphite shells reacting at only 3 - 4% of the rate of the synthetic graphite. Molecular oxygen was an order of magnitude more reactive than CO_2 or steam, but if due allowance is made for the concentrations of these gases in the exhaust their contributions to the overall erosion rate are $H_2O \gg CO_2 \gg O_2$ for high temperature propellants, with CO_2 assuming greater importance at lower temperatures.

CARBON is in many respects an excellent constructional material for high temperature applications: it has a high sublimation temperature, high strength-to-weight ratio and its strength increases with temperature. However, its usefulness is generally limited by its reactions with oxidising gases: for example, most commercial graphites are unsuitable for prolonged exposure to air at temperatures in excess of 500°C. Despite this drawback, various improved grades of carbon have been found to perform satisfactorily as nozzle materials in solid propellant rockets of short firing times (of the order of seconds).

The aim of the work to be described in this paper was to investigate the reactions of oxidation resistant forms of carbon with gases present in solid propellant rocket exhausts (especially the major constituents, carbon dioxide and steam); these reactions were to be studied at temperatures up to about 3000°K and at pressures above atmospheric, in order to provide chemical kinetic data which could be extrapolated with a reasonably high degree of confidence to rocket nozzle pressures, of the order of 1000 p.s.i. (70 kg/cm^2).

The main obstacle to the achievement of this objective was the difficulty of creating experimental conditions in which true chemical rates, free from boundary layer diffusion control, could be measured. This problem can best be understood by considering the five consecutive steps involved in a typical gas-solid reaction. These are:

(i) Transport of reactant to surface

(ii) Adsorption of reactant

(iii) Reaction between adsorbed species and surface

(iv) Desorption of product

(v) Transport of product from surface

The overall reaction rate will be governed by the slowest of these steps: thus, at low temperatures and pressures the reaction may be adsorption-controlled, while at high pressures the rate of desorption may become more important. In highly reactive conditions, i.e. when steps (ii), (iii) and (iv) become very rapid (as in the high temperature, high pressure combustion of carbon), the overall rate tends to be limited by the rate of diffusion of the reactant and product gases to and from the surface respectively. This "diffusion control" may be overcome in one of three ways.

(a) Reduction of the reaction pressure (specifically excluded by the terms of reference of the present work).

(b) The use of a solid reactant in the form of fine particles: this technique has a number of disadvantages and was, in particular, regarded as too far removed from the rocket nozzle geometry.

(c) The use of high gas velocities, with the object of reducing the boundary layer thickness to a minimum. This approach was preferred, mainly because of its compatibility with experimental geometries broadly comparable with that of the rocket nozzle.

APPARATUS

Two main types of reaction system were employed, both designs being based on the considerations discussed above. All the initial work was carried out in tubular flow reactors of the type illustrated in Figs. 1 and 2, this geometry being chosen as the closest practicable approach to that of a nozzle. A weighed and measured tubular specimen of the carbon under investigation, approximately 1.3 cm i.d. x 1.6 cm o.d. x 1.3 cm long, was mounted in a graphite support (Morganite EY9 or Le Carbone 5580) with a tightly fitting graphite seal ring at the upper end to minimise reaction on the outside and end surfaces of the specimen. The assembly was heated by R.F. induction in a stream of inert gas (argon or nitrogen) to a temperature slightly above or below the desired reaction temperature, depending upon whether the reactant gas was carbon dioxide (endothermic) or oxygen (exothermic). The temperature of the inside (reacting) surface of the specimen was measured continuously by means of a Land (silicon solar cell) pyrometer coupled to a Honeywell potentiometric strip chart recorder. The alignment of the Land pyrometer was checked immediately before each run by comparing its reading with that of a disappearing filament pyrometer directed at the hot specimen surface near the centre of the area to be reacted. Corrections were applied for emissivity and for reflection losses at the two surfaces of the quartz glass window (see Appendix).

When conditions were steady, the inert gas stream was replaced by reactant gas by means of a solenoid valve change-over system. Manual control of the R.F. output subsequently maintained the surface temperature within close limits, usually $\pm$ 10°K or better. At the end of the reaction period, usually of the order of 1 min., the R.F. power and reactant gas flow were shut off and the reactor purged with inert gas, all three operations being controlled by a single switch. The specimen was cooled in inert gas, removed from the reactor and weighed and measured again; the area taken for the calculation of specific reaction rate was the average of the initial and final areas of the inside surface, plus a small empirical correction to allow for reaction on part of the end surface due to leakage of gas past the seal ring.

With the gas supply system available, it was found difficult to achieve gas flows in excess of about 8000 cm^3/sec through the tubular reactor, even at atmospheric pressure. This corresponded to a mean linear velocity in the specimen of 4000 cm/sec, which proved to be insufficient to overcome diffusion control in the most reactive conditions studied. Increasing the velocity by reduction of the specimen diameter caused difficulties in heating and in the measurement of temperature; the creation of artificial turbulence by the incorporation of a vortex generator in the gas inlet had

the effect of substantially reducing the gas flow rate required to achieve chemical control, but also resulted in higher heat transfer rates from the surface with a consequent sharp increase in the power required to maintain a given surface temperature.

The problem was eventually overcome by the use of impingement (stagnation flow) reactors (Figs. 3 and 4) similar to that used by Strickland-Constable[1] and others. The specimen, in the form of a cylindrical rod approximately 6.0 x 0.5 cm, was mounted between two massive graphite end-blocks and heated by the passage of an electric current. A jet of gas was directed at right angles to the surface of the specimen near its centre; by the use of jet diameters of 0.48 and 0.75 cm, velocities could be achieved which were an order of magnitude greater than in the tubular reactor. The temperature of the reacting surface, directly above the jet, was recorded continuously by means of the Land pyrometer, which was focussed on the specimen via the quartz glass window, gas entry tube and jet.

The experimental procedure was similar to that described for the tubular reactor, except that the reaction rate was determined by casting an image of the specimen on a screen and measuring the recession rate of the reacting surface. Although some use was made of time-lapse photography, most of the results quoted were obtained either by measuring with a stop-watch the time taken for the image to recede by a given amount on a graduated screen, or by means of the photo-electric monitor illustrated in Fig. 5. This was based on a linear array of 40 silicon photodiodes with a total length of 4.0 mm; selected diodes were connected via a "triggering" circuit and selector switch to a millisecond timer in such a way that the times for image recessions of 0.1, 0.2, 0.5, 1.0, 2.0 or 3.9 mm could be recorded automatically; actual surface recessions were about one fifth of these figures, due to five-fold magnification of the image by the lens arrangement used. It was found necessary, in the interests of reproducibility, to operate the photodiode assembly within a limited range of illumination: this was ensured by attaching a silicon photocell to the screen within the image area and adjusting the output of the photocell to a fixed value by means of the iris diaphragm on the projection lens. The spacing of the diode pair in use was calibrated before each run against a clock gauge with a sensitivity of 0.0005" (approximately 0.001 cm).

The photoelectric monitor was of particular value in the measurement of rates too rapid for the visual technique. It had the further advantage that rates could be measured from a non-zero reference time, thus eliminating errors due to (a) the fluctuation of conditions immediately after the change-over to reactant gas and (b) losses of carbon occurring in the inert gas (i.e. before the start of the reaction) at the highest temperatures studied; the latter error was particularly troublesome in the tubular reactor but could be reduced to a tolerable level by reducing the heat-up period in inert gas to a minimum.

The advantages and disadvantages of the tubular and impingement types of reactor for the present purpose may be summarised as follows: The tubular reactor has the advantage of greater geometrical similarity to the rocket nozzle, is simple to use but of limited applicability because of the comparatively low maximum gas velocities which can be achieved in it. The impingement reactor represents a totally different flow geometry, is less convenient to use (especially in the high pressure version) and is subject to the further objection that allowance must be made for the effect of dynamic (pitot) pressure on the true reaction pressure (it was found, in practice, that the only satisfactory way to do this was empirically, i.e. by measuring pitot pressures directly over a wide range of flow and static pressure conditions, fitting the results to an empirical equation and writing a computer programme to give an output of pitot pressure versus flow and static pressure in tabulated form). However, these disadvantages were outweighed by the advantages of high gas velocities and automatic measurement, without which the highest reaction rates reported here would have proved exceedingly difficult, if not impossible, to measure.

Materials. The carbons studied were:

(a) Vitreous carbon, prepared by the controlled thermal degradation of a phenolic resin. (abbreviated to VC in the text).

(b) Pyrolytic graphite, supplied by Union Carbide and by Supertemp Corporation in the form of plates about 1.25 cm thick, and subsequently machined into hollow cylinders with the c-axis parallel to the cylinder axis, for the study of "edge-surface" reactivity (PG-edge).

(c) Pyrolytic graphite, supplied by Le Carbone and by the Rocket Propulsion Establishment in the form of thin cylinders with basal planes running circumferentially round the cylinder, for the study of "basal plane surface" reactivity (PG-basal).

(d) Le Carbone 5890 graphite, a close-grained synthetic graphite which has found application as a rocket nozzle material.

The gases used were supplied mainly by Air Products Ltd. Nitrogen and argon typically had dew-points of -189°C and oxygen contents of 4 v.p.m. (parts per million by volume), while carbon dioxide contained about 5 v.p.m. each of oxygen, nitrogen and water vapour as its main impurities. The gas supply system to the reactor incorporated four separate gas feeds with drying columns packed with Union Carbide molecular sieves (type 5A), "Gapmeter" (tapered tube) flow gauge assemblies capable of measuring flows of 20-1000 l/min, a mixing chamber, a dust filter for the removal of entrained particles down to 1 μm in diameter, and "test" quality pressure gauges for measuring supply and reaction pressures. Steam was supplied by a Clayton steam generator via a steel pipe-line, fitted with an orifice-plate recording flow meter, and a heated filter unit of sintered stainless steel to remove liquid water droplets and any entrained solid impurities.

RESULTS AND DISCUSSION

DEPENDENCE OF REACTION RATE ON GAS VELOCITY. The effect of gas velocity on reaction rate is commonly used as an indication of the presence or absence of diffusion control. The effect was initially studied in the tubular reactor, for the reaction of carbon dioxide with vitreous carbon (low reactivity) and 5890 graphite (comparatively high reactivity). Some of the results obtained for vitreous carbon at 1 atmosphere pressure are shown in Fig. 6; in general, the reaction rate was only slightly dependent upon the gas velocity except near the lower end of the surface temperature range investigated (1700-3000°K). Anomalous results were obtained at 2250°K, a temperature close to the maximum in the rate/temperature curve (see below), in that nearly all of the 14 runs carried out gave rates lower - in some cases by an order of magnitude - than those obtained at higher or lower temperatures. At surface temperatures above T_{max}, the critical velocity (at which the reaction rate became independent of velocity) was less than 3000 cm/sec. The much higher velocity-dependence exhibited by 5890 graphite, the most reactive of the carbons studied, is illustrated in Fig. 7; it is probable that most of the results obtained for the reaction of carbon dioxide with this material in the tubular reactor were depressed to a significant extent by boundary layer diffusion effects, while true chemical rates were generally obtained for vitreous carbon and both surfaces of pyrolytic graphite.

Critical velocities for the steam-carbon reaction were much higher; even for vitreous carbon at the comparatively low temperature of 2090°K, the jet velocity required to overcome diffusion control was approximately 33,000 cm/sec (i.e. ½ sonic); at 2407°K (near the temperature at which the apparent activation energy begins to decrease), experimental points were subject to a much more pronounced scatter, but a general tendency for the reaction rate to increase with jet velocity, up to and beyond sonic velocity, can be seen (Fig. 8). Because of the intense localised cooling effect of such high velocity steam jets it was found necessary to limit the jet velocity to 0.5 - 1.0 times sonic, and reaction rates above about 0.1 g/cm^2 sec (i.e. of the order of 10 mils/sec) are therefore likely to have been depressed to some extent by diffusion effects. (The problem might be overcome by pre-heating the steam to a temperature near that of the surface; using higher heating currents through the specimen, to offset the cooling effect at the impingement area, merely causes over-heating of other parts of the specimen, usually leading to failure by erosion or evaporation).

CARBON DIOXIDE REACTION

DEPENDENCE OF REACTION RATE ON SURFACE TEMPERATURE AND TYPE OF CARBON. As a result of previous work on the gaseous oxidation of carbon at high temperatures, mainly carried out at low pressures (2-5) to avoid the problems of diffusion control, the general shape of the rate/temperature curve is by now well known. The reaction rate does not increase monotonically with temperature, but passes through a maximum, followed by a range of temperature (which in some cases amounts to several hundred degrees) in which the rate decreases with temperature. Further increase of temperature causes the rate to reach a minimum and then increase sharply again. These general features have recently been confirmed for pressures near (6-9) and above (9) atmospheric.

Results obtained for all four carbons in the tubular reactor at 16.0 p.s.i.a. (pounds per square inch absolute pressure), with a mean CO_2 velocity of 3000 cm/sec, are shown in Fig. 9. (Mean velocity = flow rate in cm^3/sec divided by internal cross-sectional area of specimen in cm^2). The basal plane surface of PG was the least reactive of the four carbons studied, while the synthetic graphite (5890) was the most reactive, over the entire temperature range (1500-3000°K); the 5890 results were, as stated above, affected by boundary layer diffusion control, and weight loss rates for this material in the impingement reactor (also shown in Fig. 9) were up to 3½ times those obtained in the tubular reactor. However, part of this discrepancy must presumably have been due to mechanical erosion in the impingement reactor, since specific reaction rates below about 0.06 g/cm^2 were shown (by rate velocity plots) to be independent of velocity in the tubular reactor at 3000 cm/sec. Rates obtained on the tubular reactor at low temperatures and near T_{min} are therefore regarded as more reliable than the impingement reactor results. The reactivity ratio between VC and PG (edge) depends markedly on temperature, the PG being the more reactive material at temperatures below 2000°K and above 2800°K while VC is the more reactive at intermediate temperatures.

BATCHWISE VARIATION OF REACTIVITY. All the carbons exhibited appreciable variations in reactivity to carbon dioxide, as shown in Figs. 10-12. The best overall reproducibility was exhibited by vitreous carbon, with a maximum variation of ± 30% for the four batches studied. The 5890 graphite gave fairly reproducible results at temperatures below the rate maximum, but varied by ± 38% near the rate minimum. Five batches of pyrolytic graphite from a single manufacturer varied by ± 47% below the rate maximum with rather wide variations within each batch; however, above T_{max} PG was the most reproducible material (± 23%).

It is clear from these results that, at present, accurate predictions of nozzle erosion rates from kinetic data obtained in the laboratory can only be made if the batch reactivity has first been established by reaction rate determinations under standard conditions. The only way in which this rather unsatisfactory situation can be improved is by further investigation of the factors affecting reactivity, with a view to producing carbons with much more closely reproducible properties.

THE ORDER OF REACTION with respect to pressure of CO_2 was investigated for PG (edge) in the tubular reactor, with some support from impingement reactor experiments, and for 5890 graphite (which required higher gas velocities to overcome diffusion control) in the impingement reactor.

Results for PG (edge) are shown in Figs. 13 and 14. As may be seen from Fig. 13, the reaction rate is approximately independent of pressure at temperatures below T_{max}, and at the highest pressures

and temperatures studied (i.e. in the region of 3000°K). At temperatures between T_{max} and T_{min}, the average reaction order over the range 16.0 – 45.0 p.s.i.a. was about 1.2. The agreement between impingement and tubular reactor results depended on the pressure, as follows:

16.0 p.s.i.a.	:	very good agreement
24.0 p.s.i.a.	:	rates close to 150% of 16.0 p.s.i.a. rates, indicating a reaction order of 1.0
32.0 p.s.i.a.	:	unexpectedly high results near T_{max}, with rates approximately equal to the 45.0 p.s.i.a. rates in the tubular reactor. No complete explanation can be offered for these very high rates; however, it is possible that the "edge" surface, which is more susceptible to damage than the basal plane surface, was mechanically eroded by the high velocity, high pressure gas jet. The rate of this erosion would be expected to increase with gas pressure and with the rate of the simultaneous chemical attack on the surface.

Results for 5890 graphite are shown in Fig. 15. These results may have been affected by the contribution of mechanical erosion to the observed erosion rate (as discussed above, with reference to Fig. 9). Anomalously low rates were observed at 16.0 p.s.i.a. at temperatures above T_{max}, in that a sharp decrease in rate occurred at about 2100°K, followed by a very flat minimum extending to 2800°K. As can be seen from Fig. 15, the number and distribution of experimental points is such that they cannot be fitted satisfactorily to a smooth curve of the type normally obtained. The same effect occurred at 21.0 p.s.i.a. over a more limited temperature range (2100-2200°K), but was not observed at higher pressures.

A possible explanation for this anomalous behaviour was suggested by the observation that specimens exhibiting a low reaction rate developed a "sooty" coating during oxidation. This coating, being non-coherent and presumably of low electrical and thermal conductivity, would be expected to lead to a drop in the surface temperature as "seen" by the radiation pyrometer; increasing the heating power to compensate for this temperature drop would cause the underlying carbon to become heated above the nominal reaction temperature and therefore (since the reaction rate decreases with increase of temperature in this range) to react more slowly. Mechanical removal of the "soot" by the reactant gas jet may account for the absence of the effect at the highest pressures.

In view of the wide departure of these low rates from the expected smooth curves, and the explanation proposed, results obtained at 16.0 and 21.0 p.s.i.a. in the temperature range quoted are regarded with suspicion and have therefore not been used in the reaction order plots (Fig. 16).

Reliable rate measurements have not yet been made on the basal plane surface of PG; large specimens suitable for the tubular reactor were difficult to obtain and inordinately expensive, while small bore tubes for the impingement reactor were subject to a thickness limitation of about 0.025 cm to avoid de-lamination; these very thin specimens tended to fail by over-heating of the surface outside the impingement area, as previously mentioned. A few experiments were made with vitreous carbon in the tubular reactor at pressures up to 48 p.s.i.a., but the results were apparently subject to partial diffusion control and are therefore not reproduced here; in view of a recent decrease in interest in vitreous carbon as a nozzle material, the work has not been repeated in the impingement reactor.

EFFECT OF ADDITIONS OF CARBON MONOXIDE. The first step in the reaction of carbon with carbon dioxide is generally agreed to involve the transfer of an oxygen atom from the CO_2 molecule to the surface:

$$C + CO_2 \longrightarrow CO + C(O) \qquad \ldots\ldots(1)$$

This is followed by gasification of the adsorbed oxygen as carbon monoxide:

$$C(O) \longrightarrow CO \qquad \ldots\ldots(2)$$

Retardation of the reaction by carbon monoxide at comparatively low temperatures (usually below 1300°K) is well known and has been discussed in a large number of papers over the past 30 years (see, for example, refs. 10-18). Two main mechanisms of retardation have been proposed, namely (a) the regeneration of carbon dioxide by the interaction of carbon monoxide with a reaction intermediate, e.g. the reversal of reaction (1), and (b) the reversal of reaction (2) by adsorption of CO on active sites, making such sites unavailable for reaction with the CO_2.

No previous work appears to have been reported on the effect of carbon monoxide on the CO_2-carbon reaction at or near rocket exhaust temperatures. Walls and Strickland-Constable (7) reacted pile grade graphite with CO_2 to which 30% CO had been added to inhibit the dissociation of the CO_2; the assumption appears to have been made that the CO had no other effect on the reaction rate, and no comparisons with 100% CO_2 or with other mixtures were reported). Composition data for typical solid propellant exhausts, based on thermodynamic calculations, indicate that the CO:CO_2 ratio in the combustion chamber varies from approximately 2:1 to 20:1 for different propellants. It was considered possible that these high concentrations of CO might have a significant effect on the rate of reaction of CO_2 with a carbon nozzle; an experimental investigation of the reaction of each of the four carbons with CO/CO_2 mixtures was therefore made, using the tubular reactor (Fig.2).

The gases used were supplied by Air Products Ltd., to the following specifications:

Carbon dioxide: CO_2 99.9%, O_2 5 v.p.m., N_2 5 v.p.m., $SO_2 < 1$ v.p.m., $H_2S < 0.01$ v.p.m., CO < 1 v.p.m., Ar 1 v.p.m., B 1 v.p.m., hydrocarbons < 1 v.p.m., H_2O 6 v.p.m.

Carbon monoxide: O_2 + Ar 130 v.p.m., $N_2 < 10$ v.p.m., CO_2 40 v.p.m., $H_2 < 5$ v.p.m., $CH_4 < 5$v.p.m., $C_2H_2 < 0.5$ v.p.m., total hydrocarbons < 5 v.p.m., H_2O 8 v.p.m.

(The concentration of water vapour, and possibly also of some of the other impurities present in both gases, was probably reduced to an even lower level by passage through a molecular sieve column, 5 ft. long x 6 in. diameter, packed with Union Carbide 5A sieves and incorporated in the gas supply system).

Separate streams of the two gases were metered through Platon flow gauges and passed through a multi-baffle mixer and a Vokes air filter with a paper element capable of removing entrained particles down to 1 μm in diameter. Samples of the mixed gases were analysed by absorption of the CO_2 in "Carboscrb" tubes: the CO_2 contents of the mixtures varied from 10.2% to 74.8%.

Results obtained for the reaction of PG (edge) with pure CO_2, one CO_2/Ar mixture (as a "control") and four different CO_2/CO mixtures are shown in Fig. 17. Comparison of the curve for 50.5% CO_2, 49.5% CO with those for 100% CO_2 and for 50.5% CO_2, 49.5% Ar shows that at temperatures above about 2150°C the CO acted merely as a diluent; however, at lower temperatures a pronounced retarding effect occurred. the rate at 1800°K (near the normal T_{max} in CO_2) being only 3% of the rate in 100% CO_2. Similar effects were observed with the other CO_2/CO mixtures; a progressive increase in the CO concentration depressed the rate maximum and displaced it to higher temperatures, until with 10.2% CO_2, 89.8% CO the rate maximum virtually disappeared.

Rate measurements on the other three carbons indicated that the retarding effect of CO was much less pronounced than on the edge surface of PG. These results are summarised in Table 1, which gives the ratio of the rate in mixed gas to that in CO_2 for all four carbons, in two CO_2/CO mixtures and at three temperatures: T_{max}, T_{min} and 2250°K (which lies between T_{max} and T_{min} for all the carbons). T_{max} and T_{min} here represent the temperatures at which the rate maximum and minimum occur, for each carbon, in 100% CO_2.

Type of Carbon	ρmixture/ρCO_2 at T_{max} for CO_2		ρmixture/ρCO_2 at 2250°K		ρmixture/ρCO_2 at T_{min} for CO_2	
	x_{CO_2} = 0.012	x_{CO_2} = 0.505	x_{CO_2} = 0.102	x_{CO_2} = 0.505	x_{CO_2} = 0.102	x_{CO_2} = 0.505
PG (Edge)	0.01	0.03	0.075	0.47	0.16	0.49
PG (Basal)-Le Carbone	-	0.43	-	0.63	-	0.6
PG (Basal)-R.P.E.	-	0.50	-	-	-	-
VC	-	0.54	-	0.50	-	0.42
5890	0.043	0.42	0.035	0.48	0.063	0.69

If the reaction order with respect to CO_2 concentration, for mixtures of CO_2 with an inert diluent, is assumed to be 1.0, then values of ρmixture/ρCO_2 which are appreciably less than the value of x_{CO_2} (i.e. the mole fraction of CO_2) indicate retardation by CO. If allowance is made for an apparent order of about 1.2, as indicated by the effect of dilution of the CO_2 with argon, the only carbon exhibiting significant retardation in 50.5% CO_2, 49.5% CO in the temperature range quoted is PG (edge). The retardation effect in 10.2% CO_2, 89.8% CO is pronounced for PG (edge) and much smaller, but probably significant, for 5890 graphite, at T_{max} and at 2250°K.

Consideration of the combustion temperatures and exhaust compositions of typical solid propellants, together with the above results, suggests that retardation of the CO_2-carbon reaction by the CO present in the exhaust will in general not be important. This is because the cooler, non-aluminised propellants, with combustion temperatures in the region of 2800°K, yield a comparatively low CO/CO_2 ratio (~1.75) in the exhaust: retardation by such a small concentration of CO will be significant only for PG (edge) nozzles with surface temperatures below about 2200°K; for the other carbons, and for PG (edge) at higher temperatures, the CO will act only as a diluent. With aluminised propellants, with higher combustion temperatures (up to about 3500°K), surface temperatures will be higher and therefore the CO is again likely to act only as a diluent, even if PG (edge) nozzles are used.

KINETICS AT TEMPERATURES ABOVE T_{min}: THE CONTRIBUTION OF EVAPORATION OF CARBON. The work to be described in this section arose from the suggestion that since the temperatures of preparation of all the carbons studied were below the maximum reaction temperature, their reactivity might be affected by the preliminary heating-up period in nitrogen or argon. Specimens were therefore heated for various periods at temperatures above 2800°K with a view to determining the effect on their subsequent reactivity. This treatment had the unexpected result of causing surface re-orientation of vitreous carbon and edge-surface pyrolytic graphite, with the formation of a skin of carbon, nodular in structure, having a highly preferred orientation of basal planes parallel to the surface (19).

It was considered that this re-orientation effect might have a bearing on the kinetics of weight loss in one of two ways:

(a) If, as suggested by much of the experimental evidence (19), the effect occurs via an evaporation-condensation mechanism, interruption of the process by homogeneous reaction of evaporating species with an oxidising gas would lead to a high rate of removal of carbon, with a high temperature coefficient.

(b) Whatever the mechanism, mobile carbon atoms involved in the re-orientation process would be expected to be temporarily more reactive, so that the rate of the heterogeneous reaction would increase.

An assessment of the contribution of evaporation of carbon to the kinetics was made by comparing weight loss rates in oxidising gases with evaporation rates in an inert gas or a vacuum.

Because of the disturbing effect of R.F. discharges in argon, weight loss rates were measured in a stream of nitrogen in the tubular reactor. (The reaction between nitrogen and carbon is comparatively slow and was not expected to lead to serious errors at the high temperatures under investigation, particularly in view of the high heat of vaporisation of carbon).

The measured evaporation rates in nitrogen, and the calculated vacuum evaporation rates quoted for an unspecified carbon by Dushman (20), are compared with the weight loss rates in CO_2 in Figs. 10-12. The actual values and the temperature dependence of the weight loss rates of PG (edge) in N_2 and VC in CO_2 agreed closely with the calculated evaporation rates at temperatures well above T_{max}; the rates for 5890 graphite in CO_2, while showing a trend towards the calculated evaporation rates at high temperatures, were still much higher in value and less steeply dependent on temperature. Measured evaporation rates in nitrogen were much lower than the calculated rates, except for PG (edge) where fairly close agreement was obtained, especially at the higher nitrogen velocity of 5500 cm/sec; rates in nitrogen were in all cases much lower than in CO_2, but the PG (edge) and VC results agreed well with the extrapolation of vacuum evaporation rate measurements made on these materials at 2200-2600°K by U.K.A.E.A., Harwell.

In discussing the significance of these results, it is necessary first of all to consider the reasons for the discrepancy between the calculated evaporation rate curve and the measured evaporation rates of VC and 5890 graphite. The agreement between the measured rates for VC in nitrogen and in vacuo shows that the usual depression of the evaporation rate by an inert gas is not responsible, and it would appear that the discrepancy is entirely due to the Dushman assumption that the condensation coefficient $\alpha = 1$, whereas determinations of α by the Knudsen cell technique (21) have given values of the order of 0.1. However, the close agreement of the VC/CO_2 and PG (edge)/N_2 curves with the calculated curve suggests that α may indeed approach 1 on some carbon surfaces, e.g. a surface undergoing oxidation or the "edge" surface of PG. (Unpublished work by Diefendorf (22) has confirmed that the evaporation rate from the "edge" surface is higher than from the basal plane surface, and that the condensation coefficient of the "edge" surface is approximately 1.0. This result is in agreement with the present results for evaporation in a nitrogen stream; as far as is known, Knudsen cell measurements have not been made on this form of carbon).

The following explanation may therefore be proposed for the experimental results in nitrogen and carbon dioxide at temperatures above T_{min}. In the first place, evaporation rates in nitrogen are expected to be lower than in vacuo; the effect of an inert gas in depressing the evaporation rate of a solid is usually attributed to gas-phase collisions between the evaporating species and gas molecules, resulting in the return of some of the former to the surface, where they may condense again. This effect will be greatest for a static inert gas atmosphere and will become less pronounced as the streaming velocity of the gas over the surface increases, because of the increasing probability that vapour will be swept away in the gas stream before it can return to the surface. At high velocities it is expected that the vapour concentration near the surface will be reduced to such an extent that conditions become comparable to those obtaining in vacuum evaporation; this prediction is consistent with the results of experiments in which the nitrogen flow-rate was varied (see Fig. 10).

If the gas is a reactive one, however, collisions of evaporating molecules with gas molecules may result in reaction, again reducing the vapour concentration near the surface to a very low level. Furthermore, the occurrence of a surface reaction would be expected to disturb the bond structure of the surface to such an extent that significant evaporation rates could occur at lower temperatures than in the vacuum or inert atmosphere, and weight loss rates at high temperatures might then exceed the vacuum evaporation rates, as observed for PG (edge) and 5890 graphite in CO_2. It is possible that the rate of the surface reaction may also be increased in a similar way, as a result of enhancement of the surface reactivity by the formation of free valencies as some of the surface carbon atoms are evaporated.

Support for the suggestion that evaporation of carbon makes an important contribution to the kinetics of carbon-gas reactions at high temperatures has been obtained from two other recent investigations (23, 24, 36). Work by Walsh et al (23,24) has shown that above about 1000°K there is some correlation between the weight loss rates of PG (basal) in inert and oxidising gases. Rates in argon were only about half those expected for $\alpha = 0.07$ (as found by Burns et al (21) for the basal plane surface); this is probably because the argon velocity (2700 cm/sec) used by Walsh was too low to prevent some build-up of carbon vapour near the surface. In carbon dioxide, weight loss rates were higher than evaporation rates calculated for $\alpha = 0.07$ but showed the same very steep temperature dependence. The authors suggested two possible explanations of the enhanced rates in CO_2:

(a) Rapid removal of evaporating carbon by gas-phase reaction with CO_2 may lead to an increase in the concentration gradient of carbon vapour and hence of the evaporation rate. This suggestion cannot account for the high weight loss rates of PG (edge) in the present work, which exceed (by a

factor of about 5) the experimental evaporation rates and those calculated for $\alpha = 1$ (see Fig. 10).

(b) Alternatively, Walsh suggests, the higher weight loss rates in CO_2 may correspond to a simple summation of the surface reaction rate and the evaporation rate. Results obtained in the present investigation show that the summation of measured evaporation rates and surface reaction rates obtained by extrapolation of the straight-line portion of the Arrhenius plot at temperatures between T_{max} and T_{min} to higher temperatures, yields calculated weight loss rates which are much smaller than the observed rates in CO_2; this consideration also applies to the data obtained by Walsh et al themselves. It is therefore necessary to assume either that the evaporation and surface reaction rates are subject to mutual enhancement as suggested above, or that a minimum occurs in the surface reaction rate (due, for example, to a "surface annealing" effect of the type postulated by Strickland-Constable (2,6) and others (25,26)) and that extrapolation of the rates observed below T_{min} to higher temperatures is not justified. The evidence at present available is insufficient to enable a choice to be made between these two possibilities; however, the decrease in the order of reaction above T_{min}, at temperatures where the normal evaporation rate of PG is still an order of magnitude less than the weight loss rate in CO_2, is apparently at conflict with the Strickland-Constable theory, which predicts a first order reaction at these temperatures.

KINETICS AT TEMPERATURES BELOW T_{min}. Duval (25), Strickland-Constable (2,6) and Blyholder, Binford and Eyring (26), have put forward theories based on "annealing" of active sites on the surface to explain the observed decrease in reaction rate with temperature over part of the temperature range studied. The last-mentioned authors developed a mathematical treatment capable of explaining the general shape of the rate/temperature curves obtained by previous workers, but quantitative agreement with the experimental results was not good; better agreement has since been obtained by Strickland-Constable (1), who has found one rate equation applicable to his experimental results for the oxygen-carbon reaction over a wide range of pressures. However, rate maxima have been observed in a large number of other gas-solid reactions and attributed to entirely different mechanisms. In the cases of the oxidation of tungsten (27-30), tantalum (31) and niobium (32,33) the effect has been explained either by the formation of a protective skin of oxide, the permeability of which varies with temperature as a result of phase transitions, or by a mechanism involving dissociation of an oxide at high temperatures followed by desorption of molecular or atomic oxygen. The latter type of mechanism has also been proposed to explain rate maxima in nickel-halogen reactions (34) and in the nickel-carbon monoxide reaction (35) at 0-120°C, at which temperatures self-migration as postulated by Duval and Strickland-Constable for the carbon case is not likely to occur on nickel to any significant extent.

The oxide dissociation mechanism may be applicable to the gaseous oxidation of carbon only if oxygen atoms or molecules can be desorbed as such from carbon surfaces at high temperatures. It is generally assumed that oxygen can be desorbed only as oxides of carbon, but the experimental evidence is based on the results of desorption at high temperatures after adsorption at low temperatures, and may not be valid for a dynamic adsorption-desorption process at high temperatures. One possibility, again involving the concept of surface heterogeneity, is that reaction cannot occur at every adsorption site, but that adsorbed species must migrate to a certain type of active site for dissociation or reaction to occur, and may be desorbed before reaching such a site.

Tsu and Boudart (37) have shown that this type of mechanism, originally proposed by them to explain their results on the dissociation of hydrogen on glass, could lead to a negative apparent activation energy over a limited temperature range in certain heterogeneous reactions.

Although the occurrence of similar abnormalities in the rate-temperature curves for different reactions is not necessarily indicative of similar reaction mechanisms, there would appear to be scope for mass-spectroscopic studies of the gaseous oxidation of carbon at high temperatures, along the lines already pursued by Schissel and Trulson (27) for the tungsten case; their results established that large amounts of atomic oxygen were desorbed at temperatures above about 2100°K, and a mechanism involving this desorption was shown to account for the observed reaction rate.

A further possibility is that a decrease in reaction rate with increase in temperature may be a direct result of a change in some parameter such as sticking probability or residence time of an adsorbed molecule on the surface. The residence time and concentration of an adsorbed species decreases with increase in temperature, but this effect would be insufficient to account for the rather steep drop in reactivity observed unless the heat of adsorption is of the order of tens of kilocalories per mole. Measured heats of adsorption of carbon dioxide on carbon at room temperature are low (5-8 kcal/mole), but the possibility of a transition to higher energy adsorption, as for the oxygen-carbon system but at much higher temperatures, cannot at present be discounted.

STEAM REACTION

Since the calculated concentration of water vapour in solid-propellant exhausts may be as high as 40% by volume, i.e. several times the carbon dioxide concentration, and since the rate of the steam-carbon reaction at lower temperatures has been reported to be greater than that of the CO_2-carbon reaction (38), information on steam-carbon reaction kinetics in conditions similar to those obtaining in a rocket nozzle is essential to any investigation of the factors affecting the chemical corrosion of the nozzle. An experimental investigation of the effects of carbon type, surface temperature and (to a limited extent) pressure has therefore been made.

APPARATUS. Steam was supplied via a 1¼" galvanised steel pipeline from a Clayton steam generator. The flow rate was controlled by a Drayton pneumatic valve and "Dialset" controller, and measured by a Kent orifice meter with a circular chart recorder. Steam pressures in the pipeline and the impingement reactor were also recorded continuously. The final section of the pipeline,

between the control valve and the reactor, incorporated a solenoid valve system to permit rapid changeover from nitrogen to steam and vice-versa, and was surrounded by heating tapes and pre-formed fibreglass lagging to prevent condensation. As an additional precaution, a heated sintered stainless steel filter unit was fitted to the reactor inlet, to remove any condensate droplets and entrained particles from the steam. The general layout of the system is shown in Fig. 18.

As already mentioned, the jet velocities used in this work were in the range 0.5-1.0 of sonic velocity; these velocities appear to be the highest so far used for the investigation of carbon-gas reactions, and probably represent the closest approximation yet to rocket nozzle conditions. The observation that, despite these high velocities, the highest erosion rates measured were still apparently subject to diffusion control emphasises the extreme difficulty of measuring true chemical rates for these reactions at high temperatures and pressures.

Recession rates were measured, as previously described, at various temperatures in the range 1800-3000°K; radiation from the specimen was insufficient for satisfactory operation of the diode detector below about 2000°K so erosion rates at lower temperatures were measured by the visual (stop-watch) technique previously described. For comparison with the earlier carbon dioxide work, based on weight losses, recession rates were converted into specific reaction rates by multiplying by the density of the carbon concerned (1.48 for VC, 1.85 for 5890, 2.20 for PG).

Attempts to measure erosion rates for PG by the use of square-section rods, 6.0 x 0.3 x 0.3 cm (cut from a flat plate so that the long side lay along the a - axis of the material, thus exposing two "basal" and two "edge" surfaces, each 6.0 x 0.3 cm) were unsuccessful: in all cases, whether the steam jet was made to impinge on the "basal" or the "edge" surface, the latter oxidised more rapidly and led to failure of the specimen before any measurable recession had occurred on the projected image of the specimen. Detailed examination of the specimens after reaction showed that the recession rate on the "edge" surface varied sharply with distance from the two "basal" surfaces, the edges of these surfaces being virtually unattacked. The shape of the oxidation crater thus formed was as illustrated in Fig. 19, i.e. roughly a segment of an ellipsoid with the major axis up to 6-7 times the minor axis; the depth of the crater was at a maximum of 0.1-0.15 cm near the centre of the reacting surface, and fell to zero near the edge AA (Fig. 19). This phenomenon was eventually attributed to a sharp drop in temperature near the edge of the "edge" surface, due presumably to the loss of heat by radiation from the "basal" surface and the low thermal conductivity of PG in the c - direction. The temperature gradient was not detectable with an ordinary disappearing filament pyrometer, but was discovered by means of a micro-pyrometer giving much higher image magnifications.

Further PG work was therefore carried out with hollow cylindrical specimens in which the curved surface was entirely "edge". These were prepared by machining 1.25 cm thick plates into cylinders, 1.25 cm long x 0.6 cm o.d. x 0.35 cm i.d., with the axis of the cylinder parallel to the c-axis of the material; surface debris was removed by ultrasonic washing in distilled water and drying in an oven before use. Experiments with the 0.025 cm thick cylinders with the curved surface entirely "basal" were unsuccessful, even at only 18 p.s.i.a. steam pressure, because of the high erosion rates outside the impingement area (as for high pressure CO_2, previously discussed).

Results obtained for one batch of PG (edge) and three batches each of 5890 graphite and VC, in steam at 19.0 p.s.i.a. total pressure, are shown in Fig. 20. The main conclusions to be drawn from the work are as follows:

Activation energies in the range 2000-2500°K are high for VC and PG (edge), ~55 kcal/mole and ~60 kcal/mole respectively. The slope of the Arrhenius curve for VC decreases above 2500°K, while that for PG (edge) becomes negative. Diffusion control and skin re-orientation effects may both play a part in these changes of slope: as Fig. 8 shows, the VC reaction rate is markedly more dependent on velocity and less reproducible at about this temperature; moreover, examination of PG (edge) specimens reacted at about 2700°K revealed the presence of surface skins similar in appearance to those previously reported (19), which might be expected to exhibit reduced reactivity by virtue of the high degree of orientation of basal planes parallel to the surface.

The reactivities, as well as the activation energies, of PG (edge) and VC are comparable in the temperature range studied. However, 5890 graphite exhibited much higher reaction rates and a much lower activation energy, probably due to the kinetic importance of physical effects such as boundary layer diffusion, penetration of the pore structure and mechanical erosion.

Boundary layer diffusion effects are expected to be significant throughout the temperature range studied for this graphite, since even at the lowest temperatures (1650-1700°K) the erosion rates observed were approximately the same as for VC at 2470°K, where the rate was shown to increase with jet velocity up to and beyond sonic velocity.

Evidence for both pore penetration and mechanical erosion was obtained by visual examination of the projected image of the specimen during oxidation in steam: the surface was seen to become non-uniform in appearance, with patches of apparently cooler (i.e. darker) material forming and then suddenly disappearing, as though carried away mechanically in the gas stream. Further investigation of this effect revealed that at the lowest temperature weight losses occurred without any visible regression of the surface, over a period of a minute or more. Very rapid regression then occurred, apparently due to mechanical breakdown of a thin skin of unreacted graphite: if the reaction were stopped at this stage, i.e. before all of the surface skin had been removed, it was found that oxidation had been proceeding internally to form a cavity below this unreacted skin. As the reaction temperature was increased, the apparent "induction period" (during which weight losses occurred without surface regression) decreased, from 65 sec at 1660°K to 2 sec. at 2220°K. At higher temperatures, the effect was too rapid to follow visually, but temperature fluctuations still occurred as a

result of surface "scaling" followed by mechanical loss of "scale" to reveal an underlying, apparently much hotter, surface.

It would appear, therefore, that even at the very high jet velocities used in this work, chemical reaction rates could not be measured for the 5890/H_2O system because of the occurrence of the physical effects described. It should be emphasised that despite this limitation, which also applies to the results for PG (edge) and VC above 2500°K, the highest reaction rates observed were much higher than those occurring in actual rocket motor tests. For 5890 graphite, for example, the highest specific reaction rate (1.25 g/cm^2 min) corresponded to a surface recession rate of about 130 mils/sec, roughly two orders of magnitude higher than the average rates observed in motor tests. Various factors may contribute towards this discrepancy:

1. Recent theoretical and experimental work has shown that surface temperatures at the throat are much lower, especially in the early stages of a firing, than the highest temperatures used in the kinetics experiments reported above.
2. The reaction rate due to steam in the exhaust may be subject to diffusion effects and also to chemical retardation by other gases present: a small amount of work on CO_2/H_2O mixtures, for example, has indicated that reaction rates in such mixtures are less than the sum of the rates due to the individual partial pressures of CO_2 and H_2O.
3. Rates measured in the impingement reactor may, as a result of the differences in geometry, include a larger contribution from mechanical erosion than in the rocket motor tests.

ORDER OF REACTION. In view of the very high reactivity of 5890 graphite and the thin wall of PG (basal) specimens, both of which led to premature "burn-out" of specimens in high pressure steam, the limited time available for this stage of the work was devoted almost entirely to investigation of the reactivity of PG (edge) specimens at pressures up to 40-50 p.s.i.a. Graphs of log ρ versus log p for three different temperatures in the range investigated are shown in Fig. 21.

At the lowest temperature, 2071°K, the order of reaction was close to 1.0; however, at 2234°K only a small proportion of the experimental points could be fitted to a straight line of slope 1.0 while a much larger proportion fell close to a line of slope 2.0. This, together with the observation that pronounced local variations in reaction rate occurred over the surface, with the formation of crevasses of depth approximately equal to the mean surface recession, suggests that two different types of reacting site are present and that one is associated with a first order reaction and the other with second order. Two different types of site are, of course, to be expected for the "edge" surface of a turbostratic carbon, or one with a high degree of mis-orientation between layer planes (as is usual with "as deposited" PG); moreover, Thomas (39) has reported slightly different reactivities and orders of reaction for the two "edge" directions in reactions with oxygen at comparatively low temperatures.

The preponderance of the first order reaction at lower temperatures, and of second order at higher temperatures, may be explained by a difference in activation energies; however, further investigation of the reaction mechanisms is necessary before this suggestion can be confirmed. The decrease in the order at the highest temperatures may be due to one or more of the following effects:

(i) Re-orientation, yielding a "basal plane" surface skin

(ii) Evaporation of carbon

(iii) Diffusion control

OXYGEN REACTION

In view of the high rate and exothermicity of the carbon-oxygen reaction, and the low concentrations of oxygen present in solid propellant exhausts, the reaction was studied in oxygen-argon mixtures containing 0.4-10.0% O_2. Reaction rates were measured for PG (edge), VC and 5890 graphite in the tubular reactor at 16 p.s.i.a. pressure and at surface temperatures of 1500-3000°K, with a gas velocity of 3000 cm/sec. Subsequent experiments in the impingement reactor at surface temperatures near T_{max} and gas velocities of 1400-1500 cm/sec gave rates which were 2-4 times as high, suggesting that the tubular reactor results were not entirely free from diffusion control; the results are therefore not reproduced in detail here, but the general conclusions are still valid and may be summarised as follows:

(i) O_2 is typically only one order of magnitude more reactive than CO_2 at these high temperatures, compared with five orders at 1073°K and 0.1 atm. (38).

(ii) Since a non-aluminised propellant exhaust contains approximately 1000 times more CO_2 and 5000 times more H_2O than O_2, the contribution of O_2 to the overall erosion rate may be neglected. Indeed, diffusion control is likely to be even more pronounced in the nozzle than in the tubular reactor experiments because of the very low concentration of O_2 in the exhaust (0.01%), thus reinforcing this conclusion.

(iii) Erosion by atomic oxygen, if in the chemical regime, would be more important: Rosner and Allendorf (40) have shown that, at 1800-2000°K (the highest temperatures studied in their work) and at pressures of the order of 10^{-2} torr, atomic oxygen is 30-60 times more reactive than molecular oxygen. If this reactivity ratio is maintained at high pressures, the contribution of atomic oxygen to the nozzle erosion rate might become comparable with that of CO_2, since even a non-aluminised propellant may contain approximately 0.005% O. However, as with O_2, the reaction rate will almost certainly be limited by diffusion, the rate of which will be very low as a result of the low concentration gradient:

Diffusion rate $= \frac{D}{\delta}(c_e - c_w)$ where D = diffusion coefficient

δ = boundary layer thickness

c_e and c_w = concentrations in bulk and at wall, respectively.

Since c_e is very small, the value of $\frac{c_e - c_w}{\delta}$ (and therefore the diffusion rate) will also be very small.

Direct confirmation of these predictions by reacting carbons with an inert gas containing appropriate concentrations of atomic oxygen, at high total pressures, would be extremely difficult in practice because of the high recombination rates; however, an approximate measure of the relative reactivity of atomic and molecular oxygen under such conditions might be obtained by pre-heating an argon-oxygen mixture to a temperature at which the degree of dissociation of the molecular oxygen was sufficient to produce an equilibrium concentration of (say) a few percent of oxygen atoms. The latter concentration could be varied by changing the pre-heat temperature, the total pressure, or the partial pressure of argon. Such experiments have not yet been carried out, although feasibility studies of a gas pre-heater based on an argon plasma torch have been reported (9).

REFERENCES

1. J.R. Walls and R.F. Strickland-Constable, Carbon 1, 333 (1964).
2. R.F. Strickland-Constable, Thesis, "The Oxidation of Carbon", Oxford 1939; Trans. Far. Soc. 40 333 (1944) and 43, 776 (1947).
3. L. Meyer, Z. Phys. Chem. B17, 385 (1932).
4. H. Martin and L. Meyer, Z. Electrochem. 41,(3), 136 (1935).
5. Sihvonen, Trans. Far. Soc. 34, 1062 (1938).
6. J. Nagle and R.F. Strickland-Constable, 5th Carbon Conf. (1961), 1, 154.
7. J.R. Walls and R.F. Strickland-Constable, 7th Carbon Conf. (Abstract in Carbon 3, 350 (1965)).
8. J.R. Ladd and P.N. Walsh, Carbon 4, 539 (1966).
9. J.C. Lewis, I.J. Floyd and F.C. Cowlard, 8th Carbon Conf. (1967).
10. A.P. Semechkova and D.A. Frank-Kamenetzkii, Acta Physicochim. U.R.S.S. XII, 879 (1940).
11. J. Gadsby, F.J. Long, P. Sleightholm and K.W. Sykes, Proc. Roy. Soc. A.193, 357 (1948).
12. A.E. Reif, J. Phys. Chem. 56, 785 (1952).
13. V.A. Evropin, N.V. Kulkova and M.I. Temkin, Zh. Fiz. Khim. 30, 348 (1956), C.E. Trans. 1990 (C.E.G.B.).
14. J.D. Blackwood and F.K. McTaggart, Austr. J. Chem. 12, 533 (1959).
15. J.D. Blackwood and A.J. Ingeme, Austr. J. Chem. 13, 194 (1960).
16. J.D. Blackwood, Ind. Chem. 36, 171 (1960).
17. J.D. Blackwood, Austr. J. Appl. Sci. 13, 199 (1962).
18. M. Mentser and S. Ergun, Carbon 5, 331 (1967).
19. J.C. Lewis and I.J. Floyd, J. Matls. Sci. 1, 154 (1966).
20. S. Dushman, "Scientific Foundations of Vacuum Technique", 2nd Edn. (1962), p.696.
21. R.P. Burns, A.J. Jason and M.G. Inghram, J. Chem. Phys. 40, 1161 (1964).
22. R.J. Diefendorf, personal communication.
23. J.R. Ladd and P.N. Walsh, Carbon 4, 539 (1966).
24. P.N. Walsh, "Principles Governing the Behaviour of Solid Materials in Severe High Temperature Environments", Quarterly Progress Report, Sept. 30, 1965, Army Missile Command Contract No. DA-01-021-AMC-11926(Z); R.P.E. Ref. No. R.24071.
25. X. Duval, Ann. de Chimie 10, 903 (1955).
26. G. Blyholder, J.S. Binford and H. Eyring, J. Phys. Chem. 62, 263 (1958).
27. P.O. Schissel and O.C. Trulson, J. Chem. Phys. 43, 737 (1965).
28. J.H. Singleton, J. Phys. Chem. 45, 2819, (1966).
29. P.N. Walsh, J.M. Quets and R.A. Graff, J. Chem. Phys. 46, 1144 (1967).
30. J.A. Becker, E.J. Becker and R.G. Brandes, J. Appl. Phys. 32, 411 (1961).
31. P. Kofstad, J. Electrochem. Soc. 110, 491 (1963).
32. D.W. Bridges and W.M. Fassell, J. Electrochem. Soc. 103, 325 (1956).
33. P. Kofstad and H. Kjollesdal, Trans. Met. Soc. A.I.M.E. 221, 285 (1961).
34. J.D. McKinley, J. Chem. Phys. 40, 576 (1964).
35. A.S. Brown, Ph.D. Thesis, University of London, 1965.
36. J.F. Clarke and B.R. Fox, J. Chem. Phys. 46, 827 (1967).
37. K. Tsu and M. Boudart, 2nd Int. Conf. Catalysis, Paris 1962.
38. P.L. Walker, F. Rusinko and L.G. Austin, Adv. in Catalysis XI, 133 (1959).
39. J.M. Thomas, Chemistry and Physics of Carbon 1, 122 (1965).
40. D.E. Rosner and H.D. Allendorf, Carbon 3, 153 (1965).
41. L.G. Carpenter, A Survey of the Radiation Emissivity of Carbon and Graphite (R.P.E., Westcott, January 1969).
42. M.R. Null and W.W. Lozier, J. Appl. Phys. 29, 1605 (Nov. 1958).
43. M.R. Null and W.W. Lozier, WADD-TR-61-72, Vol. XXI (Nov. 1963).

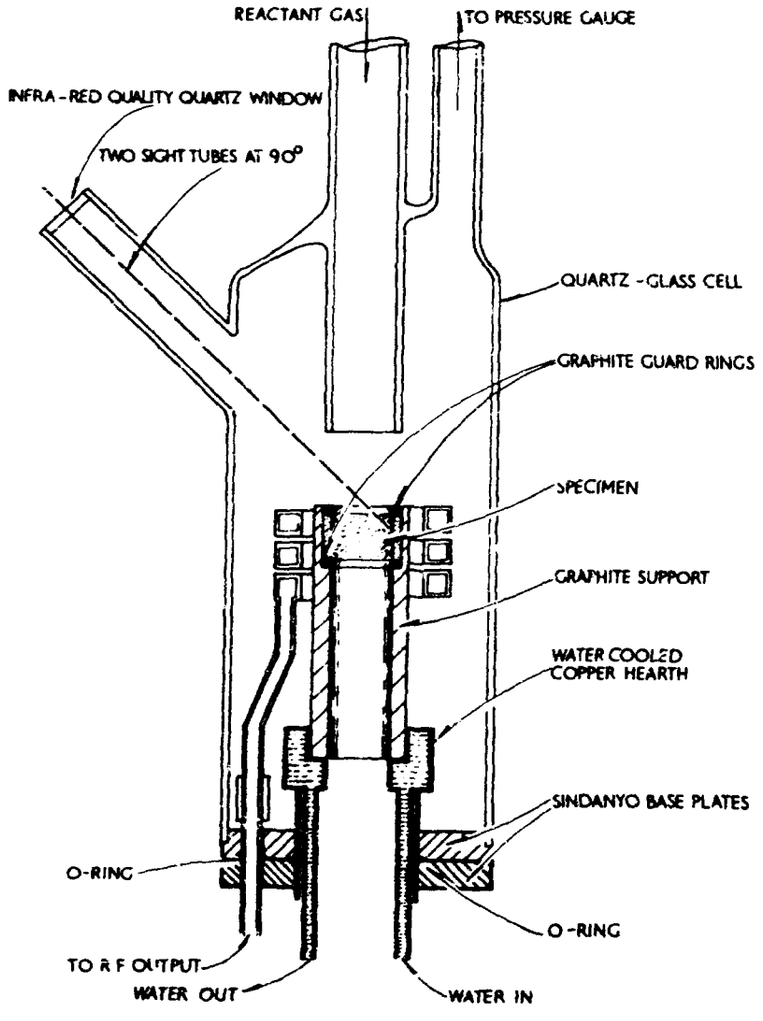

Fig.1 Tubular reactor: atmospheric pressure

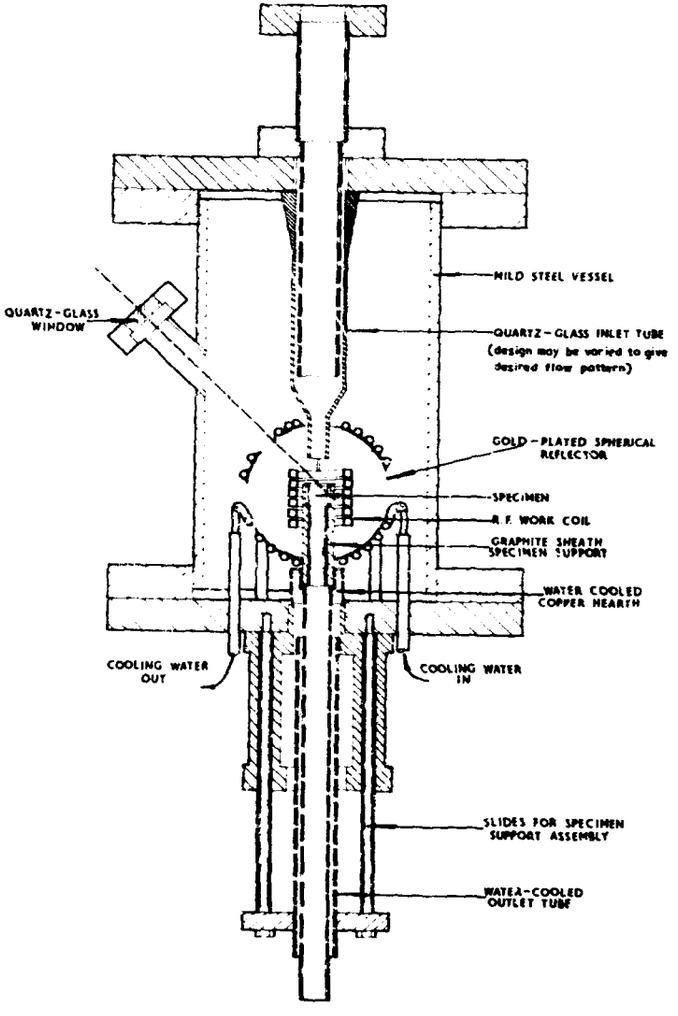

Fig.2 Tubular reactor: high pressure

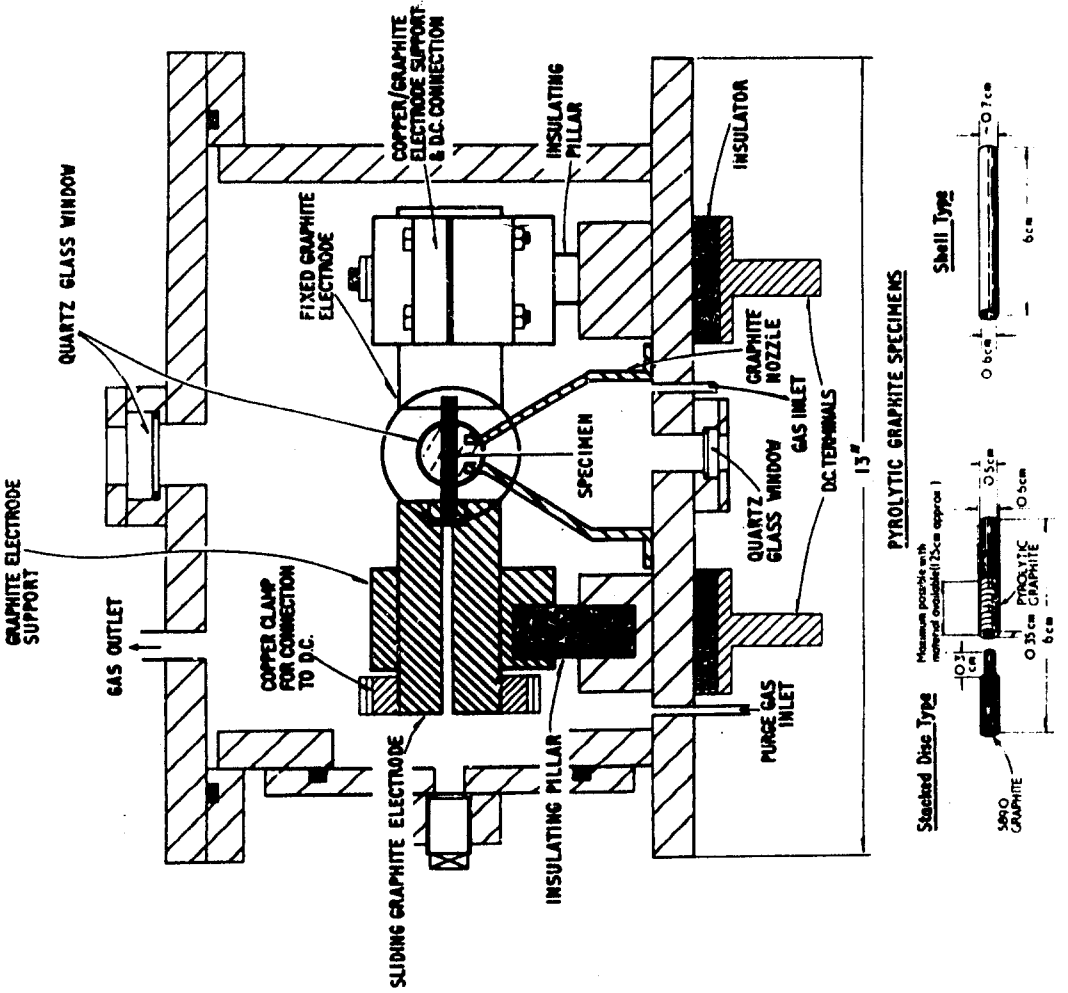

Fig.4 Impingement reactor: high pressure

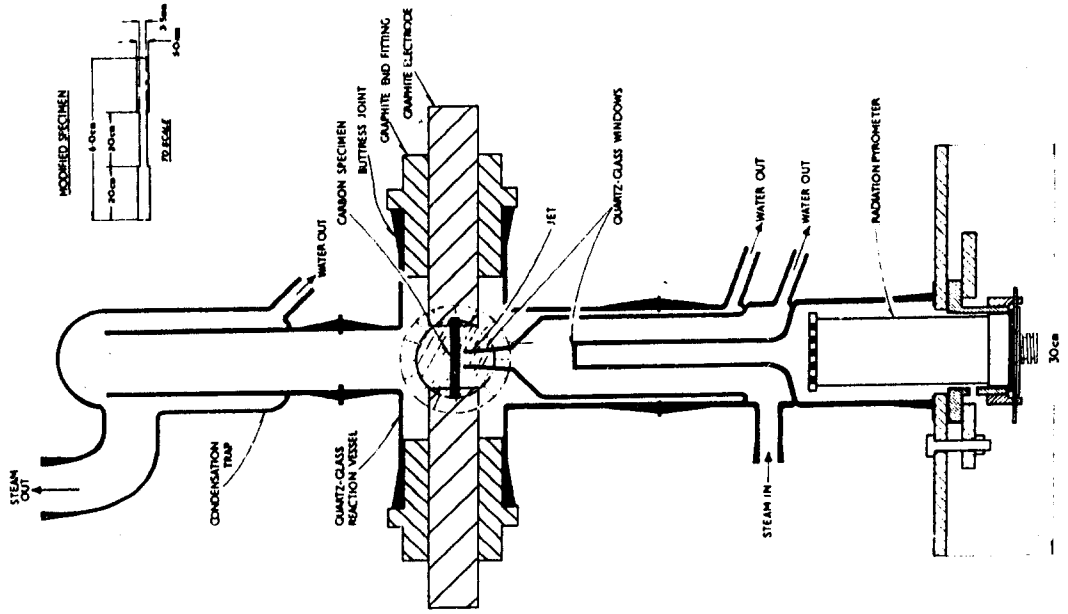

Fig.3 Impingement reactor Mark I

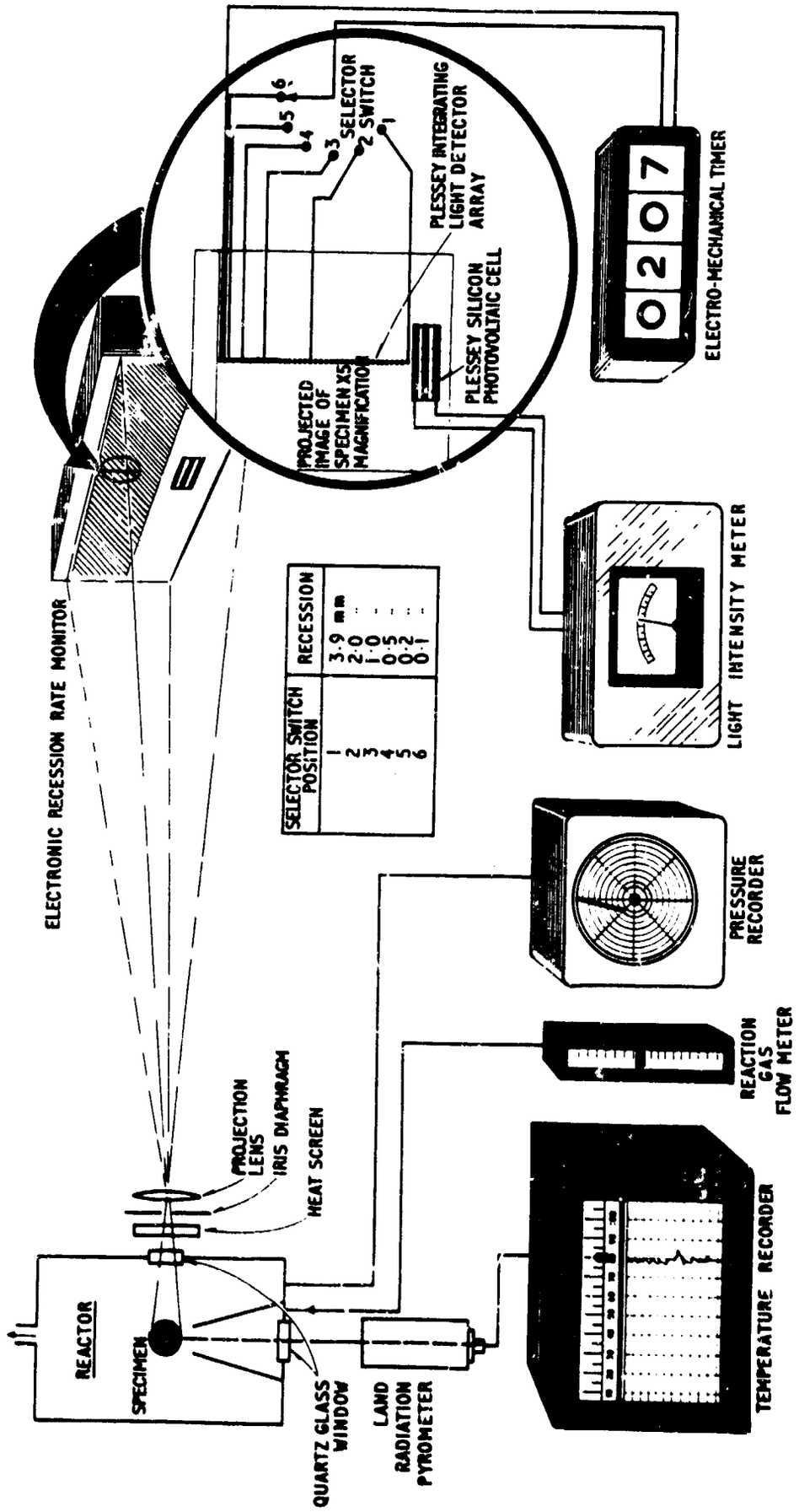

Fig.5 Photoelectric measurement of recession rates

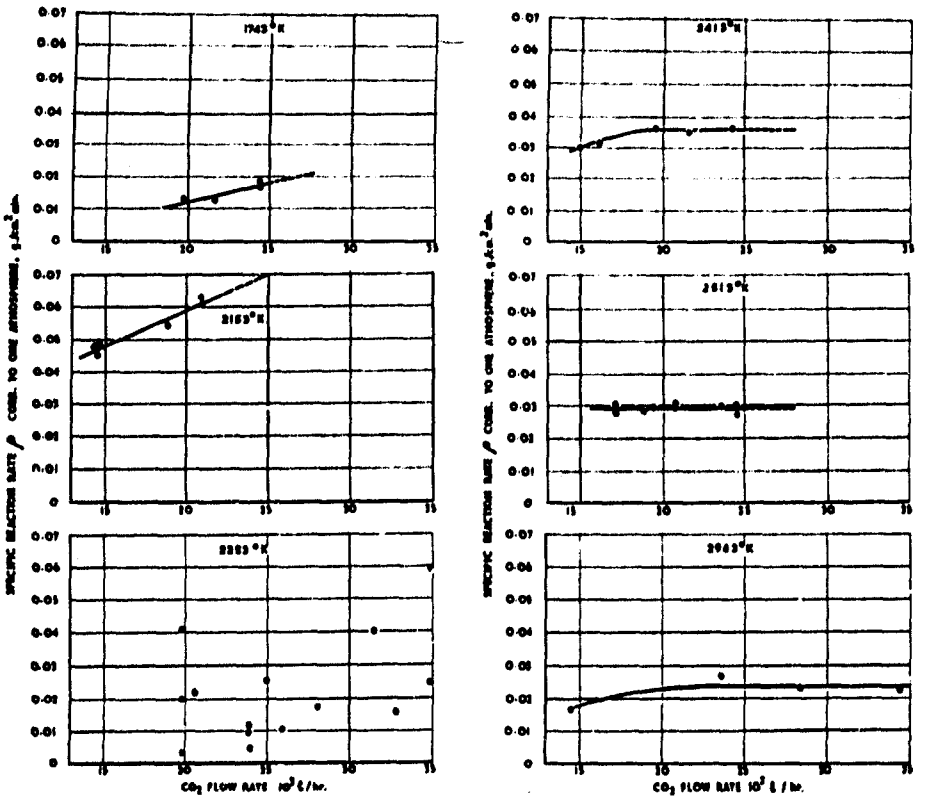

Fig.6 Variation of reaction rate with flow rate: vitreous carbon in CO_2 (tubular reactor, specimen I.D. 1.6 cm)

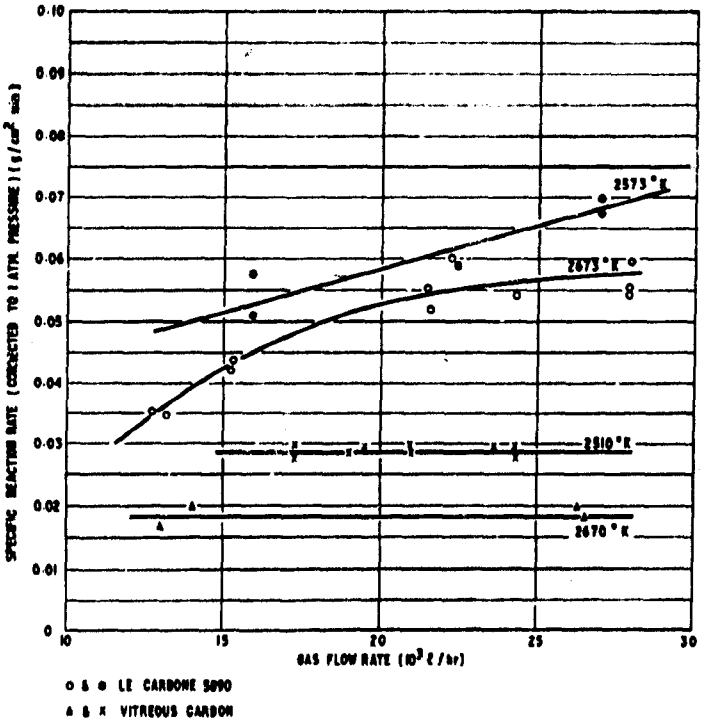

Fig.7 Comparison of flow dependence of reaction rates for vitreous carbon and le carbone 5890 graphite in CO_2 (tubular reactor, specimen I.D. 1.6 cm)

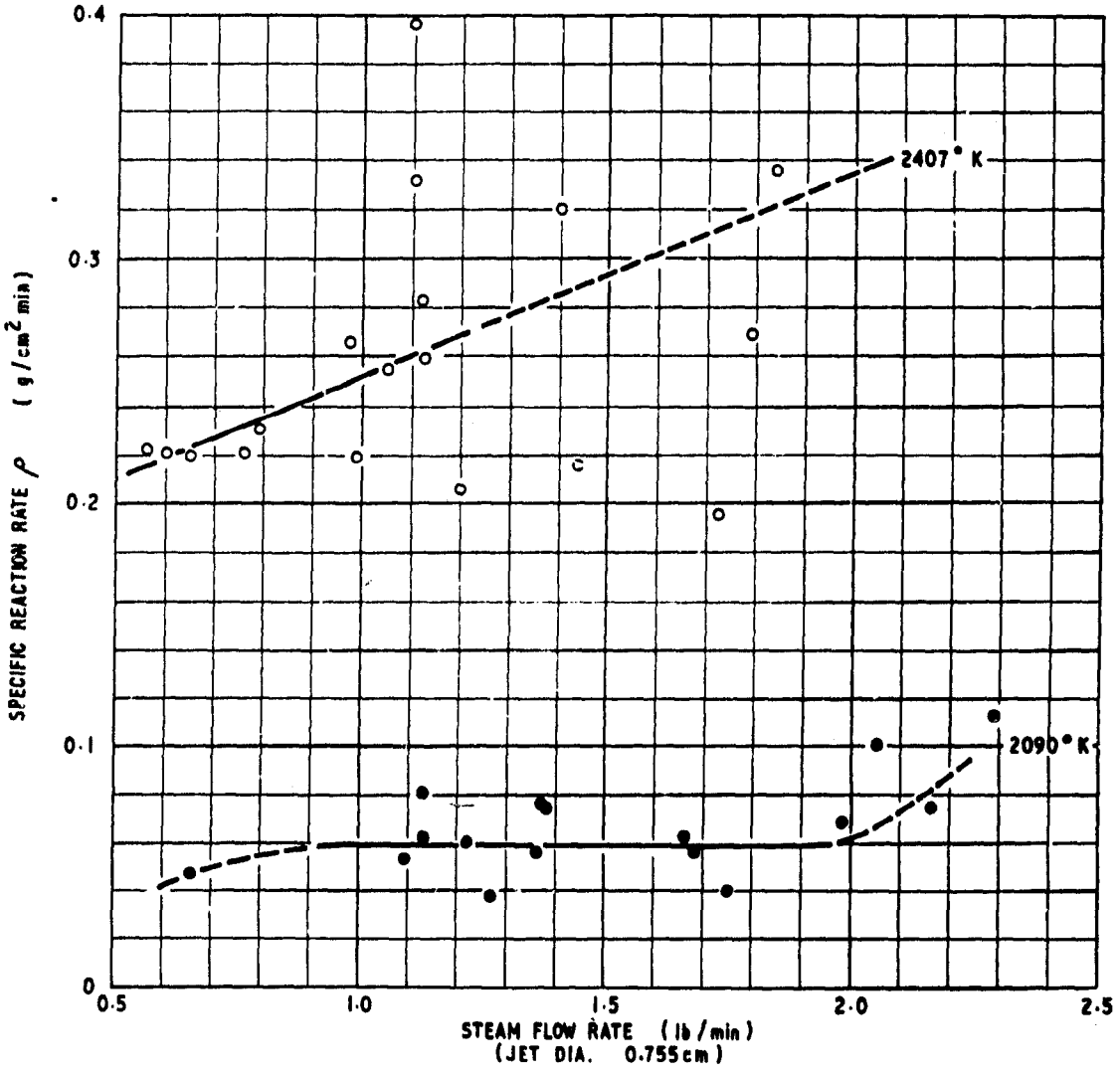

Fig.8 Variation of specific reaction rate with flow rate: vitreous carbon in steam (corrected to 16 p.s.i. assuming order of reaction = 1.0)

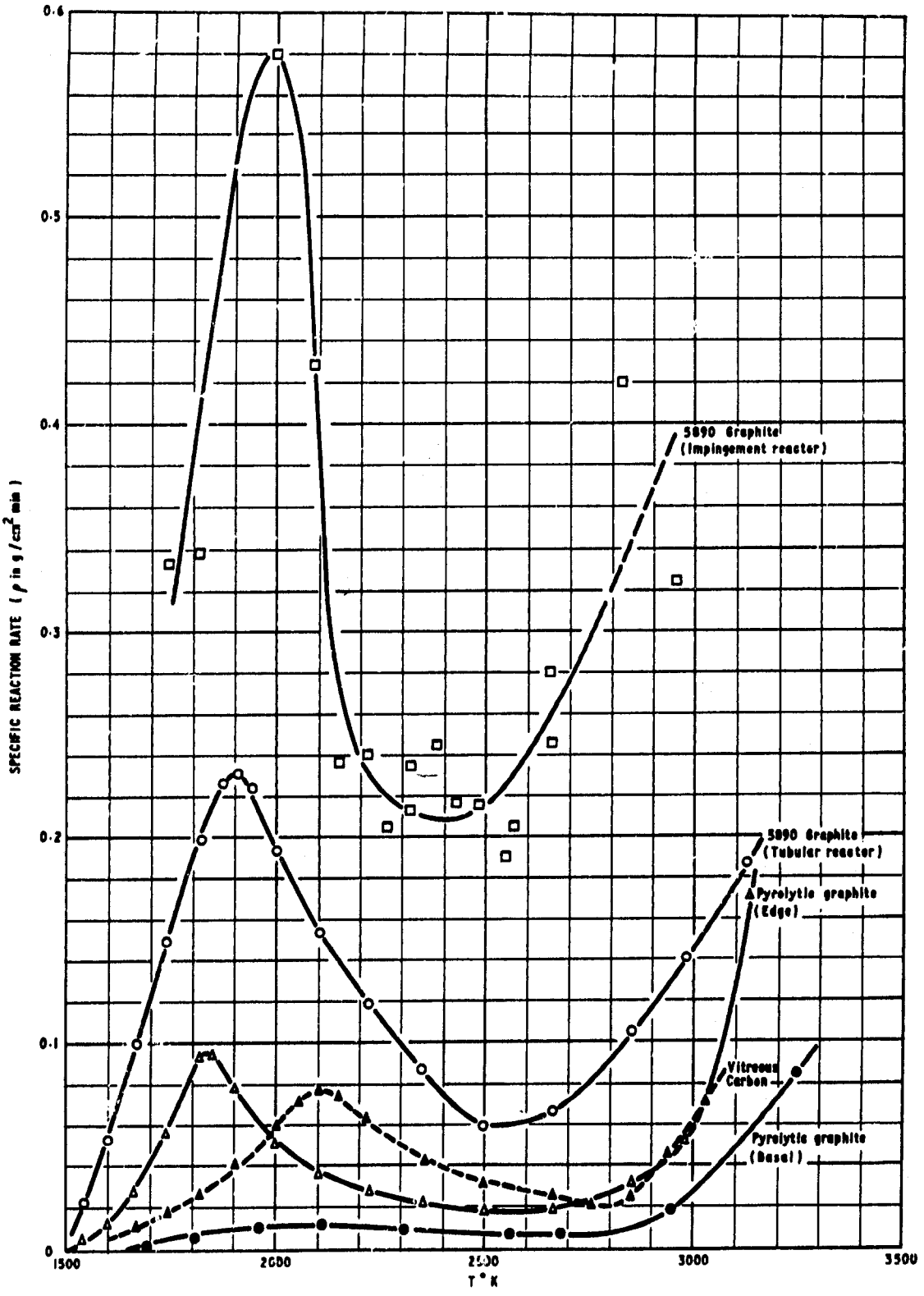

Fig. 9 Variation of specific reaction with surface temperature for various carbons in CO_2 at 16 p.s.i. absolute pressure

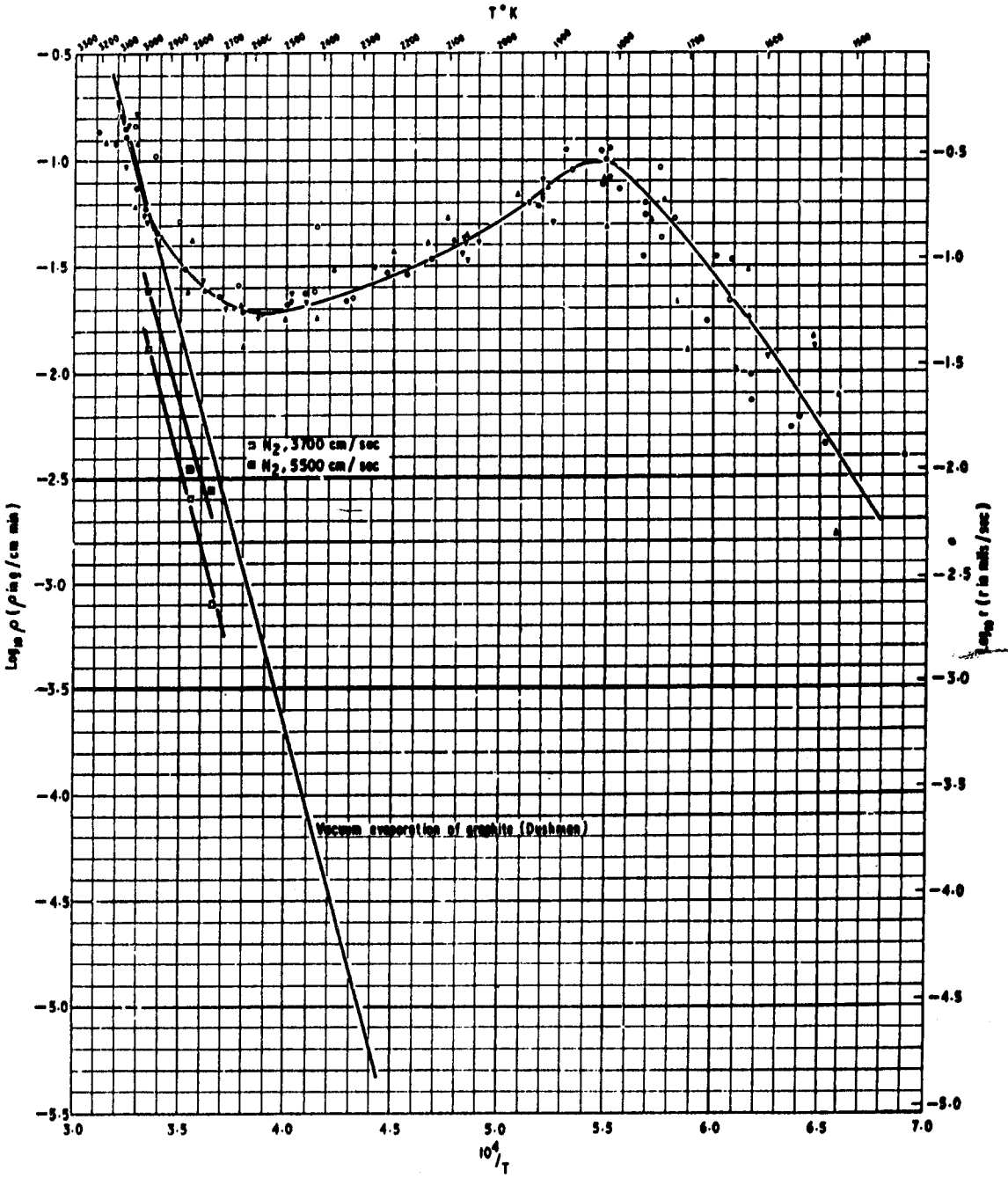

Fig.10 Variation of specific reaction rate with surface temperature for six batches of pyrolytic graphite (edge surface) in CO_2 at 16.0 p.s.i. absolute pressure

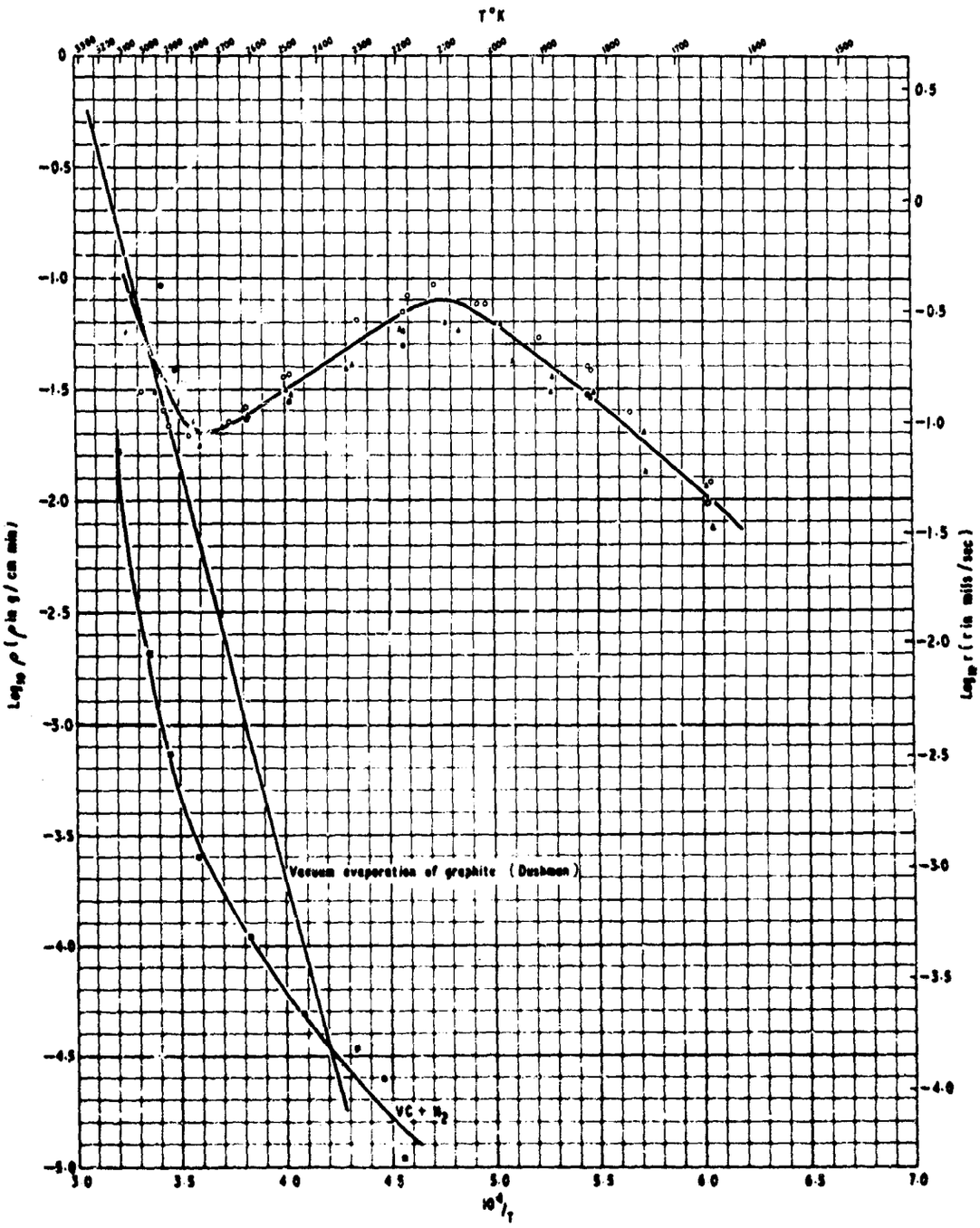

Fig. 11 Variation of specific reaction rate with surface temperature for four batches of vitreous carbon in CO_2 at 16.0 p.s.i. absolute pressure

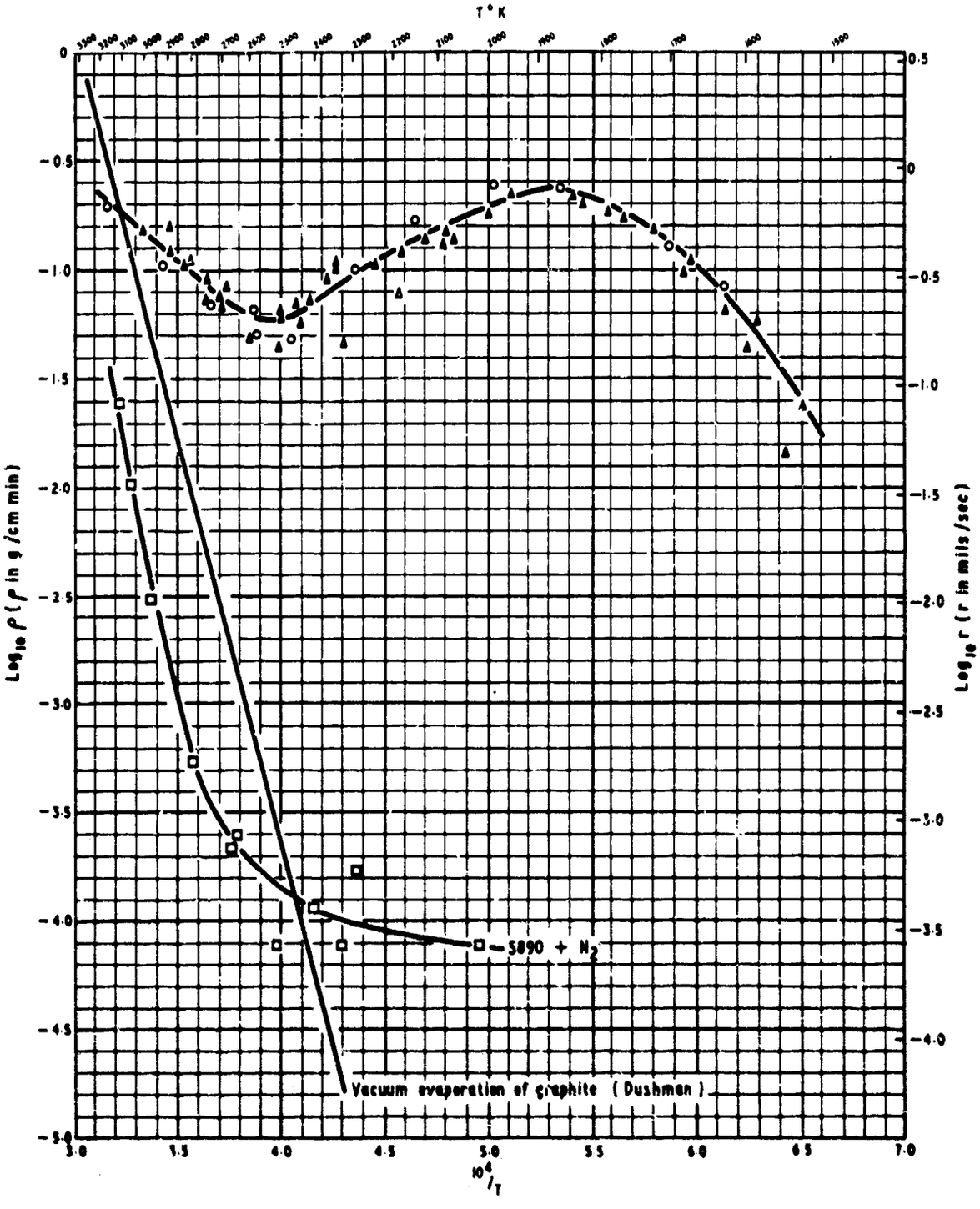

Fig. 12 Variation of specific reaction rate with surface temperature for three batches of 5890 graphite in CO_2 at 16.0 p.s.i. absolute pressure

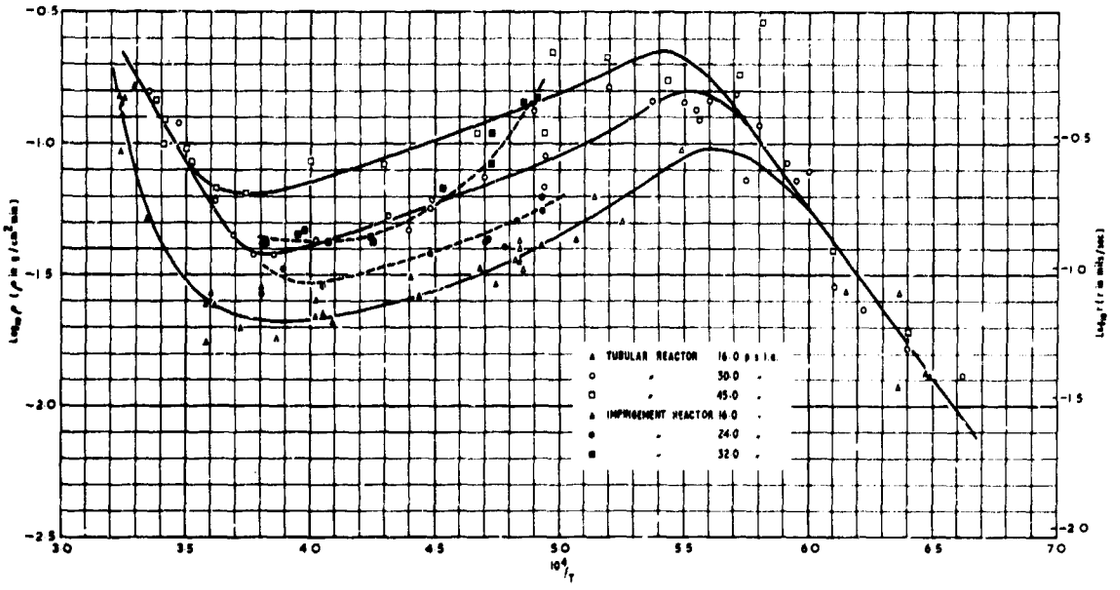

Fig.13 Variation of specific reaction rate with surface temperature: PG (edge) in CO_2 at 16.0 ~ 45.0 p.s.i.a.

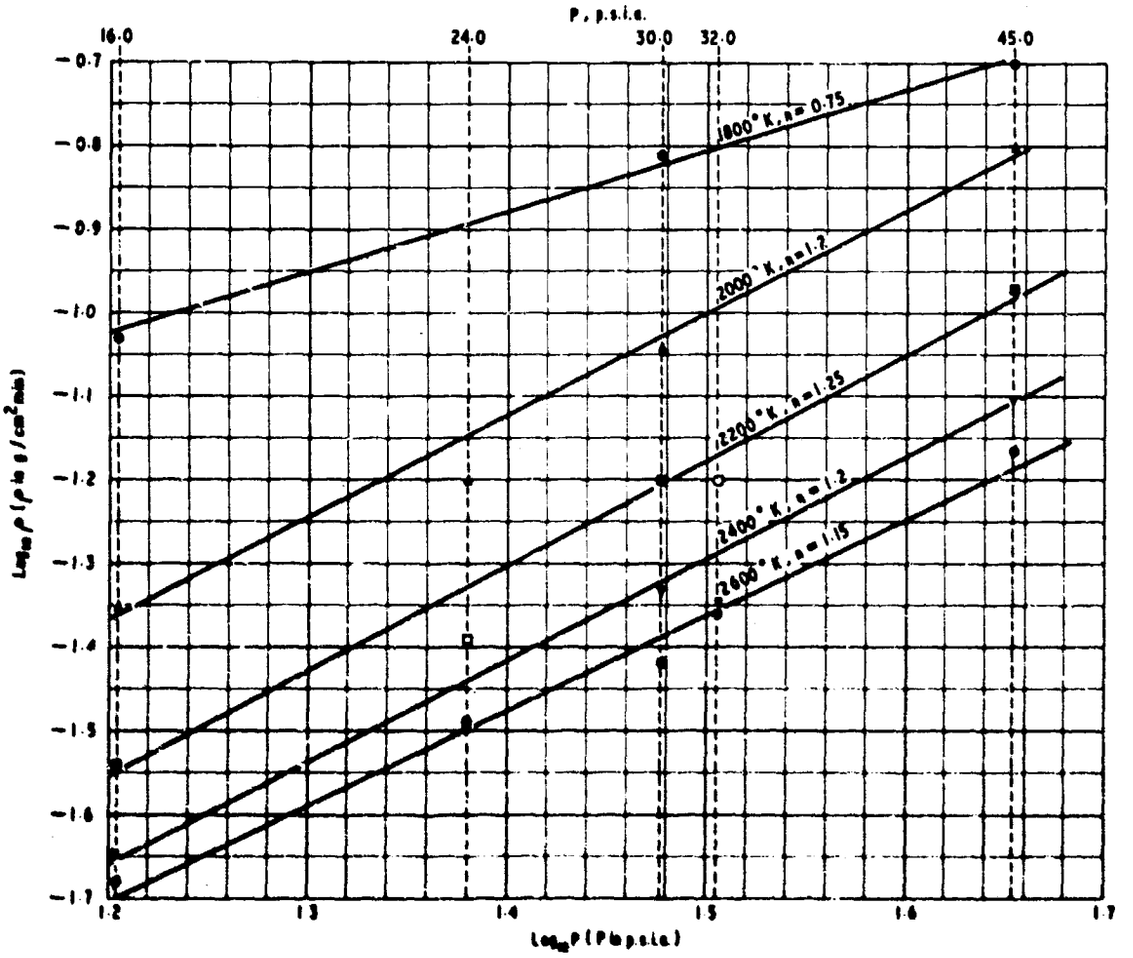

Fig 14 Reaction order graph for PG (edge) in CO_2

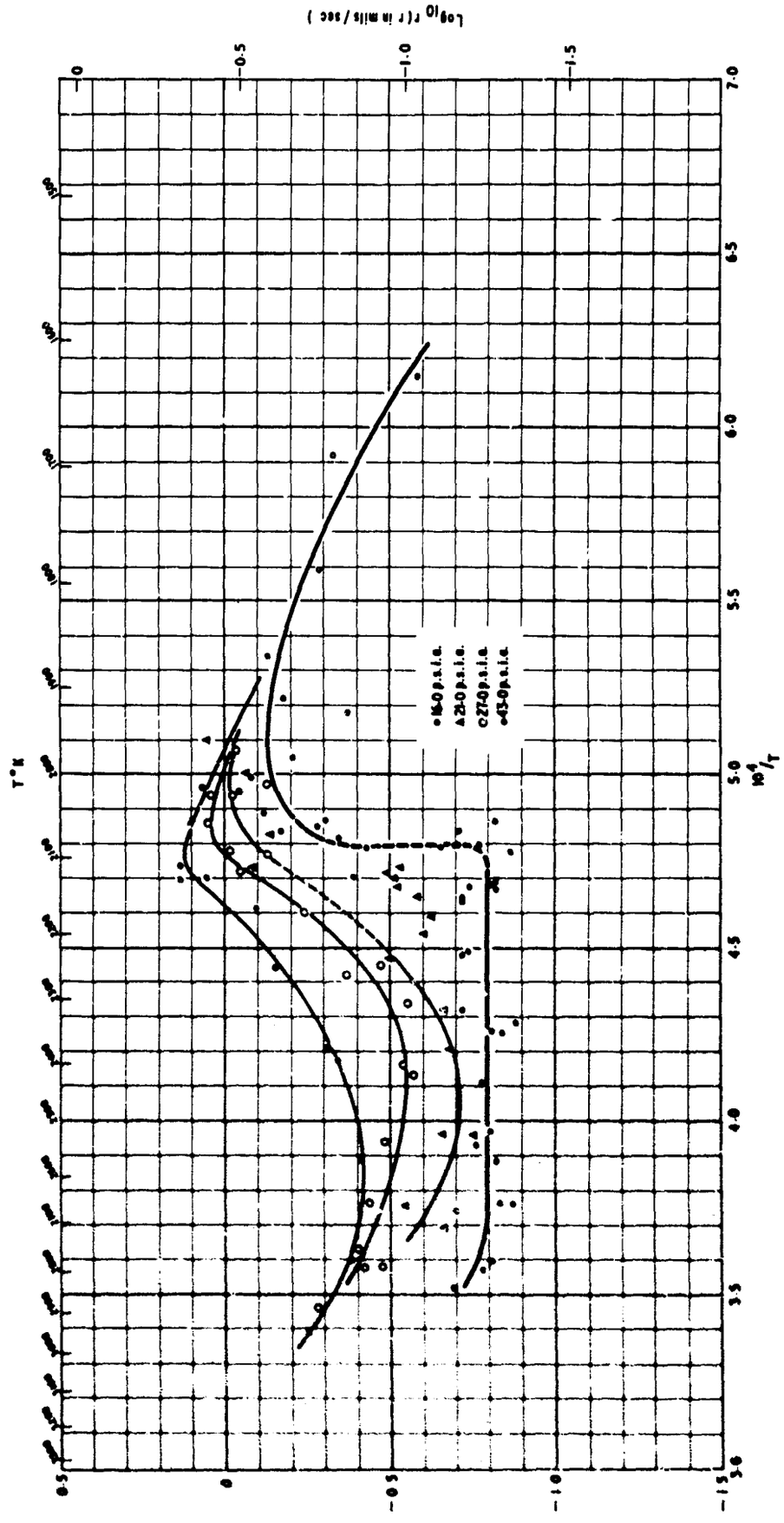

Fig. 15 Variation of specific reaction rate with surface temperature: 5699 graphite in CO_2 at 16.0 – 43.0 p.s.i.a. (impingement reactor, jet velocity > 10,000 cm./sec.)

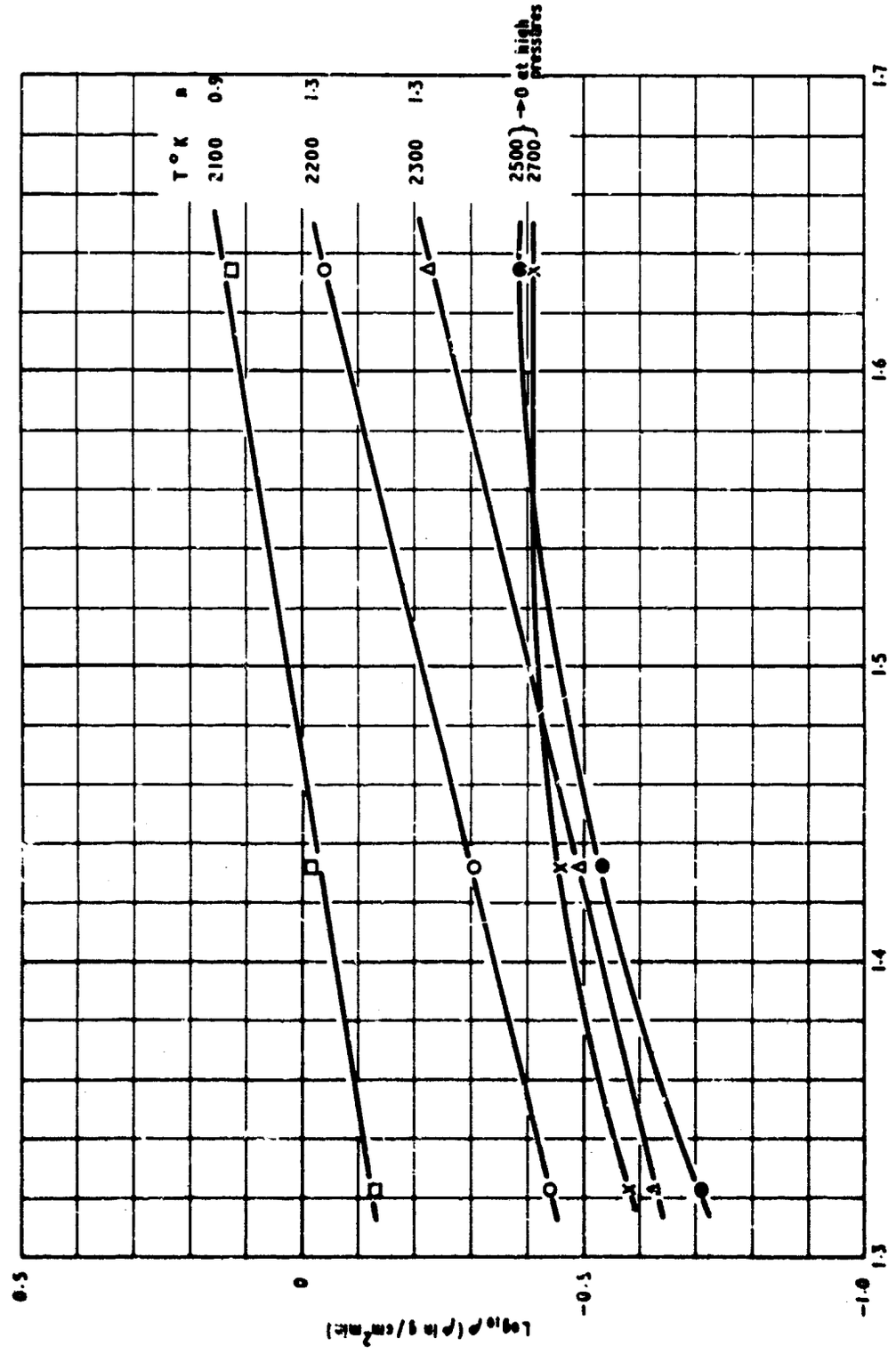

Fig. 16 Reaction order graphs for 5890 graphite in CO_2

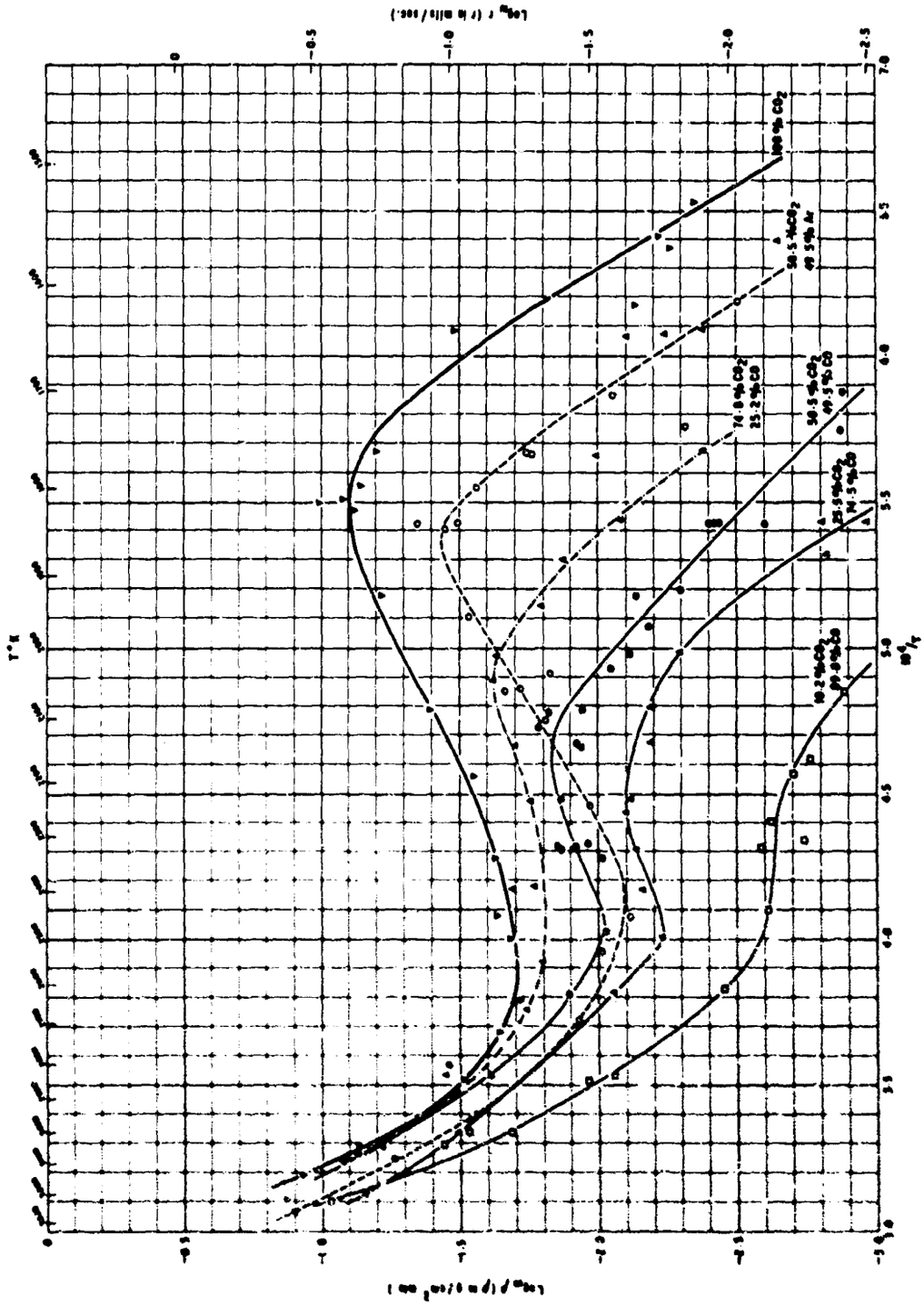

Fig. 17 Variation of specific reaction rate with surface temperature: pyrolytic graphite (edge surface) in CO_2/CO mixtures at 16 p.s.i. absolute pressure

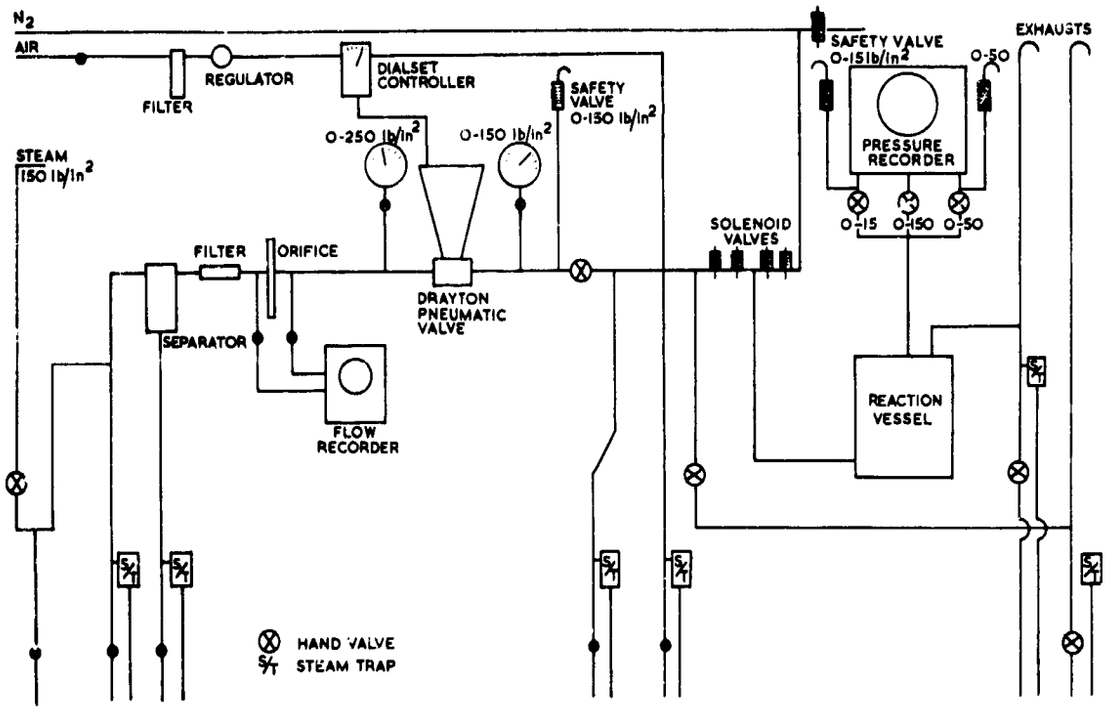

Fig. 18 Steam supply system

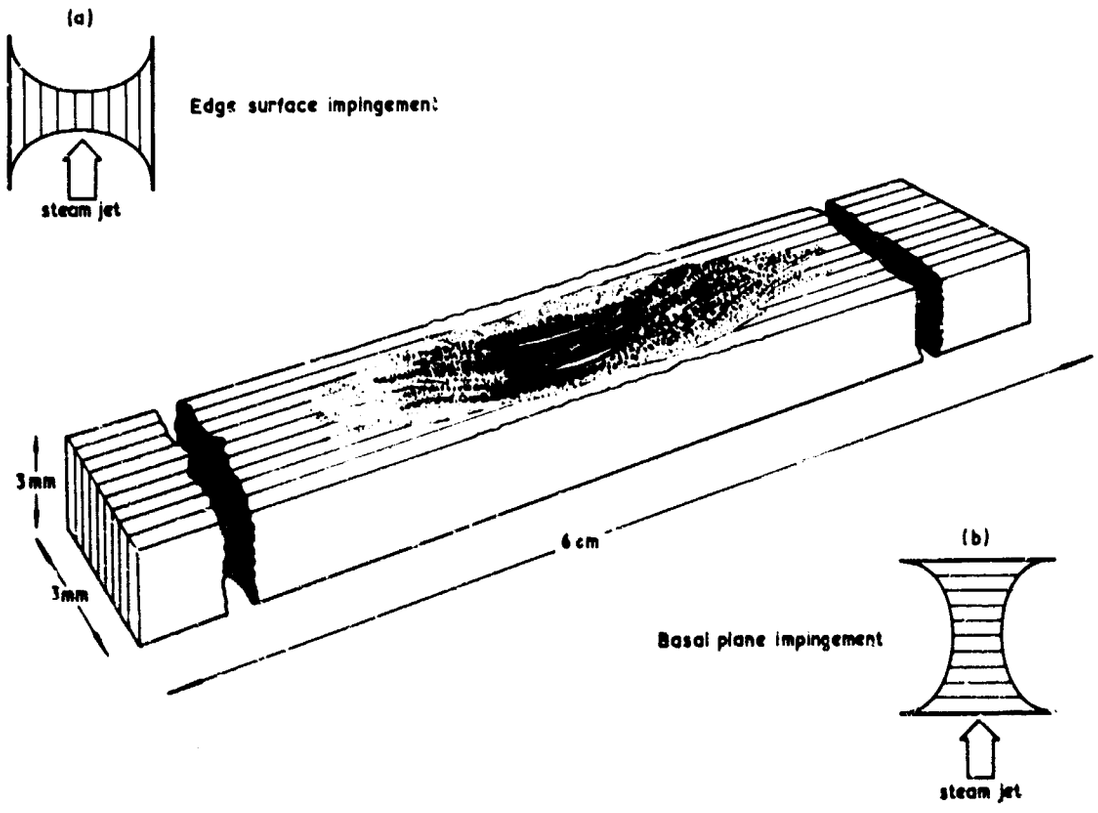

Fig. 19 Pyrolytic graphite rods after oxidation in steam at approx. 2000°K

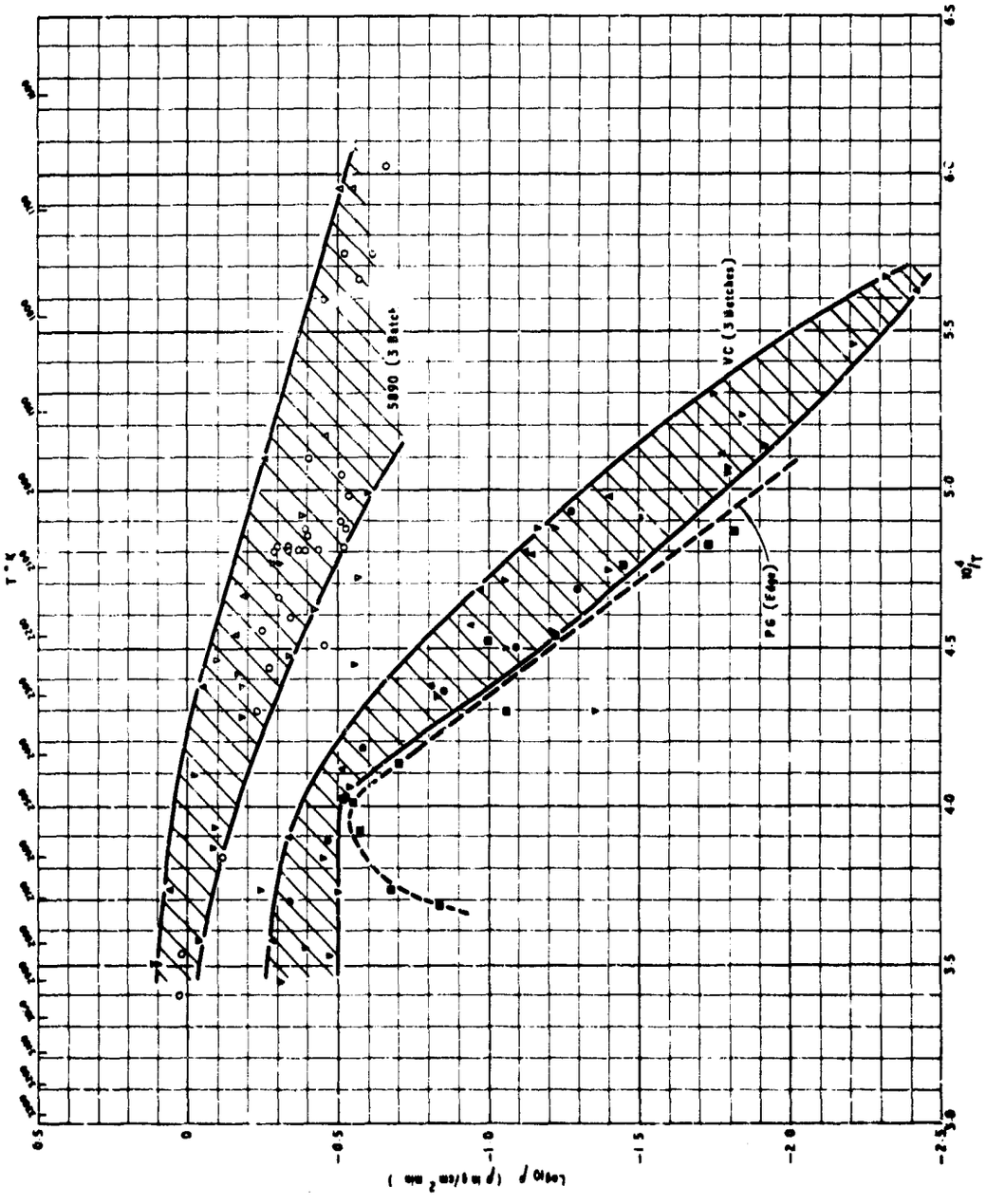

Fig.20 Variation of specific reaction rate with surface temperature for PG (edge), 5890 graphite and VC in steam at 19 p.s.i.a.

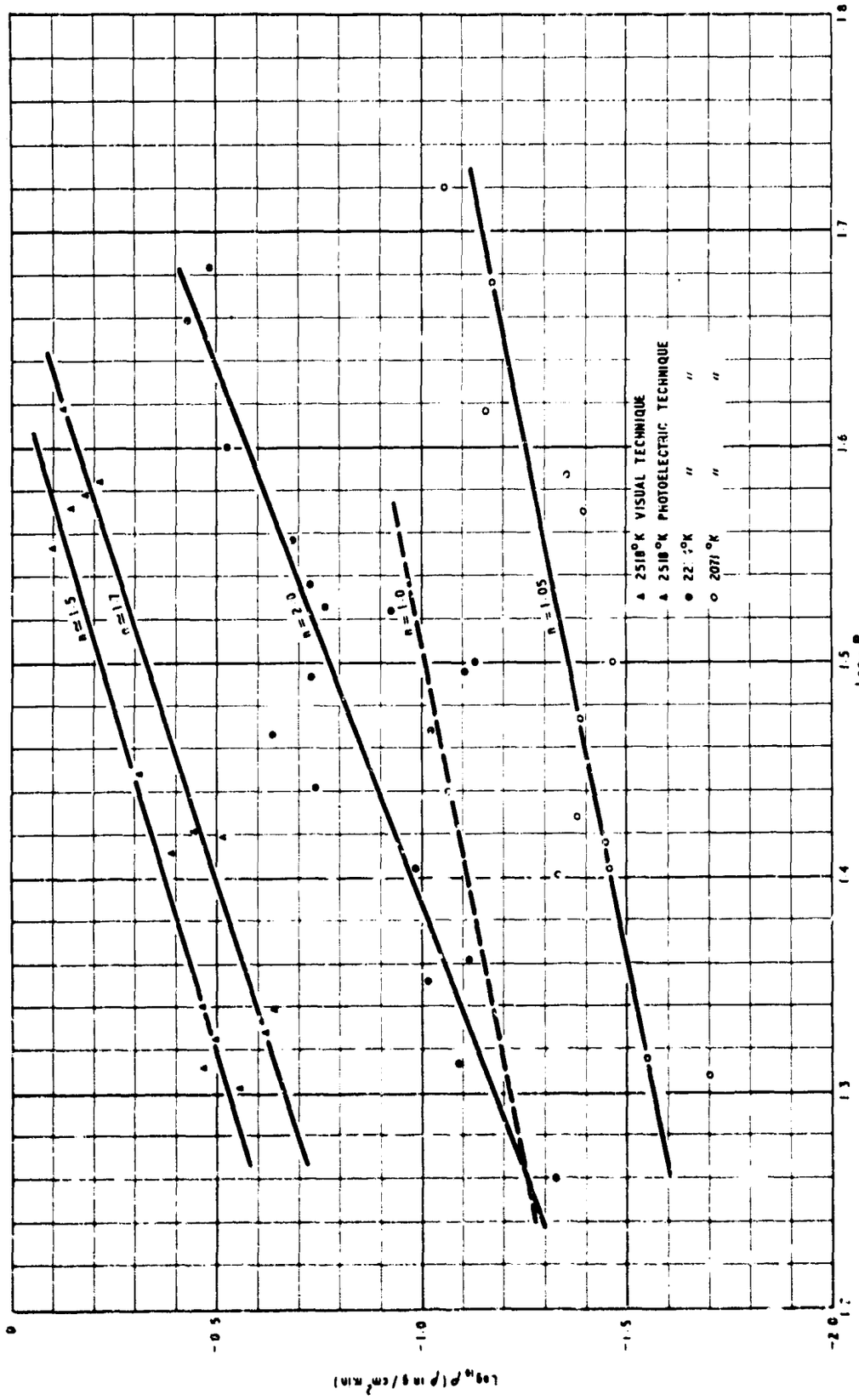

Fig. 21 Reaction order graph for PG (edge) in H_2O at 2071, 2234 and 2518°K

APPENDIX 1

EMISSIVITY CORRECTION TO TEMPERATURE MEASUREMENT ON REACTING SURFACE

In order to make a reasonably accurate assessment of the reflected component of the total emission from the target area, which is approximately half-way down the inside surface of the tubular specimen, it is necessary to integrate the contribution from all elements of a total solid angle of π, making due allowance for the variation of temperature with distance.

FIG. 22

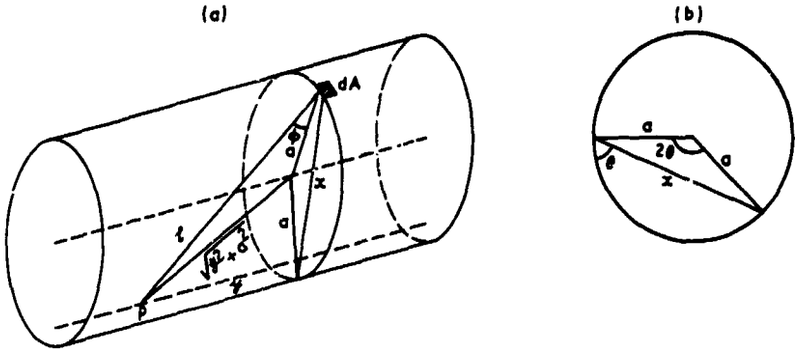

Consider an element of area dA situated a distance l from a point target P on the inside surface of a hollow cylinder (Fig. 22a). Let the displacement of dA from P along the length of the cylinder be y; let the angle between the lines l and y at the point P be θ and let the third side of the triangle so formed be x.

From Fig. 22b, $x^2 = 2a^2(1-\cos 2\theta) = 4a^2\sin^2\theta$ .....(1)

From Fig. 22a, $l^2 = y^2+x^2 = y^2+2a^2(1-\cos 2\theta) = y^2+4a^2\sin^2\theta$ .....(2)

Now $dA = x \cdot d\theta \cdot dy$ so the subtended area normal to the line and therefore 'seen' by P is $\frac{x \cdot d\theta \cdot dy \cos\phi}{\sin\theta}$.

The solid angle subtended by dA at P is therefore $\frac{x\cos\phi \cdot d\theta \cdot dy}{l^2\sin\theta}$

But $\cos\phi = \frac{l^2-y^2}{2al} = \frac{2a\sin^2\theta}{l}$ (from equation 2)

And $x = 2a\sin\theta$ (from equation 1)

Therefore solid angle subtended by dA at P $= \frac{4a^2\sin^2\theta \cdot d\theta \cdot dy}{(y^2+4a^2\sin^2\theta)^{3/2}}$

Now the total energy emitted from the area dA $= \epsilon\sigma T^4 dA$ where T = temperature of dA, σ = Stefan's constant.

∴ Total energy received per unit area at P from all elements dA (by direct emission only, i.e. neglecting energy reflected by dA)

$$= 4a^2\sigma \int_{-\infty}^{\infty}\int_{0}^{\pi} \frac{\epsilon T^4 \sin^2\theta \, d\theta \, dy}{(y^2+4a^2\sin^2\theta)^{3/2}}$$

∴ Reflected energy per unit area from P $= 4a^2\sigma(1-\epsilon_p)\int_{-\infty}^{\infty}\int_{0}^{\pi} \frac{\epsilon T^4 \sin^2\theta \cdot d\theta \cdot dy}{(y^2+4a^2\sin^2\theta)^{3/2}}$

where ϵ_p = emissivity at point P (= 0.8 for vitreous carbon).

Emitted energy per unit area from P $= \epsilon_p \sigma T_p^4$

$$\therefore T_{app}^4 = \epsilon_p T_p^4 + 4a^2(1-\epsilon_p)\int_{-\infty}^{\infty}\int_{0}^{\pi} \frac{\epsilon T^4 \sin^2\theta \cdot d\theta \cdot dy}{(y^2+4a^2\sin^2\theta)^{3/2}} \quad \text{.....(3)}$$

where T_{app} = apparent temperature at P $= \frac{\text{total energy per unit area}}{\text{Stefan's constant}}$

In order to solve equation 3 for T_p, the integral must be evaluated; this may be done numerically by a computer if T and ϵ are expressed as functions of y. From empirical observations, it appears reasonable to assume as a first approximation that the specimen and both guard rings are at

a uniform temperature T_p, that the surroundings (above and below the sheath) are at 293°K (effectively zero) and that the temperature of the graphite sheath varies linearly from T_p at the lower guard ring to 500°K at the lower end of the sheath. Calculations have shown that even if this temperature were in fact 1000°K the error in the corrected specimen temperature would be only 1°K. Emissivity values may be assumed to be 1.00 for the cold surroundings, 0.90 for vitreous carbon and 0.93 for graphite. The variations of T and ϵ with y are illustrated below (Fig. 23).

FIG. 23

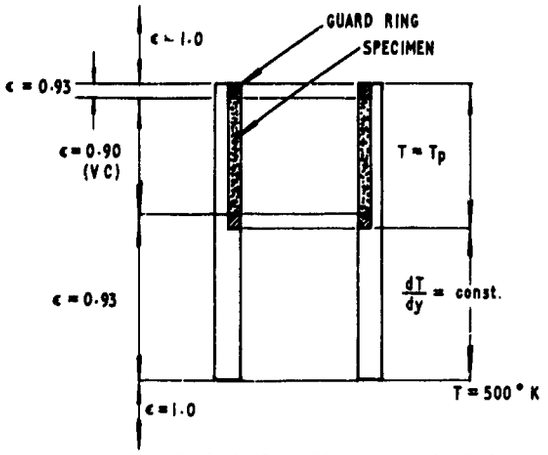

Results of the computation showed that the effective emissivity halfway down the specimen, ϵ' ($\epsilon T_{app}^4/T_p^4$) was only very slightly dependent on the temperature and length of the specimen, and that the difference between the effective emissivity and the actual emissivity ($\epsilon'-\epsilon$) was so small that second order and higher reflections could be neglected.

To allow for the reflection of energy by the quartz window, including multiple reflections, it may be shown that the values of ϵ' obtained by the above treatment must be multiplied by $\tau = \sqrt{\frac{1-\alpha^2}{1+\alpha^2}}$ where $\alpha = \frac{\mu-1}{\mu+1}$ (μ = refractive index). For quartz, $\mu = 1.54$ and so $\tau = 0.9135$.

The values taken for the actual emissivities of the four carbons studied were based on measurements made by Land Pyrometers Ltd. The method used (comparison of the energy reflected from the specimen in a black body furnace with the energy emitted from the furnace itself) neglects any variation of spectral emissivity with specimen temperatures; however, such variations are reported to be small and it was considered preferable to use this data, obtained by measurements on actual specimens oxidised at various temperatures within the range of interest, rather than rely on the scanty published data on the particular carbons being studied. (A recent review of the emissivities of carbons (41) leads to the conclusion that the most reliable data are likely to be obtained by the technique of Null and Lozier(42-3), but the apparatus used is somewhat complex and the work involved in making emissivity measurements by this method could not be incorporated into the kinetics programme).

Emissivity values used throughout this paper, for the correction of measured (apparent) temperatures to "true" surface temperatures, are listed below:

CARBON TYPE	FOR UNOXIDISED CARBON	FOR OXIDISED CARBON
VC	0.91	0.90
PG (edge)	0.94	0.945
PG (basal)	0.70	$0.64 + 4 \times 10^{-5} T_{app}$*
5890	0.93	0.93

*T_{app} = temperature (°K) of oxidation (in CO_2 at 16.0 p.s.i.a.).

IMPINGEMENT REACTOR

Emissivity and reflectivity corrections for this reactor were simpler than for the tubular reactor, the true temperature being given by

$$T^4 = \frac{T_{app}^4}{0.9135}$$

EXPLOSIVE ELECTRODE EROSION IN NANOSECOND HIGH DENSITY SPARKS

H. Fischer and K. Schönbach

Laboratory of Applied Physics, Technische Hochschule Darmstadt, Germany

SUMMARY

Tree shape optical phenomena erupting from the anode of high density nanosecond spark discharges were studied by means of time resolved photography and identified by spectroscopy as explosive erosion jets of electrode material. Observations with different electrode materials and alterations of current density and duration of current flow established conditions for the existence of the jets. Current densities larger 10^6 A/cm^2 were required.

The mechanism explaining this explosive anode erosion is derived from comparison of the different electrode materials. It is understood that the effect is produced by a thin-layer melting and evaporation of the spot area of the anode. Thus materials with a low melting point and low heat and electric conductivity favor the existence of directed erosion jets.

PROBLEM

Tree shape optical phenomena had been photographed arising from the copper anode of a high density 20-nanosecond spark and were identified tentitatively (1) being jets of the anode material as the result of a directed explosion.

Spectrally, however anode material could not be identified. It was assumed that the discharge was too shortlived in time in order to allow thermalisation and spectral excitation of the copper vapor. The tree shape structure appeared aprox 25 ns after the spark current had ceased. Noteworthy was that the "jets" were extraordinary stable and reproduceable as well in shape and location as also in the time of appearance.

Figure 1 shows the development of the spark channel and the appearance of the anode "jet" as a function of time in a 20-nanosecond spark of aprox 4000 A in 1 atm air, gap was 0,85 mm, breakdown voltage = 4,3 kV, capacity 3,6 nF, inductivity 1,5 nHy. Anode was copper (down), cathode tungsten (up). The current had its first maximum after 7 ns, went to zero after 11 ns, had an overswing of aprox 35 % and tapered off to zero after aprox 30 ns.

The tree shape "jet" grows from the bubble-like anode spot and appears after aprox 50 ns after current begin. The pictures were taken from successive shots and photographed thru a 6-nanosecond Kerrcell shutter. The timing was controlled by delay cables of various lengths. The discharge was triggered by pulse-charging with a time jitter substantially under 1 ns.

Since this first publication Schönbach at the Laboratory of Applied Physics in Darmstadt, Germany has studied the phenomenon in detail. He observed a number of relationships which I want to discuss in the following.

Most important results are the spectral identification in lead and aluminum proving the tree shape structure consisting of the anode material. Tilting the electrode surface confirmed the assumption of a directed jet perpendicular to the anode surface. A weak jet appearing at the cathode in figure 1 is the result of current reversal which temporary turns the cathode into an anode. Most of all the existence and appearances of the jet phenomenon strongly depend upon the metallic properties of the anode material. Jets were observed with current densities exceeding 10^6 A/cm^2.

EROSION JETS

Figure 2 shows the time resolved spectrum of the spark discharge in air as seen thru the Kerrcell shutter. Anode is lead. CdHg-comparison spectra are first and last. The spectrometer slit is paralell to the gap axis, anode is up.

We see that the spark spectrum is purely continuous during current flow. Widened ionised N^+ lines grow out of the fading continuum after the current has ceased after aprox 30 ns. The Pb^+ lines appear at the location of the anode jet after aprox 50 ns, i.e. shortly after appearance of the tree shape structure.

Figure 3 shows that the tree structure stays perpendicular to the anode surface, when the surface of the anode is tilted in relation to the spark channel axis. This proves that this phenomenon is tied to the anode surface, confirming the assumption of a jet erupting from the anode.

After having established the existence of the erosion jet, I should like to discuss its relation upon the discharge parameters and anode materials. We compare jets with tungsten-, copper-, lead- and aluminum anodes and change the current density and time integrated current flow by altering the capacity of the spark circuit. Secondary differences in the inductivity are being considered in the current calculation.

First we regard the photography of an erosion jet with aluminum anode. The discharge parameters in figure 4 are slightly different (L = 2,3 nHy) from those in figure 1.

Figure 4 shows the time development of the erosion jet with an aluminum anode. We observe that the jet grows uniformly from the bubble of the anode spot; time of appearance is also aprox 50 ns after current begin, i.e. aprox 20 ns after current cutoff. The jet remains very uniform, looks like a fountain with its outer rim curling backwards towards the anode. This effect is probably caused by a counterstream of gas ions released from the cathode sheet after current cutoff (2). The stem of the anode spot is wider as in copper (see figure 1). These differences of the aluminum jet in comparison to copper may be understood from the lower molecular weight, lower melting point and smaller heat conductivity of aluminum.

The lead-jet has spikes yet not quite as sharp as in copper (figure 1). The jet

appears turbulent. The stem is even wider than that of aluminum, appearantly due to the lower melting point. Also the heat conductivity is low in comparison. The jet is shorter in length than that in aluminum, probably because of the larger molecular weight of lead.

AREAS OF EXISTENCE

Figure 6 demonstrates the conditions under which jets have been observed when the current density and time of current flow has been changed. Jets in this particular case were observed with current densities exceeding 10^6 A/cm^2 between times of current maximum of aprox 3 ns to 90 ns. All discharges had a high rate of current rise which is determined by the factor $di/dt \sim$ breakdown voltage/inductivity.

It is apparent that the jet develops in lead with the smallest current density and shortest current flow. Lead has the lowest melting point and a relatively low heat and electric conductivity. Aluminum, copper and tungsten follow in the sequence of their melting points.

With increasing time duration of the current flow the jet disappears first with aluminum, which has a low melting point however high heat and electric conductivity. Tungsten in comparison has a high melting point and lower heat and electric conductivity. Thus an important factor appears the quantity - thermal conductivity divided by density times specific heat.

MECHANISM

Preceding experimental observations suggest a mechanism in which the evaporation jets are produced by a strong local heating, melting and evaporation of the anode surface by electrons entering thru the anode spot. Jet condition will be favored by a low melting point of the anode and a relatively low heat conductivity which increases the surface temperature by reducing the heatflow into the deeper regions of the anode material. The temperature gradient between surface and interior will increase with decreasing heat conductivity. Reduced electric conductivity on the other hand increases the surface temperature by Joule heating. Thus we may expect a thin melted surface layer under jet conditions with a large heat gradient to the interior.

With a long time current flow (current maximum after 90 ns) the stem of the jet in general is wider as in the short time discharge (current maximum after 3,5 ns), obviously due to an expansion of the melted area. Jets with long current flow appear more uniform, i.e. thermalised. The effect of directed explosion shows up with lower current density in case of longer current flow, however tends to disappear or thermalise as should be expected.

It appears to me that I have read similar thaughts in some Russian articles which I cannot locate at the moment. The experiments in this paper on the other hand for the first time appear to prove such mechanism.

FUTURE STUDIES

We presently are trying to understand quantitatively the mechanism of jet-erosion by calculating existence, diameter and expansion velocity of the jets from material constants. We shall study the influence of gas environment and shall try to understand the basic differences in anode and cathode erosion. At the present we have no feeling whatsoever wy the copper jet persistently shows 5 spikes - always at the same location.

Finally we should like to be able to extend our understanding into the longer duration electrical discharges, possibly with lower current densities, where thermalisation will take over the directed explosion.

REFERENCES

(1) H. Fischer and [illegible]agher, Appl. Opt. 6, 2176 (1967)

(2) R.S. Sigmond, Proc. Phys. Soc. 85, 1269 (1965)

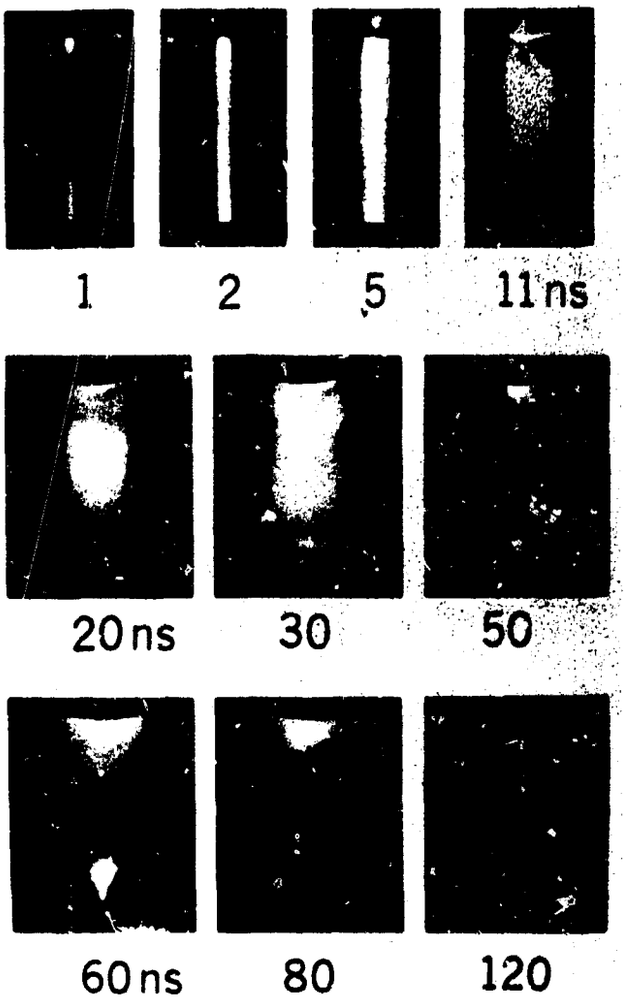

Fig. 1 Time development of spark channel and anode "jet"; anode copper (down)

Fig. 3 Anode jet with anode tilted towards spark axis; aluminum electrodes (anode down)

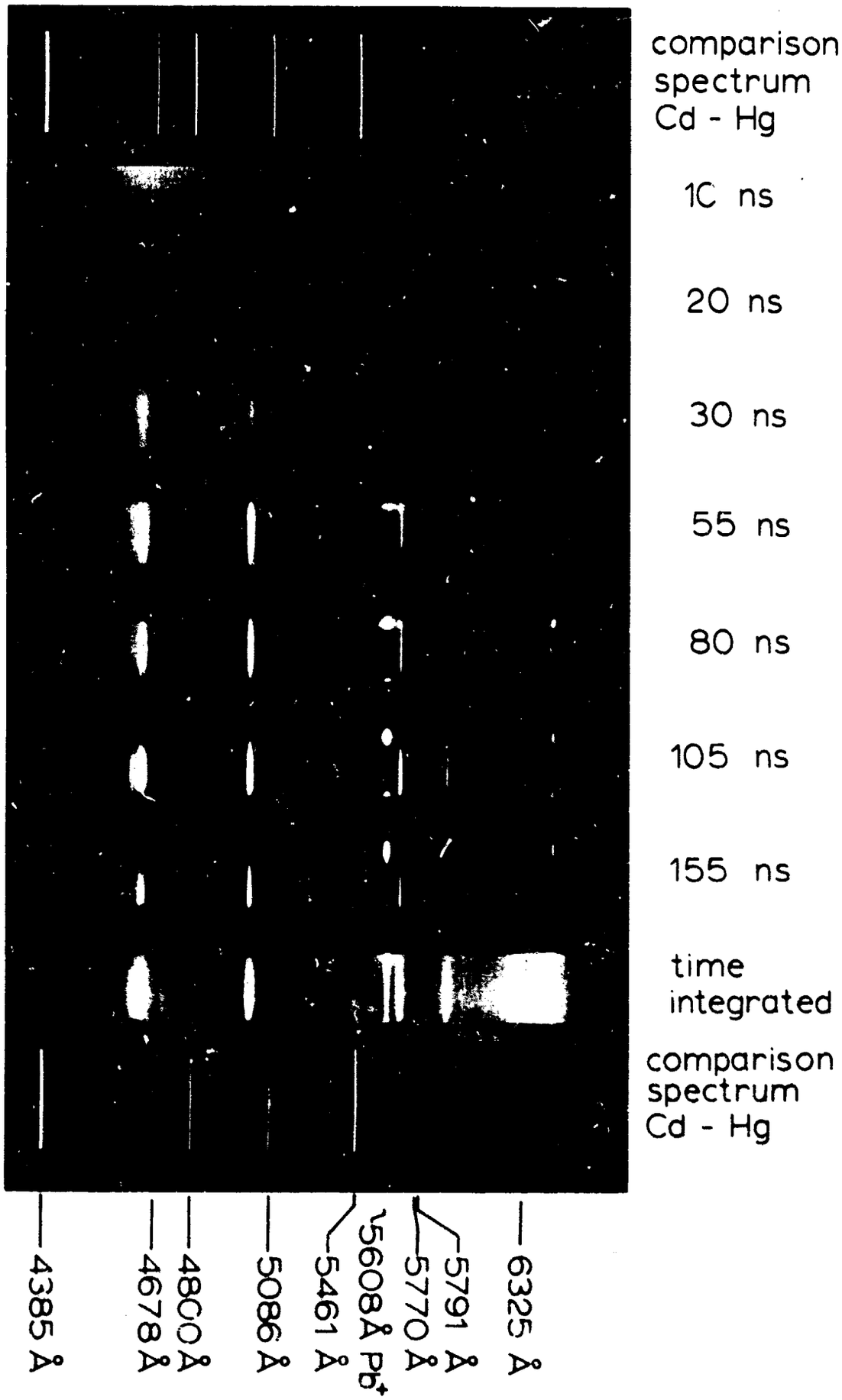

Fig. 8 Time resolved spectrum of the spark channel in 1 atm air; anode lead (up)

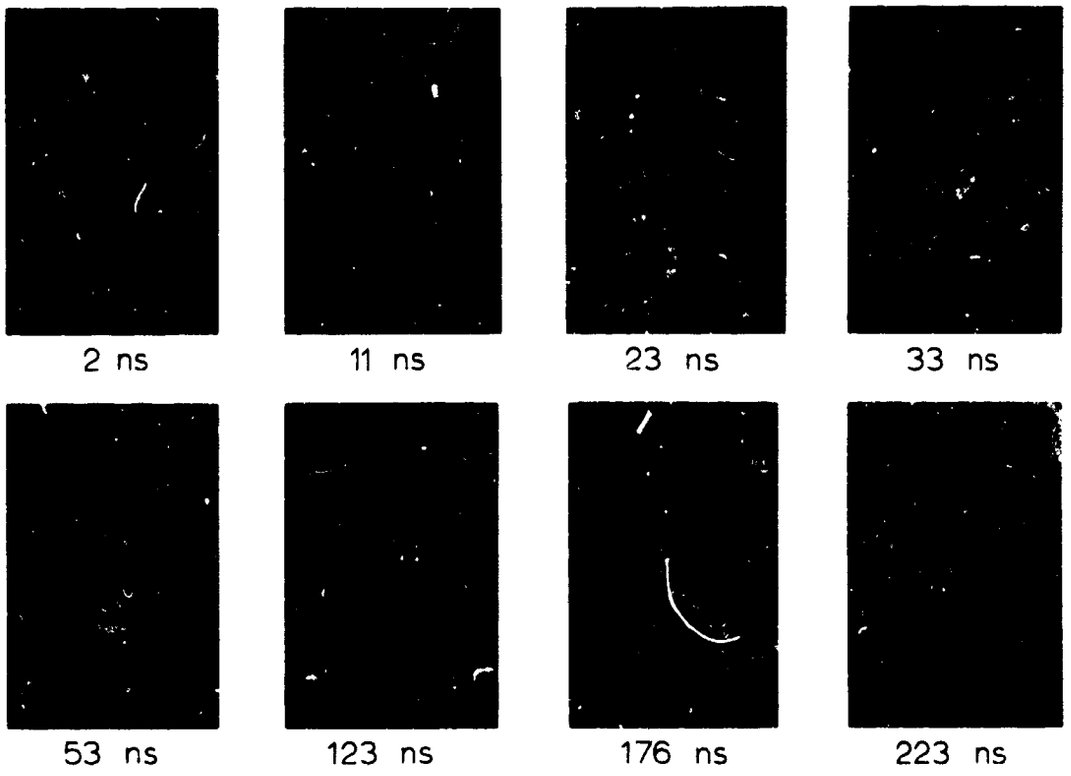

Fig.4 Time development of spark channel and erosion jet with aluminum electrodes (anode down)

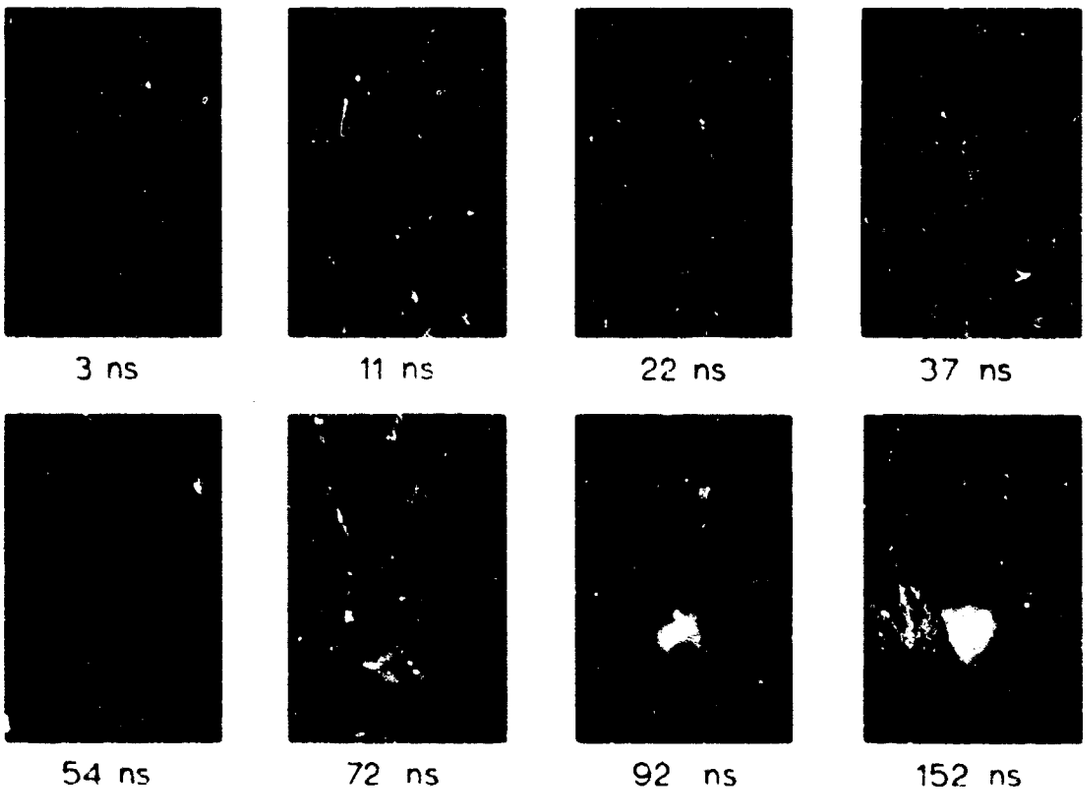

Fig.5 Time development of spark channel and erosion jet with lead anode (down)

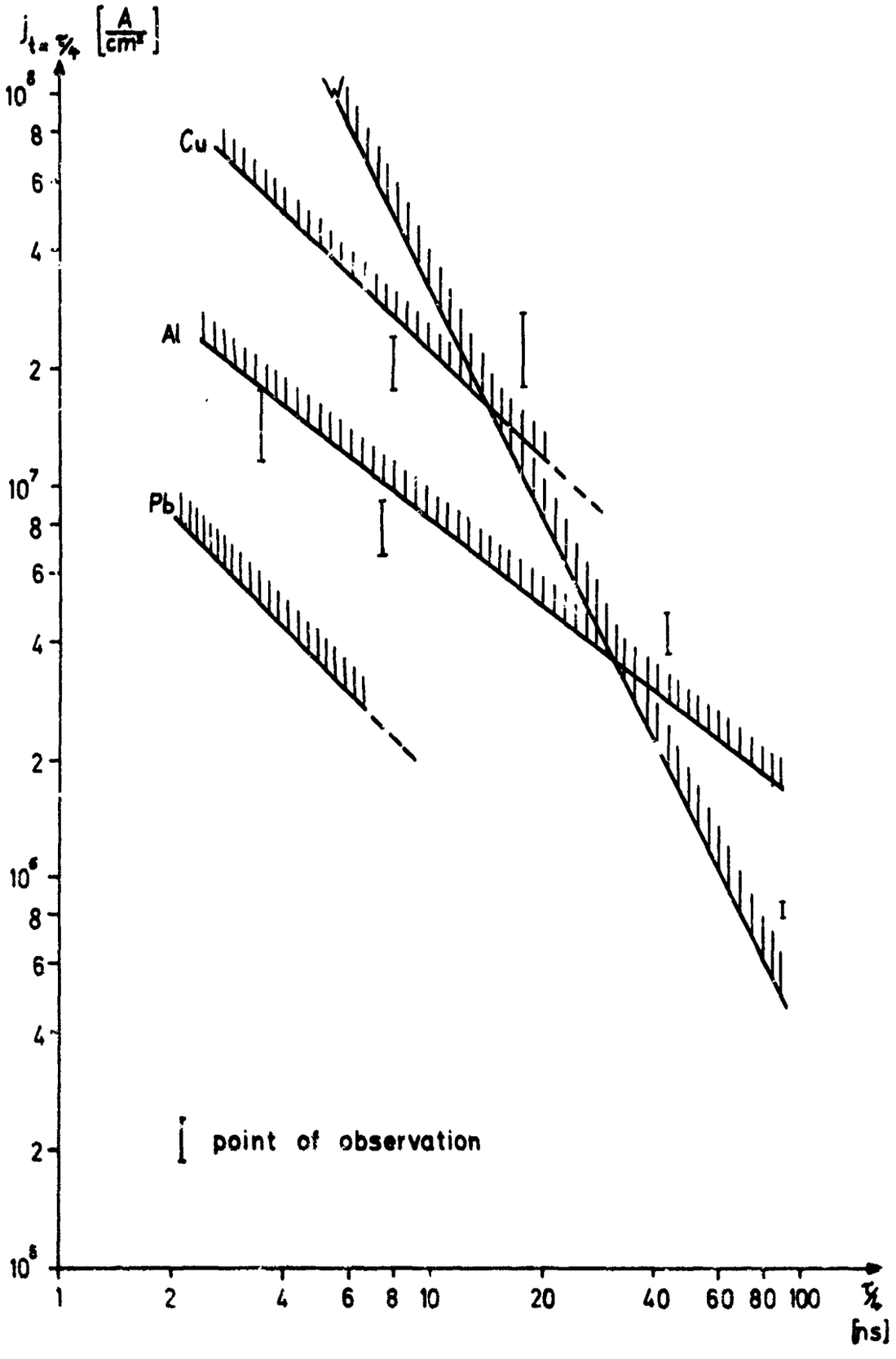

Fig. 6 Approximate areas of existence of the erosion jet (above curves)

REPRESENTATION SCHEMATIQUE DES PROCESSUS D'ABLATION

A SCHEMATIC REPRESENTATION OF ABLATION PROCESSES

par Jacques Jules NICOLAS, Samuel KOHN et Georges TAGUET

Office National d'Etudes et de Recherches Aérospatiales (ONERA)

92 - Châtillon (France)

RESUME :

L'introduction de mécanismes chimiques simples permet d'expliquer quelques exemples caractéristiques d'intérêt pratique de l'ablation des parois. En absence d'érosion mécanique on peut appliquer sous une forme simplifiée les lois de la cinétique chimique et des transferts à travers la couche limite.

Les résultats expérimentaux obtenus dans des conditions bien définies sont en bon accord avec ceux calculés selon les méthodes proposées dans le cas des matériaux suivants : résine phénolique pure, résine phénolique renforcée par des fibres de graphite, résine phénolique renforcée par des fibres de silice.

SUMMARY :

With the introduction of simple chemical mechanisms it is possible to explain some characteristic examples of practical interest of parietal ablation. In the absence of mechanical erosion we can apply under a simplified form the laws of chemical kinetics and the laws of transfer through the boundary-layer.

The experimental results obtained in well specified conditions are in good agreement with those given by the proposed methods in the case of the following materials : pure phenolic resin, phenolic resin reinforced with graphite fibers, phenolic resin reinforced with silica fibers.

NOTATIONS

ρ masse volumique g/cm^3

u vitesse m/s

p pression (bars)

R constante de gaz pour l'unité de masse

$\mathcal{R}$ constante universelle de gaz

T température °K

T_p température de paroi

H_g enthalpie d'échauffement de l'écoulement (composition d'équilibre à T_p) cal/g

H_p enthalpie de l'écoulement ramené à la température T_p cal/g

St nombre de Stanton pour la paroi en cours d'ablation

St^* nombre de Stanton pour une paroi nonablative

ϕ_p flux de convection reçu par la paroi en cours d'ablation cal/cm^2 s

ϕ_p^* flux de convection reçu par la paroi non-ablative cal/cm^2 s

$\dot{m}_p$ débit massique gazeux émis par la paroi en cours d'ablation g/cm^2 s

$\dot{m}_g^{(o)}$ débit transféré à la paroi du corps simple O à travers la couche limite g/cm^2 s

$\delta_g^{(o)}$ fraction massique du corps simple O contenu dans l'écoulement

δ_p^o fraction massique du corps simple O à la paroi

Γ_g^o, Γ_p^o respectivement fractions disponibles du corps simple O dans l'écoulement et à la paroi

$\mathcal{M}^o$ masse atomique du corps simple O

φ richesse de l'écoulement

ΔH_M^p variation d'enthalpie subie par le matériau consommé cal/g

Q chaleur liée à une transformation subie par le matériau

$Q_{efficace}$ chaleur efficace d'ablation.

1 - INTRODUCTION

La nécessité d'assurer les protections anti-thermiques des engins modernes a conduit à expérimenter de nombreux matériaux dans des conditions aussi voisines que possible de celles rencontrées dans les applications en vue.

Mais il est difficile de simuler correctement dans les essais de laboratoire à la fois toutes les conditions aérodynamiques, thermiques et chimiques et suivant les techniques utilisées on aboutit à des classements de matériaux de protection différents, ce qui rend d'ailleurs malaisé l'interprétation des essais effectués.

Le but principal de ce travail n'est pas de proposer une méthode d'essai nouvelle ou un classement supplémentaire de matériaux de protection, mais d'essayer d'introduire des mécanismes chimiques pour expliquer quelques exemples caractéristiques et d'intérêt pratique de l'ablation des parois.

Les exemples se classent en deux catégories, suivant que la régression de la paroi est due à des réactions chimiques qui s'accomplissaient principalement entre les gaz de l'écoulement et le matériau, ou bien résulte de transformations qui s'effectuent au sein même du matériau et sont entretenues par le flux thermique de convection.

Ils ont été étudiés dans des conditions reproductibles où l'érosion mécanique est négligeable et qui autorisent sous une forme très simplifiée l'application des lois de la cinétique chimique et des transferts à travers les couches limites.

Les schémas d'ablation auxquels on est conduit, peuvent éventuellement faciliter l'interprétation de la masse des résultats expérimentaux disponibles et leur conférer un aspect plus fondamental que ne le permettent en général les seules considérations physico-thermiques.

2 - ETUDE EXPERIMENTALE DE L'ABLATION PAR LA TECHNIQUE DES BRULEURS

2.1 - Matériaux expérimentés

Les matériaux expérimentés dont l'ablation est gouvernée par les réactions entre gaz de l'écoulement et paroi sont :

- la résine phénolique pure, et le composite phénolique fibres de graphite;
- le troisième matériau étudié est un stratifié à plis perpendiculaires à l'écoulement, résine phénolique tissu de verre lavé. Il se distingue des précédents par la formation d'un film de silice fondue qui protège sa surface des actions chimiques de l'écoulement et son ablation s'explique par des transformations qui prennent place dans les couches sous-jacentes.

Les maquettes d'essai qui ont été réalisées dans ces matériaux ont la forme d'un convergent suivi d'une partie cylindrique de l'ordre d'un diamètre. Elles sont montées à l'arrière d'un générateur de gaz chauds dont elles constituent la tuyère d'éjection, la partie cylindrique formant col sonique (ϕ = 20 mm) (fig. 1).

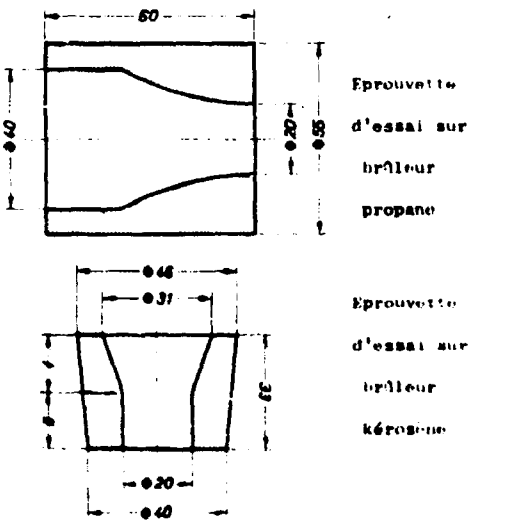

FIG. 1

2.2 - Générateur de gaz chauds

Les générateurs de gaz chauds sont des brûleurs dont le comburant est l'oxygène. Suivant le cas, on utilise un brûleur oxygène propane ou un brûleur oxygène kérosène. Le premier, de par sa conception même fournit des écoulements de gaz brûlés de composition très homogène et convient dans les cas où des flux thermiques modérés sont suffisants. Lorsque des flux thermiques assez élevés ont été nécessaires le brûleur oxygène kérosène a été employé.

Les caractéristiques moyennes des conditions réalisées avec ces moyens d'essais sont présentées dans les figures 2 et 3.

2.3 - Mesures

Les mesures principales effectuées au cours des essais sont la pression de chambre du générateur dont la variation est fonction de l'ablation des maquettes et la température de paroi par pyromètre I.R.

Les maquettes sont pesées et mesurées avant et après essai. Des examens physico-chimiques des diverses couches du matériau sont effectués et complétés par des pyrolyses d'échantillons dans des fours de laboratoires avec analyse des produits dégagés.

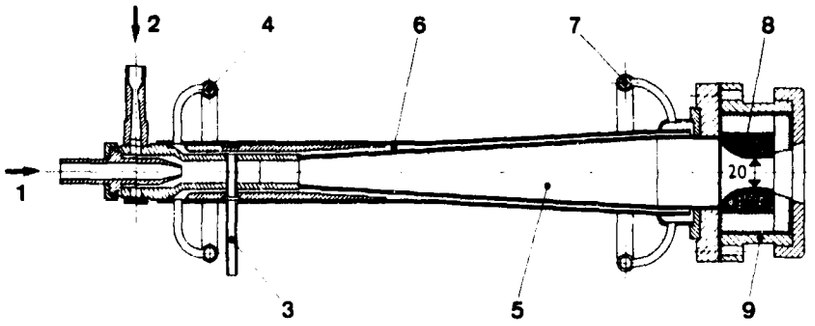

FIG. 2 - BRULEUR OXYGENE-PROPANE.

1. Arrivée d'oxygène.
2. Arrivée de propane.
3. Stabilisateur.
4. Sortie d'eau.
5. Chambre de combustion.
6. Chemise d'eau.
7. Entrée d'eau.
8. Matériau expérimenté.
9. Tuyère.

Caractéristiques de fonctionnement.

Débit g/s	Richesse φ	P_{ch} bars	V* m/s	Enthalpie (Hg-Hp) (T_p = 2100°K)	Flux thermique ϕ_c^* T_p = 2100°K	Composition des gaz T_p = 2100°K moles/kg					
						H_2	H_2O	CO	OH	CO_2	O,H
56,5	1,3	2,65	1650	1120 cal/g	38 cal/cm²s	4,4	19,5	9,7	0,015	8,6	traces

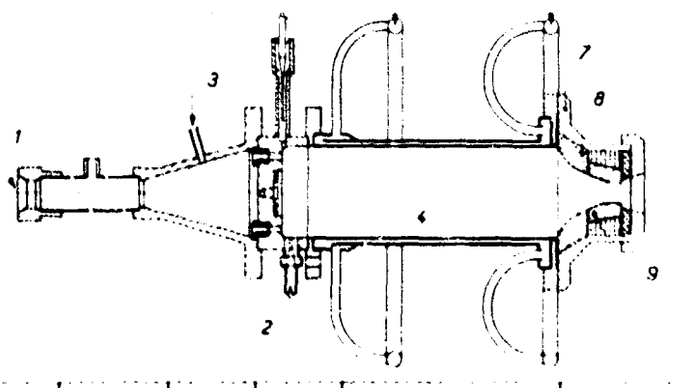

FIG. 3 - BRULEUR OXYGENE-KEROSENE.

1. Arrivée d'oxygène.
2. Arrivée du kérosène.
3. Allumage.
4. Chambre de combustion.
5. Sortie d'eau.
6. Entrée d'eau.
7. Tuyère.
8. Graphite.
9. Matériau expérimenté.

Caractéristiques de fonctionnement.

Débit g/s	Richesse φ	P_{ch} bars	V* m/s	Enthalpie (Hg-Hp) (T_p = 2250°K)	Flux thermique ϕ_c^* T_p 2250°K	Composition des gaz moles/kg					
						H_2	H_2O	CO	OH	CO_2	O,H
151	1,4	7,8	1640	985 cal/g	90 cal cm²s	4,7	15,3	13	0,1	8,8	traces

2.4 - Résultats expérimentaux

Les courbes de pression de chambre et de température de surface sont présentées dans les figures 4, 5 et 6.

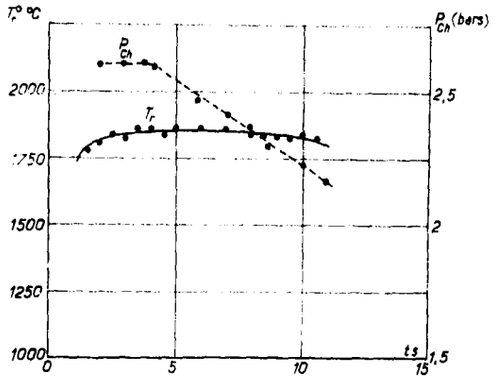

FIG. 4 - TUYERE EN RESINE PHENOLIQUE PURE (NON RENFORCEE)

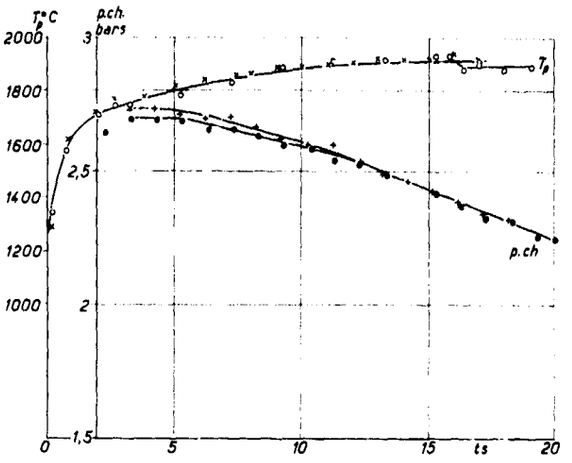

FIG. 5 - TUYERES EN RESINE PHENOLIQUE RENFORCEE DE FIBRES DE GRAPHITE
o• T. 652
+x T. 653

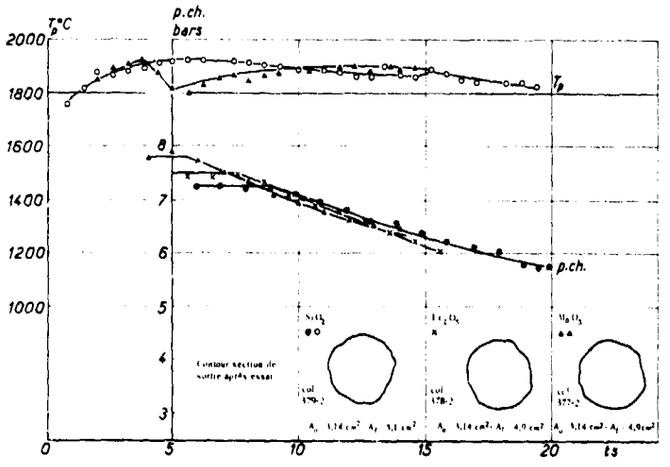

FIG. 6 - TUYERES EN RESINE PHENOLIQUE RENFORCEE DE FIBRES DE SILICE

Dans les tableaux 1 et 2 sont inscrits les principaux résultats qui seront utilisés comme base de comparaison avec les calculs qui suivent. Les résultats ont été obtenus après de nombreux tatonnements qui ont permis de réaliser une résine phénolique résistant bien au choc thermique et donnant un coke peu friable d'une part, et d'autre part de faire un choix parmi les qualités des fibres de graphite et les techniques de moulage, le critère étant l'obtention après essai d'états de surface satisfaisants.

Egalement les conditions expérimentales dans les essais des maquettes en composite phénolique silice ont été choisies de manière à ce que les quantités de silice fondues entraînées par l'écoulement soient pratiquement négligeables afin de réaliser une ablation non-perturbée par une érosion mécanique.

TABLEAU 1 - ESSAIS DU BRULEUR OXYGENE-PROPANE

MATERIAU	VALEURS EXPERIMENTALES			COMPARAISON DES RESULTATS EXPERIMENTAUX ET THEORIQUES					
	masse volumique g/cm³	vitesse d'ablation mm/s	épaisseur de coke mm	$\dot{m}_p$ exp. g/cm²s	$\dot{m}_p$ th. g/cm²s	ϕ^*_p exp. cal/cm²s	ϕ^*_p th. cal/cm²s	$Q_{eff.}$ exp. cal/g	$Q_{eff.}$ th. cal/g
résine pure F/P 2,5	1,19	0,1175	1,5	0,014	0,0142	38,5	40,5	2600	2750
	1,22	0,1175	1,5	0,0143	0,0142	38,5	40,5	2550	2750
graphite phénolique F/P 2,5	1,30	0,076	2,5 à 3	0,010	0,011	37	36	3600	3250
	1,26	0,076	2,5 à 3	0,095	0,011	38	36	3700	3250

TABLEAU 2 - ESSAIS DU BRULEUR OXYGENE-KEROSENE

MATERIAU réfrasil CRFH résine F/P 2,5	VALEURS EXPERIMENTALES			COMPARAISON DES RESULTATS EXPERIMENTAUX ET THEORIQUES					
	masse volumique g/cm³	vitesse d'ablation mm/s	épaisseur cokefiée mm	$\dot{m}_p$ exp. g/cm²s	$\dot{m}_p$ th. g/cm²s	ϕ_p^* exp. cal/cm²s	ϕ_p^* th. cal/cm²s	$Q_{eff.}$ exp. cal/g	$Q_{eff.}$ th. cal/g
maquettes non traitées	1,36 à 1,41	0,200 à 0,242	5 à 6	0,0272 à 0,0329	0,028	92,5 à 77	90	3400 à 2750	3150
maquettes ayant subi des traitements divers	1,52 à 1,55	0,160 à 0,177	5	0,0248 à 0,0273	0,028	102 à 92	90	3600 à 3300	3150

3 - BASES DE LA REPRESENTATION DES PROCESSUS D'ABLATION

L'interprétation des phénomènes d'ablation qui ont été observés, s'appuie :

a) d'une part sur un choix des mécanismes chimiques probables fondés sur des réactions connues entre les divers réactifs en présence, dans les conditions de température et de pression établies au cours des essais;

b) d'autre part sur l'établissement en régime stationnaire des bilans thermiques et massiques entre les transformations subies par le matériau et les transferts par diffusion turbulente à travers la couche limite.

Avant d'aborder l'étude des mécanismes chimiques qui dépendent du cas considéré, il convient de rappeler les règles qui gouvernent les transferts à travers les couches limites turbulentes.

3.1 - Flux thermique à la paroi

On sait que l'expression du flux thermique de convection reçu par une paroi est :

$$(1) \qquad \phi_p = \rho u \, \delta t \, (H_g - H_p)$$

ρ masse volumique
u vitesse de l'écoulement
St nombre de Stanton
H_g enthalpie d'échauffement
H_p enthalpie à la paroi.

Les hautes températures engendrées par la combustion d'un hydrocarbure dans l'oxygène font que les écoulements réalisés sont en partie dissociés.

Cependant les mesures de flux thermique et le calcul du nombre de Stanton montrent que la valeur de l'enthalpie H_g est équivalente à l'enthalpie d'échauffement pour la composition chimique d'équilibre déterminée par la température T_p de la paroi.

Il suffit d'ailleurs d'un taux de recombinaison élevé pour avoir des conditions énergétiques voisines de celles de composition d'équilibre, taux qui, compte tenu des temps de séjour dans la couche limite, a toutes chances de se réaliser.

La valeur H_p se déduit de H_g par la quantité de chaleur qu'il faut extraire pour amener sans réaction chimique la composition d'équilibre d'enthalpie H_g à la température T_p de la paroi.

Par définition même des régimes stationnaires considérés, le flux ϕ_p reçu est totalement absorbé dans les diverses transformations qui conduisent à l'ablation d'une quantité $\dot{m}_p$ de matériau par seconde et par cm² d'où :

$$(2) \qquad \phi_p = m_p \, \Delta H_m^p$$

ΔH_m^p étant la variation d'enthalpie qui accompagne l'ensemble de ces transformations depuis l'état initial du matériau. On en déduit :

$$(3) \qquad \dot{m}_p = \rho u \, St \, \frac{H_g - H_p}{\Delta H_m^p}$$

Dans les cas étudiés, le débit $\dot{m}_p$ est constitué de gaz émis par la paroi et ce débit engendre un flux de convection qui se superpose au flux habituel de diffusion turbulente dans la couche limite. Cependant $\dot{m}_p$ représente ici une fraction assez petite du flux de diffusion caractérisé par le produit $\rho u \, St^*$ et il suffit, pour tenir compte des effets de l'émission pariétale de corriger le nombre de Stanton St^* de la paroi non-émissive. Diverses corrections ont été proposées elles conduisent dans les conditions présentes pratiquement au même résultat [1] , [2] , [3] . On a choisi pour des raisons de forme et de commodité l'approximation de Spalding [4] qui est

$$(4) \qquad \frac{St}{St^*} = \frac{Ln\left(1 + \frac{H_g - H_p}{\Delta H_m^p}\right)}{\frac{H_g - H_p}{\Delta H_m^p}}$$

3.2 - Transferts de masse à la paroi

Les couches limites étant turbulentes, il est permis de supposer un nombre de transport de masse communs à toutes les espèces chimiques et égal au nombre de Stanton. Comme conséquence du principe de la conservation de la masse le débit transféré $\dot{m}_g^\circ$ d'un corps simple O contenu dans l'écoulement s'exprime par la relation :

$$(5) \qquad [\dot{m}_g^\circ] = \rho u \, St \, [\delta_g^\circ - \delta_p^\circ]$$

δ_g° et δ_p° étant respectivement les fractions massiques de O dans l'écoulement et à la paroi. Les corps simples sont en général combinés entre eux et certaines liaisons chimiques particulièrement stables font que seulement une fraction Γ dite fraction disponible peut réagir avec le matériau.

Dans le cas particulier où cette fraction disponible du corps O s'unit avec la fraction Γ^c du matériau de la paroi pour former un produit gazeux défini, il y a un rapport simple entre les masses ablatées et les masses transférées.

En effet le débit masse $\dot{m}_p$ fourni par l'ablation contient

$$\dot{m}_p \Gamma^c \frac{1}{[\mathcal{M}_c]} \text{ atomes grammes de } C$$

et le débit masse transféré apporte

$$\rho u St [\Gamma_g^\circ - \Gamma_p^\circ] \frac{1}{[\mathcal{M}_o]} \text{ atomes grammes de } O$$

$\mathcal{M}_c$ et $\mathcal{M}_o$ étant les masses atomiques.

Si les corps O et C se combinent suivant la réaction

$$x C + y O \rightarrow C_x O_y$$

il y a évidemment la relation

$$\dot{m}_p \Gamma^c \frac{1}{[\mathcal{M}_c]} \cdot \frac{1}{x} = \rho u St (\Gamma_g^\circ - \Gamma_p^\circ) \frac{1}{[\mathcal{M}_o]} \times \frac{1}{y}$$

ou

$$(6) \quad \dot{m}_p = \rho u St \frac{\Gamma_g^\circ - \Gamma_p^\circ}{\Gamma^c} \frac{[\mathcal{M}_c]}{[\mathcal{M}_o]} \frac{x}{y}$$

Comme dans le cas des transferts d'énergie, on doit tenir compte de l'émission gazeuse pariétale mais l'approximation de Spalding s'étend à toute propriété conservative

$$(7) \quad \frac{St}{St^*} = \frac{Ln\left[1 + \frac{\Gamma_g^\circ - \Gamma_p^\circ}{\Gamma_e} \cdot \frac{[\mathcal{M}_c]}{[\mathcal{M}_o]} \frac{x}{y}\right]}{\frac{\Gamma_g^\circ - \Gamma_p^\circ}{\Gamma^c} \frac{[\mathcal{M}_c]}{[\mathcal{M}_o]} \frac{x}{y}}$$

Dans les cas étudiés, les réactions à la paroi qui gouvernent l'ablation sont globalement équivalentes à une réaction unique de ce type.

4 - ABLATION REGIE PAR LES REACTIONS CHIMIQUES ENTRE GAZ DE L'ECOULEMENT ET LE MATERIAU

4.1 - Schéma chimique de l'ablation

En ce qui concerne les maquettes en résine phénolique et en composite phénolique graphite la couche solide en contact avec l'écoulement devient rapidement une couche essentiellement constituée de carbone et la régression de la paroi est le résultat d'une gazéification de ce carbone. Bien qu'on connaisse assez mal les mécanismes de cette gazéification [5], il apparaît comme certain que l'action d'un gaz comburant sur les carbones, conduit à la formation d'oxyde de carbone et dans les essais effectués l'oxydation du carbone est représentée par les réactions :

$$CO_2 + C \longrightarrow 2\,CO \text{ (gaz)}$$

$$H_2O + C \longrightarrow CO + H_2 \text{ (gaz)}$$

L'oxyde de carbone et l'hydrogène étant les produits finaux, on peut voir que la fraction disponible d'oxygène dans les écoulements issus de la combustion d'un hydrocarbure est égale à la fraction d'oxygène présente avant combustion diminuée de la fraction qui peut s'unir avec le carbone du combustible pour former du CO.

Ainsi pour le brûleur oxygène-propane la composition du mélange de richesse φ est avant combustion

$$\varphi C_3H_8 + 5\,O_2$$

l'oxygène disponible est proportionnel à

$$5\,O_2 - 3/2\,\varphi\,O_2$$

et la fraction disponible de Γ° est :

$$(8) \quad \Gamma^\circ = \frac{[5\,O_2 - 3/2\,\varphi\,O_2] \times 32}{[\varphi\,C_3H_8] \times 44 + [5\,O_2] \times 32}$$

D'autre part tout se passe à la paroi comme si l'oxygène transféré qui est sous forme de CO_2, H_2O etc, se combine avec le carbone de la paroi suivant la réaction

$$2\,C + O_2 \longrightarrow 2\,CO$$

et le rapport entre les quantités transférées et les quantités ablatées est bien celui d'une réaction unique où $x = y = 1$; $[\mathcal{M}_c] = 12$; $[\mathcal{M}_o] = 16$ c'est-à-dire est de la forme (6) et

$$(6') \quad \dot{m}_p = \frac{12}{16} \rho u St \frac{\Gamma_g^\circ - \Gamma_p^\circ}{\Gamma^c}$$

Lorsque les temps chimiques des réactions à la paroi sont petits les fractions d'oxydants disparaissent au fur et à mesure qu'elles sont transférées à la paroi et Γ_p° devient négligeable. Plus précisément si la vitesse de production de CO à partir du carbone de la paroi est représentée par une expression de la forme :

$$K (p^{(o)})^n \exp \frac{E}{\mathcal{R} T} \quad (p^\circ \text{ pression partielle de l'oxygène disponible})$$

les vitesses de transfert d'oxygène disponible étant égales d'autre part aux vitesses de formation de CO en régime stationnaire on a :

$$\rho u St [\Gamma_g^\circ - \Gamma_p^\circ] \sim K [p^{(o)}]^n \exp \frac{E}{\mathcal{R} T_p}$$

ou

$$\Gamma_p^\circ \sim \frac{\Gamma_g^\circ}{1 + \frac{K [p^{(o)}]^{n-1}}{\gamma H St} \sqrt{\gamma R T_g} \exp \frac{E}{\mathcal{R} T_p}}$$

Il suffit que le dénominateur du 2ème membre soit grand pour pouvoir négliger la fraction sans avoir besoin de connaître les vitesses de réaction. En réaction hétérogène le facteur K dépend essentiellement de l'état de surface de la phase solide souvent caractérisé par l'étendue de la surface accessible aux gaz déterminée par exemple par la méthode BET.

4.2 - Bilans massique et thermique

a) Cas de la résine phénolique pure

La résine phénolique est entièrement gazéifiée par une suite de trois processus chimiques indiqués dans la figure 7. Les essais d'ablation montrent que ces trois processus s'accomplissent dans une couche d'épaisseur faible et quasi constante et qu'un régime stationnaire s'établit dans un laps de temps petit. En outre, la structure particulièrement poreuse du coke indique une surface accessible aux gaz très grande ce qui compte tenu des températures de paroi élevées doit conduire à des temps chimiques très courts $[\Gamma_p^\circ \sim 0]$.

La composition élémentaire pondérale des résines utilisées est

$C = 0,77$ $\quad H_2 = 0,057$ $\quad O_2 = 0,173$

Si l'on admet que tous les corps oxygénés de la pyrolyse sont réduits à l'état d'oxyde de carbure, la quantité de carbone disponible est :

$$(10) \quad \Gamma^c = 0,77 - \frac{12}{16} 0,173 = 0,64$$

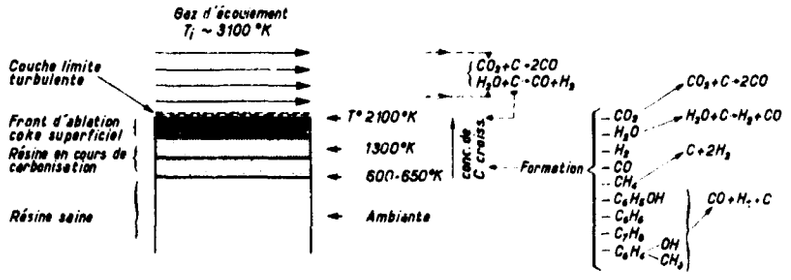

FIG. 7 - SCHEMA DE L'ABLATION D'UNE TUYERE EN RESINE PHENOLIQUE

Dans les pyrolyses effectuées au four en atmosphère inerte, l'analyse des produits dégagés à haute température indique qu'ils sont formés de CO, H_2 avec de petites quantités de CH_4 et le résidu solide correspond à une teneur en coke de 0,59 [6].

La différence 0,64 - 0,59 représente le carbone contenu dans les hydrocarbures gazeux dégagés qui peuvent être oxydés par les gaz de l'écoulement. De toute manière la différence entre carbone disponible et teneur en coke étant faible il est permis en première approximation d'établir les bilans sur la base la plus simple c'est-à-dire en fonction de la fraction de carbone définie par (10).

bilan de masse. Les maquettes en résine ont été expérimentées sur le brûleur oxygène-propane avec les conditions suivantes :

$\rho u = 16,3$ g/cm² s

$\varphi = 1,3$

$St^* = 2,10^{-3}$

La fraction d'oxygène disponible dans l'écoulement est d'après (8) :

$$\Gamma_g^\circ = \frac{[5\ O_2 - 1,3\ 3/2\ O_2]\ 32}{1,3\ C_3H_8 \times 44 + 5\ O_2 \times 32} = 0,448$$

celle du carbone disponible est Γ

$$\Gamma_c = 0,64$$

Le bilan de masse est alors représenté par l'équation

$$\dot{m}_p = \rho u St \frac{12}{16} \frac{\Gamma_g^\circ}{\Gamma^c} = 0,0142 \text{ g/cm}^2 \text{ s}$$

avec

$$\frac{St}{St^*} = \frac{Ln\ 1 + \frac{12}{16}\frac{\Gamma_g^\circ}{\Gamma^c}}{\frac{12}{16}\frac{\Gamma_g^\circ}{\Gamma^c}} = 0,81$$

Bilan thermique. En négligeant la fraction d'énergie rayonnée qui est petite, le bilan thermique est :

$$\phi_p = \dot{m}_p \Delta H_M^p = \dot{m}_p \left[Q_{\text{pyrolyse}} + Q_{\text{échauf.}} + Q_{\text{réaction}}\right]$$

la somme $Q_{\text{pyrolyse}} + Q_{\text{échauffement}}$ représente la quantité de chaleur qu'il faut fournir pour transformer 1 g de résine prise à la température ambiante en produits de pyrolyse à la température de paroi T_p. L'étude thermique d'échantillons de résine pyrolysée en atmosphère inerte montre que :

$$Q_{\text{pyrolyse}} + Q_{\text{échauffement}} \sim 550 \text{ cal/g}$$

le terme $Q_{\text{réaction}}$ représente la chaleur des réactions qui se produisent entre gaz de l'écoulement et le carbone résiduel de la résine pyrolysée.

Les réactions en jeu, dans les conditions réalisées, sont essentiellement :

$$H_2O + C \longrightarrow H_2 + CO + \sim 28600 \text{ cal}$$

$$CO_2 + C \longrightarrow 2\ CO + \sim 41000 \text{ cal}$$

à $T_p = 2100$°K.

D'après les concentrations respectives de H_2O et CO_2 dans le gaz de l'écoulement (composition d'équilibre à T_p) l'oxydation d'un gramme de carbone absorbe 2730 cal et

$$Q_{\text{réaction}} = 2730 \times 0,64 = 1750 \text{ cal/g de résine ablatée.}$$

On en déduit :

$$\Delta H_M^p = \left[Q_{\text{échauf.}} + Q_{\text{pyrolyse}} + Q_{\text{réaction}}\right] =$$

$1750 + 550 = 2300$ cal/g

et le flux absorbé a pour valeur :

$$\phi_p = \dot{m}_p \Delta H_M^p = 32,7 \text{ cal/cm}^2 \text{ s}$$

Il est d'usage de prendre comme référence le flux ϕ_p^* reçu par une paroi non émissive qui est égal, dans le cas de l'expérience à

$$\phi_p^* = \phi_p \times \frac{St^*}{St} = 40,5 \text{ cal/cm}^2 \text{ s}$$

il correspond, à ce flux, une chaleur efficace d'ablation :

$$Q_{eff} = \Delta H_M^p \times \frac{St^*}{St} = 2750 \text{ cal/g.}$$

4.3. - Composite phénolique graphite

a) Mécanisme chimique probable de l'ablation

Les composites phénolique graphite ne diffèrent de la résine pure que par une proportion plus élevée en carbone. Les hypothèses admises pour le cas de la résine s'étendent par conséquent à celui du composite ; toutefois la surface accessible aux gaz des fibres de graphite est assez grande pour qu'il n'y ait pas de différence sensible entre les vitesses d'ablation des fibres et celles du coke poreux de la résine. Cette condition avec les composites utilisés paraît assez bien satisfaite

et l'ablation s'effectue suivant le mécanisme décrit précédemment.

b) Bilan de masse

Les bilans de masse et thermique s'établissent egalement comme dans le cas de la résine pure. Le matériau expérimenté d'après les analyses a la composition pondérale élémentaire suivante :

$C = 0,92 \qquad H_2 = 0,0225 \qquad O_2 = 0,0575$

A partir de ces données le bilan de masse pour les essais du brûleur oxygène-propane est :

$$\dot{m}_p = \rho u St \frac{12}{16} \frac{\rho_o}{\rho_c} = 0,0111 \text{ g/cm}^2 \text{ s}$$

avec $\frac{St}{St^m} \simeq 0,86$.

c) Bilan thermique

En adaptant à cette nouvelle composition les valeurs trouvées pour la résine, on a :

$$\Delta H_M^o = 2780 \text{ cal/g}$$

le flux absorbé est :

$$\phi_p \simeq 31 \text{ cal/cm}^2 \text{ s} \qquad \text{et}$$
$$\phi_p^m \simeq 36 \text{ cal/cm}^2 \text{ s}$$

la chaleur efficace d'ablation étant :

$$Q_{eff.} = \Delta H_M^o \times \frac{St^m}{St} = 3250 \text{ cal/g.}$$

4.4 - Comparaison avec les résultats expérimentaux.*

Le tableau 1 résume les résultats des essais et ceux des calculs précédents. On constate un accord très satisfaisant entre ces résultats dans le cas des maquettes en résine pure ce qui constitue une bonne présomption pour la validité du schéma d'ablation proposé. L'aspect régulier légèrement rugueux de la paroi après essai, permet raisonnablement d'écarter l'hypothèse d'arrachement du coke qui aurait pour effet un abaissement systématique du résultat expérimental par rapport au résultat théorique.

En ce qui concerne les maquettes en composite phénolique graphite, on trouve que les vitesses massiques d'ablation expérimentale sont en moyenne inférieures de 12 % aux vitesses théoriques mais les flux thermiques déduits de ces vitesses théoriques sont en bon accord avec ceux déduits des mesures. En réalité la détermination expérimentale de la vitesse d'ablation est entachée d'une erreur provenant du fait qu'on néglige la perte de matière subie dans les couches carbonisées du matériau et ces couches sont nettement plus épaisses que dans le cas de la résine pure.

5 - EXEMPLE D'ABLATION GOUVERNEE PAR DES REACTIONS ENTRE CONSTITUANTS DU MATERIAU

5.1 - Mécanisme chimique probable de l'ablation du composite silice phénolique

Dans tous les essais des maquettes en résine phénolique renforcée de fibres de verre lavé (98 % de SiO_2) on a constaté la disparition d'une fraction importante de silice sans récupération en quantités notables d'autres dérivés silicés. Il faut donc admettre une élimination sous forme gazeuse de la silice.

On sait qu'aux températures élevées la silice se dissocie suivant la réaction :

$2\ SiO_2$ liquide $\rightleftharpoons 2\ SiO$ gaz $+ O_2$ gaz $+ 360$ kcal.

Mais en présence du carbone et de l'hydrogène provenant de la pyrolyse de la résine phénolique, la silice est également réduite avec formation de SiO.

Trois séries de réactions peuvent être envisagées [7] et ces réactions sont des réactions d'équilibre dont les vitesses dépendent des pressions partielles des gaz formés et des températures.

La discussion des équilibres entre Si, O_2, C et leurs composés laisse assez bien prévoir les réactions qui contrôlent l'ablation. Mais il est plus probant de s'appuyer sur certains de nos résultats expérimentaux récents [8].

Les thermogrammes d'échantillons silice phénolique étudiés par thermogravimétrie montrent qu'en atmosphère inerte les vitesses de perte de masse tendent vers zéro entre 1200 et 1400°C puis augmentent rapidement au-dessus de 1400°C. Cet accroissement de vitesse de décomposition qui n'est pas observé dans le cas de la résine pure s'accompagne d'un dégagement important de CO et d'une corrosion rapide des thermocouples platine-platine rhodié qui est attribuée à la diffusion de SiO.

Parallèlement des essais d'analyse thermique différentielle rapide avec chauffage par haute fréquence mettent en évidence dès 1400°C une réaction suffisamment endothermique et rapide pour limiter les températures maximales atteintes dans le domaine des puissances fournies par le générateur H.F. On observe un fort dégagement gazeux dont la partie condensable est identifiée comme SiO et l'autre partie comme CO.

Il ressort de ces expériences que la disparition de la silice provient essentiellement de la réaction globale :

$SiO_2 + C \rightleftharpoons SiO$ gaz $+ CO$ gaz.

D'ailleurs aux températures de surface ($\sim 2100°C$) mesurées au cours des essais d'ablation sur brûleur les pressions partielles de SiO sont

---

* Le graphite massif se distingue des matériaux précédents par certaines de ses propriétés physiques qui sont en contradiction avec les hypothèses admises. En effet sa conductibilité thermique élevée s'oppose à l'établissement d'un régime thermique stationnaire où les flux de convection sont entièrement absorbés dans les processus d'ablation et sa faible porosité initiale ne donne pas une surface accessible aux gaz suffisante. Toutefois, on a observé des régimes d'ablation stationnaire et lorsque la pression partielle des gaz oxydants est assez élevée les vitesses d'ablation sont voisines de la vitesse théorique. Ceci s'explique par la formation d'une multitude de microcratères dont l'effet évident est un accroissement de la surface accessible au gaz. D'autre part des essais de col en graphite avec des écoulements neutres chauffés par arc électrique ont montré qu'il n'y avait pas d'ablation. Ceci confirme, s'il en est besoin, l'hypothèse d'une ablation chimique.

(1) dissociation de la silice 10^{-3} bars
(2) réduction de SiO_2 par H_2 $5\ 10^{-2}$ bars
(3) réduction de SiO_2 par C 1 bar.

Elles indiquent que la réaction (3) doit s'effectuer à une vitesse beaucoup plus élevée que les deux autres qui peuvent être négligées.

Il faut tenir compte de l'action oxydante des gaz de l'écoulement qui concurrence celle de la silice sur la résine pyrolysée. Toutefois aux températures de paroi observées, la silice non réduite est un liquide visqueux qui forme un film protecteur et les réactions entre constituants peuvent s'effectuer normalement tout au moins lorsque la température de la couche réactionnelle est suffisamment élevée.

5.2 - Bilan thermique

Pour le composite silice phénolique les transformations essentielles dépendent peu de la composition de l'écoulement gazeux et en régime stationnaire elles se développent pratiquement de telle manière qu'il y a égalité entre les quantités de chaleur transmises par convection et celles absorbées dans l'ablation. C'est donc par bilan thermique qu'on peut déterminer la vitesse d'ablation.

En admettant que la réaction :

$$SiO_2 + C \rightleftharpoons SiO \text{ gaz} + CO \text{ gaz} \quad (3)$$

est la réaction dominante, elle consomme dans le cas du composite utilisé (70 % de silice, 30 % de résine phénolique) 0,140 g de carbone par gramme de matériau. Avec la résine employée il reste 0,052 g de carbone en excès et on suppose dans la suite que ce carbone excédentaire est oxydé par le gaz de combustion.

D'après la référence [9] la quantité de chaleur absorbée par la réaction (3) compte tenu de la chaleur d'échauffement des réactifs et de celle de la pyrolyse de la résine est :

$$\left[Q_{\text{pyrolyse}} + Q_{\text{échauff.}} + Q_{\text{réaction}}\right]_{2250°K}$$

$\sim$ 196 kilocalories/mole SiO_2 réduite.

Cette valeur ramenée au gramme de matériau consommé est égale à 2500 calories et l'ablation de la résine excédentaire contenue dans ce gramme absorbe 180 calories. Au total la chaleur absorbée par gramme de matériau est :

$$\Delta H_M^P = 2500 + 180 = 2680 \text{ cal/g.}$$

L'équation du bilan thermique est

$$\dot{m}_p \, \Delta H_M^P = \rho u \, St \, (H_g - H_p)$$

ou

$$\dot{m}_p = \rho u \, St \, \frac{H_g - H_p}{\Delta H_M^P}$$

Dans les essais effectués au brûleur oxygène-kérosène les conditions expérimentales moyennes sont :

$$\rho u = 48 \text{ g/cm}^2\text{s} \qquad St^* = 1{,}35\ 10^{-3}$$

$$(H_g - H_p)_{2250°K} = 985 \text{ cal/g.}$$

On trouve

$$\frac{St}{St^*} = \frac{Ln\left(1 + \frac{H_g - H_p}{\Delta H_M^P}\right)}{\frac{H_g - H_p}{\Delta H_M^P}} = 0{,}85$$

et $\dot{m}_p = \rho u \, St \, \frac{H_g - H_p}{\Delta H_M^P} = 2{,}8\ 10^{-2}$ g/cm^2 s.

La chaleur efficace d'ablation étant :

$$Q_{eff.} = \Delta H_M^P \times \frac{St}{St^*} \simeq 3150 \text{ cal/g.}$$

Bilan de masse

En l'absence des mesures des concentrations à la paroi, l'équation du bilan de masse ne peut être résolue de la même manière que celle du bilan thermique.

Si on considère le corps simple silicium qui est présent dans le matériau mais absent dans l'écoulement, on a :

$$\left[\Gamma^{Si}\right]_g = 0$$

$$\left[\Gamma^{Si}\right]_M = 0{,}326 \text{ pour le composite étudié.}$$

D'autre part la comparaison des équations de base montre que

$$\frac{\Gamma_g^{(Si)} - \Gamma_p^{(Si)}}{\Gamma_p^{(Si)} - \Gamma_M^{(Si)}} = \frac{H_g - H_p}{\Delta H_M^P}$$

(l'émission pariétale fournissant une quantité $\dot{m}_p \left[\Gamma_M^{Si} - \Gamma_p^{Si}\right]$ de silicium)

d'où

$$\Gamma_p^{Si} = \frac{\Gamma_M^{Si} \, \frac{H_g - H_p}{\Delta H_M^P} + \Gamma_g^{Si}}{1 + \frac{H_g - H_p}{\Delta H_M^P}} = 0{,}088.$$

Ce silicium se trouve sous forme de SiO et compte tenu des masses molaires en jeu la fraction de SiO à la paroi est :

$$\Gamma_p^{SiO} \sim 0.137$$

ce qui correspond à une pression partielle dans les conditions d'essais de l'ordre de 0,23 bars.

5.3 - Comparaison avec les résultats expérimentaux

Les valeurs expérimentales de $\dot{m}_p$ et des chaleurs efficaces d'ablation $Q_{eff.}$ des maquettes en composite silice phénolique sont assez dispersées mais les ordres de grandeur sont en bon accord avec les valeurs théoriques.

Cette dispersion ne paraît pas liée à la densité du matériau mais les vitesses d'ablation les plus faibles correspondent aux profils d'ablation les plus réguliers. Dans ce cas la vitesse expérimentale est environ 12 % plus faible que la valeur théorique ; le sens de l'écart s'explique d'une part par les quantités de chaleur absorbées dans la couche pyrolysée relativement épaisse et d'autre part par la transparence au rayonnement de la silice qui peut fausser la mesure de la température de paroi par pyromètre I.R.

Le diagramme 8 établi suivant les données de Poch et Dietzel [9] représente les isothermes d'équilibre des phases solides SiO_2 - SiC ; SiO_2 - Si et SiO_2 - C en fonction des logarithmes des pressions de CO et SiO.

L'analyse des résidus pyrolysés des maquettes révèle la présence en quantité très faible de SiC et de Si indiquant par là une priorité absolue à la formation des produits volatiles. En phases condensées le processus d'ablation s'effectue nécessairement dans une couche d'épaisseur finie c'est-à-dire à cause de la faible conductibilité

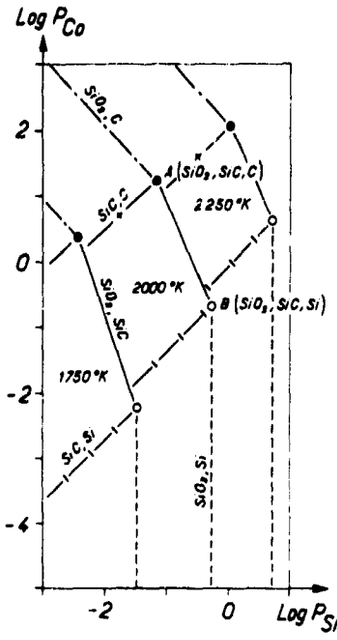

FIG. 8 - ISOTHERMES DU DIAGRAMME DE PHASES DU SYSTEME Si-C-O.

—— Equilibre SiO, SiC, phase gazeuse.
— — — Equilibre SiO_2-Si, phase gazeuse.
— · — Equilibre SiO_2C, phase gazeuse.
— | — | Equilibre SiC-Si, phase gazeuse.
— + — + Equilibre SiC, C.

thermique du matériau en présence de forts gradients thermiques. Il faut également que la pression des gaz formés soit supérieure à la pression de l'écoulement pour qu'ils puissent s'échapper.

En négligeant l'apport gazeux de la pyrolyse de la résine, le diagramme montre que la pression totale des gaz formés peut être suffisamment élevée lorsque la température de la couche réactionnelle est supérieure à 1750°K et que la pression partielle de SiO peut être de l'ordre de la valeur calculée (0,28 b) lorsque la température y est supérieure à 2000°K. Pour la température de paroi mesurée (~2250°K) la pression d'équilibre de SiO est voisine du bar. Ainsi le résultat calculé n'est pas incompatible avec les valeurs d'équilibre et d'autre part on voit que les transformations doivent s'effectuer essentiellement dans la couche de matériau dont la température est supérieure à 1750°K. Il est permis de penser que l'épaisseur de la couche réactionnelle est un facteur important et des résultats assez différents de ceux obtenus seraient observés si cette épaisseur était insuffisante.

CONCLUSION

L'étude de la pyrolyse de matériaux à base de résine phénolique effectuée au laboratoire par des méthodes classiques de chauffage et d'analyse a montré qu'à haute température, les produits gazeux formés sont peu nombreux, essentiellement CO et H_2 ou bien SiO et CO [6], [8] et que le processus chimique conduisant à ces produits peut être représenté globalement par une simple équation chimique.

A partir de ces résultats il devient possible d'établir une représentation schématique de l'ablation d'un de ces matériaux lorsqu'il est soumis à l'action d'écoulements de caractéristiques connues, ces écoulements fournissant l'énergie nécessaire et les réactifs complémentaires suivant les lois habituelles des transferts à travers les couches limites turbulentes.

Les essais effectués sur des brûleurs ont confirmé de manière satisfaisante ce point de vue et dans le tableau 3 on résume les principes de base de cette représentation schématique de l'ablation.

Il convient de remarquer qu'en raison des valeurs élevées des chaleurs d'ablation observées au cours des essais on ne voit pas quels autres processus que ceux qui ont été mentionnés pourraient expliquer les résultats obtenus.

TABLEAU 3

I - Ablation gouvernée par les réactions chimiques entre gaz de l'écoulement et la paroi
par bilan de masse

Equation chimique fondamentale	Apport massique du matériau	Apport massique de l'écoulement	Bilan	Effet de l'émission pariétale de gaz (approximation de Spalding)
$C_{(s)} + O_{(g)} \rightarrow CO_g$ $m_c = 12$ $m_o = 16$	$\dot{m}_p \Gamma^c$ Γ fraction disponible	$\rho u St \Gamma^o$	$\dot{m}_p \frac{\Gamma^c}{12} = \rho u St \frac{\Gamma^o}{16}$ $\boxed{\dot{m}_p = \rho u St \frac{12}{16} \frac{\Gamma^o}{\Gamma^c}}$	$St = St^* \frac{Ln\left(1 + \frac{12}{16}\frac{\Gamma^o}{\Gamma^c}\right)}{\frac{12}{16}\frac{\Gamma^o}{\Gamma^c}}$ St^* nb de Stanton de la paroi non émissive (si $\frac{\dot{m}_p}{\rho u St^*}$ assez petit)

II - Ablation gouvernée par les réactions chimiques entre constituants du matériau
par bilan thermique

Equation chimique fondamentale	Energie absorbée (matériau)	Energie fournie (écoulement)	Bilan	Effet de l'émission pariétale de gaz (approximation de Spalding)
$SiO_{2(l)} + C_{(s)} \rightarrow SiO_{(g)} + CO_{(g)}$	ΔH_m { $Q_{pyrol.\ résine}$, $Q_{échauf}$, $Q_{réact}$ (SiO_2 + C)	$\rho u St (H_g - H_p)$	$\dot{m}_p \Delta H_m^* = \rho u St (H_g - H_p)$ $\boxed{\dot{m}_p = \rho u St \frac{H_g - H_p}{\Delta H_m^*}}$ ou	$St = St^* \frac{Ln\left(1 + \frac{H_g - H_p}{\Delta H_m^*}\right)}{\frac{H_g - H_p}{\Delta H_m^*}}$ (si $\frac{\dot{m}_p}{\rho u St^*}$ assez petit)

REFERENCES

[1] H. A. BETHE, M. C. ADAMS -
A theory of the ablation of glassy materials.
J. A. S. vol. 26, n° 6 (1959).

[2] L. LEES -
Convective heat transfer with mass addition and chemical reactions.
Third Combustion and Propulsion Colloquium
AGARD NATO Palermo Sicily (1958)

[3] M. C. ADAMS -
Recent advances in ablation.
ARS Journal vol. 29, n° 9 (1959).

[4] D. B. SPALDING -
Transfert de chaleur et le transport de masse dans la technique aéronautique.
Traduction SDIT 59-60 (1960).

[5] GROUPE FRANCAIS D'ETUDE DES CARBONES -
Les Carbones, Tome II,
Collection de Chimie Physique, Masson & Cie (1965).

[6] a S. KOHN, G. TAGUET -
Etude de l'ablation des plastiques renforcés.
Document CNERA non publié (1965).

[6] b G. GAUTHEROT, S. KOHN -
Méthode d'analyse continue des produits gazeux formés au cours de la dégradation des résines phénoliques.
La Recherche Aérospatiale n° 124, (1968).

[7] S. KOHN, J. NICOLAS, G. TAGUET -
Contribution à l'étude de l'ablation de quelques matériaux à base de résine phénolique.
La Recherche Aérospatiale n° 117 (1967).

[8] a G. TAGUET -
Analyse des cokes d'ablation.
Non encore publié.

[8] b J. JAMET -
Analyse thermique différentielle à haute température accouplée à un spectrographe de masse.
Société chimique de France, Groupe de Thermochimie - Journée du 28 février 1969 Marseille.

[9] W. POCH, DIETZEL -
Die Bildung von Silizium Karbid aus Silizium Dioxyd und Kohlenstoff.
Ber. der Deut. Keramischen Gesel.39, (8) (1962) p. 413-446.

THERMODYNAMICS OF VAPORIZATION PROCESSES OF SOLIDS AT HIGH TEMPERATURES[♦]

G. De Maria - Istituto di Chimica Fisica ed Elettrochimica
Università di Roma. Rome, Italy

♦ The research reported in this paper has been sponsored in part by the Air Force Materials Laboratory, Research and Technology Division, AFSC. through the European Office, Office of Aerospace Research, United States Air Force and in part by the Consiglio Nazionale delle Ricerche through the Centro di Chimica delle Alte Temperature.

SUMMARY

THE MASS SPECTROMETRIC method has proved to be a powerful tool for identifying new high temperature species. The principle of the method is discussed together with the thermodynamic procedures employed in the treatment of the data. In particular the thermodynamic behavior of the evaporation process of metal-carbon systems at high temperatures is discussed, in the light of recent mass spectrometric results. A comparison with the thermodynamic properties of gaseous metal-oxide species is presented. A correlation between isosteric and isoelectronic molecules composed of IV-IV, III-V and II-VI group elements is reported.

LIST OF SYMBOLS

A = Constant equal to 215 kcal

D_o^o = Dissociation energy

e. u. = Entropy unit

$\frac{G_T^\circ - H_o^o}{T}$ = Free energy function

$\Delta\left(\frac{G_T^\circ - H_o^o}{T}\right)$ = Free energy function variation for the specified reaction

ΔH_o^o = Standard enthalpy of reaction at 0°K

$\Delta H_{o\ atom}^o$ = Atomization energy of crystals

ΔH_T = Enthalpy of reaction at temperature T

I_i^+ = Ion intensity of the isotope i of the species detected

K = Equilibrium constant of reaction

P = Partial pressure of gaseous species

Q = Total partition function

Q_{el} = Electron contribution to the total partition function

Q_{tr} = Translational contribution to the total partition function

Q_{vibr} = Vibrational contribution to the total partition function

Q_{rot} = Rotational contribution to the total partition function

S = Sensitivity factor of the mass spectrometer

T = Absolute temperature

α = Dimentionless parameter equal to $\frac{\Delta H_o^o \text{ [atom, Me]}}{D_o^o}$

σ_i = Total electron ionization cross-section

γ = Electron multiplier gain

R = Gas constant

THE STUDY of the thermodynamic behavior of the evaporation process of solids at high temperatures is strictly related to the knowledge of the composition of the gas-phase in thermodynamic equilibrium with the condensed-phase. One of the most important generalizations which can be established in high temperature chemistry is the so called "Brewer's paradox". It asserts that for the vast majority of systems of interest in high temperature chemistry the complexity of the gas-phase in thermodynamic equilibrium with the condensed systems increases with rising temperature. This proposition finds its justification on the basis of simple statistical-thermodynamic arguments (1).

THE COMPLEXITY of the gas phase shows itself not only in the variety of the molecular species, but also in the presence of unfamiliar oxidation states. One finds for instance for Lithium the 2+ oxidation state in the stable LiO molecule, while Aluminum gives rise to molecules Al_2O and AlO in which the Aluminum is in the 1+ and 2+ oxidation state. Some inorganic systems vaporize predominantly to polymers: e. g. C_3 from graphite (2); $(CuCl)_3$ in equilibrium with solid CuCl (3); and Mo_3O_9, Mo_4O_{12} and Mo_5O_{15} over solid MoO_3 (4). Only a limited number of high temperature molecular species were known from spectroscopic studies. In particular the presence of C_3 and SiC_2 was ascertained by spectroscopic observations of cool stellar atmospheres. The existence of other species could be deduced through a skilful use of thermodynamics in treating Knudsen effusion data.

THE ADVENT of the mass spectrometric technique has given an important impulse to the furthering of the wealth of knoledge of high temperature molecules, disclosing at the same time some of the patterns of behavior that can be found for high-temperature inorganic systems.

IN THIS PAPER the principle features of the mass-spectrometric method will be described together with the thermodynamic methods used in the elaboration of experimental data, while, for more comprehensive coverage of the subject, other specialized articles may be consulted (5, 6).

THE COUPLING of the Knudsen molecular source with a mass spectrometer of the Inghram-type, vertical mounting is shown in Fig. 1. The identification of the molecular species is normally accomplished by this method in four steps:

a. mass-to-charge ratio determination
b. isotopic distribution
c. appearance potential
d. intensity distribution in the molecular beam.

AN EVALUATION of the bond strenght in the molecule can be derived in some cases from the shape of the ionization efficiency curve showing the occurrence of dissociative ionization processes. The intensity distribution in the molecular beam allows one to discriminate species effusing through the cell orifice from species vaporizing from the surrounding shields. Partial pressures of the species detected can be directly determined by means of the relation:

$$P = \frac{I_i^+ \, T}{S \sigma_i \gamma_i a_i}$$

where I_i^+ represents the ion intensity of the isotope i of abundance a_i, T the temperature of the cell, S the sensitivity factor of the mass spectrometer, σ_i the electron ionization cross-section and γ the electron multiplier gain.

THE THERMODYNAMIC treatment of the evaporation data can be carried out using two independent methods, namely the so called second-law and third-law methods. The second-law method consists essentially in the use of the Van't Hoff equation:

$$\frac{d \ln K}{d \left(\frac{1}{T}\right)} = - \frac{\Delta H_T}{R}$$

THE THIRD-LAW method is based on the relation:

$$\frac{\Delta H_o^o}{T} = - R \ln K - \Delta \left(\frac{G_T^* - H_o^o}{T}\right)$$

where $\left(\frac{G_T^* - H_o^o}{T}\right) = - R \ln Q$ and the total partition function is taken as $Q = Q_{el} Q_{tr} Q_{vibr} Q_{rot}$.

ΔH_o^o, according to the cases considered, may correspond to the heat of the reaction at 0°K, or be a measure of the cohesive energy of crystals, or the dissociation energy of diatomic molecules, or their atomization energy. The knowledge of the free energy functions of the molecular species is implied in the application of the third-law method. There is a lack of knowledge of spectroscopic data for accurate free energy functions calculations for a large number of high temperature species. Nevertheless a reliable evaluation of these parameters can be made in most cases, following analogic criteria and resorting to empirical correlations between interatomic distances and force constants (7, 8, 9).

TABLE I CONTAINS a summary of the spectroscopic assumptions utilized for the calculations of the free energy functions for a number of dicarbide molecules. Free energy functions variations relative to a set of rare-earth dicarbide species are included in Fig. 2.

An analysis of the diagram shows that the corresponding values differ from each other by about one entropy unit. A rough estimate of about 16 e. u. of this parameter for the remaining rare-earth carbides can be made. One can point out that such an estimate at 2000°K would be reflected in an uncertainty for ΔH^{o}_{o} of reaction of about 4 Kcal.

THE EVALUATION of physical and chemical stabilities (10, 11) of high temperature species is of particular importance in deriving correlations between thermodynamic properties of compounds along the periodic system. Comparison of isosteric and isoelectronic molecules for a number of systems makes it possible to predict, from knowledge of the heat of atomization of the solid phase, the dissociation energy of the heteronuclear gaseous species and, therefore, the experimental conditions for their observation. GaAs molecules was observed using double-oven technique coupled with a mass spectrometer, as was deducted from thermodynamic considerations (12). A typical example of this type of correlation is represented by Table II which contains α value for isoelectronic molecules composed of IV-IV, III-V and II-VI group elements.

A CORRELATION between monoxide and dicarbide gaseous species has been established (13) and is summarized by the relation:

$$\ln \frac{P\,(MeC_2)}{P\,(Me)} = -\frac{A - D^{o}_{o}\,(MeO)}{R\,T} - \frac{1}{R}\,\Delta\,\frac{(G^{\circ}_{T} - H^{o}_{o})}{T}$$

where P (MeC_2) and P (Me) represent the equilibrium partial pressures of the dicarbide and the metal species over carbon-rich metal-carbide phase; A a constant equal to 215 kcal and D^{o}_{o} (MeO) the dissociation energy of the corresponding gaseous monoxide species.

$\Delta\,\frac{(G^{\circ}_{T} - H^{o}_{o})}{T}$ is relative to the pressure independent reaction: $Me_{(g)} + 2C_{(s)} \rightarrow MeC_{2(g)}$. The relation allows one to predict the relative concentration of dicarbide species to metal atoms for metal-carbon systems, when the thermodynamic properties of the corresponding monoxide gaseous species are known. The "inversion temperature point" can be evaluated from this equation showing the onset of the temperature range in which the dicarbide vaporizes congruently. Table III indicates a comparison between bond energy of gaseous dicarbide and gaseous monoxide species which have been studied to date.

IN ADDITION to dicarbide molecules, tetracarbide species of high physical stability were observed in the evaporation of rare-earth carbon systems (14). These findings suggested the extention of the above correlation to the dioxide molecules, as CeO_2 and HoO_2 for which atomization energies of about 370 and 350 kcal/mole^{-1} were predicted.

RARE-EARTH CARBON systems have been extensively studied in our laboratory (15, 16, 17, 18). For calculations of the thermodynamic properties of vaporization processes the following reactions were considered:

$MC_{2(s)} \rightarrow M_{(g)} + 2C_{(s)}$

$MC_{2(s)} \rightarrow MC_{2(g)}$

$M_{(g)} + 2C_{(s)} \rightarrow MC_{2(g)}$

$MC_{2(g)} + 2C_{(s)} \rightarrow MC_{4(g)}$

ON THE BASIS of the data so far accumulated, some general considerations can be made as to the composition of gas-phase and volatility of the lanthanide dicarbides. The less volatile rare-earth dicarbides vaporize predominantly to elements and carbides gaseous molecules (the gaseous dicarbide being the predominant polyatomic species) while, Samarium and Ytterbium give rise only to gaseous metal as equilibrium vapor species in the ranges of temperature explored. The MeC_2/Me ratios range from 1.6 to 1 at 2500°K for La, 0.77 at 2273°K for Ce and < 0.0001 for Yb in the range 1280-1485°K. The enthalpy of evaporation of a dicarbide to $MC_{2(g)}$ is usually greater than the enthalpy of evaporation to $M_{(g)} + 2C_{(s)}$ and, consequently, the evaporation by the dicarbide mode is favoured by increasing temperature. The characteristic bahavior of Ce-C system is shown in Fig. 3.

ACCURATE VALUES of total vapor pressures of carbon-rich rare-earth dicarbide phase are poor. From mass-spectrometric results one can make an evaluation of the volatility of these systems, obtaining at 2000°K typical total pressures ranging from $10^{-7.8}$ for LaC_2, 10^{-7} for CeC_2, 10^{-6} for HoC_2, to $10^{-3.2}$ for SmC_2, $10^{-1.5}$ for EuC_2 and $10^{-1.4}$ for YbC_2.

THE IDENTIFICATION of new, unfamiliar vapor species threw new light on the understanding of the thermodynamic behavior of the evaporation process of solids at high temperature. The mass spectrometric method has proved to be the most powerful tool for analysing the composition of high temperature gas-phase. However this technique presents some limitations, particularly in connection with the lack of direct informations as to the conformation and structure of the detected molecules. In addition relatively large uncertainties are associated in some cases to the electron ionization cross sections values, which are reflected directly in the determination of the equilibrium partial pressures of the species.

AN INCREASING number of high temperature scientists is nowadays being interested in the application of optical-spectroscopy to the study of high temperature molecules. Infrared spectroscopy, the matrix isolation technique for trapping high temperature species, electron diffraction and microwave spectroscopy are supplementing mass spectrometry as tools for the study of high temperature gas phase-condensed phase problems and, even though intrinsic and severe difficulties are encountered, their use is highly promising.

REFERENCES

1. Brewer L., Paper 7 in "Chemistry and Metallurgy of Miscellaneous Materials: Thermodynamics", National Nuclear Energy Series IV - 19B, (ed. by L. L. Quill) Mc Graw-Hill Book Co., New York, N. Y. 1950
2. Drowart J., Burns R. P., De Maria G. and Inghram M. G. - J. Chem. Phys. 31, 1131 (1959)
3. Brewer L. and Lofgren N. L. - J. Am. Chem. Soc. 72, 3038 (1950)
4. Berkowitz J., Inghram M. G. and Chupka W. A. - J. Chem. Phys. 26, 842 (1957)
5. Inghram M. G. and Drowart J. - in "Proceedings of the International Conference on High Temperature Technology", Asilomar, California, October 1959. McGraw-Hill, New York
6. Grimley R. T., in "The Characterization of High Temperature Vapors" (J. L. Margrave, Ed.), p. 195, J. Wiley and Sons, 1967
7. Baughan E. C. - Trans Faraday Soc. 48, 121 (1952)
8. Badger R. M. - J. Chem. Phys. 3, 710 (1935)
9. Herschbach D. R. and Laurie V. W. - J. Chem. Phys. 35, 458 (1961)
10. Verhaegen G., Stafford F. E., Goldfinger P. and Ackerman M. - Trans Faraday Soc 58, 1926 (1962)
11. Colin R. and Goldfinger P. - in "Condensation and Evaporation of Solids" (E. Rutner, P. Goldfinger and J. Hirth Editors) p. 165, Gordon and Breach Inc., N. Y. 1964
12. De Maria G., Malaspina L. and Piacente V. - to be published
13. De Maria G. - in "Proceedings of First International Conference on Material Science" Sept. 1968, Tremezzo, in press.
14. Balducci G., Capalbi A., De Maria G. and Guido M. - J. Chem. Phys. 43, 2136 (1965)
15. De Maria G., Balducci G. Capalbi A. and Guido M. - in Proc. Brit. Ceram. Soc., No. 8, June 1967, Stoke-on-Trent.
16. Balducci G., Capalbi A., De Maria G. and Guido M. - J. Chem. Phys. 50, 1969-1974 (1969)
17. Balducci G., Capalbi A., De Maria G. and Guido M. - Tech. Rept. AFML 68, July 1968, MAYT, Wright-Patterson, Ohio
18. Balducci G., De Maria G. and Guido M. - Tech. Rept. AFML 69, January 1969, MAYT, Wright-Patterson, Ohio.

TABLE I - Summary of spectroscopic assumptions for free energy functions calculations of gaseous dicarbides.

Molecule	K_{Me-C} dyn/cm	r_e Å	ω_1 cm^{-1}	$\omega_{2(d.d.)}$ cm^{-1}	ω_3 cm^{-1}	$-(\frac{G_T-H_o^\circ}{T})_{2000°K}$ cal. $mole^{-1} \cdot deg^{-1}$
BC_2 (a)	--	1.28	1300	550	2200	66.7
SiC_2	$2.9 \cdot 10^5$	1.90	591	465	1742	67.9
ScC_2	$3.3 \cdot 10^5$	1.75	600	310	1710	74.1
GeC_2	$2.4 \cdot 10^5$	1.99	460	454	1718	66.58
YC_2	$5.74 \cdot 10^5$	2.39	659	436	1761	72.91
LaC_2	$5.56 \cdot 10^5$	1.94	630	400	1772	67.20
CeC_2	$6.24 \cdot 10^5$	1.98	655	458	1773	78.94
PrC_2	$5.64 \cdot 10^5$	1.98	629	458	1757	77.78
NdC_2	$5.64 \cdot 10^5$	1.98	628	458	1757	77.85
HoC_2	$5.94 \cdot 10^5$	1.98	636	458	1765	78.11
ThC_2	$5.5 \cdot 10^5$	1.90	592	399	1756	74.60

(a) analogy with C_3

TABLE II - α values for isoelectronic molecules composed of IV-IV, III-V and II-VI group elements.

$$\alpha = 0.5\ \Delta H_o^\circ\ [at.MeX]\ /D_o^\circ\ (MeX)$$

IV-IV	III-V	II-VI
C_2 = 1.19	BN = 1.48	BeO = 1.32
Si_2 = 1.45	AlP = 1.82	MgS ≥ 1.68
Ge_2 = 1.37	GaAs = 1.61	ZnSe = 1.92
Sn_2 = 1.57	InSb = 1.90	CdTe ≥ 1.55
Pb_2 = 2.1	TlBi = 1.98	

TABLE III - Comparison between bond energy of gaseous dicarbides and gaseous monoxides.

Metal	D_o^o (Me - O) eV	D_o^o (Me - C_2) eV	D_o^o (Me - O) - D_o^o (Me - C_2) eV
Sc	7.2	6.3	0.9
Y	7.4	6.7	0.7
La	8.3	6.9	1.4
Ce	8.0	7.1	0.9
Pr	7.4	6.6	0.8
Nd	7.2	6.4	0.8
Gd	7.5	6.9	0.6
Tb	7.5	6.6	0.9
Dy	6.5	5.8	0.7
Ho	6.6	5.8	0.8
Er	6.6	5.9	0.7
Th	8.3	7.4	0.9
B	8.0	6.6	1.4
Ti	6.8	6.3	0.5
Si	7.2	7.2	0.0
Ge	6.8	6.3	0.5
V	6.4	5.9	0.5

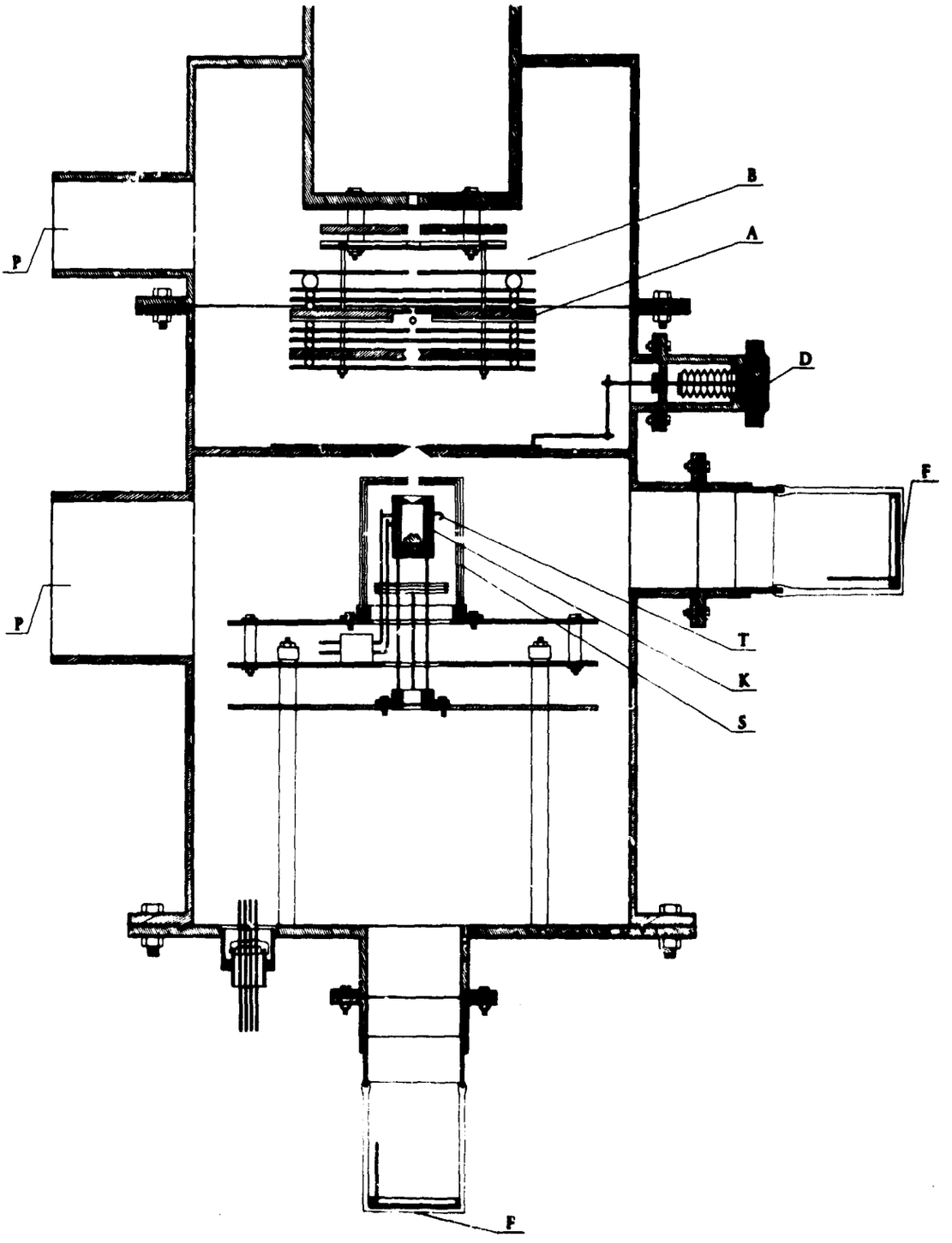

Fig. 1 - Knudsen effusion cell and ionization source assembly for thermodynamic equilibrium studies.

K- Knudsen cell; T- bombarding filament; S- radiation shields; F- windows for temperature measurement; D- movable beam defining slit; A- ionization chamber; B- ion beam defining and accelerating system; P- to pumps.

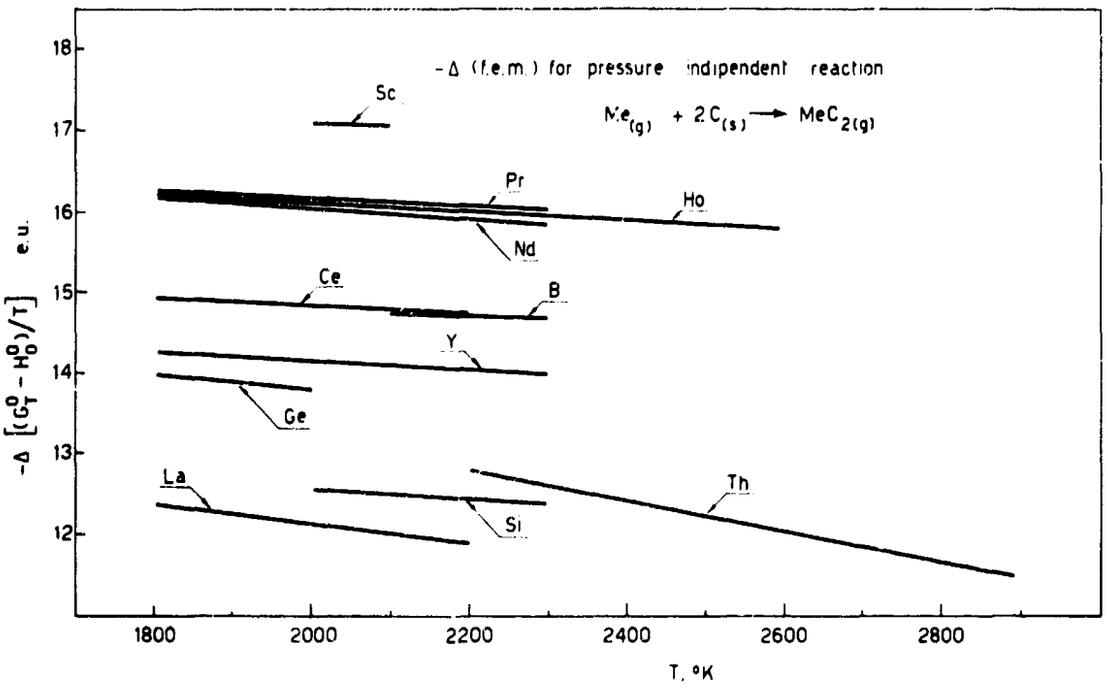

Fig. 2 - Free energy functions variations for a number of metal-carbon systems relative to the reaction: $Me_{(g)} + 2C_{(s)} \rightarrow MeC_{2(g)}$

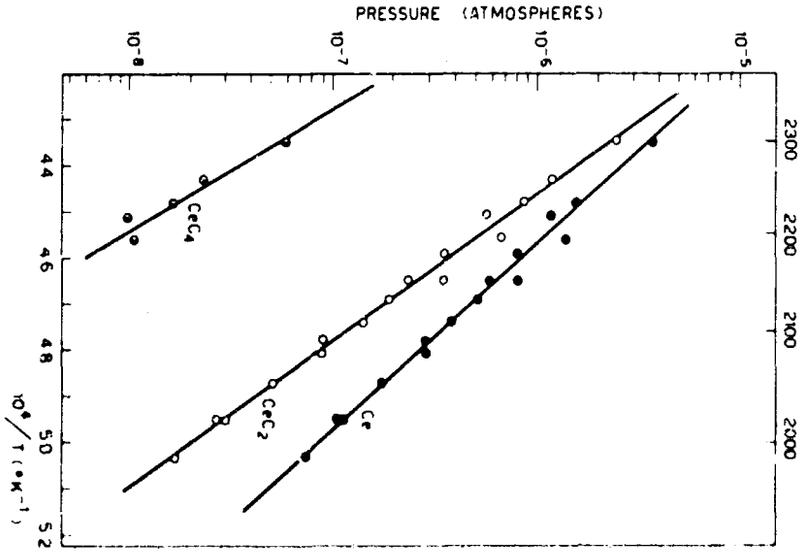

Fig. 3 - Partial pressures of the vapor species over cerium-graphite condensed system as a function of $1/T \times 10^4$ ($^\circ K^{-1}$)

"LA VITESSE LINEAIRE DE REGRESSION DU PERCHLORATE D'AMMONIUM DANS UN ECOULEMENT GAZEUX COMBUSTIBLE"

par

Prof.Ing. Corrado CASCI et Dott. Ing. Luigi DE LUCA

C.N.P.M.

(Centro Nazionale di Ricerca sulla Tecnologia della Propulsione e dei Materiali Relativi)

MILAN - ITALY

RESUME

On a déterminé expérimentalement la vitesse linéaire de régression d'échantillons cylindriques comprimés de perchlorate d'ammonium dans un écoulement gazeux combustible. Les paramètres pris en considération sont: la nature et l'épaisseur de l'inhibiteur latérale de combustion; la géométrie des spécimens; la granulométrie des poudres; la nature et le débit du gaz combustible; la dilution du gaz combustible; la nature et le pourcentage des additifs métalliques; la nature et le pourcentage des catalyseurs de la décomposition thermique du perchlorate d'ammonium; l'état de surface des additifs; l'addition du perchlorate de lithium. L'effet de la pression a été lui aussi examiné mais en conditions statiques. D'autres résultats concernent l'allumage et le délai d'ignition de mélanges non comprimés contenant le perchlorate d'ammonium et des métaux.
Les résultats expérimentaux montrent que les additifs les plus valides pour faciliter la combustion du perchlorate d'ammonium sont les métaux légers et le titanium; une influence particulière est due à Cu_2O et au cuivre réduit. L'effet du dernier est encore plus sensible si l'on opère sous pression: dans ces conditions un mélange comprimé du comburant avec le cuivre réduit brûle très rapidement dans une atmosphère soit d'hydrogène soit d'azote. L'aluminium et le magnésium résultent, au contraire, bien plus efficaces que le cuivre réduit pour diminuer le délai d'ignition de propergols composites contenant le perchlorate d'ammonium et un métal.
Les mésures de vitesse linéaire de régression ont été effectuées dans un dispositif qui rappelle la bombe Crawford; les expériences relatives au délai d'ignition ont été réalisées à travers une cellule photoélectrique.

LISTE DES SYMBOLES

AP	perchlorate d'ammonium NH_4ClO_4
LiP	perchlorate de lithium $LiClO_4$
P	pression relative (atm)
Q	débit volumétrique (lm^{-1})
V	vitesse linéaire de régression (mm/sec^{-1})
X	$\frac{\text{poids métal}}{\text{poids comburant}} \times 100$
α	$\frac{\text{débit gaz diluant}}{\text{débit gaz diluant + débit gaz combustible}} \times 100$
τ	délai d'ignition (10^{-2} sec)

L'IMPORTANCE des propergols composites dans le domaine de la propulsion justifie les nombreux études dédiés aux comburants solides pendant ces dernières années. En général on utilise comme oxydants des sels cristallines (nitrates et perchlorates) d'éléments chimiques ayant un poids moléculaire pas élévé.
Le perchlorate d'ammonium NH_4ClO_4 (que nous indiquerons en suite plus brièvement par le sigle AP) est actuellement le comburant le plus employé et par conséquent le plus étudié. Cela dépend aussi du fait que AP manifeste des propriétés bien particulières et que l'étude en laboratoire de tel perchlorate résulte moins difficulteux que pour d'autres comburants.
Puisque AP brûle sans laisser des résidus, il peut être facilement employé comme oxydant solide dans un processus de combustion hybride. La vitesse de régression de l'oxydant est dans ce dernier cas un paramètre fondamental pour le projet; en outre cette vitesse influence de façon remarquable la thermodynamique de la combustion puisqu'elle détermine la richesse du mélange et donc la température de la flamme, une fois choisi le débit de combustible.
La vitesse de décomposition de AP a fait l'objet d'une attention spéciale. Dans les laboratoires de l'ONERA (1) (2) (3) on a mesuré la vitesse de combustion de sphères de AP placées dans un écoulement gazeux combustible, en considérant ce modèle le plus convenable pour représenter la combustion réelle d'une poudre composite. En effet on peut assimiler les cristaux de AP à des sphères très petites se découvrant d'une manière progressive pendant que le combustible servant comme liant pyrolyse.
D'autres rechercheurs ont examiné la vitesse de pyrolyse (4) (5) ou de déflagration (6) (7) (8) (9) (10) (11) de AP dans la convinction que la vitesse de combustion du même est contrôlée respectivement par le processus de pyrolyse ou déflagration. Enfin la vitesse de combustion des poudres composites basées sur AP a été étudiée directement (12) (13) (14) (15) (16) (17) (18).
Toutefois la compréhension des complexes phénomènes qui se rattachent à la combustion de AP a demandé un remarquable effort pour la connaissance des propriétés de base du perchlorate, en particulier pour ce qui concerne le comportement de AP au chauffage (19) (20) (21) (22) (23) (24). On a étudié aussi l'influence de la presence de différents additifs qui catalysent les réactions de décomposition thermique (25) (26) (27) (28) (29) (30) (31) (32) et d'ignition (31) (32) (33) (34).
En général la recherche relative à AP est essentiellement expérimentale et a suivi jusqu'à ce moment deux directions principales:
- détermination directe des paramètres concernant la combustion de AP pur ou en mélange dans des poudres composites;
- étude des propriétés physico-chimiques de AP.

Le premier point de vue emmène à des résultats intéressant la technologie de la propulsion par fusées, le deuxième point de vue a surtout pour but de proposer des modèles qui expliquent ces résultats et puissent prévoir les comportements de AP dans des différentes conditions opératoires. D'autre côté des traitaisons mathématiques de la combustion de comburants ont été aussi essayées (8) (12) (35), mais elles ne semblent pas avoir complètement résolu le problème.
Le présent travail, en considèrant l'importance future de la propulsion hybride et l'actualité des poudres composites, a été développé selon le prenier point de vue.
Nos mesures se rapportent surtout à la vitesse linéaire de régression d'échantillons de AP, purs ou contenant différents additifs, placés dans un écoulement gazeux combustible. Les expériences ont été donc faites selon le modèle utilisé chez les laboratoires de l'ONERA, c'est à dire en conditions dynamiques plutôt que statiques, bien que les mesures soient effectuées selon le système mis au point par Crawford (36) pour la bombe omonyme.

DISPOSITION EXPERIMENTALE

Les mesures sont effectuées en plaçant les échantillons de AP à l'interieur d'un réacteur aux parois transparents dans lequel on envoie le gaz combustible. L'ignition est donnée par un fil chauffé électriquement.
Le circuit pneumatique de l'installation est rapporté dans la fig. 1. Le réacteur, en acier inoxydable, est constitué par deux flanges simétriques renfermant un cylindre en pyrex (fig. 2). Les spécimens sont soutenus par des supports en pyrex.
Les échantillons de comburant sont des cylindres obtenus par compression de particules précédemment pulverisées. Pour que la combustion soit "à sigarette", c'est à dire par surfaces parallèles, les cylindres sont enrobés latéralement par un inhibiteur. Enfin les échantillons sont percés diametralement pour loger les fils de repère.
Pour ce qui concerne les autres détails de la disposition expérimentale voir (37) (38) (39).
La vitesse linéaire de régression est déterminée par le temps nécessaire pour brûler la longueur de l'échantillon comprise entre les deux repères.
Le perchlorate d'ammonium est fourni par B.D.H. avec un titre pas inferieur au 99% les principales impuretés en étant SO_4 (0,02%), Cl (0,01%), Fe (0,001%), Pb (0,001%); les gaz purs sont fournis par S.I.O.; les poudres métalliques, les catalyseurs de la décomposition thermique de AP et tout autre réactif sont fournis par C. Erba.

La partie électrique et les systèmes électroniques de mesure ont été mis au point par le group électronique du C.N.P.M.

TECHNIQUE EXPERIMENTALE

On mesure la vitesse linéaire de régression, définie comme la vitesse à laquelle la surface de combustion bouge en direction perpendiculaire à elle-même, dans le cas des spécimens inhibés latéralement. Au contraire, si la surface latérale de l'échantillon participait elle aussi aux réactions de redox, la mesure se rapporterait plutôt à la vitesse de combustion, définie comme la vitesse de propagation de la réaction chimique entre le comburant solide et le combustible gazeux. La surface de réaction est plate dans le cas de vitesse linéaire de régression, tandis qu'elle est conique dans le cas de vitesse de combustion. Cela explique l'importance de l'inhibition latérale à la combustion et des petites sections transversales des spécimens (compatiblement avec la possibilité de réaliser par compression les cylindres). Il a paru nécessaire avant tout d'établir le type et la quantité d'inhibiteur à employer pourqu'on puisse mesurer des vitesses linéaires de régression d'un côté et pour ne pas influencer le procés de combustion d'autre côté. Ces expériences ont été faites en fixant le débit de gaz combustible.
La géometrie des échantillons a été le deuxième paramètre pris en consideration: on a réalisé des cylindres ayant différents diamètres Ø = 6, 8, 10, 13 mm et on a examiné l'effet sur la vitesse linéaire de régression en fonction du débit de gaz, ayant choisi pour chaque série d'expériences une certaine valeur du diamètre des spécimens. Dans la même façon on a déterminé l'effet de la granulométrie des poudres de AP. Après ces expériences préliminaires on a étudié la loi de la vitesse linéaire de régression en fonction du débit de gaz combustible (c'est à dire de sa vitesse), de la nature du gaz combustible (H_2 et les hydrocarbures CH_4, C_2H_4, C_2H_6 et C_3H_8) et de la dilution de ce dernier avec azote.
L'effet de la présence de poudres métalliques (Al, B, Be, Mg, Cd, Cu, Fe, Mn, Ti et Zn) ou de catalyseurs de la décomposition thermique de AP (charbon et oxydes de Al, Ca, Cd, Co, Cu, Fe, Mn et Ni) est déterminé en considerant soit la nature de l'additif (les spécimens contiennent un pourcentage fixe de l'1% par rapport au seul comburant) soit le pourcentage du même (1%, 5%, 10%, 15%). En outre on a consideré aussi l'état de la surface de l'additif et la addition d'autres comburants à AP (mélange avec $LiClO_4$). Toutes ces expériences on été faites à la pression atmosphérique et en conditions dynamiques, c'est à dire dans un écoulement continu de gaz combustible.
Enfin on a étudié l'influence de la pression sur la vitesse linéaire de régression de AP, mais en conditions statiques. D'autres résultats concernent l'ignition de mélanges non comprimés contenant AP.

RESULTATS ET DISCUSSIONS

Les résultats sont généralement illustrés par des graphiques qui rapportent la vitesse linéaire de régression V des échantillons en fonction du débit Q du gaz combustible. La vitesse linéaire de régression V est exprimée en mm/sec; le débit Q de gaz combustible en l/m.

NATURE ET EPAISSEUR DE L'INHIBITEUR de combustion. Les figg. 3 et 4 rapportent la vitesse linéaire de régression V en fonction de l'épaisseur S en mm d'inhibiteur. On a employé comme inhibiteurs le satoflan (fig. 3), un type de teflon non synthérisé, et le teflon (fig. 4). Le débit de gaz combustible est constant: on a examiné le cas d'un débit de 3 l/m de H_2 (courbe a) et le cas d'un débit de 3 l/m de H_2 dilué avec 3 l/m de N_2 (courbe b).
La vitesse V diminue toujours lorsque l'épaisseur S augmente: cette diminution est plus rapide quand on utilise le teflon. Puisque dans le cas du teflon les deux lignes se rapprochent, cela signifie que l'inhibiteur influence les réactions de redox en déterminant la vitesse linéaire de régression par sa propre vitesse d'ablation. Au contraire, à condition d'éviter de trop faibles épaisseurs que d'ailleurs il ne faut pas employer si l'on mesure des vitesses linéaires de régression, le satoflan ne modifie pas le procès de combustion. Pour toutes les expériences suivantes on a donc utilisé le satoflan comme inhibiteur.

DEBIT DU GAZ COMBUSTIBLE. Les résultats sont rapportés dans les figg. 5 (courbe a et b) et 11 (courbe a, b et c), relatives respectivement à l'emploi comme combustible de H_2, CH_4, C_2H_6 et C_3H_8.
En général on peut remarquer une loi de la vitesse V croissante avec le débit Q de gaz jusqu'à un point de maximum: au delà de ce point la vitesse V diminue lentement. En effet, après la valeur du débit de combustible optimum pour obtenir le maximum de V, l'excès de débit de gaz ne pourra qu'augmenter la diffusion de chaleur loin de la flamme. La zone stationnaire autour du point de maximum est très étendue dans le cas de H_2 et cela probablement dépend des excès locaux de débit dus à la facilité de diffusion du gaz dans la flamme. Le type de courbe indique que le phénomène de transport de masse borne la vitesse V aux basses valeurs du débit de gaz, tandis que le phénomène chimique de redox borne pour les valeurs élévées de débit de gaz.
En tout cas les courbes ainsi trouvées sont très semblables à celle qui exprime la vitesse de combustion d'un propergol composite, constitué par AP et polystirène,

en fonction du pourcentage en poids de polystirène (15). Cette analogie semble prouver que pour AP c'est le comburant qui détermine la loi de combustion si bien dans un propergol composite que dans un processus hybride.

GRANULOMETRIE DES POUDRES DE AP. En général la diminution des dimensions moyennes des poudres et donc l'augmentation de la surface réactive permet une plus grande vitesse de réaction dans tous les procès physico-chimiques.
La fig. 6 illustre les résultats obtenus dans nos laboratoires à propos de l'influence de la granulométrie des poudres de AP sur la vitesse linéaire de régression des échantillons de ce comburant. On a étudié trois types de poudres: type gros (courbe c), type moyen (courbe b) type fin (courbe a). Les particules de type gros passent à travèrs un tamis avec 750 mailles/cm^2 et sont retenues par un tamis avec 1600 mailles/cm^2; les particules de type moyen passent à 1600 mailles/cm^2 et sont retenues à 6400 mailles/cm^2; les particules de type fin passent à travèrs un tamis avec 6400 mailles/cm^2.
Les courbes de la fig. 6 se présentent moins douces par rapport à celle de la fig. 5 (courbe a) relative à des spécimens dont la granulométrie n'a pas été contrôlée. Il est intéressant de noter que les courbes de la fig. 6 ont toutes le même aspect: en particulier la loi linéaire dans le domaine des forts débits est bien caractéristique. En tout cas la diminution des dimensions moyennes favorise clairement la vitesse linéaire de régression, au moins dans le domaine des granulométries expérimentées, bien que l'accroissement des valeurs de vitesse ne soit pas très sensible. Par rapport à la courbe a de la fig. 5 on obtient toujours une amélioration, à part le domaine des grands débits pour les poudres de type gros.
McAlevy III et Lee (40) ont trouvé des courbes tout à fait semblables en employant la technique du lit poreux et en utilisant méthane comme gaz combustible.

NATURE DES POUDRES METALLIQUES. La présence de poudres métalliques dans un propergol est un moyen très utilisé dans la technologie de la propulsion pour élever les valeurs de la température de combustion et donc de l'impulse spécifique. Mais les metaux peuvent présenter d'autres effets positifs: par exemple l'aluminium diminue dans certaines limites l'instabilité de combustion de propergol solides (41) et ses composés peuvent soit faciliter l'ignition de particuliers mélanges (42) soit prolonger la vie de spéciales suspensions hypergoliques (43). En tout cas les poudres métalliques augmentent la densité des propergols et permettent ainsi des économies de poids et de volume dans les structures du vecteur. D'autre côté les produits d'oxydation des metaux ont un poids moléculaire relativement élévé et donc provoquent un effet negatif sur l'impulse spécifique.
Les métaux essayés sont: Al, B, Be et Mg (fig. 7); Cu électrolytique, Fe et Mn (fig. 8); Cd, Mo, Ni et Ti (fig. 9) et Zn (courbe a de la fig. 10). La quantité ajoutée est toujours de l'1% par rapport à la masse du seul AP. Les échantillons sont préparés en mélangeant avant la compression les particules de AP et des métaux bien pulverisées.
On remarque de la fig. 7 que le type de la courbe V, Q est le même pour tous les métaux légers et est caractérisé par une brusque discontinuité de V. En comparaison de la courbe a de la fig. 5 concernant AP pur on note que Al, B et Be comportent une générale augmentation de V, pendant que la présence de Mg provoquent une légère augmentation seulement pour les valeurs élévées de débit de combustible.
Le type de la courbe relative à Cu électrolytique, Fe et Mn résulte de la fig. 8 tout à fait différent: il n'y a pas de discontinuités et les valeurs de V augmentent faiblement avec le débit de gaz. En comparaison de la courbe a de la fig. 5 on observe que Fe et surtout Cu électrolytique permettent un gain de vitesse dans toute la région explorée, pendant que Mn augmente les valeurs de V seulement dans le domaine des faibles débits gazeux.
La fig. 9 montre que les courbes relatives à Mo et Ni sont pratiquement les mêmes et que l'effet de leur présence sur la vitesse linéaire de régression est négligible, tandis que Ti favorise la vitesse V dans toute la région des débits de gaz. Il est intéressant de noter que la courbe AP + 1% Ti est qualitativement la même que celle concernant AP pur: cela signifie que Ti accélère la vitesse linéaire de régression indépendamment du gaz combustible. La courbe AP + 1% Cd part elle aussi d'une manière ripide mais en suite elle se stabilise. En tout cas Cd aussi permet un gain de V, surtout dans le domaine des faibles débits.
Dans la fig. 10 (courbe a) est rapportée la courbe relative à l'addition de Zn: on remarque que la présence de l'1% de Zn n'a pas une sensible influence sur la vitesse linéaire de régression.
En conclusion les métaux peuvent soit faciliter la vitesse linéaire de régression dans tout le domaine des débits (Ti, Al, B) soit aplatir la courbe V, Q (Fe, Mn, Cu électrolytique).
Dans le premier cas les métaux agissent directement sur la décomposition thermique du comburant en la favorisant. Dans le deuxième cas ils imposent une nouvelle vitesse limite pratiquement indépendante du débit de combustible. En considérant que les métaux influencent pas seulement la vitesse linéaire de régression et la température de combustion, mais aussi le poids moléculaire moyen des produits de réaction, on peut retenir que Be et Al sont les additifs métalliques les plus auspicables. Cependant Ti peut être considéré compétitif avec les métaux légers.

NATURE DU GAZ COMBUSTIBLE. L'effet de la nature du gaz combustible concerne les valeurs quantitatives de la vitesse V plutôt que l'aspect des courbes, comme on peut voir dans les figg. 5 (courbe a et b) et 11. En tout cas à la courbe bien marquée, dans le sens ci-dessus spécifié, relative à H_2 s'opposent les courbes bien moins marquées des autres gaz combustibles. Bien que chaque gaz ait sa propre courbe V, Q, quantitativement aussi la différence entre les valeurs de vitesse linéaire de régression dues à H_2 et aux autres combustibles est sensible.
Une difference analogue a été trouvée par Barrère et Nadaud (2) (3) pour la combustion de sphères de AP dans un écoulement gazeux combustible. La loi qui exprime la variation du diamètre d des sphères en fonction du temps t est:

$$d^n = d_o^n - kt$$

où d_o est le diamètre initiale des sphères, k une constant qui dépend de plusieurs paramètres opératoires, n est un coefficient qui change avec la nature du combustible et qui vaut 2 pour CH_4, C_3H_8 et NH_3 et 3 pour H_2. Donc la loi exponentielle de variation du diamètre en fonction du temps est supérieure d'un ordre de grandeur dans le cas de H_2.
La vitesse de diffusion de H_2 pourrait expliquer la plus grande rapidité de combustion de AP avec H_2 plutôt qu'avec les autres gaz. Les résultats obtenus pourraient en outre être expliqués par la flamme très caloriphique de l'hydrogène, ce qui ferait penser à une plus grande diffusion de chaleur de la flamme vers la surface de l'échantillon dans le cas de H_2 et par conséquent à une plus élévée température de surface et débit massique de comburant. Mais cette hypothèse est à repousser du moment que la température de surface de AP (500°C) est indépendante de la nature du gaz combustible (44) (45) (46).
Le processus à vitesse limite est donc situé en phase gazeuse et concerne probablement l'oxydation du gaz combustible par les produits de décomposition de $HClO_4$ contenu en AP. En effet l'influence de la nature du gaz combustible sur la vitesse linéaire de régression ne supporte pas l'idée que le processus à vitesse limite puisse consister dans une flamme de décomposition NH_3 + $HClO_4$ du perchlorate d'ammonium. Ce résultat est d'ailleurs confirmé par d'autres expériences conduites sur des propellants composites contenant AP (47).
On sait d'autre côté que la combustion de H_2 suit un processus en chaîne qui demande la présence des radicaux OH et des atoms O et H, pendant que la combustion de tous les hydrocarbures ne présente pas de grandes différences si la valeur de pression n'est pas trop élévée. En tout cas l'oxydation des hydrocarbures paraffiniques en phase gazeuse suit le mécanisme en chaîne de CH_4, qui demande lui aussi l'existence de radicaux et dont la formation de CH_3 constitue le passage principale. En outre les hydrocarbures avec un poids moléculaire élévé peuvent dégrader vers les hydrocarbures avec un poids moléculaire inférieur en donnant origine au radical méthylique. En conclusion les vitesses linéaires de régression de AP dans un écoulement d'hydrocarbures ne peuvent pas avoir de grandes différences.
La fig. 12 montre qu'avec des échantillons de AP + 1% Zn on trouve des résultats tout à fait analogues. La combustion dans un écoulement de propane a présenté des grandes difficultés d'ignition et des fortes instabilités de flamme. En tout cas les différences dues à l'emploi des combustibles sont les mêmes pour les spécimens de AP pur et de AP + 1% Zn.

DILUTION DU GAZ COMBUSTIBLE. Dans la fig. 13 (courbe a) est rapportée la courbe relative à l'emploi comme gaz combustible de H_2 dilué avec N_2. Définissons un paramètre α comme le pourcentage volumétrique d'azote par rapport au volume totale des gaz: par example Q=2 l/m et α = 50% signifient que l'écoulement gazeux est constitué par 2 l/m de H_2 et 2 l/m de N_2. Le symbole Q indique toujours le débit du seul gaz combustible.
Le type qualitative de la courbe est toujours le même, mais on remarque un effet inhibiteur sur la vitesse linéaire de régression, dû à la présence de N_2, sensible dans tout le domaine exploré de débits. On a trouvé des résultats semblables avec méthane et propane. Même en présence de N_2, le combustible le plus réactif est l'hydrogène. En effet la combustion de AP a lieu dans un écoulement de H_2 jusqu'à α = 75% sans aucune anomalie. Au contraire la combustion est instable pour α = 75% en méthane et pour α = 50% en propane.
L'effet inhibiteur de la dilution du gaz combustible sur la vitesse linéaire de régression est bien clair aussi pour des échantillons de AP + 1% Zn (courbe b de la fig. 10, α = 50%) même si qualitativement la loi V, Q ne change pas en comparaison de l'hydrogène pur. On remarquera que la présence de Zn n'apporte de sensibles modifications des valeurs de V ni dans un écoulement combustible pur (courbe a de la fig. 10) ni dans un écoulement dilué.

GEOMETRIE DES ECHANTILLONS. On a rapporté dans la fig. 13 les courbes V, Q concernant la combustion des échantillons de AP ayant un différent diamètre ϕ dans un écoulement d'hydrogène dilué dans l'azote (α = 50%). Les cylindres ont été inhibés de façon que le rapport entre l'épaisseur d'inhibiteur et le diamètre du spécimen soit constant. La courbe a est relative à ϕ = 6 mm, la courbe b à ϕ = 8 mm, la courbe c à ϕ = 10 mm et la courbe d à ϕ = 13 mm.
On remarque que l'augmentation du diamètre des échantillons provoque une diminution de la vitesse linéaire de régression. La courbe d manifeste une loi croissante

plus forte que dans les autres cas, mais cela peut dépendre du système employé pour les mesures. En effet l'importance de la section transversale pour ϕ = 13 mm détermine aux grands débits de gaz une surface de combustion plutôt conique. Il en suit que la fusion du deuxième repère est avancée par rapport à la fusion du premier repère, qui a lieu lorsque la surface de combustion est encore plate. Des résultats semblables ont été obtenus pour des échantillons ayant ϕ = 6 mm (courbe b de la fig. 5) et ϕ = 13 mm (courbe c de la fig. 5) dans un écoulement de CH_4.

NATURE DES CATALYSEURS DE LA DECOMPOSITION THERMIQUE DE AP. Le perchlorate d'ammonium manifeste deux différents mécanismes de réaction (20) (21) lorsque il est chauffé dans le vide:

- aux basses températures (< 280°C) AP se décompose à travers un procès de surface se bornant au 20%-30% de la masse initiale et laissant un résidu chimiquement identique au produit mis à réagir mais avec une densité inférieure;
- aux températures plus élévées (≥ 380°C) AP se décompose totalement à travers un procès de disgrégation pénétrant à l'intérieur de chaque cristal. En tout cas un procès de sublimation est toujours présent pendant la décomposition thermique de AP.

Généralement l'étude expérimental des catalyseurs est limité par les rechercheurs aux températures inférieures à 300°C (décomposition thermique de la basse température) pour éviter des phénomènes trop rapides et donc impossible à suivre en laboratoire. La présence des catalyseurs (ce terme est généralement employé pour entendre un accélérateur de la décomposition thermique du perchlorate) peut changer radicalement la cinétique et les procès de réaction, en modifiant ainsi la quantité de solide décomposé et la vitesse de décomposition. Par consequent les produits de réaction changent et la sublimation aussi est influencée (elle disparaît si la décomposition thermique est trop rapide). De toute façon il ne faut pas croire que l'addition des catalyseurs provoque des effets pareilles sur la décomposition thermique et la combustion de AP, puisque les passages à vitesse limite sont differents dans les deux cas.

Les substances les plus employées comme catalyseur sont des oxydes métalliques. Nous avons expérimenté dans nos laboratoires l'effet de l'addition de CaO, Cu_2O, CuO et Fe_2O_3 (fig. 14); Al_2O_3, MnO_2 et Ni oxyde (fig. 15) et CdO, Co_3O_4 et Co oxyde noir (fig. 16). Le pourcentage en poids des catalyseurs ajouté est toujours 1% par rapport au seul AP. Les échantillons sont réalisés en mélangeant avant la compression les particules bien pulverisées de AP et des catalyseurs.

On observe de la fig. 14 que CaO (courbe b) et CuO (courbe c) favorisent la combustion de AP dans le domaine des faibles débits de gaz combustible, pendant que Fe_2O_3 (courbe d) ne change pas d'une façon sensible la loi V, Q. Au contraire Cu_2O (courbe a) manifeste une considérable action catalytique dans toute la région explorée des débits gazeux. On sait d'autre côté que CaO ne facilite pas la décomposition thermique de AP (20) et qu'en diminue la sublimation (22), alors que Fe_2O_3 favorise légèrement la décomposition thermique (20). D'ailleurs les oxydes Cu_2O (29) et CuO (30) sont tous les deux des énergiques catalyseurs de la décomposition thermique de AP. Les courbes V, Q concernant l'addition des métaux montrent que Fe (courbe a de la fig. 8) augmente la vitesse linéaire de régression des spécimens oxydants de façon bien plus sensible que l'oxyde correspondant, tandis que Cu électrolytique (courbe b de la fig. 8) ne facilite pas la combustion de AP dans la même mesure que Cu_2O, bien qu'il soit plus efficace que CuO.

La fig. 15 montre que la présence de l'1% de Ni oxyde (courbe a) explique un certain effet positif sur la vitesse linéaire de régression de AP, pendant que MnO_2 (courbe b) accélère légèrement la combustion et qu'Al_2O_3 (courbe c) n'apporte pas de grandes variations. D'autre côté MnO_2 est connu comme un des catalyseurs les plus valides de la décomposition thermique du perchlorate (20) (28), alors que Al_2O_3 n'a absolument aucun effet. Au contraire on a vu que Al (courbe b de la fig. 7) augmente clairement la vitesse linéaire de régression de AP pendant que Ni (courbe d de la fig. 9) et Mn (courbe d de la fig. 8) n'apportent pas de grandes modifications.

Pour les oxydes de Co aussi (courbes a et b de la fig. 16) les variations sont peu sensibles, bien qu'ils décomposent (28) rapidement AP même aux basses températures. Il résulte en outre que CdO (courbe c de la fig. 16) comporte une réduction de vitesse linéaire de régression pour les forts débits de combustible. D'autre côté CdO (31) favorise légèrement la décomposition thermique et Cd influence d'une manière assez considérable la vitesse linéaire de régression (courbe b de la fig.9). L'addition des poudres métalliques se révèle donc plus convenable que l'addition des catalyseurs de la décomposition thermique du perchlorate pour favoriser la vitesse linéaire de régression des spécimens de AP dans un écoulement gazeux combustible. En effet les temps d'induction pour les réactions de décomposition catalytique sont en général trop longs par rapport à l'extrême rapidité des phénomènes de combustion et donc la réaction de décomposition ne peut pas avoir une trop grande importance dans le mécanisme de redox.

Pendant que l'effet positif des catalyseurs dépend seulement des propriétés chimiques de AP et des oxydes, l'action favorable des poudres métalliques est due à des phénomènes physiques concernant les procès de combustion des métaux. De toute façon les additifs modifient le mécanisme de combustion de AP soit en phase gazeuse soit en phase solide, puisque ils changent d'un côté les produits de combustion et

d'autre côté la vitesse linéaire de régression.
En conclusion l'addition des poudres métalliques est plus avantageux par rapport aux catalyseurs, à part Cu_2O, en considérant que les métaux permettent un gain pas seulement sur la vitesse linéaire de régression mais aussi sur l'impulse spécifique.

ETAT DE LA SURFACE DE L'ADDITIF. Dans la fig. 8 (courbe a) est représentée la courbe V, Q concernant l'addition de Cu réduit, c'est à dire de particules métalliques ayant une surface de réaction très extendue, au perchlorate d'ammonium dans le pourcentage de 1'1% en poids par rapport à la masse du seul comburant. On note que la vitesse linéaire de régression augmente d'une façon sensible dans tout le domaine des débits gazeux par rapport aux échantillons soit de AP + 1% Cu électrolytique (courbe b de la fig. 8) soit de AP + 1% Cu_2O (courbe a de la fig. 14), qui était jusqu'à ce moment l'additif le plus valable. Il est intéressant de remarquer que les types de courbes concernant Cu réduit (courbe a) et Cu électrolytique (courbe b) sont différents et qu'en particulier la courbe AP + 1% Cu réduit ressemble au type de AP pur (courbe a de la fig. 5). Cela indique que Cu réduit favorise la combustion en agissant directement sur la décomposition thermique de AP: en effet on peut penser que les particules métalliques, ayant une grande valeur du rapport surface de réaction spécifique au volume, constituent des centres actifs particulièrement efficaces pour le mécanisme de décomposition à température élevée du perchlorate.
D'autre côté Cu électrolytique, Cu_2O et Cu réduit spécialement facilitent l'ignition des spécimens en diminuant sensiblement la puissance électrique nécessaire. Cela prouve la générale activité catalytique du cuivre.

POURCENTAGE DES ADDITIFS. Nous avons examiné expérimentalement l'influence du pourcentage de certains additifs sur la vitesse linéaire de régression du perchlorate d'ammonium. Les additifs pris en considération sont: Ni (fig.17), Cu réduit (fig. 18) et le charbon C (fig. 19), qui est connu lui aussi comme un catalyseur de la décomposition thermique de AP (26). Les pourcentages essayés, toujours définis comme rapport entre les poids de l'additif et du comburant, sont: 1%, 5% et 10%; pour Ni on a examiné le cas 15% aussi.
Dans la fig. 17 sont représentées les courbes relatives à l'addition d'un pourcentage variable de Ni; la courbe AP + 1% Ni est caracterisée par une discontinuité qui pourrait dépendre du système employé pour les mesures. On remarquera quand-même que, en augmentant le pourcentage de Ni, la vitesse linéaire de régression croît avec une certaine régularité. Le mélange AP + Cu réduit (fig. 18) présente le maximum de rapidité de combustion.
En considérant la facilité d'ignition du mélange et l'aspect très soutenu de la flamme bien différent des autres flammes de diffusion, on a pensé que AP + Cu réduit puisse brûler indépendamment du gaz combustible comme un propellant solide composite. On a donc fait brûler des échantillons dans un milieu d'azote, ce gaz servant pour pressuriser la chambre de combustion et aussi pour avoir une atmosphère complètement inerte. A la pression atmosphérique les spécimens de AP + 15% Cu réduit, dans les mêmes conditions opératoires que pour les mesures dans un écoulement gazeux combustible, brûlent rapidement et l'ignition ne présente aucune difficulté. La vitesse linéaire de régression dépend maintenant du débit d'azote: elle diminue lorsque le débit augmente, puisque un grand débit d'azote favorise la diffusion d'énergie thermique loin de la flamme(une valeur indicative pourrait être V = 2-3 mm/sec).
Au contraire la combustion du mélange AP + 10% Cu réduit à la pression d'une atmosphère d'azote n'est pas très stable et demande en tout cas une ignition prolongée et avec une forte puissance électrique.
A propos du mélange AP + C (fig. 1) on notera que la deuxième partie de la courbe AP + 1% C répète celle concernant AP pur (courbe a de la fig. 5), tandis que la première partie est pratiquement indépendante de débit de gaz et permet un gain de vitesse V par rapport au perchlorate pur. En effet aux forts débits de combustible le spécimen de comburant, étant donnée la très petite quantité de charbon ajouté, se comporte comme s'il était AP pur. Aux faibles débits du combustible gazeux, au contraire, l'importance en poids du combustible solide croît et on peut penser à un phénomène de collaboration entre charbon et hydrogène, qui comporte un plus grand débit massique de combustible et donc une vitesse linéaire de régression plus élévée par rapport à AP pur.
En augmentant le pourcentage de charbon contenu dans l'oxydant la vitesse V croît régulièrement et les courbes deviennent de plus en plus plâtes. En effet la quantité de combustible solide diminue de plus en plus l'effet du combustible gazeux: si pour AP + 1% C l'influence de débit d'hydrogène est bien claire dans la deuxième partie de la courbe, pour AP + 5% C cette influence est à peine visible et pour AP + 10% C elle disparaît complètement. Cela signifie que le mélange AP + C a la tendence à se comporter comme un propellant solide composite et donc de manière indépendante du débit de gaz.
En conclusion en augmentant le pourcentage des additifs la vitesse linéaire de régression généralement croît, parfois de façon très considérable (voir Cu réduit). Il faut remarquer que le pourcentage de l'additif influence pas seulement les valeurs numériques de vitesse mais aussi la loi qualitative V, Q d'un même mélange. Enfin en augmentant le pourcentage de l'additif quelque mélange se comporte comme un propellant solide déjà à la pression atmosphérique.

ADDITION DE $LiClO_4$. Le perchlorate de lithium $LiClO_4$, malgré les inconvenients d'un prix élévé et d'une forte hygroscopicité, intéresse beaucoup la technologie de la propulsion merci à son contenu d'oxygène et à sa densité. On a donc mesuré la vitesse linéaire de régression du perchlorate de lithium (que nous indiquerons brièvement par le single LiP) mélangé au perchlorate d'ammonium. En considérant la difficulté d'ignition de tels mélanges, on a ajouté un certain pourcentage de Cu réduit (fig. 20), que nous avons trouvé faciliter la combustion de AP, et de CuO (fig. 21), qui est connu comme un accélérateur de la décomposition thermique de LiP (48). Le pourcentage de l'additif est maintenant défini comme le rapport en poids entre l'additif et le mélange des perchlorates.
La courbe a de la fig. 20 concerne l'addition du 5% de Cu réduit à un mélange qui contient en poids une partie de AP contre deux parties de LiP (1 AP + 2 LiP): ce mélange est très proche à la composition eutectique des comburants (49). On voit de la courbe b de la fig. 18 le fort effet inhibiteur sur la vitesse V dû à l'addition de LiP; de la courbe a de la fig. 5 il résulte une certaine influence négative même par rapport à AP pur, malgré la présence du 5% de Cu réduit. Si l'on augmente la quantité de AP par rapport à LiP (2 AP + 1 LiP) tout en gardant le pourcentage du 5% de Cu réduit, on observe (courbe b) que la loi V, Q est pratiquement la même. En diminuant à tel mélange la quantité de l'additif (courbe c), toute la courbe se baisse légèrement. L'addition de CuO (fig. 21) semble favoriser la combustion des mélanges à fort contenu de LiP (courbe a) et laisse pratiquement inaltéré le mélange 2 AP + 1 LiP (courbe b).
Il résulte en général qu'aux forts débits d'hydrogène les mélanges oxydants riches en LiP (1 AP + 2 LiP) ont une combustion plus rapide que les mélanges riches en AP; le contraire arrive pour les faibles débits de combustible. Naturellement tout cela vaut dans les limites des petites variations de vitesse qu'on a pu observer. Il faut remarquer qu'il n'a pas été possible de brûler des échantillons de LiP pur dans un courant d'hydrogène: on a obtenu au maximum, après des allumages très difficulteuses, quelques flammelets qui disparaissent immédiatement une fois qu'on a perdu le contact entre le fil chauffant et la surface de réaction. La grande quantité de chaleur nécessaire pour l'ignition de LiP par rapport à celle de AP s'explique par la présence d'une phase liquide qui n'existe pas dans le cas de AP et par la température relativement élévée à la quelle LiP très pur commence à se décomposer (≈ 450°C).

INFLUENCE DE LA PRESSION. Les essais sous pression, tout en gardant le circuit pneumatique de la fig. 1, ont été faits dans une chambre de combustion en acier inoxydable avec des hublots pour la vision directe du phénomène.
La pression est mesurée électroniquement par un capteur à quartz, à haute vitesse de réponse, refroidis par un courant d'eau (fig. 22). La charge électrique fournie par le capteur est proportionnelle à la pression dans la chambre de combustion et est transformée dans un signal de tension. Ce signal est successivement amplifié avec un grain variable par moyen d'un amplificateur verticale qui constitue le premier canal verticale du tube cathodique. Au deuxième canal du tube cathodique, au contraire, sont envoyés des impulses pour marquer le temps dont l'interval est mesuré par un compteur électronique à I MHz, c'est à dire avec une précision de 1 microseconde sur 1 minute. La base des temps de l'oscilloscope est substituée par un autre amplificateur piloté par un générateur de balayage très lent (balayage maximum 1 minute). Le balayage est commandé manuellement à l'extérieur. Le tube cathodique est du type à memnoscope. La courbe obtenue est tout d'abord memorisée sur l'ecran du tube et après elle est photographiée par une polaroid land camera. La calibration générale du système est effectuée par une balance manométrique à haute précision (10^{-4} atm) avant de commencer les essais.
Le domaine des pressions explorées arrive jusqu'à 10 atm: les expériences sont maintenant conduites statiquement et non plus dans un courant continu de gaz combustible. Une valve reductrice de pression, qui précède immédiatement la chambre de combustion, permet de garder une pression constante pendant la durée du phénomène de redox. Pour ce qui concerne les autres variables opératoires tout a été fait comme dans les expériences en conditions dynamiques. Les résultats sont illustrés dans les figg. 23 et 24, qui rapportent la vitesse linéaire de régression V en mm/sec des spécimens comprimés en fonction de la pression relative P en atm. La pression comporte une augmentation de la vitesse V qui n'est pas très sensible pour AP et AP+1% Zn(fig.23) et qui résulte au contraire bien considérable pour Cu réduit (fig.24). Dans ce dernier cas on peut observer que la pression accentue de façon remarquable l'effet du pourcentage: pour le mélange AP + 15% Cu réduit et une valeur de pression p > 5 atm l'ordre de grandeur de V est de plusieurs dizaines de mm/sec. Cela montre encore une fois la validité de Cu réduit comme accélérateur de la combustion de AP, en considérant aussi que des essais sur des échantillons contenant des pourcentages variables de différents additifs ont donné des résultats très semblables soit qualitativement soit quantitativement à ceux de la fig. 26: les courbes n'ont pas été représentées pour eviter la superposition des lignes. Puisque, au contraire, la présence de Cu_2O permet un gain de vitesse linéaire de régression très sensible même à la pression atmosphérique, on peut affirmer, sur la base des connaissances bibliographiques aussi (30) (32) (50), la générale activité accélératrice du cuivre et de ses composés.
On a essayé en outre la combustion de AP + Cu réduit comme propergol solide composite en employant azote comme gaz de pressurisation Les mélanges AP + 15% Cu réduit

et AP + 5% Cu réduit brûlent à peu près à la même vitesse dans une atmosphère si bien d'hydrogène que d'azote, mais la dispersion des valeurs expérimentales dans ce dernier cas est sensible. Il faut noter que AP + 5% Cu réduit brûle assez facilement à l'air libre aussi. Les figg. 25 et 26 montrent les oscillogrammes de la pression dans la chambre de combustion en fonction du temps. La figure 25 concerne la combustion d'un spécimen de AP pur dans une atmosphère d'hydrogène à 6 atm: pour accentuer la caractéristique du phénomène on a employé un fort coéfficient d'amplification (chaque division verticale correspond à 0,2 atm). La fig. 26 concerne, au contraire, la combustion d'un échantillon de AP + 20% Cu réduit dans une atmosphère d'azote à 4 atm: chaque division verticale correspond maintenant à 0,8 atm. Dans la photographie on peut observer la ligne de zéro de pression (respectivement 6 atm et 4 atm) et les points marque-temps. Dans les deux cas le pic de pression au moment de l'ignition est bien visible, mais surtout est bien mise en évidence la loi de la pression dans le cas de la combustion hybride et dans le cas de la combustion composite. Les oscillations de pression dues à la flamme de diffusion, avec une fréquence parfois élévée, manquent dans la flamme du propergol.

MELANGES NON COMPRIMES. Puisque un fort pourcentage de l'additif transforme les mélanges essayés en propellants composites solides, il a paru utile de voir à partir de quel point les mélanges AP + métal peuvent être considérés propergols composites plutôt que des oxydants énergétiques. Cela signifie étudier la facilité d'ignition des poudres, ce qui dépend de la nature et du pourcentage des composants, de l'état physique des particules, de la pression etc. Cet étude a été developpé en considérant deux paramètres: le pourcentage minimum de métal nécessaire pour la combustion à l'air libre des poudres et le délai d'ignition du mélange.

Malheureusement la coérence des poudres limite le pourcentage de l'additif au moment de la fabrication des échantillons comprimés et il a donc fallu préparer des mélanges non comprimés: les pourcentages de l'additif ajouté au perchlorate d'ammonium couvrent alors tous les domaines de 1'1% au 100% de poids du métal par rapport au poids du comburant. Les poudres, bien pulverisées et mélangées, sont contenues dans un cylindre en acier ayant un diamètre $\varnothing$ = 8 mm, l'ignition étant effectuée par moyen d'un "squib" noyé dans la masse du propellant. Les métaux essayés sont Al et Mg, à cause de l'importance qu'ils ont dans la technologie de la propulsion, et Cu réduit, à cause de son particulier état physique de surface.

Le dispositif employé pour la mesure du délai d'ignition est réprésenté dans la fig. 27; à travers une cellule photoélectrique on mesure le temps qui passe entre l'instant de commande de l'allumage du squib et l'instant où la flamme du mélange apparaît bien stable. La mesure ainsi effectuée comprend le délai τ_1 du squib aussi: ce délai a été alors mesuré à part et on a obtenu, après une série d'expériences, une valeur moyenne $\tau_1 = 0{,}15 \cdot 10^{-2}$ sec. Cette valeur n'a pas donc grande influence sur le délai d'ignition du mélange, qui résulte supérieur d'un ordre de grandeur.

Les résultats sont illustrés dans le graphique de la fig. 28, qui rapporte le délai d'ignition τ du mélange en fonction du pourcentage X du métal. Le délai d'ignition est exprimé en 10^{-2} sec. Puisque chaque mesure a été répétée plusieurs fois, sur le graphique on a représenté les valeurs moyennes de chaque série d'essais: les courbes toutefois ont été tracées par interpolation, suivant la méthode des carrés minimums, avec l'aide d'un computer.

Pour Al (granulométrie très fine) la combustion à l'air libre n'a pas lieu ou est incomplète jusqu'à X = 20; elle devient stable pour X = 30 au moins. Lorsque X augmente (courbe c de la fig. 28) le délai d'ignition τ diminue jusqu'à se stabiliser: on peur considérer comme valeur (interpolée) de minimum $\tau = 2{,}5 \cdot 10^{-2}$ sec. Pour Mg la combustion à l'air libre, parfois incomplète pour X = 5 et 10, devient assez stable pour X = 20 au moins. Pour ce qui concerne le graphique τ, X (courbe b), il faut avant tout noter une certaine dispersion des valeurs expérimentales, ce qui dépend des particules métalliques employées granulométrie non controlée). En tout cas la courbe est assez semblable à celle relative au mélange AP + Al, mais avec une valeur moyenne de délai plus élévé à cause de la différente granulométrie. On peut considérer comme délai minimum $\tau = 3{,}3 \cdot 10^{-2}$ sec. La courbe c concerne le mélange AP + Cu réduit: la combustion est maintenant complète pour X = 1 aussi, mais le délai d'ignition est important (entre autre chose la granulométrie n'est pas si fine que celle relative aux particules de Al). Le délai minimum vaut $\tau = 4{,}6 \cdot 10^{-2}$ sec.

CONCLUSION

Les expériences conduites montrent que la vitesse linéaire de régression de spécimens comprimés de perchlorate d'ammonium dans un écoulement gazeux est:

- favorisée surtout par l'emploi d'hydrogène, ce résultat ayant déjà été trouvée chez l'ONERA pour une différente géométrie des échantillons (sphères au lieu de cylindres) mais dans des conditions opératoires pareilles;
- accélérée de façon bien remarquable par des additifs ayant une grande surface de réaction;

- facilitée par l'addition de métaux légers et, en général, de métaux ayant une grande chaleur de combustion;
- diminuée sensiblement par l'addition du perchlorate de lithium, même à la presence d'accélerateurs de la décomposition thermique des deux comburants;
- augmentée par la pression, mais de façon pas très sensible à moins d'ajouter des accélérateurs de combustion.

Si d'une côté la rapidité de combustion des échantillons de AP pur apparaît limitée, tout au moins à la pression atmosphérique et cause l'indépendance de la température de surface de la nature du combustible gazeux, par la flamme de diffusion du gaz avec les produits oxydants de la décomposition de $HClO_4$, d'autre côté il est difficile d'admettre que la température de surface du solide ne soit pas modifiée par l'addition de certains métaux. D'ailleurs plusieures expériences ont mis en évidence une variation de la température de surface du comburant soit aux pressions subatmosphériques (40) soit aux pressions très élévés (51). Les additifs métalliques valides comme accélérateurs de la combustion de AP pourraient, donc, par moyen de la diffusion des produits actifs des réactions de redox favoriser la transmission de chaleur de la phase gazeuse vers la phase solide si bien que constituer des centres actifs pour la décomposition du perchlorate. Les autres additifs métalliques, au contraire, bornent la rapidité de combustion de AP à travers la formation de composés intermédiaires assez stables et donc de façon indépendante du débit gazeux.

L'effet des catalyseurs de la décomposition thermique de AP pourrait enfin s'expliquer sur la base de questions proprement chimiques. En effet on a trouvé (52) que les catalyseurs les plus efficaces sont ceux qui augmentent la quantité d'oxygène dégagé pendant la décomposition du solide: dans ces conditions le perchlorate, en considérant la concentration des produits oxydants, résulte plus réactif. Cette hypothèse s'accorde très bien avec nos résultats expérimentaux, puisque les composés du cuivre et en particulier Cu_2O facilitent sensiblement la formation de O_2 par rapport à N_2O et NOCl.

Cependant les résultats obtenus peuvent intéresser la technologie de la propulsion dans la mesure de validité des expériences conduites dans un dispositif comme la bombe Crawford plus ou moins modifiée. D'ailleurs l'importance du perchlorate d'ammonium dans la préparation des propellants composites et le développement que AP pourrait avoir en agissant comme comburant solide dans un procès de combustion hybride demande une connaissance des propriétés balistiques de tel perchlorate qui ne soit pas seulement dérivée des expériences sur les fusées. A propos il faut remarquer que des essais de combustion hybride de grains solides de AP avec un débit d'hydrogène ont été déjà faits chèz nos laboratoires. Des travaux sont en cours de réalisation pour déterminer la vitesse de régression du grain solide et la confronter donc avec celle des spécimens cylindriques comprimés.

REMERCIEMENTS

Les auteurs désirent remercier le dr. A. Coghe de sa valide collaboration, le prof.ing. O. Tuzunalp de son assistance pour ce qui concerne les problèmes de nature électronique, la P.I. V. Boldrini pour la réalisation des mesures de vitesse linéaire de régression et M. Marchetti pour les mesures du délai d'ignition.

REFERENCES

1) M. Barrère and L. Nadaud - "Combustion of AP sphères in a flowing gaseous fuel" - X Symposium on Combustion, pp. 1381 - 1394, 1965.

2) L. Nadaud - "Experimental study of the combustion of AP sphères in a gaseous fuel flow" - La Recherche Aérospatiale, pp. 39 - 51, 108, 1965.

3) M. Barrère and F.A. Williams - "Analytical and experimental study of the steady state combustion mechanism of solid propellants" - ONERA TP 240, 1965.

4) G. Rosen - "Burning rate of solid propellants" - J. Chem. Phys., pp. 89-93, 32, 1960.

5) W. Nachbar and F.A. Williams - "On the analysis of linear pyrolysis experiments" - IX Symposium on Combustion, pp. 345-358, 1963.

6) R. Friedman, G.G. Nugent, K.E. Rumbel and A.C. Scurlock - "Deflagration of AP" - VI Symposium on Combustion, pp. 612-618, 1957.

7)J.B. Levy and R. Friedman - "Further studies of pure AP deflagration" - VII Symposium on Combustion, pp. 663-672, 1962.

8) W.E. Johnson and W. Nachbar - "Deflagration limits in the steady linear burning of monopropellant with application to AP" - VIII Symposium on Combustion, pp. 678-689, 1962.

9) O.R. Irwin, P.K. Salzman and W.H. Andersen - "Deflagration characteristics of AP at high pressure" - IX Symposium on Combustion, pp. 358-365, 1963.

10) L.J. Shannon and E.E. Petersen - "Deflagration characteristics of AP strands" - AIAA Journal, pp. 168-169, 1964.

11) J.D. Hightower and E.W. Price - "Combustion of AP" - XI Symposium on Combustion, pp. 463-472, 1967.

12) M. Summerfield, G.S. Sutherland, M.J. Webb, H.J. Taback and K.P. Hall - "Burning mechanism of AP propellants" - Progress in Astronautics and Rocketry, Vol. I - "Solid Propellant Rocket Research" - pp. 141-182, Academic Press, New York and London, 1960.

13) D.W. Blair, E.K. Bastress, C.E. Hermance, K.P. Hall and M. Summerfield - "Some research problems in the steady state burning of composite solid propellants" - Progress in Astronautics and Rocketry, Vol. I -"Solid Propellant Rocket Research" - pp. 183-206, Academic Press, New York and London, 1960.

14) J. Vandenkerckhove and A. Jaumotte - "Remarks on the burning mechanism and erosive of AP propellants" - VIII Symposium on Combustion, pp. 689-693, 1962.

15) G.K. Adams, B.H. Newman and A.B. Robins - "Combustion of propellants based upon AP" - VIII Symposium on Combustion, pp. 693-705, 1962.

16) E.A. Arden, J. Powling and W.A.W. Smith - "Observation on the burning of AP" - Combustion Flame, pp. 21-33, 6, 1962.

17) J. Powling - "Experiments relating to the combustion of AP based propellants" - XI Symposium on Combustion, pp. 447-456, 1967.

18) J.D. Hightower and E.W. Price - "Experimental study relating to the combustion mechanism of composite propellants" - Astronautica Acta, pp. 11-21, 14, 1968.

19) M. Dodé - "Sur la décomposition thermique du AP" - Bulletin de la Societé chimique de France, pp. 170-176, V, 1938.

20) L.L. Bircumshaw and B.H. Newman - "The thermal decomposition of AP.I" - Proc. Roy. Soc., A 227, pp.115-132, 1954

21) L.L. Bircumshaw and B.H. Newman - "The thermal decomposition of AP.II" - Proc. Roy. Soc., A 227, pp 228-241, 1955.

22) L.L. Bircumshaw and T.R. Phillips - "The kinetics of the thermal decomposition of AP" - J. Chem. Soc., pp. 4741-4747, 1957.

23) A.K. Galwey and P.W.M. Jacobs - "High temperature thermal decomposition of AP" - J. Chem. Soc., pp. 837-844, 1959

24) A.K. Galwey and P.W.M. Jacobs - "The thermal decomposition of AP at low temperatures" - Proc. Roy. Soc., A 254, pp. 455- 469, 1960.

25) A.K. Galwey and P.W.M. Jacobs - "The thermal decomposition of AP in the presence of manganese dioxide" - Trans. Farad. Soc., pp. 1165 - 1172, 55, 1959.

26) A.K. Galwey and P.W.M. Jacobs - "The thermal decomposition of AP in the presence of carbon" - Trans. Farad. Soc., pp. 581-590, 56, 1960.

27) F. Solymosi and L. Révész - "The thermal decomposition of AP in presence of zinc oxide" - Nature, pp. 64-65, 192, 1961.

28) A. Hermoni and A. Salmon - "The catalytic decomposition of AP" - VIII Symposium of Combustion, pp. 656-662, 1962.

29) P.W.M. Jacobs and A.R.T. Kureishy - "The effect of additives on the thermal decomposition of AP" - VIII Symposium on Combustion, pp. 672-677, 1962.

30) F. Solymosi and E. Krix - "Catalysis of solid phase reactions. Effect of doping of cupric oxide catalyst on the thermal decomposition and explosion of AP" - Journal of Catalysis, pp. 468-480, I, 1962.

31) F. Solymosi and K. Fónagy - "Effect of cadmium oxide and cadmium perchlorate on the decomposition and ignition of AP" - XI Symposium on Combustion, pp. 429-437, 1967.

32) P.W.M. Jacobs and A. Russel-Jones - "The thermal decomposition and ignition of mixtures of AP + copper chromite" - XI Symposium on Combustion, pp. 457-462, 1967.

33) M.W. Evans, R.B. Beyer and L. MacCulley - "Initiation of deflagration waves on the surfaces of AP - copper chromite - carbon pellets" - J. Chem. Phys., pp. 2431-2438, 40, 1964.

34) F. Solymosi - "Initiation of AP ignition by chromic oxide - titanium dioxide catalysts" - Combust. Flame, pp. 141-148, 9, 1965.

35) R.F. Chaiken - "A thermal layer mechanism of combustion of solid composite propellants: application to ammonium nitrate propellants" - Combust. Flame, pp. 285-300, 3, 1959.

36) B.L. Crawford, C. Huggett, F. Daniels and W.P. Wilfong - "Direct determination of burning rates of propellants powders" - Anal. Chem., pp. 630-633, 19, 1947.

37) C. Casci e L. De Luca - "Studio sperimentale dei comburenti solidi. Velocità lineare di regressione e meccanismi di reazione di AP" - La Rivista dei Combustibili, pp. 165-178, 1969.

38) C. Casci e L. De Luca - "Studio sperimentale dei comburenti solidi. Influenza di polveri metalliche sulla velocità lineare di regressione di AP" - La Rivista dei Combustibili, pp. 222-233, 1969.

39) C. Casci e L. De Luca - "Studio sperimentale dei comburenti solidi. Influenza dei catalizzatori e della granulometria sulla velocità lineare di regressione di AP" - En cours de publication sur La Rivista dei Combustibili.

40) R.F. McAlevy III and S.Y. Lee - "A porous plug burner technique for the study of composite solid propellant deflagration on a fundamental level and its application to hybrid rocket propulsion" - Progress in Astronautics and Aeronautics, Vol. 15, "Heterogeneous Combustion" - pp. 583-608, Academic Press, New York and London, 1964.

41) L.A. Watermeier, W.P. Aungst and S.P. Pfaff - "An experimental study of the aluminium additive role in unstable combustion of solid rocket propellants" - IX Symposium on Combustion, pp. 316-327, 1963.

42) R. Freeman and R. Anderson - "The effects of aluminium fluoride on the combustion of aluminium in the presence of potassium perchlorate and oxygen" - Combust. Flame, pp. 337-340, 10, 1966.

43) M. Pugibet - "Amélioration du délai d'allumage du kérosène par des additifs solides" - La Recherche Aéronautique, pp. 21-22, 66, 1958.

44) J. Powling and W.A.W. Smith - "Measurement of the burning surface temperatures of propellant compositions by infra-red emission" - Combust. Flame, pp. 173-181, 1962.

45) J. Powling and W.A.W. Smith - "The surface temperature of burning AP" - Combust. Flame, pp. 269-275, 7, 1963.

46) J. Powling and W.A.W. Smith - "The surface temperature of AP burning at elevated pressure" - X Symposium on Combustion, pp. 1373-1380, 1965.

47) J. Burger et A. Van Tiggelen - "Etude de la combustion de propergols hybrides et composites" - Bull. Soc. Chim. France, pp. 3122-3130, 1964.

48) F. Solymosi and M. Ranics - "The thermal stability of AP - LiP mixture. The role of eutectic formation" - Combust. Flame, pp. 398-390, 10, 1966.

49) M.M. Markowitz and R.F. Harris - "The differential thermal analysis of perchlorates. III. The system LiP - AP" - J. Phys. Chem. pp. 1519-1521, 1959.

50) A.A. Shidlovskiy and L.F. Shmagin - "Thermal decomposition and burning of AP" - Izvestiya Vysshikn Uchebnikn Zavedeniy, Khmiya i Khimicheskaya Tekhnologiya, pp. 529-532, 5, 1962.

51) V.K. Bobolev, A.P. Glazkova, A.A. Zenin and O.I. Leipunskii - "Temperature distribution in AP when burning " - Dokl. Akad. Nouk., USSR, pp. 604-607, 151, 1963.

52) K. Kuratani - "Some studies on solid propellants. Part III. Analyticat results of the combustion gases" - Aeron. Res. Inst., University of Tokyo, Report 374, 1962.

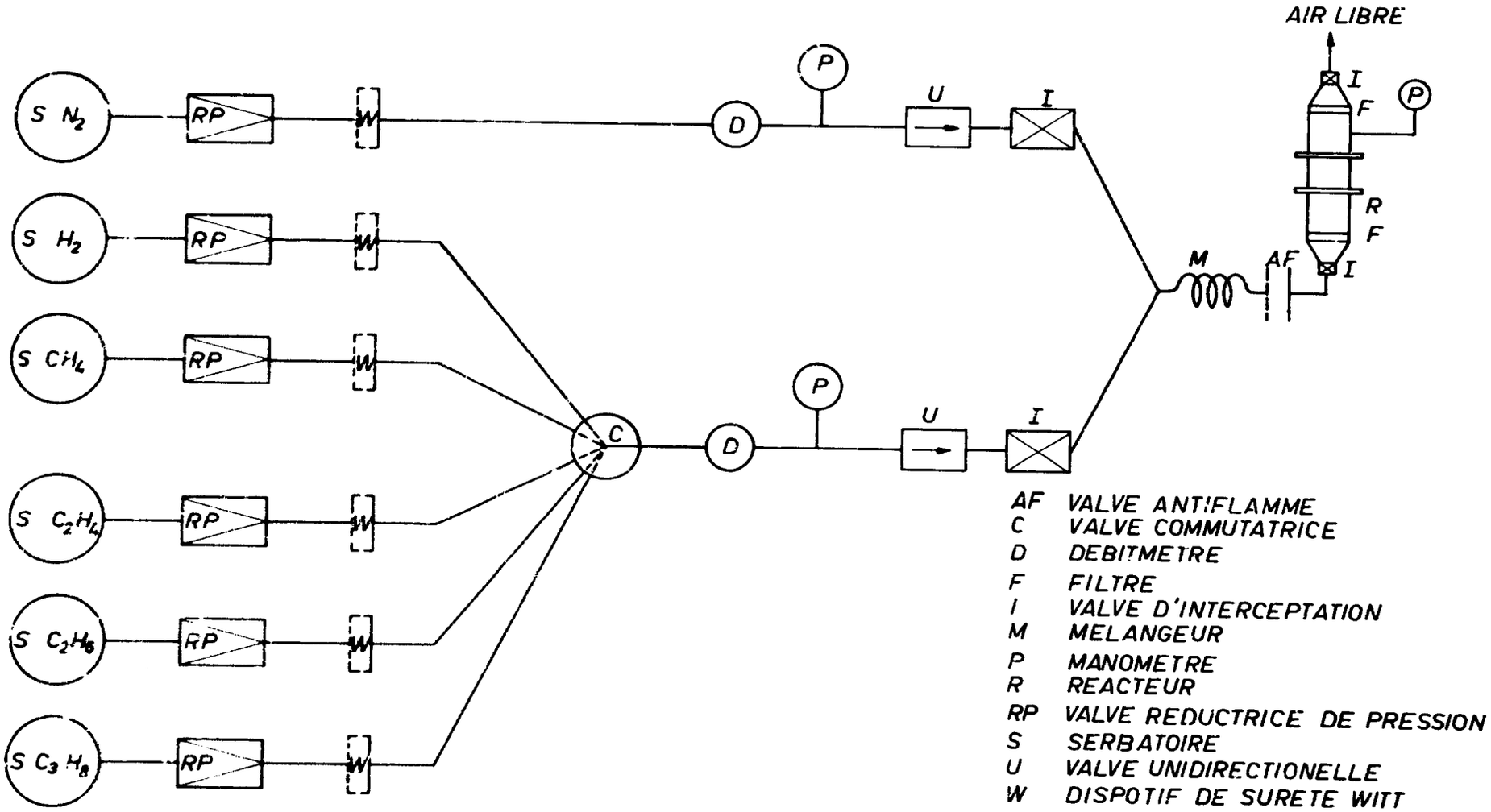

Fig. 1 - Circuit pneumatique de l'installation expérimentale.

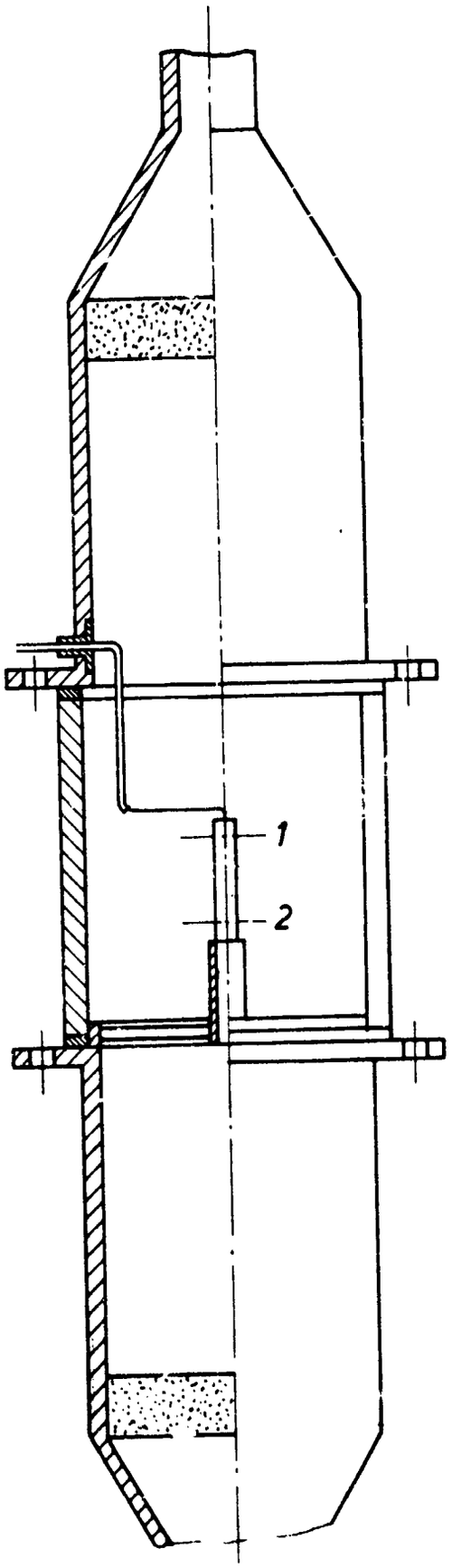

Fig. 2 - Schéma du réacteur.

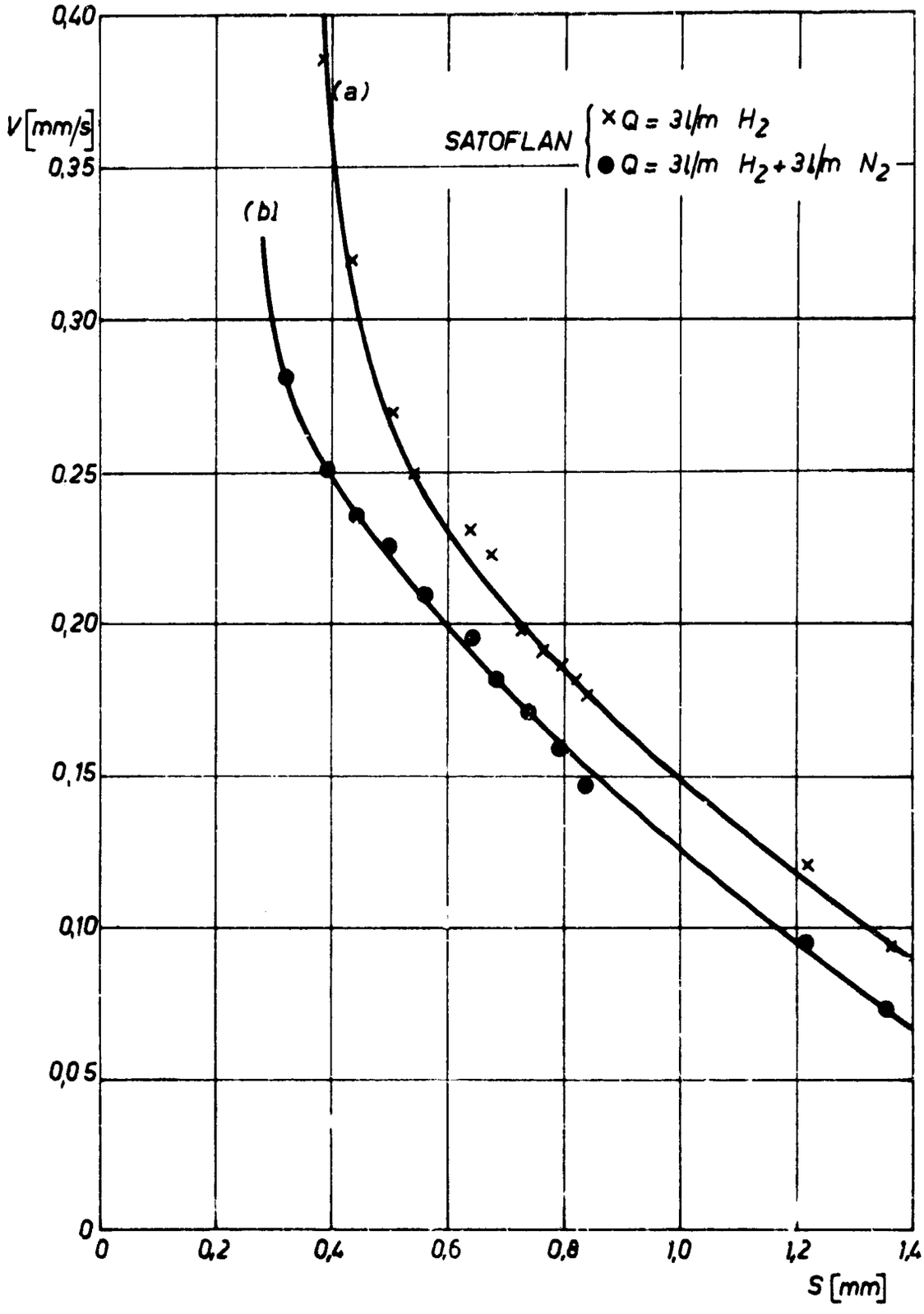

Fig. 3 - Influence du satoflan sur la vitesse linéaire de régression de AP.

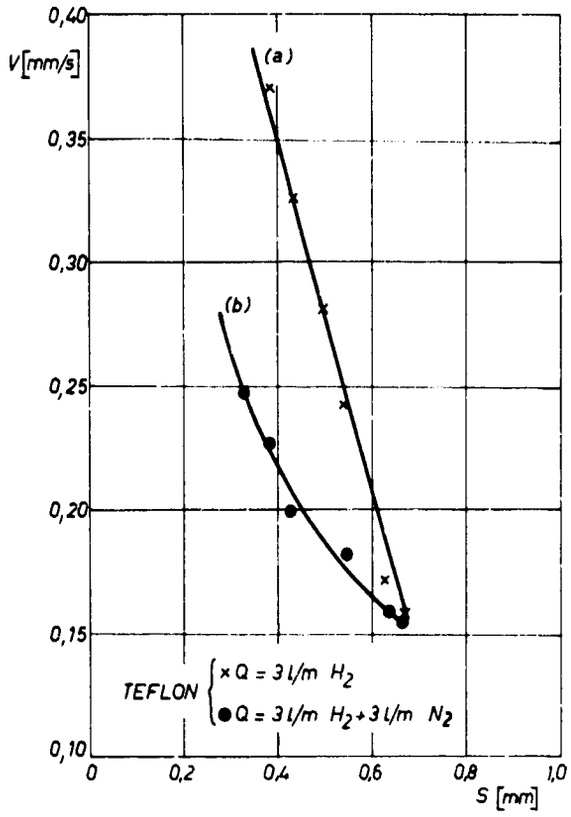

Fig. 4 - Influence du teflon sur la vitesse linéaire de régression de AP.

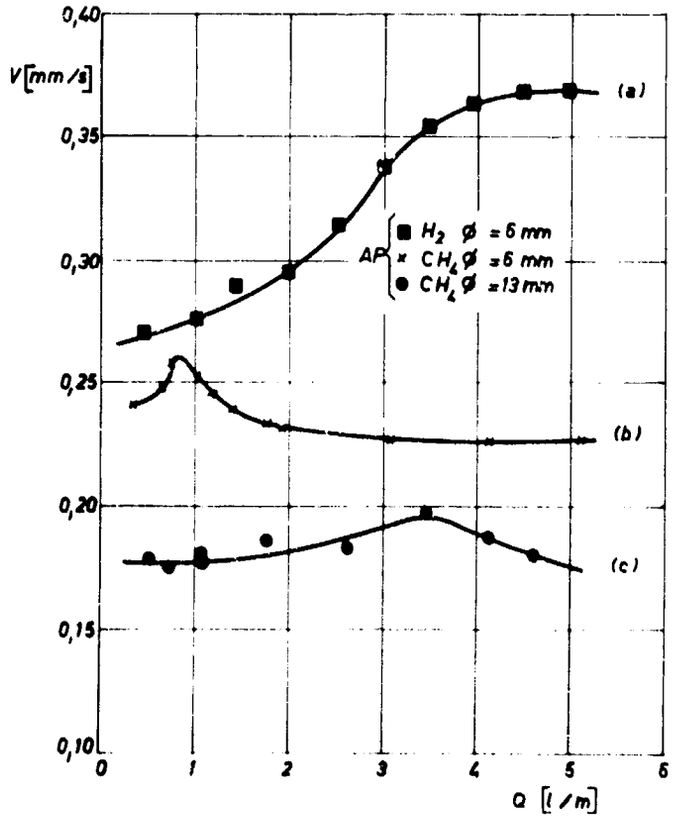

Fig. 5 - La vitesse linéaire de régression de AP dans un écoulement de H_2 et CH_4.

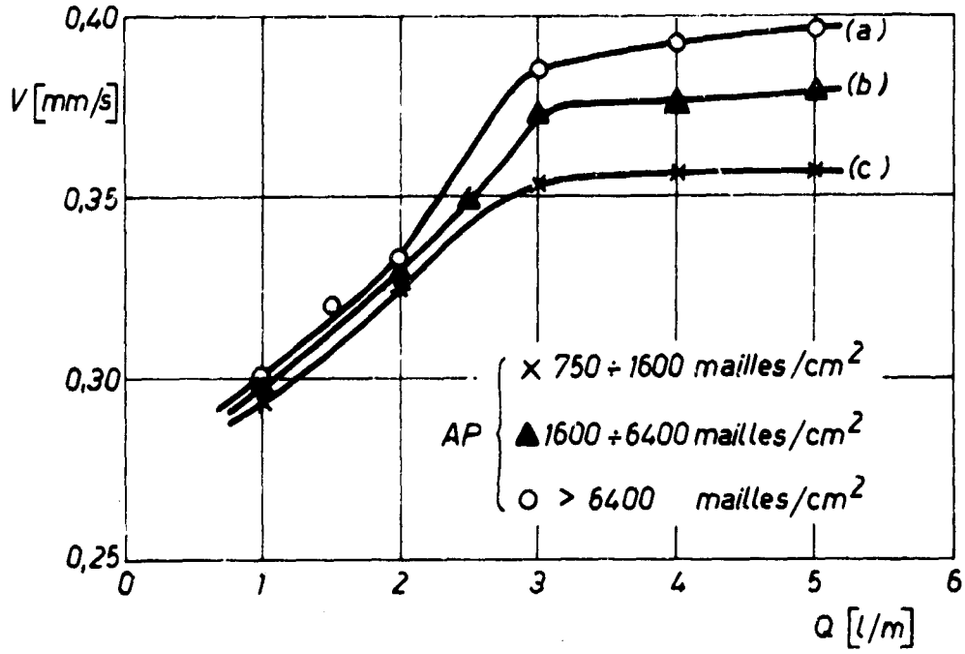

Fig. 6 - Influence des dimensions moyennes des particules de comburant sur la vitesse linéaire de régression de AP.

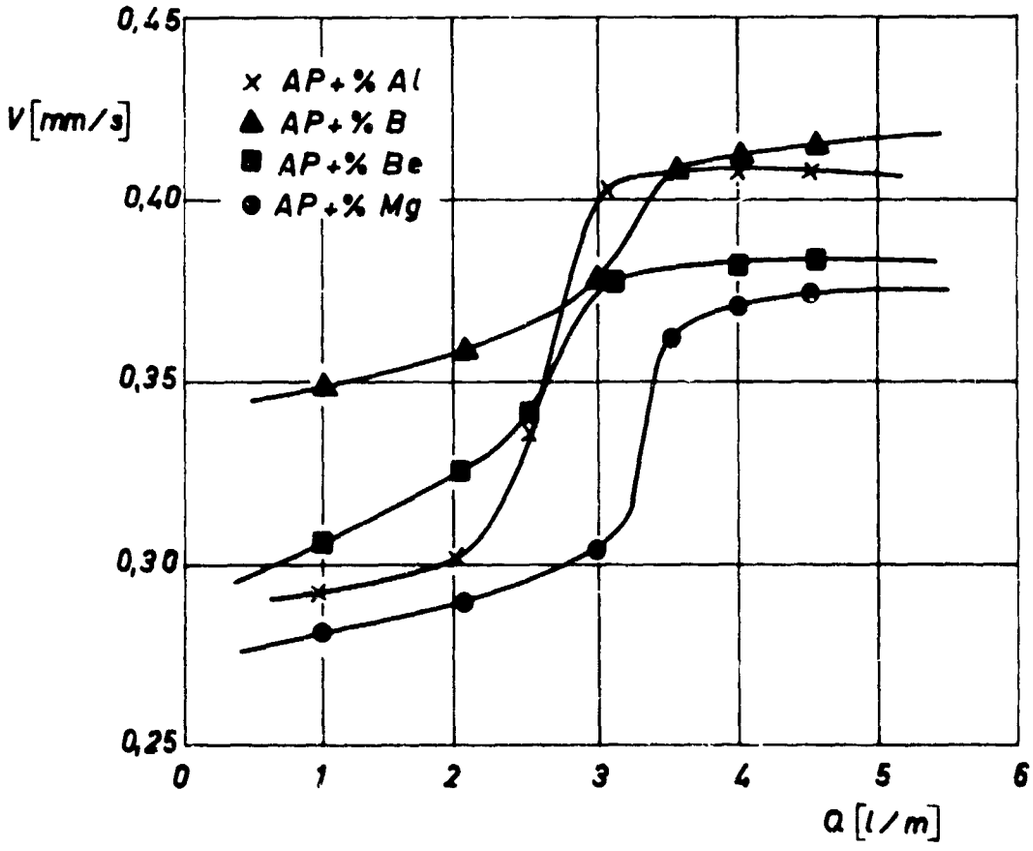

Fig. 7 - Effet de 1'1% de Al, B, Be et Mg sur la vitesse linéaire de régression de AP.

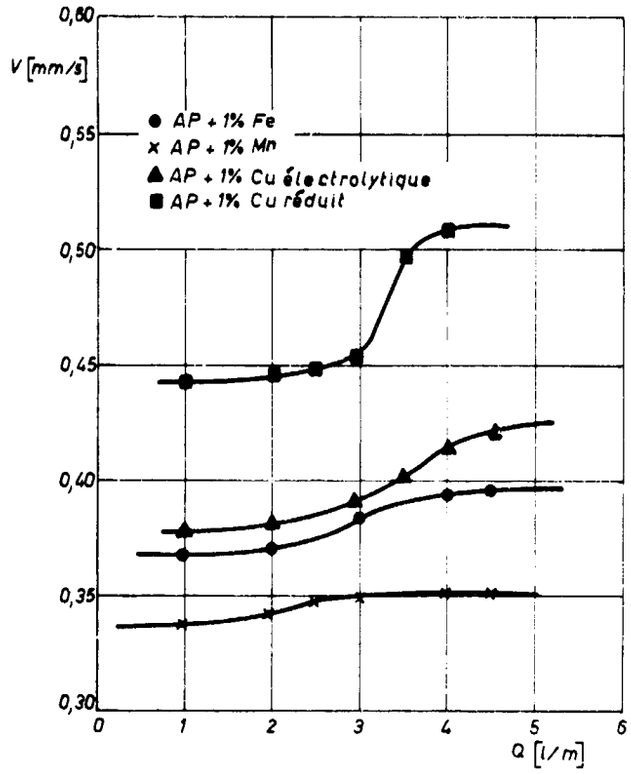

Fig. 8 - Effet de 1'1% de Cu électrolytique, Cu réduit, Fe et Mn sur la vitesse linéaire de régression de AP.

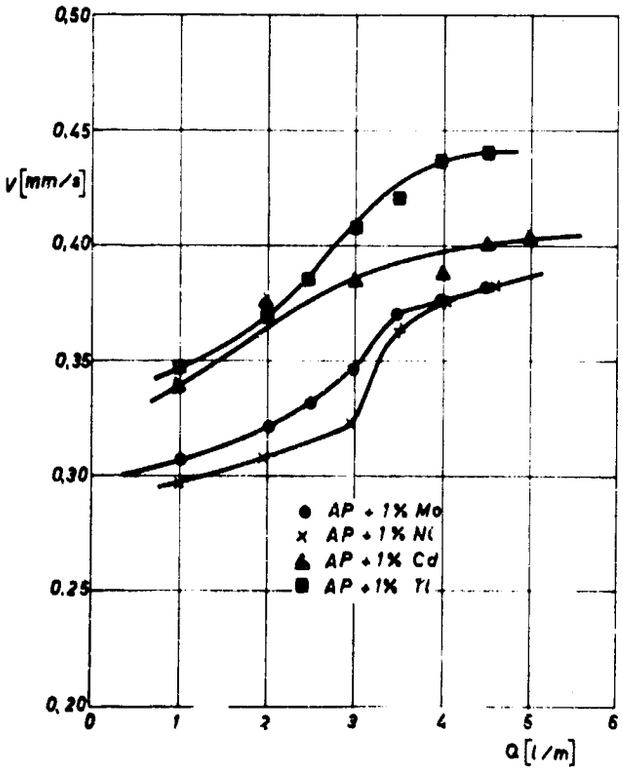

Fig. 9 - Effet de 1'1% de Cd, Mo, Ni et Ti sur la vitesse linéaire de régression de AP.

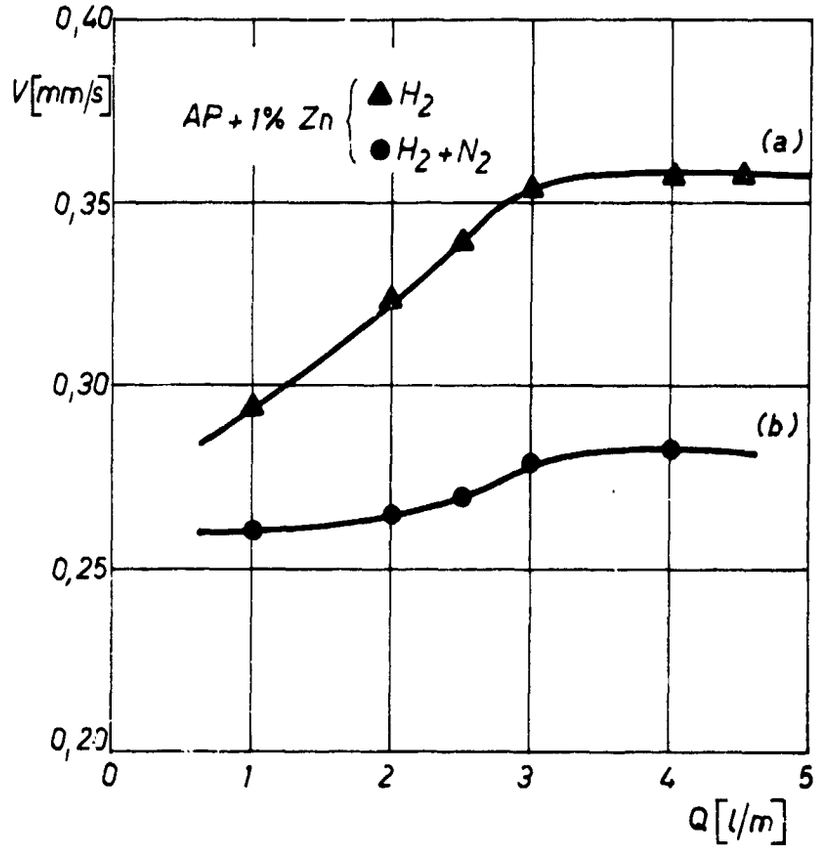

Fig. 10 - Effet de 1'1% de Zn sur la vitesse linéaire de régression de AP dans un écoulement gazeux combustible pur et dilué

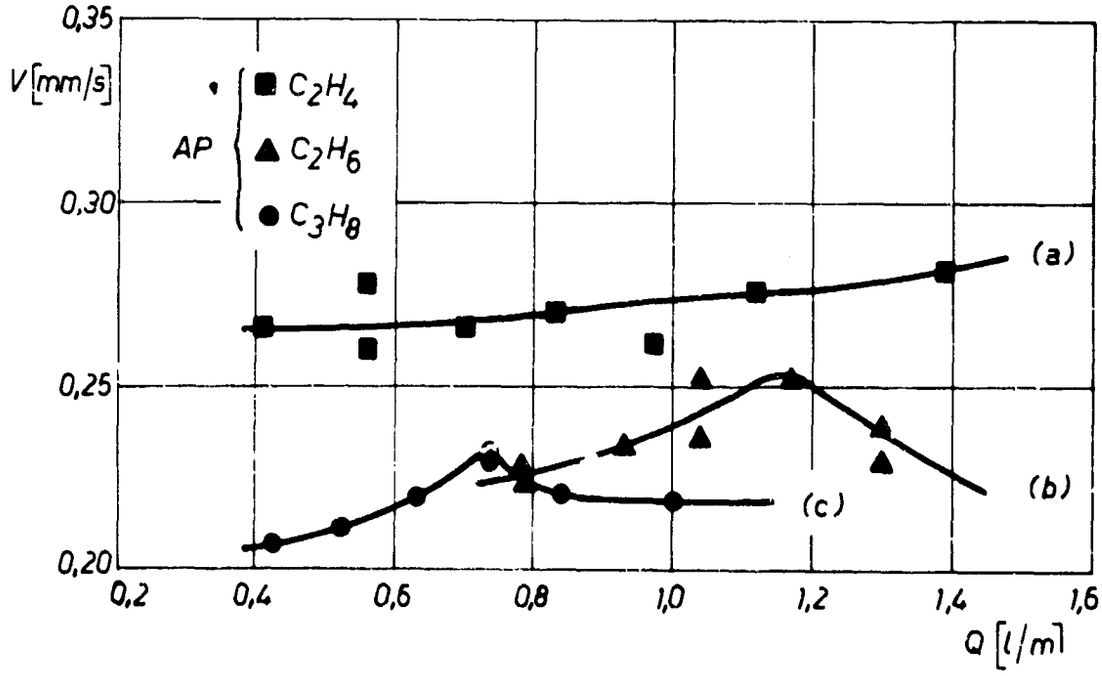

Fig. 11 - La vitesse linéaire de régression de AP dans un écoulement de C_2H_4, C_2H_6 et C_3H_8.

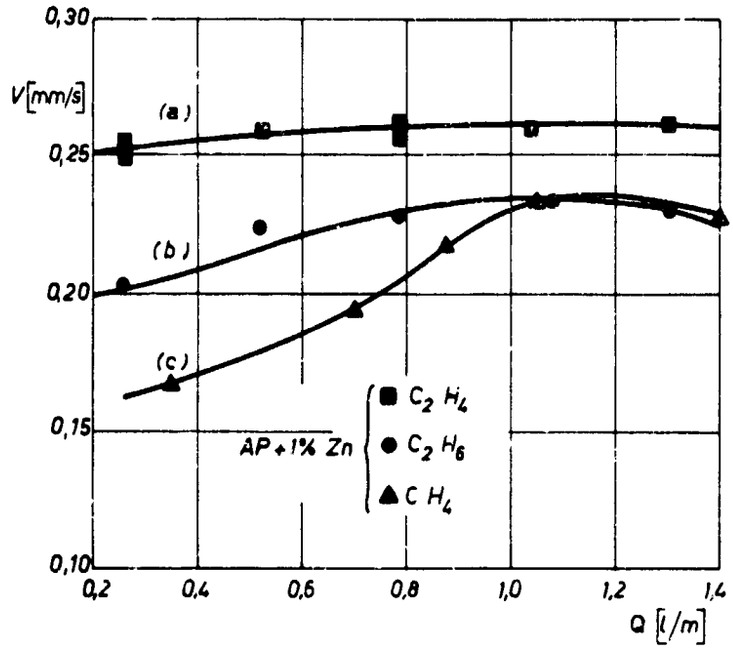

Fig. 12 - La vitesse linéaire de régression de AP + 1% Zn dans un écoulement de CH_4, C_2H_4 et C_2H_6.

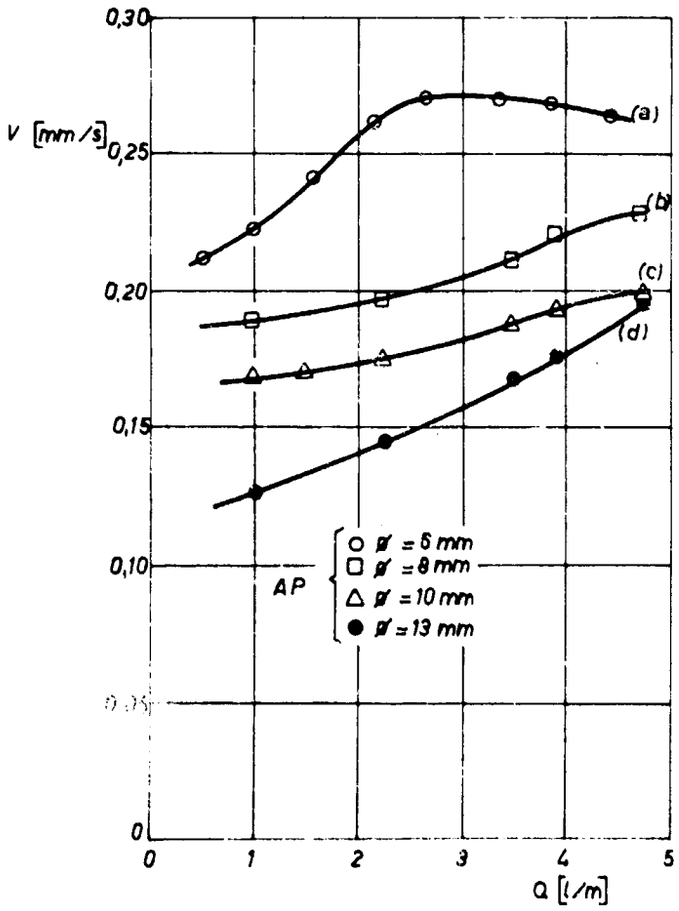

Fig. 13 - Influence du diametre des échantillons sur la vitesse linéaire de régression de AP.

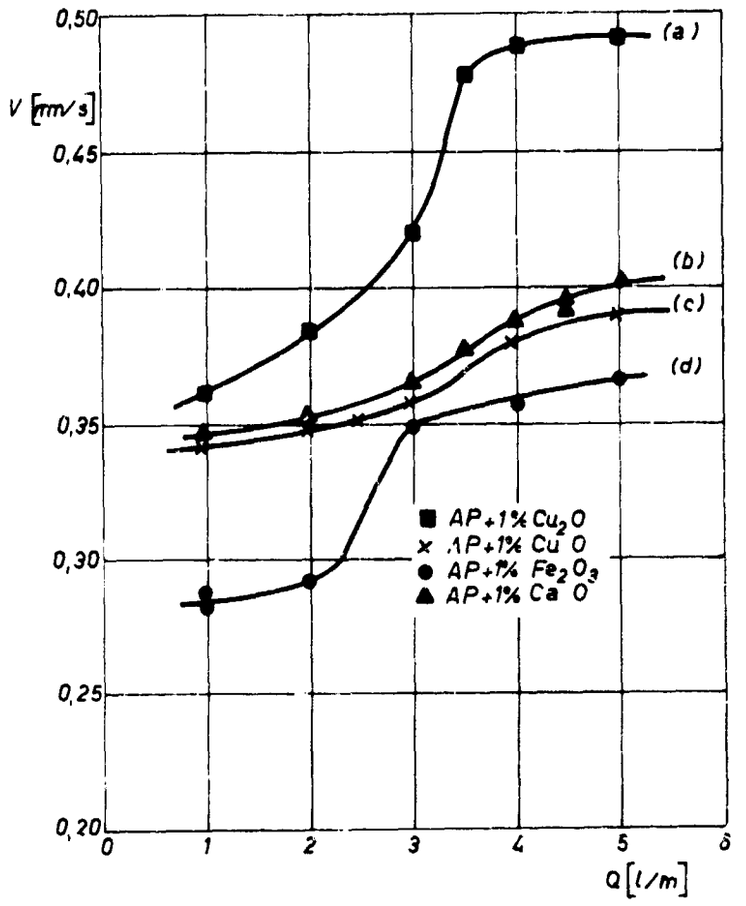

Fig. 14 - Effet de 1'1% de CaO, Cu_2O, CuO et Fe_2O_3 sur la vitesse linéaire de régression de AP.

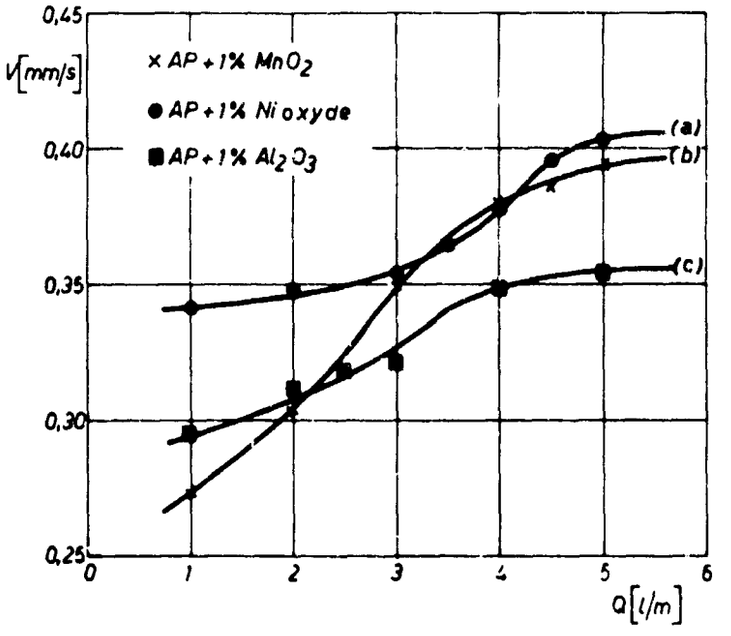

Fig. 15 - Effet de 1'1% de Al_2O_3, MnO_2 et Ni oxyde sur la vitesse linéaire de régression de AP.

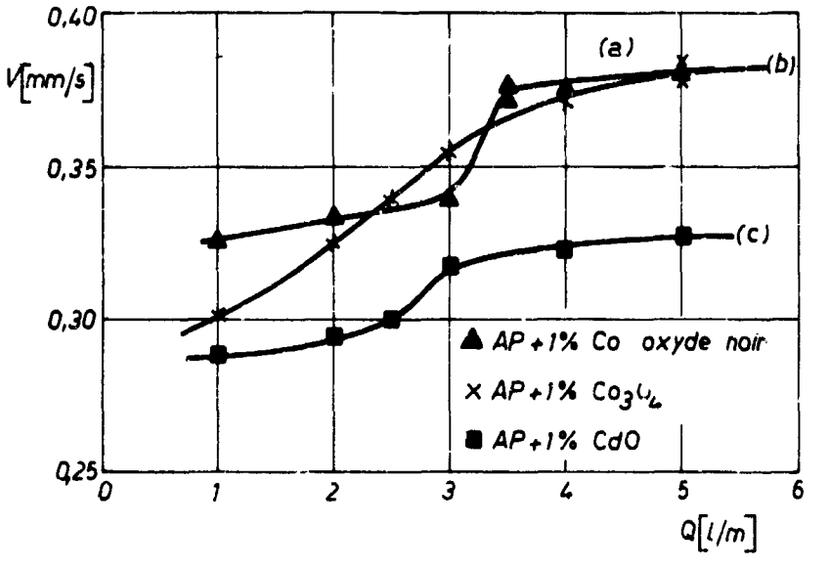

Fig. 16 - Effet de 1'1% de CdO, Co_3O_4 et Co oxyde noir sur la vitesse linéaire de régression de AP.

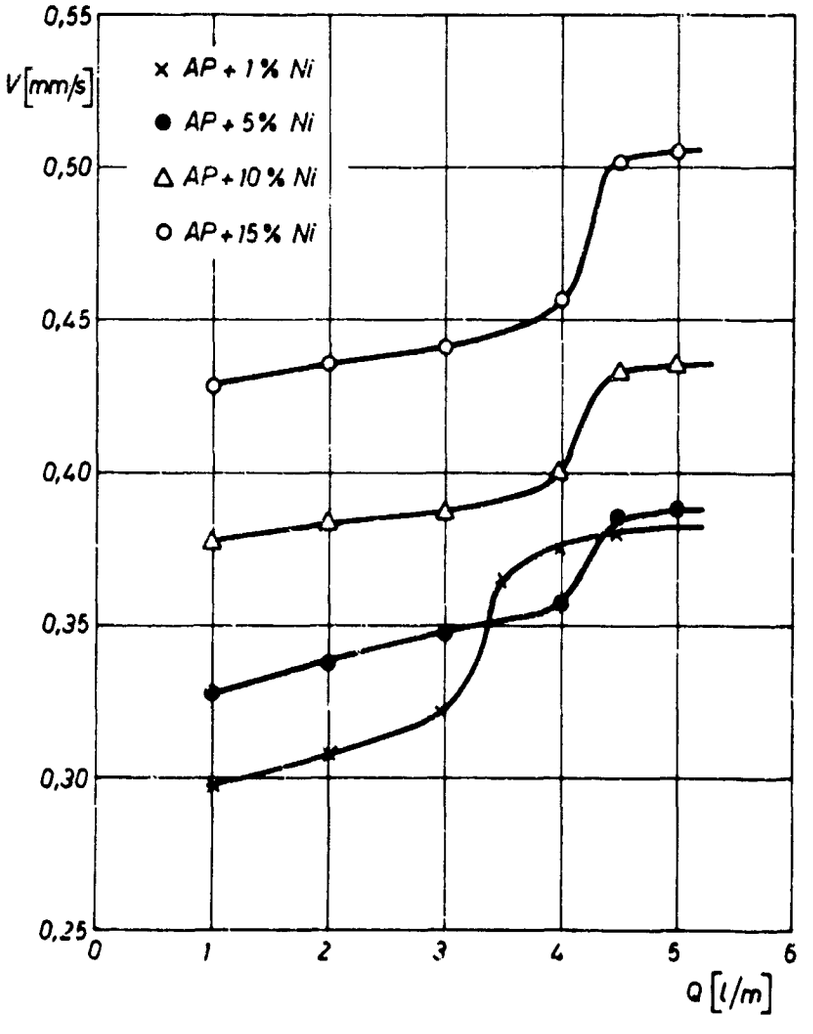

Fig. 17 - Effet du pourcentage de Ni sur la vitesse linéaire de régression de AP.

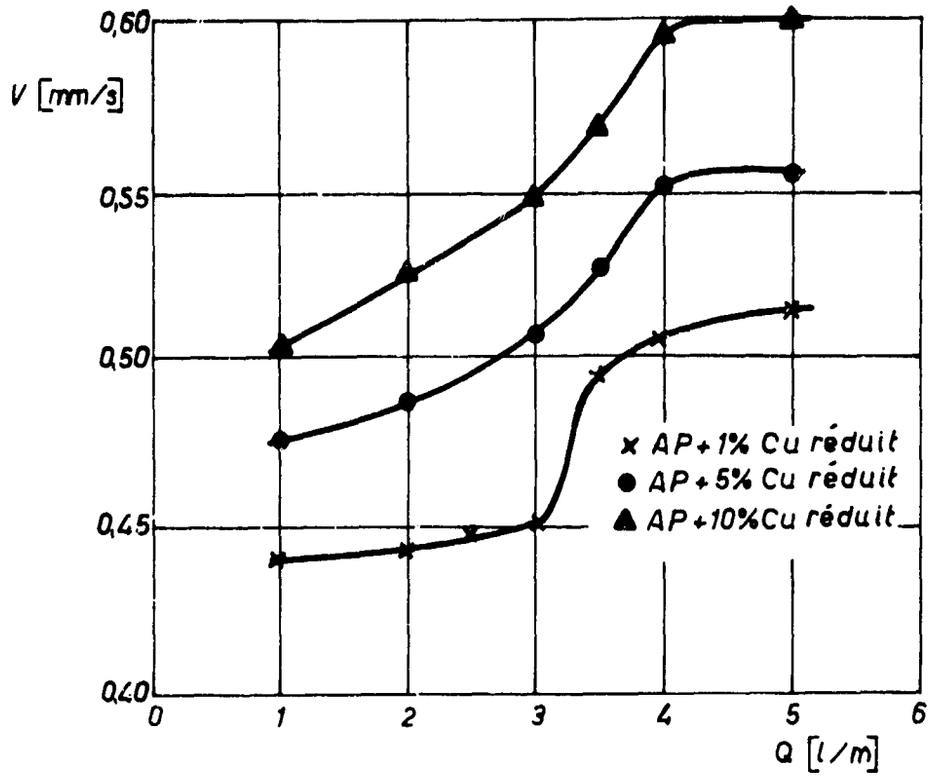

Fig. 18 - Effet du pourcentage de Cu réduit sur la vitesse linéaire de régression de AP.

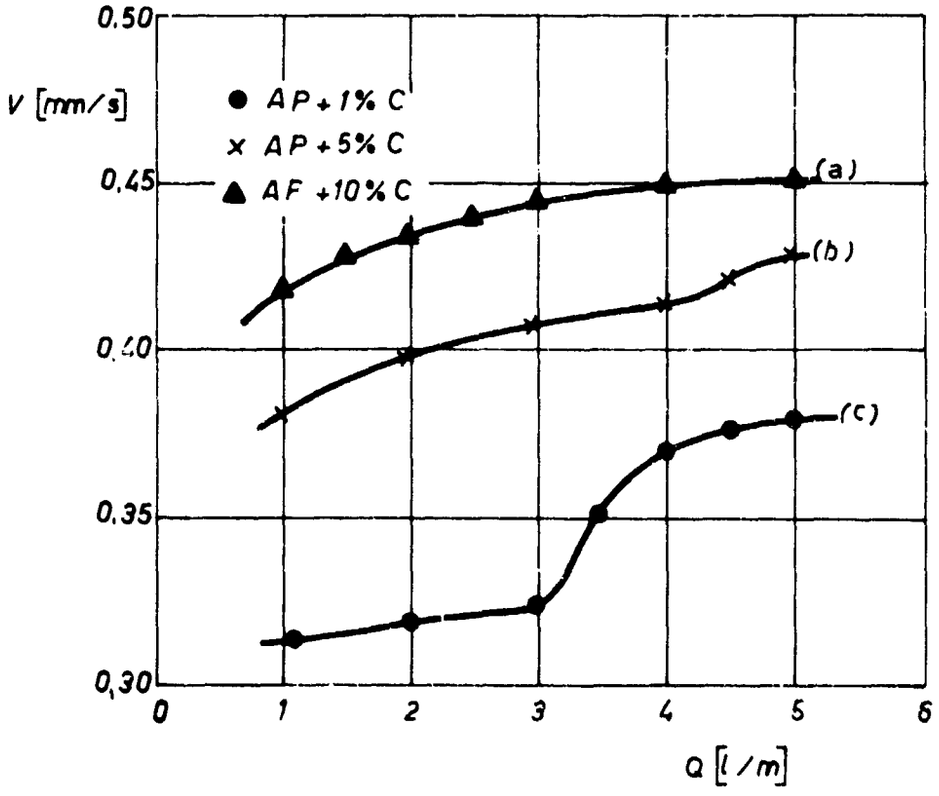

Fig. 19 - Effet du pourcentage de charbon sur la vitesse linéaire de régression de AP.

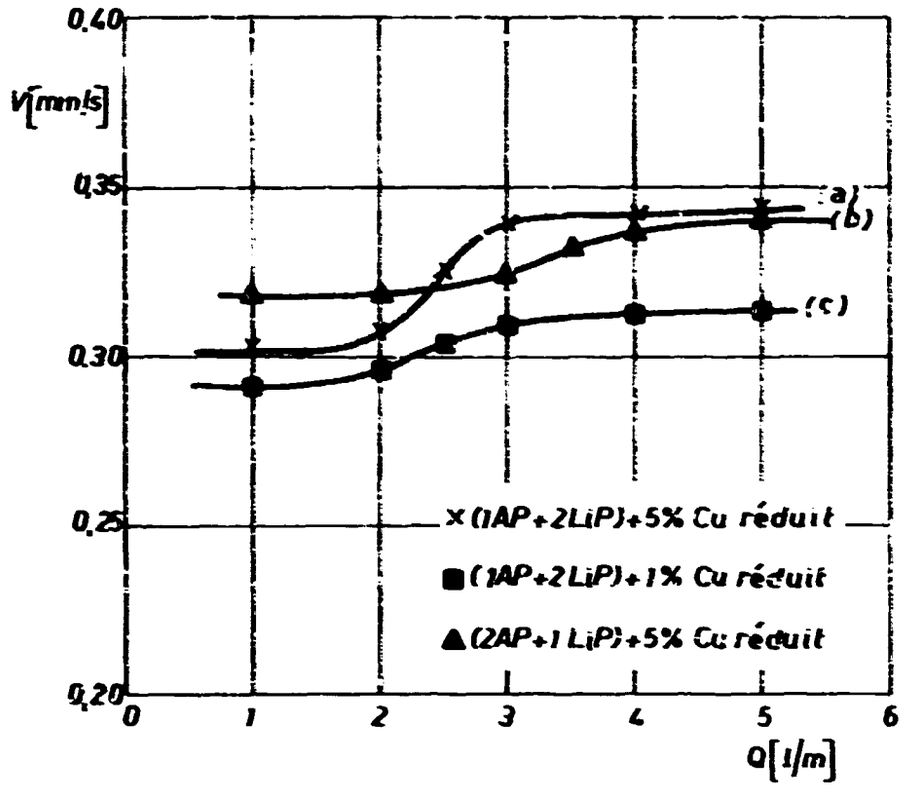

Fig. 20 - Effet de l'addition de $LiClO_4$ et Cu réduit sur la vitesse linéaire de régression de AP.

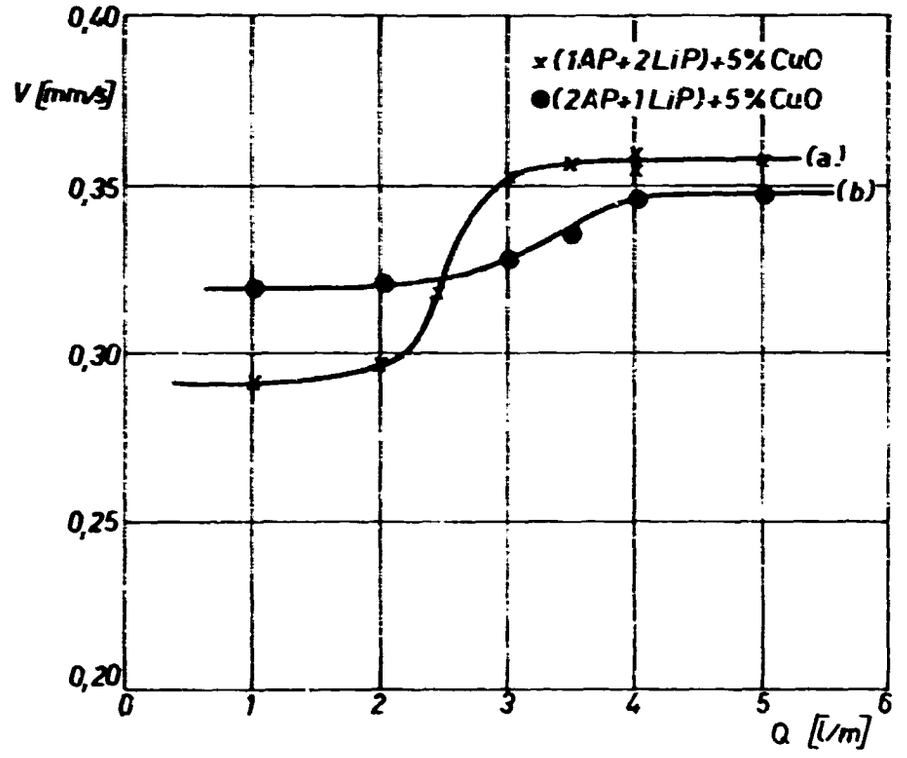

Fig. 21 - Effet de l'addition de $LiClO_4$ et CuO sur la vitesse linéaire de régression de AP.

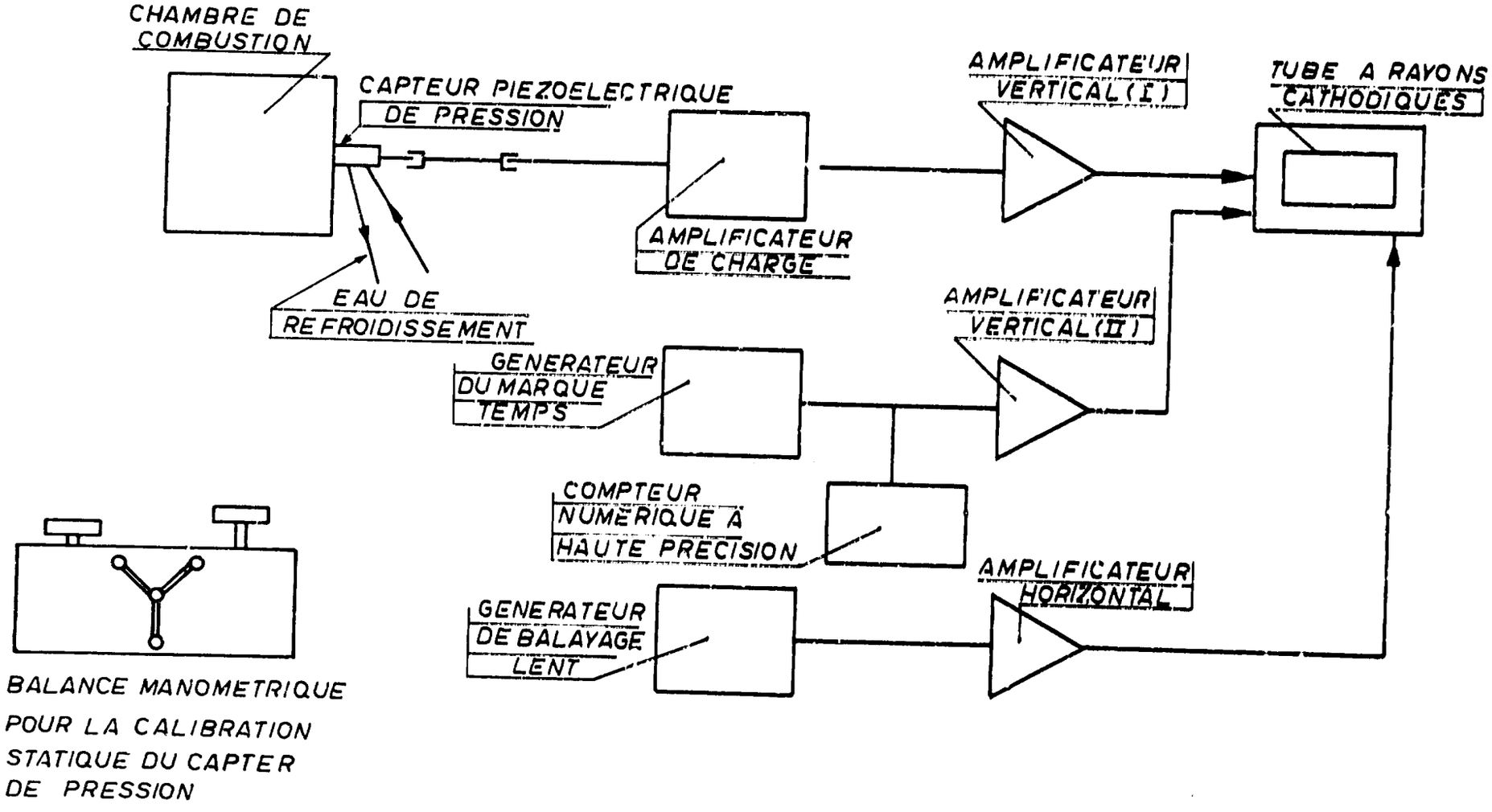

Fig. 22 - Schéma du système de mesure de la pression par un capteur piézoélectrique.

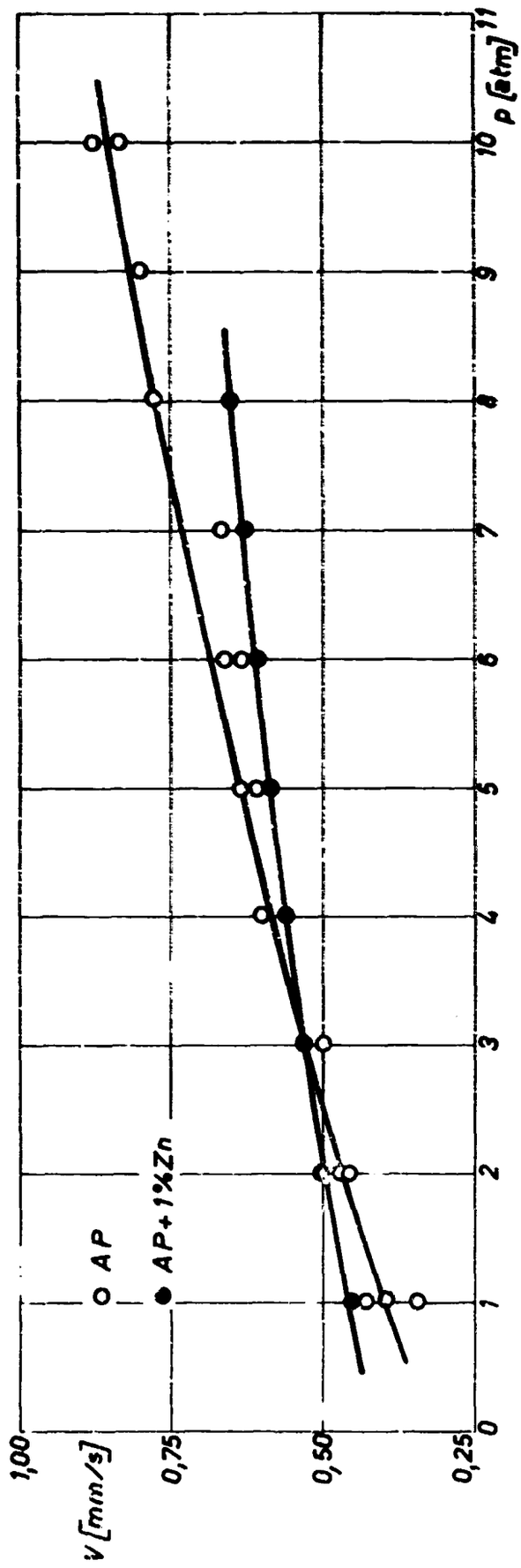

Fig. 23 - Influence de la pression sur la vitesse linéaire de régression de AP et AP + 1% Zn.

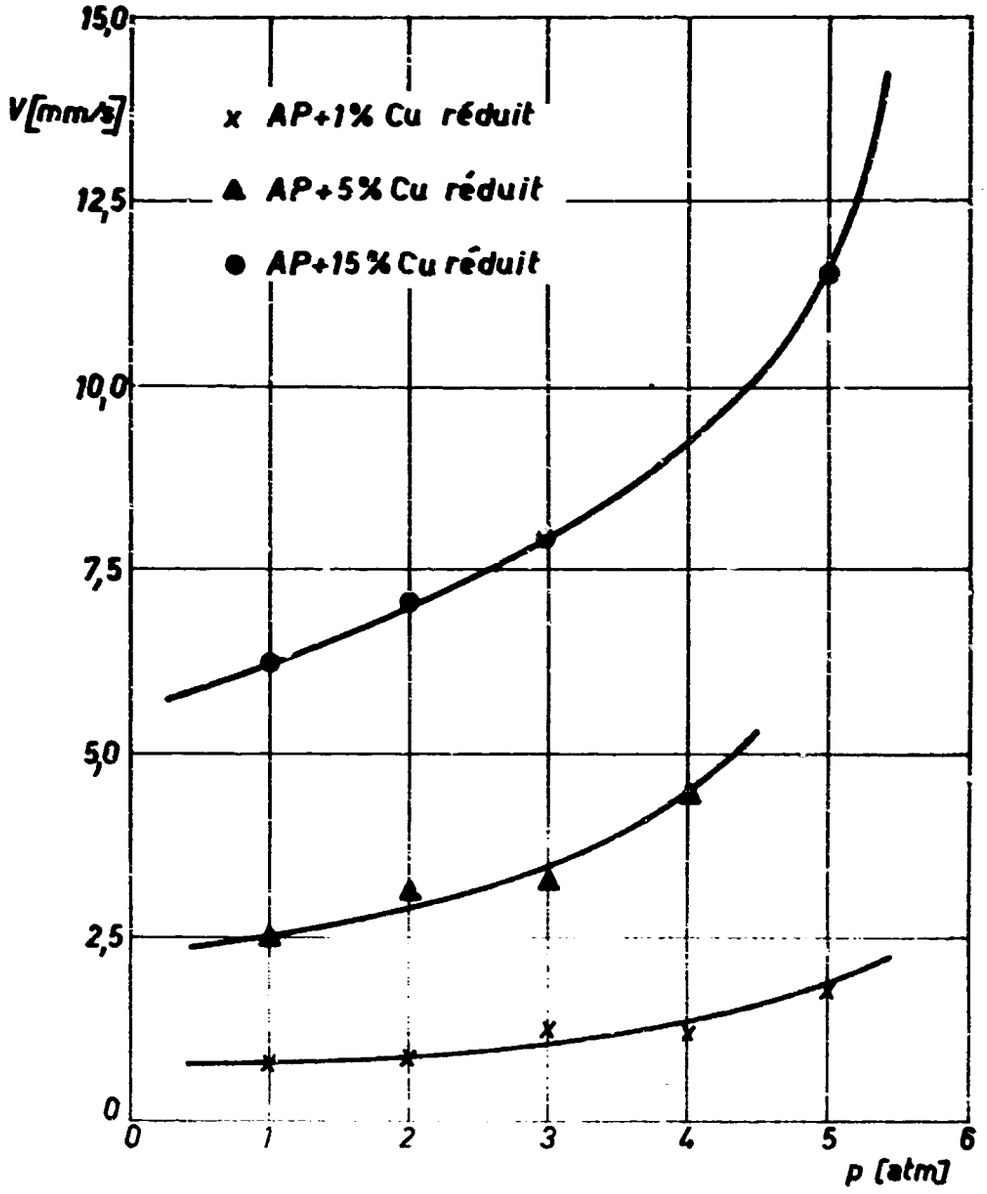

et AP + 1% Zn.

Fig. 24 - Influence de la pression sur la vitesse linéaire de régression de AP + + Cu réduit.

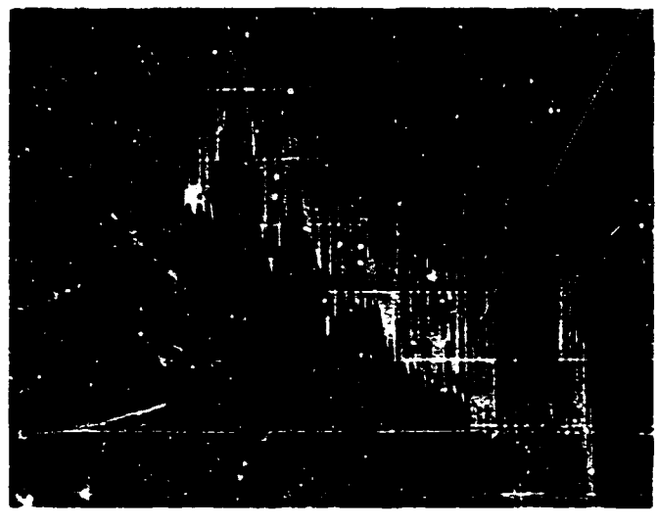

Fig. 25 - Oscillogramme de la pression pendant une combustion hybride.

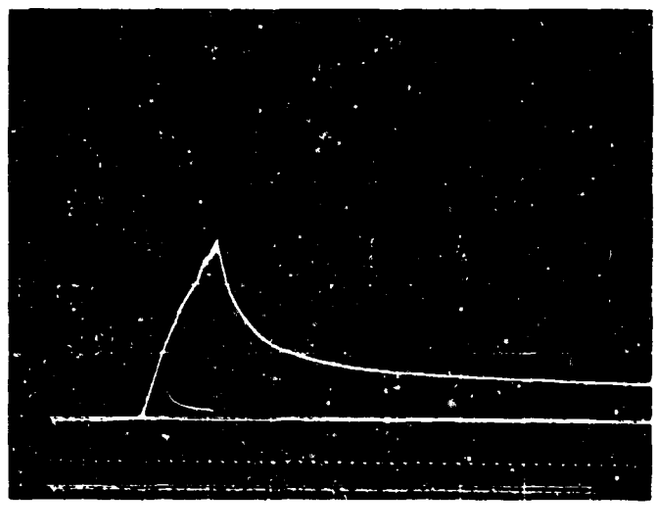

Fig. 26 - Oscillogramme de la pression pendant la combustion d'un propergol composite.

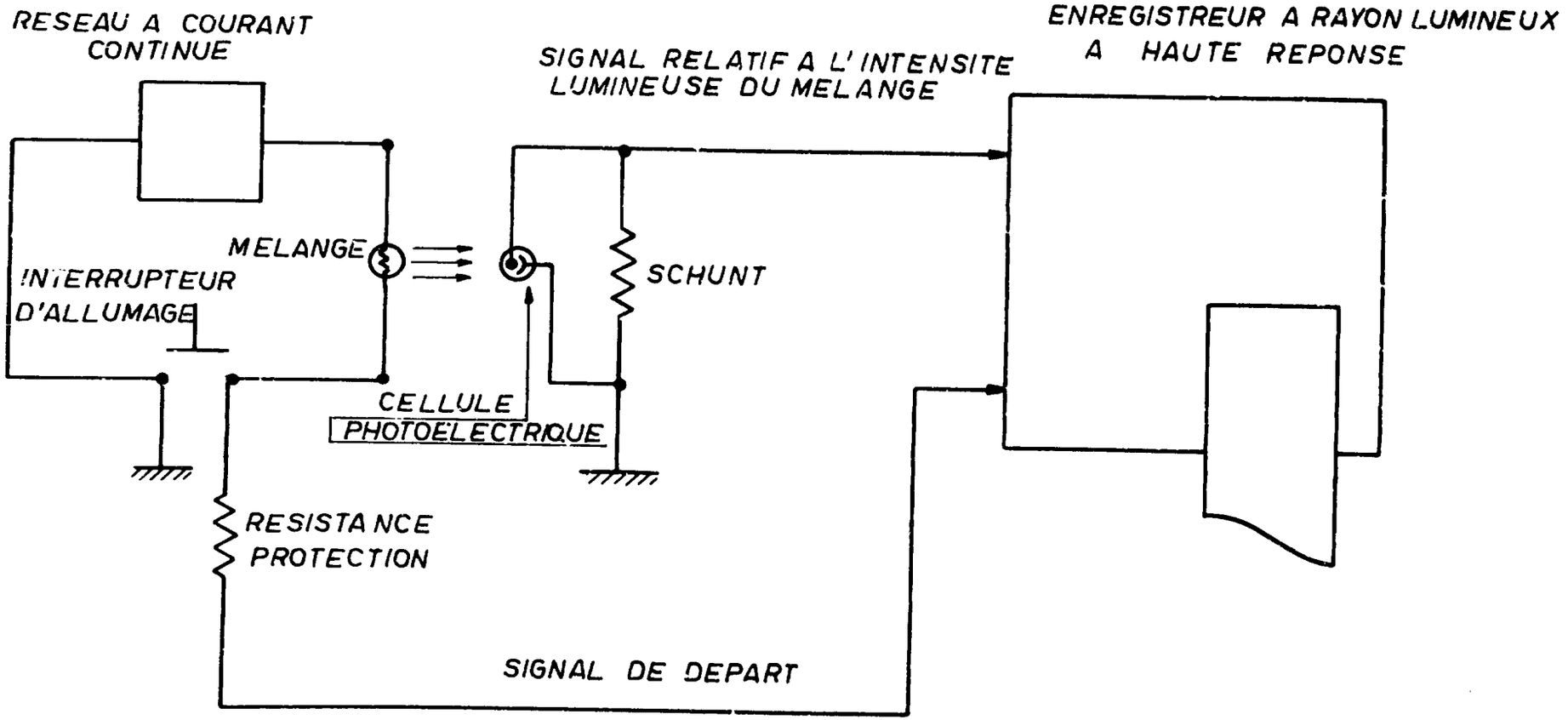

Fig. 27 - Schéma du système de mesure du délai d'ignition d'un mélange non comprimé.

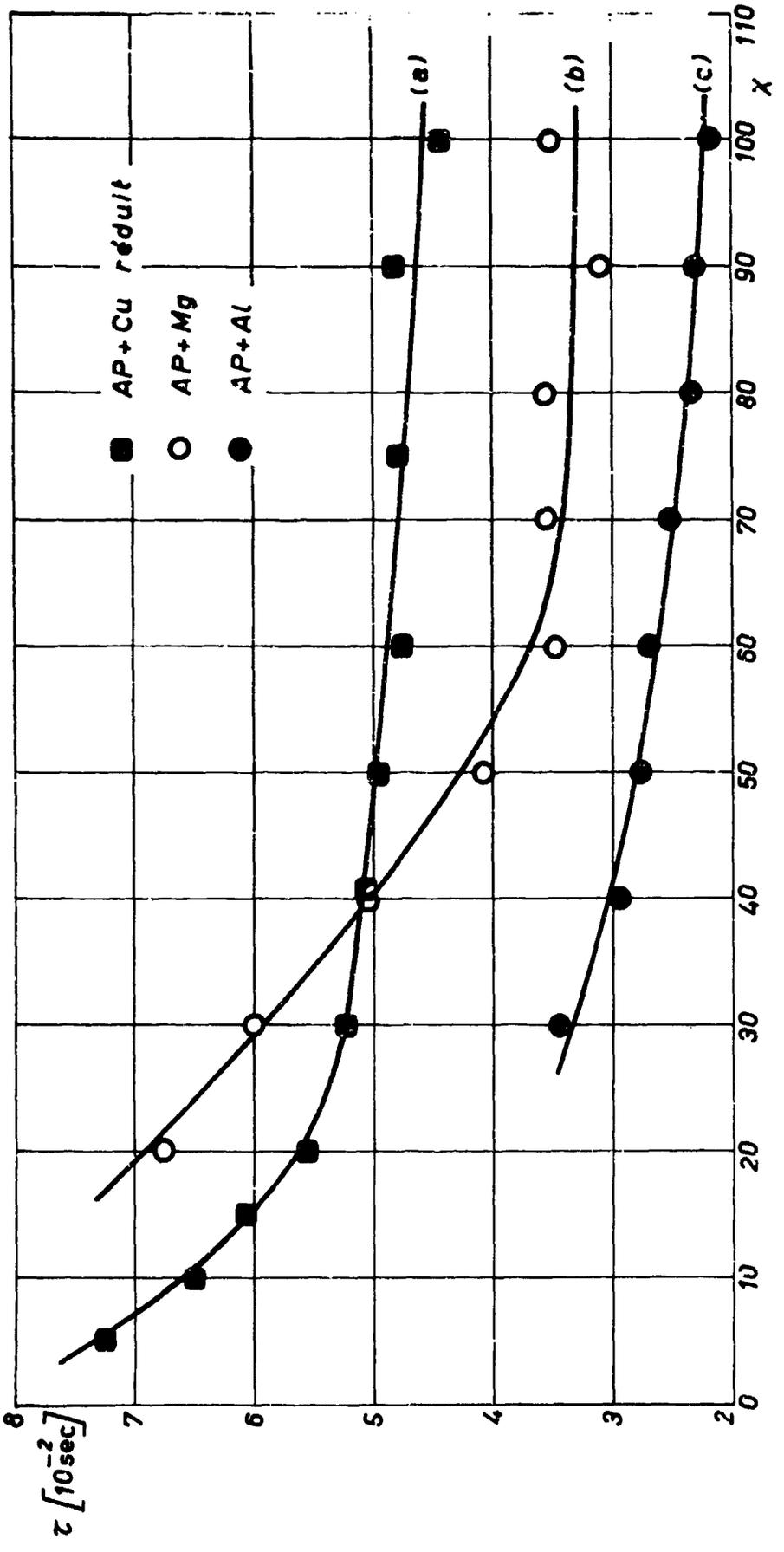

Fig. 28 - Influence du pourcentage de métal sur le délai d'ignition du mélange.

APPENDIX

DISCUSSIONS

This Appendix contains those discussions (following the presentations of papers at the meeting) for which written texts were later furnished, by the commentators and responding authors, for incorporation in the Proceedings.

LIST OF COMMENTATORS

Clark, J.	AF Flight Dynamics Laboratory, Wright-Patterson AFB, Ohio, USA
Davin, A.	Centre National de Recherches Métallurgiques, Liège, Belgium
Davis, H.M.	Metallurgy & Ceramics Division, US Army Research Office, Durham, NC, USA
Fuhs, A.E.	AF Aero Propulsion Laboratory, Wright-Patterson AFB, Ohio, USA
Glassman, I.	Guggenheim Laboratories, Princeton University, NJ, USA
Grabke, H.J.	Max-Planck-Institut für Metallforschung, Stuttgart, Germany
Graham, H.C.	Aerospace Research Laboratories, Wright-Patterson, AFB, Ohio, USA
Hancock, P.	University of Glasgow, Scotland
Heath, G.A.	Rocket Propulsion Establishment, Westcott, Bucks., England
Hutcheon, J.M.	UKAEA Reactor Materials Laboratory, Culcheth, Lancs., England
Jaarsma, F.	National Aerospace Laboratory, Amsterdam, Netherlands
Jones, R.M.	AF Rocket Propulsion Laboratory, Edwards AFB, California, USA
Kirkpatrick, H.B.	AF Materials Laboratory, Wright-Patterson AFB, Ohio, USA
Lewis, J.C.	Allen Clark Research Centre, Plessey Co. Ltd, Caswell, Northants, England
Lieberherr, J.F.	ONERA, Châtillon-sous-Bagneux, France
McAlevy, R.F.	Combustion Laboratory, Stevens Institute of Technology, Hoboken, NJ, USA
Monti, R.	Institute of Aerodynamics, The University, Naples, Italy
Osgerby, I.T.	Von Kármán Facility, Tullahoma, Tennessee, USA
Pearson, G.S.	British Embassy, Washington, DC, USA
Penner, S.S.	University of California-San Diego, La Jolla, California, USA
Povinelli, L.A.	Lewis Research Center, NASA, Cleveland, Ohio, USA
Rapp, R.A.	Ohio State University, Columbus, Ohio, USA
Rosner, D.E.	Department of Engineering & Applied Science, Yale University, Connecticut, USA
Scherberg, M.G.	Aerospace Research Laboratories, Wright-Patterson AFB, Ohio, USA
Sheasby, J.S.	University of Western Ontario, London, Ontario, Canada
Wittig, S.L.K.	Purdue University, Lafayette, Indiana, USA
Wolfson, B.T.	AF Office of Scientific Research, Arlington, Virginia, USA
Zeamer, R.J.	Hercules Incorporated, Magna, Utah, USA.

Discussion on the Paper
THE REACTION OF METALS AND ALLOYS WITH GASES AT ELEVATED TEMPERATURES
(Paper 2)
presented by
R. A. Rapp, USA

J. S. Sheasby

In your paper you attribute the pressure dependence of the parabolic rate constant of niobium to the effect of impurities in the oxide. Are you sure that this is the whole story? I do not think it matters too much whether the diffusion coefficient is impurity controlled or not; the difficult part is explaining why the apparent dissociation pressure of $\gamma - Nb_2O_5$ is about 10^{-4} atm.

R. A. Rapp

The complex oxidation behavior of niobium is certainly not yet completely understood, despite recent significant progress. The experimentally observed P_{O_2}-dependence of parabolic scaling rates cannot be rationalized within the classical theory which assumes absolutely pure oxides, and indeed, our oxidation specimens are highly impure. Kofstad's theory* is a self-consistent rationalization of the experimental observations in terms of a doped scale.

I am not aware of any experimental evidence indicating such a highly irregular dissociation pressure for $\gamma - Nb_2O_5$.

P. Hancock

I would like to make two comments on Dr Rapp's paper.

Firstly, on the work of Quets and Dresher, the diagrams produced apply to equilibrium conditions, but in sulphidation conditions internal attack of the material usually occurs. Under these conditions equilibrium data can be very misleading for the corrosion reactions are determined by kinetic rather than equilibrium thermodynamic considerations. For instance it has been shown that internal sulphur corrosion of nickel-chromium alloys results in both nickel and chromium sulphide being present in the alloy†, whereas thermodynamic considerations suggest that only chromium sulphide should be present.

Secondly, a comment on the excellent pictures by Howes showing voids at the oxide-metal interface. It is interesting to note that if the oxide is not strongly adherent then voids form at the interface as shown. However, if the oxide is highly adherent, as in nickel, then the vacancies do not principally precipitate at the interface but progress into the metal forming voids at the internal grain boundaries, as shown by work at Glasgow in 1966. Therefore we have this interesting balance that if the oxide is adherent, vacancies move into the metal and ruin its creep resistance, whereas if the oxide is non-adherent the voids precipitate at the oxide-metal interface rendering the oxide even more liable to spalling and causing subsequent accelerated corrosion of the alloy. This raises the question of what is the type of interface that is needed for a material for high temperature service?

R. A. Rapp

The use of thermodynamic considerations and the assumption of local equilibrium in the analysis of kinetic processes has often provided useful rationalizations and predictions. In the sulfidation of nickel-chromium alloys, the chromium sulfides are found at a greater depth in the alloy than the nickel sulfides which is in agreement with the thermodynamic stability diagram of Figure 3. The formation of Ni_3S_2 (even beneath a NiO scale) is allowed by the stability diagram. That CrS and Ni_3S_2 might be found together in a microstructure over some range of P_{S_2} and P_{O_2} does not agree with the stability diagram, but only indicates that the rate of their reaction to eliminate the unstable phase is too slow to achieve local equilibrium. Nevertheless, thermodynamics and local equilibrium are of great utility in analyzing the kinetics of solid-state reactions involving processes like diffusion, precipitation, dissolution, displacement reactions, etc.

Your comments concerning the effect of oxidation on creep resistance are interesting. The best available solution to the alloy oxidation problem (and this solution is emphasized by aluminide coatings) seems to be the formation of a scale which grows at a very, very slow rate (Al_2O_3, even though it's brittle), with enough of the alloying element available to renew the scale after a fracture. As an aid to scale adherence, rare-earth additions (as either solute or oxide) seem to decrease the sensitivity of the scale to thermal and mechanical stresses. The mechanism for this effect has not been sufficiently clarified in the literature.

---

* See Reference 33, page 2-8.

† Hancock, P. Proc. 1st Internal Conf. on Metallic Corrosion, Butterworth, London, 1962, pp 193-201.

Discussion on the Paper
PARAMETRES THEORIQUES ET DETERMINATIONS EXPERIMENTALES DANS L'ETUDE DE MATERIAUX SOUMIS A L'ABLATION
(Paper 3)
presented by
E. Guérini and R. Joatton, France

M. G. Scherberg

What were the shapes of the bodies used in the plasma tests? Certain shapes cause ablation striation in the exposed surfaces and hence are of interest.

E. Guérini

Les maquettes d'essais constituent la 4ème paroi d'un tube carré, les 3 autres étant en cuivre refroidi.

Nous n'avons jamais remarqué dans ces conditions de striures après essais, mais simplement des ondulations dans le cas de matériaux résistant mal à l'ablation.

D. E. Rosner

In view of the high reported concentrations of hydrogen in the pyrolysis gases, to what extent is the coke outer surface "protected" from direct attack by oxygen (via combustion in the boundary layer) in the atmospheric pressure environmental tests discussed?

E. Guérini

C'est un problème, actuellement, que de connaître la quantité d'oxygène qui atteint la surface. Il est fort probable que les gaz de pyrolyse constituent un écran; il faut savoir dans quelles proportions.

J. F. Lieberherr

Les résultats présentés par MM. Guérini et Joatton sont très intéressants, en particulier en ce qui concerne la disparition des fils de silice, ce qui semble indiquer une réaction de SiO_2 avec C à une température relativement basse. La question est de savoir si une telle réaction peut se produire dans des conditions réalistes d'utilisation des matériaux ablatifs sur une tête de réentrée. En effet, si l'oxygène ambiant, lorsqu'il y en a, parvient difficilement à la surface dans certaines conditions d'essai citées (chauffage par rayonnement), un peu plus facilement dans d'autres (chauffage convectif par écoulement tangentiel), il n'en est plus de même quand il y a un point d'arrêt de l'écoulement à la surface du matériau. Les résultats obtenus à l'ONERA montrent que l'oxygène du gaz extérieur a un effet notable et que les conditions ne sont pas du tout les mêmes avec un chauffage par plasma d'argon et par plasma d'air. Dans le premier cas on peut imaginer une réduction de SiO_2 par C alors que le dans le deuxième SiO_2 semble inerte et c'est le carbone qui réagit avec l'oxygène de l'air.

E. Guérini

1. Les essais que nous avons commentés présentent une température de paroi de 2200°C. Il ne s'agit donc pas de températures modérées.

2. Les réactions silice-carbone seront étudiées en faisant varier la teneur en oxygène. Nous tiendrons alors compte de ces résultats pour les applications en fonction de la teneur en oxygène de la couche limite.

Nous pensons toutefois que les essais au jet de plasma en écoulement tangentiel sont assez représentatifs de la section courante d'un corps de rentrée. Le point d'arrêt, toujours dimensionné surabondamment n'est pas pris en considération.

G. A. Heath

Have you observed any formation of silicon carbide during the ablation process? Silicon carbide has a brown colour and should be distinguishable from the carbon char zone. Do you think that the formation of silicon carbide, which has the desirable effect of absorbing a large amount of heat (endothermic reaction), should be encouraged by the addition of suitable catalysts to the ablative material?

E. Guérini

Nous n'avons jamais observé de dépôt de carbure de silicium après essai.

Toutefois, la réaction

$$SiO_2 + 3C \rightarrow SiC + 2CO$$

est possible.

Mais en présence d'une autre réaction telle que

$$SiO_2 + C \rightarrow SiO + CO$$

réaction qui est très vraisemblable, on peut avoir:

$$SiC + SiO \rightarrow 2Si + CO$$

ce qui expliquerait la disparition de SiC.

Nous n'avons pas envisagé la catalyse de la réaction

$$SiO_2 + 3C \rightarrow SiC + 2CO .$$

Il est bien évident que la forte chaleur d'absorption de cette réaction (132Kcal/mole) est intéressante dans les bilans thermiques.

Discussion on the Paper
TRANSFERT DE CHALEUR ET DE MATIERE AU DESSUS D'UNE SURFACE CATALYTIQUE DANS UN ECOULEMENT TURBULENT
(Paper 5)
presented by
M. Trinité et P. Valentin, France

D. E. Rosner

For this general class of flows, there should be a nonequilibrium region in which partial chemical kinetic control is encountered sufficiently close to the discontinuity in catalyst activity (cf. e.g. Rosner, D.E., Eleventh Symposium (International) on Combustion. The Combustion Institute, 1967, pp. 181-196). Is this chemical "relaxation length" large enough to be measurable at any of the reported Pd-catalyst temperature levels?

M. Trinité and P. Valentin

In our problem, the chemical reaction is only controlled by the diffusion and not by the chemical kinetics. This has been verified by the concentration profiles near the wall, it means $C = 0$ if $y = 0$, this proves that the catalyst combustion is complete at the wall. It is however certain that in the first millimeters, we may not affirm that the catalyst combustion is complete because our measurements are not sufficiently well defined very close to the discontinuity.

The results about eddy diffusivity which are presented in the paper do not take into account the first millimeters after the discontinuity, but the latter are the most important ones concerning the chemical kinetics.

Discussion on the Paper
KINETICS OF PHASE BOUNDARY REACTIONS BETWEEN GASES AND METALS
(Paper 8)
presented by
H. J. Grabke, Germany

D. E. Rosner

The rate-limiting role of dissociative adsorption in A_2 gas/solid reactions (A = O, Cl, F, ...) forming volatile reaction products recently prompted us to systematically study the corresponding reactions in *atomic* streams under otherwise comparable conditions (cf. e.g. Rosner, D.E. and Allendorf, H.D., J. Electrochem. Soc., Vol. 114, pp. 305-314, 1967). In the same spirit, it would appear fruitful to examine phase boundary-controlled dissolution reactions in dissociated gas systems in which the need for dissociative adsorption (or, dissociation of pre-adsorbed molecules) is thereby circumvented.

While the emphasis in your present paper is understandably on methodology and potentialities rather than experimental technique, I am nevertheless curious about the sensitivity of such kinetic results to impurity level in either gas feed or the iron filament. Have you had the opportunity to exploit the thin foil technique to study the (sometimes dramatic) poisoning effect of foreign gases on the kinetics and mechanism of dissolution of non-metallic elements in metals?

H.J. Grabke

It certainly would be very interesting to study the dissolution reactions of gases in metals with predissoziated gases. In that way one could get informations on the reaction steps other than the dissoziation step, which comprise the phase boundary reaction.

To answer the other part of your question I must say that I have always tried to use very pure materials, gases and metals, and to avoid the influence of impurities. But it is known from the results of L.S. Darken and E.T. Turkdogan (in Proceedings Int. Conf. Metallurgy and Materials Science, "Heterogeneous Kinetics at Elevated Temperatures", University of Pennsylvania 1969) that especially surface active atoms like sulfur and oxygen can have a pronounced effect on kinetics at metallic surfaces.

Discussion on the Paper
OXIDATION STUDY OF ZIRCONIUM DIBORIDE WITH VARIOUS ADDITIVES
(Paper 9)
presented by
H.C. Graham and W.C. Tripp, USA

D.E. Rosner

For ultimate application to lifting vehicle leading-edges, and for refractory composites including silicon carbide and/or carbon, our previous work[5,6] leads me to suggest that these materials be characterized and optimized in well-defined *dissociated* oxygen/nitrogen mixtures at suitably low pressures rather than in $O_2(g)$ alone. Have subatmospheric pressure arc jet tests been completed on this class of boride composites, and, if so, in what ways do the recession or weight change kinetics differ significantly from those illustrated in your paper?

H.C. Graham and W.C. Tripp

Under Contract AF33(615)-3859 entitled "Stability Characterization of Refractory Materials Under High Velocity Atmospheric Flight Conditions" sponsored by the Air Force Materials Laboratory, arc jet test has been conducted on these materials. There is a series of final reports[7] on this contract which summarize the results. We have not compared these results to ours since the two experiments were carried out under quite different experimental conditions.

J.C. Lewis

In view of the applications envisaged and the high temperatures of operation mentioned, and the practical difficulties involved in thermogravimetric analysis at such high temperatures, the measurement of recession rates, rather than weight loss rates, may be both easier and more relevant - don't you agree? After all, what we are interested in is the change in geometry, rather than in the weight, of a nozzle or nose cone.

H.C. Graham

In answer to the first part of the question I would say that, yes, the measurement of recession rates may be both easier and more relevant, but would add - for any given configuration or environment. I would not agree that we are only interested in the change of geometry. Our measurements are designed to determine the transport properties of the material as a function of ambient conditions. We also accurately determine the kinetics of the processes. Using both these determinations it is possible to accurately predict the behavior under various environmental conditions.

Reference 5. Rosner, D.E. *Supersonic Flow, Chemical Processes and Radiative Transfer*, AGARD - Pergamon Press, pp. 439-483, 1964.

Reference 6. Rosner, D.E; Allendorf, H.D. *Nitrogen as an Ablative Reactant in Dissociated Air* AIAAJ. in press; see also ibid., Vol.6, pp.650-654, 1968.

Reference 7. - AFML TR69-84, Part I, Vol.I; Part II, Vols.I, II and III; Part III, Vols.I, II and III; Part IV, Vols.I and II, December 1969.

H.J. Grabke

How do you explain that the vaporization rate of B_2O_3 remains constant, in spite of the growing layer of zirconia?

Do you assume that the liquid B_2O_3 goes through pores in the zirconia layer to the surface?

H.C. Graham and W.C. Tripp

We have been able to measure independently total oxygen consumption, net weight change, and vaporization rates. From these measurements we have found that the following equation described the oxidation of Material I, ZrB_2 with no additives,

$$\Delta m/A = 17.65\, e^{\frac{-6000}{T}}\, t^{1/2} + 9.15 \times 10^{4} e^{\frac{-23000}{T}}\, t ,$$

where $\Delta m/A$ is the total oxygen consumed in mg/cm^2, t is time in minutes, and T is the temperature in degrees Kelvin. The first term on the right represents the net sample weight change, i.e., the oxygen consumed in forming ZrO_2 and B_2O_3 minus the weight of any B_2O_3 vaporized. The second term on the right is the weight of any B_2O_3 that has vaporized.

Our experiments have shown that ZrB_2 oxidizes stoichiometrically, at least over the temperature range of 800° to 1400°C. In this temperature range there will always be more $B_2O_3(l)$ on the specimen than can evaporate and the vaporization rate is constant. However, for long periods of time or higher temperatures, the vaporization can reach a rate equal to the rate of formation. This time and temperature can be calculated from the equation. As this point is reached, the vaporization rate might not remain constant, but would be expected to follow the kinetics of the formation of B_2O_3. We have not, as yet, made these measurements.

Berkowitz* has shown from microstructure examination evidence that ZrB_2 oxidizes by the inward diffusion of oxygen. Microstructure studies on these materials present some difficulties because B_2O_3 is liquid above 450°C and hydrates rapidly in air. However, some recent microstructure examinations we have done certainly indicate that the B_2O_3 is distributed through the porous zirconia layer.

* See Reference 4, page 9-3.

Discussion on the Paper
OXIDATION OF SILICON AND SILICON CARBIDE IN GASEOUS ATMOSPHERES AT 1000-1300°C
(Paper 10)

presented by

J.E. Antill and J.B. Warburton, UK

D.E. Rosner

The inapplicability of a quasi-thermodynamic active-passive transition criterion for the oxidation rate of silicon carbide in systems free of external (gas phase) transport limitations has been verified in our recent experimental studies of the behavior of SiC(s) in dissociated oxygen and nitrogen (Rosner, D.E. and Allendorf, H.D.) J. Phys. Chem., submitted). A more reasonable estimate in such cases follows directly from a general expression for the steady state silica film thickness (resulting from a balance between parabolic-type scale growth and outer-surface sublimation) by inquiring into the environmental conditions ($P^*_{O_2}, T^*$) that would cause this film to be of "atomic" dimensions. This latter method also rationalizes the large difference in transition locus we have observed upon oxygen dissociation.

From the existing literature on the high temperature transition from passive to active behavior one gets the erroneous impression that the condition of net specimen *weight loss* is a suitable criterion for "active" oxidation. However, it is also evident from our high temperature measurements (*loc. cit.*) that the true transition from passive (i.e. SiO_2(c)-surface layer) to active (i.e. "bare" surface) behavior can occur well *within* the weight loss régime, and is better distinguished kinetically by (i) a marked reduction in the sensitivity of the reaction rate to specimen temperature (i.e. reduction in apparent activation energy) and (ii) an increase in reaction order with respect to oxygen. Thus, net specimen weight loss is only a necessary (but not sufficient) condition for true bare surface behavior.

J.E. Antill and J.B. Warburton

The data of Professor Rosner showing the inapplicability of the mass transport theory for the active-passive transition is most welcome support for our data. With regard to the physical interpretation of the results, two possibilities exist, the one mentioned by Professor Rosner and one in which there is an incomplete silica film during active oxidation. We favour the latter with the silica films being either porous or more probably associated with particular areas (e.g. grains) of the carbide surface. SiO formation would then occur to a

considerable extent at the triple environment-silica-silicon carbide boundaries as well as at the "bare" surface. The definition of active oxidation would therefore be one where the partial pressure of SiO at the specimen surface would be greater than that given by the dissociation of silica

$$SiO_2 \rightarrow SiO + \tfrac{1}{2}O_2 ,$$

rather than the existence of a completely "bare" surface or the condition of a net specimen weight loss.

P. Hancock

I would like to ask the author two questions.

Firstly - do you really have parabolic behavior, did you try to fit the best equation to the results.

Secondly, a general point, I think it is true that we all stopped automatically plotting $\log k_p$ vc $1/T$. The errors involved in these plots are extremely large and I think that the values of "activation energy" obtained have little use. I'm glad to see that Dr. Antill deliberately did not mention an activation energy, but I would like to ask him whether he has any comment on "energies" obtained in this way in view of the scatter obtained in his results (Fig. 4 and 5). This scatter despite the fact that he had a thin uniform scale with no internal penetration.

J. E. Antill and J. B. Warburton

Parabolic and Arrhenius plots have been used primarily as a convenient means of reporting the data, but also because they have fundamental bases. The adherence to a parabolic law was in general good, especially for silicon (e.g. Figure 6). However, as stated in the paper, with both silicon and silicon carbide after long exposure periods the reaction rates occasionally decreased at a greater rate than predicted by the parabolic law.

No "errors" are involved in reporting data in this manner and criticism can only arise from interpretation of the plots. As Dr Hancock points out activation energies have not been calculated because the extent and reproducibility of the data are not sufficient to obtain meaningful values for these energies.

R. Monti

From Figure 5 it is hard to conclude about the decreasing of the reaction rate k with increasing temperature for silicon; there appears to be only one experimental point (around 1000°C) - Is it possible that, for instance, the high k at 1000°C is due to an uncontrolled higher contamination with air?

J. E. Antill and J. B. Warburton

The decrease in the rate constant with increasing temperature for silicon in water vapour has been well substantiated. At each of the two pressures duplicate experiments were carried out at each temperature, the trend being obtained at each pressure. Also the experiments during which the pressure was changed (Fig. 6) provided further confirmation. The results could not be attributed to air contamination as in the experiments where this did apply, reaction rates were high and similar for both silicon and silicon carbide. In contrast the experiments without air contamination produced markedly different behaviour for the two materials, and therefore if contamination was responsible for the odd temperature dependence it would have to have been confined to one material at one temperature, and to have been reproduced five times.

H. J. Grabke

I should like to propose to Dr Antill to use H_2O-H_2 mixtures for his oxidation studies - then he has a defined oxygen potential in the gas atmosphere. In his oxidation studies with water vapor solely he has a very undefined oxygen activity at the surface, established by a stationary state of the reaction: oxygen transfer from the H_2O, giving H_2. Thus the oxygen potential is dependent on the rate of this transfer. It is impossible to calculate the gradient of oxygen potential in the silica layer in that case, whereas it is possible if H_2O-H_2 mixtures are used.

J. E. Antill and J. B. Warburton

I agree that the use of H_2O-H_2 mixtures is a convenient means to obtain a range of oxygen potentials in a gas, but was unfortunately not possible in this work for experimental reasons. However, the oxygen potential was fixed for a particular temperature, but varied with the experimental temperature according to the equilibrium

$$H_2O \rightleftarrows H_2 + \tfrac{1}{2}O_2 .$$

Removal of oxygen by the corrosion of the silicon or silicon carbide will not have significantly disturbed this equilibrium as the corrosion rates were slow by comparison with the gas reactions associated with the equilibrium.

R. A. Rapp

Did you experience any increased vaporization with the oxidation of Si and SiC by H_2O vapor? In other words, is there any evidence for volatile silicon hydroxides?

J. E. Antill and J. B. Warburton

Evidence for the formation of volatile silicon hydroxides was specifically sought in tests with small blocks of vitreous silica, but none was found.

G. A. Heath

I should like to ask a question on a practical aspect of this work. I am interested in the use of silicon carbide as an oxidation protection coating for graphite. Have you studied the oxidation of silicon carbide in the form of thin coatings on graphite where residual stresses at the surface could possibly affect rates of oxidation?

J. M. Hutcheon

This is an old problem in the Atomic Energy field. One problem is the matching of thermal expansion coefficients. This has led to the development of special graphites to match the silicon carbide.

J. C. Lewis

I recall some work on SiC coating of graphite, reported to the British Ceramic Research Association some years ago, which suggested that the main disadvantage of these coatings was not so much thermal mismatch with the substrate material as of pinholes in the coatings. The solution proposed at that time was the rather unsatisfactory one of sealing the holes with molten silicon. Can anyone say whether the situation has improved since then?

J. E. Antill and J. B. Warburton

One of the main problems with silicon carbide coatings on graphite is the filling or bridging of open pores in the graphite as these areas represent regions of structural weakness in the coating. Cracks are often present in these areas, leading to an undermining of the coating on oxidation over the long term, although appreciable benefits are usually obtained over the short term.

D. E. Rosner

Regarding the use of silicon carbide to "protect" graphite, it is interesting to note that at sufficiently high temperatures (e.g. above about 1850°K at an O_2-pressure of 3×10^{-2} Torr) our recent measurements reveal higher reaction probabilities for $O_2(g)$ on pyrolytic SiC(s) than on graphite (Rosner, D.E. and Allendorf, H.D.) Carbon, Vol. 7, pp. 515-518, 1969; AIAA J., Vol. 6, pp. 650-654, 1968). We also find that a high temperatures silicon carbide is far more readily attacked by *atomic* nitrogen than is graphite.

J. E. Antill and J. B. Warburton

The point made by Professor Rosner would be relevant to the performance of coatings when active corrosion of silicon carbide was operative. The behaviour of graphite and the carbide would then be analogous. However, if the oxygen pressure was sufficiently high to form appreciable amounts of silica as distinct from SiO, passive oxidation would be obtained and the carbide would be markedly less reactive than graphite.

Discussion on the Paper
THE OXIDATION OF NIOBIUM IN THE TEMPERATURE RANGE 350°-600°C
(Paper 11)
presented by
J. S. Sheasby, Canada

H. B. Kirkpatrick

In earlier work on the low temperature oxidation of niobium, we observed the development of globules of a new phase at the metal-metal oxide interface during the transition from parabolic to linear kinetics. Has Dr Sheasby observed this?

At temperatures around 275°C we also observed the growth of thick, glassy oxide layers. Did Dr Sheasby observe this?

We concluded that the transition from "parabolic" to linear kinetics was caused by breakdown of the protective oxide film due to growth of the new phase at the interface.

J. S. Sheasby

No. I have seen only niobium oxide of the interference colour film and niobium pentoxide when oxidizing below 440°C.

No. I have not oxidized specimens at 275°C, but as a general observation, the outermost oxide surface is more shiny than the surface of inner layers.

That is a fair description of the transition to linear kinetics when oxidizing below about 450°C, though there is controversy as to whether it is a new phase that is nucleating.

H. C. Graham

In reference to the slide showing the oxide-metal interface where there were areas which showed a thick oxide and areas which did not have an oxide layer:

What is the proposed reason for this difference?

Is it stress enhanced oxide growth or is the difference due to difference in metal grain orientation?

J. S. Sheasby

This phenomena is definitely related to the metal grain orientation. Though what exactly is happening and why it should be so marked is not known. This is the subject of a continuing study.

P. Hancock

I should like to ask Dr Sheasby how he is sure that all the cracks he observes at temperature were present at temperature and did not occur during cooling. In particular, Figure 7(b) appears that it could have formed during cooling.

J. S. Sheasby

At the higher oxidation temperatures it is quite easy to distinguish between cracks that formed on cooling and cracks that formed during oxide growth, for the latter can be followed by oxidizing specimens for increasing periods of time. At lower oxidation temperatures this is much more difficult, but fortunately in the arguments presented for below 660°C, it is not necessary to know the exact pore structure. However, in fact at least part of the corner crack shown in Figure 7(b) was present at temperature.

R. A. Rapp

In reply to Dr Hancock's question concerning Figure 7(b), it seems reasonable that the lack of accelerated reaction at the corner (where because of geometric contraints an accelerated reaction at the corner always accompanies "protective" oxidation on the flat surfaces) indicates that the scale of Figure 7(b) is not at all protective, and the presence of any visible crack in this scale is not of importance.

The work of Roberson and Rapp (*Trans. Met. Soc. AIME*, 239 1327 (1967)) involving the oxidation of Nb in a Cu_2O vapor shows that Cu is deposited at the reduction sites, and these sites are present (after fractures at *temperature*) throughout the oxide scale. Therefore, these Nb_2O_5 scales do, indeed fracture at the elevated temperature.

J. S. Sheasby

Thank you for your support; though I must point out that your work was performed at a temperature where the TT to H-Nb_2O_5 transition is very rapid and should, therefore, be extrapolated with caution to the present work

H. J. Grabke

It's extraordinary that the lower oxides do not appear in the oxidation of Nb to Nb_2O_5. In that connection it is very interesting to know if the Nb under the growing Nb_2O_5 is saturated or oversaturated concerning dissolved oxygen?

J. S. Sheasby

The metal at the oxide-gas interface is super-saturated with oxygen.

Discussion on the Paper
THE OXIDATION OF NI-BASE SUPERALLOYS UNDER AIRCRAFT ENGINE CONDITIONS
(Paper 12)
presented by
C. S. Wukusick, USA

A. Davin

Concerning the influence of additional elements on the oxidation and hot corrosion resistance of super alloys, at CNRM we have performed tests on Co-Cr alloys in air, H_2S/H_2 mixture and in combustion gas atmospheres produced by combustion of fuel polluted with S and NaCl*. Among a lot of addition elements, we have observed that Aluminium and Yttrium improved greatly the sulfidation resistance of the basic Co-Cr alloys. Addition of Tantulum improved the oxidation resistance, while in combustion gases in addition to Cr, alloying elements such as Ta, Al and Y, were beneficial. With regard to the influence of these elements on the morphology of the scale, in sulfidation tests we have observed that elements such as W, Nb, Al formed a sulfide layer adjacent to the metal while Cr formed an intermediate layer and Co was rejected in the outer layer as shown in the two figures (Figure 1 and 2). While in the case of additional elements such as Ni and Fe, these elements were rejected with cobalt in the outer layer.

Fig. 1. — Optical micrograph of sulphide scale formed on the Co-10Cr-15W alloy exposed for 5 hours at 800 C in a hydrogen sulphide atmosphere.

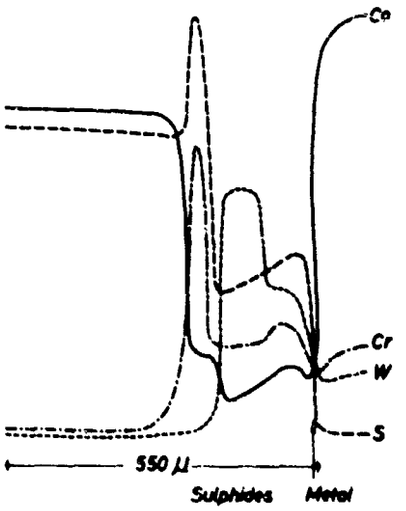

Fig. 2. — Variation of the Co, Cr, W and S contents across the scale formed on the Co-10Cr-15W alloy exposed for 5 hours at 800 C in a hydrogen sulphide atmosphere.

C. S. Wukusick

No reply necessary.

---

* Davin, A., Coutsouradis, D. and Habraken, L. Cobalt No. 35, June 1967, pp. 69-77.

R. A.

Recent work by Giggons and Pettit which will appear soon in Trans. Met. Soc. AIME has cleared up the effect of surface abrasion on the kinetics of oxidation of Ni-Cr alloys of intermediate compositions. I have summarized these results in my paper.

C. S. Wukusick

Giggons and Pettit relate the surface effects to recrystallization of the surface layers upon heating to the test temperature. However, in the more complex Ni-CrAl alloys such as U-700 recrystallization is retarded by the gamma-prime precipitate and thus does not occur below 2000°F during initial oxidation. Therefore, some contribution of the deformation to increased diffusion rates in the 1600-2000°F temperature range is possible. This effectively lowers the temperature at which selected oxidation of Al to form an Al-rich surface oxide occurs. Also partial solution of the (Ni_3Al) phase occurs, thus releasing Al for surface reaction. Again, increased diffusion rates may contribute to increased availability of Al for surface reactions.

Discussion on the Paper
REACTIONS BETWEEN HIGH-TEMPERATURE-RESISTANT ALLOYS AND GASES
(Paper 13)
presented by
H. Pfeiffer, Western Germany

P. Hancock

I would like to ask for clarification concerning green-rot attack. This type of corrosion usually occurs as Dr Pfeiffer says in atmospheres which alternate between carburising and oxidising. However I think it is usually accepted that the mechanism of corrosion is by internal carburisation removing chromium as chromium carbides which allows the chromium-denuded material to be subsequently oxidised. However in the paper Dr Pfeiffer refers to a mechanism whereby the chromium is first removed by internal oxidation. I would like to ask if he has any experience of green-rot having been produced under systems other than those containing combustion products where there is a distinct likelihood of localized reducing conditions applying periodically?

H. Pfeiffer

May be that internal carburisation promotes the green-rot attack but I think it is not a necessary condition. For instance this kind of corrosion has been observed by Spooner, Thomas and Thomassen* at NiCr-thermocouples with 10 wt% Cr and NiCr-alloys with 20 wt% Cr heated in narrow tubes containing air as annealing atmosphere. Another example of green-rot attack without the influence of carbon is the observation of this reaction in metal sheathed tubular elements†. In both cases no carbon was available.

I think green-rot attack is to be expected, whenever the corrosion reaction is started as an internal reaction on the grain boundaries, independently whether it is initiated by carburisation or not. Several conditions have to be assumed to give rise to this kind of attack, the one of them is an oxygen pressure of the annealing atmosphere between the dissociation pressures of Cr_2C_3 and NiO.

N. N. Davis

Does the "green-rot" arise only during exposure to dry oxygen, or will it develop in a moist atmosphere? In other words, will it develop in an atmosphere of H_2/H_2O in which the oxidizing potential is too low to promote the oxidation of other elements in the alloy (Ni,Fe)?

H. Pfeiffer

The main condition to get green-rot attack is a very low oxygen pressure, low enough to prevent the oxidation of other elements than chromium in NiCr(Fe)-alloys. If this condition is fulfilled, moisture seems to have only a little effect. Copson and Lang◆ observed green-rot attack annealing nickel-chromium alloys both in dry and wet carbon monoxide. The difference in the behaviour was only small. But it has to be noted too that tests in wet hydrogen were unsuccessful, demonstrating the low oxygen pressure to be only one of the conditions to get green-rot

---

* Spooner, N.F., Thomas, [illegible] Thomassen, L. Trans. AIME, Vol.197, 1953, p.844.

† Pfeiffer, H. Werkstoffe und Korrosion, Vol.12, 1961, p.669.

◆ Copson, H.R. and Lang, F.S. Corrosion (Houston) Vol.15, 1959, p.194.

Discussion on the Paper
MECHANICAL PROPERTIES OF SURFACE OXIDE FILMS AND THEIR EFFECT ON THE KINETICS OF OXIDE GROWTH
(Paper 15)
presented by
P.Hancock, UK

J.S.Sheasby

I would like to point out that the mechanical properties of the oxide are not always the most important in affecting the oxidation rate. C.Roy has recently shown that the parabolic-linear oxidation kinetics of zirconium coincide with the beginning of creep in the metal - not the oxide.

P.Hancock

I agree with Dr Sheasby that the mechanical properties of the oxide are not always the most important factor affecting the oxidation rate. For instance results with nickel, on the particular specimen geometry chosen, show that the mechanical properties of the oxide are such that continuous scale growth and adhesion are possible and therefore the oxidation rate is determined by other factors, in this case probably ion diffusion through the scale. However, with materials such as iron the mechanical properties are a very important factor in determining the oxidation rate and cannot be neglected.

Discussion on the Paper
REACTION BETWEEN SOLIDS AND GASES IN RADIATION FIELDS
(Paper 16)
presented by
J.M.Hutcheon, UK

J.Clark

Have any studies been made of the effect of the radiation on the flow characteristics (viscous losses) of gaseous coolants through a reactor?

J.M.Hutcheon

I am not aware of any experiments along the lines you indicate.

D.E.Rosner

Your initial argument concerning the insensitivity of radiolytic corrosion rate to (internal) surface area is apparently based on the heterogeneous deactivation probability per strike being unity. However, if the active species are O-atoms, and their average gas phase "range" (homogeneous recombination length) is indeed much larger than the prevailing pore dimensions, most O-atoms should have multiple opportunities to gasify graphite at the quoted temperatures. Available kinetic measurements of the C-atom removal probability when O-atoms strike graphite (cf. e.g. Rosner, D.E. and Allendorf, H.D., Carbon, Vol.7, pp.515-518, 1969) and recent measurements of the *sum* of the oxidation and recombination probabilities (J.B Berkowitz-Mattuck, work in progress) would indicate appreciable reflection (or "restitution") of C-atoms - especially at temperatures below 800 K, where perhaps 9 out of 10 incident atoms would return to the gas phase, and thereby, have another opportunity to strike the graphite surface. Upon second thought, however, to guarantee the reported insensitivity to (internal) surface area, isn't it merely sufficient that almost every O-atom formed by radiolysis be *ultimately* consumed as a result of a *wall* interaction (rather than requiring *each* such encounter to be successful)? Thus, *in the limit of negligible gas phase quenching*, atoms formed radiolytically will on the average have the same number of opportunities to strike internal graphite surfaces, regardless of the magnitude of the external surface area per gram of material.

Regarding the increased dependence of the Zircaloy alloy oxidation rate on effective oxygen pressure in the presence of reactor radiation, it is perhaps of interest to note that in a gaseous oxidizing environment, if radiation merely produced atomic oxygen in the gas phase, an increased oxygen pressure dependence would also be expected. D.Cubicciotti, Heckingbottom and Linnett (Trans. Faraday Soc., ca. 1969) have recently reported a number of cases for which dissociation increases the oxygen pressure dependence of the parabolic rate constant for p-type scale forming materials.

J.M.Hutcheon

I am grateful to Professor Rosner for directing my attention to these recent measurements. The hypothesis of unit heterogeneous deactivation probability per strike is obviously too simple. The essential feature is that the rate of reaction is determined by the rate of supply of active species, and not by the area available for the active species to strike.

Discussion on the Paper
LOW-TEMPERATURE REACTIONS BETWEEN SOLIDS AND GASES
(Paper 18)
presented by
K.Hauffe, Germany

J.Clark

Have any attempts been made to vary the ion transport rate through the semiconductor crystal lattice by the application of external electric fields or by reverse or forward electric biasing?

K.Hauffe

We have performed oxidation experiments by means of an electrochemical cell technique for the bromination of silver at 400°C in the following set-up

$$Pt|Ag|AgBr|Pt(Br_2) \qquad (I)$$

and for the oxidation of zirconium at 800°C in oxygen in the following set-up

$$Ag|Zr|ZrO_2|Ag(O_2) \qquad (II)$$

It could be demonstrated that by a short-circuit of the cell (I), the rate of bromination could be strongly increased. The same phenomenon could be detected for the oxidation of zirconium and also theoretically predicted, since in both cases electrons flowing very slowly through the layer of the reaction product (AgBr, ZrO_2), could be transported very fast via an external short-circuit wire to the reaction front $AgBr/Pt(Br_2)$ or $ZrO_2/Ag(O_2)$. A low-voltage dc device with the negative pole to silver or zirconium causes a decrease in the rate of corrosion (see Eriksen J. and Hauffe, K., Z. phys. Chem. (N.F.), 1968).

R.Rapp

Because of the bipolar nature of the (001) face of ZnO relative to the $(00\bar{1})$ face, which of the photoelectric and other effects which you have studied behave differently on the differing basal planes of ZnO?

K.Hauffe

The sensitized photocurrent is indeed smaller if the $(000\bar{1})$ face of the zinc oxide crystal is contacting the electrolyte. Both the non-sensitized photo-current and the dark-current, however, are equal for the two faces.

Discussion on the Paper
RESULTATS EXPERIMENTAUX RECENTS SUR LA COMBUSTION DE L'ALUMINIUM ET D'AUTRES METAUX
(Paper 20)
by M.Barrère, France
(presented by J.F.Lieberherr, France)

I.Glassman

Several comments are appropriate to the discussion of the combustion of aluminium particles, in particular as regards the observation of an oxide cap on the metal particle and the appearance of hollow oxide spheres in the combustion products.

The mechanism of formation of the hollow oxide spheres has been explained* as resulting from the dissolved gases in the metal. It was suggested that the hollow oxide spheres were bubbles which were blown from the oxide cap which forms on the metal particle.

---

* Brzustowski, T.A. "Comments on the Paper 'Estimating Aluminium Particle Combustion Kinetics' by Bartlett et al.". Comb. and Flame, Vol.8, 1964, pp.339-342.

The recent work of Prentice* shows significant results regarding the above comments. The accumulation of oxide on the metal particle is now referred to as a "fumarole" rather than a "lens-shaped cap". Numerous bubbles are observed in the oxide cap. In addition, Prentice demonstrates that the formation of the oxide deposit is dependent on the presence of nitrogen (other gases may also cause similar results) in the ambient atmosphere. The phenomena associated with the presence of the oxide, namely spinning, shedding of oxide spheres, and fragmentation can be eliminated by burning aluminium particles in high purity oxygen-argon mixtures.

J.F. Lieberherr

Nous avons noté qu'on peut observer des particules d'alumine massive ainsi que des sphères creuses. Le fait que l'alumine soit solide à la température de surface de la goutte d'aluminium permet assez mal d'imaginer que les sphères creuses sont obtenues de façon similaire à des bulles de savon. Leur apparence au microscope électronique indique de plus une structure vraisemblablement poreuse. On peut donc imaginer l'explication suivante pour la formation de sphères pleines et creuses d'alumine, en se fondant sur le mécanisme de formation des deux lobes de Prentice:

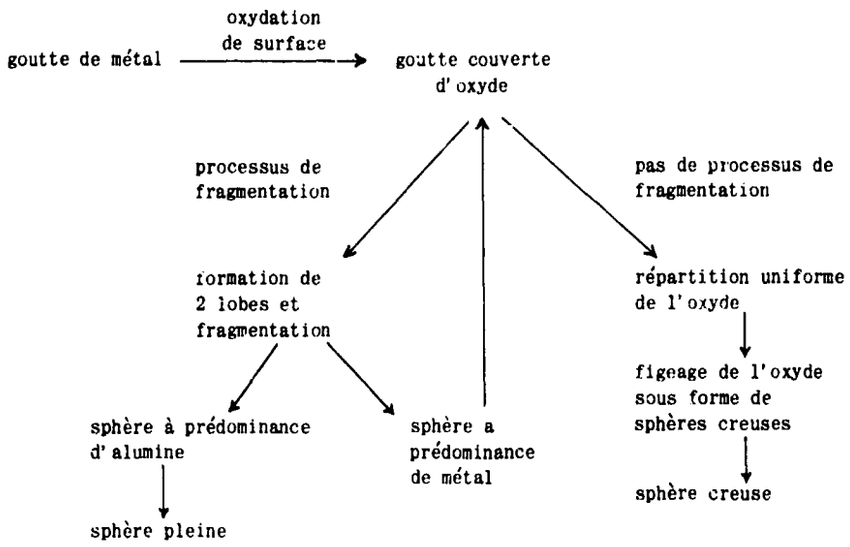

En ce qui concerne la calotte d'alumine, je vois mal ce que l'on désigne par "fumarole". D'après les photographies de Prentice on voit des calottes qui ont grandi par vagues successives et ont une structure irrégulière là où la croissance a commencé. Prentice a établi le rôle différent joué par l'azote et l'argon dans le processus de combustion mais la différence réside à mon avis dans le fait que l'argon est réellement un diluant alors que l'azote est réactif. La formation des calottes est liée au rapport combustible/comburant à la surface de la goutte. Un film tourné à l'ONERA† montre que pour des mélanges de perchlorate d'ammonium (PA) et d'aluminium la formation de la calotte est liée au pourcentage de PA. S'il décroît la formation de la calotte est favorisée. La figure 9 du texte et les conclusions de ses auteurs (Référence 11 du texte) conduisent aux mêmes conclusions. Ceci peut être interprété par la coexistence des mécanismes en phase gazeuse et de surface. Le mécanisme de surface domine aux fortes concentrations en oxygène, ce qui évité l'accumulation de l'oxyde puisque la goutte est très chaude, tandis que s'il y a peu d'oxygène disponible les mécanismes en phase gazeuse dominent et il peut y avoir formation de calottes.

Si maintenant nous comparons l'oxygène dilué dans l'azote à celui dilué dans l'argon, le mélange doit traverser la zone de flamme avant d'atteindre la surface et dans le premier cas il peut s'appauvrir en oxygène par la formation de divers oxydes d'azote dans la flamme très chaude. Le rapport combustible/comburant sera ainsi plus faible dans le premier cas que dans la deuxième, d'où formation de calottes.

---

* Prentice, Jack L. "Combustion of Pulse-Heated Single Particles of Aluminium and Beryllium". Preprint 69-2 1969 Spring Meeting, Western States Section of the Combustion Institute, China Lake, California.

† Bourianes Combustion de mélanges de perchlorate d'ammonium et d'aluminium. Film ONERA.

Discussion on the Paper
COMBUSTION OF SOLID PARTICLES IN A TURBULENT STREAM WITH RECIRCULATION
(Paper 21)
presented by
M.M Gibson and B.B.Morgan, UK

S.S.Penner

It is somewhat surprising that a highly simplified radiant heat-transfer model may be used successfully in a system in which the effect of radiation is of first-order importance. Unless the diffusion limit obtains, one would expect that radiant heat transfer in a direction normal to the axis is less important than transfer in the axial direction. Of course, a proper calculation must involve an appropriate average over the complete field of view at each location.

B.B.Morgan

In evaluating radiant transfer we integrate intensity over all solid angles, easing the integration by assumptions of (i) axial symmetry; (ii) uniform axial intensity at constant radius; and (iii) isotropic values in directions of positive and negative radius vector. I readily accept (witness the concluding section of the paper) that assumption (ii) contributes to the errors in our predictions; its result is to exaggerate temperature variations along the chamber.

But the most important effect of radiation is to transfer heat from the flame to the cooled wall; as much as 50% of the energy released by combustion is lost in this way. Remembering that the chamber has a radius only one-eleventh of its length, I am of the opinion that it is the radial flux that is the more important and that assumption (ii) is acceptable in the context of our calculation. This is not to say that one should rest content with it.

Discussion on Paper
PHENOMENES DE FUSION ET REACTIONS DE SURFACE DANS LA COMBUSTION DES LITHERGOLS
(Paper 23)
presented by
J.F.Lieberherr, France

L.A.Povinelli

The downstream rippling pattern you showed of the polythylene recalls to mind the similar patterns observed at the Naval Weapons Center some years ago when combustion instability studies were made with composite solid propellants. Is it possible that oscillatory burning was occurring during your tests? Were high frequency transducers used to detect pressure oscillations that might occur at the acoustic frequencies of the chamber?

J.F.Lieberherr

Les vagues observées à la surface du polyéthylène me semblent/surtout causées par les conditions de l'écoulement liquide qui, bien qu'étant d'une épaisseur très faible, peut être le siège d'instabilités de surface dont on observe l'effet cumulatif dans le temps. Nous n'avons pas observé d'oscillations de pression pendant la combustion. Les capteurs de pression que nou avons utilisé sont du type capacitif et les plus hautes fréquences détectables sont de l'ordre de 20 kHz. Cependant en admettant une vitesse du son de l'ordre de 1000 m/s et une longueur d'onde de 5 cm (mesurée sur la surface du polyéthylène) nous pouvons calculer une fréquence de 20 kHz correspondant à la limite supérieure ci-dessus. Nous pensons qu'il n'y a pas eu d'oscillations de pression mais le fait que la fréquence calculée soit à la limite des possibilités du capteur nous oblige à ne pas rejeter cette possibilité.

F.Jaarsma

I would like to congratulate Mr Lieberherr on his paper presenting a new approach to the regression rate problem. I have one comment and two questions. The comment concerns the introduction where you indicated that the observed regression rates in practical systems are poorly predicted by a heat transfer mechanism only. However, at NLR, we have been quite successful in predicting the regression along the fuel block based on heat transfer. The system used in decomposed H_2O_2 (99%) plus an organic fuel (polyethylene or PMMA) yielding regression rates up to 4 mm/sec. We make use of heat transfer measurements with water that have been performed elsewhere (Krall and Sparrow, Journal of Mass and Heat Transfer, February 1966) for similar geometries and Reynolds numbers. Using a single perforated diaphragm up stream of the fuel block, the heat transfer at the surface can increase up to nine times with respect to that for fully turbulent boundary layers. Doing this we

predict $\dot{m}_f \sim (\rho v)^{0.5} \cdot Mox^{1/6} \cdot d^{-2/3}$ where d is the diameter of the diaphragm hole. This equation has been checked for many sizes (30 mm to 150 mm diameter fuel blocks), pressures (20 atm to 60 atm), oxidizer flow rates and port sizes. The thrust levels involved range from 13 kgf to 225 kgf. Also surface roughness has been found and the correct increase in friction coefficient has to be taken into account. However, at large diameters of the bore in the fuel block and high pressures, a higher regression is measured than predicted. We have a strong indication that this is due to radiation heat transfer from the hot gases.

The first question I would like to ask is that you assumed no surface blowing effect on the friction coefficient, whereas it is generally assumed that this coefficient is decreased by a factor $\log\left[\frac{(1+B)}{B}\right]$. Does it really have no influence? The second question concerns the probable influence on regression of rotation, either on axis or out-off axis, of easily melting fuels. Such conditions might be encountered in sounding rockets. Tests at NLR have indicated that in our system no influence of rotation exists, though rough estimates show some influence, especially if a liquid layer is present.

J.F. Lieberherr

J'ai exprimé dans cette communication l'idée que les théories fondées sur le transfert de chaleur prévoient mal la vitesse de régression dans les systèmes hybrides qui ont un combustible solide à haute vitesse de régression, mais que pour des vitesses de régression de l'ordre de quelques dixièmes de millimètres par seconde les théories de transfert de chaleur ont été applicables, encore qu'il ait souvent fallu introduire des effets chimiques. La régression derrière un diaphragme, citée par le Dr Jaarsma, représente un cas très particulier.

L'hypothèse implicite que l'injection pariétale n'a pas d'effets sur les coefficients de transfert en phase gazeuse est une simplification faite afin de déterminer une expression explicite de la vitesse de régression. Le résultat est donc approximatif mais nos connaissances limitées en ce qui concerne la conductivité thermique, la chaleur spécifique et la viscosité de la phase liquide issue d'un polymère ou d'un hydrure métallique ne justifiaient pas un calcul complet. Nous avons voulu montrer que les fortes vitesses de régression observées dans certains cas doivent être attribuées à une fusion, ce qui est confirmé par l'observation visuelle dans des moteurs réels, et que l'exposant de 0,5 du débit massique unitaire peut également être expliqué par la fusion.

Bien que nous n'ayions pas effectué à l'ONERA d'études exhaustives sur la rotation d'un moteur hybride, il est possible de répondre à la seconde question. Je pense que la rotation du moteur peut avoir un effet sur la vitesse de fusion si l'épaisseur de la couche liquide est importante. La rotation tendrait alors à uniformiser l'épaisseur de liquide, donc à expulser une fraction appréciable de combustible fondu par l'arrière. Cependant l'observation visuelle et le calcul montrent que l'épaisseur de liquide est faible et il ne faut pas s'attendre à ce phénomène, sauf dans des cas limites.

Un autre effet possible de la rotation est de modifier la convection libre mais les effets de cette convection libre sont suffisamment faibles pour rester en dessous de ceux de la convection forcée. En effet si nous considérons un élément de gaz, il sera soumis à la différence de pression axiale dans le moteur entre la partie amont et la partie aval. Nous supposerons cette différence de pression égale à la pression dynamique $\Delta p_1 = \rho V^2/2$. Cet élément sera également soumis à une pression radiale engendrée par la rotation du moteur

$$\Delta p_2 = g \Delta \rho d .$$

Les effets de convection libre seront négligeable si:

$$L = \Delta p_2 / \Delta p_1 = (g \Delta \rho d)/(\rho V^2/2) \ll 1 .$$

Notons que si l'on tient compte de la viscosité il faut considérer:

$$Gr = L \cdot (Re)^2/2 ,$$

mais comme ici le nombre de Reynolds est très grand, nous négligerons l'effet de la viscosité.

Pour évaluer numériquement L nous utiliserons les résultats de la référence* qui donnent: $g = 4.10^4$ cm/s^2, $\Delta\rho = \rho = 2{,}5\,10^{-3}$ g/cm^3, $d = 3$ cm, $V = 6500$ cm/s et $\rho V = 16$ g/cm^2-s. Il en résulte $L = 5{,}8\ 10^{-3}$. Les effets de convection libre seront donc bien faibles que les effets de convection forcée, même en tenant compte de ce que les distances à parcourir radialement seront plus faibles que les distances axiales.

---

* Groothoff, C.C. *The Influence of Rotation on the Burning Rate of a small Hybrid Rocket Motor.* Symposium DGLR – Propulsion Spatiale II, Hannover, 22 May 1969.

Discussion on the Paper
SURFACE REACTIONS IN SOLID PROPELLANTS
(Paper 24)
presented by
H.Selzer, Germany

R.McAlevy III

I congratulate the author on his fine paper.

There is some information on the effect of irradiation on the burning rate of AP particles in a gaseous fuel environment in my paper in Vol 15, *Heterogenous Combustion*. It was found that the burning rate was *increased* by 30% or so. However, irradiation exposure *decreased* the burning rate of polymer particles in an oxygen environment by about half this amount. In both cases the dose was about 10 Mrads.

When actual AP propellants were irradiated there was a burning rate *increase* of about 10%, but it was sensitive to the nature of the binder. This was reported in a Technical Note in the AIAAJ by Henly, Odien and myself published in 1965 I think.

H.Selzer

I thank Prof.McAlevy very much for his contribution though there are some other investigators denying the influence of irradiation on the burning rate. If one thinks of the time necessary to produce a propellant and considers the annealing effects then the contradictory results are plausible. But as the burning rate was influenced in some cases, the lattice defects must be considered in connection with the combustion.

G.S.Pearson

I should like to ask whether the evidence for the post quenching reaction as shown in Figures 3 and 4 may be interpreted differently. The burning surface of an ammonium perchlorate propellant is not planar but three-dimensional and it would seem reasonable to expect that regions of the propellant with small AP particles would burn faster than areas with large particles. Thus a quenched surface would be expected to show very few small particles and more large particles than the initial cut surface.

H.Selzer

This is true and we have considered how to avoid this effect. As reported in the paper we extinguished the propellants by different means. There was no time to measure the particle size distribution in all cases, but these measurements are underway and will separate the various influences.

J.F.Lieberherr

Dr Selzer's approach to the surface mechanisms of AP combustion is a most promising one, in view of the little success obtained up to now in explaining the various characteristics of the AP burning mechanism of AP and composite propellants in general. It however does not seem to be justified to exclude melting phenomena from the discussion. The excellent photographs shown here indicate a glassy amorphous surface (Fig.5), similar to that of a resolified melt. Experiments by Hightower and Price* also show melting on the surface at all pressures studied. Visual observation of burning AP (alone at atmospheric pressure with external heating or within a propellant) made at ONERA led us to the tentative conclusion that melting does occur at low pressures but not at high pressure (above 21 atm). Later experiments by Boggs† also prove the existence of a molten phase at all pressures, except perhaps at high pressures (above 100 atm). In our present state of knowledge, it seems that the existence of a molten phase or a liquid phase must be accepted, although we do not yet know under which conditions it is formed nor what its incidence on the combustion process is.

H.Selzer

As mentioned in both the paper and the comment there are some evidences for the existence of a melt in the AP system. However, an indisputable proof of the melt has not yet been brought forth. The cited SEM-pictures are only able to show the surface of extinguished samples and one has to be very careful in the interpretation with regard to the steady combustion. One feature of a melt is the very weak pressure-dependence of the melting point, this means an increase of about 3 degrees only in the pressure range up to 300 atm. The consequences of such a fixed surface temperature can easily be seen and are incompatible with the need of a greater energy transfer due to the increased burning rate at high pressure. As the burning rate is influenced by lattice defects the proposed melt must have a very high viscosity with a very limited mobility of the molecules. Then, the difference between the liquid and the solid phase probably lies in the uniform orientation of the ions within a small domain instead of the whole crystal. But these ideas are more or less vague as the usual terminology might not be specific for such a highly reactive system as AP. Therefore the basic question should not ask for the existence but for the consequences of the melt.

---

* Hightower, J.D. Price, E.W. Experimental Studies relating to the combustion mechanism of composite propellants. Astron. Acta. Vol.14, 1, pp.11-21.

† Boggs, T.L. The deflagration of pure single crystals of ammonium perchlorate. AIAA paper No.69-142, 7th Aerospace Sciences Meeting, 20-22 January 1969.

Discussion on the Paper
MIXING AND COMBUSTION OF SOLID PARTICLES IN TURBULENT STREAMS
(Paper 25)
presented by
P.O. Baronti and A. Ferri, USA

F. Jaarsma

Except for boron, what is the order of magnitude of increase in burning rate due to turbulent washing with respect to that at stagnant conditions, say for Al, Mg and Be?

P.O. Baronti and A. Ferri

Turbulent washing is intended to identify the mechanism of particle combustion in turbulent media. Turbulent washing applies to combustion of large size particles, say with a radius of 50μ or more; in particular, it appears to be the controlling mechanism for the combustion of particles, as Al, Mg and Be, that otherwise would burn by vapor phase reaction. However, we have not made any calculation of the combustion of Al, Mg and Be particles in turbulent fields.

R.M. Jones

You mentioned that you needed additional data to verify your theory. What *type* of data do you need to verify your theory?

P.O. Baronti and A. Ferri

The ideal data should come by performing an experiment where a burning particle or a burning rod is vibrating at established frequencies and amplitudes in an oxidizing field.

L.A. Povinelli

In practical propulsion devices, the mean flow velocity tends to be relatively large, i.e. greater than several hundred feet per second. Turbulence level (intensities) tend to be relatively low with the exception of the region near an injection port or shear layer. Consequently it would appear that the relative velocity between particles and gas would be the controlling factor in removing boron oxides or combustion products from the region of particles and the turbulence contributes only in a minor way.

P.O. Baronti and A. Ferri

The mean velocity lag between particles and surrounding fluid undoubtedly enhances particle combustion, but it is the high frequency components of the turbulence that produce turbulent washing. In combustion chambers, of relative short length, the turbulence level remains high because combustion itself enhances turbulence. We expect, therefore, that the effects of turbulence on particle combustion will prevail throughout the entire combustion region.

Discussion on the Paper
DIFFUSION FLAMES OF MAGNESIUM VAPOUR AND OXYGEN AT LOW PRESSURES
(Paper 26)
presented by
B.E.L. Deckker and B.K.G. Rao, Canada

L.K. Wittig

Did you come to a conclusion based on your results, favoring one of the existing mechanism models or do you have suggestions for modifications?

I am sure you tried everything possible to obtain the right temperature with your thermocouples. However, I think, in the light of the low pressures and the reactions occurring, your calibration method is not sufficient. Do you see any method to back up your experiments.

B.E.L.Deckker

As we have emphasized in our paper, the conclusions we have reached as a result of our investigations must be regarded as tentative only. It is clear that the nature of the experiments we have described does not allow us to take up a valid position with regard to a model of the Mg-O_2-Ar flame. However, other evidence* we have since obtained from the dispersion and particle size of the deposits at different radial positions, collected on thin glass slides inserted through the apparent centre of the flame, appear to favour a model similar to that proposed by Sullivan†. We believe that we can distinguish an inner zone in which there is a heavy concentration of pure magnesium (particle size 12-16μ), with, what must be, magnesium-oxide nuclei whose dimensions cannot be ascertained by optical microscopy. Outside of this zone the magnesium particles are dispersed and are clearly evaporating, while the MgO particles grow slowly from 0.1μ to 0.3μ at the outermost edge of the luminous zone. The size of the inner zone depends on the concentration of oxygen, varying from a diameter of approximately 3 mm at 20 percent oxygen to 8 mm for 5 percent oxygen. In these two cases, the vaporiser tube temperature is 610°C, the total pressure in the combustion chamber is 0.9 mm Hg and the carrier gas concentration is 8 percent. There is evidence also that the MgO particles tend to pile-up outside the inner zone for the higher oxygen concentrations. We have referred to this aspect in the text of the paper.

The tentative conclusion that the bulk of the reaction is homogeneous hinges on the validity of our interpretation of the thermocouple data. The additional evidence that we have briefly given here indirectly confirms our earlier view of the nature of the reaction. While it is clear that further experiments can be devised to test the correctness of what we regard as the flame temperature, at present one must also account for the systematic agreement between our temperatures and those predicted by the temperature-pattern method of Reference 13. As we have pointed out in the text, the implication here is that the activation energy is only weakly dependent on the temperature, and one cannot, therefore, ignore the possibility of a termolecular reaction.

Discussion on the Paper
THE ROLE OF CARBON-GAS REACTIONS IN THE EROSION OF ROCKET NOZZLES
(Paper 28)
presented by
G.A.Heath and R.W.Thackray, UK

R.J.Zeamer

The recession of rocket throat surfaces during firings has been measured at Allegany Ballistics Laboratory, Cumberland, Maryland, by the technique of imbedding microthermocouples at successively increasing depths in the material of the nozzle throat. As the throat erodes, a discontinuity in each temperature trace indicates when its thermocouple has reached the surface.

G.A.Heath and R.W.Thackray

I am grateful to Mr Zeamer for this information. This procedure will give the nozzle throat diameter at discrete intervals during the firing. We shall now consider the use of this method in our own work.

J.S.Sheasby

You mention that you intend to measure kinetic rates of erosion. How will you do this?

G.A.Heath and R.W.Thackray

At present we measure the total erosion at the end of the firing. In order to be able to make direct comparisons between experimental results and theoretical predictions (as given in Figures 2, 3 and 4) it is necessary to have a measure of the nozzle throat diameter at any instant during the firing. Continuous precise measurement of thrust, combustion pressure and mass flow rate of propellent will enable this information to be obtained. We have already begun to apply this procedure to a liquid propellent rocket engine where it is possible to continuously measure propellent flow rates. The solid propellent rocket motor presents more difficulties. However, the mass burning rate is dependent on the combustion pressure, usually by a known relationship, and also on the burning area, which can be estimated from measurements with the same type of solid propellent charge using a non-eroding nozzle.

---

* Dinnendahl, F.P. Unpublished work. Department of Mechanical Engineering, University of Saskatchewan, Saskatoon.

† Glassman, I., Nellor, A.M., Sullivan, H.F., and Laurendeau, N.M. A Review of Metal Ignition and Flame Models. Paper No 19, presented at this Conference.

Discussion on the Paper
A LABORATORY INVESTIGATION OF CARBON-GAS REACTIONS OF RELEVANCE TO ROCKET NOZZLE EROSION
(Paper 29)
presented by
J.C.Lewis, I.J.Floyd and F.C.Cowlard, UK

J.S.Sheasby

I notice that you used cold gases for reaction. Have you considered any effects this might have on rate of reaction?

J.C.Lewis

At one time, we were planning to pre-heat our reactant gas to the temperature of the carbon surface and did in fact develop a small heater, based on an R.F. induction plasma torch, for this purpose. The power available on this heater was only about 10 kW, and the kinetic experiments which we did with it were therefore restricted to low flow rates; thus, although the reaction rate was increased slightly by pre-heating the gas, we could not be sure that this effect was not due to a change in boundary layer thickness (or to the generation of excited species by the plasma, although an attempt was made to minimise this by injecting the reactant gas into the "tail" of an argon plasma rather than into the plasma zone itself). The limited effort available did not permit the development of more powerful heaters for the high temperatures, pressures and flow rates we required, so most of our work has been done with initially cold gas (as, of course, has nearly all the work on gas-solid reactions in this temperature range: a notable exception is the B.C.U.R.A. work* on the reactions of pulverised coal with plasma-heated gases). The question of whether complete thermal accommodation is achieved in the cold gas/hot surface system before reaction is still an open one: I would like to see more work done with pre-heated gases.

Our work certainly established that the rate maximum is not due to any thermal accommodation effect: the general shape of the rate/temperature curve was unaltered by pre-heating the reactant gas.

D.E.Rosner

Our recent experiments with OH-radicals (generated from the reaction $H + NO_2 \rightarrow NO + OH$) and H-atoms (generated by passing H_2-Ar mixtures through a microwave discharge) may be of interest in making a preliminary assessment of the possible role of these "unstable" species as reactants in rocket exhaust gases. Figure 22, taken from Reference 44†, compares the relative collision efficiencies of OH, H, O and O_2 in causing surface recession (i.e. C-atom loss) of an isotropic synthetic graphite (density $\approx 1.73\ gm\,cm^{-3}$). Near 2000°K the sequence of reactivity is evidently $O > O_2 > OH \gg H$, with about one order of magnitude seperating each of the first three. While non-uniform surface attack of this graphite also precluded our inference of a well-defined reaction probability for $H_2O(g)$, these kinetic data, combined with the extensive (higher pressure) kinetic data of Lewis, Floyd and Cowlard, should provide a useful starting point in understanding the chemical ablation behavior

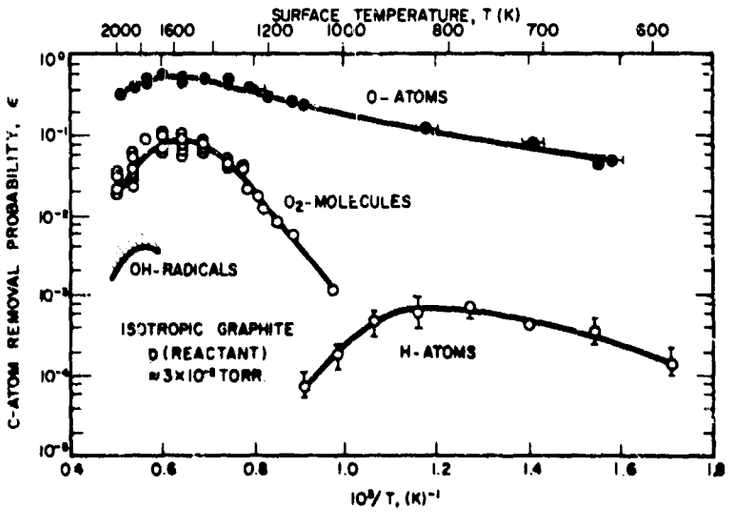

Fig. 22 Temperature dependence of the attack of isotropic graphite by O, O_2, H and OH

---

* Gray, M.D. and Kimber, G.M. Nature, Vol.214, 1967, p 797.

† Rosner, D.E. and Allendorf, H.D. "Kinetics of the Attack of Refractory Materials by Dissociated Gases", to appear in *Proc. Int. Conf. on Heterogeneous Kinetics at Elevated Temperatures* (in press).

of graphites. However, at this point it is appropriate to reiterate the danger of assuming (without experimental verification) that all of the reactants discussed above act independently of one another. In general, one must anticipate complex "coupling" behaviour - which can lead to large (positive or negative) deviations from simple estimates based on individual gas data (scaled in accord with their respective (i) partial pressures and (ii) reaction orders).

J.C.Lewis

Professor Rosner's warning is a valid one, as shown by the results (not included in our paper) of a very limited amount of work which we did on the reaction of vitreous carbon with mixtures of CO_2 and H_2O. This showed that for high H_2O/CO_2 ratios (e.g. 9:1) additivity was approximately maintained; however, for an H_2O/CO_2 ratio of 2:1, the reaction rate at temperatures below about 2300°K was lower than for CO_2 or H_2O alone.

Much more experimental work is required before due allowance for non-additivity can be made in the calculation of erosion rates in complex mixtures such as exhaust gases; the error involved in assuming additivity is likely to be small for aluminised propellants with high H_2O/CO_2 ratios, but may be significant with liquid and non-aluminised propellants with H_2O/CO_2 ratios of about 5.1*.

Discussion on the Paper
REPRESENTATION SCHEMATIQUE DES PROCESSUS D'ABLATION
(Paper 33)
presented by
J.J.Nicolas, S.Kohn and G.Taguet, France

J.C.Lewis

Does your mass balance treatment allow for the difference in reactivity of oxygen in different forms, e.g. in our work we found H_2O to be more reactive than CO_2 at high temperatures.

G.Taguet

No, we have admitted that in our test conditions the rate of all the considered chemical reactions was sufficiently high to neglect any activation energy terms. However, using a different test method we have found that the H_2O was more reactive than CO_2 at temperatures around 2100-2500°K.

Discussion on the Paper
LA VITESSE LINEAIRE DE REGRESSION DU PERCHLORATE D'AMMONIUM DANS UN ECOULEMENT GAZEUX COMBUSTIBLE
(Paper 35)
presented by
C.Casci and L.De Luca, Italy

G.S.Pearson

I should like to make a few comments on the interesting data presented by Professor Casci. First, on the effect of different fuel gases. The flows at which the regression rates are maximum show a correlation with the stoichiometric amounts of fuel required for complete combustion with a constant amount of oxidizer

Fuel	Experimental Maximum Flow	Moles Fuel for Stoichiometry with $2O_2$
H_2	5	4
CH_4	1	1
C_2H_6	0.9	4/7
C_3H_8	0.7	2/5

The effect of the different fuels on AP and on AP unit additive was compared for an AP mixture containing 1% Zn. However, as Figure 5, curve (a), and Figure 10, curve (a), show, the addition of Zn has little effect on the regression rate, hence different fuel gases would be expected to have similar effects on AP and on AP with 1% Zn, which was confirmed by Figures 12 and 11.

---

* Heath, G.A. and Thackray, R.W. Paper 28 of this Colloquium.

However, I would suggest that this may not be true for AP with small amounts of oxides, as some recent experiments (AIAA Journal, Vol.5, p.344, 1967) have shown that transition metal oxides are effective catalysts for the ignition of impinging gas streams of ammonia or iso-butene and perchloric acid. Less ready ignition was obtained with ethylene but ignition was not observed with methane. A closer simulation of the combustion process in composite propellants would be to use unsaturated hydrocarbon in place of hydrogen as the transition metal oxides may then have a larger effect on the regression rates.

The second point concerns the high activity of reduced copper. Other experiments (Combustion and Flame, in press) have been made with copper chromate and copper chromite. These have been shown to contain appreciable amounts of cupric oxide - for example, Harshaw copper chromite CuO2O2 is approximately $CuCr_2O_4$, 7CuO. Alternate exposure of these materials is 400°C to fuel gas (NH_3, C_2H_4 and iso-butene but not CH_4) and to oxygen results in transient appreciable heat releases. Weight measurements show that weight changes are reproducible and correspond to a redox cycle between cupric oxide and copper. It is very necessary in all work with catalyst/AP mixtures to characterize the particle size of the different catalysts and thus to compare the relative efficiency of the catalysts on a metal mole percent basis.

Finally, two brief points. Figure 28 shows that the ignition delay of AP/metal mixtures is a minimum at 100% metal. This indicates that the ignition process is that of AP/metal in atmospheric air and is not that applicable to AP/fuel mixtures in solid propellant rockets. Secondly, Figure 18 shows that an AP/5% reduced copper mixture has a regression rate of 0.47 to C.52 mm/sec in flowing hydrogen at 1 atmosphere. Under static conditions shown in Figure 24 the regression rate at 1 atm is 2.5 mm/sec. Do you have any suggestion as to why a hydrogen flow should decrease the regression rate by a factor of 5.

C. Casci and L. De Luca

Pour ce qui concerne le premier point il faut remarquer que, sélon nos définitions, le mélange AP/métal au 100% est constitué à moitié de AP et à moitié de métal et donc le procès d'ignition n'a pas lieu à l'air atmosphérique.

Pour la seconde question nous n'avons pas jusqu'à ce moment une expliquation valable à donner: une série systématique d'experiences est en cours de réalisation pour mieux illustrer les propriétés de mélanges AP/additifs sous pression. En tout cas il est bien de noter que la Figure 18 se rapporte à des mesures effectuées à la pression rélative 0.

J.F. Lieberherr

Les résultats très intéressants obtenus par le Professeur Casci et Mr de Luca complètent heureusement ceux que nous avons obtenus à l'ONERA. Je voudrais faire trois remarques: L'écart à la loi classique en D^2 dans la combustion de sphères observé par L.Nadaud peut être attribué à un nombre de Lewis différent de l'unité mais il semble également, d'après une étude actuellement en cours, que cet écart puisse être attribué à la non constance de la vitesse de réaction au cours de la vie de la goutte ou de la sphère en combustion. Il me semble ensuite que la différence entre les fluctuations de pression observées lors de la combustion de PA dans un gaz combustible et celles observées pour un propergol composite doive être attribuée à la différence d'échelle d'hétérogénéité entre les deux cas. Dans le premier cas l'échelle est comparable au diamètre de l'échantillon et les irrégularités de l'écoulement se traduisent par des irrégularités de combustion, tandis que dans le deuxième cas l'échelle est beaucoup plus petite et les irrégularités de combustion se compensent. Enfin il serait intéressant de distinguer dans les expériences de ce type entre les effets des additifs et ceux dûs à la température de surface qui peut quand même varier un peu, bien que dans un domaine étroit, en considérant comme acquis que les gaz ambiants n'atteignent pas la surface du PA. Nos expériences de pyrolyse indiquent que les vitesses de régression mesurées ici correspondent à des températures de surface de l'ordre de 640°C et il me semble qu'il serait donc intéressant de définir des conditions opératoires standard assurant par exemple des conditions adiabatiques qui permettraient de comparer utilement les résultats obtenus par différents expérimentateurs.

C. Casci and L. de Luca

En remerciant le Dr Lieberherr de son intervention, nous ne pouvons qu'être d'accord avec ses remarques et en particulier avec l'observation relative aux fluctuations de pression lors de la combustion hybride ou comme propergol solide composite de AP.

AGARD Conference Proceedings No. 52 North Atlantic Treaty Organization, Advisory Group for Aerospace Research and Development REACTIONS BETWEEN GASES AND SOLIDS Published February 1970 497 pages The kinetics and equilibria of gas-solid interactions are encountered in connection with a diversity of phenomena – combustion, ablation, corrosion, erosion, catalysis – each of which is usually studied and practised as a separate engineering speciality. This colloquium brings together workers in all these disciplines. Research papers describe P.T.O.	541.124.012.4	AGARD Conference Proceedings No. 52 North Atlantic Treaty Organization, Advisory Group for Aerospace Research and Development REACTIONS BETWEEN GASES AND SOLIDS Published February 1970 497 pages The kinetics and equilibria of gas-solid interactions are encountered in connection with a diversity of phenomena – combustion, ablation, corrosion, erosion, catalysis – each of which is usually studied and practised as a separate engineering speciality. This colloquium brings together workers in all these disciplines. Research papers describe P.T.O.	541.124.012.4
AGARD Conference Proceedings No. 52 North Atlantic Treaty Organization, Advisory Group for Aerospace Research and Development REACTIONS BETWEEN GASES AND SOLIDS Published February 1970 497 pages The kinetics and equilibria of gas-solid interactions are encountered in connection with a diversity of phenomena – combustion, ablation, corrosion, erosion, catalysis – each of which is usually studied and practised as a separate engineering speciality. This colloquium brings together workers in all these disciplines. Research papers describe P.T.O.	541.124.012.4	AGARD Conference Proceedings No. 52 North Atlantic Treaty Organization, Advisory Group for Aerospace Research and Development REACTIONS BETWEEN GASES AND SOLIDS Published February 1970 497 pages The kinetics and equilibria of gas-solid interactions are encountered in connection with a diversity of phenomena – combustion, ablation, corrosion, erosion, catalysis – each of which is usually studied and practised as a separate engineering speciality. This colloquium brings together workers in all these disciplines. Research papers describe P.T.O.	541.124.012.4

current advances in NATO laboratories and authoritative surveys afford a perspective to show the common thread of basic knowledge that connects these technologies as well as the differences in goals and emphasis that make each field unique.

Direct communication between specialists, crossing inter-disciplinary boundaries, is intended to stimulate new insights in dealing with the many practical problems which involve some aspect of gas-solid reactions.

Papers presented at the Propulsion and Energetics Panel 34th Meeting 8th Colloquium held at the Aerospace Research Laboratories, Wright-Patterson Air Force Base, Dayton, Ohio, USA, 13-17 October 1969.

current advances in NATO laboratories and authoritative surveys afford a perspective to show the common thread of basic knowledge that connects these technologies as well as the differences in goals and emphasis that make each field unique.

Direct communication between specialists, crossing inter-disciplinary boundaries, is intended to stimulate new insights in dealing with the many practical problems which involve some aspect of gas-solid reactions.

Papers presented at the Propulsion and Energetics Panel 34th Meeting 8th Colloquium held at the Aerospace Research Laboratories, Wright-Patterson Air Force Base, Dayton, Ohio, USA, 13-17 October 1969.

current advances in NATO laboratories and authoritative surveys afford a perspective to show the common thread of basic knowledge that connects these technologies as well as the differences in goals and emphasis that make each field unique.

Direct communication between specialists, crossing inter-disciplinary boundaries, is intended to stimulate new insights in dealing with the many practical problems which involve some aspect of gas-solid reactions.

Papers presented at the Propulsion and Energetics Panel 34th Meeting 8th Colloquium held at the Aerospace Research Laboratories, Wright-Patterson Air Force Base, Dayton, Ohio, USA, 13-17 October 1969.

current advances in NATO laboratories and authoritative surveys afford a perspective to show the common thread of basic knowledge that connects these technologies as well as the differences in goals and emphasis that make each field unique.

Direct communication between specialists, crossing inter-disciplinary boundaries, is intended to stimulate new insights in dealing with the many practical problems which involve some aspect of gas-solid reactions.

Papers presented at the Propulsion and Energetics Panel 34th Meeting 8th Colloquium held at the Aerospace Research Laboratories, Wright-Patterson Air Force Base, Dayton, Ohio, USA, 13-17 October 1969.